

Geotechnique, Construction Materials & Environment

VOLUME 3(1)



**Edited by
Md. Zakaria Hossain
Hossain Md. Shahin**



GEOMATE 2013 NAGOYA, JAPAN
GEOTECHNIQUE, CONSTRUCTION MATERIALS AND ENVIRONMENT

PROCEEDINGS OF THIRD INTERNATIONAL CONFERENCE – GEOMATE 2013
GEOTECHNIQUE, CONSTRUCTION MATERIALS AND ENVIRONMENT NAGOYA, JAPAN
13-15 NOVEMBER, 2013

Geotechnique, Construction Materials and Environment

Edited by

Md. Zakaria Hossain
*Graduate School of Bioresources
Mie University*

Hossain Md. Shahin
*Graduate School of Engineering
Nagoya Institute of Technology*



THE GEOMATE INTERNATIONAL SOCIETY

Copyright @ 2013 by The GEOMATE International Society

All rights reserved. In principle, no part of this publication or the information contained herein may be reproduced in any form or by any means, translated in any language, stored in any data base or retrieval system, or transmitted in any form or by any means without prior permission in writing from the publisher.

Disclaimer: The editors and the publisher have tried their best effort to ensure the integrity and the quality of this publication and information herein. However, they give no warranty of any kind, expressed or implied with regard to the material contained in this book, and will not be liable in any event for the consequences of its use.

Published by:
The GEOMATE International Society
Tsu city, Mie, Japan
E-mail: geomate@gi-j.com
www.gi-j.com

ISBN Number: 978-4-9905958-2-1 C3051

Table of Contents

Preface	x
Organization	xi
<i>ID Keynote Papers</i>	1
GROUND DEFORMATION DURING AND AFTER EARTHQUAKES	2
1k –SIMULATION AND PREDICTION BASED ON ELASTO-PLASTIC SOIL MECHANICS- Akira Asaoka	
2k USE OF RECYCLED AGGREGATES FROM CONSTRUCTION AND DEMOLITION WASTES FOR THE CONSTRUCTION OF FLEXIBLE PAVEMENTS	12
Márcio Muniz de Farias, Alejandra María Gómez Jiménez and Ferney Quiñones Sinisterra	
3k EFFECTIVE STRESS IN UNSATURATED GRANULAR MEDIA IN THE PENDULAR REGIME	24
Richard Wan, Sarah Khosravani and Mehdi Pouragha	
4k RECENT GEOTECHNICAL RESEARCH ADVANCES IN UNIVERSITY PUTRA MALAYSIA	32
Bujang B.K.Huat and Afshin Asadi	
<i>Technical Papers</i>	40
<i>ID Geotechnique</i>	41
3102 LANDSLIDES IN BANGLADESH: CAUSES AND RECOMMENDATION	42
Musahaq Ali, Zakaria Hossain and Shigeko Haruyama	
3110 PRECAST SPREAD FOUNDATION IN INDUSTRIALIZED BUILDING SYSTEM	47
Ramli Nazir, Ehsan Momeni, A. Kadir Marsono, Houman Sohaie	
3114 CATEGORISING GEOTECHNICAL PROPERTIES OF SUBSOIL IN SURFERS PARADISE USING GEOGRAPHIC INFORMATION SYSTEM (GIS)	53
Haider Al-Ani, Leila Eslami-Andargoli, Erwin Oh and Gary Chai	
3116 EVALUATION OF CONSTITUTIVE MODEL IN SIMULATING THE BEHAVIOR OF CEMENT-TREATED SOIL	59
Ay Lee Saw, C F Leung and S A Tan	
3122 UPDATING THE PREDICTIVE MODEL FOR THE VERTICAL COLLAPSE PERCENTAGE OF COLLAPSIBLE SOIL SUBGRADES	65
Moshe Livneh and Noam A. Livneh	
3123 INFLUENCE OF FREEZE-THAW ACTION ON AIR-PERMEABILITY OF UNSATURATED SOIL GROUND	71
Tatsuya Ishikawa, Tetsuya Tokoro, Dai Nakamura and Satoshi Yamashita	

3144	EFFECT OF ROCK SOCKET CHARACTERISTICS ON LOW STRAIN INTEGRITY TEST OF PILES Ramli Bin Nazir and Osman El Hussien	77
3148	CHARACTERISTICS OF SLOPE FAILURES IN MAKINOHARA, JAPAN Jun Sugawara	83
3151	S-PSA WITH USING FEM FOR AN EXISTING ESTUARY DAM T. Hara, M. Iwata, Y. Otake, Y. Honjo, T. Kato, A. Nishida and H. Yukimoto	89
3155	THE ROTATIONAL HARDENING RULE WITHOUT THE LIMIT SURFACE OF HARDENING Hiroyuki Kyokawa, Ryoki Ohashi and Teruo Nakai	95
3157	A STUDY OF THE FORMATION MECHANISM OF BEACHROCK IN OKINAWA, JAPAN: TOWARD MAKING ARTIFICIAL ROCK Takashi Danjo and Satoru Kawasaki	101
3161	A STUDY ON THE SLAKING-INDUCED CREEP DEFORMATION CHARACTERISTICS OF CRUSHED MUDSTONE Sharma Keshab, Kiyota Takashi and Kyokawa Hiroyuki	107
3163	ASTUDY ON GROWTH OF VETIVER GRASS IN TROPICAL REGION FOR SLOPE PROTECTION Mohammad Shariful Islam, B. A. M. Shahriar, Md. Shahidul Islam and Hossain Md. Shahin	113
3164	INTERACTION MECHANISMS OF SOIL-GEOSYNTHETIC REINFORCEMENT Mabrouk Touahmia	119
3165	SIMULATION AND PREDICTION OF LARGE-SETTLEMENT IN ULTRA-SOFT PEAT GROUND BY DEDUCING THE IN-SITU INITIAL CONDITIONS CONSIDERING ARTESIAN PRESSURE Mutsumi Tashiro, Toshihiro Noda and Nguyen Hong Son	124
3175	SEISMIC RESPONSE ANALYSIS OF GEOTECHNICAL STRUCTURES BUILT OF CEMENT-TREATED DREDGED SOIL Takayuki Sakai, Masaki Nakano and Shotaro Yamada	130
3176	DEVELOPMENT OF SPH METHOD WITH AN ELASTO-PLASTIC CONSTITUTIVE MODEL CONSIDERING SOIL SKELETON STRUCTURE AND ITS APPLICATION TO EXCAVATION PROBLEMS Hideto Nonoyama, Masaki Nakano and Toshihiro Noda	136
3178	SOUNDNESS EVALUATION OF THE EMBANKMENTS FOR EFFECTIVE MAINTENANCE AND LONG-LIFE OF SHIN-TOMEI EXPRESSWAY Masaya Hinokio, Hiroshi Yamato, Kazunari Suzuki, Takayuki Sakai, Masaki Makano and Minoru Kawaïda	142
3184	EVALUATION OF GLASS FIBERS DERIVED-THREE DIMENSIONAL GEOMATERIAL FOR PROBLEMATIC SOIL APPLICATIONS Donovan Mujah, Hemanta Hazarika, Fauziah Ahmad and Muhammad Ekhlaur Rahman	148
3193	STUDY ON MONITORING METHOD OF RETAINING WALL BEHAVIOR USING MEMS SENSOR NETWORK N Minakata, S Nishiyama, T Yano, D.H Lee, J Wu and M Ryu	154
3211	CASE STUDY ON THE USE OF HIGH-RESOLUTION SURFACE WAVE SURVEY FOR EXAMINING THE CAUSE OF SUBSIDENCE OF RECLAIMED ROAD Miura Minami and Shibuya Satoru	160
3217	MODIFICATION OF KAOLIN MINERALOGY AND MORPHOLOGY BY HEAT TREATMENT AND POSSIBILITY OF USE IN GEOTECHNICAL ENGINEERING Nurmunira Muhammad, Ideris Zakaria and Abdoullah Namdar	164
3223	SIMULATING THE EFFECT OF FLOW VOLUME ON SCOURING PROCESS AROUND BREAKWATER UNDER TSUNAMI CONDITION BY SPH METHOD M.R. Islam, K. Hayano and A.M.K.N. Nadeesha	169

3226	DEVELOPING A NUMERICAL MODEL FOR THE STABILITY DESIGN OF TUNNEL HEADING Jim Shiau and Ryan Kemp	175
3228	INVESTIGATION OF THE OPTIMAL SUPPORT PATTERNS IN BRACED EXCAVATION USING GROUND ANCHORS H. M. Shahin, Teruo Nakai, Okuda Kazuaki and Kato Morihiro	181
3232	SHEAR MODULUS REDUCTION CURVES OF GUAYURIBA SANDS BY CYCLIC TRIAXIAL AND BENDER ELEMENT TESTS J.F. Gaitán-Serrano, M.P. Ortiz-Pulido and J.F. Camacho-Tauta	187
3234	WATER DIVERSION AND DRAINAGE IN SHALLOW LAND WASTE REPOSITORY CONSTRUCTED USING CAPILLARY BARRIER OF SOIL Toshihiro Morii, Kaoru Kobayashi, Kazunobu Matsumoto and Satoru Nakafusa	193
3236	REINFORCING EFFECT OF GEOSYNTHETICS ON BEARING CAPACITY Masuda Saki, H. M. Shahin, Nakai Teruo, Morikawa Yukihiro and Mio Susumu	199
3237	INFLUENCE OF THE STRESS HISTORY ON THE STIFFNESS OF SOIL Asano Kanako, H.M. Shahin, Hiroyuki Kyokawa, Teruo Nakai and Ohashi Ryoki	205
3238	EFFECTIVENESS OF CRASHED TILE IN COUNTERMEASURE AGAINST LIQUEFACTION Morikawa Yukihiro, Maeda Kenichi and Zhang Feng	211
3246	PREDICTION OF NATM TUNNEL EXCAVATION UNDER SHALLOW OVERBURDEN IN PAHANG-SELANGOR RAW WATER TRANSFER TUNNEL PROJECT, MALAYSIA Mohd Ashraf Mohamad Ismail, Goh Chin Ong, Romziah Azit, Zulkifli Nordin, Norzani Mahmood	217
3250	FUNDAMENTAL STUDY ON LATERAL RESISTANCE CHARACTERISTICS OF BALLASTED TRACKS SUBJECTED TO PSEUDO-STATIC INERTIA FORCE Ryuta Ogawa and Kimitoshi Hayano	223
3251	USE OF ACOUSTIC EMISSION TECHNOLOGY TO STUDY THE MECHANICAL BEHAVIOUR OF VARIOUS SANDSTONES: GEOTHERMAL ENERGY Shao, S.S., Ranjith, P.G. and Chen, B.K.	229
3262	UNCONFINED COMPRESSIVE STRENGTH OF CEMENT TREATED SOIL/RAP MIXTURE Jirayut Suebsuk, Aniroot Suksan, Suksun Horpibulsuk and Apichit Kumpala	235
3267	INVESTIGATION OF STRESS REDUCTION EFFECT ON STRUCTURE DUE TO BASEMAT UPLIFT USING ENERGY CONCEPT Takafumi Inoue and Atsushi Mikami	241
3271	SWELLING DEFORMATION OF BENTONITE MIXED WITH INORGANIC MATERIALS IN ALKALINE SOLUTION Yuki Yokoyama and Kenichiro Nakarai	247
3274	USE OF FULLY SOFTENED VERSUS PEAK STRENGTH TO PREDICT THE CAPACITY OF FOOTINGS ON GEOSYNTHETIC REINFORCED SOIL Melia K. Iwamoto, Phillip S.K. Ooi, Jennifer E. Nicks and Michael T. Adams	252
3296	THREE DIMENSIONAL FINITE ELEMENT ANALYSIS OF SOIL NAILS IN GRANITIC SOILS G. Ren and H. Tokhi	258
3298	SIMPLIFIED DYNAMIC AXIAL HEAD PILE STIFFNESS IMPROVEMENT ANALYSIS FOR EXISTING PILED VIADUCT WITH BASE REINFORCEMENT Aglipay Mary Roxanne and Konagai Kazuo	262
3312	PFC3D NUMERICAL EXPERIMENTS OF SELF-BORING IN-SITU SHEAR PRESSURE-METER MODEL TEST Yafei Zhang, Guangli Xu and Jidong Teng	268

3318	DYNAMIC ANALYSIS OF SLOPE FAILURE USING THE MESH-FREE SPH METHOD N. Hiraoka, A. Oya, Ha H. Bui, P. Rajeev and R. Fukagawa	274
3320	ELECTRICAL RESISTIVITY TOMOGRAPHY TO INSPECT BRIDGE FOUNDATIONS Helsin Wang, Chih-Hsin Hu, and Chung-Yue Wang	280
3323	ULTIMATE BEARING CAPACITY ANALYSIS OF GROUND AGAINST INCLINED LOAD BY TAKING ACCOUNT OF NONLINEAR PROPERTY OF SHEAR STRENGTH Du N L, Ohtsuka S, Hoshina T, Isobe K, and Kaneda K	286
3326	PREDICTION OF SLOPE DEFORMATIONS BY ELASTIC WAVE VELOCITIES IN RELATION TO LANDSLIDE FAILURES Muhammad Irfan and Taro Uchimura	292
3329	BOX-SHAPE RETAINING WALL SYSTEM: EXPERIMENT AND NUMERICAL PREDICTION C.T. Nguyen, Ha H. Bui, and R. Fukagawa	298
3343	PERMEABILITY AND CONSOLIDATION BEHAVIOR OF COMPOSITE GROUND REINFORCED WITH SAND COLUMNS B. A. Mir and Ashish Juneja	304
3347	LABORATORY EVALUATION OF PHYSICO-CHEMICAL VARIATIONS IN BENTONITE UNDER ELECTROKINETIC ENHANCEMENT Nasim Mosavat, Erwin Oh and Gary chai	310
3358	FLOW PATTERN FOR MULTI-SIZE SILOS Yi Yang, Na Li, PengYin and YM Cheng	317
ID	<i>Construction Materials</i>	322
3132	IMPROVING ENGINEERING PROPERTIES OF FINE-GRAINED SOIL WITH STEEL SLAG FOR USING IN EMBANKMENT EARTHFILL Je-Min Baek, Satoru Shibuya, Jin-Suk Hur and Tara Nidhi Lohani	323
3156	EVALUATION EQUATION OF DIFFUSION COEFFICIENT OF CHLORIDE ION FOR CRACKED CONCRETE Junpei Saito and Satoru Shimobe	327
3160	OPTIMIZATION OF EFFECTIVE DEPTH OF COMPACTION FOR FINE-GRAINED SOILS Girum Y. Yesuf, Inge Hoff and Jan Vaslestad	333
3197	COMPRESSIVE STRENGTH OF CEMENT PASTES EXPOSED TO ELEVATED TEMPERATURE AND DETERIORATION MITIGATION Abdoullah Namdar, Ideris Bin Zakaria and Gurumurthy Hegde	339
3201	PARTICLE SIZE AND OTHER FACTORS AFFECTING THE PULLOUT BEHAVIOR OF GEOCELLS EMBEDDED IN GRAVELLY SOIL BACKFILL Xinye Han, Takashi Kiyota, Michiyuki Harata and Fumio Tatsuoka	345
3202	EFFECT OF LOADING RATE ON STRENGTH CHARACTERISTICS OF GRANULAR BASE COURSE MATERIAL Yuan Zhang, Tatsuya Ishikawa and Tetsuya Tokoro	351
3207	EXPERIMENTAL STUDY OF PLYWOOD COMPARING TO FOAM FILLED HONEYCOMB STRUCTURE Phacharaporn Bunyawanchakul, Chattarin Sunsinn, and Thammakorn Sasanawin	357
3249	X-RAY IMAGE ANALYSIS OF POROSITY OF POROUS CONCRETES Jaehun Ahn, Jinwoo Jung and Seungbae Kim	363

3252	STRESS - STRAIN BEHAVIOUR OF SLAG CEMENT CONCRETE Mustapha Boukendakdji	367
3256	ESTIMATION AND EXPERIMENTAL STUDY ON DIVERSION LENGTH OF CAPILLARY BARRIER USING CRUSHED SHELL PARTICLES Kazunobu Matsumoto, Kaoru Kobayashi , Satoru Nakafusa and Toshihiro Morii	373
3268	EXPERIMENTAL STUDY OF CONCRETE AND MORTAR MIXING WASTE TIRE RUBBER Man-Kwon Choi, Yuki Hasegawa, Shushi Sato, Shinsuke Matsumoto and Hyeon-Tae Kim	379
3287	PILE DRIVING EFFECTS ON NEARBY BUILDING Adhilla Ainun Musir and Abdul Naser Abdul Ghani	384
3317	LABORATORY STUDY ON THE PERFORMANCE OF RECYCLED CONCRETE AGGREGATES BLENDED WITH RECLAIMED ASPHALT PAVEMENT AS A PAVEMENT GRANULAR MATERIAL S. Jayakody, C. Gallage, J. Ramanujam, A.Kumar	389
3322	BEHAVIOR OF PENETRATION AND LEACHING OF CESIUM IN MORTAR HAVING VARIOUS FINE AGGREGATES AND MOISTURE CONTENT Masashi Ito, Kenichiro Nakarai Akihiko Hayashi and Kenji Kawai	394
3324	EFFECTS OF COARSE AGGREGATE CONTENT ON THE EROSION RATE OF CONCRETE DUE TO SULFURIC ACID ATTACK Yuji Hatano, Yutaka Okame and Kenji Kawai	400
3357	STUDY ON PHYSICAL PROPERTIES AND USABILITY OF SOME SELECTED RECYCLED FINE AGGREGATES Mohammad Raihanul Islam, Satoru Ishiguro	406
ID	<i>Environment</i>	410
3145	COMPUTER MODELING AND ANALYSIS OF THREE PHASE INDUCTION MOTOR UNDER TEMPORARY SHORT CIRCUIT FAULT IN STATOR USING WAVELET TRANSFORM Dicky Nova Wardana, Dimas Anton Asfani, Ardyono Priyadi, and Mauridhi Hery Purnomo	411
3147	ANALYTICAL SOLUTION TO CONTAMINANT EXTRACTION CONSIDERING SMEAR EFFECT H.Y Wang , X.W Tang and B. Bai	416
3152	MECHANISM OF C6H6 OXIDATION IN THE THREE-WAY CATALYTIC CONVERTER EQUIPPED A GASOLINE ENGINE Akio Takigawa, Akihiro Mieda and Yongzhen Peng	422
3177	ROLE OF CURBSIDE CRACK OF ROAD IN URBAN BIODIVERSITY Taizo Uchida, Xue J. Huan, Daisuke Hayasaka, Teruo Arase, William T. Haller and Lyn A. Gettys	427
3185	DYE TRACER EXPERIMENTS FOR IDENTIFYING SOLUTE DISPERSIVITY IN UNSATURATED POROUS MEDIA Kazuya Inoue, Takayuki Fujiwara and Tsutomu Tanaka	433
3188	REUSE OF AGRICULTURAL AND FOOD RESIDUES FOR RETARDING AND ATTENUATING NITRATE IN POROUS MEDIA Kazuya Inoue, Saki Matsuyama and Tsutomu Tanaka	439
3196	MICROSCOPIC RANGE OF IMMOBILIZATION BETWEEN HEAVY METALS AND AMENDMENT IN SOIL THROUGH WATER MIGRATION Shouhei Ogawa, Masahiko Katoh and Takeshi Sato	445
3198	SUB-DARCY-SCALE MODELING OF NON-UNIFORM FLOW THROUGH POROUS MEDIA WITH MIXED WETTABILITES Junichiro Takeuchi, Takuya Takahashi, and Masayuki Fujihara	452

3218	CAPTURING PEDESTRIAN MOVEMENT SAFETY AND SECURITY ISSUES AT MAJOR TRANSPORTATION INTERCHANGES Zulfadly Azizi Bohari, Syahriah Bachok and Mariana Mohamed Osman	458
3222	ASSESSMENT OF CHROMIUM CONTAMINATION IN SEDIMENTS OF SOUTHERN KAOHSIUNG HARBOR, TAIWAN Cheng-Di Dong, Chih-Feng Chen and Chiu-Wen Chen	464
3224	GPS/GIS IDENTIFICATION OF POTENTIAL BUS STOP LOCATIONS AND PASSENGER'S ACCESS AND EGRESS POINTS Syahriah Bachok, Zakiah Ponrohono, Mariana Mohamed Osman, Zulfadly Azizi Bohari	469
3243	GEOCHEMISTRY OF PALEOGENE RED BEDS IN THE NORTHERN IRAQ FORELAND BASIN: EVIDENCE FOR PROVENANCE Muatasam Hassan, Brian G. Jones, Ali Ismail Al Jubory, Sabah Ahmed Ismail, Abdual Salalm Mehdi Saleh	475
3244	DEVELOPMENT OF BASE MATERIALS FOR SEAWEED BEDS USING VOLCANIC ASHES AND RECYCLING MATERIALS OF INDUSTRIAL WASTES K. Yamamoto, T. Negami, T. Nakajima, H. Yano, Y. Futsuhara and K. Shima	481
3247	CARBON FOOTPRINT AWARENESS – AN INVESTIGATION FROM TRAVEL DIARY SURVEY Nur Sabahiah Abdul Sukorand Nur Khairiyah Basri	487
3248	OPTIMAL MONITORING NETWORK DESIGN FOR EFFICIENT IDENTIFICATION OF UNKNOWN GROUNDWATER POLLUTION SOURCES Om Prakash and Bithin Datta	493
3257	SPATIAL DISTRIBUTION CHARACTERISTICS OF SUBTERRANEAN HOT WATER EVALUATED USING WATER QUALITY CONCENTRATION DATA Takamitsu Kajisa, Si Senfi, Yasunori Mori, Homayoon Ganji, Abdul Saboor Rahmany, Masaaki Kondo and Hajime Narioka	499
3258	IDENTIFICATION OF POLLUTANT SOURCE CHARACTERISTICS UNDER UNCERTAINTY IN CONTAMINATED WATER RESOURCES SYSTEMS USING ADAPTIVE SIMULATED ANEALING AND FUZZY LOGIC Mahsa Amirabdollahian and Bithin Datta	505
3270	POINT-BASED RENDERING FOR MASSIVE POINT CLOUD VISUALIZATION Masafumi Nakagawa	511
3325	REDRAWING AN UNKNOWN MASONRY CAISSON BY GEOPHYSICAL METHODS Ming-Hung Chen, Shun-Min Lee, Yung-Chuan Chou, Yao-Jen Hsu and Chih-Hsin Hu	517
3335	CONTRIBUTION OF GEOLOGICAL MAPPING AND NEW TECHNOLOGIES TO THE IDENTIFICATION OF A MAJOR, PRE-EXISTING AND ACTIVE FAULT OVER THE CAPITAL OF TUNISIA Adnène Kassebi and Fouad Zargouni	523
3338	EFFECT OF GRAIN SIZE ON MINERAL CARBONATION OF COAL COMBUSTION FLY ASH FOR CO ₂ SEQUESTRATION N. L Ukwattage and P.G Ranjith	530
3349	STUDY SEISMICITY PARAMETERS OF RUDBAR REGION AND SEISMOLOGICAL ASSESSMENT OF RUDBAR-MANJIL (IRAN) EARTHQUAKE OF JUNE 1990 Noushin Naraghi Araghi, Mohd. Nawawi and Syed Mustafizur Rahman	535
3351	UNDERSTANDING TO PREDICT SOIL BEHAVIOR J. Rajaraman, K.Thiruvengkatasamy and S. Narasimha Rao	540
3356	CASE STUDY ON SHALLOW FAILURE OF CONGLOMERATE AND SILTSTONE SLOPES DUE TO A HEAVY RAINFALL Satoshi Kagamihara, Satoru Shibuya, Byeong - su Kim, Shunzo Kawajiri, Tara Nidhi Lohani and Takashi Okimura	545
	Authors index	551
	Contents of GEOMATE 2011 – Volume 1(1) & 1(2)	557
	Contents of GEOMATE 2012 – Volume 2(1)	564

Preface

On behalf of the GEOMATE 2013 Organizing Committee, it is our great pleasure to welcome you to the International Conference on Geotechnique, Construction Materials and Environment held at the Meitetsu New Grand Hotel, Nagoya, Japan organized in conjunction with Nagoya Institute of Technology, GEOMATE International Society, Japanese Geotechnical Society, AOI-Engineering, Useful Plant Spread Society, HOJUN and Glorious International. On Friday 11 March 2011, at 14:46 Japan Standard Time, the north east of Japan was struck and severely damaged by a series of powerful earthquakes which also caused a major tsunami. This conference was dedicated to the tragic victims of the Tohoku-Kanto earthquake and tsunami disasters. Since this is the third conference in this series, we have received a lot of positive feedback from the participants.

The conference covers three major themes with 17 specific themes including:

- Advances in Composite Materials
- Computational Mechanics
- Foundation and Retaining Walls
- Slope Stability
- Soil Dynamics
- Soil-Structure Interaction
- Pavement Technology
- Tunnels and Anchors
- Site Investigation and Rehabilitation
- Ecology and Land Development
- Water Resources Planning
- Environmental Management
- Public Health and Rehabilitation
- Earthquake and Tsunami Issues
- Safety and Reliability
- Geo-Hazard Mitigation
- Case History and Practical Experience

This year we have received many paper submissions from different countries all over the world, including Albania, Algeria, Australia, Bahrain, Bangladesh, Belarus, Benin, Canada, China, Colombia, Czech Republic, Egypt, Ethiopia, Germany, Hong Kong, India, Indonesia, Iran, Iraq, Japan, Kenya, Libya, Malawi, Malaysia, Norway, Poland, Romania, Russia, Saudi Arabia, Singapore, South Korea, Sri Lanka, Sudan, Taiwan, Thailand, Tunisia, Ukraine, United Arab Emirates, United States and Vietnam. The technical papers were selected from the vast number of contributions submitted after a review of the abstracts. The final papers in the proceedings have been peer reviewed rigorously and revised as necessary by the authors. It relies on the solid cooperation of numerous people to organize a conference of this size. Hence, we appreciate everyone who support as well as participate in the joint conferences. Last but not least, we would like to express our gratitude to all the authors, session chairs, reviewers, participants, institutions and companies for their contribution to GEOMATE 2013. We hope you enjoy the conference and find this experience inspiring and helpful in your professional field. We look forward to seeing you at our upcoming conference next year.

Best regards,

Prof. Teruo Nakai, Conference Chairman



Dr. Md. Zakaria Hossain, Conference General Secretary



Dr. Hossain Md. Shahin, Conference Secretary



Organization

Scientific Committees:

Conference Chairman: Prof. Dr. Teruo Nakai, Nagoya Institute of Technology, Japan

Conference Honorary Chairman: Emeritus Prof. Dr. Sohji Inoue, Mie University, Japan

Conference Organizing Committee:

Prof. Dr. Teruo Nakai, Nagoya Institute of Technology, Japan

Prof. Dr. Feng Zhang, Nagoya Institute of Technology, Japan

Prof. Dr. Kenichi Maeda, Nagoya Institute of Tech., Japan

E/Prof. Dr. Sohji Inoue, Mie University, Japan

A/Prof. Dr. H.M. Shahin, Nagoya Institute of Tech

A/Prof. Dr. Zakaria Hossain, Mie University

National Advisory Committee:

Prof. Dr. Fumio Tatsuoka, Tokyo University of Science, Japan

Prof. Dr. Toshinori Sakai, Mie University, Japan

Prof. Dr. Masaki Nakano, Nagoya University, Japan

Prof. Dr. Toshihiro Noda, Nagoya University, Japan

Prof. Dr. Jing-Cai Jiang, University of Tokushima, Japan

Prof. Dr. Noriyuki Yasufuku, Kyushu University, Japan

Prof. Dr. Masuya Hiroshi, Kanazawa University, Japan

Prof. Dr. Toshihiro Morii, Niigata University, Japan

Prof. Dr. Nishimura Tomoyoshi, Ashikaga Inst. of Tech., Japan

Prof. Dr. Yoshihiro Kimura, Tohoku University, Japan

Prof. Dr. Kimitoshi Hayano, Yokohama National Univ., Japan

A/Prof. Dr. Kenichiro Nakarai, Hiroshima University, Japan

International Advisory Committee:

Prof. Dr. Sai Vanapalli, University of Ottawa, Canada

Prof. Dr. M. Bouassida, National Sch. of Engg. of Tunis

Prof. Dr. L.R. Austriaco, Angles Univ. Found., Philippines

Prof. Dr. A.S.M. Abdul Awal, Univ. Technology Malaysia

Prof. Dr. M. Ibn Ibrahimy, Int. Islamic Univ., Malaysia

Prof. Dr. Md. Zahurul Islam, BUET, Bangladesh.

Prof. Dr. Bujang B.K. Huat, Univ. Putra Malaysia

Prof. Dr. Nemy Banthia, UBC, Canada

Prof. Dr. Ian Jefferson, Univ. of Birmingham, UK

Prof. Dr. John Bolander, Univ. of California, USA

Prof. Dr. Shamsul Chowdhury, Roosevelt Univ., USA

Prof. Dr. Isabel Pinto, University of Coimbra, Portugal

Prof. Dr. Mark Jaksa, University of Adelaide, Australia

A/Prof. Dr. Mohamed Shahin, Curtin University, Australia

A/Prof. Dr. Jim Shiau, Univ. of Southern Queensland Toowoomba

A/Prof.. Dr. Hj. Ramli Bin Hj. Nazir, UTM, Malaysia

A/Prof. Dr. Aly Ahmed, Beni-Suef University, Egypt

Dr. J.N. Mukabi, President of Kenya Geotech Soc., Kenya

Conference Secretariat:

Dr. H.M. Shahin, Secretary, A/Prof. NIT, Japan
Dr. Zakaria Hossain, General Secretary, A/Prof. MU, Japan
Mr. Musahaq Ali, Assistant Secretary
Division of Environmental Science and Technology
Graduate School of Bioresources
Mie University, 1577 Kurima Machiya-cho
Tsu-city, Mie 514-8507, Japan
E-mail: geomate@gi-j.com
Tel+Fax: +81-59-231-9578

Editorial Committee:

Dr. Md. Zakaria Hossain
Dr. Hossain Md. Shahin

Executive Committee:

A/Prof. Dr. Md. Zakaria Hossain
A/Prof. Dr. Hossain Md. Shahin
Prof. Dr. Teruo Nakai
E/Prof. Dr. Sohji Inoue
Mr. Musahaq Ali

Note- A: Associate, E-Emeritus

Keynote Papers

GROUND DEFORMATION DURING AND AFTER EARTHQUAKES –SIMULATION AND PREDICTION BASED ON ELASTO-PLASTIC SOIL MECHANICS–

Akira Asaoka¹

¹Association for the development of earthquake prediction, Japan

ABSTRACT

Specialization may be an unavoidable accompaniment to development in science but specialization that runs to excess can actually hinder development. This paper tries to explain briefly how the current level of knowledge in civil engineering, particularly in geomechanics and geotechnical engineering, is useful in analysis and prediction of surface ground deformation caused by earthquakes. The paper is delivered under the two content heads of “What are the difference between sand and clay?” which will be the introduction of the advanced SYS Cam-clay constitutive model, and “four application examples” in which subsurface ground deformation during and after an earthquake. All calculations in this paper have been performed using a single analysis tool i.e., GEOASIA.

Keywords: Elasto-plastic soil mechanics, Seismic response analysis, SYS Cam-clay model, GEOASIA

INTRODUCTION

This paper tries to explain briefly how the current level of knowledge in civil engineering, particularly in geomechanics and geotechnical engineering, is useful in analysis and prediction of surface ground deformation caused by earthquakes. The essence of geomechanics and the elasto-plastic constitutive equation of soils are outlined first in Sections 1 and 2 so as to make it easy to read and understand Section 3, which deal with ground deformation due to earthquakes. Although only the mechanics of saturated soils are discussed here, the author believes that this is quite sufficient for the purpose.

Whether it be sand or clay, soil consists of numerous soil particles forming a skeleton structure, and the pores are filled with water (in case of saturated soil). By themselves, both soil particles and pore water cannot be compressed by the forces that are encountered in civil engineering and architecture. However, accompanied by expulsion of the pore water, the soil skeleton structure will easily undergo large compression when it is subjected to external forces. Vice versa, it can also exhibit large expansion by absorbing water into the pores. In such cases, since the pore water movement will tend to conform to Darcy's Law of potential flow, the mechanics of saturated soil essentially possess the quality of being non-localized. To put it differently, saturated soil is a material in which any volumetric change in the soil skeleton is constrained by the incompressible pore water, and the reaction to this constraint force appears as (excess) pore water pressure. The mechanical behavior of saturated soil is described by the continuum mechanics of the two

mixed phases, the soil skeleton and pore water. To deal with the stresses in this case, they are divided into two types. One is the pore water pressure mentioned above and the other is the effective stress, which is obtained by subtracting the pore water pressure from the stress (total stress). It is the variations in the effective stress that produce the changes in the state of deformation of soils (the principle of effective stress).

Volume changes in soil is dependent on water and air, moving in and out of its pores. Such movements are, of course, due to variations in the effective stress that acts on the soil skeleton. Consider sand that has been placed into a tea can so that it is deposited loosely at the bottom of the can. No one would try to compress the sand by placing a circular disc weight on top of it. The sand would remain almost uncompressed by the forces produced by such a weight. However, if the side of the can is tapped lightly so as to subject the sand to marginal cyclic shear forces, the sand will exhibit large compression. This is known as “compaction”. Compaction is characterized by the fact that compression occurs although there has been no increase in the effective stress p' (i.e., no increase in the forces acting on the sand). This compression is plastic compression because the sand, once it has been compressed, will not loosen even if tapping is then applied from the opposite side of the can. In the above example, the sand is dry and only air exists within the pores. If the pores are saturated with water, liquefaction will occur first. After that, accompanied by the drainage of water, consolidation settlement will occur because of recovery of self-weight by the sand. Because of the difference in the history of effective stress experienced, there is a

slight difference between the amount of compression in dry sand due to compaction and the amount of compression in saturated sand after liquefaction. But all in all, the level of difference is small. Therefore, it can be said that compaction and liquefaction are contrasting phenomena that are dependent only on whether volume change is permitted or not during cyclic shear. The compaction behavior of loose sand is illustrated in Fig. 1¹⁾ by the calculation of responses using the elasto-plastic constitutive equation that is described later in this paper. It can be observed that large compression has occurred after the first few cycles.

Next, consider the situation that clay saturated with water, somewhat like Japanese bean jelly, is placed in the tea can instead of sand. In this case, lightly tapping the side of the can would have no meaning. The only way of compressing the clay is to place a porous disc on top of the clay, place a heavy weight on top of that disc, and then wait a sufficient amount of time for the water to seep out. This type of compression is called “consolidation”. Unlike compaction, an increase in the effective stress p' is indispensable for compression to occur by consolidation. That is to say, the force needs to be applied continuously for a certain length of time.

As described above, sand and clay behave quite differently. Then, is there no consolidation of sand or no compaction of clay? How should one think about compaction and consolidation for the intermediate soils?

DIFFERENCE BETWEEN SAND AND CLAY

If it were possible to describe the behavior of both sand and clay within the same framework using elasto-plastic mechanics, it would permit to describe the elasto-plastic behavior of the many intermediate soils that actually exist in a state between sand and clay too. The reason why there is no necessity to deal with sand and clay separately is that the concepts of both “structure^{2), 3)}” and “overconsolidation” are common to sand and clay. It was only in 1997 that the concept of structure, which had been an intuitive concept until then, was successfully described through elasto-plastic mechanics. This paper explains first the concepts of structure and overconsolidation using the most recent elasto-plastic constitutive equation of soils named the SYS Cam-Clay model^{1), 4)} and then proceeds to clarify the differences between sand and clay.

The compaction of loose sand illustrated in Fig. 1 occurs because the highly developed structure of the soil skeleton is destroyed rapidly by plastic deformation accompanied by cyclic shear. (It may appear strange for plastic deformation to occur due to cyclic loads of the same amplitude. How this could be understood is explained in a later section

that deals with “overconsolidation.”) In fact, although its state is different from that of sand, clay also possesses a structure. This is depicted in Fig. 2. Along with the progress of plastic deformation, the developed structure of naturally deposited clay collapse gradually until the compression line overlaps from above the normal consolidation line of clay that has been remolded and has lost its structure. The entire behavior can be explained by introducing the concept of a superloading surface^{1), 4)}, which lies outside the normal yield surface and is similar to it in shape with respect to the origin as shown in Fig. 3.

In Fig. 3, p' and q are the mean effective stress and deviator stress, respectively, which are defined by the effective stress tensor \mathbf{T}' ((tension positive) and the deviator stress tensor \mathbf{S} as $p' = -\text{tr}\mathbf{T}'/3$, $q = \sqrt{3/2}\mathbf{S} \cdot \mathbf{S}$ and $\mathbf{S} = \mathbf{T}' + p'\mathbf{I}$. Although the normal yield surface is described by the modified Cam-Clay model⁵⁾, its explanation is omitted here because anisotropy is not brought up as a topic in

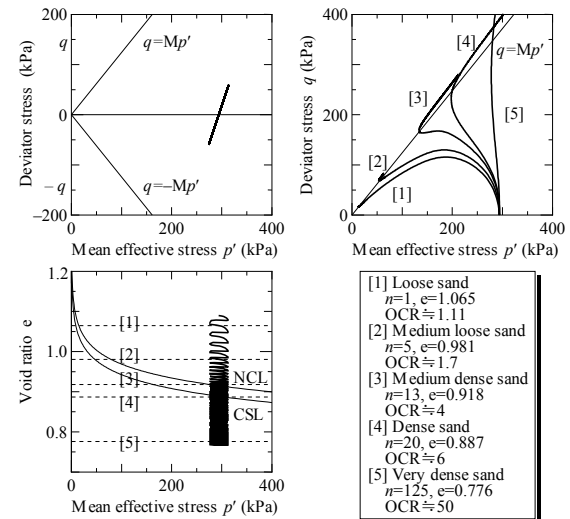


Fig. 1 Compaction of loose sand and various types of undrained shear behavior exhibited by the same sand with different densities

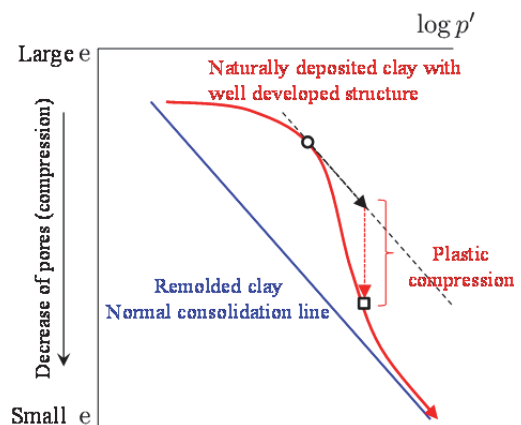


Fig.2 Compression behavior of naturally deposited clay with well-developed structure

this paper. Along with the collapse/decay of the structure due to progress of plastic deformation, the superloading surface gradually moves from the outside to overlap the normal yield surface. Therefore, the similarity ratio R^* ($0 < R^* \leq 1$) of the superloading surface to the normal yield surface approaches 1 gradually from lower values as the plastic deformation progresses. The structure, expressed by R^* , indicates the bulkiness of the soil skeleton. The collapse/decay of structure is accompanied by the loss of bulkiness, that is to say, plastic compression (see Fig. 2). This corresponds to the saying, "The structure falls apart like a house of cards, and the soil undergoes massive compression."

Overconsolidation and loss of overconsolidation are explained next. In the table within Fig. 1, the overconsolidation ratio (OCR, described below) has become larger along with the degree of compaction. This is because, with the current stress level remaining the same, sand shows an elasto-plastic response for each repeated load during cyclic loading, which leads to expansion of both the superloading and normal loading surfaces. In other words, because of compaction/cyclic shear, the sand is in a condition that is apparently the same as that reached by massive unloading from a very highly pressurized state. As explained above, the fact that soil that has undergone unloading once (overconsolidated soil) exhibits an elasto-plastic response and not an elastic response when it is reloaded is as important as the concept of structure. This is illustrated in Fig. 4 using the compression curve for clay.

If, during reloading from the unloaded (overconsolidated) state, the soil exhibits only an elastic response (i.e., if the symbol \blacksquare were to overlap \circ), which is the basis of the old elasto-plastic theory, there would be no accumulation of plastic deformation due to cyclic loading. This would mean that nothing will happen to the soil due to an earthquake. The above is the reason why the elasto-plastic response of the soil during reloading is important, and it can be expressed by introducing again a subloading surface⁶⁾ (Fig. 3), which lies inside the superloading surface and is similar to it in shape with respect to the origin. The current stress always lies on the subloading surface. The unloaded soil, which is in an overconsolidated state, gradually loses its overconsolidation with the progress of plastic deformation during reloading, and the subloading surface gradually moves from the inside to overlap the superloading surface to approach the state of normal consolidation. This is always accompanied by plastic expansion as shown in Fig. 5. The expansion phenomenon corresponds to the saying, "Soil will exhibit large expansion when the strong forces of engagement between the soil particles are relaxed." The level of overconsolidation is expressed by the similarity ratio R ($0 < R \leq 1$, Fig.

3) of the superloading and subloading surfaces. The inverse of R is the overconsolidation ratio OCR shown within Fig. 1.

Naturally deposited soils, whether sand or clay, have developed structures and are more or less in an overconsolidated state. These can be considered to

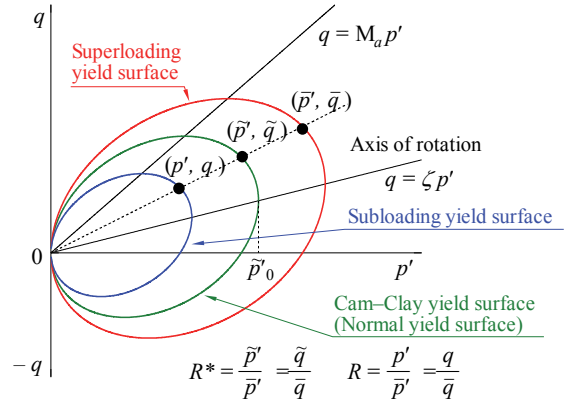


Fig. 3 Three yielding surfaces of the SYS Cam-Clay Model

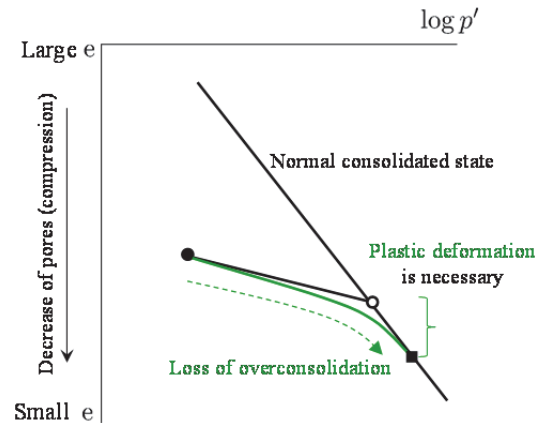


Fig. 4 Elasto-plastic behavior during reloading

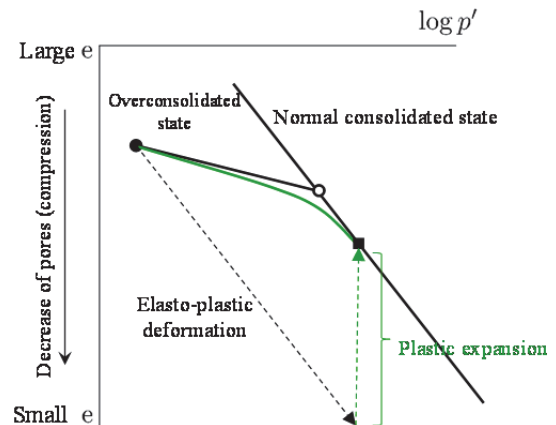


Fig. 5 Plastic expansion resulting from loss of overconsolidation

be living soils. When a living soil undergoes plastic deformation, collapse/decay of structure will progress ($R^* \rightarrow 1$) while compression occurs, or loss of overconsolidation will progress while expansion occurs ($R \rightarrow 1$). This gives rise to the following straightforward question: for a given unit of plastic deformation, which is faster, the decay of structure or the loss of overconsolidation? The difference between sand and clay lies in this aspect.

To answer this question first, even a slight plastic deformation causes very rapid decay/collapse of structure in sand, whereas loss of overconsolidation is extremely slow. Very large plastic deformation that is quite unlikely to occur in a practical situation would be required for sand to reach the state of normal consolidation. On the other hand, clay is the complete opposite of sand. Under even slight plastic deformation, loss of overconsolidation occurs rapidly in clay, and it will approach the state of normal consolidation (in Fig. 4, ■ is close to ○). However, its structure will not collapse easily. A large plastic deformation would be required to cause decay of structure in clay. The above is illustrated in Fig. 6. If someone ask which is faster, the answer would be that it is a matter of level. It is likely that there would be soils that exhibit the same level of rapidity or the same level of slackness. In other words, between sandy soils and clayey soils, there is various number of real soils, as represented by the color gradation in Fig. 6.

Consider the case of liquefaction of sandy soil in Fig. 6. In sand, the structure collapses first, and large plastic volumetric compression occurs during this stage. Under cyclic shear during earthquakes, etc., if there is not sufficient time for the pore water to escape, the collapse of structure occurs nearly under undrained conditions (constant volume conditions), and large elastic expansion is necessary to compensate for the plastic compression. Elastic expansion is related to the mean effective stress p' . Since the total stress (pore water pressure + effective stress) remains nearly constant during an earthquake, the pore water pressure will increase steadily, and this increase will continue until the effective stress p' approaches zero. In other words, liquefaction of the sand occurs. The accumulation of overconsolidation during cyclic shear loading caused by an earthquake is the same as the phenomenon of compaction shown in Fig. 1. In sand, for the state of overconsolidation to return after the earthquake to the original state of effective stress (near the state of normal consolidation) while recovering its own weight, large plastic deformation is necessary (in Fig. 4, ■ is far removed from ○). It is for this reason that the amount of consolidation settlement of sand after liquefaction is larger than what would usually be expected. It is only through these two concepts of structural decay and loss of overconsolidation that one is able to obtain a

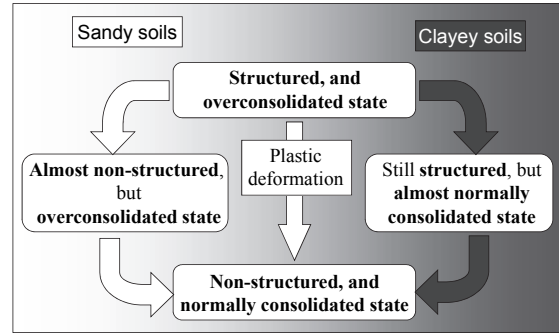


Fig. 6 Differences between sand and clay

continued understanding of not only compaction of sand but also the phenomena of liquefaction of saturated sand and the subsequent large settlement that occurs in it.

Next, consider the behavior of clay in Fig. 6. A slight plastic deformation causes a clayey soil to first approach the state of normal consolidation (in Fig. 4, ■ is close to ○). This is followed by gradual decay/collapse of structure accompanied by large plastic deformation. Of course, the decay of structure is accompanied by large compression as in the case of sand. However, since the permeability of clay is less than $1/100,000^{\text{th}}$ of that of sand, the time required for compression to occur is long. Furthermore, the delay in compression is aggravated by the decrease in rigidity that results from structural decay. These phenomena were referred to as “delayed compression/secondary consolidation” in the past. “Secondary consolidation” tends to take place in the loading range that straddles the states of overconsolidation and normal consolidation, and in addition, the time required for large settlement to

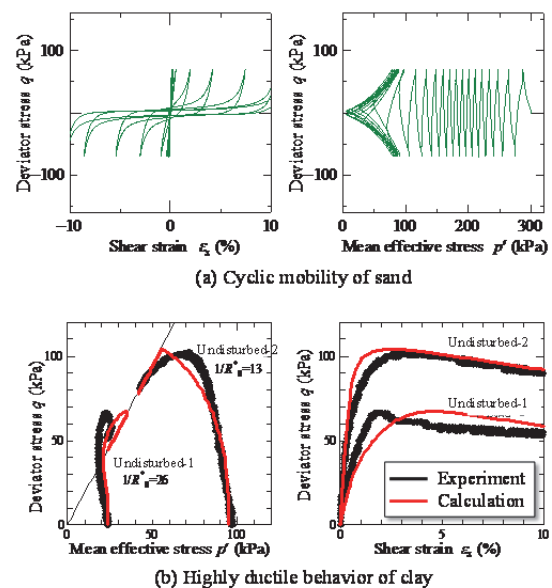


Fig. 7 Attainment of a high degree of structure during plastic expansion

occur is very long. These phenomena can be understood fully only by recognizing that both loss of overconsolidation and decay/collapse of structure take place at a sluggish pace⁷⁾. In addition, from the fact that decay/loss of structure is a phenomenon common to both sand and clay, it can be understood that compaction/liquefaction of sand is the same phenomenon as delayed compression/secondary consolidation of clay. It would be correct to say that the phenomena of compaction/liquefaction of sandy ground and delayed compression/secondary consolidation that continues forever in clayey ground occur only because all these soils are still living soils that possess structure and are in a state of overconsolidation. However, it would be unfortunate if Fig. 6, which illustrates the concept of living soils, were to give one the impression that progress of plastic deformation takes the soils on a one-way path leading to death only. It has been mentioned earlier that the state of overconsolidation is recovered by cycling loads such as those caused by earthquakes.

Fig. 7 illustrates the cyclic mobility of sand in triaxial testing and the high ductility of naturally deposited diluvial clay⁸⁾. Both of these cannot be replicated without the attainment of a high degree of structure during plastic expansion, i.e., without the regeneration of structure.

ANALYSIS EXAMPLES OF GROUND DEFORMATION DURING AND AFTER EARTHQUAKES

The so-called “trampoline effect”

During the 2008 Iwate-Miyagi Nairiku earthquake, a strong earthquake motion (3-component synthesis value: 4022 gal) was recorded on the ground surface at KiK-net station Iwth25 (West-Ichinoseki) located almost directly above the epicenter. Aoi and his colleagues have stated that the accelerometers on the ground showed clear asymmetric pulsating waves in the vertical (up-down) direction. They observed that the acceleration in the upward direction reached nearly 4000 gal, whereas that in the downward direction was limited only to 1 gal (See Fig. 8), and they named this phenomenon the “trampoline effect”^{10), 11)}. On the same ground surface, no pulsating waves were observed in the horizontal direction, and at a depth of 260 m, the tremors in the horizontal and vertical directions were symmetric, as is normal, without any asymmetric pulsations (See Fig. 9). As a result, the ground surface rose up an additional 28 cm compared with the ground interior, and the soil layer on the ground surface exhibited significant expansion.

The ground's surface layer is a terrace sediment layer of Tuffaceous sandstone in an air-dried condition. Samples taken after the earthquake showed that the soil in this layer consisted of

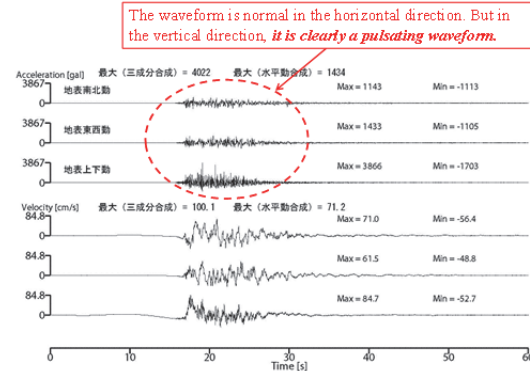


Fig. 8 Pulsating wave in vertical direction observed on ground surface

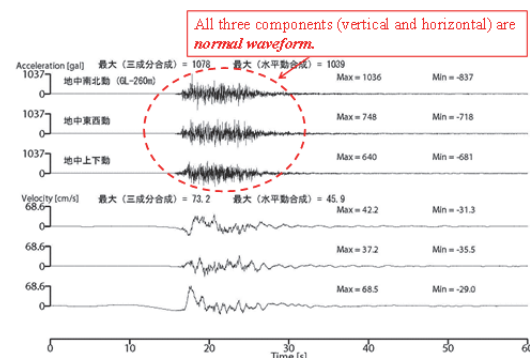


Fig. 9 Normal waveform observed within ground

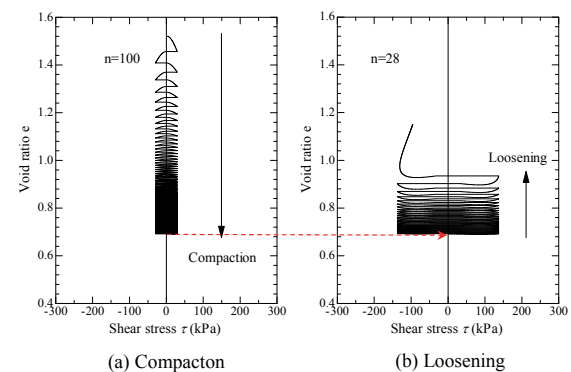


Fig. 10 Compaction of sand and the loosening that follows it

crunchy porous gravel mixed in sand. Focusing attention on this layer (thickness=approx. 20 m), the swelling that appeared on the ground surface in the vertical direction due to the nonlinear response to the horizontal cyclic shear that it was subjected to is replicated here using elasto-plastic geomechanics. That the above replication is not difficult can be understood from Fig. 10, which illustrates at the level of elements the constitutive equation response of sand during compaction and the subsequent “loosening” that occurs.

During compaction, the first few cycles produce

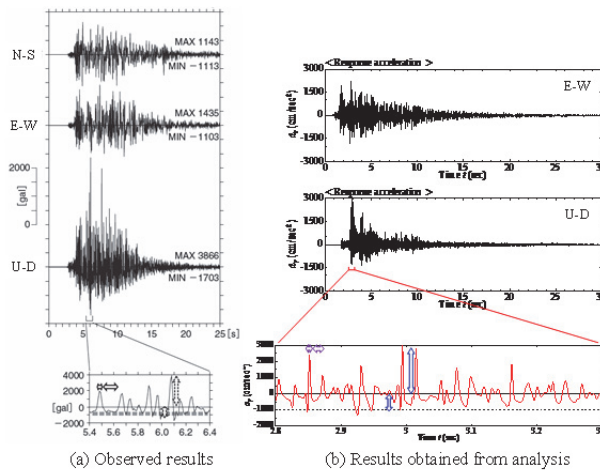


Fig. 11 Comparison of the results obtained through analysis with observed results

large compression. However, as can be seen in Fig. 10, when sand that has been compacted once is subjected to horizontal cyclic loading with greater amplitude than previously, the sand will not loosen in the beginning, but does so suddenly during the last few cycles. Utilizing the above results as background knowledge, the soil layer was extracted horizontally, and the horizontal component only of the seismic wave that had been observed at a depth of 260 m was input at the extracted layer's bottom surface. Figure 11 is a comparison of the results of analysis with the results of actual measurements. (Material constants, initial conditions, other analytical conditions, and a discussion can be found in reference 12.)

Although quantitative comparison is insufficient, there is very close resemblance between the observed results and the results of analysis with respect to the "asymmetry" of the acceleration waveform at the ground surface in the vertical direction (U-D direction). The observed and calculated results both show that the acceleration in the downward direction does not exceed 1 g. This may be thought to be logical for soil that cannot withstand tension, but the result is a natural outcome of the computational boundary condition of not allowing expansion of the ground in the downward direction. In the calculated results, the magnitude of the vertical component of the upward acceleration is somewhat small but becomes a little larger if the actually measured vertical component of acceleration is added to the seismic wave motion that was input at the bottom surface of the layer. What is important is to observe that although only the horizontal component of the seismic wave was input, the response motion of the ground surface in the up-down direction is larger than what was input. Dilatancy, which is never seen in elastic bodies and does not appear in the case of metal plasticity either, is a type of plastic deformation that is unique to soil

as an elasto-plastic body. It needs to be added that according to the results of the calculations, the trampoline effect appears in the high frequency range above 10 to 100 Hz, and that is in agreement with the actual observations made at the site¹⁰⁾.

Post-seismic slope failure

The phenomenon of expansion of the ground during earthquakes such as the trampoline effect described above is rare. However, there are many instances of ground deformation that are caused by plastic expansion occurring in compacted soils and embankments due to earthquakes. A number of embankments built on inclined ground along highways and other locations in Japan collapsed during the Chuetsu, Noto Hanto, Chuetsu-Oki, and Suruga Bay Earthquakes. In many of these instances, the collapse occurred not during the earthquake but after a period of delay ranging from tens of minutes to a few hours following the earthquake. Sliding of the valley fill embankment at Takarazuka occurred only on the day after the Great Hanshin-Awaji Earthquake. A computational replication of the delayed collapse of an embankment built on inclined ground along the Noto toll road during the 2007 Noto Hanto Earthquake is presented here as an example¹³⁾. Although the inclined ground, which was composed of tuff breccia, did not deform during the tremors, embankment that had been built with crushed tuff stone suffered extensive damage. A part of the computed replication is shown in Fig. 12.

From the shear strain distribution within the embankment approximately 10 seconds after earthquake occurrence soon after the main motion, some slippage between the incline and the embankment is observed, but no abnormality is seen in the embankment body. After sufficient time has elapsed after earthquake occurrence, the slip shape exhibited by the embankment body is a traditional

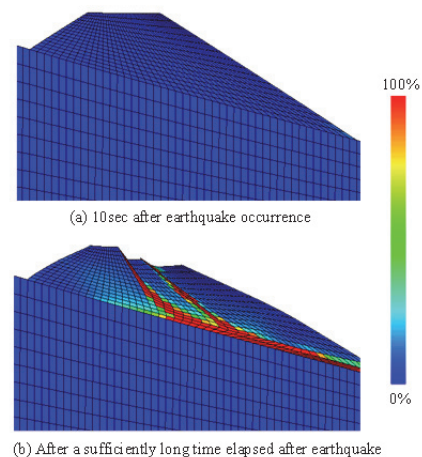


Fig. 12 Delayed failure of an embankment on inclined ground (shear strain distribution)

circular slip. Since a circular slip is a type of failure that is caused by the weight of the soil acting in the vertical direction and does not occur if there are inertial forces, the lower figure in Fig. 12 clearly indicates that the failure occurred after the earthquake ended. During the earthquake, because of the large cyclic shear produced on the incline, plastic expansion tends to occur in the embankment material (compacted sand gravel). However, since replenishment of water and air in the soil pores is not possible within the very short duration of the tremors, there is not sufficient time to allow volumetric expansion of the soil to take place. For this reason, large elastic compression is generated during the earthquake, and the effective constraint pressure on the soil skeleton increases. As a result, the embankment does not fail during the quake. Therefore, it is only after the earthquake that embankment failure eventually occurs as a result of the expansion (decrease of effective stress) that takes place due to water/air absorption. Even now, more than two years after the March 2011 earthquake, slippage and arrest of embankments, etc. have been taking place repeatedly in the housing area on the hill behind Tohoku University. The surface soil is made up of unsaturated soil. Study and clarification of the mechanism of such delayed progressive failures is one of the research tasks of The Japanese Geotechnical Society's concerted efforts in response to the March 2011 earthquake¹⁴⁾.

Liquefaction phenomenon in Urayasu

The March 2011 earthquake caused liquefaction to occur in wide areas centered on the reclaimed land along the Tokyo Bay. Not only the ground surface deposit of naturally deposited alluvial sand but also the soil layer above it, which contained large amounts (20 to 60%) of fine fraction (clay, silt), was liquefied extensively, and the amount of sand boil was great¹⁵⁾. Although the acceleration on the ground surface was less than 100 to 200 gal, the long duration of the earthquake led to the extensive

liquefaction. Based on initial studies made in the Urayasu area, where there was much damage to houses, the distinctive nature of this liquefaction phenomenon is described very briefly in this section.

When compared with loose sand, whose

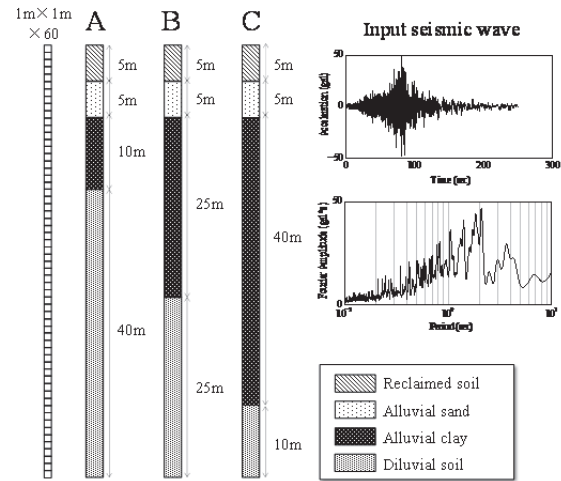


Fig. 14 One-dimensional seismic response analysis based on the ground's geological profile

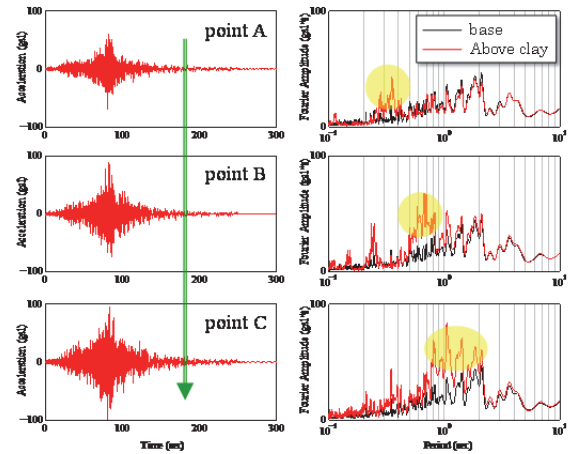


Fig. 15 Horizontal acceleration responses and Fourier amplitude spectra after the seismic wave passed through the alluvial clay layers

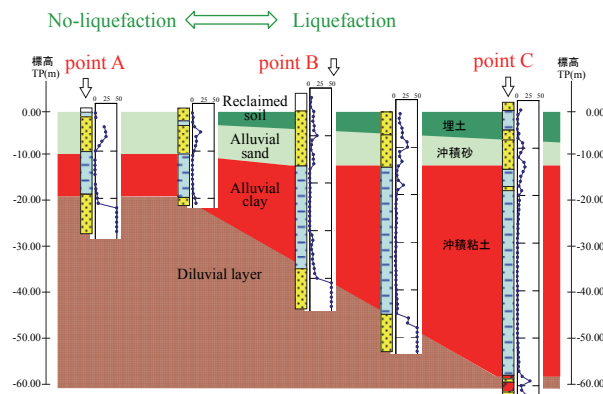


Fig. 13 Cross-section showing the geological profile of the ground in Urayasu City

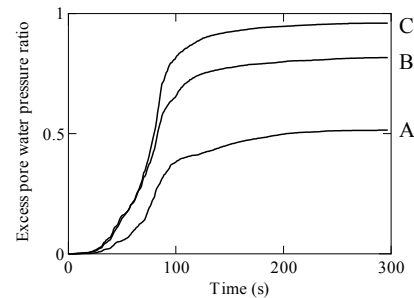


Fig. 16 Excess pore water pressure ratios at each location

structure can collapse easily, accumulation of greater plastic deformation is required to cause decay of the structure in backfill soils that contain large fine fraction. Therefore, if liquefaction extends up to such layers, it is expected that ① the seismic motion input to this layer was a long-period wave and that ② the duration of the earthquake motion was long (i.e., the number of cycles was large).

Figure 13 outlines the geological profile in Urayasu City. The bottom alluvial clay deposit

thickens from about 10 m at location A, where liquefaction damage was light, to about 50 m at location C, where heavy liquefaction damage occurred. Taking into consideration the above, the 1-dimensional analysis illustrated in Fig. 14 was carried out. The results are shown in Fig. 15. (Since the soil properties of the backfill soil layer, alluvial sand layer, and alluvial clay layer are still provisional, the results shown in this figure are preliminary.) It is seen that due to seismic motion

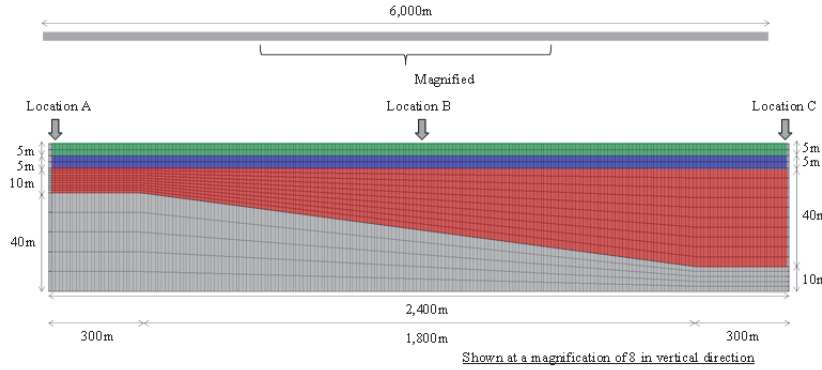


Fig. 17 Conditions for 2-dimensional analysis

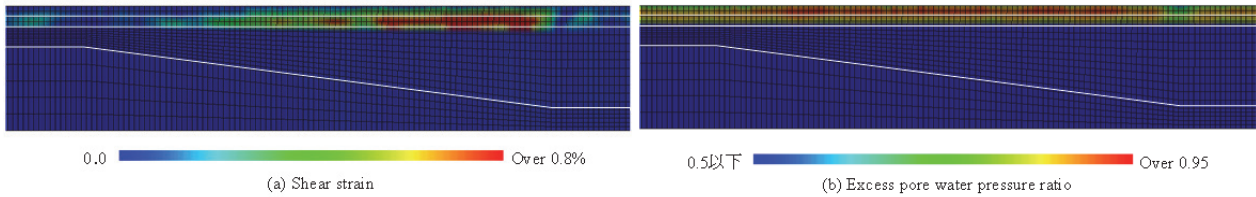


Fig. 18 Shear strain and excess pore water pressure ratio distributions 300 sec after earthquake occurrence

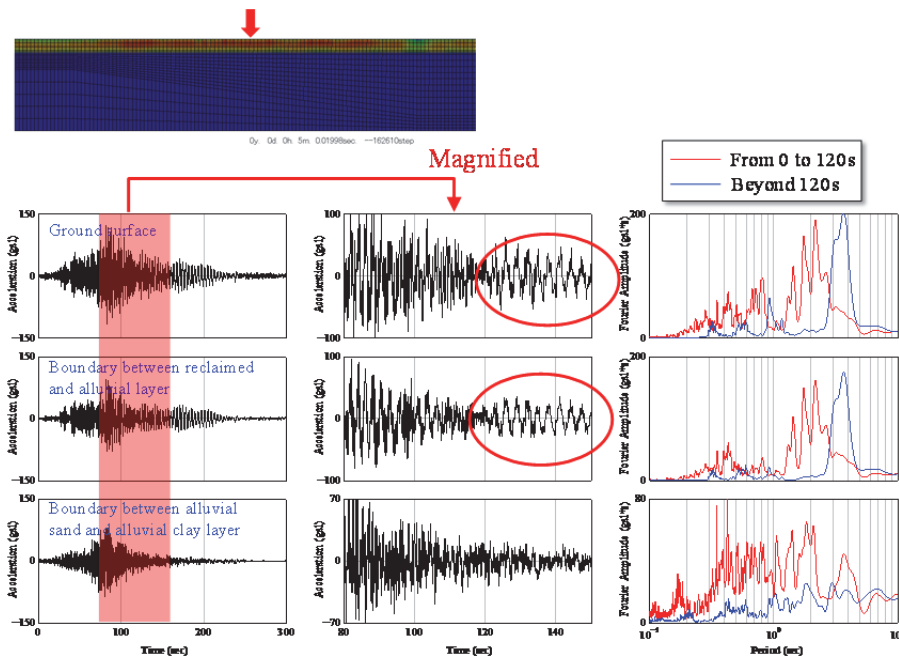


Fig. 19 Acceleration responses at the interlayer boundaries in liquefied locations of the sloped layers

transmitted from the alluvial clay layer to the top liquefied layer, the longer-period components of acceleration amplify as the clay layer thickness increases. As depicted in Fig. 16, although the pore water pressure has peaked 120 to 130 seconds after earthquake occurrence, liquefaction has not occurred at locations A and B. This result is inconsistent with the actual liquefaction damage observed at Urayasu.

Therefore, 2-dimensional analysis was carried out under the conditions set out in Fig. 17, although the stratum organization was significantly simplified for the analysis. It was assumed that the soil properties were uniform along the horizontal direction. Only the variation of the alluvial clay layer thickness was taken into account. The analytical results are illustrated in Figs. 18 and 19. Figure 18 shows the conditions 300 sec after earthquake occurrence. Liquefaction has occurred widely from location A to location C, not only in the alluvial sand layer, but also in the backfill soil layer above it. Comparing Fig. 19 with the input seismic waveform in Fig. 14, it can be observed that in the 120 sec before liquefaction occurred, the long-period components in the above strata have been amplified significantly—roughly four fold. It can also be seen from the acceleration responses of the ground surface that at any point between locations A and C, a wave with a period of about 20 sec has been overlapped by another wave with a period of about 4 sec (figure omitted), indicating that these seismic tremors were such that they could even cause sea sickness (as some readers may have seen in YouTube videos of the March 2011 earthquake). The calculations also indicated that the amount consolidation settlement occurring within 2 to 10 days after the earthquake in the liquefied layers would be roughly 20 cm at location A and 50 to 60 cm at locations B and C, the settlement at location B being the largest. These values too were in good agreement with the actual amount of settlement that occurred.

The degree of liquefaction damage to houses in the area varied in a complex manner in the horizontal direction. For this reason, the non-uniformity of the soil properties of the surface layer has become a major issue at Urayasu. This, of course, is true. However, the current analysis makes it clear that the non-uniformity in the degree of liquefaction is heavily influenced even by a slight inclination of the stratum as shown in Fig. 17. The ground surface deformation shown in Fig. 18 is indeed quite uneven, and the ground surface accelerations obtained in the course of the calculations vary greatly by as much as 100 to 160 gal at locations that are just a few meters apart. More important than the above is that comparison of Figs. 16 and 18 should not make anyone jump to the conclusion that 1-dimensional analysis is without meaning. That would be equivalent to saying that in practical civil

engineering and architecture, “accurate prediction of liquefaction is not possible anymore.” This is why the author has stressed that the analysis is preliminary. Please note that the effects of aftershocks have not been taken into account here.

Ground deformation resulting from delayed compression of alluvial clay

Runway D at Haneda International Airport was constructed on reclaimed land and encountered the March 2011 earthquake about a year after its construction had been completed. Under the landfill is a naturally deposited alluvial clay stratum that is approximately 20-m thick. This stratum is subjected to eccentric earth pressure from the landfill. There was a possibility of structural decay in this clay being promoted by cyclic shear. It has been explained earlier that it takes time for deformation to occur in clayey ground due to structural decay. Figure 20 shows the predicted deformation of Runway D at Haneda International Airport obtained through analysis (details of the analytical conditions are omitted).

To the right of Point 2, the runway is a pier type, and Point 2 is the interface that connects the runway on the landfill with that on the pier. The amount of settlement at Point 2 is a few centimeters and has nearly reached a steady state already. Calculations indicate a lateral displacement of about 20 cm

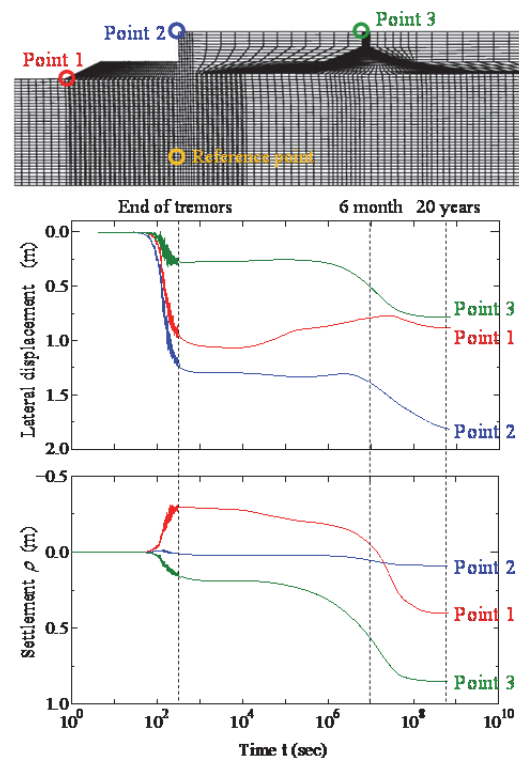


Fig. 20 Prediction of future ground behavior of Haneda Airport's Runway D

towards the pier between now (1.5 years after the earthquake) and the next 20 years. The revetment will slant about 1 degree towards the pier during the next 20 years. Since the soil properties allotted to the landfill were on the hazardous side, the calculated value seems to be somewhat large. Even so, this level of deformation can be absorbed easily by maintenance and repair operations in the future. Although Urayasu is a painful contrast, the author believes that virtually no damage was caused to Runway D by the March 2011 earthquake.

CONCLUSION AND REMARKS

This introduction to geomechanics, in spite of having taken up a few pages of space, paints only a part of the whole spectrum because it has limited itself to soil structure and overconsolidation only without touching on the evolution laws of anisotropy. Anisotropy too, is closely connected to re-liquefaction, which is an important issue¹⁶⁾. At long last, it has become possible to calculate surface ground deformation during and after earthquakes. However, as ground surfaces are the places of daily activities of people and society, it may be natural to expect that certain restrictions need to be applied on the disclosure of the true picture of ground deformation behavior and mechanism. Therefore, high-level engineering ethics would be expected from research personnel too.

REFERENCES

- [1] Asaoka, A., Noda, T., Yamada, E., Kaneda, K. and Nakano, M.: An elasto-plastic description of two distinct volume change mechanisms of soils, *Soils and Foundations*, 42 (5), pp. 47-57, 2002.
- [2] Mikasa, M.: On the significance of soil structure in soil mechanics (IN JAPANESE), *Proceedings of the Annual Meeting of the JSCE*, 1962.
- [3] Mikasa, M.: A classification chart for engineering properties of soils (IN JAPANESE), *Tsuchi to Kiso*, 12 (4), pp. 14-24, 1964.
- [4] Asaoka, A., Nakano, M. and Noda, T.: Super-loading yield surface concept for highly structured soil behavior, *Soils and Foundations*, 40 (2), pp. 99-110, 2000.
- [5] Roscoe, K. H., and Burland, J. B.: On the generalized stress-strain behavior of 'wet' clay, in J. Heyman and F. A. Leckie (eds.), *Engineering plasticity* (Cambridge: Cambridge University Press), pp. 535-609, 1968.
- [6] Hashiguchi, K.: Plastic constitutive equations of granular materials, *Proc. of US-Japan Seminar on Continuum Mechanics and Statistical Approaches in the Mechanics of Granular Materials* (Cowin, S.C. and Satake, M. eds.), Sendai, JSSMFE, pp. 321-329, 1978.
- [7] Noda, T., Asaoka, A., Nakano, M., Yamada, E. and Tashiro, M.: Progressive consolidation settlement of naturally deposited clayey soil under embankment loading, *Soils and Foundations*, 45 (5), pp. 39-51, 2005.
- [8] Noda, T., Asaoka, A., Nakai, K. and Tashiro, M.: Structural upgradation in clay and sand accompanying plastic swelling, *Proc 13th Asian Reg. Conf. on Soil Mech. Geotech. Eng.*, pp. 175-178, 2007.
- [9] Noda, T., Asaoka, A., Nakano, M.: Soil skeleton-water coupled finite deformation analysis based on a rate-type equation of motion incorporating the SYS Cam-clay model, *Soils and Foundations*, 48 (6), pp. 771-790, 2008.
- [10] Aoi, S., Kunugi, T. and Fujiwara, H.: Trampoline effect in extreme ground motion, *Science*, Vol. 322, pp. 727-730, 2008.
- [11] Aoi, S.: Discovery of asymmetric ground motion and the "trampoline effect" (IN JAPANESE), *Science*, Vol. 79, No. 4, pp. 366-370, 2009.
- [12] Asaoka, A., Sawada, Y., Noda, T., Yamada, S. and Shimizu, R.: An Attempt to Replicate the So-Called "Trampoline Effect" in Computational Geomechanics, *Proc. of 15th World Conference on Earthquake Engineering*, Lisbon, 2012.
- [13] Sakai, T., Nakano, M.: Reproduction of large-scale failure after an earthquake of an embankment on inclined ground through soil-water coupled finite deformation analysis (IN JAPANESE), *Japanese Geotechnical Journal*, 7 (2), pp. 421-433, 2012.
- [14] Research Committee on Ground Deformation Mechanisms (Chairman: Asaoka, A.) of the Japanese Geotechnical Society's Investigative Commission for Research Response to the Great East Japan Earthquake.
- [15] Yasuda, S., Harada, K., Ishikawa, K.: Damage to structures in Chiba Prefecture during the 2011 Tohoku-Pacific Ocean Earthquake (IN JAPANESE), *Japanese Geotechnical Journal*, 7 (1), pp. 103-115, 2012.
- [16] Yamada, S., Takamori, T. and Sato, K.: Effects on liquefaction resistance produced by changes in anisotropy during liquefaction, *Soils and Foundations*, 50 (1), pp. 9-25, 2010.

USE OF RECYCLED AGGREGATES FROM CONSTRUCTION AND DEMOLITION WASTES FOR THE CONSTRUCTION OF FLEXIBLE PAVEMENTS

Márcio Muniz de Farias,¹ Alejandra María Gómez Jiménez and Ferney Quiñones Sinisterra²
¹Faculty of Technology, University of Brasília, Brazil; ²Universidad del Tolima, Colombia

ABSTRACT

The industry of civil construction generates huge amounts of wastes during the construction of new buildings and the demolition or reformation of old structures. Construction and demolition wastes (CDW) comprise soils from excavations, asphalt concrete from old pavement surfaces, and a large variety of material from buildings, such as concrete, ceramics, sand and rock chips, gypsum boards, among others. These materials may be recycled and reused for the construction of road pavement layers. This kind of application was chosen taking into account the large amount of materials required and the possible economic impacts. CDW was recycled to produce aggregates that could be used as granular layers or asphalt concrete. The materials were used raw or mixed with other ingredients. The research shows the pros and cons of using recycled aggregates in different pavement layers. The major problem is related to aggregate crushing and high porosity. Overall the research concludes for the economic, environmental and technical feasibility of recycling construction and demolition wastes for pavement construction.

Keywords: Construction and Demolition Wastes, Recycled Aggregates, Flexible Pavements, Particle Crushing

INTRODUCTION

The amount of construction and demolition waste (CDW) generated in global and local levels are significant. The volume of these materials is increasing with the construction of new buildings and the demolition of old structures that have reached their project life, or due to natural hazards such as earthquakes, storms and floods and anthropic disasters like wars.

Around 300 million tons/year of CDW are generated in Europe, about 170 million tons/year in the United States and 68 million tons per year are produced in Brazil. The Federal District (Brasília, Brazil) has a daily production of 6000 tons, equivalent to a production of 2.2 million tons/year. The volume of CDW in Brazil has increased dramatically in cities that will host the 2014 Soccer World Cup due to the demolition of old stadiums and the construction of new facilities, such as road and airport expansions.

Innovation and development of wastes recycling technology are necessary to make these materials suitable for reuse. Applications of CDW, recycled concrete aggregates (RCA), and reclaimed asphalt pavement (RAP) in civil engineering works and infrastructure are now common practice in many countries [1]. Several researches show that CDW is an attractive alternative material for bases and sub-bases of highway pavements due to its high resistance and its non-expansive behavior [2]-[5]. However, there are a few disadvantages such as high

porosity, particle crushing and heterogeneities. The problem of particle crushing and its impacted of some relevant properties for the use of recycled aggregates for the construction of flexible pavements are analyzed in the following sections.

CDW FOR GRANULAR BASE LAYERS

Typical construction and demolition wastes are a mixture of reinforced concrete blocks, mortar, plaster, ceramics, soils, steel, plastic, wood, ink and solvents. Most of these can be recycled and those which can be ground or directly used as granular materials are classified as class A for recycling purposes according to the Brazilian environmental regulation CONAMA N°307/2002. Class A materials, subjected to other requirements, may be used as sub-base and base layer in high pavements. When the amount of granular material exceeds a minimum of 85%, besides other requirements to be described later, the material is classified as recycled aggregates and may even be used as component of concrete mixtures.

Characterization of the CDW

The recycled material investigated in this research was collected from wastes of the National Soccer Stadium of Brasília, which was imploded to give rise to a brand new stadium for the 2014 World Cup in Brazil. For this study a representative sample of about 1.6 tons of CDW aggregate was used for

the laboratory evaluation. Two grinding process were necessary to obtain the CDW aggregate with the desired grain size distribution required for this investigation.

Composition of the CDW used

In order to determine the composition of the CDW used in this study, the coarse aggregate fraction retained in the 4.75 mm sieve was examined visually and segregated manually. The CDW aggregate was separated into four main groups: (i) cementitious materials (the major component of the CDW aggregate, comprised mainly of concrete and mortar, 41%); (ii) crushed rock chips (about 15%); (iii) red ceramics (bricks and roof tiles, 1%); and (iv) white ceramics (floor and wall tiles, 1%).

The fine aggregate fraction, passing the 4.75 mm sieve but retained in the 0.075 mm sieve (#200), represented 42% of the total sample. Undesirable materials retained in sieve #200 such as metals, wood and plastic represented only a very small proportion in weight of 0.6% of the total sample. This value is far below the limit value of 3% imposed by Brazilian standards for the use of construction and demolition wastes in pavement layers.

Physical properties of the CDW used

The physical properties of CDW used in this research were determined using Brazilian (NBR) and American (ASTM) standards. Tests like water absorption, grain shape, grain-size distribution, sand equivalent, soundness and Atterberg limits were used to determine the physical properties of the recycled aggregate and to define whether it was suitable as base material for highway pavements. The results are summarized in Table 1.

Table 1 Physical characteristics of CDW aggregates

Property	Value	Limit**
Uniformity coef. (C_u)	61	≥ 10
% Passing sieve N°40	15	10-40
% Passing sieve N° 200	12%	15%
% of contaminants	0.56	≤ 3
Liquid limit %	32	≤ 25
Plasticity index %	NP	≤ 6
Expansion %	0	≤ 0.5
Solid specific gravity, G_s	2.14 - 2.38	-
Absorption %	7.7	-
Sand equivalent	≥ 70	≥ 30
Soundness in $MgSO_4$ (%)	6.0 – 11.0*	30%
Shape Index	0.9 – 0.8	-
Los Angeles Abrasion (%)	35 – 38*	$\leq 55\%$

Note: * 1st value refers to tests performed on coarse (gravel) fraction and 2nd value to tests performed on fine (sand) fraction. ** Limits according to Brazilian

norm DNIT – ES 141/10.

All the results above comply with the minimum requirements for the material to be used in granular pavement layers. For base layers the norm requires a plastic index inferior to 6% and expansion inferior to 0.5%. The material is non-plastic and does not show swelling characteristics. This is due to the low amount of grains passing sieve #200, which shows little contamination by silt and clay size particles. This is corroborated by the good value (70%) of sand equivalent ratio, higher than minimum norm requirements of 30% for base layers.

In fact the grain size analysis with less than 15% passing sieve #200 qualifies the material by Brazilian standards as construction and demolition aggregates (CDA) rather than wastes (CDW). The additional tests (abrasion, shape, soundness) indicate that the CDA can be considered even for applications on asphalt concrete mixes to be used in flexible pavement surface layers.

The low value of particle specific gravity is due to the presence of ceramics chips and also mortar adhered to the rock chips used in the Portland cement concrete and wall rendering. These materials are responsible for the high water absorption value and the characteristic particle breakage to be analyzed in the next sections.

Breakage of Particles from CDW

Research results from [3] show that the bulk of CDW particle breakage occurs during compaction process rather than other tests emulating service life. In order to evaluate particle breaking the grain-size distribution curves before and after the compaction process were compared. Due to the expected breakage, the initial grain size distribution was adjusted to the so called envelope or “band C”, prescribed by Brazilian code (DNIT – ES 141/10). This envelope is commonly used for base and sub-base materials in highways with medium to heavy traffic volume.

The material was then compacted at its optimum conditions determined using Modified and Intermediate Proctor energy (1263 kN.m/m³). The laboratory compaction tests were performed according to the American Standard procedure (ASTM D1557-07). The observed values of optimum water content and maximum dry density were 13.0% and 16.5 kN/m³, respectively, for the intermediate Proctor energy. Other water contents (8%, 10%, 14% and 19%) were also investigated to check the effect of this index on particle breakage.

Index for CDW particle breakage

Reference [6] developed a measure of particle breakage during the construction of earth and rockfill dams. His method was originally based on

large-scale triaxial compression tests and computes the changes in individual particle sizes between the initial and final grain size distributions. The difference in the percentage retained is computed for each sieve size. This difference will be positive or negative. Marsal's breakage factor (B_g) is the sum of the differences having the same sign:

$$B_g = \sum_k \langle W_k^i - W_k^f \rangle \quad (1)$$

in which W_k^i and W_k^f are the initial (before compaction) and final (after compaction) percentages in weight retained in sieve "k". Only positive differences are considered in the summation as indicated by the Mc Cauley bracket $\langle x \rangle$. The lower limit of Marsal's index is 0% and the theoretical maximum is 100%.

Results of particle breakage and B_g index

The original and after compaction grain size distribution curves for different initial values of water content (8%, 10%, 14% and 19%) are shown in Figure 1.

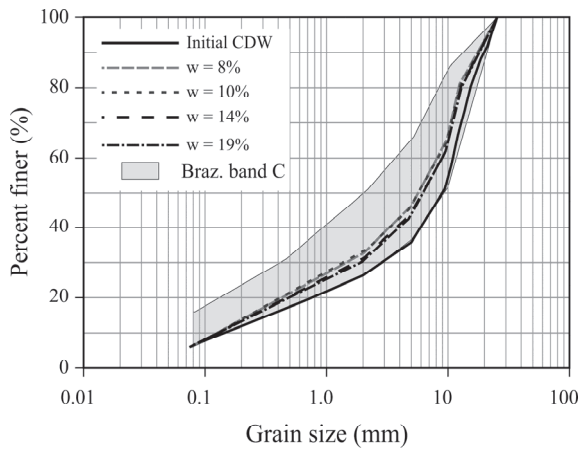


Figure 1 Grain-size distribution of CDW and effect of water content during compaction.

The change of grain sizes is evident from the leftwards shift in the curves towards the center of the gradation envelope, the gray zone in Figure 1. The most significant change occurs for the samples with lower initial water content (8%). Less crushing is observed as the water contents increases. This is due to the fact that water absorbs part of the compaction energy.

The effect of compaction water content and energy can be better appreciated by computing Marsal's degradation indices (B_g) for different compaction conditions. Figure 2 shows lines of equal degradation (iso- B_g). Note that by increasing the energy of compaction, there is an increase in

breakage index and the same parameter decreases with the increase in moisture content, as indicated by the arrow in the figure.

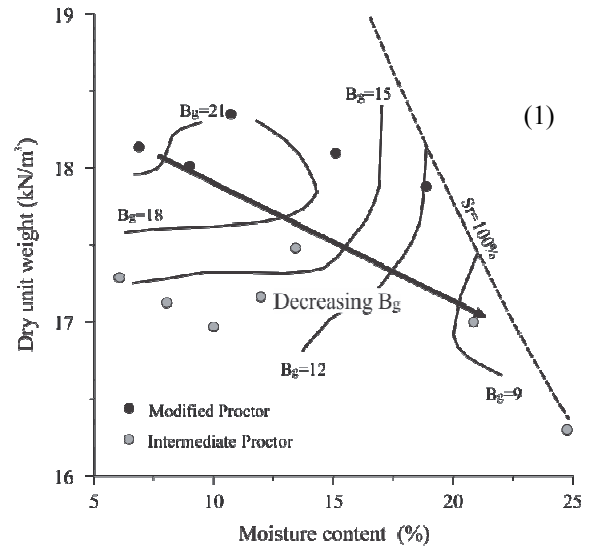


Figure 2 Lines of equal degradation indices according to compaction energy and water content.

Water Absorption and Suction in CDW Aggregates

The particle breakage and compaction characteristics discussed above are explained by the presence of ceramics and mortar in the constitution of the CDW. This also explains the high value of water absorption of 7.7 % shown in Table 1. This value is rather high when compared to natural rock chips, but it is not uncommon in CDW which can reach absorption values as high as 15%.

The absorption value of 7.7% also explains the high value of *apparent* optimum water content (w_{opt}) around 13% for the intermediate Proctor energy. Natural granular materials and rock chips tend to show lower values of w_{opt} . The *effective* compaction water content, discounting water absorption, should be in the range of 5%. In fact the optimum water content of 13% was rather arbitrary, because the compaction curves were erratic or very flat. However the samples would not stand for water contents lower than 8% and would exude water for contents higher than 20%.

The discussion above prompts to the existence of at least two families of pores: inter-particles and intra-particles. The water inside these pores should affect the mechanical (and the hydraulic) behavior in different ways. In order to investigate these conjectures the authors carried out a series of studies about the Soil Water Characteristic Curves (SWCC) or water retention curves (WRC) of the CDW.

Water retention properties

Specimens of CDW were specially prepared for determination of the WRC. The samples were compacted using intermediate Proctor energy and different water contents (9%, 13% and 17%). The samples were 100 mm in diameter and 35 mm in height and the original grain size distribution fitted the coarser limit of envelope C, shown in Figure 1. The water retention tests were performed using a specially devised pressure plate apparatus based on the axis translation technique (ATT) for suction values between 3 and 200 kPa and the filter paper method (FPM) for the remainder of the WRC [7].

The water retention curves were obtained primarily by following a drying or desorption process. Figure 3 shows the curves that describes the change in gravimetric water content in the CDW with respect to the change in matric suction. It is noted that for suction values below 100 kPa, where the desaturation process of the CDW begins, the results of with the filter paper method (FPM) are lower than those obtained by the axis translation technique (ATT).

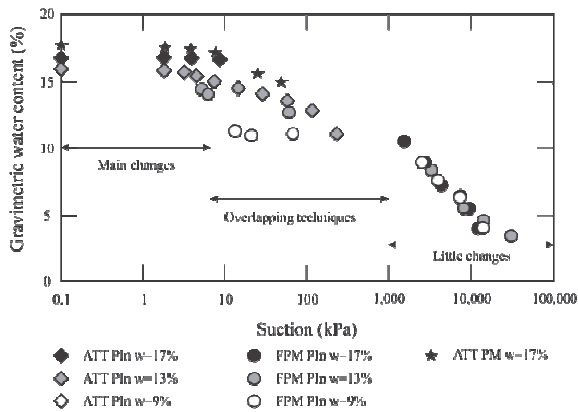


Figure 3 Water retention curve of CDW.

Observing the results in Figure 3, very little change is noted between the WRC of the different samples for the higher suction values at the right end of the curves. Most differences in the water retention capacity of the samples are observed in the initial part of the WRC. These changes in the initial form of the WRC have a connection with the breakage of the particles during the compaction process which is primarily affected by the initial compaction water content and the compaction energy as discussed in the previous section.

The shape of each curve suggests a multi-modal distribution of pores. This is clear for the WRC of the CDW with 13% water content in

Figure 4, where it is possible to distinguish at least three dominant pore sizes, from the sharp changes of inclination in the $w\text{-}\log(s)$ curve. The larger pores with diameter around 113 μm

correspond to the voids between the finer sand grains. The intermediate pores with diameter around 1.6 μm correspond to voids in the finer silt and clay particles originally present in the CDW and further generated due to particle breakage during compaction. It is supposed that the smaller pores (around 0.03 μm) correspond to voids within the mortar or even within the calcareous aggregate chips used to make the concrete, however this hypotheses should be checked later using nitrogen absorption technique directly in the aggregate chips.

The dominant pores can be better visualized by plotting the pore size density (PSD) curves. These curves are obtained from axis transformations on the water retention curves. The ordinates are changed from gravimetric water content (w) to air void indices (e_a) as follows:

$$e_a = e - G_s w \quad (2)$$

in which e is the total void ratio and G_s is the specific gravity. On the other hand the abscissa axis is transformed from capillary suction (s) to pore diameter (D), assuming that in each pore, water and air are separated by a concave interface represented by Laplace equation from which:

$$D = \frac{4\sigma}{s} \quad (3)$$

in which σ is the surface tension of the water assumed as 0.072 N/m at 20 °C. The transformed $e_a\text{-}\log(D)$ curve has a shape similar to that of the WRC in Figure 3, and its slope (first derivative) for each diameter value represents the pore density from which the pore size density curve is constructed as shown in Figure 5.

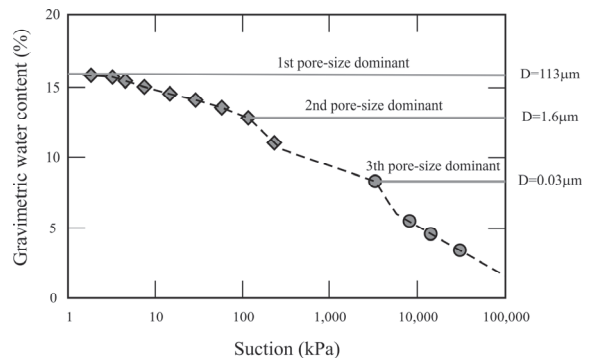


Figure 4 Multi pore shape in the water retention curve for the compaction water content of 13%.

Similar curves were obtained for other values of initial water content, but the shapes of the WRCs for low suctions (i.e. <100 kPa) were affected by

compaction water content. As compaction water content grows, the magnitude of the first air entry value increases; this value is related to the largest pore size. The final part of the curves converges. This occurs for water content values lower than 9%, which is close to the amount of water absorbed by the recycled aggregates studied.

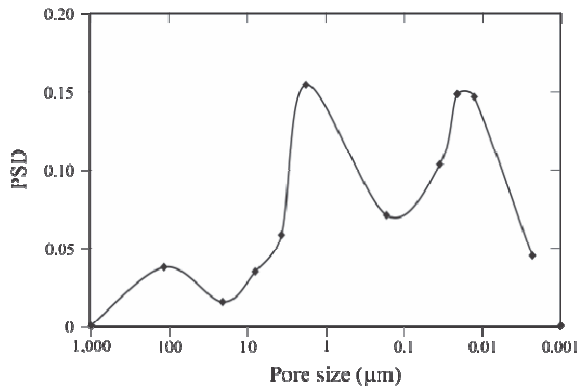


Figure 5 Pore size density (PSD) curve for the compaction water content of 13%

Mechanical Properties of the CDW

The most important engineering properties of granular materials such as stiffness moduli, shear strength, volumetric compressibility, consolidation coefficient, and permeability depend on the integrity of the particles or the amount of particle crushing that occurs due to changes in stress. Therefore, it is important to be able to identify and quantify the effects of particle crushing on these engineering properties [8].

The basic mechanical properties of granular materials of interest for the design of flexible pavements were investigated. These include California bearing ratio (CBR), conventional uniaxial compression and cyclic triaxial tests (CTT) for the determination of Modulus of Resilience (MR).

California bearing ratio (CBR)

Despite generalized criticism, the design of flexible pavements based only on the CBR properties is still a reality in many countries, including Brazil, and any research about materials for pavement construction would be incomplete without this test.

Different compaction efforts were studied corresponding to Normal (PN), Intermediate (PI) and Modified Proctor (PM) compaction energies. Samples were prepared at maximum dry density and optimal water content condition for each compaction energy. The CBR standards generally require that the samples should be soaked in water during four days, during which swell or expansion index should

be computed. Both soak and unsoaked tests CBR tests were performed and the results are summarized in Table 2 according to the Proctor energy applied.

The results shown in Table 2 are quite interesting. First the absolute values of CBR qualify the CDW as potential material to be used in sub-base layers ($\text{CBR} \geq 20\%$ at PN) and base layer even in the case of highways with heavy volume of traffic ($\text{CBR} \geq 80\%$ at PI).

Table 2 Results of CBR test.

Compaction Energy	Soaked	Unsoaked
Normal	43%	55%
Intermediate	96%	128%
Modified	175%	247%

Second the soaked CBR in all cases were higher than the unsoaked values. For natural soils, it is generally expected a decrease in soaked CBR since the increase in water degree of saturation causes the collapse of aggregates or lumps of fine particles that are produced during the sample preparation.

The increase in soaked or immerse CBR is attributed to chemical reactions of the pozzolanic materials remaining in the mortar and Portland cement concrete fractions. This was further investigated using unconfined compression tests in samples aged with different curing periods.

Unconfined compression strength (UCS)

The gain in soaked CBR values prompted the possibility of pozzolanic reactions that should be variable with time. This was investigated by preparing compacted samples of 100 mm diameter by 200 mm of height in the optimum conditions for the intermediate Proctor energy (1263 kN.m/m^3).

The samples were allowed to rest or *cure* under constant humidity and temperature conditions for the following time periods: 0, 1, 7, 30, 60 and 90 days. Later the samples were sheared under static unconfined tests and dynamic confined triaxial tests described in the next subsection.

The results of unconfined compression tests are shown in Figure 6 in which each point represents an average of three tests. The result for the samples tested immediately after compaction (without cure or 0 curing days) gave an average unconfined strength of 120 kPa. This value was used to normalize the strengths obtained after different curing periods as shown in Figure 6.

The results clearly show the increase of unconfined strength and corroborate the initial hypothesis that further pozzolanic reactions are taking place due to the reminiscent cementitious material present in the CDW. The increase was around three folds after three months tending to stabilize after that.

Dynamic triaxial tests

The modern trend in most countries is to move from the empirical design methodology based on CBR and migrate to more advanced procedure as the one prescribed in the MEPDG, Mechanistic-Empirical Pavement Design Guide [9]. In this case the most relevant mechanical property of granular materials is the modulus of resilience which is obtained from a dynamic triaxial test normalized by AASHTO T307-99. The procedure prescribes variable confinement stresses and variable cyclic deviatoric stresses performing a total of 16 determinations of moduli for each test batch.

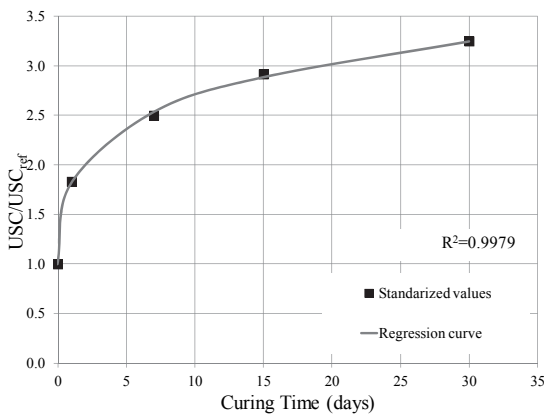


Figure 6 Average normalized unconfined compression strength versus curing days.

Similar to the unconfined compression tests the value of modulus of resilience (MR) also varied with curing time. The lower values were observed for uncured samples and MR varied between a minimum of 70 MPa and a maximum of 250 MPa, depending on the stress state. The highest values were obtained after 7 days of curing and varied in the range between a minimum of 300 MPa and a maximum of 600 MPa. These values are in accordance with those expected for good natural rock chips used for base layers in heavy traffic highways.

The variation of MR with curing time is shown in

Figure 7. The average values increase rapidly from 172 MPa immediately after compaction to a value of 426 MPa after 7 days of curing. Then an unexpected drop of stiffness is observed after 15 days of cure and after that the moduli turns to increase and maybe stabilize as curing time proceeds. The long term increase in stiffness might be related to real cementation due to pozzolanic reactions as discussed in the previous subsection. The apparent decrease of MR after 90 days is not in line with expectations and should be further investigated.

The authors believe that the initially erratic behavior of MR with time is due to stabilization of suction between the different families of pore sizes within the CRW sample. It was shown in previous sections that three dominant pore sizes are present in the CDW specimens.

In recent publications it is assumed that the mechanical behavior is primarily controlled by suction in the inter-granular pores and that strength and deformability is less or little affected by suction in the intra-granular pores present in lumps of clay particles and in the mortar in the case of CDW [1], [7], [10].

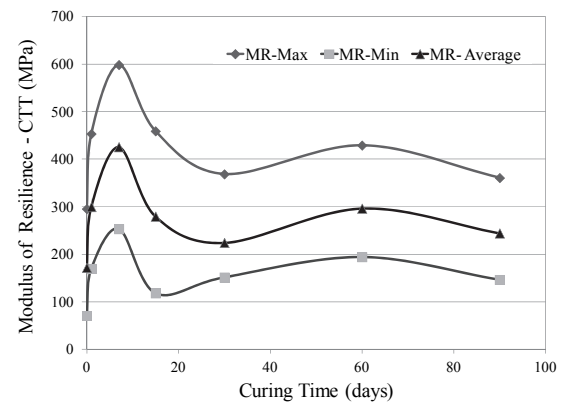


Figure 7 Change in the modulus of resilience with curing time.

Inter-granular suction takes little time to equalize in the larger pores and tend to increase stiffness initially. The water tends to migrate to the interior of the porous aggregates where internal suction is higher. This would lead to decrease in inter-particle suction and hence a decrease of deformability modulus. In the absence of further evidence this is just a conjecture, but the authors sustain it as a feasible explanation.

Modeling the variation of MR

The value of the dynamic modulus of resilience tends to vary both with the confining pressure and the deviatoric stress. The effect of confinement is greater in loose granular materials and correlates positively with the increase of modulus of resilience. On the other hand, the effect of the cyclic deviatoric stresses is more pronounced in cohesive materials and generally tends to correlated negatively with the MR in the case of natural clays.

Several models have been proposed in the literature of pavements for the non-linear behavior of the modulus of resilience with the stress state. One widely accepted is the so-called Universal model proposed originally by [11] which takes the following mathematical expression:

$$MR = k_1 p_a \left(\frac{\theta}{p_a} \right)^{k_2} \left(\frac{\tau_{oct}}{p_a} + 1 \right)^{k_3} \quad (4)$$

in which p_a is the reference atmospheric pressure, θ is the first invariant of stress, τ_{oct} is the octahedral shear stress and k_1 , k_2 and k_3 are non-dimensional materials properties obtained from regression of experimental data.

The numeric results for the constants of the model described above were obtained from regression for all tests performed and the best fit is summarized in Table 3.

Table 3 Coefficient of Universal MR model.

Curing time (days)	Universal Model			
	MR (MPa)	k_1	k_2	k_3
0	171	745	0.84	-0.35
1	299	1764	0.64	-0.49
7	425	2754	0.55	-0.45
15	280	1318	0.52	0.37
30	224	1302	0.01	1.25
60	293	1747	-0.07	1.52
90	239	1480	0.45	0.00

The value of k_1 gives a measure of MR at the reference atmospheric pressure. It controls the overall trend observed. The value of k_2 is related to the nonlinearity typical of unbound granular materials like natural sands and gravels. The values show that this behavior is dominant in the initial periods up to one or two weeks of curing time. Later this parameter is approximately zero indicating the dominance of cementation factors. Finally the value of k_3 is related to the nonlinearity caused by the deviatoric stress. This value is initially negative as for natural clays where shear stresses tend to decrease stiffness due to structural damage. The results corroborate with the conjecture of an initial stage dominated by inter-aggregate suction effects. For longer curing times the value of k_3 becomes positive indicating the dominance of bonding effects over suction. Again the value obtained for 90 days requires further analysis.

The overall adherence between the model and the experimental values is excellent. This can be appreciated in Figure 8 where all experimental values are plotted against the theoretical values computed using the universal model and the parameters described in Table 3. The equality line (at 45° degrees) is also plotted.

CDW IN HOT MIX ASPHALTS FOR SURFACE COURSES

Flexible pavements demand a high amount of

rock chip aggregates for the construction of surface courses with Hot Mix Asphalt (HMA) concrete. Unfortunately, in the Central Highland of Brazil the only type of rock available is calcareous and it is mainly exploited for the production of Portland cement. The portion which is not consumed for the production of cement is sold as aggregate chips for the ever expanding building industry. The road construction sector is left with the residues.

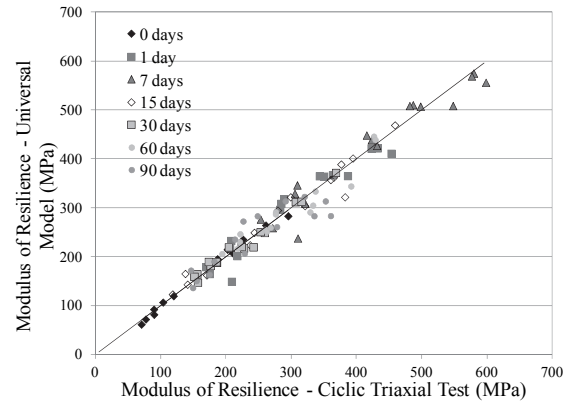


Figure 8 Experimental values of MR versus Universal model predictions.

Although the use of calcareous in pavement surface is limited or even forbidden in some countries, there is other alternative within viable economic distance to be used in Brasilia. In other regions like the Amazon, which is a huge sedimentary basin, there is also very little rock available. This shortage of natural aggregates for the construction of unbound and cohesive pavement layers in the many regions of Brazil has led to an increasing interest for the use of recyclable materials, such as construction and demolition waste – CDW. However, all these researches concentrated on the use of CDW for sub-base or base layers as described in the previous section. Very little has been done about the potential use of CDW in Hot Mix Asphalts. Previous researches by [3] showed that a CDW from the demolition of the old National Soccer Stadium in Brasilia met all the requirements to be used as base layer, even in the case of heavy traffic, although the material showed clear tendency of changing grain size distribution depending on several factors, such as compaction energy and water content. These results encouraged the investigation about the feasibility of using the recycled aggregate from this CDW to produce dense graded hot mix asphalt (HMA) concrete for the surface course of medium and low traffic pavements in the region. However, particle breakage and high water absorption of the recycled aggregate remained a major cause of concern.

On the other hand the advantages of asphalt rubber for the reduction of permanent deformation and increase in fatigue life of flexible pavements has

been widely reported in many paper journals and the proceedings of five editions of the Asphalt Rubber conference for instance [12].

The main assumption here is that asphalt rubber may also help to mitigate crushing of the recycled CDW aggregates due to the elastic behavior of the remaining particles of crumb rubber. In order to check this hypothesis the authors prepared several samples of dense graded asphalt concrete using recycled aggregates and asphalt rubber with different rubber contents. Different energies were applied during the sample compaction and the samples were later destroyed to recover the aggregates and the final grain size distribution curves were analyzed. The degradation was measured by the index described in the next sections.

Physical and Mechanical Properties of the Modified Asphalt Binder

The straight asphalt binder used in this project is classified as CAP 50-70, according to the penetration grade used in Brazilian standards. This was chosen because it is the main binder used in the region of the Federal District in Brasilia as well as in Brazil as whole. The binder was tested at the Highway Engineering Laboratory at the University of Brasilia for quality control and to verify if it satisfied the Brazilian Standard requirements.

The binder was subjected to conventional tests such as penetration grade, softening point, ductility, flame and fire temperature, etc. Non-conventional tests prescribed by the Superpave Standards were also carried out, including Dynamic Shear Rheometer (DSR) for the determination of complex shear modulus (G^*) and phase angle (δ), Rotational Viscosity and aging tests in a Rolling Thin Film Oven (RTFO). The results are shown in Table 4 and satisfied all reference intervals required by the Brazilian Petroleum Agency ANP N°19/2005.

Table 4 Asphalt binder characterization test.

Test	Unit	Reference limits	Results for CAP 50-70
Penetration (100g,5s,25°C)	0,1mm	50-70	53
Softening Point	°C	>46	47
Viscosity @ 150 °C, sp21 (20rpm)	cP	>112	165
$G^*/\sin\delta$ (46°C)	kPa	>1	22
(RTFOT) @ 163°C, 85 min			
Loss of mass	%	≤ 0.5	0.16%
Inc. Softening point	°C	≤ 8	1.5
Inc. penetration	%	≥ 55	73%
$G^*/\sin\delta$ (46°C)	kPa	>2	33

Asphalt Rubber properties

The crumb rubber used in this research was recycled from scrap tires in a commercial recycling plant in Sao Paulo, Brazil. It was tested at the University of Brasilia (UnB) according to the recommendations of the American Standard ASTM D 6114/97. The rubber grains were loose, dry and did not foam in contact with the asphalt binder. The results of control tests for textile and metallic fiber contents, water content and density met all requirements for the production of asphalt rubber.

The gradation of the crumb rubber grains was controlled in order to meet the standards prescribed by the Arizona Department of Transportation (ADOT). Figure 9 shows the ADOT limits and adopted grain size distribution curves.

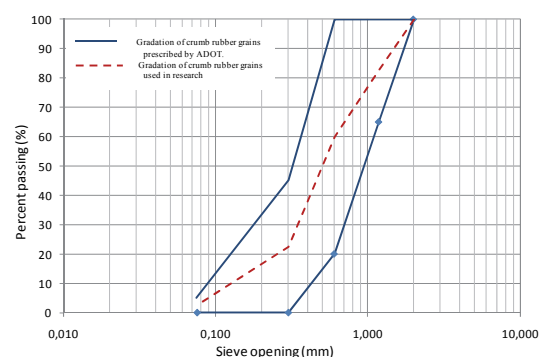


Figure 9 Crumb rubber grain size distribution curve and ADOT limits.

Modified asphalt rubber binder was manufactured in laboratory at UnB. The equipment consists of a mechanical agitator coupled with a rotational bar with a helicoidal blade at its ending, a metallic recipient to heat the binder and rubber mixture and a thermometer to control the mixing temperature. The mixing speed varied in the range of 250 to 300 rpm in order to assure a homogenous mixture. The digestion process was carried out at a temperature of 170°C during a period of one hour following suggestions from [13]. Modified binders were prepared mixing CAP 50-70 (penetration grade) with 10% and 20% in weight of crumb rubber (AR-10 and AR-20).

Asphalt Rubber HMA

Different types of hot mix asphalts were prepared in order to check the influence of the amount of crumb rubber and the compaction energy. All fractions of aggregates (coarse, fine and filler) were recycled from civil construction and demolition wastes (CDW-RA). The aggregates grading fitted a dense gradation envelope (C) prescribed by the Brazilian authorities. This envelope is not the same as band C used in base

layers. The binders include the straight CAP 50-70, the modified CAP 50-70 with 10% of crumb rubber (AR-10) and with 20 % of crumb rubber (AR-20). The following cases were tested:

- Case 0-0: Unbound CDW-RA (only the recycled aggregates)
- Case 6-0: HMA 6% of straight binder (recycled aggregates + CAP 50-70)
- Case 6-10: HMA 6% of asphalt rubber AR-10 (recycled aggregates + CAP 50-70 +10% of crumb rubber)
- Case 6-20: HMA 6 % of asphalt rubber AR-20 (recycled aggregates + CAP 50-70 +20% of crumb rubber)

The case nomenclature uses two numbers B-R, in which B is the percentage of binder (0 or 6%) and R is the percentage of rubber in the binder (0, 10 or 20%). The idea was to test initially the crushing potential of the unbound recycled aggregate under Marshall energy, then to verify the mitigating effect of the binder with different amounts of crumb rubber (0%, 10% and 20%) on the particle breakage process. Hence the binder content was kept constant at 6% in the HMA.

The amount of binder in the dense graded hot mix asphalt concrete was determined using the conventional Marshall design procedure with an automatic compactor: 50 blows in each face of the sample using a 4.54 kg hammer falling from a height of 457 mm. The ideal amount of 6% was obtained using straight binder CAP 50-70 and it was kept constant for the asphalt-rubber mixes for the sake of comparison. The initial number of 50 blows was chosen because this HMA was initially intended to be applied in medium traffic highways.

This binder content of 6% is slightly higher than the usual amount (around 5%) obtained for hot mix asphalt concrete manufactured with calcareous aggregate chips, commonly used in the Federal District region of Brazil. This higher asphalt consumption is believed to be related to the porous nature of the recycled aggregate chips used in this research, which had water absorption of about 7.7%.

Besides the rubber content, the authors also investigated the influence of the compaction energy on the crushing of the recycled aggregate particles, by varying the number of hammer blows in each face of the sample (35, 50 and 75). According to the Brazilian standards, the number of hammer blows in each face of the Marshall samples varies with the forecasted traffic during the project life: 35 blows for low volume traffic, 50 blows for medium volume traffic and 75 blows for high volume traffic. Therefore the number of hammer blows varied accordingly for all combinations proposed. In the compaction of the unbound aggregates, it was necessary to use filter paper in both faces of the

samples in order to avoid the loss of fine crushed particles.

The mixing temperatures for the binders and aggregates, besides the compaction temperature are summarized in Table 5. In order to assure statistical significance, each test was repeated two times, thus resulting in a total of 24 samples (4 cases, 3 energies, 2 repetitions). The samples are illustrated in Figure 10. The reader may see the recycled aggregates chips, including pieces of bricks and ceramics in the cut and polished samples.

Table 5 Mixing and compaction temperatures.

Temperatures (°C)	CAP 50-	Asphalt
Binder temperature at	153	170
Aggregates temperature	166	190
Compaction temperature	138	164

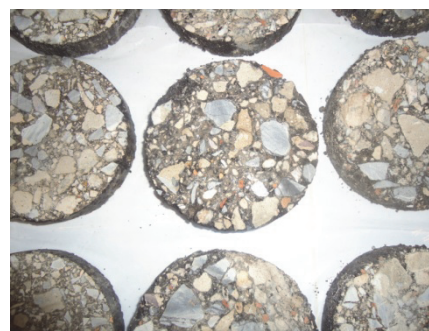


Figure 10 Cut and polished samples.

Binder extraction and final grain size evaluation

After compaction, the samples were extracted from the metal cylinders and immediately taken to a centrifuge (Rotarex) with organic solvent. This facilitated the separation process. The binder extraction process continued with several solvent soaking and centrifuging stages until the aggregates were completely clear. Figure 11 illustrates the aggregate recovery process. The clean aggregates were then subjected to a new sieving process in order to determine any changes in the grading curves due to recycled aggregate particle crushing.

For the quantification of particle breakage in flexible pavements, the Brazilian Department of Transport Infrastructure (DNIT, former DNER) prescribes the so-called Marshall Degradation Index, denoted by ID_M , when the aggregate is unbound (without asphalt binder), or ID_{ML} , when the aggregate is coated with asphalt binder. The test is described in the Brazilian norm DNIT ME-401/99. It uses a standard gradation curve and determines the differences (D_i) between the percentages before and after compaction passing through six sieves with pre-determined openings. In the case of ID_{ML} the asphalt binder should first be extracted using an

appropriate procedure as previously described. The degradation index ID is computed as follows:

$$ID = \frac{1}{6} \left(\sum_{i=1}^6 D_i \right) \quad (5)$$

where D_i is the % passing before compaction minus the % passing after compaction. The following sieve openings are prescribed: 25.4 mm (1"), 12.5 mm (1/2"), 9.5 mm (3/8"), 4.75 mm (#4), 2.0 mm (#10), 0.425 mm (#40) and 0.075 mm (#200).



Figure 11 Extraction of asphalt binder and aggregate recovery.

Results of Marshall compaction degradation

Figure 12 shows the effect of the compaction energy on the degradation of the unbound recycled aggregates. The initial gradation fitted the coarser limit of the gradation envelope known as “gradation C”, prescribed by the Brazilian Department of Transportation Infrastructure (DNIT). In normal cases, the ideal is to aim the center of the envelope when using conventional rock chipped aggregates, but the authors purposely choose to upper limit (lower curve in the figure) in order to account for possible particle crushing of the recycled aggregate. This was based on previous experience using this recycled material for granular pavement base layer [3].

The reader can clearly see the shift of the gradation curve towards the center of the envelope in Figure 12. This shift increases with the increase in compaction energy; however the influence of compaction energy on the unbound particle breakage is more evident when this is quantified by means of the unbound Marshall Degradation index (ID_M). The authors obtained: $ID_M=6.98\%$ for 35 blows; $ID_M=7.81\%$ for 50 blows and $ID_M=8.59\%$ for 75 blows.

The Brazilian standard for dense graded asphalt concrete (ES-031/2006) suggests “tentative” limiting values of $ID_M \leq 8\%$ and $ID_{ML} \leq 5\%$ (supposedly for 75 blows) for rock aggregate chips. However this condition should be verified only in cases when the rock aggregate fails the limit value of 50% for the Los Angeles abrasion loss. There is no standard for

recycled aggregates for HMA yet in Brazil, but the aggregates used in this research presented maximum abrasion loss of 38% [3] and therefore satisfies the requirements of ES-031/2006.

The introduction of asphalt binder leads to a significant reduction of aggregate crushing, irrespective of the compaction energy. This is illustrated in the grain size distribution curve shown in Figure 13 for the cases with 75 blows of compaction energy. Observe that the gradation curves of the HMA are below that of the crushed unbound aggregate (0% asphalt). Again the effect of the binder type on aggregate crushing is better captured by means a single numerical measure such as the IDML. The absolute reduction in crushing index varied between a minimum of 1.0% and a maximum of 3.5%, depending on the type of binder and compaction energy. The relative differences with respect to the original degradation indices vary between 14% and 41%.

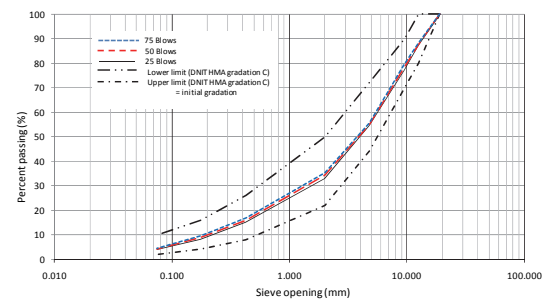


Figure 12 Unbound recycled aggregate. Effect of compaction energy.

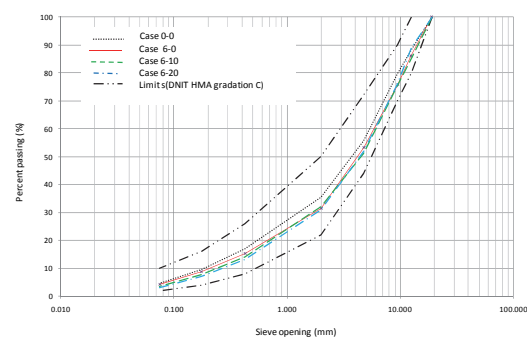


Figure 13 Effect of binder on the crushing index of the recycled aggregate. 75 blows.

Table 6 summarizes the results for all cases investigated. The overall picture is illustrated in Figure 14. Here the effect of compaction energy and type of binder can be clearly appreciated. It is interesting to observe the effect of the crumb rubber on the degradation index of the recycled aggregate. For 75 blows, for instance, the ID_{ML} was 6.47% in

the case with straight binder (case 6-0), 6.15% in the case with 10% of rubber (case 6-10) and 5.05% in the case with 20% of crumb rubber (case 6-20). The differences are statistically significant using analysis of variance (ANOVA). Hence it may be concluded the rubber grains act as elastic springs, absorbing the shock impact from the compacting hammer and therefore reducing the crushing of the recycled aggregates.

Table 6 Marshall degradation index for all cases investigated.

Case B-R	Binder, B(%)	Rubber R(%)	ID _{ML} or ID _M (%)		
			Number of blows		
			35	50	75
0-0	0%	0%	6.98	7.81	8.59
6-0	6%	0%	5.69	6.39	6.47
6-10	6%	10%	5.94	6.07	6.15
6-10	6%	20%	5.63	5.69	5.05

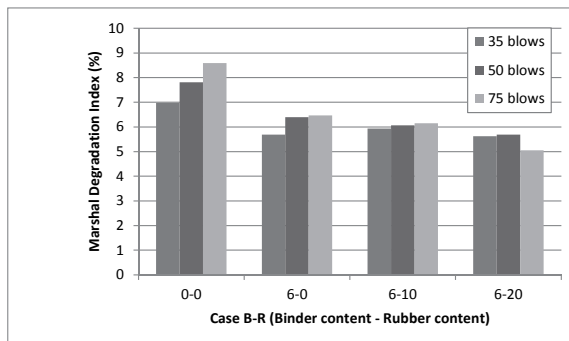


Figure 14 Marshall degradation indices for all cases.

Results of Marshall compaction degradation

Besides particle crushing degradation indices, the most important is to investigate which impact this characteristic might have on the relevant properties of HMA to be used on flexible pavement surface courses. The properties to be investigated depend on the specific requirements of each country. In the case of Brazil, besides Marshall Stability values, the pavement authorities require the determination of indirect tensile strength by means of the Brazilian test. For types of dense HMA were prepared at their optimum Marshall design conditions: (a) Calcareous aggregates with straight CAP 50-70 asphalt binder (the reference mixture); (b) Recycled aggregates CDW-RA and straight CAP 50-70 asphalt binder; (c) Calcareous aggregates with modified AR-17 asphalt rubber binder; (d) Recycled aggregates CDW-RA with modified AR-18 asphalt rubber binder.

Optimum binder contents were 5.1%, 7.3%, 6.8% and 8.9%, respectively. The binder contents are typically higher for asphalt-rubber HMA due to

the higher binder viscosity and therefore thicker binder films coating the aggregates. This is actually observed in cases (b) and (d) and the values are in accordance with typical binder contents published in the AR literature. For these cases, it is also observed a higher binder content for case (d), and the authors attribute this fact to the higher absorption of the recycled aggregates.

The values of indirect tensile strength (ITS) are shown in Figure 15. All mixtures satisfy the strength minimum requirement of 0.65 MPa set by Brazilian standards (DNIT 031/2004 - ES). The HMA using asphalt rubber presented low ITS which not uncommon for this type of binder.

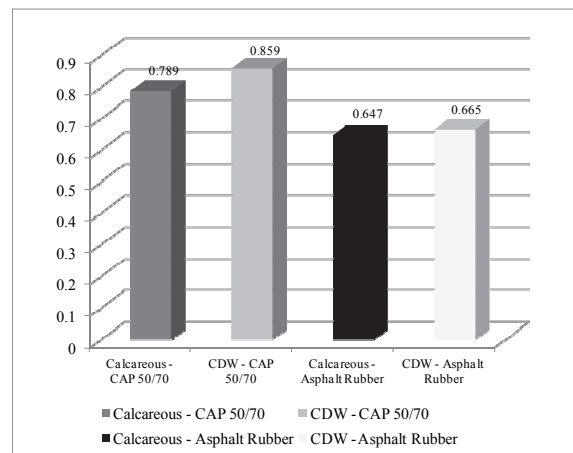


Figure 15 Indirect Tensile Strength.

Indirect tensile stress is an important property related to mixture design or composition. However, from a mechanistic design point of view, the most relevant structural properties are those related to fatigue-life and rutting due to permanent deformations. The later aspect was analyzed using a LCPC traffic simulator prescribed by French standards. The test is illustrated in Figure 16.



Figure 16 Traffic simulation.

The values of permanent deformation after 30.000 load cycles are summarized in Figure 17. The HMA using recycled aggregates, with straight binder and asphalt-rubber, presented the best performances and met the French requirements of permanent deformation inferior to 10%. The conventional mixture using natural calcareous

aggregate normally used in Brasilia presented the highest rutting and does not meet the requirements of French standards. This bad performance is attributed to the poor lamellar shape of the calcareous chips. The performance improves when asphalt-rubber is used due to the better resilience and elastic properties attained with this kind of modified binder.

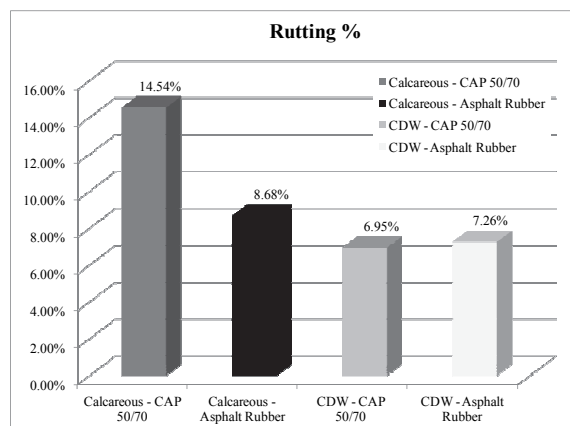


Figure 17 Rutting in LCPC traffic simulator.

CONCLUSIONS

This paper analyses the feasibility of using construction and demolition wastes (CDW) for the construction of different layers of flexible pavements.

Aggregates were recycled from the demolition of the National Stadium in Brasilia, Brazil, and subjected to a series of laboratory test. The results were compared with the requirements necessary for use in granular sub-bases and bases, and also for dense asphalt concrete surface courses.

The loose aggregates met all the requirements set by Brazilian standards to be used in sub-base and base layers, even for the case of pavements of highways with heavy traffic.

When used in dense hot mix asphalts, with conventional and modified asphalt-rubber binders, the recycled mixtures also met all requirements set by Brazilian standards. In some case, such as rutting in traffic simulator, the recycled mixtures performed even better than traditional mixtures using natural calcareous aggregates.

In both cases, granular layers and dense asphalt mixtures, the recycled aggregates tend to show particle breakage. This characteristic was analyzed carefully and some directives may be drawn with respect to compaction conditions: (1) limit the amount of brick and ceramics materials in the CDW; (2) start with a coarser grain size distribution; (3) use lower compaction energy; (4) take water absorption

into consideration in the case of granular layers.

A positive characteristic revealed in this research is the trend of recycled granular layers to gain strength and stiffness with time due to chemical reactions. This should be dependent on the amount of pozzolanic material available in the concrete mortar.

A few words of caution, however: (1) the material used in this research was exceptionally good, but general construction and demolition wastes are quite heterogeneous and must be analyzed case by case; (2) the user should pay attention to the possibility of contamination and perform the additional tests according to environmental regulations (this was done and the material was good); (3) the use of CDW in pavements must be decided on an economical bases subjected the amount available and distances of transportation.

REFERENCES

- [1] H. Rahardjo, K. Vilayvong, E. C. Leong, "Water Characteristic Curves of Recycled Materials," *Geot. Testing Jr.*, v. 34, no. 1, pp. 1–8, 2011.
- [2] F.D.C. Leite, R.D.S. Motta, K.L. Vasconcelos, and L. Bernucci, "Laboratory evaluation of recycled construction and demolition waste for pavements," *Constr and Building Materials*, v. 25, no. 6, pp. 2972–2979, Jun. 2011.
- [3] A.M.J. Gómez, "Experimental study of construction and demolition waste for pavement applications". In Portuguese, Univ. de Brasília, 2011.
- [4] G.M.T. Hendriks, C.F. Janssen, "Reuse of construction and demolition waste in the Netherlands for road constructions," *HERON*, v. 46, no. 2, pp. 109–117, 2001.
- [5] T. Park, "Application of Construction and Building Debris as Base and Subbase Materials in Rigid Pavement," *Transportation Eng.*, Oc, pp. 558–563, 2003.
- [6] D. Marsal, R.J. & Resendiz, *Earth and Earth-Rock Dams (in Spanish)*. Mexico, 1975, p. 546.
- [7] A.M.J. Gómez, M.M.Farias, M.V.R. Souza, and I.F.O. Otálvaro, "Water retention properties of a demolition waste," *Advances in Unsat. Soils*, 2013, pp. 237–241.
- [8] P.V. Lade, J. A. Yamamuro, and P. A. Bopp, "Significance of Particle Crushing in Granular Materials," *Geotechnical Eng.*, vol. 122, no. 4, pp. 309–316, 1996.
- [9] H. Theyse, "A Mechanistics-Empirical Design Model for Unbound Granular Pavement Layers," Univ. of Johannesburg, 2007.
- [10] S. Gupta, D. H. Kang, and A. Ranaivoson, *Hydraulic and Mechanical Properties of Recycled Materials*. MDOT 395,, 2009, p. 94.
- [11] J. Uzan, "Characterization of granular material," *Transp. Research Record*, no. 1022, pp. 52–55, 1985.
- [12] G. Zareh, A. & Way, "Asphalt-Rubber: 40 years of use in Arizona," in *Asphalt Rubber*, 2009, pp. 25–45.
- [13] Dantas Neto, S.A., Farias, M.M., Pais, J.C., Pereira, P.A. and Souza, J.B. "Influence of Crumb Rubber and Digestion Time on the Asphalt Rubber Binders". *Road Materials and Pav. Design*, v. 1, n.2, p. 131-148, 2006.

EFFECTIVE STRESS IN UNSATURATED GRANULAR MEDIA IN THE PENDULAR REGIME

Richard Wan, Sarah Khosravani and Mehdi Pouragha
Department of Civil Engineering, University of Calgary, Calgary, Alberta, T2N 1N4, Canada

ABSTRACT

The paper investigates the mechanical behaviour of a granular material at low moisture content where isolated pendular water bridges (menisci) at the interface of particles give rise to capillary forces in addition to existing interparticle contact forces. During an increase in moisture content, the contribution of the capillary forces is lost, which may give way to a collapse type of failure in the absence of any change in mechanical loading. In this connection, we derive a single effective stress tensor that encapsulates evolving liquid bridges, interfaces, particle packing, and water saturation, thus providing a link to failure through a micromechanical analysis of force transport in an unsaturated pendular-state granular material. Apart from the fact that the stress due to contact forces is dependent on fabric, it is also found that the so-called suction stress arising from liquid bridges is direction dependent, i.e. anisotropic. The latter is at odds with the common belief that suction stress is isotropic. We demonstrate that suction stress is a function of the distribution of liquid bridges, degree of saturation as well as particle packing, and thus provide an adequate effective stress definition to describe both constitutive behaviour and strength of unsaturated media.

Keywords: Unsaturated Soils, Pendular Regime, Anisotropic Suction, Generalized Effective Stress.

INTRODUCTION

Many emerging geotechnical problems implicate unsaturated or variably saturated conditions in soils. As such, unsaturated soils display rich and distinctive deformational behaviours that make their analysis quite challenging. For instance, a slope may succumb to shallow failure above the water table in the unsaturated (vadose) zone due to the loss of capillary effects under variable environmental conditions despite the absence of mechanical loading. The failure that ensues is typically of a collapse type related to changes in internal stresses resulting from capillary effects, pore water pressure, water intake, shrinkage and swelling, as well as strength reduction mechanisms akin to material instability.

In order to predict such failures, we need to understand the mechanics of the governing physical processes so as to build physically and mechanically representative analytical models. The question that is central to the above issue is whether there is a single controlling (constitutive) stress variable that would substitute for the role of the effective stress in the fully saturated conditions. The idea is that such generalized effective stress variable would give the expected irreversible deformations when used in any soil constitutive model based on elastoplasticity. For this to work, the stress variable would have to incorporate various internal processes such as partial pressures of water and air phases in the form of matric suction as well as evolving volume fractions

of the phases such as saturation, and other microstructural quantities such as fabric.

The paper presents such a generalized effective stress variable starting from basic micromechanical formulation of force transport in a three-phase system composed of idealized soil particles and isolated pore water menisci. A tensorial effective stress equation which can be viewed as a generalized Bishop's equation is explicitly written as a function of evolving spatial distribution of water menisci and skeleton fabric. In short, if the matric suction and degree of saturation are known together with fabric of both solid skeleton and water menisci distribution, a generalized effective stress can be computed that will lead to the expected irreversible deformations encountered in unsaturated soils. Other higher order effects are discussed in the context of strength such as the anisotropic nature of the suction stress and the additional surface tension created by the contractile skin formed by interfaces between water menisci and solid particle boundaries.

PRELIMINARIES

The point of departure of this study is the classic example of an unsaturated soil at the low end of water saturation ($S_r < 30\%$) in which the air phase is discontinuous with the solid particles being connected by discrete water menisci. As shown in Fig. 1, deformations in this unsaturated soil can be induced in two ways: (a) applying external mechanical loads such as in a stress increment $\Delta\sigma$,

and (b) increasing the water saturation by ΔS_r . In the former case, it is the increase in interparticle forces caused by the external loads that leads to a reorganization of particles, and hence densification. On the other hand, an increase in water saturation in the absence of mechanical loading erases any capillary forces in the water menisci, thereby disrupting the particle force equilibrium. A densification also ensues in this case due to a modification of force transport within the particle assembly.

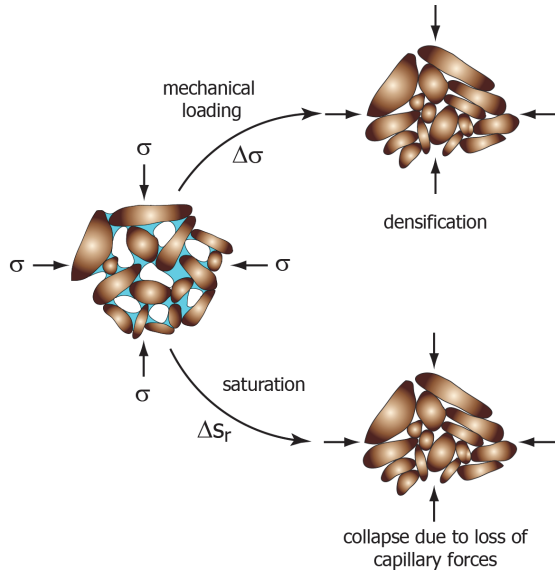


Fig. 1 Permanent skeleton deformations induced by mechanical and hydraulic loadings.

It is interesting to imagine cycles of wetting/drying inducing permanent (plastic) deformations in very much the same way as cycles of loading/unloading. In both cases, there is a single effective stress that would describe the deformations caused by both mechanical and hydraulic processes. Experimental evidences highlighting the above-mentioned observations can be found in [1] and [2] where skeleton plastic strains were measured for both water suction and mechanical loading/unloading cycles. Given the central role of force transport in such processes, a micromechanical formulation is warranted.

Bishop's Effective Stress

The presence of an air phase in an unsaturated soil was examined by Bishop [3] who extended Terzaghi's effective stress principle by intuitively introducing an average pore fluid pressure weighted over the pore air (u_a) and water (u_w) pressures. Using soil mechanics sign convention, i.e. positive stresses mean compression, Bishop's equation is given by:

$$\begin{aligned}\sigma' &= \sigma - [\chi u_w + (1 - \chi) u_a] \\ &= (\sigma - u_a) + \chi(u_a - u_w)\end{aligned}\quad (1)$$

where σ and σ' are the total and effective stresses respectively, and χ is a weighted parameter usually arbitrarily made a function of the degree of saturation S_r . Understanding the capillary (suction) stress as a function of the difference between air and water pressures as well as its dependency on the degree of saturation, void ratio and soil structure is a longstanding problem. This issue establishes a direct connection between constitutive behaviour and strength of unsaturated media in providing an adequate expression for effective stresses.

When arbitrarily confounding χ with the degree of saturation, both the dry and fully saturated conditions can be recovered readily in Eq. (1). However, due to this rather simplified hypothesis, the ability of Bishop's equation to explain the collapse of soils upon wetting has been historically challenged [4]. Also, experimental determination of the so-called effective stress parameter χ over suction ranges and wetting/drying paths is difficult [5]. The above difficulties led to the necessity of circumventing χ by introducing two independent stress variables [6], namely the net stress as $\sigma_{net} = (\sigma - u_a)$ and the matric suction as $s = (u_a - u_w)$ that would control deformations instead of the effective stress. A soil water characteristic curve (SWCC) describing how much water can be retained in the soil through a water saturation versus matric suction relationship is also introduced. With these two independent variables, Alonso et al. [7] developed their celebrated Barcelona Basic Model (BBM) within the framework of critical state and as such the phenomenon of collapse upon wetting could well be described. Many other models followed suit, adding more complexities to the already developed framework [8], [9], [10].

It is essential to know the formal meaning of χ , including its experimental verification over all suction ranges and for both wetting and drying paths. Certainly, the literature abounds with empirical relationships for defining χ [11]. Relationships using one or more parameters of the soil-water characteristic curve such as the air entry value in combination with the residual water content have been proposed; but both experimental and theoretical evidences point that void ratio and microstructural parameters such as soil fabric are also other contributing factors. With a view to account for the link between the microscopic and macroscopic properties of an unsaturated medium, many researchers have worked on the intergranular

stress in the solid skeleton under the action of pore suction and surface tension forces [12], [13], [14], [15].

For the above reasons, it appears that an alternative approach that involves micromechanical analysis is needed to get constitutive insights in unsaturated soils rather than making phenomenological assumptions that may lead to unnecessary empiricism and complexity.

STRESS DERIVATION IN A THREE-PHASE SYSTEM

We consider an ensemble of interacting solid particles in the presence of a water phase and an air phase in a representative elementary volume (REV) in equilibrium with applied loads on its boundaries as shown in Fig. 2.

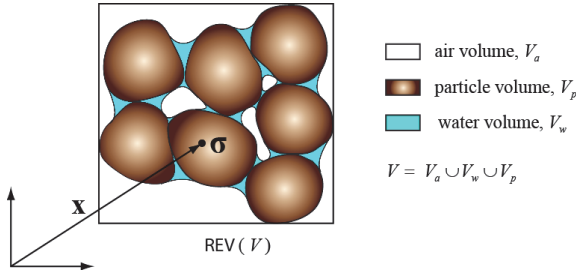


Fig. 2 Representative Element Volume (REV) with solid, air and menisci.

The (Cauchy) stress tensor for such a composite system can be readily calculated as a volume average of the various constituents (phases) just as in the case of a solid body consisting of interacting point masses in the REV of total volume V , i.e.

$$\langle \sigma_{ij} \rangle = \frac{1}{V} \sum_{V^p} \int \sigma_{ij} dV + \frac{V^w}{V} u_w \delta_{ij} + \frac{V^a}{V} u_a \delta_{ij} \quad (2)$$

where V^α , $\alpha = p, w, a$, represents solid particle, water and air phase volumes respectively, N the number of particles and δ_{ij} the Kronecker delta.

In Eq. (2), the stress in both the water and air phases has been considered to be hydrostatic and equal to u_w and u_a respectively. As a result, the last two terms on the right hand side of Eq. (2) simply refer to the partial pressures due to air and water phases with their respective volume fractions applied to each individual pressure.

Next, suppose the above system is idealized as an ensemble of mono-disperse spherical particles of

radius R joined by independent concave liquid bridges with negligible inter-particle contact area, an assumption which will become evident below. Since we are primarily interested in the transport of forces in the REV, we will then focus on the first term on the right hand side of Eq. (2) related to particle interactions. Applying Gauss' divergence theorem to the above-mentioned term as an integration over multiple particles with a closed boundary (due to negligible contacts) for the case of static and weightless media, the following so-called granular stress tensor is obtained:

$$\langle \sigma_{ij} \rangle_g = \frac{1}{V} \sum_{V^p} \int \sigma_{ij} dV = \frac{1}{V} \sum_{\Gamma^p} \int x_i t_j d\Gamma \quad (3)$$

where Γ^p is the surface of a particle, x_i the spatial position of points on Γ^p at which various surface tractions t_j act. Among the various surface tractions exerted on an individual particle, we will find contributions from pair-wise particle contact forces due to external loading, actions of air and water pressures on dry (Γ_d^p) and wetted (Γ_w^p) surfaces respectively, and surface tension forces arising from air/water/solid interfaces formed by water menisci along contour Γ_m at a particle's surface.

It can be readily shown when considering equilibrium of forces on the closed surface of each particle that:

$$\langle \sigma_{ij} \rangle_g = \frac{1}{V} \sum_{\alpha\beta} \int f_j^{\alpha\beta} \ell_i^{\alpha\beta} + \frac{u_a R}{V} \sum_{\Gamma_d^p} \int n_j n_i d\Gamma + \frac{u_w R}{V} \sum_{\Gamma_w^p} \int n_j n_i d\Gamma - \frac{R}{V} \sum_{\Gamma_m} \int T_j n_i d\Gamma \quad (4)$$

where n_j is the outward normal to the particle surface, $f_j^{\alpha\beta}$ is the mutual contact force between particle pair α and β , $\ell_i^{\alpha\beta}$ the so-called branch vector defining to the separation distance between the same two particles, T_j the surface tension forces per unit length related to water meniscus action on Γ_m formed by the intersection of the water meniscus with the particle's surface, L the number of liquid bridges, Γ_w^p is the part of the particle wetted by the liquid bridge, whereas Γ_d^p is the union of all dry parts of the particle's surface. Interestingly, the air/water interface at the particle's surface, seen as a contractile skin, allows the REV to withstand tensile stresses.

The tensor moment of force, defined by the first

term to the right hand side of Eq. (4), as a dyadic product between $\mathbf{f}^{\alpha\beta}$ and $\mathbf{l}^{\alpha\beta}$, is easily identified as the effective stress tensor that is responsible for skeleton deformation. Finally, substituting Eq. (4) into Eq. (2) and regrouping terms, we get a generalized Bishop's effective equation:

$$\sigma'_{ij} = (\sigma_{ij} - u_a \delta_{ij}) + \bar{\chi}_{ij} (u_a - u_w) \quad (5)$$

in which $\bar{\chi}_{ij}$ is a dimensionless tensor that replaces the scalar parameter χ in Bishop's equation, with

$$\bar{\chi}_{ij} = \chi_{ij} + \frac{M_{ij}}{(u_a - u_w)} \quad (6)$$

containing microstructural information through χ_{ij} which describes the spatial distributional nature of the water menisci, i.e.

$$\chi_{ij} = \phi S_r \delta_{ij} + \frac{R}{V} \sum \sum \int_{\Gamma_w^p} n_j n_i d\Gamma_w^p \quad (7)$$

where ϕ is porosity. Also, this tensorial quantity originates from the suction forces acting between particles due to water menisci.

As additional contributions emanating from the water menisci are surface tension forces whose distribution in space is represented by:

$$M_{ij} = \frac{R}{V} \sum \sum \int_{\Gamma_m} T_j n_i d\Gamma_m, \quad (8)$$

a new tensorial quantity, herein coined as the contractile skin tensor, that involves a surface integral of a dyadic products of surface tension force (\mathbf{T}) and radial normal (\mathbf{n}) along the contour of the particle-meniscus interface summed over all particles containing a liquid bridge. This represents a tensor moment of surface tension forces on the particles, easily identified as contractile (cohesive) internal force in addition to other microstructural forces.

Following the newly derived Eq. (5), the effective stress is thus governed by a net stress $(\sigma_{ij} - u_a \delta_{ij})$ and a matrix suction $(u_a - u_w)$ that gives rise to a so-called capillary stress tensor $\bar{\chi}_{ij} (u_a - u_w)$. In keeping the analogy with Bishop's equation, we denote $\bar{\chi}_{ij}$ as the tensorial effective stress parameter. It is noteworthy that the latter leads to a suction stress that is obviously anisotropic in nature following the distribution of the contractile skin surface tension and liquid bridges that in turn vary as a function of the fabric of the granular material, as well as the degree of saturation and

volumetric density of menisci. This engenders a meniscus based shear strength that increases with the anisotropy of the packing. Finally, it can be easily shown that Terzaghi's effective stress is recovered in the saturated case when $S_r = 1$ in which case $\chi_{ij} = \delta_{ij}$ and $M_{ij} = 0$ since the half filling angle α becomes 180° .

CAPILLARY STRESS AND STRENGTH

We next explore the implications of the newly derived effective stress equation (Eq. 5) by considering periodic or regular packings of mono-size spherical particles wetted in the pendular regime.

Isotropic Packings

The REV of a given packing can be described as a unit cell which essentially is the simplest repeating unit of the packing. Two limiting cases, namely simple cubic (SCP) packing (loosest state) and face centered (FCP) packing (densest state) are considered. Figures 3a,b (as insets) show SCP and FCP geometries respectively with liquid bridges between each pair of particles. The objective is to analytically compute the tensorial effective stress parameter $\bar{\chi}_{ij}$ introduced in Eq. (5) as a function of degree of saturation, among other things. Since one liquid bridge is associated with each contact and given the packing is regular, the distribution of liquid bridges is isotropic. Furthermore, if we assume a zero contact angle, the surface tension forces become orthogonal to a radial outward normal vector, and because of symmetry and isotropy conditions there is no contribution from surface tension forces arising from a meniscus/particle interface when summing over all contacts and liquid bridges within the granular assembly. The vanishing of M_{ij} under such conditions is to be expected since it represents a tensor moment of forces in the granular assembly. Thus, in this special case, $\bar{\chi}_{ij} = \chi_{ij}$ is an isotropic tensor with no contributions from surface tension forces. As a result, the diagonal terms of the tensor χ_{ij} being all equal can be identified with Bishop's effective stress parameter χ which can now be analytically calculated at various degrees of saturations for both SCP and FCP configurations. Numerical results are shown in Fig. 3c together with actual experimental data for various soils in the background for comparison purposes. It should be noted that the range of degree of saturation examined in the numerical computations

is based on idealized mono-sized spheres and falls below 30% since the menisci are not allowed to merge to give full water saturation. Also, the experimental data in this range of small degrees of saturation are scarce and not quite reliable, given known difficulties in measuring low suction in soils. The numerical results clearly show that the effective stress parameter χ is invariably a function of packing and water menisci as illustrated in Fig. 3 for the isotropic case.

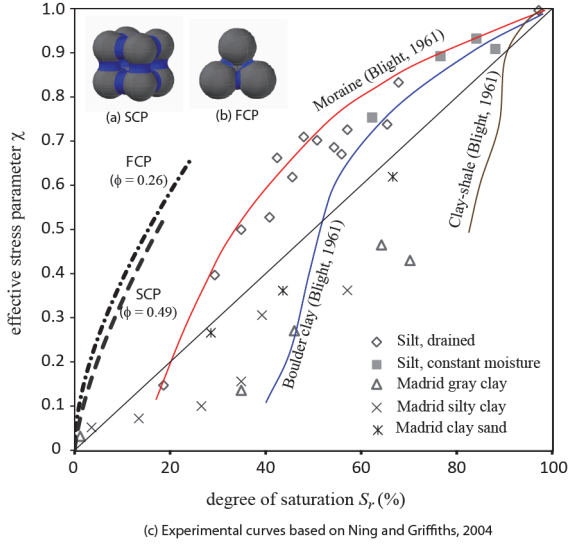
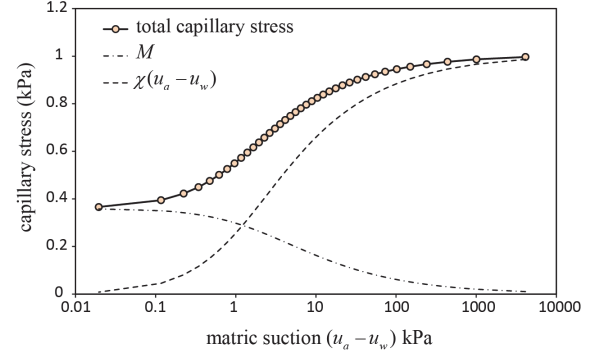


Fig. 3 Computed effective stress parameter versus degree of saturation for various packings and comparison with experimental data.

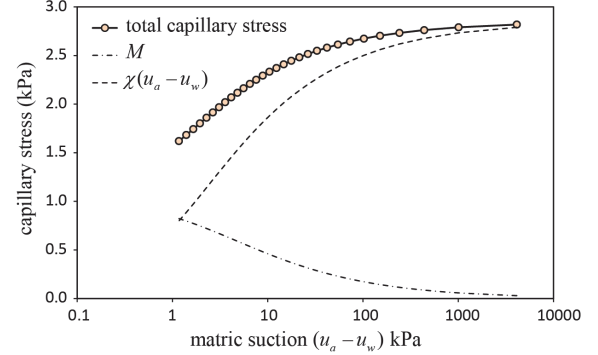
It is also interesting to investigate the relative contributions of the surface tension forces (term M_{ij}) and the suction forces between particles (term χ_{ij}) to the capillary stress $\psi_{ij} = \bar{\chi}_{ij}(u_a - u_w)$ experienced by the unsaturated granular assembly. We thus re-examine the two packings (SCP and FCP) with now a contact angle $\theta = 30^\circ$ and using a particle radius of $R = 0.1$ mm for illustrative purposes. Here again, because the packings are isotropic, the capillary stress tensor is isotropic with the difference that it has both suction and surface tension contributions.

Figure 4a shows that the relative contributions of surface tension and suction cross over at a characteristic matric suction of about 1 kPa for the loose case. At small matric suctions, the surface tension effect arising from the particle/meniscus interface dominates, but is ultimately overtaken by the suction effect at large matric suctions. Referring to the dense case in Fig. 4b, the contribution of surface tension is always smaller than that of suction. This suggests that the contractile effect of surface tension is more likely to be important for loose

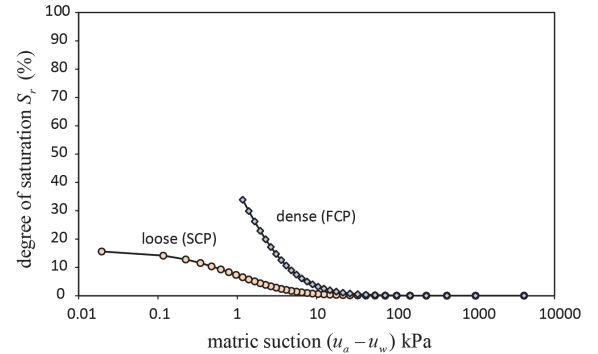
materials and at low matric suctions, i.e. high water saturations when the menisci are well developed.



(a) capillary stress contributions for loose packing



(b) capillary stress contributions for dense packing



(c) soil water characteristic curve for loose and dense packings

Fig. 4 Various computed quantities with saturation.

Finally, Fig. 4c shows the computed soil water characteristic curves (SWCC) for both loose and dense packings. The whole range of saturation cannot be covered as only the pendular regime is herein considered. However, the theory developed in this study shows that the SWCC can indeed be analytically determined rather than using empirical relationships as proposed in the literature [11].

Anisotropic Packings

We now consider anisotropic assemblies of mono-sized spheres through the tensorial effective stress parameter $\bar{\chi}_{ij}$ that confers anisotropic character to the suction stress. A body centred cubic packing (BCC) is evoked with its unit cell at a coordination number of 8 and with reference frame 1, 2 and 3 as shown in Fig. 5. By varying the size of the unit cell through lengths L and L' , a family of anisotropic BCC packings with different particle separations can be generated.

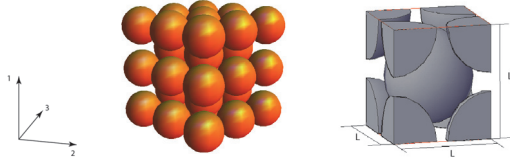


Fig. 5 Body centred cubic packing in various configurations parametrized by interparticle distance L' .

The anisotropy of the family of BCC packings can be readily evaluated through the fabric tensor F_{ij} normally defined as the summation of dyadic product of contact normals $n_i n_j$ throughout the assembly:

$$F_{ij} = \frac{1}{2N} \sum_{i=1}^{2N} n_i n_j \quad (9)$$

In principal axes relative to reference frame (1,2,3) in Fig. 5, the fabric components (F_1, F_2, F_3) for different values L' can be calculated and are given in Table 1. We herein introduce the parameter 'a' [16] to describe packing anisotropy, i.e.

$$a = \frac{5}{2} \frac{(F_1 - F_3)}{(F_1 + F_2 + F_3)} \quad (10)$$

Table 1 Values of components of the tensor F_{ij} according to packing

L'	F_1	F_2	F_3	a
2.10	0.276	0.362	0.362	-0.22
2.20	0.335	0.332	0.332	0.01
2.3094	0.333	0.333	0.333	0
2.40	0.360	0.320	0.320	0.1
2.50	0.391	0.305	0.305	0.21
2.60	0.422	0.289	0.289	0.33
2.70	0.456	0.272	0.272	0.46

Evolution of capillary stress

The components of fabric as obtained from Eq. (9) and given in Table 1 allow us to compute analytically the effective stress parameter $\bar{\chi}_{ij}$ through Eqs. (6) and (7) for various anisotropic packings. These relations ultimately define the dependence of the effective stress on degree of saturation, fabric and menisci distribution as represented in Eq. (5).

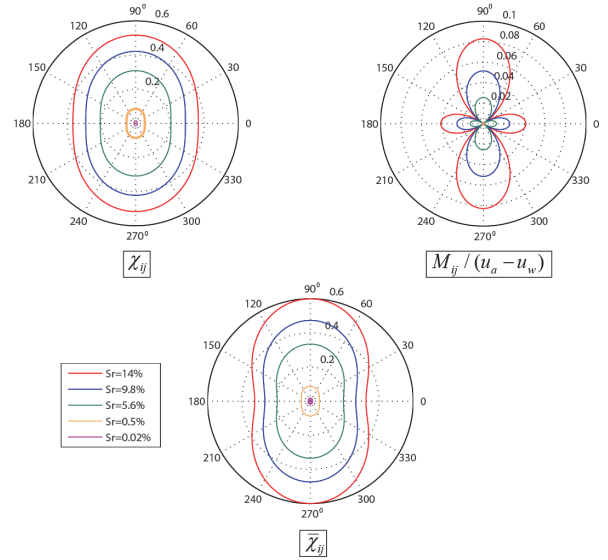


Fig. 6 Polar plot of various parameters controlling capillary stress and anisotropy

Figure 6 illustrates the evolution of various tensorial parameters $\bar{\chi}_{ij}, \chi_{ij}, M_{ij} / (u_a - u_w)$ that control the capillary stress ψ_{ij} in a BCC packing with cell spacing $L' = 2.7$ as a function of degree of saturation. The anisotropic nature of suction is clearly demonstrated with the major and minor principal directions of the capillary stress being aligned with the vertical direction 1 (axial) and 2 (lateral) respectively.

The capillary stress component in each one of the principal directions is further shown in Fig. 7 as a function of matric suction. As the wetting angle is small, the amount of capillary stress induced by surface tension forces (M_{ij}) is smaller in comparison with the capillary stress due to suction forces $\chi_{ij}(u_a - u_w)$.

Finally, Fig. 8 shows the totally induced anisotropic capillary stress which decreases with increasing degree of saturation, as expected.

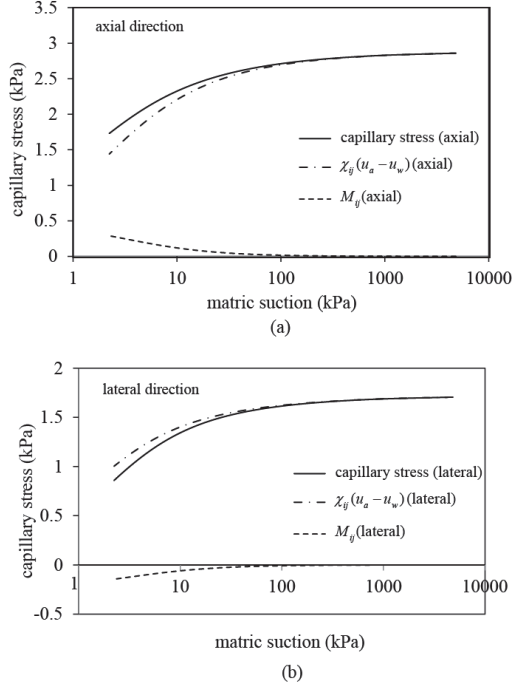


Fig. 7 Principal capillary stresses with various contributions in axial and lateral directions.

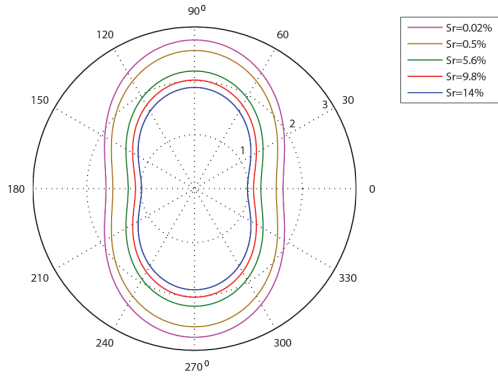


Fig.8 Decrease in capillary stresses following increased degree of saturation.

Evolution of degree of anisotropy and link to strength

There is a compelling connection between the meniscus-based anisotropic capillary stress in unsaturated granular soils and the shear strength contribution that it engenders. As an extension to the previous discussions we next analyze the evolution of such anisotropy with the degree of saturation by introducing an anisotropy factor a_ψ similar to what was defined for contact fabric, i.e.

$$a_\psi = \frac{5(\psi_1 - \psi_3)}{2 \text{trace}(\psi_{ij})} = \frac{5(\psi_1 - \psi_3)}{2(\psi_1 + \psi_2 + \psi_3)} \quad (10)$$

The origins of such factor are in the computation of the ratio of mean stress p to deviatoric stress q in a granular assembly ($\eta = q/p$) with the anisotropies of microscopic variables such as interparticle force and contact normal distribution. Thus, the anisotropy factor (a_ψ) represents an analogous fictitious ‘friction angle’ as a result of water menisci. As illustrated in Fig. 9, the meniscus-based anisotropy (a_ψ) for each packing coincides with packing anisotropy (Table 1).

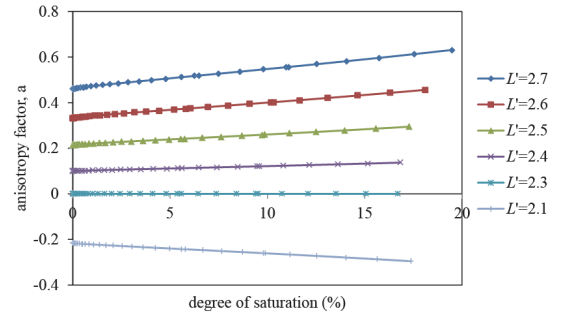


Fig. 9 Meniscus-based anisotropy with saturation for various anisotropic BCC packings.

Upon wetting, the degree of saturating increases since liquid bridges develop between particles, resulting into an increase in anisotropy of the capillary stresses following the anisotropy of the packing in the background. This increase in anisotropy is induced by the enlargement of the wetted contours of the menisci with higher degrees of saturations, while at the same time, the capillary stresses decrease (Fig. 8). The rate of increase in meniscus-induced anisotropy is greater the more prominent the anisotropy of the packing is, i.e. increasing values of L' in Fig. 9. For the isotropic packing case ($L' = 2.3$), there is obviously no meniscus-based anisotropy induced upon wetting.

Contrary to the assumption classically made with regard to isotropic pore pressures in unsaturated soil, the derived tensorial equation for effective stress shows the directional nature of the capillary stresses induced by liquid bridges. One of the consequences of this finding is that the meniscus-based anisotropy can increase drastically with water saturation the more anisotropic the packing is. As such, any perturbation to such state of high anisotropy in combination with a decrease in capillary stress may make the unsaturated sample succumb to sudden collapse. This combined increase in capillary stress anisotropy and decrease in capillary stress components with saturation can be made the basis of collapse failure in unsaturated samples in the absence of any increase in external mechanical loads.

CONCLUSIONS

The physical significance of the effective stress parameter χ as originally introduced in Bishop's equation has been formally derived through micromechanical analysis of a three phase medium (air/water/solid) with isolated water menisci, i.e. in the pendular regime. It turns out that χ is generally not a scalar, but is rather a tensorial quantity described that is generally a function of degree of saturation, particle packing as well as water menisci distribution. This leads to the possibility of the so-called capillary stress to be anisotropic in nature as dictated by the spatial distribution of water menisci and fabric of the solid skeleton evolving during deformation history. The capillary stress is shown to have two contributions: one emanating from suction between particles due to air-water pressure difference, and the second arising from surface tension forces along the contours between particles and water menisci.

Although the latter may be small at small water saturations, it becomes prominent as water saturation increases. The implication is that granular materials in the pendular regime can engender an internal suction based shear (deviatoric) effect under even isotropic loading. Also, this issue becomes particularly relevant when studying the material instability behaviour of unsaturated soils in the pendular regime where failure is characterized by a sudden collapse. In this paper, it is demonstrated that the more anisotropic the packing and capillary stress are, the higher the potential for collapse upon saturation. It is seen that the capillary stress tensor, while decreasing in magnitude upon wetting, also evolves with an increase in anisotropy that leads to a collapse failure in the absence of mechanical loading.

ACKNOWLEDGEMENTS

The authors acknowledge the Natural Science and Engineering Research Council of Canada and the Computer Modelling Foundation for their financial support through a NSERC-CRD project.

REFERENCES

- [1] Sivakumar V, "A Critical State framework for unsaturated soils", PhD thesis, University of Sheffield, UK, 1993.
- [2] Sharma RS, "Mechanical behaviour of unsaturated highly expansive clays, PhD thesis, University of Oxford, UK, 1998.
- [3] Bishop AW, "The principle of effective stress", *Teknisk Ukeblad*, Vol. 106, No. 39, 1959, pp. 859-863.
- [4] Jennings JE, Burland JB, "Limitation to the use of effective stress in partly saturated soils", *Géotechnique*, Vol. 12, No. 2, 1962 pp. 125-144.
- [5] Blight GE, "Effective stresses evaluation for unsaturated soils", *J. of Soil Mechanics and Foundations Division, ASCE, USA*, Vol. 93, 1967, pp. 125-148.
- [6] Fredlund DG, Morgenstern NR, "Stress state variables for unsaturated soils", *J. Geotech. Eng. Div., ASCE*, Vol. 103, No. 5, 1977, pp. 447-466.
- [7] Alonso EE, Gens A, Josa A, "A constitutive model for partially saturated soils", *Géotechnique*, Vol. 40, No. 3, 1990, pp. 405-430.
- [8] Wheeler SJ, Sivakumar V, "An elasto-plastic critical state framework for unsaturated soil", *Géotechnique*, Vol. 45, No. 1, 1995, pp. 35-53.
- [9] Cui YJ, Delage P, "Yielding, plastic behaviour and critical state of a collapsible unsaturated silty soil", *Géotechnique*, Vol. 46, No. 2, 1996, pp. 465-477.
- [10] Khalili N, Loret B, "An elasto-plastic model for non-isothermal analysis of flow and deformation in unsaturated porous media: formulation", *Int. J. Solids Struct.*, Vol. 38, 2001, pp. 8305-8330.
- [11] Garven E, Vanapalli SK, "Evaluation of empirical procedures for predicting the shear strength of unsaturated soils", *American Society of Civil Engineers Geotechnical Special Publication No. 147*, Vol. 2, 2006, pp. 2570-2581.
- [12] Pietruszczak S, Pande GN, "On the mechanical response of partially saturated soils at low and high degrees of saturation", *Numerical Models in Geomechanics*, 1995, pp 33-38, Balkema, Rotterdam.
- [13] Cho G, Santamarina J, "Unsaturated particulate materials, particle-level studies. *Journal of Geotechnical & Geo-environmental Eng.*", 2001, pp. 84-96.
- [14] Molenkamp F, Nazemi A, "Micromechanical considerations of unsaturated pyramidal packing", *Geotechnique*, Vol. 53, 2003, pp. 195-206.
- [15] Lu N, Likos W, "Suction stress characteristic curve for unsaturated soil", *Journal of Geotechnical and Geo-environmental Eng.*, Vol. 132, 2006, pp. 131-142.
- [16] Radjai F, "Particle-scale origins of shear strength in granular media", arXiv:0801.4722v1 [cond-mat.soft].

RECENT GEOTECHNICAL RESEARCH ADVANCES IN UNIVERSITY PUTRA MALAYSIA

Bujang B.K.Huat¹ and Afshin Asadi²

¹Department of Civil Engineering, Faculty of Engineering, Universiti Putra Malaysia, 43400 UPM, Serdang, Selangor, Malaysia

²Housing Research Centre, Faculty of Engineering, Universiti Putra Malaysia, 43400 UPM, Serdang, Selangor, Malaysia

ABSTRACT

This paper aims to present the recent geotechnical research advances in the field of geotechnical engineering in Universiti Putra Malaysia as follows; (i) Electro-biogrouting method for soft soil stabilization. In this method, the live bacteria or their production are induced by electrical gradient. The soft soil is then stabilized through a physicochemical reaction. (ii) Soil improvement using nano particles, in this method, the effect of nano SiO₂ on residual soil treated by cement was investigated. The results showed that nano SiO₂ increased the shear strength of the soil effectively. (iii) Effect of coir fiber on flexural strength of the soil was investigated to evaluate the mechanical properties of reinforced marine soft clay as earth structures. The results revealed that the coir fiber increased the flexural strength of the marine soil. (iv) Effect of acid rain on engineering properties of soil was investigated. Significant changes in engineering properties of soils under effect of acid rain were shown.

Keywords: Electro-biogrouting, Bacteria, Nano particle, Shear strength, Coir fibre, Flexural strength, Acid rain

ELECTRO-BIOGROUTING STABILIZATION OF SOFT SOILS

This project was carried out by Hamed Keykhah under supervision of Prof. B.K.Huat and Dr. Afshin Asadi. A new method of soil stabilization was developed. Electro-biogrouting method is a novel combined techniques of electrokinetic and biogrouting /biocement. The most advantages of this invention are explained as follows:

(i)The method is able to be applied in fine grain soils with low permeability. The method uses the electrical gradient to flow and transport of bacteria, *Bacillus pasteurii*, and essential materials (i.e. urea and calcium chloride) instead of hydraulic gradient in the soil.

(ii)The bacteria are transported in the soil. The most bacteria have a net negatively charged surface at high pH values and a net positive charge at low pH value due to a number of polymers, which carry ionizable groups in the membrane. Since electrokinetic technique is capable to induce charged particles and biocolloids such as bacteria, it is able to distribute bacteria in porous media of soils uniformly by electrophoresis.

(iii)This method is able to control the direction of materials movement in soil fabric. The distribution of bacteria, urea, Ca⁺² and CO₃⁻² in EK depends on position, power and the period of applied electrical

gradient. The uniform injection can be acquired by selection of appropriate position of electrodes. Therefore, it is possible to control the direction of the materials movement.

(iv)In this method, the pH can be controlled to optimize the condition for the culture media of the bacteria. During EK process, H⁺ and OH⁻ are generated from the anode and the cathode, respectively. The pH is reduced at the anode, and increases at the cathode. Since, the growth and activity of the bacteria are often pH dependent, this EK system is able to regulate appropriate environment for them.

(v)In this method, the oxygen released in EK helps the bacterial activity. The electrolyzing of water in the anode and cathode chambers cause to release oxygen and hydrogen. Since, the applied bacteria are aerobic and need O₂ for growth and activity, the system is able to regulate appropriate environment for them.

The EK not only is capable to transport the bacteria in soils, but also is able to transport CO₃⁻² which is the production of bacterial activity in soil. The hydrolysis of urea by bacteria releases CO₃⁻². Then, the Ca⁺² and CO₃⁻² can be injected in the soil by electrokinetics, resulting precipitation of CaCO₃ [1]-[5].

There are two possible methods as follows;

(a) Elector-biogrouting by bacteria injection; we injected 2M CaCl_2 and 1M urea solution in the anode chamber, waiting to be transferred by electromigration and electroosmotic procedures completely in the soil for 72 hours. Then, the live culture bacteria were added with optical density around 0.5 into the cathode chamber to transport as particles by electromigration process. When the bacteria were exposed to the urea, they released the enzyme and made bicarbonate (CO_3^{2-}) which quickly joined to the calcium ions (Ca^{+2}) and precipitate CaCO_3 (Fig.1).

(b) Elector-biogrouting by bacterial products injection; we initially added 2 M CaCl_2 into the anode chamber to be induced from anode to cathode by electromigration. Then, the mixed bacteria and urea solution were added to the cathode chamber. The bacteria quickly released enzyme to hydrolyze urea, and the bicarbonate (CO_3^{2-}) is produced in the cathode chamber. Then, the bicarbonate which has a negative charge was moved directly to the anode in the soil. Finally, the calcium carbonate was precipitated in the soil (Fig.1).

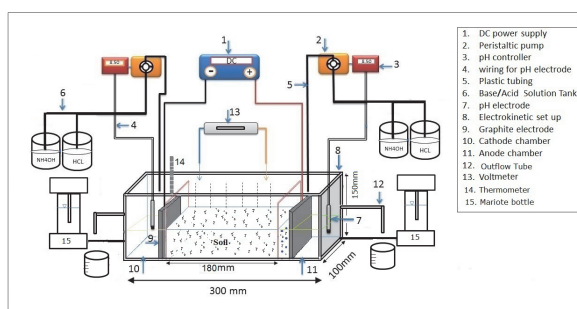


Fig.1. a) Schematic diagram of Electro-biogrouting setup



Fig.1. b) Electro-biogrouting setup

Figure 2 shows the undrained shear strength changes of the soil under electrical potential of 5-10 mV/cm after 72 hours EBM treatment in two different described methods. The undrained shear strength was measured using a vane shear apparatus. The study revealed that the method (b) was more effective than method (a) because of some reasons as follows [5]-[10];

- (i) The usage of bacterial production (CO_3^{2-}),
- (ii) The movement of CO_3^{2-} ions in an electrical field was easier than the bacterial movement in the soil, and
- (iii) Reduction of bio clogging as a result of bacterial concentration in porous media.

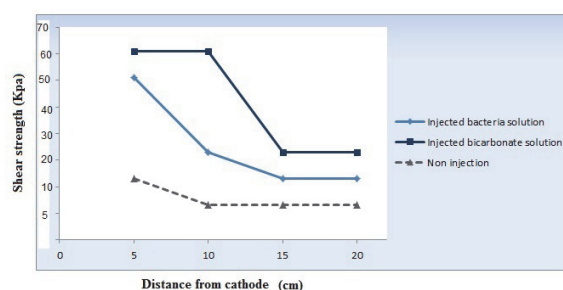


Fig.2. Undrained shear strength of the soil before and after treatment

EFFECT OF NANO PARTICLES ON PROPERTIES OF RESIDUAL SOIL

The research was conducted by Sayed Hessam Bahmani, MSc student, under supervision of Prof. Bujang B.K.Huat and Dr. Afshin Asadi. Nanoparticles are small objects, which are sized between 1 and 100nm, Because of extremely small size in nano-scale (10^{-9}m) and ultra-high surface area, some nano particles show unique properties that can improve physical and mechanical properties of the materials. Engineered nanomaterials can be categorized into four groups as follows; (i) carbon-based materials, usually including fullerene, single walled carbon nanotube (SWCNT) and multi walled carbon nanotube (MWCNT); (ii) Metal-based materials such as quantum dots, nanogold, nanozinc (nano-Zn), nanoaluminum (nano-Al), and nano scale metal oxides like SiO_2 , TiO_2 , ZnO and Al_2O_3 ; (iii) dendrimers, which are nano-sized polymers built from branched units capable of being tailored to perform specific chemical functions; and (iv) composites, which combine nanoparticles with other nanoparticles or with larger bulk-type materials. The first two types are common and are often studied.

Silicon dioxide as a nanoparticle, also known as silica, is the oxide product of silicon (SiO_2) with commonly spherical morphology (Fig. 3) [11]-[15].

A typical residual soil, which is residual granite soil in Malaysia, the SiO_2 nanoparticles and ordinary Portland cement (OPC) were used in this study. The nano particles and distilled water were mixed by stirrer. The mixture was then sprayed on the different mix proportions for exchanging moisture among the particles, forming homogenous blend, and prevent agglomeration of nano particles. The mixtures were kept in sealed plastic bags for 24hours. Finally, geotechnical tests were carried out on the specimens.



Fig. 3 SiO_2 nano particles

Effect of Nano Particles on Engineering Properties of Soil

The effect of cement and nanoparticles on liquid limit (LL) and plasticity index (PI) of the soils are shown in Fig. 4. It can be observed that addition of cement initially increased the LL and PI. However, higher percentages of the additives have led to reduction in PI. In this context, it is illustrated that reduction in the plasticity of cement/nanoparticles stabilized-residual soils was as a result of the increase in LLs and PLs. Variation of OMC and MDD weight of the soils at different mixture content are shown in Fig. 5. It can be clearly seen that the addition of cement and nano particles led to an increase in OMC. The increasing OMC is may be caused by the additional water held with the flocculent soil structure resulting from cement and cement/nanoparticles. It also can be observed that MDD of the treated soils decreased slightly as a result of cement and nanoparticles treatment.

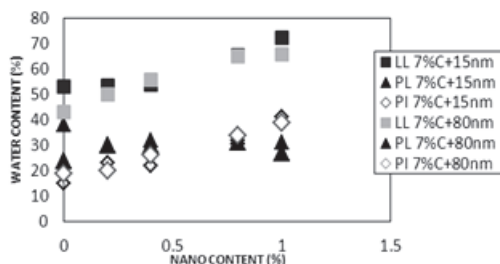


Fig. 4. Effect of nano particles SiO_2 on Atterberg limits of soil treated by cement

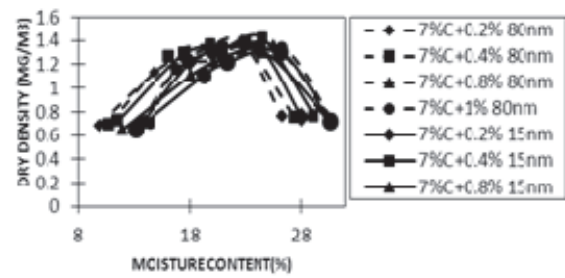


Fig. 5. Variation of compaction characteristics soil treated by cement and nano particles

Effect of Nano Particles on Unconfined Compressive Shear Strength of Soil

The effect of the addition of SiO_2 nanoparticles (15 and 80 nm) and cement on the unconfined compressive strength of the soil is shown in Fig. 6. It can be observed that both cement and nanoparticles led to increase the shear strength and lower SiO_2 nanoparticles ratios in both sizes 15-80nm resulted in higher strengths.

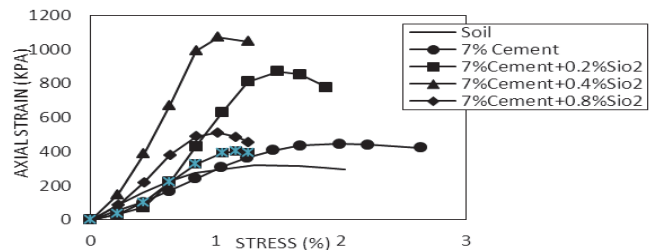


Fig.6 Variation of shear strength characteristics soil treated by cement and nano particles

The addition of nano particles (SiO_2) in Portland cement marks a novelty in the high performance soil stabilization technology. The nano particles silica behaved not only as a filler to improve soil/cement microstructure, but also as a promoter of pozzolanic reaction by transforming portlandite into C-S-H gel (Fig. 7) [15]-[20].

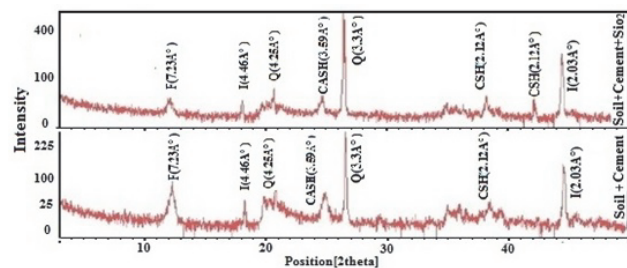


Fig. 7 XRD from soil treated by cement and nano particles

EFFECT OF COIR FIBRE ON FLEXURAL STRENGTH OF SOFT MARINE SOIL

The research was conducted by Vivi Anggraini, Ph.D student, under supervision of Prof. Bujang B.K.Huat and Dr. Afshin Asadi. Soft marine clay deposit used in the construction of earth structures has recently come under focus because of its potential to resist cracking of the compacted layer after construction. Due to that soft marine clay is weak in tension and gives rise to the risk of certain areas of the layer being subjected to flexure, a testing program was undertaken to determine the effects of compaction and internal reinforcement on the potential failure of clay liners. A schematic illustration of localized subsidence due to post closure decomposition for a landfill site is shown in Fig. 8 along with the flexural distress caused due to differential settlements.

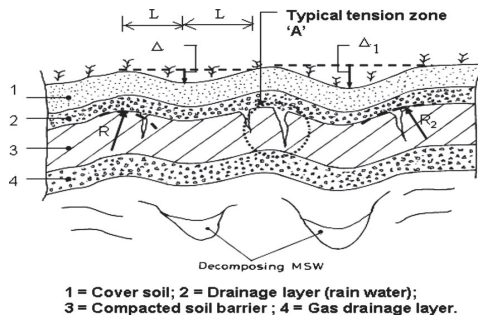


Fig.8 Flexural Distress in clay-based cover system.(Viswanadham, 2010)

The stabilization of soft marine clay soil with randomly inserted natural fibres for earth structures applications has been investigated in this research. The methods of in-situ reinforced soil are based on the principle of stabilizing natural soils by the inclusion of elements capable of resisting forces associated with tension and/or bending [21]-[25].

Three-point bending test is a conventional mechanical test which is generally used for concrete specimens. It represents the case of a plane beam placed on two simple supports and subjected to a vertical load at the middle. The test is attracting due to the fact that the Young's modulus obtained from the three-point-bending tests may represent the behaviour of the earth platform under surface loads.

Bending moment is equal to:

$$M = \frac{FL}{4} \quad (1)$$

Where F is the maximal applied load; L is distance between the supports.

Flexural stress for circular section of the specimen is equal to:

$$\sigma_f = \frac{FL}{\pi r^3} \quad (2)$$

Where r is the radius of the specimen.

Then the Young's modulus of the specimen is calculated as follows;

$$E = \frac{FL}{12\pi r^4 y} \quad (3)$$

Where y is the deflection at the centre of the beam.

Effect of Coir Fibres on Mechanical Properties of Soft Marine Clay Soil

The load deflection response of the soil fibre inclusion subject to extended deformation is shown in Fig 9.

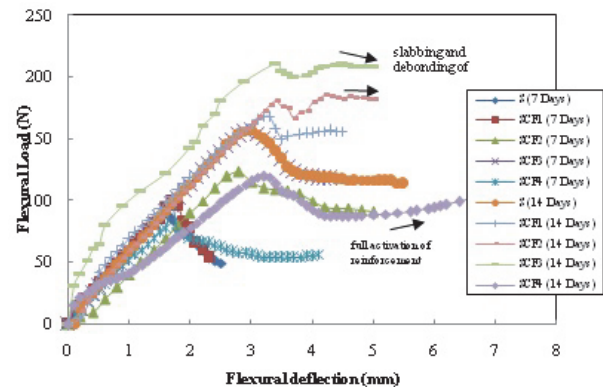


Fig. 9 Flexural load-extension relationship with various fibre contents at 7 and 14 day-curing

This initial peak load is directly related to the flexural tensile strength of the coir fibre reinforced soft marine clay, the region in which pronounced cracking occurs within the middle third of the specimen. An increasing the fibre content enhances the degree of plastic straining at constant load, with the load deflection response a ductile plastic deformation.

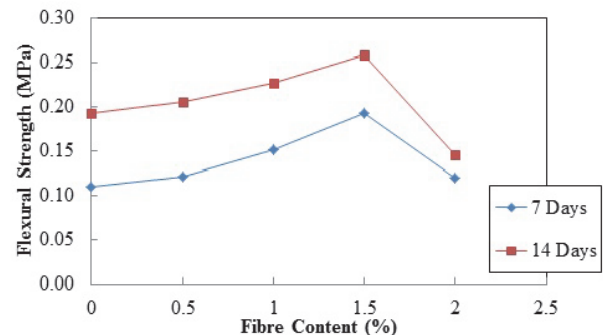


Fig 3 The values of flexural strength of specimen tested at 7 and 14-days curing

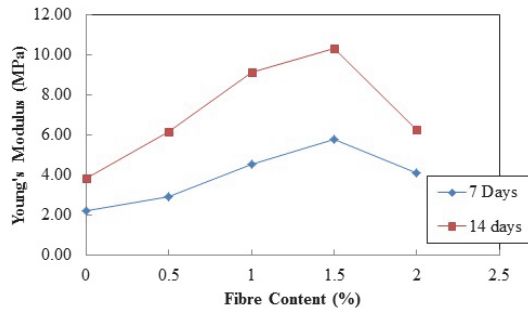


Fig. 11 The values of young's modulus of specimen tested at 7 and 14 day- curing

From the results presented in Fig 9, the computed flexural strength from in Eq.(1) and (2) was evaluated based on the maximum applied load. The distance between the supports applied was 60 mm specimens and radius 25 mm applied for all specimens. Young's modulus of the specimen was calculated from the deflection of the specimen after testing in Eq (3). The maximum value of flexural strength and young's modulus are shown in Fig 10 and Fig.11. Due to the slab action of the soil layers, the result of flexural tension test was appropriate to evaluate the mechanical properties of reinforced marine soft clay as earth structures [26]-[28].

EFFECT OF ACID RAIN ON ENGINEERING PROPERTIES OF SOILS

This research is being conducted by Zeinab Bakhshipour, PhD student, under supervision of Prof. Bujang. B.K.Huat, and Dr. Afshin Asadi. Acid rains is a broad term referring to a mixture of wet and dry deposition (deposited material) from the atmosphere containing higher than normal amounts of nitric and sulfuric acids. The precursors, or chemical forerunners, of acid rain formation result from both natural sources, such as volcanoes and decaying vegetation, and man-made sources, primarily emissions of sulfur dioxide (SO_2) and nitrogen oxides (NO_x) resulting from fossil fuel combustion. Acid rain occurs when these gases react in the atmosphere with water, oxygen, and other chemicals to form various acidic compounds. The result is a mild solution of sulfuric acid and nitric acid with an acidic pH lower than 5.6 (Fig. 12)[29]-[33].

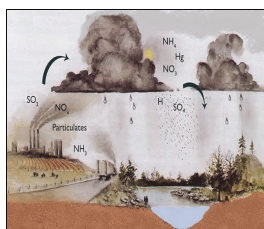
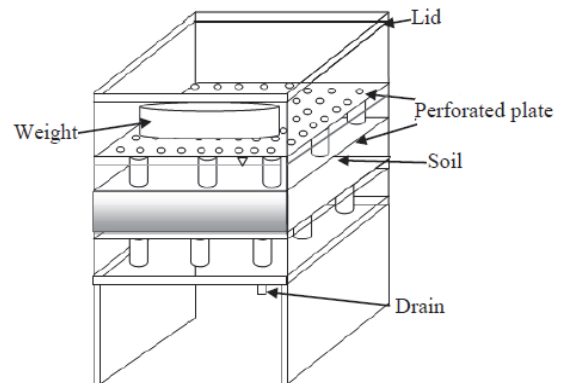
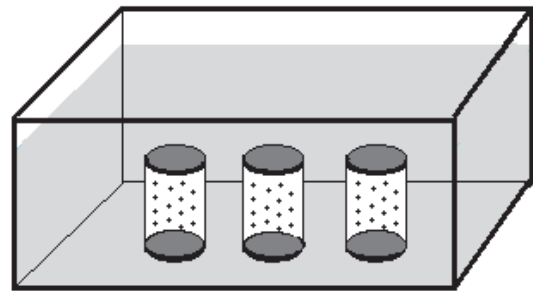


Fig. 12 Formation of acid rain in the environment by anthropogenic sources

Artificial acid rain used in this experiment was prepared by diluting sulfuric acid H_2SO_4 and nitric acid HNO_3 . Tests were conducted at five pH levels: pH 2.0, pH 3.0, pH 4.0, pH 5.0 and pH 5.6, which were arranged using 1N H_2SO_4 and HNO_3 in distilled water. Two test methods of infiltration and soak methods were selected to investigate the physico-chemical and engineering behavior of soils eroded due to acid rain. Infiltration and soak tests simulating the erosion process of soils due to acid rain were made for this study.



(a) Infiltration setup



(b) Soak setup

Fig. 13 Experimental setup for (a) infiltration and (b) soak test

Fig. 14 and 15 show the consistency and unconfined compressive shear strength of the soil in different pH respectively. The liquid limit significantly decreased in the artificial acid rain with pH 2.0 because of a large of exchangeable cations were exchanged. In addition, the diffuse double layer became thinner because the concentration of the water-soluble cations increased. The unconfined compressive strength of the soils increased with an increase in pH. The reason for this is the formation of the crystalline CaSO_4 and CaCO_3 , which may plug the pores of the specimens to cement the soil particles together.

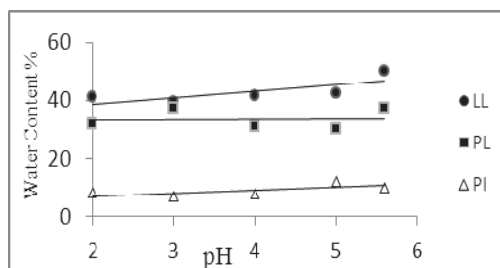


Fig. 14 Soil consistency in different pH value

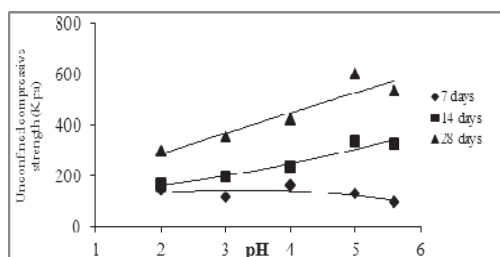


Fig. 15 Unconfined shear strength of soil in different pH value

The infiltration and soak methods were used in this study, to illustrate the erosion process of the soil due to acid rain. We have obtained some evidence of the engineering behaviors of acidified soils by means of an experiment simulating the erosion process. This data may be helpful in assessing the damaged condition of the soil due to acid rain and to estimate the effects of acid rain on soil in the future. The erosion by acid rain caused an increase in the sensitivity ratio of the soils. There was a comparably increase in the liquid limit of the soils. An increase in the unconfined compressive strength of them could be observed in higher ranges of pH. We are planning to investigate the underlying behavior of different soils and their mechanisms under effect of acid rain with different compositions. The physico-chemical properties of the soils will also be investigated in this project. It can be predicted that the effect of acid rain on the properties of soils will become serious if the rainwater is further acidified due to industrialization in the future. However, the project is ongoing further information will be released in the future.

CONCLUSION

This paper presents the recent geotechnical research advances in the field of geotechnical engineering in Universiti Putra Malaysia. Concurrently, there are some research projects as follows; (i) Electro-biogrout method for soft soil stabilization which is a new method. The live bacteria or their production are injected to the soil using an electrical gradient. The soft soil is then stabilized through the CaCO_3 precipitation. (ii) Soil

improvement using nano particles. In this study, the effect of nano SiO_2 on residual soil treated by cement was investigated. The results showed that the nano SiO_2 increased the shear strength of the soil effectively. (iii) Effect of coir fiber on flexural strength of the soil was investigated to evaluate the mechanical properties of reinforced marine soft clay as earth structures. The results revealed that the coir fiber increased the flexural strength of the marine soil well. (iv) Effect of acid rain on engineering properties of soil. In this study, effect of acid rain on soil consistency and shear strength of soil are being investigated. However, the research is ongoing and the outcomes will be released in the future[34]-[38].

ACKNOWLEDGEMENTS

Financial supports from research grants No.5527094 (ERGS), No.5524133 (FRGS), and No.9346000 (RUGS), for conducting these experiments are gratefully acknowledged.

REFERENCES

- [1] Acar YB, Gale RJ, Hamed J and Putnam G. "Electrochemical processing of soils; theory of pH gradient development by diffusion and linear convection". Journal of Environmental Science and Health, Part (a); Environmental Science Vol. 25(6), 1990, pp. 687-714.
- [2] Achal V, Mukherjee a, Basu PC, & Reddy MS "Strain improvement of *Sporosarcina pasteurii* for enhanced urease and calcite production". Journal of industrial microbiology & biotechnology, Vol. 36 (7), 2009, pp. 981-8.
- [3] Alshawabkeh AN, Sheahan TC, "Soft soil stabilization by ionic injection under electric fields". Ground Improvn. Vol 7, 2003, pp.177-185.
- [4] Asavadorndej P, Glawe U, "Electrokinetic strengthening of soft clay using the anode depolarization method. Bull". Eng. Geol. Environ., Vol. 64, 2005, pp. 237-245.
- [5] Chang-Yu Ou, Shao-Chi Chien, and Hsuan-Hsiang Chang, Soil improvement using electroosmosis with the injection of chemical solutions: field tests . Can. Geotech. J. Vol. 46, 2009, pp.727-733.
- [6] De Jong JT, Fritzges MB, and Nusslein, K, "Microbially induced cementation to control sand response to undrained shear." J. Geotech. Geoenviron. Eng., Vol. 132(11), 2006, pp. 1381-1392.
- [7] Whiffin VS, "Microbial CaCO_3 precipitation for the production of biocement." Ph.D. thesis, School of Biological Sciences and Bio-

- technology, 2004, Murdoch Univ., Perth, Australia.
- [8] Whiffin VS, Van Paassen LA, and Harkes MP "Microbial carbonate precipitation as a soil improvement technique." *Geomicro- biol. J.*, Vol. 24 (5), 2007, pp. 417–423.
 - [9] Van Paassen LA, Daza CM, Staal M, Sorokin DY, Van der Zon W, and Van Loosdrecht MC M, "Potential soil reinforce- ment by microbial denitrification." *Ecol. Eng.*, Vol. 36 (2), 2010, pp. 168–175.
 - [10] Van Paassen LA, Harkes MP, Van Zwieten G A, Van der Zon WH, Van der Star WRL, and Van Loosdrecht, MCM, "Scale up of BioGrout: A biological ground reinforcement method.", 17th Int. Conf. on Soil Mechanics & Geotechnical Engineering (ICSMGE), M. Hamza, M. Shahien, and Y. E. Mossallamy, eds., 2009, pp. 2328–2333.
 - [11] Taha, Mohd Raihan, and Omer Muhie Eldeen Taha. "Influence of nano-material on the expansive and shrinkage soil behavior." *Journal of Nanoparticle Research* 14.10, 2012, 1-13.
 - [12] Steyn, Wynand JvdM. "Applications of Nanotechnology in Road Pavement Engineering." *Nanotechnology in Civil Infrastructure*. Springer Berlin Heidelberg, 2011, 49-83.
 - [13] Basha, E. A., et al. "Stabilization of residual soil with rice husk ash and cement." *Construction and Building Materials* 19.6, 2005, 448-453.
 - [14] Naji Givi, Alireza, et al. "The effects of lime solution on the properties of SiO_2 nanoparticles binary blended concrete." *Composites Part B: Engineering* 42.3, 2011, 562-569.
 - [15] Givi, Alireza Naji, et al. "Particle size effect on the permeability properties of nano- SiO_2 blended Portland cement concrete." *Journal of Composite Materials* 45.11, 2011, 1173-1180.
 - [16] Tremblay, Helene, et al. "Influence of the nature of organic compounds on fine soil stabilization with cement." *Canadian Geotechnical Journal* 39.3, 2002, 535-546.
 - [17] Ingles, Owen Graeme, and John B. Metcalf. *Soil stabilization principles and practice*. Vol. 11. No. Textbook, 1972.
 - [18] Tang, Chaosheng, et al. "Strength and mechanical behavior of short polypropylene fiber reinforced and cement stabilized clayey soil." *Geotextiles and Geomembranes* 25.3, 2007, 194-202.
 - [19] Kamon, Masashi, and Supakij Nontananandh. "Combining industrial wastes with lime for soil stabilization." *Journal of geotechnical engineering* 117.1, 1991, 1-17.
 - [20] Sariosseiri, Farid, and Balasingam Muhunthan. "Effect of cement treatment on geotechnical properties of some Washington State soils." *Engineering Geology* 104.1, 2009, 119-125.
 - [21] Okay, US, and D Dias. "Use of Lime and Cement Treated Soils as Pile Supported Load Transfer Platform." *Engineering Geology* 114, no. 1, 2010, 34-44.
 - [22] Indraratna, B, and G Lasek. "Laboratory Evaluation of the Load-Deflection Behaviour of Clay Beams Reinforced with Galvanised Wire Netting." *Geotextiles and geomembranes* 14, no. 10, 1996, 555-73.
 - [23] Prabakar, J, and RS Sridhar. "Effect of Random Inclusion of Sisal Fibre on Strength Behaviour of Soil." *Construction and Building Materials* 16, no. 2, 2002, 123-31.
 - [24] Vinod, P, Ajitha B Bhaskar, G Sreelekshmy Pillai, and S Sreehari. "Use of Sand–Coir Fiber Composite Columns in Stabilization of Soft Clay Deposits." *Journal of Natural Fibers* 6, no. 3, 2009, 278-93.
 - [25] Sivakumar Babu, GL, and AK Vasudevan. "Strength and Stiffness Response of Coir Fiber-Reinforced Tropical Soil." *Journal of materials in civil engineering* 20, no. 9, 2008, 571-77.
 - [26] Hejazi, Sayyed Mahdi, Mohammad Sheikhzadeh, Sayyed Mahdi Abtahi, and Ali Zadhoush. "A Simple Review of Soil Reinforcement by Using Natural and Synthetic Fibers." *Construction and Building Materials* 30, 2012, 100-16.
 - [27] Dexter, AR, and B Kroesbergen. "Methodology for Determination of Tensile Strength of Soil Aggregates." *Journal of Agricultural Engineering Research* 31, no. 2, 1985, 139-47.
 - [28] Viswanadham, BVS, BK Jha, and SN Pawar. "Experimental Study on Flexural Testing of Compacted Soil Beams." *Journal of Materials in Civil Engineering* 22, no. 5. 2009, 460-68.
 - [29] Gratchev, Ivan, and Ikouo Towhata. "Compressibility of natural soils subjected to long-term acidic contamination." *Environmental Earth Sciences* 64.1, 2011, 193-200.
 - [30] Jozefaciuk, Grzegorz. "Effect of acid and alkali treatments on surface-charge properties of selected minerals." *Clays and Clay Minerals* 50.5, 2002, 647-656.
 - [31] Kamon, Masashi, T. Katsumi, and C. Ying. "Effect of acid rain on physico-chemical and engineering properties of soils." 1997, 23-31.
 - [32] Kashir, Mansor, and Ernest K. Yanful. "Hydraulic conductivity of bentonite permeated with acid mine drainage." *Canadian Geotechnical Journal* 38.5, 2001, 1034-1048.
 - [33] Sridharan, A., and K. Prakash. "Mechanisms controlling the undrained shear strength behaviour of clays." *Canadian Geotechnical Journal* 36.6, 1999, 1030-1038.

- [34] Sridharan, A., S. M. Rao, and N. S. Murthy. "Liquid limit of montmorillonite soils." *ASTM geotechnical testing journal* 9.3 ,1986, 156-159.
- [35] Wang, Y-H., and W-K. Siu. "Structure characteristics and mechanical properties of kaolinite soils. I. Surface charges and structural characterizations." *Canadian geotechnical journal* 43.6 ,2006, 587-600.
- [36] Gratchev, Ivan B., and Kyoji Sassa. "Cyclic behavior of fine-grained soils at different pH values." *Journal of geotechnical and geoenvironmental engineering* 135.2 ,2009, 271-279.
- [37] Spagnoli, Giovanni, et al. "Undrained shear strength of clays as modified by pH variations." *Bulletin of Engineering Geology and the Environment* 71.1 ,2012, 135-148.
- [38] Gajo, Alessandro, and Benjamin Loret. "The mechanics of active clays circulated by salts, acids and bases." *Journal of the Mechanics and Physics of Solids* 55.8 ,2007, 1762-1801.

Technical Papers

Geotechnique

LANDSLIDES IN BANGLADESH: CAUSES AND RECOMMENDATION

Musahaq Ali, Zakaria Hossain and Shigeko Haruyama
Graduate School of Bioresources, Mie University, Japan

ABSTRACT

This paper gives an account of the investigation carried out to review and analyses of floods and landslides in some selected areas in Bangladesh. The study aimed to determine the main causes of failure of slope or landslides and to suggest remedial measures for minimizing natural disasters in the country. Information on landslide and slope failure were collected from daily newspapers, available internet sources, statistical yearbook, and technical research reports. On the basis of such information, five major devastations were taken into consideration in this paper for detailed study. The results of analyses and discussion revealed that the major causes of landslides were due to illegal cutting of slope by public. Other causes were identified as poor planning and faulty construction of structures neighboring to landslides sites. Analyses of slope stability with and without pore water demonstrated that the factor of safety of slope decreased with an increase in pore water pressure during rainfall causing the landslide devastation in Bangladesh during rainy season.

Keywords: Landslide, Flood, Heavy Rain, Bangladesh, Stability Analysis

INTRODUCTION

Heavy rains and landslides in Bangladesh occurred during the last couple of years had killed at least 329 people and left stranded over 1950000 people in the south-east Bangladesh. The landslides are also a great concern in Bangladesh as they threaten the life and property of the people in the hilly areas of Bangladesh such as Chittagong, Rangamati, Cox's Bazar, Hobigonj and like other natural disasters those frequently occurred in Bangladesh such as tropical cyclone, flood, draught etc. The recent Cox's Bazaar, Bandarban and Chittagong landslides in 2012 that occurred on June 27 is another devastating natural disasters since the independent of Bangladesh in terms of human casualties damage and personal. The indiscriminate cutting of hill that made it very steep slope, faulty construction of homes, embankments, roads and miscellaneous structures in the mountainous areas, worsen by the heavy rains; had increased the occurrences of frequent landslides especially during the last two decades in the southern part of Bangladesh [1]. A catastrophic super landslide like that took place in 2007 was the most damaging one, claimed 130 lives, rendered nearly 150 families homeless and left over 300000 people without secure accommodation.. The tragic landslide of 1986 and 1989 claimed 51 and 300 lives respectively [2].

In recent years, the loss of life and property which occurred due to these landslides still causing staggering situation such as landslides in 2009, 2010 and 2011 had killed at least 81 peoples and affected more or less all the seven landslide prone districts of the hilly region. Landslides and related slope instability phenomena was not only the problem in

Bangladesh but also outbreak many parts of the world [3]. In Japan, a lot of devastating landslides occurred almost every year. It can be noted that a wealth of experience in understanding, recognition and treatment of landslide hazards is needed [4]. Particular area requiring attention concerning the selection and design of appropriate, cost-effective remedial measures which in turn requires a clear understanding of the mechanisms and processes that caused the landslide [5]. Especial attention had been required for the hills of Chittagong in Bangladesh as it was particularly badly hit caused devastation due to heavy monsoon rainfall. Sudden landslides not only destroying lives, crops, agricultures, poultry, fisheries and many other things but also it creates simultaneous accumulation of silts in the river beds and floodplains. Unfortunately, very little or no study is available which specifies the main reasons for such disasters. It is therefore felt that a research reviewing the causes of landslide in Bangladesh should be undertaken. In order to fulfill the above objectives, information on landslides or failure of slopes was collected from different sources such as daily newspaper, web page, statistical year book and technical reports. Discussion has been made to reveal the causes of landslides and recommendations are made for minimizing the landslide hazard in Bangladesh

LOCATION OF LANDSLIDES

The geographical position of landslide occurred in Bangladesh is shown in Fig. 1. The place of occurrence is mainly Chittagong and Cox's Bazar district as shown in the south-East location on the map of Bangladesh.



Fig.1 Geographical location of landslide

Death of People During Past Five Years

The number of death of people occurred during the past five years are given in Table 1. It is noted that there were many other landslides took place after the independence of Bangladesh in 42 year. In this paper, the recent casualties are emphasized. As can be seen in Table 1, the devastation that took place in 2012 claimed over 118 lives along with over 250000 peoples left homeless or stranded without proper accommodation.

Table 1 Recent death of people due to landslide

Date of occurrence	Death of people	Left stranded	Place
2007 June 11	130	300000	Chittagongj
2009 July 4	6	500000	Hobi-gonj
2010 June 15	58	200000	Cox's Bazar
2011 July 1	17	700000	Chittagong
2012 June 27	118	250000	Chittagong, Cox's Bazar

Fact findings

The Chittagong district is second largest city and

Cox's Bazar top tourist city of Bangladesh close to Bay of Bengal facing heavy rains during monsoon season in the month of June and July. Large part of the port city of Chittagong are badly affected by floods (Fig.2) causing multiple landslides (Fig.3).



Fig.2 Heavy rain causing flood in Chittagong city (source: BBC)[6]



Fig.3a Destruction of houses due to landslide (2012) (source:: reliefweb)[7]



Fig.3b Destruction of houses due to landslide (2007) (source: reliefweb)[8]

It is known that there are lot of illgal cutting of hills in the Chittagongcity took place every year by the influencial people. Owing to cutting of natural slope, the slope became heay stiff and sometimes the inclination were over 70 to 80 degree or close to

vertical as can be seen in Fig.4.



Fig.4 Natural slope was illegally cut to stiffer inclination susceptible to failure (source: Daily star)

CHECKING STABILITY OF SLOPE BEFORE AND AFTER CUTTING

In order to check the effect of rainfall on the stability of slope, it is necessary to perform the analyses considering the existence and non-existence of pore water inside the slope for both the natural and cut slopes. Considering the facts above, the analyses were performed using the method of determination. The main feature of this method is that it calculates the factor of safety of a slope based on moment equilibrium of simultaneous blocks dividing the whole slope into two major blocks of left and right sides as shown in Fig.5.

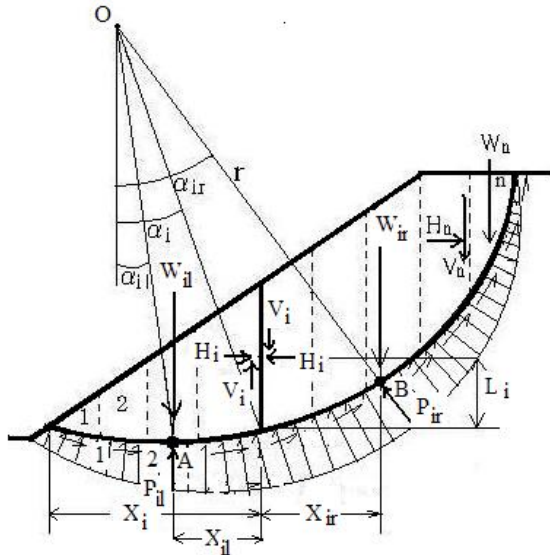


Fig.5 Forces acting on a slope for stability check

Where, H_i is the horizontal component of internal force and V_i vertical component of internal force both are acted at the vicinity of i-section owing to the self-weight of the right-side soil-block when considering the free-body of left side soil block. In the same way, considering the free body of the right-

side soil-block, the H_i and V_i are acted in the opposite direction due to the reaction of the left-side soil-block. The self-weight of right-side soil-block is denoted by W_{ir} . The center angle formed by the lines connecting to the center of the arc and the point which is the cross-section of slip line and acting line of W_{ir} is denoted by α_{ir} . The horizontal distance between the i-section and the acting line of W_{ir} is denoted by X_{ir} and the vertical distance between the point of action of internal forces and the slip line is given by L_i .

Alike the right-side soil-block, the parameters W_{il} , α_{il} , X_{il} are also defined in the case of left-side soil-block. Another feature of this method is that the point of action of internal forces to the slip circle (L_i) is common for both left and right group. The radius of the circular arc is defined by r . The horizontal distance between the bottom edge of the slip circle and i-section is defined as X_i and the center angle formed by the line passing through the cross-section of i-section and slip-line with the vertical direction is defined as

□i. The details of

method can be found elsewhere (Hossain and Inoue, 2007). By using the determinate method, the factors of safety of the landslide section are calculated by the following equation.

$$F_s = \frac{\{H_{n-1} \sin \alpha_n + (W_n - V_{n-1}) \cos \alpha_n - u_n l_n\} \eta}{(W_n - V_{n-1}) \sin \alpha_{n-1} - H_{n-1} \cos \alpha_n} \quad (1)$$

where, n indicates the number of vertical slices, indicates effective angle of internal friction and indicates effective cohesion of soil. Here, H is the horizontal force component, V is the vertical force component, W is the self weight of slice, α is the angle to the center of the circle, u is the pore water pressure and l is the base length of the slice along the circle. The η given in the above equation is defined as follows.

$$\eta = \tan \phi' + c' l \quad (2)$$

Figures or Tables should be sized the whole width of a column, as shown in Table 1 or Fig.1 (Figs. 1 and/to n) in the present example, or the whole width over two columns. Do not place any text besides the figures or tables. Do not place them altogether at the end of manuscripts.

RESULTS AND DISCUSSION

The properties of soil obtained by laboratory tests are given in Table 2. The results of analyses of natural slope (Fig.6) are compared to that of the cut slope (Fig.7) in Table 3.

Table 1 Materials properties used in stability checking

Parameters	Values
Dry density, t/m^3	01.64
Optimum water content, %	21.4
Specific gravity	02.723
Cohesion, kN/m^2	95.71
Angle of internal friction, degree	24.21
Sand, $>75\mu m$ (%)	16.00
Silt, $5-75\mu m$ (%)	44.00
Clay, $<5\mu m$ (%)	40.00
Liquid limit	52.0%
Plastic limit	29.7%
Plasticity index	22.3
Unified Classification System	CH

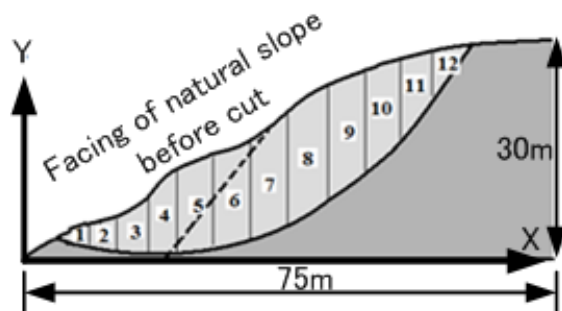


Fig.6 Before cut: facing of natural slope

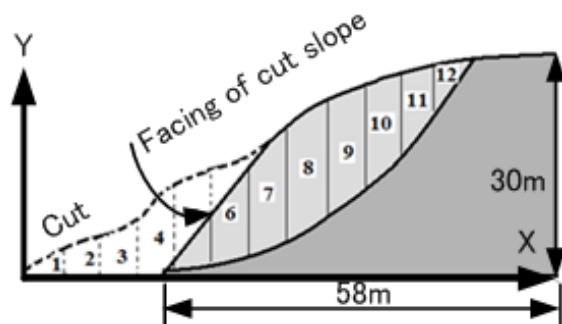


Fig.6 After cut: facing of natural slope

The factors of safety of the natural slope before cutting are 1.98 and 2.35 with and without pore water pressure respectively. This indicates that the stability of the slope decreases due to the increase in the pore water pressure during rainfall. After cutting the hill, the safety values are obtained as 1.48 and

1.10 respectively indicating that the factor of safety decreased significantly with the increase in pore water pressure which leads to the failure of the slope during rainfall because the recommended factor of safely values are over 1.8 or more.

Table 3 Results of stability checking

Pore water pressure condition	Factor of safety before hill cutting	Factor of safety after hill cutting
Without pore water	2.35	1.48
With pore water	1.98	1.10

CONCLUSION

From the results and discussion given above, the following conclusions can be drawn:

1. The natural slope in the failure location in Bangladesh was stable both in the dry season and rainy season as the factor of safety are found to be equal or more than the required factor of safety of a stable slope.
2. The major cause of landslide was found to be man-made through illegal hill cutting by influential people of Bangladesh.
3. The other causes of landslides were identified as the increase in pore water pressure during rainfall.
4. It is recommended that unless serious steps are taken to correct this way of hill, the landslides in Bangladesh are plausible to turn into even worse with time and achieve eventually devastating magnitude.

REFERENCES

- [1] Roy, P. (2007) Mindless hill-cutting caused mudslide, The Daily Star, 2007-06-12.
- [2] Schuster, R.L. (1991) Landslides analysis and control, National Research Council, p.1-10.
- [3] Sikdar, Z.H. (2007) Over 100 people were killed and hundreds more injured due to devastating landslides in these areas on June 11, The Daily Star, 2007-06-12.
- [4] Iai, S., Mimura, M., Chigira, M., Kamai, T., Sidle, R.C., Suwa, H., Saito, T and Tobita, T. (2006) Geo-disaster prediction and geo-hazard mapping in urban and surrounding areas, progress report in FY 2005, Annuals of Disas. Prev. Res. Inst., Kyoto Univ., (49) C, 23-38.
- [5] Chigira, M. and Yokoyama, M. (2005) Weathering profile of non-welded ignimbrite and the water infiltration behavior within it in

- relation to the generation of shallow landslides,
Engineering Geology, 78, 187–207.
- [6] BBC“Heavy rains and landslides in Bangladesh
kill 90”
- [7] reliefweb“Bangladesh: Situation Report No.233
(as of 26 June 2012)”
- [8] reliefweb“Bangladesh Landslide and Flood
Situation Report No.234”

PRECAST SPREAD FOUNDATION IN INDUSTRIALIZED BUILDING SYSTEM

Ramli Nazir¹, Ehsan Momeni², A. Kadir Marsono³, Houman Sohaie⁴
Faculty of Civil Engineering, Universiti Teknologi Malaysia, Malaysia^{1,2,3,4}

ABSTRACT

The use of IBS in construction is of interest mainly due to its relatively green technology and the fact that by implementing IBS, the cost of construction and its required time are decreasing remarkably. Finding a total precast solution for low to moderate rise buildings is the aim for Malaysian Construction Industry Development Board (CIDB). However, the aim is not totally achieved yet, although many precast structures have been built, none of them are totally precasted. In fact, the substructures are cast in place. The current aim of the research in Universiti Teknologi Malaysia (UTM) is to develop and introduce a new thin wall precast spread foundation known as IBS footing for low to moderate rise buildings to complete the cycle of using precast elements for affordable houses. This study reviews developed precast spread foundation as well as investigates the axial bearing capacity of a new proposed IBS footings as this parameter plays an important role in the design of footing. For this reason, a set of parametric studies using finite elements code, PLAXIS, were conducted to evaluate the optimum shape of spread foundation suitable for rapid construction. The parametric study results show that the effect of increasing the length of foundation thin walls on axial bearing capacity is much more than that of wall thickness. Based on the results of the parametric study, the new IBS footing was proposed. Consequently, the proposed IBS footing was analyzed numerically by implementing the finite element software, ABAQUS. The numerical results reveal that the bearing capacity of the proposed IBS footing is 380 kPa for 25 mm settlement. In general, numerical results confirm that the proposed IBS footing can be considered for further investigation to be used as a substructure system in low to moderate rise buildings.

Keywords: ABAQUS, Bearing Capacity, Granular Material, PLAXIS, Precast Spread Foundation

INTRODUCTION

Implementation of Industrial Building System (IBS) has recently become highlighted in construction industry [1]. Among many technical definition of IBS [2]-[6] Warszawski [7] expounded that an industrialization process is an investment in equipment, facilities, and technology with the objective of maximizing production output, minimizing labor resource, and improving quality while a building system is defined as a set of interconnected element that joint together to enable the designated performance of a building. However, Kamar [8] mentioned that in Malaysia, IBS definition represents the concept of prefabrication and industrialization of construction. A survey on the usage of IBS [9] in Malaysian construction industry shows that almost 70 percent of engineers have positive point of view towards IBS implementation in construction. This is due to numerous advantages of IBS implementation in comparison to the conventional method of construction. Many researchers have investigated the advantages of IBS usage. Among others, study by Cheong [10] shows that through IBS implementation, the cost of project can be reduced up to 46% of the total cost.

Apart from economical perspective, the use of IBS has other advantages such as rapid construction, reduction in site workers and wastes, less affection by weather condition, relatively higher quality and safer construction. On the other hand, IBS implementation has some disadvantages such as the need for high initial capital cost, competent and certified assembler, and site accessibility requirement [11]. Although IBS implementation has some disadvantages, the advantages of IBS usage outweighed the disadvantages. The use of precast elements such as beam, column, wall and panels is well established. However, when it comes to precast spread footing, only a relatively few numbers of reported cases can be found in literature. This excludes the use of precast driven piles as a kind of deep foundations. In fact, from the economical point of view, many studies show that spread foundations are more preferable. In other words, the use of shallow foundations instead of deep foundations can reduce the cost of project from 20 to 70 percents [12].

INTRODUCTION OF A NEW PRECAST THIN WALL FOUNDATION

The idea of precast thin wall foundation originated from the Malaysian's ancestors usage of

invert bottles or barrels as a foundation for their houses. In order to investigate the geotechnical performance of such thin wall foundation as well as develop its optimum shape, the initial idea was evolved and extended through a comprehensive parametric study.

The finite element code, PLAXIS [13], was used for the course of the parametric study mainly due to its availability and ease of use. In this parametric study, the effect of some parameters including the effect of both wall length and wall thickness on the bearing capacity of the proposed IBS footing is investigated.

It is apparent that soil strength and foundation width also can effectively increase the bearing capacity of foundation [14]. However, due to their obvious effects on bearing capacity, these factors are excluded in the parametric study.

Parametric Study

In order to conduct a parametric study for precast thin wall spread foundation or IBS footing, some plane strain models were considered in PLAXIS version 2010 (see Figure 1). A working area of 10 m width and 10 m depth was used to minimize the boundary effects. The width and wall length of default footings (Figure 1-b) were equal to 1 m and default wall thickness was equal to 10 cm. The cap was set to be 20 cm by 20 cm.

The soil was modelled as one layer of sand. The Mohr-Columb (MC) model was considered for soil constitutive model. The drained behavior was assumed due to the type of material i.e sand.

On the other hand, for concrete material *i.e* footing, a Linear Elastic (LE) model was selected to define the concrete behavior. The concrete was selected as a non-porous material.

The coefficient of earth pressure, K_o , in analysis was approximated by considering Jacky's estimate of $K_o=1-\sin\phi$ [15]. The materials properties for parametric study were taken from the study conducted by Momeni et al.[14] and they are tabulated in Table 1.

To define boundary conditions, standard fixities PLAXIS tool were used. These boundaries are defined in a way that for vertical geometry line, there is a horizontal fixity while the bottom horizontal geometry line is fixed vertically and horizontally.

According to a study conducted by Lebeau[16] in sandy soils, the size of mesh in PLAXIS does not have considerable effect on output curves. Therefore, in this study, course mesh size was considered for the further finite element analysis as shown in Figure 2.

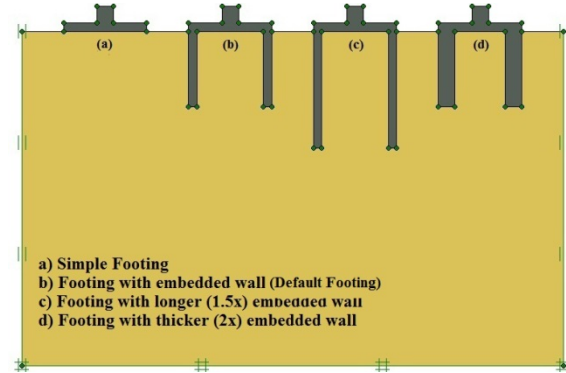


Fig.1 Different foundations used for parametric study

The prescribed displacement method for which a certain displacement will be imposed on the top of the footing was considered for analysis. The maximum allowable settlement was considered to be 20 mm [13]. The calculation was divided into two phases. In the first step, water level was defined and the initial effective stresses are generated by K_o procedure.

Table 1 Material Properties for parametric study

Material	Symbol	Sand	Footing	Unit
Material Model	-	MC	LE	-
Unit Weight	γ	18	24	kN/m ³
Stiffness	E	14.4	26E3	MPa
Poisson's Ratio	ν	0.35	0.15	-
Friction Angle	ϕ	30.5	-	degree
Cohesion	c	0.06	-	kPa

The initial phase also dealt with generating the hydrostatic pore water pressure based on the water level. The water was leveled on the bottom geometry line to represent the dry condition. In the second phase, the static plastic analysis was selected for the type of analysis. Since the analysis was static, the whole analysis can be applied in one stage. Both stage construction and total multiplier techniques could have been used in this study, however, the results are obtained using stage construction method.

Different analyses were performed to investigate the effect of important structural elements on the bearing capacity of IBS footing. In fact, the parametric study dealt with the effect of wall and its size variation on geotechnical performance of footing. The analysis began with bearing capacity estimation of simple footing (Figure 1-a). The analysis was then repeated for default footing (Figure 1-b).

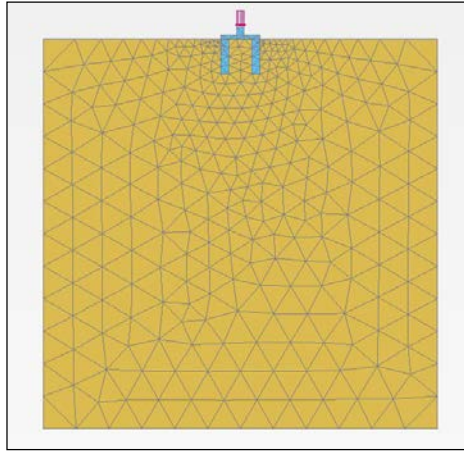


Fig. 2 Generated mesh for footing before analysis.

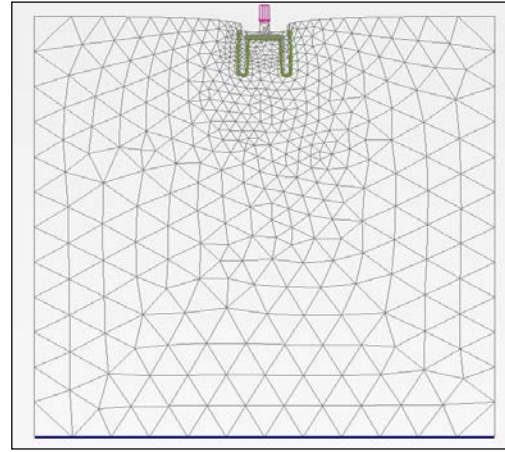


Fig. 3 Deformed mesh after analysis

In order to investigate the effect of wall length on the bearing capacity, third analysis was conducted on the aforementioned footing except that the length of walls was increased 1.5 times (See Figure 1-c). For last analysis, to investigate the effect of wall thickness on bearing capacity, the wall thickness of default footing was increased two times while the wall length was kept constant (Figure 1-d). the deformed mesh of one of the footing in addition to the results of four different analyses is shown in Figure 2 and 3 respectively.

Figure 4 shows that, for 20 mm settlement, the maximum axial bearing capacity is almost 90 kN/m. However, by adding the embedded walls, the axial bearing capacity was increased up to 110 kN/m. This is almost 25% higher than simple footing which shows the importance of such walls on the axial bearing capacity. Figure 4 also depicts the effectiveness of wall length and thickness on the geotechnical performance of footing.

As shown in this schematic figure, for the case that wall length is increased 1.5 times and the wall thickness remained constant (Figure 1-c), the rate of the increase in bearing capacity is much more than the case that wall length is kept constant and the wall thickness increased two times (Figure 1-d).

In other words, in comparison to the default footing (Figure 1-b), there is 10% increase in bearing capacity for the latter case while for the former case this rate is 15%. In interpreting the results, it is worthy to note that the wall length is increased 1.5 times while the thickness of the walls is increased two times. In fact, it can be determined from the results of the parametric study, the effect of increasing wall length on axial bearing capacity is much more than that of wall thickness.

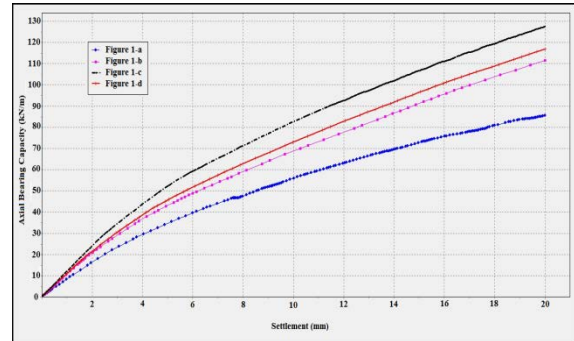


Fig.4 Schematic figure of the parametric study results

Proposed IBS Footing

Based on the results of parametric study, and engineering judgment, a thin wall precast spread foundation (IBS footing) suitable for low to moderate rise buildings is proposed. The proposed IBS footing is shown in figure 5. In the proposed footing, some other factors such as transportability are considered. Hence, the wall thickness which does not have remarkable effect on the bearing capacity of footing is considered to be 5 cm. On the other hand, to prevent the walls from brittle failure, a bracing system was developed as shown in figure 5(b). The wall length was set to be 1.1 m and the whole square IBS footing was selected to be 1.5 m by 1.5 m. Other dimensions are shown in the Figure 5.

FINITE ELEMENT ANALYSIS OF THE IBS FOOTING

The proposed precast thin wall spread foundation (IBS footing) was modelled numerically using finite element technique. Discretization of continuous media by finite number of elements is known as Finite Element (FE) method [17]. Due to specific

shape of the proposed IBS footing, the finite element code, ABAQUS [18], was implemented in this study.

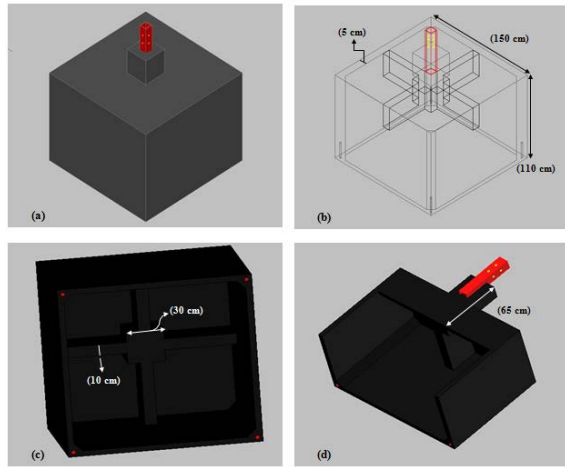


Fig.5 Proposed IBS footing: a) isometric view, b) Bracing system, c) bottom view, d) cross sectional view

One layer of sand with $c'=0$ kPa and $\phi'=37^\circ$ was considered for FE analysis. The surface area of sand stratum was 81 m^2 while its depth was 7m. The boundaries were selected in accordance to previous literature suggestions [13]. However, in order to reduce the computation time, only one-fourth of the footing was modelled. This can be done due to symmetry of the problem.

For successful numerical analysis to be performed, the soil behavior should be defined properly and realistically. Hence, modified Drucker-Prager constitutive model with cap was considered for defining the soil behavior. It is well established that the soil behavior is stress dependent [20] and the cap model used in this study considers this significant factor. The cap eccentricity value, R , used in this study was 0.4 [19]. Table 2 shows other cap model parameters which are taken from Helwany [19].

The IBS footing was considered to be rigid and it is assumed to be in perfect contact with soil. Study by Merifield and Nguyen [21] shows that the soil-footing interface strength has little or no effect on the calculated bearing capacity. In order to model a rigid footing, a downward displacement boundary condition was applied on the soil stratum [22]-[24]. Since the maximum allowable settlement for buildings is often considered to be 25 mm, this amount was applied on the soil body in 25 subsequent steps. In each step, 1 mm prescribed downward displacement was applied over the normal soil-footing interfaces area. The sand bottom

layer is fixed in all directions while for vertical boundaries only the horizontal movement is fixed.

The automatic meshing technique was employed mainly due to the specific shape of the IBS footing. Nevertheless, in the vicinity of the footing, finer mesh was considered because of significant displacement change in this area as well as the fact that this zone is the zone of stress concentration.

It is worthy to note that Four-node linear tetrahedron coupled displacement-pore pressure elements (C3D4P) were considered for FE analysis. The finite element mesh used in the analysis consists of 5571 nodes and 27652 elements. The generated mesh is shown in Figure 6.

In the analysis of the foundation, as mentioned earlier, the load is applied using a constant downward displacement boundary condition at the normal soil-footing interface areas. This type of boundary condition causes the footing to settle uniformly. The sum of reaction forces over the area, in which the downward displacement boundary condition is defined, is considered as the bearing capacity of the footing [21], [25].

Due to the static nature of the problem, static analysis was performed. In the beginning of the analysis, gravity loads were applied to the soil body. Subsequently, geostatic command was invoked for determination of the initial stresses in all soil elements and to make sure that equilibrium is satisfied within the sand layer.

Table 2 The Modified Drucker-Prager (D-P) Parameters for sand layer

Parameters	Symbol	Sand	Unit
Density	ρ	1923	kg/m^3
Initial void ratio	e_0	1.5	-
Elasticity	E	182	MPa
Poisson's ratio	ν	0.28	-
Cohesion	d	10^{-5}	kPa
Friction Angle (3-D model)	β	55	degree
Eccentricity	R	0.4	-
Coefficient of transition surface	α	0.05	-
Initial Yield	—	0	-

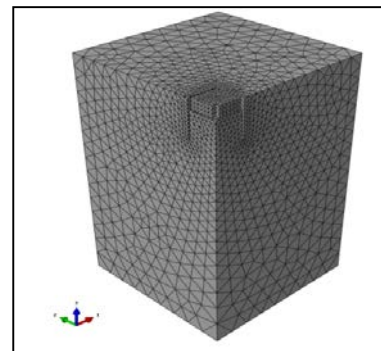


Fig. 6 IBS footing Generated Meshes

RESULTS AND DISCUSSION

The results of the aforementioned finite element analysis are discussed in this section. The deformed mesh is shown in Figure 7 while the influenced zone of the soil due to vertical displacement is shown in Figure 8. The blue color indicates zero displacement. As shown in this figure, the soil defined boundaries are assigned properly. It is worthy to note that, in Figure 8, the ABAQUS mirror tool was used for visualization purpose. Based on the results, the significant displacement occurs within vertically $2B$ (B is the footing's width) below the footing and horizontally $1.5B$ from the center point of the footing which is in good agreement with Boussinesq theory and the well-established experimental study by Briaud and Gibbens [12]. According to the well-established literature, the horizontal influenced zone is often $2.5B$ to $3B$ for simple footing. Nevertheless, the remarkable decrease in horizontal influenced zone might be due to embedded thin walls.

The load-settlement curve of the footing for 25 mm settlement is shown in the figure 9. As shown schematically in this figure, the bearing capacity of the proposed IBS footing for allowable settlement is 380 kPa. It is discussed earlier that the bearing capacity of the footing is obtained by summation of reaction forces over the applied prescribed displacement area using history output menu in ABAQUS.

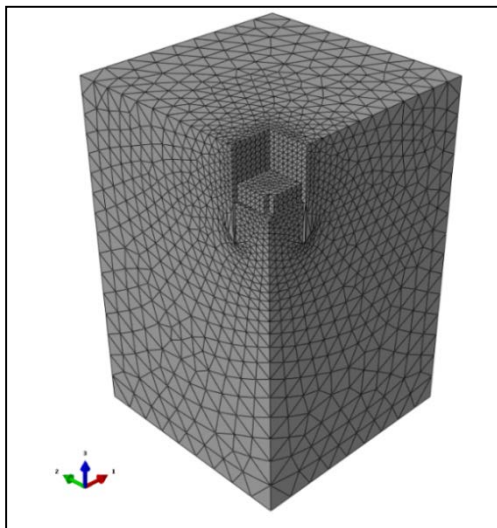


Fig. 7 IBS footing deformed mesh

SUMMARY AND CONCLUSION

The importance of IBS and precast spread foundations was investigated through a critical review. Apart from that, a parametric study for developing a new precast foundation was conducted. The results of the parametric study reveal that the effect of embedded wall on bearing capacity is

remarkable. Based on the results of the parametric study and some other factors such as transportability of the footing, a precast thin wall spread foundation known as IBS footing was introduced.

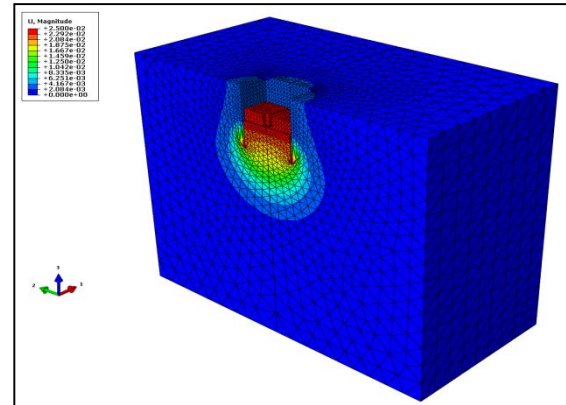


Fig.8 Influenced zone of the soil under 25 mm settlement

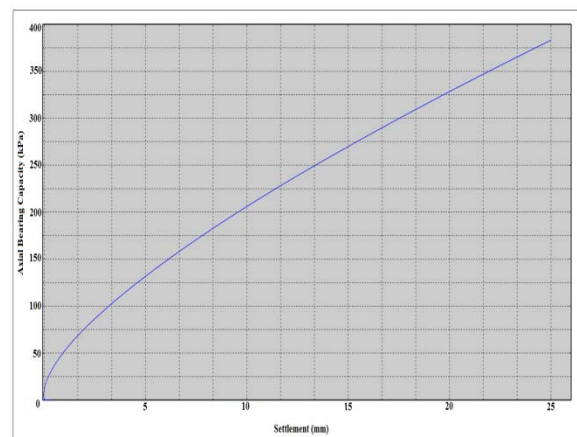


Fig. 9 Load-displacement curve under the IBS Footing

The proposed IBS footing was analyzed numerically by using the finite element software, ABAQUS. From the finite element analysis, it is found that the bearing capacity of the proposed footing is 380 kPa for 25 mm settlement. Apart from that, the numerical analysis of the IBS footing shows that the vertical zone of influence of the soil body is within $2B$ from the center point of the footing while horizontal zone of displacement is located in area between the center of the footing and $1.5B$ after it.

The influenced zone of the sand layer considered in this analysis lies inside the suggested range of influenced zone of displacement provided by researchers in well-established empirical studies.

ACKNOWLEDGEMENT

The authors would like to thank the Research Management Centre of Universiti Teknologi Malaysia (UTM) and Ministry of Science, Technology and Innovation (MOSTI) for providing financial support through research vote: R.J130000.7822.4L130 for bringing the idea into fruition.

REFERENCES

- [1] Elliot KS, Precast concrete structures. Spon Press, 2002.
- [2] CIB. New Perspective in Industrialization in Construction- state-of-art Report, CIB Publication 329, 2010.
- [3] Richard RB, Reproduction before automation and robotics. Journal of Automation in Construction, Vol. 14, 2005, pp. 251-441.
- [4] Cooper R, Progress management in Design and Construction, Oxford London: Blackwell Publishing, 2005.
- [5] Trikha DN, Industrialised Building System: Prospect in Malaysia. Kuala Lumpur: In Proceeding of World Engineering Congress, 1999.
- [6] Junid SMS, Industrialised Building System- Proceedings of a UNESCO/FEISEAP Regional Workshop, 1986.
- [7] Warszawski A, Industrialised and Automated building systems. Technion-Israel Institute of Technology, E & FN Spon, 1999.
- [8] Kamar KAM, Industrialized building System (IBS): Revisiting Issue of Definition and Classification. International Journal of Emerging Sciences, Vol. 1(2), 2011, pp. 120-132.
- [9] Shaari and Nizar, Survey on the Usage of Industrialised Building Systems (IBS) in Malaysian Construction Industry, CIDB Malaysia Publication, 2003.
- [10] Cheong GK, Fully precast system at Choa Chu Kang. Precastech Newsletter On Line, Vol. 8, 1997.
- [11] Badir YF, Kadir MRA, and Ahmed HH, Industrialized building systems construction in Malaysia, Journal of Architectural Engineering 8, Vol. 1, 2002, pp. 19-23.
- [12] Gibbens RM, and Briaud JL, Load tests on five large spread footings on sand and evaluation of prediction methods, Rep. to the Fed. Hwy. Admin., Dept. of Civ. Engrg., Texas A&M University, College Station, Tex, 1995.
- [13] US Army Corps of Engineers, Bearing Capacity of Soils, Engineering Manual, 1992.
- [14] Momeni, E, Maizir, H, Gofar N, Ramli, N, Comparative Study on Prediction of Axial Bearing Capacity of Driven Piles in Granular Materials. Jurnal Teknologi, Vol. 61, 2013.
- [15] Jaky J, The Coefficient of Earth Pressure at Rest. In Hungarian (A nyugalmi nyomás tenyezője), J. Soc. Hung. Eng. Arch. (Magyar Mernok és Építész-Egylet Közlönye), 1944, pp. 355-358.
- [16] Lebeau JH, FE-Analysis of piled and piled raft foundations, Graz University of Technology. Project Report, 2008.
- [17] Chen WF, Limit Analysis and Soil Plasticity, US: Ross J, Publishing, 2008. Ch. 12.
- [18] Abaqus 6.9 FEA software manual, SIMULIA, Rising Sun Mills, 166 Valley Street, Providence: RI 02909-2499, USA, 2009.
- [19] Helwany S, Applied soil mechanics with ABAQUS` applications. Hoboken, New Jersey: John Wiley & Sons, INC, 2007.
- [20] Brinkgreve RBJ, Selection of Soil Models and Parameters for Geotechnical Engineering Application, Journal of Geotechnical and Geoenvironmental Engineering, ASCE, 2005.
- [21] Merifield RS, Nguyen VQ, Two- and three-dimensional bearing-capacity solutions for footings on two-layered clays." Geomechanics and Geoengineering: An Intl. J., Vol. 1(2), 2006, pp. 151-162.
- [22] Gu J, Computational Modeling of Geogrid Reinforced Soil Foundation and Geogrid Reinforced Base in Flexible Pavement, Louisiana State University. PhD Dissertation, 2001.
- [23] Zhu M, and Michalowski RL, Shape factors for limit loads on square and rectangular footings. J. Geotech. Geoenviron. Eng., Vol. 131(2), 2005, pp. 223-231.
- [24] Gourvenec S, Randolph M, Kingsnorth O, Undrained Bearing Capacity of Square and Rectangular Footings, International Journal of Geomechanics, Vol. 6, 2006, pp. 147-157.
- [25] Zhu M, Bearing Capacity of Strip Footings on Two-layer Clay Soil by Finite Element Method, ABAQUS Users' Conference, 2004.

CATEGORISING GEOTECHNICAL PROPERTIES OF SUBSOIL IN SURFERS PARADISE USING GEOGRAPHIC INFORMATION SYSTEM (GIS)

Haider Al-Ani¹, Leila Eslami-Andargoli², Erwin Oh¹, and Gary Chai³

¹ School of Engineering, Griffith University, Australia

² School of Environment, Griffith University, Australia

³ Centre for Infrastructure and Engineering Management, Griffith University, Australia

ABSTRACT

Peat is a highly organic and compressible soil. Surfers Paradise (as a study area) has problematic peat layer which has different thickness at different locations between R.L. -10 to -19.6 m below the ground surface. Buildings in Surfers Paradise are using piled foundations to avoid the high compressibility and low shear strength peat layer. In this paper, geotechnical borelogs are compiled from 51 sites in the study area. These borelogs data are then imported into ArcGIS10 as digital layers and converted into assessable formats by Geographic Information System (GIS). This technique has been utilised to produce digital zonation maps for the study area. The application of interpolation techniques allows the production of zonation maps and bring together years of geotechnical data. Standard Penetration Test (SPT) N values have been selected to determine the soil stiffness in the study area. These SPT-N values are then categorised to produce different zonation maps. The occurrence of peat layers can be located using these zonation maps. These GIS-based zonation maps will provide a better overview of subsurface geology, bed rock elevations, and geotechnical properties of the various soil types found in the study area.

Keywords: Peat, Geographic Information System, Standard Penetration Test, Spatial Analyst.

INTRODUCTION

GIS has the capability to manage, store, and referencing geotechnical data to its geographic locations. It has been used to integrate existing data such as soil investigations aided by geographic coordinates with specific project data to identify potential geotechnical challenges. For instance, a case study has been presented by [1] where a geotechnical investigation data has been managed by using GIS for design purposes in transportation projects. The outcome of this study was an early identification of the geotechnical problems which require an additional budget and time consuming design's substantial changes. It is generally accepted that the organic matter presence in soils causes a detriment of their geotechnical and engineering qualities [2]. Peats and organic clays cause typical geotechnical problems as a result of their characteristics such as compressibility, lightness, creep ability, weatherability, and low strength and stiffness [3].

GIS Application in Geotechnical data

GIS has been used in many geotechnical applications ubiquitously over the world. For example, in Brazil, GIS used for geotechnical and environmental risk management of Brazilian oil pipeline in 2010 [4].

In addition, in Greece, GIS has been used to produce a thematic map for the geotechnical, geological, seismological, and geomorphological data of Athens [5]. In Turkey, reference [6] has used GIS to produce zonation maps and to estimate if a further precaution is required for a safer area. Cross sections which include SPT-N blow count with depth have been performed to determine the soil strength. Further, GIS-based geotechnical information systems have been established in the USA, Singapore, Brazil, and Japan in 2003, 2005, 2003, and 2010 respectively. The purpose of this is a web-based easy access to the geotechnical data of any area of interest to have an idea about geotechnical conditions of this area. In addition, four case studies of small scale geotechnical projects have been studied by [7] to verify the benefits of using GIS in geotechnical engineering in The United Kingdom. The outcome of this study indicated that GIS output improved the analytical and technical range of these projects in comparison with traditional techniques and the high quality produced maps are comprehensible and popular with engineers.

This paper shows the identification of peat layer occurrence in Surfers Paradise as a case study in Australia. The occurrence of peat has been identified by producing the interpolated SPT-N value zonation maps by using the Spatial Analyst extension and interpolation

techniques. Peat occurrence's depth and thickness have been also determined in the study area.

METHODOLOGY

Two approaches have been utilised to produce GIS-based SPT-*N* value zonation maps. The first approach was by collecting the geotechnical data from the geotechnical investigation reports. These data were available in many different locations and forms. Next, data has been tabulated by using Excel to make it familiar with the GIS environment. The spatial locations of boreholes have been designated by using Google Earth based on boreholes actual locations on each project's site plan. By calculating the distances between separate boreholes and the distance between the borehole itself and the adjacent boundaries on the site plan, boreholes' coordinates can be acquired from Google Earth. Randomly chosen boreholes have been chosen to validate coordinates before transferring these coordinates into GIS environment.

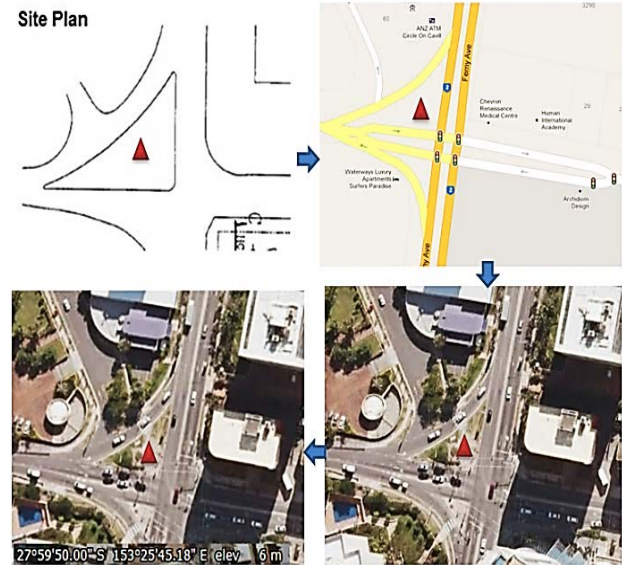


Fig 1 Designation of boreholes geographic coordinates.

Figure 1 shows the procedure of obtaining the boreholes coordinates from a project site plan. Figure 2 illustrates the transformation of geotechnical data from Excel spread sheets into ArcMap. The red dots on the GIS map represent the borehole's spatial locations. Each borehole has its own spatial data as well as geotechnical data which have been uploaded from Excel. It can be observed from Fig.3 that the geotechnical data has been horizontally tabulated in Excel sheet in a way to be compatible with the GIS setting.

The second approach has been achieved by examining eight interpolation techniques in the Spatial and Geostatistical Analyst in ArcMap10. The purpose of this approach is to interpolate the SPT-*N* value and producing the zonation maps.

The eight interpolation techniques examined were:

- (1) Geostatistical Analyst Tools, IDW method
- (2) Geostatistical Analyst Tools, Diffusion method
- (3) Geostatistical Analyst Tools, Global Polynomial method
- (4) Geostatistical Analyst Tools, Kernel method
- (5) Spatial Analyst Tools, Ordinary Kriging
- (6) Spatial Analyst Tools, Universal Kriging
- (7) Spatial Analyst Tools, Spline
- (8) Spatial Analyst Tools, IDW method.

The interpolation technique of Spatial Analyst Inverse Distance Weighting method (IDW) was the most suitable technique which gives a better representation for the SPT-*N* data in Surfers Paradise with specific parameters. This is consistent with what [8] has found.

The spatial analyst extension employs the Inverse Distance Weighting (IDW) interpolation method to create these maps. The interpolation, in turn, is a procedure being used to predict the values of cells at certain locations that lack sampled points [9].

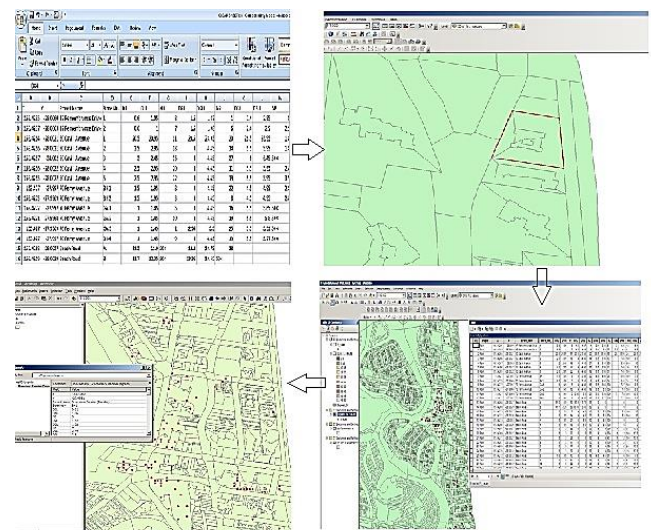


Fig. 2 Geotechnical data transformation into GIS environment

STUDY AREA

Surfers Paradise has a unique prominent location which increases the tourism and commercial activities in Gold Coast in the state of Queensland, Australia. It has been an iconic tourist destination since 1950s and it is the most famous location in Australia. Surfers Paradise has an area about 4 by 1.3 km² and the Nerang River divided it into two main parts Nerang River parts and Beach side part. The study area includes the area which is located between the Nerang River and the Coral Sea (Fig.3).

The soil profile of the study area is based on [10] and it is as follow:

- Loose to medium dense sand starts from the ground surface to R.L. 2.3 m.
- Medium dense to dense sand is underlain from (R.L. 2.3 m) to (R.L. -3.2 m).
- Very dense sand is encountered from (R.L. -3.2 m) to (R.L. -20 m).
- Within the very dense sand layer, a varying thickness peat layer is occurred at depth between (R.L. -10 to R.L. -19.6 m) at different locations with thickness ranges from (0.1 – 7 m).
- An interbedded firm to very stiff clay layers are found up to (R.L. -26.6 m) where a layer of firm to hard clay is occurred below it until the depth (R.L. -29 m).
- The last layer of this soil profile varies within the study area where in some locations there is an interbedded layer of medium dense sand, gravelly sand, clayey sand, sandy clay, or hard silty clay can be observed.

This soil profile is consistent with the description given by [10] and [11].

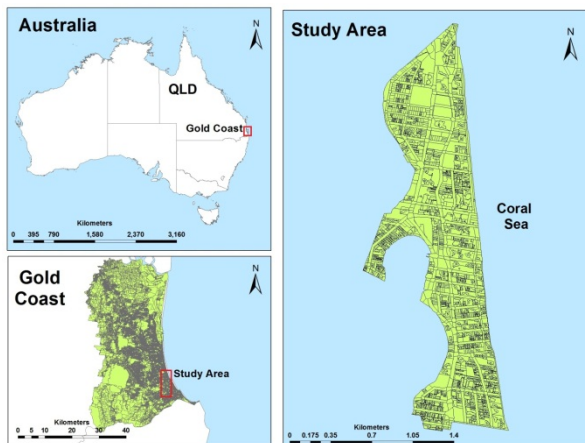


Fig. 3 the location of the study area

RESULTS

Twenty six interpolated maps have been performed for the study area at depths ranged between the ground surfaces until depth of R.L. -40. These maps have been produced by using the Spatial Analyst IDW technique which has been selected among eight interpolation techniques to give a better representation of the data with specific parameters. These parameters are: output cell size: 2.719E-05, power 2, search radius: fixed, and distance 0.25.

In this paper, only four GIS-based SPT-*N* value zonation maps have been provided to represent different depth classes. These four zonation maps represent different depth levels (near the surface until R.L. -26.6 m). Also, it shows variety of soil classes in terms of SPT-*N* values.

Further, peat existence locations map is also presented for the study area. These locations are associated with its boreholes to show the peat depth and thickness in each location.

The first zonation map is nearly shallow in depth R.L. 2.3 to 0 m. The Australian Height Datum (AHD) has been used for the depth considerations. Figure 4 shows the distribution of the soil stiffness values in the study area. It can be observed that the SPT-*N* value in the northern parts of the study area was between 0-10 blows for very loose to loose sand. Whereas, in the southern parts was quite high > 30 blows which represents dense sand. The sand classification has been adopted based on [12] in terms of number of blows of the SPT. There are some locations within the study area are not spatially interpolated and it seems to be blank due to the lack of geotechnical data in this depth at these locations.

The second SPT-*N* value zonation map has been performed for the depth between R.L. -13 to -15 m (Fig. 5). It can be seen that the dominant soil stiffness value for this depth is between 31-49 blows which can be classified as dense sand. There are also some locations of very loose sand and loose sand of SPT-*N* value between 0-10 blow.

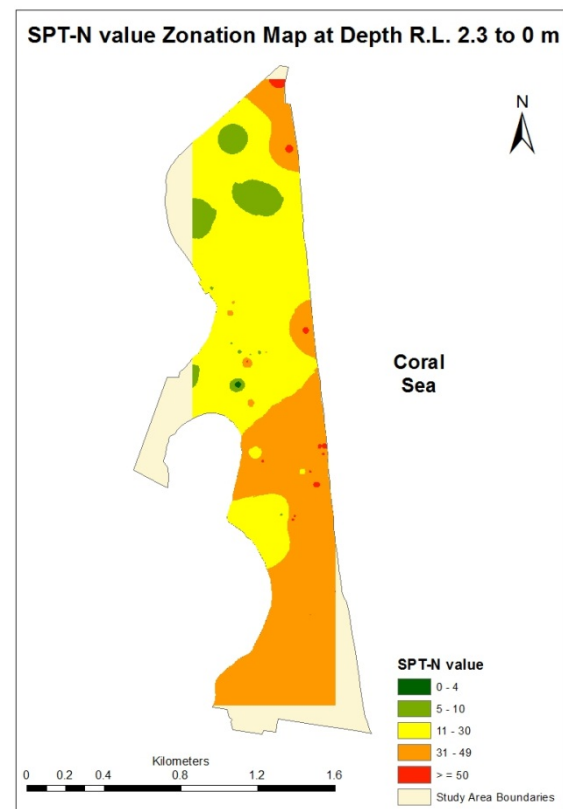


Fig.4 SPT-*N* value zonation map at depth R.L. 2.3-0 m.

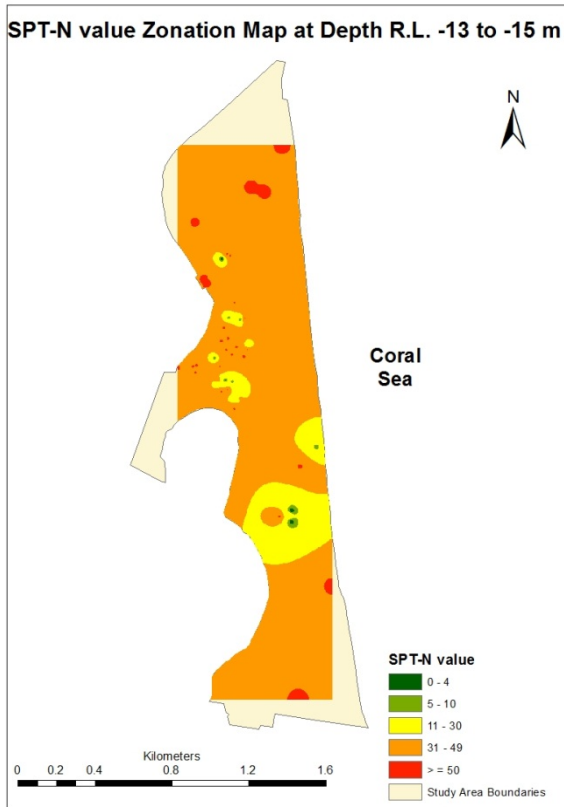


Fig. 5 SPT-N value zonation map at depth R.L. -13 to -15 m.

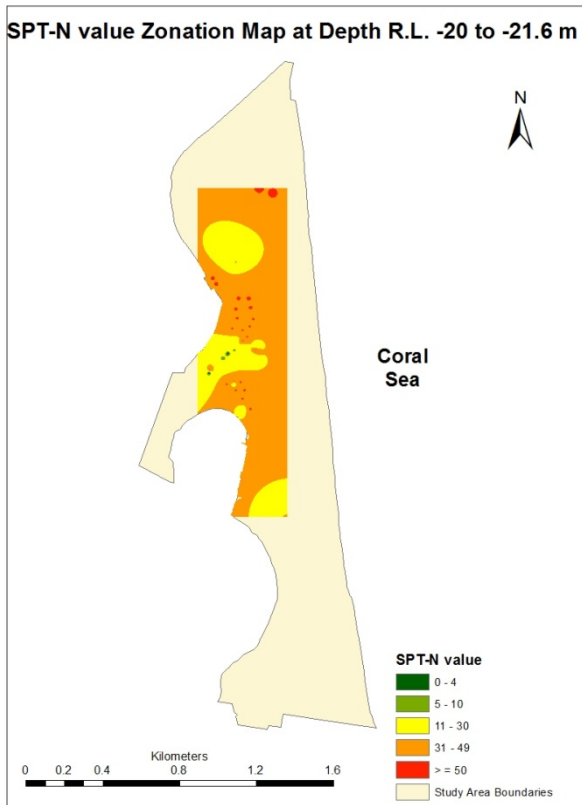


Fig.6 SPT-N value zonation map at depth R.L. -20 to -21.6 m.

Figure 6 shows the third zonation map for the SPT-N value at depth between R.L. -20 to -21.6 m. It can be noticed that the extent of this zonation map is smaller than the previous zonation maps. That is because the lacks of data at this depth level which prevent the interpolation process to be completed in the unclassified (un-interpolated) areas.

The last zonation map for the soil stiffness in this paper is located at depth between R.L. -25 to -26.6 m. Figure 7 shows the distribution of the SPT-N value within the study area and indicates that the dominant value for this depth is between 11-30 blows. This is because of interbedded layers of soft to firm clay and medium dense sand. Very loose sandy clay is also existed in the northern part of the study area.

Nonetheless, Peat locations have been identified within the study area in 16 locations (Fig. 8). These locations represent already existed buildings and other engineering structures in Surfers Paradise [10]. Each location in this figure has been given a number to denote peat's depth and thickness in this particular location (Table 1). Figure 9 shows the borehole distribution of these locations within the study area. These boreholes contain peat in its soil profile.

It can be seen from Table 1 that peat layer has a varying thickness which ranges between 0.1-7.0 m at depth between R.L. -10 to -19.6 m below the ground surface. As mentioned, peat is geotechnically problematic soil and many engineers try to avoid the adventure of construction over peat. Therefore, attention should be required for the already existed buildings and safety precaution is also necessary for the proposed new engineering structures in the peat locations. Approximately all the buildings in the study area are supported by pile foundations. Thus, this study will be useful for the potential engineering structures to take into account the depth and the thickness of peat for a suitable, economic, and safe design in Surfers Paradise.

CONCLUSION

To conclude, eight interpolation techniques have been used to characterise the subsoil conditions in Surfers Paradise. The Inverse Distance Weighting (IDW) technique within the Spatial Analyst in ArcMap10 showed a better representation for the Standard Penetration Test (SPT) N values with a certain parameters. Based on this, 26 interpolated SPT-N values zonation maps have been performed to characterise the soil in terms of soil stiffness by using the IDW technique.

Peat is highly organic and compressible and it has been considered as a geotechnically problematic layer. This layer has a varying thickness ranges between 0.1-7.0 m at depth between R.L. -10 to -19.6 m below the ground surface in the study area.

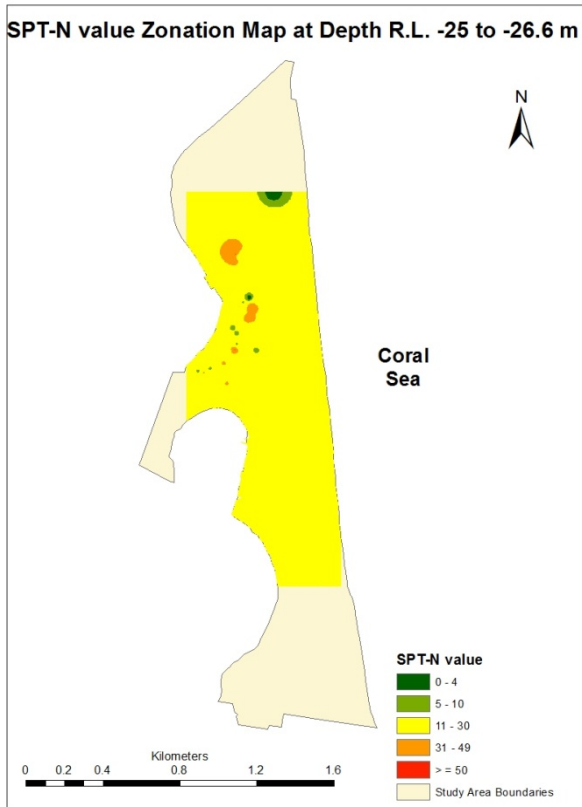


Fig. 7 SPT-N value zonation map at depth R.L. -25 to -26.6 m.

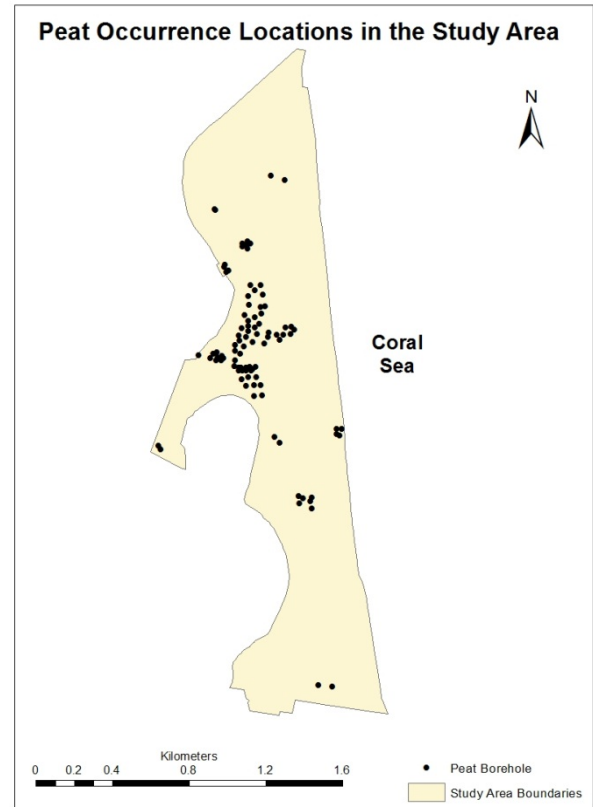


Fig. 9 Peat contained boreholes in the study area.

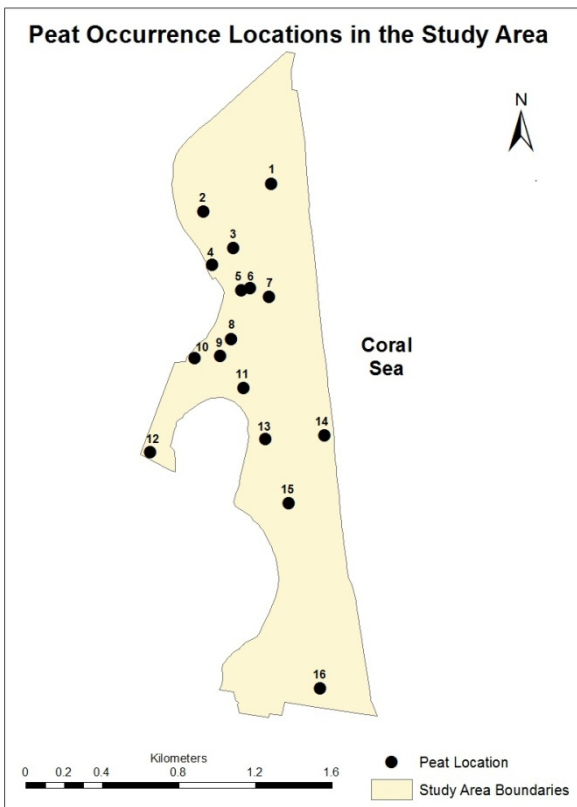


Fig. 8 Peat occurrence locations in the study area

In addition, attention should be paid in terms of potential foundations challenges, to locations which have a high thickness of peat such as a location in the core of the study area which has a peat thickness of 7.0 m. This study might be beneficial for public agency geotechnical engineers and decision makers at local and state levels.

This paper is a part from an ongoing research to characterise physical and engineering properties of peat and soil in Surfers Paradise in Southeast Queensland, Australia.

REFERENCES

- [1] Player RSV, "Geotechnical Engineering for Transportation Projects", GeoTrans 2004, 2004, p.p. 886-893.
- [2] Malkawi AIH, Alawneh, AS & Abu-Safaqah, "Effects of organic matter on the physical and the physicochemical properties of an illitic soil", Journal of Applied Clay Science, Vol. 14, no. 5-6, 1999, pp. 257-78,
- [3] Haan EJ and Kruse GAM, "Characterisation and engineering properties of Dutch peats", Vol. 3, Ed. Tan TS , Phoon KK , Hight DW & Leroueil S, Taylor & Francis Group, London, , 2007, pp. 2101-33.

Table 1 Peat thickness and its depths below the ground surface in the study area.

Location	Peat Depth (m)	Peat Thickness (m)	Location	Peat Depth (m)	Peat Thickness (m)
1	27.2 - 32.2	5.0	9	17.0-20.0	3.0
2	1.2-6.7	5.5	10	15.4-19.4	4.0
3	14.9-17.5	2.6	11	17.7-21.7	4.0
4	12.6-14.4	1.8	12	11.6 -12.4	0.8
5	16.0-23.0	7.0	13	11.3-12.5	1.2
6	17.75 - 21	3.25	14	21.4 - 23	1.6
7	17.1-18.3	1.2	15	17.0 - 22.0	5.0
8	18.0-22.5	4.5	16	0 - 1.5	1.5

- [4] Augusto FO, Hirai JN, Oliveria AS & Liotti ES, "GIS applied to geotechnical and environmental risk management in a Brazilian oil pipeline", *Bulletin of Engineering Geology and The Environment*, Vol. 69, 2010, pp. 631-41.
- [5] Antoniou AA, Papadimitriou AG & Tsiambaos G, "A geographical information system managing geotechnical data for Athens (Greece) and its use for automated seismic microzonation", *Natural Hazards*, Vol. 47, 2008, pp. 369-95.
- [6] Orhan A and Tosun H, "Visualization of geotechnical data by means of geographic information system: a case study in Eskisehir city (NW Turkey)", *Environmental Earth Sciences*, Vol. 61, 2010, pp. 455-65.
- [7] Hellawell EE, Lamont-Black J, Kemp AC, and Hughes J, "GIS as a toll in Geotechnical Engineering", *Geotechnical Engineering*, Vol. 149 (2), 2001, pp. 85-93.
- [8] Haider A., Oh E, Leila E, Chai G, "Subsurface Visualization of Peat and Soil by using GIS in Surfers Paradise, Southeast Queensland, Australia", *Electronic Journal of Geotechnical Engineering*, Vol. 18, June 2013, Bund.I, 171.
- [9] Childs, C, "Interpolating Surfaces in ArcGIS Spatial Analyst", *ArcUser*, Vol. July-September, 2004, pp. 32-5.
- [10] Al-Ani H, Oh E, Chai G, "Engineering properties of peat in estuarine environment", in in *Proc. 1st Int. Conf. on Foundation and Soft Ground Engineering Challenges in Mekong Delta*, 2013, pp. 181-191.
- [11] Oh, EYN, Huang M, Surarak, C, Adamec, R & Balasurbamaniam, AS, "Finite Element Modelling for Piled Raft Foundation in Sand", in *Eleventh East Asia-Pacific Conference on Structural Engineering & Construction (EASEC-11) "Building a Sustainable Environment"*, Taipei, Taiwan, 2008, p. 8.
- [12] Look, BG, "Handbook of Geotechnical Investigation and Design Tables", London, Taylor & Francis, 2007, ch.5.

EVALUATION OF CONSTITUTIVE MODEL IN SIMULATING THE BEHAVIOR OF CEMENT-TREATED SOIL

Ay Lee Saw¹, C F Leung² and S A Tan³

^{1,2&3}Centre for Soft Ground Engineering, National University of Singapore, Singapore

ABSTRACT

Owing to presence of thick soft marine clay in Singapore, it is often required to improve the in-situ weak soil for various construction purposes especially for excavation works. One such ground improvement technique is to treat the soft clay with cement. The treatment may be conducted at shallow depths not far below the ground level to facilitate an open excavation or at greater depths as embedded struts to support deep basement excavation works. However, relatively little studies had been performed to study the former treatment method. The current design practice evaluates the problem as an embankment stability situation where the focus is drawn to the shearing and sliding failure modes. Very often, elastic-perfectly plastic soil model using the material shear strength is adopted to simulate the behavior of cement-treated soil in the analyses. However, other failure modes such as bending and tensile failure may be overlooked. In this study, the use of three types of constitutive model, i.e. elastic-perfectly plastic Tresca, isotropic hardening/softening and concrete damage plasticity model in simulating the cement-treated soil behavior are examined. Available compression and tension laboratory tests for cement-treated sand are calibrated to compare the use of selected constitutive models. Calibration results show that the concrete damage plasticity model is able to capture the softening behavior of cement-treated sand in both compression and tension. This constitutive model is further validated by simulating a full scale test of cantilever cement-treated soil column under lateral load. 3-D finite element analysis result shows that the load-deflection relation is in good agreement with field measurement. Moreover, the predicted crack development in the treated column agrees well with the field observation.

Keywords: Cement-treated soil, Constitutive model, Concrete damage plasticity, Tension-softening

INTRODUCTION

Cement is often used as a binder in ground improvement work to increase the strength and stiffness of in-situ soft soil. Generally, a soft soil layer of certain thickness is improved by installing overlapping treated columns and employed as an embedded strut supporting the retaining wall system in deep basement excavation work. The successful case histories of adopting this method to facilitate deep excavation work in soft clay have been well documented [1]-[3]. In view of the cost and time savings as compared to the conventional method, constructing a shallow depth ground improvement layer not far below ground level has been attempted to facilitate an open excavation in Singapore in recent years.

For shallow open excavation, column-shaped cement-treated soil in different layouts is an alternative design to retaining wall. In current design practice, engineers often regard the improved layer as a composite material gravity wall. As such, two stability analyses involving external and internal wall stability are evaluated. For external stability analysis, three failure modes of the treated soil mass (assuming no failure occurred within the treated soil and untreated soil): sliding, overturning, and bearing

capacity are examined. Generally, the weighted average method is adopted to obtain the average properties of the improved ground. For internal stability analysis, rupture breaking failure is examined by a slip circle analysis where the shear failure of treated column is assumed and the induced stress on the column should be less than the allowable strength. Nevertheless, some studies revealed several failure modes that are not covered by current design practice such as bending and tensile failure [4]. It is also proposed that finite element (FE) analysis should be conducted to study the development of stress and strain in the improved ground by CDIT 2002.

In this paper, numerical constitutive models in simulating the cement-treated soil are evaluated. Three types of constitutive soil model, i.e. Tresca, isotropic hardening/softening and concrete damage plasticity (CDP) are compared to examine the most appropriate model to describe the behavior of cement-treated soil. Then, a full scale bending test of laterally loaded cantilever cement-treated column is analyzed using the CDP model. The simulations are modeled with finite element software Abaqus/Standard 6.10.

CONSTITUTIVE MODEL FOR CEMENT-TREATED SOIL

Behavior of Cement-treated Soil

Cement-treated soil is a product of mixing cement to in-situ soil aiming to increase the strength and stiffness by bonding the particles together. The increase in strength of the mixture is mainly attributed to three reactions happened during the mixing, namely: hydration, ion exchange (flocculation), and pozzolanic reaction. Many researchers had studied the behavior of cement-treated soil experimentally. It is established that addition of cement has transformed the in-situ soil from ductile into brittle behavior [5-6]. As shown in Fig. 1 and Fig. 2, the brittle behavior is manifested both in tension and compression. Generally, the treated soil stress increases abruptly associated with a low strain followed by sudden reduction of post peak stress to a very low value.

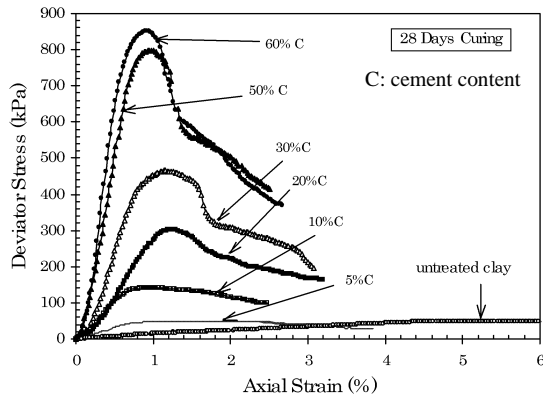


Fig. 1 UCT stress-strain curve for cemented marine clay with various cement content [5]

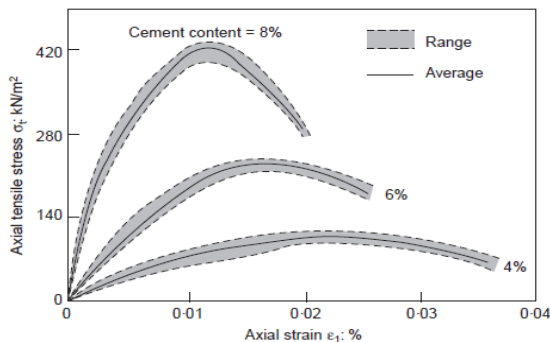


Fig. 2 Direct tensile test stress-strain curve for cemented sand [6]

Constitutive Model

Finite element analysis can simulate the cement-treated soil behavior accurately only if an

appropriate constitutive model is adopted to simulate the material behavior. Therefore, the constitutive model prediction is first examined in the present study using available laboratory test results. Laboratory data by [7] and [8] for cement-treated sand in triaxial compression test and direct tensile test respectively are adopted in the present study. Three constitutive models, i.e. elastic-perfectly plastic Tresca, isotropic hardening/softening and concrete damage plasticity model are adopted to calibrate the laboratory test data. These three constitutive models are the built-in material model available in Abaqus/Standard.

Model and Parameters

An elastic-perfectly plastic Tresca model can be used to define a material which upon reaching certain stress state, undergoes irreversible deformation. This model is commonly used in practice due to its simplicity with few parameters needed. The required design parameters are E and ν defining the elastic regime; and C_u used to define the yield surface. In addition, a tension truncated Tresca yield criterion is considered in present study by adopting a tension cut-off parameter.

For isotropic hardening/softening model, the yield surface changes size (increase/decrease) uniformly in all directions as plastic straining occurs. In Abaqus, the yield stress σ^I can be defined as a tabular function of equivalent plastic strain, $\varepsilon^{pl(i)}$. The elastic regime is similarly defined in Tresca model.

Concrete damage plasticity (CDP) model has been widely used to simulate the crack development and strength degradation due to damage for quasi-brittle material such as concrete. Therefore, it is strongly believed that this model can work reasonably well for cement-treated soil which is also known as a quasi-brittle material. CDP model assumes that the two main failure mechanisms as tensile cracking and compressive crushing. The design parameters needed for CDP model can be extracted from the experimental $\sigma - \varepsilon$ curve for both uniaxial compression and tension tests as shown in Fig. 3 and Fig. 4, respectively. Details regarding this model are available in Abaqus manual.

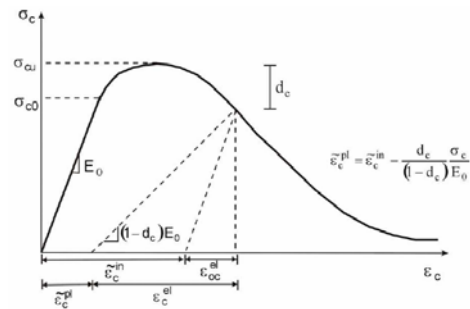


Fig. 3 Dependence $\sigma - \varepsilon$ in compression for CDP

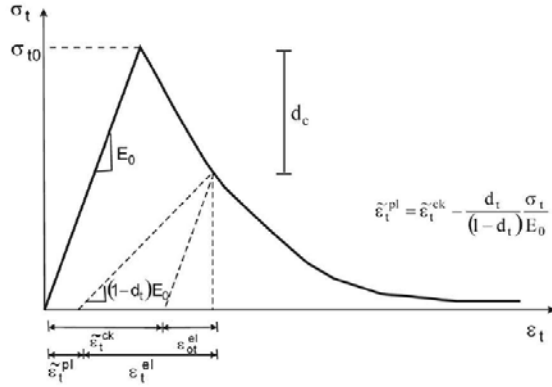


Fig. 4 Dependence $\sigma - \varepsilon$ in tension for CDP

Laboratory Data

The stress-strain relationships for a drained triaxial compression test and direct tensile test for cement-treated Toyoura sand are calibrated in the present study. The specimen test results are shown in Fig. 5 and Fig. 6, while the test details are available in [7-8].

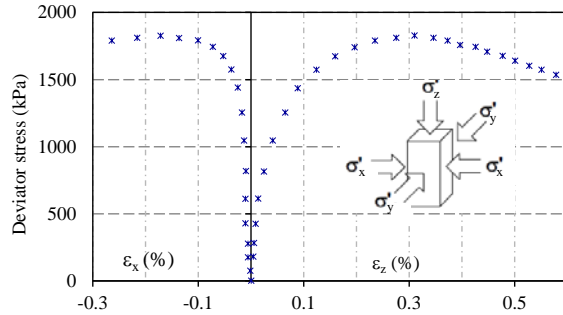


Fig. 5 Stress-strain curves for drained triaxial compression test (initial confining stress=49kPa) [7]

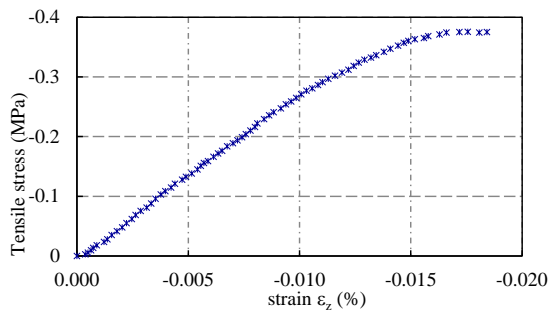


Fig. 6 Stress-strain curve for direct tensile test [8]

Finite Element Model

The drained triaxial compression test was simulated using a 3-D single element as displayed in Fig. 7. The boundary condition was modeled by constraining the bottom plane from moving

vertically. The cell pressure of 49 kPa was represented by distributed load acting around all the planes except the bottom plane. The testing process using vertical displacement control was simulated by applying prescribed displacement from top. The element type used in this model was an 8-node linear brick (C3D8R).

For direct tensile test, the test was simplified with one quarter model where the symmetric condition was modeled by constraining the tangential degree of freedom on the bottom plane and left plane from moving. The test using vertical displacement control was simulated by applying prescribed displacement from top. 4-node bilinear axisymmetric quadrilateral (CAX4R) element was adopted in this case.

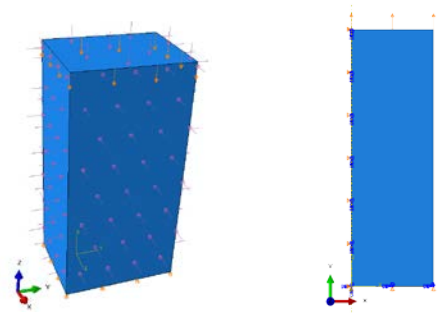


Fig. 7 Finite element model: drained triaxial compression test (left) and direct tension test (right)

The parameters used to simulate elastic regime were similar for three aforementioned constitutive models with Young's modulus $E = 2400$ MPa and Poisson's ratio $\nu = 0.167$. The parameters used to describe the yield criterion of the three models are summarized in Tables 1-3.

Table 1 Model parameters for Tresca model

Cohesion	Tension Cutoff
900kPa	380kPa

Table 2 Model parameters for Isotropic model

Yield Stress	Plastic Strain
1200kPa	0
1800kPa	0.0015
1800kPa	0.0032
1500kPa	0.0053

Table 3 Model parameters for CDP model

Compression Yield	Inelastic Strain	Tensile Yield	Fracture Energy
1100kPa	0	380kPa	9N/m
1650kPa	0.0015		

1650kPa	0.0032
1400kPa	00053

Result and Discussion

The calibration results are shown in Figs. 8-9. In compression test, the elastic-perfectly plastic Tresca model is not able to simulate the material stress-strain behavior after the specimen experiences 0.05% axial strain. Owing to a single stiffness and perfectly plastic criteria assumed in this model, the hardening as well as the softening behavior after the specimen undergoes 0.05% axial strain cannot be simulated by this model. On the other hand, isotropic hardening/softening and CDP are capable in capturing the material nonlinear behavior and the calibrated results yield closely with experimental results.

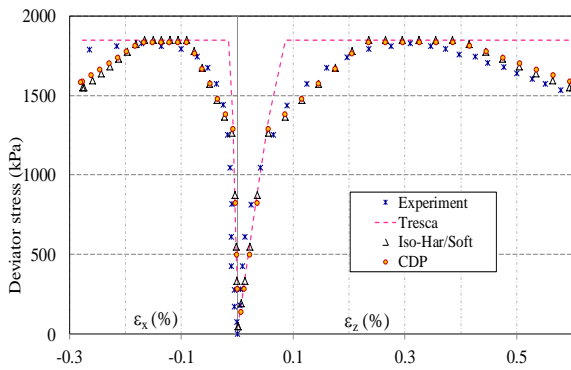


Fig. 8 Calibration results for compression test modeled by 3 types of constitutive model

Nevertheless, a representative model shall be able to capture both the compressive and tensile behavior of the cement-treated soil. As shown in Fig. 9, the post peak stress modeled by Tresca model remains at the input tension cut-off strength 380kPa. However, in reality the material experiences post peak tensile softening as illustrated in the test result. Although the isotropic hardening/softening model could simulate the compression test well, the isotropic yield criterion which allows for the development of any value of tensile stress has overestimated the actual material strength. This is evident in the calibration result shown in Fig. 9 where the predicted tensile stress-strain curve always exceeds the experimental peak tensile strength. Without the tension cut-off function as built in Tresca model, the isotropic hardening/softening model is not able to evaluate the tensile behavior of cemented soil. Nonetheless, the above mentioned shortcoming of the two models can be overcome by CDP model. In CDP model, the tensile softening behavior of the material can be simulated by the parameters of tensile stress and fracture energy G_f . Fracture energy G_f proposed by [9] is defined as the energy required to open a unit of

crack using brittle fracture concept. This model then assumes a linear loss of strength after cracking. Despite of G_f , this fracture energy cracking model can be invoked by specifying the post-failure stress as a tabular function of cracking displacement. These built-in functions make the CDP model capable of better simulating the behavior of cement-treated soil, as illustrated in Fig. 9.

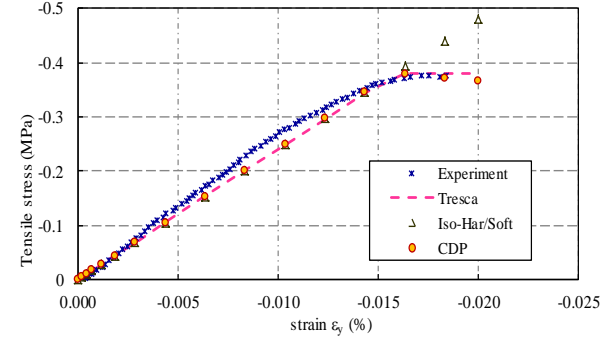


Fig. 9 Calibration results for direct tensile test modeled by 3 types of constitutive model

FE ANALYSIS OF A FULL SCALE TEST

A full scale test of cantilever cement-treated soil column under lateral load (Fig. 10) was simulated here to validate the use of CDP model in simulating an actual field problem. Details of the in-situ full scale test can be referred to [10]. The design parameters for untreated soil, concrete and steel plate are similar to those given in [11] while the parameters for treated columns using CDP model are summarized in Table 4.

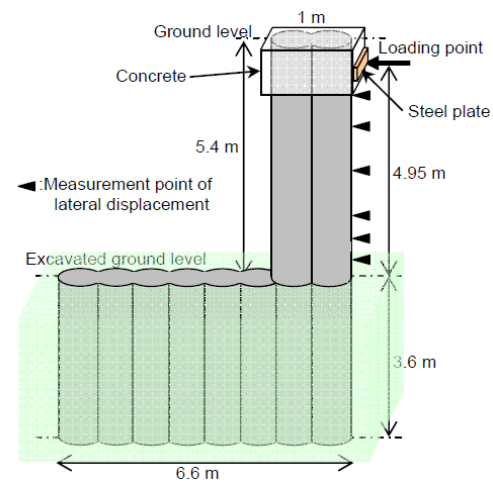


Fig. 10 Full scale test by [10-11]

A 3-D finite element analysis was conducted using 4-node linear tetrahedron (C3D4) element. The element length varied from 0.05m to 0.015m. Fig. 11 shows the finite element model and its

boundary conditions for this field test. Generally, the embedded surrounded soil was not permitted from moving tangentially. Although cyclic loading was applied in the field test, a monotonic loading condition was assumed in the present analysis. The test was modeled by applying prescribed displacement at the center point of the steel plate.

Table 4 Parameters for CDP model in full scale test

Compression Yield	Inelastic Strain	Tensile Yield	Fracture Energy
4400kPa	0	440kPa	9N/m
Density	E	ν	
1700kg/m ³	8800MPa	0.167	

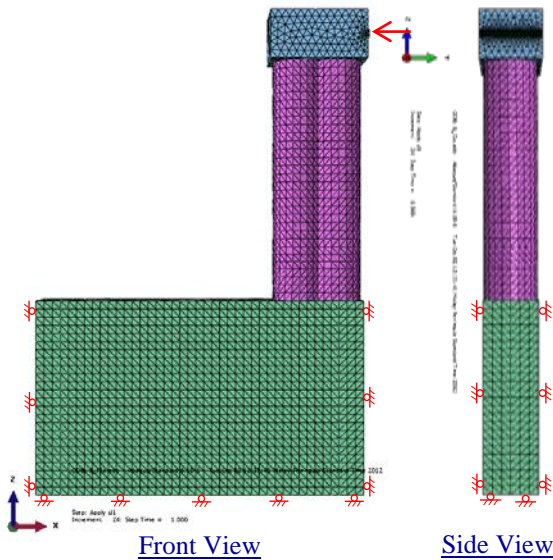


Fig. 11 FE model used to analyze the full scale test

Result and Discussion

The analysis result for lateral load-displacement relation is presented in Fig. 12 for the CDP model, which shows that there is good agreement between the analysis and the field measurement. Furthermore, the crack development in the cantilever treated column can be reasonably well modeled as displayed in Fig. 13a. In CDP model, the tensile damage is represented by the tensile damage variable, d_t which takes values from zero, representing the undamaged material, to one, which represents a total loss of strength. The first damage crack occurs approximately at 300 mm above the ground level in finite element analysis coinciding with the field observation (Fig. 13b). Hence, the use of CDP model in simulating cement-treated soil problem in the field is promising.

Beyond this, an attempt of using tension truncated Tresca model to simulate the cemented

column was conducted. However, the analysis was not stable due to the convergence problem once the tensile stress reached peak. As a result, classical Tresca model was adopted and the analysis results compared with CDP model are displayed in Fig. 14.

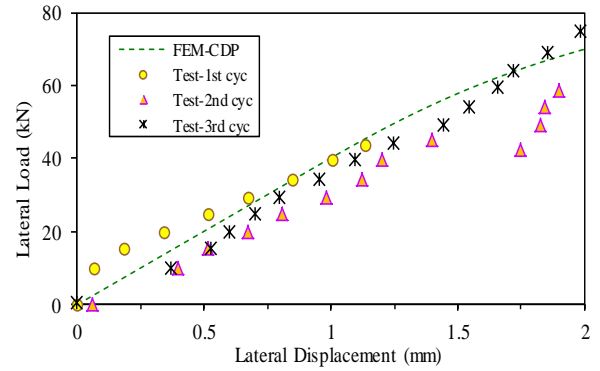


Fig. 12 Lateral load-displacement relations for field test and FEM

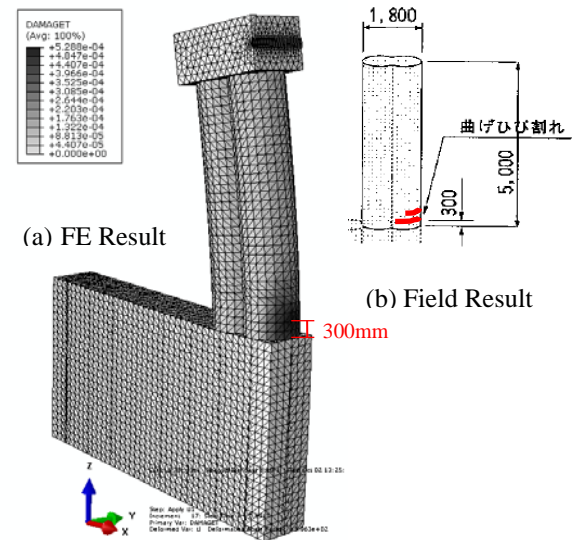


Fig. 13 Crack formation in cemented column

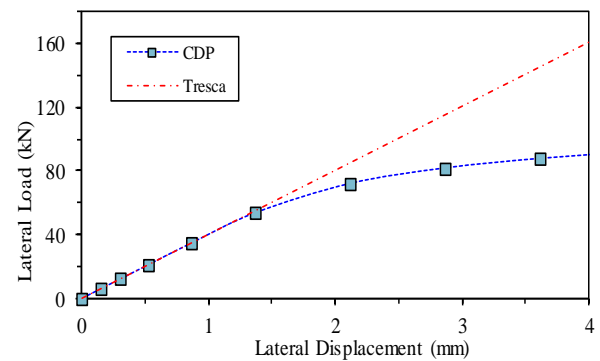


Fig. 14 Lateral load-displacement relations for CDP model and Tresca model

Prior to damage, both materials yield similar load-displacement relationships within the elastic state. Once damage has occurred, the increment of lateral load resistance is significantly reduced. Classical Tresca model shown in Fig. 13 grossly overestimates this load. This is believed to be attributed to the shear failure mechanism assumed, thus any tensile or bending failure is not captured by the classical elastic-perfectly plastic Tresca model. Although Tresca model is commonly used in practice to simulate cement-treated soil, it is not an appropriate model for this kind of problem involving lateral stresses as demonstrated in the present study.

CONCLUSION

Three constitutive models, namely Tresca, isotropic hardening/softening and concrete damage plasticity (CDP) were used to simulate the behavior of cement-treated sand. Analysis result shows that CDP model is able to simulate both compressive and tensile behavior of cemented soil. The lack of tension-softening feature in the other two models tends to grossly overestimate the tensile strength. Back-analysis of a field problem also shows that CDP model performs well in modeling the tensile crack development for a cantilever cement-treated soil column under lateral load. In conclusion, CDP is a more appropriate model so simulate cement-treated soil behavior compared to elastic-perfectly plastic Tresca and isotropic hardening/softening model.

REFERENCES

- [1] Gaba AR, "Jet grouting at newton station, Singapore", 10th Southeast Asian Geotechnical Conf., Taipei, 1990, pp. 77-79.
- [2] Sugawara S, Shigenawa S, Gotoh H, and Hosoi T, "Large-scale jet grouting for pre-strutting in soft clay", Grouting and Deep Mixing, Rotterdam: Balkema, 1996, pp. 353-356.
- [3] Lim PC and Tan TS, "A floating type braced excavation in soft marine clay", Underground Space Singapore, 2003, pp. 326-337.
- [4] Kitazume M, "Stability of group ground column type DM improved ground under embankment loading behavior of sheet pile quay wall" Report of the Port and Airport Research Institute, Nagase, Yokosuka, Japan, Port and Airport Research Institute, Vol. 47, 2008.
- [5] Kamruzzaman AHM., "Physico-chemical and engineering behavior of cement treated Singapore marine clay", Ph.D, NUS, 2002.
- [6] Das BM and Dass RN, "Lightly cemented sand in tension and compression", Geotech. and Geol. Eng., Vol. 13, 1995, pp. 167-177.
- [7] Namikawa T, "Study on tensile and shear failure characteristics of cement-treated sand", Ph.D, Uni. Of Tokyo, 2006.
- [8] Koseki J, Sato T and Nishimoto T, "Anisotropy in strength characteristics of cement-treated sand prepared by compaction", Proc. Symp. Cement-Treated Soils, JGS, 2005, pp. 365-368.
- [9] Hillerborg A, Modeer M and Petersson PE., "Analysis of crack formation and crack growth in concrete by means of fracture mechanics and finite elements", Cement and Concrete Research, Vol. 6, 1976, pp. 773-782.
- [10] Babasaki R, Suzuki Y, Nakama T and Yamada K, "Study for reinforced earth retaining wall by deep mixing method (Part 2)", Proc. 32th Annual Conf. of JGS, 1997, pp. 1733-1734.
- [11] Namikawa T, Koseki J and Suzuki Y, "Finite element analysis of a full scale bending test of cement treated soil column", IACMAG, India, Oct 2008, pp. 3635-3641.

UPDATING THE PREDICTIVE MODEL FOR THE VERTICAL COLLAPSE PERCENTAGE OF COLLAPSIBLE SOIL SUBGRADES

Moshe Livneh¹ and Noam A. Livneh²

¹Civil and Environmental Engineering Faculty, Technion-Israel Institute of Technology, Haifa, Israel

²Noam Livneh Engineering Ltd., Haifa, Israel

ABSTRACT

Since the publication of the Israeli model for the vertical collapse percentage of collapsible soil subgrades in 2012, new collapse test results have become available (all together, for 123 undisturbed and remolded silt or silty clay specimens), enabling an updating of the existing collapse model. In addition, old available collapse test data that do not contain all the necessary parameters of the materials tested (all together, for 189 undisturbed silt or silty clay specimens) have also become available for use. Thus, updating is logical so as to obtain a more accurate prediction of vertical collapse under a given vertical pressure exerted on the silt or silty clay under consideration. This paper concentrates on the required updating, together with (a) a search for the true impact of the vertical induced pressure on the predicted vertical collapse values and (b) an elaboration of the practical use of the updated model in collapse settlement calculations for a given local project, together with its limited local collapse test-results, all in order to enhance the accuracy of collapse settlement calculations. The final recommendation is to use the new updated vertical collapse model together with the limited local collapse tests results of a given project. This is done in a combined way that adjusts the new updated model to fit the specific collapse characteristics of the given project.

Keywords: Collapse, Embankment, Settlement, Silty characteristics

INTRODUCTION

Pavement and railway bed design involves a stability analysis of their earthwork material. In this respect, predicting the vertical collapse of embankments based on silts or silty clays is a necessary step. To recall, silts or silty clays in semi-arid zones are conventionally considered problematic, since they exhibit a high potential for collapse under loading. All soils settle upon loading, but the amount of settlement varies from soil to soil and is dependent on load-induced stresses. Although such settlement will eventually cease after a certain period of time, subsequent wetting under certain conditions may cause additional settlement, known as collapse.

The required prediction of the vertical collapse of these embankments is aided by a collapse model that reflects the relationship between the predicted vertical collapse and the vertical surcharge acting on the silt or the silty clay at a given depth. The development of this model is shown by the authors in [1]. To summarize, this collapse model was obtained from laboratory tests on 73 undisturbed silt or silty clay specimens. The curves of this model are dependent on knowledge of the following parameters that characterize the silt or silty clay being studied: (a) liquid limit, (b) the ratio between in-situ moisture content and plasticity limit, and (c) in-situ dry density.

The suggested collapse model is based on 73 local collapse tests that were conducted according to the

instructions of the single-odometer test, known also as the ASTM D 5333 collapse test. In this test, an undisturbed or remolded specimen is first driven into the odometer ring and then subjected to increasing vertical loads. The specimen is permitted to attain equilibrium deformation at each level of pressure. It is then inundated at a prescribed applied pressure, and the deformation is measured. The deformation induced by the addition of water, divided by the initial height of the specimen, expressed in percentage terms, defines the collapse potential, which this paper also terms vertical collapse.

Since the publication of the aforementioned Israeli collapse model in 2012 [1], new collapse test results have become available (all together, from 123 undisturbed silt or silty clay specimens), enabling an updating of the existing collapse model. In addition, old available collapse test data that do not contain all the necessary parameters of the materials tested (all together, from 119 undisturbed silt or silty clay specimens) have also become available for use. Thus, it seems to be only logical to update the existing model in order to obtain a more accurate prediction of vertical collapse under a given vertical pressure exerted on the silt or silty clay under consideration.

To sum up, this paper concentrates on the required updating, together with (a) a search for the true impact of the vertical induced pressure on the predicted vertical collapse values; (b) an elaboration of the practical use of the upgraded model in collapse

settlement calculations for a given local project, together with its limited local collapse test results, all in order to enhance the accuracy of collapse settlement calculations.

EXISTING VERTICAL COLLAPSE MODEL

As mentioned, predicting the settlement of an embankment-base surface as a result of subgrade collapse necessitates knowledge of the collapse-pressure characteristics of the silt or the silty clay strata under consideration, and these are usually obtained from laboratory tests on undisturbed and disturbed silt or the silty clay specimens. This prediction model denotes a statistical relationship between the vertical collapse (C_p), in percentages, that is due to applied vertical pressure (P_p), in kPa, and the following parameters characterizing the silt or the silty clay specimens under examination: moisture content (W) in percentages, in-situ dry density (D) in kN/m^3 , and dry density at liquid limit (D_{LL}) in kN/m^3 as defined by Eq. (2). For 73 local specimens extracted from a silt or a silty clay subgrade situated in the southern part of the country, more specifically from the construction site of Goral Junction-Netivot railway line, the best formulation of this model, reproduced from [1], is as follows:

$$C_p = 28.5354 - 27.0305 \times (D/D_{LL})^{0.9825} + 0.0001196 \times [\log(P_p)]^{11.3741} / (W/PL)^{1.4908} \quad (1)$$

$$D_{LL} = 9.807 \times 100 / (100/G + LL) \quad (2)$$

In Eq. (2), G denotes the solid specific gravity of the silt or the silty clay specimen, and LL denotes its liquid limit in percentages. Here it should be noted that Eq. (1) was derived with the aid of the Excel Solver command.

As shown in Fig. 1, the R^2 (coefficient of determination) value obtained for the vertical collapse model presented in Eq. (1) is 0.535. In addition, the accompanying SE (standard error) value obtained is 4.206%, and the SE/SY (ratio of standard error to standard deviation of the measured vertical collapse values) is 0.707. In other words, 68 percent of all predictions using Eq. (1) may be expected to be accurate within $\pm 4.206\%$, and 95 percent to be accurate within $\pm 8.412\%$.

Here, it should be mentioned that Eq. (1) was formulated to yield the highest R^2 value from among all possibilities that (a) include the independent variables of the soil's plasticity and (b) yield true physical behavior as clearly described in [3] (i.e., an increase in C_p with increasing P_p , and a decrease in C_p with increasing W , D , and LL). The density-ratio (D/D_{LL}) variable of Eq. (1) follows this finding exactly as given in [4] or indirectly as given by a similar finding in [5].

In addition, Fig. 2 depicts Eq. (1) graphically for the silt or the silty clay material. For comparison purposes, this figure also includes the collapse results obtained from the laboratory testing of the 73

specimens of Fig. 1. The average value of the W/PL measured values for these specimens is 0.565.

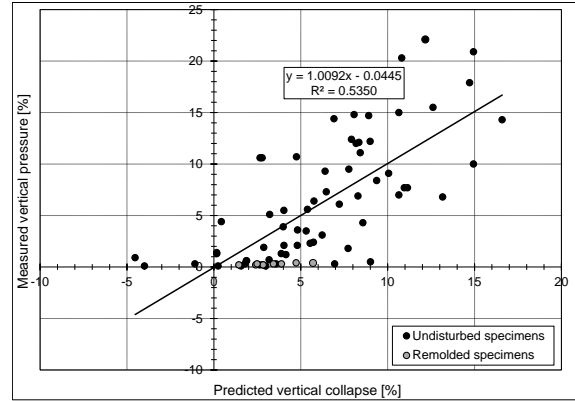


Fig. 1: Measured vertical collapse versus vertical collapse predicted from Eq. (1) for the 73 local specimens of [1]

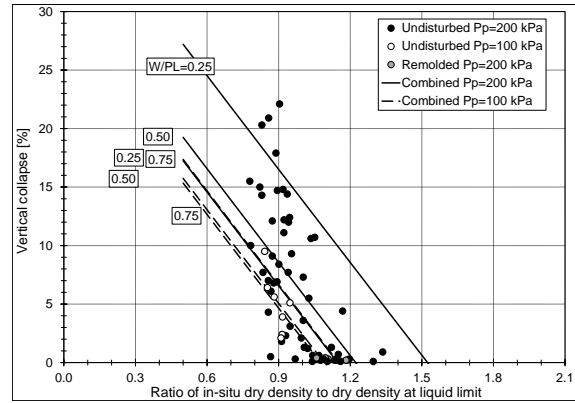


Fig. 2: Vertical collapse versus density ratio (D/D_{LL}) for vertical pressures of 100 kPa and 200 kPa as derived from Eq. (1) for the 73 local specimens of [1]

Finally it is worthwhile mentioning that (a) Eq. (1) and Eq. (2) have recently served as the vertical collapse model in the settlement calculations carried out in [2]; and (b) in the following sections, silt also refers to silty-clay.

USE OF ADDITIONAL TEST DATA

Recently, an additional 50 new collapse test results have become available from another construction site in the southern part of the country, more specifically from the southern part of Highway No. 6 (Section No. 21) near the city of Beersheba. Combining these new results with the 73 old ones yields the following modified vertical collapse model:

$$C_p = 1.7341 \times 10^5 - 1.7341 \times 10^5 \times (D/D_{LL})^{0.00008} + 0.6840 \times [\log(P_p)]^{0.9941} / (W/PL)^{1.4739} \quad (3)$$

As shown in Fig. 3, the R^2 (coefficient of determination) value obtained for the vertical collapse model of Eq. (3) is 0.312, or lower than that of Eq. (1). In addition, the accompanying SE (standard error) value obtained is 4.591%, and the SE/SY (ratio of standard error to standard deviation of the measured vertical collapse values) is 0.847. In other words, 68

percent of all predictions from Eq. (1) may be expected to be accurate within $\pm 4.591\%$, and 95 percent to be accurate within $\pm 9.182\%$.

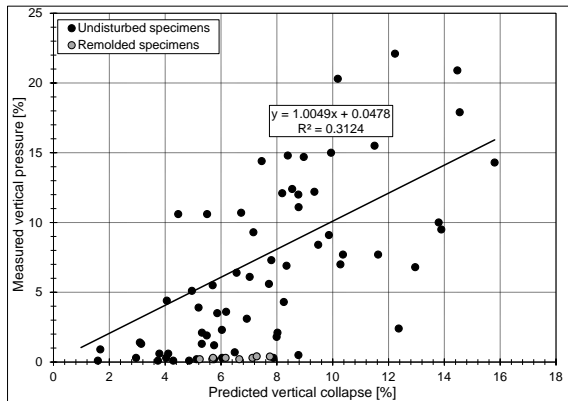


Fig. 3: Measured vertical collapse versus predicted vertical collapse from Eq. (3) for the old 73 and new 50 local specimens

Fig. 4 depicts Eq. (3) graphically for the silt material. For comparison purposes, this figure also includes the collapse results obtained from the laboratory tests of the 123 specimens of Fig. 3. For these specimens, the average value of the W/PL measured values is 0.560; i.e., almost identical to the previous value of the 73 specimens, which was 0.565.

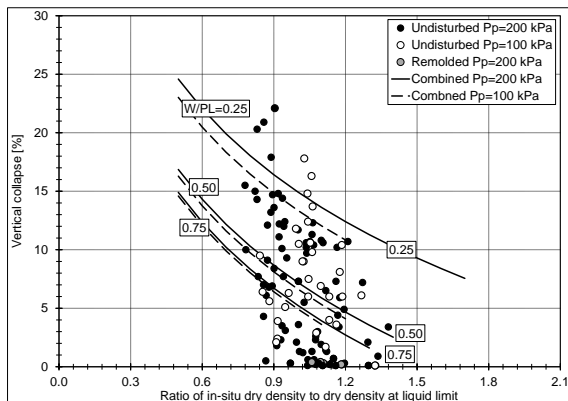


Fig. 4: Vertical collapse versus density ratio for vertical pressures of 100 and 200 kPa as derived from Eq. (3) for the old 73 and new 50 local specimens

Moreover, Fig. 4 indicates that the modified vertical collapse model is practically not sensitive to variations in the induced vertical pressure. The increase in C_p values when P_p varies between 100 kPa and 200 kPa is almost zero for $W/PL=0.75$, and about 1.5% for $W/PL=0.25$. This behavior should be regarded as totally unacceptable when compared with that characterized by the curves of Fig. 2 or with that defined by other sources, such as [6].

The main conclusion drawn from the findings of the present section is that the use of Eq. (3) is not acceptable for prediction purposes and that the 123 test-results data should be analyzed in a way that maintains the impact of the P_p input on the C_p calculated results.

INDUCED VERTICAL PRESSURE IMPACT

In order to determine the impact of the induced vertical pressure on the calculated vertical collapse results, additional old collapse test-results data, reported in [5] and [7], the latter for three airbase locations again in the southern part of Israel, were analyzed as described in following paragraphs. As these data do not contain all the necessary parameters for characterizing the tested soil, it was not possible to include them in the previous calculations of Eq. (1) or Eq. (3).

The test-results data from these three sites, when gathered in a united pool, yield the following regression equation:

$$C_p = 2.3953 - 12.9186 \times (D/D_{LL}) + 7.7727 \times \log(P_p) \quad (4)$$

The use of the linear regression model of Eq. (4) instead of that of Eq. (1) was necessary in order to overcome the absence of the measured W values in the data tested. The following values hold for Eq. (4): (a) P_p is given in kPa, (b) the R^2 value equals 0.491, and (c) the SE value equals 2.460%.

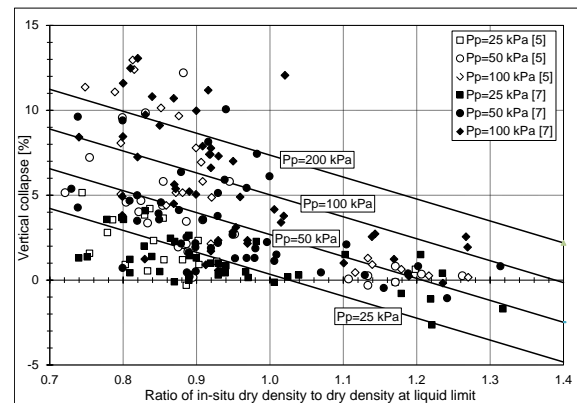


Fig. 5: Vertical collapse versus density ratio for vertical pressures of 25, 50, 100 and 200 kPa as derived from Eq. (4) for the old 189 local specimens of [5] and [7]

Eq. (4) indicates that the dependence of C_p values on the induced vertical pressure is characterized by the $7.7727 \times \log(P_p)$ expression. Thus, it is interesting to compare the contents of this expression to other sources. To this end, the regression equation of [6] is given below:

$$C_p = 48.496 + 0.102 \times C_u - 0.457 \times W - 3.533 \times D + 6.447 \times \log(P_p) \quad (5)$$

For Eq. (5), P_p is given in kPa, D in kN/m^3 , and W and C_u in percentages. The R^2 value of this equation obtained for its experimental data (138 remolded specimens) was rather high, 0.94. Furthermore, the associated SE value obtained for its experimental data was rather a low value, 1.94%.

It is to be noted that Eq. (5) contains an additional independent variable, C_u , which denotes the coefficient of uniformity of the prescribed silt. For the case of the 73 specimens of Fig. 2, the average C_u value equals 80%. This equation also indicates that the dependence of C_p values on the induced vertical pressure is characterized by the $6.447 \times \log(P_p)$

expression, which is very similar to that of Eq. (4). As for the comparison with the regression equation of the data of the 73 specimens (Fig. 2) and also that of the 123 specimens (Fig. 4), the following linear regression study should first be conducted.

The regression equations for the old 73 specimens that serve as other regression options for Eq. (1) are shown in the two expressions that follow, for which $R^2=0.493$ and $SE=4.327\%$ in the first expression, and $R^2=0.452$ and $SE=4.467\%$ in the second expression:

$$C_p = 14.5465 - 6.7860 \times W/PL - 29.9013 \times D/D_{LL} + 10.9013 \times \log(P_p) \quad (6)$$

$$C_p = 5.0010 - 32.9836 \times D/D_{LL} - 14.7602 \times \log(P_p) \quad (7)$$

In a similar manner, the regression equations for the old 73 specimens and the new 50 specimens that serve as other regression options for Eq. (3) are shown in the next two expressions, for which $R^2=0.351$ and $SE=4.421\%$ in the first expression, and $R^2=0.235$ and $SE=4.781\%$ in the second expression:

$$C_p = 40.6598 - 11.1960 \times W/PL - 16.2179 \times D/D_{LL} + 4.9255 \times \log(P_p) \quad (8)$$

$$C_p = 38.8035 - 19.9464 \times D/D_{LL} - 5.1744 \times \log(P_p) \quad (9)$$

Now, the dependence of C_p values on the induced vertical pressure as characterized by Eq. (6) and Eq. (7) is more pronounced than that characterized by Eq. (4). As for the comparison of the dependence of C_p values from Eq. (8) and Eq. (9) with that from Eq. (4), the latter is much less pronounced. Thus, it seems that the vertical collapse model of Eq. (1) in regard to the induced vertical pressure impact is more appropriate than that of Eq. (3).

UPGRADED VERTICAL COLLAPSE MODEL

The main conclusion from the previous section is the necessity of keeping the P_p impact on C_p values, as defined by Eq. (1), in the present updated regression analysis for the total available 123 specimens. The equation obtained in this analysis, which presents the final upgraded vertical collapse model, is (see Fig. 6):

$$C_p = 1.73415 \times 10^5 - 1.73410 \times 10^5 \times (D/D_{LL})^{0.0001} + 0.0001196 \times [\log(P_p)]^{1.3741} / (W/PL)^{1.0532} \quad (10)$$

Eq. (10) is limited for the following range of values: 0.25-1.10 for W/P values and 0.75-1.35 for D/D_{LL} values. In addition, although the accuracy of this equation is very low ($R^2=0.195$ and $SE=4.947\%$), it is still considered to be preferable to Eq. (1), for which $R^2=0.535$ and $SE=4.206\%$. In any case, the ratio of the calculated vertical collapse, Eq. (10), in contrast to Eq. (1), versus the density ratio (D/D_{LL}) is close to the value of 1.0 for high (critical) C_p values (see Fig. 7). It can be seen, furthermore, that the computed C_p values of Fig. 5 are almost identical with those of the $W/PL=0.5$ curves of Fig. 6. Indeed, the 0.5 value for W/PL is actually the average of the experimental data of Fig. 5. This fact may serve as another justification for the preference of Eq. (10).

Finally, the P_p impact on the calculated C_p values as defined by Eq. (10)--i.e., its increased capacity for lower W/PL values when D/D_{LL} is kept constant--seems to be compatible with the physical behavior of the collapse process. In other words, for lower W/PL values when D/D_{LL} is kept constant, the initial degree of saturation is lower, thus the collapse potential is higher.

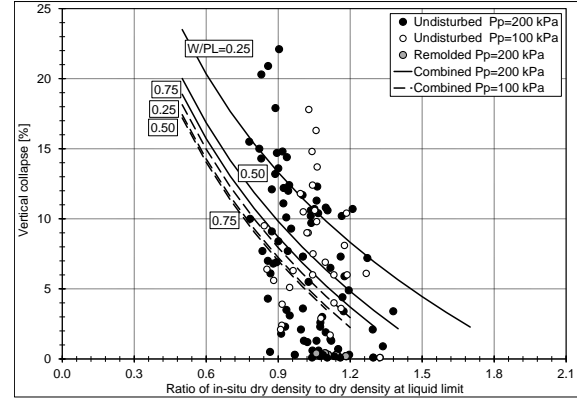


Fig. 6: Vertical collapse versus density ratio for vertical pressures of 100 kPa and 200 kPa as derived from Eq. (10) for the old and new 123 local specimens

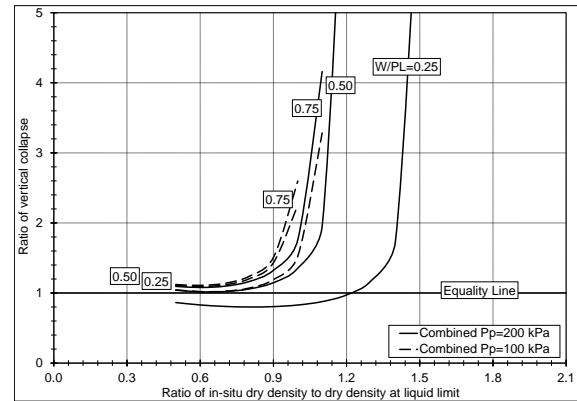


Fig. 7: Ratio of calculated vertical collapse, Eq. (10), as opposed to Eq. (1), versus density ratio

SPECIFIC VERTICAL COLLAPSE MODEL

The specific equation for predicting the vertical collapse percentage that characterizes the specific data values prevailing at a given project (say, the specific values of liquid limit, ratio of moisture content to plastic limit, and dry density of the subgrade site) is determined by combining Eq. (2) and Eq. (10) with the specific, limited results of the laboratory collapse tests, which are conducted as part of the in-situ investigations for a given project. Following the procedure given in [8] for the vertical swell model, the local values and the two given equations are combined by determining the regression coefficients α and β of the linear regression carried out between the dependent variable C_p and the independent variable, the latter as specified in Eq. (11). In other words, the formulation of this linear regression equation is as follows:

$$C_p = \alpha + \beta \times [1.73415 \times 10^5 - 1.73410 \times 10^5 \times (D/D_{LL})^{0.0001} + 0.0001196 \times \log(P_p)]^{11.3741} / (W/PL)^{1.0532} \quad (11)$$

where α and β are the linear regression coefficients.

In greater detail, the α -coefficient of Eq. (11) is the intercept value with the measured C_p -axis (Y-axis) and the β coefficient is the slope value with the Eq. (10) C_p axis (X-axis). Here it should be noted that when $\alpha=0$ and $\beta=1$, Eq. (11) is the same as Eq. (10), which, as mentioned, constitutes the accepted general vertical collapse model for settlement calculations. In addition to the regression of Eq. (11) (known also as the simple linear regular regression), a supplementary regression is suggested, in which the prerequisite constraint of $\alpha=0$ exists. For this type of regression (known also as the zero-intercept regression, or regression through the origin), the β -coefficient serves as the multiplier for the increase or decrease in the general vertical collapse percentage. In this regression, furthermore, the predicted vertical collapse value is equal to 0% for the same input data of the tested material that causes the predicted vertical collapse value to be equal to 0% when the general model--i.e., Eq. (10)--is followed. Similarly, in the simple linear regular regression, the predicted vertical collapse value is equal to α % for the same input data of the tested material that, again, causes the predicted vertical collapse value to be equal to 0% when the general model--i.e., Eq. (10)--is followed.

This calculation method to find the equation of the specific vertical collapse model that defines the vertical collapse percentage value as a function of the vertical induced pressure is based on the following assumption: the internal interrelationship of W/PL , D/D_{LL} , and P_p is a predetermined system, characterized by the outputs of Eq. (10). Hence, Eq. (11) contains only one independent variable. The sample size needed for making this kind of regression is much smaller than that needed for making the full regression, which contains six regression parameters. It should be emphasized that for a given project, the use of limited specific collapse tests for conducting an Excel-solver analysis using six regression parameters from Eq. (2) and Eq. (10) can cause a substantial distortion of the true collapse picture. Therefore, the method based on Eq. (11) is to be preferred.

As a result of the foregoing argumentation and in order to implement the preferred method, it is important that limited collapse tests be carried out under several values of vertical pressure, such as 100 and 200 kPa. These vertical pressures will cover the potential vertical pressures that act along the depth of the wetted zone of the silt. For these tests, furthermore, undisturbed subgrade specimens are to be extracted from at least three borings each at two depths, depending on the size of the given site and the statistical distribution of its subgrade properties. It is important to emphasize that when the number of specimens is below the minimum required value (about twelve), the derivation of the specific collapse

model is questionable. In this context, it is worth noting that the average of these twelve specimen results according to the ASTM E122-09 standard represents the average of the results of the entire population, with an accuracy of about 0.55 of the true standard deviation and at a 95% reliability level.

An example illustrating the derivation procedure of the aforementioned α and β coefficients for 12 undisturbed specimens extracted from the silt subgrade of a railway line construction site in the southern part of Israel is shown in Fig. 8. These 12 undisturbed specimens were tested for their vertical collapse percentage under an induced vertical pressure of 100 and 200 kPa. The undisturbed specimens were also tested to obtain their LL , PL , W , and D values.

Fig. 8 indicates that the regular regression yields an α -coefficient of 3.609 and a β -coefficient of 0.847. As for the constrained regression (i.e., the zero intercept regression), the value yielded for the latter is 1.097. These coefficients characterize the local vertical collapse model according to Eq. (11).

Finally, the question arises as to the specific regression that is to be preferred, the simple linear regression or the zero-intercept regression; The answer lies in the comparison of the two rates of the collapse settlements calculated for a given embankment, using these two models and the procedure outlined in [2]. The higher of the two calculated rates is considered to be the determinant value. However, when the number of local tests is less than the minimum required--i.e., 12--or when the coefficient of determination (R^2) obtained from the above two regressions is very low, the calculated rate according to $\alpha=0$ and $\beta=1.0$ is considered to be the determinant value.

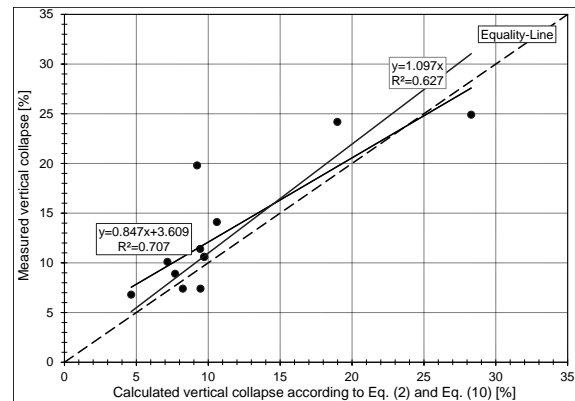


Fig. 8: Derivation of the α and β coefficients for 12 undisturbed specimens extracted from the silt subgrade of a railway line construction site

SUMMARY AND CONCLUSIONS

This paper dealt with the issue of (a) updating the general vertical collapse model given previously by the authors in [1] and [2] and (b) deriving the specific vertical collapse model for a given site by combining

limited vertical collapse test results obtained for this site with the general vertical collapse model.

The routine updating procedure using the old 73 collapse test results together with the new 50 collapse test results yields an unacceptable model with respect to the impact of the vertical induced pressure on the vertical collapse results.

Thus, an additional study was needed to confirm the impact of the vertical induced pressure calculated from the existing model presented in [1] or [2] on the vertical collapse results. This study was performed using old available collapse test data (all together, 119 undisturbed silt specimens) that do not contain all the necessary parameters of the materials tested. This showed that the impact of the vertical induced pressure on the vertical collapse results is actually similar to that of the existing model found in [1] or [2].

Given the above findings, it was understandable that a new regression analysis had to be run on the 123 collapse test results of the undisturbed and disturbed specimens of Fig. 3. The new regression equation (Eq. 10) in this analysis maintained the impact of the vertical induced pressure on the vertical collapse results as defined by the existing model--i.e., Eq. (1) and Eq. (2).

The appropriate vertical collapse model should be employed for vertical collapse settlement calculations. As developed in the paper, three models exist: (a) the general vertical collapse model derived from the Excel-solver analysis carried out on 123 undisturbed and disturbed specimens, using the impact of the vertical induced pressure on the calculated vertical collapse results as defined by Eq. (2) and Eq. (10); (b) the specific vertical collapse model derived from the simple linear regression analysis carried out on the data of the specific local tests, combined with the general updated vertical collapse model--i.e., Eq. (2) and Eq. (10); (c) the specific swelling model derived from the zero-intercept linear regression analysis carried out, again, on the data of the specific local tests, combined with the general updated vertical collapse model--Eq. (2) and Eq. (10)--in which, however, the α -coefficient always equals 0.

For the latter two vertical collapse models, it is recommended that the one that yields the higher calculated settlement rate should be adhered to as the final result. It should be emphasized, furthermore, that in order to use the specific vertical collapse model described above, collapse tests must be performed on a sufficient number (at least 12) of undisturbed specimens, as this will better reflect the site's silt variability along both the horizontal axis and the vertical axis. When the coefficient of determination (R^2) obtained for the above two models is, however, very low, the calculated rate according to $\alpha=0$ and $\beta=1.0$ is considered to be the determinant value. In the absence of local tests, moreover, only the general updated vertical collapse model need be adopted; namely, Eq. (2) and Eq. (10). In any case, the use of

the specific collapse tests for applying the Excel-solver analysis directly to a given project is inappropriate, as it may lead to erroneous results.

The final conclusion is that all the above findings can serve as a proper tool for calculating the vertical collapse settlement of the base of an embankment constructed on a collapsible silt subgrade. This is illustrated in [1] and [2] by utilizing an Excel spreadsheet for a given practical example.

ACKNOWLEDGMENTS

The paper is based on engineering studies conducted for Olizky Earthworks Roads & Development Ltd. under assignment by Israel Railways Ltd., and on the data taken from the engineering study conducted by M.N.M. Engineers Ltd. for Cross-Israel Highway Ltd. Thanks are due these firms.

REFERENCES

- [1] Livneh, M. and Livneh, N.A., "Collapse-Settlement Calculations for Embankments Founded on a Collapsible Soil Subgrade," Proc. of the 2nd Int. Conf on Geotechnique, Construction Materials and Environment, GEOMATE 2012, Kuala Lumpur, Malaysia, 2012.
- [2] Livneh, M. and Livneh, N.A., "On Collapse-Settlement Calculations for Heterogeneous Collapsible-Soil Subgrade," International Journal of GEOMATE, Vol. 3, No. 2 (Sl. No. 6), 2012, pp. 363-368.
- [3] Lawton, E.C., Frigaszy, R.J., and Hardcastle, J.H., "Collapse of Compacted Clayey Sand," Journal of Geotechnical Engineering, Vol. 115, No. 9, 1989, pp. 1,252-1,267.
- [4] Zur, A. and Wiseman, G., "A Study of Collapse Phenomena of an Undisturbed Loess," Proc. of the 7th Int. Conf. on Soil Mechanics and Foundation Engineering, Vol. 2.2, Moscow, 1973, pp. 265-269.
- [5] Austerlitz, G., Ishai, I., and Komornik, A., "Prediction of Collapse Potential in Israeli Loess Subgrade," Proc. of the 7th Asian Regional Conf. on Soil Mechanics and Foundation Engineering, Vol. 1, Haifa, 1983, pp. 106-111.
- [6] Basma, A.A. and Tuncer, E.R., "Evaluation and Control of Collapsing Soils," Journal of Geotechnical Engineering, Vol. 118, No. 10, 1992, pp. 1491-1504.
- [7] Livneh, M., "The Engineering Properties of Local Loess as Subgrade for Roads and Runways," Publication No. 80-32, Transportation Research Institute, Technion, Haifa, Israel, 1980.
- [8] Livneh, M., "Recent Developments in the Swelling Model of Expansive Clays for Pavements Upheave Calculations," Journal of Testing and Evaluation, JTEVA (ASTM), Vol. 40, No. 2, 2012, pp. 310-318.

INFLUENCE OF FREEZE-THAW ACTION ON AIR-PERMEABILITY OF UNSATURATED SOIL GROUND

Tatsuya Ishikawa¹, Tetsuya Tokoro², Dai Nakamura³ and Satoshi Yamashita³

¹Faculty of Engineering, Hokkaido University, Japan; ²Tomakomai National College of Technology Japan; ³Faculty of Engineering, Kitami Institute of Technology, Japan

ABSTRACT

This study proposes a testing method of air-permeability for unsaturated soil ground subjected to freeze-thaw action and to evaluate the effects of freeze-thawing and moisture content on air-permeability of soil ground. In this study, we develop a new test device for the evaluation of air-permeability of unsaturated model soil ground and perform a series of air-permeability tests for soil ground made of non-frost susceptible sand and frost susceptible volcanic cohesive soil under various freeze-thaw histories and moisture contents. As the results, it was revealed that the test device could evaluate air-permeability of freeze-thawed geomaterials in unsaturated condition, and that the freeze-thaw action has strong influences on the air-permeability of frost-susceptible geomaterials in unsaturated condition.

Keywords: Unsaturated soils, Air-permeability, Freeze-thaw action, Moisture content, Frost susceptibility

INTRODUCTION

At frozen soil grounds where gases (e.g., toxic gases or greenhouse gases) are stored and accumulated, in some cases these gases are ejected to the ground surface in thawing season, thereby causing the gas leakage accident from subsurface layer and the global warming. In this case, there is a possibility that freeze-thaw action affects the air-permeability in cold regions because it results in the fluctuation of moisture content and frost heave phenomenon. For example, Seyfried and Murdock [1] reported that if the soil temperature falls below 0 °C, the air permeability decreases very rapidly by performing air permeability tests on frozen sand. Moreover, Kamiya et al. [2] showed that the air permeability drops with increasing the degree of saturation based on the results of air permeability tests on unsaturated sandy soil and silty soil. Accordingly, it is important for the preventive maintenance of the above-mentioned geotechnical disasters to develop a testing method for the evaluation of the air permeability in unsaturated soil grounds subjected to freeze-thaw actions.

However, there are few researches which examine the effect of freeze-thaw action on air-permeability of unsaturated soils. For example, although the “Method for Air Permeability Test In Vadoze Zone (JGS1951-2006)” [3] has been standardized for testing the air-permeability of unsaturated soils, the objective is not to measure the coefficient of air-permeability for soils subject to freeze-thaw actions because the standard only evaluates the air-permeability in the horizontal direction. Therefore, currently in Japan, there is no

method that can assess the variations in the air permeability of unsaturated soils in the vertical direction, which are attributable to the changes in the temperature like freeze-thaw of soil ground.

The objective of this study is to propose a testing method of air-permeability for unsaturated soil ground subjected to freeze-thaw action and to evaluate the effects of freeze-thaw and moisture content on the air-permeability. To this end, we develop a new test device suitable for the evaluation of air permeability of model soil ground in unsaturated condition and perform a series of air-permeability tests for soil grounds made of non-frost susceptible sand and frost susceptible volcanic cohesive soil under various freeze-thaw histories and moisture contents. Based on the test results, first, the applicability of the newly developed test device to the air permeability test for unsaturated geomaterials was examined by comparing the results with those in existing literatures. Next, the effects of freeze-thaw and moisture content on the air-permeability of soil ground were examined.

TEST DEVICE FOR MODEL TEST

Figure 1 shows a schematic diagram of the air permeability test device for model soil ground, which consists of a polyvinyl chloride pipe (1.12 m in height and 0.59 m in diameter), a vacuum pump for suction of air, a flowmeter and differential pressure gauges attached to monitoring wells. The device causes a flow of air within the model soil ground by applying a negative pressure in the lower end of the device with a vacuum pump, and measures the air flow rate (1atm, 20°C) at that time,

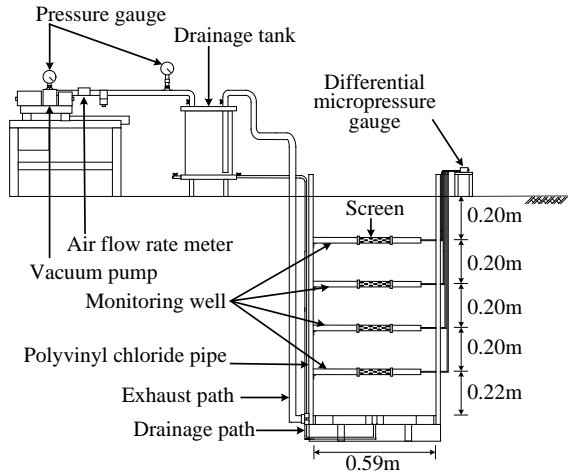


Fig. 1 Air permeability test device of soil ground.

the pore air pressure, the moisture content by volume, and the temperature distribution inside the model soil ground. The coefficient of air permeability between two adjacent monitoring wells, or between the ground surface and the monitoring well (referred to below as “layers”), was calculated using Darcy’s law (Eq.(1)). In this case, in the calculation of the air pressure gradient (i), to exclude the effect of the compressibility of the permeated gas, corrections are applied according to the temperature and pressure using Eq.(2) [4].

$$Q = Ak_a i \quad (1)$$

$$i = \frac{\left\{ \left(h_{a0}' \frac{T_1}{T_0'} + h_{a1} \right) \frac{T_0}{T_1} \right\}^2 - \left\{ \left(h_{a0}' \frac{T_2}{T_0'} + h_{a2} \right) \frac{T_0}{T_2} \right\}^2}{2h_{a0}l} \quad (2)$$

where, k_a : coefficient of air permeability (m/s), Q : flow rate (m³/s), A : cross-sectional area (m²), i : air pressure gradient (m/m), T_0 : 293.15 (K), h_{a0} : 10.332 (m), T_0' : air temperature at the time of the test (K), h_{a0}' : atmospheric pressure at the time of the test (m), T_1 : soil temperature of the upper monitoring well (K), h_{a1} : differential pressure of the upper monitoring well (m), T_2 : soil temperature of the lower monitoring well (K), h_{a2} : differential pressure of the lower monitoring well (m), and l : thickness of the layer (m).

TESTING METHOD

Test Samples

The samples used in this study are Japanese standard sand (Toyoura sand) and a volcanic cohesive soil sampled in Kitami, Japan (hereafter referred to as “Touryo soil”). The compaction curves obtained

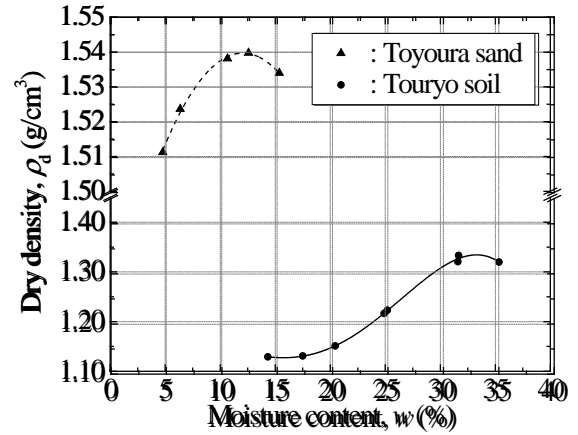


Fig. 2 Compaction curves of samples.

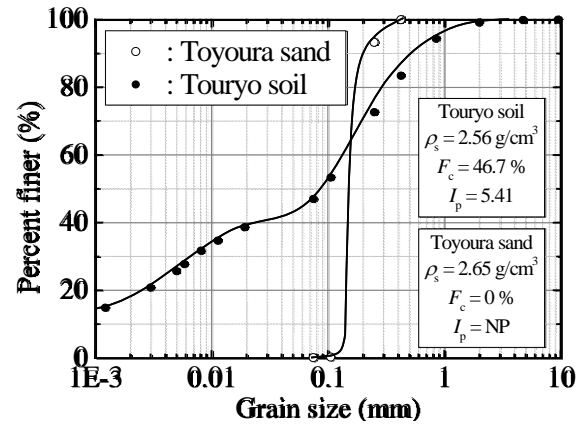


Fig. 3 Grain size distribution curves of samples.

from the compaction test (JIS A1210, A-a method) are shown in Fig. 2, and the grain size distribution curves and the physical properties are shown in Fig. 3. Toyoura sand has an optimum moisture content of $w_{opt}=13.2\%$ and the optimum dry density of $\rho_{dmax}=1.85\text{g/cm}^3$, and it is a non frost-susceptible material without fine fraction. In contrast, Touryo soil has a higher optimum moisture content ($w_{opt}=32.5\%$) than Toyoura sand and a smaller optimum dry density of $\rho_{dmax}=1.34\text{ g/cm}^3$. Also, Touryo soil has a high fine fraction content of 46.98%, and in frost heave tests (JGS 0172-2003) it showed a frost heave ratio of 89.7%, which indicates high frost susceptibility.

Air Permeability Test

The air permeability tests were conducted as indoor (Fig. 4a) and outdoor (Fig. 4b) tests in a closed-system frost heaving condition where the supply or drainage of water to or from the specimen during the freeze-thaw was not allowed, as described below.

Indoor tests

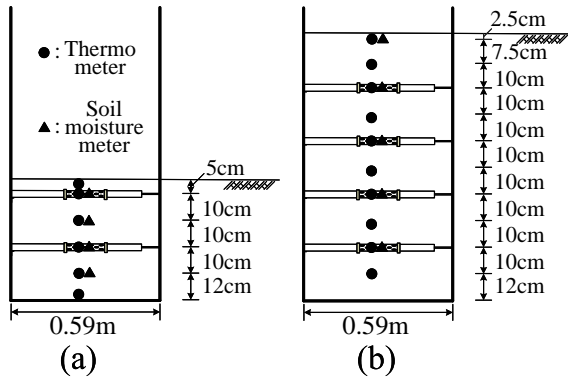


Fig. 4 Measurement in air permeability tests.
(a: indoor test, b: outdoor test)

A model soil ground ($H=0.47\text{m}$, $D=0.59\text{m}$) were prepared by placing a sample with adjusted moisture content into the cylinder soil tank in 5 cm layers to obtain a given initial degree of saturation (Toyoura sand: $S_{r0}=0, 20, 40, 60\%$, Touryo soil: $S_{r0}=15, 37.5, 60, 80\%$), and each layer compacted for the desired initial dry density (Toyoura sand: $\rho_{d0}=1.51\text{g/cm}^3$ ($D_c=82\%$), Touryo soil: $\rho_{d0}=1.10\text{g/cm}^3$ ($D_c=82\%$)). At this procedure, soil moisture sensors and T-type thermocouple thermometers were buried at equal intervals.

After specimen preparation, a negative pressure (from -1 to -10 kPa) was applied in stages in order to calculate the coefficients of air permeability (k_a) for unfrozen soil ground by using Eqs.(1) and (2) with measured values. Next, dry ice was put on top of the model soil ground to artificially freeze it down to the monitoring well with a depth of 5 cm from the surface, after which the k_a for frozen soil ground was found by carrying out the air permeability test in the same way as for unfrozen soil ground. For only Touryo soil, in addition to the test described above, air permeability tests on the frozen soil ground under conditions that easily give rise to the frost-heave phenomenon were conducted by reducing the freezing rate (U) with a heat insulating material. For example, in case of $S_{r0}=60\%$, the freezing rate (U) was 16.07 mm/h without any heat insulating material, while was 1.28 mm/h with the insulating material. Finally, the air permeability test on freeze-thawed soil ground was conducted after model soil ground had thawed at room temperature.

Outdoor tests

The moisture content of a sample used was adjusted for the desired initial degree of saturation (Toyoura sand: $S_{r0}=40\%$, Touryo soil: $S_{r0}=60\%$), and a model soil ground ($H=1.02\text{m}$, $D=0.59\text{m}$) was prepared by compacting the sample to achieve an initial dry density (Toyoura sand: $\rho_{d0}=1.51\text{g/cm}^3$, Touryo soil: $\rho_{d0}=1.10\text{g/cm}^3$) in the same way as for the indoor test. The air permeability test was carried out using a

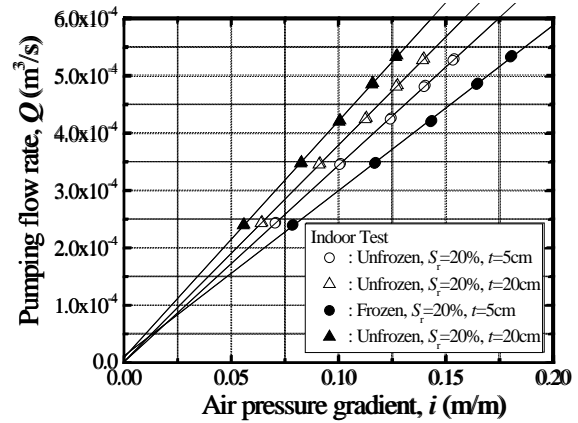


Fig. 5 Examples of air permeability test results.

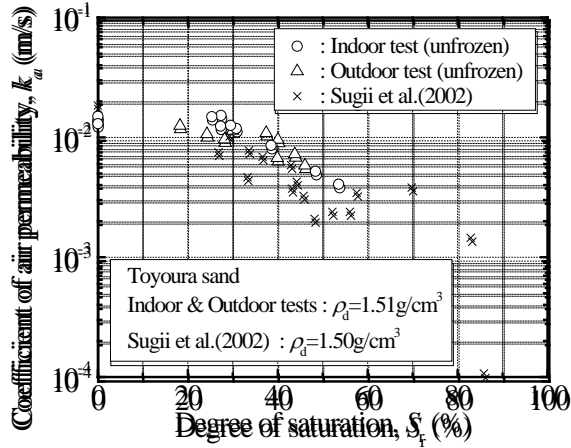
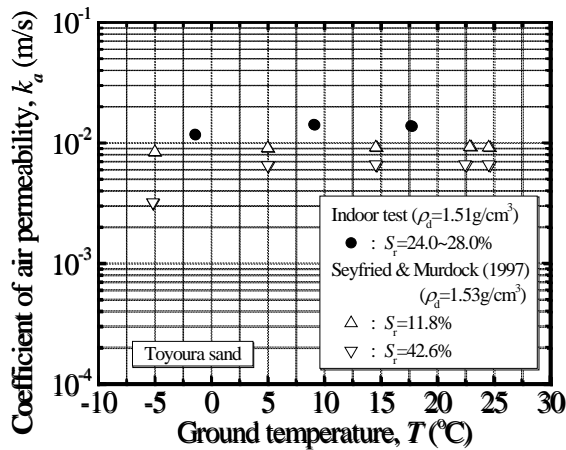
similar procedure to the indoor test to obtain the coefficient of air permeability for both unfrozen and frozen soil ground. However, for the air permeability test with frozen soil ground, it was performed at the time that the frost depth reached each of the monitoring wells, as estimated from the ground temperature measured by the thermometers. Note that the freezing index in Kitami city at the year when the outdoor tests were conducted was $461^\circ\text{C}\cdot\text{days}$ with an average temperature from December to February of -5.6°C , and a freezing rate was approximately 0.7 mm/h. Here, the freezing index is defined as the number of cumulative degree-days during freezing season.

RESULTS AND DISCUSSIONS

Applicability of Device to Air Permeability Test

The relationships of each layer between flow rate (Q) and air pressure gradient (i) are shown in Fig. 5 for the indoor test using Toyoura sand under $S_{r0}=20\%$. The Q - i relationships seems to be linear, regardless of freeze-thaw history and depth of the layer. Similar tendency was observed at the air permeability tests under different experimental conditions, irrespective of moisture content, soil sample, and testing location. Accordingly, Darcy's law is applicable to the calculation of the coefficient of air permeability (k_a).

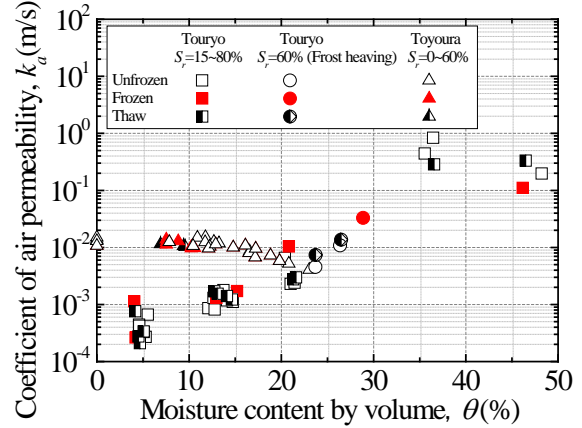
Figure 6 shows the relationships between k_a and degree of saturation (S_r), which were obtained from the indoor and outdoor tests on Toyoura sand, together with past test results conducted under the similar experimental conditions [5]. The coefficient of air permeability increases with decreasing S_r , and this increasing tendency of k_a is in fair good agreement with that in the previous test results. As pointed out in past studies, this is because the increment of moisture content in voids decreases the air channels, thereby obstructing the air permeability of soils. Besides, Fig. 7 compares the relationship between the coefficient of air permeability and the


 Fig. 6 Effect of moisture content on k_a .

 Fig. 7 Effect of ground temperature on k_a .

ground temperature during freezing, which were obtained from the indoor tests for Toyoura sand with roughly the same degree of saturation ($S_r=24\sim28\%$) with that in the past study [1]. Over the ground temperature of 0°C , the change in k_a with the decrement of ground temperature can hardly be seen, while below 0°C , together with the drop in the ground temperature, the k_a slightly decreases. In Fig. 6, for the plots with the same S_r , the k_a of frozen soil is a little smaller than that of unfrozen soil. This is because the air channels in the frozen soil became narrow in comparison with those in the unfrozen soil due to the volume expansion of pore water during phase-change from fluid to solid. The dependence of k_a on the ground temperature in this study can be recognized even in the previous test results. Accordingly, it seems reasonable to conclude that a test device newly developed in this study can evaluate air-permeability of soil ground.

Effect of Moisture content on Air Permeability

The relationships between the coefficient of air permeability (k_a) and moisture content by volume


 Fig. 8 Effect of freeze-thaw action on k_a .

(θ), which were obtained from the indoor tests on Toyouryo soil, are shown in Fig. 8, together with those for Toyoura sand (Fig. 6). Note that in the case of in-situ freezing, assuming that the volume of the pore water expands by 9%, the θ for frozen soils on the horizontal axis was found to be 1.09 times the θ before freezing, while in the case of frost heaving, the θ for frozen soils was 1.09 times the θ after freeze-thawing since the moisture content in the layers with frost heaving increases beyond that when unfrozen. According to the frost heave ratio obtained from the freezing procedure of each air-permeability test, the frost-heave phenomenon has not occurred in other tests except the indoor test with Toyouryo soil at an initial degree of saturation of 60% and a freezing rate of 1.28 mm/h, and in these tests the model soil ground is assumed to have been frozen in the manner of in-situ freezing.

As for Toyoura sand, k_a decreases with an increase in the moisture content by volume, regardless of frozen or unfrozen soils. In addition, although there was no difference in the coefficients of air permeability before and after freezing and thawing, the coefficient for frozen soil is slightly smaller than that for unfrozen. This can be reasonably explained by the fact that for high moisture content, or when the pore water contained within the unfrozen soil freezes and expands, the proportion of pore air that forms the channels for the permeating air is reduced.

As for unfrozen Toyouryo soil, it shows the different tendency to Toyoura sand in that the k_a increases with increasing moisture content at the range lower than the optimum moisture content (equivalent to about $\theta=36\%$) but it dramatically decreases at higher moisture content. This is thought to be because at a low moisture content the addition of water increased the aggregation of soil particles only for Toyouryo soil and resulted in an increase in the number and size of voids. For example, Nikol et al. [6] showed that the aggregation occurs in clay as a result of the increased moisture content, and that

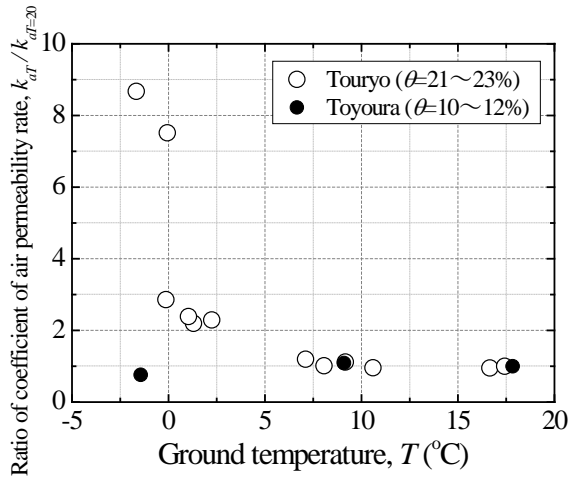


Fig. 9 Dependency of k_a on ground temperature.

the number of large-sized pores increases, which implies that the phenomenon may therefore occur in Touryo soil with particles that are similar in size to those in clay. Besides, Sugii et al. [7] showed that in aggregated soil that has a double-pore structure, the aggregation is formed due to macropores (50 nm or larger) which contribute to its permeability, and micropores (2 nm or smaller) which contribute to its water retentivity. From this fact, the macropores may also contribute to the air permeability of soils, but the effect of aggregation on the air permeability requires further study.

Effect of Freeze-Thaw on Air Permeability

To reveal how ground temperature affects the air permeability of the soil, Fig. 9 compares the relationships between the ratio of the coefficient of air permeability and the ground temperature for the specimens with roughly the same degree of saturation ($S_r=37\sim40\%$ for Touryo soil, $S_r=23\sim28\%$ for Toyoura sand) with each other. Here, the ratio of the coefficient of air permeability is defined as a normalized value of k_a for a specimen at a given temperature with the k_a for the specimen at the temperature of 20°C. At the temperature range over 0°C, the k_a remains invariant regardless of the ground temperature in test results for both samples, while below 0°C, with decreasing the ground temperature, the k_a drops very slightly for Toyoura sand but increases very rapidly for Touryo soil. Therefore, both samples show the temperature dependency of the coefficients of air permeability.

Next, the influence of the experimental condition during freezing on the air permeability is discussed. As can be seen in Fig. 8, with no frost heave, no difference is observed in the k_a of Touryo soil before and after freeze-thawing, as is the case for Toyoura sand. However, up to a low moisture content by volume of 30%, the k_a for frozen soil is larger than that for unfrozen soil. In contrast, at the initial

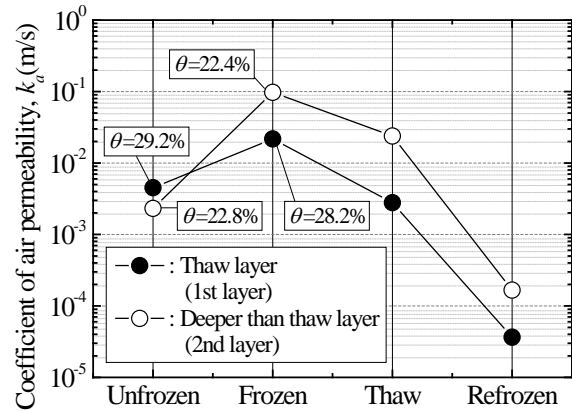


Fig. 10 Change in k_a during cyclic freeze-thawing.

degree of saturation of 80% (close to $\theta=40\%$), though the k_a for unfrozen soil showed a high value despite the high moisture content since the aggregation had occurred to an extent by which it could be verified visually, the k_a for frozen soil decreased. The reason for these can be explained as follows. At a low moisture content, pore water inside unfrozen soil ground moves along with the flow of air and as the result air is less likely to pass through, while when frozen, the air can easily pass through as the pore water freezes on the spot. Whereas, at a high moisture content, the existence of a large amount of pore water makes air flow more difficult because the volume expansion of frozen pore water is bigger as compared to the low moisture content.

Furthermore, from the circles in Fig. 8, the k_a for frozen soil with frost heave has a high value compared to that for unfrozen soil, and it showed a different tendency to the non-frost heave case in that the k_a after thawing also slightly increased over the value before freezing. This is because in addition to the increase in the k_a when freezing compared to the unfrozen case, due to the voids increasing with the locally occurring frost-heave phenomenon, voids still remain following thawing, thus increasing the coefficient compared with the unfrozen case.

Effect of Cyclic Freeze-Thaw on Air Permeability

Figure 10 compares the coefficients of air permeability (k_a) obtained from outdoor tests conducted at four different timings during freeze-thawing, that is, the unfrozen case ("unfrozen" in the Fig. 10), the time when frozen to a depth of about 80 cm ("frozen"), the time when thawed uniformly down to a depth of approximately 1 cm by pouring warm water after freezing nearly the whole specimen ("thaw"), and finally, the time when refrozen after being thawed out ("refrozen"). Here, the filled circle symbol in the figure represents the uppermost layer of the specimen that has been

thawed down to roughly 1 cm, and the hollow circle symbol represents deeper layers.

There was little visible difference in the coefficient of air permeability in the depth direction for the unfrozen case; however, in the frozen and frost heaving cases, the coefficient became different depending on the moisture content by volume. Further, after thawing by warm water, the amount of pore water increased compared with that amount before thawing, which resulted in a decreased coefficient of air permeability. When the pore water was subsequently refrozen, the coefficient further decreased. Thus, for Touryo soil, increasing the moisture content by volume beyond a constant value makes it more difficult for air to pass through, and the coefficient of air permeability tends to decrease further with the added moisture content freezing and frost heaving.

CONCLUSION

In this study, a series of air-permeability tests for soil ground were conducted on non-frost-susceptible sand and frost-susceptible volcanic cohesive soil under various freeze-thaw histories and moisture contents. Based on the test results, together with demonstrating the validity and usefulness of a newly developed test device and a proposed new testing method when evaluating a temperature-dependent coefficient of air permeability for unsaturated soil ground subjected to freeze-thaw action, we revealed that due to the experimental fact that the air permeability of unsaturated soil ground is dependent on the moisture content and freezing rate of soils, it is significantly affected by material properties of soils such as the frost susceptibility, the soil water characteristics, and the compaction characteristics in addition to being affected by environmental factors such as ground temperature and groundwater level.

ACKNOWLEDGEMENT

This research was supported in part by Grant-in-Aid for Challenging Exploratory Research (21651080 & 24651204) from Japan Society for the Promotion of Science (JSPS) KAKENHI.

REFERENCES

- [1] Seyfried MS, Murdock MD, "Use of air permeability to estimate infiltrability of frozen soil", *Journal of Hydrology*, 202, 1997, pp. 95-107.
- [2] Kamiya K, Bakrie R, Honjo Y, "The measurement of air permeability coefficient of unsaturated soil with controlling water retentivity", *Journals of the Japan Society of Civil Engineers Division C*, 62(3), 2006, pp. 679-688 (in Japanese).
- [3] Japanese Geotechnical Society, "Method for air permeability test in vadoze zone (JGS 1951-2012)", *Japanese Standards and Explanations of Geotechnical and Geoenvironmental Investigation Methods*, 2013, pp. 23-27 (in Japanese).
- [4] Japanese Geotechnical Society, "Evaluation of unsaturated soil ground behavior", 2004, pp. 25-35 (in Japanese).
- [5] Sugii T, Yamada K, Yogo T, "Study on air permeability test for unsaturated soils", in *Proc. of the 37th Japan National Conference on Geotechnical Engineering*, 2002, pp. 1275-1276 (in Japanese).
- [6] Kochmanová N, Tanaka H, "Effects of microstructure on compacted clay properties", in *Proc. of Technical report of the Annual Meeting of the JGS Hokkaido branch*, Vol. 50, 2010, pp. 193-198 (in Japanese).
- [7] Sugii T, Fang F, "Study on hydraulic properties of aggregated soils", in *Proc. of the 46th Japan National Conference on Geotechnical Engineering*, 2011, pp. 1025-1026 (in Japanese).

EFFECT OF ROCK SOCKET CHARACTERISTICS ON LOW STRAIN INTEGRITY TEST OF PILES

Ramli Bin Nazir¹ and Osman El Hussien²

¹Associate Professor, Faculty of Engineering, Universiti Teknologi Malaysia, ²PhD Student, Faculty of Engineering, Universiti Teknologi Malaysia

ABSTRACT

Recently constructed piles are usually tested in order to evaluate their integrity as part of foundation construction quality control. The low strain integrity test is routinely performed, because it is fast and cost effective. However, integrity of piles socketed in hard rock strata is usually difficult to assess. This difficulty is attributed to the dissipation of the stress wave as a result of hard rock resistance effects. A new method is presented, which used to evaluate rock socket characteristics including rock strength and socket length on integrity test results. Rock damping effects applied on stress wave were quantified for both skin resistance and toe reaction for different rock strengths and socket lengths using numerical solution of wave equation after incorporating soil effects. The generated results were compared with a wave propagation simulation software output, and the accuracy of the model was validated. It was found that rock socket characteristics play a major role in evaluating integrity of piles cast in hard rock, using low strain test method, and may lead to inconclusive assessment of piles integrity.

Keywords: Pile, Integrity, Rock, Socket

INTRODUCTION

Currently there is no clear idea about the effect of soil resistance on the stress wave propagation into piles as well as the soil impact on the applied analysis methodologies. This fact had caused engineers to go through assumptions in order to compensate for lack of proper identification of pile/soil interaction, which may jeopardize the quality of the test output. In addition, soil resistance and damping effects may lead to inconclusive assessment of pile integrity, while it is difficult to distinguish soil response from pile response [1].

Soil resistance effects are required to be properly considered for calculation of impedance profile. However, soil effects are never definitely known and for that reason engineering judgment may seriously affect the results [9]. Note that direct measurement of soil resistance or other soil parameters is not the objective of low strain integrity testing. Therefore no attempt has been made to formulate mathematical expressions relating soil resistance as a function of any of the parameters from the mobility spectrum [7]. In construction practice, piles are commonly socketed in hard strata such as rocks in order to transfer the structural loads to the competent deep layers. However, in such condition the hard layer, which surrounds pile toe, may affect the accuracy of low strain test of pile, while the increase in soil resistance force results in a decrease in the measured pile top velocity [4].

MODEL FORMULATION

During integrity test, the pile is subjected to an impact with a light hammer. Upon hammer strike, the impact will produce the following:

- 1- Downward displacement of pile body.
- 2- Mobilization of soil friction at the surface area of the pile.
- 3- Stress wave propagation through pile body, which will be:
 - a) Attenuated by soil friction.
 - b) Partially reflected at pile toe after been attenuated by soil resistance.

Hence, soil effects on pile tested by low strain integrity test can be categorized as follows:

- 1- Skin friction mobilization.
- 2- Soil – Pile interaction at pile toe.

Assuming a bar as shown in Fig. 1 having density (ρ) is subjected to dynamic force (F) resulted in linear displacement (w) in the (x) direction at time (t). The basic mathematical formulations based on force equilibrium and Newton's second law of motion will be as follows:

$$-\sigma + \sigma + \frac{\partial \sigma}{\partial x} dx = \rho dx \frac{\partial^2 w}{\partial t^2} \quad (1)$$

$$E = \frac{\sigma}{\epsilon} \quad (2)$$

$$\epsilon = \frac{\partial w}{\partial x} \quad (3)$$

Substituting Eq. (2) and Eq. (3) in Eq. (1), the partial differential equation, which known as the wave equation, can be arrived:

$$\frac{\partial^2 w}{\partial t^2} = c^2 \frac{\partial^2 w}{\partial x^2} \quad (4)$$

Where,

$$c = \sqrt{\frac{E}{\rho}} \quad (5)$$

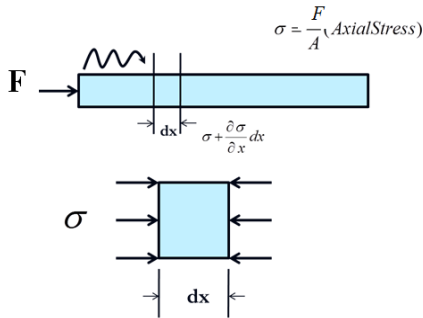


Fig. 1 Schematic diagram for a bar subjected to dynamic impact

For the pile segment shown in Fig. 2, which shows the axial force acting on segment top and the frictional forces acting on segment circumference, the numerical solution for the wave equation after incorporation of soil friction will be as follows:

$$F_i - F_{i-1} = \rho A \Delta z \frac{v_i(t + \Delta t) - v_i(t)}{\Delta t} \quad (6)$$

$$v_i = \frac{w_i(t + \Delta t) - w_i(t)}{\Delta t} \quad (7)$$

$$F_i = EA \frac{w_{i+1} - w_i}{\Delta z} \quad (8)$$

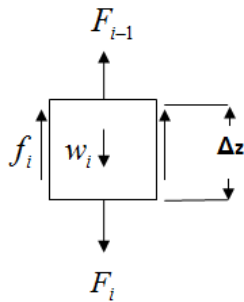


Fig. 2 Forces acting on pile segment

The skin friction is assumed to be proportional to displacement as per the following friction-displacement correlation [6]

$$f_i = \frac{G}{r_0 \cdot \ln\left(\frac{r_m}{r_0}\right)} w_i \quad (9)$$

Where (G) is soil shear modulus, (r_0) is pile radius and (r_m) is the pile influence zone, which can be estimated using ground vibration attenuation equation [2] as follows:

$$A_1 = A_0 (r_0 / r_1)^{(\gamma)} e^{\alpha(r_0 - r_1)} \quad (10)$$

Where, (A_0), (A_1) are vibration amplitudes at (r_0), (r_1) distances respectively, (γ) is a coefficient depends on wave type and (α) is material damping coefficient. Summary of some published values of geometric attenuation coefficient (γ) and material attenuation coefficient (α) are shown in Tables 1 and 2, respectively.

When the incident force (F_i) reaches pile-soil interface of a pile cast in hard soil, the following is expected to occur:

- 1- Partial transmission of force (F_t).
- 2- Partial reflection of force (F_r).
- 3- Generation of soil reaction at toe (F_R).

Force transmission/reflection at interface is caused by impedance change. Figure 3 illustrates the above mentioned scenario.

Table 1 Some published (γ) values [2]

Investigator	Soil Type	(γ)
-Wiss	Sands	1.0
	Clays	1.5
-Brenner & Chittikuladilok	Surface sands	1.5
	Sand fill over soft clays	0.8–1.0
-Attewell & Farmer	Various soils (firm)	1.0
-Nicholls, Johnson & Duvall	Firm soils and rock	1.4–1.7
-Martin	Clay	1.4
	Silt	0.8
-Amick & Ungar	Clay	1.5

Table 2 Some published (α) values [2]

Investigator	Soil Type	(α)
-Forssblad Richart	Silty gravelly sand	0.13
	4-6 in. concrete slab over compact granular fill	0.02
-Woods	Silty fine sand	0.26
-Dalmatov, et al.	Sand and silts	0.026–0.36
-Barkan Clough and Chameau	Marly chalk	0.10
	Sand fill over Bay Mud	0.05–0.20
	Dune sand	0.026–0.065
-Peng	Soft Bangkok clay	0.026–0.44

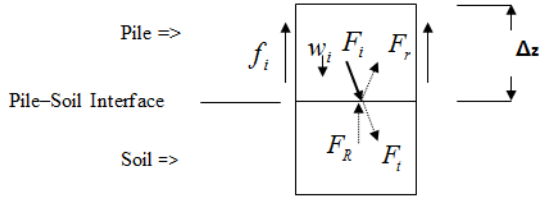


Fig. 3 Forces acting on pile bottom segment

At the pile-soil Interface, the force caused by the reflected wave (F_r) in terms of the incident wave caused force (F_i) is

$$F_r = \left[\frac{\frac{\rho_s v_s}{\rho_c v_c} - 1}{\frac{\rho_s v_s}{\rho_c v_c} + 1} \right] F_i \quad (11)$$

Where, (ρ_s) is soil density, (v_s) is wave velocity in soil and (v_c) is wave velocity in concrete.

Soil reaction (F_R) at pile toe is calculated as per Kagawa correlation [5]

$$F_R = E_{sb} r_{0b} \delta_{0b} z + 2(1 + \nu_{sb}) \sqrt{\rho_{sb} G_{sb}} r_{0b}^2 \delta_{0b} T_3 v_p \quad (12)$$

Where:

F_R : Soil reaction at pile tip

E_{sb} : Young's modulus of soil

r_{0b} : Radius of pile tip

δ_{0b} : Soil reaction coefficient

z : Pile tip displacement

ν_{sb} : Poisson's ratio of soil at pile tip

ρ_{sb} : Soil density at pile tip

G_{sb} : Shear modulus of soil at pile tip

T_3 : Polynomial function coefficient

v_p : Pile tip velocity

Based on the above mentioned theories, the model was assembled and executed using computer programmed spreadsheets. The input data in the analysis are the dynamic load details in addition to pile and soil characteristics. The pile is discretized into small segments as in Fig. 2. Force, velocity and displacement values are calculated for each pile segment utilizing the numerical solution of wave equation after incorporation of soil friction provided in equations 6, 7 and 8. Soil friction was calculated using the friction-displacement and attenuation correlations provided in equations 9 and 10, respectively. The toe segment is analyzed based on impedance change as well as soil reaction effects, which are provided in equations (11) and (12), respectively.

Based on the above methodology, the force and velocity values were obtained for both downward and upward movement of stress wave in order to identify stress wave characteristics at different pile depths.

MODEL VERIFICATION

The numerical formulation output is compared with PIT-S computer software output. PIT-S is simulation software, which takes soil properties, pile details and low strain hammer impact information, and displays force and velocity curves versus time and pile length. Specific soil, pile and dynamic load data were used in the comparison between both methods. The PIT-S software is based on wave equation analysis and Smith model of pile driving. In Smith model, the resistance to driving force is simulated by series of springs and dashpots, and the spring stiffness is defined by ratio of maximum elastic deformation or quake. Typical quake values are in 2.0 to 5.0mm range. However, soils with high rebound have high quake values in excess of 25.0mm [3]. Hence, in Smith model, soil resistance to pile driving is given as follows [8]:

$$R_t = R_s (1 + Jv) \quad (13)$$

Where, (R_t) is total soil resistance to driving, (R_s) is static soil resistance, (J) is soil damping coefficient and (v) is velocity of pile toe.

The analysis for both PIT-S software and the numerical model was carried out assuming concrete pile cast in very dense granular soil. The set data used in the analysis is shown in Table 3

Table 3 Soil, pile and load data used in the analysis

Item	Value
Pile Length, L (m)	10.0
Concrete Density, ρ_c (t/m ³)	2.5
Pile elastic modulus, E (kN/m ²)	4x10 ⁷
Pile Radius, r_0 (m)	0.18
Soil Density, ρ_s (t/m ³)	2.0
Poisson's Ratio, ν	0.4
Soil Shear Modulus, G (kN/m ²)	50,000
Force Amplitude, F (kN)	5.0
Pulse duration, (sec)	0.00025
Attenuation coefficient(γ)	1.0
Attenuation coefficient(α)	0.13

Pile influence zone (r_m) was calculated based on the assumption that pile influence zone is the distance where 95% attenuation in vibration amplitude occurs. PIT-S software generated velocity curve and the proposed model generated velocity curve for a signal received at pile top using the data shown in Table 3, for circular concrete pile cast in very dense granular soil, are provided in Fig. 4 and Fig. 5, respectively.

To compare both models, force and velocity amplitudes versus time are plotted at signal receiving depths of 0.0m, 5.0m and 9.875m. It has been found that the force and velocity amplitudes produced using the proposed model and PIT-S

software are close to each other for signals received at 0.0m and 5.0m depths of pile as shown in Fig. 6 and Fig. 7.

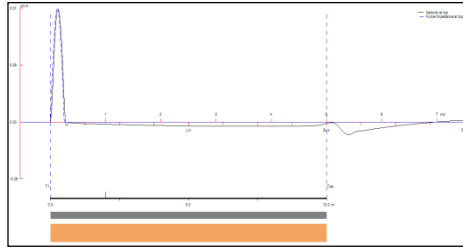


Fig. 4 PIT-S velocity curve at pile top

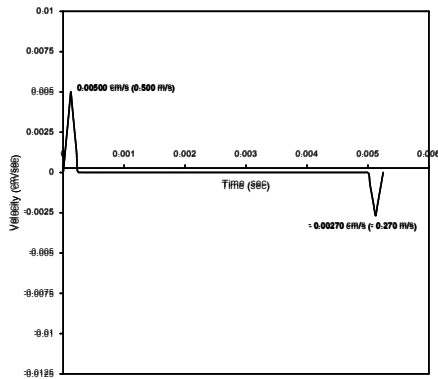


Fig. 5 New model velocity curve at pile top

As shown in the figures, relatively higher differences between PIT-S software and model generated force and velocity values were observed near pile toe. These differences are attributed to the differences between pile-soil interactions assumptions incorporated in both models.

PIT-S software is based on Smith modeling for pile driving, which incorporates static soil resistance; however, in low strain integrity test, the dynamic load is very light compared to pile driving load and does not mobilize full static resistance of soil. For this reason, the proposed model had utilized a dynamic reaction theorem for pile toe analysis, which does not require full mobilization of soil resistance.

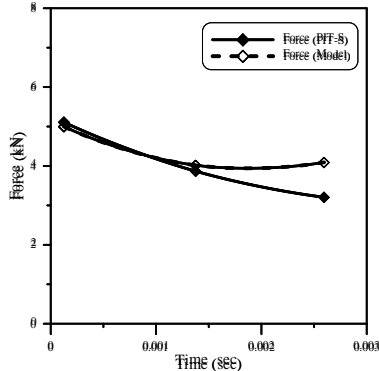


Fig. 6 Force amplitudes from model and PIT-S

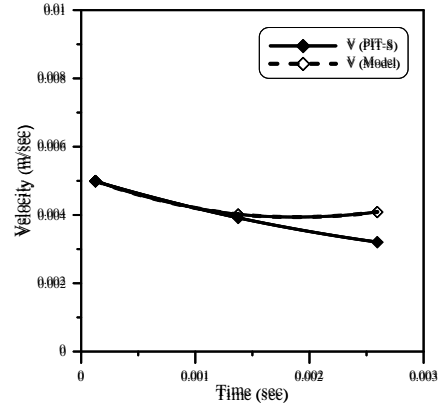


Fig. 7 Velocity amplitudes from model and PIT-S

ROCK SOCKET EFFECT

Effect of strength of rock in terms of dynamic shear modulus value and the effect of rock socket length were evaluated using the numerical analysis illustrated above. Pile, soil, rock and impact load data for a sample integrity test used for the analysis is shown in Table 4.

Table 4 Soil, rock, pile and load data used in evaluation of rock socket effect

Item	Value
Pile Length, L (m)	10.0
Concrete Density, ρ_c (t/m ³)	2.5
Pile elastic modulus, E (kN/m ²)	4x10 ⁷
Pile Radius, r_0 (m)	0.18
Soil Density, ρ_s (t/m ³)	2.00
Rock Density, ρ_s (t/m ³)	2.25
Soil Poisson's Ratio, ν_s	0.40
Rock Poisson's Ratio, ν_r	0.25
Soil Shear Modulus, G (kN/m ²)	50,000
Force Amplitude, F (kN)	5.0
Pulse duration, (sec)	0.00025
Attenuation coefficient(γ) for soil	1.0
Attenuation coefficient(α) for soil	0.13
Attenuation coefficient(γ) for rock	1.7
Attenuation coefficient(α) for rock	0.10

Effect of Rock Strength below Pile Tip

The first run of analysis was carried out assuming that the study pile is resting on a rock stratum, which does not extend above pile tip level (i.e. zero length rock socket). The analysis was conducted for two different rock strength values in terms of shear module. The first rock type has a shear modulus of 250,000 kN/m², while the second rock type has 500,000 kN/m² shear modulus value. This change in shear modulus values facilitates the study of rock strength effect, in terms of its shear modulus value, on the generated pile tip reaction. A reduction in stress wave force and velocity amplitudes of 15.4%

and 19.8% were observed when the shear modulus value was changed from 250,000 kN/m² to 500,000 kN/m². These reductions are attributed to the impedance change as a result of changing rock strength and to the produced soil reaction at pile toe for different rock strata. Force and velocity amplitude values for both rock types at zero length rock sockets are provided in Tables 5 and 6.

Table 5 Force and velocity amplitudes for different socket lengths for $G = 250,000$ kN/m² rock

Socket Length (m)	Force (kN)	Velocity (m/s)
0.0	3.190	0.00319
2.0	2.878	0.00288
4.0	2.605	0.00260
6.0	2.343	0.00234

Table 6 Force and velocity amplitudes for different socket lengths for $G = 500,000$ kN/m² rock

Socket Length (m)	Force (kN)	Velocity (m/s)
0.0	2.698	0.00270
2.0	2.165	0.00216
4.0	1.748	0.00175
6.0	1.393	0.00139

Effect of Rock Socket Length

The effect of rock socket length on stress wave was studied through analyzing the sample pile for 0.0m, 2.0m, 4.0m and 6.0m socket lengths. These analyses were carried out for shear modulus values of 250,000 kN/m² and 500,000 kN/m². For the rock having 250,000 kN/m² shear modulus, the increases of rock socket length from 0.0 to 2.0m, from 2.0m to 4.0m and from 4.0m to 6.0m were found to cause reductions in stress wave force and velocity amplitudes by 9.8%, 9.5% and 10.1%, respectively, while reductions of 19.8%, 19.3% and 20.3%, respectively, were observed for the rock having shear modulus of 500,000 kN/m². These observed attenuations in stress wave amplitudes were caused by the increase of frictional resistance forces when the socket length is increased. Furthermore, the increase in rock shear modulus is found to have remarkable effect on increasing the attenuation values as illustrated in the following section. Socket lengths versus force and velocity amplitudes for both rock types are plotted in Fig. 8 and Fig. 9, respectively.

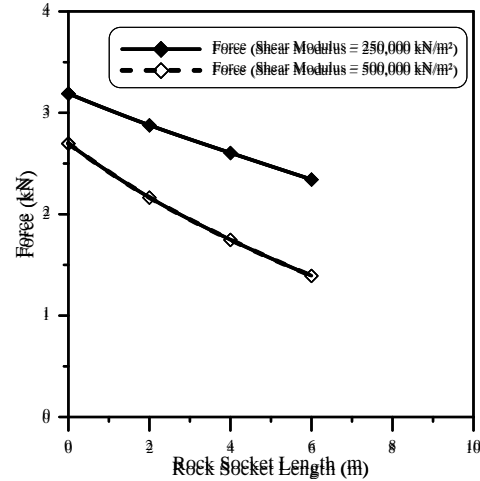


Fig. 8 Force amplitudes for different rock socket lengths of two rock types

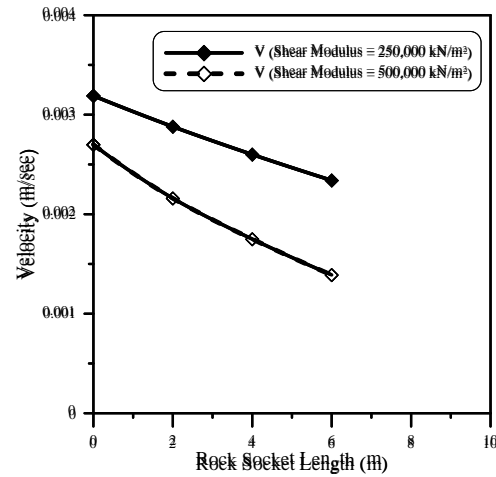


Fig. 9 Velocity amplitudes for different rock socket lengths of two rock types

Effect of Rock Shear Modulus

It had been noticed that for changes of socket lengths from 0.0 to 2.0m, from 2.0m to 4.0m and from 4.0m to 6.0m, the reduction in stress wave amplitudes were found to change from 9.8% to 19.8%, 9.5% to 19.3% and from 10.1% to 20.3% when the rock shear modulus changed from 250,000 kN/m² to 500,000 kN/m². Hence, 100% increase in dynamic shear modulus of rock had caused about 100% reduction in stress wave force and velocity amplitudes.

CONCLUSION

Soil resistance effects on stress wave that propagates during pile integrity test were quantified using new numerical method to solve the wave equation after incorporation of soil effects.

The skin friction mobilized as a result of light impact load on pile top during pile integrity test is assumed to be directly proportional to pile displacement.

Soil reaction at pile toe is assumed to be proportional to pile segment displacement and velocity. This assumption was found to be suitable for light dynamic loading on piles such as in the low strain integrity test, while small and instantaneous soil reactions can still be quantified.

Generated soil reaction at pile tip was found to be less sensitive for change of dynamic shear modulus of the strata below pile toe. This is attributed to the indirect proportional relation between soil reaction and pile toe displacement and velocity.

Rock socket characteristics like socket length and rock strength in terms of dynamic shear modulus were found to have remarkable effect on stress wave attenuation.

This method of analysis for pile tested under light dynamic loads can be used further to evaluate the efficiency of low strain integrity test for piles socketed inside hard rock. This method can provide good tool to evaluate the stress wave absorption phenomenon by the hard strata, which surround the pile.

ACKNOWLEDGEMENTS

The authors would like to thank the Research Management Centre of Universiti Teknologi Malaysia (UTM) and Ministry of Science, Technology and Innovation (MOSTI) for providing financial support through research vote: R.J130000.7822.4F118 for this research, and Pile Dynamic Incorporation for providing the technical support related to PIT-S software.

REFERENCES

- [1] American Society of Testing and Materials (ASTM), 2007. Section 4, Vol. 04.09, Standard "Test Method for Low Strain Impact Integrity Testing of Deep Foundations".
- [2] Amick, H., and Gendreau, M., "Construction Vibrations and Their Impact on Vibration-Sensitive Facilities". 2000. Proc., ASCE Construction Congress 6, Orlando Florida, pp. 1-10.
- [3] Hussein, M., Woerner, W., Sharp, M. and Hwang, C. "Pile Driveability and Bearing Capacity in High-Rebound Soils", Geo-Congress 2006: Geotechnical Engineering in the Information Technology Age, Georgia, USA.
- [4] Johnson, M., Rausche, F., "Low Strain Testing of Piles Utilizing Two Acceleration Signals". September, 1996. Proceedings of the Fifth International Conference on the Application of Stress-wave Theory to Piles 1996: Orlando, USA, FL; pp. 859-869.
- [5] Kagawa T., "Dynamic Soil Reaction to Axially Loaded Piles", Journal of Geotechnical Engineering, Vol. 177, No. 7, July 1991.
- [6] Kraft, L. M., Ray, R. P., and Kagawa, T. (1981). Theoretical t-z curves, Journal Geotechnical Engineering Division, Proceedings Paper 16653, American Society of Civil Engineers, Vol 107(GT11).
- [7] Liang, M and Wu J, "Predicting the Integrity of Existing Concrete Bridge Deck Using Sonic Method", Journal of Marine Science and Technology, Vol. 9, No. 1, pp. 45-52, 2001.
- [8] Mc Vay M. and Kuo C., "Estimate Damping and Quake by using Traditional Soil Testings", Final Report for Florida Department of Transportation, Nov. 1999.
- [9] Rausche, F., Likins, G. E., Ren-Kung, S., September, 1992. "Pile integrity testing and analysis". Proceedings of the Fourth International Conference on the Application of Stress-Wave Theory to Piles, Netherlands, pp. 613-617.

CHARACTERISTICS OF SLOPE FAILURES IN MAKINOHARA, JAPAN

Jun Sugawara¹

¹Golder Associates, Australia

ABSTRACT

Makinohara City, located in south-central Shizuoka Prefecture in Japan, is renowned for the production of high quality Japanese green tea. Approximately 25% of Makinohara City's land is used as tea plantation fields and annually 5,800 tonnes of tea is produced. However, slopes in this region are occasionally subject to failures following construction activities. In this light, this paper investigates characteristics of slope failures in Makinohara region. Based on the author's experience, a number of recommendations are also made for slope analysis and mitigation works.

Keywords: Makinohara Plateau, Tea Plantation Fields, Slaking, Slope Mitigation, Surface Protection

INTRODUCTION

Makinohara City, founded by the merger of Sagara Town and Haibara Town in 2005, is located in the south-central region of Shizuoka Prefecture in Japan. The city is known for production of Japanese green tea for a long period. Approximately 25% of Makinohara City's land is used as tea plantation fields [1]. The Makinohara City Hall also has a unique department called Tea Promotion Section which specifically deals with tea related matters. Today Makinohara City produces 5,800 tonnes of tea, which is approximately 6% of Japan's overall tea production.

In this region, a number of major transportation networks have been developed. These include Tomei Expressway, Japan National Routes 15 and 473, Tokaido Shinkansen (Japanese high speed train), Omaezaki Port, and Mt Fuji Shizuoka Airport which newly opened in 2009.

The author has noted that slopes in this region are occasionally subject to failures following construction activities. The author also identified that the landslide prone areas often impinge on the tea plantation fields [2]. The recent landslide which occurred in the tea plantation fields in Hamamatsu, Shizuoka is a good example illustrating the association between landslide prone areas and the tea plantation fields.

In this light, this paper investigates the characteristics of slope failures in the Makinohara region. Based on the author's experience, a number of recommendations are made for slope analysis and mitigation measures.

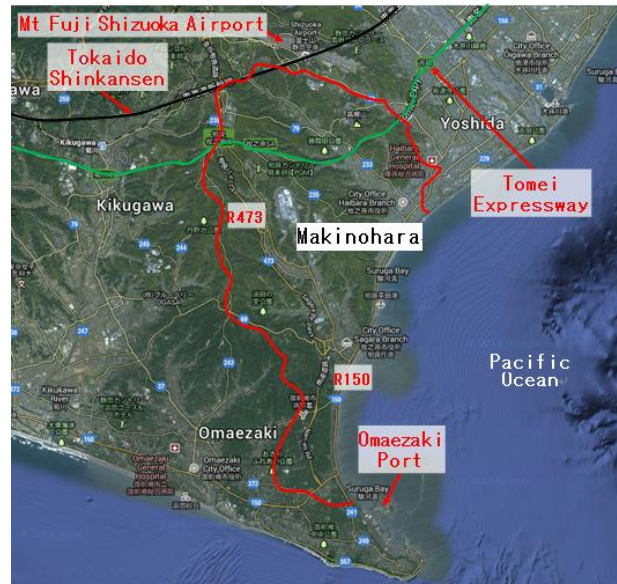


Fig. 1 Google Map of Makinohara Region (after [3])

GEOGRAPHY AND GEOLOGY

This region principally consists of the Makinohara Plateau with an elevation of less than 200m. A number of gullies are developed on this plateau. A narrow alluvial plain of the Katsuma River also lies in the middle of the Makinohara City.

According to relevant geological maps [4 and 5], the Makinohara Plateau comprises the Makinohara river terrace gravelly layers, which are in turn underlain by layers of various degrees of decomposed Neogene (Miocene) age Kakegawa Group and Sagara Group siltstones. The tolerance of these siltstones to the weathering is relatively low and their structure often includes advanced fragmentation and softening. The overlying soils are usually suitable for growing tea plants due to

their weakly acidic characteristics.



Photo 1 Typical Tea Plantation Fields in the Makinohara Region

TYPE OF FAILURES AND SLIP SURFACE IDENTIFICATION

In the Makinohara region, slope failures are often triggered by the earthwork excavations [6]. The author also observed a number of failures caused by earthworks during the road and pond constructions associated with the airport construction. There are also slope instabilities caused by the construction of embankments near the crest of past landslide sites.

According to the classification proposed by [7], slope failures in this region can be broadly classified into the following categories:

- Weathered rock type: the shape of slope failure is the convex hill type or the concave mono hill type. Scarps and a strip of depression zone are often observed near the slope crest. This type is typically triggered by the intensive rainfall events after the construction of medium to large size earthworks.
- Clayey soil type: the shape of slope failure is usually the concave poly hill type. This type consists of a number of shallow and small past failures. Gully features are developed and the terrain topography is generally disturbed. The groundwater table is usually high.

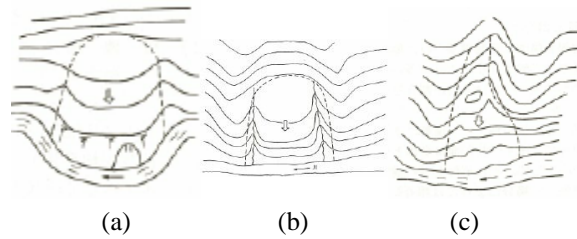


Fig. 2 Shape of Slope Failures: (a) Convex Hill Type, (b) Concave Mono Hill Type and (c) Concave Poly Hill Type (after [7])

In many cases, determination of the slip surface based on borehole core observation or monitoring results (e.g. inclinometer or pipe strain gauge) may not be difficult in this region. This is because the core is often slickensided and monitoring results typically show clear movement at the location of the slip surface. The slip surface is also occasionally seen on the faces of excavations.

It is noted that when the slope movement is significant, boreholes and inclinometer casings may bend making the monitoring of the slip surface impossible. This is not unusual in this region due to the relatively fast movement of the slope. Based on the author's experience, this phenomenon could happen within a very short period (e.g., 2 to 3 weeks) if the strength of geomaterial is low. When this is anticipated, the pipe strain gauge needs to be used for the slip surface monitoring.



Photo 2 Slope Failure Triggered by Excavation

FACTOR OF SAFETY AND ANALYSIS

The following design Factor of Safeties (FOS) are usually used for the slope mitigation works in Japan:

- Temporary works: $FOS \geq 1.05$
- Permanent works: $FOS = 1.12 - 1.20$, depending on the importance of assets to be mitigated or protected.

In Japan, the design of slope mitigation works is

undertaken by back-calculating strength parameters for the slope, based on certain assumptions regarding groundwater levels and cohesion. However the choice of the highest groundwater level (HWL) as the groundwater level for the back-analysis is a relatively arbitrary choice, that may be affected by a limited duration of monitoring. In addition, there are always uncertainties in determination of the slip surface. The required force to achieve the design FOS could differ significantly even with a slight difference in the shape of the slip surface.

Moreover, the following factors need to be carefully considered during analyses and design of slopes in this region:

- Many clayey soil type slopes appear to be marginally stable, i.e., their FOS is close to 1.0. Landslides in this area could be reactivated even with relatively minor triggering events.
- The regional geology tends to dip to southeast direction. This structural geological setting as well as other adverse geological conditions (e.g., advanced weathering) often have significant influence on the stability.
- Strong slaking and erosion events often cause creep of slope and as a result overall FOS decreases with time possibly within a short time. The author encountered a number of instances of temporary remediated slopes being damaged prior to the start of permanent mitigation works.

Taking into account all of these factors as well as the low design FOS commonly adopted in Japan, the author considers that a slightly conservative approach is required particularly during temporary works in this region.



Photo 3 Damage to Temporary Slope Mitigation Works Prior to Permanent Works

SELECTION OF MITIGATION MEASURES

Fig. 3 shows the commonly used landslide mitigation measures in Japan. They consist of landslide control measures and landslide restraint

measures [8].

Among those measures, earth removal, buttress fill, groundwater control and anchors which are commonly used in this region will be discussed in the following sections.

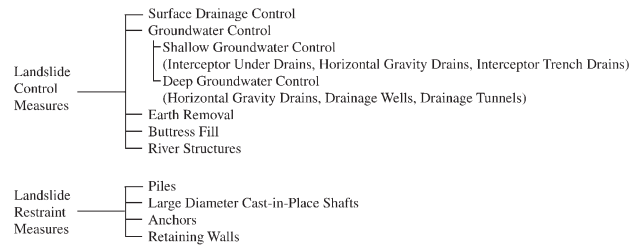


Fig. 3 Landslide Mitigation Measures (after [9])

EARTH REMOVAL AND BUTTRESS FILL

Among various slope mitigation measures, cutting back the upper portion of the slope or buttress filling near the slope toe is usually the quickest and the most economical mitigation option. Groundwater can be also effectively lowered by earth removal.

Japan has one of the highest population densities in the world. Therefore slopes are often designed as steep as possible in order to minimise the disturbance to the surrounding areas. For instance, cut slopes in weathered siltstones are often designed at 1:1.0 (V:H) in this region. However the author observed a number of failures under the following adverse conditions:

- Long and intensive rainfall events. The average annual rainfall in this region is more than 2,200mm [1].
- Abundant seepage from the Makinohara gravelly layers. After daily rainfall events with more than 100mm, groundwater seepage typically lasts for a few days in tea plantation fields and a few weeks along cliffs [10].
- Adverse geological structural setting. The regional geology tends to dip to southeast, thus bedding is dipping out on slopes facing between the east to the south.

When earth removal or buttress fill is selected as a slope mitigation measure, the author considers that the following slightly conservative slope angles are appropriate in this region:

- Cut Slope = 1:1.5 (V:H) or flatter for moderately weathered or better siltstones
- Fill Slope = 1:2.0 (V:H) or flatter

It is also prudent to apply surface protection even to the temporary slopes in order to minimise exposure of the cut surface. It is evident that many cut slope failures in this region occur following the first heavy rainfall event after slope construction.

When buttress fill is adopted, it is important not to use failed materials as buttress fill materials since

surface water tend to concentrate around these impermeable materials and causes further instability of the slope.

It is noted that earthworks which will be affecting existing tea plantation fields are often considered inappropriate by landholders and governmental administration bodies since tea farming is a very important source of income in this region. In such a case, more rigorous mitigation measures (e.g., anchors) need to be considered.



Photo 4 Erosion occurring on 1:1.0 (V:H) Temporary Cut Slope

GROUNDWATER CONTROL

The tea plants grow well in areas with yearly rainfall of more than 1,400 mm [11]. While rainfall is essential to the growth of tea plants, there are a number of sediment related disasters due to heavy rainfall events.

In particular in this region, the steady seepage flow is located around RL 170m to RL190m. Even if the groundwater level is low during the dry season, the rise of groundwater could be significant following long intensive rainfall events. The research conducted by [10] also revealed that the volume of seepage fluctuates significantly at higher RL. Therefore groundwater control is one of the key slope mitigation measures in this region.

According to manuals commonly used in Japan (e.g., [9], [12] and [13]), the planned groundwater level (PWL), which is the groundwater level taking into account effects of groundwater control measures, is often set lower than HWL, i.e. 3m (gravity drains) and 5m (drainage wells). While lowering groundwater to the PWL in gravelly layers is usually achievable, the response of groundwater in siltstones is often not fast enough to lower the groundwater due to their relatively low permeability. As a result, an increase of FOS by these groundwater control measures could be much less than 3% when they are installed in siltstones.

In order to maximise effects of these

groundwater control measures, it is essential to carry out detailed investigations to identify the groundwater table relative to the slip surface. In addition, the groundwater logging test is useful to determine the groundwater flow so that drains can be installed at locations where the groundwater flow is fast (i.e., the permeability is high).

In cases where the site is located within or adjacent to the tea plantation fields, it is important not to drain groundwater completely so that they remain suitable as tea plantation fields.

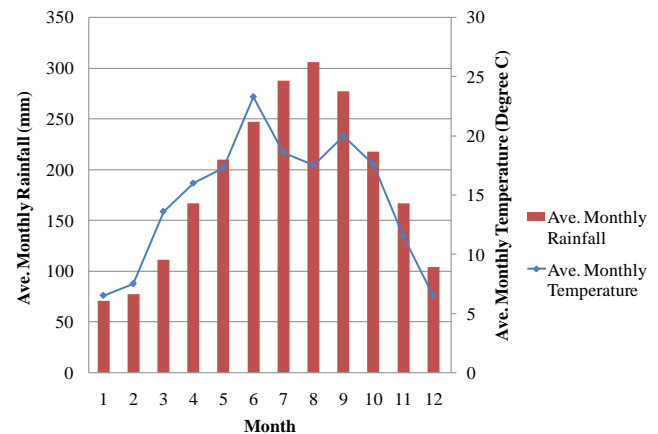


Fig. 3 Rainfall and Temperature of Makinohara City (after [1])



Photo 5 Horizontal Gravity Drains Installed on Temporary Cut Slope

ANCHORS

Anchors are often required for both temporary and permanent works in Japan. In the Makinohara region, tensioned anchors are preferable to compression anchors for weathered siltstones because:

- The extent of anchor forces acting along the tendon is greater in the tension type than in the compression type for rocks consisting of fine particles (e.g., siltstone) [14].
- The compression type tends to create the stress concentration at the bottom of the anchor [15].

The design of anchors in this region is often based on the circumferential skin friction (τ) of 0.6 MN/m^2 , which is the smallest τ value for weathered rocks in accordance with [16]. However many case studies revealed that the actual τ value could be

potentially smaller than this value in this region. Therefore it is strongly desirable to confirm the τ value by anchor pullout tests.



Photo 6 Pullout Test Revealed $\tau = 0.5 \text{ MN/m}^2$ for a Project in the Makinohara Region

Due to the potentially low τ values, additional anchors may be required in this region in order to achieve the design FOS. A larger anchor bearing plate is also often necessary due to the low bearing capacity. Meanwhile increasing the number of anchors and using a larger anchor bearing plate allows restraint to a wider area of the slope surface, resulting in a reduction of the risk of surface erosion. In addition to these measures, providing surface protection and appropriate drainage systems (e.g., shotcrete and gravity drains / weepholes) is also highly desirable.

In this region, installation of anchors is preferably undertaken in the dry season. The following steps are also recommended for anchor installation:

- Undertake excavation and anchor installation in stages from top down.
- Install anchors as soon as the slope is trimmed in order to minimise the unsupported period.
- Fabrication of the precast anchor bearing plate in a factory prior to anchor installation to minimize the lead time associated with acquisition of the anchor bearing plate.

After initial tensioning, anchor bearing plates occasionally settle in this region. Slopes also often show creep movement and the anchor lift off stress could be much lower than the design stress. Taking into account these facts, re-tensioning of anchors is often required and therefore an initial tensioning to approximately 80% or less of design anchor load is usually considered appropriate.



Photo 7 Photograph of Anchor Bearing Plate Indicating Creep Movement of Slope

CONCLUSION

In this paper, characteristics of slope failures in the Makinohara region are described. Based on the author's experience in this region, various recommendations are made for slope mitigation works. From a series of studies, the following conclusions can be drawn:

- Slope failures are often triggered by earthworks excavations. These failures can be broadly classified into the weathered rock type and the clayey soil type.
- Due to various adverse conditions and the low design FOS commonly used in Japan, a slightly conservative approach (e.g., conservative slope angle) is required particularly during temporary works in this region.
- Protection of the slope surface and the control of groundwater and surface water are key to the mitigation of slope instability since siltstones show strong slaking phenomenon in this region.
- The τ value could be smaller than the commonly adopted design value in this region, and performing anchor pullout tests is highly desirable. Re-tensioning of anchors is also often required and therefore an initial tensioning to approximately 80% or less of design anchor load is usually considered appropriate.

ACKNOWLEDGEMENTS

Valuable comments were made by Makinohara City Hall, Aya Green Tea and David Starr during the preparation of this paper and I am most grateful to them for their suggestions.

REFERENCES

- [1] Makinohara City, "Makinohara City Gaikyo", 2012, http://www.city.makinohara.shizuoka.jp/ftp/05gt04/1_gaikyou.pdf (in Japanese)

- [2] Sugawara J, “Landslides in Tea Plantation Fields in Shizuoka, Japan”, Int. J. of GEOMATE, Vol. 4, No. 1 (Sl. No. 7), March, 2013, pp. 495-500.
- [3] Google Map, <http://maps.google.co.jp/>, 2013
- [4] Shizuoka Prefecture, “Shizuoka Geological Map”, 2013, <http://www.shimizu-arc.jp/images/sumaino/geology/geologymapwest.pdf> (in Japanese)
- [5] Japanese Geology Chubu Region Editors, “Japanese Geology (4) Chubu Region I”, 1988 (in Japanese)
- [6] Makinohara City, Personal Communication, 2013
- [7] Watari M. and Kobashi S, “Prediction and Mitigation of Landslides and Slope Failures”, Sankaido, 1987 (in Japanese)
- [8] Japan Landslide Society and National Conference of Landslide Control, “Landslides in Japan (The Sixth Revision)”, Japan Landslide Society and National Conference of Landslide Control, 2002, pp.30
- [9] Japan River Association, “Manual for River Works in Japan: Investigation”, Sankaido, 1997 (in Japanese)
- [10] National Agriculture and Food Research Organisation, 2002, <http://www.naro.affrc.go.jp/project/results/laboratory/vegetea/2002/vegetea02-42.html> (in Japanese)
- [11] Rural Cultural Association, “Cha-Daihyakka”, vol. 1, Rural Cultural Association, 2008, pp. 269 – 302. (in Japanese)
- [12] Japan Construction Engineers Association, “Saigai Techou”, 2006, pp. 361. (in Japanese)
- [13] Japan Road Association, “Guidelines for Slope Stabilization Works and Slope Stability”, Japan Road Association, 1999 (in Japanese)
- [14] Sung CH, Bo JL, Wei H, and Juir RL, “Modeling of Anchors in Gravel Formation Using Discrete Element Method”, Advanced Materials Research, Vols. 189 – 193, 2011, pp. 1726 – 1731.
- [15] Institute of Slope Technology, Personal Communication, 2006
- [16] Japanese Geotechnical Society, “Manual for Design and Construction of Ground Anchors”, Japanese Geotechnical Society, 2000 (in Japanese)

S-PSA WITH USING FEM FOR AN EXISTING ESTUARY DAM

T. Hara¹, M. Iwata¹, Y. Otake¹, Y. Honjo¹, T. Kato², A. Nishida² and H. Yukimoto²

¹Department of Civil Engineering, Gifu University, Japan; ² Japan Water Agency, Japan

ABSTRACT

This paper presents an example of S-PSA, Seismic Probabilistic Safety Assessment, applied to seismic verification of an existing estuary dam. Dynamic effective stress FEM analysis was adopted in this S-PSA, in order to estimate the seismic response of the target structure built on liquefiable ground during earthquake. In this paper, details of S-PSA with using FEM is introduced, and seismic safety and seismic retrofit necessity are discussed from both results of severe damage occurrence probabilities in respective parts constituting the dam and probabilistic damage curves of the parts corresponding to increscent seismic intensity.

Keywords: S-PSA, FEM, Probabilistic seismic hazard, Damage occurrence probability, Existing structure

INTRODUCTION

Seismic design with considering occurrence probability of larger earthquake than the design one has been an important issue in Japan, because several large earthquakes caused tremendous damages to human and social economy, such as Kobe quake in 1995 and Tohoku quake in 2011.

Therefore, the authors have conducted a study on application of S-PSA, Seismic Probabilistic Safety Assessment [1], [2], to common infrastructures except nuclear plant. In this paper, an example of S-PSA applied to seismic verification of an existing estuary dam is presented. Effective stress dynamic FEM analysis is adopted in this S-PSA, in order to estimate the seismic response of the dam built on liquefiable ground during earthquake, by using response surface method [3]. And following uncertainties are considered in the reliability analysis.

Response uncertainties: Earthquake intensity based on probabilistic seismic hazard curve at the site, reproducibility of the FEM analysis adopted in this study with respect to experimental responses of the structure built on liquefied ground, and reproducibility of the assumed response surface with respect to the seismic responses estimated by FEM analysis.

Resistance uncertainties: Strength estimation of the structural members and bearing capacity of pile foundation, and spatial variation and transformation error of geotechnical parameters.

In this paper, details of S-PSA with using FEM is introduced, and seismic safety and seismic retrofit necessity are discussed from both results of severe damage occurrence probabilities in respective parts constituting the dam and probabilistic damage curves of the parts corresponding to increscent seismic intensity.

TARGET STRUCTURE

The target facility is an existing estuary dam to supply city, industrial and agricultural water due to prevent running up of seawater to the river. The facility length is 192.3m and it consists of six gates (25m in width, 7.3m in height) and seven hanging up structures of the gates. Fig.1 shows the external appearance of the dam. The target structure in this study is the hanging up structures of the gates. This structure is built on the liquefiable ground during earthquake with steel pipe pile foundation ($\phi 600$, $t = 9\text{mm}$, $l = 25\text{m}$, $n = 35$).



Fig. 1 External appearance of the target dam.

PROCEDURE FOR S-PSA

Fig.2 shows the procedure for the S-PSA in this study. At first, the uncertainty of seismic intensity is set as a probabilistic density function from the published probabilistic seismic hazard curve at the site, which corresponds to residual service term of the target facility. And then, response surfaces (RS) of respective verification points are estimated from sensitivity analyses with respect to contribution factors to each response of the points. At last, damage occurrence probabilities and probabilistic damage curves of the verification points are

estimated by Monte Carlo Simulation (MCS) with both uncertainties of response and resistance. And safety verification is conducted from both the comparison with allowable damage occurrence probability determined by one of recently built similar structures, and the probabilistic damage curve in the extent close to predictable large earthquake level.

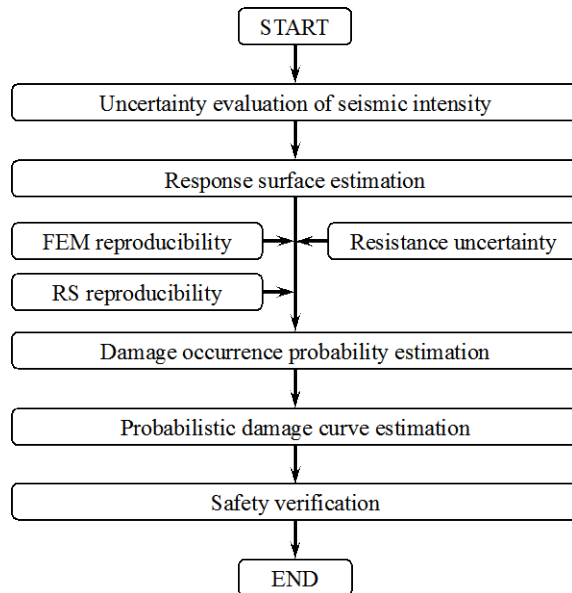


Fig. 2 Procedure for S-PSA.

UNCERTAINTY OF SEISMIC INTENSITY

Uncertainty of Seismic Intensity

Residual service term of the target facility, “30-years”, is determined as a basic term though, “50-years” is also considered in this study from a concern of the safety in case that the term is postponed.

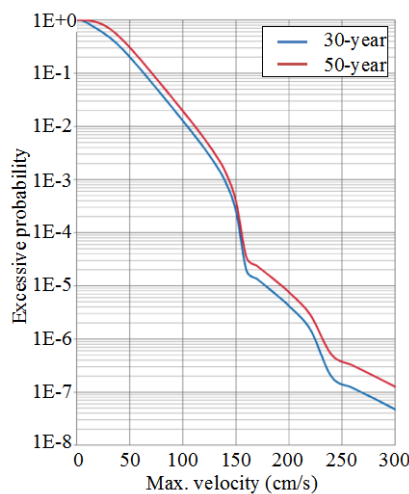


Fig. 3 Probabilistic seismic hazard curve.

The probabilistic seismic hazard curve corresponding to 30 and 50 years term at the target site (J-SHIS, 2010) is shown in Fig.3. And Fig.4 and Table 1 present the probabilistic density function, the uncertainty of seismic intensity at the site, which is assumed from the hazard curve.

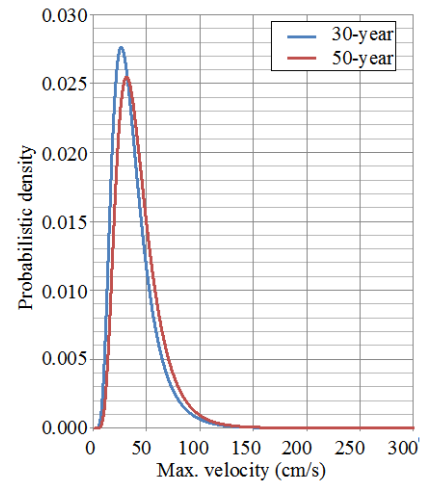


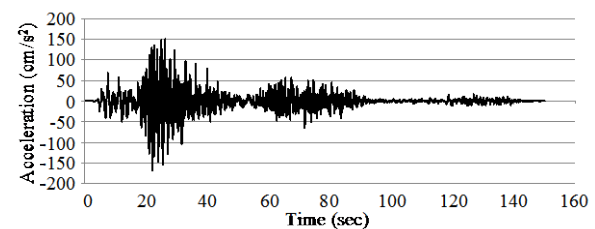
Fig. 4 Uncertainty of seismic intensity.

Table 1 Uncertainty of seismic intensity

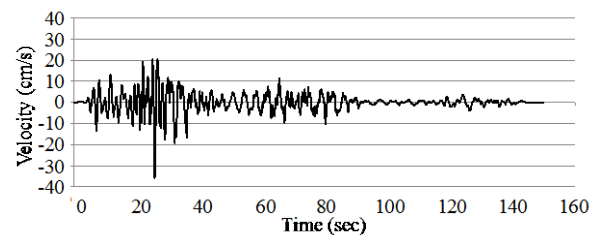
Design term	Mean (cm/s)	SD (cm/s)	Distribution
30-years	34.9	19.4	Lognormal
50-years	42.6	20.2	Lognormal

Basically seismic wave

Fig.5 shows the basically seismic wave [4] adopted in this study. The seismic effect in this study is considered from the basically seismic wave calibrated by the uncertainty of seismic intensity.



(a) Acceleration wave.



(b) Velocity wave.

Fig. 5 Basically seismic wave.

RESPONSE SURFACE (RS) ESTIMATION

Response Estimation Method

Effective stress dynamic FEM analysis, FLIP (Ver. 6.0.6), is adopted in this study, in order to evaluate the seismic response of the dam built on liquefiable ground during earthquake, by using response surface method [3]. Fig.6 shows the FEM mesh of both river axis cross section and dam axis one. Ground condition of top three strata is presented on Table 2 and A_{s2} stratum is the liquefiable ground during earthquake.

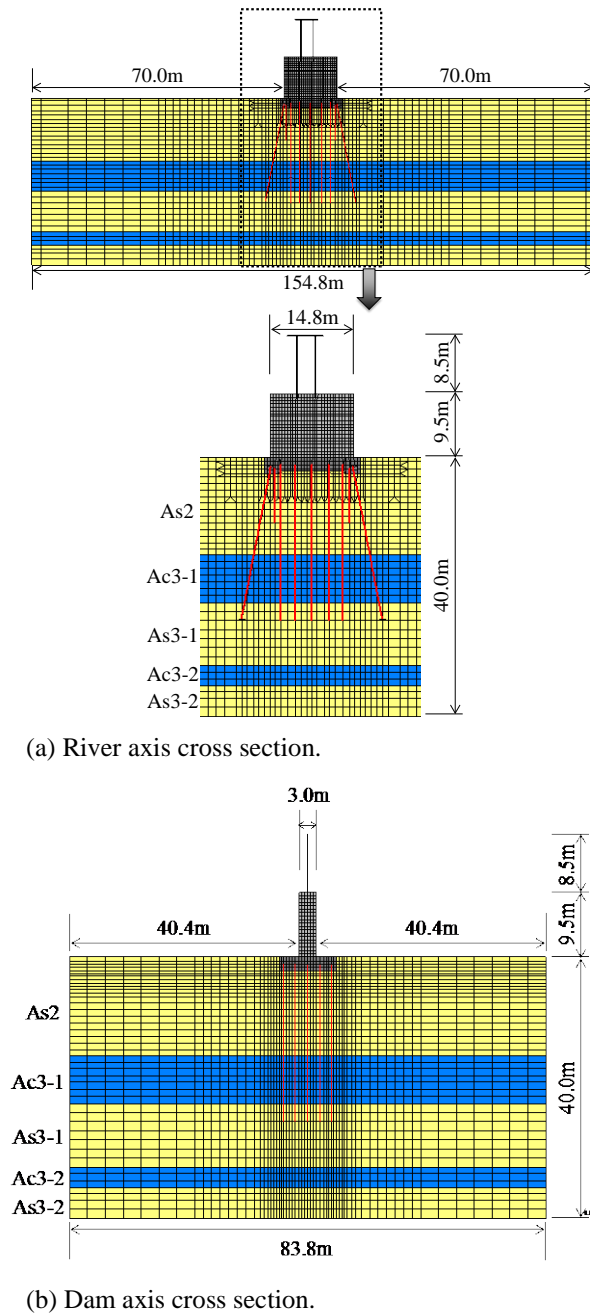


Fig. 6 FEM mesh.

Table 2 Ground condition

	Thickness (m)	SPT-N value	
		Mean	SD
A_{s2}	14.5	15.2	4.4
A_{c3}	7.0	12.4	3.0
A_{s3}	10.0	33.4	10.4

The uncertainty of the FEM reproducibility with respect to the experimental responses of structure built on liquefied ground during earthquake, which were obtained from blind tests [5], is shown in Fig.7. Because of blind test, the transformation error of the geotechnical parameters used in the FEM is included in the uncertainty. Although the reproducibility of the FEM was obtained from analyzed ones with respect to experimental data of river dike, it was referred as one to estimate response of piled structure in this study.

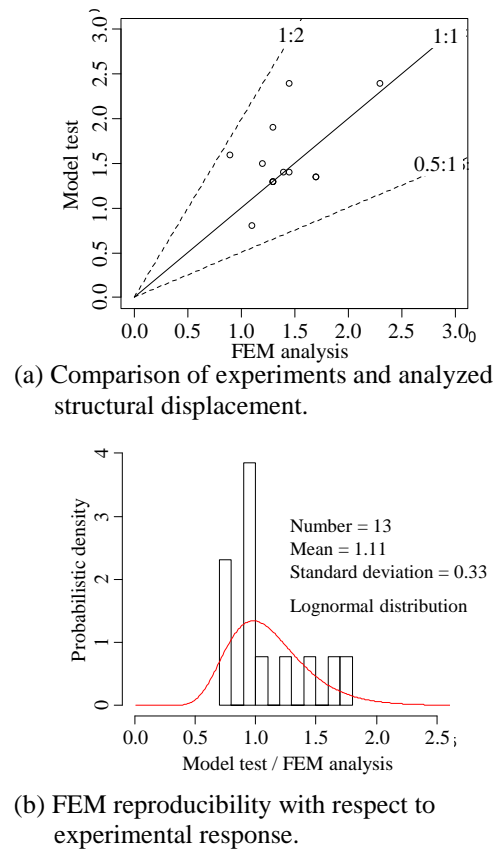


Fig. 7 Uncertainty of FEM reproducibility.

Verification Points

A lot points have to be verified in normal seismic design though, in this study, the minimum verification points, which possess the possibility that the response corresponding to increscent seismic intensity exceeds the limit state, are selected from sensitivity analyses of responses at each point. The selected verification points are presented on Table 3

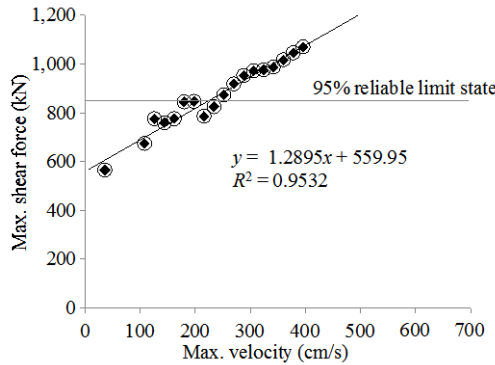
Table 3 Verification points

		Verification axis	
		River	Dam
Gate Pier	Curvature	Verify	N/A
	Shear force	Verify	Verify
Dam Pier		N/A	N/A
Pile	Displacement	Verify	Verify
Entirely structural inclination		Verify	Verify

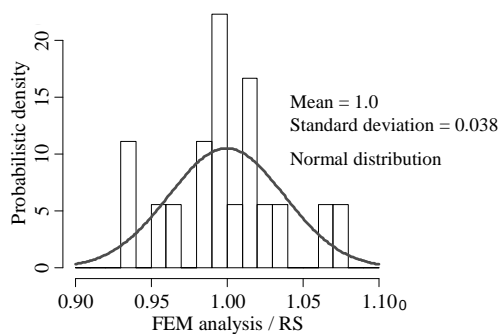
In this paper, because of paper limitation, safety assessments of gate pier shear force in the dam axis cross section with respect to 30-years term are only introduced.

Response Surface

It was confirmed that the uncertainty of seismic intensity is only influential one to the response of the respective verification points from sensitivity analyses with respect to uncertainties of seismic intensity, ground condition, deformation characteristic of gate pier and pile. Therefore, response surfaces (RSs) focused on only seismic intensity are estimated. Equation (1) and Figure 8 show RS of gate pier shear force in the dam axis cross section and its uncertainty of reproducibility with respect to the responses estimated by FEM analyses.



(a) Estimation of RS.



(b) Uncertainty of RS.

Fig. 8 RS of maximum shear force of gate pier.

$$T = 1.2985 \cdot V_m + 559.95 \quad (1)$$

where, T = maximum shear force of gate pier (kN), V_m = maximum velocity of seismic wave (cm/s)

LIMIT STATE UNCERTAINTY

The uncertainty of shear strength is presented on Table 4, which was referred from the existing research on the reproducibility of the shear strength estimated by Eq. (2)-(4) with respect to experimental ones [6].

Table 4 Model error of shear strength estimation

Mean	SD	Distribution
1.93	0.273	Normal

$$P_s = S_c + S_s \quad (2)$$

$$S_c = c_c \cdot c_e \cdot c_{pt} \cdot \tau_c \cdot b \cdot d \quad (3)$$

$$S_s = \frac{A_w \cdot \sigma_{sy} \cdot d \cdot (\sin \theta + \cos \theta)}{1.15 \cdot \alpha} \quad (4)$$

where, P_s = shear strength of reinforced concrete structure (N), S_c = shear strength boar by concrete (N), S_s = shear strength boar by reinforcing bar (N), c_c , c_e and c_{pt} = compensation coefficients concerning cyclic loading action, effective height of the section (d) and, ratio of axial tensile reinforcing bars' area and sectional one, τ_c = mean shear stress boar by concrete (N/mm²), b = section width (mm), A_w = area of shear reinforcing bars (mm²), σ_{sy} = yield strength of shear reinforcing bar (N/mm²), θ = angle of shear reinforcing bar and vertical axis (deg), α = pitch of reinforcing bars (mm).

DAMAGE OCCURRENCE PROBABILITY AND PROBABILISTIC DAMAGE CURVE

Damage occurrence probability and probabilistic damage curve are estimated by MCS with one million runs with considering respective uncertainties.

Damage Occurrence probability

Equation (5) expresses the performance function. And the shear collapse occurrence probability of gate column (dam axis) for 30-year term, 0.27%, is shown in Fig.9

$$g = \delta_T \cdot T - \left(1.2985 \cdot \delta_v \cdot V_m \right) \cdot \delta_{FEM} \cdot \delta_{RS} \geq 0 \quad (5)$$

where, δ_T , δ_V , δ_{FEM} , and δ_{RS} = random variables of shear strength (kN), maximum seismic velocity (cm/s), FEM reproducibility and RS reproducibility, presented on Table 5.

Table 5 Random variables for estimation of shear collapse occurrence probability (30 years)

	Mean	SD	Distribution
δ_T	1.93	0.27	Normal
δ_V	37.6	19.4	Lognormal
δ_{FEM}	1.11	0.33	Lognormal
δ_{RS}	1.0	0.038	Normal

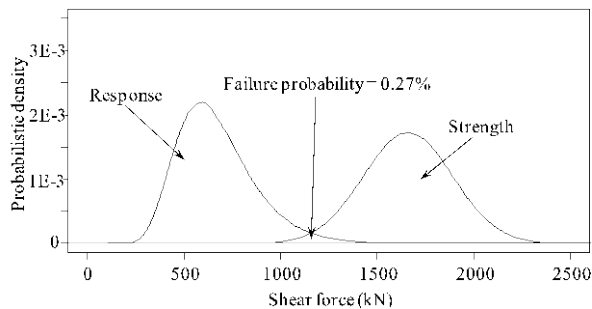


Fig. 9 Shear collapse occurrence probability.

Probabilistic Damage Curve

Equation (6) expresses the performance function. And the probabilistic shear collapse curve of gate column (dam axis) corresponding to increscent deterministic seismic intensity is shown in Fig.10 together with other results of respective verification points.

$$g = \delta_T \cdot T - \text{Res}_T \cdot \delta_{FEM} \geq 0 \quad (6)$$

where, Res_T = shear force occurring in the gate column estimated by FEM with respect to each deterministic seismic intensity. And random variables are the same as ones presented on Table 5.

SAFETY VERIFICATION

Allowance damage occurrence probability

Damage occurrence probability of the recently built similar structures [7]-[9] is referred to specify the allowable ones for the target facility in this study. Table 6 presents the allowance damage probabilities.

Safety verification with respect to probabilistic earthquake

The comparison of the allowable damage occurrence probabilities and estimated ones of all verification points in this study on Table 7 and 8. In

the Tables, the values noted in the brackets are the damage probability in 50-year term. According to the results, shear collapse occurrence probability of the gate column in dam axis cross section is only not satisfied the allowable one

Table 6 Allowable damage probability

		Allowable probability (%)	
		Probabilistic earthquake	Deterministic earthquake
Gate column	Flex.	0.15	1.5
	Shear	0.15	1.0
Pile		0.35	7.5
Incline		0.15	1.5

Table 7 Safety verification, dam axis, 30 (50) years

		Damage probability (%)	
		Estimated	Allowable
Shear collapse of gate column	0.27 (0.29)	0.15	NG
Group pile displacement	2.7E-3 (3.1E-3)	0.35	OK
Residual incline	< 1.0E-4 (< 1.0E-4)	0.15	OK

Table 8 Safety verification, river axis, 30 (50) years

		Damage probability (%)	
		Estimated	Allowable
Flex. collapse of gate column	1.0E-4 (2.0E-4)	0.15	OK
Shear collapse of gate column	7.7E-3 (0.01)	0.15	OK
Group pile displacement	7.0E-4 (9.0E-4)	0.35	OK
Residual incline	1.0E-4 (1.0E-4)	0.15	OK

Safety verification with respect to probabilistic damage curve (deterministic earthquake)

Fig.10 shows normalized probabilistic damage curves by allowable probabilities (deterministic earthquake) of respective verification points in dam axis. In this figure, the intensity of Nankai-trough earthquake [10] that the occurrence is predicted in the near future is also presented.

According to the results, it can be confirmed that shear collapse occurrence probability of gate column in dam axis, which is judged as NG in the safety verification with respect to probabilistic earthquake, rises sharply at the point exceeded the seismic intensity of Nankai-trough earthquake. Namely, the dangerous of the gate column is also confirmed in safety verification with respect to probabilistic damage curve from viewpoint of seismic intensity uncertainty.

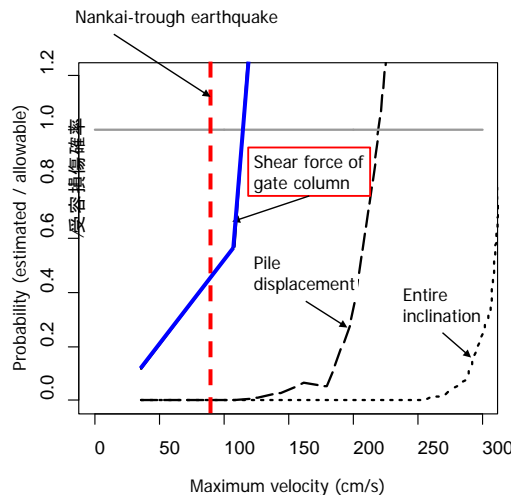


Fig. 10 Probabilistic damage curve (dam axis).

CONCLUSIONS

A concrete example of S-PSA application with using FEM analysis to an existing facility was introduced in this paper. This paper can be concluded as follows;

- Application of S-PSA to common infrastructure is not so difficult.
- S-PSA with using FEM is possible by response surface method.
- Both damage occurrence probability and probabilistic damage curve are available for safety assessment.

Furthermore, if the damage probability is expressed as risk with considering damage cost, it can be expected that this approach apply to making priority decision for seismic retrofit of multiple facilities despite building region and structural type and so on. The authors recommend to apply S-PSA to common infrastructures from the viewpoints of accountability to public and reasonable use of limited public investment to seismic retrofit.

REFERENCES

- [1] International Atomic Energy Agency (IAEA). 1993. Probabilistic safety assessment for seismic events.
- [2] International Atomic Energy Agency (IAEA). 2009. Evaluation of seismic safety for existing nuclear installations.
- [3] Honjo, Y. 2011. Challenges in geotechnical reliability based design: Proc. of the 3rd intern. symp. on Geotechnical Safety and Risk, 11-27, Munich, 2-3 June 2011. Germany: Bundesanstalt fur Wasserbau.
- [4] Cabinet Office, Government of Japan (COGJ). 2006. Tonankai-Nankai seismic (acceleration)

wave on engineering basement ($V_s = 400$ m/s): www.bousai.go.jp/jishin/chubou/. html.

- [5] Japan Institute of Construction Engineering (JICE). 2002. Analysis method of seismic river dike deformation: JICE Document, Vol. 102001.
- [6] Watanabe, H., Koga, H. & Nakamura, H. 2007. A study on installation of International standard of design on concrete structure: Report of general research by government subsidy.
- [7] Osumi, M., Unjo, S., Adachi, S. & Hoshikuma J. 2000. A study on seismic reliability evaluation of highway bridges: proc. of the 4th symp. on seismic design based on ductility design method for bridges: 13-16.
- [8] Unjo, S. & Zhang, K. 2009. A study on partial factor design for highway bridge seismic design: Report of road development research by government subsidy.
- [9] Nakatani, S., Shirato, M., Kono, T., Nakamura, Y., Nomura, T., Yokomaku, K. & Iochi, H. 2009. A study on stability verification method of bridge foundation based on performance based design concept: Technical Note of Public Works Research Institute (PWRI), No.4136.
- [10] Cabinet Office, Government of Japan (COGJ). 2012. Nankai-trough seismic (acceleration) wave on engineering basement ($V_s = 350-700$ m/s): www.bousai.go.jp/jishin/chubou/nankai_trough/data_teikyou/. html.

THE ROTATIONAL HARDENING RULE WITHOUT THE LIMIT SURFACE OF HARDENING

Hiroyuki Kyokawa¹, Ryoki Ohashi² and Teruo Nakai³

¹Institute of industrial science, University of Tokyo, Japan; ²Nagoya city office, Japan; ³Nagoya Institute of Technology, Japan

ABSTRACT

The rotational hardening rule has been used for describing the induced anisotropy of the geo-materials, especially the Bauschinger effect, in a constitutive modeling. Some of the evolution rules of the back stress ratio tensor indicating the center axis of the yield surface have also been proposed. In a lot of those evolution rules, the back stress ratio tensor shifts with the plastic deformation, and the limit surface of hardening is required to satisfy the appropriate failure condition. However, the physical meaning of the limit surface and its transition due to some properties of soil seem to be not clear. Fully new evolution rule of the back stress ratio tensor is proposed in this study. The proposed method, which distinctly considers the development of the stress history during non-monotonic loading path, and its decay with plastic deformation, can suitably address the complicated strength and deformation characteristics of soil due to stress history without the limit surface.

Keywords: Constitutive model, Soil, Elastoplasticity, Rotational hardening rule, Stress induced anisotropy

INTRODUCTION

Soil shows a complicated anisotropic behavior due to the stress history. For instance, in the reloading shear process, the shear stiffness is larger than that of virgin shear. Conversely, since the yield strength decreases when the direction of loading is changed, the shear stiffness becomes lower in the reverse loading process. This sort of property in reverse loading is, particularly, well known as the Bauschinger effect. These mechanical characteristics of soil due to the stress history are, moreover, collectively called as “the stress induced anisotropy”. The stress induced anisotropy is considerable feature for the failure and deformation prediction of ground and earth structure, and should be properly considered in a constitutive model of soils.

In order to represent the soils induced anisotropy, the rotational hardening rule, in which the yield surface and/or the plastic potential is rotated by the back stress ratio tensor, namely the center axis of surface, has been used in the ordinary model. In addition, some evolution rule of the back stress ratio has also been proposed, and most it is continuously rotated with the plastic deformation. The monotonic shear behavior of the rotational hardening model is, therefore, different from that of the original model without rotational hardening. Furthermore, the limit surface of hardening indicating the motion space of the back stress ratio is required to satisfy the prescribed failure state. It seems, however, that the physical meaning of the limit surface arbitrarily

given is not clear. In addition, the size of the limit surface is basically a constant determined by a material parameter. Since the (peak) strength of soil is fairly changeable due to the influences of some mechanical factors (e.g. density, cementation, temperature, suction and others), it is natural that the size of the limit surface of hardening is not constant but changes under the influence of some factors as with the strength. It would be, however, quite complicated to change the size of the limit surface of hardening taking every factor into consideration.

A new rotational hardening rule, in which the yield surface is shifted faithfully reflecting on the stress history, is developed in this study. The back stress ratio develops when the stress path deviate from the monotonic loading path, i.e., the stress history occurs, in the proposed method. It would be, therefore, a rational method that the proposed model shows different behavior from the original model without the rotational hardening only when soil has the stress history. By describing not only the development of the stress history but also its dissipation, the proposed method can appropriately describe the failure state without the limit surface of hardening.

The proposed rotational hardening rule is applied to subloading t_{ij} model [1] considering the influence of the relative magnitude of the intermediate stress, thus the proposed rotational and isotropic hardening model describes the influence of the intermediate stress and the stress history simultaneously. In this paper, the outline of the proposed rotational hardening rule and the formulation of the proposed

Table 1 Comparison of stress and strain increment parameters in ordinary stress σ_{ij} and t_{ij} concept

	ordinary concept	t_{ij} concept
transform tensor to modified stress	-	$a_{ij} = \sqrt{I_3/I_2} t_{ij}^{-1}$ ($t_{ik} t_{kj} = \sigma_{ij}$)
unit tensor normal to reference plane	δ_{ij} (Oct. plane)	a_{ij} (SMP)
stress tensor	σ_{ij}	$t_{ij} = a_{ik} \sigma_{kj}$
mean stress	$p = \sigma_{ij} \delta_{ij} / 3$	$t_N = t_{ij} a_{ij}$
deviatoric stress tensor	$s_{ij} = \sigma_{ij} - p \delta_{ij}$	$t'_{ij} = t_{ij} - t_N a_{ij}$
deviatoric stress	$q = \sqrt{(3/2)} s_{ij} s_{ij}$	$t_s = \sqrt{t'_{ij} t'_{ij}}$
stress ratio	$\eta = q/p$	$X = t_s/t_N$
strain increment normal to reference plane	$d\epsilon_v = d\epsilon_{ij} \delta_{ij}$	$d\epsilon_N = d\epsilon_{ij} a_{ij}$
deviatoric strain increment tensor	$de_{ij} = d\epsilon_{ij} - d\epsilon_v \delta_{ij} / 3$	$d\epsilon'_{ij} = d\epsilon_{ij} - d\epsilon_N a_{ij}$
strain increment parallel to reference plane	$d\epsilon_d = \sqrt{(2/3)} de_{ij} de_{ij}$	$d\epsilon_s = \sqrt{d\epsilon'_{ij} d\epsilon'_{ij}}$

model are presented, and the proposed model is verified by comparison with the experimental results of triaxial test and isotropic compression test on medium dense Toyoura sand.

THE MODIFIED STRESS t_{ij} CONCEPT

In most of isotropic hardening models such as Cam clay model [2], their yield functions are formulated using parameters of Cauchy stress tensor σ_{ij} and the flow rule is given in σ_{ij} -space. Such models, however, cannot describe the strength and the deformation of soils under three-dimensional stresses in a uniform manner. Nakai & Mihara proposed a method, in which the yield function is formulated using the parameters of the modified stress t_{ij} ($= a_{ik} \sigma_{kj}$) and the flow rule is assumed in t_{ij} space [3]. This method can suitably consider the influence of the intermediate principal stress by the parameters of stress and strain increments based on the specially mobilized plane: SMP [4] listed in Table 1. Only by replacing the ordinal stress and strain parameters of the ordinary model with the corresponding parameters of t_{ij} concept, the ordinary model can be automatically extended to consider the influence of the relative magnitude of the intermediate stress.

Although the proposed rotational hardening rule and constitutive model are explained and formulated by using the modified stress t_{ij} in this study, it is possible to apply the concept to models based on the Cauchy stress tensor σ_{ij} just by replacing t_{ij} with σ_{ij} .

THE ROTATIONAL AND ISOTROPIC HARDENING MODEL WITHOUT THE LIMIT SURFACE OF HARDENING

Various models adopt different approaches to

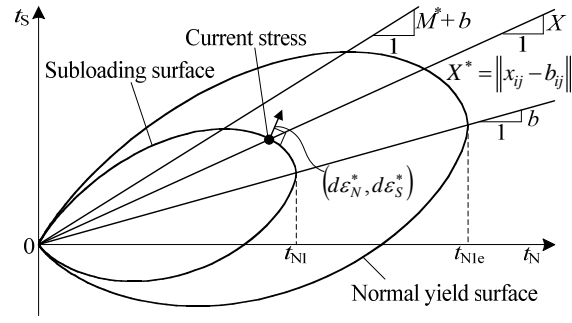


Fig. 1 Yield surface based on the rotational hardening

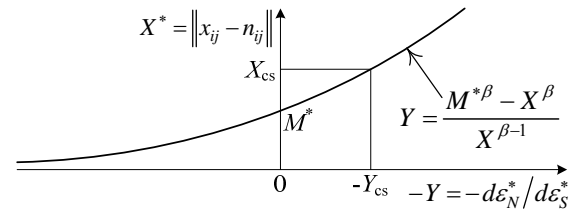


Fig. 2 Relation between stress ratio and dilatancy

describe anisotropic behavior of soils. Among them, Sekiguchi and Ohta model [5], in which the yield surface is oriented around the origin of ordinary stress space for describing the anisotropic behavior of initially K_0 -overconsolidated soil, is a simple extension of the original Cam clay model and has been commonly used in practice. However, this model cannot represent the induced anisotropy, since the oriented yield surface is not mobilizing with any stress change which means that the anisotropy is persistent like the inherent anisotropy in this model. On the other hand, Hashiguchi [6] proposed the rotational hardening and its evolution rule by extending the concept of Sekiguchi and Ohta model. Hashiguchi and Chen [7] developed the rotational and isotropic hardening model with subloading surface [8]. The proposed rotational and isotropic hardening model based on the t_{ij} concept is formulated in the track of those models.

The Rotational and Isotropic Hardening Constitutive Model Based on t_{ij} Concept

In this paper, a rotational hardening model is proposed and it applied to the isotropic hardening model named subloading t_{ij} model which considers not only the influence of the intermediate stress by the modified stress t_{ij} concept, and the influence of density and/or confining pressure by using the concept of subloading surface [8]. Since the details of the original model are explained in another paper [1], the application of the proposed rotational hardening rule is mainly presented here.

The yield function of soil is formulated as a logarithmic function of the mean stress plus an

increasing function of the stress ratio in the original Cam clay model [1]. Similarly, considering an orientation of the yield surface, the yield function of the proposed rotational and isotropic hardening model based on subloading t_{ij} model is presented as

$$f = \ln t_N + \zeta(X^*, M^*) - \ln t_{N1} = 0 \quad (1)$$

$$= \ln \frac{t_N}{t_{N0}} + \frac{1}{\beta} \left(\frac{X^*}{M^*} \right) - \ln \frac{t_{N1e}}{t_{N0}} + \ln \frac{t_{N1e}}{t_{N1}} = 0$$

Schematic yield surface on $t_N - t_s$ plane is shown in Fig. 1. X^* is the modified stress ratio, and given as follows using the back stress ratio tensor b_{ij} .

$$X^* = \sqrt{x_{ij}^* x_{ij}^*} \text{ where } x_{ij}^* = x_{ij} - b_{ij} \quad (2)$$

where β is a material parameter which determines the shape of the yield surface. M^* is a vertex of the nonrotating (original) yield surface, and composed of the principal stress ratio at the critical state in triaxial compression $R_{CS} = (\sigma_1/\sigma_3)_{CS}$. The stress-dilatancy relation is illustrated in Fig.2. t_{N1} and t_{N1e} are the value of t_N at $X^* = 0$ of the subloading surface on which the current stress state always exist, and the normal yield surface. Defining t_{N1e} as the isotropic hardening parameter and t_{N10} is its initial value, the third term in right side of Eq. (1) is linked with the plastic volumetric strain and is given as

$$\ln \frac{t_{N1e}}{t_{N0}} = \frac{1 + e_0}{\lambda - \kappa} \varepsilon_v^p \quad (3)$$

Similarly, the forth term in right side of Eq. (1) is a function of the density parameter ρ , which represents the distance between void ratio on the normally consolidated line and the current void ratio under t_{N1} and is given as

$$\ln \frac{t_{N1e}}{t_{N1}} = \frac{\rho}{\lambda - \kappa} \quad (4)$$

Additionally, the following function is assumed as the evolution rule of the density parameter ρ .

$$d\rho = -\Lambda(1 + e_0) \frac{a\rho^2}{t_N} \quad (5)$$

Finally, Eq. (1) is rewritten as

$$f = \ln \frac{t_N}{t_{N0}} + \frac{1}{\beta} \left(\frac{X^*}{M^*} \right) - \frac{1}{C_p} \left(\varepsilon_v^p - \frac{\rho}{1 + e_0} \right) = 0 \quad (6)$$

Here, C_p indicates $(\lambda - \kappa)/(1 + e_0)$. The plastic strain increment is obtained by assuming the associated flow rule in t_{ij} -space as

$$d\varepsilon_{ij}^p = \Lambda \frac{\partial f(t_{ij}, b_{ij})}{\partial t_{ij}} \quad (7)$$

The Evolution Rule of the Back Stress Ratio b_{ij}

The evolution rule of the back stress ratio tensor is b_{ij} determined reflecting on the following experimental evidences. (a) Soil shows complicated anisotropic behavior due to the stress history only when non-monotonic loading is applied, (b) The

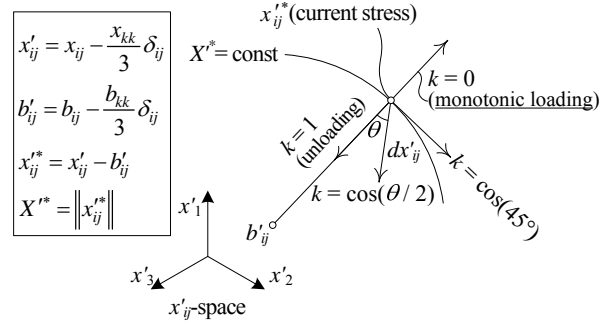


Fig. 3 Judgment of loading condition by stress ratio tensor and its increment in x'_{ij} space

strength and deformation characteristics of soils are independent of the stress histories at the failure state even if soils had the complex stress path histories [9]. The essentials of the evolution rule of b_{ij} are summarized as follows.

- b_{ij} is equal to zero during monotonic loading paths, and the stress history develops ($db_{ij} \neq 0$) when stress path deviate from monotonic loading path (non-monotonic loading path).
- The stress history: b_{ij} develops in the direction of the current stress state: $x_{ij}^* (= x_{ij} - b_{ij})$ with change in stress ratio: dx_{ij} .
- The stress history decays with progress of the plastic deformation ($b_{ij} \rightarrow 0$ with $d\varepsilon_{ij}^p$), and completely disappears at failure state even undergoing complex loading history ($b_{ij} = 0$ at failure state).

An evolution rule of b_{ij} which satisfies all of the above conditions is given as

$$db_{ij} = kx_{ij}^* - lb_{ij} \quad (8)$$

$$= -\xi \left(\cos \frac{\theta}{2} \right) \left(n_{ij}^* dx_{kl} \right) n_{ij}^* - \mu \| d\varepsilon_{kl}^p \| b_{ij} \left(n_{ij}^* = \frac{x_{ij}^*}{\|x_{ij}^*\|} \right)$$

First term of right side in Eq. (8) represents the development of the stress history, and is composed of the direction: n_{ij}^* , the magnitude of development: $\xi n_{kl}^* dx_{kl}$ (ξ is a newly added material parameter), and the loading judgment, namely, monotonic loading ($\cos(\theta/2) = 0$), non-monotonic loading ($0 < \cos(\theta/2) < 1$), and unloading ($\cos(\theta/2) = 1$). θ is given as follows and a schematic view of the loading judgment is shown in Fig. 3.

$$\theta = \cos^{-1} \left\{ \frac{(b'_{ij} - x'_{ij}^*) \cdot dx'_{ij}}{\|b'_{ij} - x'_{ij}^*\| \cdot \|dx'_{ij}\|} \right\} \quad (9)$$

Note that new parameter x'_{ij} and its space are used here to consider every stress state on the same reference plane, since the reference plane of t_{ij} concept whose normal is a_{ij} changes continuously with stress state.

Conversely, second term of right side in Eq. (8)

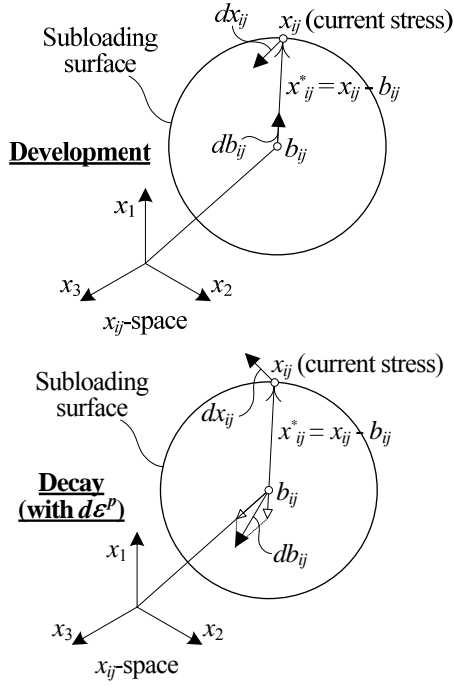


Fig. 4 Evolutions of the back stress ratio when the influence of the stress history develops and decays

indicates the decay of the stress history, which is represented as b_{ij} going to zero with the plastic deformation. l is proportional to the magnitude of the plastic strain increment, while μ is also a newly added material parameter controlling the rate of the decay of the influence of stress history. Figure 4 illustrates the evolution of the back stress ratio when the stress history develops and decays respectively.

Stress and Strain Relation

The proportionality constant Λ representing the magnitude of the plastic strain increment in Eq. (7) is obtained by solving Prager's consistency equation ($df = 0$).

$$\Lambda = \left\langle \frac{\left\{ \frac{\partial f}{\partial \sigma_{ij}} - \xi \left(\cos \frac{\theta}{2} \right) \frac{\partial f}{\partial b_{mn}} n_{mn}^* \left(n_{kl}^* \frac{\partial x_{kl}}{\partial \sigma_{ij}} \right) \right\} d\sigma_{ij}}{\frac{1}{C_p} \left(\frac{\partial f}{\partial t_{kk}} + \frac{a\rho^2}{t_N} \right) + \mu \frac{\partial f}{\partial b_{ij}} b_{ij} \left\| \frac{\partial f}{\partial t_{kl}} \right\|} \right\rangle \quad (10)$$

The elastic strain follows the generalized Hooke's law as

$$d\varepsilon_{ij}^e = \frac{1+\nu_e}{E_e} d\sigma_{ij} - \frac{\nu_e}{E_e} d\sigma_{kk} \delta_{ij} \quad (11)$$

Young's modulus E_e is expressed in terms of the swelling index κ and Poisson's ratio ν_e as

$$E_e = \frac{3(1-2\nu_e)(1+e_0)p}{\kappa} \quad (12)$$

Although the influence of stress path on the plastic flow is also considered in the proposed model

Table 2 Constitutive parameters for Toyoura sand

λ	0.0700	
κ	0.0045	
e_{NC} at $p=98$ kPa & $q=0$ kPa	1.1	Same parameters as Cam clay model
$R_{cs} = (\sigma_1/\sigma_3)_{cs(comp)}$	3.2	
ν_e	0.2	
β	2.0	Shape of yield surface (same as original Cam clay if $\beta=1$)
a	$\frac{a_{AF}}{a_{IC}}$	Influence of density and confining pressure
ξ	2.0	Development of stress history
μ	100.0	Dissipation of stress history

in the same manner as the original model, the details are handed over to reference [1].

RESULT AND DISCUSSION

In this section, the feature of the proposed rotational and isotropic hardening model describing the influence of the intermediate principal stress and the stress history simultaneously is verified by the comparison of the calculated results with the experimental results of triaxial tests and isotropic compression test with non-monotonic loading path on medium dense Toyoura sand ($e_{max} = 0.95$, $e_{min} = 0.58$, $G_s = 2.65$, $D_r = 72\%$). The material parameters of the proposed model are listed in Table 2. ξ and μ are newly added to the material parameters of original model for controlling the development and decay rate of the stress history respectively. Other parameter values are the same as those of the original subloading t_{ij} model for Toyoura sand. These parameters can be determined from isotropic compression and triaxial compression test.

Triaxial Tests – Reverse Loading and Reloading

Figure 5 presents the non-monotonic loading paths of triaxial test, namely, reverse loading (ABCD) and reloading (ABCE). Fig. 6, 7 and 8 show the observed results, the computed results by the original isotropic hardening model, and those by the proposed rotational and isotropic hardening model, respectively. The monotonic shear behavior is also indicated in each figure for comparison. Diagram (a) and (b) indicate the relation between axial strain and stress ratio, and the relation between stress ratio and volumetric strain, respectively.

It can be observed from these figures that, during triaxial compression test (path A→B), the results of the proposed model coincide with those of the original model, and both agree well with the experimental result though the volumetric contraction is slightly overestimated. During unloading (B→C) and subsequent reverse loading

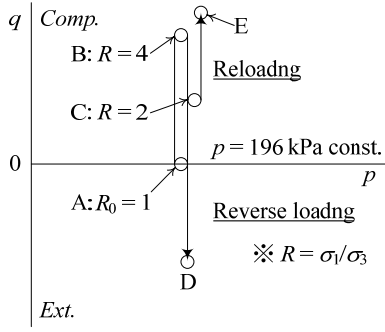
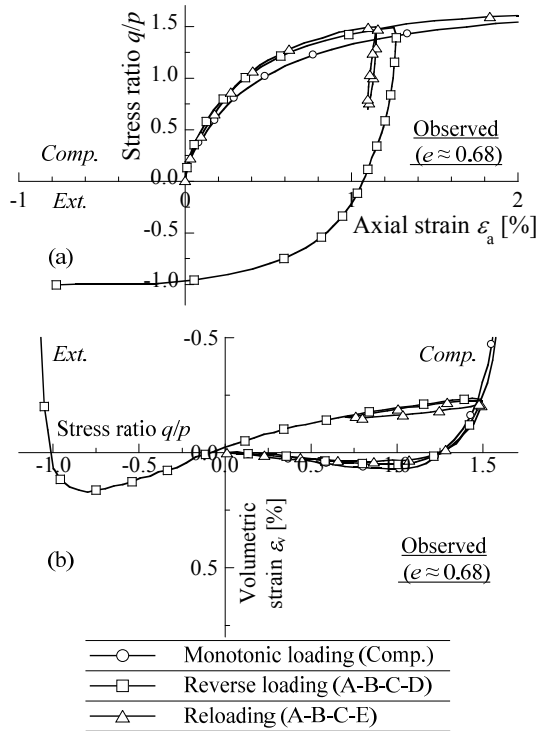


Fig. 5 Stress paths of reverse loading and reloading



(C→D), the proposed model is capable of suitably describing both the reduction of the shear stiffness and the dilatancy before isotropic stress state as can be seen in the observed results, i.e. the Bauschinger effect, while the original isotropic hardening model exhibits only elastic deformation. An overestimated volume contraction by the proposed model in reverse loading is, additionally, assumed to not be due to the rotational hardening, since the computed results evaluate more compressible behavior than the observed ones even in monotonic loading path. On the other hand, during reloading path (C→E), the proposed model represents the increasing of stiffness in the direction of past shear history as well as the observed results. It is finally worth observing that, in the simulation by the proposed model, the gradual dissolution of the influence of the stress history along with the plastic deformation is well described. Therefore, the shear strength reaches its appropriate

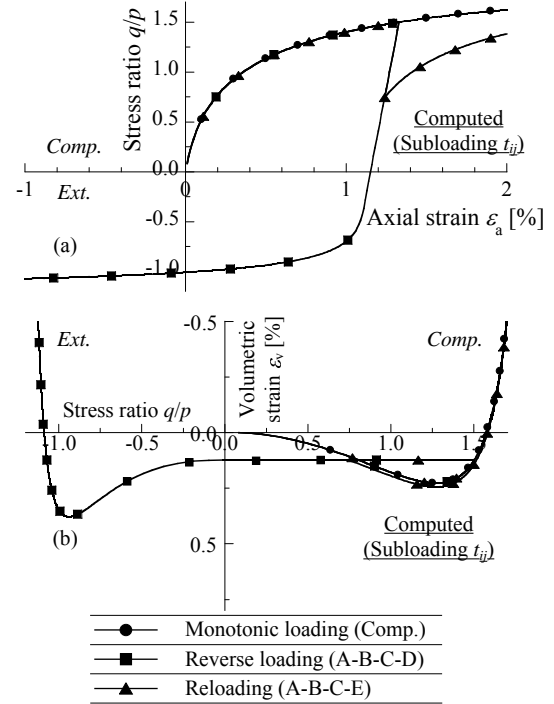
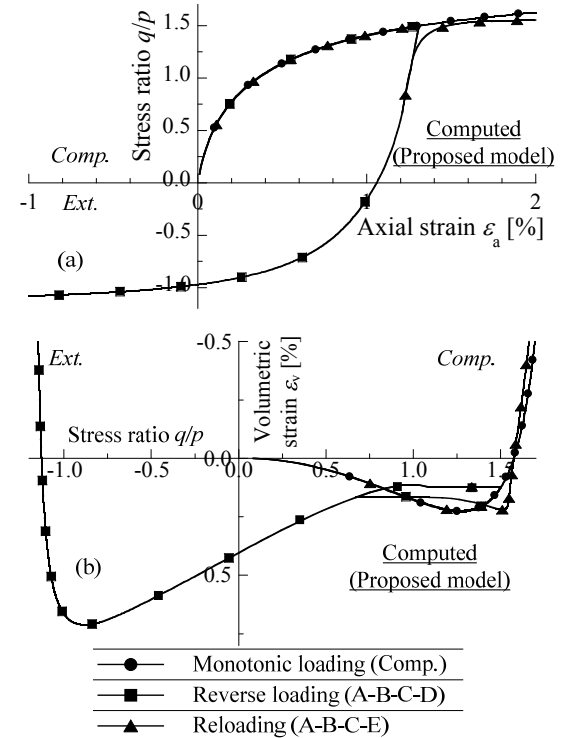

 Fig. 7 Computed results by the isotropic hardening model (subloading t_{ij} model)


Fig. 8 Computed results by the proposed rotational and isotropic hardening model

final value without the limit surface of hardening, and the orientated yield surface coincides with the yield surface of the original isotropic hardening model, i.e., $b_{ij} = 0$ at failure state. Naturally, the proposed model considers the final state depending on the relative magnitude of the intermediate stress.

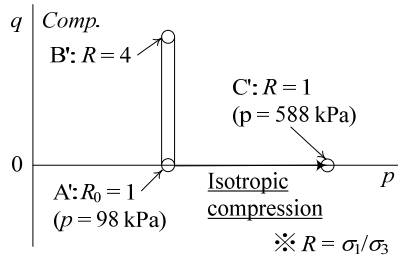


Fig. 9 Stress path of isotropic compression with shear history

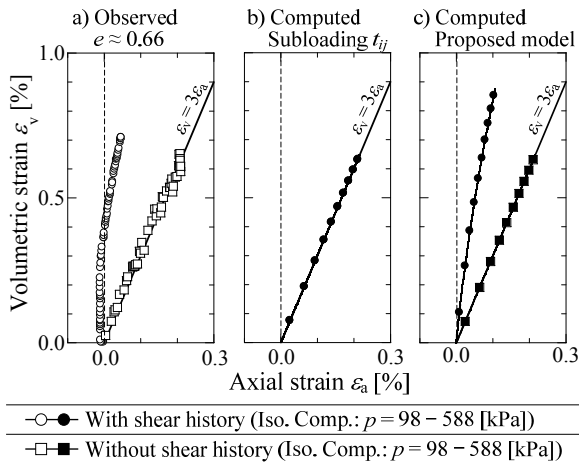


Fig. 10 Results of isotropic compression test with shear history

Triaxial Test – Isotropic Consolidation Test with Shear History

Figure 9 illustrates the stress path of isotropic compression test with shear history, and Figure 10 shows its observed and computed results, which are organized as the relation between axial and volumetric strain during isotropic compression path (A→C'). It can be seen from observed result that soil deforms anisotropically even under isotropic compression, once it experienced shear history. However, from the gradient $d\epsilon_v/d\epsilon_a$ gradually decreasing with increasing of means stress, it can be assumed that the influence of the stress history also ceases with progress of the plastic deformation under isotropic condition. Although the computed result by the proposed model slightly underestimates the influence of the stress history, it fairly describes such development and decay of the influence of the stress history.

CONCLUSION

A new rotational hardening rule describing the evolution rule of the back stress ratio was proposed in this paper. Unlike the ordinary rotational hardening rule, the back stress ratio develops when the stress state deviates from monotonic loading path

in the proposed one. In addition, by considering the decay of the influence of the stress history with progress of the plastic deformation, the failure state could be described without the limit surface of hardening.

The proposed rotational hardening rule is applicable to most constitutive models, and the isotropic hardening model named subloading t_{ij} model was extended to describe induced anisotropy of soil. It was indicated from a comparison with the experimental results that the proposed model well describes a complicated anisotropic behavior by controlling the development and decay of the influence of stress history.

ACKNOWLEDGEMENT

We would like to thank Mr. Anteneh Biru Tsegaye, PhD candidate at Norwegian University of Science and Technology, for valuable discussion and reading the manuscript.

REFERENCES

- [1] Nakai T. and Hinokio M, "A simple elastoplastic model for normally and over consolidated soils with unified material parameters", Soils and Foundation, Vol. 44, No. 2, 2004, pp. 53-70.
- [2] Schofield A. N. and Wroth C. P., "Critical State Soil Mechanics". McGraw Hill, London, 1968.
- [3] Nakai T. and Mihara Y, "A new mechanical quantity for soils and its application to elastoplastic constitutive models", Soils and Foundations, Vol. 24, No. 2, 1984, pp. 82-94.
- [4] Matsuoka H. and Nakai T, "Stress-deformation and strength characteristic of soil under three different principal stresses", Proc. JSCE, 232, 1974, pp.59-70.
- [5] Sekiguchi H and Ohta H, "Induced anisotropy and time dependency in clays", Proc. 9th ICSMFE, 1977, pp. 229-238.
- [6] Hashiguchi K, "An expression of anisotropy in a plastic constitutive equation of soils", Proc. 9th ICSMFE, 1977, pp. 302-305.
- [7] Hashiguchi K and Chen X. P., "Elasticplastic constitutive equation of soils with the subloading surface and the rotational hardening", Int. J. for Numerical and Analytical Methods in Geomechanics, Vol. 22, 1998, pp. 197-227.
- [8] Hashiguchi K, "Subloading surface model in unconventional plasticity", International Journal of Solids Structure, Vol. 25, 1989, pp. 917-945.
- [9] Nakai T et.al., "Formulation of the influence of the density and the stress path dependency of plastic flow in sand", Proc. of Powders and Grains, 2001, pp. 217-221.

A STUDY OF THE FORMATION MECHANISM OF BEACHROCK IN OKINAWA, JAPAN: TOWARD MAKING ARTIFICIAL ROCK

Takashi Danjo¹ and Satoru Kawasaki²

¹ Graduate School of Engineering, Hokkaido University, Japan; ² Faculty of Engineering, Hokkaido University, Japan

ABSTRACT

Beachrock is coastal sediment that has been cemented mainly by calcium carbonate within the intertidal zone in tropical and subtropical regions. Man-made beachrock has the potential to inhibit coastal erosion. Considering this important application, we performed field investigations and laboratory tests to understand the formation mechanism of beachrock in Nago, Okinawa, Japan. We performed a needle penetration test, microbial population count and urease activity test, and conducted elemental and mineral analyses of the beachrock and sand. Some microorganisms at the site showed urease activity and the beachrock cement comprised high Mg calcite (HMC). Our investigation showed that evaporation of seawater and/or urease activity of bacteria may have resulted in precipitation of HMC, leading to formation of the beachrock, with partial solidification of some sandy specimens.

Keywords: Beachrock, Formation Mechanism, Cement, Microorganism, Urease Activity

1. INTRODUCTION

On the world's coasts, erosion is a significant problem. To preserve coastlines, various countermeasures are used to combat coastal erosion. These include construction of artificial reefs, headlands, detached breakwaters and hard shore protection, all of which control the amount of drift sand and/or beach nourishment and sand bypassing, thus overcoming shortages of drift sand. However, these solutions are expensive, and require long time periods for implementation, as well as the engineering of large amounts of materials, especially for heavyweight sand coasts [1], [2].

We consider here a new method to protect coastlines – the use of artificial rock that auto-repairs by means of sunlight, seawater, and bacteria. Our model of artificial rock is beachrock. Beachrock is a type of sedimentary deposit that generally occurs on tropical and subtropical beaches as a result of intertidal lithification of loose beach sands and gravels by carbonate cementation [3]. Beachrocks around the world have been reported to form over several thousand years [4] owing to interactions among sand supply, cement precipitation from seawater and coastal erosion by ocean waves. Therefore, it may be possible to slow the erosion of coasts by making man-made beachrock from coastal sands. Because this artificial rock is made of local materials, it has the potential to be an eco-friendly product.

In this study, we examined the formation mechanism of beachrock in Okinawa, Japan, because understanding this mechanism is an

important step in making artificial beachrock. As part of this analysis, we performed a needle penetration test, determined the viable bacterial count, conducted a urease activity test and performed elemental and mineral analyses of the beachrocks and sand. Our focus is on the cement formation mechanism of beachrock, which occurs in the intertidal zone. Cement type and content have the potential to influence the strength of the material; hence, detailed knowledge of beachrock cements is valuable for producing a man-made equivalent. In addition, we conducted laboratory solidification experiments using local bacteria.

2. STUDY SITE AND METHODS

2.1 Study Site

The geology of Sumuide, Nago, Okinawa, Japan (Fig. 1) comprises limestone and calcarenite of the Quaternary Ryukyu Group [5]. The location is 26° 40' 74" N and from 126° 00' 73" to 126° 00' 74" E.

2.2 Needle Penetration Test

At the site, needle penetration inclination (N_P) values of some beachrock samples were measured five closely spaced points at each location by using a needle penetration device (SH-70, Maruto Testing Machine Company, Tokyo, Japan). Samples measured exposed beachrock at the shoreline (two test sections) and buried beachrock underneath the coastal sand (one test section). Unconfined compressive strength, q_u , was estimated from N_P by

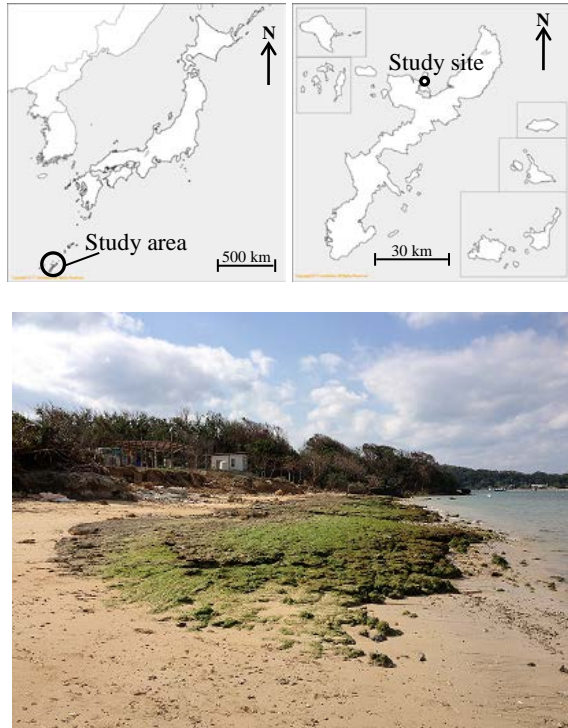


Fig. 1 Maps showing study site and view of exposed beachrock.

the correlation chart of N_p and q_u described in the instruction manual.

2.3 Microbial Population Count

Seawater, some beachrock samples, and sand at both sites were sampled in sterile test tubes and refrigerated at 4 °C in our laboratory. Subsequently, 1.0 g of each sample was mixed with 9 mL of artificial seawater or saline solution, and 10 μ L of the supernatant was added to ZoBell2216E medium (for marine bacteria) or polypeptone-yeast extract medium [6] (for viable bacteria). After inoculation, the media were incubated at 25 °C for 7 days. Subsequently, each population (colony count) was counted by the plating method.

2.4 Urease Activity Test

We isolated colonies from the sand adjacent to the beachrocks using ZoBell2216E medium. Each colony was mixed with 20 mL of solution (25 g/L $\text{CO}(\text{NH}_2)_2$ and 20 mL/L cresol red solution with distilled water) in a 20 mL bottle. Under sealed conditions, the samples were left standing at 45 °C for 2 hours. To determine whether the colonies have urease activity, we observed the solution color after 2 hours. For cresol red, a change from yellow to purple can be observed from pH 7.2 to pH 8.8. Those samples that changed to purple were measured for their pH values. For comparison, a non-bacterial sample also was measured.

2.5 Elemental Analysis and SEM Observations

Samples of exposed beachrock, buried beachrock, and adjacent sand were analyzed by X-ray fluorescence analysis (XRF). The surfaces of the samples were observed microscopically and elemental measurements were made using scanning electron microscopy (SEM) (SuperScan SS-550, Shimadzu Corporation, Kyoto, Japan) and energy-dispersive X-ray spectroscopy (EDX) (SEDX-500, Shimadzu Corporation).

2.6 Mineralogical Analysis

The same samples used for XRF and EDX analyses were further subjected to mineralogical study using X-ray diffraction (XRD) (MultiFlex 2kW, Rigaku Corporation, Tokyo, Japan) with Cu-K α radiation, with 2θ between 5 and 70°.

3. RESULTS

3.1 Needle Penetration Test

The q_u values of exposed beachrocks were larger than those of buried beachrock (Table 1). This result is similar to that of Voudoukas et al. [4]. Furthermore, to the best of our knowledge, this study is the first to report q_u of buried beachrock. Only three previous studies from Japan and Scotland [7]–[9] have addressed the mechanical properties of exposed beachrocks.

Table 1 Unconfined compressive strength, q_u of the beachrocks estimated by the needle penetration test, and microbial population counts.

Test Section	Needle Penetration test		Microbial population count	
	N_p N/mm	q_u MPa	Marine $\times 10^4$ CFU/ mL	Viable $\times 10^4$ CFU/ mL
Seawater	-	-	1.3	0
Exposed Beachrock 1	80 \pm 22	28 \pm 6.9	410	45
Exposed Beachrock 2	51 \pm 12	19 \pm 4.7	1500	8.15
Buried Beachrock	8.9 \pm 5.4	3.4 \pm 2.2	460	13.6
Sand	-	-	500	5.4

3.2 Microbial Population Count

For each sample, marine microbial populations showed viable values (Table 1). Bacterial morphologies and colors differed on ZoBell2216E medium and polypeptone-yeast extract medium (e.g. Fig. 2). The populations in the beachrock samples tended to be smaller than bacterial populations reported from soil (10^6 to 10^{14} g⁻¹) [10], but larger than in the seawater, despite the fact that the beachrock is washed by seawater every day. Therefore, this result suggests that the microbiological properties of the beach at this site affect beachrock formation.

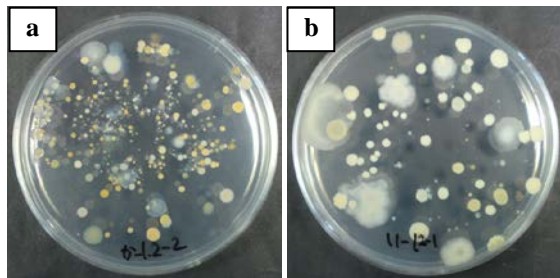


Fig. 2 Microorganisms in exposed beachrock 1 on (a) ZoBell2216E medium and (b) polypeptone-yeast extract medium.

3.3 Urease Activity Test

About 156 colonies were isolated from the soil near beachrocks. Of these, five colonies changed the solution color to purple after 2 hours at 45 °C, indicating urease activity. Moreover, the pH range of the five samples was 9.0–9.3. In comparison, the pH value of the non-bacterial sample was 7.1.

3.4 Elemental Analyses and SEM Observation

Results of XRF analysis of the samples are shown in Figure 3. All samples were composed mainly of CaO, and beachrock samples contained more MgO than adjacent sand. By contrast, the sand contained more SiO₂.

Subsequently, to identify the beachrock cement, we analyzed sample surfaces by performing SEM-EDX. Figure 4 shows that, only in association with the beachrocks, the microparticulates covered with sand particles and the morphologies (Fig. 4 (b) and (d)) were similar to that of high Mg calcite, HMC [11]. HMC is a polymorph of CaCO₃, containing more than 4 mol% MgCO₃, or 1.2 wt%. Moreover, the MgCO₃ found in the microparticulates was calculated to be 16–18 wt% (>1.2 wt%) based on the Mg percentage about P1–P6 in Figure 5. Therefore, we can conclude that the cement of beachrock at site O is HMC.

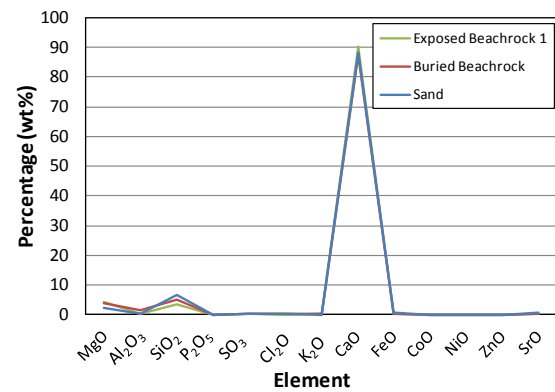


Fig. 3 Elemental percentage of site O samples by using XRF.

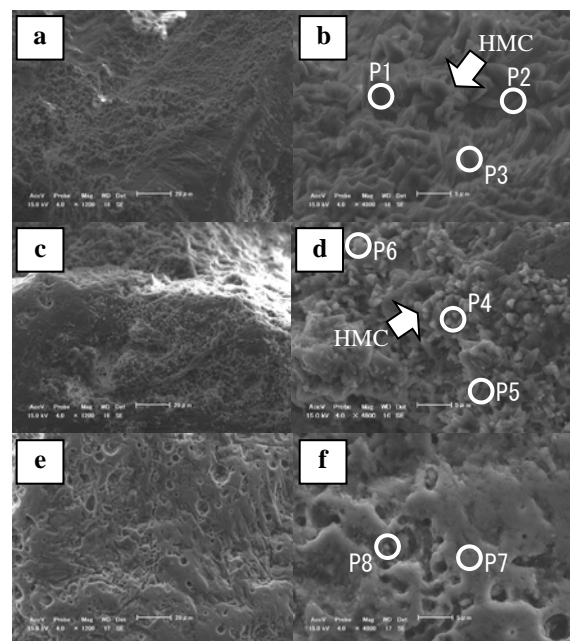


Fig. 4 SEM images of the samples. (a), (b): exposed beachrock 1 ($\times 1200$, $\times 4800$), (c), (d): buried beachrock ($\times 1200$, $\times 4800$), (e), (f): sand in site O ($\times 1200$, $\times 4800$).

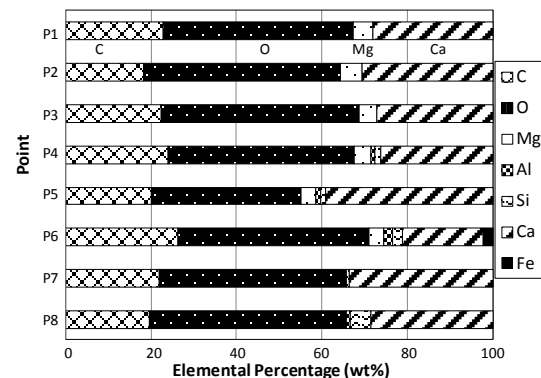


Fig. 5 Elemental percentage from P1 to P8 of Fig. 4 using EDX.

3.5 Mineralogical Analysis

The samples contained the following minerals: Mg calcite (MC), aragonite, and quartz (Fig. 6). MC can be divided into HMC and low Mg calcite (LMC). LMC contains less than 4 mol% MgCO_3 [4]. The highest peaks (around 30°) of the samples were closer to the peak of HMC than that of LMC, about 2θ value [12].

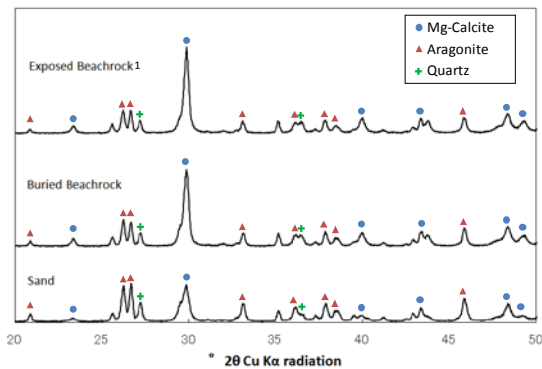


Fig. 6 XRD patterns of (a) exposed beachrock 1, (b) buried beachrock and (c) sand.

4. DISCUSSION

4.1 Formation Mechanism of the Beachrock

Beachrocks cemented by HMC have been reported at 16 sites [4], [13] around the world, and their formation mechanisms are shown in Figure 7.

We focused further investigations of the beachrock cements on the influence of precipitation from seawater and/or seawater evaporation (PSW), and on surface microorganisms, which we considered as one biological process (BIOL). This is because (1) PSW is the factor most reported to be related to the formation mechanism of beachrock cemented by HMC (Fig. 7) and (2) microbiological

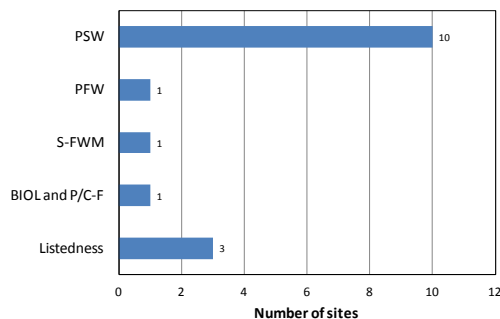


Fig. 7 Formation mechanisms of beachrocks that contain HMC cements. [4], [13] (PSW, Precipitation from seawater/seawater evaporation; PFW, precipitation from fresh water; S-FWM, Sea – fresh water mixing; BIOL, biological processes; P/C-F, Physico/chemical factors)

properties may affect beachrock formation at this study site based on the above microbial population count. Other effects on beachrock formation are outside the scope of this study and require further consideration in the future.

First, with respect to PSW, Raz et al. [14] reported that to better understand the depositional process of high-magnesian calcitic skeletons, they studied the CaCO_3 precipitates formed from solutions with Mg/Ca ratios ≥ 4 . We conducted water analyses at the study site by performing ion chromatography (ICS-1000, Dionex Corporation, Osaka, Japan) (Table 2). The molar ratio Mg/Ca of the seawater was approximately 6.3; this ratio satisfies the conditions under which HMC could precipitate. In addition, according to experiments by Kitano et al. [15], sodium citrate and sodium malate favor the precipitation of MC, whereby an increase in concentration of magnesium ion and these organic materials cause formation of Mg-rich calcite. The present study site is rich in organic matter, such as sea algae, shells, corals, and bacteria, which may be sources of citrate and malate.

Table 2 Chemical composition of seawater at the study site.

Na^+ (ppm)	Mg^{2+} (ppm)	K^+ (ppm)	Ca^{2+} (ppm)	pH	EC (mS/cm)
11000	1330	486	348	7.9	51

A second factor—the microbiological effect—was indicated by the microbial population count and urease activity test. We found five colonies of bacteria exhibiting urease activity in the sand near the beachrock. The bacteria stimulate the hydrolysis of urea, $\text{CO}(\text{NH}_2)_2$. This reaction leads to an increase in pH and precipitation of CaCO_3 , as shown Eq. (1) and (2) [16]. At this site, there are abundant organisms, and the mammalia, amphibia and chondrichthyes void urea.

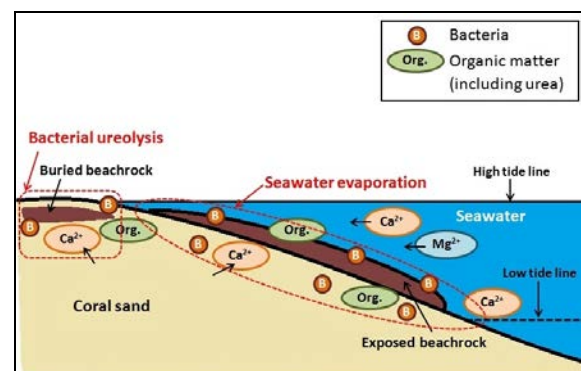
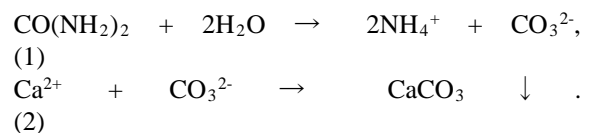


Fig. 8 Proposed formation mechanism of beachrock at the study site.

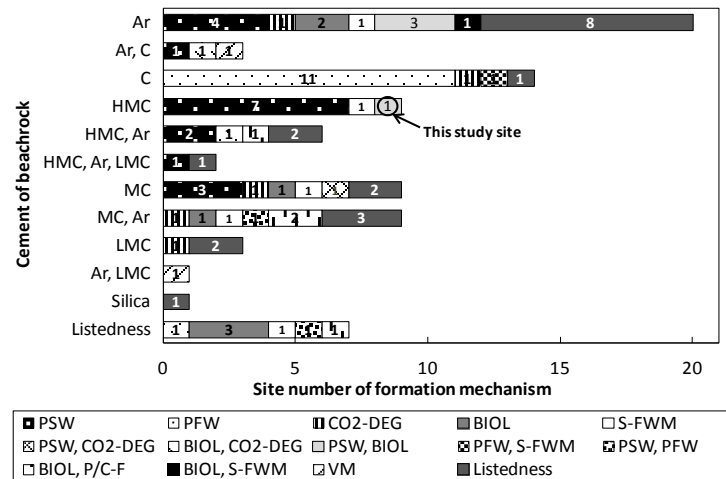


Fig. 9 Cements and formation mechanisms of beachrocks in the world including the study site. [4], [17] (Cement type: Ar, Aragonite; C, Calcite; HMC, High Mg calcite; LMC, Low Mg calcite; MC, Mg calcite; Al, Element of Al; Si, Element of Si. Formation process: CO₂-DEG, CO₂ – degassing; VM, Various mechanisms.)

Moreover, MgCO_3 is expected to precipitate with CaCO_3 . To the best of our knowledge, this is the first time that bacteria exhibiting urease activity have been recorded near beachrock.

Therefore, our investigation into the formation mechanisms of beachrock at this study site (Fig. 8) has shown that the evaporation of seawater and/or the urease activity of microorganisms might have resulted in the precipitation of HMC, leading to formation of beachrock.

Furthermore, we considered the relationship of cements and formation mechanisms of beachrocks around the world, including the present study site (Fig. 9). We found six processes to be reported: PSW; precipitation from fresh water (PFW); CO₂-degassing; BIOL; sea-fresh water mixing; physico/chemical factors; and various other mechanisms. Some beachrock sites have developed from more than one mechanism. Moreover, the beachrock examples cemented by calcite tend to have been formed by PFW. In contrast, aragonite and MC tend to have been precipitated from seawater, as beachrock cements. In addition, the beachrocks formed by BIOLs are cemented by HMC, MC and/or Ar (Fig. 9).

4.2 Ground Solidification using the Bacteria

We discuss here the tendency for solidification of sand using microorganisms from the study site.

Recently, several investigations of microbial ground improvement technologies have been reported globally. The major cementation method is to stimulate calcium carbonate to precipitate by the ureolytic reaction of *Sporosarcina pasteurii*, a well-known urease positive bacterium [16], [18], [19]. The solidification technique using local bacteria is

novel and expandable.

Based on the method of Inagaki et al. [18], we conducted a solidification test using a local microorganism that raised the pH value to the highest with respect to the above urease activity test. The microorganism was estimated as *Paracoccus sp.* by the analysis of a partial base sequence of 16S rDNA using the Apollon DB-BA 8.0 database. First, the bacterium was shaken in the ZoBell 2216E culture solution for 3 days at 30 °C. Second, coral sand dried at 110 °C for more than 2 days was added into a 15 mL syringe (inner diameter 15 mm). Third, the culture medium solution and 0.3 equimolar urea and calcium chloride solution were sequentially injected into the syringe and drained up to 1 mL above the top surface of the sand. The specimens were kept in wet conditions throughout. Thereafter, in the same manner, the urea and calcium chloride solution was injected and drained once a day and the syringe test was conducted at 30 °C.

Results indicate that the upper, side portions, and bottom areas of the specimens were solidified after 2 weeks (Fig. 10). The q_u values were estimated, by the needle penetration test, up to 2 MPa. This maximum strength was obtained from an upper



Fig. 10 Solidified parts of sediments using a

bacterium obtained from near the Okinawa beachrocks.

solidified part that was ≤ 10 mm thick and 54 mm high). To the best of our knowledge, this is the highest q_u measured by all reported solidification methods using local bacteria.

Hereafter, by finding optimal compositions of the solutions and curing temperatures, we plan to make higher mechanical strength materials and larger specimens to create artificial beachrock.

5. CONCLUSIONS

We performed needle penetration tests, viable bacterial count and urease activity tests, as well as conducted elemental and mineral analyses of beachrock and sand to investigate the formation of beachrock at Okinawa in Japan. These results revealed a probable formation mechanism.

In particular, evaporation of seawater and/or urease activity of microorganisms may have resulted in precipitation of HMC, leading to formation of beachrock. In addition, the microorganisms partly solidified coral sand specimens.

For future studies, we plan to conduct solidification tests with bacteria and an evaporation test with seawater to create artificial beachrock on a large scale.

ACKNOWLEDGEMENTS

This research was supported by JSPS Grants-in-Aid (21300326 and 24·1036). We are grateful to Suguru Shimazaki and Nao Aoki of Hokkaido University for conducting the urease activity test.

REFERENCES

- [1] Pranzini E, Williams A, Coastal and Erosion and Protection in Europe. New York: Routledge, 2013.
- [2] Torii K, "Recent Trend of the Beach Erosion Control", Suikougaku ni kansuru kaki kensyukai kougisyu, JSCE, 2002 (in Japanese).
- [3] Ginsburg RN, "Beachrock in South Florida", J. Sediment. Petrol, Vol. 23, 1953, pp. 85-92.
- [4] Voudoukas MI, Velegakis AF, Plomaritis TA, "Beachrock occurrence, characteristics, formation mechanisms and impacts", Earth-Science Reviews, Vol. 85, 2007, pp. 23-46.
- [5] Kamiya K, "Geography and Geology of Yagaji Island" Okinawa Prefectural Museum, Vol. 27, 2001, pp. 15-28 (in Japanese).
- [6] Oshima T, Imahori K, "Description of *Thermus thermophilus* (Yoshida and Oshima) comb. nov., a Nonsporulating Thermophilic Bacterium from a Japanese Thermal Spa.", Int. J. Syst. Bacteriol, Vol. 24, 1974, pp. 102-112.
- [7] Danjo T, Kawasaki S, "Physical and Mechanical Properties of Beachrocks in Okinawa Island", Journal of JSEG. Vol. 53, 2012, pp. 191-200 (in Japanese with English abstract).
- [8] Ogasawara H, Yoshitomi K, Jijyu K, "Beachrock in Sosogi coast, Wajima, Japan", In Proceedings of the JSEG Tyugoku-shikoku Meeting, 2004, pp. 31-34 (in Japanese).
- [9] Selby MJ, "Hillslope Materials and Processes", Oxford University Press, Vol. 2, 1993.
- [10] Pandey S, Singh DK, "Total bacterial and fungal population after chlorpyrifos and quinalphos treatments in groundnut (*Arachis hypogaea* L.) soil", Chemosphere, Vol. 55, 2004, pp. 197-205.
- [11] Erginal AE, Kiyak NG, Bozcu GM, Ertek A, Gungunes H, Sungur A, Turker G, "On the Origin and Age of the Ariburnu Beachrock, Gelibolu Peninsula, Turkey", Turkish J. Earth Sci., Vol.17, 2008, pp. 803-819.
- [12] Henderson GM, Slowey NC, Fleisher MQ, "U-Th dating of carbonate platform and slope sediments", Geochimica et Cosmochimica Acta, Vol. 65, 2001, pp. 2757-2770.
- [13] Erginal AE, Kiyak NG, Ozturk B, "Investigation of Beachrock Using Microanalyses and OSL Dating: A Case Study from Bozcaada Island, Turkey", Journal of Coastal research, Vol. 26, 2010, pp. 350-358.
- [14] Raz S, Weiner S, Addadi L, "Formation of High-Magnesian Calcites via an Amorphous Precursor Phase: Possible Biological Implications", Adv. Mater, Vol. 12, 2000, pp. 38-42.
- [15] Kitano Y, Kanamori N, "Synthesis of magnesian calcite at low temperatures and pressures", Geochemical Journal, Vol. 1, 1966, pp. 1-13.
- [16] Whiffin VS, Van Paassen LA, Harkes MP, "Microbial carbonate precipitation as a soil improvement technique", Geomicrobiology Journal, Vol. 24, 2007, pp. 1-7.
- [17] Kneale D, Viles HA, "Beach cement: incipient CaCO_3 -cemented beachrock development in the upper intertidal zone, North Uist, Scotland", Sedimentary Geology. Vol. 132, 2000, pp. 165-170.
- [18] Inagaki Y, Tsukamoto M, Mori H, Nakajima S, Sasaki T, Kawasaki S, "A centrifugal model test of microbial carbonate precipitation as liquefaction countermeasure", Japanese Geotechnical Journal, Vol. 6, 2011, pp. 157-167 (in Japanese with English abstract).
- [19] Van Paassen LA, Daza CD, Staal M, Sorokin DY, Van Der Zon W, Van Loosdrecht CM, "Potential soil reinforcement by biological denitrification", Ecological Engineering, Vol. 36, 2010, pp. 168-175.

A STUDY ON THE SLAKING-INDUCED CREEP DEFORMATION CHARACTERISTICS OF CRUSHED MUDSTONE

Sharma Keshab¹, Kiyota Takashi² and Kyokawa Hiroyuki³

¹Former student, University of Tokyo, Japan; ²University of Tokyo, Japan; ³University of Tokyo, Japan

ABSTRACT

In order to study the slaking induced creep deformation characteristics of crushed mudstone, a series of direct shear tests were conducted on the crushed mudstone under different stress ratio by using a modified direct shear apparatus. Similar tests were also performed on the crushed sand stone, silica sand and glass beads to compare the creep deformation characteristics with crushed mudstone. In each cyclic wetting and drying test, three cycles of drying and wetting were carried out under constant shear load. Creep shear deformation in the first wetting becomes larger as increase in the stress ratio, while it decreases with the progress of cyclic wetting and drying, almost zero in third wetting. During the drying process, initially, no appreciable creep deformation is found to occur at higher water content. When the water content of specimen has reached a certain value, creep deformations occur progressively with water loss. These tests show that the creep deformation during the drying is more significant than during the wetting with the progress of wetting and drying cycles. On the other hand, the influence of cyclic wetting and drying on crushed sand stone, silica sand and glass beads is almost negligible.

Keywords: Slaking, Mudstone, Creep, Deformation, Wetting and Drying

INTRODUCTION

Mudstone tends to slake and has given rise to numerous stability and settlement problems around the world. For example, the landslide dam formed by the 2005 Kashmir earthquake was breached in 2010 during moderate rainfall. It is assumed that the dam was breached due to the slaking of mudstones [1]. Mudstones can also accelerate soil creep and are physical processes that have been recognized as causal factors of landslide development on slopes [2], [3]. In addition, when high embankment made of these materials is considered, long term stability and settlement problems may possibly arise from the occurrence of slaking of geo-materials due to repeated wetting and drying cycles [4], [5].

This deformation behavior becomes more complicated when mudstone is exposed to cyclic wetting and drying [6]. Structures, pavements, concrete slab and other engineering structures can experience significant damage from this slaking induced shrinkage and swelling process if not designed for the presence of mudstone [7], [8].

Similarly, structures have experienced heave in many parts of the world, including Saudi Arabia, Canada, Australia, Oman, UK, USA, Japan, Norway, and Ireland [9], [10]; for example, approximately 1000 homes in Japan were damaged by mudstone heave in 2002 [11] and in Canada ongoing mudstone heave issues have already impacted upon an estimated 10,000 buildings [12].

It is necessary to evaluate the creep deformation characteristics of mudstone against slaking and

ultimately the stability of the natural and artificial slopes. Slaking of mudstone has been studied by many researchers [13]-[17]. Traditionally, these phenomena have very often been dealt with solely from the viewpoint of durability, not deformation and strength. Only slaking or durability tests have been carried out in various forms which deal with the change in physical properties such as density, particle size distribution etc. of mudstone due to slaking. The precise mechanism of creep deformation due to slaking is imperfectly understood [18].

A large creep deformation of crushed mudstone after immersion was reported by many authors (e.g., [1], [19]). Some researchers tried to evaluate the impact of slaking on the engineering behaviour of mudstones under unconfined condition. However, cyclic wetting and drying in the field typically occurs under anisotropic stress condition. Similarly, deformation characteristics of these mudstones have generally been studied either at a constant water content equal to the initial one, or after soaking at zero suction, or at dry condition. Since these conditions only represent the two extreme conditions of the mudstone, however, ones are lacking for investigating the deformation behavior of mudstones under variable water contents and stress condition. Therefore, in order to predict the long term response of various natural slopes and other geotechnical structures, a better understanding of the deformation characteristics of mudstones undergoing slaking is essential. So, the author tries to achieve a better understanding of mudstone through this research.

In this study, a series of direct shear tests were performed with advanced direct shear apparatus under different stress ratio. Specimens were consolidated at prescribed stress ratio, then they were wetted and dried alternatively under constant shear loading. During the test, vertical and shear loads, and vertical and shear displacements were monitored, recorded, and processed in a personal computer.

TESTING APPARATUS AND MATERIALS

The Hattian Bala mudstone used in this investigation as shown in Fig. 1, was obtained from the earthquake induced landslide dam, formed by the 2005 Kashmir earthquake, which is located southeast of Muzaffarabad, Pakistan. As already mentioned, the earthquake induced landslide dam was suddenly breached on 9th February, 2010 just after moderate rainfall preceded by drought. Slaking of mudstone was assumed to be one of the major causes of the failure [1], [20]. The specimens of oven dried crushed mudstone were prepared by removing particles finer than 2 mm and larger than 4.75 mm as a necessary adjustment to the apparatus dimension. The specimens were not thoroughly compacted to prevent from particle breakage and to make similar conditions as those of the landslide dam, which was dynamically deposited without strong compaction. The slaking index (JGS 2132) of the mudstone was evaluated as level 1, while the slaking ratio (NEXCO-110, 2006) was 96.86 %. Similarly, the crushed sand stone, silica sand and glass beads were also used for the comparative study with crushed mudstones. The specimen of oven dried sand stones also consist of particles finer than 4.75 mm and larger than 2 mm. Similarly, the mean size of glass beads and silica sand is 4 mm and 0.48 mm respectively.



Fig.1 Hattian Bala mudstone

The performed laboratory tests comprise a series of direct shear tests with a modified direct shear apparatus in order to study slaking induced creep

deformation of crushed mudstones. The inside specimen size is 20cm x 20cm x 9.14cm. The initial opening between upper and lower boxes was fixed as 10 mm. The apparatus has the following essential features: 1) a possible feedback control on both normal load and shear load to impose any prescribed stress path in the shear stress-normal stress space; 2) a lower shear box moving on a very low-friction rail, with two friction load cells to evaluate any friction at the bottom of the lower shear box; 3) shear load applied by a high precision gear loading device driven by a servo-motor, allowing easy and exact control of arbitrary shear displacement ratio as well as sustained loading (by a feedback control on the shear load). The importance of all these features to obtain reliable data of direct shear tests on granular material was demonstrated by [21]. A moisture sensor was inserted into shear box to measure the water content of the specimen instantaneously as shown in Fig. 2.

In this study, loading process during the test consisted of two stages: 1) the specimen was subjected to shear and average normal stresses keeping their ratio, $R (= \tau/\sigma_v)$ constant ($R = 0.3, 0.5$ and 0.7). Both shear stress (τ) and normal stress (σ_v) were steadily increased up to respectively 15 kPa and 50 kPa for $R = 0.3$, 25 kPa and 50 kPa for $R = 0.5$ and 35 kPa and 50 kPa for $R = 0.7$; 2) After the prescribed shear (τ) and normal stress (σ_v) values were reached, these values were kept constant until the stabilization of both shear and vertical deformations are achieved. After both shear and vertical deformations stabilization, the first wetting was carried out by supplying distilled water from the bottom of shear box until the specimen was fully immersed. Two cylinders with valves were used to control the water flow inside and outside of the shear box. The overflow of water was collected by fixing an external container around the shear box as shown

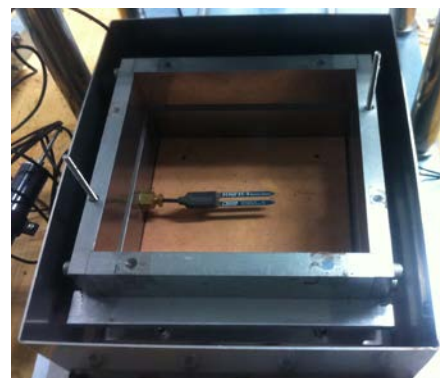


Fig. 2 Moisture sensor and shear box with large container

in Fig. 2. This creep loading process represents a situation that slope ground is saturated by rain fall under constant stress condition. When deformation

due to immersion led to stabilize, water was drained out (the first drying). Dry air was pumped from the bottom of the shear box and the shear box was covered by silica gel to absorb moisture from specimen while room temperature was maintained at 30°C. When both shear and vertical deformations as well as water content had reached an almost constant value, water was supplied again to the specimen (the second wetting). The same process of drying and wetting was repeated (the second drying and the third wetting). The detail information about testing apparatus and procedure was given by [22]. The above mentioned processes were also applied for crushed sand stones, silica sand and glass beads specimen.

TEST RESULTS AND DISCUSSION

Figure 3 shows the instantaneous response of creep deformations and water content of the crushed mudstone specimen during the wetting and drying cycles under stress ratio (R) 0.5. Each cyclic wetting and drying creep test took about one month to complete. The influence of wetting in the first cycle upon shear deformation appears to be significant for all specimens. Similarly, negative vertical deformation (expansion) occurs due to wetting. Positive value of vertical deformation is taken as contraction. This expansive behavior of crushed mudstone would consist of two phases, swelling caused by water absorption of clay mineral and dilatancy due to shearing.

For the second and third wetting processes, the increment of shear deformations are relatively small, almost 1/8 times the increment of shear deformation in the first wetting. However, substantial negative vertical deformation occurs during the second and third wetting processes. Figure 3 also shows that water content decreases gradually during the first and second drying processes. Initially, no appreciable creep deformation is found to occur at higher water content. When the water content becomes about 2.5 % (points A and B in Fig. 3), both vertical and shear deformations occur progressively with water loss and finally tend towards an asymptotic value at water content of about 0.7 %. As seen from the Fig. 3, both creep curves during drying are composed of two well defined curvilinear parts. Figure 4 shows schematic sketch of crushed mudstone particles which consist of two pore systems, inter (macro) and intra-primary (micro) porosity [23]. It is assumed that water leaves the crushed mudstones from the inter-pedal (macro) pores causing shrinkage of inter-pedal (macro) pores (first part of curvilinear). When the inter-pedal (micro) pores empty out, intra-primary (micro) pores begin to shrink, losing its water content (second part of curvilinear).

In addition, from Fig. 3 a), the creep shear deformation caused by wetting seems to be decreased with progress of wetting and drying cycle, almost zero during the third wetting. The water content of specimen before third wetting is about 0.7 %. The effect of water content before wetting on creep deformation will be discussed later.

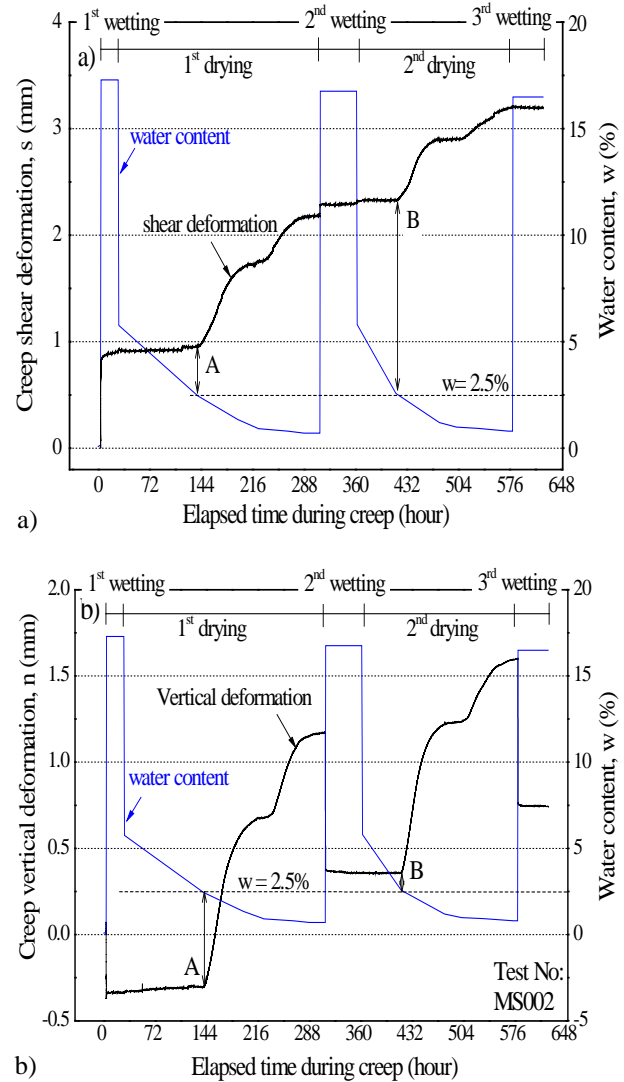


Fig. 3 Time histories of water content and creep deformation (a) Shear (b) Vertical under cyclic wetting and drying for 3 times for $R = 0.5$

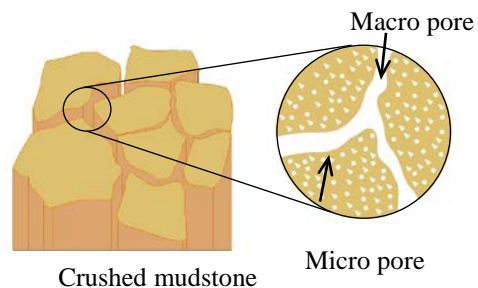


Fig. 4 Macro and micro pores system [23]

Figure 3 b) shows considerable vertical deformation that occurred in each wetting process. The vertical deformation in case of $R = 0.3$, however, is almost negligible except in the first wetting because of having higher water content (more than 3 %) of specimen before the second and third wettings. The wetting behavior would compose of contraction due to The vertical deformation in the wetting is affected by both R values during creep shear loading and the progress of wetting and drying cycles.

The above test results are summarized in Fig. 5, showing the increment values of creep shear and vertical deformations at each stress ratio, R . The wetting-induced maximum creep shear deformation of 3.4 mm was observed at $R = 0.7$ during the first wetting (see Fig. 5a). Similarly, wetting-induced creep failure was observed at $R = 0.8$ on the same material as the one in this study. Therefore, it seems that the creep shear deformation during wetting is proportional to the value of R , which would indicate high risk of slaking-induced instability at steep

slopes.

The specimens prepared at high initial dry density showed smaller shear displacement during wetting. The shear displacement of the specimen with initial dry density of about 1.50 gm/cm^3 was about 0.9 mm while 0.3 mm shear displacement occurred in case of the specimen with initial dry density of about 1.60 gm/cm^3 under $R = 0.5$ (Fig. 6).

The creep shear displacement caused by wetting seems to be decreased with the progress of wetting and drying cycle. The water content before each wetting was not same. Figure 7 shows the relationship between water content before wetting and wetting induced shear displacement. The shear displacement during wetting became higher as the water content before wetting of the specimen become lower. Reference [24] also reported that the slaking level of clay aggregates became higher as the initial water content of the specimen became lower. Therefore, it can be understood that the maximum displacement was observed during the first wetting because the specimen in this study was

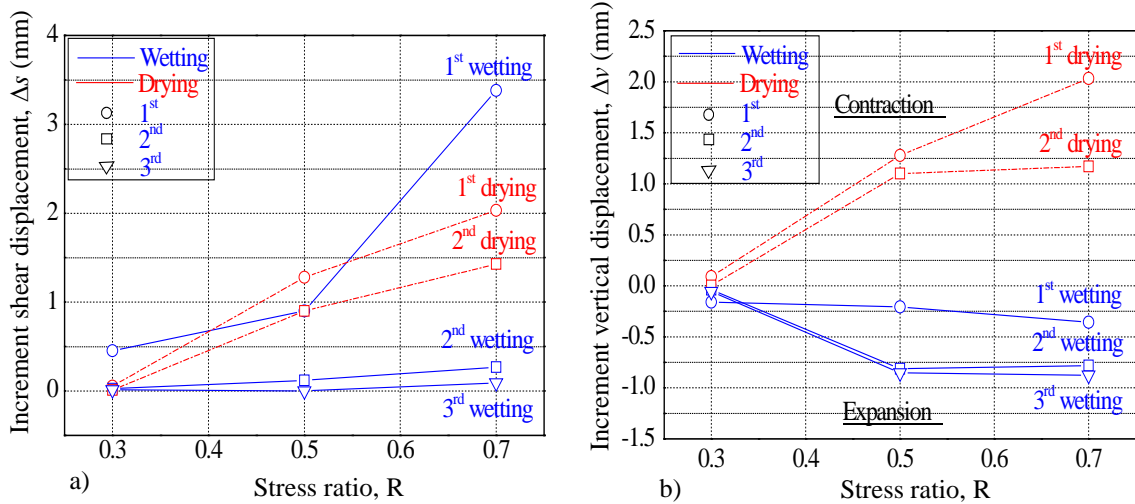


Fig. 5 Increment value of creep (a) Shear (b) Vertical displacement at each stress ratio, R

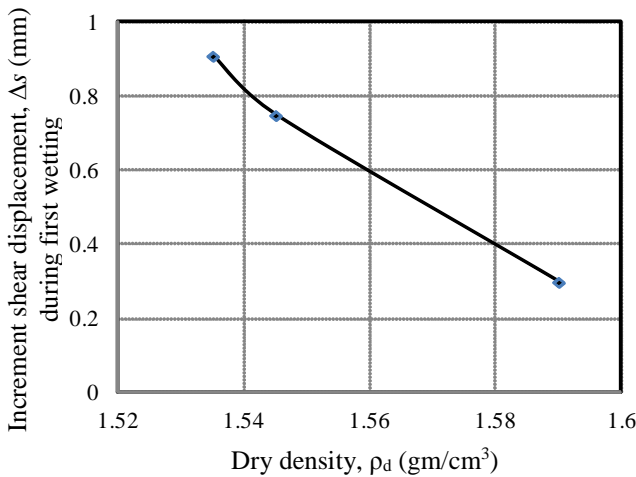


Fig. 6 Relationship between density of the specimen and shear displacement during first wetting

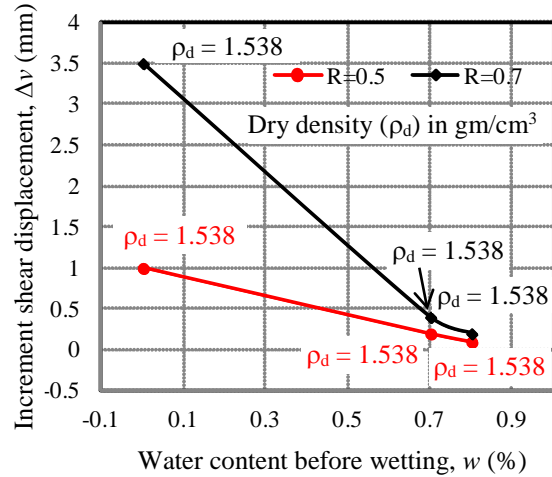


Fig. 7 Relationship between water content before wetting and creep shear displacement

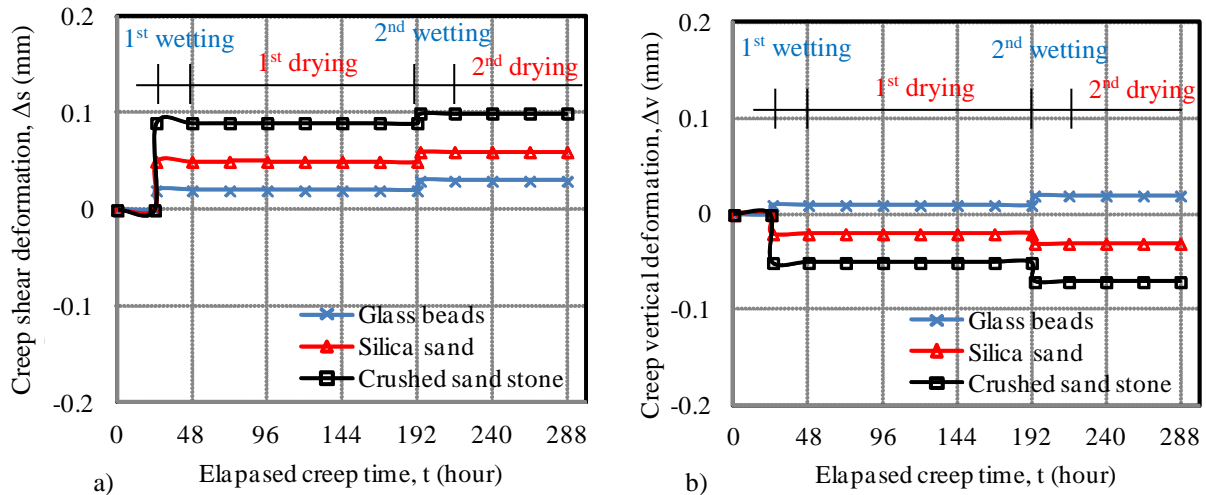


Fig. 8 Time histories of water content and creep deformation (a) Shear (b) Vertical deformation under cyclic wetting and drying for 2 times for $R=0.5$

prepared by oven-dried crushed mudstone. The lowest water content during drying step is quite large (about 3 %) in case of $R=0.3$. This may be reason for almost negligible creep shear displacement during the second wetting process at $R=0.3$. It can be deduced from this result that longer and more severe droughts before rainfall events could be more detrimental to slope stability as reported by [1].

One of the noticeable behaviors observed in these experiments is a quite large creep deformation during the drying processes. As shown in Fig. 5 a), the creep shear deformation during drying increase with the increase in the stress ratio, R . However, in the case of stress ratio, $R=0.3$, the lowest water content during the drying step is quite large (about 3 %). This may be reason for relatively small creep deformation during the drying process at stress ratio, R equal to 0.3.

Significant amount of mudstone particles were crushed due to slaking. After experiment, it was found that about 6 % particles became finer than 2 mm.

Figure 8 shows the instantaneous response of creep deformations of glass beads, silica sand and crushed sandstone specimen during the wetting and drying cycles under stress ratio ($R=0.5$). The water was supplied to the glass beads specimen after 24 hours creep loading. The Influence of wetting in the first cycle upon both shear and vertical displacement appears to be negligible (Fig. 8). Then, after 24 hours of creep loading under saturated condition, the water was removed from the specimen. The water content of the specimen decreased gradually and became almost zero after 6 days. As in the wetting, the influences of drying upon both shear and vertical displacements were not noticed. Similarly, for the second wetting processes, the increments of shear and vertical displacements were again almost zero. Similarly, in case of crushed mudstone and silica

sand, the influence of cyclic wetting and drying upon creep deformation seemed to be negligible i.e. no slaking effect on crushed sandstone and silica sand. The particles size distribution of all three materials i. e. glass beads, crushed mudstone and silica sand remained same even after cyclic wetting and drying which indicate the non-slakeable geomaterial does not have any influences of cyclic wetting and drying.

CONCLUSIONS

In order to study the slaking induced creep deformation of crushed mudstone, a series of direct shear tests were conducted. The following conclusions were obtained in this study.

A significant creep shear deformation could be found in the first wetting process. However, the amount of creep shear deformation during wetting is decreased with step of the drying and wetting cycles. Almost equal vertical deformation occurs in each wetting step if the water content of the specimen before wetting becomes quite smaller. Creep shear displacement during the wetting phase increases with a higher stress ratio, R which would indicate a higher slaking-induced instability at steeper slopes. Shear displacement during the first wetting phase is very large as compared to the second and third wetting. During the drying process, a significant creep deformation is found to occur when water content becomes less than 2.5 %. These tests show that the creep deformation during the drying is more significant than during the wetting with the progress of wetting and drying cycles. On the other hand, it was observed that creep deformation that occurred in the glass beads, crushed sandstone and silica sand were relatively insignificant and may not cause instability of any slopes or structures.

However, there is no doubt that extended work and further validation are required to describe this

behaviour more completely in full drying/wetting paths.

REFERENCES

- [1] Kiyota T, Konagai K., Sattar A, Kazmi ZA, Okuno D and Ikeda T, "Breaching failure of a huge landslide dam formed by 2005 Kashmir earthquake", *Soil and Foundation*, Vol. 51, No. 6, 2011, pp. 1179-1190.
- [2] Yatabe R, Yagi N, Yokota K and Bhandary NP, "Influence of Expansive Chlorite on the Strength of Weathered Green Rock at Mikabu Belt of Japan", In *Proc. International Conference on Geotechnical and Geological Engineering*, Melbourne, 2000.
- [3] Popescu, ME, "Landslide causal factors and landslide remedial options", in *Proc. 3rd Int. Conf. on Landslides, slope stability and safety of infra-structures*, Singapore, 2002, pp. 61-81.
- [4] Cetin H, Laman H and Ertunc A, "Settlement and slaking problems in the world's fourth largest rock-fill dam, the Ataturk Dam in Turkey", *Engineering Geology*, Vol. 56(3-4), 2000, pp. 225-242.
- [5] Tovar RD and Colmenares JE, "Effect of drying and wetting cycles on the shear strength of argillaceous rocks", *Unsaturated Soils – Alonso & Gens (eds)*, Taylor & Francis Group, London, 2011, ISBN 978-0-415-60428-4, 1471-1476.
- [6] Pejón OJ, Zuquette LV, "Analysis of cyclic swelling of mudstones", *Journal of Engineering Geology*, Vol. 67, 2002, pp. 97-108.
- [7] Shima H, and Imagawa S, "Compressive settlement of slakable material and its countermeasures." *Tsuchi-To-Kiso*, Vol. 28(7), 1980, pp. 45-52 (in Japanese).
- [8] Nelson JD and Miller DG, "Expansive soil: problems and practice in foundation and pavement engineering" *John Wiley & Sons*, 1997.
- [9] Mochizuki A, Mikasa M and Kawamoto S, "Investigation of settlement of clay fill at a housing development site" *Tsuchi-To-Kiso*, Vol. 33, No. 4, 1985, pp. 25-32 (in Japanese).
- [10] Noda T, and Nishi M, "A study of soft-rock embankment deformation due to water increase", in *Proc., JSCE*, Vol. 391No. 8, 1988, pp. 77-86 (in Japanese).
- [11] Yamanaka T, Miyasaka H, Aso I, Tanigawa M, and Shoji K, "Involvement of sulfur and iron-transforming bacteria in heaving of house foundations", *Geomicrobiology*, Vol. 19, 2002, pp. 519-528.
- [12] Sutton D, McCabe B, O'Connell A and Cripps J, "A laboratory study of the expansion of an Irish pyritic mudstone/siltstone fill material", *Engineering Geology*, Vol. 152, 2013, pp. 194-201.
- [13] Ladd CC, "Mechanisms of swelling by compacted clay", *Highway Research Board Bulletin*, abstract, Vol. 245, 1960, pp. 10-26.
- [14] Nakano R, "On weathering and changes of properties of tertiary mudstone related to landslide", *Soils and Foundation*, Vol. 3, 1967, pp. 1-14.
- [15] Franklin JA and Chandra R, "The slake durability test", *International journal of Rock mechanics and mineral science*, Vol. 9, 1972, pp. 325-34.
- [16] Moriwaki Y, "Causes of slaking of argillaceous materials." Ph. D dissertation, University of California, Berkeley, 1974.
- [17] Botts ME, "The effects of slaking on the engineering behavior of clay shales", Ph. D. dissertation, University of Colorado, Boulder, 1986.
- [18] Morris PH, Graham J and Williams DJ, "Cracking in drying soils", *Canada Geotechnical Journal*, Vol. 29, 1992, pp. 263-277.
- [19] Yoshida N, Enami K and Hosokawa K, "Staged compression-immersion direct shear test on compacted mudstone", *Journal of Test Evaluation*, Vol. 30, No. 3, 2002, pp. 239-244.
- [20] Sattar A, Konagai K, Kiyota T, Ikeda T and Johansson J, "Measurement of debris mass changes and assessment of the dam-break flood potential of earthquake-triggered Hattian landslide dam", *Landslides*, 2010, DOI: 10.1007/s10346-010-0241-9.
- [21] Shibuya S, Mitachi T, and Tamate S, (1997). "Interpretations of direct shear box testing of sands as quasi-simple shear", *Geotechnique*, Vol. 47, No. 4, 1997, pp. 769-790.
- [22] Sharma K, "Slaking characteristics of geomaterials in direct shear test", Master thesis, University of Tokyo, Japan, 2012.
- [23] Braudeau E, Mohtar RH and Chahinian N, "Estimating soil shrinkage parameters", *Development in Soil Science*, Vol.30, 2004, pp. 225-240.
- [24] Panabokke CR and Quirk JP, "Effect of initial water content on stability of soil aggregates in water", *Soil Science*, Vol. 83, No. 3, 1987, pp. 185-196.

STUDY ON GROWTH OF VETIVER GRASS IN TROPICAL REGION FOR SLOPE PROTECTION

Mohammad Shariful Islam¹, B. A. M. Shahriar¹, Md. Shahidul Islam¹ and Hossain Md. Shahin²

¹Department of Civil Engineering, Bangladesh University of Engineering and Technology, Bangladesh; ²Department of Civil Engineering, Nagoya Institute of Technology, Japan

ABSTRACT

River bank erosion and embankment failures happen continuously throughout Bangladesh. From a strictly economic point of view, the cost of remediating these problems is high, and the state budget for such works is never sufficient. This confines rigid structural protection measures to the most acute sections. General reasons of embankment failure are erosion due to rain splash, wave action, overtopping of storm surge. Faulty design, poor maintenance and poor construction also cause failure. The use of CC blocks, stone revetments, geo-bags, and plantation etc. are commonly used for protection of embankment in traditional practices. These materials are expensive and sometimes are not effective to protect the embankments and river bank for an expected design life. On the other hand, slopes stability can be augmented by using bio-engineering techniques. Vetiver grass (*Vetiveria zizanioides*) is being used as an efficient bio-technology for slope protection in many countries, for its special attributes like longer life, strong and long finely structured root system and high tolerance of extreme climatic condition. A few steps have only been taken recently to employ this technique for slope protection purposes in Bangladesh. This paper presents three case studies of vetiver plantation in slope protection against rain-cut erosion. It is found that vetiver grass grows in different soil and climatic conditions of Bangladesh and effective for slope protection. Prospect of vetiver plantation in protecting haor low-land is also discussed.

Keywords: Bio-technology, erosion, low-land protection, salinity, vetiver

INTRODUCTION

Bangladesh is a small riverine country located in South East Asia. In total, it has 700 rivers including tributaries which have a total length of 24,140km. It also carries two months of monsoon period in a year. As a result, embankment failure due to erosion and bank breaching is very common phenomena in this country. Embankment failure is a big setback for transportation sector of Bangladesh. High cost of land in this over populated country forces to economic design of road embankment which is often failed by the wave action of heavy tidal force.

Bangladesh managed to construct about 7,555km of embankment including 4,000km of coastal embankments during the last few decades. It protects about 24% of total land area and 39% of net cultivation area. These embankments are constructed to protect land from tidal inundation, but cannot prevent overtopping of cyclonic surges and tidal bores. In addition, due to increased agricultural production, these embankments provide good road communication and contribute in the growth of the overall socio-economic condition at the coastal zone. Coastal region of Bangladesh is about 700km long. To protect such long length of embankment against natural calamity and erosion, every year government of Bangladesh has to allocate huge amount of money in its annual budget. So, cheaper maintenance and

construction cost of embankment would be a great relief for Bangladesh.

Cultivation and export of shrimp is very successful in the coastal region and it contributes 4% of national GDP every year [1]. For shrimp cultivation, ponds are dug side by side. These ponds are separated by common dikes around each pond. Slopes of these ponds are also to be maintained for hassle free cultivation [2]. Cropping time is all round the year except November to January. During these three months farmers refurbish their ponds as it becomes a dry season. In Satkhira region, flood occurs during rainy season (July to August) in a regular basis. The whole area becomes flooded and pond boundaries go under water. Flood causes damages to the dikes boundary of the shrimp ponds. Very often farmers engage themselves in boundary deciding argument [3].

During monsoon season, basin type low lands of north eastern part of Bangladesh (called "Haor") become flooded every year under water of 2 to 6 meters. Erosion in these areas is the main cause of loss of home for a good number of people every year.

The common causes for embankment slope failure in Bangladesh are heavy rainfall, wave action from river, and inadequate protection of slopes against overtopping of storm surge. Protection against these types of failures can be divided into three types like – i) structural, ii) non-structural and

iii) biological protection. Among the structural protections revetment, guide bunds, boulders and brick matressing are common, while dredging, channelization geo-bag dumping etc. are common in non-structural protections. Biological protections refer to bank vegetation, wooden pilling, willow post, bandallings and crisscross porcupines [4]. Most of these are expensive solutions against desired design life for the protection.

Now-a-days, bio-engineering technique is becoming popular in other countries. As Bangladesh could be one of the most affected countries for global warming [5], implementation of bio-technology would be the best solution against global warming. Moreover, it is cheaper than typical structural solutions that are provided for slope protection. Vetiver grass (*Vetiveria zizanioides*) is being used as an efficient bio-technology for slope protection purpose in many countries. The special attributes of vetiver is that it can grow on sites where annual rainfall ranges from 200mm to 5000mm [6]. It can survive in temperature ranging from 0°C to 50°C. It grows on highly acidic soil types (pH ranges from 3.0 to 10.5) and also tolerant to high content of Al, Mn, As, Cd, Cr, Ni, Pb, Hg, Se and Zn in the soil. The saline threshold (EC) of vetiver is 7.8 dS/m. However, in soil with EC values of 10~20 dS/m, the yield of vetiver is reduced by 10%~50% [7]. Its roots are very strong with a diameter of 0.66 ± 0.32 mm having a high tensile strength of around 85.10 ± 31.20 MPa. It is also found that vetiver hedges can survive even for more than 100 years [8].

Recently, few efforts have been made to investigate the effectiveness of vetiver in slope protection in Bangladesh [9, 10]. In this paper, application of vetiver grass to protect road embankment, shrimp pond sides in saline zone and pond slope in barind tract zone has been presented. Finally, possibility of vetiver application in haor low-land protection is discussed.

DESCRIPTION OF STUDY AREAS

Trials are made in three different geographic regions of Bangladesh. Possibilities of using the developed method are also proposed for haor village protection. Road embankment slope, pond slope in barind tract and saline zone were selected for field trials. General descriptions, climatic data, and soil characteristics of the sites are given below.

Keraniganj Site

A road embankment named as Konakhola-Kholamura-Hazratpur-Itavara-Hemayetpur of Roads and Highway Department of Bangladesh was selected to investigate the effectiveness of vetiver at road side slope. The site is situated at Keraniganj under Savar Upazilla, Dhaka. Total length of the

road is 23.01km and average width is 3.80m. The chainage of the field trial is 17+700m to 17+800m. Annual Average Daily Traffic of the road is 71.38. Temperature and humidity of this area ranges between 14°C and 34°C and between 45% and 79%, respectively. Average annual rainfall is 1875mm.

Specific gravity of the slope soil is 2.70. Sand, silt, and clay content are 10%, 80% and 10%, respectively. Mean grain size, D_{50} and coefficient of uniformity, C_u of the soil are 0.048mm and 7.5, respectively. It is seen that the soil is sandy silt. It seems that the soil is erodible.

Rajshahi Site

A pond was selected to evaluate the growth and effectiveness of vetiver grass to control erosion of pond bank soil. The pond is situated at Godagari Upazilla in Rajshahi District. The region consists of barind tract, Diara and Char lands. Annual average temperature ranges between 11.2°C and 37.8°C. Average annual rainfall is 1862mm.

Specific gravity of the slope soil is 2.64. Sand, silt and clay content of the soil are 13%, 75% and 12%, respectively. Mean grain size, D_{50} and coefficient of uniformity, C_u is 0.016mm and 7.4, respectively. According to percentage of contents the soil is sandy silt. It seems that the soil is erodible.

Satkhira Site

Satkhira is a district of south western part of Bangladesh under Khulna division. It is close to Bay of Bengal. Being coastal district, salinity is a key feature for soil and water of this district. The annual average maximum and minimum temperatures are 35.5°C and 12.5°C, respectively. The annual rainfall is 1710mm. Most of the population is involved with shrimp cultivation in this district. Plantation was done in two areas.

Plantation Area-1 was a plane land and part of a well maintained garden. Specific gravity of the soil sample is 2.64. Sand, silt and clay content are 2%, and 97%, and 1%, respectively. Mean grain size, D_{50} and coefficients of uniformity, C_u are 0.025mm and 11.87, respectively. It is to be noted here that this plantation area is not a slope. However, this trial was employed to compare the growth in the same region.

Plantation Area-2 was a slope of a shrimp pond. The soil of this site is organic soil with organic content of about 10%. Specific gravity of the soil sample is 2.52. Sand, silt, clay content are 3%, 88% and 9%, respectively. According to percentage of contents the soil is CH. D_{50} and C_u are 0.022mm and 9.56, respectively. Liquid limit and plasticity index of the soil are 63 and 38, respectively.

pH level of the soil varies between 6.2 and 8.4. Cation exchange capacity is 14.2 to 25.5 m.e%. Na, K, Ca and Mg content ranges are 0.5 to 0.6, 0.2

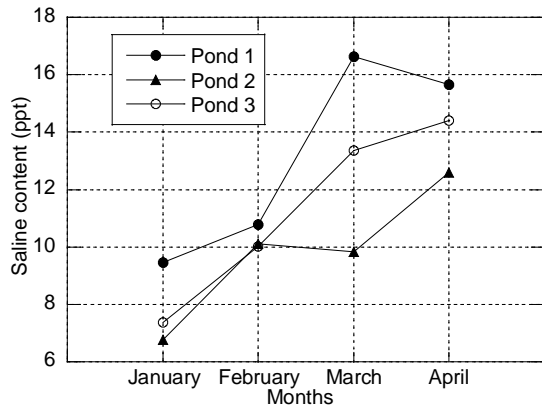


Fig. 1 Variation of salinity content of water of the ponds with time at Plantation Area-2.

to 1.2, 6.3 to 16.2 and 2.8 to 11.4 m.e%, respectively. Content of P, Zn and Cu ranged between 12 to 24, 0.1 to 0.8 and 0.08 to 0.30 ppm, respectively. Saline content of three ponds near the Plantation Area-2 are given in Fig. 1. Salinity is highest in March.

Haor Area

Haor is a basin type low land area in the north eastern part of Bangladesh. This zone contains about 400 haors and beels. The haor basin is a remote and difficult access area that is flooded every year during monsoon. The climate of the area is subtropical monsoonal with an average annual rainfall of 4,000 mm. Temperature varies between 26°C and 31°C. The surface soil of the area is mainly composed of yellowish grey silts which are very erosion prone and problematic from filtration point of view.

Index and physical properties of the soils from Keraniganj (Site-1), Rajshahi (Site-2), Satkhira (Plantation Area-1: Site-3; Plantation Area-2: Site-4) are presented in Table 1. It is seen that soil from Keraniganj and Rajshahi are sandy silt. Soil of the Plantation Area-1 of Satkhira is mainly silt while the soil from Plantation Area-2 is organic clay.

FIELD TRIALS

Application in Road Embankment

Field trial was conducted at the Keraniganj site for a road slope. Before vetiver plantation, site was prepared by plucking out unwanted grasses and leveling the soil bed. Then geo-jute was placed over the soil bed using fixing pins at a fixed interval. 700gsm geo-jute was used in this plantation purpose. After that vetiver had been planted at an interval of 20cm c/c both in horizontal and vertical direction using a stick for making hole in the ground through geo-jute. Vetiver was planted in October 2011. These vetiver grasses were collected from a place called 'Pubail' which is nearby Dhaka city.

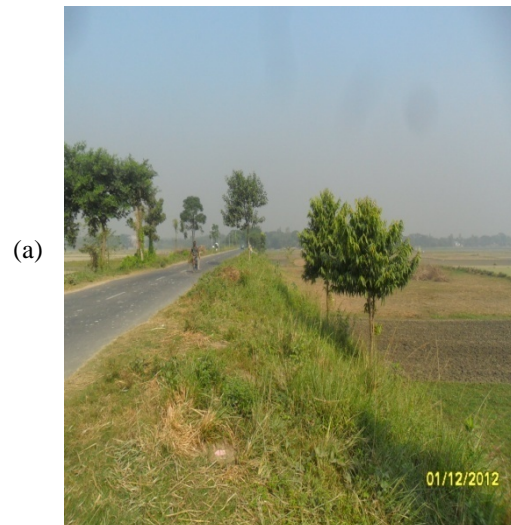
Table 1 Index and physical properties of soils

Site	G _s	Sand (%)	Silt (%)	Clay (%)	PI (%)	OC (%)
Site-1	2.70	10	80	10	-	-
Site-2	2.64	13	75	12	-	-
Site-3	2.64	2	97	1	-	-
Site-4	2.52	10	3	88	38	10

Note: G_s: specific gravity, PI: plasticity index, OC: organic content

Watering had been done for 1 month on a regular basis. Detail about this trial is presented in Islam et al., 2013 [10].

The growth of shoot and root was monitored regularly. Figure 2 presents the site view and vetiver shoot & root after 52 weeks. Figure 3 shows the shoot and root growth with time. It can be seen that root grew up to 52cm at the end of 52nd week while length of shoot was grew up to 180cm. It is found that although both the shoot and root length increased with time the rate of growth became slow after 40 weeks. No sort of geo-jute was found at the



(a)



(b)

Fig. 2 Growth of vetiver grass at Keraniganj site after 52 weeks of plantation: (a) view of the site and (b) close view of shoot and root.

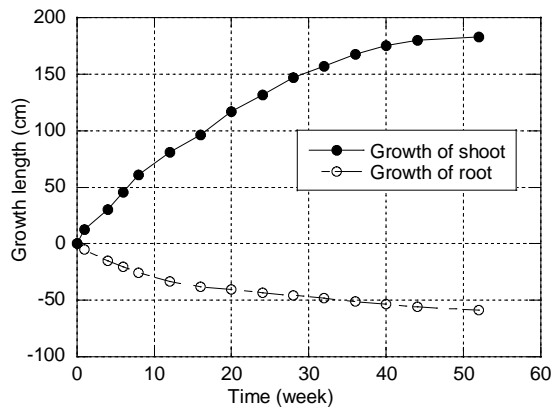


Fig.3 Growth of vetiver shoot and root with time at Keraniganj site.

site after 52 weeks which indicates that geo-jute is totally bio degradable to environment. In the opposite side of the vetiver plantation, a thick masonry wall was constructed for protecting the slope from rain-cut erosion. Some parts of the wall were damaged due to the rain water pressure while vetiver plantation part worked perfectly. Cost of vetiver plantation is 4 times lower than that of the masonry wall construction. Vetiver grass increases the factor safety of the slope from 1.7 to 2.8 [10].

Application in Pond Slope

Trial in barind tract zone in Rajshahi

Field trial was made to protect a pond slope from erosion in the barind tract zone. The periphery of the pond was about 122m. The pond is used for bathing and household purpose. There was almost no vegetation around the side slope of the pond except some banana trees. Side slope's soils of the pond were highly erodible. In rainy season, top soil is washed away by runoff which causes the pond water muddy. In dry season, the top soil is flown away from the bank by wind. The slope of the pond is not uniform. The slope at the top, middle and lower portion is 1:1.5, 1:2 and 1:3, respectively.

Vetiver grass was planted in three sides of the pond bank in June 2010 and growth of its root and shoot were monitored until November 2010. At first cow-dung was mixed with the bank soil. Vetiver collected from 'Shirajganj' was planted according to the contour line shown in Fig.4. Spacing of planted vetiver grass was 15cm both along the slope and perpendicular to the slope directions (Fig. 4). Well rooted slips was planted 15cm apart to ensure a close hedge within 6 months of plantation. It was found that the root grew up to 25.4cm and shoot grew up to 80cm in 6 months. Figure 5 show the condition of the pond before and after vetiver plantation. Water of the pond was turbid before vetiver plantation. But water became clear even in rainy season. It means that application of vetiver was effective to protect the erosion and migration of soil particles from the

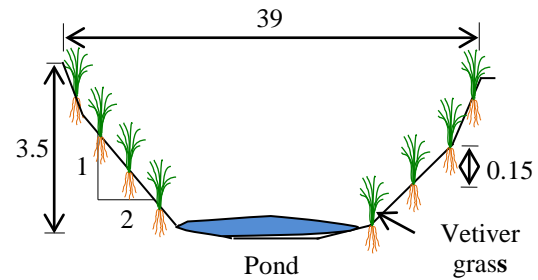


Fig. 4 Schematic diagram showing the plantation of vetiver grass along the pond slope (dimensions are in meter)



(a)



(b)

Fig. 5 Pond condition: (a) before vetiver plantation and (b) after 6 months of vetiver plantation at the Rajshahi site.

top and bank of the pond during rainy season and winter (dry season).

Application in saline zone

At Satkhira, two places were chosen for the plantation program. Plantation Area-1 was a garden with an area of 100 square meter and Plantation Area-2 was a side slope of a shrimp pond of about

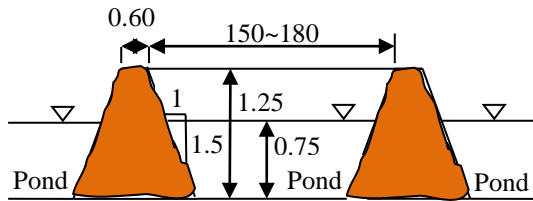


Fig. 6 Schematic diagram of a typical shrimp pond at Satkhira (all the dimensions are in meter)

100 square meter of plantation area which is 35km away from the Plantation Area-1. Vetiver grass collected from 'Pubail' site was also planted in these two areas.

For Plantation Area-1, soil bed was watered and ploughed using a garden hoe. After that, vetiver grass was planted in square grid of 30.5cm. Root of the grasses was inserted at least 7.5cm below the soil surface. Watering has been done two times every day.

On the other hand, for Plantation Area-2, which was a slope of a shrimp pond, vetiver grass was planted at 30.5cm distance both in along the slope and perpendicular to the slope. Here, it is to be mentioned that, no geo-jute was used in the slope area. Watering was done from the shrimp pond itself to make the grasses habituated with the saline condition. Figure 6 shows a typical section of shrimp pond.

After plantation, growth of the shoot of vetiver are monitored weekly. It is to be noted here that salinity content of ponds become very high during March to April and plantation work had been done in May. Plantation during high saline content period would help us to monitor vetiver's sustainability against hostile soil condition.

Condition of the root and shoot after 45 days for both the plantation area is presented in Fig.7. Growth of root and shoot with time has been presented in Fig.8. The growth in the Plantation Area-2 is less than that of the Plantation Area-1. This might be due to high salinity of the water and soil in this area. However, it is clear that vetiver grass can grow even in the saline zone. Similar results were obtained in Fiji where vetiver grown in high saline zone (Truong et al., 2002).

Comparison of vetiver roots and shoot growth in different areas that is Keraniganj, Rajshahi and Satkhira is presented in Fig.9. Growth of both the root and shoot are different for different soil and climatic conditions. The growth is different even in the same area. It is seen that in all the cases both the root and shoot grow with time.

Haor Village Protection

In the haor areas, masonry wall, revetment stone bamboo etc. are used for protecting the villages from the wave action. A comparative cost analysis for the typical slope protection measures that are used in



(a)



(b)

Fig. 7 Growth of vetiver shoot at Satkhira site in 45 days at (a) Plantation Area-1 and (b) Plantation Area-2

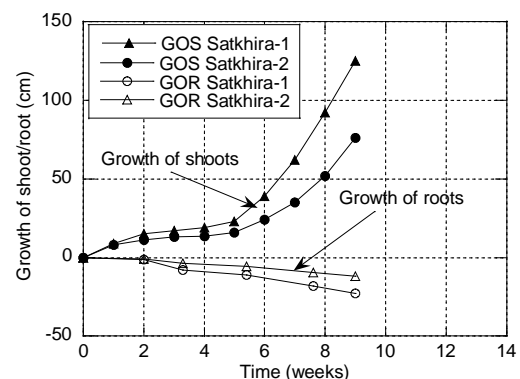


Fig. 8 Growth of vetiver shoot and root with time

haor areas are made. Unit costs are taken from the rate schedule 2011 of Public works Department (PWD) [11]. It is found that among the four solutions 'Total vegetation protection' type of protection system is less costly and very easy for construction. In general, a 300mm layer of stone is placed over geotextile. Vertical and horizontal anchor is also used to attach with ground. It is a hard nature solution and costs about US\$ 19.55 per square meter slope protection. Another hard nature protection

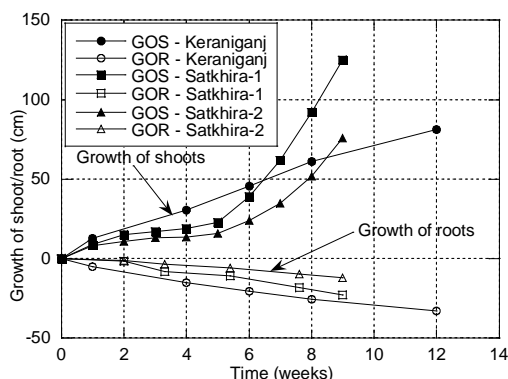


Fig. 9 Comparison of vetiver growth in different regions

system is 'Masonry wall protection system'. Its construction cost for per unit square meter is US\$38. This solution is found as the most costly solution among the others. Another two protection measures are proposed. One is vetiver grass with revetment and another is vetiver grass without revetment. Protection including revetment stone costs US\$9.53 per square meter and only vetiver plantation costs US\$ 4.7 per square meter.

FINDINGS AND RECOMMENDATIONS

Bio-technology in contrast to current practices of embankment and slope protection around the world is more sustainable, practical and efficient. In this context, field trials have been made in three different geographical locations of Bangladesh. The main findings of these studies are:

- 1) Vetiver plantation works very well on the slope of road embankment which protects the slope from rain-cut erosion and sliding. This proves that vetiver plantation is suitable in a sub-tropical climate in sandy soil.
- 2) Vetiver grass also grows well in barind tract zone and works very well against rain-cut erosion and wind induced erosion to protect pond slope.
- 3) Even in high saline zone area, vetiver plantation is a suitable green solution to protect the side slopes of shrimp ponds from flood and wave action.
- 4) From the study it is clear that vetiver plantation is suitable for protecting slopes in different geographic areas with different soil and climatic conditions. However, the growth of vetiver root and shoot are different in different areas. These are due to the difference in soil type, nutrient content and salinity.
- 5) From comparative cost analysis it is found that vetiver application is 8 times cheaper than masonry wall protection and 5 times cheaper than revetment stone slope protection system. Thus application of vetiver grass for erosion protection could be a sustainable, green and

cheaper bio engineering solution for a global warming threatened country like Bangladesh.

ACKNOWLEDGEMENTS

The authors are grateful to WAB Trading Intl. (Asia) Ltd. for their support in plantation of vetiver grass in Satkhira. The authors are also grateful to RHD, Government of Bangladesh for giving their permission in planting vetiver in road embankments.

REFERENCES

- [1] Hensler, L, "A sustainable future for shrimp production in Bangladesh?" Sustaining ethical aquaculture trade, 2013.
- [2] Alam, MN and Philips, MJ "Coastal shrimp aquaculture systems in southwestern Bangladesh", Asian Fisheries Science 17, 2004, pp. 175-189.
- [3] Haque, SA, "Salinity problems and crop production in coastal region of Bangladesh", Pak. J. Bot., Vol. 38, No. 5, 2006, pp.1359-1365.
- [4] Islam, MS, "Riverbank erosion and sustainable protection strategies", J. of Engineering Science, Vol. 2, 2011, pp. 63-72.
- [5] Rajib, MA, Rahman, MM, McBean, EA "Global Warming in Bangladesh Perspective: Temperature Projection upto 2010", Proceedings of the Global Conference on Global Warming, 2011, pp. 43-48.
- [6] Rahman, MM, Islam, MA, Rashid, SH, Mia, MMK, and Rahman, MH "Study on the distribution and potential of vetiver grass in Bangladesh." *Bangladesh J. of Plant Taxonomy*, 1996, 3(2), pp. 1-16.
- [7] Truong, PN, Gordon, I, Armstrong, F, and Shepherdson, J, "Vetiver grass for saline land rehabilitation under tropical and Mediterranean climate." Proc. Eighth National Conf. on Productive Use of Saline Lands, Perth, Australia, 2002, pp. 71-80.
- [8] Verhagen, HJ, Jaspers, Focks, DJJ, Algera, A, and Vu, MA, "The use of vetiver in coastal engineering." Proc., Copedec VII, Dubai, UAE, 2008, Paper No. 119.
- [9] Islam, MN, "Role of vetiver in controlling water-borne erosion with particular reference to Bangladesh coastal region." Proc., 3rd Int. Conf. on Vetiver (ICV3), Guangzhou, China, 2003, pp. 358-367.
- [10] Islam, MS, Nasrin, S, Islam, MS and Moury, FR, "Use of vegetation and geo-jute in erosion control of slopes in a sub-tropical climate", World Academy of Science, Engineering and Technology, Vol. 73, 2013, pp. 1162-1170.
- [11] Public Works Department, PWD, "Schedule of rates for civil works", 2011.

INTERACTION MECHANISMS OF SOIL-GEOSYNTHETIC REINFORCEMENT

Mabrouk Touahmia¹

¹Department of Civil Engineering, University of Hail, Kingdom of Saudi Arabia

ABSTRACT

The pullout performance of geosynthetic reinforcements under static and sustained loading is described in this paper. Laboratory tests were conducted to investigate the cumulative effects of loading on the pullout capacity and behaviour of geogrid reinforcements. The test methods and procedures for analyzing and interpreting the data are presented. The mechanics of load transfer and reinforcement displacement are also examined. In general, the results showed that under static loading applications the geogrid experienced a gradual deformation with load increase. No peak load was observed with the system of loading used and the deformation of the geogrid was mainly close to the point of load application. The sustained loading tests showed no cessation of creep displacement of the geogrid throughout the testing periods of this investigation.

Keywords: Geosynthetics; Geogrids; Soil Reinforcement; Static Loading; Creep

INTRODUCTION

Over the past three decades, geosynthetics have become a significant part of civil and environmental engineering practice in most part of the world. Various types of geosynthetic products have been used extensively in a range of engineering applications such as in road and highways, railways, soil reinforcement, drainage and erosion control, waste containment, retaining structures, slopes stability and embankments stabilization, and in some of these applications they have entirely replaced the conventional construction materials. The use of geosynthetics has proven to offer cost-effective environmentally sustainable alternative solutions to many soft and unstable ground problems, where the use of conventional construction materials would be restricted or significantly expensive.

However, the rapid development of geosynthetics technology has been accompanied by relatively slower development in methods of analysis and design. The selection of appropriate design parameters for geosynthetics reinforced soil systems has remained variable and sometimes confusing, due to the lack of data from field and laboratory models that can optimize current design methods [1]. Up to now, there are many uncertainties concerning the structural or load-carrying capacity of geosynthetic-reinforced soil systems. Perceptions by users concerning the durability of geosynthetic materials have caused a number of designers to be hesitant to use geosynthetics for long-term reinforcement applications. Although many research studies have been carried out in recent years to investigate the interaction properties of soils-geosynthetics [2],[3],

[4], there is still a lack of understanding about the long-term interaction mechanism of the composite system due to the absence of comprehensive and conclusive studies. Geosynthetics are widely used in structures which are subjected to constant loads throughout their service life. Under these loading conditions, geosynthetics would exhibit creep strains which may potentially cause damage to the corresponding structural system [5], [6]. Creep is the time-dependent increase in accumulative strain or elongation in the geogrid resulting from a constant applied load. Thus, the creep behaviour of geosynthetics should be properly evaluated so that the appropriate factor of safety can be incorporated into the long-term design of structural systems.

The main objective of this research was to evaluate the pullout performance of geogrid soil reinforcements under different loading conditions. Large-scale experimental program was conducted aimed at the improvement of the understanding of the interaction behaviour of soil-geosynthetic composite systems. This paper presents an examination of the pull-out performance and failure mechanisms of geogrid reinforcements under static and sustained loading.

TESTING APPARATUS AND MATERIALS

For the examination of the interaction mechanism of soil-geogrid composite systems, a large scale laboratory pullout device was developed. The testing program was designed to evaluate the interlock capacity of the soil-geogrid and to analyse the failure mode of the composite system.

The main testing apparatus used in this investigation is shown in Fig. 1. It consisted of a

rigid sand container of inside dimensions 4.0 m x 0.3 m x 0.3 m, a loading system with the capacity to apply axial pullout loads and a surcharge pressure system. The confining stresses, which could be controlled up to 300 kPa safely, were applied to the top of the soil sample via a pressure plate loaded through a water bag and connected to an air compressor through a pressure regulator. Instruments were used to measure pullout forces, pullout displacements and surcharge pressures. All data were recorded and monitored by a computer based data acquisition system connected to the testing apparatus.

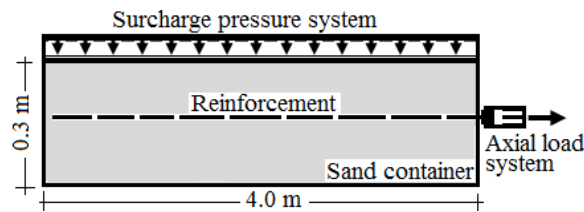


Fig. 1 Testing apparatus.

The reinforcements tested in this investigation were formed by cutting SR2 geogrids into a row of two ribs in width and 4 m in length. SR2 geogrid is a uniaxial geogrid type manufactured from copolymer grade high density polyethylene. Physical and mechanical properties of SR2 geogrids are reported from manufactures' data in Fig. 2 and Table 1. The index load (PI) of the geogrid, defined as the ultimate rupture load of an identical geogrid in air, is shown in Fig. 3.

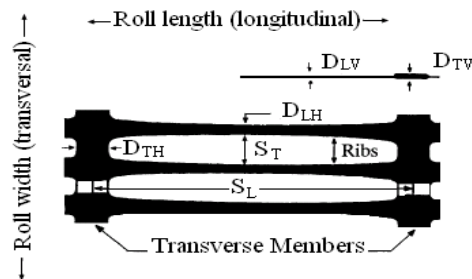


Fig. 2 Geometry of uniaxial SR2 geogrid.

Table 1 Physical properties of SR2 geogrid

Dimensional Properties	Mean
Product width (S_L)	100 mm
Transverse bar width (D_{TH})	12.69 mm
Max bar thickness (D_{TV})	4.56 mm
Min bar thickness (D_{TV})	4.36 mm
Rib width (D_{LH})	5.72 mm
Rib thickness (D_{LV})	1.34 mm
Number of ribs	44 / m
Mass per unit area	972 g/m ²

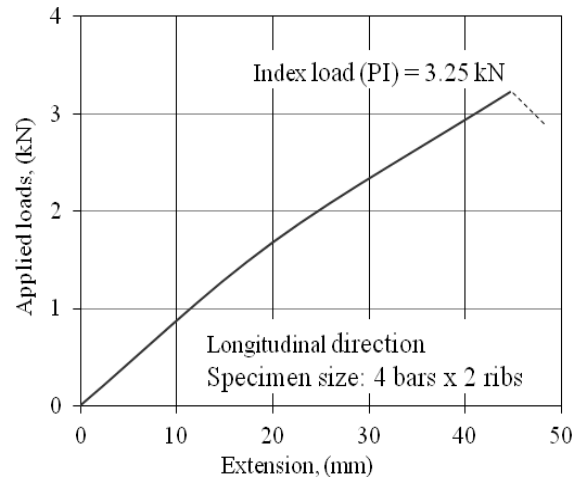


Fig. 3 Typical tensile strength extension of the geogrid (SR2).

The test specimen was located at the mid-height of the soil sample and connected to the loading levels system with a special end clamp. The displacements along the geogrid were measured using inextensible steel wires connected to the specimen, in at least eight different locations, and to LVDTs fixed to the external back side of the box.

The soil used in testing was a uniformly graded dry sand of medium size with a coefficient of uniformity $C_u = 1.9$; a specific gravity $G_s = 2.67$; a friction angle $\Phi = 39.4^\circ$; maximum and minimum densities of 1.78 Mg/m³ and 1.42 Mg/m³ respectively (Fig. 4). The sand samples were prepared in the sand container by raining method to a targeted relative density $D_r = 53\%$. To obtain a uniform density of sand throughout the filling operation, the sand was placed in equal layers of 50 mm thickness.

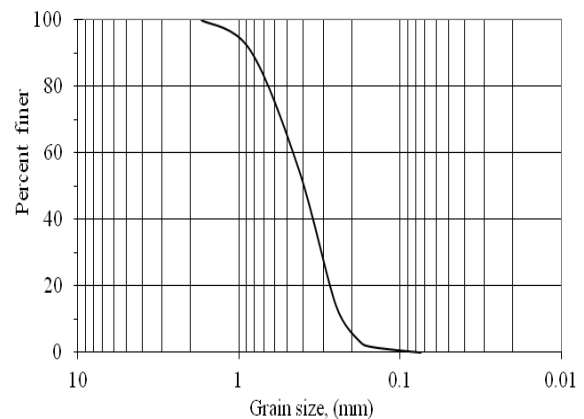


Fig. 4 Particle size distribution of the sand.

PULL-OUT BEHAVIOUR OF THE GEOGRID

A series of static pull-out tests were carried out to investigate the pullout performance of the geogrid.

The static loading of the reinforcements were carried out by applying dead weights of 20 kg each 5 minutes and then reduced to 10 kg each 5 minutes at high extension.

Figure 5 shows the load-displacement relationships for the 4 m geogrid reinforcement buried under 2 different normal stresses of 50 and 100 kPa.

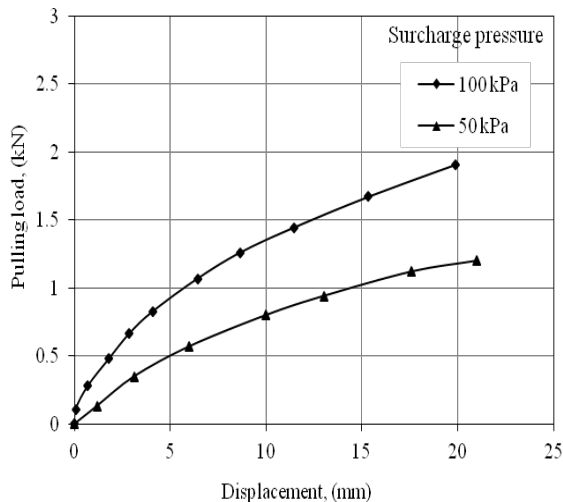


Fig. 5 Pullout load-displacement relationship of the geogrid at different confining stresses.

As can be seen, the general pattern of these relationships is characterized by a rapid increase of load with an initial small increase in the strip movement up to a certain level after which the displacement continues to increase with load increase till the end of the test. No peak load could be observed with the system of loading used and the relationship between load and deformation became linear at large displacements. The surcharge pressure was found to have a great effect on the deformation of the geogrid. The reinforcement mobilized greater resistance to pulling load when the surcharge pressure increased and that is clearly visible under high loading increments.

The recorded movements along the length of the geogrid reinforcement are given in Fig. 6. These movements were expected to be a combination of two components; the extension induced in the reinforcement together with the slip of the reinforcement. However, as can be seen, the total displacement of the reinforcement consists only of an extension of the front half part of the geogrid reinforcement and neither slip nor extension along the rear segment of the specimen length was observed. This means that no load was absorbed by the lattermost half length of the reinforcement and hence no frictional or bearing resistances were mobilized along that part of the strip. This observation would indicate that unless a very low

confining stress be used it would be impossible to pull out the reinforcement. Consequently, failure of these reinforcements by rupture appears to be an easier mode.

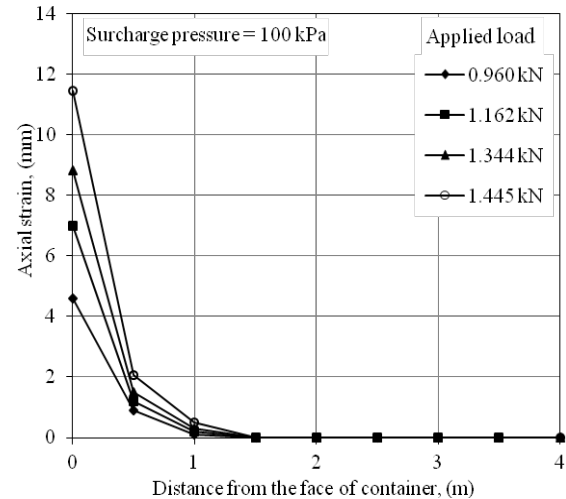


Fig. 6 Axial displacement of the geogrid with applied loads.

CREEP BEHAVIOUR OF THE GEOGRID

To examine the creep behavior of the SR2 geogrid reinforcement a series of short and long-term sustained loading tests were conducted throughout this investigation. For the short-term creep test a loading increment of 5% PI was applied each 60 minutes during which the creep deformations are recorded at 1, 2, 5, 10, 20, 40 and 60 minutes. For the long-term creep test, two loading levels, namely 25% PI and 35% PI, were chosen to be held for twelve weeks (2000 hours) time duration while the creep deformations of the geogrid reinforcement were recorded at 1, 2, 5, 10, 20, 40, 60 minutes and then after each hour. During all these tests the surcharge pressure was kept constant at 100 kPa. These tests were carried out under very small changes in temperature to minimize the effect of temperature variation on the experimental results. The temperature recorded throughout the tests was $18 \pm 1^\circ \text{C}$ with a maximum variation of 2°C .

The results of these tests showed no cessation of creep displacement of the geogrid reinforcement throughout the testing period. This trend can be clearly seen in Fig. 7 which illustrates the relationships between creep displacements and time. The results of these tests indicated that despite none of the reinforcement failed by pulling through the sand mass, their creep deformation did not cease throughout the test period and showed a significant increase with time and applied load increase.

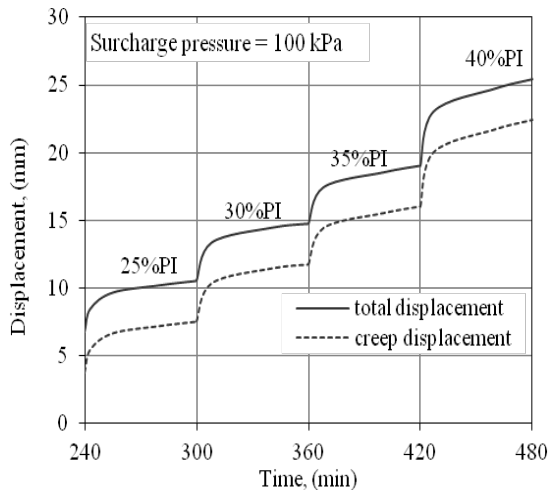


Fig. 7 Displacement-time relationship with applied load of the geogrid.

These observations are best illustrated by the form of a plot between creep deformation rate and time. It may be seen in Fig. 8 that at any sustained stress level the logarithm of the creep deformation rate decreases linearly with the logarithm of time. Furthermore, the slope of this relationship is essentially independent of the stress level, and increases in stress serve only to shift the line vertically upwards.

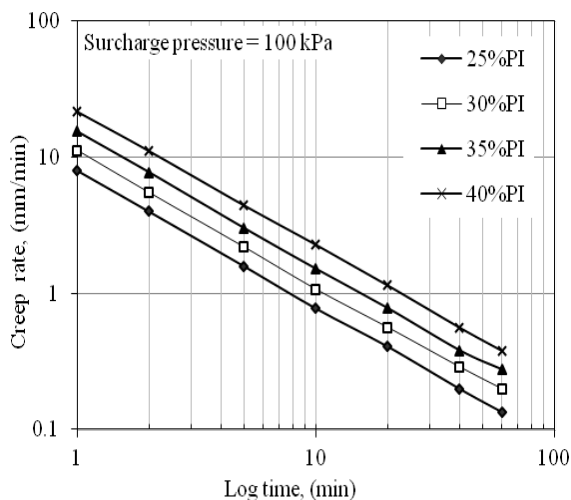


Fig. 8 Creep rate-time relationship of the geogrid.

Figure 9 shows the time-dependent deformation relationships of the geogrid on a semi-log scale for the long-term sustained tensile loading. This figure indicates that maintaining the applied load constant for several weeks results in a continuous deformation of the geogrid reinforcement. An interesting feature is that the rate of displacement-log time was constant during the first few weeks and started to decrease slightly towards the end of the test.

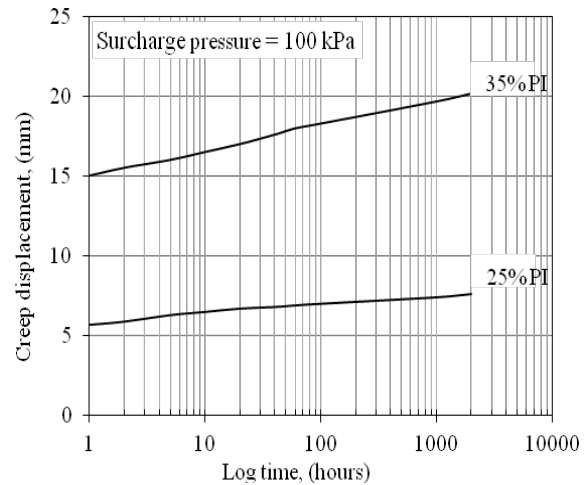


Fig. 9 Creep displacement-log time relationship of the geogrid.

CONCLUSION

The pull-out performance of the geogrid reinforcement under static and sustained loading is described in this paper. The laboratory tests results demonstrated that the geogrid reinforcement can be used in most loading conditions, although care will be required in ensuring that appropriate factors of safety are applied to control the resulting deformation.

Under static loading applications the geogrid reinforcement experienced a gradual deformation with load increase. No peak load was observed with the system of loading used and the relationship between load and deformation became almost linear at larger displacements. The total displacement of the reinforcement consists only of an extension of the front half part of the geogrid reinforcement and neither slip nor extension along the rear segment of the specimen length was observed.

The sustained loading tests data indicated that maintaining the applied load constant for several weeks results in a continuous deformation of the geogrid reinforcement without cessation. This deformation was mainly close to the point of load application. Despite none of the reinforcement failed by pulling through the sand mass, their creep deformation did not cease throughout the test period and showed a significant increase with time and applied load increase.

ACKNOWLEDGEMENTS

The author gratefully acknowledges the support of his research program by The Saudi Binladin Group. The facilities and assistance provided by the College of Engineering at the University of Hail are also appreciated.

REFERENCES

- [1] Zornberg JG and Leshchinsky D, "Comparison of international design criteria for geosynthetic-reinforced soil structures", *Landmarks in Earth Reinforcement*, Ochiai et al., Vol. 2, 2003, pp. 1095-1106.
- [2] Moraci N, Romano G and Montanelli F, "Factors affecting the interface apparent coefficient of friction in pullout conditions", 3rd European Geosynthetics Conference, Monaco, Vol. 1, 2004, pp. 313-318.
- [3] Teixeira SHC, Bueno BS and Zornberg JC, "Pullout Resistance of Individual Longitudinal and Transverse Geogrid Ribs", *Journal of Geotechnical and Geoenvironmental Engineering*, Vol. 133 (1), 2007, pp. 37-50.
- [4] Palmeira EM, "Soil-geosynthetic interaction: Modelling and analysis", *Geotextiles and Geomembranes*, Vol. 27 (5), 2009, pp. 368-390.
- [5] Yoo H, Jeon HY and Chang YC, "Evaluation of engineering properties of geogrids for soil retaining walls", *Textile Research Journal*, Vol. 80 (2), 2010, pp. 184-192.
- [6] Bathurst RJ, Huang BQ and Allen TM, "Interpretation of laboratory creep testing for reliability-based analysis and load and resistance factor design (LRFD) calibration", *Geosynthetics International*, Vol. 19 (1), 2012, pp. 39-51.

SIMULATION AND PREDICTION OF LARGE-SETTLEMENT IN ULTRA-SOFT PEAT GROUND BY DEDUCING THE IN-SITU INITIAL CONDITIONS CONSIDERING ARTESIAN PRESSURE

Mutsumi Tashiro¹, Toshihiro Noda² and Nguyen Hong Son³

^{1,3}Civil Engineering, Nagoya University, Japan;

²Disaster Mitigation Research Center, Nagoya University, Japan

ABSTRACT

In the Mukasa area of the Maizuru-Wakasa expressway in Japan, delayed settlement as large as 11m has occurred by the test embankment loading on a ground that includes approximately 50m of ultra-soft sediment layers containing peat and clay. While the construction of the embankment could not induce catastrophic sliding failure, it did dramatically impact the surrounding ground, causing substantial lateral displacement and ground upheaval of up to 2m and 1 m, respectively. In this paper, simulations of the settlement and pore water pressure observed until now and predictions of future behavior were carried out using soil-water coupled finite deformation analysis program GEOASIA. The initial in-situ conditions of the ground were deduced considering effect of the observed artesian pressure and various disturbances that might occur during sampling. The results showed that improvement of mass permeability of the ground and the slow and/or lightweight banking are effective means of providing the stability during loading and reducing the residual settlement.

Keywords: Peat, Prediction of settlement, Soil-water coupled analysis, Delayed settlement

INTRODUCTION

The soil in the Mukasa area of the Maizuru-Wakasa expressway in Japan consists of ultra-soft sediment layers comprising peat and clay with N-values on the order of 0 to 1 and a maximum depth of 50 m. Examination of a test embankment established approximately four years ago reveals that substantial settlement in excess of 11 m has occurred. While the construction of the embankment could not induce catastrophic sliding failure, it did dramatically impact the surrounding ground, causing substantial lateral displacement of up to 2 m and ground upheaval of up to 1 m as in [1].

In this paper, simulations carried out on the large-scale ground settlement observed until now, and predictions of settlement that could occur in the future are shown. In addition, the effect of countermeasures such as ground improvement by drain, replacement of existing embankment with lightweight materials, and reduction of the loading rate, were also investigated using numerical analysis. These analysis were performed using the soil-water coupled analysis program **GEOASIA** (All Soils All States All Round Geo-Analysis Integration: [2], [3]), in which the SYS Cam-clay model as in [4] was mounted as the constitutive equation for the soil skeleton. The initial in-situ conditions of the ground were deduced considering the effects of the observed artesian pressure and various disturbances that might occur during sampling.

GENERAL DESCRIPTION OF THE TEST EMBANKMENT

Figure 1 shows a longitudinal cross-section of the soil strata underlying the test embankment. Three types of test embankments were constructed using the card-board drain method (CBD), the sand drain method (SD) or no ground improvement with the aim to select an effective method for the ultra-soft ground. The soft layer of ground directly under the test embankment constructed with SD method was thickest among these three embankments and the magnitude of observed settlement was also largest. For this reason, the following discussion in this study was performed focusing on the SD section.

The total settlement estimated before construction was 8.6m in the case of considering the settlement of all layers including even the deep peat layers. However, as presented in Figure 2, the thickness of embankment (= embankment height + settlement) reached 15m when the embankment were constructed at the planned height of 7m.

The large-scale settlement was accompanied by substantial deformations in the surrounding area. Especially in the vicinity of embankment, ground uplift of up to 1m and horizontal displacement of up to 2m have been observed and inclination of irrigation ditch and cracking of ground surface were occurred. The range of these influences was about 100m away from the toe of slope. At the point, 4 years after the end of embankment loading, the settlement has reached 11 m, representing a

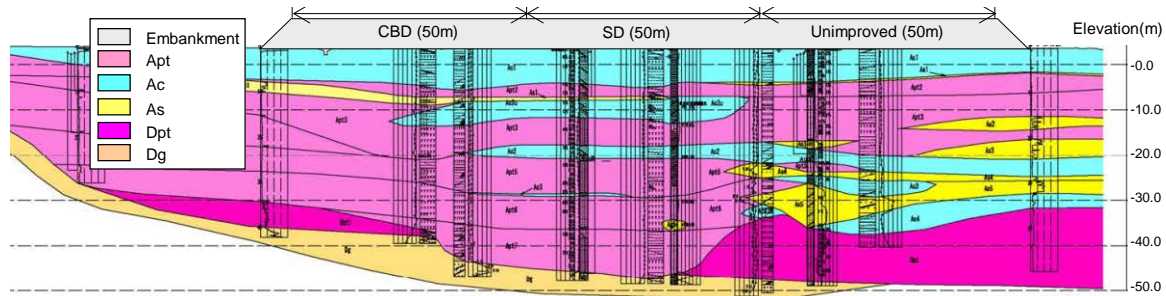


Fig. 1 Schematic of test embankment and underlying soil strata (longitudinal cross section).

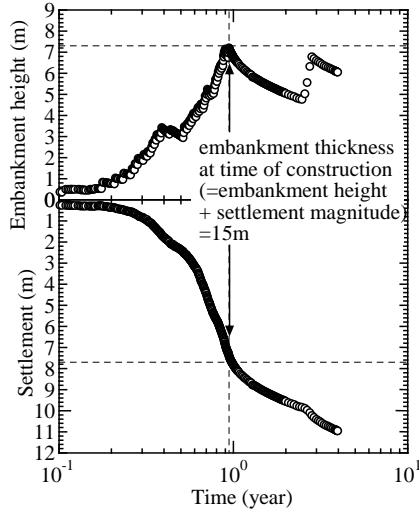


Fig. 2 Embankment height and observed settlement at the center of embankment (constructed with SD).

settlement rate of 3.0 cm/month with little sign of convergence.

DEDUCTION OF INITIAL IN-SITU GROUND CONDITIONS

Prior to performing the simulation, in order to estimate the initial in-situ ground conditions, historical data related to ground formation as well as various survey data, including pore water pressure were examined. The area is located between faults, and there is a possibility that the ground was deposited through the repeated upheaval, settlement, and deep accumulation of organic components in the valley that experienced continuous artesian conditions.

In this paper, the initial distributions of pore water pressure and effective overburden pressure of the ground prior to embankment loading was estimated in Figure 3. For reference, the distribution when artesian pressure is not taken into consideration is included as a dotted line. This represents a special case in which the initial effective overburden pressure p_0 becomes greater than the consolidation yield stress p_c ($p_0 > p_c$). In this region, it is expected that the increase in artesian pressure accompanying the increase in soft ground thickness resulted in a continuous low effective pressure in the deep ground.

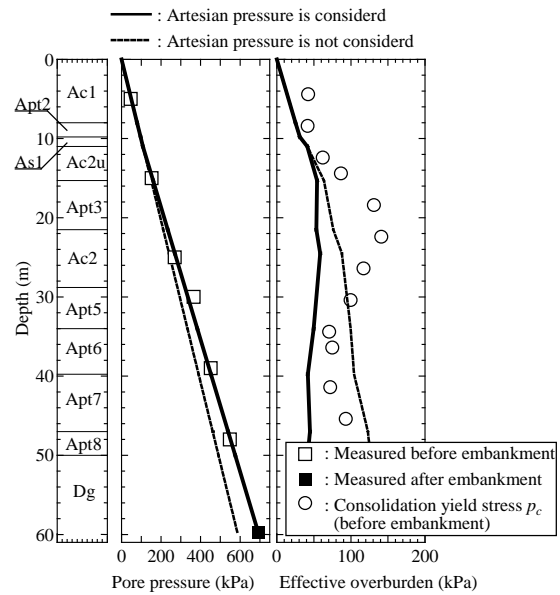


Fig.3 Estimated distribution of initial pore water pressure and effective overburden pressure

Subsequently, the material constants and initial in-situ conditions of each layer are estimated from laboratory test results.

In previous studies as in [5] and [6], the authors proposed a novel method for predicting long-term settlement of soft clay ground accompanied by delayed compression. Natural deposited clays with high compressibility possess high degree of structure and are sensitive to disturbance, i.e. the compressibility tends to become significantly low in this type of clay because of the “disturbance” that might be occurred between sampling from in-situ and preparing samples for laboratory tests. Therefore, it would be necessary to consider the effect of disturbance in order to deduce a higher compressibility of in-situ soils.

In this paper, the various insights gained from soft clay ground were applied to peat ground. In comparison with inorganic clays, peats are expected as more desirably impacted by “disturbances” due to extremely high water content, and low shear strength. In addition, considerable heterogeneity among deep-peat-layers samples regarding to factors such as mixing of plant fibers was observed. For these reasons, simulations were conducted based on a

range of assumed initial in-situ conditions deduced from as many compression curves for undisturbed samples as possible, and determined the initial conditions that best reproduced the measured settlement magnitude. Figure 4 shows the examples of compression curves for laboratory and in-situ soils.

With regard to the permeability of ground, given the high compressibility of the peat layers, a positive relation between the void ratio e and coefficient of permeability k were assumed by the expression $e = C \ln k / k_0 + e_0$, and for the other layers, constant permeability coefficient were assumed. In addition, in order to represent the improvement in permeability due to the SD, 100 times as large as permeability were assigned to finite elements corresponding to the improved area. Based on these assumptions, permeability values were also determined that could simulate the observations as sufficiently as possible.

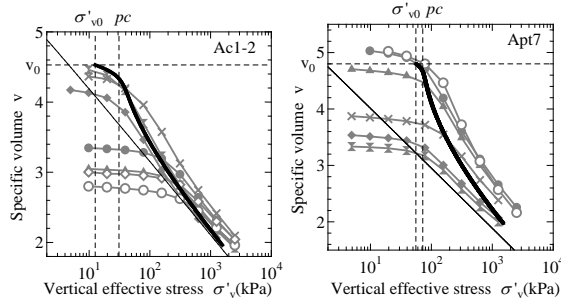


Fig. 4 Examples of compression curves for undisturbed samples (gray lines) and estimation for in-situ soil (thick black lines).

SIMULATION AND PREDICTION OF LARGE-SCALE SETTLEMENT

The finite element mesh and boundary conditions are presented by Figure 5. The SD installation section of the embankment of Figure 1 was modeled and ground in state of horizontal stratification was assumed for simplicity.

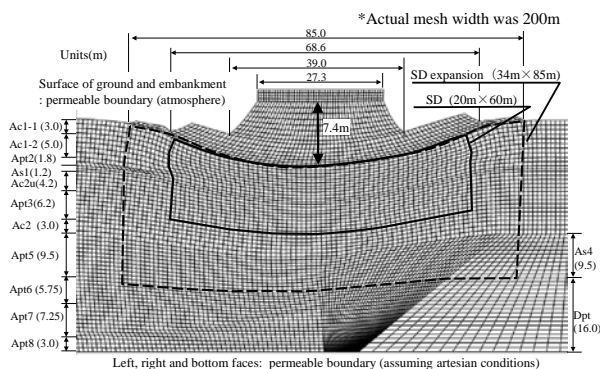


Fig. 5 Finite element mesh (after embankment construction).

Figure 6 shows the measured and calculated results on settlements at surface and boundary of each layer directly below the center of embankment. After simulating the observed settlements and adjusting the initial in-situ conditions and permeability of each layer, the prediction of future behaviors was performed by continuing the numerical analysis using the same parameters. As a result, additional residual settlement on the order of 1.5m was estimated to occur over the next 70 years. Measured and simulated pore water pressures were compared in Figure 7 at approximately 1400 days (about 4 years) after the entry of embankment loading (dotted line in Figure 6). It can be observed that the measured distribution of pore water pressure has also reproduced well through the above computations.

Figures 8 and 9 show the settlements of ground surface and the horizontal displacements directly below the both toes of slope, respectively. The large-deformations observed the Mukasa-side (uplift of ground surface and lateral displacement to the outside of embankment) were also reproduced. It was estimated that ground deformations of the Tana-side were restrained by the deep rigid layers (As4 and Dpt layers). With the progress of consolidation, the directions of deformations in shallow layers were shifted to the inside of embankment. In the Tana-side, especially, it could be expected that the surface layers might be transformed to the inner side than the initial location. In addition, in the deep layers around Apt5 layer where their permeability were gradually changed lower as a result of large compression, lateral displacement to the outside of embankment was estimated to occur at the end of consolidation.

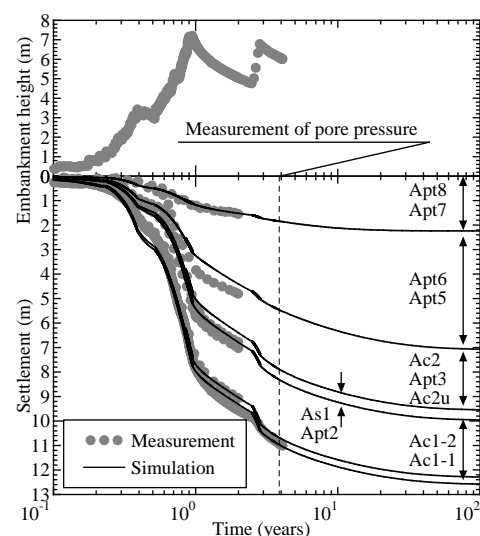


Fig. 6 Simulations and predictions of settlements directly below the center of embankment.

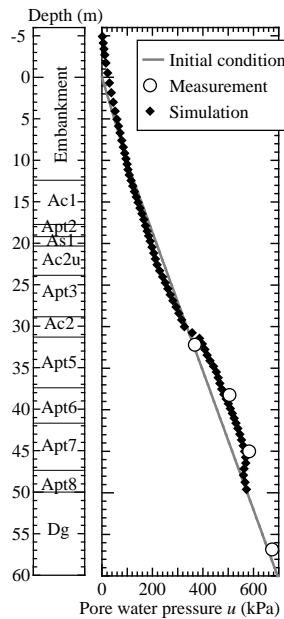


Fig. 7 Comparison of measured and simulated pore water pressures (about 1400 days after the entry of embankment loading).

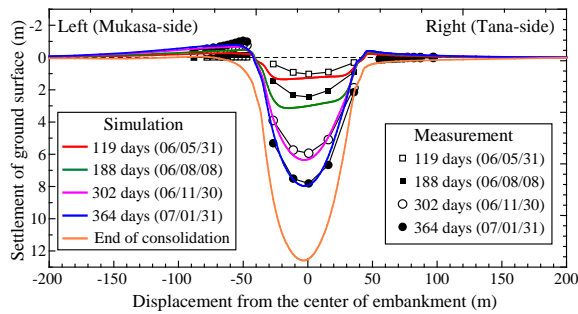


Fig. 8 Deformations of ground surface.

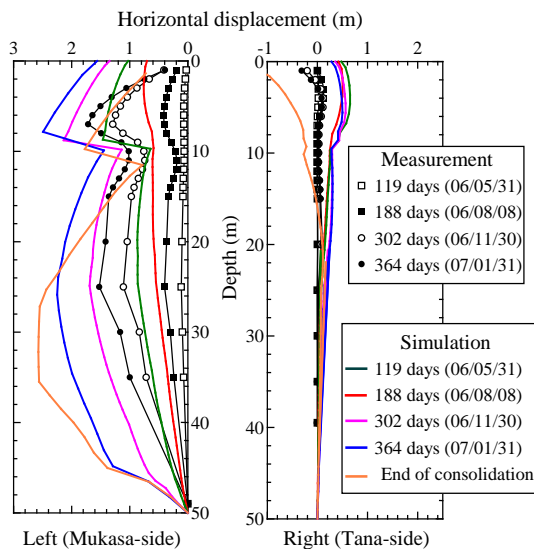


Fig. 9 Horizontal displacements directly below the both toes of slope

As examining in the previous chapter, the deep peat layers (Apt5-8) in Mukasa area possess lower

consolidation yield stress derived from their depositional environments. Therefore, when a relatively high embankment was constructed on the ground, the stress conditions of even deep layers were reached beyond the consolidation yield stress easily and rapid compressions were occurred. After a certain degree of volume compression, peats exhibit extremely poor permeability and have trouble dissipating excess pore pressure, particularly, in the area of ground without drain improvement.

EVALUATION OF COUNTERMEASURES FOR ULTRA-SOFT GROUND CONTAINING PEAT

Effects of Mass Permeability Improvement

In order to evaluate the effect of ground improvement on the test embankment using SD method, numerical analyses were performed in three cases as follows:

Case 1: Simulating the actual SD-improved area of the test embankment ($20 \times 60\text{m}$ (L \times W))

Case 2: No SD-improvement

Case 3: Expanding the SD-improved area (length and wide) for simulating the condition of actual constructions ($34 \times 85\text{m}$ (L \times W), i.e., the whole area under the embankment down to the Apt5 layer)

In each case, based on the records on the actual construction, the simplest construction history was used (constant increasing the embankment thickness at a rate of 2.35 cm/day). And as the same as the above simulation and prediction, the effect of improvement by SD method was represented by the change of mass permeability on the assumption that the SD method is equivalent to improve permeability 100 times in comparison with the original soil.

Although the magnitude of the settlement during initial embankment loading is lowest in Case 2, a large-scale circular slip extends suddenly to the deep ground layers below the embankment center as shown in Figure 10, because the poor permeability induces shear deformation under undrained condition. From this result, it appears that ground improvement by SD-method in this area was effective in preventing catastrophic slip failure.

Case 3 resulted in most stability, particularly, of the deep peat layers, and early settlement convergence. Figure 11 shows the settlement of ground surface for case 1 and 3. The residual settlement starting at a point 2 years (assuming the entry into service) after embankment construction is also illustrated in the lower figure. Expansion of the SD-improved area, particularly in the deep peat layers, reduces lateral displacement due to undrained shear deformation and settlement associated therewith. The total settlement is reduced by 55 cm

across the entire area of ground under the embankment. Furthermore, residual settlement was reduced by approximately half due to the fact that the settlement approached convergence earlier. However, because consolidation of the deep peat layers also occurred earlier, deformation was concentrated in the upper peat layers, and upheaval of areas near the toe of the slope increased (Figure omitted). As countermeasures for this problem associated with expansion of SD-improved area, it might be better to expanding the area and load of the counterweight embankment and reducing the rate of embankment loading, particularly in the initial stages.

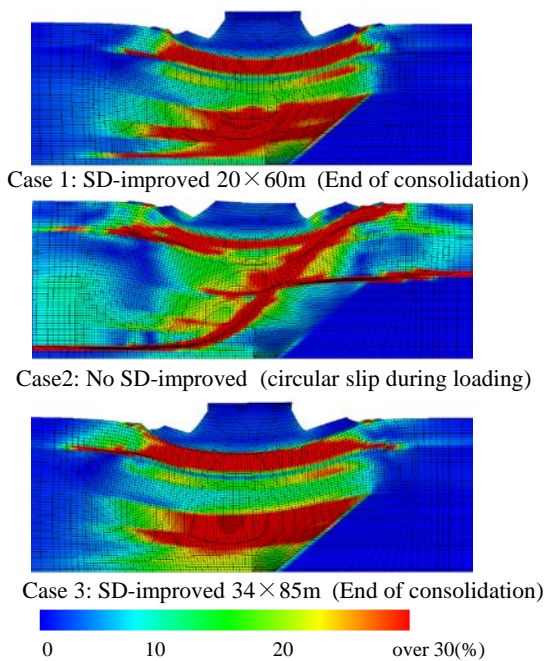


Fig. 10 Effect of ground improvement by SD method (distribution of shear strain).

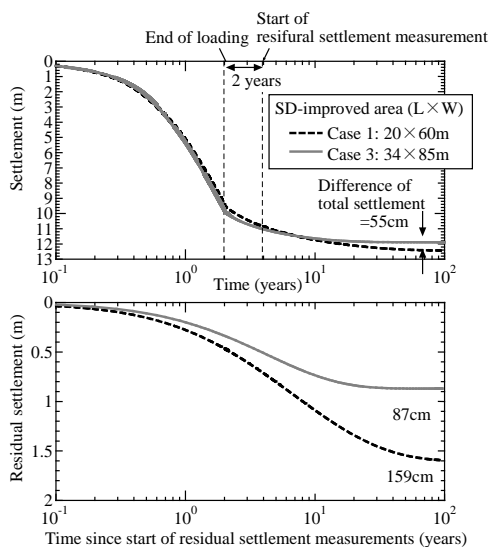


Fig. 11 Comparison of SD-improvement area.

Effects of Slow Banking Method

Table 1 shows the results of simulations performed under the same conditions as Case 3 above, but with lower (1.5 cm/day) or higher (3.0 cm/day) rates of embankment loading. Reducing the rate of loading allowed for greater drainage during loading, which resulted not only in earlier convergence of settlement and reduction in residual settlement but also a slight but significant reduction in total settlement.

Figure 12 shows the effect of loading rate to the lateral displacement at the ends of construction and consolidation. The lower loading rate was effective in reducing lateral displacement of the shallow ground layers, and although the data is not presented here due to space constraints, also upheaval of the soil surface. And it resulted in an earlier shift from outward deformation to inward deformation in the embankment loading process.

Table 1 Effect of rate of embankment loading

Loading rate (increase in embankment thickness/day)	Total settlement (m)	Residual settlement (cm)
1.5 cm/day	11.7	74
2.35 cm/day	11.9	87
3.0 cm/day	12.0	94

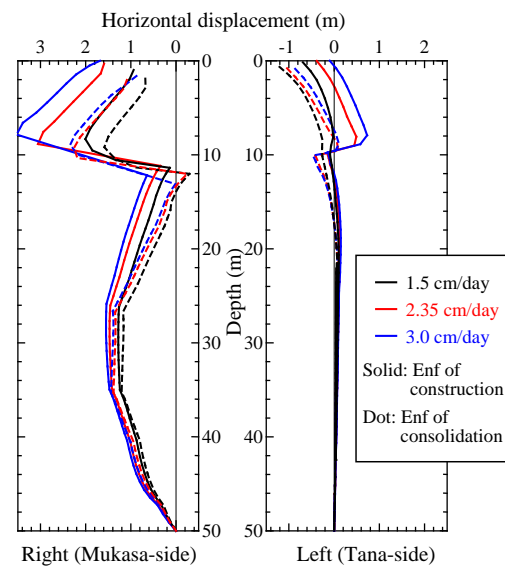


Fig. 12 Horizontal displacements directly below the both toes of slope (comparison of loading rate).

Although construction of the test embankment shown in Figure 6 was managed so that the embankment “height” generally increased at a rate of 3.0 cm/day, because obvious settlement occurred during embankment construction, the actual rate of loading per unit time (increase in embankment

“thickness”) was higher than that specified in any of the above-mentioned simulations. Although no catastrophic slip failure occurred, this rapid construction resulted in increased lateral displacement and upheaval.

As discussed above, slow embankment loading is effective not only for increasing stability during construction but also for reducing residual settlement and impacts on the surrounding ground. When it is not possible to secure adequate time for embankment construction, combinations with other countermeasures such as vacuum consolidation should be considered.

Effects of Lightweight Banking Method

Figure 13 shows the effect of weight reduction of the existing embankment with lightweight materials. For simplicity, the reduced loading was represented by removal of the embankment in the calculation. Greater reduction in loading was accompanied by less residual settlement and earlier occurrence of settlement convergence. Furthermore, although not shown here, it was demonstrated that greater reduction in loading resulted in reduced inward deformation of the ground surrounding the embankment.

Based on these simulations, the culvert in actual construction site has been designed with a 1.2-m freeboard, and in order to reduce differential settlement, the material of the embankment in the vicinity of the culvert is planned to be replaced with lightweight material.

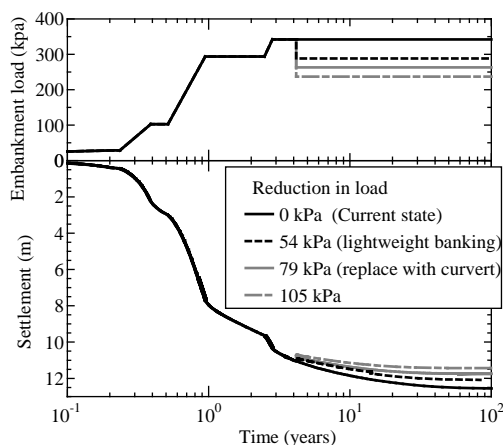


Fig. 13 Effect of weight reduction of the existing embankment.

CONCLUSION

In this paper, simulations of the large-scale settlement in excess of 11 m and predictions of future settlement of ultra-soft ground containing peat due to loading by a test embankment were performed by deducing the initial in-situ conditions of ground considering the effect of the depositional

environment, the “disturbances” that might occur during sampling and the heterogeneity among samples. In this region, it is expected that the increase in artesian pressure accompanying the increase in soft ground thickness resulted in a continuous low effective pressure in the deep ground. Therefore, when a relatively high embankment was constructed on the ground, the stress states of even deep layers exceed the consolidation yield stress easily and rapid compressions were occurred. The undrained shear deformation resulting from poor permeability causes the large lateral displacement to occur, which can lead in severe cases to slip failure. Furthermore, because rapid compression occurs even under drained conditions in peat layers, permeability improvement using SD, reduction of the loading rate, and the more drastic countermeasure of reducing the load itself are effective in increasing stability during loading, reducing the deformation of the ground surrounding the embankment, and reducing residual settlement after the enter into service.

REFERENCES

- [1] Inagaki, M., Sakakibara, K., Yamada, K., Tashiro M, Noda T, Nakano A and Asaoka A, “Estimation of the initial conditions of a very soft peat ground which causes large delayed settlement due to test embankment loading”, 45th Japan National Conf. on Geotechnical Engineering, 2011, pp.751-752 (in Japanese).
- [2] Asaoka A and Noda T, “All soils all states all round geo-analysis integration”, Int. Workshop on Constitutive Modeling - Development, Implementation, Evaluation, and Application, Hong Kong, China, 2007, pp.11-27.
- [3] Noda T, Asaoka A and Nakano M, “Soil-water coupled finite deformation analysis based on a rate-type equation of motion incorporating the SYS Cam-clay model”, Soils and Foundations, Vol.48. 6, 2008, pp.771-790.
- [4] Asaoka A, Noda T, Yamada E, Kaneda K and Nakano M, “An elasto-plastic description of two distinct volume change mechanisms of soils”, Soils and Foundations, Vol. 42. 5, 2002, pp.47-57.
- [5] Inagaki M, Nakano M, Noda T, Tashiro M and Asaoka A, “Proposal of a Simple Method for Judging Naturally Deposited Clay Grounds Exhibiting Large Long-term Settlement due to Embankment Loading”, Soils and Foundations, Vol.50.1, 2010, pp.109-122.
- [6] Tashiro M, Noda T, Inagaki M, Nakano M and Asaoka A, “Prediction of Settlement in Natural Deposited Clay Ground with Risk of Large Residual Settlement due to Embankment Loading”, Soils and Foundations, Vol.51.1, 2011, pp.133-149.

SEISMIC RESPONSE ANALYSIS OF GEOTECHNICAL STRUCTURES BUILT OF CEMENT-TREATED DREDGED SOIL

Takayuki Sakai¹, Masaki Nakano² and Shotaro Yamada³

¹ Disaster Mitigation Research Center, Nagoya University, Japan;

^{2,3} Civil Engineering, Nagoya University, Japan

ABSTRACT

In this study, firstly, the mechanical properties of cement-treated soil are comprehended through laboratory tests. Secondly, the mechanical test results are reproduced by using an elasto-plastic constitutive model based on the action of the soil skeleton structure, SYS Cam-clay model to determine material constants and to interpret the treatment principle based on concept of soil skeletal structure. Finally, seismic response analysis of geotechnical cement-treated structure is carried out through a soil-water coupled finite deformation analysis code, GEOASIA. The new findings are summarized as follows; 1) The effective stress path of the cement-treated soil approached the tension cut-off line as the cement content is large and confining stress is low. 2) The cement-treated soil can be regarded as a highly structured and heavily overconsolidated soil. 3) In the case of this study (the treated soil with a cement content of 50kg/m³), the cement-treated geotechnical structure does not exhibit failure, a large deformation by earthquake, and a long-term deformation occurs partition bank after earthquake.

Keywords: cement soil stabilization, mechanical property, seismic response analysis, dredged soil

INTRODUCTION

About 1.0 million m³ of dredged soil is produced annually in Nagoya Bay. However, the temporary storage capacity for the soil at Nagoya Port Island is limited, so effective use of the soil has become a pressing issue. A method of the effective use is to improve the dredged soil by adding cement to use as a geomaterial. Currently, a lot of cement-treated soil is used for reclamation, backfilling and surface stabilization in the bay area. However, cement-treated geotechnical structures are almost designed by unconfined compression strength. Besides, seismic stability of these structures has not been examined.

In this study, firstly, the mechanical properties of cement-treated soil are comprehended through laboratory tests. Secondly, the mechanical test results are reproduced by using an elasto-plastic constitutive model based on the action of the soil skeleton structure, SYS Cam-clay model as in [1] to determine material constants and to interpret the treatment principle based on a concept of soil skeleton structure. Finally, seismic response analysis of cement-treated structures is carried out through a soil-water coupled finite deformation analysis code, GEOASIA as in [2].

MECHANICAL BEHAVIOR OF CEMENT-TREATED SOIL

The Pneumatic Flow Method was adopted as a soil improvement method in this study. This method

is widely used for improvement of dredged soil. In this method, the cement-treated soil must have suitable fluidity and strength. The unconfined compressive with strength in curing 28days should be more 100kPa, and flow value should be 90-100mm. In the result of design of mixture, water content of dredged soil is $w=120\%$ and cement content is of $C=50\text{kg/m}^3$. Compared with the specimen of $C=50\text{kg/m}^3$, the specimens of cement content is $C=30, 70 \text{ kg/m}^3$ are made.

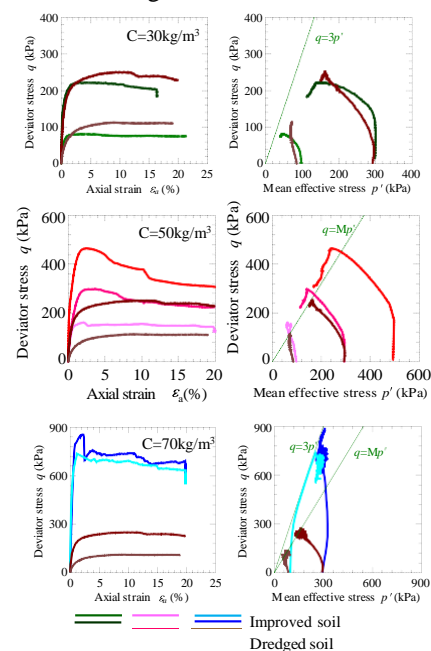


Fig. 1 Triaxial test results for cement-treated soil

Figure 1 shows the test results for the CU triaxial tests for the cement-treated soils. For the specimen of $C=30$ and 50kg/m^3 , an increase in deviator stress q associated with a reduction in mean effective stress p' is seen before peak q . Also, a reduction in q associated with a reduction in p' is seen after peak strength. This behavior is similar to the one soft natural deposited clay. Peak strength of $C=50\text{kg/m}^3$ is higher than $C=30\text{kg/m}^3$. For cement content of $C=70\text{kg/m}^3$, the peak of q appears clearly and the stiffness is very high. The peak of $C=70\text{kg/m}^3$ is the highest of all the cement-treated soils. The effective stress path goes up to almost vertical in the beginning of shearing. From the above, the peak of q increases as the cement content increases. The effective stress path of the cement-treated soil approaches the tension cut-off line as the cement content is large and confining stress is low. Especially, the results of cement content $C=70\text{kg/m}^3$ under confining pressure 100kPa shows q becomes large along the tension cut-off line. This is special behavior of cement-treated soil of high cement content.

Figure 2 shows the result of oedometer tests for the cement-treated soils and a dredged soil. A compression line of the cement-treated soil is located above a compression line of the dredged soil. As the cement content increases, the consolidation yield stress increase and compression value decreases up to consolidation yield stress. But, high compressibility appears when the consolidation yield stress is exceeded.

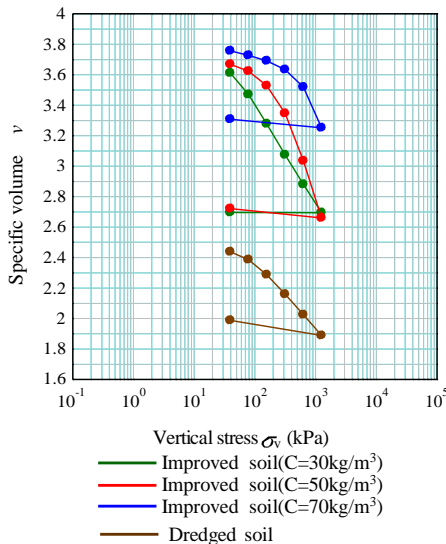


Fig. 2 Oedometer test for cement-treated soil

REPRODUCING MECHANICAL BEHAVIOR OF CEMENT-TREATED SOIL BY SYS CAM-CLAY MODEL

The past study as in [3] shows elasto-plastic parameters are obtained by reproducing mechanical

behavior of remolded samples of treated soil. Figure 3 shows the results of reproducing mechanical behavior of remolded treated soil of each cement content. The solid line shows result of calculation and the dotted line shows results of laboratory test. The mechanical behavior of each remolded treated soils is reproduced by the SYS Cam-clay model. The elasto-plastic parameters are determined by the reproduction is shown in Table1. Elasto-plastic parameters change with cement content. Therefore, it can be seen that the cement-treated soil becomes the different materials according to cement constant. As the cement content increases, compression index and NCL intercept (98.1 kPa) increase especially.

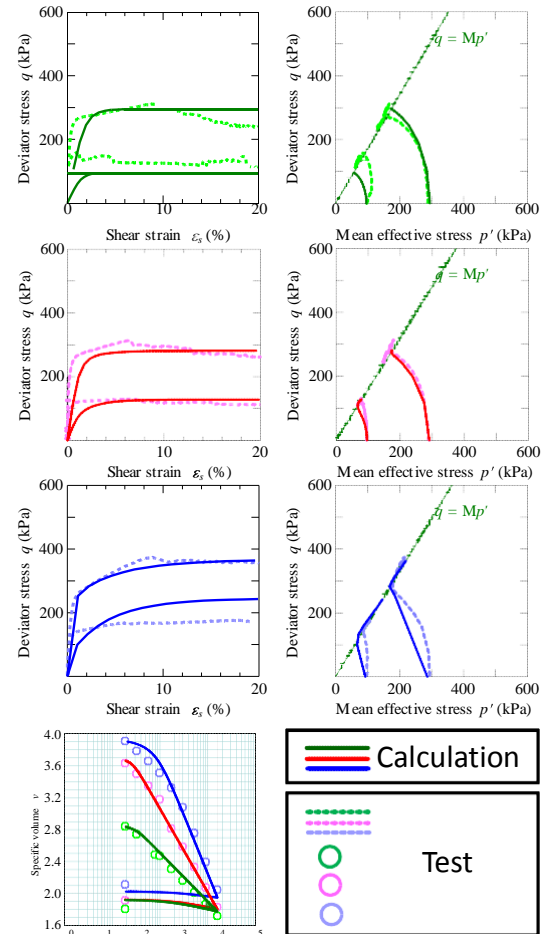


Fig. 3 Reproducing mechanical behavior of remolded treated soil

Table 1 Elasto-plastic parameters

Plasticity parameters		Treated soil		
Cement content (kg/m ³)		C=30	C=50	C=70
Compression index	λ	0.21	0.36	0.51
Swelling index	κ	0.05	0.05	0.03
Limit state constant	M	1.70	1.60	1.65
NCL intercept	N	2.70	3.40	4.20
Poisson's ratio	ν	0.30	0.30	0.30

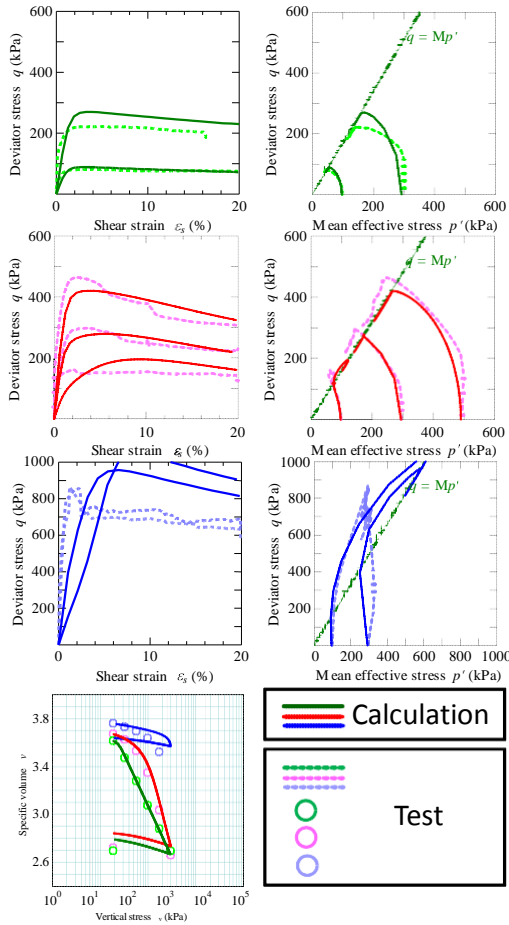


Fig. 4 Reproducing mechanical behavior of cement-treated soil

Table 2 Evolution rule parameters and Initial values

Plasticity parameters		Treated soil		
Cement content (kg/m ³)		C=30	C=50	C=70
Evolution rule parameters				
Normal consolidated soil index	m	0.01	0.60	5.00
Structure degradation index	a	0.25	0.60	1.50
	b	1.00	1.00	1.00
	c	1.00	1.00	1.00
Plastic shear:plastic compression	c _s	0.20	0.50	0.10
Rotation hardening index	b _r	0.00	0.00	0.00
Rotation hardening limit index	m _b	0.50	0.50	0.50
Initial values				
Overconsolidation ratio	1/R ₀	1.03	20.9	63.8
Extent of structure	1/R ₀ [*]	260	10.00	5.00
Vertical stress	σ _v	19.6	19.6	19.6
Specific volume	v ₀	3.94	3.75	3.80
Stress ratio	η ₀	0.00	0.00	0.00
Initial anisotropy	ζ ₀	0.00	0.00	0.00

The mechanical behaviors of the cement-treated soils are reproduced using obtained elasto-plastic parameters. Figure 4 shows the results of reproducing mechanical behavior of cement-treated soil. The solid line shows result of calculation and the dotted line shows results of laboratory test. The mechanical behavior of each cement-treated soils is reproduced mostly. However, as the cement content

increased, reproducibility goes down.. Especially, it is difficult to reproduce softening behavior with plastic compression above critical state line. Table 2 shows evolution rule parameters and initial values for this calculation. The cement-treated soil can be regarded as a highly structured and heavily overconsolidated soil. It can be seen that large deformation is caused when cement-treated soil decays structure and loses overconsolidation. The overconsolidation ratio increased as the cement content increased, on the other hand, the degree of structure reduced. Evolution rule parameters changes by cement constant. As the cement content increases, the rate of change of the evolution of structure and overconsolidation increases.

SEISMIC RESPONSE ANALYSIS OF GEOTECHNICAL STRUCTURES BUILT BY PNEUMATIC FLOW METHOD

In this section, the seismic response analysis of a partition bank. The partition bank was constructed in the Third Port Island in Nagoya Port through the Pneumatic Flow Method to prevent contamination from spreading. The partition bank is not an eternal structure because the partition bank is buried by dredged soil in the future. Therefore, its function is not lost by a settlement and a deformation of the bank, and its stability problem is important.

Figure 5 shows a cross-section of the partition bank and seabed ground used in the analysis. The seabed ground is modeled in reference to boring investigation.

The bank is 10m in height with the slopes of 1:1.5. Its crown is 14m in width. The reclamation of the dredged soil on the west of the bank is 10m in height and on the east 16m in height. The hydraulic boundary conditions are as shown in Fig. 5; the edges on the left, right and bottom are impermeable boundaries, and the top edge is a permeable boundary (atmosphere). Also, the water level is

always constant at the ground surface. In other words, the ground and embankment are always saturated. The movement boundary conditions before the earthquake are as follows: all the nodes on the left and right edges are fixed horizontally, and all the nodes on the bottom surface are fixed horizontally and vertically. During and after the earthquake, the boundary condition which gives simple shear deformation to the finite elements of a side boundary as in [4] was set to both lateral sides of the ground. In addition, in order to prevent all reflections of the seismic waves, a viscous boundary as in [5] is provided in the horizontal direction on the bottom edge during the earthquake.

Table 3 Material constants of seabed ground for this calculation

		AcL	As	AcU3
Elasto-plastic parameters				
Compression index	λ	0.18	0.05	0.18
Swelling index κ		0.019	0.0002	0.019
Limit state constant	M	1.60	1.1	1.60
NCL intercept N		2.22	1.95	2.22
Poisson's ratio ν		0.30	0.30	0.30
Evolution rule parameters				
Normal consolidated soil index	m	3.00	0.12	3.00
Structure degradation index	a	0.30	5.00	0.30
	b	1.10	1.00	1.10
	c	1.00	1.00	1.00
Plastic shear:plastic compression	c_s	0.40	1.00	0.40
Rotation hardening index	b_r	0.00	3.00	0.00
Rotation hardening limit index	m_b	1.00	0.90	1.00
Initial values				
Overconsolidation ratio	$1/R_0$	distribution depending on earth pressure		
Extent of structure	$1/R_0^*$	4.00	2.00	5.00
Specific volume	v_0	2.20	1.84	2.30
Stress ratio	η_0	0.23	0.23	0.23
Initial anisotropy	ζ_0	0.00	0.23	0.00
		AcU2	AcU1	Bc
Elasto-plastic parameters				
Compression index	λ	0.18	0.18	0.18
Swelling index κ		0.019	0.019	0.019
Limit state constant	M	1.60	1.60	1.60
NCL intercept N		2.22	2.22	2.22
Poisson's ratio ν		0.30	0.30	0.30
Evolution rule parameters				
Normal consolidated soil index	m	3.00	3.00	3.00
Structure degradation index	a	0.30	0.30	0.30
	b	1.10	1.10	1.10
	c	1.00	1.00	1.00
Plastic shear:plastic compression	c_s	0.40	0.40	0.40
Rotation hardening index	b_r	0.00	0.00	0.00
Rotation hardening limit index	m_b	1.00	1.00	1.00
Initial values				
Overconsolidation ratio	$1/R_0$	distribution depending on earth pressure		
Extent of structure	$1/R_0^*$	7.00	9.00	20.0
Specific volume	v_0	2.40	2.5	2.80
Stress ratio	η_0	0.23	0.23	0.00
Initial anisotropy	ζ_0	0.00	0.00	0.00

Table 2 shows material constants and initial values of seabed ground. Material constants and initial value are obtained by reproducing mechanical behavior of seabed soils as in [6]. AcU layer is very soft clay, As layer is rather dense sand and AcL layer is rather soft clay. The material constant of partition bank is the ones of cement-treated soil ($C=50\text{kg/m}^3$). Figure 6 shows input seismic wave. The input seismic wave is Tokai-Tonankai-Nankai multiple-segment type earthquake as in [7]. This analysis intends for construction of partition bank, reclamation, consolidation after construction, to input seismic wave and consolidation after the earthquake by using GEOASIA. Process of construction of partition bank and reclamation of the dredged soil is the same as a real construction history generally. After 20 years finishing construction, the seismic wave is inputted into the ground finish construction after 20 years. The calculations are carried out under the conditions of plane strain over the entire cross-section.

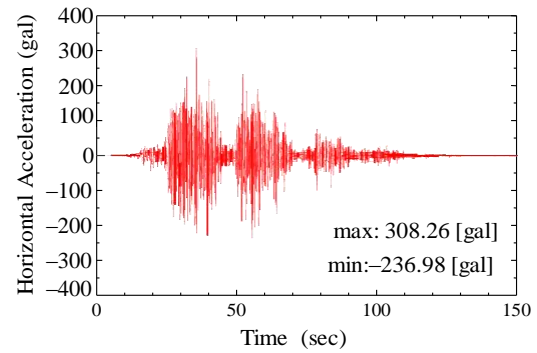


Fig. 6 Input seismic wave

Figure 7 shows the shear strain distribution before and after the earthquake, 12 years after the earthquake and end of calculation. The bank does not exhibit failure, while a long-term deformation

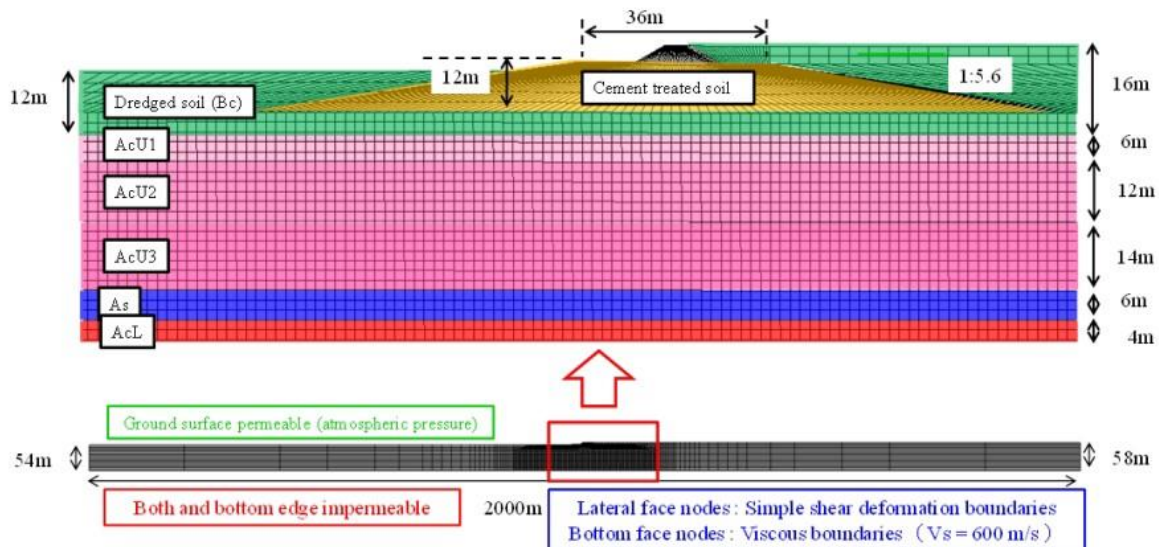


Fig. 5 A cross-section of the partition bank and seabed ground used in the analysis

occurs after earthquake. The largest shear strain occurs at the layer of dredged soil under the partition bank, while the shear strain due to the earthquake does not extend at the partition bank. After the earthquake, the shear strain on the boundary between the embankment and the ground increases.

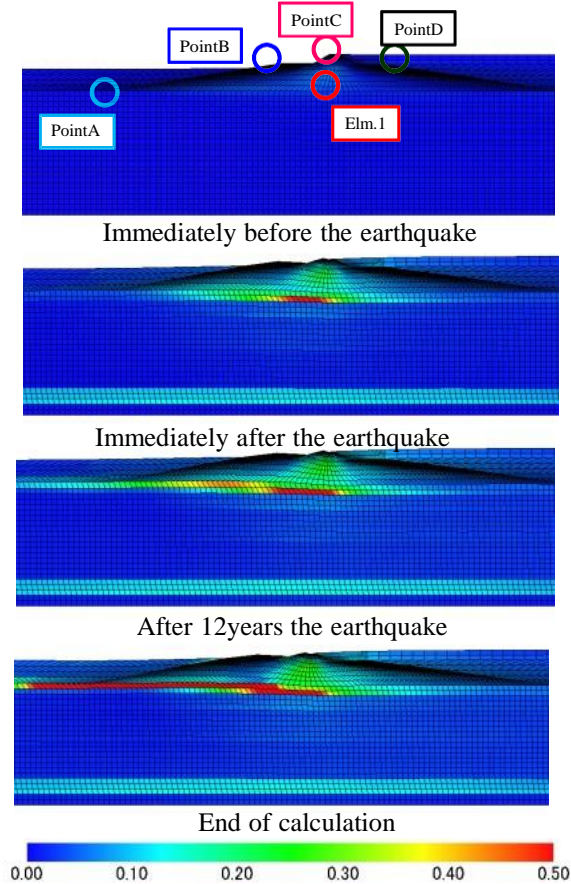


Fig. 7 Shear strain distribution

Figure 8 shows settlement during and after earthquake. The amount of settlement at the crown is about 1.5m. After the earthquake, settlement progressed in the long term and about 3.2m settlement occurred finally. Settlement of only partition bank is about 1.0m. In the west, partition bank and reclamation soil swelled during earthquake and the amount of settlement was smaller than east finally.

Figure 9 shows the mechanical behavior of the element 1 in Figure 7. The mean effective stress of cement treated soil decreased by shearing repeatedly due to the earthquake, and the shear strain progresses to around 15%. For the degree of structure and overconsolidation, the cement treated soil does not lose structure and overconsolidation. Therefore, the cement treated soil keep stability and the partition bank is not failure by the earthquake.

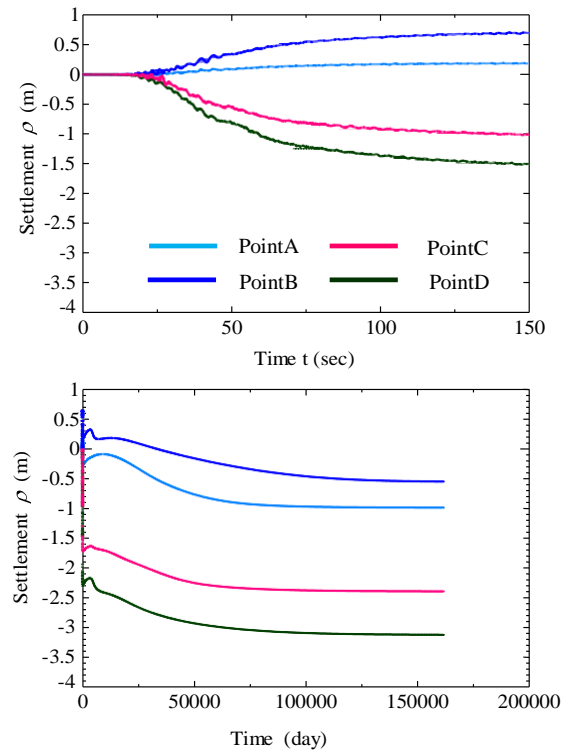


Fig. 8 Settlement

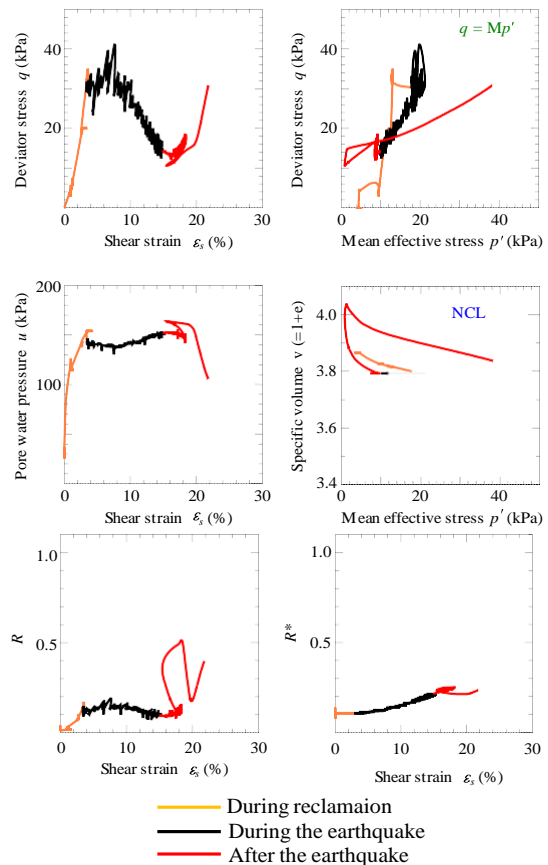


Fig. 9 Element behavior of cement-treated soil

CONCLUSION

In this study, firstly, the mechanical properties of cement-treated soil are comprehended. Secondly, the mechanical test results are reproduced by using an elasto-plastic constitutive model based on the action of the soil skeleton structure, SYS Cam-clay model to interpret the treatment principle based on concept of soil skeletal structure. Finally, seismic response analysis of cement-treated structures is carried out through a soil-water coupled finite deformation analysis.

The following are the conclusions obtained from this study.

1) The mechanical behavior of cement-treated soil is similar to soft natural deposited clay. In other words, the behavior of cement-treated soil shows like behavior of overconsolidated and high structured soil. The increase in peak strength and stiffness associated with the increase in cement content. Especially, cement-treated soil with $C=50$ kg/m³ shows clear improved effect. The effective stress path of the cement-treated soil approached the tension cut-off line as the cement content is large and confining stress is low.

2) The mechanical behavior is reproduced by the SYS Cam-clay model. It is difficult to reproduce softening behavior with plastic compression above critical state line. The obtained parameters shows the cement-treated soil can be regarded as a highly structured and heavily overconsolidated soil. The overconsolidation ratio increased as the cement content increased, on the other hand, the value of structure reduced. Also, the compression index and the NCL intercept (98.1 kPa) increase and the rate of change of the evolution of structure and overconsolidation increases. The cement-treated soil becomes the different materials according to cement constant.

3) In the case of this study (the treated soil with a cement content of 50kg/m³), the partition bank does not exhibit failure, and a long-term deformation occurs after earthquake. A characteristic of the cement-treated soil is that large deformation is caused when cement-treated soil loses structure and

overconsolidation. However, cement-treated soil does not lose structure and overconsolidation. Therefore, the cement-treated soil keep stability and the Partition bank is not failure by the earthquake.

REFERENCES

- [1] Asaoka A., Noda T., Yamada E., Kaneda K. and Nakano M. 2002. "An elasto-plastic description of two distinct volume change mechanisms of soils" *Soils and Foundations* Vol. 42, No. 6, 2002, pp.47–57.
- [2] Noda T., Asaoka A. and Nakano M. "Soil-water coupled finite deformation analysis based on a rate-type equation of motion incorporating the SYS Cam-slay model" *Soils and Foundations* Vol. 48, No. 6, 2008, pp. 771–790.
- [3] Yamada, S., Nakano, M., Noda, T., Horiuchi, S., and Yoda, H., Sasayama, T. "Mechanical behaviour of cement-treated soil and remolded cement-treated soil and simulation of that by SYS Cam-clay model", 45th Japan National Conf. on Geotechnical Engineering, 2011, pp.643-644 (in Japanese).
- [4] Yoshimi, Y. and Fukutake, K., "Physics and evaluation technology of soil liquefaction including mitigation method", 2005, Gihodo-Shuppan. (in Japanese)
- [5] Joyner W.B., Albert T. and Chen F. "Calculation of nonlinear ground response in earthquakes. *Bulletin of the Seismological Society of America*" Vol. 65, No. 5, 1975, pp. 1315–1336
- [6] Sun. K., "Seismic analysis of reclaimed ground with dredged soil and effective utilization of dredged soil treated stabilizers", Doctor Dissertation, Department of Civil Engineering, Nagoya University, Nagoya, Japan. (in Japanese), 2010, pp.43-53.
- [7] Central Disaster Prevention Council Cabinet Office, Government of Japan, Published data of Tohankai-Nankai earthquake, 2004

DEVELOPMENT OF SPH METHOD WITH AN ELASTO-PLASTIC CONSTITUTIVE MODEL CONSIDERING SOIL SKELETON STRUCTURE AND ITS APPLICATION TO EXCAVATION PROBLEMS

Hideto Nonoyama¹, Masaki Nakano¹ and Toshihiro Noda²

¹Department of Civil Engineering, Nagoya University, Japan;

² Disaster Mitigation Research Center, Nagoya University, Japan

ABSTRACT

In order to solve large deformation problem of geomaterials, the SPH method is used which is a kind of particle method based on the mesh-less Lagrangian scheme. The method can solve large deformation problems without mesh distortion. Moreover, it can handle the governing equations and existing constitutive models for geomaterials based on a continuum mechanics. To express various states of the soil, the elasto-plastic constitutive model taking account of soil skeleton structure is introduced into the method. In this paper, the excavation problems from loose to dense sand ground are simulated. In order to determine the material parameters and initial value of the evolution rules, a simulation of simple shear test is carried out. From a series of the numerical results, it is demonstrated that the different deformation behaviors for sand ground can be described by the states of soil.

Keywords: SPH method, Elasto-plastic Constitutive Model, Excavation Analysis

INTRODUCTION

In the field of geotechnical engineering, the infinitesimal deformation theory and the finite deformation theory have been widely used in conventional deformation analysis of geomaterials. These theories have been successfully implemented in several numerical methods, such as the finite element method (FEM). As a result, it is now possible to predict a variety of geomaterial deformation behaviors. However, there are still difficulties in large deformation analysis. It is therefore difficult to solve the entire deformation process, from the initial state to subsequent large deformations. In conventional methods such as the FEM, numerical instabilities arise in the large deformation region due to mesh distortion. In the large deformation problems, important problems such as slope failure and lateral flow of liquefied ground are included from the engineering viewpoint. To solve such problems, various numerical approaches have been proposed.

In this study, in order to solve large deformation problem of geomaterial, the Smoothed Particle Hydrodynamics (SPH) method [1], [2], a kind of particle method based on the mesh-less Lagrangian scheme, is used. The method can solve large deformation problems without mesh distortion. Moreover, it can handle the governing equations and existing constitutive models for geomaterials, since it is based on a continuum approximation. The method has already been used to solve many types of geotechnical problems, and a number of

interesting achievements have been published (e.g., [3]). However, since the geomaterial is assumed to be an elastic or elastic-perfectly plastic material in many researches using the SPH method, it is necessary to introduce the high performance elasto-plastic constitutive model to describe complicated deformation behavior of geomaterial precisely. In this study, the elasto-plastic constitutive model taking account of soil skeleton structure [4], [5] is introduced into the SPH method.

In this paper, firstly, basic theory of the SPH method and formulation of the SPH method based on solid mechanics are summarized. Then, the excavation problems from loose to dense sand ground are solved. In order to determine the material parameters and initial value of the evolution rules, a simulation of simple shear test is carried out. From a series of the numerical results, the effectiveness of the SPH method with the constitutive model of high performance is demonstrated.

NUMERICAL METHOD

Basic Theory of the SPH Method

In the SPH method, an object is expressed as an assembly of particles. If the motions of the particles are solved individually, the deformation behavior of the continuum cannot be represented by this technique. In order to treat an object as a continuum, a unique interpolation theory is used. This interpolation theory includes two key approximations: a kernel approximation and a

particle approximation. The first step is a kernel approximation of the field functions. The kernel approximations are based on neighboring particles β located at points x^β within the support domain κ^{dh} of a smoothing function W for a reference particle α located at point x^α , as shown in Fig.1. In the first step of the interpolation, we define a smoothed physical quantity $\langle f(x^\alpha) \rangle$ for the physical quantity $f(x^\alpha)$ at the reference particle α as follows,

$$\langle f(x^\alpha) \rangle = \int_{\Omega} f(x^\beta) W(r, h) dx^\beta \quad (1)$$

where $r = |x^\alpha - x^\beta|$, h is the radius of the influence domain, and Ω is the volume of the integral that contains x^α and x^β .

In the second step of the interpolation, the physical quantity $\langle f(x^\alpha) \rangle$ for the reference particle α is expressed as the summation of the distribution of the assumed physical quantities $f(x^\beta)$ for each particle. Thus, the physical quantity can be expressed in terms of N discrete points:

$$\langle f(x^\alpha) \rangle = \sum_{\beta} \frac{m^\beta}{\rho^\beta} f(x^\beta) W^{\alpha\beta} \quad (2)$$

where m^β is the mass, and ρ^β is the density of neighboring particles β . N is the numbers of neighboring particles in the support domain, and $W^{\alpha\beta}$ is the smoothing function that expressed the contribution from the neighboring particles β to the reference particle α . In this study, Cubic spline function [6] is used.

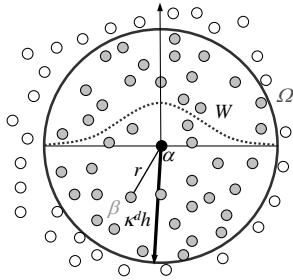


Fig. 1 An image of basic concept of the SPH method.

Equation (2) is a formula for evaluating a physical quantity via the SPH method. It is also possible to approximate the spatial gradient of a physical quantity in a similar way, using the spatial derivative of the smoothing function. The spatial derivative of Eq. (2) can be written as

$$\frac{\partial \langle f(x^\alpha) \rangle}{\partial x_i} = - \sum_{\beta} \frac{m^\beta}{\rho^\beta} f(x^\beta) \frac{\partial W^{\alpha\beta}}{\partial x_i} \quad (3)$$

Based on the two-step interpolation procedure, it

is possible to calculate any physical quantity and its special derivative of a physical quantity.

SPH Method Based on the Solid Mechanics

The governing equations used in this study are based on solid mechanics. The equation of continuity and the equation of motion can be defined as follows,

$$\frac{d\rho}{dt} = -\rho \frac{\partial u_i}{\partial x_i} \quad (4)$$

$$\frac{du_i}{dt} = \frac{1}{\rho} \frac{\partial \sigma_{ij}}{\partial x_j} + F_i \quad (5)$$

where u_i is the velocity vector, ρ is the density, σ_{ij} is the stress tensor and F_i is the external force vector. Applying the SPH interpolation theories, the equations are expressed as follows,

$$\frac{d\rho^\alpha}{dt} = - \sum_{\beta} m^\beta (u_i^\beta - u_i^\alpha) \frac{\partial W^{\alpha\beta}}{\partial x_i} \quad (6)$$

$$\frac{du_i^\alpha}{dt} = \sum_{\beta} m^\beta \left(\frac{\sigma_{ij}^\alpha}{(\rho^\alpha)^2} + \frac{\sigma_{ij}^\beta}{(\rho^\beta)^2} - \delta_{ij} \Pi^{\alpha\beta} \right) \frac{\partial W^{\alpha\beta}}{\partial x_j} + F_i^\alpha \quad (7)$$

where δ_{ij} is the Kronecker's delta, $\Pi^{\alpha\beta}$ is the artificial viscosity used to decrease the numerical instability. In this study, an artificial viscosity introduced in an earlier study [7] is employed.

In order to describe the complex behavior of soils, the Super-subloading Yield Surface Modified Cam-clay model [4], [5] are used as follows,

$$f(p', \eta) = M D \ln \frac{p'}{\tilde{p}'_0} + M D \ln \frac{M^2 + \eta^2}{M^2} + \quad (8)$$

$$M D (\ln R^* - \ln R) - \varepsilon_v^p = 0$$

$$D = \frac{\lambda - \kappa}{M(1 + e_0)} \quad (9)$$

where M is the critical state parameter, D is the dilatancy parameter, p' is the mean effective stress, $\eta (=q/p')$ is the stress ratio, q is the deviatoric stress, R is the inverse of degree of overconsolidation ratio, R^* is the inverse of degree of structure, ε_v^p is the plastic volume strain, λ is the compression index, κ is the swelling index and e_0 is the initial void ratio. The \tilde{p}'_0 is found to be the mean effective stress on the modified Cam-clay yield surface that coincides with the initial mean effective stress p'_0 of the soil in the reference state. The anisotropy is not taken into account in this study. Then, the evolution rules for sub and super loading defining the soil skeleton structures are expressed as follows, respectively:

$$\dot{R} = U \|\mathbf{D}^p\|, \quad U = -\frac{m}{D} \ln R \quad (10)$$

$$\dot{R}^* = U^* \left\{ (1 - c_s) (-D_v^p) + c_s \sqrt{\frac{2}{3}} \|D_s^p\| \right\}, \quad (11)$$

$$U^* = \frac{a}{D} R^{*b} (1 - R^*)^c$$

where $\|\cdot\|$ is the norm, \mathbf{D}^p is the plastic stretching, D_v^p and D_s^p are the volume and deviation components of plastic stretching. U and U^* are the positive scalar functions of R and R^* . The parameter groups for the evolution rules in Eqs. (10), (11) all consists of constants, and from their respective functions we may call m the degradation index of overconsolidation, a , b , c , c_s the degradation indices of structure.

NUMERICAL RESULTS

Determination of Material Parameters and Initial Values of the Evolution rules

In order to determine the material parameters and initial values of the evolution rules, a simulation of simple shear test under plane strain condition is carried out using the SPH method considering the soil skeleton structure. Figure 2 illustrates the numerical model used in the simulation. As the figure indicates, the specimen is a square object (10 cm by 10 cm), and a virtual area surrounded the specimen to prevent errors at the free surface. The solid line denotes the initial configuration of the specimen, and the dashed line denotes the configuration after deformation. In the simulation, the virtual area is forcibly deformed with a constant displacement to represent simple shear conditions, and the deformation of the specimen is calculated. The parameters used in this simulation are summarized in Tables 1 and 2. Four different cases (case1: loose sand, case2: medium dense sand, case3: dense sand, case4: very dense sand) are considered in this simulation. Also, parameters of typical sand under constant mean stress and four different values of the initial degree of overconsolidation, structure and the initial specific volume are utilized.

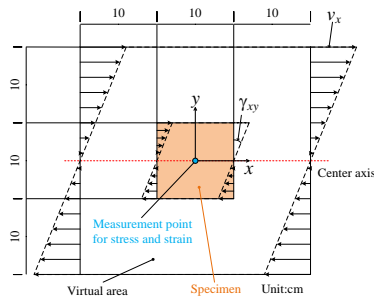


Fig. 2 Numerical model.

Table 1 Material parameters

<elasto-plastic parameters>		
compression index	λ	0.050
swelling index	κ	0.012
critical state constant	M	1.0
NCL intercept	N	1.98
Poisson's ratio	ν	0.3
<evolution parameters>		
degradation index of overconsolidation	m	0.06
degradation index of structure	a	2.2
degradation index of structure	b, c, c_s	1.0

Table 2 Initial values

Case		1	2	3	4
<initial value>					
initial degree of overconsolidation	$1/R_0$	1.25	4.23	6.58	39.65
initial degree of structure	$1/R_0^+$	73.62	2.84	2.01	1.13
initial specific volume	v_0	2.08	1.91	1.88	1.79
initial mean stress	p_0 [kPa]	294			

Figure 3 shows obtained (a) shear stress - shear strain relation, (b) stress paths, (c) R - shear strain relation and (d) R^* - shear strain relation at the center of the specimen.

In the case 1 for a loose sand, q increased while with decreasing p , then q exhibits the peak. After that, p and q move toward zero. In the case 2 for a medium dense sand, after reducing q , q increased again, accompanied by an increase in p . In the cases 3 and 4 for dense and very dense sand, q did not decrease, and q increased with the increase of p . The decay of the structure with shearing occurs, and its gradient for loose sand is greater than that for dense sand as shown in Fig. 3(d).

From these numerical results, although it is a constant volume condition, it is possible to simulate the shear behaviors of loose and dense sand using the SPH method, shown in the previous research [8].

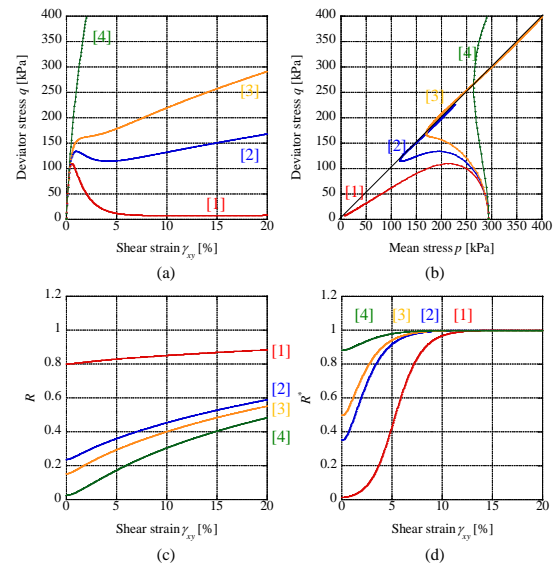


Fig. 3 Numerical results.

Excavation Analysis from Loose to Dense Sand Ground

An excavation analysis from loose to dense sand ground is carried out, using the SPH method considering the soil skeleton structure. In this simulation, the depth of the initial ground is 9m and the width is 20m. After excavation, the slope height is set to be 4.5m and slope angle is set at an inclination of 1H: 2V. Figure 4 illustrates the numerical model in this simulation. As the figure shows, the time histories of displacements at the top of the slope (point A), R (points B, C, D), R^* (point B) are checked. The material parameters and initial values of the evolution rules determined by the simple shear simulation in the previous section are used. In this simulation, the ground has homogeneous initial structure and initial specific volume in the depth direction. Also, the initial overconsolidation ratio is calculated from the value of initial structure and initial specific volumes. The initial values of the evolution rules used in this simulation are listed in Table 3. The isotropic stress corresponding to static earth pressure is used as the initial stress. For the boundary conditions, the horizontal direction at the side wall of the ground is fixed, and the vertical direction is free. The horizontal and vertical directions at the bottom of the ground are fixed. Fixed boundary particles are used to describe the walls. In this simulation, a static analysis is carried out until the ground is stable, then removed particles instantly in the excavation area as shown in Fig.4.

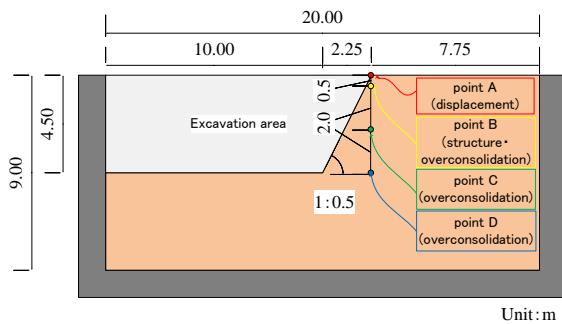


Fig. 4 Numerical model.

Table 3 Initial values

Case		1	2	3	4
<initial value>					
initial degree of overconsolidation	$1/R_0$	5.30	17.92	27.93	167.71
initial degree of structure	$1/R_0^*$	73.62	2.84	2.01	1.13
initial specific volume	v_0	2.08	1.91	1.88	1.79

Figure 5 shows the simulated displacement at the top of the slope at point A between before and after excavation for each case. Figures 6 and 7 show the time histories of R^* and R at point B between before

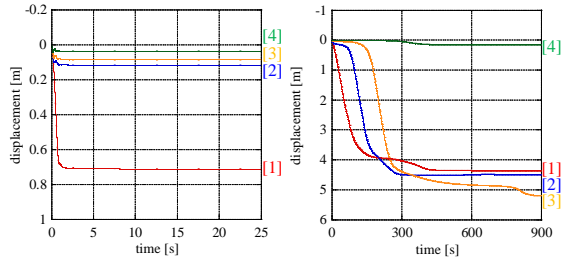
and after excavation. Figure 8 shows the time history of R at points C and D after excavation. Figure 9 shows the distribution of accumulation of the maximum shear strain ($\gamma_{\max} = (\epsilon_1 - \epsilon_2)/2$) at different times for cases 1 to 4, respectively. Figure 10 shows the distribution of the overconsolidation ratio after excavation (0, 900s) for cases 1 to 4, respectively. Boundary particles were used for the wall, but are not shown in these figures.

Before excavation, in the case 1 for loose sand, it was found that the structure decayed along with the compression of the ground in the initial stage of static analysis as shown in Figs. 5(a) and 6(a). On the other hand, in the cases 2 to 4 for medium dense, dense and very dense sand, it was found that the compression of the grounds were not larger than one of case 1 in the stage of static analysis. For after excavation, the time of failure was different in each case as shown in Fig. 9. In the case 1, a slope failure was occurred immediately after excavation. Also, in the cases 2 and 3, a slope failure was occurred with the progression of time. In the case 4, a slope failure didn't occur.

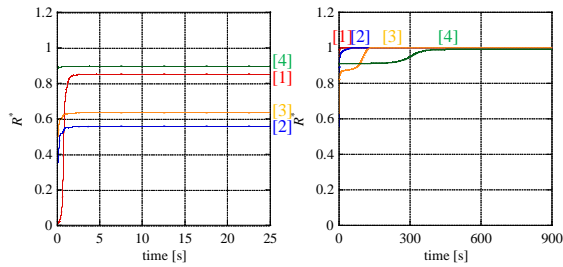
As the cause of these results, it was shown that the structure of loose sand can easily decay ($R^* \rightarrow 1.0$) compared with dense sand as shown in Fig. 3(d). Also, the ground was highly structured soil in this simulation as shown in Fig. 6(b), and the loss of overconsolidation ($R \rightarrow 1.0$) occurred after the decay of the structure ($R^* \rightarrow 1.0$) as shown in Figs. 6 and 7(b). Then, the slope failure occurred because the state of ground changed from overconsolidation state to normal state. In the case 1, as the results of focusing on the time history of R at the failure point (Points B and C), the state of ground reached the normal state as shown in Figs. 7(b) and 8(a). Also, at the non-failure point (Point D), the state of ground remained the overconsolidation state as shown in Fig. 8(b). On the other hand, in the cases 2 and 3, it was confirmed that the time of failure was slower than the case 1, because the structure was less likely to decay than loose sand as shown in Fig. 6. In the cases 2 and 3, as with the case 1, the state of ground reached the normal state at failure point (Point B), and the state of ground remained the overconsolidation state at the non-failure point (Points C and D) as shown in Figs. 7 and 8. In the case 4, although the decay of the structure occurred after excavation, the state of the ground remains the overconsolidation state and the slope failure didn't occur because the loss of the overconsolidation didn't occur. As shown in Fig. 10, it could be seen that the loss of the overconsolidation at the ground, which is in the overconsolidation state after excavation, occurred along with the slope failure, and the state of the failure part changes normal state.

From a series of the numerical results, the different deformation behaviors from loose to dense sand are obtained qualitatively. With the

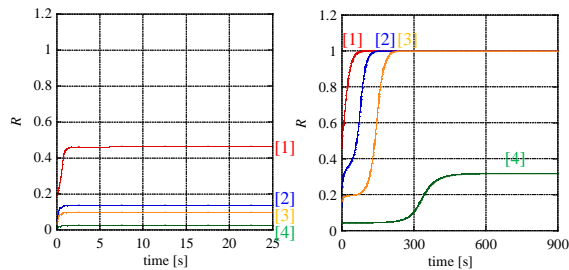
introduction of the Super-subloading Yield Surface Modified Cam-clay model into the SPH method, it can be said that it was applicable to the various ground, such as the highly structured naturally deposited grounds in the overconsolidation state, which is difficult to simulate using the simple constitutive model.



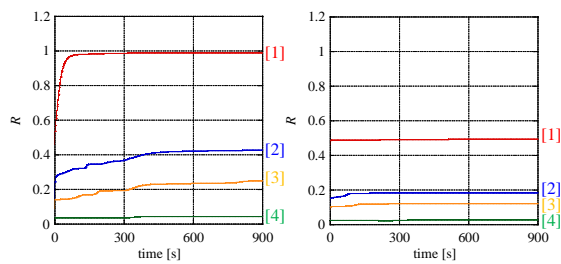
(a) before excavation (b) after excavation
Fig. 5 Time history of the displacement at the top of the slope at point A.



(a) before excavation (b) after excavation
Fig. 6 Time history of R^* at point B.



(a) before excavation (b) after excavation
Fig. 7 Time history of R at point B.



(a) point C (b) point D
Fig. 8 Time history of R .

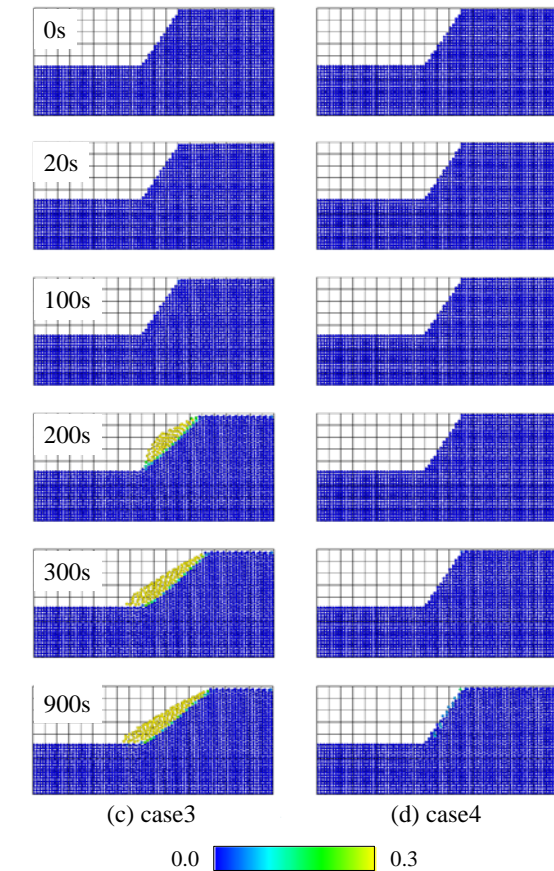
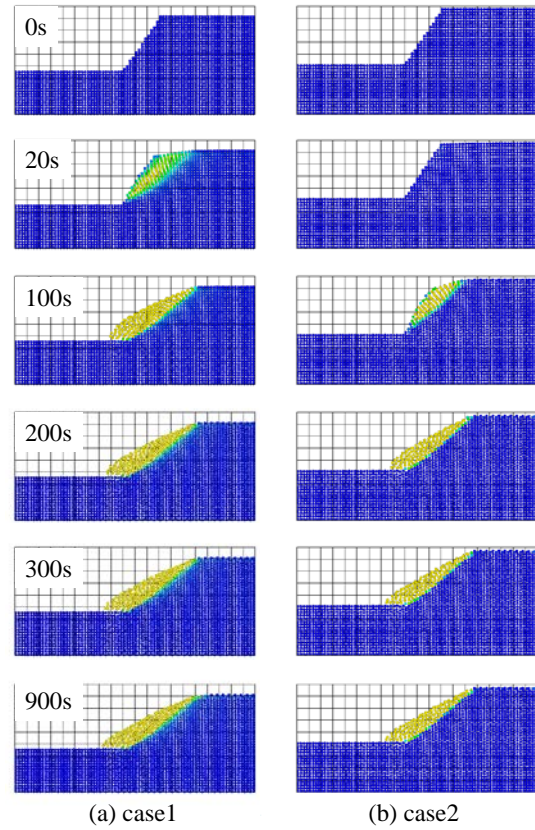


Fig. 9 Distribution of accumulation of the maximum shear strain at different time.

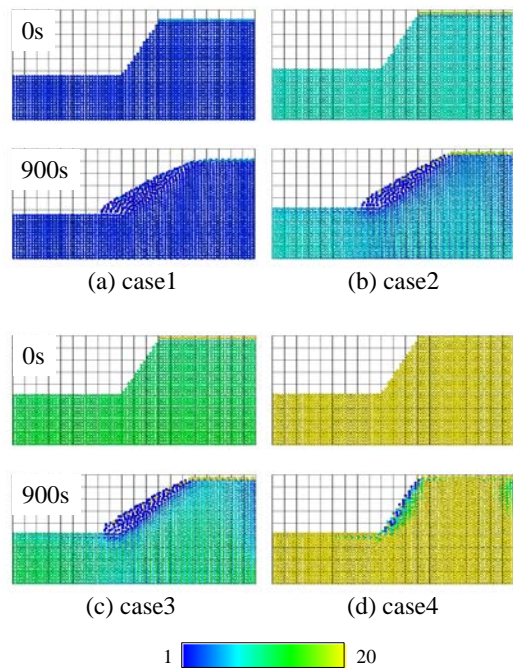


Fig. 10 Distribution of the overconsolidation ratio after excavation (0, 900s).

CONCLUSION

In this paper, the elasto-plastic constitutive model taking account of soil skeleton structure is introduced into the SPH method. Also, the simulation of the excavation problem from loose to dense sand ground was carried out. The findings are summarized as follows.

The excavation problems from loose to dense sand ground were simulated. In the case for loose sand ground, the slope failure occurred immediately after excavation. Also, in the cases for medium dense and dense sand ground, the slope failure was occurred with the progression of time after excavation. On the other hand, in the case for very dense sand ground, the slope failure didn't occur after excavation. As the cause of these results, the dense sand didn't easily decay the structure than the loose sand. Moreover, in the case that occurred slope failure, due to the loss of the overconsolidation after the decay of the structure, the states of ground changed from overconsolidation state to normal state.

As the issue on future, we should compare the experimental results and exciting the numerical

results for the validation and also try to improve the numerical method to be able to take into account the pore water pressure introducing the two phase mixture theory. Moreover, we want to reproduce deformation behavior of the real phenomenon of the ground in the framework of the SPH method with an elasto-plastic constitutive model considering soil skeleton structure.

REFERENCES

- [1] Lucy, L.B., "A numerical approach to the testing of the fission hypothesis", *Astronomical Journal*, Vol.82, 1977, pp.1023-1024.
- [2] Gingold, R.A. and Monaghan, J.J., "Smoothed particle hydrodynamics: theory and application to non-spherical stars", *Monthly Notices of the Royal Astronomical Society*, Vol.181, 1977, pp.375-389.
- [3] Maeda, K. and Sakai, M. "Development of seepage failure analysis procedure of granular ground with Smoothed Particle Hydrodynamics (SPH) method", *Journal of Applied Mechanics, JSCE*, Vol.7, 2004, pp.775-786 (in Japanese).
- [4] Asaoka, A., Nakano, M. and Noda, T., "Superloading yield surface concept for highly structured soil behavior", *Soils and Foundations*, Vol.40, No.2, 2000, pp.99-110.
- [5] Asaoka, A., Noda, T., Yamada, E., Kaneda, K. and Nakano, M., "An elasto-plastic description of two distinct volume change mechanisms of soils", *Soil and Foundations*, Vol.42, No.5, 2002, pp.47-57.
- [6] Swegle, J.W., Attaway, S.W., Heinsteins, M.W., Mello, F.J. and Hicks, D.L., "An analysis of smoothed particle hydrodynamics", SAND93-2513, Sandia National Laboratories, Albuquerque, NM, 1994.
- [7] Monaghan, J.J. and Gingold, R.A., "Shock simulation by the particle method SPH", *Journal of Computational Physics*, Vol.52, pp.374-389, 1983.
- [8] Nakai, K., "An elasto-plastic constitutive modeling of soils based on the evolution laws describing decay of soil skeleton structure, loss of overconsolidation and development of anisotropy", PhD. Dissertation of Nagoya University, Japan, 2005.

SOUNDNESS EVALUATION OF THE EMBANKMENTS FOR EFFECTIVE MAINTENANCE AND LONG-LIFE OF SHIN-TOMEI EXPRESSWAY

Masaya Hinokio¹, Hiroshi Yamato¹, Kazunari Suzuki¹, Takayuki Sakai¹, Masaki Makano¹ and Minoru Kawaide²

¹Department of Civil Engineering, Nagoya University, Japan; ² Central Nippon Expressway Company Limited, Japan

ABSTRACT

Road embankments are important infrastructure for modern human life. And it is needed that the performance of such road embankment is always kept in good condition. For this, they must be well maintained. However, taking current economic situation into consideration, it is difficult to spend large amounts of cost on infrastructure construction; therefore, it is important to extend the life of existing structures effectively and economically. Generally, it has been thought that structures like embankments become more stable with time and hence the quality of the embankment is ensured through site management during construction. However, in recent years there have been a series of cases of embankment collapse due to heavy rains or earthquakes. In this study, the Surface Wave Propagation tests are carried out on embankments of Shin-Tomei expressway to evaluate soundness of the embankments. Furthermore, laboratory tests using the soil materials which are collected from those embankments are carried out to grasp mechanical properties of soils. The laboratory tests reveal that soils of embankments are easy to compress and have enough strength and stiffness. Moreover, from results of the Surface Wave Propagation tests, the S-wave velocity are more than 250m/sec at most places of embankment. From the Surface Wave Propagation test and laboratory test results, it is judged that these embankments are compacted enough.

Keywords: Embankment, Maintenance, Evaluation, Surface wave propagation test, Triaxial test

INTRODUCTION

In generally, construction of embankment is cheaper than other structures. In addition, it has been thought that embankments become more stable over time. If collapse do not occur during construction period, then embankments are safer afterwards. So, during construction appropriate management is carried out, after construction maintenance is generally not carried out. However, in recent years there have been a series of cases of embankment collapse due to heavy rains or earthquakes. In these cases, in addition to collapse due to unexpected external forces, the loss of soundness of the embankments themselves has contributed to collapse. In other words, stability of the embankment can be gradually lost with time due to differences in materials of soils or different surrounding situations. In particular, embankments are constructed on slope and valley where rainwater can easily infiltrate. They weaken the embankment and the loss of fine materials can easily reduce the soundness of embankment [1]. It is difficult to determine risk of such embankment from the surface before the occurrence of failure and collapse. Therefore, to perform effective maintenance, it is needed to confirm the soundness of the inner part of the

embankment.

To confirm the soundness of inner part of embankment, surface wave propagation tests [2] are carried out. In addition to surface wave propagation, various laboratory tests are performed to investigate mechanical characteristics of embankment. From results of surface wave propagation tests and Laboratory tests, it is tried to carry out a simple soundness evaluation of embankment.

SURFACE WAVE PROPAGATION TESTS

Surface wave propagation test is one of nondestructive inspection techniques. This test has these properties.

- Can find distribution of S wave velocity of the ground.
- Can measure without damage of structure.
- Can easily measure.

To perform effective maintenance, surface wave propagation tests have to be carried out at the three stages:

- 1) Inspection immediately after construction (new embankments only)
- 2) Periodic inspection after entering service
- 3) Inspection after deformation occurs

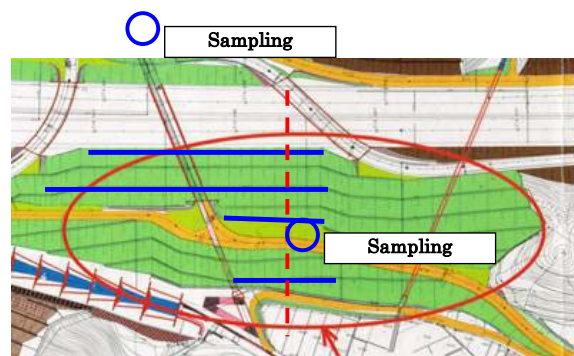
From a comparison of the results at each of the

stages, it is possible to make a simple evaluation



a) The plan view of site 1

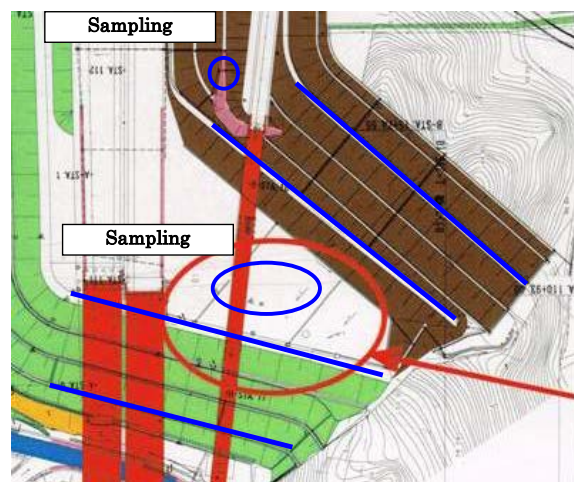
measurement sites. The blue lines indicate the



b) The plan view of site 2



c) The plan view of site 3



d) The plan view of site 4

Figure 1 The plan view of sites

from the change of results. In addition, by understanding the point where the change of the S wave velocity is remarkable, the point where a sounding test should be performed can be chosen.

An understanding of the initial state of the embankment is essential for these evaluations. Just before and just after start of service of Shin-Tomei Expressway, surface wave propagation tests are carried out on embankments not only to evaluate the internal state of embankments but also to obtain the initial value that would become the standard when a future soundness evaluation is carried out. 4 sites are selected and measurements are made along a total of 14 lines. The embankment of Site 1 consists of mudstone, sandstone and gravel as main materials. Site 2 consists of mudstone and gravel soil as main materials. Site 3 consists of sand and sandy gravel as main materials. Site 4 consists of clay slate, tuff, limestone and gravel as main materials. In addition to surface wave propagation test, various laboratory tests are performed using the soil samples which are gathered from 4 sites.

Figure 1 shows the plan views of the four

location of the measurement lines and blue circles indicate locations at which soils are sampled.

Figures 2, 3, 4 and 5 show the measurement results for the four sites. In these figures, the results of each measurement line locate them in the same way as location in the plan view. From these figures, S wave velocity is more than 250 m/sec at most locations, and the largest measurement at some locations is more than 500 m/sec. Therefore, it is considered that these embankments are compacted enough. When these tests are performed regularly, and the S wave velocity of the same point decreases, it is considered that stability of the embankment has decreased. Therefore a simple soundness judgment can be performed.

However, such an evaluation is a qualitative evaluation, and it is difficult to directly evaluate it quantitatively for all embankments. In addition, to know the initial soundness of the embankments quantitatively is difficult and to evaluate how much soundness is lost with passage of time is more difficult. Because mechanical properties and compaction properties differ greatly with the type of

soil, quantitative evaluation cannot be performed by

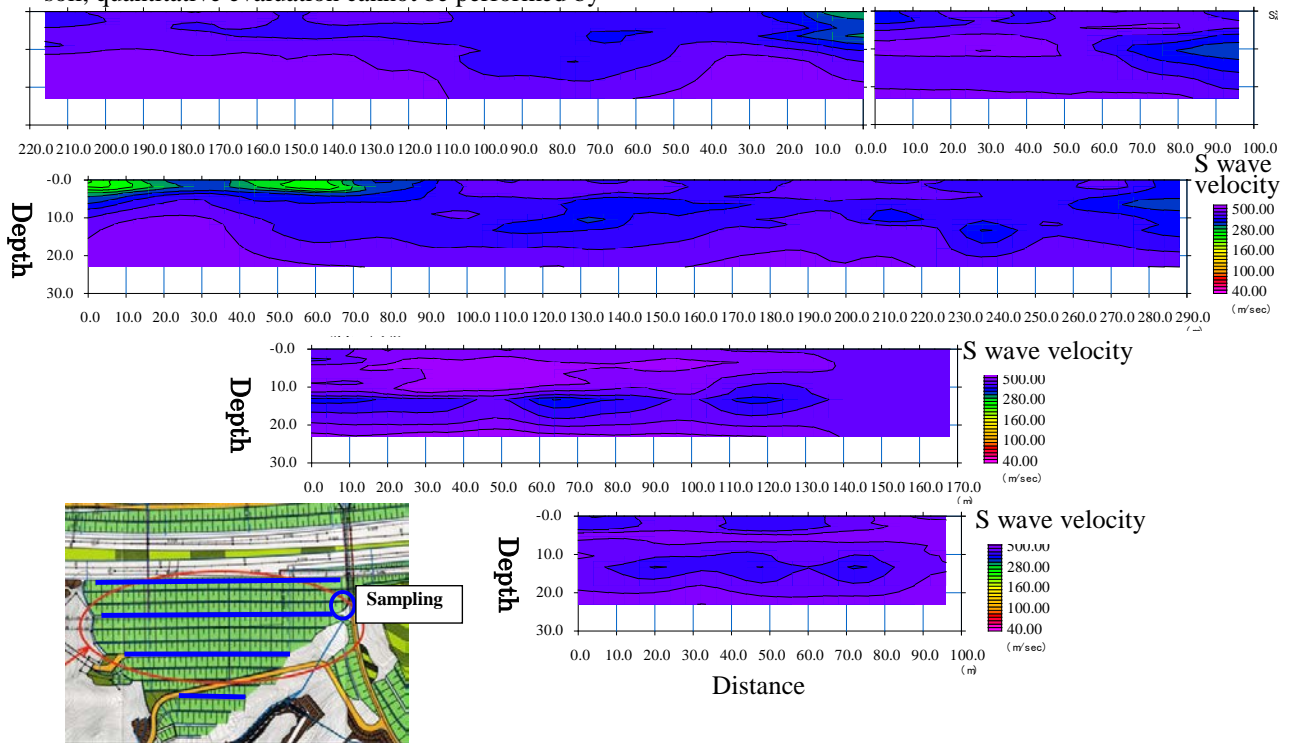


Figure 2 The result of site 1

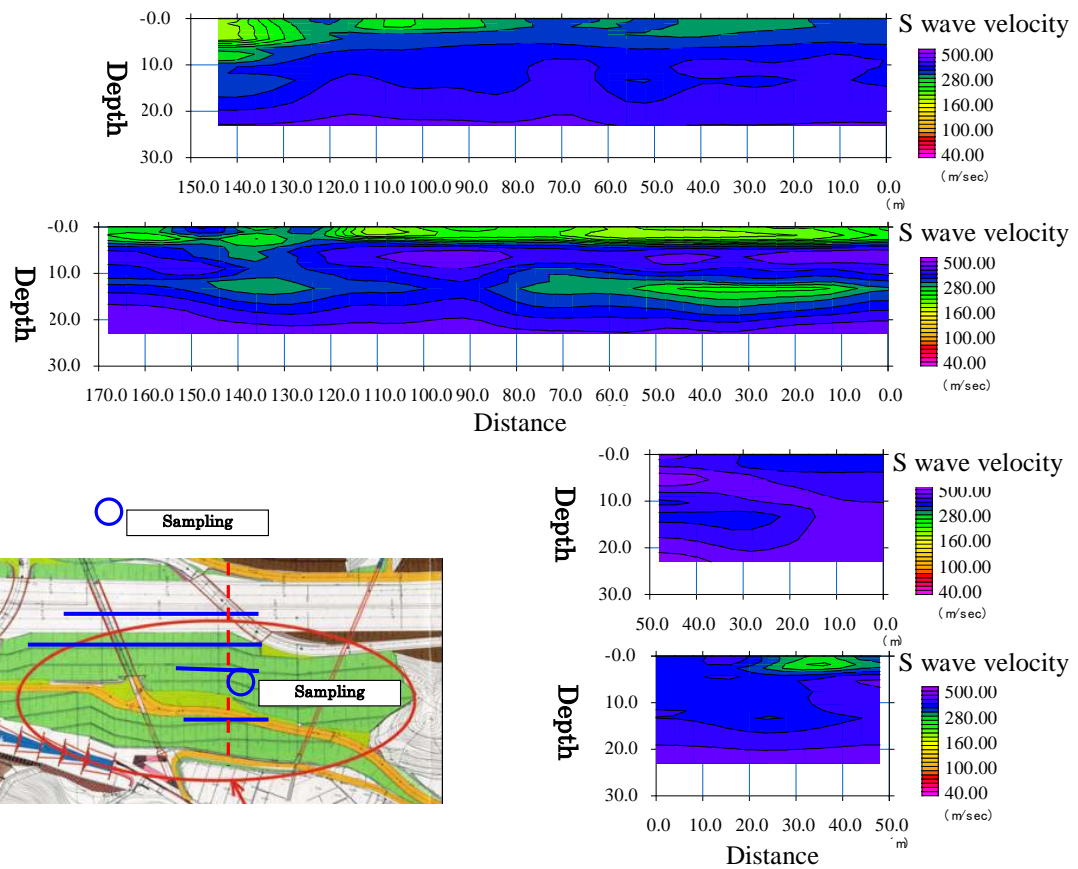


Figure 3 The result of site 2

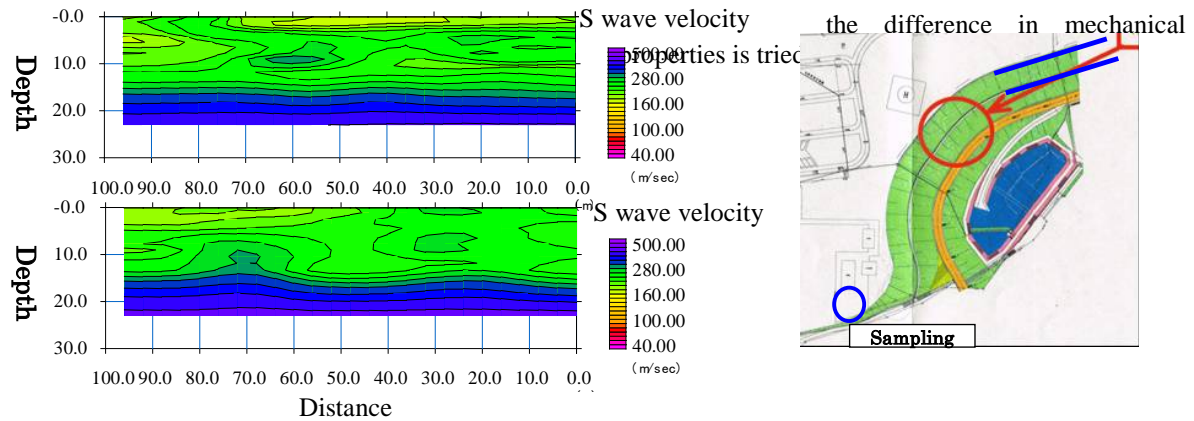


Figure 4 The result of site 3

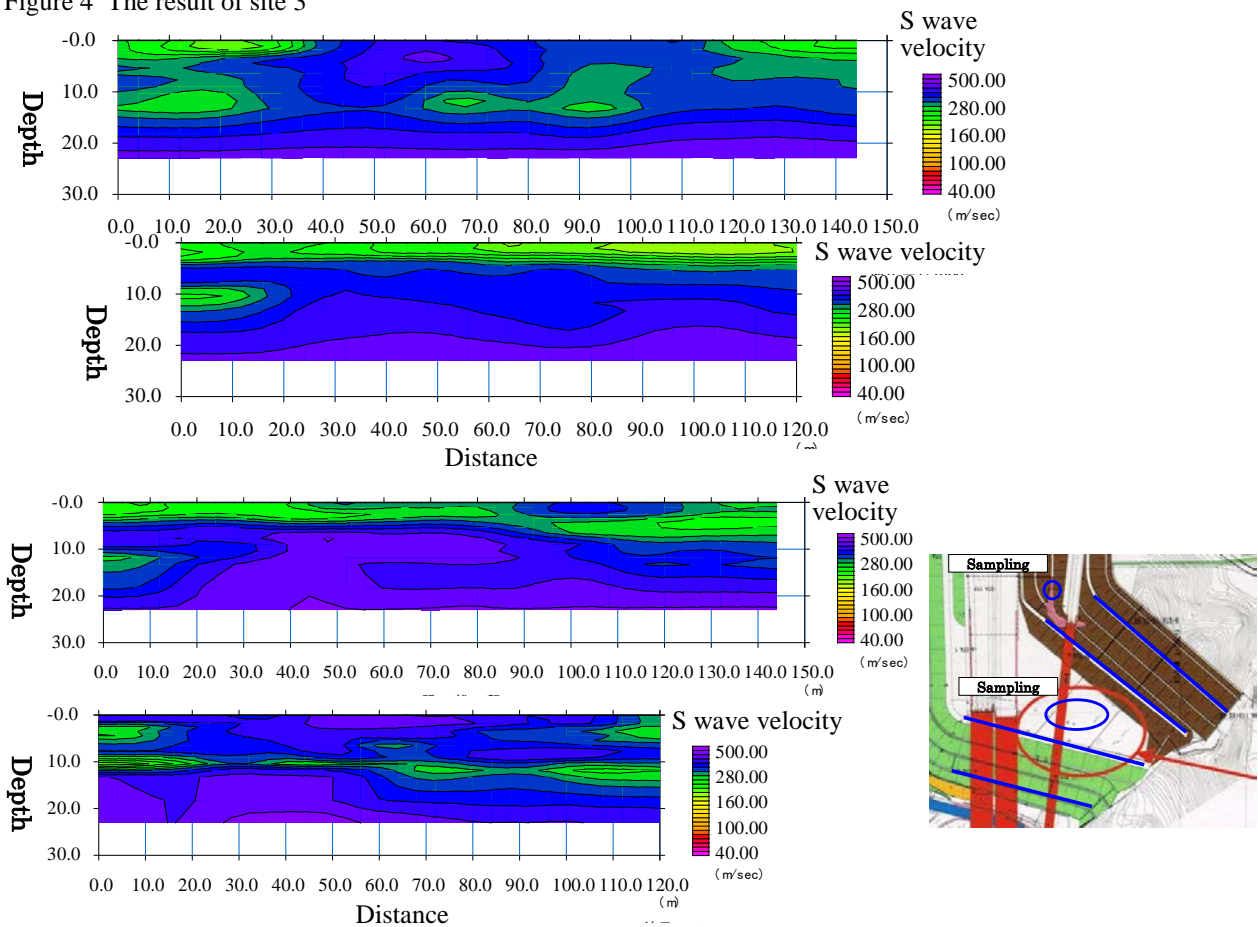


Figure 5 The result of site 4

only considering S wave velocity with disregard of the characteristics of the soil. In other words, because there is a large difference in soundness based on the differences of soil types of embankments, even if the same S wave velocity is measured, the valuation of soundness cannot be performed uniformly only with numerical values. Therefore, it is necessary to clarify S wave velocity and the association with mechanical properties, properties of compaction, and the density of the soil. Therefore, laboratory tests are performed for the different soils of embankments and an evaluation

LABORATORY TESTS

Laboratory tests are carried out using soils obtained from the sites of surface wave propagation tests. Six soil samples are collected. From Sites 1 and 3, one sample is collected. And two samples from each of Sites 2 and 4 are collected. Using each sample, density of soil particle test, particle size distribution test, compaction test, and undrained triaxial compression test are carried out. In particle size distribution test and compaction test are performed on samples adjusted below particle size of 19 mm. The results of density of soil particle test and particle size distribution test are shown in Table

Table 1 The Density of soil particle

Sample	site1	site2-a	site2-b	Site3	site4-a	site4-b
Density of soil particle ρ_s (g/cm ³)	2.762	2.708	2.700	2.679	2.822	2.685

1 and Figure 6. From this Table it can be shown that most soils have almost the same density of around 2.7g/cm³. From Figure 6, it is seen that Site 3 has the largest proportion of fine particle fraction than other sites. In consideration of these test results, compaction test and undrained triaxial compression test are carried out only for soils of site 2-a and 3. The soil of Site 3 has the largest proportion of most fine particle fraction and soil of Site 2-a has the largest proportion of coarse-grained fraction. And from S wave propagation test, result of site 3 is the lowest velocity.

The results of compaction test are shown in this Figure 7. From this Figure, it is understood that it is easy to compact soil of Site 2-a. This is because soil of Site 2-a comprises the most coarse-grained fraction.

Figures 8 and 9 show the results of undrained triaxial compression tests. The results include two additional specimens (7.5cm in diameter, 15cm in height) with degree of compaction Dc=85 and 100%. These figure show that shear strength greatly increases with the rise in degree of compaction. Furthermore, it is seen that the effective stress path of Dc=85% shows behavior similar to that of normally consolidated soil from q-p' relations. On the other hand, the effective stress path of Dc=100% rises along the critical state line. In addition, negative pore water pressure occurs by shear deformation, showing behavior similar to that of dense sand. From this, it can be supposed that overconsolidation accumulated by compaction. In addition, from v-p' relations, it can be supposed that

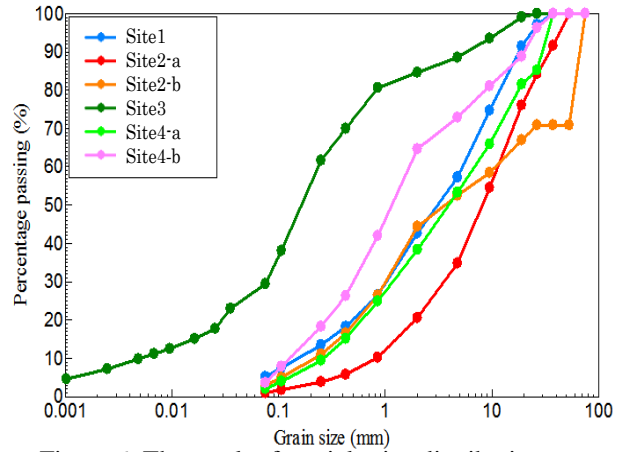


Figure 6 The result of particle size distribution test

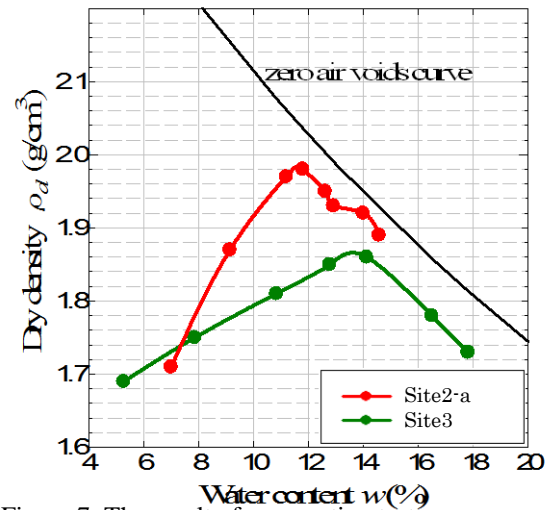


Figure 7 The result of compaction test

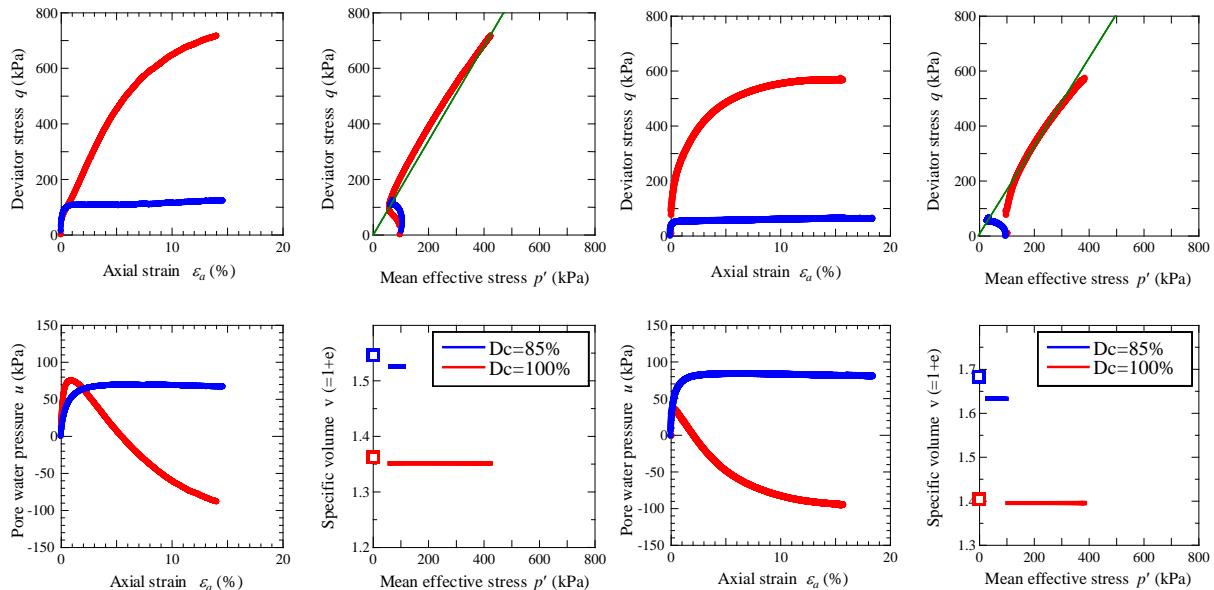


Figure 8 The result of triaxial tests(Site 2-a)

Figure 9 The result of triaxial tests(Site 3)

as the degree of compaction becomes higher, the quantity of compression becomes small. The aptitude of these two soils (Site 2-a and Site 3) is judged by comparing the soils with soils from Soil A (generally high quality soil) and Soil B (generally not good quality soil). Figure 10 and 11 show the results of particle size distribution test and compaction test. From result of compaction test, it can be seen that compaction curve of Site 2-a and Site 3 are steeper in comparison with that of Soil A, and the value of the peak is big. Therefore, soil of Site 2-a and Site 3 are easy to compact, and they are high quality soils.

Figure 12 shows the results of undrained triaxial compression test. From this Figure, it can be seen that the shear strengths of Site 2-a and Site 3 are bigger than those of Soil A and Soil B with $D_c=100\%$. And, the shear strength of Soil B does not rise with the rise in degree of compaction that much, but the shear strength of Site 2-a and Site 3 greatly rises with the rise in degree of compaction. From this, it is thought that compaction has a big effect on the increase in shear strength, and that these soils are suitable for embankment.

CONCLUSIONS

The following conclusions are obtained from Surface wave propagation tests and Laboratory tests.

- From surface wave propagation tests, the S wave velocity is more than 200m/sec. It shows the embankment were well compacted.
- From laboratory tests, the soils of embankments are easy to compact and the strength is high. Therefore, these soils are suitable for embankment.
- By checking distribution of S wave velocity in the ground two-dimensionally, it can be investigate a relative difference with the initial state. And it can be developed to simple evaluation of embankments.
- By collecting these information, the detailed position that should be examined is pinpointed.
- It leads to the rationalization of the maintenance and its high efficiency.

REFERENCES

- [1] M. Hinokio, M. Nakano and M. Kawaida, "Model tests of embankment subjected to seepage water", Proc. 6th International Workshop on New Frontiers in Computational Geotechnics, 2012.
- [2] Koichi Hayashi and Haruhiko Suzuki, "Surface-wave propagation in two-dimensional models and its application to near-surface S-wave delineation", The 5th SEGJ International Symposium -Imaging Technology-, 2001.

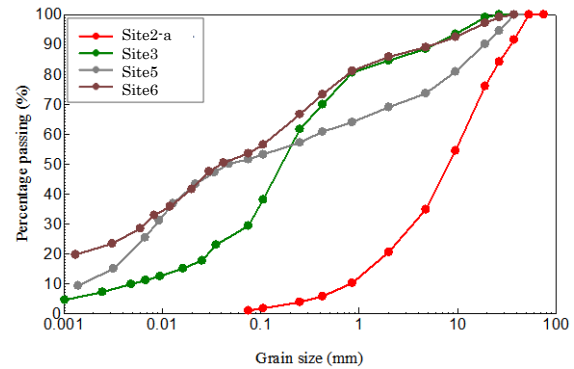


Figure 10 The result of particle size distribution test

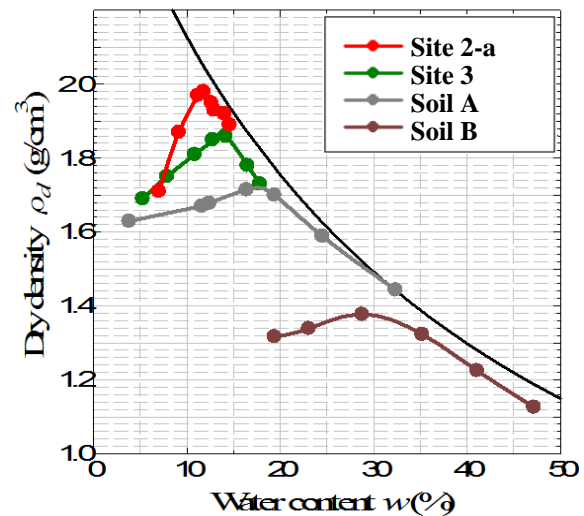


Figure 11 The result of compaction test

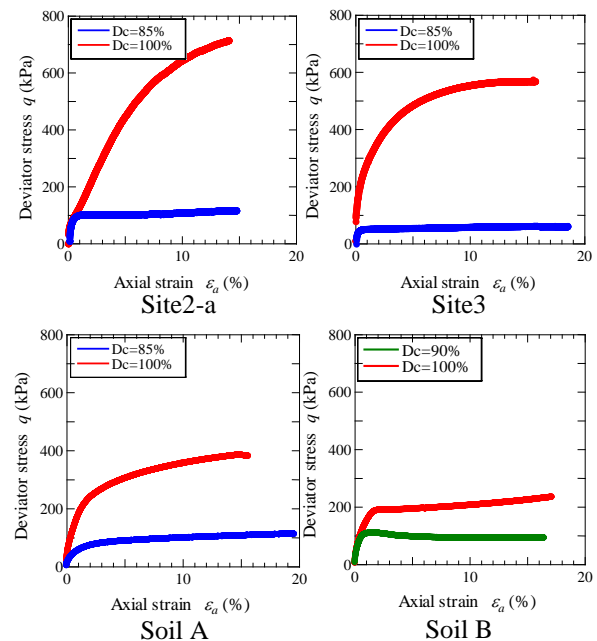


Figure 12 Comparison the other site

EVALUATION OF GLASS FIBERS DERIVED-THREE DIMENSIONAL GEOMATERIAL FOR PROBLEMATIC SOIL APPLICATIONS

Donovan Mujah¹, Hemanta Hazarika², Fauziah Ahmad³ and Muhammad Ekhlasur Rahman⁴

^{1,4} Department of Civil and Construction Engineering, Curtin University Sarawak, Malaysia

² Department of Civil and Structural Engineering, Kyushu University, Japan

³ School of Civil Engineering, Universiti Sains Malaysia, Malaysia

ABSTRACT

This research was aimed to study the potential reuse of recycled glass fiber-derived three dimensional geomaterial obtained from industrial glass fiber wastes to innovate a sustainable, cost-effective geosynthetic for ground improvement in problematic soil application. The ready availability, high tensile strength, lightweight and non-biodegradable characteristics of glass fibers further elevate their advantages as compared to the presently adopted geosynthetics in soft soil reinforcement condition. In this study, mechanical properties of rectangular strip shape, '8' shape and bolted screw '8' shape samples and pullout resistance force of glass fibers geomaterials were investigated by considering glass fibers' layer thickness, shape formation and orientation in a laboratory scale model. It was observed that the tensile and yield strengths of overall geomaterial samples significantly increase as strip layers thickness increase. Results from both the tensile strength and pullout resistance force indicated similar trend of increasing in strength values with test conducted using other type of geosynthetics in various soil media to simulate the action of different soil conditions at real sites.

Keywords: Recycled Glass Fibers, Ground Improvement, Tensile Strength, Pullout Resistance Force.

INTRODUCTION

Recently, researchers have engaged in the use of glass fibers as ground improving geomaterial [1]–[4]. [5] states that glass fibers' amorphous structures are able maintain internal stability along and across the fibers without further intrusion by foreign additives thus ensuring structural durability. In contrast to carbon fibers, glass fibers are able to undergo considerably more elongation before rupture when demonstrated by tensile test. Likewise, [1] reported that glass fiber is an attractive reinforcing agent because of their high strength, stiffness, high ratio of surface area to weight and dimensional stability.

Although earlier studies of glass fiber [1], [5] mentioned its unique properties however none of them described their potential use as reinforcing agent for ground improvement. In this paper, a new geomaterial called 8FG MAT made from recycled glass fibers derived from industrial glass wastes is proposed as a sustainably driven innovative effort for ground remediation technique whereby its mechanical properties in terms of the tensile strength and pullout resistance force were verified through laboratory tests in various soil conditions.

MATERIALS AND METHODOLOGY

Materials

Soil Samples

The laboratory work consisted of testing three soil samples reinforced and unreinforced with geomaterial were used in the experiment to simulate different kinds of soil conditions on site. The particle size distribution of the various soils used in the study is shown in Figure 1.

Glass Fibers

Polymeric glass fibers derived from industrial glass wastes were sterilized in an autoclave in a temperature of 120 °C – 150 °C for 1 hour to get rid of micro-organism impurities. Some portions of the fibers were coated with acrylic butadiene styrene (ABS) thermoplastic before proceed to mechanical testing. Subsequently, fiberglass yarns were molded into '8' shape form using a prefabricated mold 1000 mm length, 200 mm width and 150 mm height. Furthermore, strands of glass fibers were glued together using resin to ensure that glass fibers were

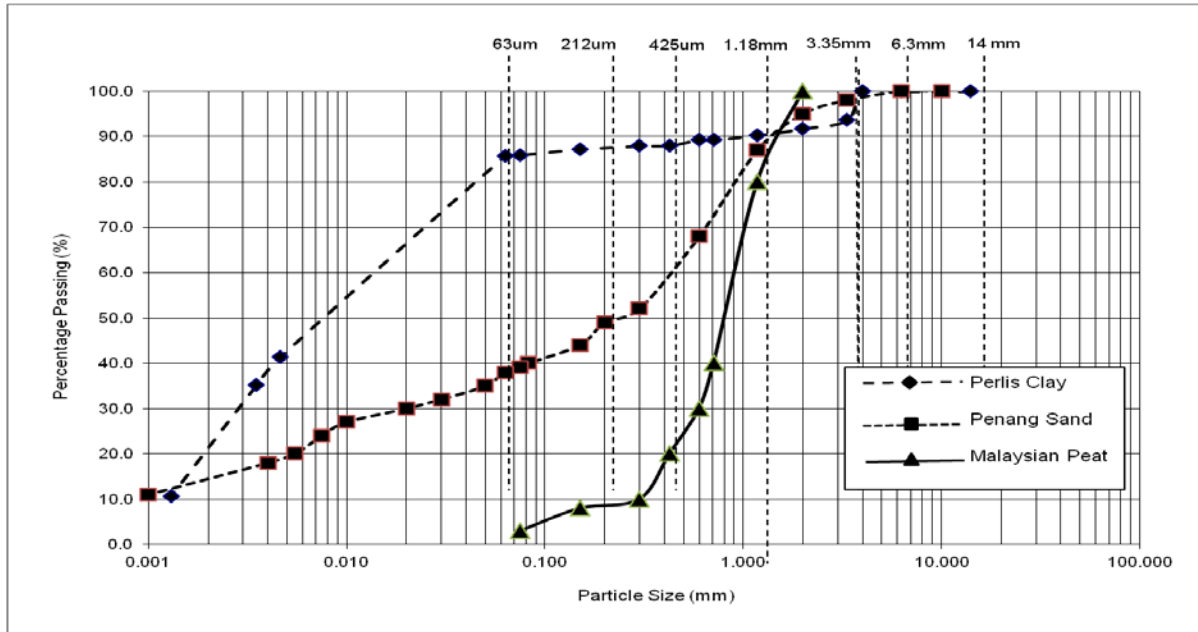


Fig. 1 Particle size distribution curves of the various soil media used in the study.

intently intact. Any presence of air bubbles were closely observed as they may lead to voids formation which may result into a lower volume of glass fibers thus affecting geomaterial's overall strength. The sample was then allowed to harden for two hours before mold was removed.

Samples of glass fiber geomaterials were prepared into four categories accordingly to their layers which included (a) 10 mm (b) 20 mm (c) 30 mm and (d) 40 mm thickness as shown in Figure 2.



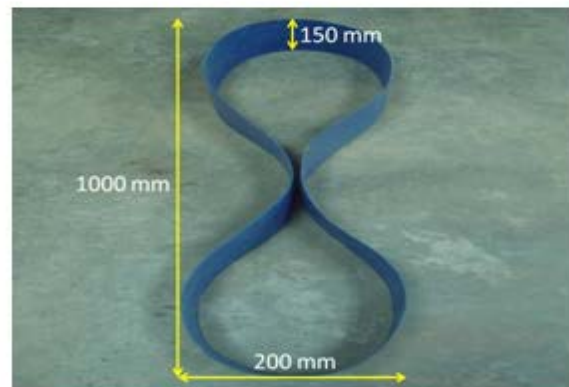
(a) Polymeric glass fibers



(c) '8' shape glass fiber geomaterial preparation



(b) Glass fiber strand by layer



(d) 8FG MAT dimension

Fig. 2 Step by step preparations of the 8FG MAT.

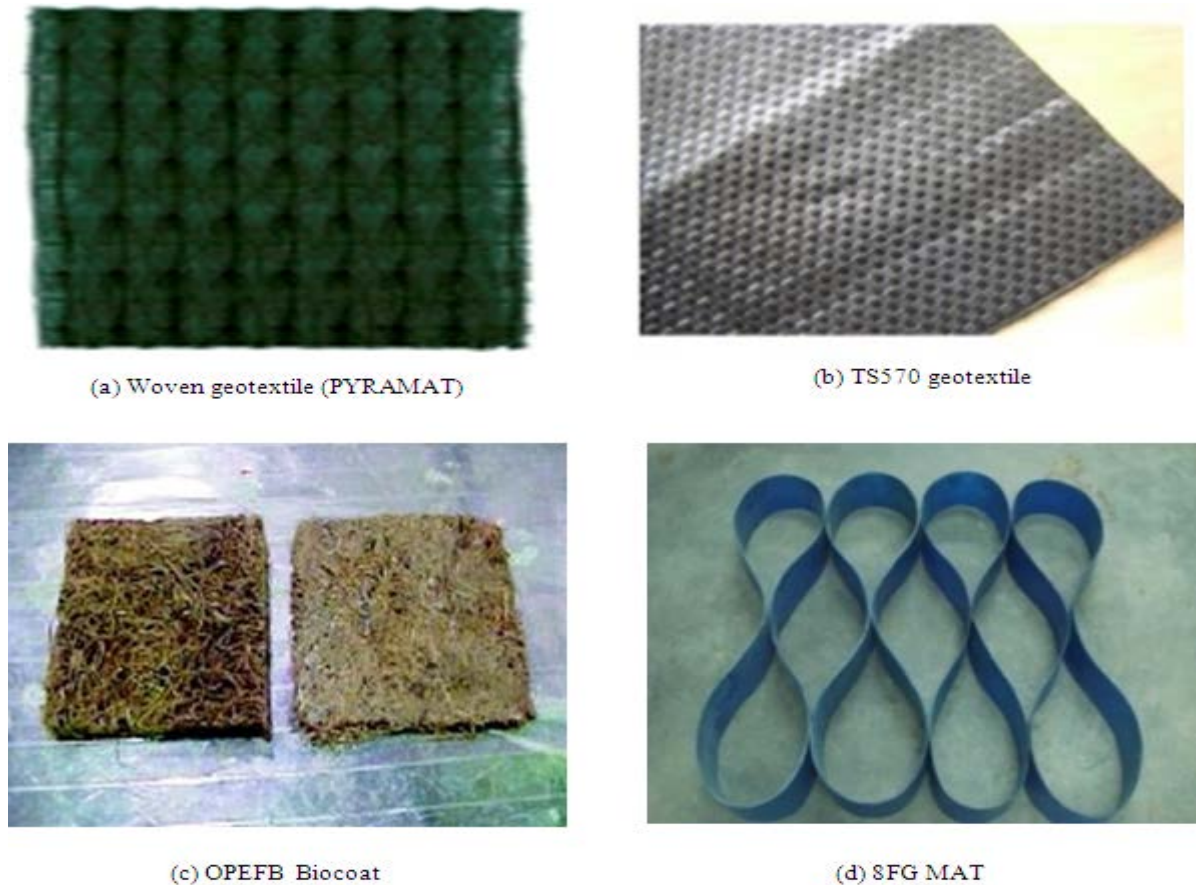


Fig. 3 Different type of geosynthetics used in the tensile test experiment.

Methodology

Shear Box Apparatus

In this research, a rigid steel soil box was used having 1200 mm length, 1000 mm width and 500 mm depth. The pullout apparatus system which comprised of steel box, steel rod and ready filled soil media was equipped with an electric motor that rotates with a constant displacement rate of 4.6 mm/min connected to a high tensile 20 mm diameter steel rod that was clamped to the geomaterial embedded in the soil box by means of four numbers of 1 mm diameter wire connections. The inlet and outlet ports were installed at the front and back sides of the box to enable connections to four number of linear variable displacement transducers (LVDT) located at the back side and on top of the box respectively. During experiment, LVDT's readings that record horizontal displacement of geomaterial and settlement of soil media were monitored through a data logger.

Tensile Test

Two sets of tensile tests were conducted to verify the tensile strength of glass fibers. Firstly, tensile

strength of polymeric yarns of glass fibers were tested and compared to coated glass fibers and natural fibers extracted from oil palm empty fruit bunch (OPEFB). Stress-strain relationship of glass fiber strands was observed using INSTRON 3690 Electro-Hydraulic Actuator and Universal Tensile Machine (UTM) according to ASTM C1557-03: Standard Test Method for Tensile Strength and Young Modulus of Fibers. Consequently, the tensile test for '8' shape glass fiber geomaterial was carried out according to the modified version of ASTM D7004-03: Standard Test Method for Grab Tensile Properties of Reinforced Geomembranes. To our knowledge, this is the first '8' shape form of geomaterial glass fibers ever attempted other than the presently available steel mesh geocell. The ultimate tensile strength of the molded '8' shape glass fiber geomaterial (8FG MAT) is compared to other available geosynthetic products such as woven geotextile (PYRAMAT), TS570 geotextile and oil palm empty fruit bunch (OPEFB) Biocoat as shown in Figure 3.

Pullout Test

The pullout resistance force of glass fiber geomaterial was observed through pullout test based on ASTM D6706: Standard Test Method for Measuring Geosynthetic Pullout Resistance in Soil. Pullout test is commonly adapted as a crucial experimental indicator for any geosynthetic validation because it provides not only soil-structure interaction between reinforced soil and reinforcing agent but also visible trend in reinforced soil failure mechanism. As illustrated in Figure 3, soil media were filled in and compacted manually using 60 N weights, 120 mm diameter circular base hammer dropped from a height of 300 mm for 25 blows per layer.

RESULTS AND DISCUSSION

Tensile Test Experiment

The result from fibers tensile test experiment by considering the effect of ABS thermoplastic coating between natural and glass fibers is shown in Figure 4. The result shows typical linear relationship of a brittle material due to the fact that both natural and glass fibers exhibit the absence of yield point and strain hardening region after undergoing elastic deformation. Compared to the uncoated fibers specimens, coated fibers show higher peak tensile stress at the same corresponding strain.

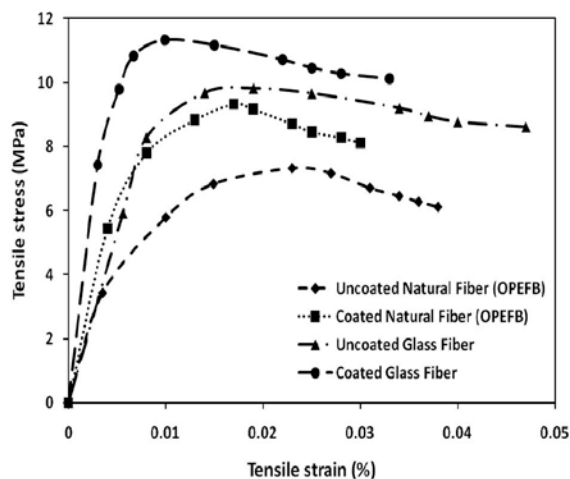


Fig. 4 Tensile stress-strain relationship of the coated and uncoated fibers.

Figure 5 shows the stress-strain relationship of the molded '8' shape 8FG MAT by considering

different layer thickness. It was observed that the addition of layer thickness in molded specimens contributed to the increased values in tensile stress. However, the effect of molding glass fibers into the '8' shape form does not greatly affecting the peak tensile stress of glass fiber specimens. The recorded peak tensile stress of uncoated and coated glass fibers are 9.83 MPa and 11.33 MPa in which are almost equivalent to the peak tensile stress of the three and four layers thickness of molded '8' shape specimen at 9.52 MPa and 11.43 MPa respectively. In the case of both one and two layers thickness, alteration of glass fibers into '8' shape form recorded lower tensile stress values than uncoated glass fibers. This suggests that the process of converting glass fibers into bundle of layered strands does not necessarily enhance the overall tensile strength of glass fibers in bulk.

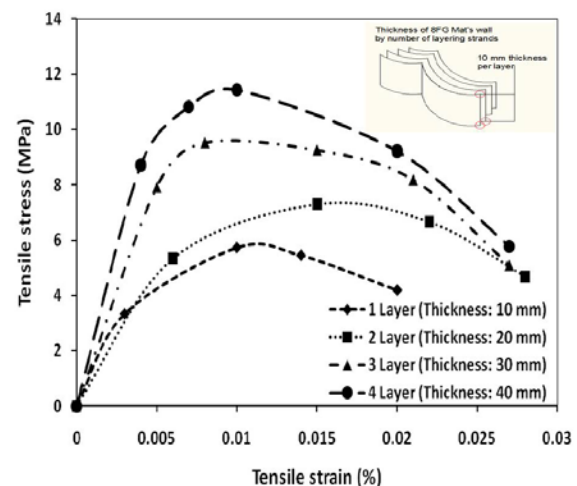


Fig. 5 The effect of layer thickness towards the tensile stress-strain behavior of 8FG MAT.

The tensile strength of two commonly used slope protection materials such as woven geotextile (PYRAMAT) and TS570 geotextile together with naturally based fibrous oil palm empty fruit bunch (OPEFB) biocoat were compared with '8' shape glass fiber geomaterial (8FG MAT) as shown in Figure 6. The ultimate tensile strength of all specimens in ascending order were recorded as 0.59 kN, 0.61 kN, 0.76 kN and 0.86 kN respectively [PYRAMAT > 8FG MAT > TS570 geotextile > OPEFB biocoat]. It was observed that both ultimate tensile strength values for TS570 geotextile and OPEFB biocoat were almost similar. However, due to the randomly distributed natural fibers that existed in its structure, biocoat specimen was observed to

undergo large horizontal strain before rupture. The ultimate tensile strength value of 8FG MAT is shown to be higher than that of both TS570 and OPEFB but lower than that of PYRAMAT. This is mainly due to the effect of 8FG MAT grabbing during tensile test, in which the region where construction joint is located. The construction joint is the line where layers of glass fiber strands were connected using resin to harden. The occurrence of failures in all samples of 8FG MAT at the construction joint regardless of their layer thickness proved the joint susceptibility in resisting applied force.

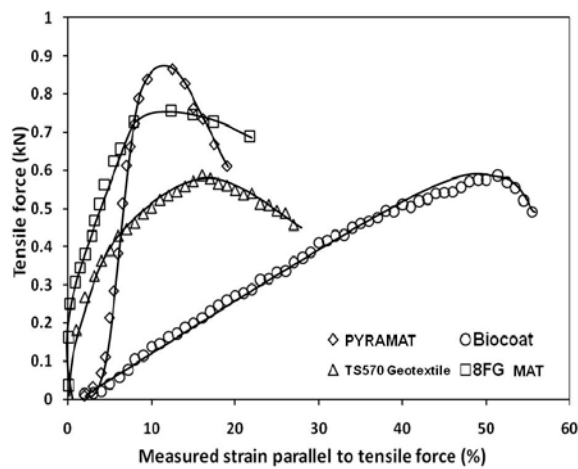


Fig. 6 Comparison of tensile strength values of the various geosynthetics.

Pullout Test Experiment

The pullout relationship between sand and peat reinforced with 8FG MAT is shown in Figure 7. The result shows linear relationship between pullout force in sand and that in peat. The slope of the regression line is the pullout force coefficient. The pullout force coefficients in ascending order of different layer thickness are 0.47, 1.02, 1.63 and 2.02 respectively with all regression coefficients over than 0.995.

Similarly, Figure 8 shows the pullout relationship between clay and sand reinforced with 8FG MAT. The result shows linear relationship between pullout force in clay and that in sand. The pullout force coefficients in ascending order of different layer thickness are 0.93, 1.53, 2.40 and 2.61 respectively with all regression coefficients over than 0.997. Although the addition of layer thickness linearly proportional to the pullout force in both peat and sand soil samples, the pullout coefficients in three and four layers of geomaterial

reinforcement in clay and sand soil samples are almost similar indicating further increase in thickness will not yield further increase in pullout force.

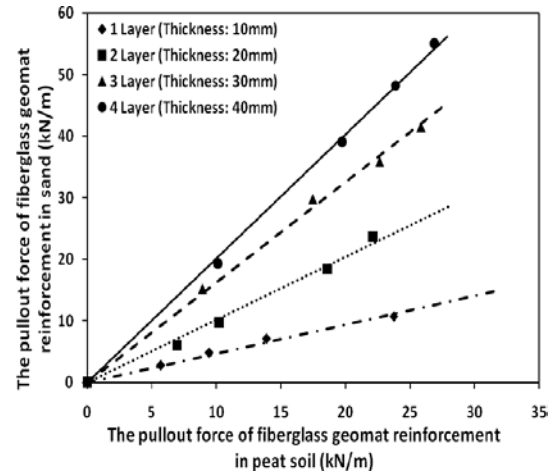


Fig. 7 Pullout force relationship between sand and peat.

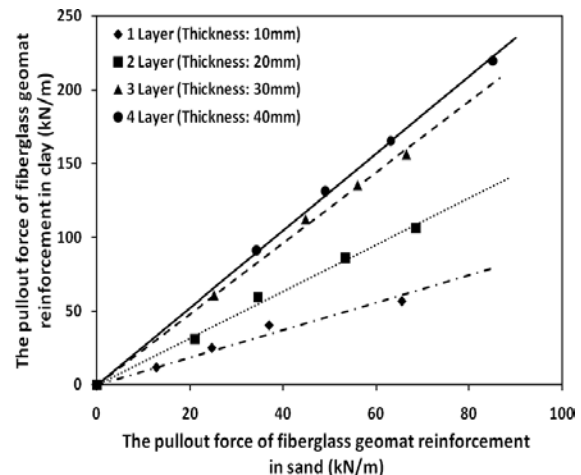
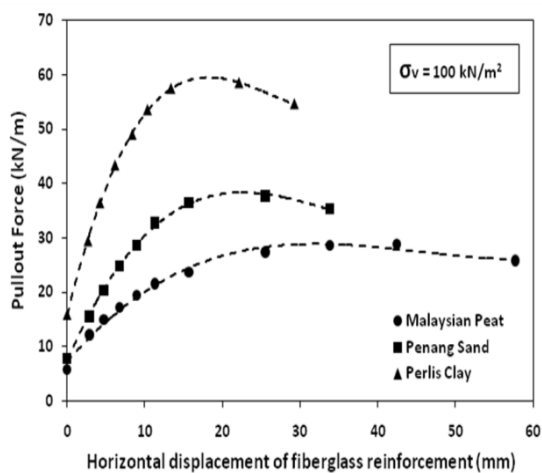
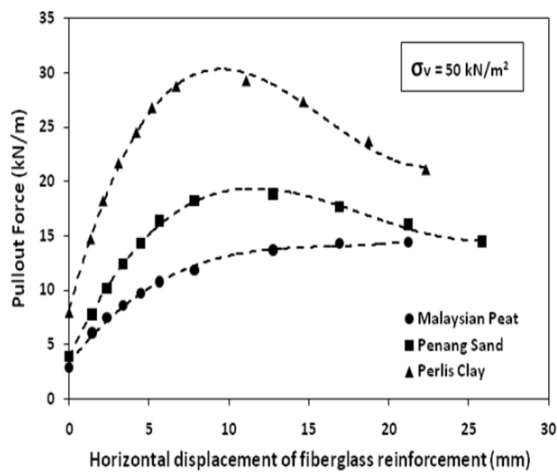


Fig. 8 Pullout force relationship between clay and sand.

The pullout force of 8FG MAT was investigated in different types of soil media to show its reliability as ground improvement agent. Figure 9(a) and Figure 9(b) show the pullout-displacement relationship of reinforced soil media with 8FG MAT in two different confining vertical stresses conditions $\sigma_v = 100 \text{ kN/m}^2$ and $\sigma_v = 50 \text{ kN/m}^2$ respectively. The results from both figures clarify that the pullout force is directly proportional to the applied confining pressure. The increase of confining pressure was observed to increase the corresponding pullout force for all soil samples.



(a) Confining vertical stress $\sigma_v = 100 \text{ kN/m}^2$



(b) Confining vertical stress $\sigma_v = 50 \text{ kN/m}^2$

Fig. 9 Pullout–displacement relationship of the reinforced soil media with 8FG MAT in two different confining vertical stress conditions.

CONCLUSIONS

In this research, the mechanical properties of molded ‘8’ shape glass fiber geomaterial derived from industrial glass waste was studied. From the findings, the following conclusions could be made:

- 1) The tensile strength of glass fiber geomaterial was significantly increased with the addition of layer thickness while fibers alteration in terms of coating with ABS thermoplastic showed that coated fibers exhibit higher peak tensile stress at

the same corresponding strain in that of uncoated fibers.

- 2) The pullout test results revealed a linear relationship between the pullout force values in different soil samples as the thickness of glass fiber strands’ layers and confining pressures were increased.
- 3) The ready availability, high tensile strength, lightweight and non-biodegradable characteristics of glass fibers proved to be an advantage for long term ground improvement remediation especially in soft soil condition. The ‘8’ shape form of 8FG MAT provide strength into reinforced soil by confining effect of its layer that maintains the intactness between glass fibers and soil particles thus, improving friction at their interface.

ACKNOWLEDGEMENTS

The financial supports granted by E-Science Fund (MOSTI) Malaysia and the Japan-East Asia Network of Exchange for Students and Youths (JENESYS) Program are gratefully acknowledged.

REFERENCES

- [1] Lutz JT and Grossman RF, “Polymer modifiers and additives”, Emerging Material for Civil Infrastructure: State of the Art, Roberto A. Lopez-Anido, Tarun R. Naik, Gary T. Fry, David A. Lange, & Vistasp M. Karbhari (Eds.), ASCE, 2001, pp. 233–240.
- [2] Mujah D, Ahmad F, Hazarika H, Yasafuku N, Omine K and Kobayashi T, “Evaluation of fiberglass as ground improving geomaterial”, in Proc. 10th Japan-Korea-France-Canada Joint Seminar on Geoenv. Eng, Japan, 2011, pp. 189–194.
- [3] Ahmad F, Mujah D, Hazarika H, and Safari A, “Assessing the potential reuse of recycled glass fibre in problematic soil applications”, J. of Cleaner Production, Vol. 35, 2012, pp. 102–107.
- [4] Mujah D, Ahmad F, Hazarika H, and Safari A, “Evaluation of the mechanical properties of recycled glass fibers-derived three dimensional geomaterial for ground improvement”, J. of Cleaner Production, accepted, 2013.
- [5] Pinzani GP and Sauli G, “Long term efficiency of erosion control geomats”, Millpress, Rotterdam, Netherlands, 2006, pp. 103–114.

STUDY ON MONITORING METHOD OF RETAINING WALL BEHAVIOR USING MEMS SENSOR NETWORK

N Minakata¹, S Nishiyama², T Yano³, D.H Lee⁴, J Wu⁵ and M Ryu⁶

Department of Urban Management, Graduate school of Engineering, Kyoto University, Japan
Graduate school of Engineering, Okayama University, Japan

Department of Urban Management, Graduate school of Engineering, Kyoto University, Japan
Department of Civil Engineering, National Cheng-Kung University, Taiwan
Earthtech Toyo Co.,Ltd, Japan

ABSTRACT

For the evaluation of infrastructures, the authors have developed the monitoring method of the stability of civil engineering structures using MEMS sensors. MEMS sensors have various advantages as follows. First, the authors can design the arrangement of MEMS sensors easily and save the monitoring cost. Secondly, the authors can send data with wireless equipment. Finally, the authors can transform the data of acceleration into the value of angle, which means the high possibility of calculating the two dimensional angles of inclination of retaining walls. More specifically the authors can use the acceleration sensors as inclinometers. In addition, the authors demonstrated that the resolution of MEMS sensors was less than 0.1 degree as the results of the experiments and also investigated the applicability of monitoring method reported herein at the actual field. From the monitoring results, it is found that measurement values with using MEMS sensors has the temperature characteristics and that the temperature correction is very important for the authors to get an exact monitoring data, so that the authors revealed the temperature characteristics of MEMS sensors. In this paper, the authors showed that the low pass filter the authors designed for deleting this temperature effect and monitored the retaining wall behavior with a high accuracy.

Keywords: Inclinometer, Acceleration, Retaining Wall, MEMS, Wireless Sensor Network

INTRODUCTION

Recently the number of natural disaster increases all over the world, and maintenance of the civil engineering structure for disaster prevention is becoming more and more important. Asian countries are characterized by geological conditions under which rocks weather quickly, and these countries often suffer natural disasters such as earthquakes, typhoons as well as localized torrential downpours. Moreover, in many Asian countries, rapid urban development has been carried out, and lots of slope hazard damages occur. The prevention of resultant damages caused by slope hazard requires the establishment of sound slope behavior monitoring technology. Considering this situation, the authors focus on the micro machine technology which has been greatly advanced, and have developed an early warning system for the prediction of landslides and the prevention of resultant damages with the MEMS sensor network [1]. This system has the following characteristics. The first one is installation of the sensor is easy because the size of the sensor is small.

The second one is the authors can install sensors in any positions because the authors transmit and receive measurement data by radio. Finally, it is possible to reducing a labor and costs required for management of the measurement system. The function of MEMS sensor is being developed, but there are few examples of the practical use in the field of civil engineering works. The MEMS has been used as a clinometer mainly until now. We also make a sensor network using MEMS to measure the tilt angles of a retaining wall for the prevention of landslides. In this study, the authors develop a sensor network system in which measurement data transmitted from a sensor is prevented from being affected by vegetation, a distance between a sensor and a base station collecting the measurement data is made long, and in addition, precision of a sensor signal is not affected by temperature. This paper argues the practicability of the proposed measurement system by evaluating the precision of the slope behavior monitoring.

DEVELOPED MONITORING METHOD

The authors pay attention to MEMS sensor and wireless network systems, and the authors developed the new monitoring method by utilizing both of them.

The Developed MEMS Sensor

Figure.1 shows the MEMS sensor used in this study. The size of the MEMS sensor is W123mm × D76mm × H57mm, therefore the MEMS sensor is very compact, lightweight, and inexpensive. That is why the problem that conventional measurements have been widely used everywhere in the world and have been effective but resulting in a limited application only for a few infrastructures because of high costs, can be solved [2]-[4]. The measurement principle of the MEMS sensors is shown in Fig.2. The MEMS sensors used in this monitoring system can measure two-direction accelerations, and the MEMS proposed herein can measure two-direction angles by calculating with Eq.(1). As a result, the authors can use the MEMS sensor proposed herein as an inclinometer. Simultaneously, the MEMS sensors can measure temperature.

$$\theta_i = \text{Arccos} \left(\frac{Acc_i}{\sqrt{Acc_x^2 + Acc_y^2}} \right) \quad (1)$$

$i = x, y$

Experiments

For evaluating the accuracy of the MEMS sensor, the authors performed the experiment. Figure.3 shows the relation between measured values with using the MEMS sensors and changed angles. It is concluded that the precision of the MEMS sensor network system proposed herein gets the very high accuracy with the high precise that is 0.1 degree, which is much higher than conventional methods. To verify the temperature characteristics of the MEMS sensor network system, the authors performed another experiment. The result of this experiment is shown in Fig.4, which shows the relation between temperature and inclinations measured using the MEMS sensors. From the result, it is found that the temperature characteristic of the new developed MEMS sensors is less than 0.001 degree per a degree centigrade. This temperature characteristic is much lower than the MEMS sensors which the authors developed before. This is because the MEMS sensors are filled with a bulking agent, resulting in the temperature characteristics get very small.

The Developed Sensor Network

The authors installed wireless device into the developed MEMS sensor. That is why the MEMS sensor can send measured values without using any wires to the base station as shown in Fig.5. Therefore it is possible to decrease the risk of damage caused by the thunderbolt. After the data measured using the wireless communication with frequency of 434 MHz are sent to the base station, the sent data are uploaded to the Web site designated via the Internet. This is why the authors can access the collected data via the Internet and the authors can access the data anywhere a terminal via the Internet browser is utilized, and the acquisition process is automatic and requires no technicians on site [5]. Even if it is far from the site to the office, it is possible that the authors monitor the actual civil engineering structures in real time. For example, the authors need not to go to the site in order to collect the measured data and in order to check how to operate normally [6]. Therefore the authors can save labor. Also this monitoring system is set in sleep mode except for completing start-up, measurement, and transmission in a while time. Thus this monitoring system achieves low power consumption and can be free of maintenance.

From these result of experiments performed by the authors, it is found that the MEMS sensor can measure very small magnitudes of an inclination of the civil engineering structures even if the measured value includes the temperature characteristics. Therefore the authors applied this monitoring method to assess an actual retaining wall in Taiwan for disaster prevention.

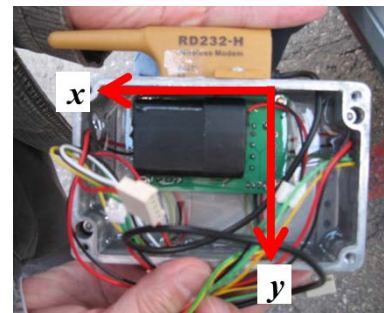


Fig.1 This figure shows the MEMS sensor used in this paper. The red lines show the coordinate system of the MEMS sensors.

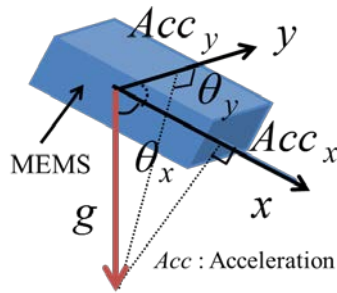


Fig.2 This figure shows the measurement principle for the MEMS sensors. The red line shows the gravity direction and the black lines show the coordinate system of the MEMS sensors.

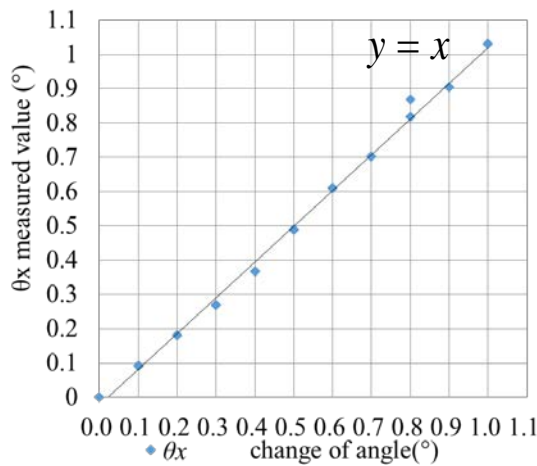


Fig.3 This figure shows the result of the experiment. The blue figures show the relation between changes of angle and measured values.

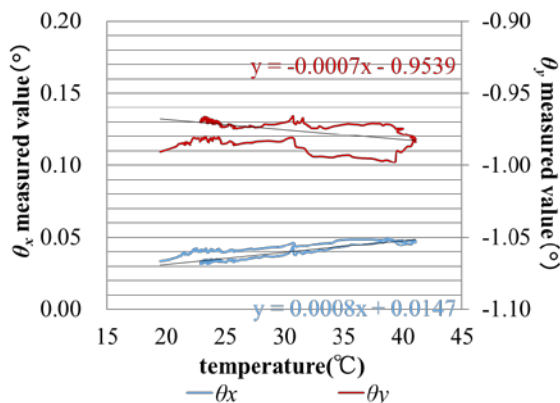


Fig.4 This figure shows the result of the experiment for verifying the temperature characteristics. The blue line shows the relation between temperatures and θ_x measured values and the red line shows the relation between temperatures and θ_y measured values, and the black lines show the linear approximate curves.

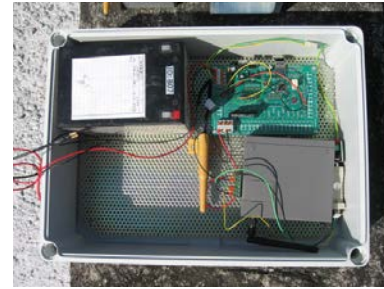


Fig.5 This figure shows the base station. The unit is W380mm × D270mm × H130mm. The measured values are sent to this base station, and after that, the sent data are uploaded to Web site.

APPLYING THE ACTUAL RETAINING WALL

Retaining Wall Monitored

The authors applied the monitoring system developed in this paper to the actual retaining wall in Taiwan. The retaining wall is shown in Fig.6 and the red point of Fig.6 are respectively locations of installation of MEMS S11, S12, and S13. The overall length of the retaining wall is 90m and the maximum height is about 30m. This retaining wall was damaged by Morakot in 2009 and collapsed by the deep sliding as shown in Fig. 7 [7]. Because of the collapse of this retaining wall, the government of Taiwan began the reinforcement work of the retaining wall monitored and it was completed as shown in Fig. 8. For preventing the slope sliding and the collapse of the retaining wall, the authors monitor this repaired retaining wall in order to check whether the deep sliding is moving or not, and simultaneously whether this retaining wall is safe or not.

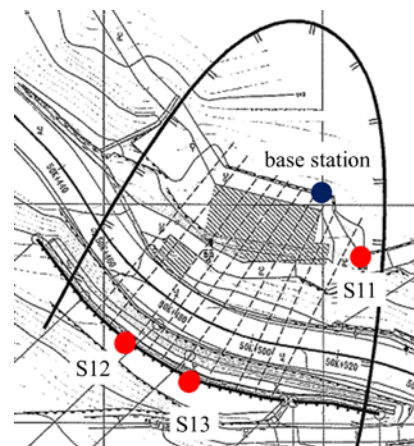


Fig.6 This figure shows the retaining wall monitored using the MEMS sensors shown in the red points, and the base station is shown in the blue point.



Fig.7 This shows the retaining wall damaged by deep sliding when Morakot happened in 2009.



Fig.8 This shows the reinforced retaining wall.

The authors installed 3 monitoring points and the base station, and the setting situation is respectively shown in Fig.9, Fig.10 and Fig.11. The distance between MEMS and the base station is approximately 20m, and measured values are sent to the base station via the wireless communication at 1 minute interval, and the data is then uploaded to the Web site which the authors made in advance. In this monitoring system, the sampling time is set 1 minutes, and the MEMS sensors equip two dry cells. In this setting, it is not necessary to change the batteries for three years.



Fig.9 This shows S11 on the retaining wall.



Fig.10 This figure shows S12.



Fig.11 This figure shows S13.

Monitoring Result of Actual Retaining Wall

In this paragraph, the monitoring result measured using the MEMS sensors S11, S12 and S13 is shown. The measured angles are respectively shown in Fig.12, Fig.14 and Fig.16, and the measured temperatures are shown in Fig.13, Fig.15 and Fig.17. The measured values are shown in solid lines, and the calculated values by using moving average are shown in dashed black lines. The amount of change of the calculated values of S11- θ_x is approximately 0.2 degree. The amounts of changes of the calculated values the others MEMS sensors which are S11- θ_y , S12- θ_x , S12- θ_y , S13- θ_x , S13- θ_y are less than 0.1 degree. In this paper, when the amount of change is more than 0.1 degree, the authors regard this movement as the deformation of this retaining wall. Considering the definition the authors proposed here and the result of the calculated values, it is found that the measurement point of S11 is moving gradually while the other measurement points are not moving. Therefore it is recognized that the deep sliding is moving gradually. In summary, it is necessary to set more measurement points and monitor the retaining wall and the deep sliding more densely, and it is required to reveal the relation between the retaining wall behavior and the deformation of the deep sliding. Additionally, the earthquake happened in Taiwan on 2nd June. In regard to this, each of MEMS sensors could capture the movement caused by the earthquake.

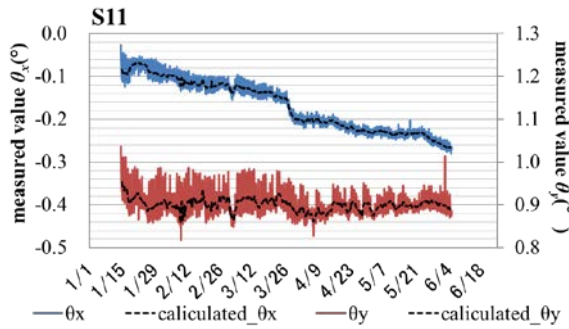


Fig.12 This figure shows the measured values. The blue line shows θ_x measured values and the red line shows θ_y measured values, and the black dashed lines show the calculated values using average moving.

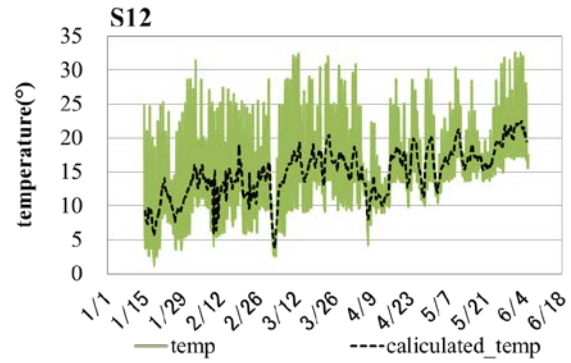


Fig.15 This figure shows measured temperatures. The solid line shows the measured temperatures and the black dashed line shows the calculated values using average moving.

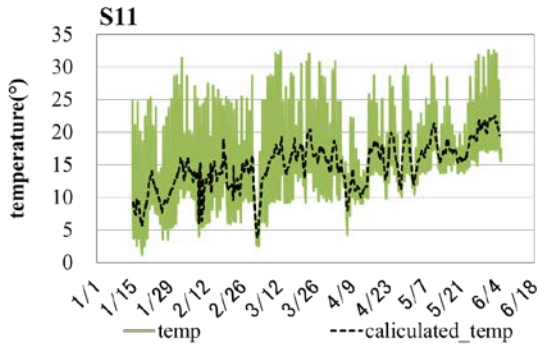


Fig.13 This figure shows measured temperatures. The solid line shows the measured temperatures and the black dashed line shows the calculated values using average moving.

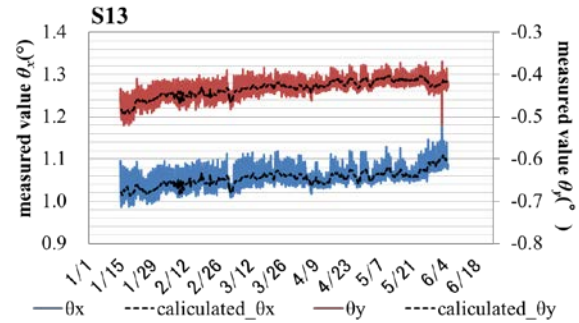


Fig.16 This figure shows the measured values. The blue line shows θ_x measured values and the red line shows θ_y measured values, and the black dashed lines show the calculated values using average moving.

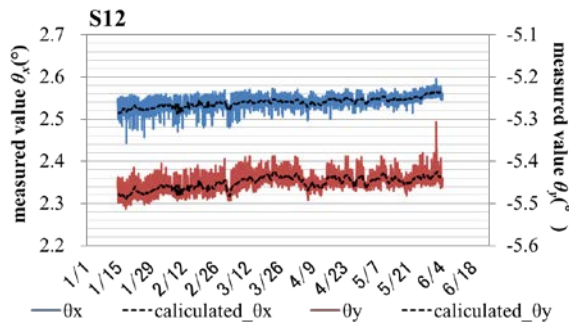


Fig.14 This figure shows the measured values. The blue line shows θ_x measured values and the red line shows θ_y measured values, and the black dashed lines show the calculated values using average moving.

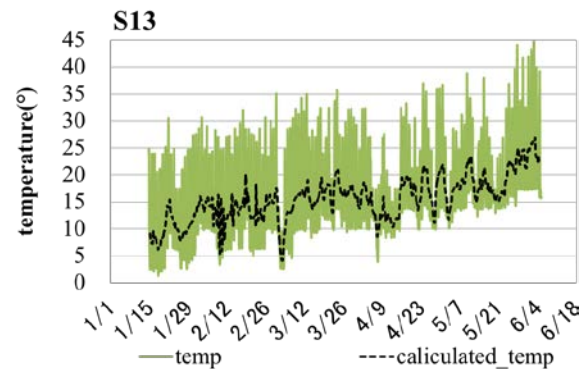


Fig.17 This figure shows measured temperatures. The solid line shows the measured temperatures and the black dashed line shows the calculated values using average moving.

CONCLUSION

The purpose of this paper is to develop the establishment of the slope behavior monitoring technology for disaster prevention. That is because

the authors focus on the micro machine technology and developed an early warning system for the prediction of landslides and the prevention of resultant damages. As a result of the development the monitoring technology for evaluating the soundness of the slope, the MEMS sensor could detect very small magnitudes of a deformation of the retaining wall and proposed monitoring system featuring simple measurement work and a high degree of precision was found to be possible. Therefore the authors applied the measurement system and monitor the retaining wall behavior and the deformation of the slope. From the monitoring result, it was concluded that the retaining wall is moving partially and simultaneously the deformation of this slope is increasing gradually.

ACKNOWLEDGEMENTS

The authors are grateful to National Cheng Kung University in Taiwan for their matchless technical competence and friendly support. This research was supported by Zengwun Improvement Engineering Office, The fifth Maintenance Office, Directorate General of Highways, Ministry of Transportation and Communications, and SHINOTECH ENGINEERING CONSULTANTS, INC.

REFERENCES

- [1] Lee S, "Reliability Assessment of Advanced Materials And Structure", J. of Solid Mechanics and Materials Engineering, vol.4, 6, 2010, pp. 639-651.
- [2] Bourgeois E, Soye L, Le Kouby.A, "Experimental and numerical study of the behavior of a reinforced-earth wall subjected to a local load", J. of Computers and Geotechnics, Vol. 38, 6, 2011, pp. 515-525.
- [3] Bhattacharya S, Murali Krishna A, Lombardi D, Crewe A, Alexander N, "Economic MEMS based 3-axis water proof accelerometer for dynamic geo-engineering applications", J. of Soil Dynamics and Earthquake Engineering, Vol. 36, 5, 2012, pp.111-118.
- [4] Uchihara T, Towhata I, Trnh T, L A, Fukuda J, Bautista B J C, Wang L, Seko I, Uchida T, Matsuoka A, Ito U, Onda Y, Iwagami S, Kim M, Sakai N, "Simple monitoring method for precaution of landslides watching tilting and water contents on slopes surface", J. of Landslides, Vol. 7, 10, 2010, pp. 351-357.
- [5] Yin Y, Wang H, Gao Y, Li X, "Real-time monitoring and early warning of landslides at relocated Wushan Town, the three gorges reservoir, china", J. of Landslides, Vol. 7, 5, 2010, pp. 339-349.
- [6] Nakagawa M, Sato M, Hagiwara I, Ono K, Nishiyama S, "Development and Applications of Nanosensor Devices for Detection of Slope Disaster", Proc. the International Workshop on ICT in Geo-Engineering, 2012, pp. 259-265.
- [7] Justin Chun-te Lin, Ja-Jang Chen, Duu-Jong Lee, Wan-Mu Guo, "Treating high-turbidity storm water by coagulation-membrance process", J. of the Taiwan Institute of Chemical Engineers, Vol. 43, 3, 2012, pp. 291-294.

CASE STUDY ON THE USE OF HIGH-RESOLUTION SURFACE WAVE SURVEY FOR EXAMINING THE CAUSE OF SUBSIDENCE OF RECLAIMED ROAD

Miura Minami¹, Shibuya Satoru²

¹ Graduate student, Kobe university, Japan; ² Professor, Kobe University, Japan

ABSTRACT

This case study deals with the problem of ground subsidence, which took place after backfilling the sewage pipeline in a small town in Hyogo Prefecture, Japan. The settlement brought about serious damage to the neighboring houses by showing harmful inclination of fence, garage shutter etc. The local government commissioned to find out the cause of ground subsidence for the remedial work planned in near future. In an attempt to get an overall image regarding the current conditions of the backfilled portion of the road, a high-resolution surface wave survey was performed. The 2-D profile of S-wave velocity provided us with an crucially important clue that the S-wave velocity of the backfill where the surrounding houses were damaged was obviously lower than those for the undamaged areas. In order to manifest the cause of ground subsidence, a series of tests in the laboratory, i.e., the compaction test, direct shear box test etc., was carried out for soil samples retrieved at various spots along the surveyed line. It was found that i) the backfilled gravelly soil was similar in all the spots; however, ii) the fines content of soil where the subsidence took place was noticeably higher. It was concluded that the surface wave survey was of great use for promptly finding out potentially under-compacted portion of the backfill without damaging the cited ground.

Keywords: Surface Wave Method, Submergence, Settlement, Direct Shear Test

INTRODUCTION

A high-resolution surface wave (HR-SW) survey enables us of manifesting a 2-D depth profile of elastic shear wave (S-wave) for a site if interest in a non-destructive manner [1]. Rayleigh wave has dispersibility. The short wavelength Rayleigh wave passes a shallow layer and the long wavelength Rayleigh wave passes a deep layer. Additionally, a velocity of Rayleigh wave and a velocity of S-wave are even approximately. Therefore, it is possible to get a 2-D depth profile of elastic S-wave by measuring the Rayleigh wave velocity. The HR-SW survey is quick to perform and cost-effective compared to other soundings method in geotechnical engineering practice. This paper describes a case study in which a ground subsidence of recently reclaimed road in Taka-Cho, Hyogo Prefecture, Japan is cited. The ground subsidence had developed at some places over several years since the sewage pipe was mounted and backfilled with a gravelly soil. In the year of 2011, the ground deformation had eventually triggered a serious damage to local houses and the local government commissioned us to investigate the cause of the ground subsidence, together with countermeasure to prevent further damage. Accordingly, the HR-SW survey was performed so as to manifest the 2-D profile of S-wave velocity over the reclaimed portion along the road. The basic physical properties, together with the

compaction aspect and settlement measurement of the gravelly soil on submergence were examined in the laboratory. The HR-SW survey provided a vital clue about the weakly-compacted state of the site that was the cause behind group subsidence and therefore, was considered to be a vital tool for such investigations.

RESULTS OF HIGH-RESOLUTION SURFACE WAVE (HR-SW) SURVEY

Figure 1 shows ground subsidence around a sewage manhole, whereas Fig. 2 shows an inclined fence of a local house due to the ground deformation,



Fig. 1 Subsidence around a manhole at B1



Fig. 2 Inclined fence of a house at B1

respectively. Figure 3 shows the survey lines A (95m long) and B (143m long) along the local roads, for which the HR-SW survey was carried out. It should be mentioned that the ground deformation as well as the damage to the adjacent houses took place in a narrow area at B1. In the survey, two adjacent receivers were fixed at 1m interval.

The profile of S-wave velocity, V_s , with depth is shown in Fig. 4 As can be seen in Fig. 4 , the

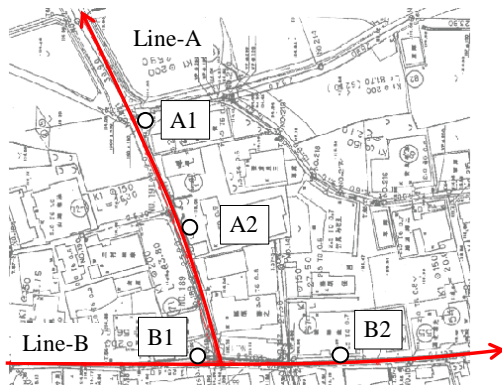


Fig. 3 HR-SW survey performed

boundary between the original ground and the fill lies at around 2m depth, below which the V_s exceeds 300 m/sec. Note that the V_s for the point B1, where the ground subsidence is significant, is lower at around 150 m/sec when compared to the V_s of about 200m/sec at other points A1, A2 and B2, all showing no subsidence. The difference of V_s between B1 and the others certainly suggests that the gravelly soil in the deformed zone at B1 may be somewhat in a looser (or under-compacted) by showing lower V_s .

Figure 5 shows the profile of SPT N-value when estimated by using the following empirical relationship;

$$V_s = a N^b \quad (1)$$

where the constants of $a = 80$ and $b = 0.33$ as suggested by IMAI et al (1975) were employed for the estimation. As shown in Fig. 6, the estimated N-value is close to the measured value. Note also that the measured N-value of the fill is about 5 on average to what depth, suggesting a loose state of the fill.

RESULTS OF LABORATORY TESTS

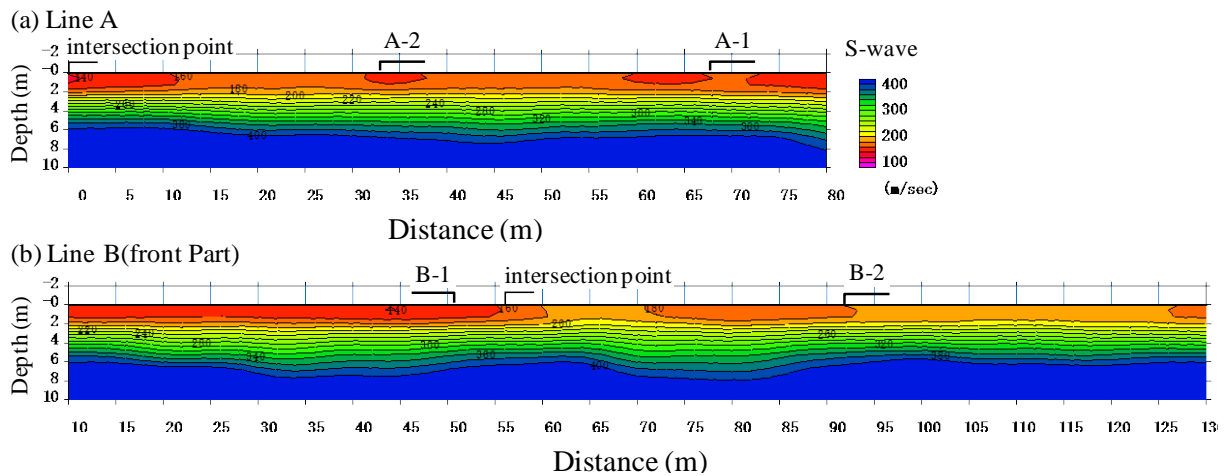


Fig. 4 Profile of V_s along the survey lines A and B

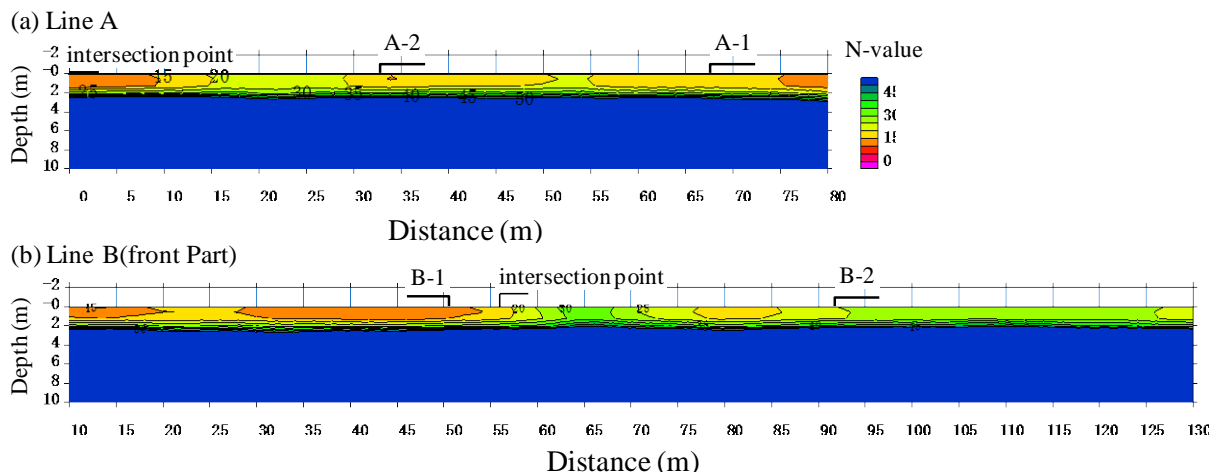


Fig. 5 Profile of SPT N-value along the survey lines A and B

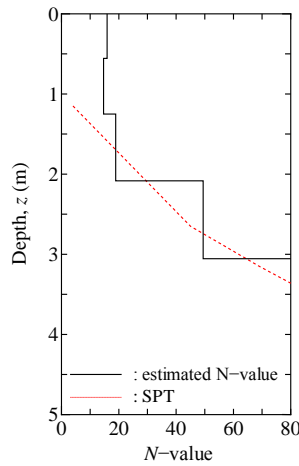


Fig. 6 Measured and estimated SPT N-value

Table 1 Physical properties of four samples

Samples	A1	A2	B1	B2
Soil density, ρ_s g/cm ³	2.656	2.627	2.643	2.646
Coefficient of uniformity U_c	33	20	33	23
Coefficient of curvature U_c'	0.9	1.3	1.8	0.7
Category	SG-F	SG-F	GFS	GS-F

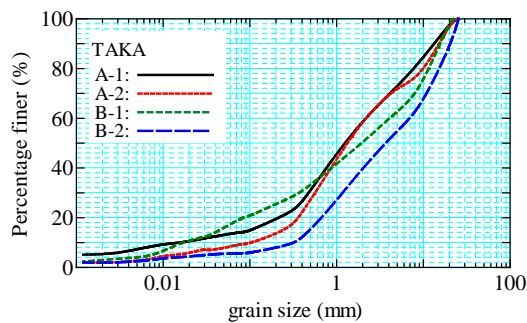


Fig. 7 Grading curves (original grading)

Soil samples were retrieved at points A1, A2, B1 and B2, bearing in mind that the observed ground deformation was significant at A1, A2 and B1 (refer to Fig. 3). Table 1 shows physical properties, whereas the grading curves of these four samples are shown in Fig. 7 [3]. All the samples are gravel-rich coarse-grained soil, which is in general suitable for the fill geomaterials. However, a subtle difference can be noticed in terms of fines content, F_c ; i.e., the F_c was the largest in sample B1 as compared to the rest.

Figure 8 shows the result of Proctor test for these four samples. As can be seen in Fig. 6, the maximum dry density and the optimum water content of the

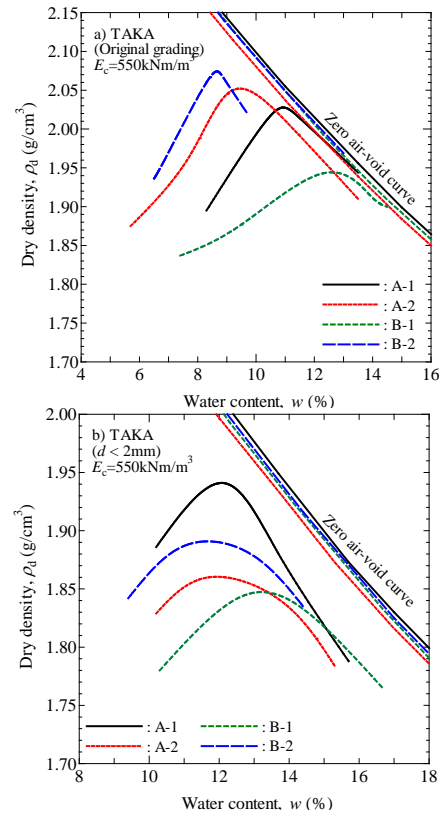


Fig. 8 Compaction curves of four samples; a) original grading and b) grading less than 2mm [3]

original grading of sample B1 are the lowest and the largest than those of the other samples, respectively. The trend is reasonable since the F_c of sample A1 and B1 is the largest among all the samples.

The settlement of the samples on submergence was measured in the laboratory. In a rigid-box consolidometer, the partly-saturated sample having the optimum water content and the dimension of 6cm in diameter and 4cm in height was subjected to the prescribed vertical stress of 40 kPa. It was then subjected to submergence while the vertical stress was kept constant at 40 kPa. The results are shown in Fig. 9 In each of these figures, the variation of compressive strain with time is examined for three samples having the degree of compaction of 80%, 85% and 90%. It should be mentioned here that the amount of settlement on submergence increased as the nominal degree of compaction increased. The trend is more clearly seen in Fig. 10, in which the axial strain on submergence is plotted against the degree of compaction. The following should be noted;

- For all the samples, the settlement when submerged was almost zero when the degree of compaction was larger than 80 %, and
- The settlement of sample A1 and B1 at loosest state with the degree of compaction of 78 % was significant.

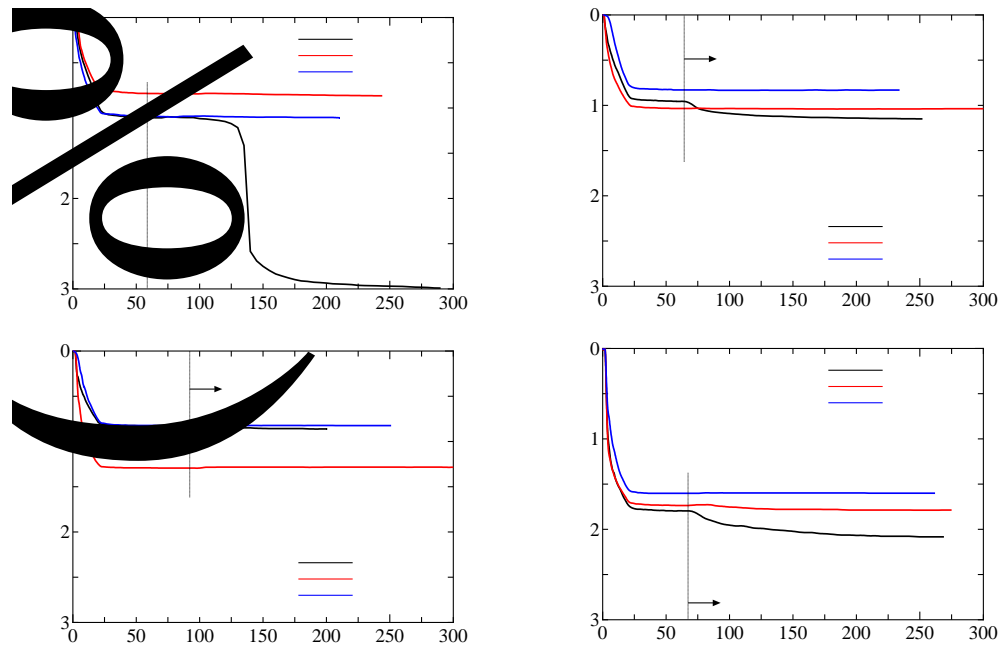


Fig. 9 Results of submerge test [3]

Based on these observations, the soil at B1 having higher fines content could have been backfilled at loose state with the degree of compaction less than 80%, which in turn had resulted in lower Vs as compared to the other points. The ground subsidence is concentrated over a narrow area around B1, the cause of which may be attributed to under-compaction. To avoid ground settlements, such as above, it seems very important to compact the gravel-rich soil properly. Similarly, finer particles should be washed out when using the gravelly soil as a fill material.

CONCLUSION

In this case study, the value of high-resolution seismic survey was well demonstrated in a manner that the deformed ground was properly pin-pointed by showing the low profile of elastic shear wave velocity. The area, where the ground subsidence was observed, was backfilled with the gravelly soil having higher fines content as compared to the other non-deformed areas. Based on the results of compaction and submerge tests in the laboratory, the soil could have been backfilled at a degree of compaction less than 80%. To avoid ground settlement as such, it seems quite important to properly compact even the gravel-rich soil. Similarly, fine grains should be washed out when using the gravelly soil as a fill material.

ACKNOWLEDGEMENT

The Authors are grateful to Dr T.N. Lohani for his

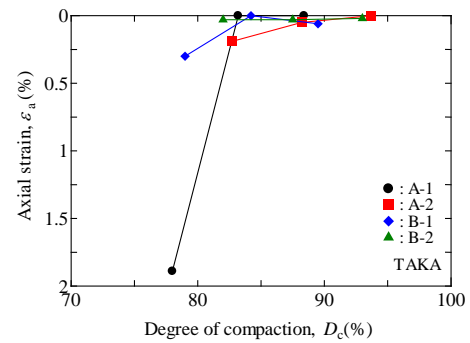


Fig. 10 Relationship between axial strain on submergence and the degree of compaction [3]

comments on the manuscript. Mr. Lee. J-H was generous in providing his test data in the laboratory.

REFERENCE

- [1] Hayashi K, "CMP Analysis of Multi-channel Surface Wave Data", Proceeding of the SEGJ Conference, 105th, Society of Exploration Geo-physicists of Japan, 2001, pp. 13-16.
- [2] Imai T, Fumoto H, Yokota K, "The Relation of Mechanical Properties of Soils to P- and S-wave Velocities in Japan", Proceedings of Japan Earthquake Engineering Symposium, 4th, Japan, 1975, pp. 89-96.
- [3] Lee J-H, Shibuya S, Yamamoto T, Okamoto K, T N Lonani, "Laboratory Investigation on the One-dimensional Settlement Characteristics of Fill Materials due to Submergence", 4th, Japan-Korea Geotechnical Workshop, 2013.

MODIFICATION OF KAOLIN MINERALOGY AND MORPHOLOGY BY HEAT TREATMENT AND POSSIBILITY OF USE IN GEOTECHNICAL ENGINEERING

Nurmunira Muhammad¹, Ideris Zakaria¹ and Abdoullah Namdar¹

¹Faculty of Civil Engineering & Earth Resources, University Malaysia Pahang, Malaysia.
aira.munira@gmail.com

ABSTRACT

This paper presents an experimental work on the effect of heat treatment on the mineralogy and morphology of kaolin. Kaolin, which is moderately expansive, was preheated at temperatures ranging from 200°C to 800°C by increment of 200°C and cooled at room temperature before it was mixed with peat. Peat represents a compressible soil and has low bearing value. The main aim of the work is to study the effect of heat treatment on shear strength parameters of peat-kaolin mixture. The mixtures are prepared at different proportions, and at each proportion triaxial samples were prepared and tested in the undrained condition to study the shear strength parameters. Untreated kaolin-soil mix was also prepared to provide a comparison between the treated and untreated soil mix in terms of the shear strength behaviour. XRD and FESEM were also carried out to investigate the change in soil micro-structure due to heat treatment. The tests showed that there was a slight improvement in the strength of peat-kaolin mixture when kaolin was preheated to a temperature of up to 400°C. Finally results were discussed and conclusions were made for the preheated kaolin-peat mixture.

Keywords: Kaolin, Peat, Heat treatment, Triaxial, Shear strength

INTRODUCTION

Kaolin is a subgroup of the clay family of mineral which contains polytypes such as kaolinite, dickite, nacrite and halloysite [1]. Mineral compositions of the tropical residual soils in Malaysia are mostly dominated by kaolinite which occurs from weathering or hydrothermal processes. Kaolinite is the principal mineral element in Kaolin which is used in various industries and has a natural moisture content between 16 to 49% [2],[3].

Kaolinite crystals are usually 0.2–2 micrometers in size. Kaolinite ($\text{Al}_2\text{Si}_2\text{O}_5(\text{OH})_4$) is a 1:1 type clay mineral composed of stacked layers of SiO_4 tetrahedral (silica) sheets and $\text{AlO}_2(\text{OH})_4$ octahedral (alumina) sheets. The ideal chemical composition is Al_2O_3 39.53%, SiO_2 46.51% and H_2O 13.96% [4]. The particles tend to agglomerate more strongly at a higher temperature and produce higher amount of coarse particles. Yilmaz [5] had mentioned that the thermal treatment affects the behaviour of clays through the influence of absorbed water. It may cause dispersion of flocculation effects depending on kaolinite mineral and the type of ion exchange. The disintegration of soil particles is completed when the water around the particles is removed. This situation may lead to particle growing to larger sizes. The XRD pattern study shows that only a small part of kaolinite mineral remains when kaolin is heated at 500°C. Some changes are observed in mineral

composition like the transformation from kaolinite to metakaolinite when kaolin is heated to between 650°C and 850°C [6].

A number of researchers recently studied the replacement of the synthetics products for ground improvement by more natural additive such as fly ash, coal ash, lime slurry, bentonite, recycled gypsum and waste plastic trays [7]. In fact, naturally occurring weak soils are the types of soil that need more attention to improve their engineering properties. The term ‘weak soil’ mentioned in this study refers to an organic soil that has high compressibility but low permeability, bearing capacity and shear strength.

In engineering projects, weak soils have unacceptable physical and mechanical properties. For example peat is a problematic soil. In Malaysia peat is found mainly in low-lying poorly drained depressions or basins in the coastal areas that occupies over a total of 2.7 million hectares, which represents about 8% of the total land area of the country [8]; hence, the need to find solutions to strengthen this problematic soil before any projects is built on it.

In a comparative study by other researchers had found that the amendment of peat with 10% kaolin could increase the compressive strength [9]. Ref Kalantari et al [10] also found a solution for increasing compressive strength of peat by mixing it with cement and fibers. However, another study has

shown that by increasing the amount of kaolinite may increase shear strength of soil treated but cause shrinkage of cement grout in grouting method [11].

Construction industries in the United States use soil mixing technique, a low-cost method in a ratio of one to five compared with other solutions; and this technique is used to treat contaminated soft soil [12]. Soil mixing can be used to treat contaminated sand as well [13]. Deep mixing method is an option to use for mixing the binding agents such as lime or/and cement because it may improve the permeability, strength and deformation properties of weak soil [14]. But, when the depth of peat layer is less than 4m, the mixing method is not effective enough.

The present work analyzes the effect of heat treatment on the shear strength parameters of the peat-kaolin mixture. We applied the soil mix design method of peat-kaolin mixtures in laboratory conditions to assess the improvement of engineering properties.

MATERIALS AND TECHNIQUE OF CHARACTERIZATION

Materials

In the field, the predominant soil types based on texture are identified by inspection. Generally, the identification and description methods of soils have already been clarified in BS 5930 Section 6. Since the texture and colour of peat soil is different than other soils it is easier to notice. Peat soil contains sediments from woody remains such as roots, branches and tree trunks. Typically the colours of peat are from dark brown to black. The samples for this study were taken at Jalan Kuantan-Pekan, Pahang, Malaysia in the coordinate of longitude E 103.301239 and latitude N 3.650854. The area has soils that have organic content.

The commercial kaolin mineral as shown in Figure 3.4 was imported from Kaolin (Malaysia) Sdn. Bhd. This is one of the main mineral suppliers in Malaysia that extracts and process kaolin in their own factory in Tapah, Perak. Type of kaolin powdered that has been used in this study is C type. The moisture content of C type is less than 7.0% in natural condition. Average particle size of this powdered kaolin in between $2.5\ \mu - 4.5\ \mu$ and the pH of 30% solid mineral are between 3.0 – 5.0. The chemical composition of kaolin as provided by the manufacturer is summarized in Table 1.

Experimental methods

In order to investigate the changes in engineering properties of our soil samples mixed with thermally treated kaolin, tests were conducted for mixtures with raw kaolin and with kaolin thermally treated at

200°C, 400°C, 600°C and 800°C. The specimens were prepared by laboratory soil mixing method at mass ratio of peat soil mix at 90:10, 80:20, 70:30, 60:40 and 50:50%.

Table 1 Chemical composition of kaolin

Type of properties	Kaolin (Manufacturer data)
• Aluminium (Al_2O_3)	• B32.0 – 38.0 %
• Silica (SiO_2)	• 47.0 53.0 %
• Iron (Fe_2O_3)	• Below 1.3 %
• Potassium (K_2O)	• Below 2.5 %
• Magnesium (MgO)	• Below 0.5 %
• Loss on Ignition @ 1025°C	• 11.0 – 14.0 %

Laboratory furnace has been used to burn kaolin with different temperatures for 1 hour. In order to investigate the effect of peat and kaolin mix on shear strength, soil compaction tests were conducted by using automatic compactor with 1 L mould. These tests are needed to determine the optimum moisture content. After mixing thoroughly, the soil samples again were compacted with the same compactor machine and then they were extruded using an extruder to a sample cylinder with the size of 38 mm diameter and 76 mm high. All re-compacted samples were left to mature in a clear plastic tube container for at least 24 hours. The unconsolidated-undrained (UU) Triaxial test has been used in order to determine the shear strength parameters. The values of the shear strength parameters reported here were the average values. The UU tests were performed according to BS 1377:1990 Part 7. In the second part of this study, the XRD and FESEM were also carried out to investigate the change in soil micro-structure due to heat treatment to gain better understanding of improvement of soil mixing properties.

RESULT AND DISCUSSION

The weak soil properties have been analyzed based on BS1377:1990 as shown in Table 2. Before the untreated soil was tested in laboratory condition, the observation was done by visual classification according to ASTM D2487. The visualization result obtained was ML (silt content with low plasticity), but the laboratory test result refined the classification as sandy silt with organic matter. The influence of different proportions of soil mixture with different levels of temperatures has been investigated and the results are presented in tables and figures.

Table 2 The properties of untreated weak soil

Properties	Organic soil
• Moisture content (%)	• 23.15
• Organic content (%)	• 10.5
• Ash Content (%)	• 89.5
• Specific gravity, G _s	• 2.58
• Liquid Limit (%)	• 38.93
• Plastic Limit (%)	• 27.65
• Plasticity Index (%)	• 11.28
• Bulk Density (kg/m ³)	• 1986.98
• Soil Type (USCS)	• SM
• Description	• Sandy Silt with Organic Matter

Influence of soil mixing on optimum moisture content

Figure 1 shows the graph of optimum moisture content for soil mixture samples with different ratios of kaolin-peat mixtures at various temperatures. When the organic soil has been mixed with increasing proportions thermally heated kaolin, the optimum moisture content gradually increased. Theoretically, when the soils are subjected to heat, dewatering process will take over after all the moisture is trapped in voids it evaporated in. Due to this dewatering process, the natural mineral soil subjected to thermal high temperatures will go through this process. Hence, the optimum moisture content of thermally heated kaolin will be much higher than the raw kaolin.

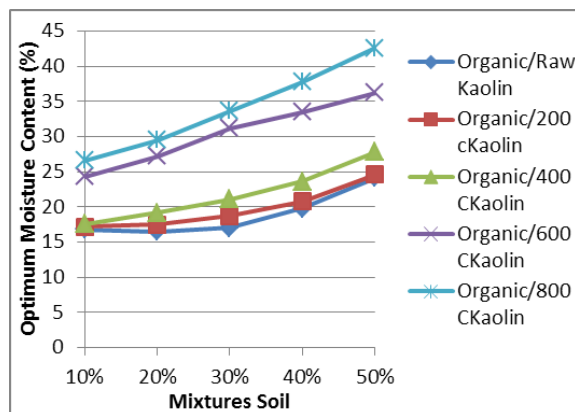


Fig. 1. Graph of optimum moisture content against soil mixture samples

Moreover, one of the factors that can also be discussed due to high OMC with low MDD are the particle rearrangement and orientation. While the preferred orientation increased as the moisture content increases, the particles, pores and other elements tend to become parallel with each other. As expected, the long platy particles seemed to be

rearrange and reorientate themselves into a new more stable position [15] but when the thermal treatment took place, the bulk density gradually decreased with temperature due to particle size distribution [16]. Eventually, when kaolin is subjected to heating process, particles are found to agglomerate more strongly and lead to have a coarser fraction. Hence, the treatment tends to reduce the density of the mixture soil samples.

Influence of soil mixing on shear strength

Shear strength was developed from both 50KPa cell pressure and deviator stress with maximum values of 182.0KPa for peat and unheated kaolin mixture at about 10% mix ratio. Figure 2 shows the pattern of the different shear strength values in term of percentage mixture. As we can see, when the proportion of mixture was increased, the shear strength value decreases.

At higher temperatures, shear strength of peat mixed with thermally treated kaolin decreases. The soil mixture at 400°C shows kaolin has lesser values in shear strength than the unheated and 200°C of heated kaolin. The main concern in shear strength development is related cohesion and the angle of friction.

The correlation coefficient (R square) by regression shows a relationship between cohesion and internal angle of friction with effects of gradient of temperature. By referring to Fig.3, the cohesion of mixture soils is found to gradually decreasing with the increasing of soil mixture temperature with R square being 0.998. In addition, the internal angle of friction (Fig.4) was increased steadily with increasing temperature of mixture and the R square is 0.997. When the soil is mixed with heated kaolin, the optimum moisture content increased but the cohesion was found to decrease steadily.

Without stabilization the untreated peat specimen has very low cohesion and internal angle of friction. This is because organic soil such peat has poor mechanical properties. Strong correlations were found between the internal angle of friction and thermal treatment of kaolin as determine by Yilmaz [5]. The internal angle of friction depends on the grain size distribution of thermal treated kaolin. The experimental results show gradually decreasing shear strength values. If we continue the experiment the results might show lower value of shear strength as the temperature increases. Hence, the investigation was stopped at 400°C.

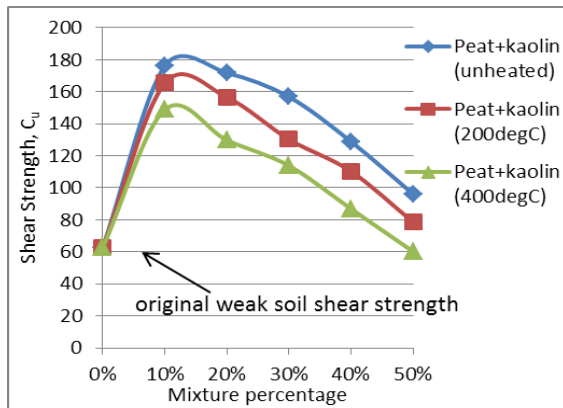


Fig. 2. Graph of shear strength against percentage of soil mixture samples

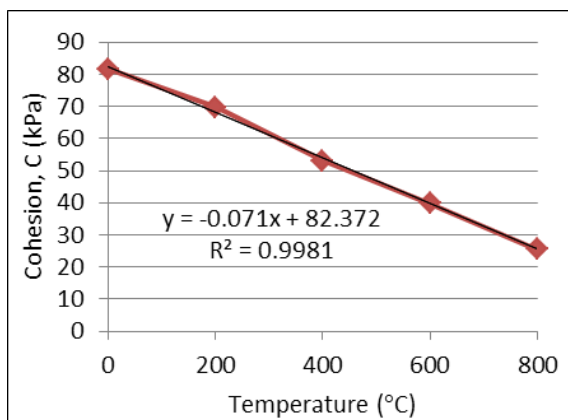


Fig. 3. Graph of cohesion against kaolin temperature of soil mixture samples

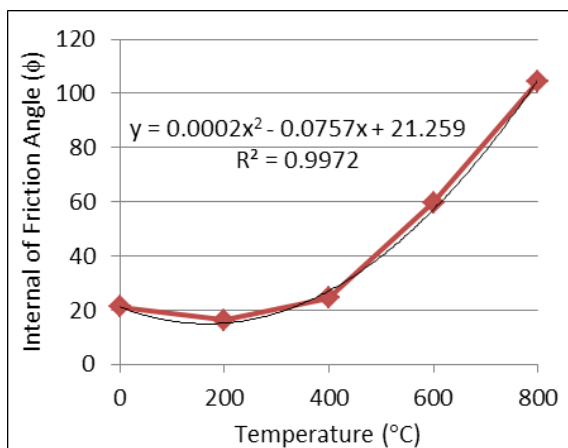


Fig. 4. Graph of internal of friction angle against kaolin temperature of soil mixture samples

Influence of mineralogy and morphology on optimal design of mixing soil

Figure 5 shows the energy dispersive X-ray characterization for optimum design of mixed soil sample that was 90% peat with 10% unheated kaolin

soil. It can be observed from this figure that other elements such as S, K and Ca are present. Table 3 lists the components identified in the 10% natural mixed soil. It has been observed that, the bonding of silica and alumina has shown major distribution effect among the elements. But the presence of some elements is detrimental to good bonding and forming strong compound of stabilizing weak soil. In their analysis of unconfined compression tests, Wong et al have shown the presence of high peaks of Ca, Si and O after curing the test specimens. These three elements would form calcium silicate hydrate as a main cementation product in stabilized soil [9].

Even though this EDAX analysis did not show a high percentage of Ca, yet this element plays an important role as a bonding agent to form an optimized mixture soil in this study. This can be clearly observed from the particle morphology of 10% mixture in Fig.6. The platy structures are closely packed together and reducing voids between the particles. Such association development is likely because the kaolin particle surface charge is compensated and hydrogen bonds can dominate instead of stronger ion-dipole interactions [17].

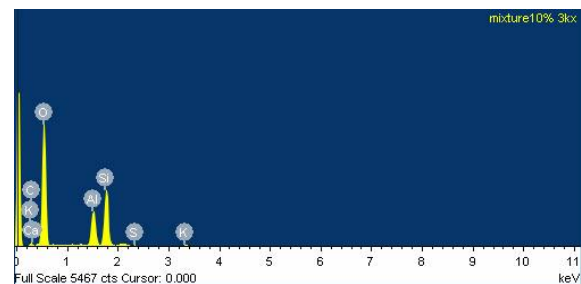


Fig. 5. The EDAX result for optimum design of mixed soil sample

Table 3. The component obtained for optimum design of mixed soil samples

Element	Weight	Formula	Compound (%)
C	7.04	CO ₂	25.80
Al	11.37	Al ₂ O ₃	21.47
Si	23.66	SiO ₂	50.62
S	0.25	SO ₃	0.63
K	0.87	K ₂ O	1.05
Ca	0.31	CaO	0.43
O	56.50		

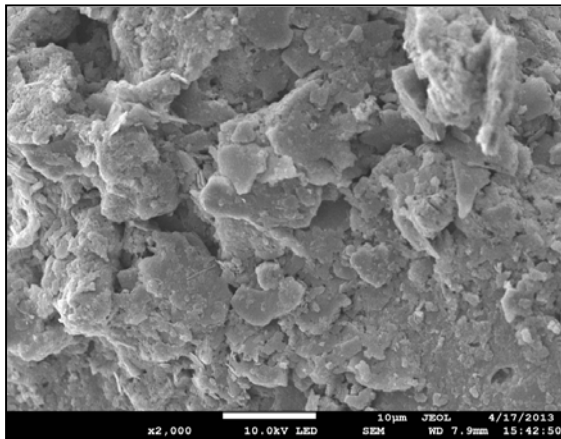


Fig. 6. The morphology photo of optimum soil mixing design by FESEM

CONCLUSION

This study was carried out to investigate the effects on shear strength of peat soil treated with unheated and thermally heated kaolin, added in different proportions. It was observed that, when cohesion increases, the internal angle of friction decreases. This phenomenon can be observed based on the effect of soil mineralogy on internal angle of friction in soil mass. When kaolin is subjected to 400°C we can see a substantial decrease of soil cohesion, and in the same time, the internal angle of friction is increased. It can be indicated that bonding sheets of silica and alumina in clay indirectly controls the internal angle of friction. The best result has been observed in the combination of 10% of unheated kaolin to the peat. This research work was limited to the specimen in the laboratory. For more investigation the subsoil or earth structure can be modelled using materials used in this research work for more application of produced materials.

ACKNOWLEDGEMENTS

The authors wish to express their gratitude to the Faculty of Civil Engineering & Earth Resources and Centralized Lab at Universiti Malaysia Pahang for the use of lab facilities.

REFERENCES

- [1] Brindley GW, "Mineralogical Studies of Kaolinite-Halloysite Clays: Part I. Identification Problems," *The American Mineralogist*. Vol., 48, 1963, pp. 897-910.
- [2] Maail S, Huat BBK, "Index, engineering properties and classification of tropical residual soils", *Tropical Residual Soils Engineering*, Taylor & Francis Group, London, 2004, pp. 37-55.
- [3] Nixon IK., Skipp BO, "Airfield construction on overseas soil: Part 5, Laterite". *Proc. Inst. Civ. Engrs.* 36(6258), 1957, pp. 253-275.
- [4] Turhan Y, Dogan M, Alkan M, "Poly(vinyl chloride)/kaolinite nanocomposites: characterization and thermal and optical properties", *Industrial and Engineering Chemistry Research* 49, 2010, pp. 1503-1513.
- [5] Yilmaz, G, "The effects of temperature on the characteristics of kaolinite and bentonite", 6(9), 2011, pp. 1928-1939.
- [6] Kakali G, Perraki T, Tsivilis S, Badogiannis E, "Thermal treatment of kaolin: the effect of mineralogy on the pozzolanic activity", *Applied Clay Science*, 20(1-2), 2001, pp. 73-80.
- [7] Masahiko et al. "Improvement of soft ground using solidified coal ash and its effects on the marine environment", *Journal of hazardous materials*, (76), 2000, pp. 285-299.
- [8] Mutalib AA, Lim J S, Wong M H, Koonvai L, ("Characterisation, distribution and utilisation of peat in Malaysia" *Proc. Int. Syrup. Tropical Peatland*, Kuching, Malaysia, May. 1991.
- [9] Wong LS, Hashim R, Ali F, "Improved strength and reduced permeability of stabilized peat: Focus on application of kaolin as a pozzolanic additive", *Construction and Building Materials*, 40, 2013a, pp. 783-792.
- [10] Kalantari B, Prasad A, Huat BBK, "Use of cement, polypropylene fibers and optimum moisture content values to strengthen peat", *International Journal of the Physical Sciences*, 7(8), 2012, pp. 1276-1285.
- [11] Kazemian S, Huat BBK., Barghchi M, "Effect of calcium chloride and kaolinite on shear strength and shrinkage of cement grout", 6(4), 2011, pp. 707-713.
- [12] Christopher RR, Brian HJ, "Deep soil mixing at jackson lake," *ASCE Geotechnical Division Specialty Conference*, vol. 1-14, no. June 25-29, 1989.
- [13] Ayotamuno M J, Martin RJ, "Soil mixing of stratified contaminated sands," pp. 53-75, 2000.
- [14] Larsson S, Rothhamel M, Jacks G, "A laboratory study on strength loss in kaolin surrounding lime-cement columns" *Appl Clay Sci* 2009;44:116-26.
- [15] Cetin H, Fener M, Söylemez M, Günaydin O, "Soil structure changes during compaction of a cohesive soil", *Engineering Geology*, 92(1-2), 2007, pp. 38-48.
- [16] Chandrasekhar S, Ramaswamy S, "Influence of mineral impurities on the properties of kaolin and its thermally treated products", *Applied Clay Science*, 21(3-4), 2002, pp. 133-142.
- [17] Kim S, Palomino A M, "Polyacrylamide-treated kaolin: A fabric study", *Applied Clay Science*, 45(4), 2009, pp. 270-279.

SIMULATING THE EFFECT OF FLOW VOLUME ON SCOURING PROCESS AROUND BREAKWATER UNDER TSUNAMI CONDITION BY SPH METHOD

M.R. Islam¹, K. Hayano¹ and A.M.K.N. Nadeesha¹

¹School of Urban Innovation, Yokohama National University, Japan

ABSTRACT

The study has attempted to simulate scouring process around the breakwater by smoothed particle hydrodynamics (SPH) method. SPH is a mesh less numerical method with a high capability of simulating large deformation of geo-material. However, SPH application in geotechnical problem is relatively new. The study has developed a simplified model arrangement with water and soil particle. Scouring process was simulated for saturated and dry soil by allowing water to fall continuously. The soil has the properties of elastic-perfectly plastic model with Mohr-Coulomb failure criteria. The water has the properties of viscous fluid. Scouring occurred as seepage force tried to drag the soil particles. Scouring process was found to advance with time and with increase in flow volume for both saturated and dry soil. The outcome of the study will help to predict the scour process around breakwater.

Keywords: SPH, Breakwater, Scour, Flow volume

INTRODUCTION

The Kamaishi seawall of 63 meters depth and 1,950 meters length was collapsed by the Great East Japan tsunami 2011. It was considered that scouring by the overtopping water had lowered the stability of the seawall foundation and caused to collapse. Scouring process consists of fluid movement and interaction with soil. To encounter such a complex problem Smoothed particle hydrodynamics (SPH) is very effective. SPH method is a particle method and does not require any mesh. A simplified 2D SPH model of water falling into the landward side of the breakwater is presented here. The study has attempted to simulate the behavior of scouring process by using the simple model. For developing the SPH code, the study has adopted the SPH theory written in Liu's book [1].

FUNDAMENTALS OF SPH

SPH is a particle method where the computational domain is discretized into a finite number of particles (or interpolating points). The material properties of a particle are evolved from the neighboring particles within support domain by using interpolation function. The interpolation process is based on the integral representation of a field function $f(x)$ follows:

$$\langle f(x) \rangle = \int_{\Omega} f(x') W(x - x', h) dx' \quad (1)$$

Where Ω is the area of the integration that contains x and x' ; and h is the smoothing length defining the

influence domain of the smoothing kernel. $W(x - x', h)$ is the kernel or smoothing function, which must satisfy the following three properties: the first one is the normalization condition,

$$\int_{\Omega} W(x - x', h) dx' = 1 \quad (2)$$

The second condition is the delta function property that is observed when smoothing length approaches zero,

$$\lim_{h \rightarrow 0} W(x - x', h) = \delta(x - x') \quad (3)$$

Additionally, the third condition is the compact condition,

$$W(x - x', h) = 0, \text{ when } |x - x'| > kh \quad (4)$$

Where k is a scalar defines the influence domain of the smoothing function.

Smoothing function

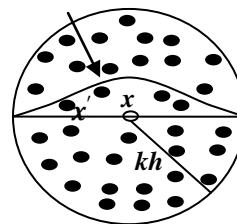


Fig. 1 Description of influence domain of a field variable 'x'.

There are many kernel functions but the study has used the cubic spline smoothing function. The cubic spline function was proposed [2]. The cubic spline function has the following form:

$$W(R, h) = \alpha_d \begin{cases} 1.5 - R^2 + 0.5R^3 & 0 \leq R < 1 \\ \frac{(2-R)^3}{6} & 1 \leq R < 2 \\ 0 & R \geq 2 \end{cases} \quad (5)$$

Where, $R = |x - x'|/h$, $\alpha_d = \frac{1}{h}, \frac{15}{7\pi h^2}, \frac{3}{2\pi h^3}$ respectively in one, two and three dimensions.

SPH Formulations for Fluid

The continuity equation used in the study is as follows:

$$\frac{D\rho}{Dt} = \sum_{j=1}^N m_j (v_i^\alpha - v_j^\beta) \frac{\partial W_{ij}}{\partial x_i^\alpha} \quad (6)$$

Where, $\frac{D\rho}{Dt}$ is the time derivative for density, m is mass, v is velocity, $\frac{\partial W}{\partial x}$ is the first derivation of kernel, i is the first particle, j is the neighboring particle, N is the number of total neighboring particle, α and β are co-ordinate direction. Moreover, the momentum equation for each particle becomes

$$\frac{Dv_i^\alpha}{Dt} = \sum_{j=1}^N m_j \left(\frac{\sigma_i^{\alpha\beta}}{\rho_i^2} + \frac{\sigma_j^{\alpha\beta}}{\rho_j^2} \right) \frac{\partial W_{ij}}{\partial x^\beta} + g^\alpha \quad (7)$$

Where, σ is the total stress tensor, and g is the external force. Total stress σ for fluid is defined as

$$\sigma^{\alpha\beta} = -p\delta^{\alpha\beta} + \tau^{\alpha\beta} \quad (8)$$

Where, p is isotropic pressure, $\delta^{\alpha\beta}$ is the Kronecher's delta, $\tau^{\alpha\beta}$ is the viscous stress for fluid. Isotropic pressure for fluid is obtained from equation of state.

$$p = B \left[\left(\frac{\rho}{\rho_0} \right)^\lambda - 1 \right] \quad (9)$$

Where λ is a constant and set equal to 7 for most cases; ρ_0 is the reference density; B is a problem dependent parameter, which sets a limit for the maximum change of the density. B is usually chosen as $B = \frac{\rho_0 c^2}{\lambda}$ where, c is the sound speed in water. However, to keep the density variation within 1% then $c = 10v_{typ}$ is chosen.

For Newtonian fluids, the viscous shear stress should be proportional to the shear strain rate denoted by ε through the dynamic viscosity μ .

$$\tau^{\alpha\beta} = \mu \varepsilon^{\alpha\beta} \quad (10)$$

$$\varepsilon^{\alpha\beta} = \frac{\partial v^\beta}{\partial x^\alpha} + \frac{\partial v^\alpha}{\partial x^\beta} - \frac{2}{3} (\nabla \cdot v) \delta^{\alpha\beta} \quad (11)$$

SPH Formulations for Soil

SPH formulation for soil is similar with fluid with some exceptions. For soil the total stress is as follows:

$$\sigma^{\alpha\beta} = -p\delta^{\alpha\beta} + s^{\alpha\beta} \quad (12)$$

where σ is total stress, p is mean stress and s is deviatoric stress. However, deviatoric stress for the soil has been calculated from Hook's law as in the equation (13)

$$\frac{ds^{\alpha\beta}}{dt} = 2G \left(\varepsilon^{\alpha\beta} - \frac{1}{3} \delta^{\alpha\beta} \varepsilon^{\gamma\gamma} \right) + s^{\alpha\beta} R^{\beta\gamma} + s^{\gamma\beta} R^{\alpha\gamma} \quad (13)$$

Where, G is shear modulus, ε is strain rate tensor, R is rotation rate tensor are defined as in Eq. (14), (15)

$$\varepsilon^{\alpha\beta} = \frac{1}{2} \left(\frac{\partial v^\alpha}{\partial x^\beta} + \frac{\partial v^\beta}{\partial x^\alpha} \right) \quad (14)$$

$$R^{\alpha\beta} = \frac{1}{2} \left(\frac{\partial v^\alpha}{\partial x^\beta} - \frac{\partial v^\beta}{\partial x^\alpha} \right) \quad (15)$$

By combining Eq. (13), (14) and (15) the deviatoric shear stress components are calculated. According to the elastic-perfectly plastic soil model, the deviatoric stress components in the plastic region are scaled back to the maximum shear stress by the Mohr-Coulomb equation

$$s_f = c + p \tan \phi \quad (16)$$

Where, c is the cohesion and p is the mean stress and ϕ is the angle of internal friction. Mean stress of soil has been calculated as the Eq. (17)

$$p = K \left(\frac{\rho}{\rho_0} - 1 \right) \quad (17)$$

Where, K is bulk modulus of soil. The study has taken the value of the K less than the actual as in the case of [4].

Soil- Water Interaction

In the preceding sections, SPH formulations for fluids and soils were described. However, it is needed how soil-water will interact with each other. The study has adopted the concept of two-phase flow for soil and water. When water will pass through the pores of the soils, it will exert drag force to the soil. This is called seepage force in soil. The seepage force acts on the soil particle and will be introduced into the momentum equation for soil and

water as in [4], [5] .

$$f_{seepage} = \gamma_w n \frac{v_{water} - v_{soil}}{k} \quad (18)$$

where γ_w is the unit weight of water, n is the porosity and k is permeability of soil.

Artificial Viscosity

The artificial viscosity terms are usually added to the pressure term in the momentum equation to diffuse sharp variations in the flow and to dissipate the energy of high frequency. The study has used Monaghan type artificial viscosity Π_{ij} . The detail formulation is as bellow:

$$\Pi_{ij} = \begin{cases} \frac{-\alpha_{\Pi} \bar{c}_{ij} \phi_{ij}}{\bar{p}_{ij}} & v_{ij} \cdot x_{ij} < 0 \\ 0 & v_{ij} \cdot x_{ij} \geq 0 \end{cases} \quad (19)$$

Where,

$$\phi_{ij} = \frac{\bar{h}_{ij} v_{ij} \cdot x_{ij}}{|x_{ij}|^2 + 0.01 \bar{h}_{ij}^2}, \quad \bar{c}_{ij} = \frac{1}{2}(c_i + c_j)$$

$$\bar{h}_{ij} = \frac{1}{2}(h_i + h_j), \quad \bar{\rho}_{ij} = \frac{1}{2}(\rho_i + \rho_j)$$

In the above equations, α_{Π} , β_{Π} are constants, in the study for water the values were taken as 0.01 and 0 respectively. However, for soil the values for the both were taken as 1.0.

With the inclusion of seepage force and artificial viscosity the momentum equation for soil is as follows;

$$\begin{aligned} \frac{Dv_i^\alpha}{Dt} = & - \sum_{j=1}^N m_j \left(\frac{p_i^{\alpha\beta}}{\rho_i^2} + \frac{p_j^{\alpha\beta}}{\rho_j^2} \right) \frac{\partial W_{ij}}{\partial x^\beta} \\ & + \sum_{j=1}^N m_j \left(\frac{s_i^{\alpha\beta}}{\rho_i^2} + \frac{s_j^{\alpha\beta}}{\rho_j^2} \right) \frac{\partial W_{ij}}{\partial x^\beta} \\ & + g^\alpha \\ & + \sum_{j=1}^N m_j \left(\frac{f_{seepage}}{\rho_{water} \rho_{soil}} \right) W_{ip} \end{aligned} \quad (20)$$

However, the momentum equation for water becomes as follow:

$$\begin{aligned} \frac{Dv_p^\alpha}{Dt} = & - \sum_{q=1}^N m_q \left(\frac{p_p^{\alpha\beta}}{\rho_p^2} + \frac{p_q^{\alpha\beta}}{\rho_q^2} \right) \frac{\partial W_{pq}}{\partial x^\beta} \\ & + \sum_{q=1}^N m_q \left(\frac{\tau_p^{\alpha\beta}}{\tau_p^2} + \frac{\tau_q^{\alpha\beta}}{\tau_q^2} \right) \frac{\partial W_{pq}}{\partial x^\beta} \\ & + g^\alpha \\ & - \sum_{q=1}^N m_q \left(\frac{f_{seepage}}{\rho_{water} \rho_{soil}} \right) W_{ip} \end{aligned} \quad (21)$$

In equation (21), p and q represent the first and second pair of the water particles. In the applications of the artificial compressibility to fluid flows, it is useful to use the 'XSPH' technique proposed by [2]. In the 'XSPH' technique fluid particle finally moves in the following way:

$$\frac{dx_p}{dt} = v_p - \varepsilon_{xsp} h \sum_{q=1}^N \frac{m_q}{\rho_q} v_{pq} W_{pq} \quad (22)$$

Where, $\varepsilon_{xsp} h$ is a constant usually in the range of 0 to 1.0. The study has used 0.001 and found good result.

Boundary Treatment

A SPH particle near or on the boundary while updating physical properties does not get neighboring particles from boundary side. This is called particle deficiency problem. The study has used symmetric image particles proposed by [3]. For each real particle located within kh distance from the boundary, an image particle is created symmetrically outside of the boundary. The image particle will have the same physical properties as the real one except the velocity and stress tensor. The velocity of an image particle normal to the boundary is taken as minus of the real one, in order to prevent the real particles from penetrating the boundary. However, velocity of an image particle tangent to the boundary is kept equal to the real one in order to simulate free-slip boundary condition on the symmetric plane. The stress tensor of an image particle is set according to the following relations:

$$\sigma_{image}^{\alpha\beta} = \begin{cases} \sigma_{real}^{\alpha\beta} & \text{if } \alpha = \beta \\ -\sigma_{real}^{\alpha\beta} & \text{if } \alpha \neq \beta \end{cases} \quad (23)$$

Time Integration

Equation (6), (20) and (21) are integrated using a standard Leap-Frog (LF) algorithm with the following integration schemes:

$$\rho_{n+1/2} = \rho_{n-1/2} + \Delta t \left(\frac{D\rho}{Dt} \right)_n \quad (24)$$

$$v_{n+1/2} = v_{n-1/2} + \Delta t \left(\frac{Dv}{Dt} \right)_n \quad (25)$$

$$x_{n+1/2} = x_{n-1/2} + \Delta t \left(\frac{Dx}{Dt} \right)_n \quad (26)$$

$$s_{n+1/2} = s_{n-1/2} + \Delta t \left(\frac{Ds}{Dt} \right)_n \quad (27)$$

Where Δt is the time step; n indicates the current time t ; and $(n+1)$ indicates the advanced time $(t+\Delta t)$. The Stability of LF scheme is guaranteed by several criteria for time step. The first one is the Courant-

Friedrichs-Levy(CFL) condition,

$$\Delta t \leq 0.25 \min\left(\frac{h}{c}\right) \quad (28)$$

And constraints due to the magnitude of particle acceleration f

$$\Delta t \leq 0.25 \min\left(\sqrt{\frac{h}{f}}\right) \quad (29)$$

And viscous diffusion

$$\Delta t \leq 0.125 \min\left(\frac{h^2}{\nu}\right) \quad (30)$$

Time step Δt for a simulation should be the minimum of value of Eq. (28)-(30).

DESCRIPTION OF NUMERICAL MODELS

A simplified model with a soil area of 0.095m X 0.25m was developed to simulated scouring process around the breakwater. Continuous water with discharges varying from 0.06m³/m/s to 0.11m³/m/s with falling heights of 0.01m was allowed to fall on the soil layer. Numerical simulations were done for the case of both saturated and dry soil. Saturated soil layer consists of both water and soil particle [4], [5] having the size of 0.005mX 0.005m. However, dry soil layer consists of soil particle only. The soil has the elastic-perfectly plastic properties with Mohr-Coulomb failure criteria. The elastic modulus of the soil was chosen as 20Mpa and Poisson's ratio was 0.3 with zero cohesion value. The density of soil was chosen as 1800 kg/m³. The water was modeled as viscous fluid having dynamic viscosity of 10⁻³ Ns/m² and density 1000kg/m³. Figure 2 depicts the initial arrangement of the simulation model.

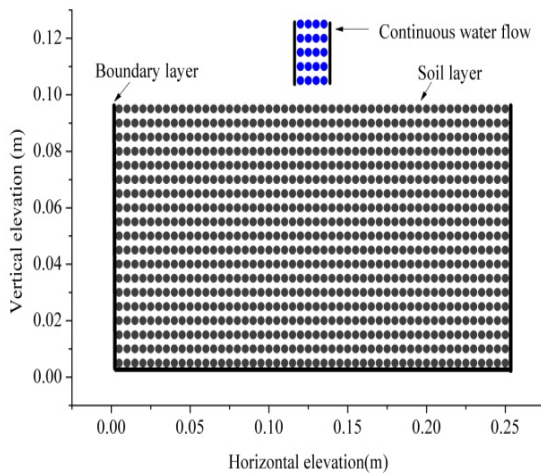


Fig. 2 Input condition of the simulation model.

Simulation Results for Saturated Soil

Saturated soil was modeled as two-phase layer of water and soil [4], [5]. Although the soil and water stay closer but their physical properties will be governed by different system. The study has used two-phase model to allow the seepage force to work properly between water and soil. From Fig. 3 to Fig. 6 describe the progress of scouring process due to falling water. The particles in the saturated soil were found to show a little disturbance with the progress of simulation. This phenomenon may be related with excessive pore water pressure development. The study has used almost fifty percent of the saturated soil mass as the water particles. Figure 7 shows the progressive scouring depths with different flow volume with same fall height of 0.01m. It shows that with increase of flow volume scour depths increase.

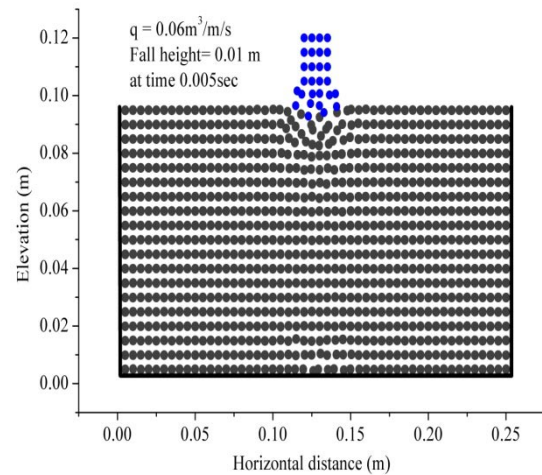


Fig. 3 Scouring progress of saturated soil at 0.005 seconds.

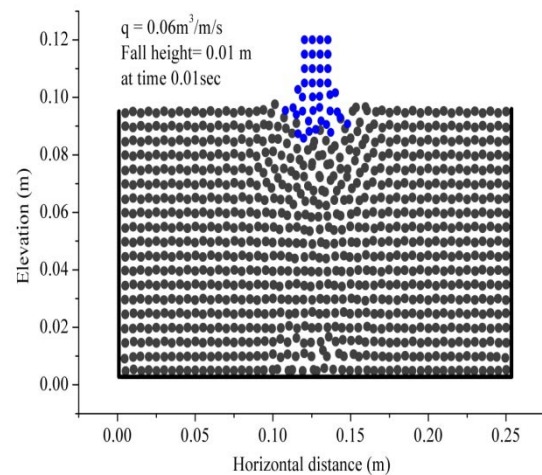


Fig. 4 Scouring progress of saturated soil at 0.01 second.

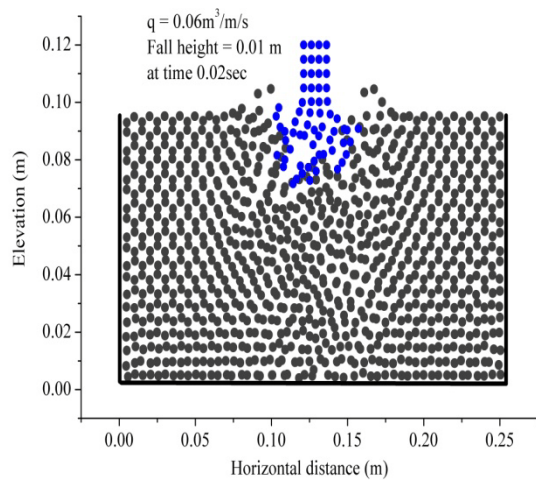


Fig. 5 Scouring progress of saturated soil at 0.02second.

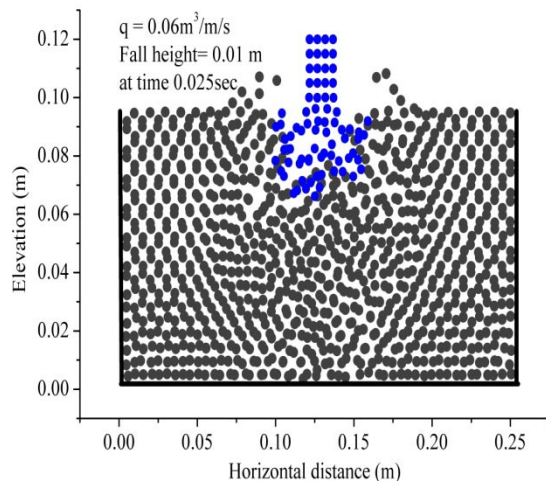


Fig. 6 Scouring progress of saturated soil at 0.025 second.

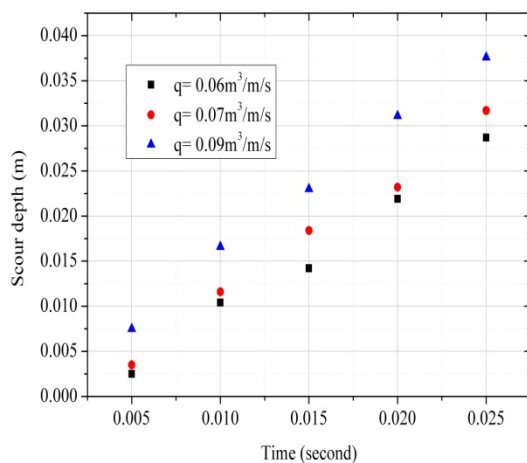


Fig. 7 Progressive scouring depths for saturated soil from 0.01m fall.

Simulation Results for Dry Soil

Dry soil layer was modeled with the soil particles only. Fig.8, Fig.9, Fig.10 and Fig.11, show the progress of scouring process. However, it is observed that soil layer has the tendency of being compressed. As the soil layer follows the principle of continuum mechanics, and drag force by the water flow was considered in the momentum equation for soil, it shows some compressive behavior after being stressed by the drag force. Fig.12 shows that with the increase of flow volume scour depth increase. From Fig.7 and Fig.12, it is found that saturated soil shows large value of scour depth comparing with that of dry soil. It is because, in the study saturated soil has porosity filled with water. However, dry soil was considered more compacted than that of saturated soil.

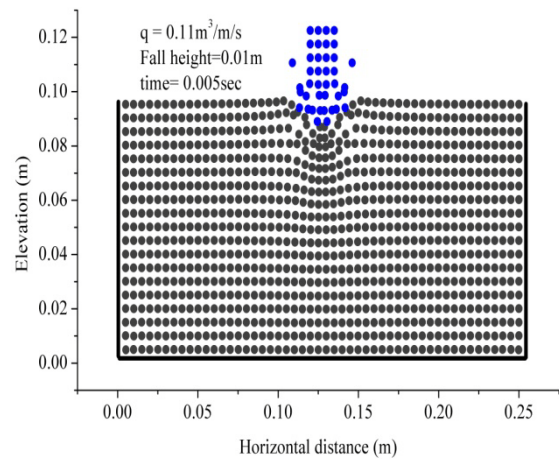


Fig. 8 Scouring progress of dry soil at 0.005second.

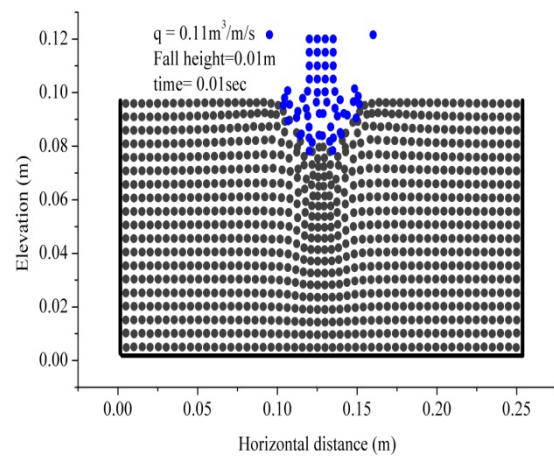


Fig. 9 Scouring progress of dry soil at 0.01second.

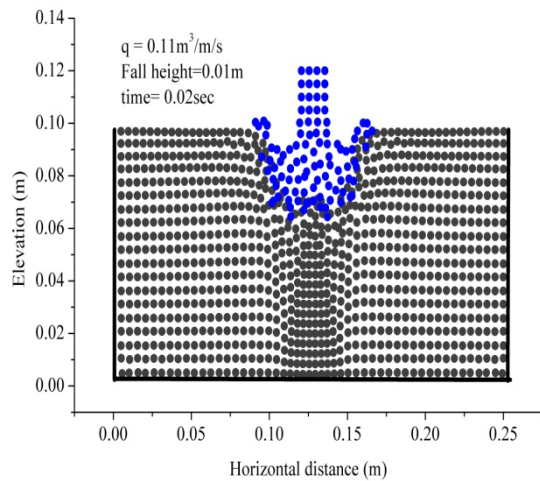


Fig. 10 Scouring progress of dry soil at 0.02second.

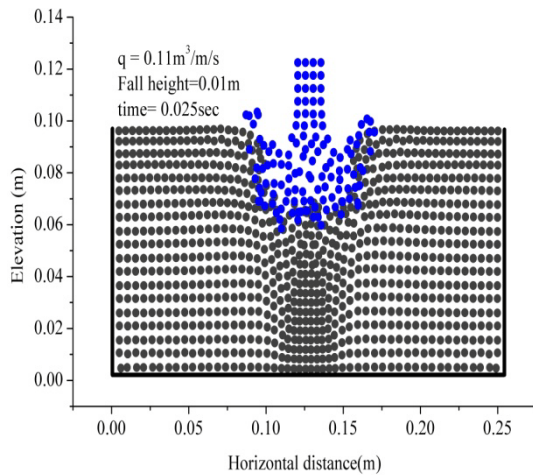


Fig. 11 Scouring progress of dry soil at 0.025second.

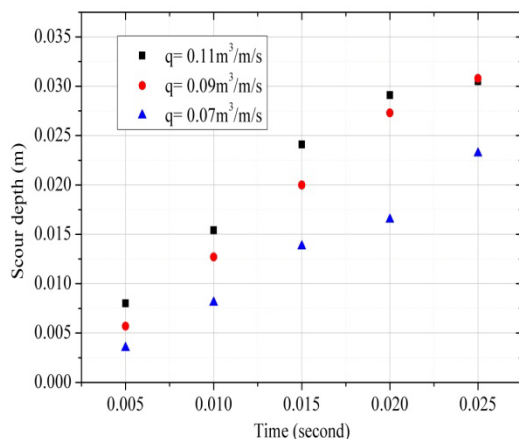


Fig. 12 Progressive scouring depths for dry soil from 0.01m fall.

CONCLUSION

The study has proved the capability of SPH method to simulate scouring process around breakwater in tsunami condition. In the simplified model, adopted here, saturated soil was modeled with water and soil particle. However, dry soil was modeled with only soil particle. It was found that scouring process progress with time and with increase of flow volume.

REFERENCES

- [1] G.R. Liu and M.B. Liu, "Smoothed Particle Hydrodynamics; a meshfree particle method", World Scientific Publishing Co. Pte. Ltd. (2003)
- [2] J.J Monaghan, "Simulating free surface flows with SPH", Computational Physics, Vol.110, (1994), pp 399-406.
- [3] Libersky LD, Petschek AG, Carney TC et al., "High strain Lagrangian hydrodynamics: a three dimensional SPH code for dynamic material response. Journal of Computational Physics 1993; 109: pp.67-75.
- [4] Bui Ha H., K. Sako and R. Fukagawa, "Numerical simulation of soil-water interaction using smoothed particle hydrodynamics (SPH) method", Journal of terramechanics 44 (2007) pp.339-346.
- [5] Maeda Kenichi, Hirotaka Sakai and Mamoru Sakai, "Development of seepage failure analysis method of ground with smoothed particle hydrodynamics", JSCE vol.7, 2004, pp.775-786.

DEVELOPING A NUMERICAL MODEL FOR THE STABILITY DESIGN OF TUNNEL HEADING

Jim Shiau¹ and Ryan Kemp¹

¹Faculty of Engineering and Surveying, University of Southern Queensland, Australia

ABSTRACT

This paper describes the development and verification of a numerical model for tunnel heading using the commercially available software FLAC. The developed model uses force relaxation techniques to simulate reductions in tunnel heading pressures. A script file was developed using the built-in program language FISH that enable automatic mesh generation for each problem analysed and allows that parametric studies to be carried out efficiently. The model results were verified by comparing stability numbers with those established results using rigorous limit analysis techniques, and were found to be within their upper and lower limits for all condition analysed. The overall aim of this paper is to provide the end user with a 'user friendly' tool for the design of preliminary face pressures to prevent instability from occurring and to control and estimate ground surface movements to tolerable limits.

Keywords: Numerical Modeling, Tunnel Heading, FLAC, Design

INTRODUCTION

As city's grow and public infrastructure become under greater pressures, governments are choosing to supplement existing infrastructure systems by constructing an underground network of tunnels. Transport infrastructure, for vehicles and trains, as well as services, for water transport, are being built under urban areas, waterways and through mountains using tunnel boring techniques.

Tunnel boring machines (TBM) have become the preferred method of underground construction in urban areas and are considered a relatively quick and safe construction technique. TBM technology has been improved significantly since its beginnings in the 1960's to where surface settlement in sensitive areas can be limited by combining state of the art TBM's with suitable construction methodologies. More research and improvements in soft soil tunnel construction is needed to better understand and control surface settlement and thus increase the applicable of tunnel boring.

In today's urban environment limiting the soils response to tunnel boring is critical to ensure that tunnel induced movements does not have an adverse impact on overlying buildings. Indeed, soil stresses are changed during construction and in turn influence the soils response [1]. These changes may be due to: (1) volume change at the heading resulting from differing heading pressures from the at-rest pressures, (2) volume change at the tail and lining annulus before grouting, (3) consolidation settlement in soft clay soils from changes in pore pressures as the TBM pushed through the soil, (4) consolidation settlement from changes in soil stress

(dependent on over consolidated ratio) and (5) poor construction techniques.

This paper is concerned with volume changes and stability at the tunnel heading as a result of changes in face pressures from the at-rest condition for soft undrained soils. This paper seeks to develop a FLAC model using the built-in program language FISH for predicting heading pressures and stability for slurry or Earth pressure balance (EPB) TBM. This will in turn provide designers with a simple but effective tool for estimating working heading pressures at the preliminary design stage and during construction.

Rigorous solutions to the tunnel heading stability problem have been presented by [2] and [3] using finite element upper and lower limit analyses for plane strain headings. It was concluded that the true solution lies within 10%, or less, of their upper and lower bounds. These accurate bounds are used in this paper to verify the results obtained using the developed FLAC model. Theoretical stability design charts were then developed. It is expected that such a development would assist the end users (industry) in their daily design work.

PROBLEM DEFINITION AND FLAC MODEL

While real soil conditions and tunnel/soil interactions are very complex, the model uses simplified assumption to predicted theoretical soil responses to tunnel construction using TBM's. The tunnel heading model assumes Mohr-Coulomb failure criteria, plane strain, and undrained condition with dimensions shown in Fig. 1. The tunnel lining is assumed to be rigid and soil conditions

homogenous having uniform properties with increasing depth.

As shown in Fig. 1, σ_s is the surface surcharge, γ is the unit weight, C is the overburden height, σ_t is the tunnel support pressure and S_u is the undrained shear strength of the soil. The tunnel support pressure, σ_t , at the at-rest condition is the state where no volume change occurs as this internal pressure theoretically matches the in-situ pressures before construction.

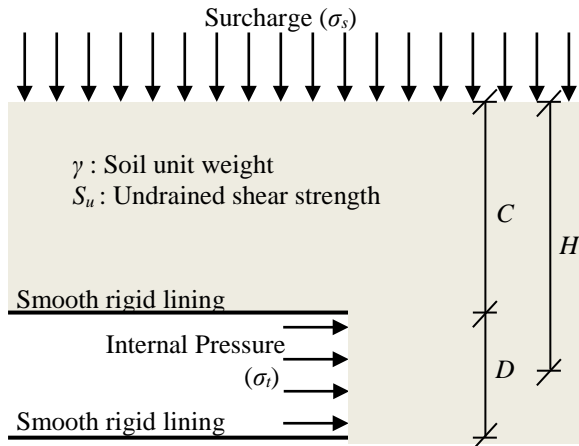


Fig. 1 Idealized plane strain tunnel heading in 2D space.

The tunnel heading problem can be approached by making use of a force relaxation technique whereby the internal pressure at the at-rest condition is determined and then relaxed by a percentage of the at-rest pressure (equilibrium reached at each relaxation step) until σ_t is equal to zero. Considering that during construction it is the slurry or earth pressures at the tunnel heading that is controlled, it is generally accepted that the use of force relaxation technique would provide a more realistic result when compared to other methods such as the displacement method. As the relaxation method better reflects the conditions at the cutter head and plenum of a slurry shield or EPM machine. Although there is some contact between the soil and cutting disk that prevents displacement at these areas, the heading is predominantly supported by the pressure balance generated at the heading during construction [4]. This is also the case when air pressure is used to support the face during maintenance.

When the heading pressure is relaxed, the heading stability decreases until yielding occurs at the point of plastic instability, or where tunnel collapse is immanent. This point is also where a sudden change in tunnel face movement takes place [4]. While reaching this point of collapse is avoided, it does provide a meaningful bound to designers in prescribing face pressure limits and in understanding the sensitivity of the soils response to changes in

face pressures during construction. Practically this means that operators could be provided with a range of upper and lower limit face pressure during construction for different materials and construction geometries.

The overall heading stability is commonly presented using the dimensionless quantities $\gamma D/S_u$ and $(\sigma_s - \sigma_t)/S_u$ and in conjunction with the geometry ratio C/D [2]. These dimensionless quantities, which are also adopted in this paper, would help to define the point of instability, providing designers and TBM operators with minimum heading pressures to prevent collapse and to estimate the sensitivity of the soil response to the tunnel boring and changes to face pressures.

A FLAC numerical model using the built-in FISH language was developed that automatically generates grid dimensions, solution commands and outputs relevant plots for prescribed condition. The developed model, using built-in program language FISH, is user friendly with only limited soil parameters and dimension inputs required by the designer to achieve relatively accurate and meaningful results for preliminary design and construction purposes.

A typical mesh generated by FLAC using the developed script is shown in Fig. 2. The grid was generated by entering the required parameters in *Heading.fis* and then calling the script from the command window.

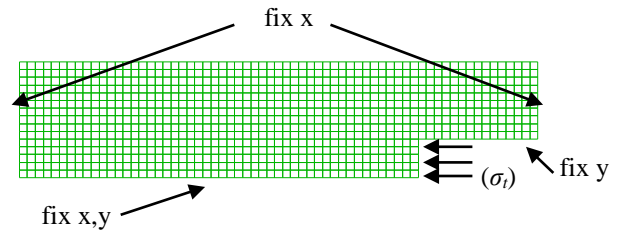


Fig. 2 A typical mesh generated by FLAC using Heading.FIS ($C/D=2$).

It is aimed to develop a design tool that requires a limited number of input, i.e. soils parameters and tunnel dimensions, as well as achieving a relatively quick computation time while still providing accurate and useable results to the designer. Fig. 3 shows a typical screen shot of the FISH input window with a total of nine soil and geometric parameters required for analysis.

$C = 2$; Height of overburden soil
$D = 1$; Diameter of the tunnel
$SOIL_DEN = 1631$; Soil density
$SOIL_COH = 80E3$; Cohesion
$SOIL_FRI = 0$; Frictional angle
$SOIL_DIL = 0$; Soil Dilation

```
Set_grav = 2*9.81      ;more g for stiff clay
Sigma_s = 0            ; surface surcharge
No_relax = 11          ;force relaxation steps
```

Fig. 3 A typical FISH input window.

The built-in program language FISH also allows efficient parametric and sensitivity analysis to be undertaken by the use of 'batch' files.

OPTIMIZATION OF MESH SIZE AND FORCE RELAXATION STEPS

One of the goals of optimizing the mesh size was to ensure accurate test results by having small enough elements to model soil behavior correctly while at the same time minimizing computational speed by limiting element sizes. With the aim of simplifying usability, a set mesh size for varying ratios of C/D needed to be determined.

This convergence between accuracy and computational efficiency was achieved by trialing different grid sizes between 0.2 m and 0.05 m. Table 1 shows a summary of the mesh size optimization results for different grid sizes for $C/D = 2$.

Table 1 Mesh size optimization ($C/D = 2$ and 10 relaxation steps).

Grid Size (m)	Stability Number $(\sigma_s - \sigma_t)/S_u$ (This paper)	Difference (%)
0.2	-1.676	N/A
0.1	-2.020	20.6
0.05	-2.155	6.6

The difference between using a grid size of 0.2 m and 0.1 m is over 20% while the difference between using a grid size of 0.1 m and 0.05 m reduces to less than 7%. Considering that the difference in stability number would be less than 7%, a grid size of 0.1 m was selected as the optimal grid size for all verification analyses.

Similarly, the number of relaxation steps required for the model verification was optimized to improve computational efficiency. Using a small number of relaxation steps while reducing computational time would decrease result accuracy. On the other hand increasing the number of relaxation step increases computational time, and therefore increases accuracy.

A number of trial runs were performed to determine the optimal number of relaxation steps for the validation and future analyses. Table 2 shows a summary of the results for a grid size of 0.1 m of $C/D = 2$. The results are also shown graphically in Fig. 4. It can be seen that convergence is achieved at

around 50 steps, and this value was selected for the model in subsequent verification analyses. This means that at each relaxation step the tunnel heading pressure is relaxed (reduced) by 2% of the at-rest earth pressure.

Table 2 Number of relaxation step optimization ($C/D = 2$ and grid size of 0.1 m).

Relaxation steps	Stability Number $(\sigma_s - \sigma_t)/S_u$ (This paper)	Difference (%)
10	-2.095	N/A
20	-1.833	12.58
50	-1.676	8.57
100	-1.676	0

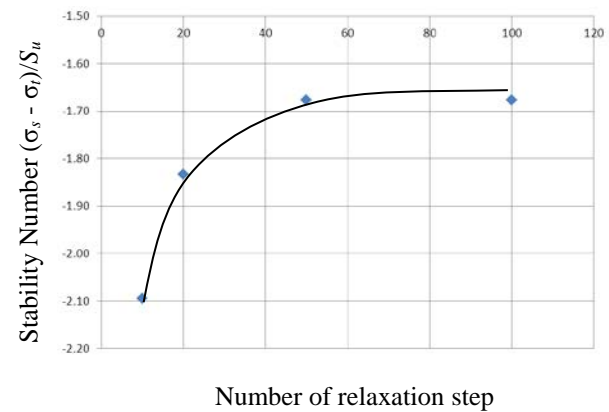


Fig. 4 Stability number against relaxation steps.

Once a grid size and reduction factor was selected based on computational efficiencies and accuracy, model verification was carried out accordingly.

MODEL VERIFICATION

To verify the developed model in this paper, stability numbers were compared to the rigorous upper and lower bounds published in [2] and [3]. The upper and lower bounds provide limits where the likely 'true collapse' would occur. The point of collapse is the point where the soil reaches plastic instability. Using the force relaxation technique, the point where the soil reaches plastic instability can be determined by inspections from the plots of plastic yields and unbalanced forces at all relaxation steps.

Figs. 5 - 8 show an example of the point where the soils progress from the stable elastic state to plastic instability. This is for the case of ($C/D = 2$ and $\gamma D/S_u = 2$). Inspection of the unbalanced forces in Figs. 5 and 6 shows that there is a relaxation step at which the soil goes from a steady balanced force state to a unbalanced force state, indicating that a

failure mechanism formed. Similarly, inspection of the plastic yields in Figs. 7 and 8 shows that there is a relaxation step where the soil surrounding the tunnel head and the soil above the head changes from the elastic state to the plastic state in a single relaxation step.

The step before plastic instability occurs, shown in Figs. 5 and 7, is considered to be the relaxation step just before true collapse of the tunnel heading would occur. The internal pressure, σ_t , at this relaxation step is the value selected to determine the stability number for the tunnel heading. The internal pressure at this point with an appropriate factor of safety would be the pressure prescribed on the construction field sheet to provide operators with a lower bound face pressure that should not be exceeded.

The step after plastic instability has occurred, Figs. 6 and 8, results in a sudden increase in soil displacement at the face and corresponding decrease of ground settlement at the surface, along with a sudden increase of unbalanced forces. At this step the soil strength with the aid of the internal tunnel pressure can no longer support the overburden weight and surface pressures, and tunnel collapse would theoretically occur. The step where plastic instability has occurred is therefore considered to be unstable and to be avoided during construction.

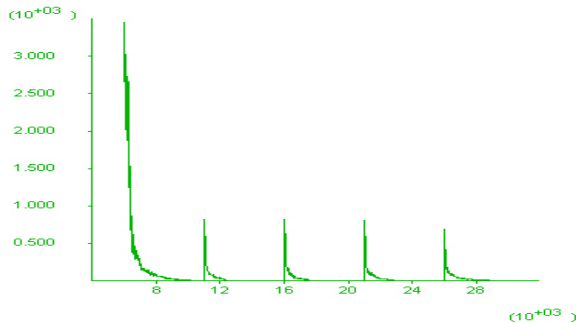


Fig. 5 Unbalanced force before plastic instability has occurred ($C/D = 2$ and $\gamma D/S_u = 2$).

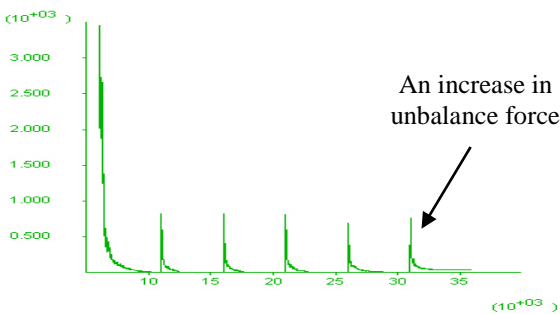


Fig. 6 Unbalanced force after plastic instability

has occurred ($C/D = 2$ and $\gamma D/S_u = 2$).

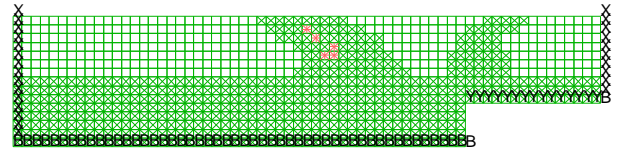


Fig. 7 Step before plastic instability has occurred for $C/D = 2$ and $\gamma D/S_u = 2$.

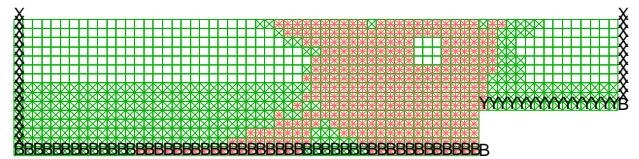


Fig. 8 Step after plastic instability has occurred for $C/D = 2$ and $\gamma D/S_u = 2$ (plastic indicators are shown in orange colour).

Table 3 shows a comparison of stability numbers between FLAC (this paper) and those in [3] using rigorous upper and lower bound techniques. This is for the case of $\gamma D/S_u = 3$. The results are also shown graphically in Fig. 9.

Table 3 Comparison of stability numbers ($\gamma D/S_u = 3$).

C/D	Lower Bound [3]	Stability Number ($(\sigma_s - \sigma_t)/S_u$) (This paper)	Upper Bound [3]
1	-0.74	-0.12	-0.11
2	-2.84	-2.02	-1.82
3	-5.03	-4.23	-4.00
4	-7.49	-6.65	-6.29
5	-10.11	-9.26	-8.80

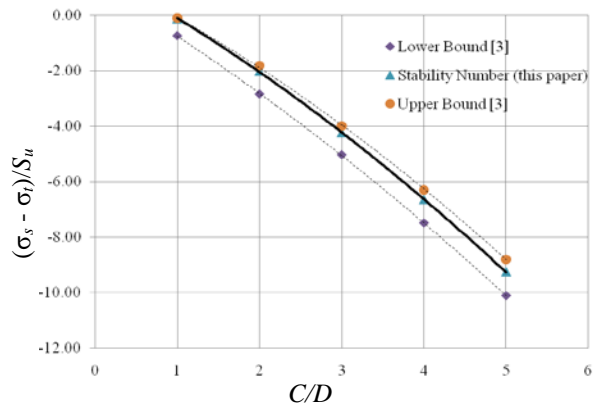


Fig. 9 Comparison of stability, this paper, with [3] and [4] ($\gamma D/S_u = 3$).

It can be seen from Fig. 9 that FLAC results are located within the upper and lower bounds. At small C/D values the stability number is near the upper bounds and with increasing C/D ratios the stability number moves slightly towards the lower bound.

These results indicate that the current developed model produce accurate results and can be used in estimating tunnel stability and provide tunnel design engineers with suitable internal pressures at the cutting face.

RESULTS AND DISCUSSION

To expand our numerical study for other TBM geometrical dimensions and for a wider range of softer soils, a series of parametric studies were performed. Nowadays, diameter (D) of TBM's can range from less than 1 m, for services such as water pipelines, to over 19 m for two level, three lane roads such as the 19.25 m TBM for the Orlovski tunnel in St Petersburg. Overburden heights (C) can range from several meters to over 50 m (English Channel). The range of C/D ratios that TBM need to operate in is therefore relatively large.

The range of strata conditions vary from hard rock to the soft collapsible soils. Practically, the definition of the strength of 'soft' soil may vary worldwide however for the purpose of this paper soft soil refers to soil strength ranging between firm to very soft with undrained shear strength between 0 kPa and 50 kPa. It is typically these 'soft' soils that require "positive" face support in order to prevent collapse and limit surface settlement.

The computed numerical results are summarised in Table 4 and a design chart using the values in Table 4 is shown graphically in Fig. 10.

Table 4 Stability of tunnel heading $(\sigma_s - \sigma_t)/S_u$

	C/D				
$\gamma D/C_u$	1	2	3	4	5
1	2.94	3.05	2.78	2.34	1.86
2	1.45	0.56	-0.69	-2.09	-3.76
3	-0.12	-2.02	-4.23	-6.65	-9.26
4	-1.66	-4.45	-7.77	-11.08	-14.45
5	-3.10	-7.05	-11.26	-15.43	-19.94
6	-4.61	-9.54	-14.68	-20.00	-26.25

In Table 4, positive values of stability number, such as those with $\gamma D/S_u = 1$ and $\gamma D/S_u = 2$ for $C/D = 1$ and 2, would require a negative σ_t (pulling pressure) to reach the point of imminent collapse. Therefore they are considered as stable and require no internal pressure to maintain the stability. However, in practice elastic settlement may need to be controlled and so face pressures would be applied

to the tunnel heading.

As $\gamma D/S_u$ increase (decrease in soil strength) negative values of stability number are obtained. From the equation $(\sigma_s - \sigma_t)/S_u$, it is known that for a negative stability number, the value of σ_t must be positive ~ a positive "pushing" pressure is required to prevent imminent collapse.

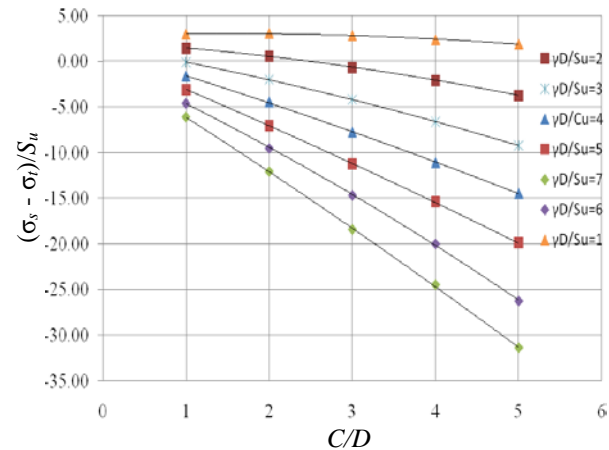


Fig. 10 Design chart for the stability of tunnel heading.

During construction, it is the softer soils that are particularly problematic and considered the most unstable, thus requiring tighter control at the face to prevent collapse or to limit surface settlement.

It should be noted that with softer soils ($\gamma D/S_u > 4$), some plastic zones may occur before 'full' plastic instability occurs. However, through inspection of the plastic yield plots at internal pressures greater than the instability pressure it can be seen that these localized plastic zones are generally located near the tunnel heading and do not remain plastic, and also do not extent all the way to the surface. It indicates that if adequate pressure head is maintained then localised failure can be prevented.

Clear differentiation can however be made between localized plastic zones with balanced internal forces and full plastic instability where internal forces remain unbalanced. An interesting observation is the areas of localized instability when $\gamma D/S_u > 4$. This confirms the general rule by [5] that bulging may occur at the tunnel heading although the face at the pressure is considered to be within acceptable limits.

Example of Estimation of Internal Pressure

A tunnel with diameter (D) 6.0 m is buried at a depth of 12 m (C) in an undrained clayey material with properties $S_u = 27$ kPa, $\phi_u = 0^\circ$ and $\gamma = 18$ kN/m³. Given the surface surcharge loading $\sigma_s = 10$ kPa, determine the theoretical tunnel heading pressure σ_t required to maintain the tunnel stability.

The following procedures are used to determine the theoretical internal pressure σ_t .

1. Given $C = 12$ m and $D = 6$ m, $C/D = 2$.
2. Given $S_u = 27$ kPa and unit weight $\gamma = 18$ kN/m³, $\gamma D/S_u = 4.0$.
3. For a 2D tunnel heading problem with $C/D = 2$, $\gamma D/S_u = 4.0$, Fig. 10 returns a value of $(\sigma_s - \sigma_t)/S_u = -4.45$.
4. σ_t can then be computed $\sigma_t \approx 10 - (-4.45 * 27) = 130.15$ kPa. Positive values of σ_t indicate an internal “pushing” pressure.

CONCLUSION

The tunnel heading stability model has been developed to provide designers with a simple but accurate tool for estimating shield or EPB face pressures within soft clay soils during the preliminary design and construction stage. Verification of stability numbers with rigorous upper and lower bound solutions in [3] and [4] confirms that the model produces accurate results for the stability problem. A simple design chart was developed to provide the user with internal pressure for a larger range of geometric situations and soil condition than typically available.

The developed FISH programme (Heading.fis) can be used for site specific parametric or sensitivity analysis. Heading.fis has nine input parameters. Once called into FLAC, it automatically generates grid dimensions, solution commands and outputs

relevant plots and table for examination and easy interpretation of results. Proposed future work on the model is to simulate situation with varying soil properties with depth and multiple soil layers.

REFERENCES

- [1] Leca, E, New, B, “Settlements induced by tunneling in soft ground”, Tunnelling and Underground Space Technology 22, 2007, pp. 119–149
- [2] Sloan, SW, Assadi, A, “Undrained stability of a plane strain heading”, Canadian Geotechnical Journal, Vol 31, 1994, pp. 443-450.
- [3] Augarde, CE, Lyamin, AV, Sloan, SW, “Stability of an undrained plane strain heading revisited”, Computer and Geotechnics, Vol 30, 2003, pp. 419-430.
- [4] Grant, RJ, Taylor, RN, “Stability of tunnels in clay with overlying layers of coarse grained soil”, International Conference on Geotechnical & Geological Engineering, 2000.
- [5] Kim, SH, Tonon, F, “Face stability and required support pressure for TBM driven tunnels with ideal face membrane-drained case”, Journal of tunneling and underground space technology, Vol 25, 2010, pp. 526-542.

INVESTIGATION OF THE OPTIMAL SUPPORT PATTERNS IN BRACED EXCAVATION USING GROUND ANCHORS

H. M. Shahin¹, Teruo Nakai², Okuda Kazuaki³ and Kato Morihiro⁴

¹Department of Civil Engineering, Nagoya Institute of Technology, Japan; ²Geo-Research Institute, Nagoya Branch, Japan; ³Penta-Ocean Construction Co. Ltd., Miyagi, Japan; ⁴Central Japan Railway, Gifu, Japan

ABSTRACT

In this research, to establish a rational design and construction process in braced excavation using ground anchors, two-dimensional model tests are carried out varying the length, number and inclination of ground anchors. Numerical simulations with finite element method using FEMtij-2D are also carried out for the same scale of the model tests. Subloading t_{ij} model is used in the analyses to model the ground material. It has been revealed that installation a longer anchor at the deeper excavation part is the most effective method in the ground anchors of earth retaining wall. Installation angle of ground anchor has significant effect on the backfill ground displacement and deformation of the retaining wall as well. The numerical analyses capture well the results of the model tests.

Keywords: Braced excavation, Ground anchor, Finite element analysis, Reinforcing

INTRODUCTION

It is well known that an open excavation causes problem to the deformation of surrounding ground. Retaining wall is commonly used to prevent the ground deformation during excavation. In addition, struts are used to make a large underground area in open excavation. However, sometimes the struts hinder the construction process as the excavated area is occupied with the struts. It is possible to excavate large section and to increase excavation depth using ground anchor as reinforcement in a retaining wall without strut, which accomplishes smooth handling of construction works. In present design method of retaining wall with anchor, earth pressure acting on the retaining wall and its deformation are evaluated by empirical procedure imitating the construction procedure of strut. Since it is expected that the construction of anchor type retaining wall will be increasing day by day, it demands a rational design procedure. Therefore, purpose of this research is to investigate the mechanism of anchor type retaining wall by model tests and numerical analyses. The analyses are performed using finite element method based on an elastoplastic constitutive model named subloading t_{ij} model [2]. This model can describe typical stress deformation and strength characteristics of soils such as the influence of intermediate principal stress, the influence of stress path dependency of plastic flow and the influence of density and/or confining pressure.

LAYOUT OF MODEL TESTS

Figure 1 shows the schematic diagram of the

two-dimensional apparatus. The size of the model ground is 680mm in width and 450mm in height. Aluminum rods of 5cm in length, having diameters of 1.6mm and 3.0mm and mixed with the ratio of 3:2 in weight, are used as the model ground (unit weight of the mass is 20.4kN/m³). The retaining wall is 300mm in length, 60mm in width and 0.5mm in thickness, which is a plate of aluminum material ($EI = 0.88 \text{ N}\cdot\text{m}^2/\text{cm}$, $EA = 4.22 \text{ kN/cm}$). It is set in the ground before excavation and is located at 200mm from the right boundary of the ground. In the experiment the model ground was excavated with a layer of 15mm in thickness up to a possible depth of excavation. The anchor plate is 50mm in length, 50mm in width and 5mm in thick, and it is made of aluminum. In the anchor plate, aluminum rods of 1.6mm diameter are glued at both sides at an interval of 10mm to maintain a certain friction between the ground and the anchor plate. Pre-stress is applied at the head of the anchors. The pre-stress of the anchor is controlled by a fly nut set up at its head, and the anchor can be set up at any arbitrary inclination (θ) from the horizontal line. The anchor is modeled connecting the head and the anchor plate by piano wire (thread) at both sides of the ground. The piano thread is 0.3mm in diameter having $EA = 1.41 \times 10^3 \text{ kN/cm}$. Biaxial strain gages attached with a thin aluminum board (30 mm in length, 60 mm in width, and 0.2 mm in thickness) are connected in the piano thread to measure tensile force. By taking photographs with a digital camera and using PIV technique the ground movements and consequently the strain of the ground are measured. The wall deformation is also measured using digitizer from the photographs of the ground. A laser type

displacement transducer is used to measure surface settlement of the ground.

Table 1 shows the experimental pattern. The anchors are set up either at 2 stages or 3 stages. Excavation depth during the installation of the 1st stage anchor is 30mm, the 2nd stage anchor is 90mm and the 3rd stage anchor is 150mm. The anchor depth for the 1st stage anchor is 15mm, the 2nd stage anchor is 75mm and the 3rd stage anchor is 135mm from the surface of the ground. A plane of active earth pressure is assumed considering the final excavation depth is 210mm and angle of internal friction is 30°. The anchor plate is set up outside of the assumed plane of active earth pressure. Case2-A and Case3-A are considered as the basic patterns, and experiments are carried out changing the length of the anchor. The initial pre-stress of the anchor is calculated from the active earth pressure using the prescribed excavation depth of each anchor as mentioned above. In this paper, only the results of the 2 stages and 3 stages anchor with the inclination of 30° will be illustrated due to the space limitation.

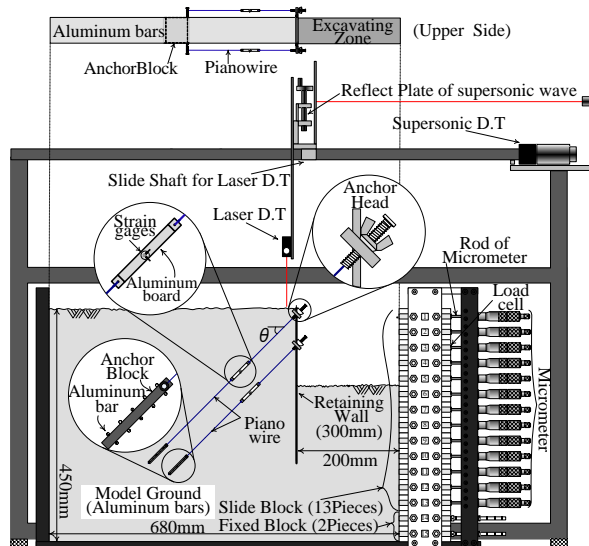


Fig.1 Apparatus of the model experiments

Table 1 Pattern of experiments

	No	Initial tensile force (N)	Anchor length L (mm)	Angle θ°
Case2-A	2	$T_1=0.31$	$L_1=150, L_2=125$	30
Case2-B			$L_1=300, L_2=125$	
Case2-C			$L_1=150, L_2=250$	
Case2-D			$L_1=300, L_2=250$	
Case3-A	3	$T_3=0.84$	$L_1=150, L_2=125, L_3=100$	
Case3-B			$L_1=300, L_2=125, L_3=100$	
Case3-C			$L_1=150, L_2=125, L_3=300$	

LAYOUT OF NUMERICAL SIMULATIONS

An elastoplastic constitutive model for soils, called the subloading t_{ij} -model [2], is used in finite element analyses. This model requires only a few unified material parameters, but can describe properly the following typical characteristics of soils: (1) influence of intermediate principal stress on the deformation and strength of soil; (2) influence of stress path on the direction of plastic flow is considered by splitting the plastic strain increment into two components; (3) influence of density and/or confining pressure. Model parameters for the aluminum rod mass are shown in Table 2. The parameters are fundamentally the same as those of the Cam clay model except for the parameter a , which is responsible for the influence of density and confining pressure. Where, λ and κ are the slope of loading and unloading curve of e - $\ln p$ graphs at the loosest state. N is the void ratio at mean principal stresses (p) 98kPa in the above mentioned loading curve and v_e is the Poisson's ratio. The parameter β controls the shape of yield surface. These parameters can easily be obtained from traditional laboratory tests. The parameters can be determined through conventional triaxial tests and consolidation test. Figure 2 shows the results of biaxial tests for the mass of aluminum rods used in the model tests. The figure shows the positive and negative dilatancy of aluminum rod mass; and it is clear that the strength and deformation behavior are very similar to those of dense sand.

Table 2 Material parameters for aluminum rods

λ	0.008	Same parameters as Cam-clay model
κ	0.004	
N (e_{NC} at $p=98kPa$ & $q=0kPa$)	0.3	
$R_{CS}=(\sigma_1/\sigma_3)_{CS(comp.)}$	1.80	
v_e	0.20	Shape of yield surface (same as original Cam-clay at $\beta=1$)
β	1.20	
a	1300	Influence of density and confining pressure

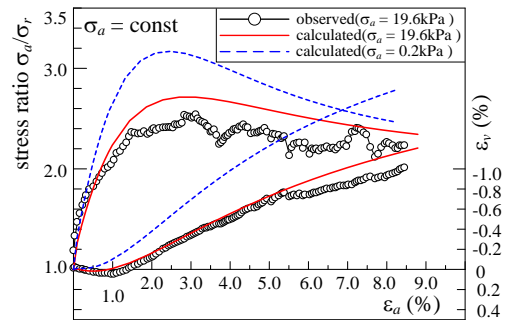


Fig. 2 Stress-strain-dilatancy relation for the mass of aluminum rods

Figure 3 shows a mesh used in the finite element analyses for the simulations of the model tests. The analyses are carried out using finite element code FEMtij-2D developed in our laboratory. Isoparametric 4-noded elements are used to represent the soil. The mesh is well refined with elements of finer mesh in most regions. The sheet pile and anchor plates are modelled using elastic beam elements. The frictional behavior (friction angle $\delta=14^\circ$) between the sheet pile and the ground is simulated using elastoplastic joint elements [1]. The frictional angle, $\delta=14^\circ$, was obtained from a laboratory model test. The anchor is modelled using truss element as it can only resist tensile force. The stiffness of the truss element considered in the analyses is the same as the stiffness of the piano wire used in the model tests. In the analyses, the excavation is simulated removing elements in the mesh corresponding to the excavation area of the model tests. The analyses are carried out under plane strain conditions, since the aluminium rods do not deform in the out of plane direction. The analyses are carried out with the same conditions of the model tests. Both vertical sides of the mesh are free in the vertical direction, and the bottom face is kept fixed. The initial stresses of the ground are calculated by applying the body forces due to self-weight ($\gamma=20.4\text{kN/m}^3$), starting from a negligible confining pressure ($p_0=9.8\times 10^{-6}\text{kPa}$) and an initial void ratio $e=0.35$. After self-weight consolidation the void ratio of the ground was 0.28 at the bottom and 0.30 at the top. The pre-stress is applied at the head of each anchor the same as the model tests.

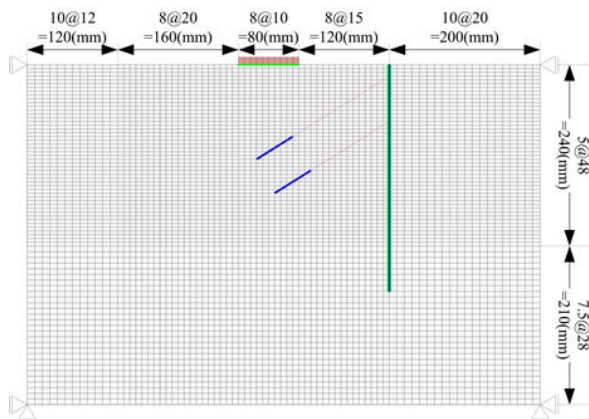


Fig.3 Mesh for Finite Element Analyses

Pullout Capacity of Anchor Block

The tensile strength of anchor block has been investigated by a pullout test. Figure 4 shows the observed and computed results of the tests. The analyses are performed applying upward vertical displacement at the top most nodal point of the

anchor block (beam element). Two tests are conducted varying the depth of the anchor from the surface of the ground (D), $D = 15$ and 30cm . In the figure the marks represent experimental results and the lines show computed results. It is seen in the test results that pullout force of anchor block increases with the increasing vertical displacement and reaches an ultimate value following a reduction to some extent. The ultimate pullout load capacity of the deeper anchor block is larger than that of the shallower one. Although the numerical analysis shows the tendency of a flatter initial slope, it can mostly evaluate the ultimate pullout capacity and variation of the capacities with the soil depths the same way as the model tests. Therefore, the modeling of the anchor block in the numerical analysis can be considered as an appropriate one.

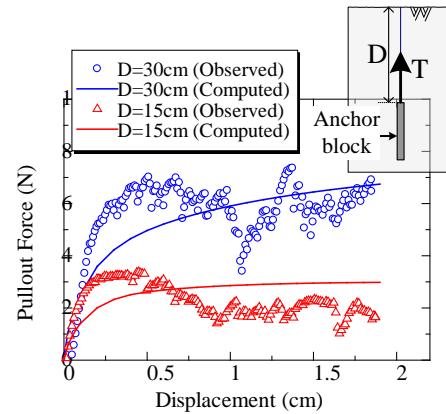


Fig.4 Tensile strength of anchor block

RESULTS AND DISCUSSIONS

Figure 5 shows the observed (Fig.5 (a)) and computed (Fig.5 (b)) wall displacements for Case2-B and Case2-C where anchors are set at two stages in the ground. Figure 6 represents surface settlement profiles for the same set of tests. The legend represents excavation depth (d). The arrows in the figures indicate the position of the upper and lower anchors. It is revealed that for the two-stage anchors it restricts the wall displacement and surface settlement till the excavation depth of 150mm irrespective of the anchor length. When excavation depth exceeds 150mm a large wall displacement is observed near 150mm depth of the wall, and the surface subsidence increases significantly as well. For the excavation depth of 180mm, the influence of anchor length is seen remarkably. In Case2-C (only the lower anchor length is longer) the wall displacement is smaller than that of Case2-B (only the upper anchor length is longer). It (Case2-C) also restricts the surface subsidence both in magnitude and in area, i.e. subsidence occur in narrower area. Therefore, if the lower anchor is longer, it is possible to make deeper excavation. The results of the

numerical analyses show the same tendency of the model tests not only in shape but also in quantity for both wall displacement and surface settlement profiles.

Figure 7 represents the maximum horizontal displacement of the wall for the excavation depth of 150mm and deeper where the wall displacement remarkably occurs. The figure shows the comparison of the results among Case2-A, Case2-B, Case2-C and Case2-D. As mentioned above, Case2-C (only the length of the lower anchor is longer) restricts the wall displacement almost the same extent as Case2-D where the lengths of both upper and lower anchors are longer. That is, the longer lower anchor produces supporting effect efficiently. On the other hand, only the longer upper anchor, Case2-B, produces almost the same effect as Case2-A where the lengths of both upper and lower anchors are shorter. In both Case2-A and Case2-B, displacement increases significantly when excavation depth crosses 180mm and the ground collapses at shallower excavation depth compare to other two cases. The numerical simulation slightly over-predicts the wall displacement of Case2-A at excavation depth of 180mm as some elements in the ground undergo into failure state. Until the collapses of the ground the analyses show good agreement with the model tests.

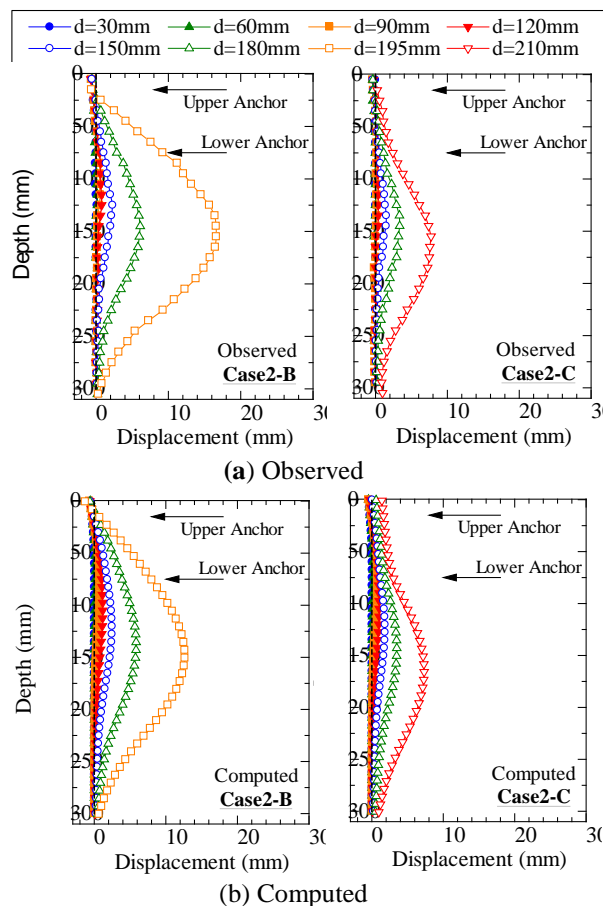


Fig.5 Horizontal displacement of wall in Case2-B, C

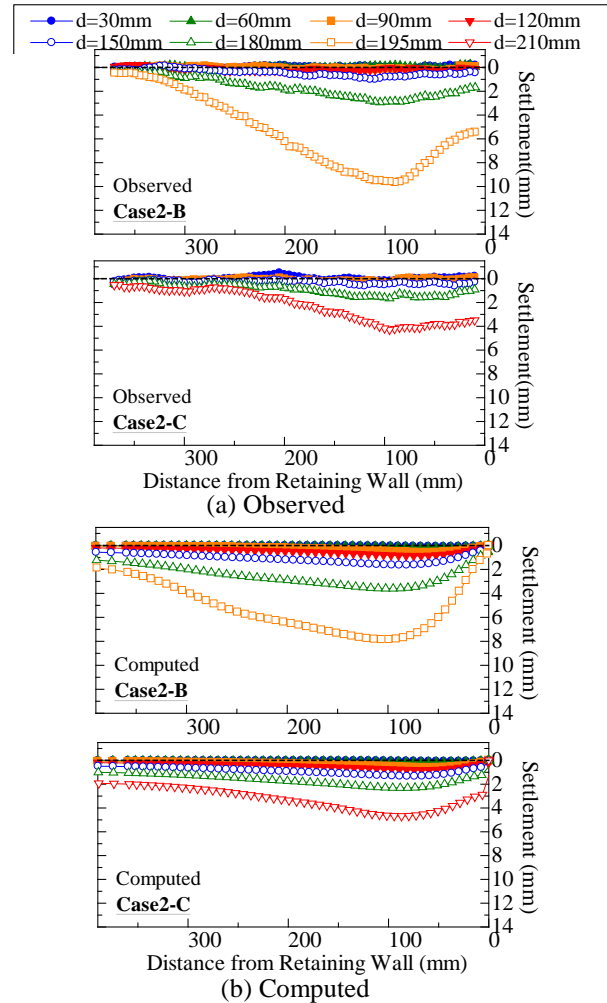


Fig.6 Surface settlement profiles in Case2-B, C

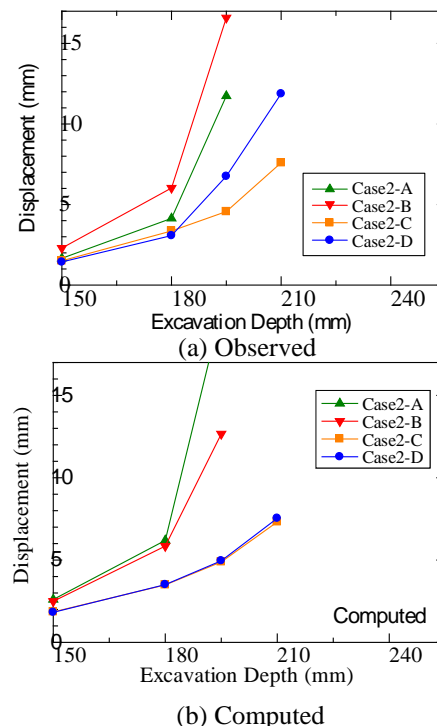


Fig.7 Wall horizontal displacement for excavation depth deeper than 150mm

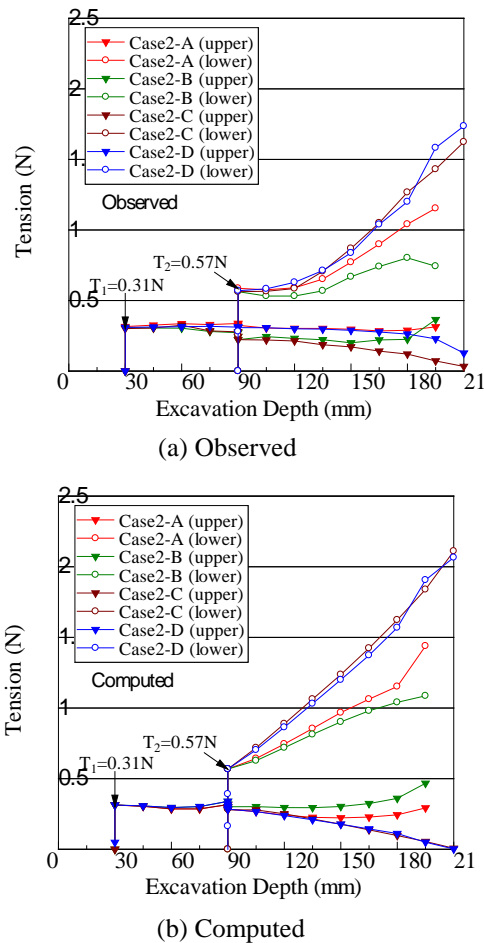


Fig.8 Variation of tensile force of anchor

Figure 8 shows the observed and computed variations of tensile force at both upper and lower anchors for Case2-A to D. It is seen that for all cases, the change of tensile force at the upper anchor is less significant compare to the lower anchor. In contrast, the tensile force at the lower anchor increases with the advance of excavation, especially, when the excavation depth is deeper than 150mm which is associated with a significant wall deformation and surface settlement of the backfill ground. In the the case of longer lower anchor (Case2-C, D), the maximum tensile force is almost 1.5times the maximum tensile force of the lower anchor of Case2-A. The numerical analyses perfectly capture the observed tensile force of both upper and lower anchors.

Figure 9 illustrates distribution of shear strain of the model tests and numerical simulations. The distributions of shear strain of the model tests are obtained using Particle Image Velocimetry (PIV) technique. In this paper, two images are divided into a finite area; the average movement rate of the mass of aluminum rods of each area is extracted as nodal displacements. The strain for one grid is calculated from these displacements by using the shape functions and the B matrix (strain- displacement

matrix) that is usually used in finite element method to relate displacements and strains. It is seen that in Case2-A, for the shorter anchor shear band develops outside the lump of the ground having the anchor block inside the lump. In the case of longer upper and lower anchors (Case2-D), the anchor blocks are located far outside the slip surface which restricts the development of shear strain significantly. Case2-C, where only the lower anchor is longer, shows almost the same distribution of shear strain as that of Case2-D. This is because, as the lower anchor is located outside the slip surface and produces sufficiently high pullout resistance it increases tensile force and hence a notable supporting effect can be speculated. On the other, though the upper anchor block of Case2-B is located outside the slip surface, there is not much difference of the distributions of shear strain between Case2-A and Case2-B. Therefore, it can be said that a longer anchor at the lower excavation part restricts the displacement of retaining wall and can be treated as an effective supporting method. The shear strain of the numerical analyses shows good agreement with the results of the model tests.

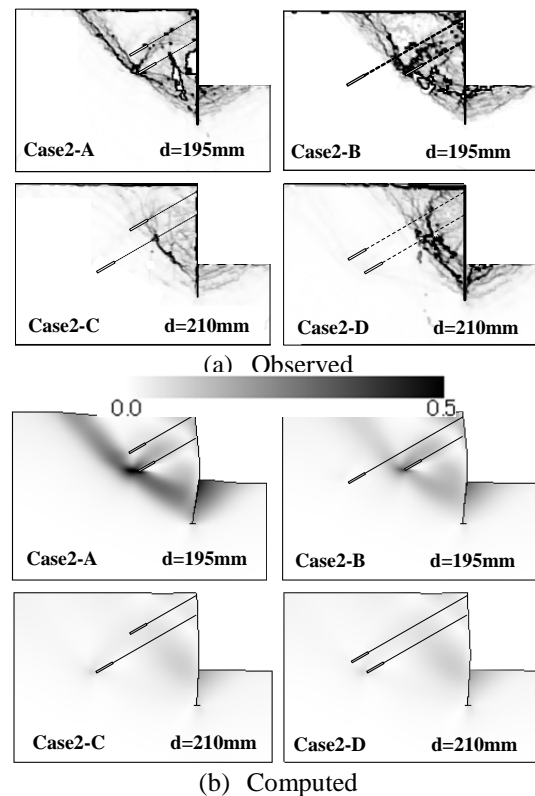


Fig.9 Distribution of shear strain: Case2-A to D

Figure 10 represents observed and computed surface settlement profiles of the backfill ground for Case3-A and Case3-C. The lengths of anchors in both cases are the same except a longer anchor is setup at the deeper excavation part in Case3-C. It is seen that when the excavation depth crosses 180mm

a larger settlement with wider area occurs in Case3-A where all the anchors are shorter in length the same way as the two stages anchor as describe before. In Case3-C where the 3rd stage (lower) anchor is longer, excavation up to the depth of 210mm is possible without a significant subsidence of the backfill ground. Figure 11 illustrates distribution of shear strain of the model tests and the corresponding numerical analyses for Case3-A and Case3-C. Case3-A shows the results of the excavation depth of 210mm as the further excavation was not possible due to the collapse of the ground. As described above the longer anchor of the deeper excavation depth grasp much pullout resistance compare to the anchors at the shallower excavation depth, it restricts the movement of the retaining wall and hence deeper excavation is possible. The numerical analyses can clearly express the difference of the surface settlement profiles and the distribution of shear strain with the variation of the anchor lengths the same way as the model tests.

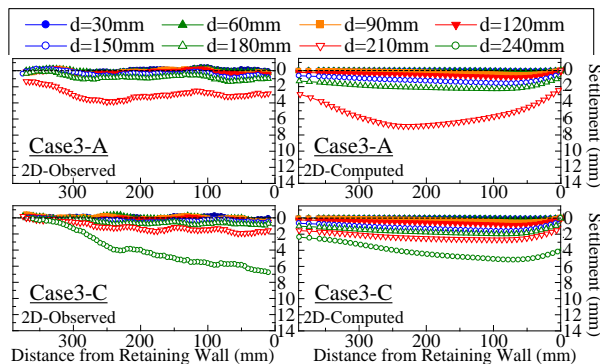


Fig.10 Surface settlement profiles: Case3-A, C

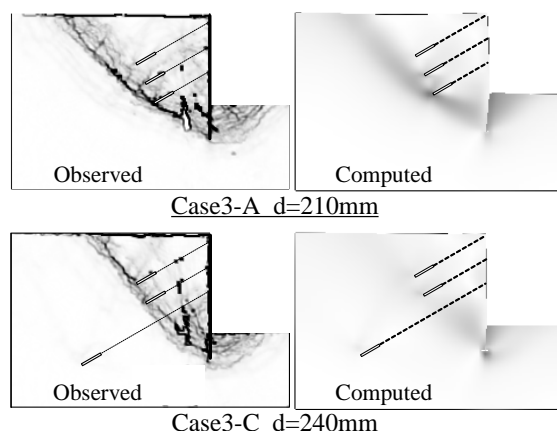


Fig.11 Distribution of shear strain: Case3-A,C

CONCLUSION

In this research, two-dimensional model tests and the corresponding numerical analyses are carryout out on anchor type braced excavation. It is revealed that supporting effect of anchor in braced excavation can be achieved if the anchor block is

setup outside the assumed slip surface developed during excavation. Especially, longer anchor in the lower part of the excavation produces a significant supporting effect resisting wall displacement and surface settlement of the backfill ground. As the wall deformation and surface settlement of the backfill ground increase with the advance of excavation it is important to install an anchor with a sufficient length in deeper excavation depth. In contrast, there are not much differences in supporting effect between a shorter and a longer anchor in shallower excavation depth. It is also revealed that the number of anchors, inclination of anchors and their interval play an important role in safe and stable braced excavation. Therefore, it is important to find out an optimum supporting pattern in anchor type braced excavation for rational design in the case economical point of view. It can also be concluded that the computed results in which typical stress-strain behavior of soils is appropriately taken into account agree well with the experimental results qualitatively and quantitatively.

REFERENCES

- [1] Nakai, T., "Finite element computations for active and passive earth pressure problems of retaining wall". *Soils and Foundations*, 25(3), 1985, pp. 98-112.
- [2] Naka T. and Hinokio T., "A simple elastoplastic model for normally and over consolidated soils with unified material parameters", *Soils and Foundations*, Vol. 44, No.2, 2004, pp. 53-70.
- [3] Nakai, T., Shahin, H. M., Iwata, N., Ninomi M. and Takei, H., "Influence of deflection process and mode of wall and existing building load on retaining wall", 13th Asian Reg. Conf. on Soil Mech. and Geotechnical Engineering, Kolkata, India, December, 2007, pp. 481-484.
- [4] Iwata, N., Shahin, H.M., Zhang, F., Nakai, T., Niinomi, M. and Geraldni, Y.D.S., "Excavation with stepped-twin retaining wall: model tests and numerical simulations", *Proc. of the 6th Int. Sym. on Geotechnical Aspects of Underground Construction in Soft Ground*, Shanghai, China, April, 2008, pp.655-661.
- [5] Shahin, H.M., Nakai, T., Kikumoto, M. and Uetani, Y., "Influence of existing foundations on retaining wall in braced excavation", 14th Asian Reg. Conf. on Soil Mech. and Geotechnical Engineering, Hong Kong, May, 2011, pp. 267.
- [6] Shahin, H.M., Nakai, T., Kikumoto, M., Sakai, R., Yoshida, Y., Saito, I., Nagao, N. and Toda, K., "Investigation of a reliable reinforcing method for embankment ground", 1st International Conference on Geotechnique, Construction Materials and Environment, Mie, Japan, November, 2011, pp. 71-76.

SHEAR MODULUS REDUCTION CURVES OF GUAYURIBA SANDS BY CYCLIC TRIAXIAL AND BENDER ELEMENT TESTS

J.F. Gaitán-Serrano¹, M.P. Ortiz-Pulido¹ and J.F. Camacho-Tauta¹

¹Faculty of Engineering, Nueva Granada Military University, Colombia

ABSTRACT

A laboratory experimental programme based on cyclic triaxial and bender element tests was performed on three particle sizes of sands from Guayuriba River (Colombia). The material from the Guayuriba River consists mostly of quartzite of the group Quetame (Paleozoic shale formation). Tests performed under different confinements (50, 100, 200 and 400kPa) allow obtaining a general view of the cyclic behavior of this material. The influence of the grain size on the shear modulus reduction curve was identified. There were good continuity between the bender element and the cyclic triaxial results. Moreover, it was verified the applicability of a unified model to predict the shear modulus reduction curves for this sand for normalized shear modulus greater than 0.4. For the material tested, this model could be used to obtain a reasonable approximation of the shear modulus reduction curve. Two parameters are required: the initial shear modulus, for example by bender element testing, and the shear strain for a normalized shear modulus equal to 0.7, which is easily recognizable by a cyclic triaxial test without internal instrumentation. These tests are less expensive than the resonant-column method and other specialized techniques.

Keywords: Bender Element Test, Cyclic Triaxial Test, Shear Modulus, Soil Stiffness

INTRODUCTION

Around the world, many authors have investigated the dynamic behavior of granular soils by laboratory testing. Kokusho [1], Santos and Gomes Correia [2], Zhou y Chen [3], Jafarzadeh and Sadeghi [4] are examples of that kind of investigations. In Colombia, there are some works with local materials, providing advances in this subject, for example Yamin et al [5], Garcia [6], Chaves [7], Rivas [8], who have made similar investigations about the behavior towards the phenomenon of liquefaction of sands of Tumaco (Chocó, Colombia) or the dynamic behavior in schists of Sabaneta (Antioquia, Colombia).

The shear modulus is one of the parameters required to estimate the dynamic response of soil layers. For example, the shear modulus is used in the assessment of seismic behavior of a sand deposit, to assess the risk from cases like the one in the middle of Atrato River (Colombia), where it presented the liquefaction of a dam formed by sandy material product of an earthquake presented on 17 and 18 October 1992 [9].

This paper aims to study the shear modulus in fluvial sands of the Guayuriba River (Colombia), by obtaining the shear modulus reduction curves. These curves were obtained by cyclic triaxial and bender element tests with different confining pressures. The results were analyzed, and a unified shear modulus reduction curve based on the model of Santos and Gomes Correia [2] has been obtained.

THEORETICAL BACKGROUND

In this section, the most relevant concepts related to the subject of this research are presented, starting by the definition of the initial shear modulus and the reduction of the modulus along different strain levels. Special attention is devoted to the unified model used in this work.

Initial Shear Modulus

The initial shear modulus (G_0), is the parameter that defines the stiffness of a soil subjected to cyclic stresses in the very small range of deformations. G_0 has been studied by different authors like Kokusho [1], Ishihara [10], Santos and Gomes Correia [2] and Richart et al. [11]. These researchers have found that a number of factors influence G_0 in sandy soils. The most important factors are the effective confining pressure (σ'_0) and the void ratio (e), as shown in Eq. (1).

$$G_0 = A \left[\frac{(B-e)^2}{(1+e)} \right] (\sigma'_0)^n \quad (1)$$

Where A , B and n are experimental constants that depend of the material. A compilation of different materials presented by some authors, shows that the most common values of B and n are 2.17 and 0.5, respectively. A fluctuates between 7000 and 14100 for G_0 and σ'_0 expressed in kPa [12].

Modulus Reduction Curves

The modulus reduction curve is a representation of the secant shear modulus divided by the initial shear modulus (i.e. the shear modulus at very small strain) as a function of the strain level [12]. The normalized curve is an advantageous representation because it can be simply multiplied by an appropriate experimentally determined G_0 to obtain the shear modulus for any strain level. This curve synthesizes the nonlinear behavior of soils. Figure 1 shows the modulus reduction curve along the shear strain [13].

The modulus reduction curve is not unique. In the case of sands, its shape and location depend mostly of the confining pressure, number of cycles and drainage conditions [1, 14].

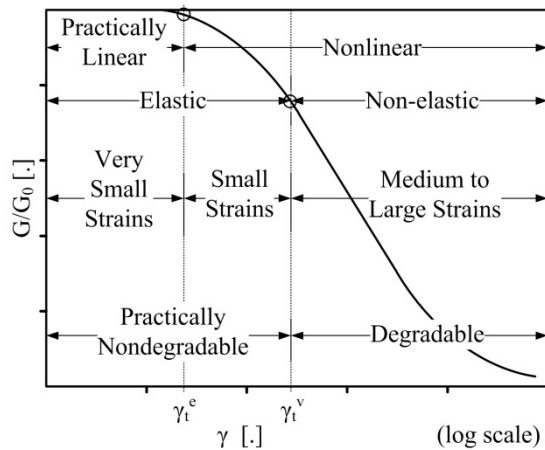


Fig. 1 Modulus reduction curve and zones of cyclic shear strain. Adapted from [13].

Elastic And Volumetric Threshold Shear Strains

The shear strain level can be classified in very small strains, small strains and medium to large strains [10]. The limit between very small and small strains was defined arbitrarily as the shear strain corresponding to $G/G_0 \approx 0.99$ [13]. This strain receives the name of linear elastic cyclic threshold strain (γ_t^e). The limit between small and medium strains is defined as the shear strain above which the microstructure is irreversibly altered by cyclic shearing [13]. This limit is known as the volumetric threshold shear strain (γ_t^v) because from this value appear irreversible changes in the volume of the sample. Kokusho [15] concludes that γ_t^v is the shear strain for which G/G_0 is between 0.6 and 0.85. Ishihara [10] proposes a mean value of $G/G_0 = 0.7$. Given the difficulty to measure γ_t^v in practice, Santos [16] proposed to use the reference threshold strain (γ_t^r), defined as the shear strain causing $G/G_0 = 0.7$. Relative locations of γ_t^e and γ_t^v are shown in Fig. 1.

Unified Shear Modulus Reduction Curve

A first proposal of a unified model was presented by Ishibashi and Zhang [17]. Based in many collected data, they proposed a set of formulas for all soil types, taking into account the effect of plasticity and confinement.

Santos and Gomes Correia [2] proposed a unified model by the normalization of the strain axis of the modulus reduction curve. The normalized shear strain (γ^*) is computed by:

$$\gamma^* = \frac{\gamma}{\gamma_t^r} \quad (2)$$

Experimental data from Vucetic and Dobry [18] and Darendeli [19] was normalized using Eq. (2) and the results are presented in Fig. 2, showing that the model works for different soil plasticity and effective confining pressures.

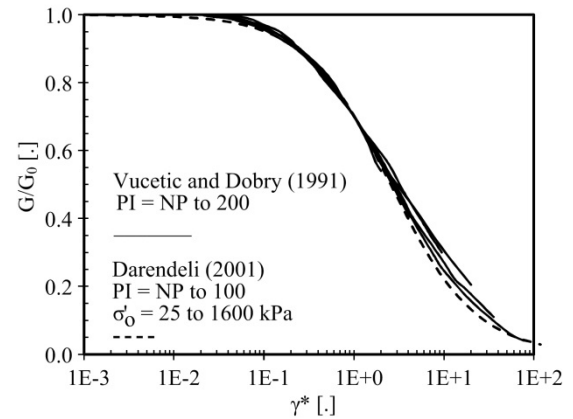


Fig. 2 Unified modulus reduction curves computed using data from Vucetic and Dobry [18] and Darendeli [19].

Based on a series of tests [2], it was demonstrated that data matches in a narrow zone delimited by the curves given by Eq. (3) and Eq. (4).

$$\frac{G}{G_0} = 1 \quad \text{for } \gamma^* \leq 10^{-2} \quad (3)$$

$$\frac{G}{G_0} = \frac{1 - \tanh\left[0.48 \ln\left(\frac{\gamma^*}{1.9}\right)\right]}{2} \quad \text{for } \gamma^* > 10^{-2}$$

$$\frac{G}{G_0} = 1 \quad \text{for } \gamma^* \leq 10^{-1} \quad (4)$$

$$\frac{G}{G_0} = \frac{1 - \tanh\left[0.46 \ln\left(\frac{\gamma^* - 0.1}{3.4}\right)\right]}{2} \quad \text{for } \gamma^* > 10^{-1}$$

Moreover, experimental data for plastic and non-plastic soils fit with good agreement with Eq. (5) [20].

$$\frac{G}{G_0} = \frac{1}{1 + (0.385\gamma^*)} \quad (5)$$

MATERIALS, EQUIPMENT AND TESTING METHODS

Materials

The material from the Guayuriba River consists mostly of quartzite of the group Quetame [21]. Three particle sizes of the same sand were used in the experiments, in order to analyze the influence of grain size on the results. The physical characterization included the determination of specific gravity of soil solids, particle-size analysis, maximum index density and minimum index density according to the ASTM standards [22]. Results of these laboratory tests are presented in Table I.

The cylindrical specimens (14 cm in height and 7 cm in diameter) were prepared by the dry pluviation method. Size and proportions of the specimens are in agreement with suggestions of previously-reported works [23-25].

Table I Physical properties of the materials

Property	Material		
	1	2	3
Minimum diameter [mm]	0.18	0.43	0.85
Maximum diameter [mm]	0.43	0.85	2.00
Uniformity coefficient [.]	1.58	1.42	1.39
Curvature coefficient [.]	0.93	0.94	1.00
Specific gravity of solids [.]	2.68	2.65	2.68
Void ratio [.]	0.81	0.91	0.99
Dry unit weight [kN/m ³]	14.8	14.1	13.5

Equipment

The dynamic test program was performed in a cyclic triaxial apparatus (Dynatriax, WF-Controls) with automatic control of cell and back pressure, equipped with submersible load cell and external displacement, volumetric change and pore pressure sensors, data acquisition unit and driver software with autonomous control of the tests stages.

The triaxial cell was equipped with a set of BE manufactured by the University of Western Australia [26]. The transmitter and receiver are located at the base cap and top cap of the triaxial device, respectively. The input signal is generated by a function generator (RIGOL, DG1022). A current amplifier stabilizes the signal and send it to the BE transmitter. The output signal of the BE receiver is amplified and both input and output signals are collected by a digital oscilloscope (Tektronics, 3S2012B). The BE system was calibrated using aluminum rods [27]. A schematic description of the BE system is presented in in Fig. 4.

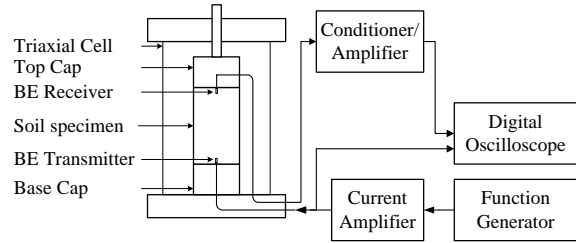


Fig. 4 Schematic of the BE system [27].

Testing Methods

Each soil specimen was installed in the cyclic triaxial cell, saturated, and then consolidated under a confining pressure of 50, 100, 200 or 400 kPa.

Bender element tests (BE)

BE tests were conducted by the following methodology:

- The function generator produces a linear sine sweep signal with frequency band between 1–20 kHz with duration of 40 ms and amplitude of 20 Vpp. This signal is sent to the BE transmitter.
- The digital oscilloscope acquires both input and output signals. The Fast Fourier Transform (FFT) computed in real time by the oscilloscope allows to identify the specific frequency in which the response of the BE receiver is higher.
- The function generator is turned to single-sine pulse mode with the frequency previously determined. The period of the signal is selected in order to allow enough time for the attenuation of the BE response before the next pulse. The output signals of a number of pulses are stacked in order to cancel out random noise, obtaining a clean response from the BE receiver.
- The arrival time is identified by the first inversion method [28]. The travel time (tt) is the difference between the arrival time and the time at the start of the sine pulse.
- The travel distance (L_{TT}) is the height of the specimen minus the length of each BE. The initial shear modulus (G_0) is computed by Eq. (6), where ρ is the mass density.

$$G_0 = \rho \left(\frac{L_{TT}}{tt} \right)^2 \quad (6)$$

Figure 5 shows a typical screen of the oscilloscope in the BE test. Channel 1 exhibits the single-sine pulse use to excite the BE transmitter and Channel 2 shows the output signal acquired by the BE receiver. Vertical cursors indicate the initial and arrival times used to compute the travel time.

According to different studies [12, 25, 29, 30], the shear strain level associated to the BE shear modulus is assumed to be 5×10^{-6} .

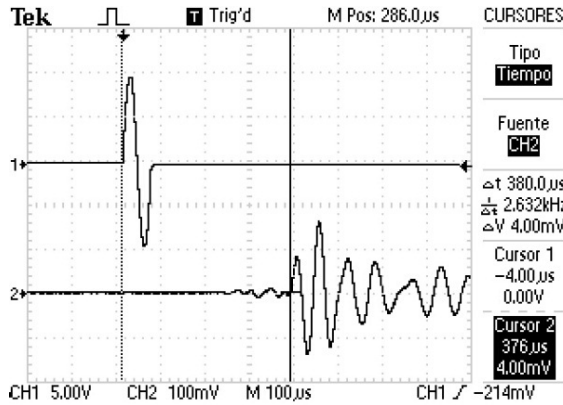


Fig. 5 Typical BE test showing input and output waveforms.

Cyclic triaxial tests (CTX)

After the bender element tests, cyclic triaxial tests were carried out according to the Method B (strain controlled) of ASTM D 3999 standard [31], with nine cyclic shear stages, each one with 40 sinusoidal cycles at frequency of 0.5 Hz. The strains were selected in a range of 0.028 mm ($\gamma \approx 1.33 \times 10^{-4}$) to 1.4 mm ($\gamma \approx 6.67 \times 10^{-3}$). The shear stress and shear strain are computed by Eq. (7) and Eq. (8), respectively.

$$\tau = \frac{q}{2} \quad (7)$$

$$\gamma = \frac{\varepsilon}{1+\nu} \quad (8)$$

Where q is the deviator stress, ε is the axial strain and ν is the Poisson's ratio, assumed to be 0.5 for saturated sands. Fig. 6 shows an example of the hysteresis loop obtained by the cyclic triaxial test, where the shear modulus is obtained as the slope of the line connecting the two extreme points of the loop.

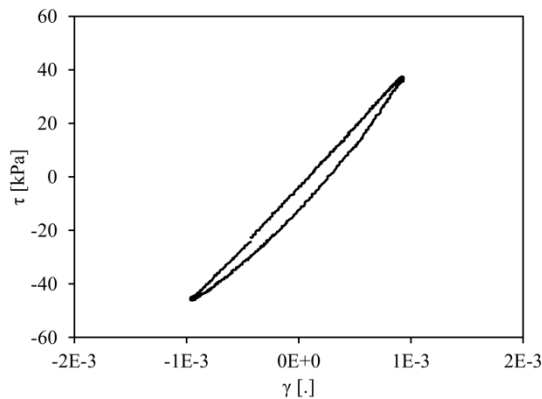


Fig. 6 Hysteresis loop of the cyclic triaxial test. Material 3, $\sigma'_0 = 100$ kPa.

RESULTS AND DISCUSSION

Figure 7 shows the curves obtained for the three sands and the different effective confining pressures. The results obtained by bender element and cyclic triaxial tests show the influence of the particle size and the confining pressure on the shear modulus reduction curves. The gap between BE and CTX tests is remarkable, not only regarding to the shear strain level, but also concerning the magnitude of the shear modulus. The use of internal instrumentation on the CTX test could reduce this difference.

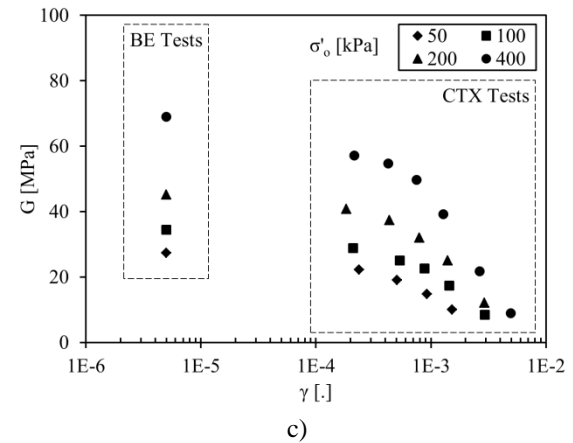
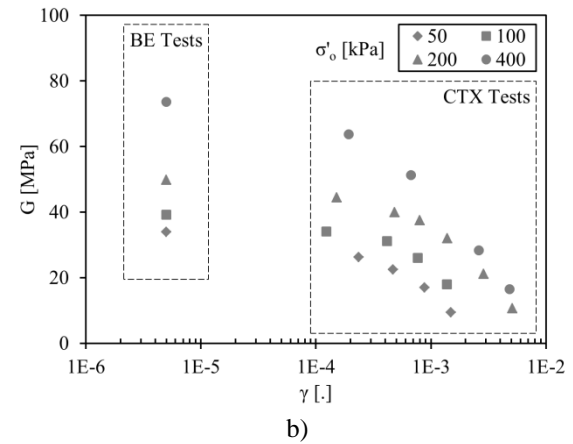
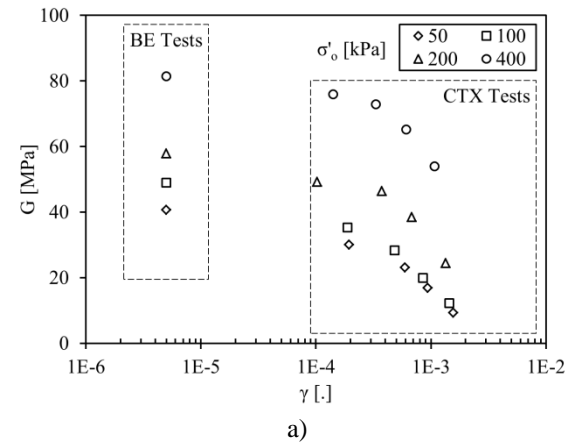


Fig. 7 Experimental modulus reduction curves: a) Material 1; b) Material 2; c) Material 3.

Shear moduli were normalized by their respective maximum shear modulus. These results are presented in Fig. 8. After a careful analysis of the figure, it is possible to observe that in general, the higher the confinement, the larger the normalized modulus for a given shear strain. This observation is in agreement with previous reported works [1]. However, the dispersion of result does not allow proposing a clear trend on this issue.

The reference shear strain (γ_{r^*}) was estimated by interpolation of the data and the normalized shear strain (γ^*) was computed by Eq. (2). These double-normalized curves are presented in Fig. 9, as well as the limits expressed by Eq. (3) and Eq. (4).

The influence of the assumed shear strain level in BE tests in results presented in Fig. 8 is insignificant because the normalized shear strain is computed using only CTX results and the magnitude of the shear modulus obtained by BE tests.

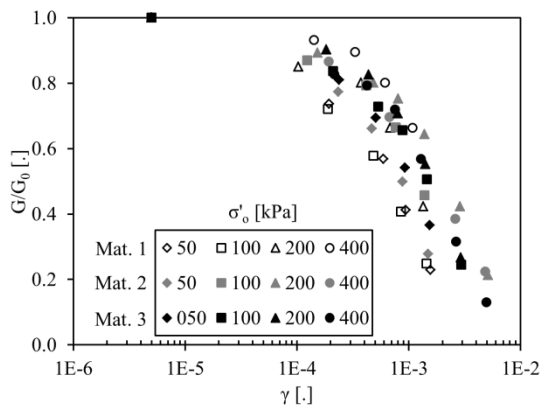


Fig. 8 Shear modulus reduction curves

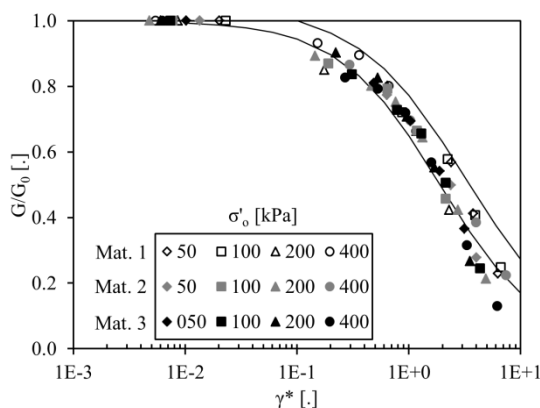


Fig. 9 Unified model for materials tested and comparison with limits proposed by Santos and Gomes Correia [2].

Deviation of the limits increases for normalized shear strains greater than 3, which is in average equivalent to a shear strain level of 3×10^{-3} . This

could be due that at this strain level, and for these loose specimens, the soil starts to exhibit cyclic liquefaction.

Results presented here suggest that a practical approximation of a shear modulus reduction curve could be obtained by a combination of BE tests and CTX tests.

CONCLUSION

The procedures for the cyclic triaxial and the bender element tests were adequately implemented. Results on Guayuriba sands were suitable when compared with the literature and the models proposed by other authors.

The model presented by Santos and Gomes Correia, is applicable to the Guayuriba sands. This model has the advantage that only needs the maximum shear modulus and the shear strain corresponding to a modulus equal to 70% of the maximum shear modulus. This simple approximation could be useful to obtain initial estimates of the soil behavior or to check values obtained by more advanced tests.

ACKNOWLEDGEMENTS

This paper is a result of the Research Project ING-1187 funded by the Nueva Granada Military University. Authors acknowledge the financial support of the Nueva Granada Military University.

REFERENCES

- [1] Kokusho T, "Cyclic triaxial test of dynamic soil properties for wide strain range", *Soils and Foundations*, Vol. 20, no. 2, June, 1980, pp. 45-60.
- [2] Santos JA and Gomes Correia A, "Reference threshold shear strain of soil. Its application to obtain an unique strain-dependent shear modulus curve for soil", in *Proc. Proceedings of the 15th International Conference on Soil Mechanics and Geotechnical Engineering*, 2001, pp. 267-270.
- [3] Zhou Y-G and Chen Y-M, "Influence of seismic cyclic loading history on small strain shear modulus of saturated sands", *Soil Dynamics and Earthquake Engineering*, Vol. 25, 2005, pp. 341-353.
- [4] Jafarzadeh F and Sadeghi H, "Experimental study on dynamic properties of sand with emphasis on the degree of saturation", *Soil Dynamics and Earthquake Engineering*, Vol. 32, Mar, 2012, pp. 26-41.
- [5] Yamin L, Caicedo B and Solano E, "Evaluation of the dynamic response of volcanic deposits and implications for seismic design" (in

- Spanish), Revista de Ingeniería Universidad de los Andes, Vol. 10, 1999, pp. 79-84.
- [6] Garcia JR, "Comparative analysis of the phenomenon of liquefaction in sands. Application to Tumaco (Colombia)" (in Spanish), Departamento de Ingeniería del Terreno, Cartográfica y Geofísica, Universidad Politécnica de Cataluña, Barcelona, 2007.
- [7] Chaves JF, "Pore pressure generation in undrained cyclic processes" (in Spanish), Facultad de Ingeniería Civil y Agrícola, Universidad Nacional de Colombia, 2011.
- [8] Rivas D, "Influence of microstructure on the dynamic behavior of residual soils of schist in Sabaneta" (in Spanish), Facultad de Minas, Universidad Nacional de Colombia, Medellín, 2010.
- [9] Velásquez A, "The Middle Atrato-Murindó earthquake in October 1992" (in Spanish), Desastres de origen natural en Colombia 1979 - 2004, E. M. Hermelin, Ed., 2005, pp. 91-108.
- [10] Ishihara K, Soil behaviour in earthquake geotechnics: Oxford Science Publications, 1996.
- [11] Richart FE, Jr., Hall JR, Jr. and Woods RD, Vibrations of soils and foundations. Englewood Cliffs: Prentice-Hall, 1970.
- [12] Camacho-Tauta J, "Evaluation of the small-strain stiffness of soil by non-conventional dynamic testing methods", PhD Thesis, Instituto Superior Técnico, Technical University of Lisbon, Lisbon, 2011.
- [13] Vucetic MV, "Cyclic threshold shear strain in soils", Journal of Geotechnical Engineering, ASCE, Vol. 120, no. 12, 1994, pp. 2208-2228.
- [14] Barros JMC, "Dynamic shear modulus of tropical soils" (in Portuguese), PhD Thesis, Escola Politécnica, Universidade de São Paulo, São Paulo, 1997.
- [15] Kokusho T, Yoshida Y and Esashi Y, "Dynamic properties of soft clay for wide strain range", Soils and Foundations, Vol. 22, no. 4, December, 1982, pp. 1-18.
- [16] Santos JA, "Soil characterization by dynamic and cyclic torsional shear test. Application to study of piles under static and dynamic horizontal loading" (in Portuguese), PhD Thesis, Department of Civil Engineering and Architecture, Instituto Superior Técnico of the Technical University of Lisbon, Lisbon, 1999.
- [17] Ishibashi I and Zhang X, "Unified dynamic shear moduli and damping ratios of sand and clay", Soils and Foundations, Vol. 33, no. 1, March, 1993, pp. 182-191.
- [18] Vucetic MV and Dobry R, "Effect of soil plasticity on cyclic response", Journal of Geotechnical and Geoenvironmental Engineering, ASCE, Vol. 117, no. 1, 1991, pp. 89-107.
- [19] Darendeli MB, "Development of a new family of normalized modulus reduction and material damping curves", PhD Thesis, Faculty of the Graduate School, The University of Texas, Austin, 2001.
- [20] Gomes Correia A, Barros JMC, Santos JA and Sussumu N, "An approach to predict shear modulus of soils in the range of 10⁻⁶ to 10⁻² strain levels", in Proc. Proceedings of the Fourth International Conference on Recent Advances in Geotechnical Earthquake Engineering and Soil Dynamics, 2001, pp. paper no. 1.22.
- [21] Amorochio R, Bayona G and Reyes-Harker A, "Controls on the composition of fluvial sands in the proximal region of tropical foreland basin (Colombia) (in Spanish)", Revista Geología Colombiana, Vol. 36, no. 1, Ago, 2011, pp. 163-178.
- [22] ASTM International, Annual Book of ASTM Standards. West Conshohocken, 2002.
- [23] Arroyo M, "Pulse tests in soils samples", PhD Thesis, Faculty of Engineering, University of Bristol, Bristol, 2001.
- [24] Rio J, Greening P and Medina L, "Influence of sample geometry on shear wave propagation using bender elements", in Proc. Deformation Characteristics of Geomaterials, 2003, pp. 963-967.
- [25] Rio J, "Advances in laboratory geophysics using bender elements", PhD Thesis, University College London, University of London, London, 2006.
- [26] Ismail M, Sharma SS and Fahey M, "A small true triaxial apparatus with wave velocity measurement", Geotechnical Testing Journal, ASTM, Vol. 28, no. 2, 2005, pp. 113-122.
- [27] Camacho-Tauta J, Jiménez JD and Reyes-Ortiz OJ, "A Procedure to Calibrate and Perform Bender Element Test", Revista Dyna, Vol. 79, no. 176, 2012, pp. 10-18.
- [28] Viggiani G and Atkinson JH, "Interpretation of bender element tests", Géotechnique, Vol. 45, no. 1, 1995, pp. 149-154.
- [29] Pennington DS, "The anisotropic small strain stiffness of Cambridge Gault clay", PhD thesis, Department of Civil Engineering, University of Bristol, 1999.
- [30] Leong EC, Yeo SH and Rahardjo H, "Measuring shear wave velocity using bender elements", Geotechnical Testing Journal, ASTM, Vol. 28, no. 5, 2005, pp. 488-498.
- [31] ASTM International, "Standard Test Methods for the Determination of the Modulus and Damping Properties of Soils Using the Cyclic Triaxial Apparatus (D3999)", Annual Book of ASTM Standards, West Conshohocken, 2008, pp.

WATER DIVERSION AND DRAINAGE IN SHALLOW LAND WASTE REPOSITORY CONSTRUCTED USING CAPILLARY BARRIER OF SOIL

Toshihiro Morii¹, Kaoru Kobayashi², Kazunobu Matsumoto² and Satoru Nakafusa³

¹ Faculty of Agriculture, Niigata University, Japan; ² Tobishima Corporation, Japan; ³ Japan Atomic Power Company, Japan

ABSTRACT

Capillary barrier (CB) is tilting soil layer system which is composed of sand layer underlain by gravel layer, and can well divert water infiltrating from a soil surface. A shallow land waste repository, in which upper CB and bottom CB were placed to divert infiltration due to rainfall and to drain water percolating through the protected waste material respectively, was proposed to isolate a hazardous waste material or a very low level radioactive waste. In this study a test shallow land waste repository was constructed to investigate the CB's performance in the field. Firstly a diversion length of the CB was determined based on the laboratory soil box test to determine the structural dimensions of the shallow land. Then soil moisture contents were measured in the test shallow land. They showed an excellent and stable water diversion of the CB in the field.

Keywords: Capillary Barrier of Soil, Shallow Land Waste Repository, Diversion Length, Test Construction

INTRODUCTION

Capillary barrier (CB) is a tilting soil layer system which is composed of a finer soil (usually sand) layer underlain by a coarser soil (usually gravel) layer. Water which infiltrates into the soil is suspended just above an interface between the soil layers and diverted downward along the interface, with the result that a vertical movement of water into deeper soil layers below the interface stops within some length along the interface. Because of this excellent diversion of infiltration water, the CB has been employed in a top cover of waste landfills and mining wastes to reduce water infiltration into the protected waste materials [1], [2]. The CB has also been proposed to be used as a soil cover for slope stabilization purpose against rainfall-induced slope failure [3], [4]. Water flow downward along the interface between finer and coarser soil layers accumulates gradually its mass of flow due to continuous infiltration from the soil surface, and, at some length along the interface, water percolates into the coarser soil layer [5], [6] as shown schematically in Fig. 1. A horizontal length or distance from the beginning of water flow to this percolation into the coarser soil layer (breakthrough) is called a diversion length of the CB, and is one of important parameters in designing structural configuration of the CB system and selecting a suitable combination of the finer and coarser soils. It is well known that the diversion length can theoretically be estimated based on the infiltration flux, saturated and unsaturated hydraulic properties of the finer and coarser soils, and the slope of the

interface [7]. Although Ross [6] discussed that the diversion length might be theoretically as much as 50 m in a dryer climate with an order of magnitude less infiltration, only 1 to 2 meters of the diversion length has been observed and published [6].

In this paper, a shallow land waste repository shown in Fig. 2, in which a top CB and a bottom CB are placed to reduce infiltration due to rainfall and to drain percolating water through the protected waste material respectively, is proposed to isolate effectively a hazardous waste material or a very low level radioactive waste. As the shallow land waste repository is constructed on ground surface, there may be no risk that groundwater enters the waste and diffuses pollutants into a surrounding environment. It should be also emphasized that the CB can maintain its function of water diversion for

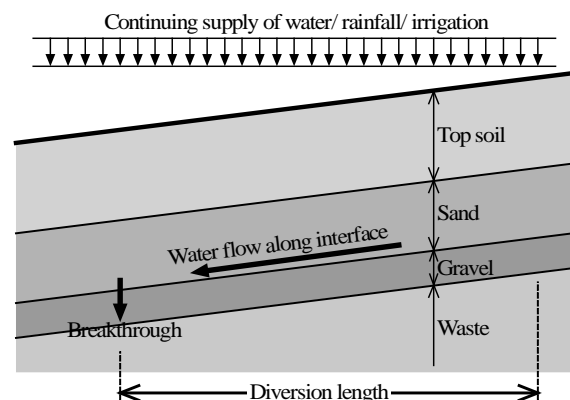


Fig. 1 Schematic layout of a capillary barrier of soil and diversion length.

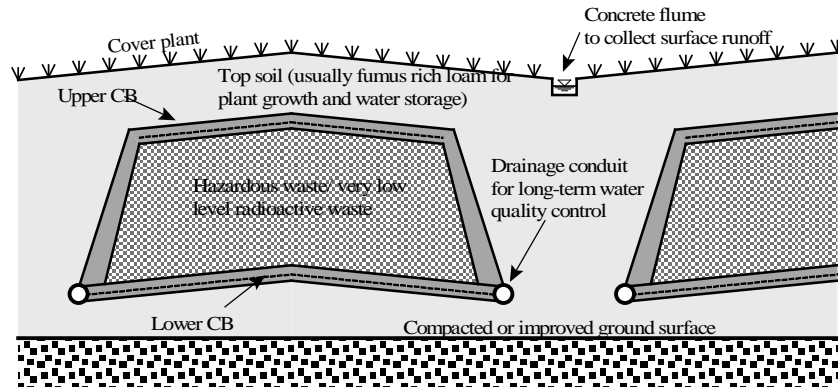


Fig. 2 Proposal of shallow land waste repository covered with upper CB and placed with bottom CB.

an extremely long duration because it consists of natural materials such as sand and gravel. In the following section, the diversion length of the CB which can be applied to structural design of the shallow land waste repository is determined based on a laboratory soil box test. Then trial construction is reported to show some feasible proposition for construction of the shallow land waste repository. Observations of soil water movement in a test shallow land waste repository are also discussed to show an effectiveness of the CB.

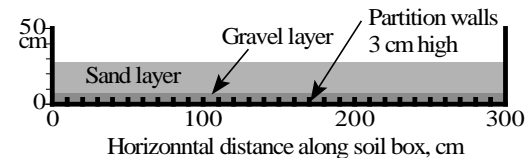
ESTIMATION OF DIVERSION LENGTH BY LABORATORY SOIL BOX TEST

Soil Box Test

In order to observe directly the breakthrough of water flowing along the interface, and to determine the diversion length, a series of laboratory soil box test was carried out. Figure 3a shows an acrylic soil box, 300 cm in length, 20 cm in width and 50 cm in height, built in a steel frame. The soil box was placed horizontally, and the gravel was compacted into the layer of 7.5 cm thickness, then the sand into 20 cm thickness as shown in Fig. 3b. A completely-permeable polypropylene net was placed over the compacted gravel layer so that the sand particles did not fall into voids formed in the gravel layer. After a gauze sheet was spread over the soil surface to protect soil erosion due to rainfall droplet, one side of the soil box was jacked up to obtain the tilting interface of the CB. The infiltration water was supplied on the surface of the upper sand layer through emitting needles (syringe needles), 0.3 mm in an inner diameter, attached to the base plate of the water reservoir. To keep the acrylic front panel clean, the emitting needles were placed so that the rainfall droplet did not fall along the front panel. Intensity of rainfall was simulated by adjusting the head of constant water in the water reservoir. Uniformity of the rainfall intensity over the soil surface was examined by measuring the water mass collected



a. Soil box (lower set) and water reservoir (upper set).



b. Partition walls attached to the bottom of the soil box.

Fig. 3 Test equipment prepared for the soil box test to measure diversion length of the CB.

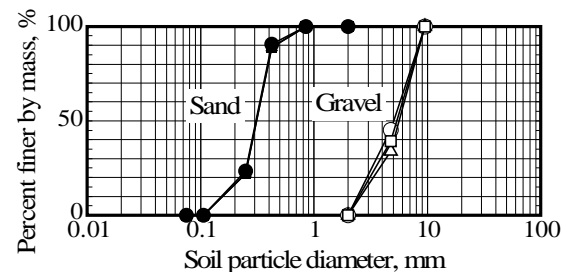


Fig. 4 Grain size distribution of sand and gravel used in the soil box test.

into a glass beaker during 10 minutes.

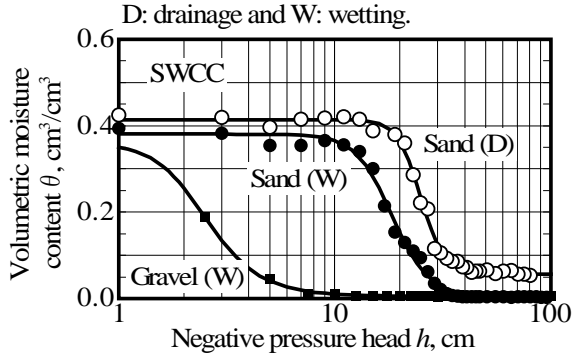


Fig. 5 Soil-water characteristic curves (SWCC) of sand and gravel measured by laboratory soil column tests.

Figure 4 shows grain size distribution curves of sand and gravel used in the soil box test. The sand has less-5% fine and coarse fractions; the gravel, commercially available, is siliceous with a mean particle size of 5 to 6mm. Relationships of negative pore pressure, h , with volumetric moisture content of sand and gravel were measured by a laboratory soil column test, and are plotted in Fig. 5. Soil-water characteristic curves are determined by using van Genuchten equation [8].

Measurement of Diversion Length

Totally 12 tests were conducted by combining two interface angles, 5 and 10 degrees, with three infiltration rate, 5, 10 and 20 mm/h, in two soil boxes. The sand layer in one of two soil boxes was compacted into 90 % of a maximum dry density, 1.616 Mg/m³, and 85 % in another soil box. Water which percolated into the lower gravel layer was collected along a partition wall 3 cm high attached transversely every 10 cm intervals onto the bottom plate of the soil box as shown in Fig. 3b, and led to a collecting beaker through a silicon tube connected to the lowest position of the side wall of the soil box as shown in Fig. 3a. The diversion length was determined by observing and measuring a volume of water collected into the collecting beaker along the bottom of the soil box. Figure 6 shows a typical measurement of the water volume collected along the distance of the bottom of the soil box in the case of 90 % compaction of the sand layer, 10 degrees in slope and 10 mm/h of infiltration rate (rainfall intensity). As a mean total amount of the water volume, 1077.4 cm³/10 min., is converted into 10.8 mm/h of the infiltration rate, it is found that a mass balance between infiltration and drainage of water is kept. In this case, the diversion length of 170 cm was determined from Fig. 6.

Estimation of Diversion Length

Some theoretical equations have been proposed

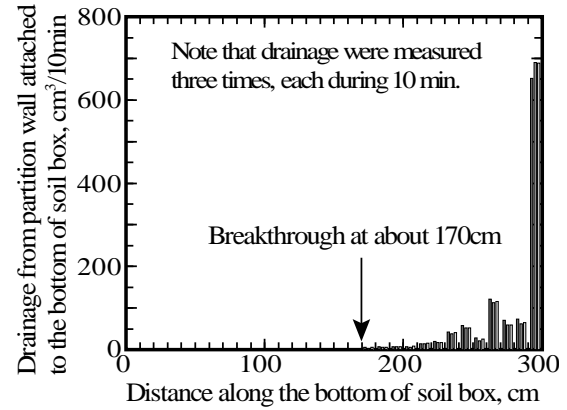


Fig. 6 Typical measurement of water volume collected along the bottom of the soil box.

to estimate the diversion length of the CB by several researchers [5], [7], [9]. Among these, the equation by Steenhuis *et al.* [7] is effectively adaptable [6], [10]. In the case where an infiltration rate, q , is much smaller than a saturated hydraulic conductivity of sand (the upper finer soil), K_s , the equation of the diversion length, L , is given by

$$L \leq \frac{K_s}{q} \tan \phi \left[\alpha^{-1} + (h_a - h_w) \right] \quad (1)$$

in which ϕ is a slope angle of interface, h_a and h_w are an air entry value of sand and a water entry value of gravel, respectively. α is an exponential constant describing the relationship between h and unsaturated hydraulic conductivity, K , of sand near saturation:

$$\begin{aligned} K &= K_s \quad |h| < h_a; \\ K &= K_s \exp[\alpha(h - h_a)] \quad |h| \geq h_a \end{aligned} \quad (2)$$

All the diversion lengths measured in the soil box test are given in Fig. 7 and compared well with the estimations calculated by Eqs. (1) and (2). K_s of 90 %-compacted sand is 1.31×10^{-4} m/s, and 85 %-compacted sand 1.91×10^{-4} m/s. The unsaturated hydraulic properties of the sand, h_a , h_w and α , are determined to be 13 cm, 1 cm and 0.12/cm, respectively, based on Fig. 5 and Nakafusa, *et al.* [11]. Some experiment data published by Walter *et al.* [6] and the observed data by Morii *et al.* [12] are also plotted in Fig. 7. The measured value of the data denoted by a small arrow would be larger because the measurement was restricted to the length of the soil box, 300 cm. A fairly good comparison of the diversion length between the measurements/observations and the estimations can be found in Fig. 7. It is thought from Fig. 7 that Eqs. (1) and (2) proposed by Steenhuis *et al.* [7] can be practically

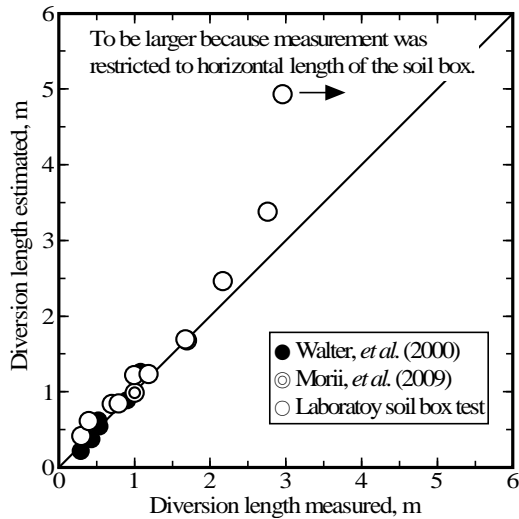


Fig. 7 Comparison of the diversion length between measurements and estimations.

employed to estimate the diversion length of the CB.

Based on the results given in Fig. 7, about four meters of the diversion length can be practically employed to design the CB in the shallow land waste repository.

SOIL WATER MOVEMENT IN TEST SHALLOW LAND WASTE REPOSITORY IN THE FIELD

Construction of Test Shallow Land Waste Repository

A test shallow land waste repository was constructed in order to monitor the soil water movement in the field and to examine an excellent water diversion by the CB. The upper CB was not included because it was planned only to observe the diversion of infiltration water. The original ground soil was compacted with the surface inclination of 5 degrees. The gravel was placed over the compacted ground surface and compacted statically by using the plate-type bucket in 10 cm thickness and in 4 m horizontal length (Figs. 8a and 8b), then the sand over it in 15 cm thickness. After constructing the CB layer, sandy soil, polypropylene soil-bags which simulated containers for waste storage, and sandy soil were placed and compacted successively higher (Figure 8c). Uniformity in density of the compacted sand layer is an important property which guarantees the water diversion in the CB system because the diversion length directly relates to the saturated hydraulic conductivity of sand as shown in Eq. (1). After constructing the CB layer, 19 cylindrical sand cores, 100 cm³ in volume and 5 cm in height, were sampled, and the densities of the sand cores were measured in laboratory. Figure 9a shows a mean value and a standard deviation of the dry density, ρ_d ,



a. Gravel layer compacted by the plate-type bucket.



b. Sand layer compacted by the plate-type bucket.



c. Test shallow land waste repository constructed..

Fig. 8. Construction of the test shallow land waste repository.

of sand cores on a normal distribution curve, together with the saturated hydraulic conductivity of sand measured by laboratory permeability test in Fig. 9b. It is found from Fig. 9 that the saturated hydraulic conductivity corresponding to a maximum density expected with 95%-confidence is about 65 % lower than that corresponding to a minimum density along an average line between K_s and ρ_d in Fig. 9b, with the result that the diversion length may varies .

Soil Water Movement

The volumetric moisture contents measured in the test shallow land waste repository from June to September are given in Fig. 10b together with the structural section in Fig. 10a. Two plots were

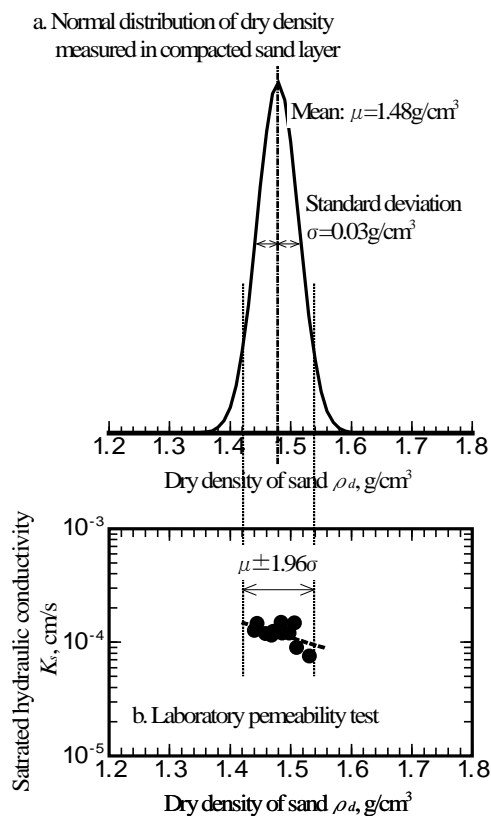


Fig. 9 Frequency distribution of dry density measured in the compacted sand layer and the saturated hydraulic conductivity measured in laboratory.

prepared in the test construction, a CB layer plot and a reference plot without the CB layer both 2 m in width (Fig. 8d). The left and right rows in Fig. 10 show the volumetric moisture contents measured in the CB layer plot and in the reference plot without the CB layer, respectively. The upper and lower lines in Fig. 11 show the volumetric moisture content measured in the sand layer and in the gravel layer, respectively. Rainfall intensity measured 5-minute intervals is given by an inverse bar with the right vertical axis of each figure. Comparing Figs. 11d with 11b and 11c, it is found that the soil water which infiltrates from the top surface of the test repository enters into the sand layer but does not into the gravel layer underlying the sand layer. This is exactly due to the excellent water diversion by the CB.

CONCLUSIONS

Shallow land waste repository, in which the upper CB and bottom CB are placed to reduce infiltration due to rainfall and to drain percolating water through the protected waste material respectively, was proposed to isolate effectively a

hazardous waste material or a very low level radioactive waste. The laboratory soil box test and the test shallow land waste repository constructed in the field reveal that:

1) The diversion length which determines the structural dimensions of the shallow land waste repository can be estimated well based on the hydraulic properties of sand and gravel employed in the CB, the inclination of the CB interface and the infiltration rate expected in the field. Equations 1 and 2 proposed by Steenhuis *et al.* [7] is recommended to estimate the diversion length of the CB.

2) The test shallow land waste repository showed the excellent and stable diversion of infiltration water provided by the CB. A continuing observation of soil water movement may be required to evaluate the CB performance for a long duration.

ACKNOWLEDGEMENTS

The present study was supported by the Grant-in-Aids for Scientific Research (B), No. 22380127, and Challenging Exploratory Research (C), No. 24658201, made by the Ministry of Education, Science, Sports and Culture of Japan. Messrs. K. Taguchi and N. Someya, TNS Co., Ltd., Japan, are sincerely grateful for their help in conducting the laboratory soil box test and in constructing the test shallow land waste repository. Their efforts done by Mr. K. Takahashi and Miss Y. Nakano, the undergraduates of Faculty of Agriculture, Niigata University, to calculate the volumetric moisture contents in the test shallow land waste repository are acknowledged.

REFERENCES

- [1] Stormont, J.C. & Anderson, C.E. 1999. Capillary barrier effect from underlying coarser soil layer. *Journal of Geotechnical and Geoenvironmental Engineering* 125(8): 641-648.
- [2] Yanful, E.K., Simms, P.H., Rowe, R.K. & Stratford, G. 1999. Monitoring an experimental soil waste cover near London, Ontario, Canada. *Geotechnical and Geological Engineering* 17: 65-84.
- [3] Tami, D., Rahardjo, H., Leong, E.C. & Fredlund, D.G. 2004. A physical model for sloping capillary barriers. *Geotechnical Testing Journal* 27(2): 173-183.
- [4] Rahardjo, H., Krisdani, H. & Leong, E.C. 2007. Application of unsaturated soil mechanics in capillary barrier system. *Proceedings of the 3rd Asian Conference on Unsaturated Soils*: 127-137.
- [5] Ross, B. 1990. The diversion capacity of capillary barriers. *Water Resources Research* 26(10): 2625-2629.

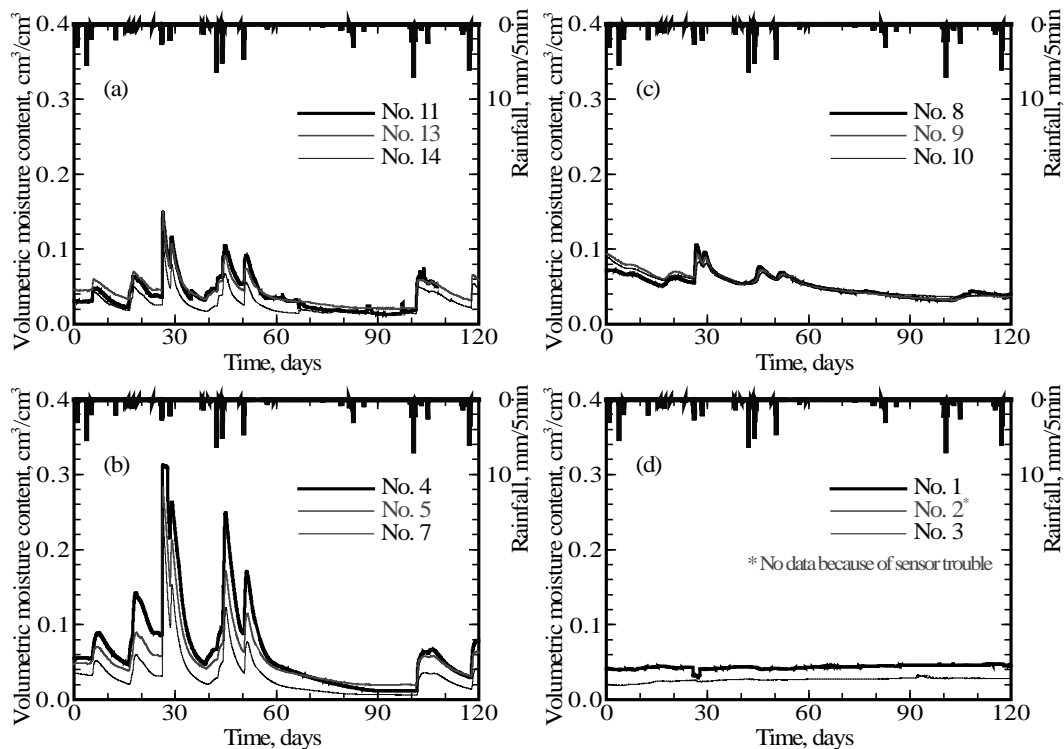
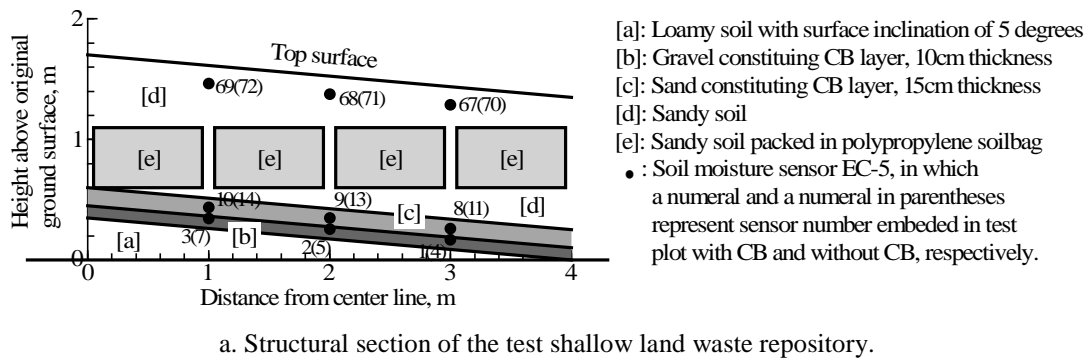


Fig. 10 Soil water movement measure in the test shallow land waste repository.

- [6] Walter, M.T., Kim, J.S., Steenhuis, T.S., Parlange, J.Y., Heilig, A., Braddock, R.D., Selker, J.S. & Boll, J. 2000. Funneled flow mechanisms in a sloping layered soil: Laboratory investigation. *Water Resources Research* 36(4): 841-849.
- [7] Steenhuis, T. S., Parlange, J.Y. & Kung, K.J. 1991. Comment on "The Diversion Capacity of Capillary Barriers" by Benjamin Ross. *Water Resources Research* 27(8): 2155-2156.
- [8] Stephens, D.B. 1996. *Vadose Zone Hydrology*. Florida: CRC Press.
- [9] Kung, K.J.S. 1990. Preferential flow in a sandy vadose soil, 2, Mechanism and implications. *Geoderma* 46: 59-71.
- [10] Smesrud, J.K. & Selker, J.S. 2001. Effect of soil-particle size contrast on capillary barrier performance. *Journal of Geotechnical and Geoenvironmental Engineering* 127(10): 885-888.
- [11] Nakafusa, S., Kobayashi, K., Morii, T. & Takeshita, Y. 2012. Estimation of water diversion provided by capillary barrier of soils. *Proceedings of the 5th Asia-Pacific Conference on Unsaturated Soils*, 2: 773-777.
- [12] Morii, T., Takeshita, Y., Inoue, M. & Matsumoto, S. 2009. Alternative measures for soil slope stability using capillary barrier of soil. *Proceedings of the 4th Asia-Pacific Conference on Unsaturated Soils*: 319-324.

REINFORCING EFFECT OF GEOSYNTHETICS ON BEARING CAPACITY,

Masuda Saki¹, H. M. Shahin², Nakai Teruo³, Morikawa Yukihiro⁴ and Mio Susumu⁵

^{1,2,3}Department of Civil Engineering, Nagoya Institute of Technology, Japan;

³Geo-Research Institute, Nagoya Branch, Japan;

⁵Nikken Wood Systems, Tokyo, Japan

ABSTRACT

In general, geosynthetics are laid under the foundation for increasing bearing capacity. This method is already established in the construction of foundation. Until now, the authors examined the reinforcement mechanism changing the length and the laying depth of reinforcement. However, for getting more clear information about the reinforcement mechanism to establish a rational design method of reinforced-soil ground some model tests have been conducted in addition to the previous research. In this research, we have investigated the reinforcement effect changing the laying depth, length and fixity conditions of the reinforcement conducting two dimensional laboratory tests referring to the past research. In real field as the load on the foundation is not always vertical, here we have also investigated the effect of loading conditions. The corresponding numerical analyses are also carried out with finite element programs called FEMtij-2D using elastoplastic subloading t_{ij} model. It is found that a significant increase in bearing capacity can be achieved if the geosynthetics are placed properly with optimum length having the boundary fixed with the ground.

Keywords: Geosynthetics, reinforcement, foundation, Bearing capacity

INTRODUCTION

In Japan, a huge area of the ground consists of soft soils having insufficient bearing capacity at the surface layer which makes trouble to engineers in design and construction process. In such cases, it is necessary to increase the bearing capacity to construct superstructures. To increase the bearing capacity ground improvement and replacement of good quality of soils are commonly used. However, these processes are expensive and also time consuming. Moreover, these processes sometimes restrict workability of the construction. In urban housing it is especially unpleasant to use cement in ground improvement which increases construction cost as well. In the case of replacing the existing soft soils with good quality soils, it needs installation of temporary structures, such as sheet pile, retaining wall, struts, etc. which causes difficulties in employing this process. Therefore, in this research it is focused on the use of geosynthetics to reinforce the ground for reducing ground deformation and increasing bearing capacity of the ground. The reinforcement in geosynthetics construction method consists of fiber materials to withstand against tensile forces acting upon the soils due to the upper surcharge. The authors [1] explained some effective reinforcing method in the previous research. They investigated the effective methods considering the optimal length and shape of reinforcement materials.

Here, the reinforcing mechanism is clarified through two-dimensional (2D) model tests of the foundations using reinforcements under vertical loading conditions – concentric and eccentric loadings, and the corresponding numerical analyses.

In practice geosynthetics is laid under a building foundation. The edges of the reinforcing members are kept fixed with the ground by hooks to increase bearing capacity. This construction method has already been proved effective after the tremor of Great East Japan Earthquake on March 11, 2011. Fig. 1 illustrates an image of tensile force around geosynthetics under a structure. As seen in Fig. 1 tensile force of the reinforcing member determines the increase of the bearing capacity of the ground.



Fig. 1 Image of tensile force around geosynthetics

However, reinforcing effect with geosynthetics is

neither a direct process of ground improvement nor a process of increasing ground strength. Therefore, at present the evaluation of reinforcing effect is very difficult. As stated before the reinforcing effect can only be achieved when tension develops in the reinforcing members depending on the extent of tensile force in the geosynthetics.

OUTLINE OF 2D MODEL TESTS AND NUMERICAL ANALYSES

Outline of 2D Model Tests

Fig. 2 shows a schematic diagram of a 2D model test apparatus for the investigation of bearing capacity of ground. The size of the model ground is 1000mm in width and 500mm in height. Aluminum rods of 5cm in length, having diameters of 1.6mm and 3.0mm and mixed with the ratio of 3:2 in weight, are used as the model ground (unit weight of the mass is 20.4kN/m^3). An aluminum plate is placed at the surface of the ground to simulate the bearing capacity of a strip (flat) foundation. Fig. 3 shows a model of the foundation. The foundation is 120mm in width and 35mm in height. Sandpaper is attached at the bottom of the foundation to attain surface friction between the foundation and the ground. Vertical load is applied at the foundation using a motor. A slider, which permits the movement of the loading rod in the horizontal direction, and a load cell for measuring the magnitude of load are set in the loading system. The model test is conducted with the aspect ratio of 1:100 between the model tests and prototype scale. Vertical displacement and rotation of the foundation are measured setting two displacement transducers at the two edges of the foundation. Photographs are taken during the experiments and they are used later as input data for the determination of ground movements with a program based on the technique of Particle Image Velocimetry (PIV).

Fig.4 shows a model of reinforcement material. Tracing paper is used as a geosynthetics which has almost no bending stiffness. In the tracing paper, aluminum rods of 1.6mm in diameter are glued with an interval of 10mm to provide frictional behavior in the reinforcement. The length of reinforcement (L) is 144mm, which is 1.2 times the width of the foundation ($B=120\text{mm}$). The fixity condition in the geosynthetics is imposed by setting an aluminum plate in both edges of the reinforcement. The dimensions of each aluminum plate for modeling the fixed boundary condition of the reinforcement are - 2mm in thick and 15mm in height having the width of 50mm. It is projected from the tracing paper (geosynthetics) with an upper part of 5mm and a lower part of 10mm. The plate is moved with the movement of the ground during the application of load.

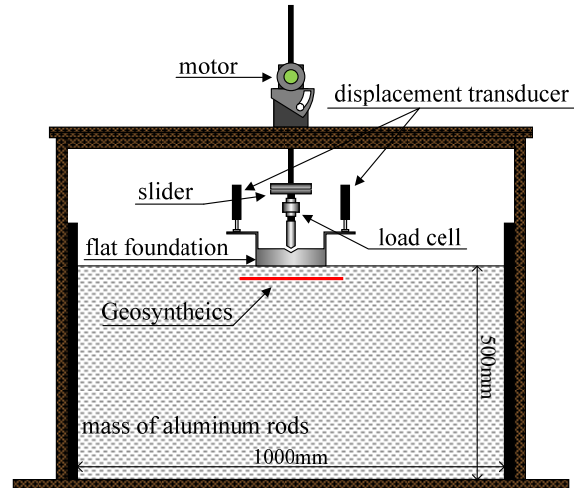


Fig. 2 Schematic diagram of apparatus

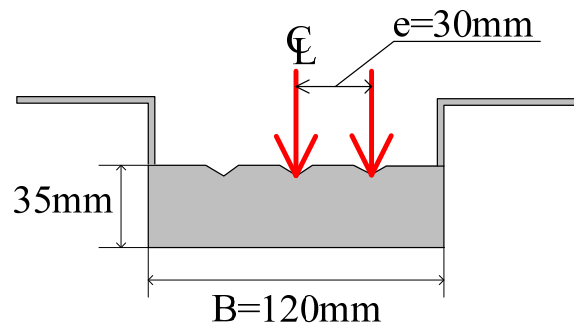


Fig. 3 Model of foundation

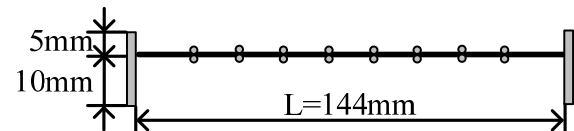


Fig.4 Model of reinforcement material

Outline of Numerical Analyses

Numerical analyses have been conducted considering the same scale of the 2D model tests. Two-dimensional finite element analyses are carried out with FEMtij-2D program which is developed in our laboratory. Fig.5 represents a typical mesh used in the numerical analyses. Isoparametric four-noded elements are used for soil elements, and elastic beam elements are used to simulate reinforcements. The frictional behavior between the reinforcement and aluminum rods, and the foundation and aluminum rods, is modeled employing the elastoplastic joint element [3]. The friction angle between reinforcement and aluminum rods, is determined by the sliding tests ($\delta=20^\circ$ for rough reinforcements). The friction angle between foundation and soil is $\delta=15^\circ$. In the numerical analyses the elastoplastic

subloading t_{ij} model [4], is used as a constitutive model for the ground. This model can describe typical stress deformation and strength characteristics of soils such as the influence of intermediate principal stress, the influence of stress path dependency of plastic flow and the influence of density and/or confining pressure. The same parameters of aluminum rods [1], [2] are used for the ground materials. The parameters of aluminum rods are listed in Table 1.

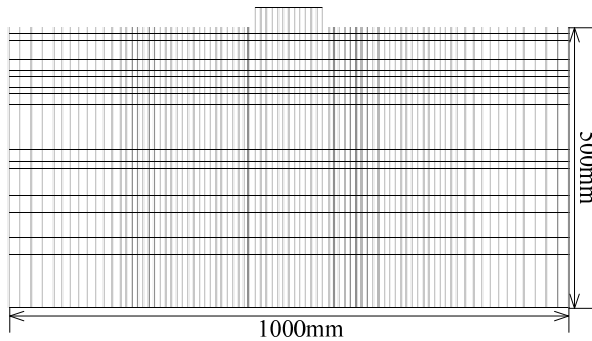


Fig.5 Finite element mesh for numerical analyses

Table 1 Values of material parameters for the mass of aluminum rods

λ	0.008	compression index	
κ	0.004	swelling index	
e_{NC}	0.3	reference void ratio on normally consolidation line at $p = 98 \text{ kPa}$ & $q = 0 \text{ kPa}$	Same parameters as Cam clay model
R_{cs}	1.8	critical state stress ratio $R_{cs} = (\sigma_1/\sigma_3)_{cs(comp.)}$	
ν_e	0.2	Poisson's ratio	
β	1.2	shape of yield surface (same as original Cam clay at $\beta = 1$)	
a	1300	influence of confining pressure	

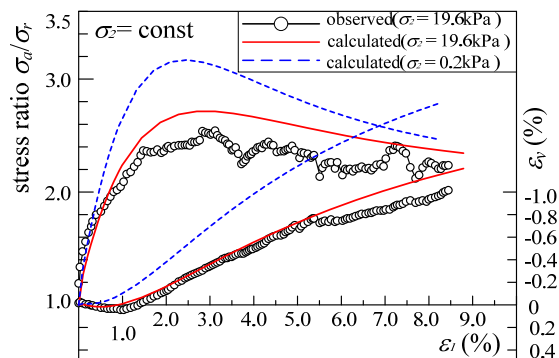


Fig.6 The results of biaxial test and analysis of aluminum rod mass

The parameters are fundamentally the same as those of the Cam clay model except the parameter a ,

which is responsible for the influence of density and confining pressure. The parameter β represents the shape of yield surface. The parameters can easily be obtained from traditional laboratory tests. Fig.6 shows the results of biaxial test and analysis of aluminum rod mass. The figure shows the positive and negative dilatancy of aluminum rod mass; and it is clear that the strength and deformation behavior are very similar to those of dense sand.

PETTERNS OF EXPERIMENTS

Table 2 shows the patterns of experiments. Tracing paper is set underneath the foundation at different installation depths (D). Five sets of reinforcement depths are considered: $D/B=0.00$, 0.05 , 0.10 , 0.20 and 0.40 , where B is the width of the foundation. In the real field the load of super structure is not always being acted at the center of the foundation. Therefore, the effectiveness of the reinforcement has been investigated for the two different loading positions, load is applied at the center (concentric loading) and at an eccentricity of $e=1/4B$ (eccentric loading).

Table 2 Patterns of experiments

	Pattern (Length of reinforcement $L/B=1.2$)				
	Depth of reinforcement D/B				
	$D/B=0$	$D/B=0.05$	$D/B=0.1$	$D/B=0.2$	$D/B=0.4$
Concentric Loading	○	○	○	○	○
Eccentric Loading	○	○	○	○	○

RESULTS AND DISCUSSIONS

Concentric Loading Condition

Fig.7 (a) and (b) show the observed and computed bearing capacity for different installation depths in concentric loading condition where the reinforcement length is 144 mm ($L/B=1.2$). The vertical axes represent vertical load q_v , which is divided by $\gamma B/2$; abscissas show normalized vertical displacement that is normalized by the width of the foundation ($B=120 \text{ mm}$). The figures also show the load-displacement curve of the ground without reinforcement. It is seen in the figures that bearing capacity increases for the installation depth of reinforcement at $D/B=0.05$, 0.10 , and 0.20 compared with the results of no-reinforcement. In addition, almost the same reinforcing effect is seen when the installation depth lies in between $D/B=0.05$ to 0.20 . On the other hand, the influence of reinforcement cannot be achieved when the installation depth is deeper than a certain depth (D/B is greater equal to 0.40). Similarly, when the reinforcement is placed on the ground surface just below the foundation, there is almost no effect of the reinforcements

except the coefficient of friction of the foundation; the behavior is similar to the case of no-reinforcement. The results agree with the results of the previous research [1], where it was found that when the depth of the reinforcement is in between $D/B=1/8$ to $D/B=1/2$, the effect of the reinforcement is the maximum. Therefore, it can be said that when the installation of reinforcement is deeper than the ground surface and is situated in the range of the influence of loading on the foundation, the effect of reinforcement can easily be achieved. When the installation depth of reinforcement is shallower tensile force develops in reinforcement due to the load application.

Fig.7(b) shows that the computed bearing capacity for different installation depths for concentric loading. As compared with observed results, the numerical analyses slightly overestimate the bearing capacity of the model tests. However, if compared with the results of the no-reinforcement, bearing capacity for the reinforcement at $D/B=0.05$, 0.10 and 0.20 increases the same way as the model tests. In addition, in the cases of reinforcement at the surface and at a depth deeper than $D/B=0.40$, there is almost no reinforcement effect. Therefore, it can be said that the analyses simulate the behavior of reinforcing effect similar to the observed results.

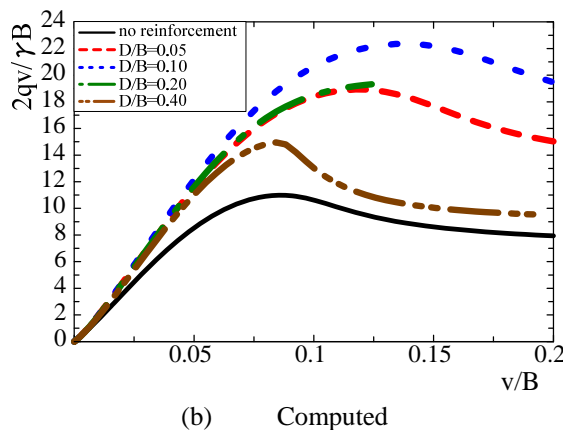
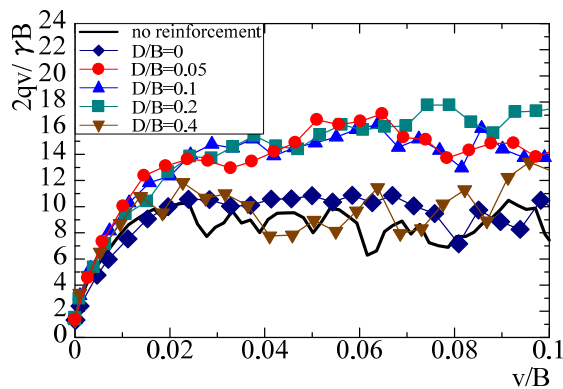


Fig.7 Vertical load vs. vertical displacement for concentric loading

Figure 8 illustrates observed and computed deviatoric strain distributions of the ground while the load approaches the peak strength, it is at $v/B=0.06$ for the model test, and for the analysis it is at $v/B=0.10$ in the case of no-reinforcement and at 0.13 when the reinforcement is setup at $D/B=0.10$ and 0.40. The distribution of deviatoric strain of the model tests is obtained from the simulation of the PIV technique taking two photographs before and after loading. The upper figure represents the results of the no-reinforcement. It is seen that where the effect of reinforcement occurs, for the reinforcement at $D/B=0.10$, a zone of large deviatoric strain spreads vertically below the foundation and it is distributed widely compared with no reinforcement. In the case of installation depth of reinforcement at $D/B=0.4$, deviatoric strain develops at narrower zone and hence bearing capacity of the ground does not increase. The computed results describe well the differences of the deviatoric strain distribution as observed in the model tests at different installation depths.

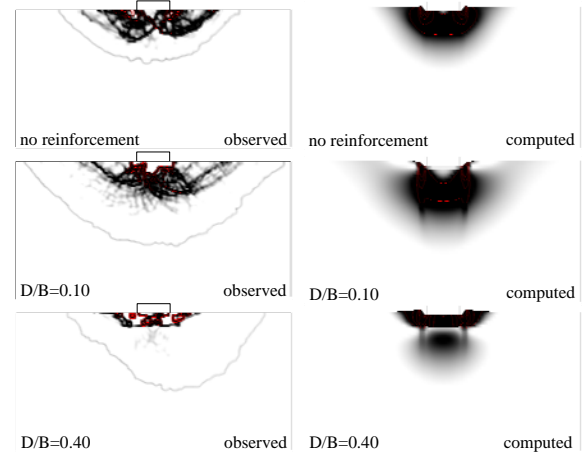


Fig.8 Deviatoric strain distributions: concentric loading

Eccentric Loading Condition

Figure 9(a) shows the observed bearing capacity for different installation depths in eccentric loading condition where the reinforcement length is 144mm ($L/B=1.2$) for the same test patterns as the concentric loading. Here, the load is applied at $2e/B=0.5$, i.e., at $1/4^{\text{th}}$ point of the strip foundation. The vertical axes and the abscissas show the same representation as described in Fig. 7. The figures also show the results of the ground without reinforcement. It is seen that the bearing capacity for the eccentric loading is smaller than that of the concentric loading (as illustrated in Fig.7) as a whole. It is seen in Fig.9(a) that bearing capacity increases for the installation depth of $D/B=0.05$, 0.10, and 0.20 compared with the results of no-reinforcement, and the influence of

reinforcement cannot be expected when the installation depth is deeper than a certain depth (D/B is greater equal to 0.40). These results are similar to that of concentric loading condition. Consequently, it can be said that when installation of reinforcement is deeper than the ground surface and is situated in the range of the influence of loading on the foundation, the effect of reinforcement can be achieved even in eccentric loading condition.

Figure 9(b) shows that the computed bearing capacity for different installation depths for eccentric loading condition. As compared with observed results, the numerical analyses slightly overestimate the bearing capacity of the model tests. However, if compared with the results of the no-reinforcement, bearing capacity in the case of reinforcements at $D/B=0.05$, 0.10 and 0.20 increases the same way as the model tests. In addition, in the cases of reinforcement at the surface and at a depth deeper than $D/B=0.40$, there is almost no reinforcement effect. Therefore, it can be said that the analyses simulate the behavior of reinforcing effect similar to the observed results. The numerical analyses not only simulate the results of the model tests for the concentric loading but also simulate the results of the model tests for the eccentric loading condition.

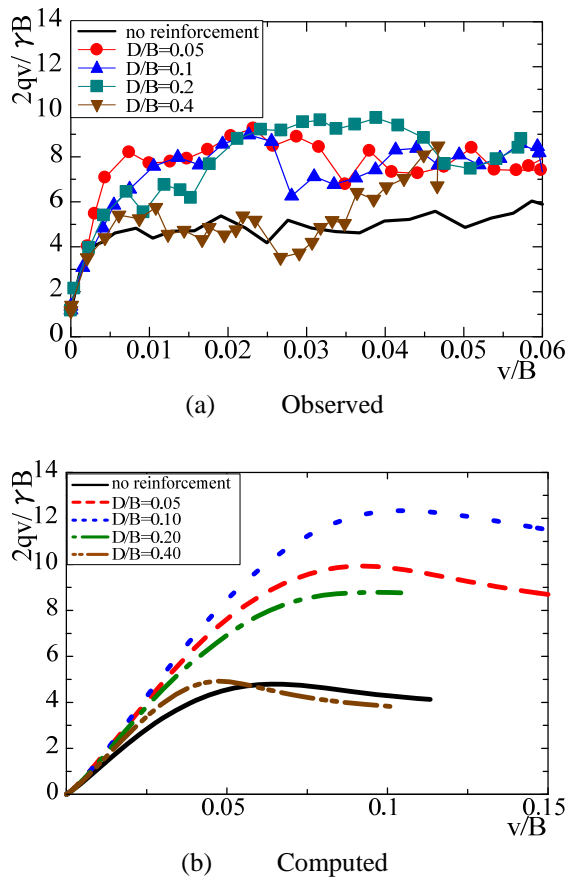


Fig.9 Vertical load vs. vertical displacement for eccentric loading

Figure 10(a) shows that the observed relation between the rotations of the strip foundation and the normalized vertical load in eccentric loading condition. Since uniform load is not applied to the foundation during eccentric loading condition, it is very important to reduce the amount of rotations which arises at the time of construction. It is seen in Fig. 10(a) that compared with the result of no-reinforcement, the rotation of the foundation starts at higher load when the reinforcement is installed at $D/B=0.05$, 0.10 due to the reinforcing effect. That is, the foundation can bear a higher load without rotating if it is reinforced properly underneath the foundation. However, the amount of load bearing capacity without any rotation of the foundation is less in the case where the reinforcement is installed at $D/B=0.20$ as compared with other two cases ($D/B=0.05$ and 0.10). On the other hand, almost the same behavior as no-reinforcement is seen when the reinforcement is installed at $D/B=0.40$. It is revealed that the rotation angle of the foundation decreases in the reinforced ground when the reinforcement is setup at $D/B=0.05$, 0.10 and 0.20. The tendency of the reinforcing effect in the reduction of rotation angle of the foundation is similar to that of the relation of bearing capacity and displacement as described before.

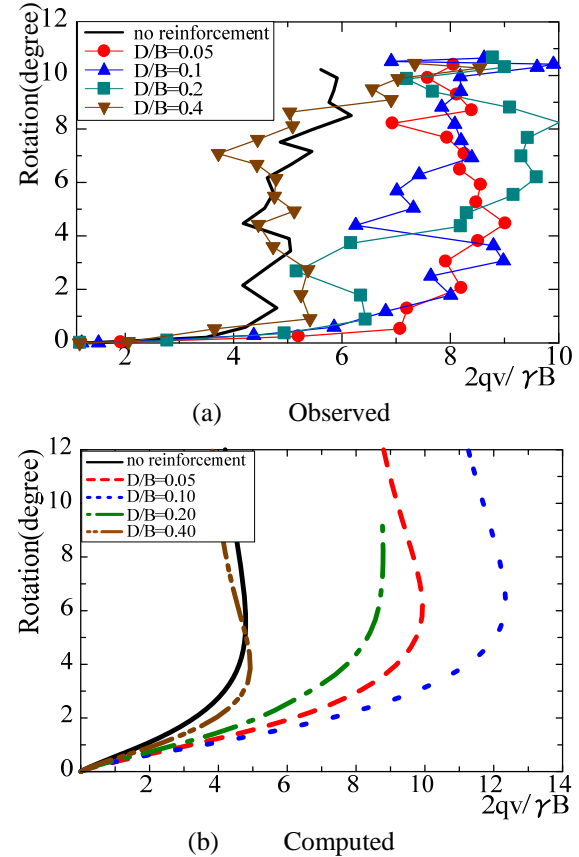


Fig.10 Rotation angle vs. load for eccentric loading: numerical analyses

Figure 10(b) represents the results of the numerical analyses corresponding to model tests shown in Fig. 10(a). As compared with the observed results, the numerical analyses slightly overestimate the amount of rotation at the initial stage. However, if compared with the results of the no-reinforcement, rotation of the foundation decreases in the case of reinforcements at $D/B=0.05$, 0.10 and 0.20 the same way as the model tests. In the case of reinforcement at $D/B=0.20$, the reinforcing effect on the reduction of the rotation of the foundation is relatively less as compared with other two cases ($D/B=0.05$ and 0.10) the same as the model tests. Similarly, the analyses do show any reinforcing effect on the rotation of the foundation in the case when installation depth is $D/B=0.40$. Therefore, it can be said there is a good agreement between the computed and observed results in the rotation of the foundation. So, laying geosynthetics under the foundation in an appropriate depth differential settlement can be controlled in eccentric loading condition.

Figure 11 illustrates observed and computed deviatoric strain distributions of the ground while the load approaches the peak strength, it is at $v/B=0.03$ for the model test, and for the analysis it is at $v/B=0.06$ in the case of no-reinforcement and at 0.10 when the reinforcement is setup at $D/B=0.10$ and 0.40 . The upper figure represents the results of the no-reinforcement. It is seen that even in the case of eccentric loading where the effect of reinforcement occurs, for the reinforcement at $D/B=0.10$, a zone of large deviatoric strain spreads vertically below the foundation and deviatoric strain is distributed widely compared to no reinforcement. In the installation depth of reinforcement at $D/B=0.40$, deviatoric strain develops at narrower zone the same way as the concentric loading. The computed results describe well the differences of the deviatoric strain distribution as observed in the model tests in the eccentric loading as well.

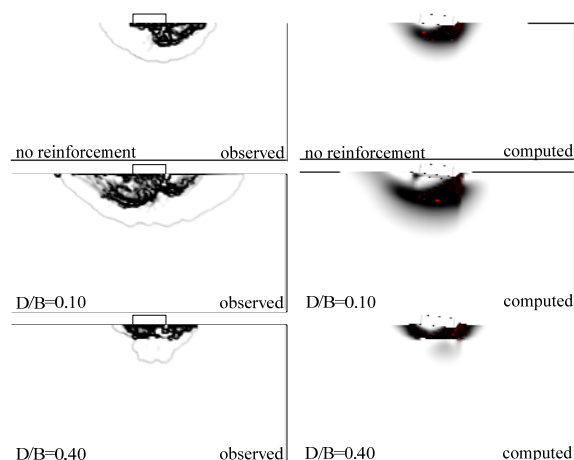


Fig. 11 Deviatoric strain distributions: eccentric loading

CONCLUSIONS

The bearing capacity of soil-reinforcement using geosynthetics has been investigated with laboratory model tests and the corresponding numerical analyses. The edges of the geosynthetics were kept fixed with the ground. It is revealed that the effectiveness of reinforcement mainly depends on the position of reinforcement and the maximum reinforcing effect can be achieved when it is set up in between $D/B=0.05$ to $D/B=0.20$ in the fixed condition. However, in the case of eccentric loading condition, the reinforcement effect decrease when the installation depth of reinforcement is $D/B=0.20$. Furthermore, if the reinforcement is setup at $D/B=0.40$ and deeper, the reinforcement effect is not achieved. If the reinforcement is situated in the range of the influence of loading, the effect of reinforcement can be achieved even in eccentric loading condition. By laying geosynthetics under the foundation in an appropriate depth differential settlement can be controlled in eccentric loading condition which is very important in real field construction. The results obtained from the numerical analyses show very good agreement with the results of the model tests in all patterns. It can be concluded that if the mechanical properties of ground material, reinforcing material and skin friction of reinforcement are appropriately considered, and the soil-reinforcement is treated as an interaction problem of the soil and structure (soil and reinforcement), it is possible to explain the reinforcement mechanism properly with such model tests and numerical simulations.

REFERENCES

- [1] Nakai T, H. M. Shahin, Watanabe A & Yonaha S., "Reinforcing mechanism of Geosynthetics on bearing capacity problems – model tests and numerical simulations", Proc. of the 17th International Conference on Soil Mechanics and Geotechnical Engineering, Alexandria, Egypt, October, 2009, pp. 917-920
- [2] Shahin, H. M., Nakai, T., Yoshida, Y. & Mio, M., "Effective reinforcing method for increasing bearing capacity", Proc. of the 5th Sino-Japan Geotechnical Symposium, China, 2012, pp. 457-463.
- [3] Nakai, T., "Finite element computations for active and passive earth pressure problems of retaining wall". Soils and Foundations, 25(3), 1985, pp. 98-112.
- [4] Naka T. & Hinokio T., "A simple elastoplastic model for normally and over consolidated soils with unified material parameters", Soils and Foundations, Vol. 44, No.2, 2004, pp. 53-70.

INFLUENCE OF THE STRESS HISTORY ON THE STIFFNESS OF SOIL

Asano Kanako¹, H.M. Shahin², Hiroyuki Kyokawa³, Teruo Nakai⁴ and Ohashi Ryoki⁵

^{1,2}Department of Civil Engineering, Nagoya Institute of Technology, Japan; ³The University of Tokyo, Japan; ⁴Geo-Research Institute, Nagoya Branch, Japan; ⁵Nagoya city office, Nagoya, Japan

ABSTRACT

The behavior of soil is influenced by the past stress history. However, it is not only the immediate last stress history to have influence on the deformation characteristic of soil, accumulation of all stress histories received in the past also affects the mechanical characteristic of soil. The number of times, magnitude and the direction of the past stress are being reflected on the accumulation of stress histories. In this research, several triaxial tests and true triaxial tests on sand have been conducted employing various stress histories. We have investigated the influence of cyclic stress history on the deformation characteristic of soils in details. We have also examined the stationary state of deformation where the change of volume converges to a stationary state by applying cyclic loading on soil. It is revealed that the stiffness of soil increases to certain extent due to the cyclic loading followed by a constant stiffness after some cycle of loading. The void ratio of soil decreases to certain limit for cyclic loading and it becomes constant after some cycle of loading the same as the soil stiffness.

Keywords: triaxial test, true triaxial test, stress history, cyclic load, stationary state

INTRODUCTION

In recent years effective use of land including underground, such as tunnels in urban areas and constructions of a subway and underground shopping malls etc., is the demand of modernization. In order to use the land more effectively, safely and economically, exact geotechnical analyses with numerical simulation are required. For this purpose, a constitutive model of soil is indispensable which can express the characteristics of the ground in detail from the viewpoints of density, time effect and anisotropy. Even if the conditions of the analysis conforming to a real problem, if the ability of the constitutive model used for analysis is insufficient, the accuracy of the solution will be poor too. In the most cases, the constitutive model used in numerical analyses of soils is either elastic or elastoplastic which cannot express the behavior of ground material fully. Therefore, it is necessary to form a constitutive model which can clearly express various characteristics of ground material such as confining stress and influence of past stress history.

Prediction of soil deformation is difficult because an internal particle structure changes at every moment and shows an anisotropic deformation characteristic according to the past stress history. This induced anisotropy affects greatly the response of soil when cyclic loading is applied, and is closely related to the main problems of geotechnical engineering, such as liquefaction which is subjected to undrained condition, compaction of the ground

which is subjected to drained condition. In order to describe stress induced anisotropy, till now a kinematic hardening law and modified stress are proposed. However, the model cannot explain completely the development and dissipation mechanism of a stationary state of soil. Moreover, it is insufficient to explain only some experimental values under limited conditions with a constitutive model. Therefore, verification of a model not only by the results of a conventional triaxial test but also by the results of a true axial test is required. For this purpose, this paper illustrates the results of some cyclic conventional triaxial and cyclic true triaxial tests under drained condition changing the amplitude of stress ratio, the direction of loading and the direction of major principal stress.

OUTLINE OF THE TEST AND THE SAMPLE USED IN THE TEST

The soil used for this research is Toyoura sand having a density of 2.65tf/m³. All the test specimens have been prepared by the water pluviation method to make a homogeneous sample. In order to maintain almost the same void ratio, the number of blows applied in all the test specimens was kept fixed which was 80. The dimension of the specimen is 12.35 mm in height, and 50 mm in diameter with saturated condition. All the experiments were carried out in drained conditions under constant mean effective stress of 196kPa. The back pressure of 98kPa is applied to the test specimens for all the tests. In

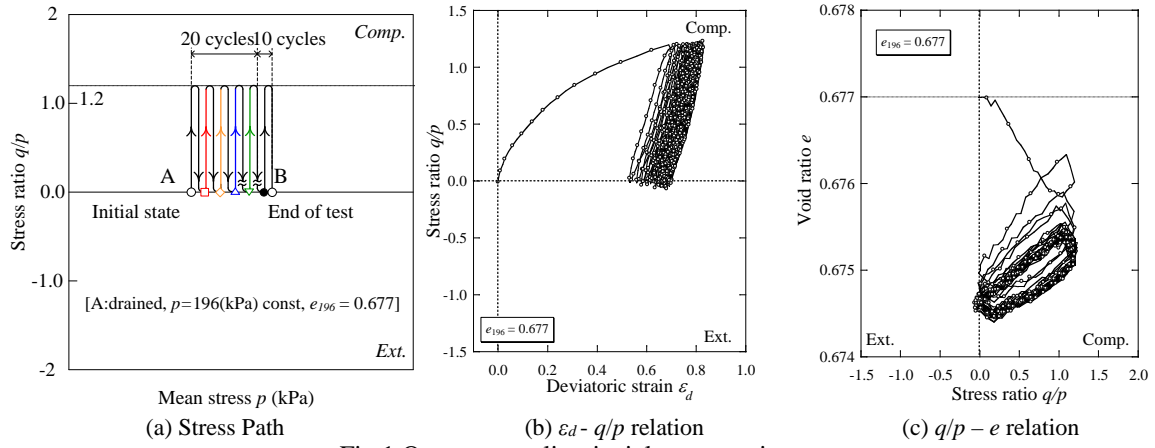


Fig.1 One-way cyclic triaxial compression test

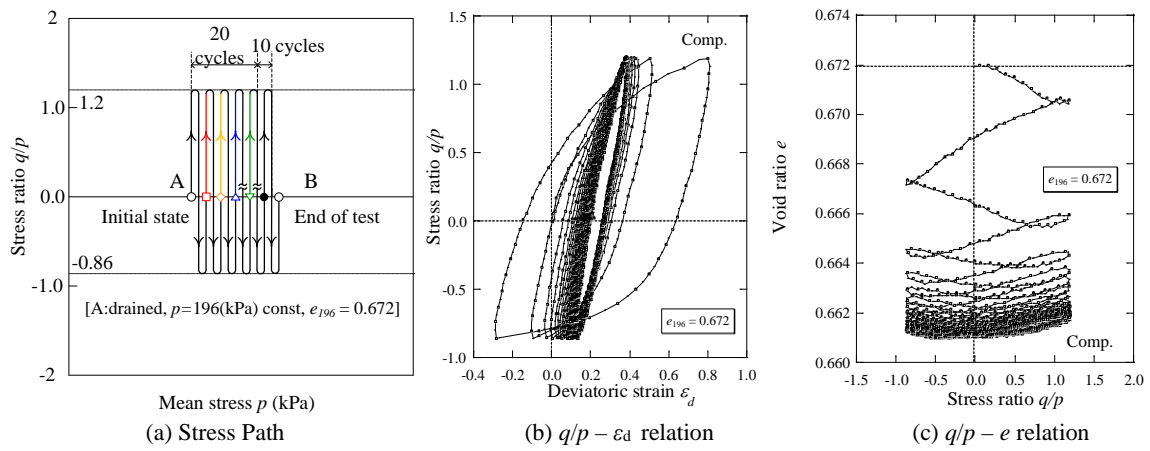
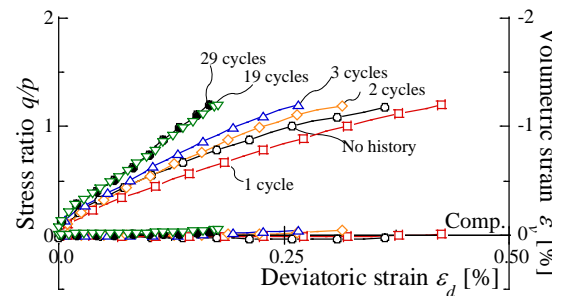
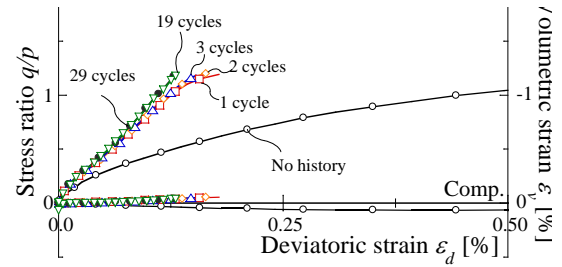


Fig.2 Two-way cyclic triaxial compression-extension test

addition, all the stresses shown in this paper are effective stresses. Strain controlled loading is applied in the tests.

INFLUENCE OF ONE-WAY AND TWO-WAY CYCLIC TESTS

In order to consider the influence of the reverse way loading in cyclic triaxial test, we have carried out both one-way cyclic triaxial compression test and two-way cyclic triaxial compression-extension test under constant stress ratio condition. The results of the one-way cyclic triaxial compression test are shown in Fig.1, and the results of the two-way cyclic triaxial compression-extension test are shown in Fig.2. The stress paths are shown in Fig. 1(a) and Fig. 2(a). Stress ratio q/p – deviatoric strain ε_d relations are shown in figure (b), and void ratio e – stress ratio q/p relations are shown in figure (c), respectively. It can be seen from figures (b) and (c) of Figs.1 and 2 that deviatoric strains and void ratio decrease remarkably in both cyclic triaxial tests. However, with the repeated loading, the amount of deformation associated with each subsequent cycle gradually decreases and finally converges to a stationary state. Comparing the results of the one-way cyclic triaxial


 Fig.3 $q/p - \varepsilon_d - \varepsilon_v$ relations at each cycle

compression test (Fig.1(c)) and the two-way cyclic triaxial compression-extension test (Fig.2(c)), it is found that more cycles of loading is required to reach the stationary state in the two-way cyclic triaxial compression-extension test than that of the one-way cyclic triaxial compression test.

Figure 3 represents the relation of stress ratio: q/p – deviatoric strain: ε_d for each cycle. The results of the one-way cyclic triaxial compression test are shown in Fig. 3(a), and the results of the two-way cyclic triaxial compression-extension test are shown in Fig. 3(b). The figures illustrate the behavior due to loading in the compression side in both cases. The numbers of cycles indicated in the figures represent the past stress history (in terms of repeated cycle) which is applied to the specimen. From Fig. 3(a) it is revealed that for the one-way cyclic triaxial

compression test, when load is applied at the second time (the first repeated loading), the stiffness increases sharply, and the stiffness in this state is almost similar to that of the final stationary state; the stiffness seldom changes even if the number of repetition of loading increases after the first cycle of loading. On the other hand, in Fig. 3(b) for the case of two-way cyclic triaxial compression-extension test it is seen that the stiffness increases gradually with the increase of the number of cycles before reaching a stationary state. It is interesting that though it needs more cycles to reach the level of the maximum stiffness (stationary state) the final stiffness in the case of two-way cyclic test is lower than that of the one-way cyclic test. In the two-way cyclic triaxial compression-extension test, since the load applied in the extension side is reverse to the compressive load,

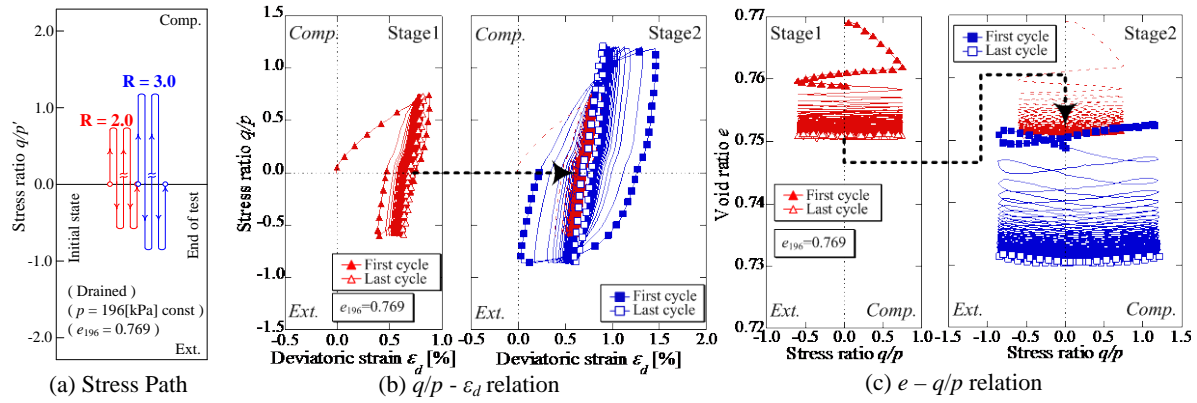


Fig.4 Results of the cyclic test with higher stress ratio

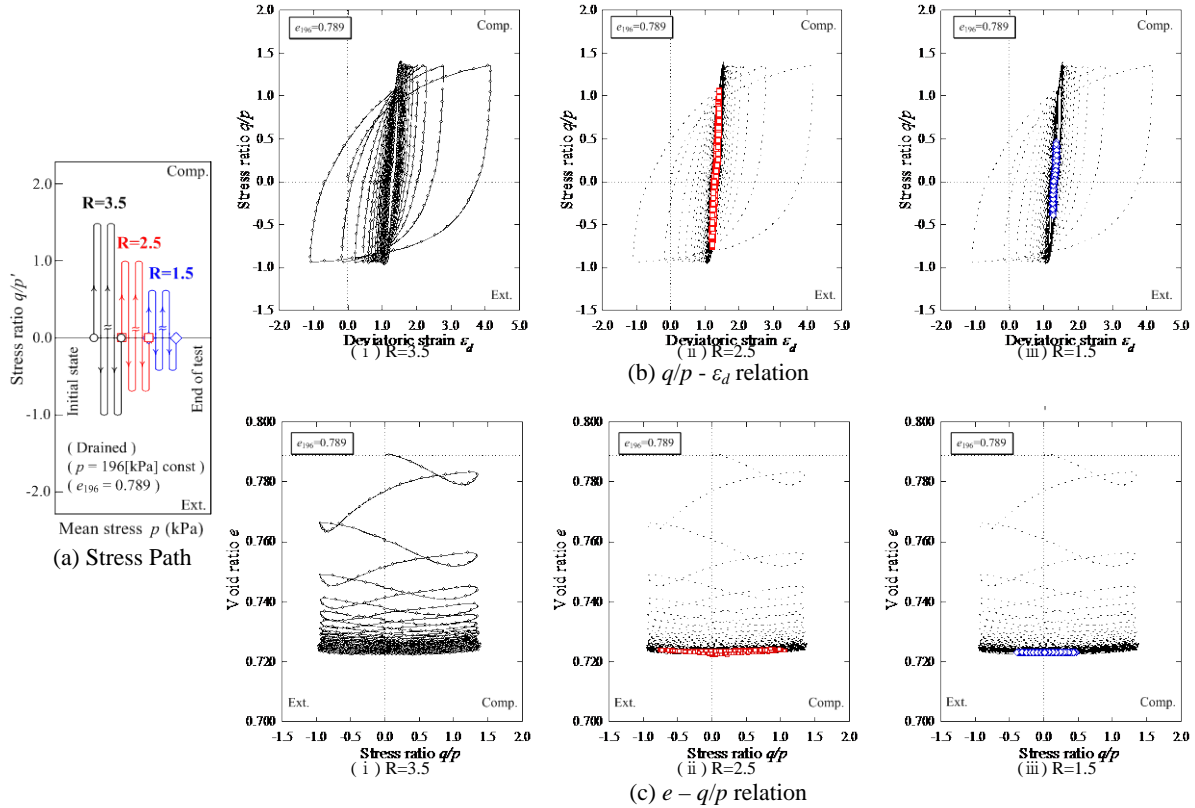


Fig.5 Results of the cyclic test reduced stress ratio

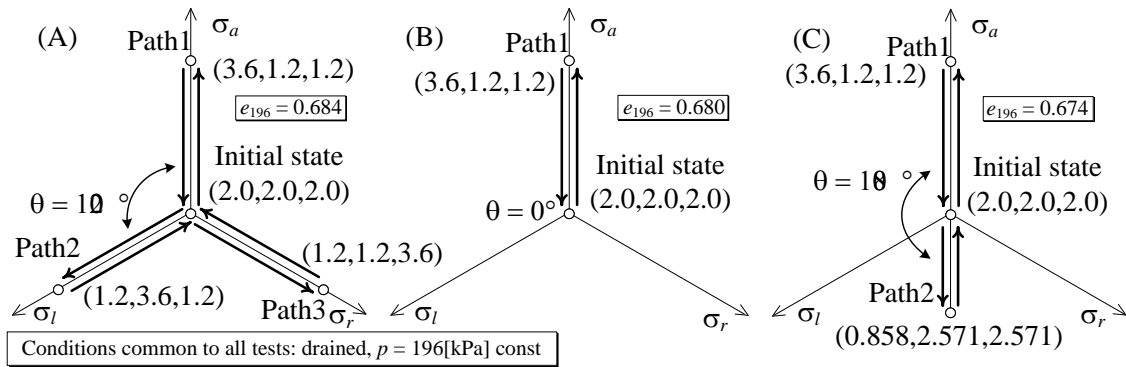
stiffness in the compression side is reduced to some extent for every cycle of loading in the extension side. Therefore, more cycles are required to reach the stationary state in the two-way cyclic test, and the stiffness at the stationary state is comparatively low.

INFLUENCE OF THE VARIATION OF THE AMPLITUDE OF STRESS RATIO

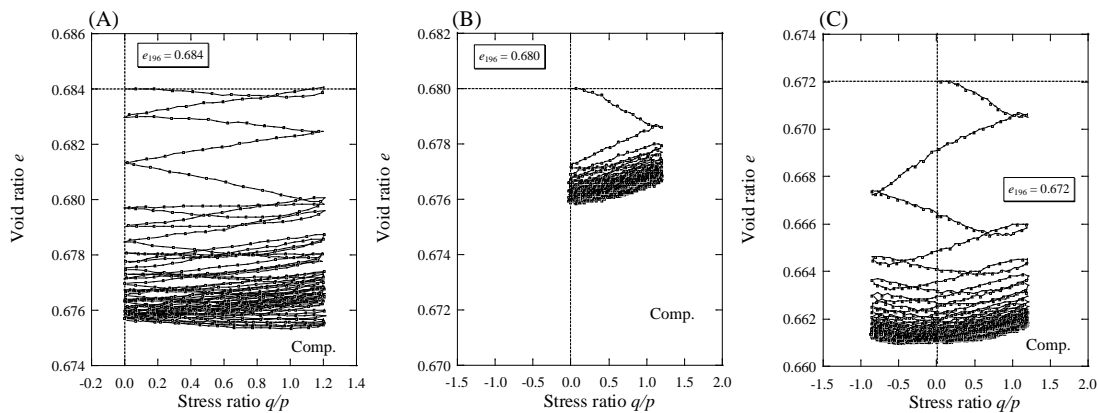
In order to investigate the influence of the amplitude of stress ratio on the stress-strain characteristics of soils in a repeated loading test, the stress ratio is being changed after reaching a stationary state by a cyclic triaxial test under constant amplitude of stress ratio. Figures 4 and 5 show the results of cyclic triaxial tests on the same specimen as described before for different amplitudes of stress ratio. Figure (b) shows the variation of stress ratio q/p against deviatoric strain ε_d , and figure (c) represents the relation of void ratio e and stress ratio q/p . In Fig.4, stress ratio R changes from 2.0 (Stage1) to 3.0 (Stage 2), i.e., stress ratio is being increased. On the other hand, in Fig.5 stress ratio R changes from 3.5 to 2.5 and finally to 1.5, i.e., stress ratio had been decreased gradually. The stress path of each test is

drawn in Fig. 5(a). In Fig.4, the solid marks represent the results of the first cycle and the open marks show the results of the last cycle. In Fig.5, black circular marks represent the results of stress ratio $R= 3.5$, red square marks show the results of $R= 3.0$, and the blue diamond marks illustrate the results of $R= 3.5$. In every test, the listed stress ratios were applied after confirmed that soil reached a stationary state.

Figure 4 shows that soil reached to a stationary state due to the application of repeated stress ratio with an amplitude of $R=2.0$ (Stage1). However, when a higher stress ratio $R=3.0$ is applied on the specimen the first stationary state is dissipated at the load application of very first cycle, and gradually soil reaches to a new stationary state with the increase of deviatoric strain and volume contraction due to the application of repeated cycles of loading. The stiffness of the soil increases as well in this case. On the contrary, it is seen in Fig.5 that when a smaller stress ratio $R=2.5$ is applied after applying a higher stress ratio $R=3.5$, the stationary state remains as it is without shifting to a new stationary state. Consequently, soil stiffness is not affected by the change of low stress ratio after it has reached the stationary state by applying higher stress ratio.



(a) Stress Path



(b) $q/p - e$ relation

Fig. 6 Results of cyclic true triaxial test, one-way cyclic conventional triaxial compression test, and two-way cyclic conventional triaxial compression-extension test

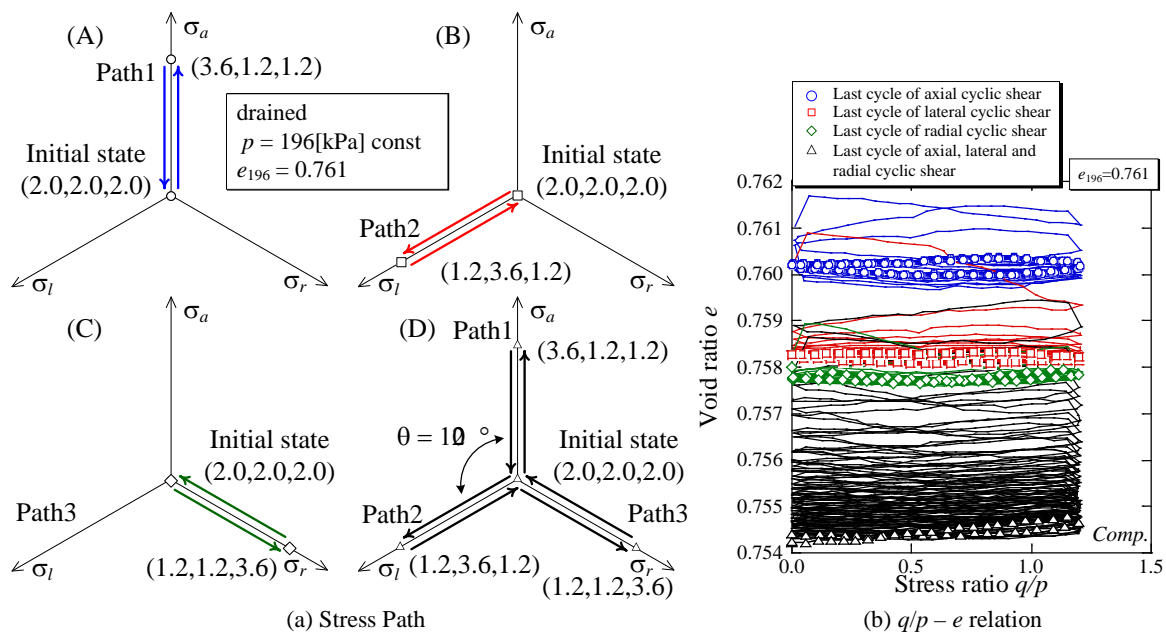


Fig.7 Results of cycle test changing the direction of principal stress

INFLUENCE OF THE DIRECTION OF MAJOR PRINCIPAL STRESS (LODE ANGLE)

The variation of the direction of the major principal stress has been investigated conducting one-way cyclic triaxial compression test. At first, compressive load with stress ratio of $R = 3.0$ ($q/p = 0.0 \Leftrightarrow 1.2$) is applied in the direction of a (axial direction) from an isotropic state of stress having $p = 196\text{kPa}$ (Path1 - Fig. 6(a)(A)); in the next step load in the direction of l (longitudinal direction) (Path2 - Fig. 6(a)(B)) is applied; and finally load in the direction of r (radial direction) (Path3 - Fig. 6(a)(C)) is applied in order. The stress paths 1 to 3 are repeated until a stationary state is reached. The results of this test (A) are shown in Fig.6. For comparison, the results of the one-way cyclic triaxial compression test (B) and two-way cyclic triaxial compression-extension tests (C) are also shown in the figure. The stress path of each test is drawn in figure (a), the relations of void ratio e - stress ratio q/p are shown in figure (b). In figure (a), θ represents the Lode angle showing the loading direction on the π plane.

In the case of principal stress path (A), an expansion of soil is seen after a compaction of soil at the initial monotonic loading paths and only compaction is seen at the unloading path the same way as the conventional triaxial compression test (B). For the subsequent repeated loading, soil rather shows compressive behavior even in unloading path in case (A); the behavior is almost the same as case (C). After some cycles of loading soil reaches to a stationary state the same way as cases (B) and (C). However, the amount of volume change until it

reaches a stationary state is different in the three different tests. The maximum volume contraction is seen in the two-way conventional triaxial compression-extension test (C) among the three stress paths, the minimum one is seen in case (B). The Lode angles of case (A) is $\theta = 120^\circ$, case (B) $\theta = 0^\circ$ and case (C) $\theta = 120^\circ$ on the π plane. Therefore, it can be said that the amount of volume change depends on the Lode angle too. For the same amplitude of stress ratio larger volume change is associated with larger Lode angle.

INFLUENCE OF THE CHANGE OF THE DIRECTION OF MAJOR PRINCIPAL STRESS

In order to study the influence of the change of the direction of major principal stress on the behavior of re-stationary state in sand, cyclic true triaxial test kept constant stress ratio in a fixed direction of principal stress have been performed. Here, after reaching a stationary state, we have changed the Lode angle and repeated the test by applying the same stress ratio in a fixed direction of principal stress. The stress path is shown in Fig. 7(a). Firstly, compressive cyclic load in the direction of a is applied until it reaches a stationary state (Path1 - (A) of Fig.7 (a)), in the next step the same amount of load is applied in the direction of l (Path2 - (B) of Fig.7 (a)) until it reaches a stationary state, and the same procedure is applied in the next step to get a new stationary state in the direction of r (Path3 - (C) of Fig.7 (a)). In the case of (D) in Fig.7, repeated compressive load is applied in the directions of a (Path1), l (Path2), and r (Path3) in order until it reaches a stationary state.

Figure 7(b) illustrates stress ratio q/p - void ratio e relation. Blue circular marks represent the results of

the last cyclic of case (A), red square marks show the results of the last cyclic of case (B), and green diamond marks illustrate the results of the last cyclic of case (C) and triangle marks show the results of the last cyclic of case (D). Figure 7(b) shows that after soil reaches a stationary state in the direction of a , as a result of changing the loading direction to the direction of l and then to the direction of r , at every time soil shifts to a new stationary state with a certain void ratio breaking the previous one. Therefore, it is revealed that soil shifts to a new stationary state with the change of the loading direction even if the amplitude of stress ratio is kept constant. Nevertheless, if cyclic load is applied in the stress path shown in (D) after the application of stress path shown in (C), soil is experienced with the maximum amount of volume contraction and reaches a stationary state with a certain void ratio. This result shows that the stress path in a cyclic load influences the amount of volume contraction of soil. The more change of the direction of principal stress in the stress path, the larger the volume contraction occurs before reaching a stationary state.

CONCLUSION

In this paper, several element tests have been carried out to investigate the factors affecting the volumetric strain and stiffness of Toyoura sand due to the stress induced anisotropy. The results can be concluded as-

(1) Influence of reverse loading -

In the one-way cyclic test, soil reaches the stiffness due to the first reloading which is almost the same as the stationary state. In the two-way cyclic test, stiffness increases gradually with the repeated loading before reaching a stationary state. More cycles of loading is required to reach a stationary state in the case of the two-way cyclic test than that of the one-way cyclic test because the stiffness is reduced due to the reverse way loading. Stiffness at stationary state is less for the two-way cyclic test compared with the one-way cyclic test as the development and dissipation of stiffness are being repeated in the two-way cyclic test.

(2) Influence of the amplitude of stress ratio -

If the amplitude of stress ratio increases or the direction of principal stress changes, soil shifts to a new stationary state from a previously developed stationary state. The amount of volume change depends on the Lode angle.

(3) Influence of the direction of major principal stress -

The stress path in a cyclic load influences the amount of volume contraction of soil. The more changes of the direction of principal stress in the stress path, the larger the volume contraction occurs before reaching a stationary state.

Therefore, in order to express stress deformation characteristics, such as the change of stiffness and volumetric strain which are subjected to the past stress history, it is necessary to consider the past direction of major principal stress and the amplitude of stress ratio during the formulation of a constitutive model.

ACKNOWLEDGEMENTS

The authors are grateful to Mr. A. Ban and Mr. Ishihara, former student of Nagoya Institute of Technology for their contribution in some experiments.

REFERENCES

- [1] Ohashi R, Kyokawa H., Kikumoto M., Nakai. T, Shahin H.M., and Ban A., "The influences of stress histories on the deformation characteristics of sand", The 23rd conference of JGS Chubu Shibu, August, 2011 (CD-ROM, in Japanese).
- [2] Naka T. and Hinokio T., "A simple elastoplastic model for normally and over consolidated soils with unified material parameters", Soils and Foundations, Vol. 44, No.2, 2004, pp. 53-70.
- [3] Ohashi R., Asano K., Shahin H.M, Nakai T, Kyokawa H., "Experimental Investigation of the Development of Stress Induced Anisotropy and its Dissipation in Sand", Proc. of the 7th conference of Japan Society of Materials Science, Tokai branch, Nagoya, Japan, March, 2013 pp. 71-72 (in Japanese).

EFFECTIVENESS OF CRASHED TILE IN COUNTERMEASURE AGAINST LIQUEFACTION

MORIKAWA Yukihiro¹, MAEDA Kenichi² and ZHANG Feng³

¹Assistant Professor, Nagoya Institute of Technology, Japan

^{2,3}Professor, Nagoya Institute of Technology, Japan

ABSTRACT

Liquefaction usually occurs in many sandy grounds during earthquake including Japan. Liquefaction causes damage of structures by making floatation or subsidence of them, and reduces the necessary performance of the structures. For example, stability of retaining wall based on skeleton weight of the structure is reduced due to subsidence and inadequate support which causes the destabilization of the structure. In addition, the light weight underground structure suffers damage such as floating due to the reduction of shear strength of soils during liquefaction. The damage occurs not only to the civil engineering structures (roads, bridges, etc.) but also to the residential buildings which makes the building unusable. On the other hand, Aichi Prefecture (Japan) is a center of the production of tiles where the crushed tile can be used as recycling materials for a measure of soil liquefaction. In this research, we have investigated the material property of the crushed tile and examined the effectiveness of countermeasure against liquefaction by shaking table tests. It is found that liquefaction of the ground can be reduced using crushed tiles because of its high friction and drainage properties. In the research, we found that the anti-liquefaction manhole which was backfilled by crashed tile floated only by 1/3 of the magnitude observed in the case of without countermeasure against liquefaction.

Keywords: Countermeasure against liquefaction, recycling materials, crashed tile, disaster mitigation

INTRODUCTION

In Great East Japan Earthquake happened on March 11 2011, huge damage was reported [1] and [2]. Especially, the damage caused by tsunami and liquefaction were the largest scale in the history of observation. Liquefaction has been intensively dealt with for a main shock in huge earthquake. In recent years, however it is found that the bearing capacity of soils may not only decrease in the main shock with relative short time period but also in multiple aftershocks with relative a long time seismic motion. In addition, the multiple aftershocks in short time period enlarged the damaged area by the liquefaction. For this reason, it is necessary to predict the damage and take counter measures, both in software and hardware, against the mixed disasters of huge earthquake that will happen with very high probability within thirty years.

Countermeasures against the earthquake for small structures such as branch lifelines and personal houses are urgently needed because they are vulnerable to not only the main shock but also the secondary disaster that had become serious problems in the past earthquakes. Therefore, it becomes social concern and more important for the research on feasible and effective countermeasures for the existed small structures against the liquefaction caused by long-time seismic motion and short-time

multiple aftershocks.

IMPORTANCE OF THE COUNTER-MEASURES AGAINST LIQUEFACTION FOR SMALL STRUCTURES

The countermeasures to protect the small structures from the damage are not so intensively dealt with compared with huge structures in civil engineering [3]. As observed in Great East Japan Earthquake, liquefaction causes the floating of underground structures such as sewage pipe, water pipes and gas pipe. Most of which became unusable for a long period (Fig.1).



Fig. 1 Damage as floating of underground structure due to liquefaction

In this research, we investigated the material properties of a crushed tile and examined the effectiveness of countermeasure against liquefaction for small structures using the crushed tile. Aichi Prefecture, Japan, is a major production source of tiles where useless or crushed tile comes out as garbage. If it can be used as recycling materials for anti-liquefaction, then it will be of great benefit.

RECYCLING MATERIAL AS ANTI-LIQUEFACTION MATERIAL

About Crashed Tile

The useless or crushed tile, called as abolished tiles, are produced in a fixed quantity each year, among which more than 80% of the abolished tiles are reused as raw materials for the production of new tile. The other 20%, however, is left unusable. Besides, the old abolished tile in the process of reroofing of houses is not recycled at all. The crushed tile is crushed to small angular particles in order to make it possible for recycling, as shown in Fig.2. Physically, the tile is stable that has no bed influence on environment because it is burnt at a very high temperature of 1150 °C.



Fig. 2 Shape of the particle of material (Left side: crashed tile, Right side: Toyoura sand)

Physical Properties of Crushed Tile

In this research, some laboratory tests are conducted in order to investigate the applicability of the crashed tile as anti-liquefaction material. A red-brown crashed tile made in Mikawa area, hereafter called as Mikawa crashed tile, is used in the laboratory tests, including 1G shaking table test.

Figures.3-6 show test results of grain size distribution curve, density test of soil particle, and minimum-maximum density test of soil (void ratio and dry unit weight). In addition, the compressive strength of the particle in crushed tile is 78MPa, and its water absorption is 6-7%.

As for crashed tile that we used in the all tests, the maximum grain size is 4.75mm, uniformity coefficient is 6.0, and coefficient of curvature is 0.8

(Fig.3). The grain size distribution of crashed tile is better than Toyoura sand, a clean sand with a maximum grain size is 0.425mm, uniformity coefficient is 1.6, and coefficient of curvature is 0.9.

As to the density of the crashed tile, because it has a lot of small voids inside the particles as shown Fig.4, the density is rather lighter ($G_s=2.56$) than the general soil ($G_s=2.65$).

As mentioned before that the grain size distribution of the crashed tile is better than Toyoura sand, the distribution of the minimum-maximum void ratio, however, ranging from $e=0.863$ to $e=1.457$, is much bigger than the other materials, e.g., Toyoura sand: $e=0.614-0.959$ (Fig.5).

As the result, the dry density of the crashed tile, as shown Fig.6, is smaller than other materials because the void ratio of crashed tile is bigger and the density of soil particle is lighter.

From the above test results, it is found that the crashed tile is light soil material that has relatively good grain size distribution but large void.

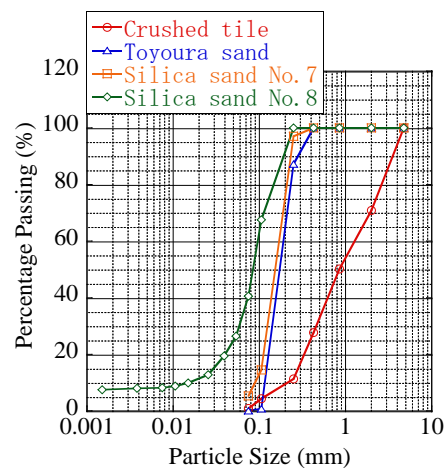


Fig. 3 Grain Size Distribution

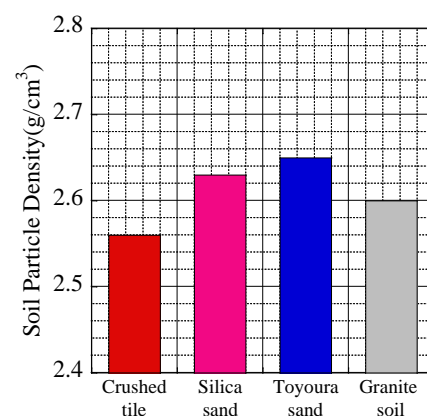


Fig. 4 Density of Soil Particle

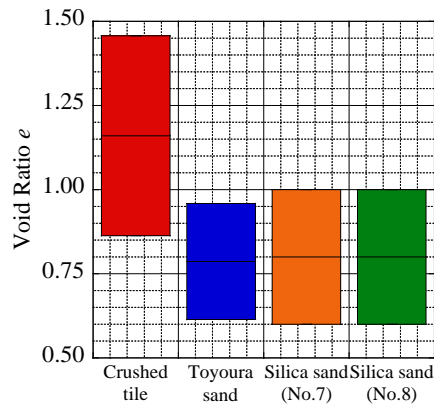


Fig. 5 Range of Void Ratio

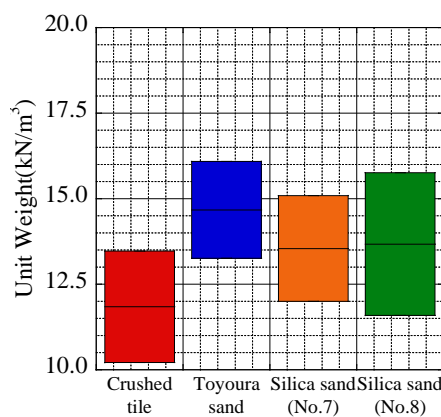


Fig. 6 Range of Dry Unit Weight

Mechanical properties of Crushed Tile

Figure 7 shows the test results of a repose test, a simplest and easiest way to examine the reposed angle of a particle material under dry condition. The reposed angle of the crashed tile is 41deg that is higher than general sand (around 30deg) from the result. The reposed angle of aluminum ball whose shape is completely round, is about 23°, which means that a particle material with angler shape will possess a high frictional resistance or, a high internal friction angle.

Figures 8-10 shows the test results of permeability test, direct shear test and conventional triaxial test. The permeability of the crashed tile is 2.76×10^{-3} m/sec, as shown in Fig.8, a higher value than that of Toyoura sand (5.77×10^{-4} m/sec) because the maximum grain size and void ratio of the crashed tile is bigger than that of Toyoura sand. The permeability of the crashed tile can be classified as a coarse sand or gravel.

Figure 9 shows the result from the direct shear test. The internal frictional angle ϕ of the clashed tile is 42deg higher than that of Toyoura sand (around 30deg). In addition, the test result of triaxial compression test is shown in Fig.10. The internal frictional angle of the crashed tile is 41.5deg.

Therefore it is reasonable to conclude that the internal frictional angle of the clashed tile is over 40deg from these mechanical tests.



Fig. 7 Repose angle of different materials

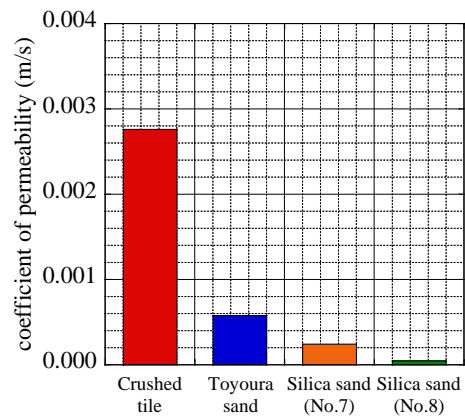


Fig. 8 Permeability Test

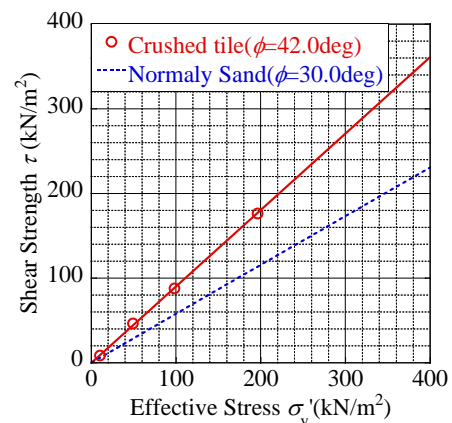


Fig. 9 Direct Shear Test

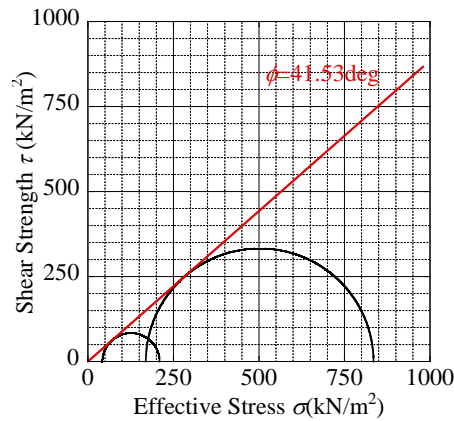


Fig. 10 Triaxial Test

Table 1 Property of Crashed Tile

Maximum density	$\rho_{d \min}$	g/cm ³	1.042
Minimum density	$\rho_{d \max}$	g/cm ³	1.374
Maximum void ratio	e_{\min}		1.457
Minimum void ratio	e_{\max}		0.863
Soil particle density	ρ_s	g/cm ³	2.56
Maximum grain size	D_{\max}	mm	4.75
60% diameter on the grain size diagram	D_{60}	mm	1.28
50% diameter on the grain size diagram	D_{50}	mm	0.847
30% diameter on the grain size diagram	D_{30}	mm	0.456
10% diameter on the grain size diagram	D_{10}	mm	0.213
Uniformity coefficient	U_c		6.0
Coefficient of curvature	U_c'		0.8
Coefficient of permeability	k	m/sec	2.76×10^{-3}
Angle of Internal friction	ϕ	deg	42.0

COUNTERMEASURE AGAINST FLOATING OF UNDERGROUND STRUCTURES

Setup of Experiment

The crashed tile is then regarded as an effective material for anti-liquefaction because its internal frictional angle and permeability is higher than those of sands. In order to confirm this factor, we conducted a floating test of manhole which is backfilled with the crashed tile on liquefiable sandy ground using 1G shaking table test, as shown in Fig.11.



Fig. 11 Shaking Table

The shaking table test device uses air-pressure actuator that has an advantage of high performance of maintenance but disadvantage of less accuracy of wave output. The maximum air pressure is 1.0MPa, the maximum stroke is 0.05m, the maximum loading capacity is 18kN, and the maximum vibration acceleration is 9.80m/s². A laminate shear box is installed on the table whose depth, length and width is 0.8m, 1.2m and 1.0m respectively. The average relative density of Toyoura sand and the crashed tile that used in the shaking table test, is 24.2% and 23.7% respectively.

Test Conditions

In the shaking table test, we use the crashed tile as a backfill material against the liquefaction and Toyoura sand as the model ground material. In the test, the apparent gravity of the manhole, an underground structure, is 1.2, its diameter is 0.10m, the height is 0.30m, and the manhole is made from acryl hollow cylinder. Figure.12 shows the plan view of the model ground. In the test, one manhole is backfilled by the crashed tile and another one is backfilled with the same sand as the model general. Both the manholes were installed in the same laminate shear box and were excited with the same earthquake motion. As shown in Fig.12, the anti-floating manhole is on the left side and the manhole without countermeasure is on the right side of the shear box. In the test, the height of model ground is 0.50m while the depth of the crashed tile as countermeasure against floating is from GL-0.30m to the top surface, which is the same depth as the manhole length. Of course it is much better to backfill the manhole by the crashed tile from in whole depth, here we only investigate a minimum improvement effect of the backfill.

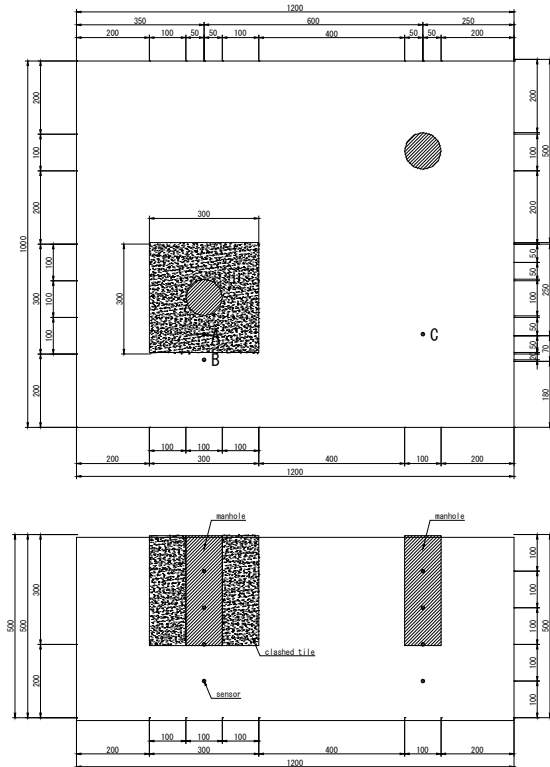


Fig. 12 Plan and x-section of the shaking table test

We installed 12 excessive pore water pressure sensors within the model ground, Point A, where is located inside the backfilling area with the crashed tile, Point B where is near the backfilled area, and Point C where is no-countermeasure area, as shown in Fig.12. In all the measurement points, the sensors were installed at 4 different depths (GL-0.10m, GL-0.20m, GL-0.30m, GL-0.40m).

Results of Shaking Table Test

Figure 13 shows the input wave which was measured on the table of the test. Its frequency is 4Hz, shaking time is 10sec, and the maximum acceleration is around 0.2 m/sec^2 .

Figures 14-17 show the excessive pore water pressure ratio (EPWPR) at each measurement point. The results shows that the EPWPR may rise over 1.0, which we consider as a measuring error, because the reason why this phenomenon occurred is due to the small initial value of the confining stress but with relative large up-down movement happened around the sensors near the surface.

From the measuring results at point A (inside of the clashed tile), it is known that the excessive pore water pressure (EPWP) decreased substantially immediately after the excitation at the depth of 30 cm, implying that the crashed tile is a good material to enhance the dissipation of EPWP and hard to be liquefied.

In addition, the EPWP at Point B (around of the crashed tile) also dissipated immediately after the excitation, the same as Point A, meaning that it is an effective countermeasure against the liquefaction using the crashed tile as backfilling material.

The EPWP at all the points below GL-0.30m, however, the effectiveness of the countermeasure against liquefaction cannot be confirmed, as shown in Fig.17.

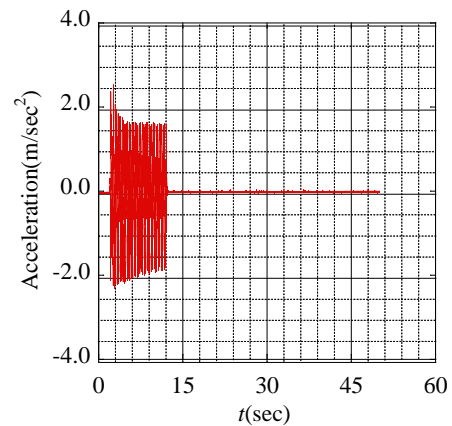


Fig. 13 Input Wave

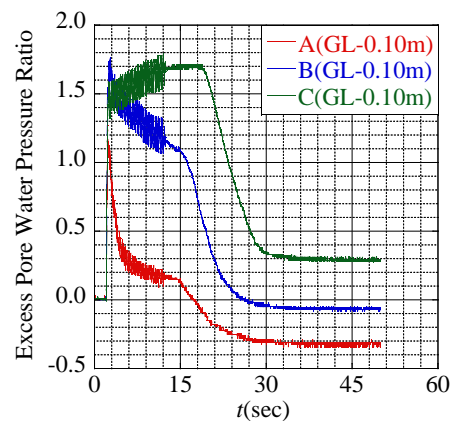


Fig. 14 Excess Pore Water Pressure Ratio (GL-0.10m)

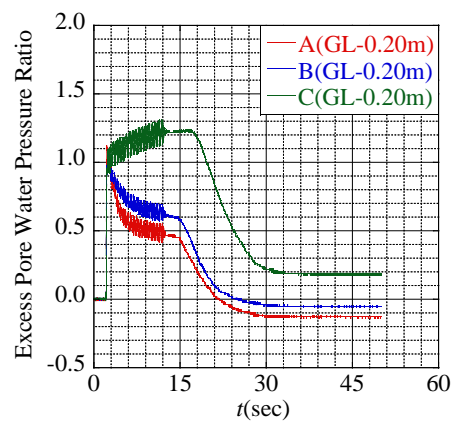


Fig. 15 Excess Pore Water Pressure Ratio (GL-0.20m)

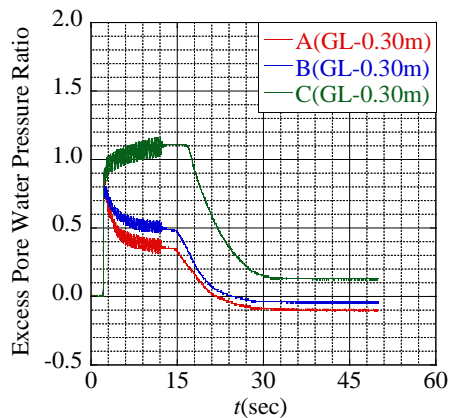


Fig. 16 Excess Pore Water Pressure Ratio (GL-0.30m)

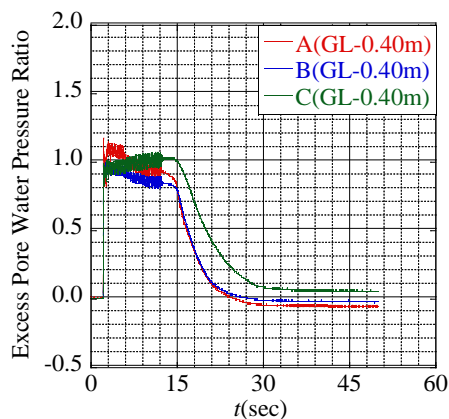


Fig. 17 Excess Pore Water Pressure Ratio (GL-0.40m)

Figure 18 shows the situation of the manhole after the excitation. In the first vibration loading, the manhole without countermeasure against liquefaction floated by 95mm, shown in Fig.18 (a), while the manhole backfilled with the crashed tile for anti-liquefaction, floated only by 31mm, shown in Fig.18 (b).

Furthermore, in the second shaking, the manhole without countermeasure floated and then fell down completely, shown in Fig.19 (a), but the damage to the manhole with anti-liquefaction measure is limited, as shown in Fig.19 (b).



Fig. 18 Situation of the Manhole (1st earthquake): (a) Manhole Without Countermeasure, (b) Manhole With Countermeasure



Fig. 19 Situation of the Manhole (2nd earthquake): (a) Manhole Without Countermeasure, (b) Manhole With Countermeasure

Based on the above results, it is clear that the crashed tile is very effective backfilling material the countermeasure against liquefaction. When an underground structure is backfilled by a material with high frictional resistance and high permeability like the crashed tile, it is possible to minimize the damage related to the floatation due to liquefaction.

CONCLUSION

The Performance of Clashed Tile

- 1) The angle of internal friction is very high.
- 2) The coefficient of permeability is very high.

Effectiveness of Countermeasure

- 1) The anti-liquefaction manhole which was backfilled by clashed tile floated only by 1/3 of the magnitude observed in the case of without countermeasure against liquefaction.
- 2) EPWP inside and around the clashed tile decreases immediately after excitation, hence clashed tile can be an effective countermeasure against liquefaction.

REFERENCES

- [1] Kazam M., " Overview of the damages of The 2011 Off the Pacific Coast of Tohoku Earthquake and its geotechnical problems" Japanese Geotechnical Journal, Vol. 7(1), 2012, pp. 1-11.
- [2] Yasuda S., Harada K., Ishikawa K., " Damage to structures in Chiba Prefecture during the 2011 Tohoku-Pacific Ocean Earthquake" Japanese Geotechnical Journal, Vol. 7(1), 2012, pp. 103-105.
- [3] Murakami Y., Goto S., Yoneyama T., " Prevention of liquefaction of shallow backfill ground and of up-lift of underground facilities by use of stabilized mud" Japanese Geotechnical Journal, Vol. 2(2), 2006, pp. 87-94.

PREDICTION OF NATM TUNNEL EXCAVATION UNDER SHALLOW OVERBURDEN IN PAHANG-SELANGOR RAW WATER TRANSFER TUNNEL PROJECT, MALAYSIA

¹Mohd Ashraf Mohamad Ismail, ¹Goh Chin Ong, ¹Romziah Azit, ²Zulkifli Nordin, ²Norzani Mahmood

¹School of Civil Engineering, Universiti Sains Malaysia, ²Pahang-Selangor Raw Water Transfer Tunnel Project, Ministry of Energy, Green Technology and Water, Cyberjaya, Selangor, Malaysia

ABSTRACT

This study deals with the prediction of NATM tunnel construction with shallow overburden at the Kerau river crossing in the Pahang-Selangor Raw Water Transfer Tunnel Project. The subsurface profiles along the shallow NATM tunnel alignment are developed based on 13 boreholes data and in-situ Lugeon tests using inverse distance weighting (IDW) interpolation together with electrical resistivity survey result. Based on the subsurface profiles developed, the tunnel excavation was simulated using filtered tunnel model to assess the rock mass weathering grade, Rock Quality Designation (RQD) and Lugeon value. From the result analyses, the weathering grade at the crown along the tunnel alignment is mainly in rock grade III and grade II at the invert with RQD from 50-90%. Additionally, the comparison between filtered model for Lugeon value and electrical resistivity result indicate the zone of potential flow path underneath the Kerau River. The prediction allows the potential risks along the critical tunnel alignment being evaluated and suggested solutions to be proposed to provide complete stabilization during the tunnel excavation and advancement.

Keywords: NATM tunnel, inverse distance weighting, Filtered Tunnel, Electrical Resistivity Test

INTRODUCTION

The construction of shallow tunnel in heterogeneous geological condition is very difficult compare to other construction projects. The construction can be more complex if the tunnel is excavated under a river with shallow overburden as there are many uncertainties and risk involved. Before the tunnel is excavated under the Kerau River, geotechnical investigations has been carried out to assess the ground condition. Rotary drilling was carried out to obtain the soil and rock samples. Meanwhile, single and multiple packers Lugeon tests were carried out to determine the permeability of the rock. According to Spencer [1], the tunnel can be submerged by the water during the construction if there is a water bearing zone surrounding the tunnel alignment. Thus, it is important to identify the water bearing zone underneath the river bed before the excavation proceed. However, rotary drilling cannot be done directly below the river bed of the tunnel alignment due to the risk presence although the geotechnical parameter and engineering properties under the river is essential for the tunnel excavation and advancement planning.

The construction of the tunnels through different ground conditions needed different methods of excavation and construction such as using Tunnel Boring Machine (TBM) or New Austrian Tunnelling Method (NATM) [3-5]. Due to the shallow tunnel overburden and occurrence of heterogeneous ground conditions, NATM was used

for the tunnel excavation under the Kerau River. Meanwhile, Japanese Highway (JH) Classification System is used to classify the rock to determine the type of tunnel support. Since the geotechnical parameter and engineering properties cannot be obtained using borehole method under the Kerau River before the tunnel construction, only probe drilling method will be used to investigate the geological condition ahead of the tunnel during the tunnel excavation [6, 7]. To stabilize the tunnel crown during the excavation, additional tunnel support such as pipe roof and forepoling must be installed during the excavation of the tunnel [8-10]. For this project, forepoling with all ground fastened (AGF) will be used as the additional support system for the tunnel crown. The construction of forepoling have been described in details by Kontothanassis, Koronakis [11] and Leca, Leblais [12]. For this project, forepoling was not only acted as support to the tunnel crown, but also act as a roof support for further tunnel advancement. In this study the potential risks along the critical alignment under the Kerau River crossing will be evaluated based on the geological and engineering properties that controls the behaviour of the NATM tunnel excavation.

SPATIAL INTERPOLATION USING IDW

In this study, subsurface models are developed using Inverse distance weighting (IDW) technique which is based on spatial interpolation between all input data points. IDW is an interpolation technique that places with a known scattered set of points nearer to the interpolated location. IDW algorithm

is a moving average interpolator that is usually applied to highly variable data. This method assumes the influence of the variable entered on the map decreases with the increase of the distance from its sampling site. In the inverse distance weighted interpolation, the interpolation value of $Z(X_0)$ in the position X_0 is calculated based on the following expression:

$$Z(X') = \sum_{i=1}^n W_i Z(X_i) \quad (1)$$

where n is the number of scatter points (data samples) in the set, $Z(X_i)$ are the values at the sampled points (e.g., the data values set), and W_i are the weights assigned to each sampled point. This weight is calculated with the following function:

$$W_i = \frac{h_i^{-p}}{\sum_{j=1}^n h_j^{-p}} \quad (2)$$

where p is a positive real number called the power parameter (typically, $p = 2$) and h_i is the distance from the sampled location to the unsampled location for which an interpolated value is required [13]. For certain data types, it is possible to return to the collection site and record a new value that is statistically different from the original reading but within the general trend for the area. It is not desirable to honour local high/low values but rather to look at a moving average of nearby data points and estimate the local trends.

The IDW technique calculates a value for each grid node by examining surrounding data points that lie within a user-defined search radius. Some or all of the data points can be used in the interpolation process. The node value is calculated by averaging the weighted sum of all the points. Data points that lie progressively farther from the node influence the computed value far less than those lying closer to the node (Fig.1).

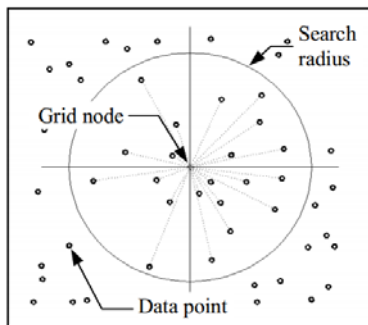


Fig.1: IDW interpolation technique

SUBSURFACE MODELING

In this study the data obtained from the Pahang-Selangor Raw Water Transfer Project is used to characterize the subsurface condition along the tunnel alignment under the Kerau River Crossing. The data is interpreted and categorized into geological and engineering parameter for subsurface characterization together with the electrical resistivity survey carried out at the site. The main parameters that important for the study are rock mass weathering grade, Lugeon value and rock quality designation (RQD) which are obtained from the borehole and rock drilling data at the study area (Fig.2). The excavation method used for the tunnel alignment under the Kerau River Crossing is NATM which is very suitable for tunnel excavated under mix ground condition.

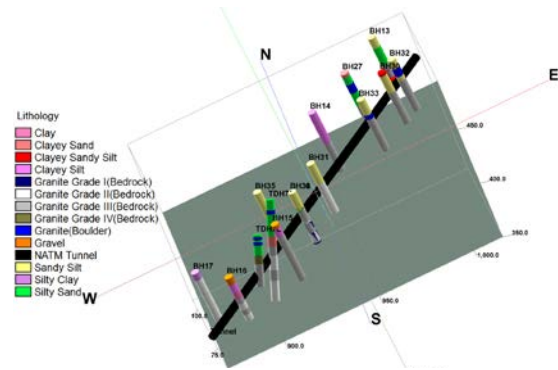


Fig.2: 3-Dimensional borehole location model

Based on the data collected, the filtered tunnel model is develop by using Inverse Distance Weighting Method (IDW) which is one of the deterministic method for multivariate interpolation with a known scattered set of data points. Rockworks 15 software package with the built in deterministic method for multivariate interpolation will be used to generate the spatial model and profile along the tunnel alignment based on the point wise data obtained from the boreholes and in-situ Lugeon tests. The results from the subsurface models were interpreted and analysed to understand the ground behaviour that will be subjected to the tunnel excavation. The evaluation is carried out based on the subsurface and filtered model developed for the rock mass weathering grade, Lugeon value and RQD. The ground was filtered along the tunnel alignment under the Kerau River Crossing based on rock mass weathering grade, Lugeon value and RQD to predict the behaviour of the rock mass that will be excavated during the construction of the NATM tunnel. The prediction of the tunnel behaviour under the Kerau river crossing will benefit the tunnel excavation project as it will provide the information of the tunnel behaviour before and during excavation of the tunnel. Hence,

safety of the tunnel construction during the excavation can be ensured by putting additional supports that are required to stabilize the tunnel.

Simulation of tunnel excavation using Filtered tunnel model

For the real Pahang-Selangor Raw Water Transfer Project, the NATM tunnel diameter was 5.5m where there is a semi-circle on the upper part and a rectangular shape at the bottom part. The dimension of the NATM tunnel was shown in Fig.3(a). Since it is unable to draw out the real shape of NATM tunnel by using Rockworks 15 software, a circular shape of tunnel with 5.6m diameter was drawn to simulate the real NATM tunnel excavation. It is acceptable as the area of a 5.6m diameter circular tunnel was covered the whole area of the real NATM tunnel. The simulated NATM tunnel was shown in Fig.3(b). From the analysis, the excavated ground is filtered to compute the rock mass weathering grade, Lugeon value and Rock Quality Designation (RQD) along the tunnel excavation. The result from the filtered ground is very important to predict the rock weathering grade, permeability and rock quality along the tunnel excavation.

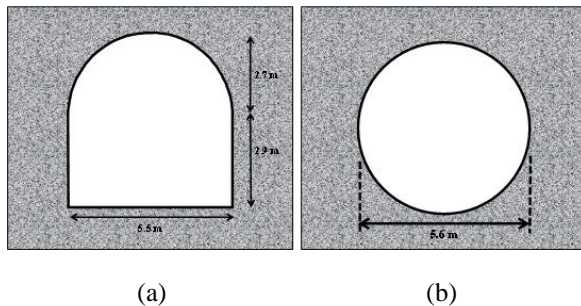


Fig.3: a) Real NATM tunnel shape. b) Simulated NATM tunnel shape

Position of Filtered Ground

The ground will be filtered according to two different lengths based on the real tunnel alignment data for the Pahang-Selangor Raw Water Transfer Tunnel Project. The length of filtered ground was carried out at a specific area under the Kerau river crossing. The detailed analyses was carried out under the Kerau river crossing because there were many uncertainties at that area, hence prediction of unfavourable risks and hazards need to be carried out to provide a reliable information of the geological condition. The information of the filtered ground was listed in Table 1. The location of filtered tunnel is shown in Fig.4 (indicated in yellow) and the example of filtered ground based on rock mass weathering grade is shown Fig. 5.

Table 1: Position of Filtered Ground

Filtered Tunnel	Location	Coordinate		Elevation (m)
		E	N	
Length A	Point A ₁	444870	373350	80
	Point A ₂	444925	373407	80

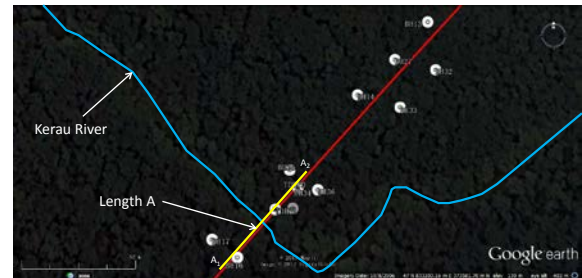


Fig.4: Location of filtered Tunnel.

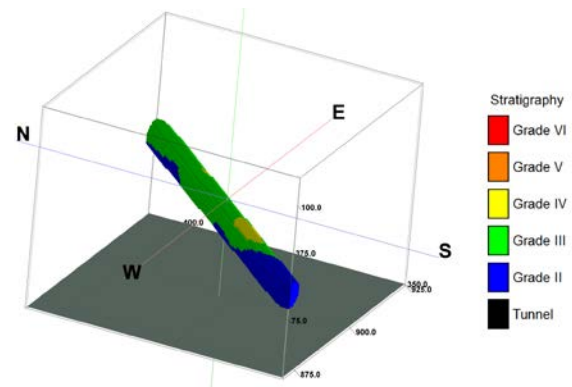


Fig. 5: Example of Filtered tunnel excavation for weathering grade

RESULT AND DISCUSSION

Simulation of tunnel excavation based on Rock Mass Weathering Grade

The result from the analysis was shown in Table 2. Based on the computed result, there are 8.3% of rock Grade IV, 45.0% of rock Grade III and 46.7% of rock Grade II existed along the critical tunnel alignment under the Kerau River. Referred to Fig.5, rock grade IV and rock grade III were existed at the top part along the tunnel alignment. Thus, top heading and bottom heading excavation was proposed in order to reduce the excavation disturbed or damage zone that might be occurred during the control blasting. In addition, to prevent roof collapse due to the tunnel excavation, forepoling with AGF was proposed to be used to strengthen the tunnel roof before the next sequence excavation. Besides that, rock bolt, shotcrete and steel rib should be installed once the tunnel excavation was done.

Table 2: Weathering grade during tunnel excavation

Soil Mass Weathering Grade	Volume (m ³)	Percentage (%)
Grade 4	156.69	8.3
Grade 3	850.06	45.0
Grade 2	881.125	46.7
Total Filtered Volume:	1887.875	100

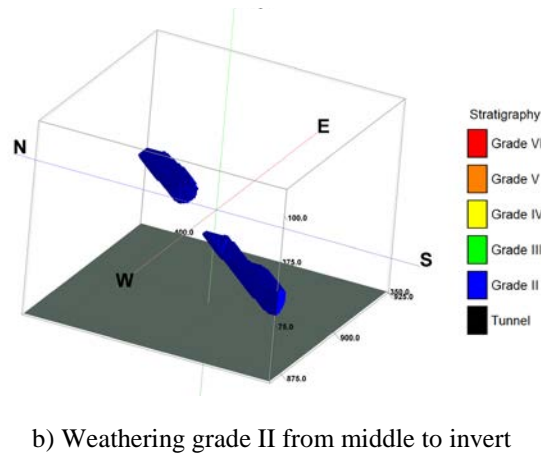
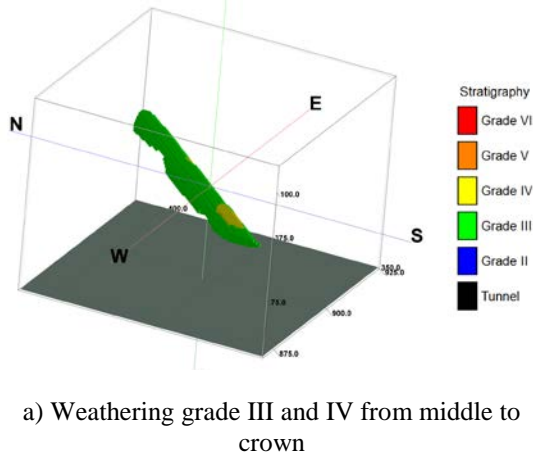


Fig.6: Filtered tunnel (rock mass weathering grade)

Simulation of tunnel excavation based on Lugeon value

Lugeon test is necessary for evaluating seepage potential and for determining whether pre-grouting is necessary or practical. In this project, the main purpose to carry out the Lugeon test is to determine permeability of the rock mass for seepage evaluation and control. The detailed result from the analysis carried out on the Lugeon tests data was shown in Table 3. Based on the computed result, there are 28.36% of rock having Lugeon value from 1 to 5 (1×10^{-5} - 6×10^{-5} cm/sec), 46.81% of rock having Lugeon value from 5 to 15 (6×10^{-5} - 2×10^{-4} cm/sec) and 24.83% of rock having Lugeon value

from 15 to 50 (2×10^{-4} - 6×10^{-4} cm/sec) existed under the Kerau River.

Table 3: Lugeon value during tunnel excavation

Lugeon Value	Volume (m ³)	Percentage (%)
<1	0	0
1-5	544	28.36
5-15	897.875	46.81
15-50	476.25	24.83
Total Volume	1918.125	100

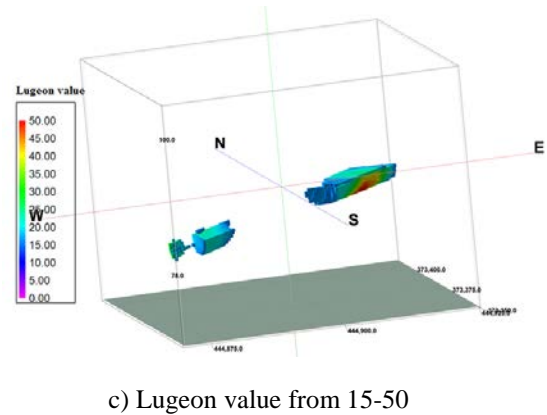
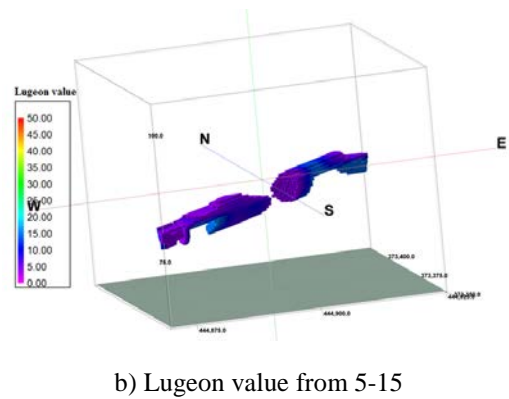
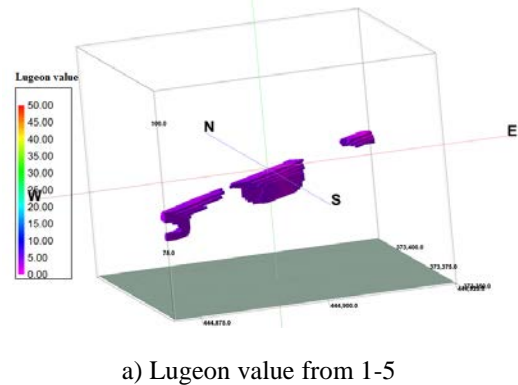


Fig.7: Filtered tunnel (Lugeon value)

Fig.7 show the area based on three classified Lugeon value classes (Lugeon value from 1-5; 5-15

and 15-50). Higher permeability in rock mass will induce ingress of water into tunnel when excavated. Hence, it will affect the working condition during construction of tunnel. From the result, due to high percentage of excavated area that will experience high permeability in rock mass, probe drilling should be done before the tunnel alignment passing through the high permeable zone in order to obtain more reliable data regarded to the rock permeability in front of tunnel face. If the high permeable zone was confirmed by probe drilling data, pre-grouting from inside the tunnel was recommended to be done before excavation in order to reduce the risk of excessive water ingress during tunnel excavation. Additionally, seepage draining should also be done so that the ingress water will not affect the working condition in the tunnel.

Evaluation of Filtered Tunnel Based on Rock Quality Designation (RQD)

The detailed result from the analysis was shown in Table 4. Based on the computed result, there are 0.41% of rock having RQD from 0 to 25, 33.23% of rock having RQD from 25 to 50, 30.87% of rock having RQD from 50 to 75, 32.03% of rock having RQD from 75 to 90 and 3.46% of rock having RQD>90 under the Kerau River. Range of RQD value from 0 to 75 indicated the weak zone that existed in rock mass during tunnel excavation. Based on Table 4 there was high percentage (64.51%) of weak zone of rock mass existed under Kerau river. Additional investigation should be carried out to assess the orientation and characteristic of the weak zone.

Table 4: RQD during tunnel excavation

RQD	Volume (m ³)	Percentage (%)
0-25	7.75	0.41
25-50	635.875	33.23
50-75	590.625	30.87
75-90	612.875	32.03
>90	66.25	3.46
Total Volume	1913.375	100

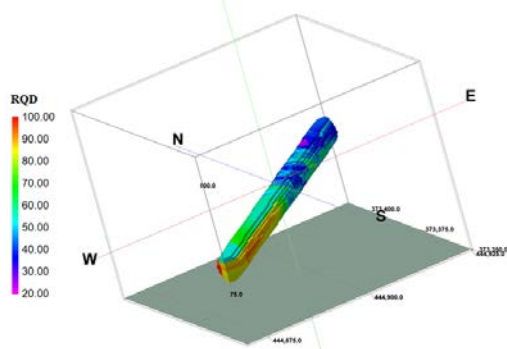


Fig.7: Filtered tunnel (RQD)

Comparison of Electrical Resistivity Test Result and Lugeon Value

Combining electrical resistivity and Lugeon tests results are important for comprehensive prediction of rock permeability which may affect greatly the progress of the tunnel excavation and advancement. The electrical resistivity profile was generated based on the measured data at site and as shown in Fig.9. Meanwhile Fig.8 shows the Lugeon value of the subsurface. Under the Kerau river the resistivity value is in low to moderate resistivity value zone. This is due to the present of fracture aquifer existed in the rock mass under Kerau river which indicated that this zone is in critical zone of high water content in the rock mass. When compared to the Lugeon value profile in Fig.8 and Fig.9, both of the subsurface profiles possessed a potential zone of high permeability under the Kerau river. Both of the results shown that the rock mass under Kerau river were experienced high in water content and permeability. Hence, the generated subsurface profile by using Lugeon value was reliable to be used as engineering judgement before and during the tunnel construction.

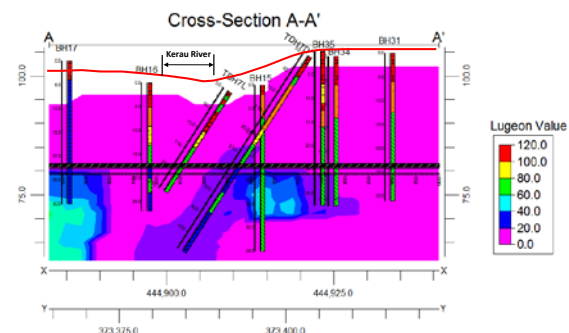


Fig.8: Lugeon value subsurface profile

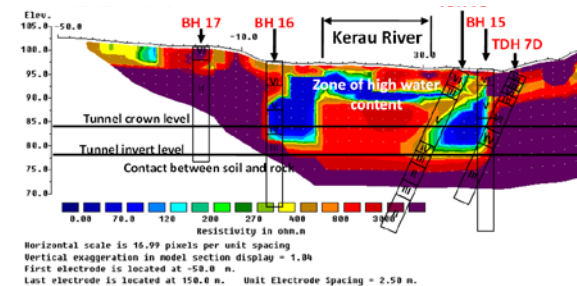


Fig.9: Electrical resistivity test result at Kerau river

DISCUSSION AND CONCLUSION

Deterministic analysis was carried out by using Rockworks software. By using Inverse Distance method, the filtered model was generated to estimate the volume of excavated tunnel under different rock grade.

Evaluation of filtered model according to rock mass weathering grade allowed the prediction of rock quality at region under Kerau River. Rock mass weathering grade was the main important factor that determine the method of tunnel excavation and also types of tunnel support used. From the simulation, Rock Granite II and Rock Grade III were predicted to exist at the route of NATM Tunnel alignment. Based on the evaluation of subsurface profile, forepoling was proposed to be installed as roof support. Besides, types of tunnel support such as steel rib, rockbolt and shotcrete were also proposed.

Evaluation of filtered model according to the Lugeon value allowed the prediction of permeability of the rock mass under Kerau River. High permeability of rock mass indicated the occurrence of discontinuities in rock mass. Thus, the analysis allow the site engineer to foresee the region that required more concerns, and able to prepare the countermeasures before the problem occurred. Based on the analyses, probe drilling was recommended to be done in order to obtain more reliable immediately before the tunnel excavation and advancement. Besides, type of grouting such as pre-grouting was also recommended to be carried out to reduce the seal the fractures and reduce the amount of water ingress.

For evaluation of RQD filtered model, the quality of the rock mass are able to be predicted based on the subsurface model developed. Condition of rock mass will affect the types of tunnel support and tunnel roof. For the region of rock mass that had low value of RQD, more support such as rock bolt with shotcrete and steel rib was needed during the excavation of tunnel. Thus, the analysis displayed a clear image for the engineer to determine the suitable type of tunnel supports needed during the construction of NATM Tunnel.

Finally, comparison between Electrical Resistivity subsurface profile and Lugeon value subsurface profile were carried out to determine the relationship between these two profiles. From the generated profiles, it had shown that the electrical resistivity subsurface and Lugeon value subsurface profile were correlated to each other which is through the similar zone of high water content.

In conclusion, filtered model based on rock mass weathering grade, Lugeon value and RQD can be used to determine the main geological and engineering properties that control the behaviour of shallow tunnel under unfavourable ground condition. At the same time the analyses allows the potential risks along the critical tunnel alignment being evaluated and suggested solutions to be

proposed to provide complete stabilization during the tunnel excavation and advancement

ACKNOWLEDGEMENT

The authors gratefully acknowledge the assistance and cooperation given by KeTHHA (Ministry of Energy, Green Technology and Water Malaysia) and Tokyo Electric Power Services Co., Ltd. (TEPSCO) to carry out this study successfully. Finally, the authors greatly appreciate the financial assistance from USM Short Term Grant that made this research possible.

REFERENCES

1. Spencer, M. Tunnel Boring Machines. in IMIA Conference Istanbul. 2009. Istanbul.
2. Ruwanpura, Y.A., M, Allouche, M, Analytical method to reduce uncertainty in tunnel construction project. Canadian Journal of Civil Engineering 31 (2), 2003: p. 345-360.
3. Messinella, M., Models for the Analysis of Tunnelling, 2010, Concordia University: Texas.
4. Rossi, L., Tunnel construction-fact about the Adelaide-Crafers Highway project, 1999, Federal Government of Australia.
5. COWI, g., Tunnel Engineering, 2004: Denmark.
6. Almén, K.-E. and L. Stenberg, Characterisation methods 2005: Sweden.
7. Australia, S.o.W., OPEN PIT MINING THROUGH UNDERGROUND WORKINGS, 2000: Western Australia.
8. Almeraris, G. and B. Mariucchi, in Rapid excavation and tunneling conference proceedings. 2009, Society of Mining, Metallurgy, and Exploration, Inc.: USA. p. 736-737.
9. Oskar, S., NATM Applications in Singapore, Ground Condition, 2010, Geoconsult Asia Singapore Pte. Ltd: Singapore.
10. CHENG, K.H., Construction of Pipe Roof and Support System, 2010: India.
11. Kontothanassis, P., et al., Design and construction of NATM underground station tunnel by using the forepoling method in difficult conditions for Athens Metro, 2005, Taylor & Francis Group: London.
12. Leca, E., Y. Leblais, and K. Kuhnenn, Underground works in soils and soft rock tunneling, 2005.
13. Mito, Y., M.A.M. Ismail, and T. Yamamoto, Multidimensional scaling and inverse distance weighting transform for image processing of hydrogeological structure in rock mass. Journal of Hydrology, 2011. **411**(1-2): p. 25-36.

FUNDAMENTAL STUDY ON LATERAL RESISTANCE CHARACTERISTICS OF BALLASTED TRACKS SUBJECTED TO PSEUDO-STATIC INERTIA FORCE

Ryuta Ogawa¹ and Kimitoshi Hayano²

¹Graduate School of Urban Innovation, Yokohama National University, Japan

² Institute of Urban Innovation, Yokohama National University, Japan

ABSTRACT

Ballasted tracks compose about 90 percent of railroad tracks in Japan. However, there is a concern that lateral resistance of ballasted tracks may be reduced when they are subjected to earthquakes owing to loosening or collapse of ballasts. For safety, it is important to evaluate effects of earthquake motions on the lateral resistance. In view of above, discrete element simulations were conducted on model grounds which were 1/5 of actual size to investigate effects of horizontal seismic inertia force on the lateral resistance. After each model ground was subjected to quasi-static inertia forces, horizontal loadings were applied on a single sleeper by displacing it. The resistance forces were measured during the loadings. The analyses results suggested that lateral resistance of sleepers would decrease with the increase of horizontal seismic coefficient. It was also found that the significant reduction of lateral resistance appeared when the railway roadbed shoulders collapsed by the combined effects of the seismic inertia force and horizontal displacement of sleepers.

Keywords: Ballast, Sleeper, Lateral resistance, Earthquake, Quasi-static inertia force, Discrete element simulations

1. INTRODUCTION

Ballasted tracks compose about 90 percent of railroad tracks in Japan. However, there is a concern that lateral resistance of ballasted tracks may be reduced when they are subjected to earthquakes owing to loosening or collapse of railway roadbed as illustrated in Fig. 1. Then, it is afraid that decrease of lateral resistance induces railway buckling as shown in Fig. 2. Therefore it is important to evaluate effects of earthquake motions on the lateral resistance for safety design [1].

In view of above, discrete element simulations (DEM) were conducted on numerical railway roadbed models which were 1/5 of actual size to investigate effects of horizontal seismic inertia force on the lateral resistance. The numerical roadbed models were subjected to quasi-static inertia forces and a constant horizontal displacement was applied on sleepers. The resistance forces of the sleepers were measured during the displacements.

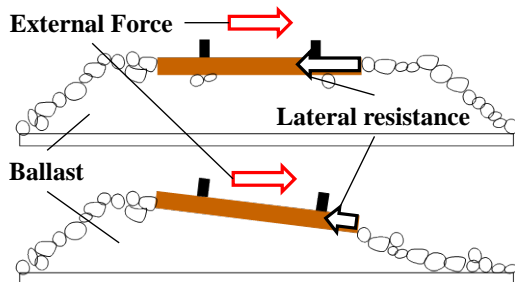


Fig. 1 Decrease in lateral resistance of ballast due to the collapse of roadbed during and after earthquake

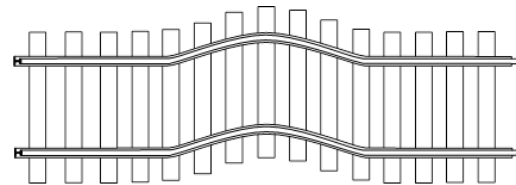


Fig. 2 Schematic image of rail buckling

2. DISCRETE NUMERICAL MODELLING

2.1 Modeling of ballasts and a sleeper

Ballast particles were modeled as spherical particles in this time. Actually, the ballast shape is not spherical. However, to reduce the computational cost the spherical shape is adapted in this study. The effect of the particle shape, for example, lower resistance of particle rotation, should be study on the lateral resistance in future research. The spherical particle sizes were 1/5 of actual ballasts and the particles size distribution was 1/5 of actual one which satisfied the Japanese standard particle size range as shown in Fig. 3.

A single sleeper was modeled as a rectangular parallelepiped solid (0.063m in width, 0.48m in length and 0.051m in height). The sleeper was embedded in ballasts as shown in Fig.4. The railway roadbed slope was set one in 1.8.

The interaction between the spherical particles is defined by the following equation of motion.

$$ma = \sum (F_n + F_s) + F_b \quad (1)$$

Here, m is the mass of particle, a is the acceleration of particles, F_n is contact normal force, F_s is contact tangential force and F_b is body force including gravitational force acting on the particle. It should be noted that, with regard to the interaction between the sleeper and particles, Eq. (1) is also satisfied.

In this study, three dimensional discrete numerical modeling was adopted with using open source software called YADE [2]. Table 1 lists parameters used in the simulations. The details are as follows.

1) Number of particles n

Number of particles n was determined so that it satisfied the ballast bed density $1,600 \text{ kg/m}^3$. In total 73,210 particles was used in this analysis.

2) Radius of particle r

Radius of particle r was set to follow the particle size distribution (see Fig. 3).

3) Density of particle ρ_s

Density of particle ρ_s , $2,700 \text{ kg/m}^3$ was used to represent the actual density of ballasts.

4) Spring constant k_n

Spring constant in the normal direction, k_n between particles is defined by the Eq. (2) using the particles' Young's modulus E . In the present analyses, although it was significantly lower than that of actual ballasts, Young's modulus 50MPa was adopted to reduce the computational time. Young's modulus will affect the analysis results. Lateral resistance of ballast becomes lower than the actual value. But in this study, the emphasis is placed on understanding the qualitative behavior of the lateral resistance of ballast.

$$k_n = \frac{2E_1r_1E_2r_2}{E_1r_1 + E_2r_2} \quad (2)$$

Here, E_1 and E_2 are Young's modulus of particle 1 and particle 2 which are in contact to each other. In the same way, r_1 and r_2 are the radius of the particle 1 and particle 2.

5) Spring constant ratio k_s / k_n

Ratio of spring constant in the tangential direction to that in the normal direction k_s / k_n , 0.3 was used [3].

6) Inter-particle friction angle ϕ_{inter}

Inter-particle friction angle, ϕ_{inter} , 60 degrees was used.

7) Coefficient of local damping α

The local damping is damping forces acting on the particles with proportion to the resultant forces. In this analysis, the local damping coefficient 0.4 was used.

8) Time step Δt

Time step $8.72\text{e-}6$ seconds was used in this study.

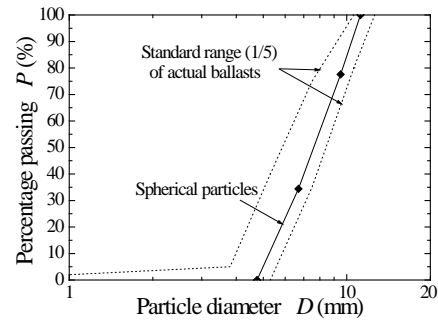


Fig. 3 Particle size distribution of spherical particles

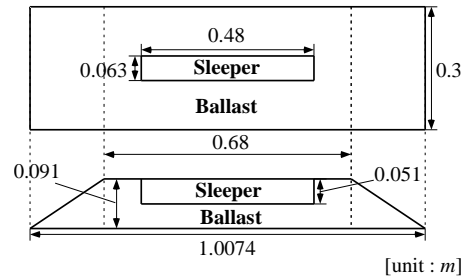


Fig. 4 Railway roadbed model prepared in DEM

Table 1 Input parameters for DEM simulations

Number of particle n	73,210
Density of particle $\rho_s (\text{kg/m}^3)$	2,700
Spring constant ratio k_s / k_n	0.3
Inter-particle friction angle ϕ_{inter} (degrees)	60
Coefficient of local damping α	0.4
Time step $\Delta t (\text{s})$	$8.72\text{E-}06$

2.2 Construction of numerical roadbed models

Fig. 5 shows construction steps of a numerical roadbed model. First, sphere particles which represent ballasts were generated in a box (box size: $0.3\text{m} \times 0.13\text{m} \times 0.211\text{m}$) (Step1). Then, the particles were set in free fall at 1G. The particles were deposited in a container which had slopes equivalent to those of roadbeds. Then a rigid plate was generated above the sphere particles together with the parallelepiped box which represented a single sleeper (Step2). The plate and the sleeper box were simultaneously settled down at 0.1 m/s and it statically compressed the deposits of sphere particles until the thickness of deposits became that of roadbed shown in Fig. 4(Step 3). The density of the ballast beds $1,600 \text{ kg/m}^3$ were achieved. Finally, the plate and the container were removed from the scene and only ballasts and the sleeper remained (Step4).

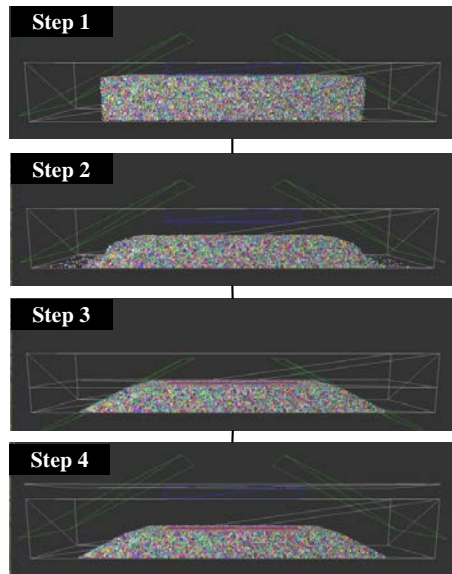


Fig. 5 Construction steps of a numerical roadbed model

2.3 Inertia Force and Horizontal Loading

To apply seismic inertia force to the roadbed in the DEM simulation, pseudo static method simulating tilt tests as shown in Fig. 6 was introduced. The situation was made so that the numerical model grounds were tilted with the angle α in the scene. That is, the predetermined horizontal acceleration G_h was given to the railroad while at the same time the vertical acceleration G_v was reduced from $1G$ to the $1G * \cos\theta$. Particles were moved by the application of the inertia force, however they gradually settled with time. After the movement became stable, the sleeper was displaced horizontally at a constant displacement rate 0.7mm/s until the horizontal displacement reached 10mm .

The roadbed constructions and the horizontal loadings were conducted four times with changing the tilting angles α from 0 to 15 degrees. The relationships between the tilting angle α and horizontal seismic coefficient k_h are shown in Table. 2.

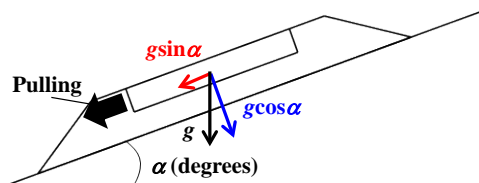


Fig. 6 Pseudo static method

Table. 2 Tilting angles and the horizontal seismic coefficients adopted in DEM simulations

case	α (degree)	K_h
1	0	0.00000
2	5	0.08749
3	10	0.17633
4	15	0.26795

3. DEM SIMULATION RESULTS

3.1 Effects of Tilting Angles on the Lateral Resistance

Fig. 7 shows the relationship between the horizontal displacement of the sleeper and the horizontal load acting on the sleeper, obtained from each DEM simulation. It is seen in the figure that the horizontal load rapidly increases just after the start of loading and become almost constant after it reaches the maximum. It is also seen in the figure that the lateral resistance of the sleeper with the tilting angle α of 10 or 15 is significantly lower than that with the angle α of 0 or 5 .

Fig. 8 shows the relationship between the lateral resistance R and the tilting angle α obtained from the results shown in Fig. 7. The lateral resistance R measured at the horizontal displacements d_h of 0.4mm and 10mm are shown in the figure. It is seen in the figure that the lateral resistance R measured at 10mm reduces with increase of α more significantly than that measured at 0.4mm .

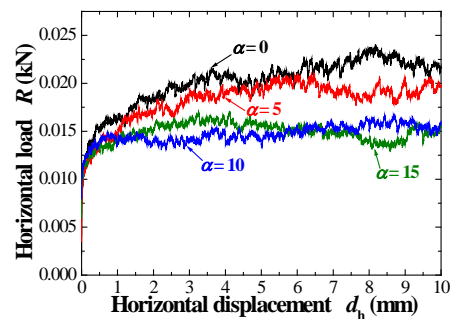


Fig. 7 Relationships between d_h and R

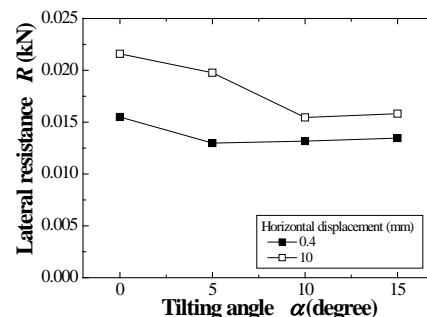


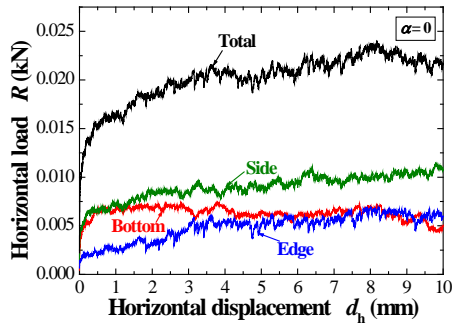
Fig. 8 Relationships between R and α

3.2 Contributions of Bottom Resistance, Side Resistance and End Resistance

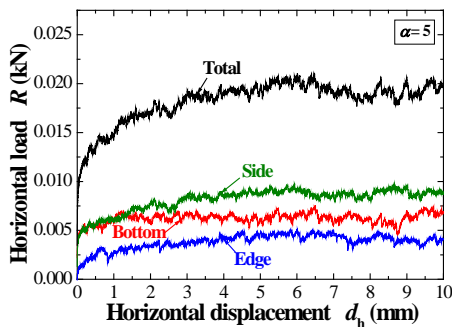
Lateral resistance of sleeper is usually induced by the friction resistance at the sleeper bottom and that at the bilateral sleeper sides as well as earth pressure acting on the sleeper ends. It is worthwhile to see the contributions of bottom resistance, side resistance and end resistance to the total resistance to clarify the development mechanism of lateral resistance.

Fig. 9 shows the bottom resistance, side resistance and end resistance of the sleeper for each tilting angle. In the figure, the total lateral resistance is also shown based on the results shown in Fig. 7. It is found in the figures that irrespective of tilting angles, the bottom and the side resistance rapidly increase just after the start of loading, while the end resistance gradually increases. This is because the end resistance is mainly induced by the passive earth pressure of ballasts, which require significant amounts of displacement to be fully mobilized. It is also seen in the figures that the maximum end resistance become lower with the increase of tilting angle.

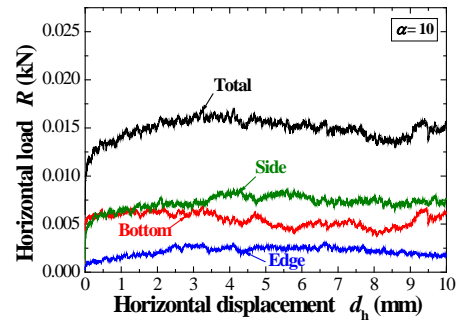
Fig. 10 shows the ratios of bottom resistance, side resistance and end resistance to the total resistance when the horizontal displacement of the sleeper was 10mm. It is found that the contribution of the end resistance becomes significantly lower when the tilting angle α becomes 10 degrees. In order to investigate the reasons, discussions will be made based on particles' movement in the next section.



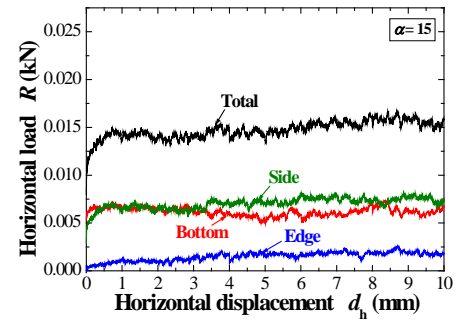
(a) $\alpha = 0$



(b) $\alpha = 5$



(c) $\alpha = 10$



(d) $\alpha = 15$

Fig. 9 Bottom, Side, Edge resistance of sleeper

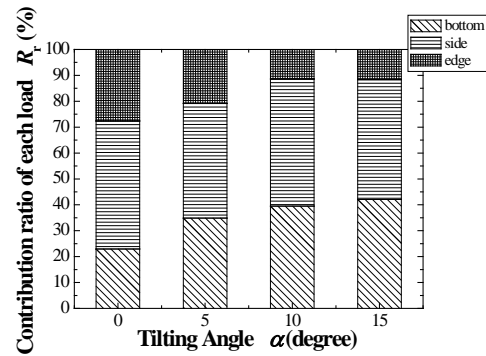


Fig. 10 Contribution ratio of each load at the time of 10mm displacement

3.3 Particles' movement

Fig. 11 shows the particles' trajectory induced by tilting, that is, application of inertia force. Significant particles' movement was observed when the tilting angle α becomes 10 or 15 degrees. In these cases, several particles in the slope could not keep their original positions and dropped down the slope. Deposits of fallen particles can be found near the toe of slope.

Fig. 12 represents the particles' trajectory induced by horizontal loading of sleepers. Again significant movement can be observed in the particles along the slope, irrespective of tilting angles. The slope angles become gentler by the application of horizontal loadings. It is also found in the figures that the slope shoulders cannot keep the

original shapes when α becomes 10 or 15 degrees. The shoulder width was just 10 cm, therefore the significant reduction of end resistance can be caused by the collapse of shoulder.

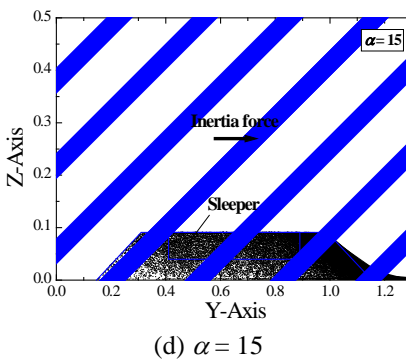
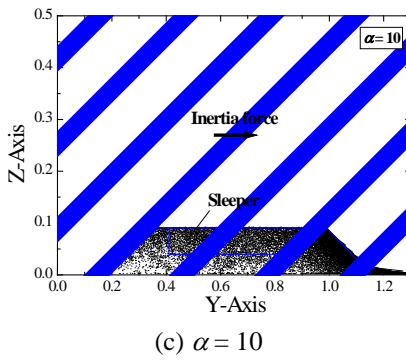
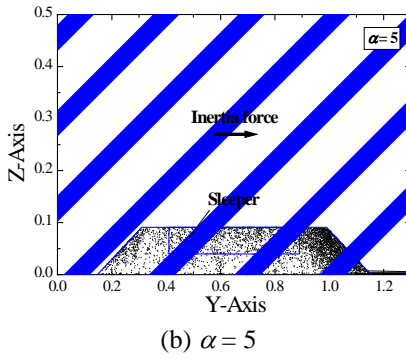
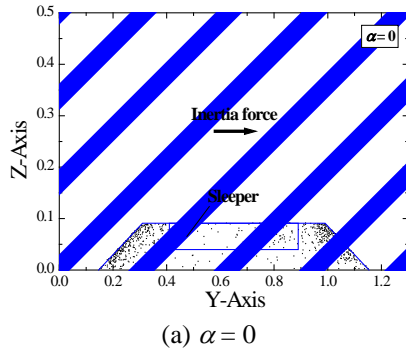


Fig. 11 Particle's movements induced by tilting

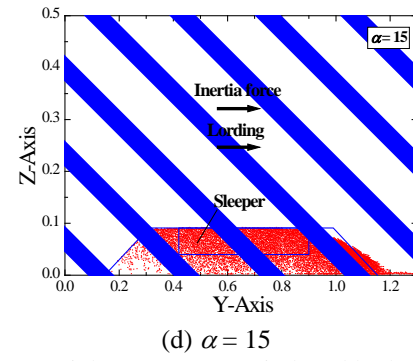
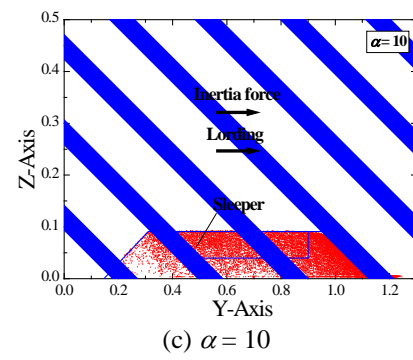
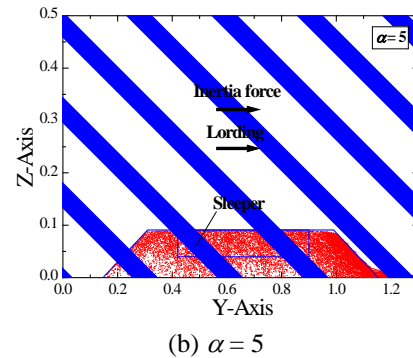
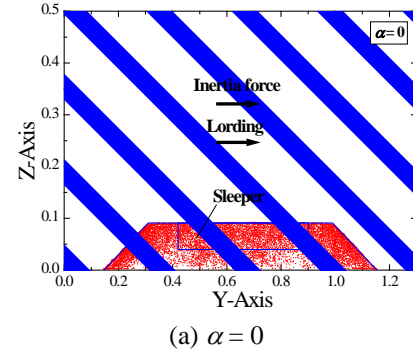


Fig. 12 Particle's movements induced by horizontal loadings

4. CONCLUSIONS

Following conclusions can be derived from this study.

- 1) Lateral resistance of sleepers would decrease with the increase of horizontal seismic coefficient.
- 2) Reduction of lateral resistance appeared predominantly when the railway roadbed shoulders collapsed by combined effects of the seismic inertia force and horizontal displacement of sleepers.
- 3) Significant reduction of end resistance can be caused by the collapse of shoulder.

REFERENCES

- [1] Sekine Etsuo, Nakamura Takahisa and Hirao Hiroki : The Model Test on the Lateral Resistance of Ballast in the Ballast Track, Japan society of Civil Engineers 2010 Annual Meeting, 2010, pp.473-474 (in Japanese)
- [2] Vaclav Smilauer : Cohesive Particle Model using the Discrete Element Method on the Yade Platform, PhD thesis, 2010
- [3] Shimizu Hiroyuki, Murata Sumihiko and Ishida Tsuyoshi : Influence of particle size distribution and number of particles on the configuration of the rock mechanical properties in granular discrete element method, Material, 59(3), 2010, pp.219-226 (in Japanese)

USE OF ACOUSTIC EMISSION TECHNOLOGY TO STUDY THE MECHANICAL BEHAVIOUR OF VARIOUS SANDSTONES: GEOTHERMAL ENERGY

Shao, S.S.¹, Ranjith, P.G.² and Chen, B.K.³

¹ Department of Civil Engineering, Monash University, Melbourne, Victoria, Australia;

² Deep Earth Energy Lab, Bld 60, Monash University, Melbourne, Victoria, Australia;

³ Department of Mechanical & Aerospace Engineering, Monash University, Melbourne, Victoria, Australia

ABSTRACT

The mechanical behavior three types of sandstones: Acrogem (Ac), Wondabyne (Wo) and Barrabool (Ba) sandstones subjected to thermal and compressive loadings was investigated. Prior to testing, samples were either maintained at ambient temperature or thermally-stressed to a pre-determined temperatures of 200, 400 600 or 800 °C. Thermal-stressing was achieved by heating the sample to the target temperature at a constant rate of 5 °C/min, holding the temperature constant for one hour, and then cooled at two different condition: (a) air/slow-cooled and (b) water/rapid-cooled. The results indicate that the axial strains of all sandstones were increasing temperature increasing. Temperature of 400 is considered critical. In general, the strength changes of rapidly-cooled strength testing accordant to the changes performed in slow-cooled strength testing. However, AEs results indicate the rapidly-cooled specimens produced more energy releases in the beginning of loading (less than 5 kN) up to 0.27%, 13.49% and 26.49% of the peak strengths of Ac, Wo and Ba at 400 °C, respectively. AE results show very direct view of the crack propagation development of the heated and cooled treated sandstones under axial loading.

Keywords: Acoustic emission, rock mechanics, high temperature, quenching

1. INTRODUCTION

Geothermal resource is now recognized as renewable on the time-scales of both technological and societal systems, with cost, reliability and environmental advantage over conventional energy resource. In the meantime, there is a new challenge for rock mechanics to deal with rock engineering problems at high temperatures. Acoustic emissions (AEs) monitoring has been recently used in various engineering applications for damage characterization, such as micro-crack nucleation and crack propagation during rock deformation, evaluation of the failure process, their mechanisms and fracture locations.

1.1 AE technology

AE is a non-destructive technique, which detects elastic waves generated due to crack initiation, crack formation and crack coalesce. Based on the recorded waves many parameters are calculated and analysed in order to characterize the distinct failure mechanisms. Under certain loads, brittle material releases sudden strain energy when the crack develops which creates an elastic stress wave which travels from the place of origin to the surface. AE is

used to detect and measure the transient wave that is generated from these discrete acoustic waves produced by each micro-crack, which can produce appropriate event data to interpret the crack propagation of the material. Although AE can provide a qualitative gauge of strain energy release, it is unable to provide quantitative results.

1.2 Identification of stress crack thresholds

According to Hoek and Bienawski[1], crack propagation process involves several stages. Based on the stress strain curve of axial and lateral deformation measurements in uniaxial compression test, fracture phases of brittle materials mainly consist of crack closure, crack initiation followed by stable crack propagation, crack damage followed by unstable crack propagation and ultimate failure. These phases can be identified using various methods such as axial stiffness and stress-strain curve, and volumetric stiffness-strain curve [2]-[3].

1.3 The effect of thermal shock influence rock strength

Thermal stresses are generated when material experiences temperature gradients e.g. during

quenching, and the transient thermal stresses generated are normally tensile at the surface and compressive in the centre of the body [4]. For instance, the shrinkage of a cooled surface of rock is constrained by the expanded hotter inner regions. In general, tensile stress is generated in the cooled surface and the constraint of the surface thermal strain is caused by the interior of the specimens. The tensile stress and the constraint of the surface strain are counterbalanced by compressive stresses in the inner part of the specimen [5]. The level of tensile stress is highest at the surface and decreases with crack depth, and the crack growth occurs in the downward direction after a certain critical quench [6]. Thermal cracks release the constraint of the thermal strains and the thermal stresses. Thermal cracks often stop before they separate the specimen into two or more parts. This paper is aimed to study the effect of high temperatures and cooling or quenching treatments on various sandstones through AEs analysis.

2. MATERIAL PROPERTIES

The tested sandstones were collected from two sources. Acrogem sandstone (Ac) is from Perth basin, Wondabyne sandstone (Wo) is from Sydney basin, Barrabool sandstone (Ba) is from Barrabool basin. Ac sandstone is buff veined and white in colour, with medium- to fine-grained composing predominantly of quartz 58%, feldspar 24% and clay 11%. The quartz exhibits a recrystallised character resulting in fusion between the majority of adjacent grains. Wo sandstone is in grey-buff colour, with medium-grained comprising about quartz 60%, matrix 30%, clay and cement (composed of calcite, quartz and siderite) 10%. It is grey when quarried and oxidises to pale buff after extended exposure to the atmosphere. Ba sandstone is highly weathered and collected from open surface. It is green-brown in colour, with medium - to fine-grained comprising quartz, feldspar, calcite, chlorite and a variety of accessory minerals. Their mechanical properties at room temperature without pre-heated though unconfined compression test are listed in Table 1. Ac sandstone has the highest peak strength and elastic modulus, as well as axial failure strain compared to Wo and Ba sandstones.

Table 1 Mechanical property of sandstones

Specimen	Peak strength (MPa)	Axial strain (%)	Elastic modulus (GPa)
Ac	66.85	1.439	7.52
Wo	39.21	0.970	6.53
Ba	52.40	0.659	3.94

2.2 Experimental procedure

Specimens of size 22.5 mm diameters and 45 mm length (shape factor of 2) were prepared. Thermal-stressing was achieved by heating the sample to the target temperature at a constant rate of 5 °C/min, holding the temperature constant for one hour, and then cooled at two different rates: (a) air/slow-cooled and (b) water/rapidly-cooled. In compressive strength tests, core samples were loaded at a constant displacement rate of 0.1 mm/min. All unconfined compressive tests were performed at room temperature (23 °C). During experimentation, AE hits were recorded if signals exceeded the set threshold of 60 dB. The amplitude and absolute energy of each AE signal were provided by the AEwin software.

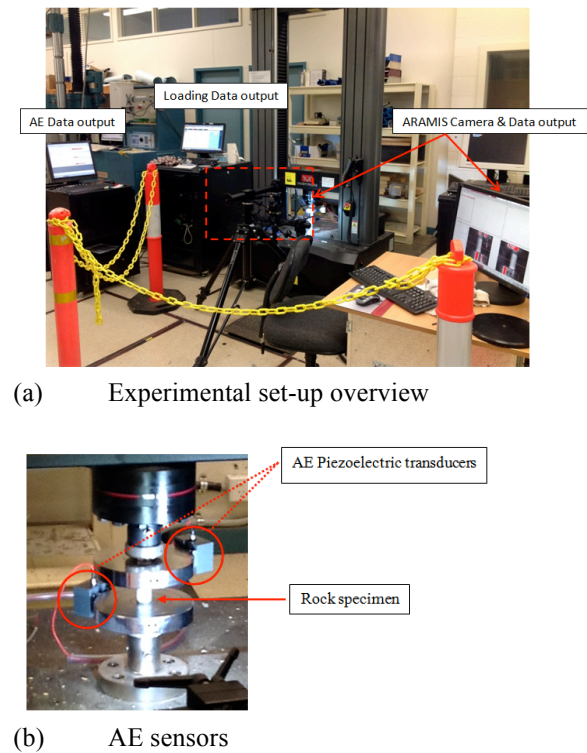


Fig. 1 This is the experimental setup

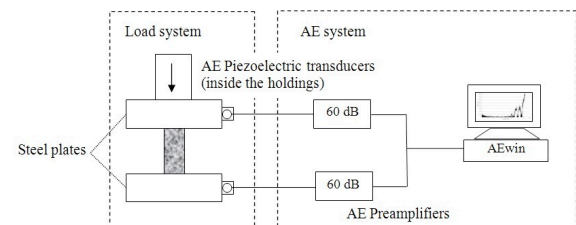


Fig. 2 This is AE schematic diagram

























3. EXPERIMENTAL RESULTS AND DISCUSSION

The effects of cooling treatments on the mechanical behaviour of various sandstones were studied by conducting compressive tests on specimens which had been either slow-cooled (air cooled) or rapidly-cooled (water cooled) at consistent compressive loading rates. AE events were analysed to determine crack formation due to combination thermo-mechanical loadings.

slow- and rapidly-cooled from different temperatures. Figure 3 presents the comparison of peak strength, elastic modulus and failure strain of the three types of sandstone.

The images in Table 2 have shown that all three types of sandstone turned into reddish colour and rapidly-cooled specimens have generally turned darker. This is due to rock oxidation under high

Table 3 Images of specimens after slow- and rapidly-cooled treatment

	Slow	Rapid		Slow	Rapid		Slow	Rapid
	Ac sandstone			Wo sandstone			Ba sandstone	
200 °C								
400 °C								
600 °C								
800 °C								

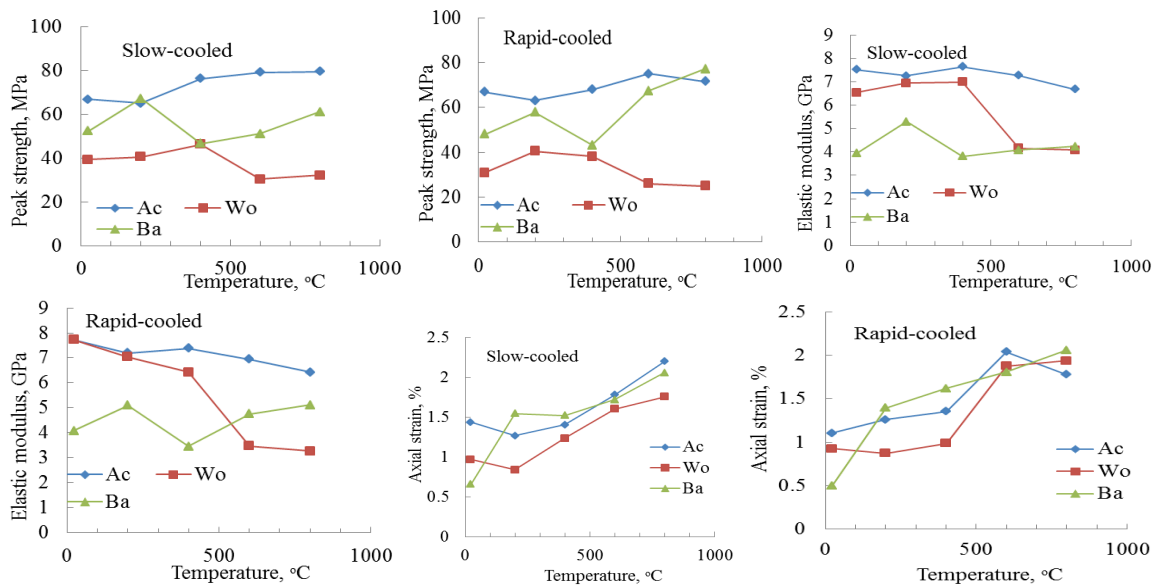


Fig. 3 This is the mechanical characteristic changes after various heated and cooled treatment

3.1 Effects of pre-heat and cooling on mechanical characteristic of sandstones

Table 3 displays the images of specimens after

temperature and direct exposed in atmosphere. Ba sandstone is relatively highly weather amount the specimens, therefore it presents the darkest colour after heat treated. The dark sparkles on some of the specimens are the burned mark when it contracted

with pincher.

All three types of granite retain well integrity up to 800 °C heat treatment followed by both slow- and rapidly-cooled. In general, Ac sandstone showed the highest rock strength followed by Ba and then Wo, as shown in Fig. 3. Quenching from temperatures below 400 °C, the peak strength of Ba sandstone sudden drop from 200 °C while Ac and Wo sandstones remain relatively constant. Quenching from temperatures above 400 °C causes the peak strengths of Ac and Ba sandstones increase while

increase when quenched from temperatures above 400 °C.

In general, the most distinct effect is that quenching from higher temperatures results in higher axial failure strain regardless of the speed of quench. However this result cannot present the distinct of slow- and rapidly-cooled effect. Therefore AE result has been used to interpret the thermal cracks development within the specimen at various cooling histories.

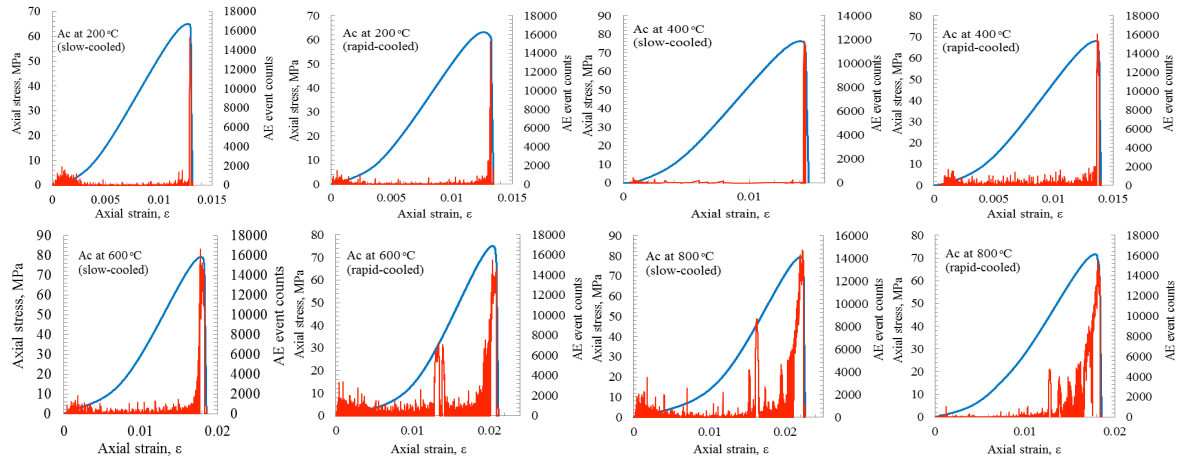


Fig. 4 This is the axial strength and AE event counts of Ac sandstone

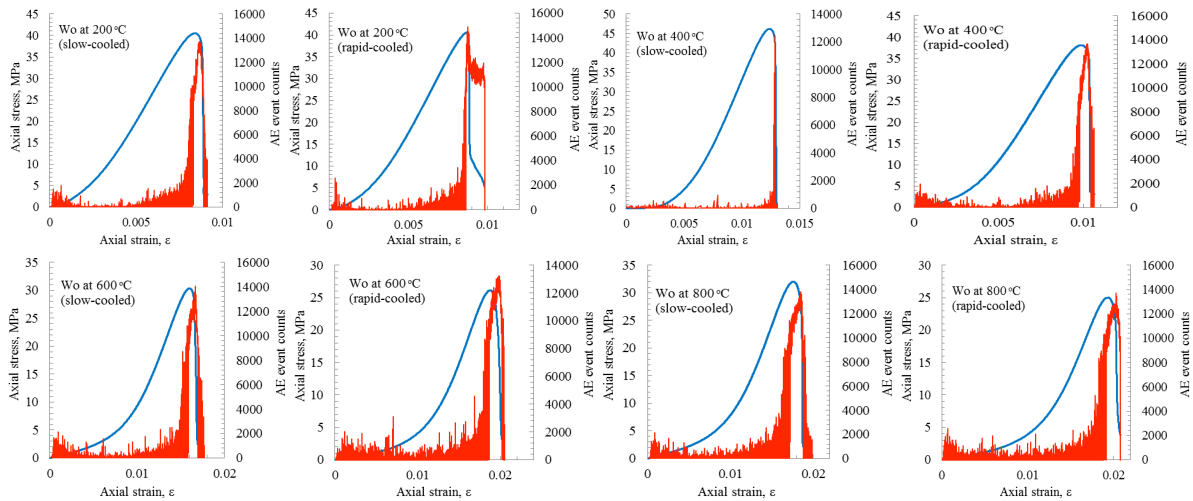


Fig. 5 This is the axial strength and AE event counts of Wo sandstone

Wo sandstone decrease. Both slow- and rapidly-cooled results showed similar trends. The elastic modulus of Ac sandstone behaved quite differently when quenched from temperature above 400 °C with Ac decreasing slightly, Wo decreasing dramatically and Ba increasing moderately. A similar pattern was found with the peak strength when quenched from temperature above 400 °C. However, these changes are in accord with the steep axial failure strain

3.2 Effects of cooling on fracture initiation

Figures 4, 5 and 6 present the different AE event counts after specimens were quenched from various temperature changes. Crack propagation can be identified from the relationship between AE event count and axial stress. Three stages of crack propagation are proposed from previous works: crack closure, crack initiation and crack damage.

Crack closure initially occurs in the pre-existing crack when sandstone specimens were subjected to the axial stress. Stress-strain response during crack closure is non-linear. However, the extent of this non-linear region is small and most of the cracks are closed when a small load is applied, and this non-linear region is determined by the initial crack density and the geometrical characteristics of the crack population. Results in Figs 4, 5 and 6, that rapidly-cooled specimens released more energy and generated numbers of AE event counts were record simultaneity with larger axial strain development for all specimens for all quenching temperatures except Ac sandstone at 800 °C. AE results indicate the rapidly-cooled specimens produced more energy

individual minerals decreases, which leads to an increase in their mutual attraction and the strength of the bonds increases. Therefore, Ac sandstone produce less AE event counts after water quenched from 800 °C may due to the volume expansion and crack closure.

Following crack closure, linear elastic deformation occurs when the majority of pre-existing cracks have closed, which is the stable crack region. The elastic modulus can be determined in the stable crack region. This region is between crack closure and crack damage. By increasing the temperature from which the specimen is quenched, crack initiation region is shortened by the earlier crack damage occurred. These stable crack regions

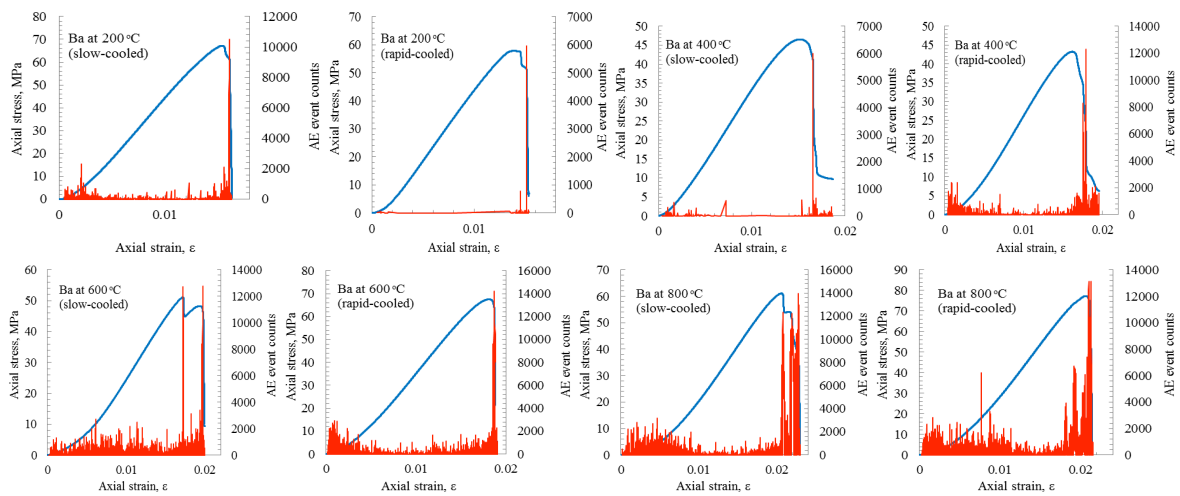


Fig. 6 This is the axial strength and AE event counts of Ba sandstone

releases in the beginning of loading (less than 5 kN) up to 0.27%, 13.49% and 26.49% of the peak strengths of Ac, Wo and Ba at 400 °C, respectively.

Besides the natural micro-cracks, pre-exist cracks also include cracks caused by tensile stress and thermal cracks which are generated during the rock heating process. When temperature increases, the crystal particles of rock fractures forming new microscopic cracks (pre-existing grain boundaries) between mineral grains, as a result of differential thermal expansion between grains with different thermo-elastic modulus and thermal conductivities [7]-[9]. Especially it occurs in crystalline rock, since the amount of quartz has a significant effect on thermally-induced micro-cracks because of the complexity of its thermal expansivity.

These thermal cracks were which developed due to thermal shock during the cooling process, as the rock specimens had cooled surface which is constrained by the expanded hotter centre region. For Ac sandstone at 800 °C, from the study of Dmitriyev et al. [7] it is known that due to volume expansion, the distance between the interfaces of the

of rapidly-cooled specimens are generally shorter than slow-cooled specimens.

As the crack grows, the fracture process involves unstable crack propagation and as so termed crack damage. In contrast to crack closure and crack initiation, rapidly-cooled specimens have greater region of unstable crack propagation untill failure occurs.

Overall, AE results showed very direct view of the crack propagation development of the heated and cooled treated sandstones under axial loading. Rapid-cooled specimens produced more AE event signals in each crack propagation stages at all appointed temperatures. Specimens have been heated above 400 °C generates dramatically greater amount of energy release. This result is consistent with the changes in strength and axial strain.

4. CONCLUSION

The results show increasing axial strains in all sandstones with increasing temperature from which the specimen is quenched. However, the changes for

peak strength and elastic modulus are inconsistent with the axial strains and it is difficult to draw firm conclusions. It was noticed in slow-cooled residual strength testing, Ac, Wo and Mw sandstones were rapidly strengthened from quench temperature of 200 to 400 °C however the axial strength of Ac sandstone gently increased up to 800 °C, while Wo sandstones decreased. Contrast to these three sandstones, Ba sandstone was sharply weakened from 200 to 400 °C and followed gentle increasing up to 800 °C. In general, changes in strength of rapidly-cooled specimens were consistent with those of from slow-cooled specimens. Quenching from temperature of 400 °C appears to be a critical transition temperature.

AE results show very direct view of the crack propagation development of the heated and cooled treated sandstones under axial loading. Rapid-cooled specimens produce more AE event signals in all three crack propagation stages (crack closure, crack initiation and crack damage) at all appointed temperatures. Specimens have been heated above critical temperature of 400 °C showed dramatically greater amount of energy release. Therefore, both from strength changes and AE results showed the temperature of 400 °C is the critical transition temperature for all three types of sandstones.

REFERENCES

- [1] Hoek, E. and Z.T. Bieniawski, Brittle fracture propagation in rock under compression. *International Journal of Fracture*, 1965. 1(3): p. 137-155.
- [2] Bieniawski, Z.T., Mechanism of brittle fracture of rock. Part II-experimental studies. *International Journal of Rock Mechanics and Mining Sciences and*, 1967. 4(4): p. 407-408,IN13-IN14,409-418,IN15-IN18,419-423.
- [3] Eberhardt, E., Stead, D., Stimpson, B., Read, R. S., Identifying crack initiation and propagation thresholds in brittle rock. *Canadian Geotechnical Journal*, 1998. 35(2): p. 222-233.
- [4] Collin, M. and D. Rowcliffe, The morphology of thermal cracks in brittle materials. *Journal of the European Ceramic Society*, 2002. 22(4): p. 435-445.
- [5] M. Fellner, P.S., Thermal shock failure of brittle materials. *Key Engineering Material*, 2002. 223: p. 97-106.
- [6] Collin, M. and D. Rowcliffe, Analysis and prediction of thermal shock in brittle materials. *Acta Materialia*, 2000. 48(8): p. 1655-1665.
- [7] Dmitriyev A. P., K.L.S., Protasov Y. I. & Yamshchikov V. S, Physical properties of rocks at high temperatures. National Aeronautics and Space Administration, NASA Technical Translation, 1972. N 72-26286.
- [8] Kranz, R.L., Microcracks in rocks: A review. *Tectonophysics*, 1983. 100(1-3): p. 449-480.
- [9] Heard, H.C. and L. Page, Elastic Moduli, Thermal Expansion, and Inferred Permeability of Two Granites to 350°C and 55 Megapascals. *J. Geophys. Res.*, 1982. 87(B11): p. 9340-9348.

UNCONFINED COMPRESSIVE STRENGTH OF CEMENT TREATED SOIL/RAP MIXTURE

Jirayut Suebsuk¹, Aniroot Suksan², Suksun Horpibulsuk³ and Apichit Kumpala⁴

^{1,4} Geomechanics and Geomaterials Research Group, Department of Civil Engineering,

Faculty of Engineering and Architecture, Rajamangala University of Technology Isan, Thailand;

^{2,3} School of Civil Engineering, Institute of Engineering, Suranaree University of Technology, Thailand

ABSTRACT

The article attempts to present the influence of reclaimed asphalt pavement (RAP) content on the compaction behavior and unconfined compressive strength of cement treated soil-RAP mixture. The laboratory compaction and unconfined compression tests on cement treated soil/RAP mixture were carried out with various RAP and cement contents. The porosity was adopted as a state parameter for assessing the strength of the mixed materials. The results show that with an increase in RAP content, the OMC tends to decrease, up to the optimum of soil/RAP ratio of 50/50. The asphalt fixation point is designated as a transitional point where less change in strength turns to a larger change. An asphalt content of 3.5% (50/50 soil/RAP ratio) is found to be the asphalt fixation point. The strengths, where the asphalt content is lower than the asphalt fixation point, can be predicted by the proposed generalized form of strength. This proposed equation can assess the laboratory strength of cement treated soil/RAP mixture under various mixed proportions, cement contents, water contents, and curing times.

Keywords: Reclaimed asphalt pavement, Lateritic soil, Unconfined compressive strength, Cement stabilization

INTRODUCTION

Reclaimed asphalt pavement (RAP) is defined as pavement materials containing asphalt and aggregates which have been removed and/or reprocessed [1]. Rehabilitation of asphalt concrete pavement includes the milling of asphalt concrete layer, which produces a great amount of RAP. Those RAP from the rehabilitation of asphalt road are a major problem for many countries. Fig. 1 shows the on-site RAP heap from the rehabilitation of asphalt pavement failure caused by flood in the Lopburi province, Thailand. RAP can be recycled by the following applications: cold in-place recycling, cold planning, hot recycling, hot in-place recycling, and full depth reclamation [2]. Although RAP can be recycled directly as a recycled proportion of new hot mix asphalt concrete, this is generally limited to 25% (or less) of the new material according to the standard. Some RAP remain and alternative methods for disposal would need to be developed.

When used as a total substitute for natural aggregates, most RAP materials do not often meet the minimum base material requirements set forth by the standard or local state guidelines [3]. The use of RAP as a granular base is one solution available for the disposal of RAP solid waste and provides good application where no suitable materials are available [4]. RAP can be replaced by natural aggregate in pavement base or subbase if mixed with other natural aggregates [5]. However, the natural soils mixed with RAP exhibit low strength and collapse on wetting. These limitations have led to the new

research efforts aimed at exploring novel stabilization methods to treat soil/RAP mixture before their use in pavement base or subbase construction [6]. The cost-effective method for stabilizing pavement material is a cold in-place mixed with cement. This method is economical and the engineering properties of materials can be controlled. The strength and resistance to deformation increase with curing time. The fundamental mechanical characteristics and some influential factors on the strength behavior (e.g., water content, cement content, curing conditions and compaction energy) of cement treated soils have been investigated extensively (e.g., [7] to [13], and others).



Fig. 1 On-site RAP heap in the Lopburi province, Thailand (photo by Jirayut Suebsuk)

RAP are becoming increasingly popular as alternative recycled solid waste materials for pavement base applications over the last decade. Laboratory and field investigation on the use of RAP material in pavement base and subbase applications has been conducted by Rutgers University [14]. Other research works on the use of RAP have been reported in the most recent literature (e.g., [6], [15] to [17]). However, there are no methodologies based on rational criteria to assess the target strength for practical use; the conventional technique to design the mixed proportions of soil/RAP mixture is based on a trial batch.

This research therefore aims to study the influence of RAP content on the compaction behavior as well as to assess the unconfined compressive strength and strength development with curing time of cement treated lateritic soil/RAP mixture, using porosity as a state parameter.

LABORATORY INVESTIGATION

Lateritic Soil

The natural lateritic soil used in this study is a local problematic soil from the Nakhon-Ratchasima province, Thailand. It contains high fine particle content over the maximum criteria according to the Department of Highways (DOH) standard. It was collected from a borrowed pit in the Nakhon-Ratchasima province, Thailand, at a depth 2 to 3 m. The fine particle accounts for the significant problems on the base course structure, especially the swelling, consolidation and collapse upon drying and wetting. The grain size distribution of the soil is presented in Fig. 2. The natural soil is composed of 2% gravel, 53% sand, 25% silt, and 20% clay. The specific gravity is 2.68. The liquid and plastic limits are approximately 23% and 5%, respectively. Based on the Unified Soil Classification System (USCS), the soil is classified as clayey sand (SC).

Reclaimed Asphalt Pavement (RAP)

The only source of RAP material was obtained from the milling of asphalt pavement for resurfacing in the cold in-place recycling (CIR) process in the Nakhon-Ratchasima province, Thailand. This RAP contains primarily crushed limestone with 7% of asphalt content. The in-situ RAP were air-dried and then passed through a 3/8" sieve for removal of particles larger than 10 mm. The grain size distribution is also presented in Fig. 2. It indicated that approximately 100% of RAP was retained on the No. 200 sieve. The bulk specific gravity is 2.49.

Compaction and Unconfined Compression Tests

The compaction of lateritic soil, RAP and mixed materials was carried out using a 100-mm standard mold under modified Proctor energy (ASTM D 1557). The optimum moisture content (OMC) and

maximum dry density ($\gamma_{d,max}$) of compacted lateritic soil under the modified Proctor are 8% and 21.2 kN/m³, respectively; while the OMC and $\gamma_{d,max}$ of compacted 100% of RAP under the modified Proctor are 6.2% and 17.5 kN/m³, respectively. The modified Proctor energy was performed on the untreated mixed materials to assess their OMC and $\gamma_{d,max}$, which are presented in Table 1.

The unconfined compressive tests were performed on the cylindrical specimens, which were compacted on the OMC of untreated materials (*vide* Table 1). The lateritic soil, mixed with RAP, was treated by various contents of Portland cement type I. The RAP content used in the mix proportions varied from 0 to 90% by weight of total material, while the cement content (C) varied from 0 to 5% by weight of solid. After 24 hours of molding, the specimens were dismantled from the mold, wrapped in vinyl bags, and stored in a humidity chamber with a constant temperature (25 ± 2 °C). Unconfined compression tests were conducted on the samples after 1, 7, 14, 28, and 60 days of curing. The rate of vertical displacement was constantly kept at 1 mm/min. After finishing the test, the moisture content of the samples was measured for evaluating the porosity.

For all mixtures at each curing time and combination of moisture content and cement content, at least five samples were tested under the same condition to check the consistency of the test. In the most cases, the results under the same testing condition were reproducible with a low mean standard deviation, SD ($SD/\bar{x} < 10\%$), where \bar{x} is the mean strength value).

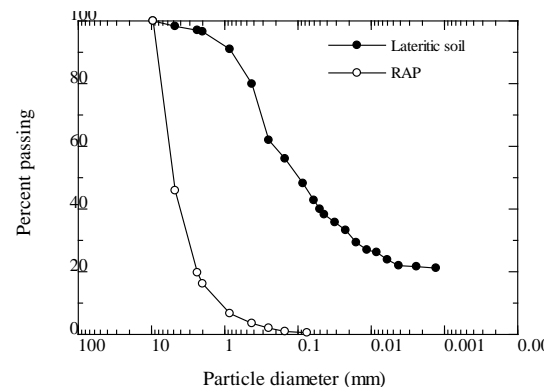


Fig. 2 The grain size distribution of lateritic soil and RAP

Table 1 The OMC and maximum dry density of soil/RAP mixtures

Soil/RAP ratio	OMC (%)	$\gamma_{d,max}$ (kN/m ³)
80/20	7.0	21.5
60/40	6.8	21.6
50/50	6.4	21.9
40/60	7.0	21.3
20/80	8.8	19.9

RESULTS AND DISCUSSIONS

Fig. 3a shows the compaction curve of the lateritic soil and RAP. The various compaction curves of mixed materials were presented in Fig. 3b under various soil/RAP ratios. The OMC tends to decrease as the RAP content increases up to the optimum RAP content, which is 50/50 of soil/RAP ratios. At this point, it provides a maximum dry density of 21.9 kN/m^3 associated with a moisture content of 6.4%. The reduction in the maximum dry density is associated with an increase in the RAP content, more than the optimum point. The reduction in the maximum dry density (increase in porosity) could be due to the larger particle size of RAP, where the soil/RAP mixture leads to a poorly graded material.

Fig. 4 shows the typical stress-strain relationships in the unconfined compression tests of cement treated soil/RAP mixture for different RAP content but with the same cement content and curing time. The RAP content in the mixed materials has played a significant role in the stress-strain-strength behavior under unconfined compression tests. The reduction in strength and stiffness of the mixed materials are associated with a decrease in dry density.

Fig. 5 shows the effect of RAP, as represented by the asphalt binder content AS (%), on the strength in unconfined compression tests of cement treated soil/RAP mixture. AS is calculated as follows:

$$AS = \frac{W_{as}}{W_s} \times 100, \quad (1)$$

where W_{as} is the weight of asphalt binder, and W_s is the weight of soil solid. As the asphalt content increases, the unconfined compressive strength significantly decreases. However, when the asphalt binder content is greater than 3.5% (50/50 of soil/RAP ratio), the change in strength is larger. The asphalt content of 3.5% can be designated as the "asphalt fixation point". The decrease in strength is due to a reduction in friction between the solid particles (soil and RAP aggregate), which is caused by the asphalt binder. The asphalt fixation point is a transitional point where less change in strength turns to a larger change. The reduction in strength is minimal when the asphalt content is lower than the asphalt fixation point; this zone is called the inert zone. The zone is also called deterioration when the asphalt content is greater than the asphalt fixation point.

Fig. 6 shows the porosity η of the cement treated soil/RAP mixture. The compacted 100% lateritic soil inherently exhibits 18.5% of porosity. The increase of asphalt content in the mixed material reduced the porosity. By adding 3.5% of asphalt content, the porosity is reduced by up to about 14%. However, when the asphalt content is greater than 3.5%, the

porosity increases. The increase in the porosity could be due to the lower specific gravity of RAP and the compaction behavior of the mixed material.

Fig. 7 shows the comparison of strength development in cement treated soil/RAP mixture under various RAP content but with the same cement content. As the higher asphalt content increases, the strength is lowered. The presence of asphalt binder reduces the bonding between RAP aggregate and soil. The asphalt binder is detrimental to cement treated soils. The typical strength development with curing time for cement treated soil/RAP mixtures under 20%, 40% and 50% of RAP content is shown in Figs. 8-10. The strength development with curing time (days) in a natural logarithmic scale can be expressed as a linear variation. The strength ratio plots after normalization are also shown in these figures. The normalized relation is presented in Eq. (2).

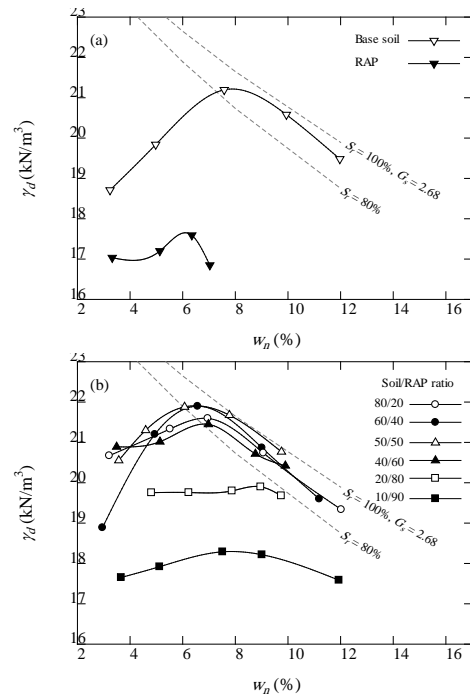


Fig. 3 Compaction curves of the lateritic soil, RAP, and mixed materials

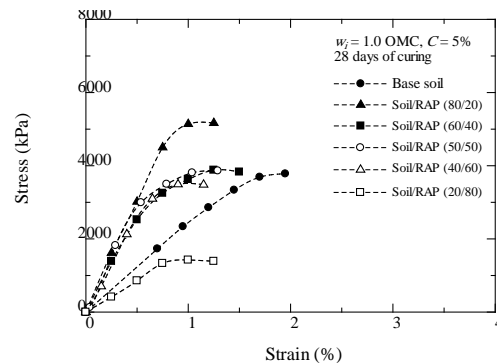


Fig. 4 Stress-strain relationships in unconfined compression test of lateritic soil and mixed materials

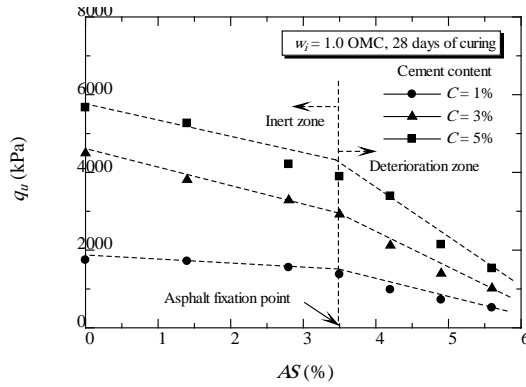


Fig. 5 Relationship between strength and asphalt content

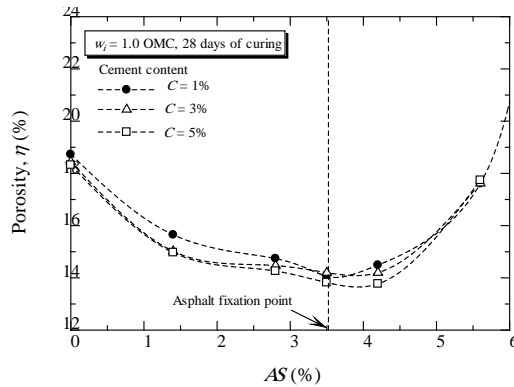


Fig. 6 Relationship between porosity and asphalt content

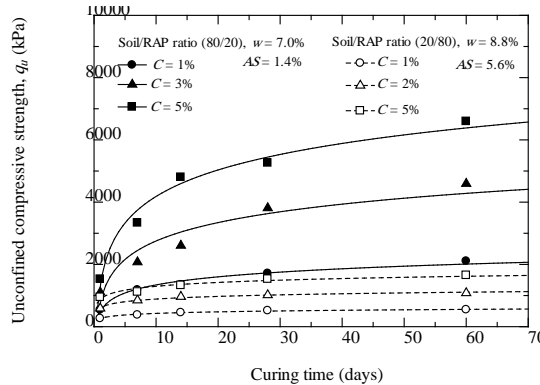


Fig. 7 The comparison of strength development in cement treated soil/RAP mixture under different RAP content

$$\frac{q_D}{q_{28}} = a + b \ln D, \quad (2)$$

where q_D is the strength after D days of curing, q_{28} is the 28-day strength, a and b are constant. From this investigation, the values of a and b are 0.248 and 0.225 for 80/20 of soil/RAP ratio, 0.297 and 0.197 for 60/40 of soil/RAP ratio, and 0.444 and 0.178 for 50/50 of soil/RAP ratio. The normalized strength development is comparable to that proposed for cement treated low plasticity and coarse grained soils [10]. It is found that these three sets of values depend on the variation of porosity and cement

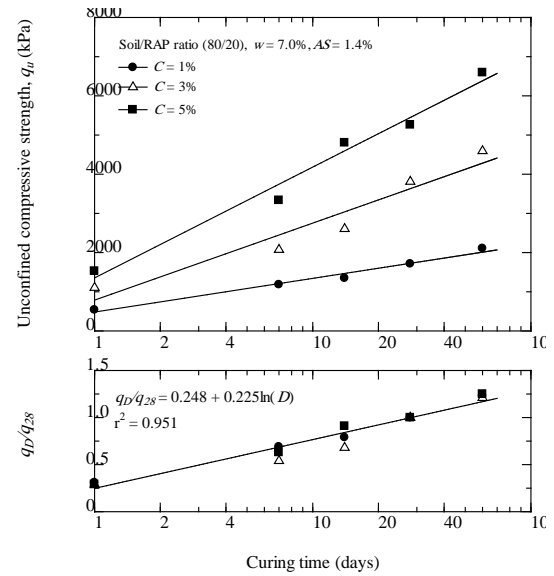


Fig. 8 Strength development in cement treated soil/RAP mixture (80/20) and its normalization

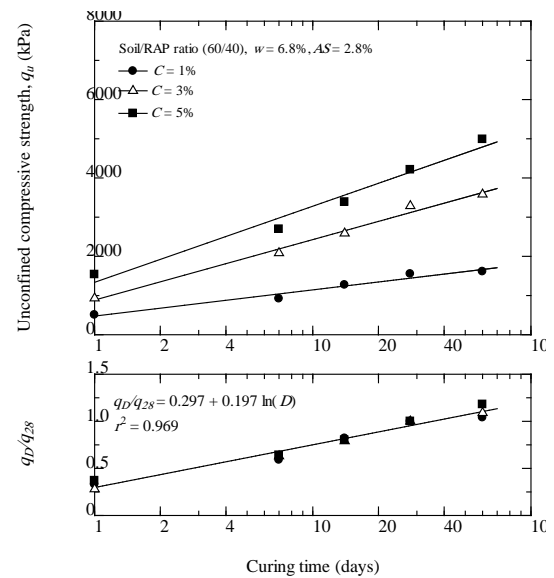


Fig. 9 Strength development in cement treated soil/RAP mixture (60/40) and its normalization

content for the range of curing time considered. The soil water/cement ratio and compaction behavior has play a significant role on the change in porosity of cement treated soil/RAP mixture. To account the material type and the water/cement ratio, the generalized relationship of strength ratio has been take the porosity into the account by the proposed generalized equation:

$$\frac{q_D}{q_{28}} \eta = a^* + b^* \ln D \quad (3)$$

where η is the porosity of treated specimens at each mixture, a^* and b^* are constant. Based on the test result of cement treated mixed materials on the inert zone, the generalization of strength development can

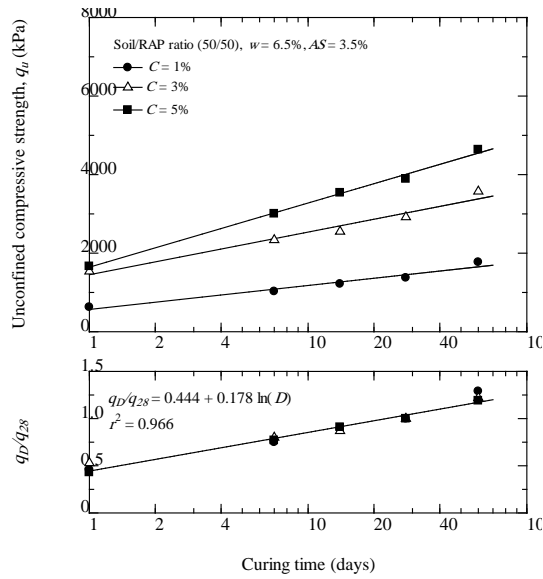


Fig. 10 Strength development in cement treated soil/RAP mixture (50/50) and its normalization

be illustrated as in Fig. 11. The linear regression analysis gives $a^* = 0.028$ and $b^* = 0.046$. This generalization accounts for the effect of the compaction behavior of different gradation. It is evident that the asphalt content is lower than the asphalt fixation point (3.5%) and valid for the range of curing time between 1 to 60 days. For predicting the strength via the generalization Eq. (3), one laboratory test value of strength and porosity measured on the 28 days of curing at the same compaction energy, same cement content, and same soil/RAP ratio is needed. Using this generalization, the strength of cement treated soil/RAP (70/30 of soil/RAP ratio) mixture was predicted and compared with those of the laboratory test as shown in Fig. 12. There is some discrepancy between the predicted and laboratory strengths. However, the error from the prediction is acceptable in common engineering practice.

CONCLUSION

This article presents the unconfined compressive strength of a problematic lateritic soil mixed with RAP. The mixed materials were treated by cement to increase their strength and engineering properties. The influence of RAP content on the compaction and strength development with curing time was studied using porosity as a state parameter. The following conclusions can be drawn:

- 1) The OMC of mixed material is dependent directly on the mixed proportions. With an increase in RAP content, the OMC tends to decrease, up to the optimum gradation with a soil/RAP ratio of 50/50.

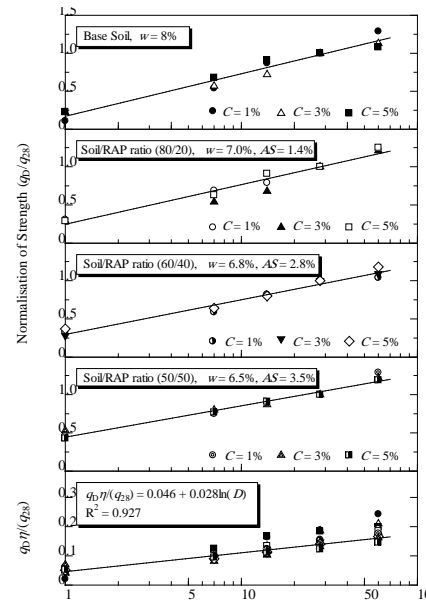


Fig. 11 Generalization of strength development in cement treated soil/RAP mixture

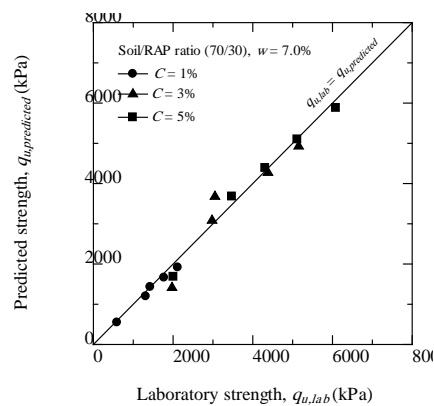


Fig. 12 Comparison between predicted and laboratory strengths

- 2) As the asphalt content increases, the unconfined compressive strength decreases due to a reduction in friction between the solid particles (soil and RAP), which is caused by the asphalt binder. The unconfined compressive strength of mixed materials is associated with the variation in porosity. Asphalt fixation point is defined as the limit point of asphalt content that separates the inert from the deterioration zones. An asphalt content of 3.5% (50/50 of soil/RAP ratio) has become the asphalt fixation point of this investigation.
- 3) The target strength of cement treated soil/RAP mixture can be predicted by the generalized form of strength if and when the asphalt content is lower than the asphalt fixation point. This proposed equation can assess the laboratory strength of cement treated soil/RAP mixture in which the

mixed proportion, cement content, water content, and curing time vary.

ACKNOWLEDGEMENTS

This research was financially supported by the Rajamangala University of Technology Isan. The facilities provided by the Department of Civil Engineering, Faculty of Engineering and Architecture, Rajamangala University of Technology are also very much appreciated.

REFERENCES

- [1] Cosentino, P.J., Kalajian, E.H., Shieh, C.H., Mathurin, W.J.K., Gomez, F.A., Cleary, E.D., and Treeratrakoon, A. (2003). "Developing Specifications for Using Recycled Asphalt Pavement as Base, Subbase or General Fill Materials, Phase II (Rep. No. FL/DOT/RMC/06650-7754)" Florida Institute of Technology.
- [2] Attia, M.I.E. (2010). "Characterization of the Structural Behavior of Reclaimed Asphalt Pavement as pavement base layer", Doctoral dissertations, North Dakota State University of Agriculture and applied science.
- [3] Rana, A.S.M.A. (2004). "Evaluation of recycled material performance in highway applications and optimization of their use" Ph.D. dissertation, Texas Tech Univ., Lubbock, TX.
- [4] Papp, W.J., Maher, M.H., Bennert, T.A., and Gucunski, N. (1998). "Behavior of Construction and Demolition Debris in Base and Subbase Applications", ASCE Recycled Materials in Geotechnical Applications, Geotechnical Special Publication No. 79, pp. 122-136.
- [5] Taha, R., Ali, A., Basma, A., and Al-Turk, O. (1999). "Evaluation of reclaimed asphalt pavement aggregate in road bases and subbases" Transportation Research Record 1652, Washington, DC, pp. 264-269.
- [6] Hoyos, L.R., Puppala, A.J., and Ordonez, C.A. (2011). "Characterization of Cement-Fiber-Treated Reclaimed Asphalt Pavement Aggregate: Preliminary Investigation", Journal of Material in Civil Engineering, ASCE, Vol. 23, No.7, pp. 977-989.
- [7] Consoli, N.C., Rotta, G.V., and Prietto, P.D.M. (2000). "The influence of curing under stress on the triaxial response of cemented soils" Geotechnique, Vol. 50, No. 1, pp. 99-105.
- [8] Consoli, N.C., Prietto, P.D.M., Carraro, J.A.H., and Heineck, K.S. (2001). "Behavior of Compacted Soil-Fly Ash-Carbide Lime Mixtures" Journal of Geotechnical and Geoenvironmental Engineering, ASCE, Vol. 127, No. 9, pp.774-782.
- [9] Consoli, N.C., Foppa, D., Festugato, L. and Heineck, K.S. (2007). "Key parameters for Strength Control of Artificially Cemented Soils", Journal of Geotechnical and Geoenvironmental Engineering, ASCE, Vol. 133, No. 2, pp.197-205.
- [10] Horpibulsuk, S., Katkan, W., Sirilerdwattana, W. & Rachan, R. (2006). "Strength Development in Cement Stabilized Low Plasticity and Coarse Grained Soils: Laboratory and Field Study", Soils and Foundations, Vol. 46, No. 3, pp. 351-366.
- [11] Horpibulsuk, S., Rachan, R., Chinkulkijniwat, A., Raksachon, Y., and Suddeepong, A. (2010). "Analysis of Strength Development in Cement-Stabilized Silty Clay based on Microstructural Considerations" Construction and Building Materials, Vol. 24, pp. 2011-2021.
- [12] Horpibulsuk, S., Rachan, R. & Suddeepong, A. (2011). "Assessment of Strength Development in Blended Cement Admixed Bangkok Clay", Construction and Building Materials, Vol. 25, No. 4, pp.1521-1531.
- [13] Horpibulsuk, S., Phojan, W., Suddeepong, A. and Liu, M.D. (2012). "Strength Development in Blended Cement Admixed Saline Clay", Applied Clay Science, Vol. 55, pp. 44-52.
- [14] Maher, M.H., and Popp, W.Jr., (1997). "Recycled Asphalt Pavement as Base and Subbase Material" ASTM STP 1275, ASTM, West Conshohocken, Pa.
- [15] Taha, R., Al-Harthy, A., Al-Shamsi, K., and Al-Zubeidi, M. (2002). "Cement Stabilization of Reclaimed Asphalt Pavement Aggregate for Road Bases and Subbases" Journal of Materials in Civil Engineering, Vol. 14, No. 3, pp.239-245.
- [16] Puppala, A.J., Hoyos, L.R., and Potturi, A.K. (2011). "Resilient Moduli Response of Moderately Cement-Treated Reclaimed Asphalt Pavement Aggregates", Journal of Materials in Civil Engineering, Vol. 23, No. 7, pp. 990-998.
- [17] Puppala, A.J., Saride, S., and Williammee, R. (2012). "Sustainable Reuse of Limestone Quarry Fines and RAP in Pavement Base/Subbase layers", Journal of Materials in Civil Engineering, Vol. 24, No. 4, pp. 418-429.

INVESTIGATION OF STRESS REDUCTION EFFECT ON STRUCTURE DUE TO BASEMAT UPLIFT USING ENERGY CONCEPT

Takafumi Inoue¹ and Atsushi Mikami²

¹Department of Civil & Environmental Engineering, The University of Tokushima, Japan

²Department of Civil & Environmental Engineering, The University of Tokushima, Japan

ABSTRACT

In order to verify seismic performance of a structure, it is necessary to evaluate the effect of dynamic soil-structure interaction appropriately. One of the reliable models that can account for basemat uplift as well as soil yielding is the macro-element model for shallow foundations. This paper studies stress reduction effects induced in structures (such as bridge piers) due to basemat uplift and soil yielding by the use of a macro-element model for foundations placed on sands. A superstructure is modeled by a lumped mass and Bernoulli-Euler beam. A foundation-soil system is modeled as four cases; (1) fixed base, (2) elastic soil, (3) elastic soil with basemat uplift and (4) elasto-plastic soil with basemat uplift. Time histories that have different frequency characteristics are considered as input motions to the models. Comparisons of responses of the models show remarkable reduction of section force due to basemat uplift and soil yielding. The degree of base shear reduction differs depending on the input motions. Therefore, it may be concluded that the degree of base shear reduction depends on the frequency characteristics of the input motions relative to the system. Regarding the case that degree of stress reduction effect is the largest, energy balance for the system are estimated. In this case, the input energy imparted to the structure by an earthquake tends to be smaller by the effect of basemat uplift.

Keywords: Bridge Pier, Stress Reduction Effect, Basemat Uplift, Macro-element, Energy

INTRODUCTION

As the design method shifts to performance-based design, it becomes more important to accurately estimate the response of superstructure accompanied by foundation rotation and basemat uplift. Basemat uplift is reportedly induced even by weak to medium ground motions [1], hence, it is necessary to incorporate the effect of basemat uplift into a design code.

Hayashi [2] assessed slightly damaged buildings standing on the most severely damaged area during the 1995 Hyogoken-Nanbu Earthquake. By using numerical simulation, he has studied damage reduction effect due to basemat uplift of buildings which were subject to strong ground motions, and showed that the damage reduction effect sometimes becomes remarkable depending on structural parameters and input motions. The finite element model was used in his analysis treating soil as a linear or equivalent linear medium.

Iwashita *et al.* [3] have examined the effect of uplift at pile head on structural response. They have discussed the input energy imparted to the structure by an earthquake. They have treated the ground as

springs and assumed that the spring doesn't resist tensile force to take the effect of uplift into account.

Authors have studied the reduction effect of a section force induced in the structure due to basemat uplift and soil yielding by the use of a macro-element model and showed that the degree of base shear reduction depends on the frequency characteristics of the input motions relative to the system [4].

This paper studies the reduction effect of a section force induced in the structure due to basemat uplift and soil yielding by the use of a macro-element model. In addition, the energy balance for the structure is estimated. A foundation-soil system is modeled as four cases; (1) fixed base, (2) elastic soil, (3) elastic soil with basemat uplift and (4) elasto-plastic soil with basemat uplift. Time histories which have different frequency characteristics are considered as input motions in the model.

MACRO-ELEMENT MODEL

In this study, a macro-element model developed by Nakatani *et al.* [5] is employed to study stress reduction effect of structures due to basemat uplift

and sand soil yielding. A brief overview is described in this section. Details can be referred to in Shirato *et al.* [6].

Relationship between displacements and loads of a macro-element model

In the macro-element model, the foundation is assumed to be rigid, and foundation-soil model which is subjected to combined loads is modeled as one element. Displacements and loads at the center of the footing are defined as shown in Fig. 1 and the following equations.

$$x = (v \quad u \quad \theta)^T \quad (1)$$

$$F = (V \quad H \quad M)^T \quad (2)$$

where the superscript T stands for transposition. The relationship between incremental displacements and loads is expressed by

$$dF = (D^{el} + D^{up} + D^{pl})^{-1} dx \quad (3)$$

where D^{el} , D^{up} and D^{pl} are elastic compliance, uplift compliance and plastic compliance, respectively.

Elastic compliance

In order to determine elastic compliance, equivalent elastic spring coefficients corresponding to the vertical, translational, and rocking component are used based on Gazetas [7]. The coefficients for a rectangular foundation are expressed by

$$K_v = \frac{4.54G(B/2)}{1-\nu} \quad (4)$$

$$K_h = \frac{9G(B/2)}{2-\nu} \quad (5)$$

$$K_r = \frac{3.6G(B/2)^3}{1-\nu} \quad (6)$$

where G and ν are shear modulus and Poisson's ratio of the underlying soil and B is the footing length. Frequency dependence of the coefficients is ignored.

Uplift compliance

Uplift compliance is determined based on the following model for uplift. $\theta^{up} - M$ relationship is expressed by

$$\theta^{up} = 0 \quad (M \leq M_a) \quad (7)$$

$$\theta^{up} = \left\{ \frac{4}{(3-M/M_a)^2} - \frac{M}{M_a} \right\} \theta_0 \quad (M > M_a) \quad (8)$$

where M_a and θ_0 are moments that are influenced by soil plasticity and rotation at which

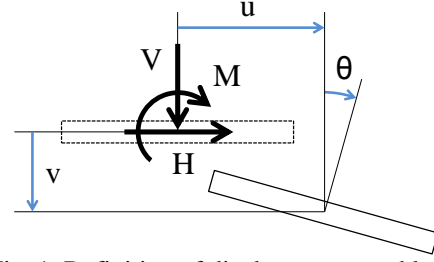


Fig. 1 Definition of displacements and loads for the macro-element model

the uplift initiates. Then $v^{up} - M$ relationship is expressed by

$$v^{up} = 0 \quad (M \leq M_a) \quad (9)$$

$$v^{up} = -\frac{B}{2} \left\{ \frac{4}{(3-M/M_a)^2} - \frac{4}{(3-M/M_a)} + 1 \right\} \quad (M > M_a) \quad (10)$$

Plastic compliance

In order to determine plastic compliance, bearing capacity surface is used. A schematic diagram of this is shown in Fig. 2. Shirato *et al.* [6] assumed following expression for bearing capacity surface.

$$f_{cr} = h^2 + m^2 - \xi^2(1-\xi)^{2c} = 0 \quad (11)$$

where $\xi = V/V_m$, $h = H/(\mu V_m)$, $m = M/(\psi B V_m)$ and V_m is bearing capacity in terms of centered vertical loading. Parameters μ and ψ are tangents at the origin on the $v-H$, $v-M$ planes, respectively. To describe plastic deformations, a yield function is defined based on Nova and Montrasio [8] as follows:

$$f_y = h^2 + m^2 - \xi^2(1-\xi/\rho_c)^{2c} = 0 \quad (12)$$

where ρ_c is the hidden parameter that specifies instantaneous size of the yield surface and translates instantaneous combined loads into the norm of an equivalent vertical force. In order to relate size of the yield surface and incremental displacements, the hardening rule and flow rule are required. As for the hardening rule, isotropic hardening, which defines similar bearing capacity surface and yield surface, is assumed. The hardening function is expressed by

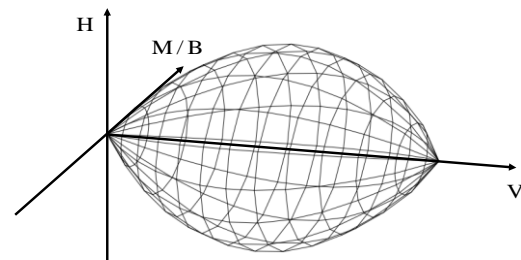


Fig. 2 Schematic of bearing capacity surface

$$\rho_c = 1 - \exp\left(-\frac{R_0 v_c}{V_m}\right) \quad (13)$$

where R_0 is initial gradient of the $v-v^p$ curve. v_c is expressed by

$$v_c = \left\{ (v^p)^2 + (\alpha_M u^p)^2 + (\gamma_M B \theta^p)^2 \right\}^{0.5} \quad (14)$$

where α_M and γ_M are non-dimensional parameters that incorporate the contribution of horizontal displacement and rotation into hardening. As for the flow rule, a non-associated flow rule is adopted. Regarding such a non-associated flow rule, a plastic potential function is defined as follows:

$$g = \lambda^2 h^2 + \chi^2 m^2 - \xi^2 (1 - \xi / \rho_s)^{2\xi} = 0 \quad (15)$$

where $\lambda = \mu / \mu_s$, $\chi = \phi / \phi_s$, μ_s and ϕ_s are parameters that specify the shape of the plastic potential surface.

STRESS REDUCTION AGAINST A REAL EARTHQUAKE

Here, stress reduction effects of a structure-foundation-soil system against real earthquakes is reviewed. The system was subjected to different types of acceleration-time histories. A foundation-soil system is modeled as four cases; (1) fixed base, (2) elastic soil, (3) elastic soil with basemat uplift and (4) elasto-plastic soil with basemat uplift.

Structure-foundation-soil system

Schematic and parameters of the structure-foundation-soil system is shown in Fig. 3 and Table 1. A superstructure was modeled by a lumped mass and Bernoulli-Euler beam. The total degrees of freedom of the system were six; consisting of three degrees of lumped mass and three degrees of the macro-element. A foundation-soil system is modeled as four cases; (1) fixed base, (2) elastic soil, (3) elastic soil with basemat uplift and (4) elasto-plastic soil with basemat uplift. The damping coefficient of the beam element was assumed to be proportional to the element stiffness matrix and 5% of the damping coefficient was taken into account. Frequency dependence of elastic compliances of the macro-element was ignored. Damping coefficients of the macro-element corresponding to the vertical, translational, and rocking component were set based on Gazetas [7]. The parameters of yield function, plastic potential and hardening function were set based on Nova and Montrasio [8] and Nakatani *et al.* [5].

Stress reduction against a real earthquake

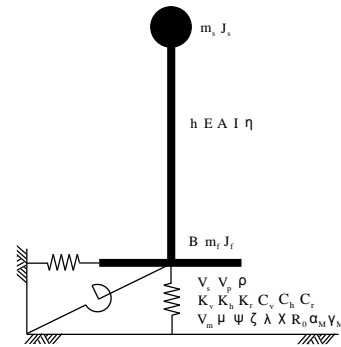


Fig. 3 Schematic of structure-foundation-soil system

Table 1 Parameters of structure-foundation-soil system

Parameter	Unit	Value
Lumped mass m_s	t	500
Moment of inertia of the structure J_s	$t \cdot m^2$	4167
Height h	m	10
Young modulus E	kN/m^2	24500000
Section area A	m^2	4.423
Second moment of area I	m^4	1.557
Damping coefficient of the structure η		0.05
Footing length B	m	10
Mass of the foundation m_f	t	100
Moment of inertia of the foundation J_f	$t \cdot m^2$	833
Shear wave velocity V_s	m/s	230
Lysmer's analog wave velocity V_{La}	m/s	356
Ground density ρ	t/m^3	1.603
Vertical elastic spring coefficient K_v	kN/m	2750000
Translational elastic spring coefficient K_h	kN/m	2240000
Rocking elastic spring coefficient K_r	$kN \cdot m/rad$	54500000
Vertical damping coefficient C_v	kNs/m	52500
Translational damping coefficient C_h	kNs/m	36900
Rocking damping coefficient C_r	$kNsm$	99800
Bearing capacity of centered vertical loading V_m	kN	96100
Parameter of yield function μ		0.9
Parameter of yield function ψ		0.48
Parameter of yield function ζ		0.95
Parameter of plastic potential λ		0.45
Parameter of plastic potential χ		0.45
Parameter of hardening function R_0		48946
Parameter of hardening function α_M		2.8
Parameter of hardening function γ_M		1.7

The degree of stress reduction effects of a structure was studied. The aforementioned structure-foundation-soil system is subjected to input motions in the time domain. Two kinds of ground motions are considered as the input motions

here; subduction type earthquake (acceleration time history that was recorded at a port in Hachinohe during the 1968 Tokachi-Oki Earthquake) and inland type earthquake (acceleration time history observed at JR Takatori station during the 1995 Hyogoken-Nanbu Earthquake). These time histories are shown in Fig. 4 and 5. For conducting nonlinear analysis with the macro-element model, time step for seismic response analysis was set at 0.0001 seconds by interpolating the input time histories which were originally recorded at 0.02 second intervals. A linear acceleration method was used for the numerical integration.

The time history of base shear that occurred in the structure for subduction zone type earthquake is shown in Fig. 6. The thin black dot-line, the thin blue line, the thick red dot-line and the thick green line correspond to responses for fixed base case, elastic soil case, elastic soil with basemat uplift case and elasto-plastic soil with basemat uplift case, respectively. The case (1) show different time responses from other cases (this difference implies the wave radiation effect). However, linear case and nonlinear cases show similar time responses. This means that significant stress reduction effect due to basemat uplift and soil yielding are not apparent in this case.

Secondly, an inland type earthquake is considered as input motion into the system. Calculated responses are shown in Fig. 7. Meanings of curves are the same as Fig. 6. Responses show significantly different waveforms. The fixed base case and elastic soil case show similar time responses (this difference implies the wave radiation effect). However, when basemat uplift is considered, the base shear becomes significantly different from linear cases. Nonlinear cases show drastic reduction of base shear, thus longer period motions are implied. When soil yielding is considered, the period of the motion becomes even longer.

We can recognize from these results that stress reduction of structures due to basemat uplift and soil yielding can occur in some cases depending on input ground motions. In order to examine factors that might bring a differences in the level of stress reduction, some artificial input motions that have different frequency characteristics are considered in the next section.

STRESS REDUCTION OF STRUCTURE FOR INPUT MOTIONS OF DIFFERENT FREQUENCY CHARACTERISTICS

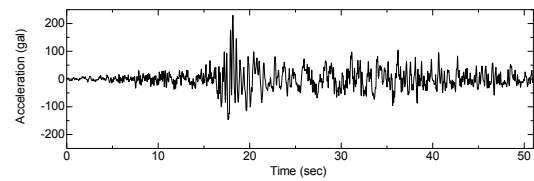


Fig. 4 Acceleration time history

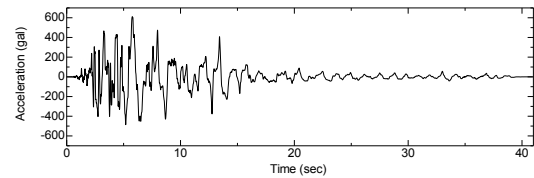


Fig. 5 Acceleration time history

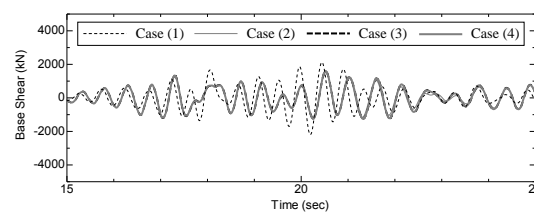


Fig. 7 Base shear time history

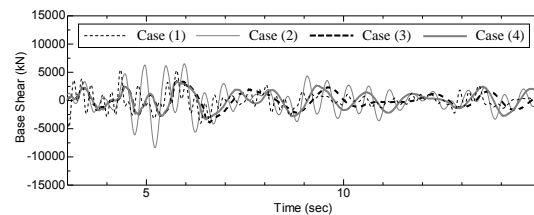


Fig. 7 Base shear time history

The same structure-foundation-soil system is considered. As the input motion, harmonic waves that have different frequency characteristics are given. An example of the harmonic seismic wave which has a natural frequency of 1.989Hz is shown in Fig. 8. The amplitude gradually increases until it reaches to the amplitude of 500gal. As the former section, foundation-soil system is modeled as four cases; (1) fixed base, (2) elastic soil, (3) elastic soil with basemat uplift and (4) elasto-plastic soil with basemat uplift. Three cases of different excitation frequencies are considered: (a) excitation frequency f_e is lower than the natural frequency of the elastic soil system f_n ($f_e/f_n=0.9$) (b) excitation frequency is the and same as the natural frequency of the elastic soil system ($f_e/f_n=1.0$) (c) excitation frequency is higher than the natural frequency of the elastic soil system ($f_e/f_n=1.1$). The natural frequency of the elastic soil system is 1.989(Hz).

Stress reduction for case (a)

The time history of base shear induced in the structure is shown in Fig. 9. The meanings of the

curves are the same as before. The base shear responses of fixed base and elastic soil model are larger than nonlinear cases. When basemat uplift effect is incorporated in the model, the base shear reduced significantly. Any clear difference can not be seen by the soil yielding effect.

Stress reduction for case (b)

Calculated responses are shown in Fig. 10. In this case, the base shear of the elastic soil model becomes much larger than others. This is because the elastic soil system reached resonance with excitation frequency becomes system frequency. Compared to the elastic soil case, base shear of the models that incorporated basemat uplift effect reduced significantly.

Stress reduction for case (c)

The result is shown in Fig. 11. In this case, excitation frequency is higher than the elastic soil system and closer to the fixed base model. For this

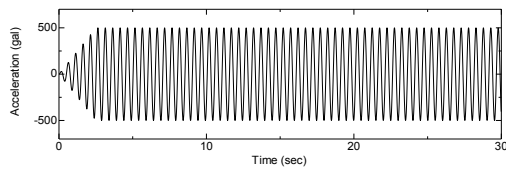


Fig. 8 Acceleration time history

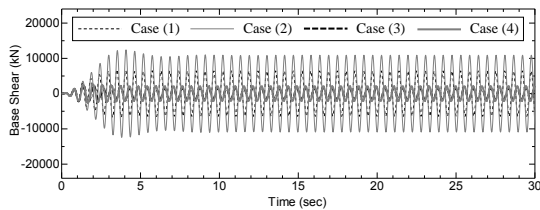


Fig. 9 Base shear time history (Case (a))

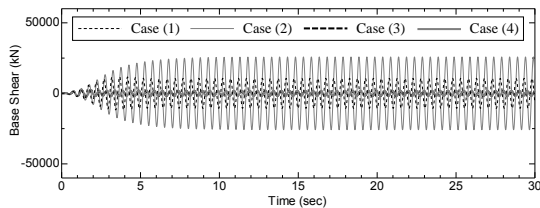


Fig. 10 Base shear time history (Case (b))

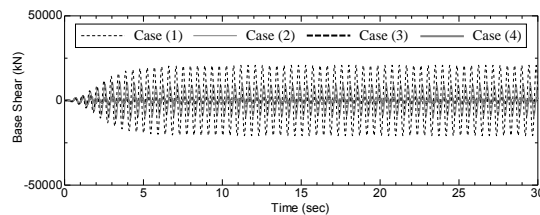


Fig. 11 Base shear time history (Case (c))

reason, base shear of the fixed base model is largest. Owing to radiation damping effect, base shear of the elastic soil model reduced significantly. Furthermore, basemat uplift effect works to drastically reduce the base shear of the structure in this case.

INVESTIGATION OF STRESS REDUCTION EFFECT USING ENERGY CONCEPT

Regarding case (c) that degree of stress reduction effect was the largest in the preceding chapter, energy balance for the system are estimated. The various energy terms can be defined by integrating the equation of motion of the system. If a macro-element model developed by Nakatani *et al.* [5] is employed, the equation of motion of the system is expressed by

$$[M]\{\ddot{u}\} + [C]\{\dot{u}\} + [K]\{u\} + \{F\} = \{P\} \quad (16)$$

where $[M]$ is the mass matrix, $[C]$ is the damping matrix, $[K]$ is the stiffnessmatrix for the pier, $\{F\}$ is the soil reaction force matrix from macro-element, and $\{P\}$ is the external force matrix. Hence, the various energy terms can be expressed by

$$\int_0^t \{\dot{u}\}^T [M] \{\ddot{u}\} dt + \int_0^t \{\dot{u}\}^T [C] \{\dot{u}\} dt + \int_0^t \{\dot{u}\}^T [K] \{u\} dt + \int_0^t \{\dot{u}\}^T \{F\} dt = \int_0^t \{\dot{u}\}^T \{P\} dt \quad (17)$$

The right side of this equation is the energy input to the system. The first term on the left side of this equation is the kinetic energy of the system associated with its motion relative to the ground. The second term on the left side of this equation is the energy dissipated by viscous damping. The third term on the left side of this equation is the potential energy of the structure. The fourth term on the left side of this equation is the potential energy of the soil. The time histories of energy for the systems are shown in Fig. 12. In this case, the input energy imparted to the structure by an earthquake tends to be smaller by the effect of basemat uplift.

CONCLUSIONS

This study examined stress reduction effects induced in a structure due to basemat uplift and soil yielding by the use of a macro-element model for foundations placed on sands. The foundation-soil system is modeled as four cases; (1) fixed base, (2) elastic soil, (3) elastic soil with basemat uplift and (4) elasto-plastic soil with basemat uplift. Time histories with different frequency characteristics were considered as input motions to the models. Comparisons of responses for the models showed

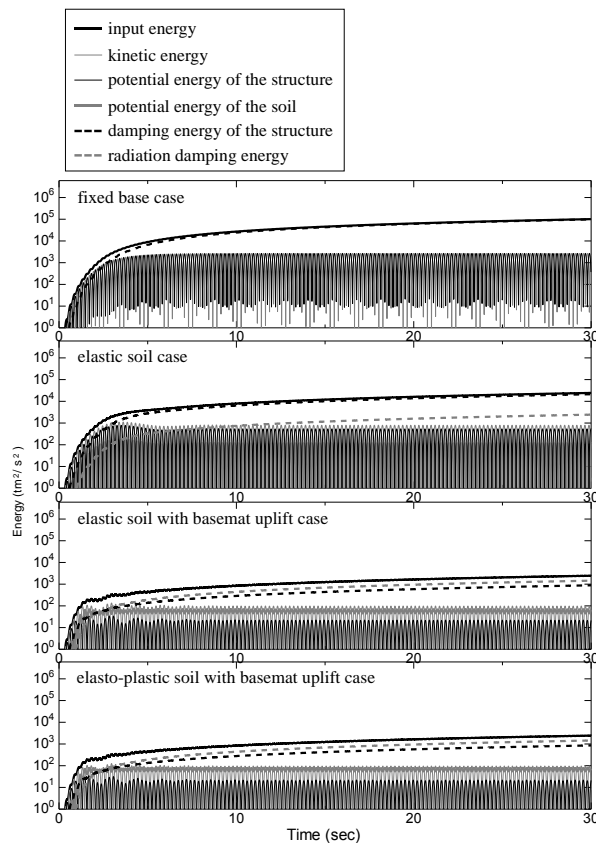


Fig. 12 Energy time history (Case (c))

remarkable reduction of section force due to basemat uplift and soil yielding. Therefore, it may be concluded that the degree of base shear reduction depends on the frequency characteristics of the input motions relative to the system. Regarding the case that degree of stress reduction effect was the largest, energy balance for the system are estimated. In this case, the input energy imparted to the structure by an earthquake tends to be smaller by the effect of basemat uplift.

ACKNOWLEDGEMENTS

Authors acknowledge the Public Works Research Institute, Tsukuba, Japan, for providing the analysis program.

REFERENCES

- [1] Fukui J, Kimura Y, Ishida M and Kishi Y, "An investigation on the response of shallow foundations to large earthquakes", Technical Memorandum of PWRI, Public Works Research Institute, (3627), 1999, (in Japanese).
- [2] Hayashi Y, "Damage reduction effect due to basemat uplift of buildings", Journal of Structural and Construction Engineering (Transactions of AIJ), 485:53-62, 1996, (in Japanese).
- [3] Iwashita K, Taniguchi H, Ishihara T, "Energy Approach to the Earthquake Response of Building Allowing Uplift at Pile Head" Journal of Structural and Construction Engineering (Transactions of AIJ), 564:23-30, 2003, (in Japanese).
- [4] Inoue T, and Mikami A, "Stress Reduction Effect of Structure due to Basemat Uplift and Soil Yielding," In: Proceedings of the 10th International Conference on Urban Earthquake Engineering, Tokyo, JAPAN, 2013.
- [5] Nakatani S, Shirato M, and Kouno T, "Development of a numerical model for the seismic nonlinear behavior and irreversible displacement of a shallow foundations" PWRI Report, Public Works Research Institute, (4101), 2008, (in Japanese).
- [6] Shirato M, Paolucci R, Kouno R, Nakatani S, Fukui J, Nova R, di Prisco C, "Numerical simulation of model tests of pier-shallow foundation systems subjected to earthquake loads using an elasto-uplift-plastic macro element" Soils and Foundations, 48(5), 693-71, 2008.
- [7] Gazetas G, "Foundation vibrations" Foundation Engineering Handbook, Fang HY (ed.), van Nostrand Reinhold: NY, 1991.
- [8] Nova R, and Montrasio L, "Settlement of shallow foundations on sand," Géotechnique, 41(2), 243-256, 1991

SWELLING DEFORMATION OF BENTONITE MIXED WITH INORGANIC MATERIALS IN ALKALINE SOLUTION

Yuki YOKOYAMA¹ and Kenichiro NAKARAI²

¹Graduate School of Engineering, Gunma University, Japan

²Graduate School of Engineering, Hiroshima University, Japan

ABSTRACT

In the radioactive waste disposal facility, sodium-type bentonite will be used as an artificial barrier material. It is expected to delay the infiltration of groundwater and fill the crack with the surrounding ground because it has high swelling performance. However, during the tens of thousands of years, the bentonite can be deteriorated and dissolved by the components leached from the surrounding cement-based materials. Then, the swelling performance of the bentonite may be lowered. In this paper, we propose a method to solve this problem by the mixing inorganic materials. From the experimental results, it was found that the mixing of small amount of silica fume or sodium carbonate to bentonite can reduce the deterioration of the bentonite in alkaline water from the viewpoint of swelling performance. But, in the case of the aged specimens 1 year after mixing, the effect of the mixing on the degradation of swelling performance of the bentonite tended to be smaller than in the case of the young specimens tested just after mixing regardless of the type of admixtures.

Keywords: artificial barrier, bentonite, silica fume, sodium carbonate, swelling deformation

INTRODUCTION

In radioactive waste disposal facilities, sodium bentonite having high swelling capacity will be used as an artificial barrier material. It is expected to delay the infiltration of groundwater and to fill cracks of the surrounding host rock. However, during tens of thousands of years, the bentonite can be deteriorated by the alkaline water with the ions leached from the surrounding cement-based materials. It decreases swelling capacity of the bentonite [1]. In order to solve this problem, we proposed a method to mix inorganic materials such as silica fume and sodium carbonate, which show reactivity with the components leached from the cement-based materials, to the bentonite. The pozzolanic materials such as silica fume and fly ash are expected to consume the leached calcium ions from the cement-based materials and hence, reduce the deterioration of the bentonite.

In our previous research [2]-[4], one-dimensional vertical swelling deformation tests proposed by Komine and Ogata [5], [6] were performed. Experimental results in the previous research showed that the mixing of the pozzolanic materials could restrain the decrease of the swelling capacity. Especially, the mix with 10~15 mass% of fly ash or the mix with 1 mass% of silica fume presented the most effectiveness on reducing the deterioration by calcium hydroxide solution.

The other proposal is the mixing of sodium carbonate to the bentonite. Here, calcite precipitation in the interface zone between the bentonite-based materials and cement-based materials was expected. The previous experimental results conducted by

Nakarai et al. [7] showed that the calcite precipitation could reduce the deterioration of the bentonite due to calcium leaching from the cement paste. Here, the immersion tests of the composite specimens consisting of cement paste and bentonite were performed. Then, the effect of the sodium carbonate mixing was investigated from the distribution of calcium measured by Electron Probe Micro Analysis (EPMA). In addition, the previous experimental results studied on swelling characteristics of bentonite showed that the mix with 0.5 mass% of sodium carbonate was the most effective in reducing the deterioration by calcium hydroxide solution.

In the previous research, the swelling-deformation tests conducted right after mixing. However, in the actual environment, it will take a long time to reach the leached ions from the surrounding cement-based materials to the bentonite. So, we have to investigate the aging effect of the mixing of the admixture in the bentonite. In this study, we investigated the time-dependent effect of mixing by comparing the results from the specimens tested right after mixing and after 1 year from the mixing in terms of the swelling characteristics of bentonite. Here, we prepared the bentonite specimens mixed with silica fume or sodium carbonate. Then, we also used the swelling-deformation tests proposed by Komine and Ogata [5], [6] and measured the swelling-deformation of the bentonite specimens in the saturated aqueous solution of calcium hydroxide or deionized water.

OUTLINE OF EXPERIMENTS

Materials

Table 1 shows the outline of specimens. In this study, we used silica fume or sodium carbonate as an admixture. Then, we prepared three kinds of specimens; pure bentonite without admixtures, bentonite mixed with silica fume, and bentonite mixed with sodium carbonate. This study used the commercial bentonite, called Kunigel-V1, extracted from the Tsukinuno Mine in Japan. This study used silica fume as an admixture. The 94.9% of silica fume was SiO_2 . And, its specific surface was $17.5 \text{ m}^2/\text{g}$. This study also used commercial sodium carbonate. Its content of sodium carbonate was 99.8%.

In the case of the young specimens tested just after mixing (experiment in the previous research [3]), the mixing ratios of silica fume to dry bentonite were 0.5, 1.0, 2.0, 5.0, 8.0 mass% while the mixing ratios of sodium carbonate were 0.2, 0.5, 1.0, 4.0 mass%. In the case of the aged specimens 1 year after mixing, the mixing ratios of silica fume to dry bentonite were 0.5, 1.0, 2.0 mass%, while the mixing ratios of sodium carbonate were 0.5, 1.0, 4.0 mass%. The water content of specimen in the both cases was set to 21 % by considering the planned value in the design of a subsurface radioactive waste repository for low level wastes in Japan.

In this paper, the names of specimens indicated the composition of the materials, the mixing ratio of admixture, and the type of solution. (W: distilled water, CH: saturated calcium hydroxide solution and calcium hydroxide powder). In the case of the aged specimens 1 year after the mixing, the asterisk (*) was attached at the end of the specimen name.

Mixing of Materials

The mixing procedures were as follows. Firstly, air-dried bentonite and admixture were mixed at low speed for 30 seconds using an Omni mixer. During the mixing, water contents of these mixtures were adjusted during low speed mixing. Here, we sprayed distilled water. After that, they were mixed at high-speed for 60 seconds. Then, they were kept in a polyethylene bag for 24 hours. In the next day, these mixtures were mixed at high-speed for 60 seconds again, and we measured water contents of these mixtures. Then, the samples were kept again in a polyethylene bag about one year. The temperature of the storage environment is 20°C . The relative humidity is 60%.

Specimens

In this study, the cylindrical specimens having diameters of 60mm and heights of 5mm were

Table1 Outline of specimens

Names of specimens	Material composition [mass%]			Type of solution	Timing of test
	Be	SF	Na_2CO_3		
Be-W	100.0	-	-	distilled water	just after mixing
BeSF-0.5-W	99.5	0.5	-		
BeSF-2-W	98.0	2.0	-		
BeSF-3-W	97.0	3.0	-		
BeSF-5-W	95.0	5.0	-		
BeSF-8-W	92.0	8.0	-	saturated calcium hydroxide solution with calcium hydroxide powder	just after mixing
Be-CH	100.0	-	-		
BeSF-0.5-CH	99.5	0.5	-		
BeSF-1-CH	99.0	1.0	-		
BeSF-2-CH	98.0	2.0	-		
BeSF-5-CH	95.0	5.0	-		
BeSF-8-CH	92.0	8.0	-		
BeN2C-0.2-CH	99.8	-	0.2		
BeN2C-0.5-CH	99.5	-	0.5		
BeN2C-1-CH	99.0	-	1.0		
BeN2C-4-CH	96.0	-	4.0		
BeSF-0.5-CH*	99.5	0.5	-	saturated calcium hydroxide solution with calcium	1y after mixing
BeSF-1-CH*	99.0	1.0	-		
BeSF-2-CH*	98.0	2.0	-		
BeN2C-0.5-CH*	99.5	-	0.5		
BeN2C-1-CH*	99.0	-	1.0		
BeN2C-4-CH*	96.0	-	4.0		

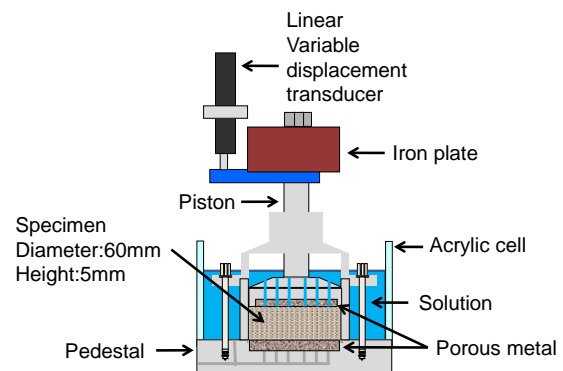


Fig.1 Schematic drawing of test apparatus

prepared. The height of the specimens was small to save time for water absorption because the compacted bentonite specimens have low conductivities. The dry density was set to $1.3\text{g}/\text{cm}^3$ to easily assess deterioration. The sample was statically compacted by vertical pressure for several hours until the height of specimens became 5mm.

Swelling Deformation Test

Figure 1 shows the test apparatus. Swelling characteristics of the bentonite specimens were evaluated by using the one-dimensional swelling deformation test under a constant vertical pressure proposed by Komine and Ogata [5,6]. An iron plate was fixed to the top of the piston applying the constant vertical pressure. We used a filter paper ($\phi 60\text{mm} \times 0.19\text{mm}$), and a porous metal ($\phi 60\text{mm} \times$

5mm) as filter. The filters were placed below the top cap and on the pedestal. They were used for mitigating the outflow of bentonite particles from specimens. After applying the prescribed vertical pressure (10kPa) to the specimen, aqueous solutions were supplied to the specimen. Then, the relationship between the axial swelling deformation and the time required from the start of water supply was then measured.

The solution supplied to the specimens was the saturated aqueous solutions of calcium hydroxide to discuss the effects of calcium ions leached from cement-based materials. And the solution was included additional calcium hydroxide powders to keep saturated concentration during the swelling tests.

In the cases of specimens of the pure bentonite without admixtures and the bentonite mixed with silica fume, the temperature during the experiments was set to 40 °C in order to promote pozzolanic reaction of silica fume. In the case of specimens of the bentonite mixed with sodium carbonate, the temperature was set to 20°C. They were determined by considering the experimental condition in the previous studies [2]-[4].) The solution was supplied from one side of specimens in this study. The method is same as the previous study [2]-[4]. Measurement period it was decided to be 7 days. It was longer than the previous study conducted by Nakarai and Shimakura [2] to improve the accuracy of data.

Evaluation Method

The swelling strain (%) is defined by

$$\varepsilon_s = \frac{\Delta S}{H_0} \times 100 \quad (1)$$

where ε_s is swelling strain (%), ΔS is swelling deformation, and H_0 is initial specimen height.

It is known that the curves of swelling strain versus time can be approximated by the hyperbola in Eq.(2) [4], [5]. The maximum swelling strain ε_{smax} (%) is obtained from the asymptotic line of the hyperbola, and can be calculated by Eq.(3)

$$\varepsilon_s(\text{time}) = \frac{\text{time}}{a + b\text{time}} [\%] \quad (2)$$

$$\varepsilon_{smax} = \lim_{\text{time} \rightarrow \infty} \varepsilon_s(\text{time}) = \frac{1}{b} [\%] \quad (3)$$

where “time” is the duration (in day) from the start of water supply, $\varepsilon_s(\text{time})$ is swelling strain at “time”, and a and b are constants determined by fitting procedures.

X-ray Diffraction Analysis

The components of specimen after the swelling deformation test were examined by X-ray diffraction. The specimen was mixed with α -Alumina (Corundum), whose volume was 10% of the sample for the XRD measurement, as a standard substance. The data was analyzed by using SIROQUANT Ver.3 to detect the mineral components from the measured peak.

RESULTS AND DISCUSSIONS

Aging Effect of Mixing of Admixture

Effect of silica fume as an admixture

Fig.2 shows the relationship between the calculated maximum swelling strain and the mixing ratio of the silica fume (included the results of the previous research [3], [4]). Here, the solid and broken lines in the figure show the predicted maximum swelling strain in W and CH, respectively. They were predicted from the maximum swelling strain of the pure bentonite specimens and the mixing ratio as references for the discussions. Fig.3 shows the results of the swelling-deformation tests for investigating the aging effect on the swelling behavior when the saturated calcium hydroxide solution (CH) was supplied to the specimens which were mixed with silica fume about 1 year ago.

According to Fig.3, in the case of the young specimens, it was found that the maximum swelling strain of specimens mixed with silica fume (0.5 ~ 5.0 mass%) became larger than the predicted maximum swelling strain indicated by the solid line. It means that the mixing of silica fume can reduce the deterioration of bentonite by alkali. Especially, the mixing of 1mass% of silica fume was most effective to suppress the deterioration. When we mixed silica fume more than 1mass%, the maximum swelling strain gently decreased as mixing ratio of silica fume increase. It was caused by the decrease in the bentonite proportion in the specimen and solidification associated with the pozzolanic reaction of silica fume in the water.

In the case of the aged specimens 1 year after mixing, the mixing of 0.5 ~ 2.0 mass% of silica fume was effective to suppress the deterioration of bentonite by the calcium hydroxide solution. However, in these aged specimens, the effect of the mixing on the degradation of swelling performance of the bentonite tended to be smaller than in the case of the young specimens tested just after mixing.

In the case of the young specimens, the mixing of

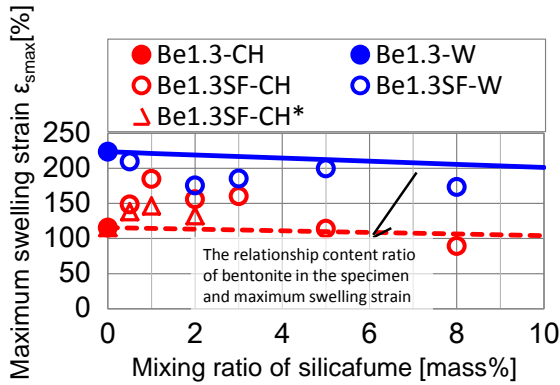


Fig.2 Relationship between maximum swelling strain and mixing ratio of silica fume

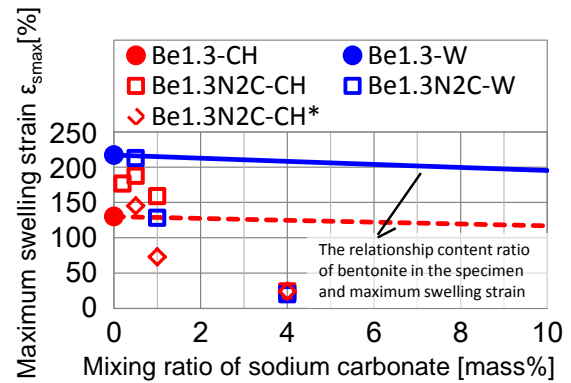


Fig.4 Relationship between maximum swelling strain and mixing ratio of sodium carbonate

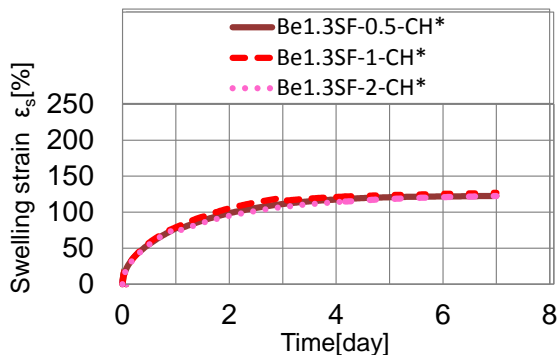


Fig.3 Curves of swelling strain versus time

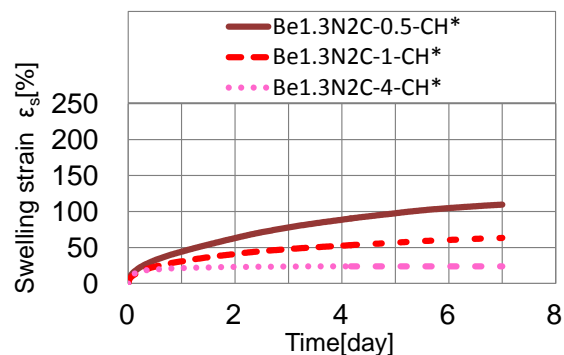


Fig.5 Curves of swelling strain versus time

1mass% of silica fume was most effective to suppress the deterioration. But in the case of the aged specimens 1 year after mixing, the effect of suppressing the deterioration was all most same regardless of the mixing ratio of the silica fume.

Effect of sodium carbonate as an admixture

Fig.4 shows the relationship between the calculated maximum swelling strain and the mixing ratio of sodium carbonate (included the results of the previous research [3], [4]). Here, the solid and broken lines in the figure also show the predicted maximum swelling strain in W and CH, respectively. Fig.5 shows the results of the swelling-deformation tests when the saturated calcium hydroxide solution (CH) was supplied to the specimens, which were mixed with sodium carbonate about 1 year ago.

According to Fig.4, in the case of the young specimens, it was found that the maximum swelling strain of specimens mixed with sodium carbonate (0.2 ~ 1 mass%) became larger than the predicted maximum swelling strain indicated by the solid line. It means that the mixing of sodium carbonate can reduce the deterioration of bentonite by alkali. Especially, the mixing of 0.5mass% of sodium carbonate was most effective to suppress the

deterioration. But, it was found that the swelling strain of Be1.3N2C-1-CH was greater than that of Be1.3N2C-1-W. It was supposed to be caused by the decrease in the ionic strength of the pore water in the particles associated with the precipitation of calcite.

In the case of the aged specimens 1 year after mixing, the mixing of 0.5mass% of sodium carbonate was only effective to suppress the deterioration of bentonite by the calcium hydroxide solution.

However, in the case of the aged specimens, the effect of the mixing on the degradation of swelling performance of the bentonite also tended to be smaller than the young specimens tested just after mixing.

Finally, we examined the component of the specimens after the swelling-deformation test using the X-ray diffraction (XRD) analysis. Figs. 6, 7 show the results of this XRD analysis. Since the dry densities of the specimens in Figs. 6 and 7 were not same, the ratio of the components in the specimens will be discussed here.

According to the results obtained by XRD analysis, the amount of the montmorillonite in the aged specimen tested 1 year after mixing sodium carbonate was significantly smaller than in the case

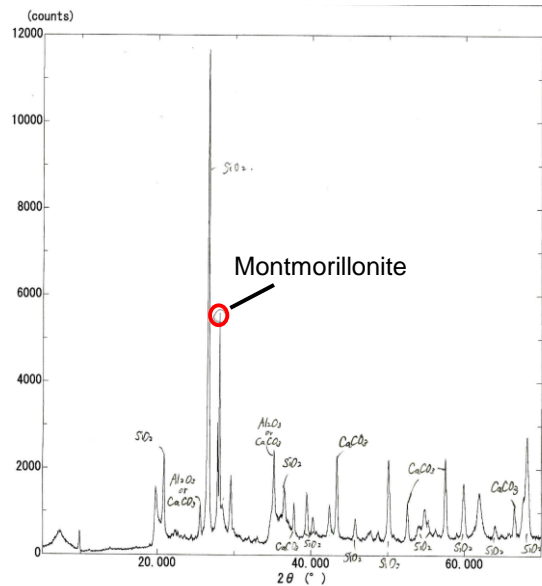


Fig.6 Result of XRD analysis (Be1.6N2C-4-CH)

of the young specimens tested just after mixing. Therefore, the decreasing the effect of suppress the deterioration of the bentonite was thought to be caused by the decreasing of the amount of the montmorillonite as a source of the swelling in the specimen.

CONCLUSIONS

In this study, we investigated the effect of admixtures such as silica fume and sodium carbonate in order to develop new composite materials suppressing the deterioration by alkali solution from the viewpoint of swelling performance in the engineered barrier system for nuclear waste management. The performance was evaluated based on the swelling deformation of specimens measured in the distilled water and the saturated calcium hydroxide solution. Then, the following conclusions were drawn from the results of the experiments.

(1) In the case of the young specimens tested just after mixing, the mixing of small amount of silica fume or sodium carbonate can reduce the deterioration of the bentonite in alkaline water.

(2) In the case of the aged specimens 1 year after mixing, the effect of the mixing on the degradation of swelling performance of the bentonite tended to be smaller than in the case of the specimens tested just after mixing regardless of the type of admixtures.

REFERENCES

- [1] Japan Society of Civil Engineers, "The method for setting nuclide migration assessment scenario in safety assessment of sub-surface

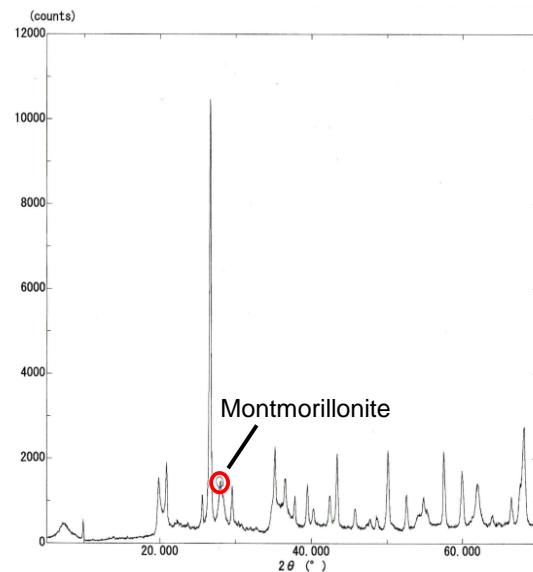


Fig.7 Result of XRD analysis (Be1.3N2C-4-CH*)

parameter used in groundwater migration disposal," 2008. (in Japanese)

- [2] K. Nakarai, and C. Shimakura: "Swelling deformation of the bentonite mixed with pozzolanic materials in calcium hydroxide solution," Proceedings of 46th Conference of the Japanese Geotechnical Society, pp.2089-2090, 2011. (in Japanese)
- [3] Y. Yokoyama, and K. Nakarai: "Swelling deformation of the bentonite mixed with silica fume or sodium carbonate in calcium hydroxide solution," Proceedings of 9th Conference of the Japanese Geotechnical Society Branch of Kanto, material3-2, 2012. (in Japanese)
- [4] Y. Yokoyama, and K. Nakarai: "Swelling deformation of the bentonite mixed with silica fume or sodium carbonate in calcium hydroxide solution," Second International Conference on Geotechnique, Construction Materials and Environment, pp.172-175, 2012.
- [5] H. Komine, and H. Ogata, "Experimental study on swelling characteristics of compacted bentonite," Canadian Geotechnical Journal, Vol.31, No.4, pp.478-490, 1994.
- [6] H. Komine, and H. Ogata, "Experimental study on swelling characteristics of sand-bentonite mixture for nuclear waste disposal," Soils and Foundations, Vol.39, No.2, pp.83-97, 1999.
- [7] K. Nakarai, M. Watanabe, H. Ishii, K. Koibuchi: "Reducing the deterioration between cement and bentonite by mixing with Na_2CO_3 ," Proceedings of the 66th Annual Conference of the Japan Society of Civil Engineers, pp.99-100, 2011.

USE OF FULLY SOFTENED VERSUS PEAK STRENGTH TO PREDICT THE CAPACITY OF FOOTINGS ON GEOSYNTHETIC REINFORCED SOIL

Melia K. Iwamoto¹, Phillip S.K. Ooi², Jennifer E. Nicks³ and Michael T. Adams⁴

¹Graduate Research Assistant, Department of Civil and Environmental Engineering, University of Hawaii at Manoa, USA ²Professor, Department of Civil and Environmental Engineering, University of Hawaii at Manoa, USA ^{3,4}Turner-Fairbank Highway Research Center, Federal Highway Administration, USA

Abstract

A database of load tests performed on geosynthetic reinforced soil (GRS - reinforcement in this study is of the extensible variety) was developed using results of recent load tests performed on large scale GRS structures at the Federal Highway Administration's Turner Fairbank Highway Research Center as well as results from the literature. The measured capacities were compared to those predicted using the Wu and Pham [1] equation utilizing both the peak and fully softened soil shear strength parameters. It was found that the fully softened strengths yielded capacities that agreed better with the measured capacities. A rationale for this finding is that the robust reinforcement in a GRS strengthens the soil considerably causing the GRS to experience large strains prior to failure. Because the soil peak strengths are mobilized at relatively small displacements/strains even in large scale direct shear or triaxial tests compared to the GRS load tests, it is postulated that the fully softened values are more appropriate to estimate the GRS bearing capacity. A follow-on to this is that since large movements are required to fail say a GRS abutment, the design of GRS abutments will most likely be governed by the serviceability limit state rather than the ultimate limit state.

Keywords: Geosynthetic Reinforced Soil, Bearing Capacity, Fully Softened Strength and Bridge Abutments

INTRODUCTION

Geosynthetic Reinforced Soil (GRS) is defined as closely-spaced (≤ 0.3 m) layers of geosynthetic reinforcement and compacted granular fill material [2]. GRS has been used for a variety of geotechnical applications but has recently been promoted by the Federal Highway Administration (FHWA) for use as abutments for single span steel or concrete bridges in their Everyday Counts Initiative, which is focused on accelerating implementation of proven, market-ready technologies. GRS-IBS, where IBS stands for Integrated Bridge Systems, consists of a reinforced soil foundation (RSF), a GRS abutment and a GRS integrated approach (Fig. 1). The RSF consists of granular fill compacted and encapsulated in geotextile. The RSF provides embedment and increases the bearing width and capacity of the GRS abutment. The GRS abutment provides load-bearing support for the bridge, which is placed directly on the abutment. GRS is also used to construct the integrated approach adjacent to the superstructure. GRS-IBS has the following advantages:

1. Fast and cost-effective method of bridge support. It eliminates the need for cast-in-place reinforced concrete abutments traditionally supported on deep foundations.
2. Quality compaction control can be realized since closely-spaced geosynthetics ensure backfill is placed in thin lifts.
3. Catastrophic collapse was not observed in numerous load tests carried out to failure; GRS abutments behave in a ductile fashion.

4. Can be built in variable weather with common labor, materials and equipment, and can be easily modified in the field.
5. Alleviates the "bump at the end-of-the-bridge" problem caused by differential settlement between the bridge abutment and the approach roadway. This is made possible by eliminating deep foundations, by using GRS to construct the integrated approach and by limiting its use to short, single-span integral bridge systems.
6. Enjoys all the advantages associated with an integral abutment bridge.
7. Very flexible system that is amenable to differential settlement and seismic loading.

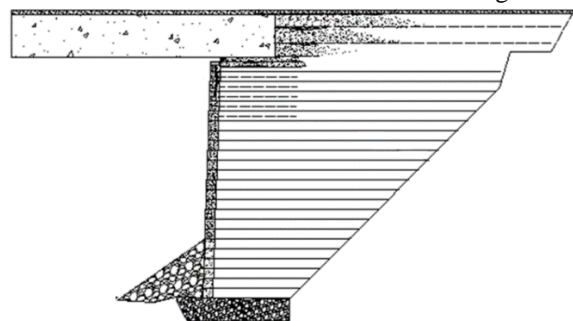


Fig. 1 Typical cross-section of a GRS-IBS [2]

Because GRS-IBS is load bearing, its capacity is an important design consideration. Many studies of the bearing capacity of strip footings supported on RSF [3]-[11] consider the RSF to extend horizontally on both sides of the footing. In the case of a GRS-IBS, the ground is limited on one side and the bearing capacity of the bridge footing on a GRS abutment wall must be known. Work in this area is rather limited. One exception is the work by Pham

[12], who performed plane strain load tests on GRS and who derived an expression for the bearing capacity of a footing on a GRS wall. The applicability of this expression is examined using results from an extensive series of load tests performed at FHWA's Turner-Fairbank Highway Research Center (TFHRC) as well as those from the literature.

Motivation for This Study

Christopher et al. [13] proposed that peak strengths of the backfill should be used when predicting bearing capacity of footings on mechanically stabilized earth (MSE) type bridge abutments reinforced using extensible elements. However, it was observed that the peak strength from large scale direct shear (LSDS) tests on granular soils in this study was mobilized at about 13 to 16 mm lateral displacements, which correspond to about 4.5 to 5.4% shear strain for a 0.3 m x 0.3 m x 0.2 m high direct shear sample. Also, the peak strength from large scale (0.15 m diameter x 0.3 m high) triaxial tests on granular soils was mobilized at about 2.3 to 5.0% axial strain [12]. As will be presented later, load tests on GRS with closely spaced (< 0.3 m) reinforcement having a wide width tensile strength of at least 70 kN/m generally fail at strains greater than 10%, implying that the soil shear strength is then past its peak.

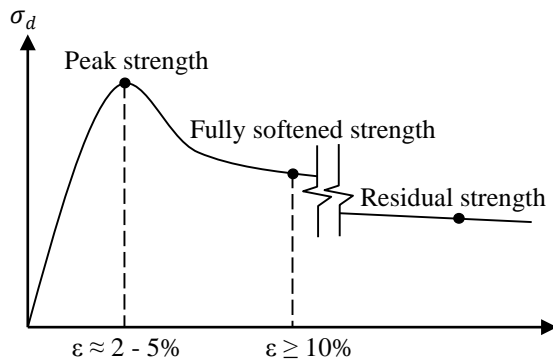


Fig. 2 Typical stress-strain curve

The notion of using fully softened strength is not new in geotechnical engineering. Duncan and Wright [14] recommend the use of fully softened strength when analyzing the stability of cuts in heavily overconsolidated soil. The rationale for this is that swelling and softening was found to have occurred along the slip surfaces during forensic studies of such slides and use of fully softened strength, or the strength if the soil was normally consolidated, provided better agreement when back-calculating the factors of safety in these failed slopes. Wu [15] indicated that the fully softened strength is typically mobilized at strains on the order of 10%. In the case of GRS, the reinforcement strengthens the soil and forces failure to occur very often at double-digit strains (see TF test series in

Table 1). Therefore, in the interest of preserving strain compatibility, a study was conducted to see whether fully softened strengths will provide a better prediction of the bearing capacity of footings on GRS abutments than peak strengths.

BEARING CAPACITY EQUATION OF A FOOTING ON A GRS ABUTMENT WALL

Pham [12] derived the bearing capacity of a footing on a GRS abutment wall (q_{ult}) as follows:

$$q_{ult} = \left(\sigma_h + W \frac{T_f}{S_v} \right) K_p + 2c\sqrt{K_p} \quad (1)$$

where σ_h is the lateral stress, T_f and S_v are the reinforcement strength and spacing, respectively, c is the soil cohesion, K_p is the Rankine passive earth pressure coefficient, defined as

$$K_p = \frac{1 + \sin \phi}{1 - \sin \phi} \quad (2)$$

ϕ is the soil friction angle. W is a dimensionless factor that amplifies the contribution of S_v to the GRS capacity, and was semi-empirically derived as

$$W = 0.7 \frac{S_v}{d_{max}} \quad (3)$$

where d_{max} is the maximum particle size of the GRS backfill. Note that the 0.7 factor was theoretically derived using the concept of "average stresses" proposed by Ketchart and Wu [16] while the exponent was empirically derived. For details on this derivation, refer to [12].

For a GRS wall with dry stacked modular block facing, σ_h = lateral stress exerted by the facing on the GRS mass, defined by Pham [12] as

$$\sigma_h = \gamma_{bl} D \tan \delta \quad (4)$$

where γ_{bl} = bulk unit weight of facing block = weight of block/volume of block assuming it is not hollow, D = depth of facing block perpendicular to the wall face and δ = friction angle between geosynthetic reinforcement and the top and bottom surface of the facing block.

GRS versus MSE

Mechanically stabilized earth (MSE) differs from GRS in many respects. The most significant difference involves the maximum reinforcement spacing (0.3 m in GRS versus 0.8 m in MSE). The basic MSE design premise is that each reinforcement layer is responsible for equilibrium within the reinforcement tributary area; i.e.; $\sigma_h = T_f/S_v$. Implied in this equation is that a GRS with reinforcement strength T_f at spacing S_v will behave the same as a GRS with reinforcement strength $2T_f$ at spacing $2S_v$, which has been shown to be untrue

by Adams et al. [17] and Pham [12]. Instead, S_v has a bigger influence on the bearing capacity than T_f . This led Pham to propose the addition of the W term in Eq. 1, without which, the equation is the expression for the bearing capacity of a footing on a MSE abutment wall.

APPLICABILITY OF BEARING CAPACITY EQUATION

Considering that most of the load tests in the database were performed on GRS columns (mostly square with some circular in plan) while a bridge footing resting on an abutment more resembles a plane strain (PS) condition, the relationship between the column tests and that of a strip footing loading the top of a GRS wall is of interest. Assume that the strength of a GRS column can be represented by the Mohr-Coulomb equation as follows:

$$\tau = c_{GRS} + \sigma \tan \phi_{GRS} \quad (5)$$

where τ = shear strength, σ = applied normal stress, c_{GRS} and ϕ_{GRS} = cohesion and friction angle of the GRS composite, respectively. In an unconfined compression load or Performance Test (PT), where the facing has been removed, the ultimate capacity of the GRS column ($q_{ult,PT}$) can be expressed as

$$q_{ult,PT} = 2c_{GRS} \quad (6)$$

For the PS condition, the bearing capacity of a footing supporting the bridge superstructure can be estimated using Meyerhof's [19] solution for a rough strip bearing on top of a slope

$$q_{ult,PS} = c_{GRS}N_{cq} + 0.5\gamma_{GRS}bN_{\gamma q} \quad (7)$$

where $q_{ult,PS}$ = ultimate capacity of strip footing under PS conditions, γ_{GRS} = unit weight of the GRS backfill, b = footing width, and N_{cq} and $N_{\gamma q}$ = Meyerhof's [19] bearing capacity factors for a strip footing with a rough base. $N_{\gamma q}$ approaches zero when the slope angle is 90° for a GRS abutment wall; thus Eq. (7) reduces to

$$q_{ult,PS} = c_{GRS}N_{cq} \quad (8)$$

Dividing Eq. (8) by (6), the ratio of the bearing capacity of a strip footing on top of a GRS abutment to that of a GRS column can be estimated as

$$\frac{q_{ult,PS}}{q_{ult,PT}} = \frac{N_{cq}}{2} \quad (9)$$

For a surface footing on top of a vertical GRS abutment, the value of N_{cq} varies with the footing offset from the edge of the wall face, a , wall height, H , footing width, b , and stability factor, $N_s = \frac{\gamma_{GRS}H}{c_{GRS}}$,

as shown in Fig. 3. c_{GRS} can be obtained from laboratory or numerical experiments.

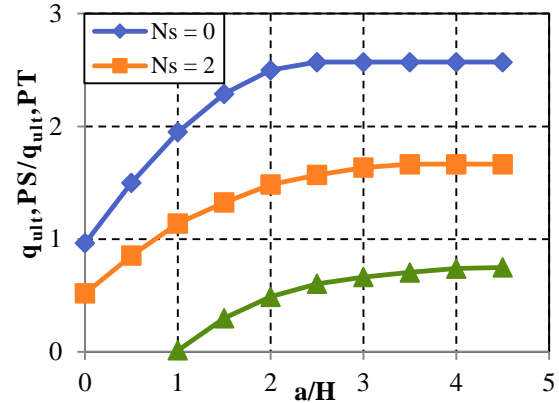


Fig. 3 Variation of N_{cq} with footing geometry and the stability factor.

For example, Pham [12] conducted a series of plane strain load tests on 1.94-m-high GRS that can be used to derive a cohesion value for the GRS. Two of the tests (GSGC2 and 5 in Table 1) were identical in every respect (Tensile strength of reinforcement = 70 kN/m, Reinforcement spacing = 0.2 m, Backfill $c = 70$ kPa and $\phi = 50^\circ$) except for the confining stresses (0 in GSGC5 and 34 kPa in GSGC2). The corresponding failure stresses were 2032 and 3396 kPa for the 0 and 34 kPa confining stresses, respectively. The resulting shear strength parameters for the GRS are $c_{GRS} = 160$ kPa and $\phi_{GRS} = 72^\circ$. The corresponding stability factor $\gamma H/c \approx 0.29$. Based on this stability factor, the ratio of plane strain capacity for a typical GRS abutment with a typical set-back $a = 0.2$ m and H varying from 3 m to 10 m (i.e. $a/H = 0.02$ to 0.07) to column (PT) capacity is close to unity. Therefore, the column PT is fairly representative of an in-service PS condition for well-graded gravels in this case.

LOAD TESTS

Eleven GRS load tests performed at FHWA's TFHRC (designated as "TF") with and without cast masonry unit or CMU facing that was frictionally connected to the geosynthetic are reported in Table 1. Each CMU block was 0.194-m-high x 0.397-m-long x 0.194-m-wide (Fig. 4a). A schematic of tests TF-1, 2, 6, 9 and 12, each 10 blocks high, is shown in Figs. 4b to 4d. Tests TF-4, 7, 10 and 11 have a similar set-up except the blocks were removed prior to testing. TF-14 (Fig. 4e) has the same area in plan but was slightly taller ($H = 2.0$ m) with 7 pairs of full- and half-height blocks. TF-13 is identical to 14 except the blocks were removed. Details of the geotextile and soil utilized are summarized in Table 1 along with other tests collected from the literature giving a total of 28 load tests in this database.

Table 1 Test parameters of GRS performance tests selected from literature and available studies

Test	d _{max} m	USCS Symbol	ϕ_{peak} °	c _{peak} kPa	ϕ_{fs} °	c _{fs} kPa	Strength Test Type	T _f kN/m	S _v m	Facing Type	σ_h kPa	Boundary Conditions	q _{ult,emp} kPa	ϵ_f^1 %	Reference
GSGC2 ²	0.0330	GS-GM	50	70	41	118	TX ³	70	0.2	⁴	34	Plane Strain	3396	6.5	[12]
GSGC3 ²	0.0330	GS-GM	50	70	41	118	TX ³	140	0.4	⁴	34	Plane Strain	2038	6.1	[12]
GSGC4 ²	0.0330	GS-GM	50	70	41	118	TX ³	70	0.4	⁴	34	Plane Strain	1783	4.0	[12]
GSGC5 ²	0.0330	GS-GM	50	70	41	118	TX ³	70	0.2	None	0	Plane Strain	2032	6.0	[12]
Elton1	0.0127	SP	40	28	41	27	DS ⁵	9	0.15	None	0	Cylindrical Column	230	1.7	[18]
Elton2	0.0127	SP	40	28	41	27	DS ⁵	9	0.3	None	0	Cylindrical Column	129	3.1	[18]
Elton3	0.0127	SP	40	28	41	27	DS ⁵	14	0.2	None	0	Cylindrical Column	306	3.9	[18]
Elton4	0.0127	SP	40	28	41	27	DS ⁵	15	0.2	None	0	Cylindrical Column	292	4.5	[18]
Elton5	0.0127	SP	40	28	41	27	DS ⁵	19	0.2	None	0	Cylindrical Column	402	4.7	[18]
Elton6	0.0127	SP	40	28	41	27	DS ⁵	20	0.2	None	0	Cylindrical Column	397	7.7	[18]
Elton7	0.0127	SP	40	28	41	27	DS ⁵	25	0.2	None	0	Cylindrical Column	459	8.5	[18]
VS-1 ⁶	0.0127	GP	54	23	51	0	LSDS ⁷	70	0.2	CMU	1.82	Square Column	1116	8.0	[20]
VS-2 ⁶	0.0191	GP	46	19	45	0	LSDS ⁷	70	0.2	CMU	1.82	Square Column	1087	7.1	[20]
VS-5 ⁶	0.0127	GP	51	0	51	0	LSDS ⁷	70	0.2	CMU	1.82	Square Column	1031	10.4	[20]
MPA ⁸	0.0254	GW-GM	54	75	53	0	LSDS ⁷	70	0.6	None	0	Square Column	225	1.9	[17]
MPB ⁸	0.0254	GW-GM	54	75	53	0	LSDS ⁷	70	0.4	None	0	Square Column	170	2.2	[17]
MPC ⁸	0.0254	GW-GM	54	75	53	0	LSDS ⁷	20	0.2	None	0	Square Column	460	6.4	[17]
TF-1	0.0127	GP	53	69	55	0	LSDS ⁷	35	0.2	CMU	1.82	Square Column	981	10.9	[20]
TF-2	0.0254	GW-GM	54	75 ⁹	53	0	LSDS ⁷	35	0.2	CMU	1.82	Square Column	1209	11.5	[20]
TF-3	0.0254	GW-GM	54	75 ⁹	53	0	LSDS ⁷	35	0.2	None	0	Square Column	837	13.8	[20]
TF-6	0.0254	GW-GM	54	75 ⁹	53	0	LSDS ⁷	70	0.2	CMU	1.82	Square Column	2095	15.7	[20]
TF-7	0.0254	GW-GM	54	75 ⁹	53	0	LSDS ⁷	70	0.2	None	0	Square Column	1271	12.5	[20]
TF-9	0.0254	GW-GM	54	75 ⁹	53	0	LSDS ⁷	70	0.4	CMU	0.91	Square Column	1068	15.6	[20]
TF-10	0.0254	GW-GM	54	75 ⁹	53	0	LSDS ⁷	70	0.4	None	0	Square Column	494	14.3	[20]
TF-11	0.0254	GW-GM	54	75 ⁹	53	0	LSDS ⁷	20	0.1	None	0	Square Column	1113	12.8	[20]
TF-12	0.0254	GW-GM	54	75 ⁹	53	0	LSDS ⁷	20	0.1	CMU	1.82	Square Column	1390	13.4	[20]
TF-13	0.0254	GW-GM	54	75 ⁹	53	0	LSDS ⁷	53	0.3	None	0	Square Column	620	12.3	[20]
TF-14	0.0254	GW-GM	54	75 ⁹	53	0	LSDS ⁷	53	0.3	CMU	2.73	Square Column	1128	12.7	[20]

Notes: 1. ϵ_f = Strain of GRS load tests at failure

2. GSGC = Generic Soil-Geosynthetic Composite

3. TX = Consolidated drained triaxial compression tests on 0.15-m-diameter and 0.3-m-high samples

4. No facing was used. Instead, a confining pressure = 34 kPa was applied using a rubber membrane wrapped all around the GRS

5. DS = direct shear test. Because soil was SP, direct shear sample was 0.063 m diameter performed in accordance with ASTM D3080

6. VS = Performance tests conducted in Defiance County, OH as part of the FHWA's Every Day Counts GRS Validation Sessions

7. LSDS = Large Scale Direct Shear tests on 0.3 m by 0.3 m by 0.2 m high specimen

8. MP = Mini pier tests or more widely referred to herein as performance tests

9. Best fit linear Mohr-Coulomb envelopes for soil used in TF-2 through TF-14 yielded values of cohesion of 75 kPa and 6 kPa, respectively for the partially saturated and saturated samples. A cohesion of 75 kPa was used when estimating the GRS capacity since soil was partially saturated during load testing in FHWA's TFHRC laboratory.

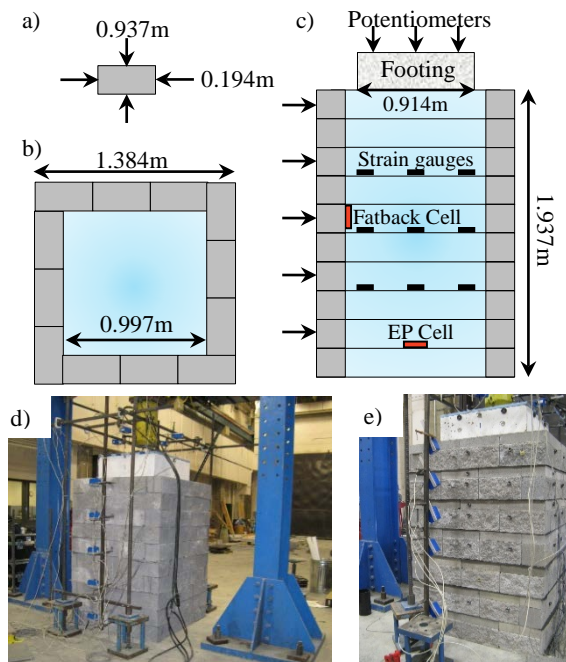


Fig. 4 (a) CMU dimensions; (b) and (c) schematic of TF 1, 2, 6, 9, and 12; (d) photo of TF-6; (e) photo of TF-14

Results

The ultimate bearing capacities of the 28 load tests were predicted using Eq. 1 and both the backfill's peak and fully softened shear strength parameters. Table 2 contains the predicted capacities ($q_{ult,peak}$ and $q_{ult,fs}$) along with the measured capacities ($q_{ult,emp}$). Also shown in Table 2 are the bias defined as the ratio of the measured to predicted capacities. The mean, standard deviation and coefficient of variation (COV) of the bias are shown at the bottom of Table 2.

The mean bias using peak strengths was 0.79 with a COV of 36%. Fig. 5a contains the corresponding plot of the histogram and normal distribution of the bias while Fig. 5b shows a plot of the predicted versus measured capacities. Clearly, Eq. 1 over-predicts the GRS capacity when using peak strengths.

In contrast, the mean bias using fully softened strengths was 1.00 with a coefficient of variation (COV) of 32%. Fig. 6a contains the corresponding plot of the histogram and normal distribution of the bias while Fig. 6b shows a plot of the predicted versus measured capacities where the data points are more centered around the line of equality. Based on these results, Eq. 1 along with the use of fully softened strengths yield a bias that is close to unity with a slightly smaller COV compared to the use of peak strengths for this dataset.

Hypothesis testing on the normal distribution of the bias indicate that using Eq. 1 and fully softened strengths will result in a mean bias of 1.0, with a

90% confidence that the bias will be within 3 standard deviations of the mean.

Table 2 Predicted ultimate bearing capacities of footings on GRS using peak and fully softened strengths

Test	$q_{ult,emp}$ kPa	$q_{ult,peak}$ kPa	$q_{ult,fs}$ kPa	Bias	
				Peak	FS
GSGC2	3396	2511	1885	1.35	1.80
GSGC3	2038	1957	1529	1.04	1.33
GSGC4	1783	1294	1102	1.38	1.62
GSGC5	2032	2260	1723	0.90	1.18
Elton1	230	250	252	0.92	0.91
Elton2	129	151	150	0.86	0.86
Elton3	306	325	329	0.94	0.93
Elton4	292	333	337	0.88	0.87
Elton5	402	393	398	1.02	1.01
Elton6	397	416	422	0.95	0.94
Elton7	459	486	494	0.94	0.93
VS-1	1116	1587	1159	0.70	0.96
VS-2	1087	1329	1155	0.82	0.94
VS-5	1031	1159	1159	0.89	0.89
MPA	225	717	259	0.31	0.87
MPB	170	1085	620	0.16	0.27
MPC	460	1070	606	0.43	0.76
TF-1	981	1080	734	0.91	1.34
TF-2	1209	1528	1055	0.79	1.15
TF-3	837	1511	1038	0.55	0.81
TF-6	2095	2585	2093	0.81	1.00
TF-7	1271	2568	2077	0.49	0.61
TF-9	1068	1134	668	0.94	1.60
TF-10	494	1126	660	0.44	0.75
TF-11	1113	2001	1520	0.56	0.73
TF-12	1390	2018	1536	0.69	0.90
TF-13	620	1296	828	0.48	0.75
TF-14	1128	1322	852	0.85	1.32
Mean Bias				0.79	1.00
Standard Deviation				0.28	0.32
Coefficient of Variance (%)				0.36	0.32

SUMMARY AND CONCLUSIONS

The current state of practice is to use the peak strength of the backfill material, as suggested by Christopher et al. [13]. However, the results of this study provide evidence that the fully softened strengths are more appropriate for estimating footing capacities on GRS.

Prediction of GRS bearing capacity improved by using fully softened versus peak strengths obtained from large scale direct shear and triaxial tests. Mean bias between measured and predicted values increased from 0.79 to 1.00 and the COV improved from 36% to 32%.

Fully softened strengths are more suitable for bearing capacity predictions because GRS with closely spaced reinforcement generally fail at large strains past the backfill's peak strengths. A follow-on to this is that since large movements are required to fail say a GRS abutment, the design of GRS abutments will most likely be governed by the serviceability limit state rather than the ultimate limit state.

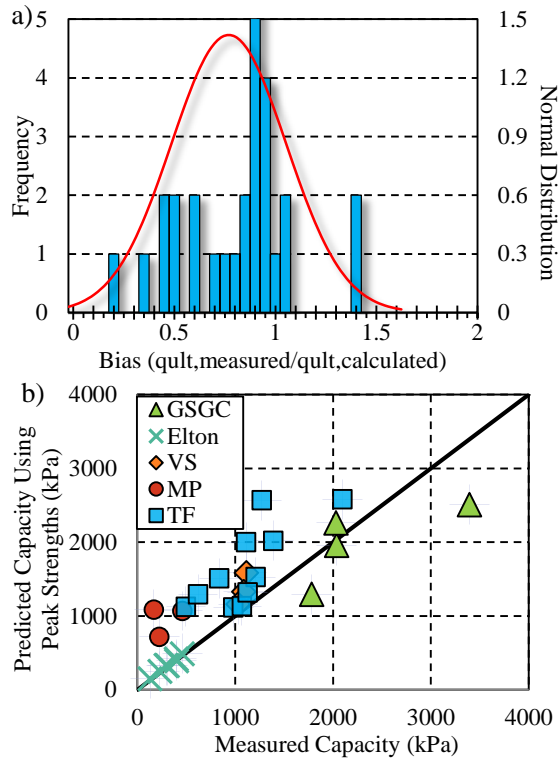


Fig. 5 (a) Histogram and normal distribution of bias using peak strength; (b) predicted versus measured capacities using peak strength

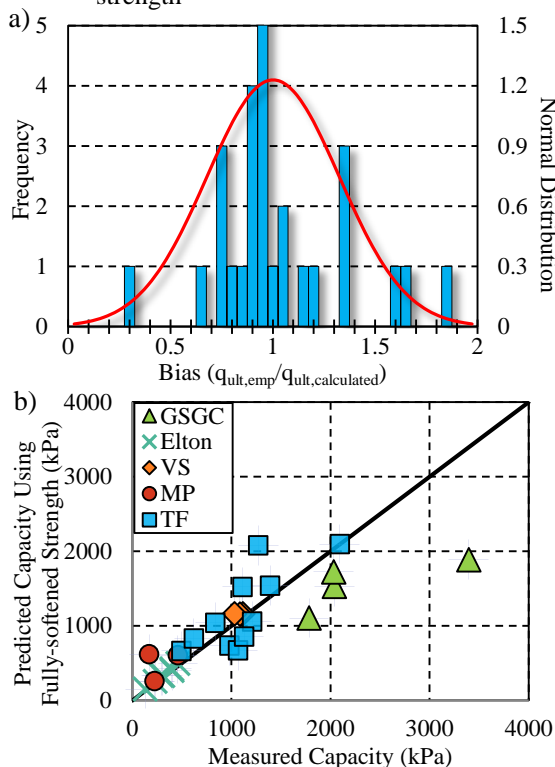


Fig. 6 (a) Histogram and normal distribution of bias using fully softened strength; (b) predicted versus measured capacities using fully softened strength

REFERENCES

- [1] Wu JTH, Pham TQ, "Load-carrying capacity and required reinforcement strength of closely-spaced soil-geosynthetic composites", *ASCE J. of Geotech. and GeoEnv. Engrg.*, Vol. 139, Jan. 2013.
- [2] Adams M, et al., *Geosynthetic Reinforced Soil Integrated Bridge System Interim Implementation Guide*. McLean: Federal Highway Administration, 2011, Report No. FHWA-HRT-11-026.
- [3] Binquet J, Lee KL, "Bearing capacity analysis of reinforced earth slabs", *ASCE J. of Geotech. Engrg. Div.*, Vol. 101, Dec. 1975, pp. 1257-1276.
- [4] Fragaszy RJ, Lawton EC, "Bearing capacity of reinforced sand subgrades", *ASCE J. of Geotech. Engrg. Div.*, Vol. 110, Oct. 1984, pp. 1500-1507.
- [5] Guido VA, Biesiadecki GL, Sullivan MJ, "Bearing capacity of geotextile reinforced foundation", in *Proc. 11th Int. Conf. on Soil Mech. and Found. Engrg.*, 1985, pp. 1777-1780.
- [6] Guido VA, Chang DK, Sweeney MA, "Comparison of geogrid and geotextile reinforced slabs", *Canadian Geotech. J.*, Vol. 23, Apr. 1986, pp. 435-440.
- [7] Huang CC, Tatsuoka F, (1988). "Prediction of bearing capacity in level sandy ground reinforced with strip reinforcement", in *Proc. Int. Geotech. Symposium on Theory and Practice of Earth Reinforcement*, 1988, pp. 191-196.
- [8] Huang CC, Tatsuoka F, "Bearing capacity of reinforced horizontal sandy ground", *Geotextiles and Geomembranes*, Vol. 9, Jan. 1990, pp. 51-82.
- [9] Karim MR, Siddiquee MSA, (2009). "Improvement of bearing capacity of strip footing on sand by using metal strip reinforcement", *J. of Civil Engrg., IEB*, Vol. 37, Dec. 2009, pp. 165-177.
- [10] Michalowski R, "Limit loads on reinforced foundation soils" *ASCE J. of Geotech. and GeoEnv. Engrg.*, Vol. 130, Apr. 2009, pp. 381-390.
- [11] Sakti JP, Das BM, "Model tests for strip foundation on clay reinforced with geotextile layers" *Trans. Res. Rec.* 1153, Transportation Research Board, 1987, pp. 40-45.
- [12] Pham TQ, "Investigating Composite Behavior of Geosynthetic Reinforced Soil (GRS) Mass", Ph.D. Thesis, University of Colorado, Denver, 2009.
- [13] Christopher B, Gill SA, Giroud JP, Juran I, Schlosser F, Mitchell JK, Dunncliff J, "Reinforced Soil Structures, Volume 1, Design and Construction Guidelines", Federal Highway Administration, Washington, D.C., Report No. FHWA-RD-89-043, Nov. 1990.
- [14] Duncan M, Wright S, *Soil Strength and Slope Stability*. Hoboken: John Wiley and Sons, Inc., 2005, Ch. 5.
- [15] Wu JTH, "Soil strength properties and their measurement", *Landslides Investigation and Mitigation*, Spec. Rep. 247, Transportation Research Board, Turner A, Schuster R, Ed. Washington, D.C., National Academy Press, 1996, pp. 319-336.
- [16] Ketchart K, Wu JTH, *Performance Test for Geosynthetic-Reinforced Soil including Effects of Preloading*. McLean: Federal Highway Administration, Office of Infrastructure R&D, 2001, Report No. FHWA-RD-01-018.
- [17] Adams MT, Ketchart K, Wu JTH, "Mini pier experiments: geosynthetic reinforcement spacing and strength as related to performance", in *Proc. Geo-Denver*, 2007.
- [18] Elton DJ, Patawaran MAB, "Mechanically stabilized earth (MSE) reinforcement tensile strength from tests of geotextile reinforced soil", Alabama Highway Research Center, Auburn University, 2005.
- [19] Meyerhof, GG, "The ultimate capacity of foundations on slopes", in *Proc. 4th Int. Conf. on Soil Mechanics and Found. Engrg.*, London, Aug. 1957, pp. 384-386.
- [20] Nicks, J.E., Adams, M.T. and Ooi, P.S.K. *Geosynthetic reinforced soil performance testing – Axial load deformation relationships*. Federal Highway Administration, Report No. FHWA-HRT-13-066, McLean, VA. 2013.

THREE DIMENSIONAL FINITE ELEMENT ANALYSIS OF SOIL NAILS IN GRANITIC SOILS

G. Ren¹ and H. Tokhi¹

¹School of Civil, Environmental and Chemical Engineering, RMIT University, 376-392 Swanston Street, Melbourne, Victoria, Australia.

Abstract: Soil nailing techniques have been widely employed in the civil engineering industry to improve the safety margin of soil slopes and excavations. In this paper, a three dimensional finite element model (FE) is developed to simulate the nail-soil interaction of soil nail during shear-box pull-out test under different overburden pressures. The behaviour of soil-nail and its interaction play an important role in overall and internal failure mechanism. The stress strain behaviour of the soil was modelled by the modified Drucker-Prager/Cap model and the interaction between the nail and soil was simulated using a penalty-type interface. The results indicate that soil nail capacity is heavily influenced by the soil-nail interaction mechanism and the shear strength developed at the soil-nail interface.

Key words: Soil nail, pull-out test, slope, surcharge, finite element.

Introduction

Soil nails have been widely used in stabilising slopes and retention systems as an efficient and economical method. Using soil nails for stabilising purposes is a relative recent development and hence the design guidelines are not fully understood and are still debated by many researchers. It is well understood that the pull-out nail resistance is influenced by factors such as the construction method, soil-nail surface interaction, soil dilation and saturation and the nail bending.

Many researchers [1,2,3] have carried out soil-nail pull-out tests. These researchers have tested physical models of grouted soil nails in typical Hong Kong soil, that is, decomposed granitic soils. The large scale pull-out tests were conducted to study the influence of factors such as grout pressure, overburden pressure and soil saturation. The large-scale pull-out tests of soil nail properly represent the behaviour of soil nail constructed in a field slope.

In this paper, a three dimensional FE model has been conducted to simulate pull-out tests of a soil nail. A general purpose FE program, ABAQUS [4] is used in this study. The soil strength and the

overburden pressures are considered in the present FE model.

Three-dimensional finite element model

The three-dimensional solid model and the finite element mesh analysed is shown in Fig.1. The model dimensions were 1mx1mx1.5m. The nail was modelled to be initially in perfect contact with the soil and the interaction between them is simulated using a penalty-type interface with a friction factor of 0.3. This type of interface sufficiently represents the frictional interaction between the soil and nail. Four noded continuum element was used in the analysis. Varying overburden pressure is applied on the top.

The problem was run in three steps. In the first step the effective self-weight of the soil material was applied using the body-force option in Abaqus. During this step, geostatic command was invoked to make sure that equilibrium was satisfied within the soil. In the second step a surcharge load was applied and the nail was pulled out in the last step. In all the steps, the loads were applied at a very slow rate to ensure effective or drained loading conditions. Also, the application of slow load will prevent the generation of excess pore water pressure anywhere within the finite element mesh.

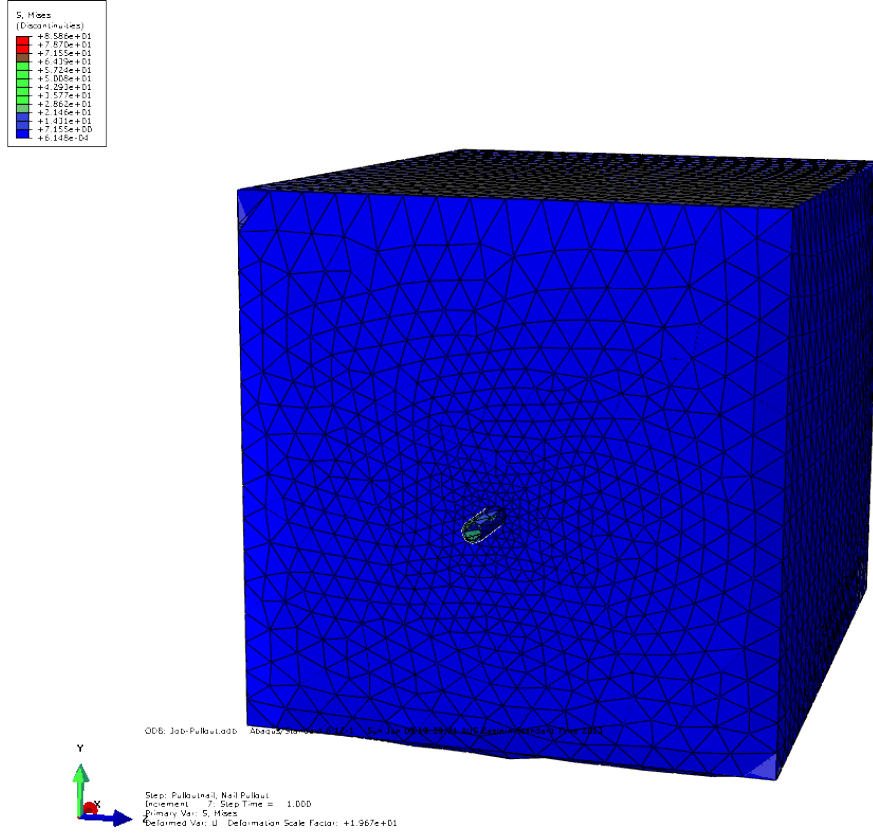


Figure 1: Three dimensional finite element model for pull out simulation.

Constitutive models and parameters

Anisotropic elastic-perfectly-plastic model using the Drucker - Prager failure criterion [13] is adopted. The model is expressed in terms of stress invariants in ABAQUS as follows:

Mean effective stress,

$$p' = \frac{\sigma'_1 + \sigma'_2 + \sigma'_3}{3} \quad 1$$

Mises equivalent stress,

$$q = \sqrt{\frac{3}{2}(S:S)} \quad 2$$

Where S = deviatoric stress and is defined as, $s = \sigma - p'I$, where I is unit tensor.

The Drucker-Prager failure surface is given by

$$F = t - p'\tan(\beta) - d = 0 \quad 3$$

Where β the soil friction angle and d is its cohesion. The yield stress on the t is given by

$$t = \frac{q}{2} \left[1 + \frac{1}{K} - \left(1 - \frac{1}{K} \right) \left(\frac{r}{q} \right)^3 \right] \quad 4$$

K = yield tension and compression stress ratio.

For tri-axial compression conditions, the Mohr-Coulomb parameters can be converted to Drucker-Prager parameters using

$$\tan(\beta) = \frac{6\sin(\phi)}{3 - \sin(\phi)} \quad 5$$

$$d = \frac{18c\cos(\phi)}{3 - \sin(\phi)} \quad 6$$

Where ϕ is the internal friction angle and c is effective cohesion of soil defined in the Mohr-Coulomb yield criterion.

Table 1: Nail and soil parameters used in FE analysis

Nail:	
Density, ρ (t/mm ³)	7.85E-9
Young's modulus, E (MPa)	210000
Poisson's ration, ν	0.2
Soil:	
Density, ρ (t/mm ³)	1.8E-9
Young's modulus, E (MPa)	30
Poisson's ration, ν	0.3
Effective cohesion, d (MPa)	0.01
Effective angle of friction, β (°)	54
Angle of dilation, (°)	2
Void ratio	0.3
Coefficient of permeability, k (m/s)	1E-5
R	1
K	0.8
α	0.01
Initial yield, $\varepsilon_{vol}^{in} _0$	0.0

Results

A three dimension finite element analysis of soil-nail pull out was conducted under soil self-weight and surcharge conditions. The soil stress and displacements are obtained from the soil-nail pull out model. The theoretical results show that the deformation and stress around the soil nail is different when compared to the conventional soil nails. Therefore, it has been shown, at least theoretically, that this failure mechanism will result in increased nail pull out capacity.

The soil parameters shown in Table 1 were adopted for the analysis and these parameters are typical for the granitic soil.

Figure 2 shown is a plane cut through the mid-section of the model. It shows the contours of the zones of high shearing. Furthermore, the relative displacements of the soil around the nail can clearly indicate that the soil-nail failure slip line is not along the soil nail interface. Therefore, it can be concluded that the nail pull out capacity inferred must be greater to the conventional soil nailing construction.

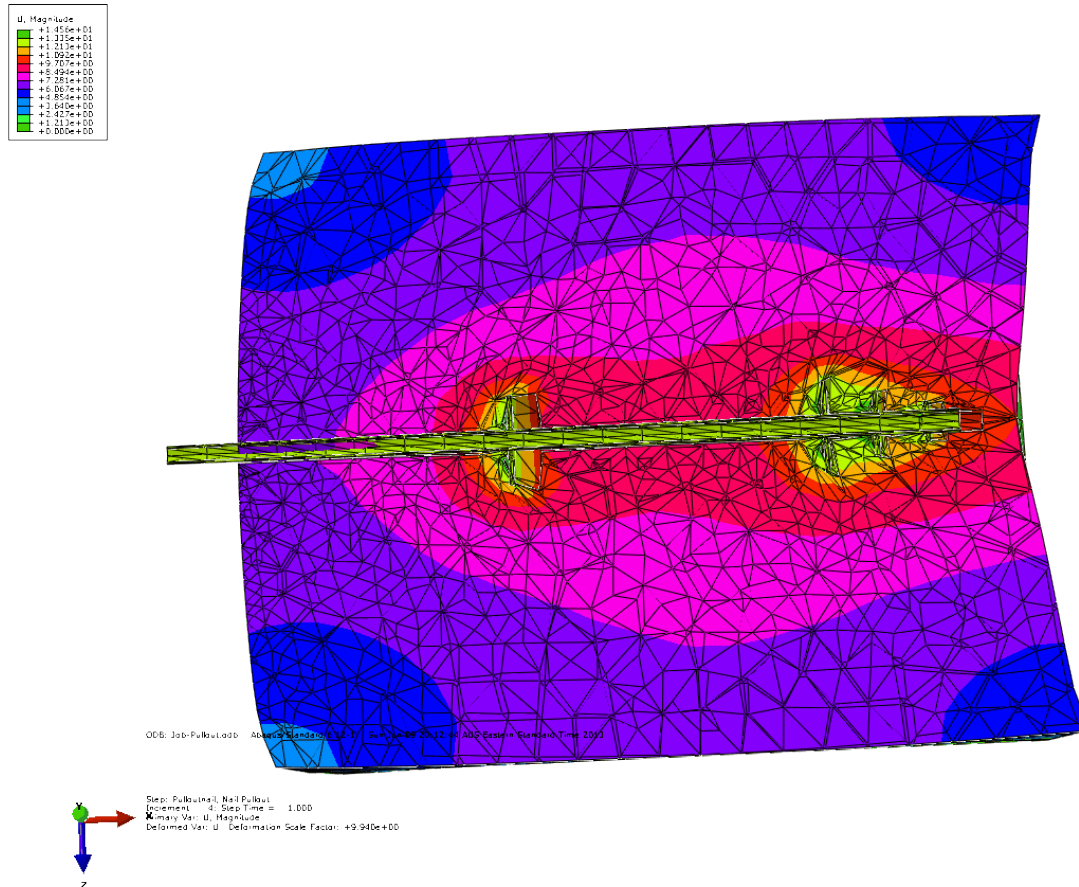


Figure 2: Soil-nail cut view showing displacements and deformations at the interface and around the nail.

Summary

It could be shown that Abaqus can be applied to solve a wide range of boundary value problems in the field of soil mechanics. This offers researchers a tool to examine some of the open problems in geomechanics like the influence of construction processes for geotechnical constructions, the optimization of geotechnical constructions regarding deformations or the optimization of construction. It should not be concealed that the presented simulations have limits caused by modelling features and hardware resources.

Simulation of the soil–nail interaction was conducted with the model. The model that has been implemented into a finite element analysis will be used in a back analysis of a laboratory test conducted on a scaled model. The soil–nail interaction can be investigated and therefore overall and internal failure mechanisms can be analysed. The information obtained from the three-dimensional FE analysis contributes to the deeper understanding of the behaviour of the reinforcing and failure mechanisms of nailed soil and can be helpful for the correct design of nailed soil structures.

References

- [1] W.-H. Zhou, J.-H. Yin, and C.-Y. Hong, "Finite element modelling of pullout testing on a soil nail in a pullout box under different overburden and grouting pressures.(Report)," *Canadian Geotechnical Journal*, vol. 48, p. 557(11), 2011.
- [2] L.-J. Su, J.-H. Yin, and W.-H. Zhou, "Influences of overburden pressure and soil dilation on soil nail pull-out resistance," *Computers and Geotechnics*, vol. 37, pp. 555-564, 2010.
- [3] K. Su and Y. Li, "Discussion of Extended Drucker-Prager Yield Criterion in Slope Stability Analysis," in *Power and Energy Engineering Conference, 2009. APPEEC 2009. Asia-Pacific*, 2009, pp. 1-4.
- [4] A. D. S. S., "User Manual," ed, 2011.

SIMPLIFIED DYNAMIC AXIAL HEAD PILE STIFFNESS IMPROVEMENT ANALYSIS FOR EXISTING PILED VIADUCT WITH BASE REINFORCEMENT

AGLIPAY Mary Roxanne¹ and KONAGAI Kazuo²

¹Graduate Student, University of Tokyo, Japan; ²Yokohama National University, Japan

ABSTRACT

Relatively high vertical accelerations were observed in some viaducts along the Tokaido Shinkansen Line supported by pile groups embedded at intermediate sandy layers of adequate bearing capacity underlain by soft soils. New piles in between existing pile groups and beam frame system at the pile head were added as part of the retrofitting works in the substructure of two viaduct segments (Viaduct “A” and Viaduct “B”) in the intention to reduce the vertical acceleration by increasing the dynamic stiffness of the foundation. Parametric analyses using Tajimi and Shimamura’s Thin Layer Element Method (TLEM) were done to determine key parameters that govern the improvement effect in the axial pile head stiffness of the retrofitted system of the two target viaducts. Based on a simple assemblage of springs representing the retrofitting elements (existing and new piles, and beams) and investigation on simple expression of axial stiffness of single pile, there are two important parameters describing the improvement of axial pile head stiffness: (1) $\mu_{new}L_{o,a,new}/\mu_{existing}L_{o,a,existing}$ and (2) $EI_b/\mu_{new}L_{o,a,new}L_s^3$. Although rigorous solutions are available, the nomographs developed as a function of these two parameters provide a quick estimate of the improvement effect. With many RC rigid frames supported by piled foundation similar to the target viaducts A and B, these nomographs will come handy for future retrofitting works.

Keywords: Soil-Pile Interaction, Dynamic Axial Pile Head Stiffness, Pile Foundations, Viaduct Retrofitting

INTRODUCTION

Background of the Study

Monitoring and maintenance of the whole railway system had always been a part of the operation throughout the 48 years of existence of the Tokaido Shinkansen line in the commitment to safety and sustainability in their service to the commuters, being one of Japan’s principal transportation system crossing over the country’s three largest metropolitan cities: Tokyo, Nagoya and Osaka.

Many of the viaducts carrying the Shinkansen were supported by piles embedded at shallow depths of adequate bearing capacity underlain by soft soils. Supporting the viaducts with floating piles back then was a rational and realistic measure to help minimize the uneven ground subsidence which had been occurring gradually over the past years primarily caused by groundwater extraction which was noticeably worst during the Japan’s post war. However, in these days during one of the regular maintenance, vertical accelerations of these viaducts supported by floating piles under train loads were observed to be relatively high. Though there are no serious signs of durability issues, long term effect of exposure to frequent vibrations is to be mitigated.

With the enactment of the three major laws in 1950’s and 1960’s, namely the Industrial Water Act (1951), the Act of Regulation of Pumping-up of Ground Water for Use in Building (1962) and the Basic Law for Environmental Pollution Control (1967), followed by implementation of regulations for practical control of pumping underground waters in 1970’s, ground subsidence has been largely stopped allowing JR Central to explore addition of end bearing piles as part of retrofitting scheme with the intention to reduce the vertical acceleration by increasing the dynamic stiffness of the foundation.

Target Viaducts

In response to the problem, retrofitting works in the substructures of two viaduct segments (Viaducts A and B) along the Shinkansen Tokaido Line located in Aichi and Shiga Prefecture respectively, had been done. The retrofitting works generally involved addition of new end bearing piles and longitudinal and transverse beams connecting the existing pile group and new piles at their head levels. This allows the foundation to act as a beam frame system.

The substructure of Viaduct “A” originally consists of 8-3x3 pile groups. In 2008, underpinning

works were done which included driving a total of 6 end bearing steel piles. Properties of the new pile are shown in Table 1. The new piles were positioned in between the existing pile groups along the longitudinal direction. Longitudinal and transverse RC beams having a cross section of 0.7m x 1.0m were added to connect the existing and new piles. A general layout of the retrofitted viaduct A in plan and elevation views is shown in Fig. 1.

On the other hand, Viaduct "B" prior to retrofitting is supported by 8-5pile groups. This viaduct was retrofitted in two stages. The first stage was around late 2010 to March 2011 which included addition of 6 concrete bored piles in between the existing pile groups along the longitudinal direction and 2 concrete bored piles, one at each end of the segment along the transverse direction. New pile parameters are shown in Table 1. The existing pile group and new piles were connected by 1.5m x 1.6m longitudinal and transverse RC beams. The second stage of retrofitting took place between March 2011 and July 2012 wherein depths of the beams were thickened to 2.1m and braces were added to the viaduct columns. General layout of the retrofitted substructure of viaduct B is shown in plan and elevation views in Fig. 2.

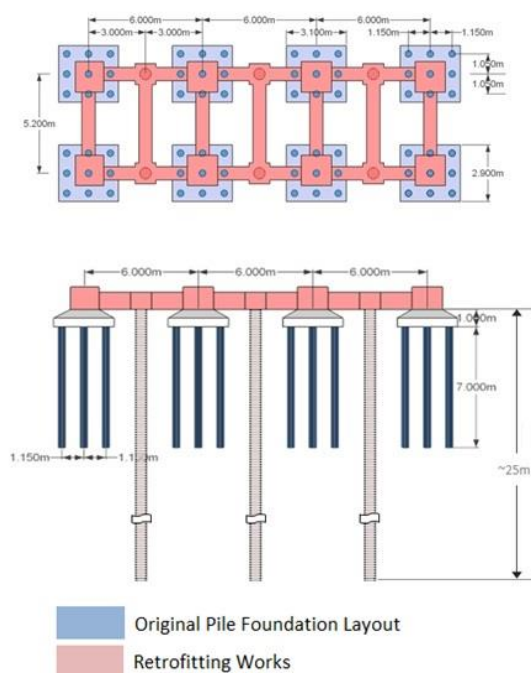


Fig. 1 Plan and elevation of viaduct "A" [1]-[4]

Objectives of the Study

With about 350 trains operating per day, the structure experiences vibration constantly due to the passing trains. The excitation induced by these vibrations affects the structural response with the

interaction between the piles and the surrounding soil. This soil-pile interaction can be described by the dynamic stiffness at the pile heads. Considering the implemented retrofitting scheme, this study aims to investigate the improvement performance and further define the key parameters contributing to such effect. Based on the parametric studies, it is important to provide simple approach for an effective retrofitting scheme that may serve as a useful guide in future retrofitting works given that some RC rigid frame viaducts along Tokaido line similar to the target viaducts are also experiencing comparatively high vertical accelerations.

SOIL PILE INTERACTION

Simplified Expression for Axial Pile Head Stiffness of Single Pile

Simple stiffness function of foundations is preferred for a straightforward superposition with the superstructure for a dynamic integrated interaction system. Pile head stiffness can be approximately expressed by an assembly of spring, damper and mass as shown in Fig. 3.

Table 1 New pile parameters for the target viaducts

New Pile	Outer radius, r_o (m)	Inner radius, r_i (m)	Young's Modulus E_s (GPa)
Viaduct A	0.300	0.288	210
Viaduct B	0.500	0.000	31

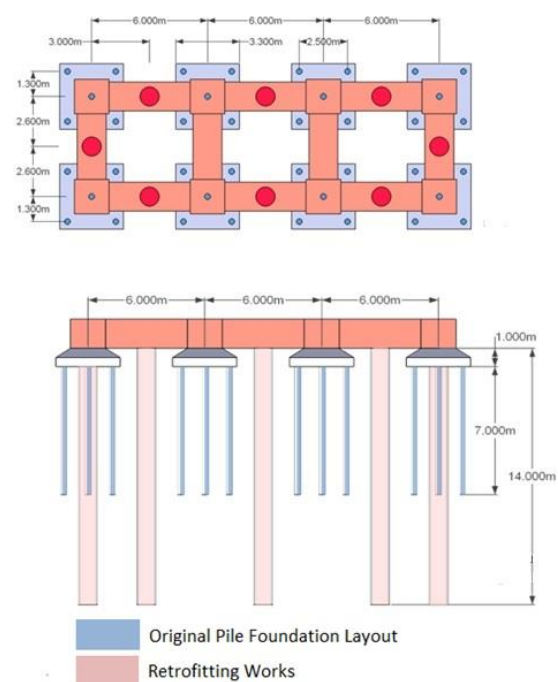


Fig. 2 Plan and elevation of viaduct "B" [1]-[4]

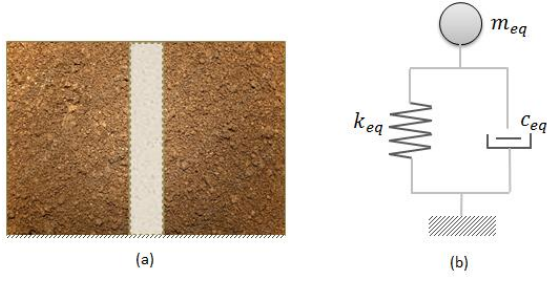


Fig. 3 Dynamic pile head stiffness model: (a) rigorous solution of pile-soil system (b) approximate spring-damper-mass system

Konagai [5] introduced an important parameter, $L_{o,l}$ as a function of pile bending stiffness and surrounding soil's shear modulus, that governs the overall behavior of a rigidly capped flexible pile group subjected to lateral loadings. Analogously, the deformation due to a vertical load for substantially long piles is largely noticeable in the upper part and becomes negligible with increasing depth. This remarkable deformation at the upper part, called active length hereafter, is considered to be dependent on characteristic length,

$$L_{o,a} = \sqrt{\frac{EA}{\mu}} \quad (1)$$

where EA is the axial stiffness of the pile and μ is the shear modulus of the surrounding soil. Thus, the side soil reaction, which contributes largely to the axial pile head stiffness is dependent on $\mu L_{o,a}$. This parameter greatly simplifies the dynamic axial pile head stiffness. It is used to normalize the dynamic axial pile head stiffness, $k_{zz,rigorous}$ and correspondingly, frequency is normalized by the ratio of shear wave velocity to the radius of pile V_T/r_o . These non-dimensional parameters describe the approximate expressions given by the following equations.

$$\text{Re}\left(\frac{k_{zz,rigorous}}{\mu L_{o,a}}\right) = k_{eq} - m_{eq}\left(\frac{\omega r_o}{V_T}\right)^2 \quad (2)$$

$$\text{Im}\left(\frac{k_{zz,rigorous}}{\mu L_{o,a}}\right) = c_{eq}\left(\frac{\omega r_o}{V_T}\right) \quad (3)$$

Parametric analysis using Tajimi and Shimamura's Thin Layer Element Method [6] was done on end bearing piles of solid cross section embedded in homogeneous infinite soil deposits. Six cases of different soil-pile configurations were considered varying one specific soil or pile parameter while keeping other variables constant.

The pile parameters considered were: (1) radius, (2) length, (3) Young's modulus of elasticity. The soil parameters: (4) shear modulus, (5) soil density and (6) Poisson's ratio were varied between the shear velocity range of 50m/s to 375m/s.

Table 2 Constant values for the parametric analysis

pile properties	
outer radius (r_o), m	0.250
Young's modulus (E_p), $(10)^6$ tf/m ²	3.161
length (L_p), m	50
soil properties	
shear modulus (μ), tf/m ²	1098
Poisson ratio (ν)	0.440
soil density (ρ), tf/(s ² /m ⁴)	0.182

For all piles with axial characteristic length less than length of pile, the imaginary and real parts lie in a unique curve. The real part forms a parabolic curve where $k_{zz,rigorous}/\mu L_{o,a}$ decreases with increasing frequency. Meanwhile, the imaginary part has a linear relationship, having an increasing trend with increasing frequency.

Based on this parametric study, a simple approximate formula of axial pile head stiffness can be suggested given by Eq. 2 and Eq. 3. The values of the equivalent stiffness, mass and damper are obtained from the best fit line on various pile and soil parameters considered. These non-dimensional constant values are 1.6, 0.001 and 2.1 respectively as seen in Fig. 4.

The parameter, $\mu L_{o,a}$, allows simple and straightforward expression for the axial pile head stiffness of single piles or equivalent single pile for pile groups. Thus, with a threshold of acceptable value of axial pile head stiffness, this simple approach serves as an easy criteria to which existing piled foundations can be categorized dependent on retrofitting priority scale.

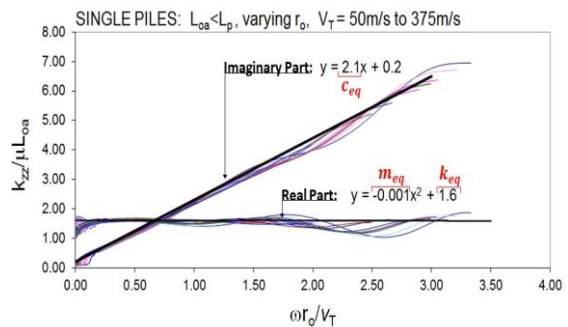


Fig. 4 Real and imaginary parts of axial pile head stiffness for $L_{o,a}/L_p < 1$

Spring Assemblage Analysis for the Retrofitted System

Rigorous solution allows derivation of pile head stiffness for any complicated soil-pile profiles. However, it is important to highlight the key parameters that govern the performance of the addition of new piles and corresponding connecting beams as a retrofitted scheme on existing pile foundations. With a simple assemblage of springs as in Fig.5, the effect of addition of new piles and the connecting beam can be described.

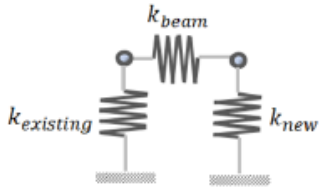


Fig. 5 Simple spring model describing the effect of new pile and connecting beam

The improved stiffness can be expressed as the equivalent spring of the system given by Eq. 4.

$$k_{zz,improved} = k_{zz,existing} + \frac{1}{\frac{1}{k_{beam}} + \frac{1}{k_{zz,new}}} \quad (4)$$

Simplifying further gives,

$$k_{zz,improved} = k_{zz,existing} + \frac{k_{beam}k_{zz,new}}{k_{beam} + k_{zz,new}} \quad (5)$$

Dividing both sides by $k_{zz,existing}$ gives the improvement effect,

$$\frac{k_{zz,improved}}{k_{zz,existing}} = 1 + \frac{\left(\frac{k_{beam}}{k_{zz,existing}}\right)\left(\frac{k_{zz,new}}{k_{zz,existing}}\right)}{\left(\frac{k_{beam}}{k_{zz,existing}}\right) + \left(\frac{k_{zz,new}}{k_{zz,existing}}\right)} \quad (6)$$

From Eq. 6, the improvement effect is essentially a function of the ratio of the stiffness of the new pile to the existing pile ($k_{zz,new}/k_{zz,existing}$) and the ratio of the vertical stiffness of the longitudinal beams to the existing pile ($k_{beam}/k_{zz,existing}$).

It has been established that the axial pile head of pile is proportional to $\mu L_{o,a}$. Therefore, the ratio between the equivalent spring constants for the existing and new piles must be dependent on the ratio of the product of the shear modulus and

characteristic lengths of new and existing piles, thus the ratio is $\mu_{new}L_{o,a,new}/\mu_{existing}L_{o,a,existing}$.

Shear moduli, μ_{new} and $\mu_{existing}$, may be cancelled out as long as both the new and existing piles are embedded in the same and homogeneous soils. However, for non-homogeneous soil deposits, there is no guarantee that μ_{new} is identical to $\mu_{existing}$, because these representative shear moduli are to be estimated over the active pile lengths, which can differ between the new and existing piles. Therefore, the shear moduli for both new and existing piles are to be left in this stiffness ration.

The vertical stiffness of the longitudinal beam is proportional to EI_b/L_s^3 where EI_b and L_s is the beam vertical bending stiffness and the space between existing and new piles respectively. Therefore, the ratio between the equivalent spring constants for beam and existing pile is dependent on $EI_b/\mu_{new}L_{o,a,new}L_s^3$.

As summary, the improvement on the axial pile head stiffness of the existing pile can be described with the two parameters: (1) $\mu_{new}L_{o,a,new}/\mu_{existing}L_{o,a,existing}$ and (2) $EI_b/\mu_{new}L_{o,a,new}L_s^3$.

Development of Dynamic Pile Head Stiffness Nomograph

Analysis on the effect of the addition of new piles and beams were done as a function of the abovementioned parameters and are summarized in nomographs. Two model configurations were considered: (1) two rows of frames connected by transverse beams and (2) same with case 1 but with addition of new piles along the transverse direction at ends of the segments (Fig. 6). Every single line of frame has 7 end bearing piles of uniform longitudinal spacing, L_s , embedded in a homogeneous soil deposit. The new piles are embedded in between existing piles. The transverse spacing is $1.73L_s$ similar to the configuration of the two target viaducts as the standard configuration throughout the entire stretch of Tokaido Shinkansen Line. The radius of the existing piles is held constant while varying the radius of the new piles to obtain different $\mu_{new}L_{o,a,new}/\mu_{existing}L_{o,a,existing}$ ratios ranging from 0 to 2.0. Note that the $L_{o,a,new}$ and $L_{o,a,existing}$ considered were less than the actual length of pile L_p . For each $EI_b/\mu_{new}L_{o,a,new}L_s^3$ ratio, there are 4 different cases of beam bending stiffness considered taken care by the change in Young's modulus ($E_b = 26.5, 80, 120, \text{ and } 200 \text{ GPa}$). From the rigorous solution, approximate axial pile head stiffness is derived with the best fit line and is divided with the simplified axial pile head stiffness for single piles for $L_{o,a} < L_p$.

Application to Real Viaducts

In application to real viaducts, the two key parameters were derived for viaduct A and B based on the pile and beam properties of their foundation and their surrounding soil characteristics. The existing pile group and new piles of the two target viaducts were assumed to be embedded in a homogeneous soil deposit by using representative shear moduli of the actual non-homogeneous stratified soil deposits along the active pile lengths. The representative shear moduli were derived along this depth by getting the weighted average of the shear moduli of the soil deposits of the viaducts.

Thus, the value of key parameters to describe the improvement effect of the retrofitting scheme

implemented in these viaducts can be easily derived as summarized in Table 3. These are subsequently plotted in their corresponding nomograph as seen in Fig. 6.

Table 3 Values of the key parameters.

	A	B
$\mu_{new}L_{o,a,new}/\mu_{existing}L_{o,a,existing}$	0.54	0.061
$EI_b/\mu_{new}L_{o,a,new}L_s^3$	2.00	0.472

Given a small value for the two key parameters, little improvement can be seen in Viaduct A. However, viaduct B exhibits increase in the improvement by a factor of ~2.0 and ~3.0 for corner and center piles.

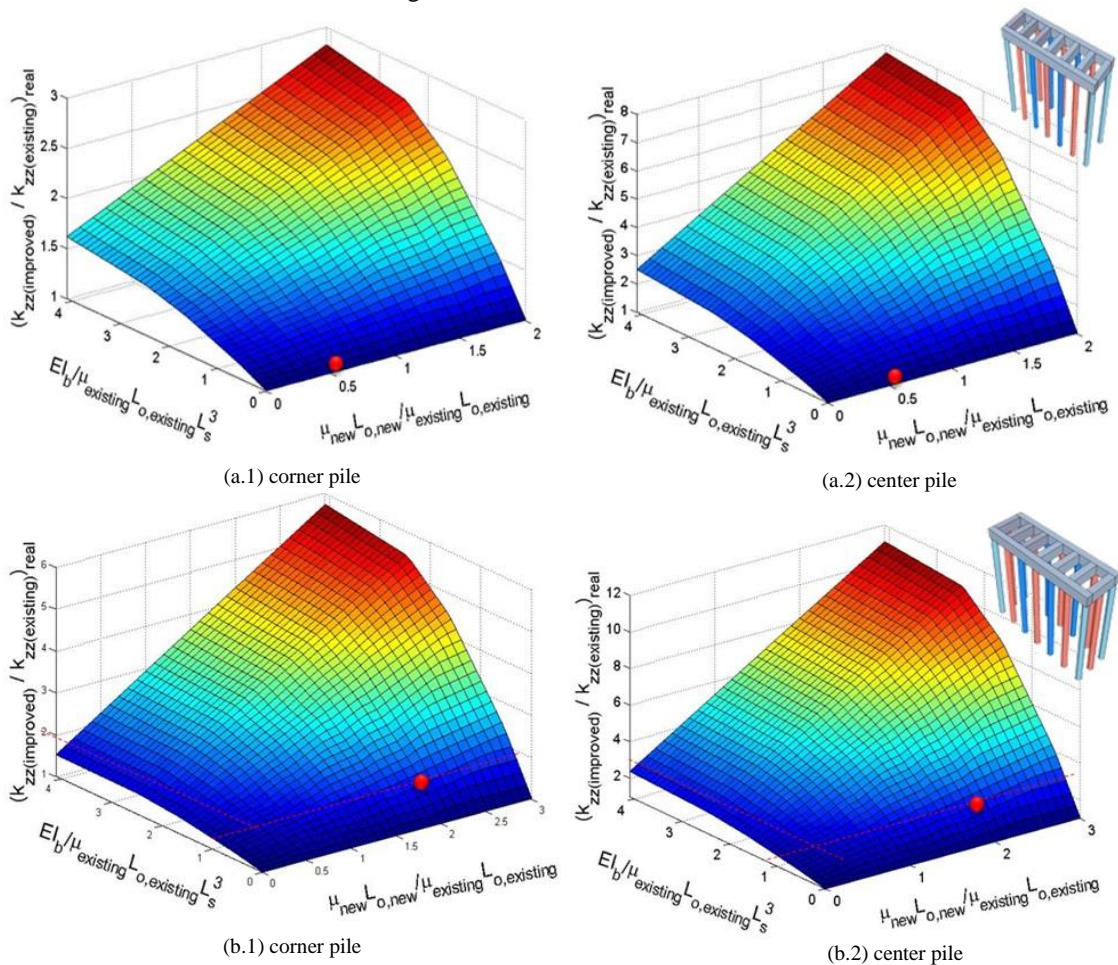


Fig. 6 Improvement in axial pile head stiffness over frequency in (a.1-a.2) viaduct A and (b.1-b.2) viaduct B

Comparison with Static Locomotive Tests and Rigorous Solution

In both viaducts, improvement is higher in center piles relative to corner piles. Stiffnesses of the immediate neighboring piles and corresponding connecting beams have predominant influence on the improvement of the axial pile head stiffness.

Having stiffer piles installed in viaduct B and thicker beams, there is a remarkable improvement in the dynamic axial pile heads stiffness having a factor of ~1.7 and ~2.5 for corner and center piles respectively while very little improvement is seen in viaduct A based on rigorous solutions. Same general trend is observed from results of the static locomotive loading test, wherein there is a twofold

increase in the average axial pile head stiffness of all 8 pile group in viaduct B while little improvement is seen in viaduct A (Table 4).

The general trends of results in the nomograph are approximately the same with that of the static locomotive tests and rigorous solutions (Fig. 7).

Table 4 Average settlement of all 8 columns in the upbound and downbound side before and after retrofitting from the static locomotive test and corresponding stiffness improvement [1]-[4].

Viaduct	Before retrofitting	After retrofitting	Stiffness Improvement
A	-0.22mm	-0.17mm	1.29
B	-0.33mm	-0.18mm	1.83

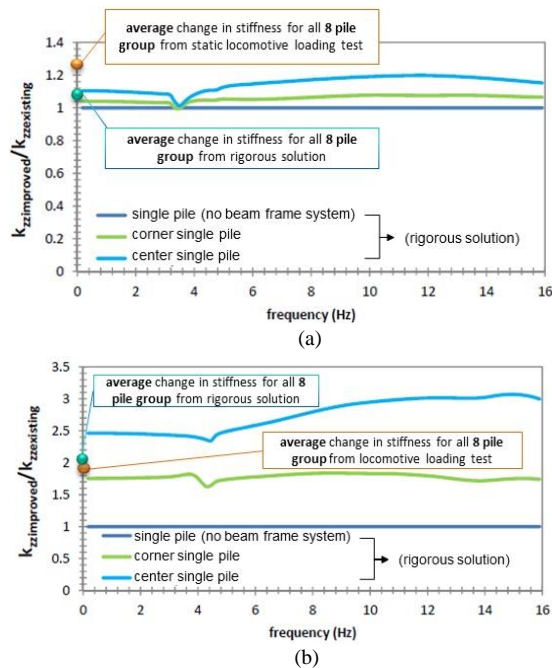


Fig. 7 Improvement in axial pile head stiffness in (a) viaduct A and (b) viaduct B

CONCLUSION

Rigorous solutions using the Thin Layer Element Method can deal with any complex soil-pile configurations, yet simplifications are needed to save time and effort. Simple expressions of axial pile head stiffness for single pile or equivalent single pile of pile groups which is largely dependent on $\mu L_{o,a}$ provide a simple and straightforward approach for determining axial pile head stiffness of existing piled viaducts. With a threshold of acceptable figure for the axial pile head stiffness, decision can be made which existing piled viaducts demands retrofitting

works to increase the dynamic axial pile head stiffness and furthermore categorize based on retrofitting priority scale.

Upon decision of needed retrofitting works, the nomographs developed in this study provide a quick estimate of the improvement effect using the two key parameters: $\mu_{new}L_{o,a,new}/\mu_{existing}L_{o,a,existing}$ and $EI_b/\mu_{new}L_{o,a,new}L_s^3$. Stiffnesses of neighboring piles and corresponding beams have predominant influence on the improvement of the axial pile head stiffness. For a non-homogeneous soil deposit present in most cases, the active length is a good parameter for getting representative shear moduli for a straightforward calculation to derive the key parameters. Tokaido Shinkansen line has 4000 RC rigid frames and approximately half of it is supported by similar foundations of viaducts A and B, having possible the same problems of relatively high vertical accelerations. The nomographs with readily available information will come handy for future retrofitting works.

ACKNOWLEDGEMENTS

Thanks to Ms. Chiho Takeguchi, Mr. Atsushi Doi and Mr. Motoyuki Azuma, and the Structural Design Team of Structural Design Group 1, Technology Research and Development Department, JR Central for providing the necessary data and to Monbukagakusho Scholarship for the financial support and making this study possible.

REFERENCES

- [1] Azuma M. et al, "Vertical Vibration Reduction of Existing RC Viaduct with Base Reinforcement", Journal of Structural Engineering, Vol. 156A, 2010.
- [2] Azuma M. et al, "Effect of Base Reinforcement of Existing Railway Viaducts with new piles and underground beams", Annual Convention of Japan Concrete Institute, Vol. 32, No. 2, July 2010.
- [3] JR Data for target viaducts (Viaduct "A" and Viaduct "B"): General Layout, Pile and Soil Properties, and numerical results.
- [4] Imai K., et al., "Maintenance and strengthening of existing Railway RC Viaducts", Bridge and Foundation Engineering 2012, No. 10.
- [5] Konagai K., Ahsan, R., Maruyama, D. "Simple Expression of the Dynamic Stiffness of Grouped Piles in Sway Motion", Journal of Earthquake Engineering, 4(3), 2000, pp. 1-22.
- [6] Tajimi H., Shimomura Y., "Dynamic Analysis of Soil-Structure Interaction by Thin Layer Element Method" (in Japanese), Architectural Institute of Japan, 1976, pp. 41-51.

PFC3D NUMERICAL EXPERIMENTS OF SELF-BORING IN-SITU SHEAR PRESSURE-METER MODEL TEST

Yafei Zhang¹, Guangli Xu¹ and Jidong Teng²

¹Faculty of Engineering, China University of Geosciences (Wuhan), China; ² Faculty of Engineering, Kyushu University, Japan

ABSTRACT

The self-boring in-situ shear pressure-meter (SBISP) has little to no disturbance to the surrounding soil. It can simultaneously determine the deformation and strength parameter of easily disturbed soil at depth. However, the deformation response of surrounding soil under multilevel loading process in SBISP test has seldom been studied up to present. At the same time, the determination of the deformation parameter of the soil is closely related to its deformation mechanism. Based on this, the SBISP model test was simulated by PFC3D (Particle Flow Code in three Dimensions) program in this study. The results of numerical experiments showed that the displacement of particles in central area increased with the shear stress imposed stepwise, and the direction of displacement vector showed a clearly preferred direction. Additionally, with the increase of the consolidation pressure, the influence area of the numerical sample diminished gradually. The motion trails of particles were step-like lines; the steps were becoming gentler as the distances from particle to the probing rob center increasing.

Keywords: Self-boring In-situ Shear Pressure-meter Test; Particle Flow; Deformation Response; Motion Trails;

INTRODUCTION

With the development of the geotechnical engineering test technology, it has been realized that obtaining undisturbed or less disturbed soil sample to conduct conventional laboratory testing is very difficult [1], which impels related researchers to develop new in-suit testing instruments to exclude the disturbance while sampling. A new in suit test instrument, the self-boring in-situ shear pressure-meter (SBISP), has been developed in 2007 [2] based on conventional in suit test methods both at home and abroad. The SBISP test is a combination of the pressure-meter test (determination of the deformation modulus) and the direct shear test (determination of the shear strength). The deformation and shear strength parameters can be directly determined simultaneously compared with previous traditional test methods. Moreover, it can reduce the disturbance of surrounding soil as much as possible by self-boring. Hence, the SBISP test is particularly suitable for soils that are difficult to sample, easily disturbed and with low strength such as sandy soil and silty soil.

The experimental studies of SBISP were few. The apparatus, mechanism and procedure of SBISP test were first applied in pile foundation engineering around 2007. And the shear strength obtained by SBISP test was compared with the test results of the uniaxial compressive test and the undrained tri-axial compressive test in a project; the comparison showed that they were almost the same, by which

the practicability of the SBISP was proved [2]. In another study, the authors confirmed that the shear strength of soil can be approximately interpreted by the friction strength of the interface of the rough probe and surrounding soil, which can be used as strength parameter of soil directly [3]. The previous study focused mainly on the introduction of test methods, the interpretation of test mechanism, and the comparison and verification with other test methods, but the deformation process of easily disturbed soil under multilevel loading condition has not been discussed. Furthermore, the deformation and destruction of easily disturbed soil is mainly due to the translation and rotation of each soil particles and their interaction, which is a macroscopic phenomenon caused by the change of micro-structure. Therefore, it is of great necessary to study the deformation response of soil particles during the SBISP test process.

The Particle Flow Code in Three Dimension (PFC3D) was put forward in 1979 to simulate the movement of spherical particles and their interaction [4]. PFC3D program has great advantages in simulating the mechanical response of granular substance [5]. Based on the laboratory model test, we establish a numerical model by PFC3D to simulate the multilevel loading process of SBISP test in this study, and then comparatively analyze the variation of displacement fields of the numerical sample under different overlaying consolidation pressures. Moreover, the motion trails of particles of different positions are monitored to study the

micromechanical characteristic of the surrounding sand in the process of expansion and shearing of the probe.

BRIEF INTRODUCTION OF LABORATORY TEST

To verify the feasibility of strength parameter of soil obtained by multilevel loading in SBISP test. The laboratory verification test [6] was conducted in a large tri-axial chamber developed in Kyushu University of Japan. The sketch of the tri-axial chamber is shown in Fig. 1.

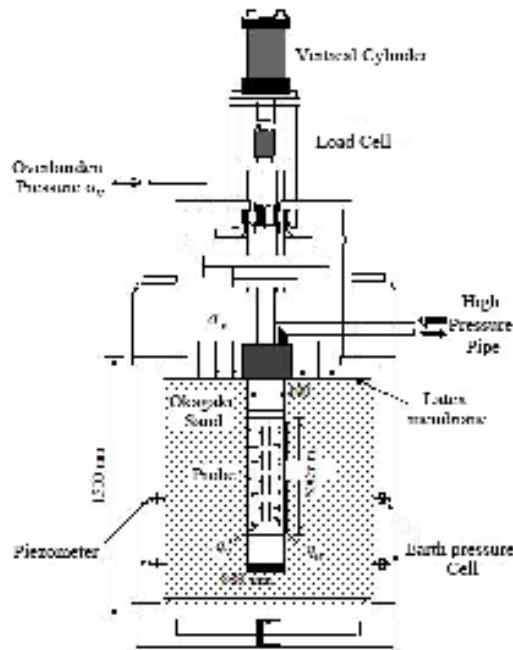


Fig. 1 Sketch of tri-axial chamber with probe of SBISP

The tri-axial chamber had a diameter of 900mm, and was 1500mm high. The diameter and height of the probe were 86mm and 500mm, respectively. The Okagaki dry sand employed in the laboratory test was got from Okagaki town, Fukuoka Prefecture. It was uniform fine sand of badly graded which mainly consists of quartz and feldspar. The soil sample was generated by air pluviating method. The soil sample during testing had a porosity n value of 0.44. The mean particle size D_{50} and the specific density ρ are 0.26mm and 2.63 g/cm³ respectively.

The tri-axial chamber had the capability to apply the overburden pressure and up-pull or down-push stresses independently. The overburden pressure was executed to the surface of the soil sample through the high-pressure air bag. And the up-pull stress was applied by the vertical loading cell. During loading process, the earth pressure was monitored by the pressure cells.

It was shown that the tested data of the tri-axial chamber can be interpreted by theoretical analysis methods mentioned in paper [3], and the interpreted results agreed well with other established testing methods. Therefore, the new test technology may be put into use in situ. The PFC3D numerical model established below is based on the verification test above.

MODEL ESTABLISHMENT OF PFC3D

Boundary and Probe Model of SBISP

To improve the computational efficiency, the size of the large tri-axial chamber and probe is properly reduced to decrease the number of particles generated. As shown in Fig. 2(1), the radius and height of test chamber are 150 mm and 350 mm respectively; it consists of one general cylindrical wall (wall 3) and two standard walls (wall 5, 6). The probe consists of three general cylindrical walls (walls 1, 7, 8; wall 1 is a cylindrical wall, but walls 7 and 8 are truncated cone walls with an inclination angle of 45°). The original radius of the probe is 15 mm, with a height of 180mm; so the probe has a length to diameter ratio (L/D) value of 6. The diameter of the chamber is 10 times that of the probe. The radius of the probing rod is 15 mm as well, and is represented by one general cylindrical wall (wall 2).

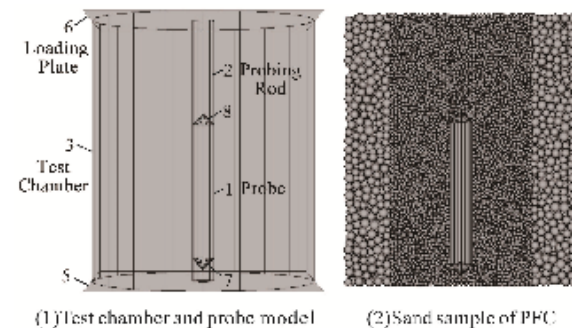


Fig. 2 Test chamber model and numerical sample

The functions of each wall are explained as follows. The initial consolidation load is applied to the top of the simulated domain by wall 6. The radial and vertical velocities are specified successively for walls 1, 7 and 8 which exerting the radial- and shear-force on the domain. To simulate a rigid probe, we specify a normal- and shear-stiffness of $1 \times 10^{10} \text{ N} \cdot \text{m}^{-1}$ for the probe. The mesoparameters of the walls are shown in Table 1.

Table 1 Meso-parameter of model walls

Number of walls	Normal stiffness k_n (N·m ⁻¹)	Shear stiffness k_s (N·m ⁻¹)	Friction coefficient f_c
1, 7, 8	1×10^{10}	1×10^{10}	0
2, 3, 5, 6	1000	1000	0.5

1	1×10^{10}	1×10^{10}	0.6
2、3、5、6	1×10^{10}	—	—
7、8	1×10^{10}	—	—

Sand Sample Model of PFC3D

The spherical particles generated can be divided into two parts from the probe outward. In order to improve the operation rate in the premise of ensuring the precision of calculation, we reduce the number of particles by generating particles of small radius in central region and large radius in outer region. The radius of the central region is 6 times that of the probing rod.

Based on the particle size in the laboratory verification test, the particles in central region are generated. To reduce the number of particles in numerical simulation, the actual grain size is enlarged properly. In this simulation, the average particle size, D_{50} of the numerical sample is 5.2 mm which is 20 times larger than the actual grain size. The large particles in the outer region are generated first, followed by the fine particles in the central region. The mesoparameters of the large particles in the outer region are deduced based on the mesoparameters of the particles in the central region. When the Young's modulus of spherical particles is constant, the relationship of particle stiffness and particle radius is [7]:

$$\bar{E} = \frac{k_n}{4R} \quad (1)$$

where \bar{E} is the Young's modulus; k_n is the particle stiffness; R is the average radius of spherical particles.

According to Eq. (1), when the same material is simulated by particles of different radius, the particle contact stiffness is proportional to the particle radius. Therefore, the stiffness of large particles in the outer region can be derived by the stiffness of fine particles in the central region. The meso-parameter of fine particles in the central region is obtained by comparison with tri-axial test simulated by PFC. Partitions and meso-parameters of numerical sample are listed in Table 2.

Table 2 Partitions and meso-parameter of numerical sample

Region	Range	Radius of particles /mm	Normal stiffness $k_n(\text{N} \cdot \text{m}^{-1})$	Density $\rho_s(\text{kg} \cdot \text{m}^{-3})$	Friction coefficient f_c
central region	1-4D	2-3.2	3×10^5	2630	2.5
outer region	4-10D	4-6.2	5.88×10^5	2630	2.5

Note: D is the diameter of the probing rod.

The eventual numerical sample of sand particles is a hollow cylinder and having a total of 89,048 particles. The numerical sample can be seen in Fig. 2(2).

Simulation of Loading Process

According to the loading process of laboratory verification test of SBISP, the loading procedure of this simulation is designed as follows: (1) The consolidation stress σ_v is applied firstly by adjusting the velocity of standard wall 6 using a servo-control function. When the requested value of the consolidation stress is reached, keep it constant. (2) Then the requested value of the first grade radial-stress q_{v1} is obtained as the consolidation stress did in procedure (1). The difference is that, at this time, the velocities we adjusting are the cylindrical walls 1, 7 and 8. Keep the requested value of q_{v1} constant as well. (3) The first grade shear-stress q_{H1} is applied to the surrounding soil by specifying a constant velocity of the probe. When it reaches the peak value, terminates the loading. The loading process of the shear-stress is automatically controlled by writing a FISH function. (4) Then the next grade radial-stress q_{v2} is applied. When it reaches the requested value, applies the next grade shear-stress q_{H2} . Repeat it five times.

For the purpose of comparing the variation characteristic of displacement field of the numerical assembly under different consolidation pressures, the pre-consolidation stresses applied are 100kPa and 200kPa respectively in this simulation. The corresponding radial-stresses of each grade are 150kPa、400kPa、600kPa、800kPa and 1MPa, respectively.

Verification of the Results of the Numerical Simulation

The applicability of the simulation of PFC is confirmed by comparing the macroscopic curve of numerical test and the results of the field experiment of SBISP. Fig. 3 is a general test curve of SBISP which describes the relationship of shear-stress and shear-displacement under the radial-stress of each level. Where q_v is radial-stress, q_H is shear-stress, and Q_H is shear-force.

Fig. 4 shows the shear stress-shear displacement curve obtained by numerical simulation of SBISP by PFC. It can be seen from Fig.4 that, when applying the shear-stress of each level at the initial stage, there is always a sharp peak with steep rise/fall which is shown in the circle in Fig. 6. This can be interpreted by the law of friction [8]: The static

friction force F_{f0} increases with the external force F when the object does not slide relative to the horizontal plane. The object is on the point of sliding as F reaches a certain value. At this point the static friction force reaches the maximum value, which is known as the maximum static friction force F_{f0m} . Experiments show that the relationship between the maximum static friction force and the positive pressure F_N is

$$F_{f0} = \mu_0 F_N \quad (2)$$

where μ_0 represents the static friction coefficient. When the object slides on the plane, the sliding friction force F_f it subjected is

$$F_f = \mu F_N \quad (3)$$

where μ is the sliding friction coefficient. The sliding friction coefficient is usually less than the static friction coefficient when the relative velocity of the object is not too large. Therefore, this can reflect the validity of the PFC3D program in simulating the actual physical phenomenon.

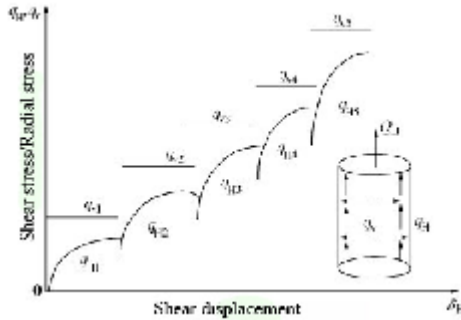
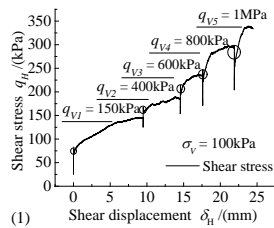
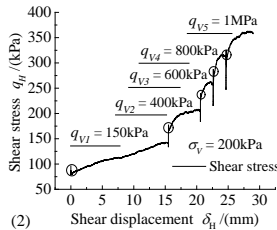


Fig. 3 The general curve of SBISP tests



(1)



(2)

Fig. 4 Numerical simulation curve of SBISP tests

Through the comparison of Fig. 3 and Fig. 4, it can be seen that the stress and deformation response obtained by numerical experiment of PFC3D is of good agreement with that of the field test of the SBISP. With the increase of radial-stress of each grade, the peak values of shear-stress of each level increase as well. However, the growth rate of shear-stress decreases with the increase of the shear displacement under the radial-stress of the same level, and approaches the peak value finally. It demonstrates that the numerical model built can reflect the general law of the sand particles in the loading process of SBISP, and the numerical model established by PFC3D in this study is reasonable.

ANALYSIS OF THE RESULTS OF THE NUMERICAL EXPERIMENT OF PFC3D

Evolution Process of the Displacement Field under Different Consolidation Pressures

The variation of the displacement field of the particles surrounding the probe is monitored under different consolidation pressures. The distribution of displacement vectors of particles, after the peak value of the shear-stress of each level has been reached under the different consolidation pressures, is shown in Fig. 5. Fig. 5(1), (2) are the distribution of displacement vectors of particles of each level under the consolidation pressure of 100kPa, and Fig. 5(3), (4) are that of 200kPa. It can be seen that, no matter the overlaying consolidation pressure is 100kPa or 200kPa, the influence area mainly lies in the central region of small particles. At the same time, the displacement field in the outer region of the large particles has no significant change. Moreover, the displacement of particles in the central region increases obviously with the peak value of shear-stress of each level increases; and the displacement vectors have a good directionality gradually. Under the peak values of the third and the fifth grade shear-stresses, displacement vectors of the particles surrounding the probe has an upward directionality obviously. The shape of the displacement vectors of particles within the height of the probe is a reverse cone.

From the comparison of the two columns of Fig. 5, it can be seen that the displacement of particles decreases as the consolidation pressure increases. This is because the bigger the consolidation pressure applied, the greater the resistance particles suffered from while moving driven by the probe.

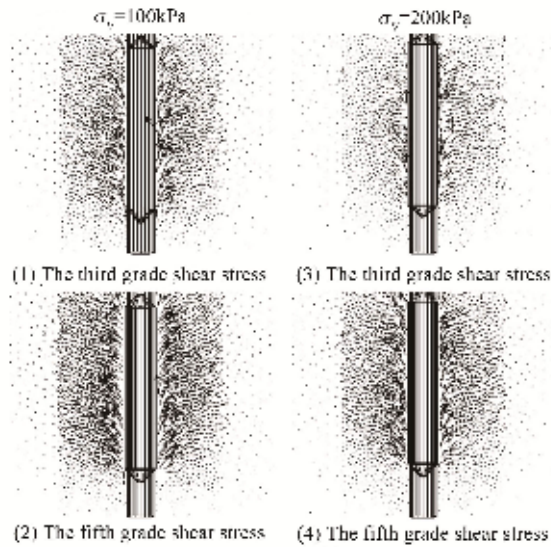


Fig. 5 Distribution of displacement vectors of particles

In order to observe the impact of inflation of the probe on the surrounding particles intuitively, the particles are painted by different colors according to the magnitude of their displacement. In this study, the displacement contour map is plotted automatically by a 'color function' written with FISH language. Fig. 6 is a displacement contour map of numerical sample.

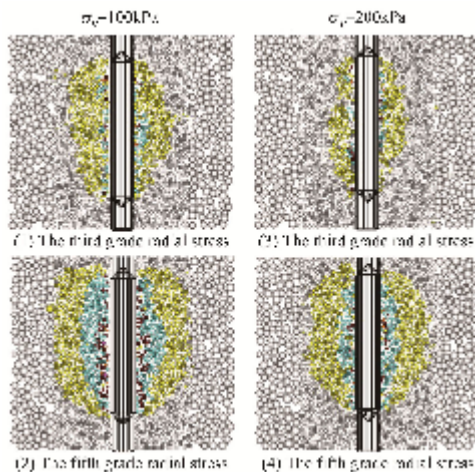


Fig. 6 Displacement contour map of numerical sample

The two figures on the left are displacement contour maps generated after the application of the radial-stress of each level under the consolidation pressure of 100kPa, while the three figures on the right are that of the consolidation pressure of 200kPa. It should be noted that the displacement of particles monitored in this diagram is that in the XY plane. As we can see, the diameter of the probe increases with the radial-stress of each level applied step by step.

Meanwhile, the influence area of the probe on the surrounding particles is increasing as well. But the influence area mainly locates at the height of the probe.

It can be found from the comparison of the figures of both sides that, although the radial-stresses of each level applied are the same, the influence area of the probe reduces obviously as the consolidation pressure increases. And the influence area of the probe is mainly located in the central region. This is in consistent with the phenomenon observed in Fig. 5.

Motion Trails of the Particles

The motion trails of particles surrounding the probe are studied. Under the consolidation pressure of 200kPa, the position of particles with different distance from the probe center is monitored and the motion trails of the particles are plotted in the XYZ space. It should be noted that the initial positions of the particles monitored mainly located in the XZ plane. The distances from the particles monitored to the probing rod center are around 15mm, 20mm, 30mm, 40mm, 50mm, 60mm, 70mm and 80mm, respectively; and two particles are selected at each distance. As space is limited, the motion trails of particles illustrated in this paper are only that at the distances of 15mm, 40mm and 70mm.

It should be noted that "id" represents the number of the particle monitored, and "r" represents the distance from the particle to the probing rod center in Fig. 8. The projection of the motion trails on the XZ plane is represented by black lines; while that on the XY plane are blue lines. It can be seen that the projection of the motion trails on the XZ plane is a step-like line. This phenomenon reflects that with the expansion and elevation of the probe, the particles surrounding the probe are moving along the radial and vertical direction continuously. When the particles contact with the probe, the steps are in a sharp corner form. However, when the distance to the probe increase, the steps are in an arc shape. Moreover, the radian of the arc is increasing as the distance increase, and becoming much gentler. It indicates that the closer the distance is, the greater the degree of the influence suffered from the probe movement. In addition, the motion trails in the XYZ space and its projection on the XY plane are irregular, but the motion trails is almost moving along a unique horizontal direction on the same step plane. Gibson and Anderson [9] put forward the method to interpret the self-boring pressure-meter test for the first time. They assumed that the pressure-meter was infinitely long, so that the deformation of the surrounding soil takes place under conditions of axial symmetry and plane strain. The phenomenon shown in Fig. 8 indirectly proves that these assumptions are reasonable in some

degree.

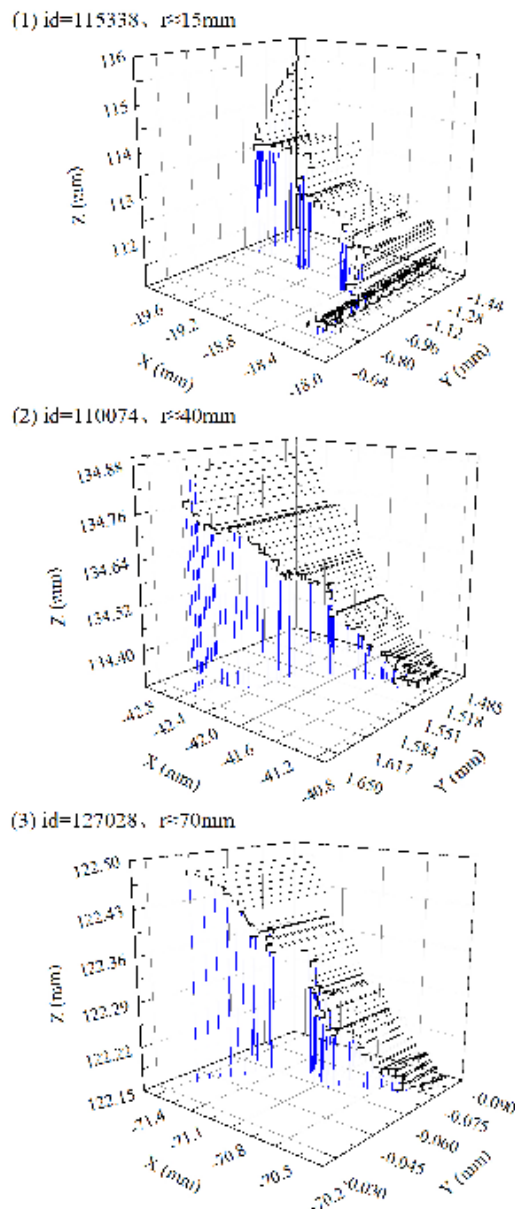


Fig. 7 Motion trails of particles

CONCLUSIONS

The results of the numerical experiment suggest the influence of the probe on the displacement of the particles has a sectionalized characteristic. The particles in the central region have been influenced significantly, but the big particles in the outer region have seldom been affected. It is found that the displacement of the particles in the central region increases with the shear-stress increases gradually, and has an upward directionality step by step; the shape of the displacement vectors of particles

surrounding the probe is a reversed cone under the fifth grade shear-stress. Moreover, the displacement of particles surrounding the probe reduces as the consolidation pressure increases, so does the influence area.

The motion trails of particles are a step-like line. Furthermore, as the distance from the particles to the probing rod increases, the steps are becoming gentler.

ACKNOWLEDGEMENTS

The authors acknowledge the financial support provided by the National Natural Science Foundation of China (Contract No: 41072218).

REFERENCES

- [1] Shen Z J, "Soil sampling on site or in-situ testing—a preliminary research on development of soil parameters testing technology". Chinese Journal of Geotechnical Engineering, Vol. 18, Sep. 1996, pp. 90–91.
- [2] Zhang X L, Xu G L, Wang C Y, et al., "Development and application of self-boring in-situ shear pressuremeter", Rock and Soil Mechanics, Vol. 28(Suup.), Oct. 2007, pp. 909–913+918.
- [3] Xu G L, Zhang X L, Wang C Y, "Development and application of self-boring in-situ shear pressuremeter", Chinese Journal of Geotechnical Engineering, Vol. 32, Jun. 2010, pp. 950–955.
- [4] Cundall P A, Strack O D L, "A discrete numerical model for granular assemblies", Geotechnique, Vol. 29, 1979, pp. 47–65.
- [5] Zhou J, Chi Y, "Mesomechanical simulation of sand mechanical properties", Rock and Soil Mechanics, Vol. 24, Dec. 2003, pp. 901–906.
- [6] Xu G L, Zhang X L, Wang C Y, et al, The new self-boring shear pressuremeter and its application. Wuhan: China University of Geosciences Press, 2009, ch.4.
- [7] Deng Y B, Zhou J, Liu W B, et al., "PFC numerical simulation of augered piling of soil displacement screw piles", Chinese Journal of Geotechnical Engineering, Vol. 33, Sep. 2011, pp. 1391–1398.
- [8] Ma W W, Physics. Beijing: Higher Education Press, 1999, ch.2.
- [9] Gibson R E, Anderson W F. "In-situ measurement of soil properties with the pressuremeter", Civil Engineering Public Works Review, Vol. 56, 1961, pp. 615–618.

DYNAMIC ANALYSIS OF SLOPE FAILURE USING THE MESH-FREE SPH METHOD

N. Hiraoka¹, A. Oya¹, Ha H. Bui², P. Rajeev² and R. Fukagawa¹

¹Department of Civil Engineering, Ritsumeikan University, Japan;

² Department of Civil Engineering, Monash University, Australia

ABSTRACT

In the past few decades, majority of dynamic behavior of slope have been conducted using the finite element method (FEM). However, earthquakes often cause large deformation and post-seismic soil deformation which is difficult to predict using the FEM due to mesh distortion issues. As an alternative numerical method, the smoothed particle hydrodynamics (SPH) has been recently applied to geotechnical field and showed to be a promising numerical technique to handle large deformation and post-failure behavior of geomaterials. In this paper, taking into consideration of this advantage, the SPH method is applied to simulate response of a slope subject to seismic loading. Reliability of SPH results was assessed by comparing with experimental data available in the literature. It is shown that the SPH method could qualitatively predict slope failure behavior observed in the experiment.

Keywords: Dynamic analysis, seismic deformation, SPH, slope failure, elasto-plastic analysis

INTRODUCTION

Seismic induced lateral displacement in a slope is traditionally determined by Newmark's sliding block approach in design and assessment [1]. However, this method has limitations because of its simplicity. Nowadays, FEM (Finite Element Method), DEM (Distinct Element Method) [2] and FDM (Finite Difference Method) are used to simulate the co-seismic and post-seismic deformation of a slope subjected to seismic load. However, FEM and FDM methods have some disadvantage such as mesh distortion due to large deformation induced by soil failure. DEM, which is based on continuum mechanics, is favorable to simulate large deformation. However, DEM is computationally expensive to simulate the large problem. Moreover, it is quite difficult to specify DEM parameters for contact models.

Alternatively, the mesh-free smoothed particle hydrodynamics (SPH) [3] [4] has been applied to dynamic analysis of geomaterials [5] and shown that the method can be used effectively to predict the large deformation due to soil failure such as slope failure. In this paper, the SPH method is used to study the seismic behavior of a slope. The co-seismic slope displacements and failure surface are calculated and compared with laboratory experimental results. The soil behavior is modeled with the elasto-plastic Drucker-Prager model. The artificial time history is used to simulate the earthquake loading. The seismic loading is applied to the slope by enforcing the motion of the model boundaries.

SIMULATION APPROACH

Soil constitutive model in SPH

As stated, soil is modeled using the elastic-plastic Drucker-Prager constitutive model. The implementation of this soil model in the SPH framework was already presented by Bui et al. [6]. The key equation used to represent the advance soil stresses are summarized here for brevity. The stress-strain relationship of Drucker-Prager's model with non-associate flow rule can be written as follow,

$$\frac{d\sigma^{\alpha\beta}}{dt} = 2G\dot{\epsilon}^{\alpha\beta} + K\dot{\epsilon}^{\gamma\gamma}\delta^{\alpha\beta} - \dot{\lambda} \left(9K \sin \psi \delta^{\alpha\beta} + \frac{G}{\sqrt{J_2}} s^{\alpha\beta} \right) \quad (1)$$

with the rate of change of plastic multiplier $\dot{\lambda}$,

$$\dot{\lambda} = \frac{3\alpha_\phi K \dot{\epsilon}^{\gamma\gamma} + (G/\sqrt{J_2}) s^{\alpha\beta} \dot{\epsilon}^{\alpha\beta}}{27\alpha_\phi K \sin \psi + G} \quad (2)$$

where G is the elastic shear modulus; K is the elastic bulk modulus; $\dot{\epsilon}$ is the deviatoric shear strain tensor; $\dot{\epsilon}$ is the elastic strain tensor; ψ the is dilatancy angle; δ is the Kronecker's delta; s is the deviatoric shear stress; J_2 is the second invariants of stress tensor; and α_ϕ is the Drucker-Prager's constant. These equations are discretized with SPH as following,

$$\frac{d\sigma_i^{\alpha\beta}}{dt} = \sigma_i^{\alpha\beta} \dot{\omega}_i^{\beta\gamma} + \sigma_i^{\beta\gamma} \dot{\omega}_i^{\alpha\gamma} + 2G\dot{\epsilon}_i^{\alpha\beta} + K\dot{\epsilon}_i^{\gamma\gamma} \delta^{\alpha\beta} - \dot{\lambda} \left(9K \sin \psi \delta^{\alpha\beta} + \frac{G}{\sqrt{J_2}} s^{\alpha\beta} \right) \quad (3)$$

$$\dot{\lambda} = \frac{3\alpha_\phi K \dot{\epsilon}_i^{\gamma\gamma} + \left(G/\sqrt{J_2} \right) s_i^{\alpha\beta} \dot{\epsilon}_i^{\alpha\beta}}{27\alpha_\phi K \sin \psi + G} \quad (4)$$

where i indicates a particle under consideration. $\dot{\epsilon}$, $\dot{\omega}$ are the strain rate and spin rate tensors, respectively, which are discretized as below,

$$\dot{\epsilon}^{\alpha\beta} = \frac{1}{2} \left(\sum_{j=1}^N \frac{m_j}{\rho_j} (v_j^\alpha - v_i^\alpha) \frac{\partial W_{ij}}{\partial x_i^\beta} + \sum_{j=1}^N \frac{m_j}{\rho_j} (v_j^\beta - v_i^\beta) \frac{\partial W_{ij}}{\partial x_i^\alpha} \right) \quad (5)$$

$$\dot{\omega}^{\alpha\beta} = \frac{1}{2} \left(\sum_{j=1}^N \frac{m_j}{\rho_j} (v_j^\alpha - v_i^\alpha) \frac{\partial W_{ij}}{\partial x_i^\beta} - \sum_{j=1}^N \frac{m_j}{\rho_j} (v_j^\beta - v_i^\beta) \frac{\partial W_{ij}}{\partial x_i^\alpha} \right) \quad (6)$$

where $j = 1, 2, \dots, N$ are particles in the influence domain of a certain particle i . W indicates function of approximation so-called “kernel function”.

The particle position is finally determined as follows,

$$\frac{dx_i^\alpha}{dt} = v_i^\alpha \quad (7)$$

Further details about SPH framework for soil can be found in [6] and [7].

Boundary conditions and earthquake loading

Accuracy and stability of computation depend on the boundary conditions. In this paper, two types of boundary condition are considered: free-roller and full-fixity. Details of these boundary conditions and their inclusion of seismic motion are discussed in the following section.

Free-roller boundary with seismic motion

Free-roller boundary condition is usually used to represent a far field boundary condition. At the free-roller boundary, soil particles are free to move in the direction which is parallel to the wall boundary. In SPH, the free-roller boundary can be simulated using ghost particles [8] which are placed symmetrically on the opposite side of the wall boundary as shown in Fig.1. The stress boundary condition is set as follow [6],

$$\sigma_G^{\alpha\beta} = \begin{cases} \sigma_R^{\alpha\beta} & \text{if } \alpha = \beta \\ -\sigma_R^{\alpha\beta} & \text{if } \alpha \neq \beta \end{cases} \quad (8)$$

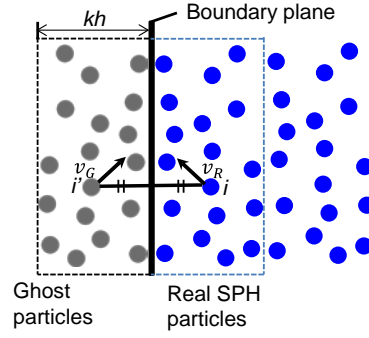


Fig.1 Arrangement and treatment of ghost particles

where σ_G and σ_R are the stress tensor of ghost and real SPH particles, respectively. The velocity of ghost particles v_G is represented as follows [6-7],

$$v_G = \begin{cases} -v_R + 2v_{wall} & \text{if } v_G \text{ is normal velocity} \\ v_R & \text{if } v_G \text{ is shear velocity} \end{cases} \quad (9)$$

where v_R is the velocity of real particles and v_{wall} is used to represent moving wall. In this paper, the seismic wave velocity on the roller boundary is enforced through v_{wall} . In addition, the roller boundary is also subjected to motion according to the seismic motion input.

Full-fixity boundary with seismic motion

The second type of boundary condition which is often used to restraint soil motions at the solid boundary is the full-fixity boundary [8]. In SPH, the fully-fixity boundary condition can be modeled using “boundary particles” which are placed outside the wall boundary as shown in Fig. 2. These particles are normally fixed in the space and carry the same material properties as soil particles [6-7], except the velocity. In this paper, the same approach presented by Bui et al. [6-7] which can be dated back to the original work proposed by Morris et al. [9] is applied. Accordingly, velocity of boundary particles are updated using the following equation,

$$v_{AB} = v_A - v_B = \bar{\beta} v_A \quad (10)$$

$$\bar{\beta} = \min \left(\bar{\beta}_{max}, 1.0 + \frac{d_B}{d_A} \right) \quad (11)$$

where v_A and v_B are the velocity of real and boundary particles, respectively; d_A and d_B are the distance from the real and boundary particles to the wall boundary; and β_{max} is a constant number which should be chosen to prevent particles getting closer to the wall boundary. In this study, $\beta_{max}=1.5$ is applied based on the recommendation by Bui et al [6].

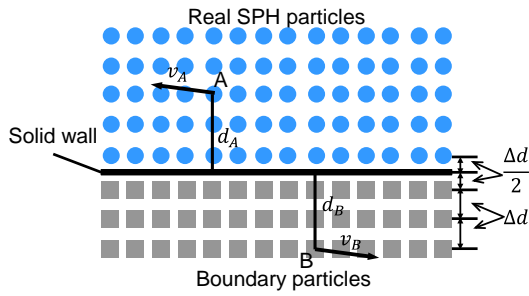


Fig.2 Arrangement and treatment of solid boundary

It is worth noting here that, although boundary particles are assigned with a virtual velocity (v_B), these particles are fixed in the space. However, for the case of moving boundary such as due to seismic motion, equation (10) must be replaced by the following equation,

$$v_{AB} = \beta(v_A - v_{wall}) \quad (12)$$

where v_{wall} is again the seismic velocity wave. As a result, the virtual velocity of boundary particles on the moving boundary can be estimated as follows,

$$v_B = (1 - \beta)v_A + \beta v_{wall} \quad (13)$$

Equation (13) assures that the velocity of real soil particles right at the solid wall will be exactly zero which satisfies the full-fixity boundary condition. However, this boundary condition does not represent the true natural seismic loading condition where the motion of boundary should be applied. In this paper, to simulate the true seismic loading boundary, the boundary particles are subjected to seismic motion which can be obtained by taking integration of the input acceleration.

NUMERICAL VALIDATION

Outline of experiment

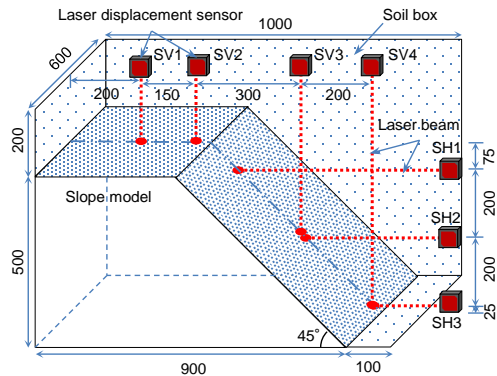


Fig. 3 Outline of the experiment (Unit: mm)



Fig. 4 View of the slope model in experiment

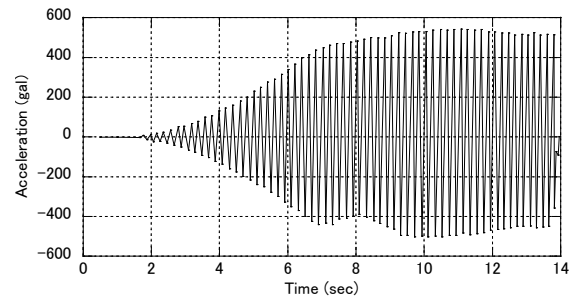


Fig. 5 Acceleration - time history used in experiment

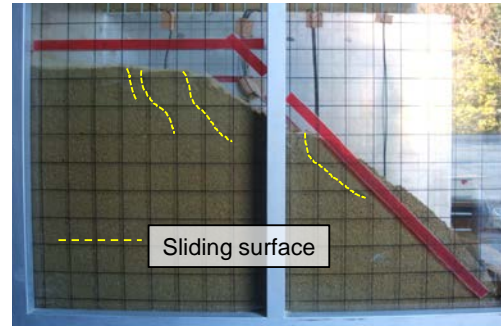


Fig. 6 Final slope configuration after loading

A small-scale cut slope shaking table experiment was conducted to verify SPH results. Figure 3 and 4 show the schematic diagram of the experimental setup and the overview of the soil slope shaking table setup respectively. A steel box of 100cm long, 60cm wide and 70cm high was mounted on top of the shaking table. The soil slope model of 90cm length, 60cm width and 50cm height was set in the shaking box, and the slope angle was 45°. The soil used in the experiment was Massa soil which is a weathered granite commonly found at Kansai area in Japan. The particle size over 5mm was eliminated and the water content of soil is set at 10%. The slope was constructed in phases using 5cm thickness compacted layers of 90cm length and 60cm width to achieve the homogeneous soil slope. Finally, the soil block was shaved to the angle of 45°. The soil

parameters are given in Table 1.

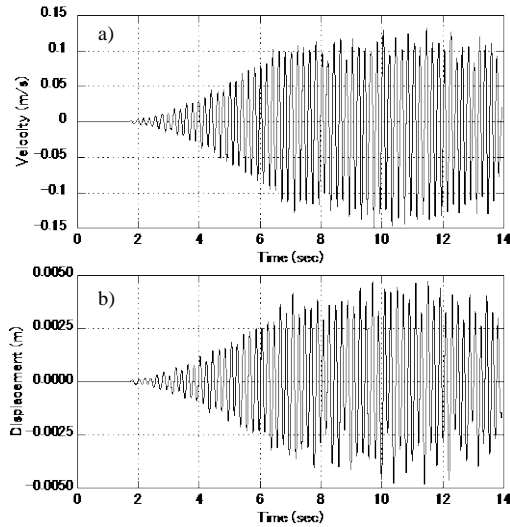


Fig. 8 Input seismic motions: a) velocity and b) displacement

Table 1 Soil parameters

Items	Values	Items	Value
ρ	1.68g/cm ³	ψ	0 - ϕ
ϕ	22.56°	E	2.57MPa
c	0.78 kPa	ν	0.33

To measure displacement within the slope, seven laser displacement sensors were used. Three sensors, named SH1, SH2, and SH3, were fixed to slope side on the soil box to measure horizontal displacement of the slope at given height (see Fig.3). Four laser displacement sensors, named SV1, SV2, SV3, and SV4, were fixed to the top of the soil box to measure vertical displacement at given locations. The shaking table can generate a maximum acceleration of 323m/s² with a corresponding displacement of 5cm in horizontal direction and a frequency of 700Hz.

The slope model was subjected to the seismic wave loading shown in Fig.5, which was recorded from the experiment. Test was run for 14 seconds until the slope was completely collapsed. Figure 6 shows the deformation pattern of the slope at the end of the testing. The top surface of the slope was settled down due to the soil compaction. Four distinct failure surfaces were identified from the side wall, suggesting that the slope was collapsed in several stages during loading. In addition, because the soil slope was constructed on the steel box, the friction at the bottom of the slope is significantly low. Therefore, the sliding along the steel box could also be considered as one of the factors triggering the slope failure.

NUMERICAL VALIDATION

A 2D-SPH model was conducted to simulate the

dynamic behavior of the slope model. Soil parameters for the constitutive model can be found in [9] and summarized in Table 1. The effect of dilatancy angle on the failure mechanism of the slope is investigated. In general, the dilatancy angle can vary from zero to the friction angle. In the case of $\psi = 0$, the plastic volume is constant, and there is no plastic volumetric expansion; however, for the case of $\psi = \phi$, the plastic volumetric expansion is maximal. Therefore, dilatancy angles of $\psi = 0, \phi/2$, and ϕ are adopted throughout this paper. Results of the failure surface and soil displacements are then compared with those observed in the experiment. The effect of pore-water pressure was assumed to be negligible and not considered in this study.

A total of 3245 SPH particles were used to create the slope model shown in Fig.3 with an initial smoothing length of 1.2cm. Boundary conditions are free-roller at the vertical and full-fixity at the base. The initial stress condition in the slope was obtained by applying the gravity loading to soil particles [7]. The slope model was then subjected to the seismic wave loading shown in Fig.8 which was computed from the acceleration time history recoded in the shaking table test. The load was applied by enforcing the seismic motions of the solid wall boundaries.

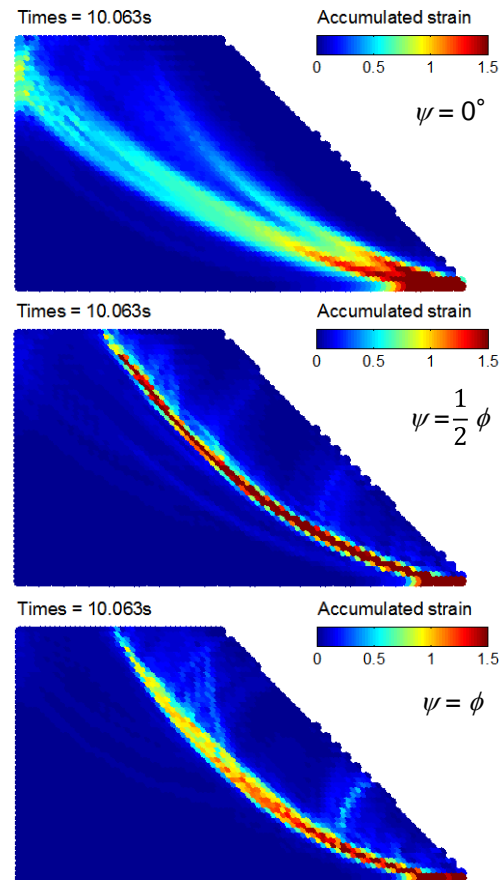


Fig. 9 Effects of dilatancy angle on the failure

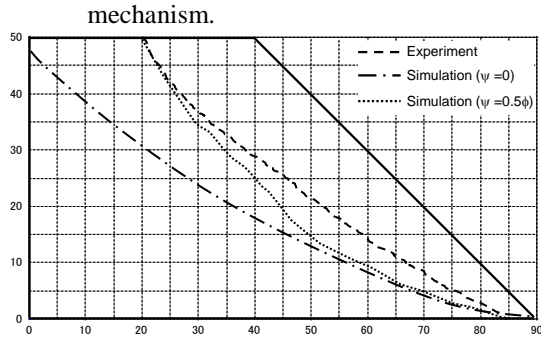


Fig. 10 Comparison between SPH simulation and experiment for the failure surface.

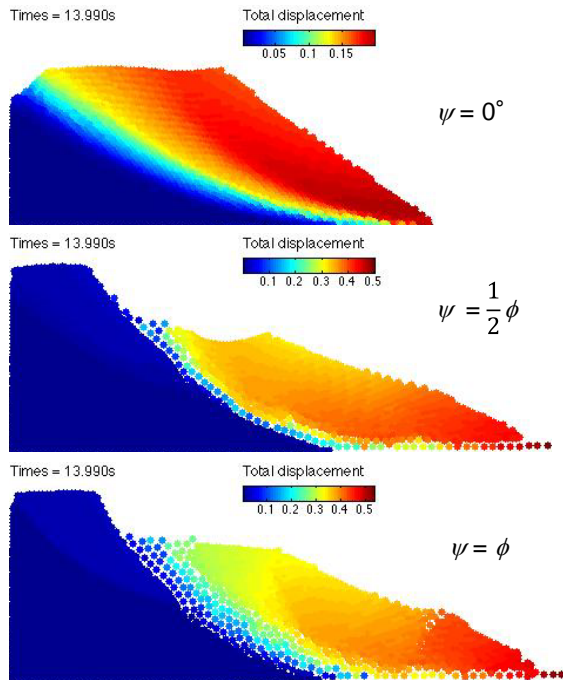


Fig. 11 Effects of dilatancy angle on the post failure behavior of the slope.

Figure 9 shows a comparison of the failure surface obtained in the simulations for different dilatancy angles. The contour plot represents the accumulated deviatoric strain. In the case of $\psi = 0^\circ$, soil underwent shear deformation without plastic volumetric expansion, which resulted in the thick shear band layer. Contrarily, when the dilatancy angle was increased, the failure occurred locally due to the development of plastic volumetric strain. As a result, the slip surface was found to be localized in a narrow band.

Figure 10 shows a comparison between experiment and simulation for the failure surface. In the experiment, the failure surface was obtained by removing collapsing soil carefully above the failure surface. It can be seen that the SPH simulation with high dilatancy angle (i.e. $\psi > 0.5\phi$) predicted fairly well the failure surface observed in the experiment.

However, the SPH model with ($\psi = 0$) overestimated the failure zone. The ends of sliding surface line are the same in both experiment and simulations. The shape of the sliding surface in the simulation was found to be almost circular, while that of experiment was a curved line having higher curvature angle. It is still not clear about this failure mechanism observed in the experiment because there might have some technical errors when removing the collapsing soil to specify the failure surface in the experiments. Further tests should be conducted to clarify this difference for a future work.

In term of the progressive failure, the experimental results showed that the slope model underwent four failure stages which correspond to four different failure surfaces as shown in Fig.6. The SPH model was unable to reproduced this failure mechanism; however, two failure surfaces were observed in the SPH simulation with ($\psi = 0$); while only one failure surface was found in the SPH model ($\psi > 0.5\phi$). On the other hand, the SPH method can simulate well the sliding process of soil after collapse.

Figure 11 shows a comparison of SPH simulations for the post-failure behavior of soil using different dilatancy angles. It can be seen that the higher dilatancy angle is utilized in the simulation, the larger final run-out distance could be predicted in the simulation. This result is conceptually correct and reflects well the behavior of the current constitutive model, that is the larger dilatancy angle is adopted in the constitutive model, the higher plastic volumetric strain could be predicted during the post-yielding process. This result suggests that if a suitable constitutive model is used, the SPH simulation could simulate well post-failure behavior of soil.

Figure 12 shows a comparison between the SPH simulation and the experiment for the vertical and horizontal displacements measured at some specific locations as outlined in Fig.3, i.e. SH1-SH4 and SV1-SV4. In both cases (i.e. $\psi = 0$ and $\psi = 0.5\phi$), the SPH simulations predicted fairly well the vertical and horizontal displacement profiles measured at different layer displacement sensors. However, simulation results over predicted the final run-out distance of soil measured in the experiment. The SPH model with zero-dilatancy angle seems providing better prediction of the displacement as compared to the SPH model utilizing high dilatancy angle. In addition, it is also noticed that the horizontal displacement at sensor SH1 in the SPH simulation of $\psi = 0.5\phi$ went negative, which is significantly different from that observed in the experiment. This can be explained due to the fact the slope collapsed and slid downward along the failure surface. Thus, the measuring location of SH1 in the simulation was no longer on the sliding soil volume, but on the failure surface. This mechanism was however not clear from the experiment. Further

research is required to confirm the mechanism.

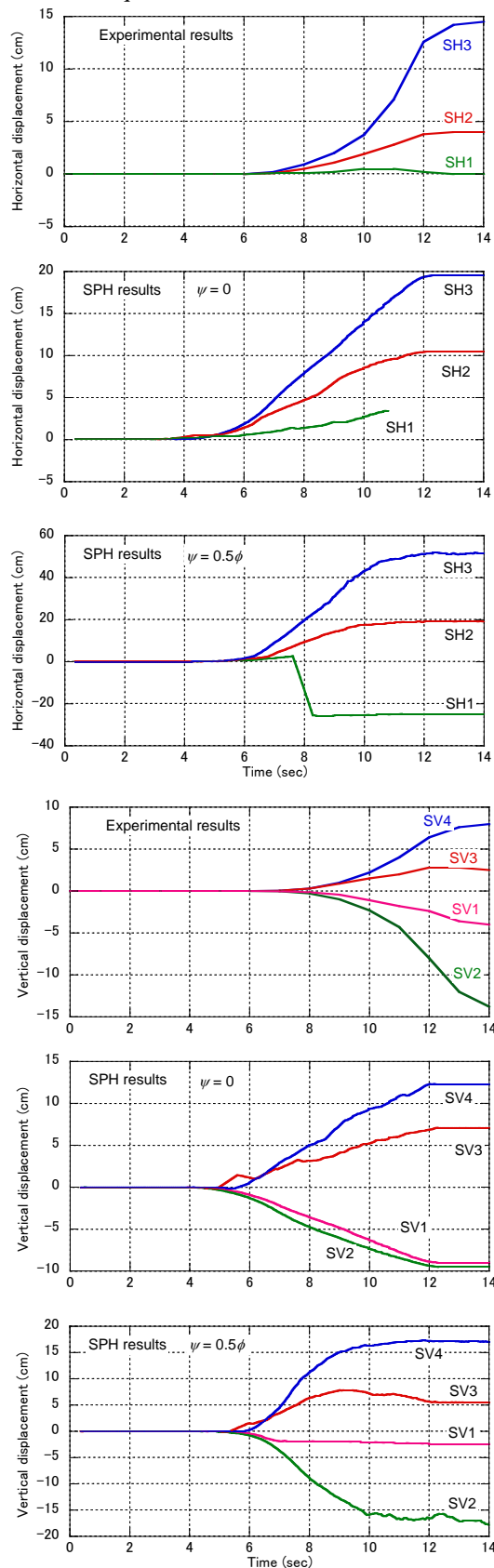


Fig. 12 Comparison between SPH simulation and experiment results for the displacements.

CONCLUSION

This study presented the application of SPH to simulate the large deformation and failure behavior of the slope subjected to dynamic loading. Results showed that SPH predicted fairly well the failure surface observed in the experiment, but significantly overestimated the slope deformation. In order to improve the accuracy of the SPH simulation, advanced soil constitutive model and damping should be taken into consideration. These are the subjects of future work

ACKNOWLEDGEMENTS

This research was supported by the JSPS institution program for young researcher overseas visits.

REFERENCES

- [1] Newmark NM, "Effects of earthquake on dams and embankments", *Geotechnique*, Vol 15, No.2, 1965, pp 139-160.
- [2] Cundall PA, Strack ODL, "A discrete numerical model for granular assemblies", *Geotechnique*, Vol 29, Issue.1, 1979, pp 47-65
- [3] Lucy LB, "A numerical approach to the testing of the fission hypothesis", *Astr. J.*, 82, 1977, pp.1013-1024.
- [4] Monaghan JJ, Gingold RA, "Smoothing particle hydrodynamics: theory and application to non-spherical stars", *Mon. Not. R. Astr. Soc.*, 181, 1977, pp.375-389.
- [5] Bui HH, Fukagawa R, Sako K, Okamura Y, "Earthquake induced slope failure simulation by SPH", *The 5th Int. Conf. Rec. Advanced Geotech. Earthquake Eng., CD*, 2010.
- [6] Bui HH, Fukagawa R, Sako K, Ohno S, "Lagrangian meshfree particles method (SPH) for large deformation and failure flows of geomaterial using elastic-plastic soil constitutive model", *Int. J. Numer. Anal. Meth. Geomech.*, 32, 2008, pp.1537-1570.
- [7] Bui HH, Fukagawa R, "An improved SPH method for saturated soils and its application to investigate the mechanisms of embankment failure: Case of hydrostatic pore-water pressure", *Int. J. Numer. Anal. Meth. Geomech.*, Vol.37, Issue 1, 2011, pp.31-50.
- [8] Randles PW, Liversky LD, "Smoothed particle hydrodynamics: some recent improvements and applications", *Com. Meth. Appl. Mech. Eng.*, Vol.139, 1996, pp.375-408.
- [9] Okamura Y, Sako K, Fukagawa R, "Analysis of seismic displacements of slopes applied vibratory conveyance theory", *Journal of JSCE (C)*, Vol.65, No.1, 2009, pp. 162-173.

ELECTRICAL RESISTIVITY TOMOGRAPHY TO INSPECT BRIDGE FOUNDATIONS

Helsin Wang¹, Chih-Hsin Hu², and Chung-Yue Wang^{1,3}

¹Institute of Bridge Engineering, CECI, Taiwan; ²HCK, Taiwan; ³Department of Civil Engineering, National Central University, Taiwan

ABSTRACT

Non-destructive testing (NDT) has been verified to efficiently know foundation conditioning. In this paper, NDT techniques were required to inspect the bridge foundations with high scour potential in Taiwan. The electrical resistivity tomography was proposed to conduct to the inspection on three commonly-used foundation types of bridges. This technique displays its unique image outcomes for each foundation type. A high reliability image can be easy-of-operation to identify both the shape and depth on shallow foundations and caissons.

Keywords: *Electrical resistivity tomography, Foundation type, Bridge, Non-destructive testing,*

INTRODUCTION

The as-built condition of foundations can affect the performance of existing bridges supported by these elements. Foundation conditioning is a crucial key to evaluate the bridge resistance to flood or earthquake and its stability for bridge engineers. For example, lacking foundation dimension could impede of rating the flood or earthquake resistance on old bridges. Furthermore, materials deterioration, scour variation, or cracking could undermine the foundation capacity of bridges as well.

For more than forty years, non-destructive testing (NDT) or instrumentation inspection has been developed to know the integrity of foundations [1], [5], [6]. Such inspection technique can provide quality assurance of construction, maintain original functions after testing, determine in-situ mechanical properties, rapidly assess a number of objects, and find aberration in existing foundations.

At present, both the surface reflection technique, such as the impulse response method or ultra-seismic method, and direct transmission technique, such as the sonic logging method or parallel seismic method, are frequently used to evaluate the integrity of concrete piles, drilled shafts, and caissons in field [1], [3]-[5].

Besides the wave-based inspection techniques, geophysical inspection methods were introduced to subsurface and substructure investigation in past few years [6], [8]. The most useful inspection technique, electrical resistivity tomography (ERT), provided an outstanding identification on the interface between foundations and surrounding soils/rocks [2].

ELECTRICAL RESISTIVITY TOMOGRAPHY

The principle of ERT is to develop an artificial potential field by probing current electrodes around

a target zone. Two extra potential electrodes are triggered to measure the ground potential difference (as shown in Fig. 1).

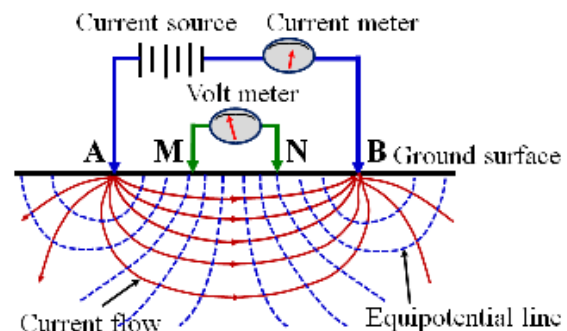


Fig. 1 A schematic representation for ERT setting.

The typical resistivity values of geomaterials and waters are shown in Table 1 as reference for identifying rock type, water content, salt content, and anomaly, such as embedded pipes, underground structures, or hollows. The measured resistivity value in field is also highly contingent to mineral composition, grain size, mineral formation, water content, and ion concentration.

As shown in Fig. 2, the upper part shows the two RC elements embedded in layered soils; the lower one presents the measured apparent resistivity image with a display mode of visible-light spectrum, which corresponds resistivity values varying from 2,000 to less than 1 ohm×m and illustrates the resistivity intensity distributions in space. The resistivity value for sediments composed of silt and sand is more than 5 ohm×m, corresponding to the pink, red, orange, yellow, or green zones. The existence of pre-cast or cast-in-place foundations and protection works, which usually consists of steel, could increase the electric conductivity value and

also form a low resistivity-content zone with a specific geometrical shape or spatial attribute. The steel-content structural pieces have a lower resistivity value, below $1 \text{ ohm}\cdot\text{m}$, corresponding to light blue and grey shades. The possible distribution of underground structures is graphically illustrated on the resistivity images.

Table 1 Resistivity range of common rocks, soils, and waters [6].

Material	Resistivity ($\text{ohm}\cdot\text{m}$)
Rocks	
Granite	$5 \times 10^3 - 10^6$
Slate	$6 \times 10^2 - 4 \times 10^7$
Marble	$10^2 - 2.5 \times 10^8$
Sandstone	$8 - 4 \times 10^3$
Shale	$20 - 2 \times 10^3$
Limestone	$50 - 4 \times 10^2$
Soils	
Clay	1–100
Sand (dry)	$5 \times 10^3 - 2 \times 10^4$
Sand (saturated)	$2 \times 10^2 - 10^3$
Gravel (dry)	$2 \times 10^4 - 8 \times 10^4$
Gravel (saturated)	$10^3 - 5 \times 10^3$
Alluvium	10–800
Waters	
Groundwater (fresh)	10–100
Sea Water	0.2

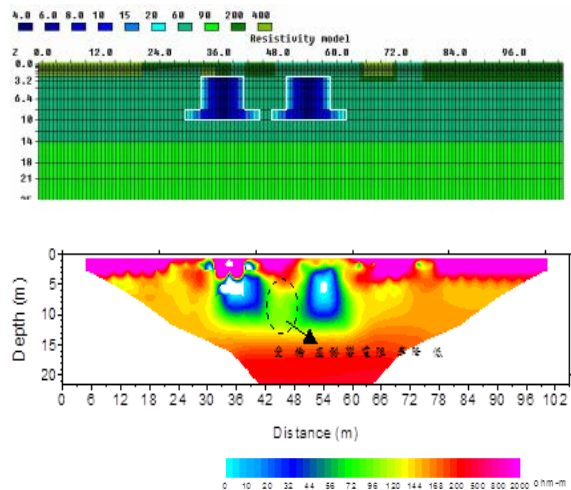


Fig. 2 ERT result of layered soils influenced by 2 embedded RC elements.

There are 4 commonly-used inspection types, including pole-pole array, pole-dipole array, dipole-dipole array, and Wenner-Schlumberger array [6]. Each inspection type has different resolutions along and perpendicular to the probing array direction and also expresses various inspection abilities in depth. In practice, ERT deployment is highly associated with subsurface characterization and environment. Its crucial information is listed as the below:

- (1).Electrode Spacing: The smaller electrode spacing is arranged, the higher image resolution and the shallower inspection depth are. Accordingly, the larger electrode spacing is used, the lower image resolution and the deeper inspection depth are. Both inspection depth and site characteristics determine the possible electrode spacing.
- (2).Layout Length: The optimal layout length is suggested to be various from 1.5 to 2 times of pier foundation depth if possible.
- (3).Inspection Type: Two or more inspection types are suggested to magnify the resolution along and vertical to the probing array direction.
- (4).Layout Deployment: The inspection depth and resolution are in terms of electrode spacing, layout length, and the probing distance to bridge piers. Furthermore, a trial and error process on sectional image is used to determine the optimal layout deployment.
- (5).In order to enhance inspection accuracy, two mutually-perpendicular inspection directions are suggested around a target bridge pier if possible.

CASE STUDY

The ERT technique was proposed to inspect the foundation conditioning on four scoured river-crossing bridges in Taiwan. The following sections describe the execution and interpretation linking ERT images and foundation conditions.

Shallow Foundation

The Guguan Bridge was a 3-span pre-stressed bridge crossing the Da-Jia Stream in middle Taiwan. The bridge stood at the bending vertex zone, and severely alternative scour and deposition occurred at the bridge site. Two bridge piers were located at the river bending zone covered with gravely riverbed overlaying upon bedrock (Fig. 3). The foundation type was determined as shallow foundations with a depth of 4 m from the ground surface.



Fig. 3 ERT inspecting a bridge shallow foundation.

A 70-m long ERT layout Line G2 was selected to set around one of bridge piers with an electrode spacing of 2 m. In order to circumvent embedded training structures found on the upstream side, Line G2 had an angle of 45° different from the bridge direction (Fig. 3). The position of the target bridge pier was set around at the position of 36~39 m on Line G2.

Two inspection types, dipole-dipole array and pole-dipole array, were applied to inspect the bridge foundation type, as shown in Fig. 4 and Fig. 5, respectively. The black dotted line represented the interface between gravel and bedrock. The white dotted line indicated the groundwater table. The ERT images also significantly revealed a pretty low resistivity zone, shown as grey-white color, at the position of 34~40 m, which overlapped the position of the bridge pier. The resistivity value ranged 1~20 $\text{ohm}\times\text{m}$ which corresponded to the resistivity value of metal. The foundation type was shaped with a black thin dotted line. This step-like image was identified as a shallow foundation. The estimated depth was around 5 m from the ground with an inspection error of ± 1 m.

In addition, the resistivity value of the gravel layer fell around 300 $\text{ohm}\times\text{m}$. The resistivity image on bedrock was distorted by overlaying bridge pier which were usually composed of steel for structural reinforcement.

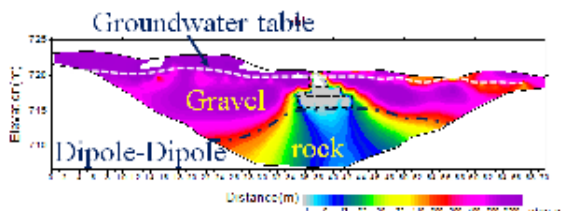


Fig. 4 ERT image crossing a shallow foundation with dipole-dipole array.

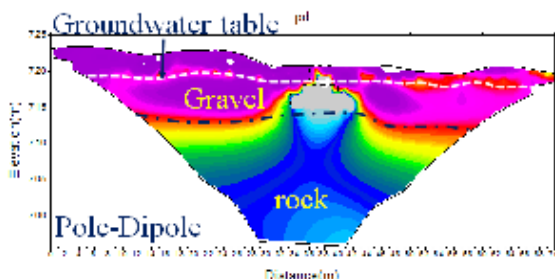


Fig. 5 ERT image crossing a shallow foundation with pole-dipole array.

Caisson

The Tienmei Bridge was a 2-span pre-stressed RC bridge crossing the Chung-Guan Stream in northern Taiwan. The single bridge pier was located

at gravelly riverbeds overlaying upon sandstone (Fig. 6). The foundation type was determined as a caisson with a depth of 8.3 ± 0.5 meters obtained from the ultra-seismic method. The scour depth around the bridge pier was deepened much more than that of the other river section due to a violent flow of bending vertex. The exposed height was around 1.5 m above the river surface. The underwater exposed height was measured as 2.5 m using a hanging weight scour measurement. A scour potential has been reported to the bridge agency for re-building a new bridge in order to replace the current old bridge.



Fig. 6 ERT inspecting a bridge caisson.

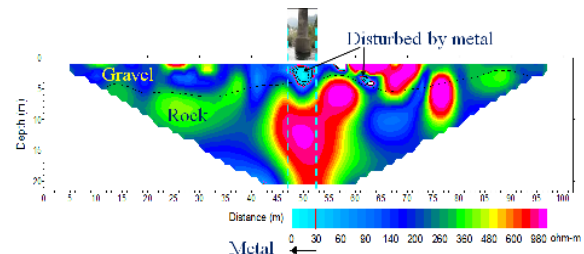


Fig. 7 ERT image crossing a bridge caisson.

The inspection type of pole-dipole array was executed to inspect the foundation type. The ERT probing Line L-1 was set perpendicularly to the bridge direction and parallel to the flow direction. Its total length was around 102 m by using an electrode spacing of 3 m. The position of the pier corresponded to around the position of 48~51 m on the ERT image (Fig. 7). A light blue zone was identified as the bridge pier. Its embedment depth was evaluated as 4.5 ± 1.5 m. The estimated height of the caisson was totally 8.5 ± 1.5 m consistent with the recorded value.

In addition, the black dotted line represented the interface of gravels and bedrock. An unknown embedded object, RC armed blocks possibly, which was marked with a low resistivity value, severely interfered with the ERT image on the downstream side.

Deep Foundation

The Sibin Bridge

The Sibin Bridge on joint Highway No.17 and Expressway No.61 provided the most downstream crossing point over the longest Chuo-Shuei Stream, around few kilometers from the Taiwan Strait in western Taiwan (Fig. 8). This 78-span bridge was 2,730 m in length and consisted of three parallel I-type pre-stressed bridges with widths of 8 m, 18 m, and 8 m supported by 35-m-long pile group each pier. The distance was around 2 m between adjacent

two bridges. Repeatedly scour and deposition around pile foundations were induced by storms or typhoons.

A 220-m ERT inspection line R-2 was aligned along the traffic direction with a distance of 1 m outside to bridge piers P11~P16. Electrode spacing as 5 m was selected to detect foundations and soils above the depth of 40 m. The corresponding positions of bridge piers P11~P16 were at the positions of 10~16 m, 45~51 m, 80~86 m, 115~121 m, 150~156 m, and 185~191 m along the inspection line, respectively. These six zones with pretty low resistivity values positively confirmed the existence of six pile groups (as shown in Fig. 9(a)).



Fig. 8 Panorama of the Sibin Bridge.

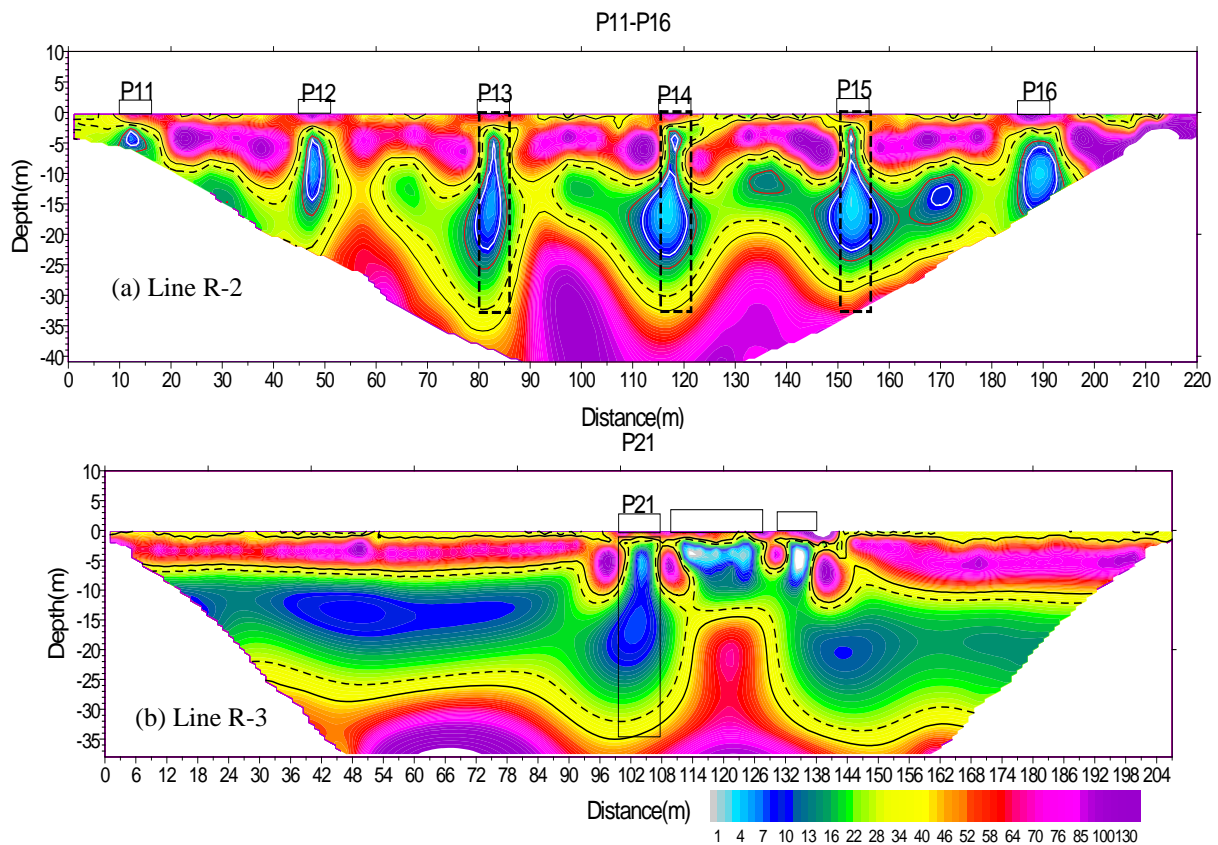


Fig. 9 ERT images (a) along the bridge direction and (b) across pier P21 on the Sibin Bridge.

A low resistivity isolines image was assumed as a rectangular shape on each pile group herein. Since both the length of pile groups and shallow embedded

protection works, RC armed blocks, or training structures, the most countermeasures used to mitigate bridge scour in Taiwan, played a key role in

ERT inspection results, these two effects severely interfered with ERT inspection ability and sheltered the electrical potential response at deeper zones. This caused a distorted water-drop-like shape, not a rectangular shape, extended from the pile cap downward into the elevations various $-25 \sim -29$ m ± 2.5 m, much less than designate depth, -35 m, on piers P13~P15 (seen in Fig. 9(a)).

A 207-m-long ERT inspection Line R-3 was aligned perpendicularly to the bridge direction with a distance of 1 m to all piers on the P21 position. Electrode spacing as 3 m was selected to detect foundations and soils below the depth of 37 m. Pier P21 was marked at the position of 100~138 m on the ERT image (Fig. 9(b)). The ERT image also exhibited that a low resistivity zone with less than 22 ohm \times m could be identified at the position of 100~108 m. Its water-drop-like shape geometrically indicated that the length of pile groups was around the 28 ± 1.5 m less than the construction length, 35 m. Unfortunately, the caps on the rest pile groups severely interfered with ERT inspection results and blocked the electrical potential response below 10 m at the position of 110~138 m. No reliable information could be provided to estimate their depth. In addition, two low resistivity zones, which ranged around the horizontal positions of 0~90 m and 141~207 m, represented unknown RC armed blocks existing at the depth of 20~25 m.

The Wanda Bridge

The Wanda Bridge on Expressway No.88 played an important transportation role over the Kaoping Stream in southern Taiwan (Fig. 10). This bridge was consisted of two parallel I-type pre-stressed bridges with a width of 24.5 m each. Each bridge was supported by two RC piers overlaying 30-m-long pile groups which were embedded in sandy

layer. The distance was 2 m between these two bridges. An increasing scour were found on the upstream right embankment. Therefore, inspection Lines L-1 and L-2 were set across and along this target zone as shown in Fig. 10.

Inspection Line L-1 had a length of 200 m and transversely crossed through around four piers at P6 position with a distance of 1 m to all piers. Electrode spacing as 5 m was selected to detect foundations and soils below the depth of 45 m. These four RC piers were located at the positions of 96~103 m, 107~116 m, 124~133 m, and 137~144 m, respectively, on its ERT image (seen in Fig. 11). These corresponding positions displayed four low resistivity-content zones (less than 26 ohm \times m). Their pile caps and an unknown aberration material severely interfered with the ERT inspection result. Therefore, the lengths of pile groups have great variations from 10 m to 28 m ± 2.5 m, less than the construction length, 30 m, marked on Fig. 11.

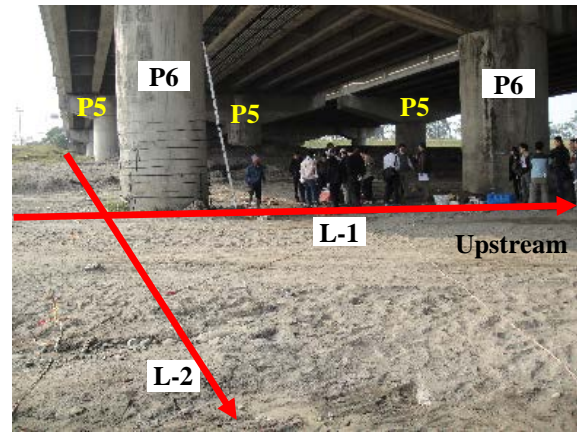


Fig. 10 ERT inspecting the pile foundations of the Wanda Bridge.

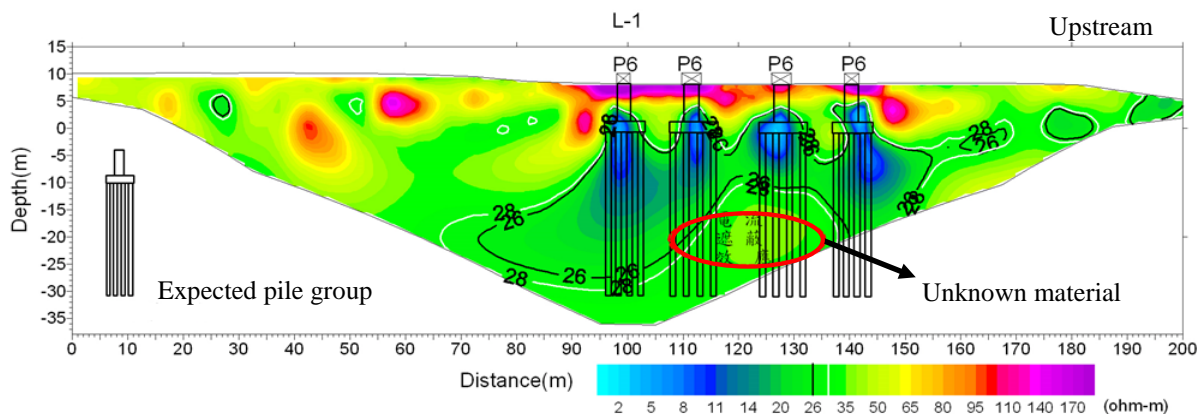


Fig. 11 ERT image across pier P6 on the Wanda Bridge.

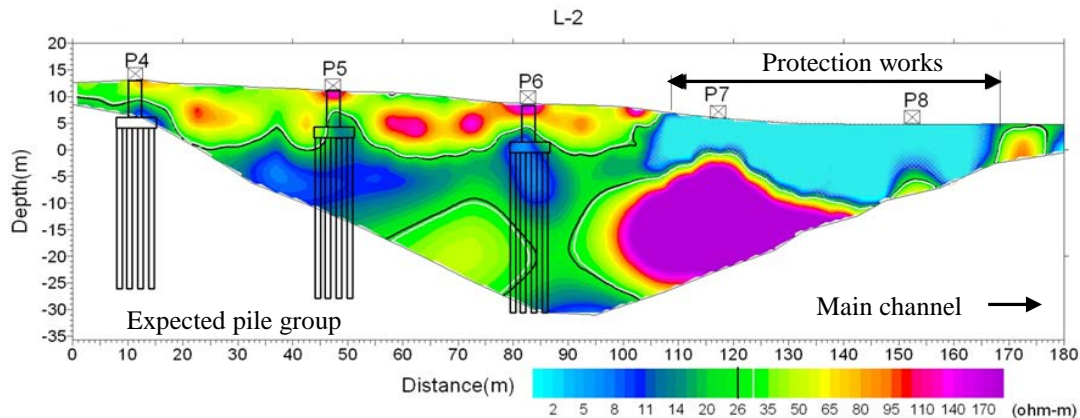


Fig. 12 ERT image along the traffic direction on the Wanda Bridge.

Line L-2 was aligned along the bridge direction and crossed five piers from P4 to P8 with a distance of 1 m to these 5 piers. Fig. 12 indicated that their corresponding positions were situated at the positions of 8~15 m, 44~51 m, 79~86 m, 115~122 m, and 150~157 m, respectively, along the inspection line. An extreme low resistivity zone (less than 10 ohm×m) was found at the positions of 105~168 m. This condition could be identified to experience embedded protection works due to continuously lateral erosion on the upstream side. Therefore, the depth of pile groups could not be recognized from this ERT deployment.

CONCLUSION

The ERT inspection technique was applied to investigate the foundations of four scoured river-crossing bridges in Taiwan. The foundation depths, as well as foundation type, could be significantly identified from the measured resistivity images on shallow foundations or caissons of bridges. However, a droplet-like resistivity shape represented the existence of deep foundations, for the shelter effect of pile groups obviously limited the cognoscible range of the electrical field on the upper part of pile groups. Therefore, their exact depth also could not be recognized on the detective ERT images. In future, according to these ERT image characteristics, bridge engineers have a chance to rapidly determine the foundation type, even its depth, of unknown foundation bridges, and their flood or earthquake resistance can be preliminarily assessed.

ACKNOWLEDGEMENTS

The paper is partially granted by the Harbor and Marine Technology Center, Institute of Transportation, the Ministry of Transportation and Communications (MOTC) in Taiwan. Authors greatly appreciate the financial support and assistances of the MOTC.

REFERENCES

- [1] Baker CN, Parikh G, Briaud JL, Drumright EE, and Mensah DF, Drilled Shafts for Bridge Foundations, FHWA Report No. FHWA-RD-92-004, McLean, VA: Federal Highway Administration, 1993.
- [2] Non-Destructive Testing Committee of the Chinese Institute of Civil and Hydraulic Engineering, Inspection Method and Application of Bridge Inspection, Taipei, Taiwan: Scientific and Technical Publishing Co., Ltd., 2010, pp. 5-27~5-32.
- [3] Davis AG and Dunn CS, "From theory to field experience with non-destructive vibration testing of piles", Proceedings of the Institution of Civil Engineers, Part 2: Research and Theory, Vol. 57, 1974, pp. 571-593.
- [4] Geo-Institute Deep Foundation Committee, "Nondestructive evaluation of drilled shafts", Journal of Geotechnical and Geoenvironmental Engineering, ASCE, Vol. 126, No. 1, 2000, pp. 92-95.
- [5] Hertlein BH and Davis AG, Nondestructive Testing of Deep Foundations, Chichester, U.K.: John Wiley & Sons Ltd., 2006.
- [6] Loke MH, Electric Imaging Surveys for Environmental and Engineering Studies— A Practical Guide for 2-D and 3-D Surveys, Sunbyberg, Sweden: ABEM Instrument AB, 2000.
- [7] Olson LD, Jalinoos F, and Aouad MF, Determination of Unknown Subsurface Bridge Foundations, NCHRP Project No. E21-5, Transportation Research Board, Washington, D.C.: National Research Council, 1998.
- [8] Wightman WE, Jalinoos F, Sirles P, and Hanna K, Application of Geophysical Methods to Highway Related Problems, FHWA Report No. DTFH68-02-P-00083, Lakewood, CO: FHWA, Central Federal Lands Highway Division, 2003.

ULTIMATE BEARING CAPACITY ANALYSIS OF GROUND AGAINST INCLINED LOAD BY TAKING ACCOUNT OF NONLINEAR PROPERTY OF SHEAR STRENGTH

Du N L¹, Ohtsuka S¹, Hoshina T¹, Isobe K¹, and Kaneda K²

¹Department of Civil and Environmental Engineering, Nagaoka University of Technology, Japan

²Takenaka corporation, Japan

ABSTRACT

In the assessment of bearing capacity of footing, the bearing capacity formula proposed by The Architectural Institute of Japan (AIJ) has been widely used in Japan for the design of building foundation. However, this formula is limited to simple conditions like simple footing shape, flat ground and uniform material property. Although the rigid plastic finite element method (RPFEM) can solve this complex problem, it has not taken into account the size effect in assessment of bearing capacity. This study newly develops the RPFEM by introducing the nonlinear shear strength property against the confining stress and proposes the rigid plastic constitutive equation of parabolic yield function, basing on the change in the angle of shear resistance of Toyoura sand. The developed method and the bearing capacity formula (established by empirical approach) provided identical results for various footing sizes showing good estimation for wider range of footing size.

Keywords: Rigid plastic finite element method, Bearing capacity, Inclined load effect, Size effect

INTRODUCTION

Assessment of bearing capacity is necessary to ensure the stability of a building. However, the bearing capacity of footing could be considerably influenced by many factors, including inclination load, eccentric load, shape, depth, size effect, etc.

Many researches have investigated these effects on bearing capacity. Terzaghi & Peck (1948) developed the classical bearing capacity equation as follow:

$q_u = \gamma \cdot D_f \cdot N_q + c \cdot N_c + 0.5 \gamma \cdot B \cdot N_\gamma$ and defined bearing capacity factors N_c , N_q , N_γ in terms of a linear strength envelope $\tau_{\max} = \sigma \tan \phi + c$.

Meyerhof (1951, 1963), and Brinch Hansen (1970) based on the limit equilibrium method and the slip line method which were extended by the original proposal of Terzaghi (1948) to apply that formula with more general factors and also derived expressions for the inclination factors. In Japan, bearing capacity formula proposed by Architectural Institute of Japan (AIJ) has been also widely used. This formula uses bearing capacity factors N_c , N_q given by Prandtl, N_γ and inclination load factors i_c , i_γ , i_q described by Meyerhof, and other extended factors: shape coefficient α, β defined on the basis of footing shape and size effect factor. In recent years, finite element method has involved as a well known method in structural analysis, a revival of interest in finite element, mainly focusing on soil mechanics problems and exploiting the kinematic.

On the other hand, rigid plastic finite element method uses only strength parameters of the ground. RPFEM is an analysis method which has been developed in the field of plastic working of metal. It is the effective analysis method to calculate the ultimate bearing capacity of the ground. Initially, RPFEM was established on the basis of the upper bound limit analysis, then it developed the rigid plastic constitutive equation to provide the similar result as in limit analysis. RPFEM with several constitutive equations is quite often utilized to predict the critical behavior. However, RPFEM does not take into account the size effect in assessment of bearing capacity. This study newly develops the RPFEM by introducing the nonlinear shear strength property against the confining stress and proposes the rigid plastic constitutive equation of parabolic yield function against the confining stress.

This paper describes a simple method of calculating bearing capacity by using rigid plastic finite element method which is derived from the rigid plastic constitutive equation, and then compares the result with those of other methods (limit equilibrium method (Meyerhof, AIJ) and, Slip line method (Hansen) with the width range of foundations from 1m to 100m.

Results obtained from this study shows that although Meyerhof, Hansen or AIJ methods are widely used in design, they are not sufficiently clarified. As we have known, although many experiments have been carried out with model tests, a conclusion for the size effect of model scale is difficult to obtain. Moreover, these formulas use the

simple linear strength model. This study develops RPFEM to solve the boundary problem with kinematical properties and provide a summary of good estimation for wider range of footing size.

RIGID PLASTIC FINITE ELEMENT METHOD (RPFEM)

Limit analysis and its application to FEM

Hill (1951) and Drucker (1951, 1952) published their ground breaking lower and upper bound theorems of plasticity theory, on which limit analysis is based. It is apparent that limit analysis would be an effective tool to provide important insights into the bearing capacity problem.

The upper bound theorem of classical plasticity theory which assumption of a perfect plastic soil model with an associated flow rule, is an useful tool to predict the stability of problems in soil mechanics. It states that the power dissipated by any kinematically admissible velocity field could be equated to the power dissipated by the external loads, and so enables a strict upper bound on the true limit load to be deduced. A kinematically admissible velocity field satisfies the conditions of compatibility, flow rule and velocity boundary. In order to provide practical solutions, the upper bound theorem is often used in parallel with the lower bound theorem.

The formula of the Rigid Plastic finite element method is built on the basic of the upper bound theorem. The arbitrary general strain rate element $\dot{\epsilon}_{ij}$ is not always allowed for the strain rate $D(\dot{\epsilon}_{ij})$ since some kind of constraint is more specific. It is assumed that no volumetric plastic strain rate occurs under the limit state. This is naturally accepted for the soil structure. Define further the subset $K_0 (\subset K_p)$

The upper bound theorem previously proved is found to be valid when we restrict $(\dot{u}_i, \dot{\epsilon}_{ij})$ to K_0 since $(\dot{u}_i^*, \dot{\epsilon}_{ij}^*)$ at the limit state also stays in K_0 .

$$\text{Minimize } \int_{\dot{\epsilon}_{ij} \in K_0} D(\dot{\epsilon}_{ij}) dV \quad (1)$$

It should be noted that this problem falls into the category of the convex programming problem, i.e., the functional to be minimum is always identical to the global one.

where

$\dot{\epsilon}$: Vector of strain rates of all elements

\dot{u} : Vector of all nodal velocities

\dot{v} : Vector of rates of volume change of all elements

Rigid Plastic constitutive equation

Tamura (1991) developed the rigid plastic constitutive equation for frictional material. The Drucker-Prager's type yield function is expressed as follow:

$$f(\sigma) = aI_1 + \sqrt{J_2} - b = 0 \quad (2)$$

where I_1 is the first invariant value of stress, J_2 is the second invariant value of shear stress, the constants of a and b express the angles of shear resistance and dilatancy.

$$I_1 = \text{tr} \sigma \quad (3)$$

$$J_2 = \frac{1}{2} \mathbf{s} : \mathbf{s} \quad (4)$$

Following the non-associated flow rule, the strain rate $\dot{\epsilon} = \dot{\epsilon}^p$ could be written as follow:

$$\dot{\epsilon} = \lambda \frac{\partial g}{\partial \sigma} = \lambda \left(\alpha \delta_{ij} + \frac{\mathbf{s}}{2\sqrt{J_2}} \right) \quad (5)$$

where λ is an indeterminate multiplier and δ_{ij} is the Kronecker's delta symbol, $\dot{\epsilon} = \sqrt{\dot{\epsilon} : \dot{\epsilon}}$ is the norm of strain rate and \mathbf{I} is a unit tensor. However, the strain rate $\dot{\epsilon}$ should satisfy the volumetric constraint condition as follow:

$$h(\dot{\epsilon}) = \dot{\epsilon}_v - \frac{3\alpha}{\sqrt{3\alpha^2 + 1/2}} \dot{\epsilon} = 0 \quad (6)$$

in which $\dot{\epsilon}_v$ and $\dot{\epsilon}$ indicate the volumetric strain rate and norm of the strain rate, respectively. The rigid plastic constitutive equation was expressed by Tamura (1991) as follow:

$$\sigma = \sigma^{(1)} + \sigma^{(2)} = \gamma \frac{\partial f}{\partial \sigma} + \beta \frac{\partial h}{\partial \dot{\epsilon}} \quad (7)$$

The variable of γ is determined by inserting Eq. (4) into the plastic potential of Eq. (2). On the other hand, the indeterminate stress parameter β still remains unknown until the whole problem with the kinematical constraint conditions of Eq. (6) is solved. The stress-strain rate relation for the Drucker-Prager's type by means of the nonassociated flow rule is finally expressed in the following form:

$$\sigma = \frac{\psi - 3\alpha\beta}{\sqrt{3\alpha^2 + 1/2}} \frac{\dot{\epsilon}}{\dot{\epsilon}} + \beta \mathbf{I} \quad (8)$$

Where the coefficient ψ is a variable, which is determined by stress σ located on the yield function, α as cohesion.

BEARING CAPACITY OF FOOTING UNDER PLANE STRAIN CONDITION

Bearing capacity formulas

Meyerhof (1951, 1953, 1963, 1965 and 1976) developed the bearing capacity equations by extending the Terzaghi's mechanism to the soil above the base of the footing. The bearing capacity factors N_c and N_q are given by Prandtl (1921). Meyerhof extended the proposal of Terzaghi (1948) and incorporated those factors as follow:

$$q = i_c c N_c + 0.5 i_\gamma \gamma_1 B N_\gamma + i_q \gamma_2 D_f N_q \quad (9)$$

In 1953, Meyerhof extended his theory for ultimate bearing capacity under vertical load to the case with inclined load. The assumed failure mechanism is confined to one side of the footing for all values of the inclination angle, and composed of three zones whose geometry is changed to account for the load inclination. Furthermore, two slightly different mechanisms were considered, one for small inclinations and another for large inclinations.

Brich Hansen (1957, 1970) used the slip – line method and provided a new expression for the semi - empirical N_γ factor, with other bearing capacity factors kept unchanged. Hansen also derived expressions for the empirical inclination factors. This expression has assumption on one sided mechanism and accounts for the adhesion between the soil and the footing base.

Bearing capacity formula of AIJ using bearing capacity factors N_c , N_q given by Prandtl and N_γ and inclination load factors i_c , i_γ , i_q described by Meyerhof

$$q = i_c \alpha c N_c + i_\gamma \gamma_1 \beta B \eta N_\gamma + i_q \gamma_2 D_f N_q \quad (12)$$

and some extended factors: shape coefficient defined based on the shape of foundations. α, β with the strip foundations are 1 and 0.5 respectively; Size effect factor (B is a width of footing and B_0 is a reference width):

$$\eta = \left(\frac{B}{B_0} \right)^n \quad (10)$$

Bearing capacity of footing for vertical load

For under concentrated vertical load, the numerical solution is used with a rigid plastic constitutive equation under plain strain condition. This is the linear shear strength properties.

This study uses the angle of shear resistance $\phi=30$ deg. The result presented from fig.1 shows that the bearing capacity of footing increases with the increase of size footing. As can be seen the value obtained from RPFEM and other methods have large difference. This difference is due to the significant effect of confining stress when calculating the bearing capacity of footing. This would be improved in the next section when using RPFEM consider

confining stress .

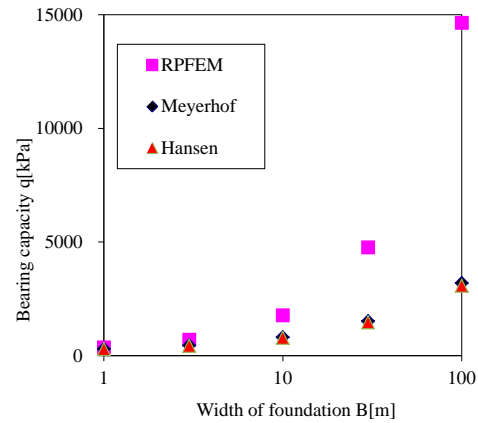


Fig. 1 Effect of footing width on bearing capacity for concentric vertical load application ($\phi = 30$ deg)

Bearing capacity of footing for inclined load

We calculate the bearing capacity regardless of size effect. The bearing capacity under vertical load is calculated for the case with inclined load and, angle of shear resistance $\phi = 30$ deg. Load inclination angle θ is inclination of load with respect to vertical. The load inclination angle changes from 10 deg to 30 deg.

As presented above, inclination load only effect when inclined load angle $\theta < 30$ deg with the Meyerhof's formula.

The empirical results shows that the values of bearing capacity of footing decrease as the load inclination angle increase, even for small inclination angles.

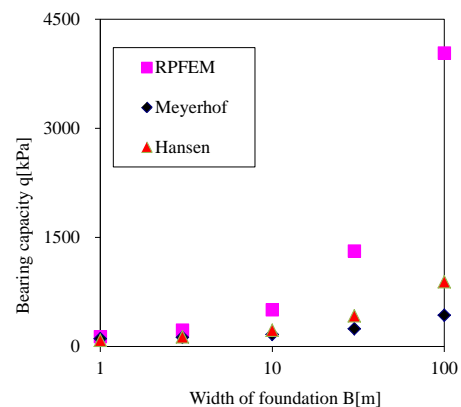


Fig. 2 Bearing capacity with angle of Inclined load $\theta = 20$ deg

Fig. 2 describes the relationship between bearing capacity and width of footing. The different values also consistently confirmed the effect of confining stress dual on bearing capacity of footing.

Furthermore, results presented in the Fig. 2 indicate the influence of size effect. The larger width of footing the larger difference between RPFEM with other methods.

RIGID PLASTIC CONSTITUTIVE EQUATION OF TOYOURA SAND

Strength tests of Toyoura sand by Tatsuoka

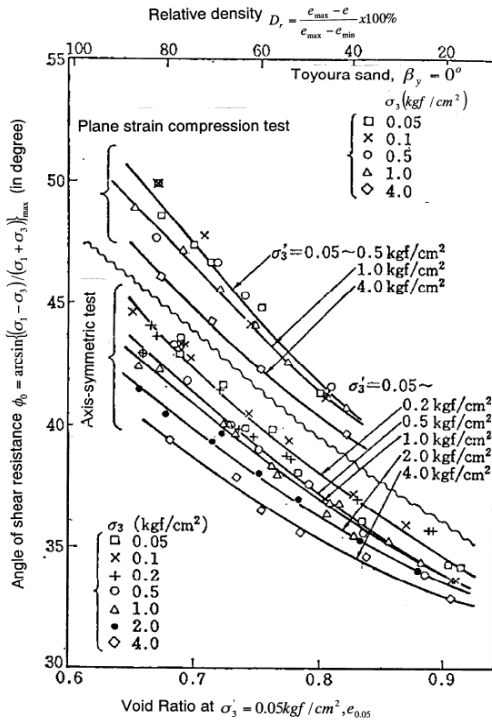


Fig. 3 Experimental result of Toyoura sand (Tatsuoka, 1986)

Applying Drucker-Prager criteria and Mohr-Coulomb criterion are based on the frictional characteristics to represent the strength of the ground. When angle of shear resistance is increased, the effect of the ultimate bearing capacity of the ground changes constantly on the extremely large ultimate bearing capacity of the ground. Therefore, when determining the angle of shear resistance and adhesion by soil test, in the compression zone, low pressure area always overestimates the strength. It is pointed out that the development of yield function by the non linear shear strength is needed to improve the accuracy when calculating the bearing capacity of footing.

As mentioned above confining stress and size effect have significant effects on the shear strength using shear strength linear properties. It is more than evident through experiments of Tatsuoka. Tatsuoka surveyed the shear strength of Toyoura sand and clarified that the angle of shear resistance varied with the confining stress as Fig. 3 above. So, the development of yield function by the non-linear

shear strength is needed. Higher yield function and parameters of the yield function are proposed on the basis of experimental results of Tatsuoka. The ultimate bearing capacity results gained through the application of high yield function in RPFEM in this study shows more consistent with the actual ground than the values obtained in the Drucker-Prager yield function. The study's results shown that it is possible to evaluate the ultimate bearing capacity values, taking into account the nonlinearity's influence of the soil strength due to confining pressure of the ground.

Based on the layout of Toyoura sand from Fig. 3, the results show that the confining stress effect on the behavior of ground in Fig. 4. So we can establish the relationship between the value of the first stress invariant I_1 and the second invariant value of shear stress J_2 . This allows us to design parameters when referring to nonlinear shear strength properties of soil for different types of soil.

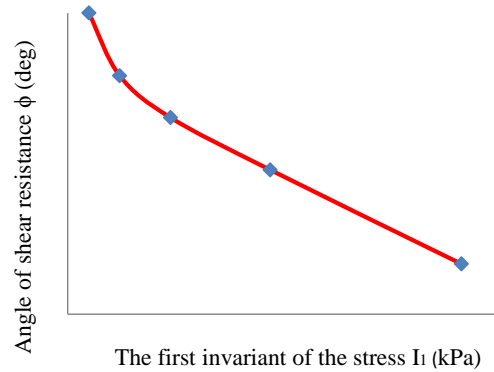


Fig. 4 Effect of confining stress to soil behavior

Non – linear rigid plastic constitutive equation for confining stress

From yield function:

$$f(\sigma) = aI_1 + (J_2)^n - b = 0 \quad (11)$$

The first invariant of the stress is decided by modifying the yield function formula, the first invariant of the stress using the second invariant of the deviatoric stress is updated by the following equation:

$$I_1 = \frac{1}{a}(b - (J_2)^n) \quad (12)$$

The strain rate for nonlinear case:

$$\dot{\epsilon} = \lambda \frac{\partial f(\sigma)}{\partial \sigma} = \frac{aI_1 + nJ_2^{n-1}s}{\sqrt{3a^2 + 2n^2(b - aI_1)^{2-1/n}}} \dot{e} \quad (13)$$

and the volumetric strain rate $\dot{\epsilon}_v$:

$$\dot{\epsilon}_v = tr \dot{\epsilon} = \frac{3a}{\sqrt{3a^2 + 2n^2(b - aI_1)^{2-1/n}}} \dot{e} \quad (14)$$

The first invariant and stress is expressed by strain rate so this relationship can be obtained as follows:

$$\sigma = \left[\frac{1}{n} \left(\frac{9a^2}{2n^2} \left(\frac{\dot{\epsilon}}{\dot{\epsilon}_v} \right)^2 - \frac{3a^2}{2n^2} \right)^{\frac{1-n}{2n-1}} \left[3a \frac{\dot{\epsilon}}{\dot{\epsilon}_v} - a\mathbf{I} \right] \right] + \frac{1}{3} \left[\frac{b}{a} - \frac{1}{a} \left(\frac{9a^2}{2n^2} \left(\frac{\dot{\epsilon}}{\dot{\epsilon}_v} \right)^2 - \frac{3a^2}{2n^2} \right)^{\frac{n}{2n-1}} \right] \mathbf{I} \quad (15)$$

In this study, we develop a rigid plastic constitutive equation incorporating a confining pressure dependence of the ground strength which is evaluated with highly accurate the ultimate bearing capacity. The first term of the above equation is determined by the stress constitutive relation and the second term is the stress component along the yield surface. So the stress σ can be shown as follows:

$$\sigma = \frac{(aI_1 + 2n(b - aI_1))}{\sqrt{3a^2 + 2n^2(b - aI_1)^{(2-1/n)}}} \frac{\dot{\epsilon}}{\dot{\epsilon}} + \kappa(\dot{\epsilon}_v - \beta\dot{\epsilon}) \left(\mathbf{I} - \frac{3a}{\sqrt{3a^2 + 2n^2(b - aI_1)^{(2-1/n)}}} \frac{\dot{\epsilon}}{\dot{\epsilon}} \right) \quad (16)$$

where κ is the variable determined by inserting Eq. (8) into the plastic potential of Eq. (3).

Through analysis of the explicitly dilatancy characteristics, computation of stable displacement velocity field can be implemented by using above nonlinear equation. Further, the advantage of the numerical analysis on the rigidity matrix is symmetrical.

APPLICABILITY OF PROPOSED CONSTITUTIVE EQUATION TO BEARING CAPACITY ASSESSMENT

Bearing capacity of footing for vertical load

As mentioned above, high pressure and low pressure area of the confining pressure of the ground is a problem which leads to the overestimate of Drucker-Prager's yield function. This is primarily due to the intensity nonlinear characteristic of confining pressure by soil. Therefore, it is reasonable to evaluate the strength by applying the intensity equation linear shear strength of the soil. In practice, non-linear strength of the ground may dominate the stability, hence it is important to incorporate the stability evaluation of the nonlinearity strength in engineering. The rigid-plastic constitutive equation, that is non-linear, should be used for higher-order yield function. In this case, the effect of compression stress on estimated values is smaller than those obtained from the linear intensity formula. In this section, we perform a numerical analysis with

respect to the horizontal ground and the comparison with theoretical solution of Meyerhof.

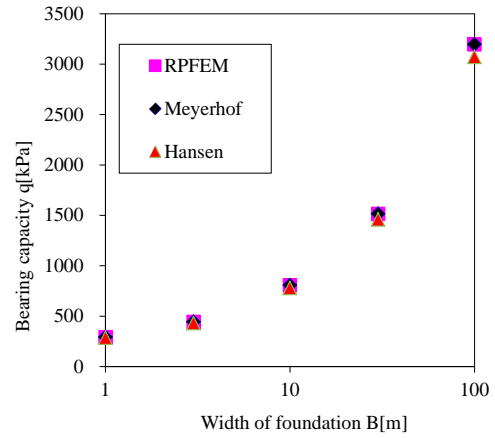


Fig.4 Bearing capacity with higher order yield function

Fig. 4 shows the development of Rigid Plastic Finite Element Method. RPFEM results coincide with the results of Meyerhof, which mean that the results obtained from non-linear shear strength properties is much better than the linear function described earlier.

Bearing capacity of footing for inclined load

Results from Fig. 5 indicates that the differences between RPFEM and other methods are significantly improved when comparing with the results calculated from linear shear strength properties.

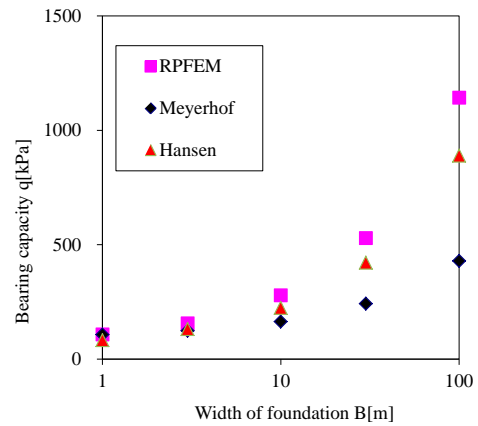


Fig.5 Bearing capacity with angle of Inclined load $\theta = 20$ deg

As can be seen from Fig. 6, with width of footing $B=30$ m when considering the influence of inclined load, the effect of confining stress is very significant and the use of nonlinear properties of shear stress to calculate the bearing capacity of footing is perfectly reasonable.

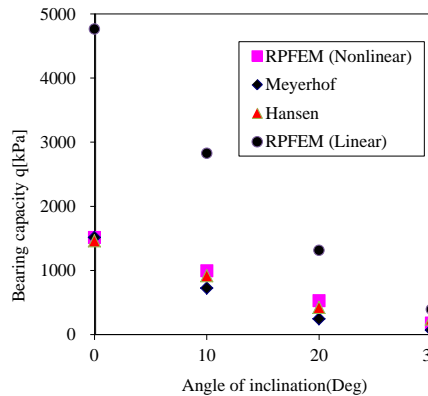


Fig. 6 Bearing capacity with Inclined load effect in case width of footing $B = 30\text{m}$

In this case, the value of bearing capacity decrease quickly under effect of inclination load. Impact of size footing is considerable. The value of bearing capacity reduces from 3 to 4 times when considering size effect. This finding is very important to insure stability of building.

The use of rigid-plastic constitutive equation with higher-order yield function proposed, which can be expressed nonlinearity strength by confining stress of the ground and checked the applicability of Drucker-Prager method to the ultimate bearing capacity problems.

CONCLUSION

This study has developed the ultimate bearing capacity analysis method using a rigid-plastic constitutive equation with higher-order yield function by confining pressure. The empirical results indicated that, ultimate bearing capacity value decreases in accordance with the increase of the load inclination angle in both cases linear and nonlinear shear strength properties. However, the values of ultimate bearing capacity from developed RPFEM is less than those values obtained from Drucker-Prager's yield function.

In addition, be evaluated properly to yield function from the change in values of the first invariant I_1 of the stress and, the effects of confining pressure of the ground can be evaluated reasonably.

However, the results from empirical investigation are still limited by the experimental method in case of size of footing. RPFEM coincided with the calculated results from the experimental method. This persuasively demonstrates the accuracy of this method. We proposed to use numerical method with large width of footing. The applicability of RPFEM is to solve more complicated problems in case of layered ground and improved ground. The developed Rigid plastic finite element method can provide the good estimation for wider range of footing size.

REFERENCES

- [1] Aysen A, "chapter 10", Soil Mechanics – Basic concepts and engineering applications, Balkema A A publisher, 2002, pp. 413 – 419.
- [2] Drucker D C, Greenberg H J, Lee E H, Prager W, "On plastic rigid solutions and limit design theorems for elastic plastic bodies", 1st US NCAM, 1951, pp. 533 – 538
- [3] Hill R, "On the limits set by plastic yielding to the intensities of singularities of stress", J. Mech. Phys. Solids, Vol. 2, 1954, pp. 278-285.
- [4] Okamura M, Takemura J, Kimura T, "Centrifuge model tests on bearing capacity and deformation of sand layer overlying clay", Soil and Foundations, Vol. 37, No.1, 1997, pp.73–87.
- [5] Fumio Tatstuoka et al, "Model tests and FEM simulation of some factors affecting the bearing capacity of footing on sand", Soil and Foundations, Vol. 41, No.2, 2001, pp. 53 – 74.
- [6] Tatsuoka F, Sakamoto M, Kawamura T and Fukushima S, "Strength and deformation characteristics of sand in plane strain compression at extremely low pressures", Soil and Foundations, Vol.26, No.1, 1986, pp.65– 84
- [7] Takeshi Hoshina, Satoru Ohtsuka and Koichi Isobe, "Ultimate bearing capacity of ground by Rigid plastic finite element method taking account of stress dependent non-linear strength property", Journal of Applied Mechanics, Vol.6, 2011, pp.191 – 200
- [8] Takeshi Tamura, "Rigid-Plastic Finite Element Method in Geotechnical Engineering", The Society of Materials Science, Japan, Vol.7, pp. 135–164.
- [9] Mohammed Hijaj, Andrei V. Lyamin, Scott W. Sloan, "Bearing capacity of cohesion-frictional soil under non-eccentric inclined loading", Vol 31, 2004, pp. 491 – 516.
- [10] Hjiag M, Lyamin A V, Sloan S W, "Numerical limit analysis solutions for the bearing capacity factor N_γ ", International Journal of Solids and Structures, Vol. 42, 2005, pp. 1681 – 1704.
- [11] Lyamin A V and Sloan S W, "Upper bound limit analysis using linear finite elements and non-linear programming", International Journal for numerical and analytical methods in geomechanics, Vol. 26, 2002, pp. 181 – 216.
- [12] Bolton M D and Lau C K, "Vertical bearing capacity factors for circular and strip footings on Mohr – Coulomb soil", Canada Geotechnical Journal, Vol 30, 1993, pp. 1024 – 1033.
- [13] Siddiquee M S A, Fumio Tatsuoka, Tadatsugu Tanaka, Kazuo Tani, Kenji Yoshida and Tsutomu Morimoto, "Model tests and fem simulation of some factors affecting the bearing capacity of a footing on sand", Soil and Foundations, Vol. 41, No.2, 2001, pp. 53 – 76.

PREDICTION OF SLOPE DEFORMATIONS BY ELASTIC WAVE VELOCITIES IN RELATION TO LANDSLIDE FAILURES

Muhammad Irfan¹ and Taro Uchimura²

^{1,2}Department of Civil Engineering, University of Tokyo, Japan

ABSTRACT

The authors propose a method for the prediction of landslide movement by using elastic wave velocity in soil. A series of triaxial tests was conducted on unsaturated sand specimens to study the variation of shear and compression wave velocities with soil yielding. Several specimens with different initial saturation ratio were prepared. To simulate the field stress path followed by soil during landslides, total radial stress (σ_3) was reduced at a constant rate while keeping the total axial stress (σ_1) constant. Shear and compression wave velocities were determined at regular intervals till failure of specimens. Soil yielding due to reduction of radial stress (σ_3) was observed to be dependent on saturation state. Shear and compression wave velocities were observed to decrease by about 40% and 15% respectively with soil yielding. An idea to predict landslides by monitoring changes in wave velocities in slope ground is schematically presented and explained.

Keywords: Landslide Monitoring; Elastic Wave Velocity; Triaxial Tests; Unsaturated Soil.

INTRODUCTION

Landslides are among the most devastating natural disasters. Every year numerous lives are lost and infrastructure is destroyed around the globe due to landslides. According to GLIDE number record of 134 landslides between 1999 and 2012, around 63% are triggered by rainfall (www.glide-number.net). Majority of landslide early warning systems around the world are based solely on the monitoring of rainfall intensity or duration and issuing warning when precipitation exceeds a certain critical value. However, for efficient prediction of landslides, consideration of soil characteristics and monitoring of actual slope displacements is integral. A variety of sensors are currently being used around the world to monitor physical movements of slope surfaces. These include draw wire displacement sensors [1], inclinometers [2-4], extensometers [5, 6], etc. A new idea to watch slope movements by monitoring elastic wave (shear wave and compression wave) velocities in soil is presented in this paper. Experimental results and relevant discussions from a series of triaxial tests, performed to explore the effect of soil yielding on elastic wave velocities, are presented in the following passages.

FIELD STRESS PATH

In conventional triaxial tests, a soil element is subjected to increasing axial stress (σ_1) while maintaining the radial stress (σ_3) constant. However, such tests do not correctly depict the in-situ stress path followed by soil during rainfall induced failure. Brand [7] postulated that the slope surface at

shallow depths is generally in unsaturated state, hence possessing negative pore water pressure (matric suction) which adds to the stability of slope. The infiltration of rain water in slope surface causes decrease in matric suction which in turn reduces effective normal stress acting on the potential failure plane. As a consequence of decreasing effective normal stress (σ_n), available shear strength (τ) also reduces, and this reduction continues to a point at which equilibrium can no longer be sustained in the slope. He further suggested that the field stress path can be simulated in laboratory element tests by one of the following tests methods;

- i. Application of constant total stress (σ_1 , σ_3 : constant) and increasing pore water pressure from initial negative value until the failure occurs.
- ii. Decreasing the radial stress (σ_3) while maintaining the axial stress (σ_1) constant.

Although both the methods yield the same stress path but the latter method is unable to simulate actual failure mechanism [7, 8]. But as water saturation distinctly reduces elastic wave velocities [9], therefore to study the effects of soil yielding on wave velocity in isolation, the latter method was adopted for this study. Hence, to achieve failure, a constant axial stress (σ_1) was maintained while decreasing the radial stress (σ_3) at a constant rate and recording wave velocities at regular intervals.

TEST PROGRAM

Experimental Setup

A stress controlled triaxial testing apparatus was

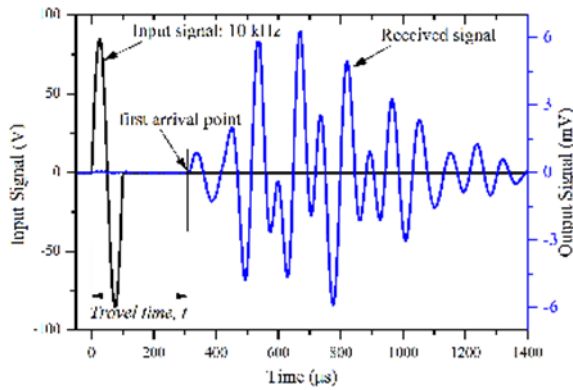
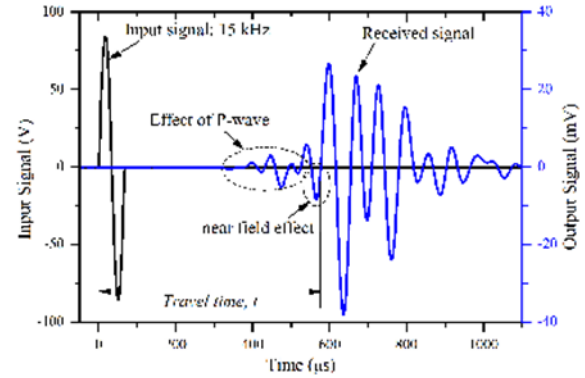

 (a) *P*-wave

 (b) *S*-wave

 Fig. 1: Typical elastic wave propagation signals in Edosaki sand, and definition of wave travel time (a) *P*-wave, and (b) *S*-wave

employed for this study. Independent control of axial and radial stress was made possible by means of electro-pneumatic transducers.

Volumetric strains of unsaturated specimens were recorded by continuously monitoring axial and radial strains. A pair of local deformation transducers (LDTs) [10, 11] attached to the surface of specimen by means of pseudo-hinges was used to measure axial strains. However, LDTs could measure axial strains only up to 2-3 %, therefore axial strains beyond this level were recorded by an externally mounted linear variable differential transducer (LVDT). Radial strains in the specimens were measured by three clip gauges mounted at different heights of the specimen.

Top cap and base pedestal of the apparatus were modified to enable measurement of shear wave (*S*-wave) and compression wave (*P*-wave) velocities in unsaturated triaxial specimens. A novel disk type piezoelectric transducer (referred as *disk transducer* hereinafter) was fabricated and sealed to the pedestal and top cap for generation and measurement of elastic wave velocities (construction details in [12]). The use of disk transducers instead of the more commonly used bender elements, not only enabled the measurement of both *P*-wave and *S*-wave velocities but also reduced sample disturbance due to its non-intrusive nature.

Transmitter disk transducer, sealed to the pedestal, was excited by a single cycle of 10 kHz or 15 kHz sinusoidal wave for generation of *P*-wave or for *S*-wave respectively. An excitation voltage of 4.5 *V_{pp}* (*V_{pp}* = *peak-to-peak voltage*) generated by a function generator was amplified to 90 *V_{pp}* and fed to the transmitter disk transducer. The wave travelled through the soil specimen and was received at the top cap by receiver disk transducer which transferred the signals to oscilloscope to be digitally displayed. Time of flight of each wave through soil specimen was then computed by analyzing received

signals as shown in Fig. 1. As compression waves are the fastest propagating waves through soil, thus were identified by the first deflection of receiver signal (Fig. 1a). However, the first arrival of *S*-wave may not correspond to the actual arrival of shear wave but rather to the arrival of the so called “near-field” component, which travel with the velocity of *P*-wave [13]. Shear wave travel time was thus calculated as the difference between the start of transmitted signal and the start of first major positively polarized up rise; i.e. “first-zero cross over” method [14]. By knowing the wave travel time ‘*t*’ from received signal, and travel distance ‘*H*’ (equivalent to specimen height), wave velocity can be computed by using a simple expression;

$$V_p \text{ or } V_s = H/t \quad (1)$$

where, *V_p* and *V_s* represents compression and shear wave velocity respectively and *t* is the corresponding travel time for compression or shear wave.

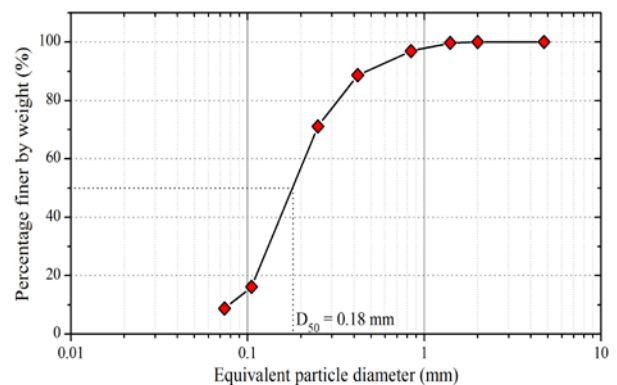


Fig. 2: Particle size distribution of Edosaki sand.

Materials & Methodology

Edosaki sand procured from a pit trench in Tsukuba, Japan was used for this study. Fig 2 shows typical particle size distribution of material used. Particles larger than 2 mm were removed through sieving. Table 1 summarizes physical properties of Edosaki sand employed for this study.

Cylindrical triaxial specimens (75 mm in diameter and 150 mm in height) were prepared by wet tamping Edosaki sand to a predefined density of 1.56 g/cm^3 ($D_r=88\%$) in ten equal layers. Placement moisture content was controlled to prepare specimens with initial saturation ratio of 10%, 20%, 45% and 75%. A saturated specimen with Skempton's B -value of 0.80 ($S_r \approx 90\%$) was also prepared. All the specimens were prepared at initial all around confining pressure of 15 kPa. Then as part of a separate study (not covered in this paper), isotropic confining pressure was first increased to 300 kPa and then gradually brought down to 150 kPa. From 150 kPa initial isotropic confining pressure, radial stress (σ_3) was gradually decreased at a rate of 0.016 kPa/s so that the specimen reached failure. The magnitude of axial load was adjusted accordingly to maintain a constant axial stress (σ_1) throughout the test. Elastic wave velocities were recorded at various points along this stress path. Stress path employed in these tests is schematically shown in Fig. 3.

Table 1: Physical properties of Edosaki sand.

Property	Value
Specific gravity, G_s	2.639
Minimum void ratio, e_{\min}	0.647
Maximum void ratio, e_{\max}	1.160
Fines (%)	9
Maximum dry density (g/cm^3)	1.762
Optimum moisture content (%)	14.6

TEST RESULTS

Effect of Initial Saturation on Landslide Failure

Field stress path tests were carried out on specimens with different initial saturation ratio, by maintaining the axial stress constant and gradually reducing the radial stress to the point of failure. Fig. 4 shows the response of various specimens when subjected to field stress path. On reducing the radial stress (σ_3) from an initial isotropic stress of 150 kPa, extremely small strain was observed during the early phase of tests. However, after sufficient reduction in radial confinement, axial strain started to increase first slowly and then at a rapid rate. Such transition in strain rate can be defined as *yield point* of specimen. Once the yield point is reached, there is

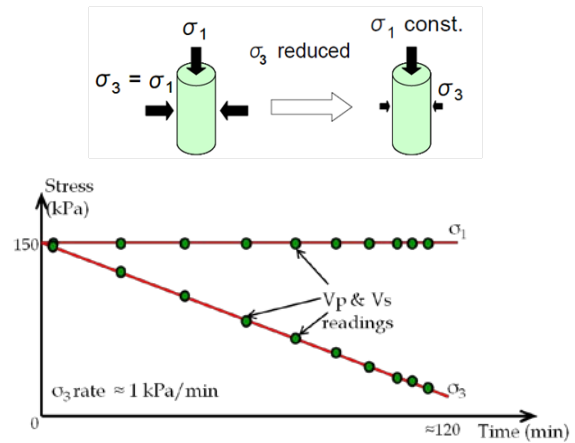


Fig. 3: Stress path adopted for this study.

continuous straining of the specimen without any appreciable change in stress. Moreover, the strains beyond yield point are irrecoverable. Hence, the yield point can be said to represent failure initiation of the specimen as indicated by “ Δ ” in Fig. 4.

A systematic approach adopted for the definition of Δ is explained in Fig. 5. Using the radial stress (σ_3) ~ axial strain (ϵ_1) plot, a tangent corresponding to 0.2% axial strain (point A) was drawn. Another line, tangent to the final part of the curve, was extended backwards to intersect the first tangent. The intersection point of these two tangents (point B) represented the yield point of soil specimen and the corresponding magnitude of radial stress indicated the yield strength. Thus, the failure was initiated when the specimen reached its yield strength, and yield point of each specimen is indicated by Δ in Fig. 4.

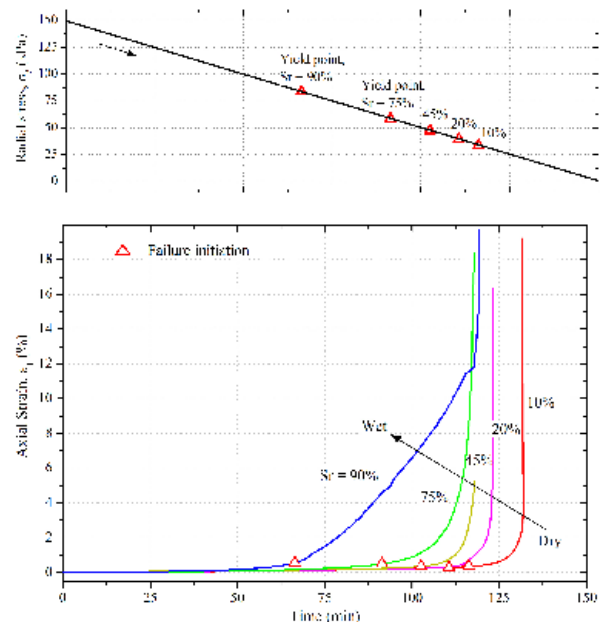


Fig. 4: Deformation time history of specimens subjected to field stress path.

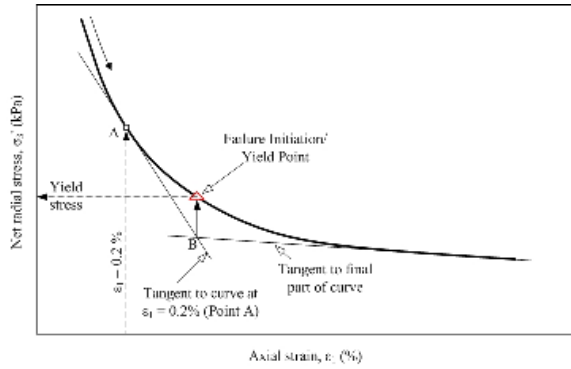


Fig. 5: Definition of failure initiation adopted for this study.

From Fig. 4, yielding of soil specimen subjected to field stress path is a function of initial saturation state. Although the rate of radial stress decrement was same for all test cases, yet specimens with higher saturation initiated failure much earlier than relatively drier specimens. Therefore, it can be surmised that wetter slopes are closer to failure stage than relatively drier slope surfaces.

Test results presented in Fig. 4 also help understand the post failure behavior of unsaturated

slopes. Post-yielding strain rate decreases with increasing saturation. For instance, 20% saturated specimen developed very large strains in a very short time after yielding. However, it took a very long time after yielding for 90% saturated specimen to reach the failure strain. Dry slopes undergoing failure process are therefore expected to fail at a rapid pace (brittle in nature) as compared to wet slopes which are rather expected to fail in a more ductile manner. Large post-yielding strain in wet slopes can hence be used as a warning before complete failure.

Effect of Yielding on Wave Velocity

As the specimens were subjected to field stress path, elastic wave velocities (V_s : shear wave velocity, and V_p : compression wave velocity) were determined at various intervals. Fig. 6 summarizes the effects of soil yielding on shear and compression wave velocities. With the reduction of radial stress (σ_3), shear wave velocity start decreasing slowly. This decrease in V_s can be attributed to the gradual loss of inter-particle contact force with the reduction of radial stress. As the radial stress

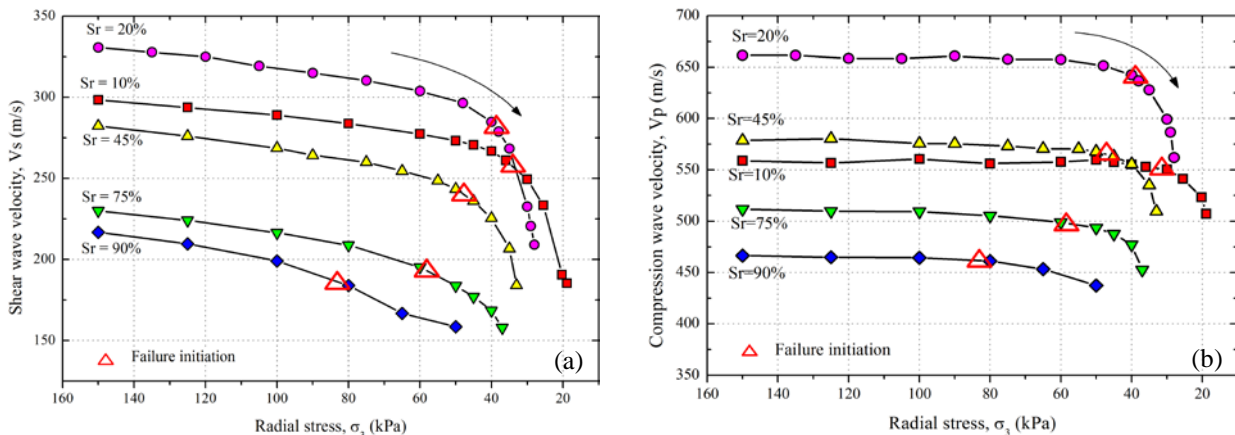


Fig. 6: Effect of radial confinement on wave velocities (a) S-wave; (b) P-wave

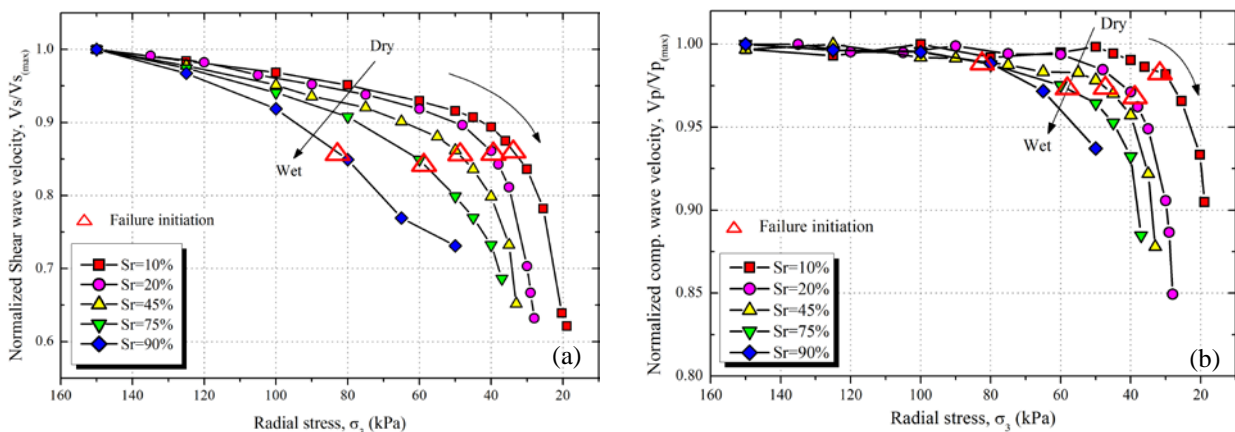


Fig. 7: Effect of radial confinement on normalized wave velocities (a) S-wave; (b) P-wave

approaches yield strength of specimen (represented by Δ), a sharp increase in rate of V_s decrement is observed. Compression wave velocity (V_p) however, nearly remains constant before failure initiation, but drops at an accelerated speed once the failure is initiated (Fig. 6b). Difference in the pre-yielding behavior of V_s and V_p is because of the difference in stress dependency of two waves i.e. V_s is a function of both axial (σ_1) and lateral stress (σ_3), whereas V_p is solely dependent on axial stress (σ_1) [15]. Therefore, decrease of radial stress (σ_3) in the pre-yielding phase only causes reduction in V_s , while V_p remains unaffected. However, once failure is initiated, the specimen starts to dilate at an accelerated pace and the structural rearrangement of particles causes rapid reduction of both V_p and V_s .

Shear strength of unsaturated specimens subjected to field stress path is function radial stress (σ_3) and soil matric suction (negative pore water pressure). Higher the saturation ratio, lower would be matric suction, and shear strength would be more sensitive to radial stress (σ_3) only. This phenomenon can be observed from Fig. 7, a plot of radial stress versus wave velocities normalized with respect to the respective maximum wave velocity. The rate of pre-yielding V_s decrement is higher for 90% saturated specimen as compared to the relatively drier specimens. Moreover, while undergoing the field stress path shear and compression wave velocities were observed to decrease by about 40% and 15% respectively. This decrease in wave velocities due to soil yielding can be used as an indicator of landslide initiation in actual field conditions.

APPLICATION FOR LANDSLIDE PREDICTION

Slope surfaces, at shallow depths, are generally in unsaturated state with soil matric suction (negative pore water pressure) playing an important role in their stability. During rainfall events, as water

percolates the slope surface, matric suction is gradually lost resulting in reduction of shear strength. With the loss of available shear strength slope surface starts to become more and more unstable and this destabilization continues to a point at which equilibrium can no longer be sustained and the slope ultimately fails.

Elastic wave velocities in soil decrease with increasing saturation [9]. Discussions in previous sections based on Fig. 6-7 also highlight the sensitivity of elastic wave velocities to soil yielding. These phenomena can therefore be utilized for the prediction of landslides. A conceptual idea of landslide prediction by using elastic wave velocities is presented in Fig. 8. A pair of exciter/receiver assembly placed on the slope surface can be used to obtain wave velocities in slope at regular intervals. Start of a rainfall event would increase soil saturation hence reducing wave velocity. Meanwhile, slope failures may occur when the slope ground is already nearly saturated and water contents are constant at a high level. Some failures happen even after the rainfall has stopped. Wave velocity should start decreasing sharply once failure is initiated and soil has started to yield. Shear wave velocity is expected to drop by about 40% due to soil yielding (Fig. 7a). This decrease in wave velocity is large enough to be used for early warning of landslides.

CONCLUSIONS

A series of triaxial tests, following the field stress path during landslides, was conducted to explore the effects of soil yielding on elastic wave velocities. The main conclusions drawn from this study are summarized below.

- Failure initiation (yielding) due to reduction of radial stress was found to be a function of initial saturation ratio. Wet specimens were found to yield earlier than dry specimens reflecting the wet slopes to be much closer to failure stage.

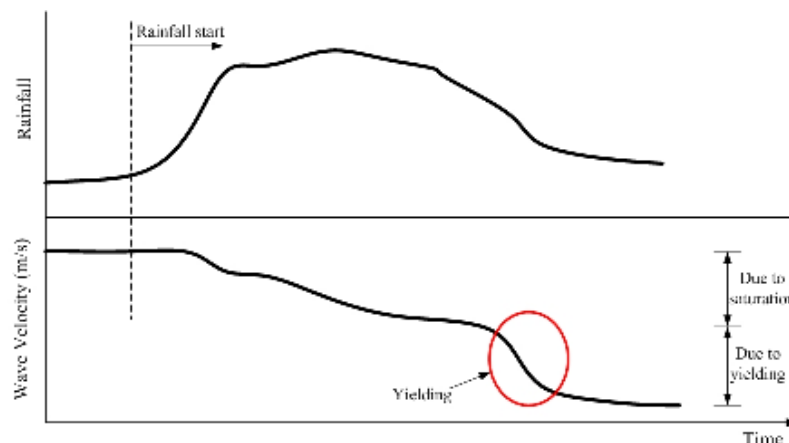


Fig. 8: Conceptual schematic of landslide prediction by monitoring wave velocities.

- Post-yielding behavior was also found to be dependent on saturation state. Time lapse between failure initiation and complete failure can be considerably large in nearly saturated slopes. However, dry slopes may tend to fail in a brittle manner i.e. very small time between failure initiation and complete failure.
- Both shear and compression wave velocities were found to decrease rapidly once failure is initiated in soil specimens. A decrease of about 40% was observed in shear wave velocity whereas the corresponding decrease in compression wave velocity was about 15%.
- An idea for the prediction of landslides by using elastic wave velocities is presented. Sensitivity of wave velocities to soil moisture and slope deformations can effectively be utilized to warn against landslide failures.

ACKNOWLEDGEMENTS

Ministry of Education, Culture, Sports, Science & Technology (MEXT) is gratefully acknowledged for their financial assistance.

REFERENCES

- [1] Arnhardt, C., et al., *Sensor based Landslide Early Warning System-SLEWS. Development of a geoservice infrastructure as basis for early warning systems for landslides by integration of real-time sensors.* Geotechnologien science report, 2007. 10: p. 75-88.
- [2] Lollino, G., M. Arattano, and M. Cuccureddu, *The use of the automatic inclinometric system for landslide early warning: the case of Cabella Ligure (North-Western Italy).* Physics and Chemistry of the Earth, Parts A/B/C, 2002. 27(36): p. 1545-1550.
- [3] Uchimura, T., et al., *Simple monitoring method for precaution of landslides watching tilting and water contents on slopes surface.* Landslides, 2010. 7(3): p. 351-357.
- [4] Uchimura, T., et al. *Miniature ground inclinometer for slope monitoring.* in *Proc. of The 14th Asian Regional Conference on Soil Mechanics and Geotechnical Engineering, ATC3 session.* 2011. Hong Kong, China.
- [5] Angeli, M.-G., A. Pasuto, and S. Silvano, *A critical review of landslide monitoring experiences.* Engineering Geology, 2000. 55(3): p. 133-147.
- [6] Uchimura, T., D. Suzuki, and S. Hongkwan. *Combined monitoring of water content and displacement for slope instability.* in *Proc. of 4th Japan-Korea Geotechnical Workshop.* 2011. Kobe, Japan.
- [7] Brand, E.W., *Some Thoughts on Rain-Induced Slope Failures.* Proc. of 10th International Conference on Soil Mechanics and Foundation Engineering, 1981. 3: p. 373-376.
- [8] Brenner, R.P., H.K. Tam, and E.W. Brand, *Field stress path simulation of rain-induced slope failure.* Proc. of 11th International Conference on Soil Mechanics and Foundation Engineering, 1985. 2: p. 991-996.
- [9] Irfan, M. and T. Uchimura. *Effects of soil moisture on shear and dilatational wave velocities measured in laboratory triaxial tests.* in *Fifth International Young Geotechnical Engineering Conference - 5iYGEC'13.* 2013. Paris, France (to appear).
- [10] Goto, S., et al., *A simple gauge for local small strain measurements in the laboratory.* Soils and Foundations, 1991. 31(1): p. 169-180.
- [11] Hoque, E., T. Sato, and F. Tatsuoka, *Performance evaluation of LDTs for use in triaxial tests.* ASTM geotechnical testing journal, 1997. 20(2): p. 149-167.
- [12] Irfan, M. and T. Uchimura, *Criteria for determining Gmax in laboratory element tests using disk type piezoelectric transducers.,* in *10th International Conference on Urban Earthquake Engineering 2013:* Tokyo, Japan. p. 555-560.
- [13] Sanchez-Salinerio, I., et al., *Analytical studies of body wave propagation and attenuation,* 1986, DTIC Document: Texas Univ at Austin Geotechnical Engineering Center Report GR 86-15.
- [14] Lee, J. and J. Santamarina, *Bender Elements: Performance and Signal Interpretation.* Journal of Geotechnical and Geoenvironmental Engineering, 2005. 131(9): p. 1063-1070.
- [15] Hardin, B.O. and F.E. Richart, *Elastic wave velocities in granular soils.* J. Soil Mech. and Found. Div., ASCE, 1963. 89(1): p. 33-65.

BOX-SHAPE RETAINING WALL SYSTEM: EXPERIMENT AND NUMERICAL PREDICTION

C.T. Nguyen^{2,3}, Ha H. Bui¹, N. Hiraoka², A. Oya², and R. Fukagawa²

¹Department of Civil Engineering, Monash University, Australia

²Department of Civil Engineering, Ritsumeikan University, Japan

³Institute of Mechanics, Vietnam Academy of Science and Technology, Vietnam

ABSTRACT

Box-shape retaining wall system has been extensively used to stabilize natural and cut-slope. Despite this fact, numerical development for prediction of the large deformation and flexible behavior of retaining wall blocks is still not advanced. To overcome this limitation, this paper presents a new numerical approach which can be used to simulate large deformation and flexible behavior of the box-shape retaining wall system. Herein, soil is modelled using an elasto-plastic constitutive model, while wall blocks are assumed rigidity with full degree of motion. A linear contact model is proposed to simulate interaction between soil and wall block. Experiments were also conducted to validate the proposed numerical framework. It is showed that the proposed numerical framework can simulate well behavior of the box-shape retaining wall system. The proposed method can be readily extended to analyze dynamic response of a general segmental retaining wall.

Keywords: Box-shape retaining wall, large deformation, elasto-plastic, SPH

INTRODUCTION

Box-type retaining walls (BRW) have been used as an effective method to stabilize cuts and fills adjacent to highways, driver-ways, embankment, etc. Because they are flexible structures, box-type retaining walls can tolerate movement and settlement without causing crack and damage, particularly under seismic loading conditions. Despite of its advantage, very few numerical studies of large deformation of the BRW systems were found in the literature. This is because it is very difficult to simulate large deformation and flexible behaviour of wall blocks (i.e. full rotational and translational motions) in the BRWs system using traditional continuum based numerical methods such as finite element method (FEM) which is suffered from grid distortions. The Discrete Element Method (DEM) proposed by Cundall & Strack [1] which is another popular numerical method in geotechnical applications may be applied to simulate dynamic behaviour of the box-type retaining wall blocks in the BRW system. However, the DEM suffers from low accuracy in predicting soil behaviour due to the difficulty in selecting parameters for contact laws. In addition, the DEM cannot make use of advanced soil constitutive models which have been extensively developed in the literature. The discontinuous deformation analysis (DDA) method proposed by Shi et al. [2] has also been applied to geotechnical applications, but is mainly used for rock engineering, etc. In order to overcome the above limitations of traditional numerical methods, continuum based

mesh-free methods such as the mesh-free Galerkin element method (EFG) [3], material point method (MPM) [4], particle in cell method (PIC) [5], etc., could be also applied to simulate large deformation of soil. However, these methods are quite time consuming and complicated to implement into a computer code as they consist of both interpolation points and the background mesh. On the other hand, the smoothed particle hydrodynamics (SPH) method, originally proposed by Gingold & Monaghan [6], has been recently developed for solving large deformation and post-failure behaviour of geomaterials [7-12] and represents a powerful way to understand and quantify the failure mechanisms of soil in such challenging problems.

In this paper, taking into consideration the unique advantage of the SPH method, the SPH method is further extended to simulate large deformation and post-failure of the BRW systems. Herein, soil is modelled using the elasto-plastic Drucker-Prager constitutive model [8] and wall blocks are assumed rigidity with complete degree of rotation. A linear contact model which is similar to the penalty contact law is proposed and is implemented in the SPH code to simulate interaction between soil and wall blocks, and between wall blocks in the BWR systems. The developed model is then applied to simulate large deformation of the BRW system and comparing to a two-dimensional experiment. Results showed good agreement with the experiment, suggesting that the proposed method is a promising approach for further design of retaining walls subject to earthquake.

SIMULATION APPROACHES

Simulation of Soil in SPH Framework

In the SPH method, motion of a continuum is modeled using a set of moving particles (interpolation points); each assigned a constant mass and “carries” field variables at the corresponding location. The continuous fields and their spatial derivatives are taken to be interpolated from the surrounding particles by a weighted summation, in which the weights diminish with distance according to an assumed kernel function. Details of the interpolation procedure and its application to soil can be found in Bui et al. [8]. The motion of a continuum can be described through the following equation,

$$\rho \frac{d\mathbf{v}}{dt} = \nabla \cdot \boldsymbol{\sigma} + \rho \mathbf{g} + \mathbf{f}_{ext} \quad (1)$$

where \mathbf{v} is the velocity; ρ is the density; $\boldsymbol{\sigma}$ is the total stress tensor, where negative is assumed for compression; \mathbf{g} is the acceleration due to gravity; and \mathbf{f}_{ext} is the additional external force(s). The total stress tensor of soil is normally composed of the effective stress ($\boldsymbol{\sigma}'$) and the pore-water pressure (p_w), and follows Terzaghi's concept of effective stress. Because the pore-water pressure is not considered, the total stress tensor and the effective stress are identical throughout this paper, and can be computed using a constitutive model.

In the SPH framework, Equation (1) is often discretized using the following form [8, 11],

$$\frac{dv_a^\alpha}{dt} = \sum_{b=1}^N m_b \left(\frac{\sigma_a^{\alpha\beta}}{\rho_a^2} + \frac{\sigma_b^{\alpha\beta}}{\rho_b^2} + C_{ab}^{\alpha\beta} \right) \nabla_a^\beta W_{ab} + g_a^\alpha + f_{ext \rightarrow a}^\alpha \quad (2)$$

where α and β denote Cartesian components x, y, z with the Einstein convention applied to repeated indices; a indicates the particle under consideration; ρ_a and ρ_b are the densities of particles a and b respectively; N is the number of “neighbouring particles”, *i.e.* those in the support domain of particle a ; m_b is the mass of particle b ; C is the stabilization term employed to remove the stress fluctuation and tensile instability [10]; W is the smoothing kernel function which is taken to be the cubic Spline function [13]; and $f_{ext \rightarrow a}$ is the unit external force acting on particle a .

The stress tensor of soil particles in Equation (2) can be computed using any soil constitutive model developed in the literature. For the purpose of soil-structure interaction, the Drucker-Prager model has been chosen with non-associated flow rule, which

was implemented in the SPH framework by Bui et al. [8] and shown to be a useful soil model for simulating large deformation and post-failure behaviour of aluminum rods used in the current paper as model ground. The stress-strain relation of this soil model is driven from the assumption of additive decomposition of the total strain rate tensor,

$$\dot{\boldsymbol{\epsilon}} = \dot{\boldsymbol{\epsilon}}^e + \dot{\boldsymbol{\epsilon}}^p \quad (3)$$

where a raised dot denotes the time derivative; $\dot{\boldsymbol{\epsilon}}$ is the total strain rate tensor; $\dot{\boldsymbol{\epsilon}}^e$ is its elastic component; and $\dot{\boldsymbol{\epsilon}}^p$ is its plastic component. The elastic component is computed using the well-known Hooke's law; while the plastic component can be calculated using the plastic flow rule [8],

$$\dot{\boldsymbol{\sigma}} = \mathbf{D} \dot{\boldsymbol{\epsilon}}^e \quad (4)$$

$$\dot{\boldsymbol{\epsilon}}^p = \dot{\lambda} \frac{\partial g_p}{\partial \boldsymbol{\sigma}} \quad (5)$$

where \mathbf{D} is the elastic stiffness matrix, $\dot{\lambda}$ is the rate of change of plastic multiplier, and g_p is the plastic potential function.

According to the plasticity theory, the plastic deformation occurs only if the stress state reaches the yield surface. Therefore, the plastic deformation will occur only if the following yield criterion is satisfied,

$$f = \alpha_\phi I_1 + \sqrt{J_2} - k_c = 0 \quad (6)$$

where I_1 and J_2 are the first and second invariants of the stress tensor; and α_ϕ and k_c are Drucker-Prager constants that are calculated from the Coulomb material constants c (cohesion) and ϕ (internal friction). In the plane strain, the Drucker-Prager constants are computed by,

$$\alpha_\phi = \frac{\tan \phi}{\sqrt{9 + 12 \tan^2 \phi}} \quad (7)$$

$$k_c = \frac{3c}{\sqrt{9 + 12 \tan^2 \phi}} \quad (8)$$

The non-associated plastic flow rule specifies the plastic potential function by [9-10],

$$g_p = \alpha_\psi I_1 + \sqrt{J_2} - \text{constant} \quad (9)$$

where α_ψ is a dilatancy factor that can be related to the dilatancy angle ψ in a fashion similar to that between α_ϕ and friction angle ϕ .

Substituting Equation (9) into Equation (5) in association with the consistency condition, that is the stress state must be always located on the yield surface f during the plastic loading, the stress-strain relation of the current soil model at particle a can be written as [10],

$$\frac{d\sigma_a^{\alpha\beta}}{dt} = 2G_a \dot{e}_a^{\alpha\beta} + K_a \dot{\epsilon}_a^{\gamma\gamma} \delta_a^{\alpha\beta} - \dot{\lambda}_a \left[3K_a \alpha_{\psi a} \delta_a^{\alpha\beta} + (G_a / \sqrt{J_{2a}}) s_a^{\alpha\beta} \right] \quad (10)$$

where $e^{\alpha\beta}$ is the deviatoric strain-rate tensor; $s^{\alpha\beta}$ is the deviatoric shear stress tensor; and $\dot{\lambda}$ is the rate of change of plastic multiplier of particle a , which in SPH is specified by [10],

$$\dot{\lambda}_a = \frac{3\alpha_{\phi a} K_a \dot{\epsilon}_a^{\gamma\gamma} + (G_a / \sqrt{J_{2a}}) s_a^{\alpha\beta} \dot{\epsilon}_a^{\alpha\beta}}{9\alpha_{\phi a} K_a \alpha_{\psi a} + G_a} \quad (11)$$

where the strain-rate tensor is computed by

$$\dot{\epsilon}_a^{\alpha\beta} = \frac{1}{2} (\nabla^\beta \dot{u}^\alpha + \nabla^\alpha \dot{u}^\beta)_a \quad (12)$$

When considering a large deformation problem, a stress rate that is invariant with respect to rigid-body rotation must be employed for the constitutive relations. In the current study, the Jaumann stress rate is adopted:

$$\dot{\hat{\sigma}}_a^{\alpha\beta} = \dot{\sigma}_a^{\alpha\beta} - \sigma_a^{\alpha\gamma} \dot{\omega}_a^{\beta\gamma} - \sigma_a^{\gamma\beta} \dot{\omega}_a^{\alpha\gamma} \quad (13)$$

where $\dot{\omega}$ is the spin-rate tensor computed by

$$\dot{\omega}_a^{\alpha\beta} = \frac{1}{2} (\nabla^\beta \dot{u}^\alpha - \nabla^\alpha \dot{u}^\beta)_a \quad (14)$$

As a result, the final form of the stress-strain relationship for the current soil model is modified to

$$\begin{aligned} \frac{d\sigma_a^{\alpha\beta}}{dt} = & \sigma_a^{\alpha\gamma} \dot{\omega}_a^{\beta\gamma} + \sigma_a^{\gamma\beta} \dot{\omega}_a^{\alpha\gamma} + 2G_a \dot{e}_a^{\alpha\beta} \\ & + K_a \dot{\epsilon}_a^{\gamma\gamma} \delta_a^{\alpha\beta} - \dot{\lambda}_a 3K_a \alpha_{\psi a} \delta_a^{\alpha\beta} \\ & + \dot{\lambda}_a (G / \sqrt{J_2})_a s_a^{\alpha\beta} \end{aligned} \quad (15)$$

Validation of the elasto-plastic Drucker-Prager soil model with SPH has been extensively documented in the literature [8-10], and readers can refer to these references for further details on the validation process.

Motion of Rigid Wall Blocks

An arbitrary motion of a rigid body can be represented as a superposition of translational motion in which all points of the body, including the centre of mass, move with the same speed along parallel trajectories, and rotation around the centre of mass. Accordingly, the motion of a rigid wall block in the BRW system can be determined by specifying the translational motion of the centre of mass and the rotational motion about its mass central. The equation of motion of the central mass is given as follows,

$$M \frac{d\mathbf{V}}{dt} = \mathbf{F} \quad (16)$$

where M is the central mass, \mathbf{V} is the velocity vector of the central mass, \mathbf{F} is total force vector acting on the body.

The equation of rotation about the central mass is,

$$I \frac{d\mathbf{\Omega}}{dt} = \mathbf{T} \quad (17)$$

where I is the inertial moment, $\mathbf{\Omega}$ is the angular velocity which is perpendicular to the plane of the motion, and \mathbf{T} is the total torque about the central mass.

In the computation, the rectangular block is represented by the set of boundary particles that are equi-spaced around the boundary. Denoting the force vector acting on each boundary particle i located on the moving block is f_i , Equations (16) and (17) can be rewritten, respectively, as follows,

$$M \frac{d\mathbf{V}}{dt} = \sum_i \mathbf{f}_i \quad (18)$$

$$I \frac{d\mathbf{\Omega}}{dt} = \sum_k (\mathbf{r}_i - \mathbf{R}) \times \mathbf{f}_i \quad (19)$$

where \mathbf{r}_i and \mathbf{R} are vector coordinates of boundary particle and central mass, respectively. The rigid body boundary particles move as a part of the rigid body, thus the change on position of boundary particle i is given by,

$$\frac{d\mathbf{r}_i}{dt} = \mathbf{V} + \mathbf{\Omega} \times (\mathbf{r}_i - \mathbf{R}) \quad (20)$$

The force \mathbf{f}_i acting on a boundary particle on the rigid body is due to the surrounding soil particles or boundary particles that belong to different rigid bodies. This force can be calculated using any suitable contact model.

Contact Force Model

In this paper, a linear soft contact model based on a concept of the spring and dash-pot system is proposed to model the interaction between soil and retaining wall blocks and between blocks. Accordingly, the radial force acting between two particles can be calculated using the following equation,

$$\mathbf{f}_{a \rightarrow i}^n = \begin{cases} -K_{ai} \delta_n - c_n \mathbf{v}_{ai}^n & h_{ai} > 2d_{ai} \\ 0 & h_{ai} \leq 2d_{ai} \end{cases} \quad (21)$$

where K is the radial stiffness; δ_n is the allowable overlapping distance between two particles; c_n is the radial damping coefficient; \mathbf{v}^n is the relative radial velocity vector between particle a and particle i ; h_a and h_{ai} are the sum of the initial separation between soil particles and between boundary particles, respectively; and d_{ai} is the distance between two particles. The overlapping distance and radial damping coefficient can be calculated using the following relationships,

$$\delta_n = d_{ai} - h_{ai} / 2 \quad (22)$$

$$c_n = 2\sqrt{m_{ai}K_{ai}} \quad (23)$$

The contact force in the shear direction which is perpendicular to the radial direction can be calculated in the same manner,

$$\mathbf{f}_{a \rightarrow i}^s = \begin{cases} -k_{ai} \delta_s - c_s \mathbf{v}_{ai}^s & h_{ai} > 2d_{ai} \\ 0 & h_{ai} \leq 2d_{ai} \end{cases} \quad (24)$$

where k_{ai} is the shear stiffness which is taken similar to K ; δ_s is the relative shear displacement between the two particles; c_s is the shear damping coefficient; \mathbf{v}^s is the relative shear velocity vector between particle a and particle i . The relative shear displacement and shear damping coefficient are calculated by,

$$\delta_s = \oint \mathbf{v}_{ai}^s dt \quad (24)$$

$$c_s = 2\sqrt{m_{ai}k_{ai}} \quad (26)$$

The current shear force must satisfy Coulomb's friction law which implies that the maximum shear force must not exceed the maximum resisting force,

$$\mathbf{f}_{a \rightarrow i}^s \leq \mu \frac{\delta_s}{|\delta_s|} |\mathbf{f}_{a \rightarrow i}^n| \quad (25)$$

where μ is the friction coefficient. Finally, these forces are converted to the conventional coordinate system and added to Equations (2), (18) and (19) to progress the motion of soil and wall block.

TWO-DIMENSIONAL EXPERIMENTS

A series of two-dimensional box-shape retaining wall system collapses were conducted to investigate the failure mechanism of the BRW system and to verify the proposed numerical framework. Fig.1 outlined the initial setting condition of the BRW system which consists of six rectangular wall blocks. The size of the model ground is 15cm in height and 50cm in width at the base. Soil was modelled using aluminum rods of 1.6mm and 3mm in diameters, 50mm in length, and mixed with the ratio of 3:2 in weights. The wall block is 3.2cm in width, 2.5cm in height, and 5cm in length, which is also manufactured from aluminum. In the experiment, the BRW system was constructed by successively placing one wall block on the top of the other with an overlapping of 1.2cm, followed by filling the model ground at each layer. The BRW system was stabilized by a stopper stand as shown in Fig. 1. To visualize the failure pattern of the model ground after collapse, square grids (2.5×2.5cm) were drawn on the soil specimen. The experiments were initiated by quickly removing the stopper stand and digital photos were taken to record the failure process as well as the final configuration of the BRW system after collapse. A series of experiments were conducted starting from one block and then gradually increasing the number of blocks in the BRW system until the retaining wall is collapsed. The experimental evidences consistently showed that the BRW system will collapse when reaching 6 blocks height. Accordingly, a numerical model consisting of six retaining wall blocks will be conducted in the next section to verify the proposed numerical framework. A total of six experiments were conducted to verify the failure mechanism of the BRW system and the final run-out distance of each block in the BRW system. In all experiments, the failure mechanism of the BRW systems was more or less the same as shown in Fig.2.

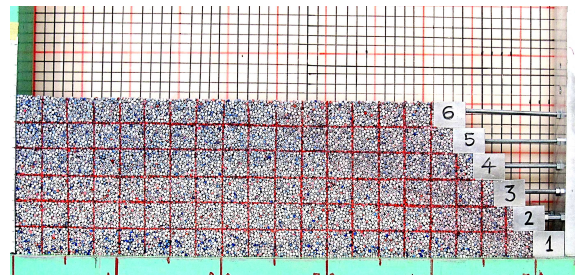


Fig. 1 Initial setup of model ground and the retaining wall blocks in the BRW system.

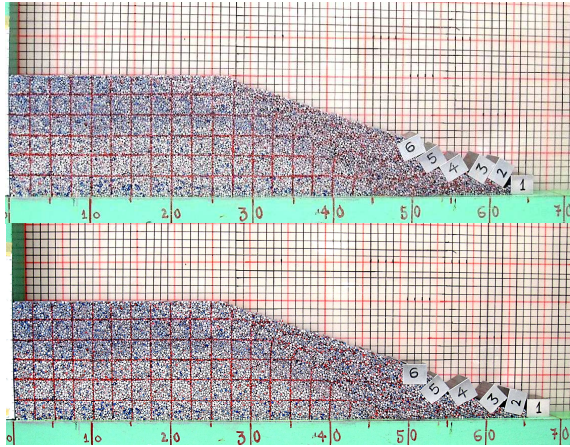


Fig. 2 Typical final configurations of the BRW system observed in the experiment after collapse for two different tests.

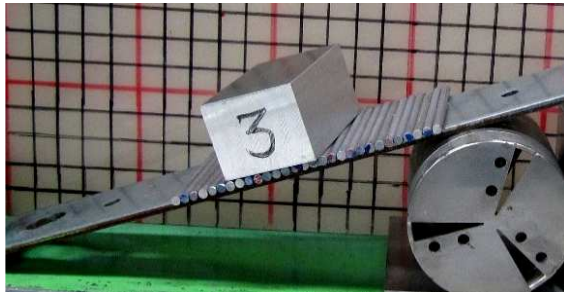


Fig. 3 Outline of sliding test to measure friction between model ground and wall block.

In addition to the retaining wall collapse experiments, sliding tests were also conducted to measure friction coefficients between the wall blocks, between the soil model and the wall block, and between the block and the bottom solid wall. Outline of these tests are shown in Fig. 2. Based on these experiment, it was found that the friction (μ) between retaining wall blocks is $\mu \sim 0.31$, between the retaining wall block and model ground is $\mu \sim 0.38$, and between wall block and the bottom wall boundary is $\mu \sim 0.49$.

SIMULATION OF BOX-SHAPE RETAINING WALL COLLAPSE USING SPH

The model test shown in Figure 1 was simulated using 11,304 SPH particles arranged in a rectangular lattice with an initial separation of 0.25cm. Rigid blocks were created by placing boundary particles uniformly around the boundary at a constant distance. In order to simulate the smooth surface, half of particle spacing was chosen for the rigid body boundary particles. Model ground parameters including elastic modulus $E = 5.84\text{MPa}$, Poisson's ratio $\nu = 0.3$, friction angle $\phi = 21.9^\circ$, dilatant angle $\psi = 0^\circ$, and cohesion $c = 0\text{kPa}$ were taken similar to

those measured by Umezaki et al. [15]. The unit weight of the ground model is $\gamma_s = 20.4\text{kN/m}^3$. In addition to the ground parameters, parameters for the linear contact model needed to be specified. In this paper, the radial and shear stiffness were assumed to be $K = k = 1 \times 10^9\text{N/m}$. The friction coefficients between the ground model and the block, between the rigid blocks, and between the block and the bases of the wall boundary were taken similar to those measured in the sliding tests as explained in the experimental section. The boundary conditions for the model ground are restrained with a free-slip boundary at the lateral boundaries and fixed in both directions at the base [8].

Fig. 4 shows the comparison between the experiment and the computation for the final configuration of the BRW system after collapse. It can be seen that the computed result could predict fairly well the behavior of all rigid blocks observed in the experiment after the BRW system was collapsed. The good agreement between experiment and simulation can be attributed to the fact that the complete degrees-of-freedom of the rigid wall was taken into consideration in the simulation and large deformation and post-failure behavior of soil could be simulated well in the current SPH framework.

Comparing the final run-out distance of each block, for instance Block No.1, it can be seen that the final position (right edge) of Block No.1 in the simulation is approximately $\sim 68.3\text{cm}$ from the left-most solid boundary. This result is in fairly good agreement with that observed in experiment which was approximately $\sim 66.2\text{cm}$. This suggests that the proposed numerical framework could be applied to simulate the soil-structure interaction in the BRW system. However, further refinement of the contact model should be considered to provide a more theoretical sound framework to specify the parameters for the contact model.

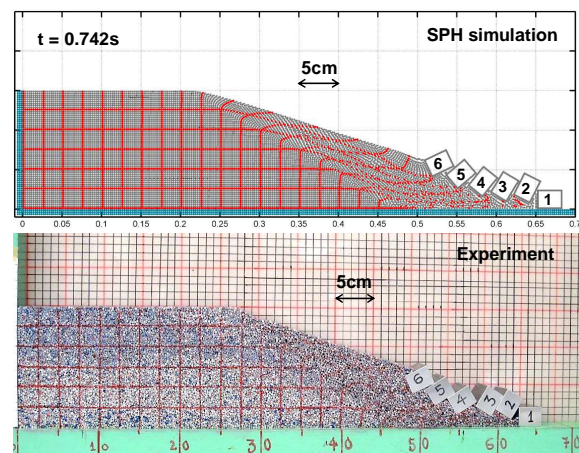


Fig. 4 Comparison between the SPH simulations and the experiment for the final configuration of the BRW system.

CONCLUSION

This paper presented a new numerical approach for simulation of large deformation and post-failure of box-shape retaining wall system. It was shown that the proposed method provides good agreement with the experimental results. One of the key advantages of the proposed method is that the complete degrees-of-freedom of the retaining wall blocks, which could not be simulated using traditional numerical approaches such as finite element method, can now be simulated in the proposed numerical framework. Large deformation and post-failure behaviour of geomaterials can also be readily simulated. In order to broaden the application of the proposed numerical approach in geotechnical engineering, generalized contact model is necessary. This work is in progress and will be reported in the near future.

ACKNOWLEDGEMENTS

The first author would like to thank the Japan Society for the Promotion of Science (JSPS) for providing doctoral scholarship through the RONPAKU Program.

REFERENCES

- [1] Cundall PA and Struck ODL, "A discrete numerical model for granular assemblies", *Géotechnique*, Vol.29, 1979, pp.47-65.
- [2] Shi GH, "Discontinuous deformation analysis: a new numerical model for the static and dynamics of block systems" Ph.D. Thesis, 1988, University of California, Berkeley.
- [3] Belytschko T, Lu YY, and Gu L, "Element-free Galerkin methods", *International Journal for Numerical Methods in Engineering*, Vol.37, 1994, pp.229-256.
- [4] Sulsky D, Chen Z, and Schreyer HL. "A particle method for history-dependent materials". *Computer Methods in Applied Mechanics and Engineering*, Vol.118, 1994, pp.179-196.
- [5] Harlow FH, Ellison MA, and Reid JH, "The particle-in-cell computing method for fluid dynamics". *Methods in Computational Physics*. Vol.3, 1964, pp.319-343
- [6] Gingold RA and Monaghan JJ, "Smoothed particle hydrodynamics: Theory and application to non-spherical stars", *Mon. Not. Roy. Astron. Soc.*, Vol.181, 1977, pp.375-389.
- [7] Bui HH, Sako K, and Fukagawa R, "Numerical simulation of soil-water interaction using smoothed particle hydrodynamics (SPH) method", *Journal of Terramechanics*, Vol.44, 2007, pp.339-346.
- [8] Bui HH, Fukagawa R, Sako K. and Ohno S. "Lagrangian mesh-free particle method (SPH) for large deformation and post-failure of geomaterials using elastic-plastic soil constitutive model, *International Journal for Numerical and Analytical Methods in Geomechanics*", Vol. 32, 2008, pp.1537-1570.
- [9] Bui HH, Fukagawa R, and Sako K, "Slope stability analysis and discontinuous slope failure simulation by elasto-plastic smoothed particle hydrodynamics (SPH)" *Géotechnique*, Vol.61, 2011, pp. 565-574.
- [10] Bui HH and Fukagawa R, "An improvement of SPH for saturated soils and its application to investigate the mechanisms of embankment failure: Case of hydrostatic pore-water pressure", *International Journal for Numerical and Analytical Methods in Geomechanics*, Vol. 37, 2013, pp.31-50.
- [11] Blanc T, and Pastor M, "A stabilized smoothed particle hydrodynamics, Taylor-Galerkin algorithm for soil dynamics problems", *International Journal for Numerical and Analytical Methods in Geomechanics*, Vol.37, 2013, pp.1-30.
- [12] Pastor M, Haddad B, Sorbino G, Cuomo S, and Drempetic V, "A depth-integrated, coupled SPH model for flow-like landslides and related phenomena" *International Journal for Numerical and Analytical Methods in Geomechanics*, Vol.33, 2009, pp.143-172.
- [13] Monaghan JJ, "SPH elastic dynamics". *Computer Methods in Applied Mechanics and Engineering*, Vol.190, 2003, pp.6641-6662.
- [14] Monaghan JJ and Lattanzio JC, "A refined particle method for astrophysical problems", *Astronomic & Astrophysics*, Vol.149, 1985, pp.135-143.
- [15] Umezaki T, Kawamura T, and Ochiai H, "Increment of Confining Pressure Due To Pull-out of Reinforcement Anh Modelling of Reinforcing Mechanics", *Geosynthetic Engineering Journal*, Vol.20, 2005, pp.241-248. (in Japanese).

PERMEABILITY AND CONSOLIDATION BEHAVIOR OF COMPOSITE GROUND REINFORCED WITH SAND COLUMNS

B. A. Mir¹ and Ashish Juneja²

¹ Faculty, Deptt. of Civil Engg., National Institute of Technology Srinagar-006, J&K., India

² Faculty, Deptt. of Civil Engg., Indian Institute of Technology Bombay-076, Mumbai., India

ABSTRACT

In this paper, the behavior of the composite ground reinforced with sand columns with and without smear effect installed in 200mm long and 100mm diameter cylindrical clay specimens was investigated using conventional triaxial consolidation tests under different confining pressures ranging from 50kPa to 575kPa. Change in volume of the specimen was measured using automatic volume change apparatus. This typically required a consolidation time of about 100minutes compared to more than 6-7days required to consolidate the specimen without the sand columns. However, specimens prepared with smear effect took slightly more time to consolidate thereby lending further confidence to the method used to create the smear zone. The test results showed that the dissipation of excess pore water pressure occur faster in the radial direction due to the greater coefficient of soil permeability in the horizontal direction and the reduced drainage path.

Keywords: Composite ground, Sand column, Smear, Soil improvement, Consolidation, Permeability

INTRODUCTION

Soft clay deposits usually have a low bearing capacity and undergo excessive settlement over a long period of time. One of the important problems geotechnical engineers are often to deal with is the accurate and reliable measurement of compressibility and permeability characteristics of soft soils. The coefficient of consolidation is an essential soil parameter required for seepage, settlement, stability calculations and for predicting the rate of settlement of soft soils. The importance of compressibility characteristics are further increased in case of environmental problems, such as waste disposal and detrimental effects on the surrounding ground due to contamination.

In the recent years, improvement of soft soils has been extensively implemented for the various development projects all over the world due to extremely limited stable construction sites. But one of the major problems associated with soft soils is the presence of thick deposits of soft clayey ground. Thus, soft clay foundations present considerable construction problems. Therefore, where poor ground conditions make traditional forms of construction expensive, it may be economically viable to attempt to improve the engineering properties of the ground before building on it. This can be done by reducing the pore water pressure, by reducing the volume of voids in the soil, or by adding stronger materials. Although there are a variety of ground improvement techniques under different categories, granular piles such as sand columns or sand compaction piles (SCPs) are

considered as cost-effective method as well as alternative solution to the problem of stability and settlement posed by construction on soft ground. In particular, the insertion of stone or sand columns into soft clay has been shown to have a positive effect on the load carrying capacity of the clay, resulting in a composite soil mass that has greater shear strength and improved stiffness compared to the unreinforced clay. In addition, sand columns generally act as vertical drains in the clay thus accelerating the dissipation of excess pore water pressures that are generated during preloading. As such, sand columns currently stand as one of the most viable and practical techniques for improving the mechanical properties of soft clays. The consolidation time can be reduced to achieve a required degree of consolidation by selecting suitable drain spacing and an appropriate installation pattern [1]. This method of ground improvement has been widely used for rapid improvement of soft ground, and also in near-shore regions for land reclamation works e.g. [2]-[4]. In India, the sand columns have been used to improve ground for container freight station at Navi Mumbai and the construction of dry dock at Pipavav shipyard Gujarat [5]. But, installation of the sand columns is known to cause disturbance due to smear in a limited zone of the soil surrounding the sand column [6]. Thickness of the disturbed zone depends upon the roughness of the casing used during the installation and, is associated with reduced permeability and high pore pressures. Laboratory and field tests previously conducted to determine the extent of the disturbance caused by pile driving into soft clay deposits have

demonstrated that the natural structure of the clay around the pile is excessively disturbed [7]-[9]. Recently, Weber TM et al. [10] compared the smear zone around model SCPs installed on the centrifuge to that observed around driven piles. The smear zone around the SCP was observed to extend up to 1.2 to 1.4 times the SCP diameter. It was perhaps not a coincidence that the thickness of the smear zone was comparable to the thickness of the disturbance, which is usually observed around piles driven in soft clays [7]. Similarly, Bond and Jardine [11] observed that the thickness of the smear zone was narrow when the piles were driven in overconsolidated clays. If the extent of the disturbance around SCPs is taken analogous to that observed around driven piles, then any change in the clay fabric during the SCP installation will also affect the permeability and pore pressure dissipation, and consequently the load-carrying capacity of the composite ground [12]-[13].

Laboratory tests on model sand drains have shown significant reduction in the horizontal permeability in the vicinity of the drain, and the extent of the smear zone caused by mandrel driven vertical drains, which otherwise was estimated based on the pore pressure generated [14]-[16]. The extent of the smear zone was also confirmed from the change in permeability of the clay layer in the smear zone obtained from oedometer tests [17].

In this paper, the behavior of the composite ground reinforced with sand columns is analyzed. The consolidation of model sand columns installed in 100mm diameter and 200mm long clay specimens was investigated using conventional triaxial consolidation tests. The composite specimens were prepared by driving a small diameter PVC casing into the specimen and then backfilling the cavity with sand column after removing the casing. The casing was painted using sand glued with araldite prior to the insertion to create smear zone. Diameter of the sand particles glued to the casing was taken as a measure of the smear zone. The composite specimens were first saturated and then consolidated isotropically under different confining pressures ranging from 50kPa to 575kPa. Change in volume of the specimen during consolidation was measured using automatic volume change apparatus. This typically required a consolidation time of about 100minutes compared to more than 6-7days required to consolidate the specimen without sand columns. However, specimens prepared with smear effect took slightly more time to consolidate thereby lending further confidence to the method used to create the disturbed zone. The results show that the dissipation of excess pore water pressure occurs faster in the radial direction due to the greater coefficient of soil permeability in the horizontal direction and the reduced drainage path. Thus, the main function of sand column application is to accelerate soil consolidation by shortening the drainage path and

activating radial drainage, thereby reducing post-construction settlement [18].

EXPERIMENTAL WORK

Materials and methods of sample preparation

Isotropic consolidated triaxial tests were performed on 100mm diameter and 200mm long specimens [19] prepared from commercially available kaolin clay. The experimental program consisted of 18 triaxial consolidation tests on composite specimen. The triaxial samples were prepared in 250mm diameter and 450mm long stainless steel cylindrical mould. Up to 3 specimens could together be prepared using this mould. De-aired clay slurry was consolidated on the laboratory floor, first under its own self-weight and later under surcharge of 211- to 404kN/m² applied in stages on top of the clay surface using a custom designed pneumatic load frame. Upon completion of the 1-D consolidation, the block of clay was extruded and trimmed into three 100mm diameter specimens using soil lathe (Fig. 1). Three additional steps were undertaken to prepare the composite samples. In the first step, a cylindrical hole was cored through the centre of the sample using a thin, smooth casing. The diameter of the hole varied between 25 and 45 mm in different tests. In the second step, air-dry sand ($d_{50} = 0.3$ mm) was poured into the hole in layers and each layer compacted at 90% relative density using a pneumatic compactor. The final diameter of the SCP was equal to the diameter of the hole (Fig. 2).

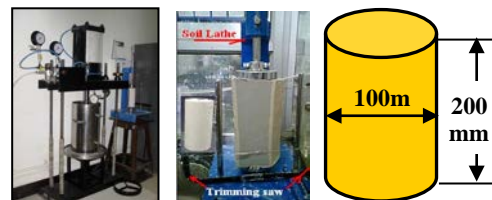


Fig.1 Consolidation set-up on the laboratory floor and specimen trimming



Fig. 2 Preparation of composite specimen

In some tests, the outer surface of the casing was made gritty by painting a paste of coarse sand mixed with araldite. This helped to create a smear zone around the compacted sand column. In the third step,

two circular rubber sheets with a hole at the centre were placed at the ends of the sample. The diameter of the hole was slightly less than that of the sand column so as to only permit radial drainage during consolidation. Table 1 shows the properties of the clay and Table 2 shows experimental program used in this study.

Table 1 Properties of kaolin clay

Clay (%)	Silt (%)	Liquid limit (%)	Plastic limit (%)	Shrinkage limit (%)	G _s
75	25	49	23	16	2.64

Table 2 Experimental program for composite samples

Test No	σ'_v * (kPa)	d _s # (mm)	Smear zone	p' _c § (kPa)	p' ** (kPa)	OCR = p' _c /p'
S1	404	25	✗(no)	285	100	3
S2	404	25	✗	285	150	2
S3	404	25	✗	285	300	1
S4	264	29	✓(yes)	187	100	2
S5	264	29	✓	187	150	1.2
S6	264	29	✓	187	300	1
S7	211	32	✗	149	450	1
S8	211	32	✗	149	200	1
S9	211	32	✗	149	50	3
S10	211	36	✓	149	450	1
S11	211	36	✓	149	200	1
S12	211	36	✓	149	50	3
S13	211	40	✗	149	375	1
S14	211	40	✗	149	575	1
S15	211	40	✗	149	75	2
S16	211	45	✓	149	575	1
S17	211	45	✓	149	375	1
S18	211	45	✓	149	75	2

*: σ'_v = Vertical stress at end of 1D loading,

#: d_s = Equivalent diameter of sand column,

§: p'_c = Preconsolidation pressure = $\sigma'_v/3 (1+2k_o)$

**: P' = mean effective stress at end of consolidation

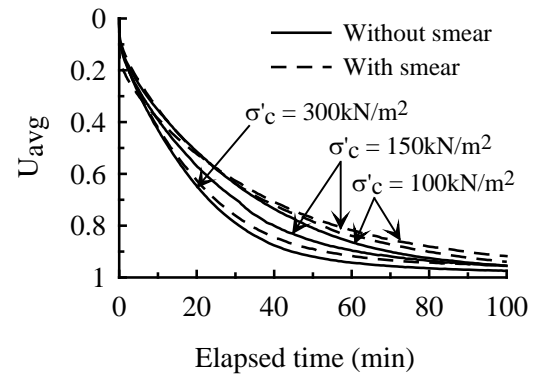
In this table, σ'_v is the 1-D vertical stress used for consolidating slurry in cylindrical mould on the laboratory floor. Mean effective stress (p') towards the end of 1-D loading was estimated using K_o (0.56) obtained from undrained shear test results.

RESULTS AND DISCUSSIONS

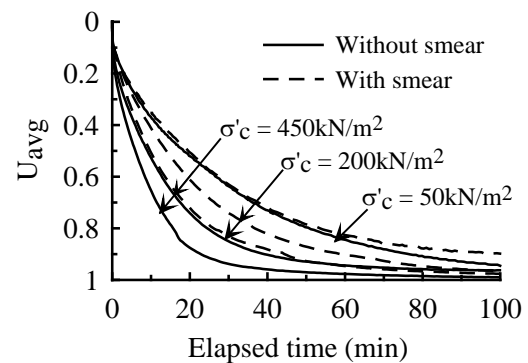
Variation of consolidation

Triaxial consolidation tests were performed on 200mm long and 100mm diameter cylindrical specimens prepared from remolded and reconsolidated commercially available kaolin clay. Two circular rubber sheets with a hole at the centre

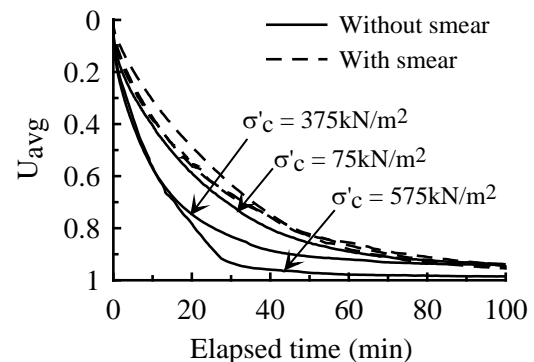
were placed at the two ends of the sample so as to only permit radial drainage during consolidation. Change in volume of the sample during consolidation was automatically measured using the volume change apparatus. The effect of smear zone was investigated by observing the change in pore pressure during consolidation of the composite specimen. Fig. 3a-c shows the average degree of consolidation, U_{avg} plotted against time during isotropic consolidation.



(a)



(b)



(c)

Fig.3a-c Variation of average degree of consolidation with time using sand columns of: (a) 25mm diameter; (b) 32mm diameter; and (c) 40mm diameter.

As can be seen, the figures show that the time to 90% consolidation reduced from about 400 min to less than 60 min with the use of sand column. However, specimens prepared with smear effect took slightly more time to consolidate thereby lending further confidence to the method used to create the disturbed zone. The figure also shows that not all specimens with smear effect were consolidated up to U_{avg} of 1. Similar results have been reported under radial drainage by many researchers [20]-[22].

Variation of coefficient of permeability and coefficient of consolidation

Figure 4a shows the variation of coefficient of permeability, k for selected soil specimens deduced from consolidation data against p' using the procedure suggested by [23].

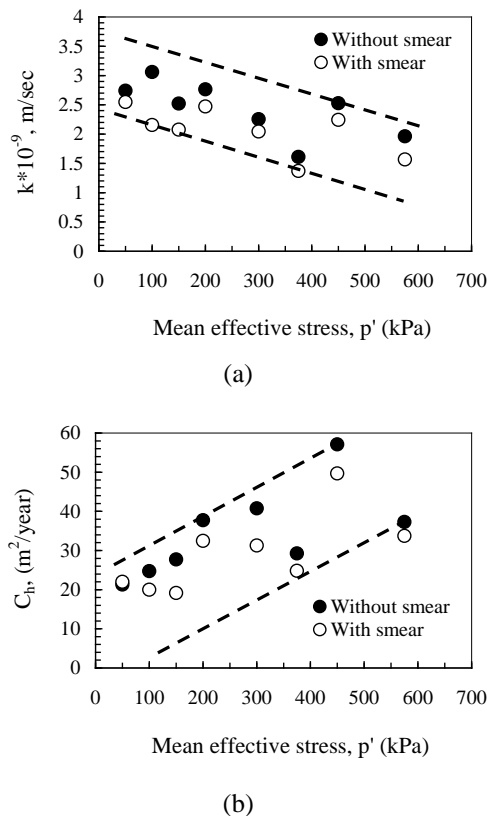


Fig. 4a-b Variation of: (a) coefficient of permeability; (b) coefficient of consolidation with mean effective stress for composite samples.

The results seem to suggest that there was a marginal reduction of permeability by about 20% when specimens were prepared using the smear effect compared to the k of the composite samples prepared without the smear zone. The variation of coefficient of horizontal consolidation with mean effective stress is shown in Fig. 4b above.

Variation of water content

Figure 5 shows water content variation at different locations measured after the completion of few selected tests with and without smear effect. The figures show that water content was not uniform throughout the sample length, and the water content was higher in the samples with the smear zone which supports the above supposition that the smear zone does not permit the complete dissipation of the pore pressure. The results seem to suggest that radial drainage can give rise to significant non-uniformities during consolidation of soil specimens. Similar results have also been reported by [20].

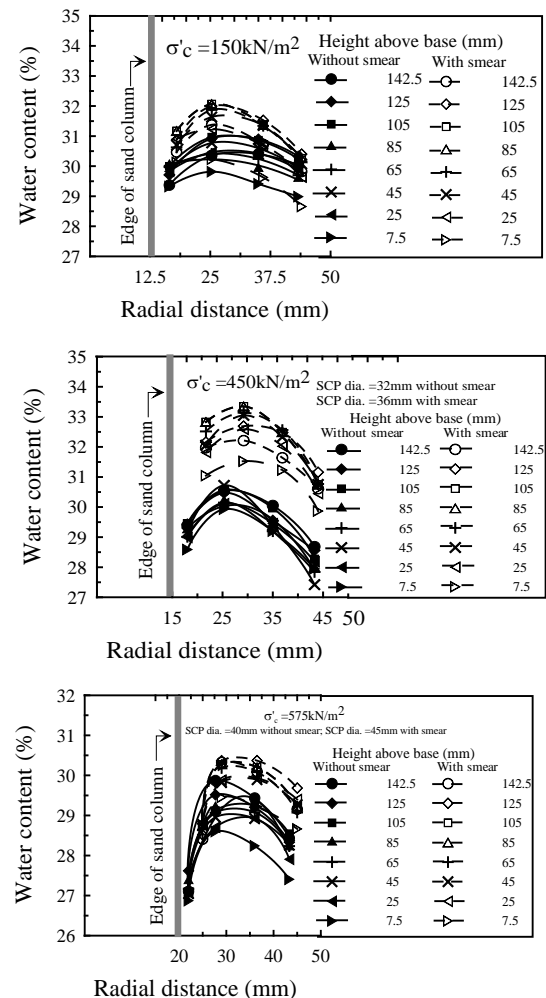
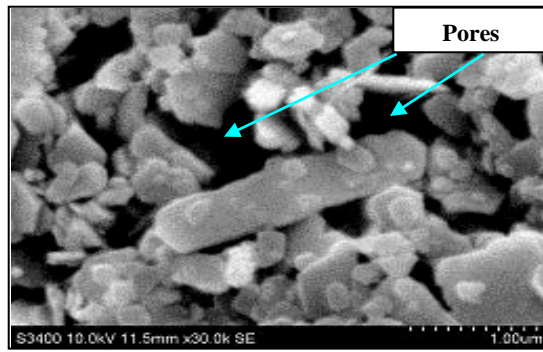
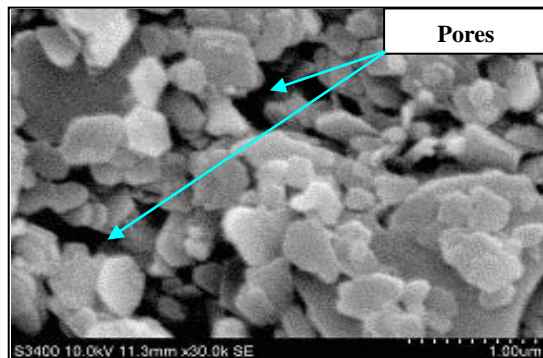


Fig. 5 Variation of water content at different locations measured after the completion of the tests for composite samples under different confining pressures with and without smear effect.

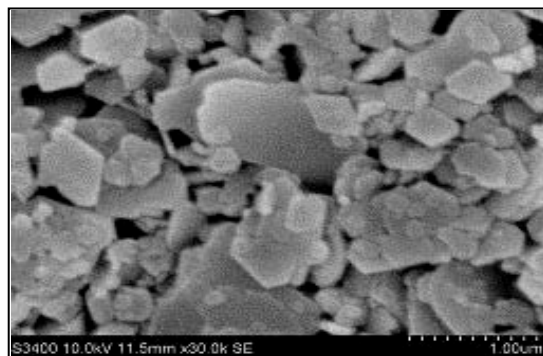
This is also evident from Scanning Electron Microscope (SEM) images (Fig. 6a-d) taken on post compression tests of specimens with and without smear. 7.5mm x 7.5mm x 7.5mm air dried samples were prepared at room temperature for SEM images.



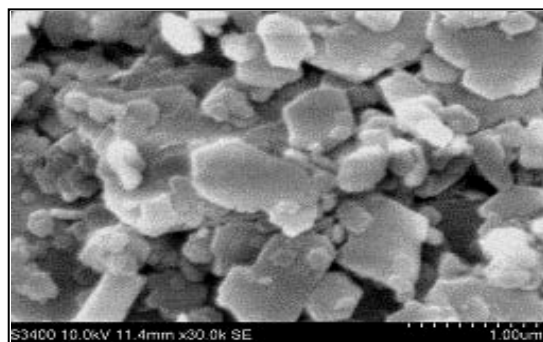
(a). Mean eff. stress at end of consolidation (50kPa)



(b). Mean eff. stress at end of consolidation (450kPa)



(c). Mean eff. stress at end of consolidation (50kPa)



(d). Mean eff. stress at end of consolidation (450kPa)

Fig. 6 SEM images: (a-b) Composite samples without smear zone, (c-d) Composite samples with smear zone.

The images of samples with and without the smear zone show differences in the microstructure. The clay minerals in the smear zone appear to be closely packed with reduced pore space. As such, permeability of the composite samples with the smear zone is reduced with reduced pore space in this zone. The properties within the smear zone are also shown to vary with the overburden pressure [24]. Notwithstanding the above, the focus of this study is to note the difference in the soil behavior when a well defined smear zone is formed surrounding the sand column.

CONCLUSIONS

The permeability and consolidation behavior of the composite ground reinforced with sand columns with and without smear effect was studied using 18 triaxial consolidation tests on composite specimens. It is seen that specimens with sand column (inward radial consolidation) is more effective to improve permeability and consolidation characteristics than compared to conventional clay specimen, which require more than 6-7 days to consolidate without the sand columns. The test results showed that the dissipation of excess pore water pressure occur faster in the radial direction due to the greater coefficient of soil permeability in the horizontal direction and the reduced drainage path. But the installation of the sand columns by means of a rough casing cause remolding of the subsoil in a limited zone of the soil surrounding the sand columns. The presence of smear zone was shown to affect the consolidation and permeability characteristics of the composite sample. Effect of smear zone surrounding the sand column was evident from the additional time taken to consolidate the composite triaxial specimen and because of reduced soil permeability. The soil permeability was reduced by about 20% which was also manifested by the water content variation and pore pressure dissipation in the composite specimen. Also, in present study, a hollow open ended casing was used to remove the soil and form a cavity for installing sand columns, which may not yields realistic pore pressures in the clay during installation. Hence, the effective stress manifested due to the all-round uniform cell pressure is not uniform throughout the specimen. The non-uniformity of consolidated ground and its consequence on subsequent construction of structures needs further study. In order to simulate the better field conditions, installation of driving-in of closed ended casing may be used. Further, amongst the various techniques for improving in-situ ground conditions, columnar inclusions such as sand columns/sand compaction piles, stone columns/granular piles etc., are considered as one of the most cost effective ground improvement techniques as well as good drainage systems.

ACKNOWLEDGEMENT

The first author would like to acknowledge the financial support from the Indian Institute of Technology Bombay (IITB) in the form of research scholarships.

REFERENCES

- [1] Jamiolkowski M, Lancellotta, R and Wolski W, "Precompression and speeding up consolidation", Proc. 8th European Conference on Soil Mechanics and Foundation Engrg., Helsinki, vol. 3, 1983. pp. 1201-1206.
- [2] Aboshi H, Ichimoto E, Enoki M and Harada K, "Composer: method to improve characteristics of soft clays by inclusions of large diameter sand column", Proceedings of the International Conference on Soil Reinforcement: Reinforced Earth and other Technique, Paris, Vol. 1, 1979, pp. 211-216.
- [3] Aboshi H and Suematsu N, "Sand compaction pile method: State-of-the art paper", Proceedings of the 3rd International Geotechnical Seminar on Soil Improvement Methods, Nanyang Technological Institute, Singapore, 1985, pp. 38-44.
- [4] Bergado DT and Balasubramniam AS, "Laboratory testing of prefabricated vertical drains (PVD)", Geotechnical Engineering Journal, Vol. 25, No. 1, 1994, pp.1.
- [5] Raj D and Dikshith CV, "Vibro replacement columns for shipyard infrastructure at Pipavav, Gujarat, India", Proceedings of the International Symposium on Ground Improvement Technologies and Case Histories, GeoSS, Singapore, 2009, pp. 763-769.
- [6] Juneja A and Mir BA, "Behavior of clay reinforced by sand compaction pile with smear", Proceedings of the ICE-Ground Improvement, 165 (2), 2012, pp. 111-124.
- [7] Randolph MF, Carter JP and Wroth CP, "Driven piles in clay-the effects of installation and subsequent consolidation", Geotechnique 29(4), 1979, pp. 361-393.
- [8] Singh G and Hattab TN, "A laboratory study of efficiency of sand drains in relation to methods of installation and spacing", Geotechnique 29(4), 1979, pp. 395-422.
- [9] Xu XT, Liu HL and Lehane BM, "Pipe pile installation effects in soft clay", Proceedings of the Institution of Civil Engineers, Geotechnical Engineering 159, Issue GE4, 2006, pp. 285-296.
- [10] Weber TM, Plotze M, Laue J, Peschke G and Springman SM, "Smear zone identification and soil properties around stone columns constructed in-flight in centrifuge model tests", Geotechnique 60(3), 2010, pp.197-206.
- [11] Bond AJ and Jardine RJ, "Effects of installing displacement piles in high OCR clay", Geotechnique 41(3), 1991, pp. 341-363.
- [12] Madhav MR, Park YM and Miura N, "Modelling and study of smear zones around band shaped drains", Soils and Foundations 33(4), 1993, pp. 137-149.
- [13] Sharma JS and Xiao D, "Characterization of a smear zone around vertical drains by large-scale laboratory tests", Canadian Geotechnical Journal 37(6), 2000, pp. 1265-1271.
- [14] Indraratna B and Redana IW, "Laboratory determination of smear zone due to vertical drain installation", J. Geotech. Engg., ASCE, Vol. 124, No. 2, 1998, pp. 180-184.
- [15] Sathananthan I and Indraratna B, "Laboratory evaluation of smear zone and correlation between permeability and moisture content", Journal of Geotechnical and Geoenvironmental Engineering, ASCE, Vol. 132, No. 7, 2006, pp. 942-945.
- [16] Sathananthan I, Indraratna B and Rujikiatkamjorn C, "Evaluation of smear zone extent surrounding mandrel driven vertical drains using the cavity expansion theory", International Journal of Geomechanics, Vol. 8, No. 6, 2008, pp. 355-365.
- [17] Andreou P, Frikha W, Frank R, Canou J, Papadopoulos V And Dupla JC, "Experimental study on sand and gravel columns in clay", Proceedings of the ICE - Ground Improvement 161(4), 2008, pp. 189-198.
- [18] Holtz RD, Jamiolkowski M, Lancellotta R and Pedroni S, "Prefabricated vertical drains: design and performance, CIRIA Ground Engineering Report: Ground Improvement", Butterworth-Heinemann Ltd, UK, 1991.
- [19] BS 1377-1, "Methods of test for soils for general requirements and sample preparation", British Standards Institute, 1990, London.
- [20] Atkinson JH, Evans JS and Ho EWL, "Non-uniformity of triaxial samples due to consolidation with radial drainage", Geotechnique 35(3), 1985, pp. 353-355.
- [21] Robinson RG and Shilpa D, "Equal strain consolidation of clays under radial drainage", Indian Geotechnical Journal, 38(2), 2008, pp. 204-220.
- [22] Mir BA, "Study of the influence of smear zone around sand compaction pile on properties of composite ground", Ph.D. Thesis, Deptt. of Civil Engineering, IIT Bombay, 2010.
- [23] Barron RA, "Consolidation of fine-grained soils by drain wells", Transactions ASCE, 113, 1948), pp. 718-754.
- [24] Bergado DT, Alfaro MC and Balasubramaniam AS, "Improvement of soft Bangkok clay using vertical drains", Journal of Geotextiles and Geomembranes 12, 1993, pp. 615-663.

LABORATORY EVALUATION OF PHYSICO-CHEMICAL VARIATIONS IN BENTONITE UNDER ELECTROKINETIC ENHANCEMENT

Nasim Mosavat¹, Erwin Oh¹ and Gary chai³

¹Griffith School of Engineering, Griffith University, Australia

²Centre for Infrastructure Engineering & Management, Griffith University, Australia

ABSTRACT

When the traditional ground improvement techniques are not practical for a particular situation, alternative technology, such as electrokinetic (EK) soil treatment can be considered. EK treatment method involves applying a low direct current (DC) or a low potential gradient to arrays of electrodes inserted in the low permeable soils simulating migration of electricity, pore water, ions and charged particles across the soil, hence modifying the physicochemical, mechanical and engineering properties of the soil. This study investigates the effects of EK treatment on conductance phenomena and physico-chemical changes of bentonite at different intervals under total applied voltage of 10V subjected to specific types of anode enhancement solutions. The cumulative electroosmotic flow and electric current through the sample was measured for 15 days of treatment. The specimens were also tested for moisture content, pH and undrained shear strength variations over different time periods of 3, 6, 9, 12 and 15 days showing good correlations between the soil parameters.

Keywords: Electrokinetic, Enhancement solutions, Bentonite, Physico-chemical

1. INTRODUCTION

The use of EK treatment, which is a comparatively new methodology, is being investigated in some parts of the world as a viable in situ soil stabilisation and treatment method [1-10]. EK soil treatment method also termed as electro-chemical soil processing, uses low intensity direct current (DC) or a low electric potential, to remove pore water and modify fine-grained soils, mud, sludge, slurries and sediments by electric potential. The transportation of charged chemical species across the soil involves several complex mechanisms such as electrolysis, electro-osmosis, electromigration and electrophoresis. In this regard, application of direct electric current (EC) has various effects such as:

- i. It results in electrolysis of water which brings about oxidation at the anode, generating an acid front, and reduction at the cathode, producing a base front [11]
- ii. It generates two migrations: an ionic migration (electromigration) and electrophoresis of colloidal particles.
- iii. It establishes an electric potential difference which will lead to generation of electro-osmosis through the sample [12].

This technique can also be enhanced by introducing desirable chemical compounds (enhancement solutions) such as lime, calcium chloride or even tap water to the soil by injecting them at the appropriate electrode, preferably anode. The introduction of an appropriate chemical enhancement solution can be

beneficial to decrease the extreme acidity at the anode; manage/neutralise anode pH; facilitate the electro-osmotic flow, and enhance the EK process across the soil. The combined effects of these processes together with various geochemical reactions alter the chemical composition of the soil porous medium and hence modify the physicochemical properties of the soil during the EK treatment.

Although the EK technology has been proven to be useful in many laboratory and field tests, the application of the technology is still limited. This may be due to the complicated and unknown features such as conductance phenomena and electrochemical reactions during this treatment. Field electro-osmotic mechanism is different from laboratory experiment and moreover, the EK treatment with the injection of lime and saline enhancement solutions (chemical stabilisers) has rarely been discussed. In this regard, there is a need for a comprehensive experimental program to be carried out for a better fundamental understanding of the changes in soil during and after the treatment. Such information would be of particular interest in the improvement of marine soils possessing high moisture content (Mc) and low bearing capacity on existing infrastructure. The aim of this study is to evaluate the conductance phenomena and several physico-chemical modifications of bentonite clay subjected to hydrated lime and saline enhancement under the total applied voltage of 10 V (0.3 V/cm voltage gradient) during 15 days of treatment.

2. EXPERIMENTAL SOIL

Some studies have shown that bentonite exhibits much higher buffering capacity (resistance to change in pH) because of higher CEC compared with other clay minerals, compared to kaolinite [13]. Despite several industrial and engineering applications of bentonite, such deposits exhibit large of swell/shrink behaviour upon moisture fluctuations and being sensitive to the changes in chemical environment. Therefore, it is known as one of the dangerous types of clay and can lead to serious engineering problems such as slope or wall failures, high swell/shrink behaviour leading to differential settlements and large cracks. Therefore, Na-bentonite was selected in this study to investigate the potential of EK treatment technique incorporated with chemical stabilisation to improve/stabilise soft soils. The original properties of the bentonite are summarized in Table 1.

Table 1. Original properties of the bentonite

Soil characteristics	Values	References
Clay mineralogy	Bentonite	-
Liquid limit (%)	650	AS 1289.3.1.1-1995
Plasticity index, (%)	450	AS 1289.3.1.1-1995 AS 1289.3.1.1-1995
Linear shrinkage, (%)	27.2	AS 1289.3.1.1-1995
Activity	4.9	PI/ Percentage of clay
Specific gravity, Gs	2.8	AS 1289.3.5.1-1995
Unified soil Classification	CH	ASTM D 2487-83
Textural classification	Heavy clay	Soil textural triangle by USDA ¹
Colour	Light grey	-
Clay (%)	92	AS 1289.3.6.2-1995
Silt (%)	6	AS 1289.3.6.2-1995
Sand (%)	2	AS 1289.3.6.2-1995
Electrical conductivity, (μS)	397	AS 1289.4.3.1-1997
pH	10	AS 1289.4.3.1-1997

3. EXPERIMENTAL MODEL AND SET UP

The laboratory experiments of EK treatment of soil samples are carried out using the test model developed at the Griffith University. The EK tests are performed in clear glass rectangular tanks of 38 cm in length and 20 cm in width, under highly controlled laboratory conditions. A compacted layer of the soil with a thickness of about 17 cm was placed in the tank to known moisture content value. Tap water having a conductivity of 187 μS at 25°C was used for the slurry preparation to resemble actual field application. Then, two hollow stainless steel tubes, possessing some drilled holes through their walls, to allow the enhancement liquids to move freely into the sample, were placed 32 cm apart at the ends of the tank to be served as electrodes. An outlet from cathode chambers is connected to the vacuum pump to facilitate collecting cathode effluent and measuring the cumulative electro-osmotic flow volume. The power distribution cables were attached to the electrodes and connected to the DC power supply, providing total voltage of 10 V. The soils at various normalised distances of 0, 0.25, 0.5, 0.75 and 1 from the anode, were tested for variations in moisture content (Mc), pH and undrained shear strength (Su) as a result of EK process for 3, 6, 9, 12 and 15 day periods. The normalised distance is defined as the distance of the testing point from anode, over the total distance between the electrodes. The schematic view of the experimental model has been shown in Fig. 1. In order to aid the EK process, soil samples were subjected to a slow continuous flow of anode enhancement solutions (hydrated lime and saline solution). The saturated hydrated lime in distilled water, had pH value of 12.4 and electro-conductivity of 8.9 mS. Similarly, 0.1 N calcium chloride was mixed with 1:100 sodium silicate solutions (by the volume of distilled water) and this saline solution was selected as second enhancement liquid during the EK treatment. The pH of this solution was found to be 9.5 and electro-conductivity value of 15 mS. The physico-chemical properties of the hydrated lime (slaked lime), calcium chloride and sodium silicate used in this study are shown in Table 2. The enhancement liquids were permitted through the soil via anode by use of a thin flexible PVC tube connected to an external plastic reservoir, at a small external hydraulic head (with very low discharge of solution, almost dripping). For testing, the upper 20 mm was first removed to ensure that any surface drying/wetting or disturbance effects were avoided.

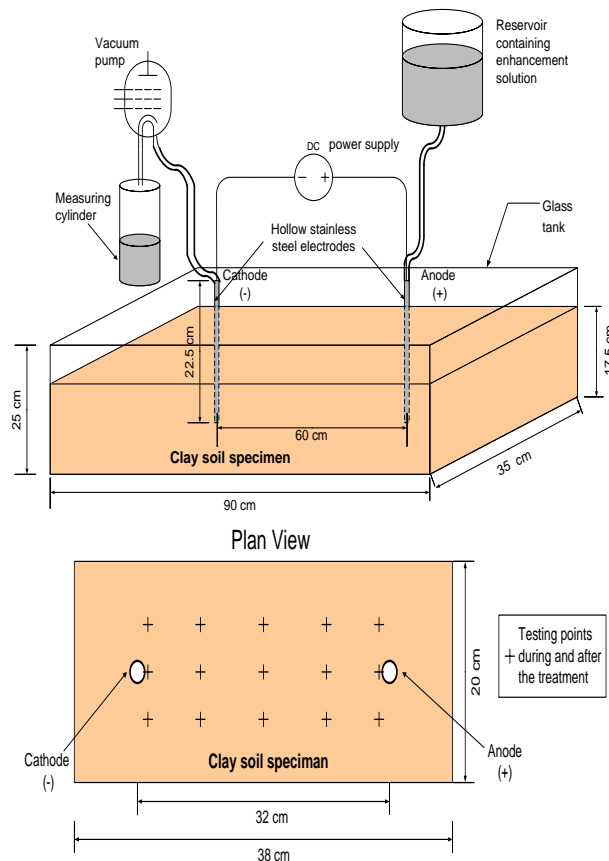


Fig. 1 (a) Schematic view and (b) plan view of the laboratory set up for the EK treatment of the clay soil (not to scale)

Table 2. Properties of the enhancement agents used in this study

Properties	Hydrated lime	Calcium chloride	Sodium silicate
Molecular formula	Ca(OH)_2	CaCl_2	Na_2SiO_3
Molar mass (g/mol)	74.093	111	122.06
Exact mass	73.968071	110.9848	
Appearance	Soft white powder	White powder	Thick liquid
Odour	Odourless	Odourless	Odourless
Solubility	Soluble in glycerol and acids. Insoluble in alcohol.	Soluble in acetone, acetic acid	Insoluble in alcohol
Toxicity	Low	Low to medium 8-9	Corrosive
Acidity	12.4	(anhydrous) 6.5-8.0 (hexahydrate)	11.5
Basicity	2.37	-	-

4. METHODOLOGY

The cathode effluent (liquid) was extracted mechanically via a vacuum pump from the cathode well to measure the accumulated electro-osmotic flow volume for period of 15 days. The electric current between the electrodes was manually monitored using a digital multimeter for everyday. The moisture content (M_c) and pH variations of the soil samples were evaluated by using the method described in Australian standard AS 1289.2.1.1-2005 and AS 1289.4.3.1-1997 respectively. The undrained shear strength (S_u) of the soil was measured directly using a hand vane shear apparatus in accordance with AS 1289.6.2.1-1997.

5. RESULTS AND DISCUSSIONS

5.1. Conductance Phenomena During EK Process

Upon the application of DC electric potential through the soil sample across the electrodes, the soil-liquid medium undergoes several complex electrochemical processes that take place within the soil porous media. Some of these processes are initiated immediately after the DC electric potential was applied (e.g. electrolysis of water, electro-osmotic flow, current flow, etc), while several other progressions develop with time (e.g. variations in M_c , pH, S_u , etc). With the increase of treatment durations, some of these modifications (e.g. electro-osmotic flow and electric current flow) appear to continue but with a gradually decreasing rate, which is due to the several other system complications developing within the porous media. The most prominent observation of these experiments was the development of wet and drier areas between the electrodes due to positive electro-osmotic flow from anode to cathode.

5.1.2. Cumulative electro-osmotic flow

When a electric potential is employed to a clay-water structure, electro-osmosis flow occurs from anode to cathode and the mobile DDL moves and drags the solution with it [14]. The variation of total liquid volumes cumulated in the cathode well for bentonite due to electro-osmotic flow subjected to hydrated lime and saline enhancement is presented in Fig. 2. As it can be seen with hydrated lime enhancement higher cumulative electro-osmotic flow volume has been recorded in comparing with saline solution. This can be described by the Helmholtz-Smoluchowsky's (H-S) theory which is the most common theoretical electro-osmotic description and is widely accepted by geotechnical researchers [13, 15]. According to this model the

electro-osmosis permeability (k_e) under an electrical gradient is indirectly proportional to the viscosity (η) of the pore fluid via the following formula:

$$k_e = \frac{D\zeta}{\eta} n \quad (1)$$

Where ζ is the zeta potential (V), n is the porosity, η is the viscosity (FT/L2) and D is the dielectric constant. Saline solution has higher viscosity (η) compared to hydrated lime due to existence of water-soluble thick liquid; sodium silicate. Therefore, with saline enhancement the viscosity of the pore fluid increases and electro-osmotic flow rate decrease. This led to delaying of electro-osmotic flow through bentonite and reduction of cumulated cathode effluent.

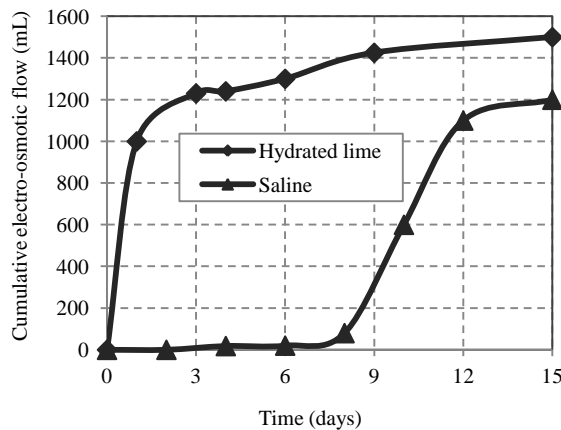


Fig. 2 Variation of cumulative electro-osmotic flow volume with time for bentonite under applied voltage of 10 V subjected to hydrated lime and saline enhancement solution

5.1.3. Electric current (EC) flow and electrical resistance(ER)

Fig. 3 represents the variation of electric current flow (EC) and electrical resistance (ER) across bentonite with respect to hydrated lime and saline enhancement solutions. It can be seen that both tests begin with relatively high EC values, while with passing processing time, the current reduces reaching almost constant values. The injection of enhancement solutions through the soil sample would increase the number of cations in the soil pore solution leading to more hydration of cations migrating towards the cathode [16]. According to the Fig 3 higher rate of EC flow was observed with saline enhancement compared to hydrated lime enhancement. This can be due to greater ionic

concentration and electro-conductivity of the saline solution, which will increase electrochemical effects (e.g. increase of cation exchange and precipitation on the surface of clay particles) leading to higher initial current through the sample. By dividing the applied voltage by the electric current, the electrical resistance (ER) of bentonite was obtained. The ER of the soil decreased initially and then increased with processing time. This is due to the fact that injection of enhancement solutions would increase the electric current in the sample, which in turn reduces the initial electrical resistance of soil. With increasing treatment time, the electrical resistance increased due to the decline of the electric current through the soil sample.

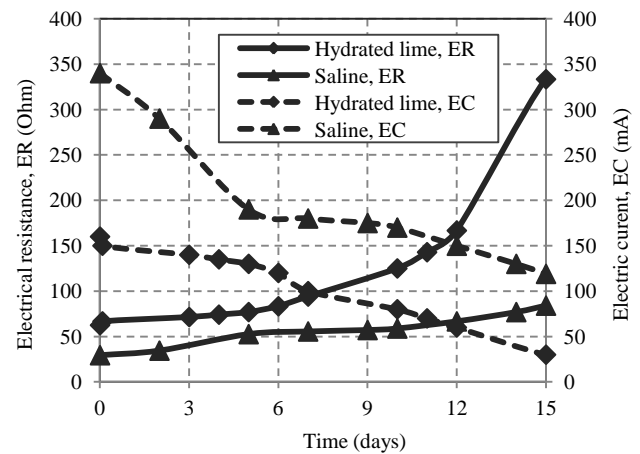


Fig. 3 Variation of electric current flow (EC) and electrical resistance (ER) across bentonite over time under applied voltage of 10 with hydrated lime and saline enhancement

5.2. EK Effect on Physico-chemical Characteristics of Bentonite Soil

EK processes can modify the system chemistry of the porous media, hence modifies several physico-chemical and engineering properties of the soils.

5.2.1. EK effect on moisture content (Mc) and undrained shear strength (Su) variations

The undrained shear strength (Su) and moisture content (Mc) variations of bentonite with time at different normalised distances from anode under 10 V applied voltage with hydrated lime and saline enhancement are presented in Figs. 4 and 5 respectively. It is noticed that under both EK processing conditions employed, a considerable Mc gradient was built up in the bentonite between the electrodes, forming wet and dry regions. The

positive electro-osmotic flow from anode to cathode formed dry regions at the vicinity of the anode and wet areas at the vicinity of the cathode. In this regard, the exact location of wet and dry regions depends on the mineralogical properties of the soil such as permeability characteristics, clay type and content, DDL characteristics, etc [17].

From the Figs. 4 and 5 it can also be observed that there is a considerable S_u gradient in soil sample between the electrodes showing very good correlations with the changes in M_c of the soil

across the sample. In general, with increasing processing time, the strength appears to increase possessing the highest strength values after 15 days of treatment at 0.25 normalised distance from the anode subjected to both enhancement solutions. Moreover, with saline enhancement, higher degree of shear strength was observed in soil sample compared with hydrated lime enhancement. From these results it can be concluded that the EK treatment with enhancement solutions, has significantly improved soil strength especially at the vicinity of the anode and in the middle of the tank.

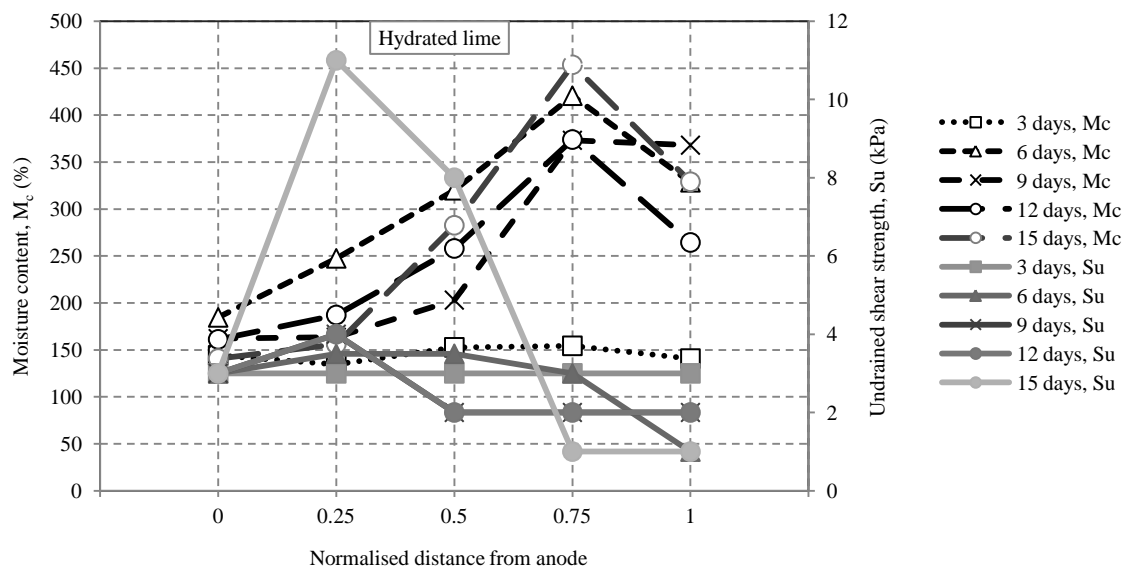


Fig. 4 Shear strength (S_u) and moisture content (M_c) variation of bentonite over time at regular normalised distances from the anode under applied voltage of 10V with hydrated lime enhancement

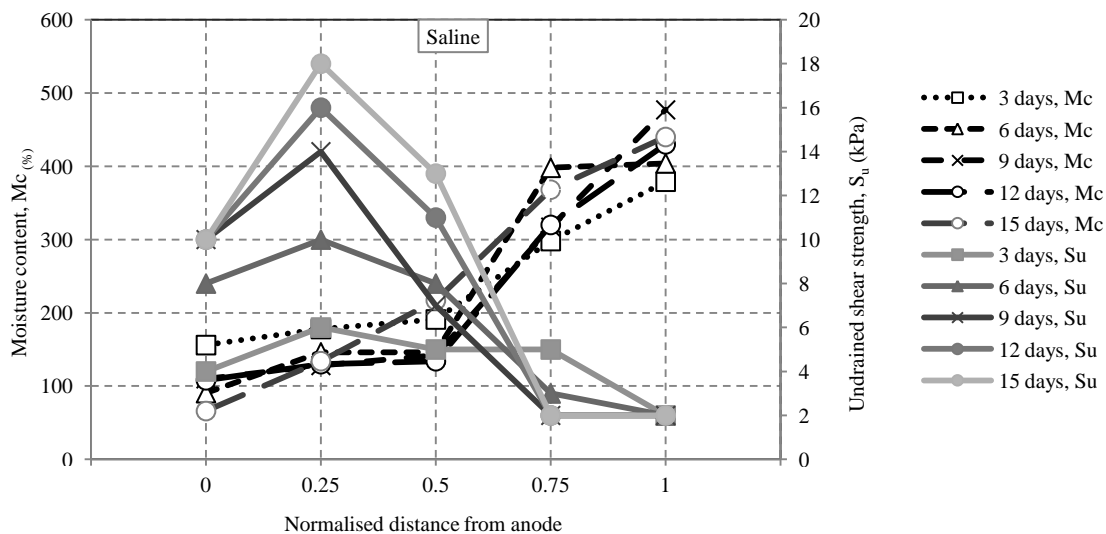


Fig. 5 Shear strength (S_u) and moisture content (M_c) variation of bentonite over time at regular normalised distances from the anode under applied voltage of 10V with saline enhancement

5.2.2. EK effect on pH variations

The development of the pH gradient across the electrodes, for bentonite versus time at regular normalised distances from the anode with hydrated lime and saline enhancement is presented in Figs 6 and 7, respectively. It can be noticed that under the both EK processing conditions, a clear pH gradient was being developed within the bentonite soil between the electrodes, forming an acid front at the anode and a base front at the cathode. However, the passage of enhancement solutions through the soil reduced the extreme acidity near the anode. As it can be observed from Figs. 6 and 7, during the early stages of EK treatment, the pH of the soil remained unchanged. This is due to the high buffering capacity of bentonite. However with the passage of processing time, the pH at the vicinity of the anode seems to drop reaching almost lowest pH value at 15 days of treatment.

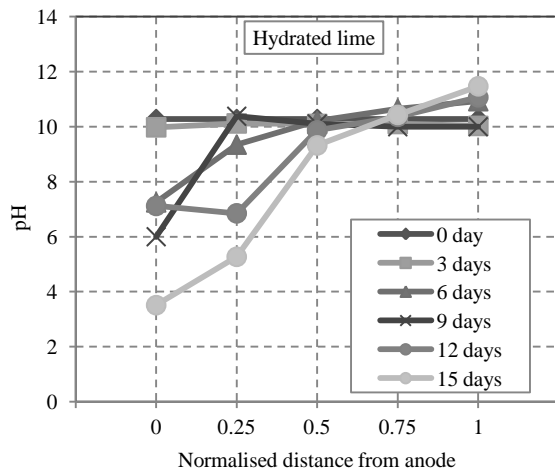


Fig. 6 Variation of pH of bentonite over time at regular normalised distances from the anode under applied voltage of 10V with hydrated lime enhancement

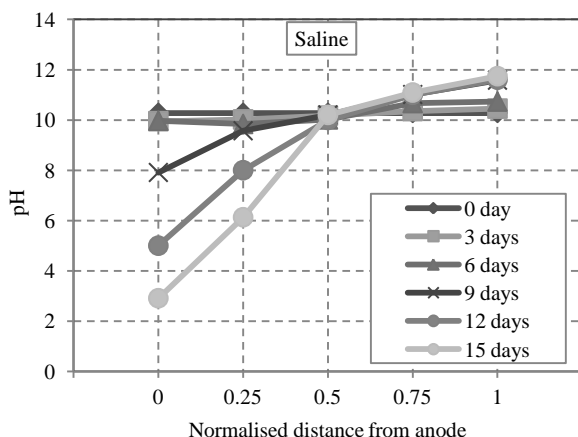


Fig. 7 Variation of pH of bentonite over time at regular normalised distances from the anode under applied voltage of 10V with saline enhancement

6. CONCLUSIONS

This paper has presented some laboratory results of a study undertaken to investigate the EK treatment effects in bentonite soil subjected to two enhancement solutions under a predetermined applied voltage gradient of 10 V. From the analysis of the test results the following conclusions can be made:

- With the application of DC electric potential through the sample, the soil-liquid medium undergoes several physico-chemical and electrical changes due to several complex electrochemical processes which take place within the soil porous media. The most prominent observation of these experiments was the development of wet and dry areas between the electrodes due to positive electro-osmotic flow from anode to cathode
- Higher rate of electro-osmotic flow is observed during the early stage of the EK process under both processing conditions while with processing time, a gradual decrease in the rate of electro-osmotic flow was noted. With hydrated lime enhancement higher cumulative electro-osmotic flow volume was recorded in comparing with saline enhancement.
- The tests began with relatively high currents, however with processing time, the current declined gradually, leading to higher ER values. The electric current through the sample found to be higher with saline enhancement.
- Under both EK processing conditions employed in this study, a clear pH gradient in soil increasing from anode to cathode was built up exhibiting very good correlations with the changes in S_u of the soil. With saline enhancement, higher degree of shear strength was observed in soil sample (at 0.25 normalised distance from the anode) compared with hydrated lime enhancement.
- Under both EK processing conditions employed, a clear pH gradient was being developed in the bentonite between the electrodes, creating an acid front at the anode and a base front at the cathode, although the passage of anode enhancement solutions through the soil reduced the extreme acidity near the anode.

REFERENCES

- [1] Acar, Y.B. and A.N. Alshawabkeh, Electrokinetic remediation .1. Pilot-scale tests with lead-spiked kaolinite. Journal of

- Geotechnical Engineering-Asce, 1996. Vol. 122.(3): pp. 173-185.
- [2] Alshawabkeh, A.N. and Y.B. Acar, Electrokinetic Remediation - Pilot-Scale Test-Results. Abstracts of Papers of the American Chemical Society, 1994. Vol. 207.(pp. 114-ENVR.
- [3] Al-Hamdan, A.Z. and K.R. Reddy, Electrokinetic remediation modeling incorporating geochemical effects. Journal of Geotechnical and Geoenvironmental Engineering, 2008. Vol. 134.(1): pp. 91-105.
- [4] Jayasekera, S., An investigation into modification of the engineering properties of salt affected soils using electrokinetics, University of Ballarat 2008.
- [5] Mohamedelhassan, E., Laboratory Model Test on Improving the Properties of Soft Clay by Electrokinetics. 2011.
- [6] Schmidt, C.A.B., M.C. Barbosa, and M.S.S. de Almeida, A laboratory feasibility study on electrokinetic injection of nutrients on an organic, tropical, clayey soil. Journal of Hazardous Materials, 2007. Vol. 143.(3): pp. 655-661.
- [7] Shang, J.Q. and K.L. Masterson, An electrokinetic testing apparatus for undisturbed/remoulded soils under in-situ stress conditions. GEOTECHNICAL TESTING JOURNAL, 2000. Vol. 23.(2): pp. 215-224.
- [8] Tjandra, D. and P.S. Wulandari, Improving marine clays with electrokinetics method. Civil Engineering Dimension, 2007. Vol. 9.(2): pp. 98-102.
- [9] Turer, D. and A. Genc, Strengthening of soft clay with electrokinetic stabilization method, in 6th symposium on electrokinetic remediation (EREM 2007), C.C. Fernández, M.A.S. Braga, and M.M.P. Currás, Editors.: Spain 2007, pp. 83-84.
- [10] Yeung, A.T., T.B. Scott, S. Gopinath, R.M. Menon, and C. Hsu, Design, Fabrication, and Assembly of an Apparatus for Electrokinetic Remediation Studies. Geotechnical Testing Journal, GTJODJ, 1997. Vol. 20.(2): pp. 199-210.
- [11] Iyer, R., Electrokinetic Remediation. Particulate Science and Technology, 2001. Vol. 19.(pp. 219-228.
- [12] Acar, Y.B., et al., Electrokinetic remediation: Basics and technology status. Journal of Hazardous Materials, 1995. Vol. 40.(2): pp. 117-137.
- [13] Acar, Y.B. and A.N. Alshawabkeh, Principles of electrokinetic remediation. Environmental Science & Technology, 1993. Vol. 27.(13): pp. 2638-2647.
- [14] Ahmad, K., K.N. Kassim, and M.R. Taha, Electroosmotic flows and electromigrations during electrokinetic processing of tropical residual soil Malaysian Journal of Civil Engineering, 2006. Vol. 18.(2): pp. 74-88.
- [15] Mitchell, J.K., Fundamentals of Soil Behaviour. 2nd ed1993, New York: John Wiley & Sons Inc.
- [16] Ou, C.Y., S.C. Chien, and Y.G. Wang, Soil improvement using electroosmotic with the injection of chemical solutions: field tests. Canadian Geotechnical Journal, 200946): pp. 727-733.
- [17] Jayasekera, S. and S. Hall, Modification of the properties of salt affected soils using electrochemical treatments. Geotechnical and Geological Engineering, 2007. Vol. 25.(1): pp. 1-10.

FLOW PATTERN FOR MULTI-SIZE SILOS

Yi Yang¹, Na Li², PengYin³ and YM Cheng⁴

Department of Civil and Environmental Engineering, The Hong Kong Polytechnic University, Hong Kong.

ABSTRACT

Silo container is a very important storage structure for coal, sand and other granular materials. Nonhomogeneous granular flow is sometimes found in ore discharging in mining engineering, but so far there are only limited studies to this topic, particularly for double opening silo. In views of that, it is necessary to figure out the details about the flow pattern behavior. In the present paper, four physical models are designed to investigate the flow patterns for silos discharge behavior with double openings. The opening spacing, height ratio, sand properties and automatic separated manners are considered in these laboratory tests. Meanwhile, two-dimensional discrete element method is used to reproduce the flow behavior as well as to evaluate the dynamic wall stresses distribution on the silo hopper from bottom to top. It is found that the flow pattern is very sensitive to the spacing between openings under close opening silos. For the wide opening silos, the discharge efficiency would change nearly 30%. The arch effect in the dead zone and ore recovery are significantly influenced by the height /spacing ratio. The results from discrete element analysis can match well with the experimental study if suitable micro-parameters are used in the analysis.

Keywords: Silos; Flow Pattern; Discharging; Laboratory Tests; Discrete Element

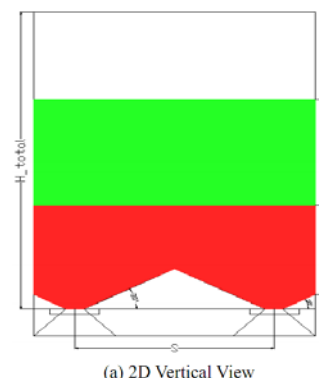
INTRODUCTION

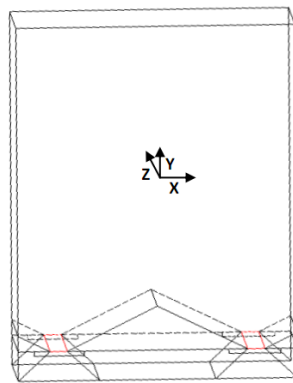
Many engineers still use the classical Janssen formula [1] to analyze the stress distribution on the wall of silo, where only homogeneous material is considered and the end effect is ignored. The limitations of this formula come from the assumption of uniform flow required in the classical continuum mechanism for analyzing discontinuous problem. Cheng et al. [2] discovered that columniform channel flow can be observed when two layers of materials with different sizes are introduced into short silos, where maximum stress can be found at the top of dead region. Cheng et al. [3] had found that the double opening silo can increase the recovery of the bottom material. The material deposition from the nature is complicated, as the columniform channel and funnel flow are required to be considered for granular discharge flow. In this paper, four physical models are designed to carry out 16 groups of tests with double openings for the silos. The effect of opening distance, height/spacing ratio and layering are investigated for the flow pattern, arching effect and ore recovery. The discrete element method [4]-[7] is also used for comparing the analysis and monitoring the stress field for the whole processing.

EXPERIMENTAL TESTS

Four different double openings silos are designed, where the opening spacing and height ratio are varied. The schematic diagram is shown in Fig. 1,

where S means the opening distance, H_{layer} is the height of each soil layer, and H_{total} is the height of each silo. The heights of the two shorter silos (silo A and silo B) are 650mm, and it is 1000mm for silos C and D. The laneway in the physical model is 30mm wide with an angle of 30 degree to the horizontal direction. The laneway can be removed to induce the initial sand drawing. The surrounding sides of the silos were made of transparent PVC sheet with scale lines for easy monitoring and capturing discharge process. The flow pattern of this test is also recorded by a high speed camera. In this experimental study, red sand and green sand, which were deposited and compacted in layers, were used for visualizing the flow behavior. The particle size distributions of the sands are nearly uniform. Cheng and co-workers [2] have used these two sands for comparing the single and double opening effects in flow patterns, where the opening distance is close and the height ratio is small.





(b) 3D Geometric Model

Fig. 1 2D and 3D double-opening schematic.

The number and types of layers are limited in this study. In this paper, multiple experiments have been carried out to capture the sensitivities of the above three factors for granular flowing pattern and ore recovery. Detailed information about these tests can be seen in Table 1, where the height of each layer is associated with layers order. For silo A model, the reverse deposition manner may directly influence the flow pattern. In test 1, the coarse red sand is at the bottom layer, where the global flow is basically a uniform discharge. In test 2, the fine green sand at the bottom will induce two twin funnel flows, and a steady dead zone with sharp geometry at the interface between the two layers were found during the flow. The speed of the red sand (coarser sand) is much greater than the fine sand, and the green dead zone will support the upper layer to generate two fast flow side zones. Red sand will firstly deposit in the deposition tank. The flow pattern of these two tests can be seen in Fig. 2.



Fig. 2 The flow patterns in test 1(left) and 2.

The discharge time in Table 1 can be influenced by the material property at each layer, which has been found by *Cheng et al.* [2]. In these experimental tests, it can be found that the opening spacing can significantly affect the discharge efficiency. The difference in the discharge time for reversing the layerings in the close opening silo A and C are not

obvious.

Table 1 Detail information of experimental tests (T means the time required for complete discharge)

Groups	Layer	Num	S (mm)	H_{layer} (mm)	T (s)
Silo A	Red	1	155	155	5.8
	Green				
	Green	2			155
Red					
Silo B	Red	3	240	240	10
	Green				
	Green	4			240
Red					
Silo C	Red	5	140	140	6.8
	Green				
	Green	6		280	7.2
	Red				
	Red	7		140	9.5
	Green				
	Green	8		420	9.7
	Red				
	Red	9		140	9.8
	Green				
	Green	10		560	10.1
	Red				
Silo D	Red	11	270	270	10.8
	Green				
	Green	12		270	13.2
	Red				
	Red	13		270	11.1
	Green				
	Green	14		405	14.6
	Red				
	Red	15		270	12.6
	Green				
	Green	16		540	16
	Red				

However, for the wide opening silo B and D, the variations are nearly 30% which can directly influence the discharge behavior. This may be induced by the couple effect of the geometry and the material properties. The frictional coefficient of fine green sand is larger than the coarse red sand, and this may impact the flow ability. Meanwhile, higher height can accelerate the whole flow velocity to increase the discharge efficiency. The dead zones at the bottom layer can be found in each test for silo C and silo D, especially at a larger height value. The dead zones are unstable in higher top layer, which will gradually decrease in the global processing

behavior. This interesting phenomenon can be seen in Fig 3. In this figure, since the opening spacing is close, the depression cone will also appear in the bottom layer. Ore recovery will be better when the height ratio is higher, where the height of bottom layer is coincident with the opening spacing. The authors here choose test 5 and test 9 for a comparison which is shown in Fig 4. These findings can be important for non-homogeneous ore mineral discharge behavior.

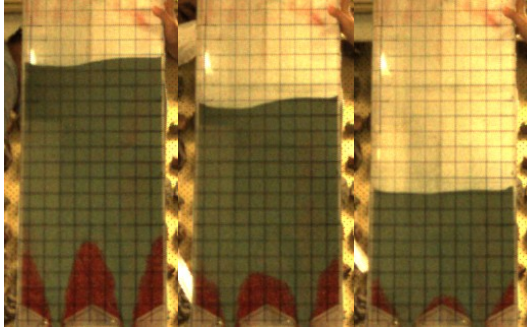


Fig. 3 The variation of dead zone in bottom layer.

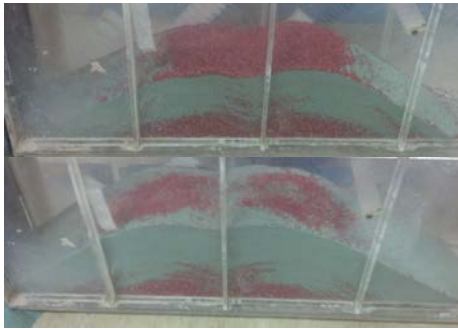


Fig. 4 The deposition view of test 5(top) and 9.

NUMERICAL COMPARISON

Two dimensional program PFC2D [4] using rigid “Disk” with soft contact is used for the present study. The governing principle in the modeling includes three models: 1) contact model; 2) bonding model; 3) slip model. For cohesionless materials such as sand in the present study, the bonding model can be ignored. The authors have chosen the linear elastic model and Coulomb slip model in the present study which is also adopted in many previous studies [2]-[7]. The micro parameters of linear contact model include the normal and shear stiffnesses and the internal frictional coefficient. Furthermore, the velocity vectors of each “Disk” consist of two plane translational components and a rotational component. The skeleton of the linear contact model in this paper is given in Fig 4. Meanwhile, the mechanical governing equations of the bond/slip model are

given by:

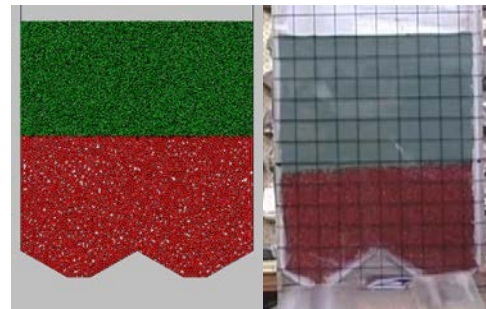
$$\begin{cases} F_i^n = K_n U_n \\ \Delta F_i^s = -k_s \Delta U_s \\ F_i^s \leq \mu F_i^n \end{cases} \quad (1)$$

Where K_n and k_s denote the normal and shear stiffness coefficients, ΔU_n is the normal overlap, ΔU_s is the incremental tangential displacement, μ is the inter-frictional coefficient.

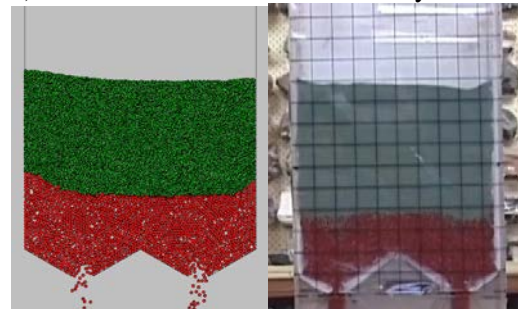
The calibration of the input micro parameters has been discussed by many researchers [2], [7]. The material physical and micro numerical parameters are given in Table 2. Particles are generated by the deposition method, which can generate a similar initial stress field as the experimental specimen initial condition. The dimensions in the numerical model are same as the physical model. The vertical and horizontal stresses can be monitored at every step in the computing procedure, which can qualitatively analyze the stress distribution on the boundary. The stress field on the boundary is another important index for optimizing the design of the silo and ore discharge.

Table 2 Physical and micro parameters

Sand	Size (mm)	ϕ	Density (kg/m ³)	K_n (N/m)	k_s (N/m)
Red	2-2.2	27	1415	4e6	4e6
Green	0.15-0.60	31	1379	1e6	1e6



a) Initial numerical and laboratory test.



b) 400,000 numerical steps

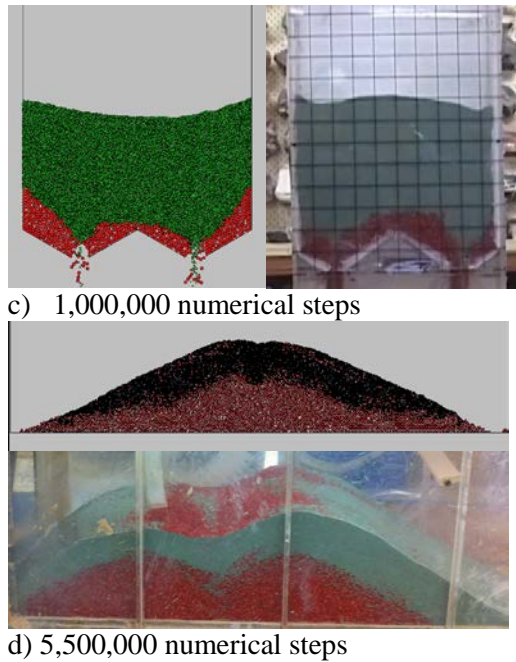


Fig. 5 Numerical and experimental comparison.

In this paper, the authors choose test 1 to carry out a numerical simulation. It was observed that the sand is drawn uniformly beginning, but it gradually becomes twin short funnel channel. The flow patterns of test 1 at different numerical time steps are shown in Fig.5, which is simultaneously compared with experimental test from the high speed cameral. These results can totally match well with the trend of the laboratory results.

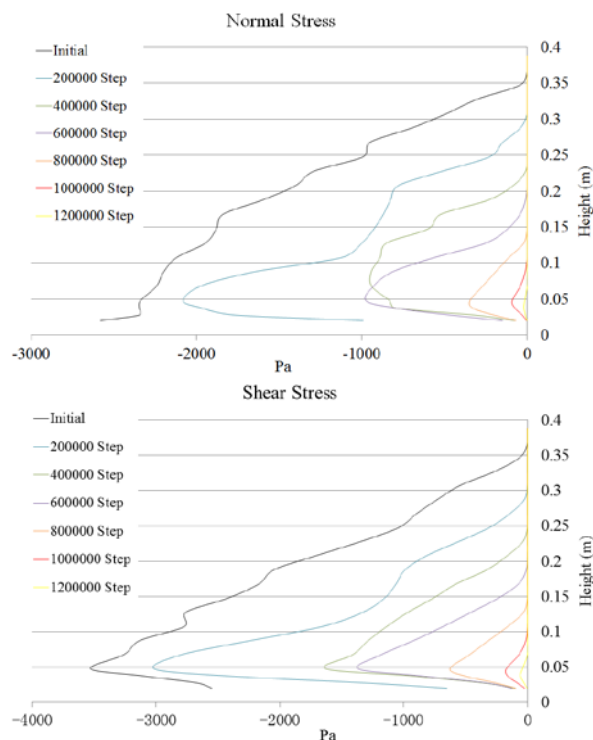
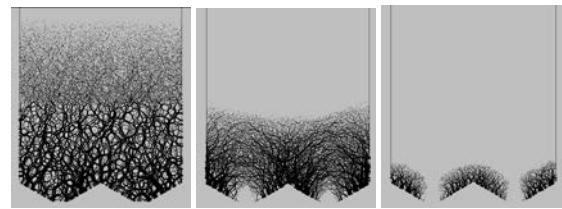


Fig. 6 Normal and shear stresses on the side wall.

The monitored normal and shear stress data can be easily analyzed to capture the qualitative trend of boundary circumstance, which is shown in Fig.6. The normal stresses in the initial stage are fluctuating dramatically and stress concentration is found at the corner of the side and bottom plates. This is induced by the instantaneous opening behavior and geometry effect. Normal stress drops very significantly in the initial stage, meanwhile, the peak stress location has also changed, which is induced by the short funnel flow pattern after 100 million numerical steps in Fig.5. Accompanied the whereabouts of red coarse sand, the normal stress variation and stress concentration location gradually change steadily. The flow pattern can't lead to a sharply variation for the shear stress, as the short funnel would just produce extra lateral compression for the boundaries dead zone, where the dynamic force is on the horizontal direction. The discrete element simulations just give some qualitative assessments for stress or other physical quantities. The flow pattern behaviors can similar be reproduced by discrete element method, which can give some visualization not possible from the model test even in the internal of each layer.



(a) Initial stage (b) 1,000,000 steps (c) 2,600,000 steps

Fig. 7 Contact force distribution of test 1.

In Fig.7, from the contact force of test 1, different contact force chains within these two sand layers can be noticed. Red sand which owns larger size generates much stronger force chains concentrated at the silo bottom and is shown in Fig. 7 (a), and its gravity transfers to the four hopper walls forming strong connections between sands and walls. On the other hand, Green sand creates much weaker force chains on the silo top, which represent more intense and sufficient contact and friction inside this layer. It can also be noted from the sequence of contact force diagram that the interaction of particles becomes stronger during the discharging process.

The circular shaped arch of distribution zone can be noticed above the caving arch near the silo openings in Fig. 7 (b). The falling velocity of sands is large within the distribution zone, while the sand draws slowly outside the arch. In the beginning of the silo flow, particles from the two sides travel the

same distance with those flow at the middle, which explains why the mass flow is formed during discharging. As sands are continuously drawn out, less contact force induces smaller stress on the silos hopper walls. Hence, the distribution zone start developing upward, so funnel flow may possibly be formed at the later stage till the end of flow.

CONCLUSIONS AND RECOMMENDATIONS

The present study in this paper has focused on nonhomogeneous granular flow behavior from both macroscopic and microscopic view points, and has revealed some interesting phenomenon for a silo flow problem with granular material. The results from the present study are particular useful for mining engineering in ore discharging.

Four sets of silos are investigated in this research. It is found that the opening spacing can significantly influence the discharge efficiency. The flow pattern and efficiency can also be influenced by the soil layerings. For close opening silos, the flow pattern is slightly changed while the efficiency of flow is not sensitive to the layerings. However, for the wide opening silos, the discharge efficiency can change by nearly 30%. Larger height ratio is also beneficial for ore recover. Depression cone can be seen in the close opening silos. Meanwhile, the dead zone in the bottom layer is unstable for relative higher top layer.

Numerical analysis can match well with the flow pattern and give some qualitative results. The porosity of the dead zone in funnel flow is larger than the mass flow. The size of opening affects the contact force in the middle of the silo, which leads to the formation of a depression cone. The nature of the internal force network is of great importance in the understanding of various properties of granular assemblies.

A good agreement between the laboratory and numerical results can be observed if suitable

microproperties are used in the analysis. It is recommended that for the further study, more in-depth numerical study needs to be carried out to capture the fundamental behavior for these interesting experimental results. Three dimensional simulations are also suggested.

ACKNOWLEDGEMENTS

The authors acknowledge the support of the postgraduate funding of the Hong Kong Polytechnic University.

REFERENCES

- [1] Janssen HA, "Getreidedruk in Silozellen", Z. Ver, Dtsch. Ing, Vol. 39, pp. 1045-1049.
- [2] Cheng YM *et al*, "Laboratory test and Particle Flow Simulation of Silos problem with non-homogeneous materials", J. of Geotechnical and Geoenvironmental Engineering, ASCE, Vol. 135, Nov. 2009, pp. 1754-1761
- [3] Cheng YM *et al*, "Flow pattern for silo with two layers of materials with single and double openings", J. of Geotechnical and Geoenvironmental Engineering, ASCE, Vol. 136, Oct. 2010, pp. 1278-1286.
- [4] Itasca Consulting Group, Inc, "Theory and Background of PFC2D". 1999
- [5] Parisi DR *et al*, "Partitioned distinct element method simulation of granular flow within industrial silos", J. of Eng. Mech., ASCE, Vol. 130, July. 2004, pp. 771-779.
- [6] Masson S and Martinez J, "Partitioned distinct element method simulation of granular flow within industrial silos", Powder Technology, Vol. 109, Apr. 2000, pp. 164-178.
- [7] Coetzee CJ and Els DNJ, "Calibration of discrete element parameters and the modeling of silo discharge and bucket filling", Computers Electronics in Agriculture, Vol. 66, Mar. 2009, pp. 198-212.

Construction Materials

IMPROVING ENGINEERING PROPERTIES OF FINE-GRAINED SOIL WITH STEEL SLAG FOR USING IN EMBANKMENT EARTHFILL

Je-Min Baek¹, Satoru Shibuya¹, Jin-Suk Hur² and Tara Nidhi Lohani³

¹Graduate school of Civil Engineering, Kobe University, Japan;

²ESCO C&E Co., Ltd., Korea; ³RCUSS, Kobe University, Japan

ABSTRACT

As part of the promotion and effective utilization of steel slag as an embankment fill material, its applicability was studied through a series of laboratory test. It was found that the steel slag, which has higher internal friction angle as compared to the normal embankment earthfill materials, has sufficient strength to be used as a fill material. When mixed with a poor natural soil containing high percentage of fines, grain-size characteristics, permeability values, compaction properties and strength properties were also significantly improved, exhibiting an excellent soil-improvement effect. The soil-slag mixture showed transitional values of physical and mechanical properties in between the steel slag and natural soil. The environmental concern is mostly alleviated by the low permeability characteristics of the soil-slag mixture. This shows that steel slag is expected to be a promising fill material for its low-cost and strong soil strength feature to be used in embankments, if proper grain-size and compaction control are done at the site.

Keywords: Soil-improvement, Steel slag, Fill material, Embankment, L-shaped geosynthetic drain

INTRODUCTION

In recent years, the disasters related to reinforced earth wall due to rainwater infiltration have been increasing. In 2004, reinforced earth wall under construction in Hyogo prefecture was collapsed due to a rapid increase in water level at its back caused by the heavy rainfall from Typhoon No.23. The prime factor behind the failure was an increase in the degree of saturation of fill material by the infiltration of stagnant water at its back and directly from the rainfall, which decreased suction value and hence, lowered the strength and stiffness of the reinforced earth embankment below the critical [1].

The significance of using locally available soil in an earthfill is quite explicable from economic reason as well as the assurance of speedy construction. However, shear strength and permeability requirement may not always be met, especially, when the local soil is a fine-grained one. In general, the cement stabilization technique is usually applied in such cases. The resulting soil acquires better strength parameters however, the low permeability might result in the water stagnation at the rear side of reinforced earth wall and therefore, becomes the candidate for failure as mentioned earlier.

In order to alleviate the damage on the reinforced embankment, it is therefore important to prevent the penetration of the rainwater inside the earthfill and also avoid the water stagnation at the rear side. References [2]-[4] suggested that the combination of the water proofing and the drainage systems inside the reinforced earth wall is quite effective for

improving its reinforcement function. This method differs from the conventional drainage system set inside the embankment in such a way that the water seeped into the reinforced wall from its back or top is smoothly lowered to the base level through L-shaped vertical geosynthetics layer inserted inside the wall. The drained water further finds its escape out of the embankment through the drainage layer installed at its base. This makes an embankment a completely a waterproof area [5].

In this research, study is done on the steel slag for its effective utilization as a fill material for embankments. The slag, although considered to have excellent strength characteristics, has a critical alkalinity concern in using as an embankment backfill material. The soil improvement effect of the slag has been examined by using a poor soil, having a lot of fines content and considered to be unsuitable for earthfill purpose, and also a soil-slag mixture. Laboratory tests were performed on the fine-grained soil, steel slag and soil-slag mixture to evaluate their physical properties, permeability, pH, compaction- and shear-strength characteristics.

CHARACTERISTICS OF THE FILL MATERIAL USED FOR THE EXPERIMENT

Table 1 shows the fundamental physical properties of the steel slag, the soil used and its mixture. The slag has relatively low water absorption rate of about 2.7% and its unit weight, $\rho_s = 3.480\text{g/cm}^3$, is quite heavy as compared to commonly available soils ($2.6\sim 2.8\text{g/cm}^3$).

Table 1 Basic physical properties of the tested soils

Name			Steel slag	Soil-slag mixture ^{*1)}	Natural soil	
Water content		w (%)	8	15	23	
Particle density		ρ_s (g/cm ³)	3.480	2.908	2.609	
Water absorption coefficient		(%)	2.7	—	—	
Void ratio ^{*2)}		e	0.468	0.474	0.655	
Degree of saturation ^{*3)}		S _r (%)	67.8	92.7	88.0	
Air porosity ^{*4)}		n _a (%)	10.3	2.4	4.8	
Grain-size characteristics	Rock	(%)	≥ 75mm	0	0	
	Gravel		2~7mm	69.0	47.9	
	Sand		0.075~2mm	27.8	43.8	
	Fines		≤ 0.07mm	3.2	8.3	
	Mean particle size		D ₅₀ (mm)	8.7	1.61	0.23
	Maximum particle size		D _{max} (mm)	37.5	37.5	26.5
	Uniformity coefficient		U _c	54.0	43.9	126.7
	Coefficient of curvature		U _c '	0.939	0.361	2.46
* 1) Steel slag : Natural soil = 4 : 6 (volume ratio)						
* 2) $e = \frac{\rho_s}{\rho_d} - 1$ * 3) $S_r = \frac{w\rho_s}{e\rho_w}$						
* 4) $n_a = 100 - \rho_d/\rho_w(100/\rho_s + w)$						

The fine-grained soil used for the test is a by-product generated at a construction site and has particle density of 2.609g/cm³. With the fines content (Fc) as high as 32.6% and containing gravel fraction as well, it can be classified as SFG from the standard soil classification system. According to the design standard of the reinforced earth [6], this type of soil is not allowed as a fill material without proper countermeasures.

In addition, soil-slag mixture was also prepared at the volume ratio of respectively, 6:4 (5:5 in terms of weight ratio) and had unit weight, $\rho_s = 2.908\text{g/cm}^3$. Figure 1 shows the grain-size distribution curves for all materials. As observed from the uniformity coefficient and coefficient of curvature values from the plot, the grain-size characteristics of the fine-grained soil is improved by steel slag addition.

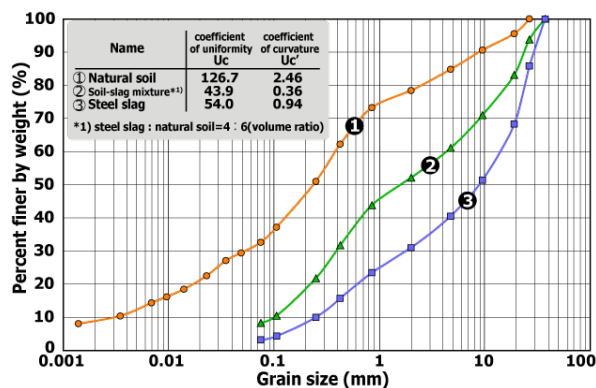


Figure 1 Grain-size distribution curves

TEST PERFORMED AND THEIR RESULTS

Soil pH Measurement

Being alkaline in nature, there is wide concern from the environmental impact point of view that the steel slag can affect the surrounding soil when it is used as an embankment earthfill. A Japanese effluent standard (water pollution prevention act of Japan) has set the allowable pH limit as 5.8~8.6 (5.0~9.0 at the sea area) [7]. However, as shown in the measured pH values for steel slag, soil-slag mixture and the soil in Table 2, strong alkalinity is

shown by the steel slag (pH = 12.9). The soil used also had a weak alkalinity (pH=10). The pH of soil-slag mixture dropped only slightly (pH = 12.7) as compared to the pure slag, probably because of this soil alkalinity. Therefore, in order to use the steel slag in the real field, some countermeasure against alkali pollution is anticipated.

Table 2 pH Measurements

Item	Volume ratio (%) Steel slag: Natural soil	pH
Soil-slag mixture	100 : 0	12.9
	40 : 60	12.7
	0 : 100	10.0

Water Permeability

The best option considered to prevent the alkali pollution of steel slag is to avoid water infiltration into the embankment. The effluent volume reduction is obviously expected. Focus was therefore, put on permeability characteristics of geomaterial.

Table 3 Permeability coefficient

Items	Material	D _c	85%	90%
Constant-head permeability test	Steel slag	k ₁₅ (m/s)	4.0×10 ⁻⁶	—
	Slag-soil mixture		2.4×10 ⁻⁶	—
Falling-head permeability test	Natural soil		—	6.84×10 ⁻⁸

Table 3 shows the result of the constant-head permeability test on slag and soil-slag mixture, and falling head permeability test on soil by using a 10cm x 12.73cm mold. In case of steel slag and soil-slag mixture, particle size above 19mm was screened out by considering mold size used in the test. The fine-grained soil used in the experiment yielded a very low permeability (10⁻⁸m/s). On the other hand, the permeability figure was also low (10⁻⁶m/s) for the slag and its mixture. This assures a very small quantity of infiltration into the earthfill and correspondingly, the effluent quantity as well. In addition, when additional safety measures in the

form of L-shaped drains [2]-[4] are adopted, infiltrating water never pass into the fill body and environmental concern is completely alleviated.

Soil Compaction

Figure 2 shows the compaction curve of each soil type performed according to JIS A1210. The compaction of steel slag and soil-slag mixture was done according to the B-c method (mold diameter 15cm, height 12.50cm, no soil reuse). On the other hand, the fine-grained soil was compacted by A-c method (mold diameter 10cm, height 12.73cm, no soil reuse). As apparently observed by comparing with the result of fine-grained soil, the increase in maximum dry density and lowering of the optimum moisture content was quite conspicuous by steel slag addition. This result is similar to the compaction characteristics of the ordinary soil when mixed with the sandy soil or gravelly soil. In other words, there is an improvement in compaction characteristics by mixing the heavy particle weight steel slag mass.

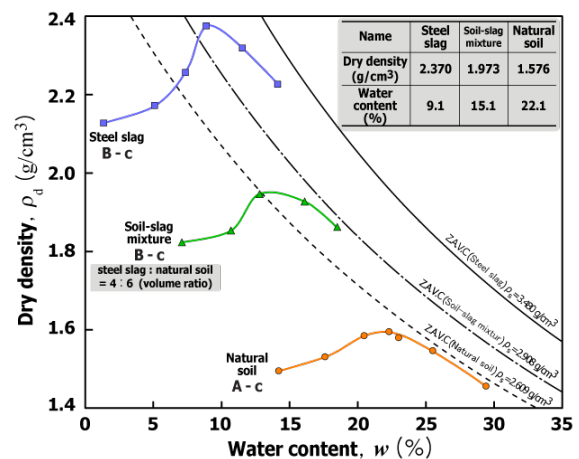


Figure 2 Compaction curve for three different soil types used in the test

Strength Characteristics

Table 4 Test conditions for triaxial compression test

Item	Volume ratio (%) Slag : Soil	Degree of compaction D _c (%)	Confining pressure σ' (kPa)	Shear strain rate (%/min)
Soil-slag mixture	100 : 0	CD Test	85	50 100 200
	40 : 60			

	0 : 100		90		
--	------------	--	----	--	--

The shear strength characteristics were examined by the triaxial compression test. Specimens of 10cm diameter and 20cm height were prepared by considering the maximum grain size of steel slag. Table 4 shows the test condition.

Mohr's circle of stress at failure is plotted in Figure 3. The angle of internal friction, ϕ_d of the soil-slag mixture ($\phi_d=37.4^\circ$) lies nearly at midway between steel slag ($\phi_d=44.1^\circ$) and the fine-grained soil ($\phi_d=29.7^\circ$). It is thus well understood that slag mixing has improved the shear strength properties of the fine-grained soil and resulted mix has enough strength to satisfy the criteria of an embankment fill material [8].

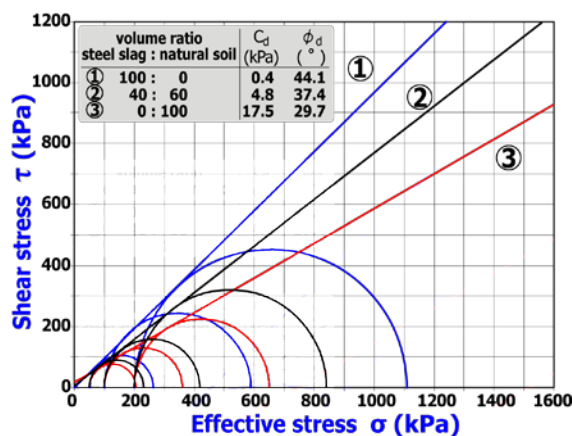


Figure 3 Results of triaxial compression test

CONCLUSION

The applicability of steel slag as a fill material for embankments was examined through a series of laboratory test. It was found that the steel slag, which is quite heavy and has higher internal friction angle as compared to the normal embankment earthfill materials, has sufficient strength to be used as a fill material.

When mixed with natural soil, grain-size characteristics, permeability values, compaction properties and strength properties were significantly improved, exhibiting excellent soil-improvement effects. The soil-slag mixture showed intermediate values of physical and mechanical properties between the steel slag and natural soil. Although, the exact values obtained in the tests could be associated to its soil-slag weight ratio of 5:5, there is a quite clear tendency that the physical properties of the composite material can be easily controlled.

Summarizing the above outcomes, steel slag is expected to be a promising embankment fill material because of its low-cost and strong soil strength features by preparing its composite with the locally available soils. The environmental concern is mostly alleviated by the low permeability characteristics of the soil-slag mixture. In addition, the impervious surface layers, such as asphaltic layers in road embankments and improved drainage system, such as L-shaped drainage system as discussed in previous sections, can keep the water out of the fill and any environmental impact to the surrounding soil could be reduced to almost zero level.

REFERENCES

- [1] Shibuya S, Kawaguchi T, Chae J-G, "Failure of Reinforced Earth wall as attacked by Typhoon No. 23 in 2004", Soils and Foundations, 2007, Vol.46, No.2, pp. 153-160
- [2] Shibuya S, Saito M, Hara K, Mitsui J, "Proposal of L-shaped geodrain for preventing seepage flow into embankment using Geosynthetics", 43th Japan National Conference on Geotechnical Engineering, July 2008, pp. 1539-1540.
- [3] Hara K, Saito M, Mitsui J, Shibuya S, "Model test and numerical simulation for L-shaped geodrain for preventing seepage flow into embankment using Geosynthetics", 43th Japan National Conference on Geotechnical Engineering, July 2008, pp. 1541-1542.
- [4] Hara K, Shibuya S, Saito M, Torii N, Chae J-G, Masuo T, "Watertight embankment using L-shaped geosynthetic drain - Full-scale test and numerical simulation", Geosynthetics Engineering Journal, Vol. 23, Japan Chapter of International Geosynthetics Society, 2008, pp. 147-154.
- [5] Shibuya S, "Embankment failure: mechanical process & remedy", Geosynthetics Engineering Journal, Vol. 23, Japan Chapter of International Geosynthetics Society, 2008, pp. 1-14.
- [6] Public Works Research Center, "Design and Construction Manual of Reinforced Soil (Terre Armee) Wall Construction Method (in Japanese) [3rd Edition]", Nov. 2003.
- [7] Ministry of Land, Infrastructure, Transport and Tourism, MLIT: <http://www.mlit.go.jp/>, Considerations about pH and bad smells, Reference 1-6-9 (in Japanese).
- [8] East, Central, West Nippon Expressway Company Limited, "Primary collection of design guidelines", July 2009.

EVALUATION EQUATION OF DIFFUSION COEFFICIENT OF CHLORIDE ION FOR CRACKED CONCRETE

Junpei SAITO¹ and Satoru SHIMOBÉ²

^{1,2}College of Science and Technology, Nihon University, Japan

ABSTRACT

The first author has built a evaluation equation (proposed equation) of diffusion coefficient of chloride ion in which the limit on the range of application has been expanded to include various crack conditions and various reinforced concrete members, by using crack area ratio (the ratio of crack area to concrete area) in the equation as the JSCE STANDARD "design" and by decreasing the constant which represents the effect of cracks according to the depth of cracks.

However, the concrete area should be appropriately defined in the equation, in order for chloride ion penetration properties calculated by the equation proposed based on the experiment results, to be assessed with appropriate accuracy on existing reinforced concrete structures with cracks.

Therefore, this study investigates appropriate concrete area set value in the proposed equation, based on the rate of chloride ion penetration from cracks into the core in a vertical direction which was obtained through the back analysis of the results of electrical migration test conducted by the first author.

Keywords: Cracked Concrete, Chloride Ion Penetration, Evaluation Equation, Diffusion Coefficient, Concrete Area

INTRODUCTION

In order to plan for the proper extension of the life of deteriorated reinforced concrete structures, appropriate diagnosis and repair is required. Out of the various factors that influence the deterioration of concrete in Japan, the effect of the airborne salt in the coastal areas, as well as the chloride ions present in snow melting agents in the mountainous and the colder regions create an environment where reinforced concrete structures are susceptible to deterioration due to salt attack. In addition, once cracks appear in reinforced concrete structures in such environments, the penetration of salt is encouraged, resulting in the structures becoming more susceptible to early deterioration. In this situation, it is therefore especially necessary to have appropriate maintenance plans, as well as future predictions based on the deterioration and diagnosis in place.

The first author has investigated the Evaluation Equation (JSCE Equation) of diffusion coefficient for chloride concentration at the location of reinforcement which is used in the examination of chloride attack. The JSCE Equation is indicated in STANDARD SPECIFICATIONS FOR CONCRETE STRUCTURES "Design" by Japan Society of Civil Engineers[1]. The author's electrical migration tests were carried out using specimens modeled concrete cover with various types of cracks in order to evaluate chloride ion penetration on reinforced concrete structures with diversified types of cracks[2]. In the results, the first author has

built to evaluate equation (proposed equation) of diffusion coefficient of chloride ion. In the proposed equation, the limit on the range of application has been expanded to include various crack conditions and various reinforced concrete members. For the expansion of limit of JSCE Equation, the first author has used the crack area ratio (the ratio of crack area to concrete area) and the decreasing of the constant which represents the effect of cracks according to the depth of cracks for the proposed equation [3][4].

However, the concrete area should be appropriately defined in the equation, in order for chloride ion penetration properties calculated by the equation proposed based on the experiment results, to be assessed with appropriate accuracy on existing reinforced concrete structures with cracks.

Therefore, this study investigates appropriate concrete area set value in the proposed equation, based on the rate of chloride ion penetration from cracks into the core in a vertical direction which was obtained through the back analysis of the results of electrical migration test conducted by the first author.

EXPANSION OF APPLICABILITY CONDITIONS IN JSCE EQUATION

Test Method

Using a cracked concrete model as a specimen, effective diffusion coefficients were calculated with experimental equipment complied with the electrical migration test method (JSCE-G571) [5] (Fig.1).

The specimens were modeled as a cube with a concrete cover set at 40mm. Crack conditions used were crack width, crack depth, and crack number; the specimens were cracked according to the conditions set (Table 1). Figure 2(a) shows a standard specimen. Figure 2(b) shows a specimen modeled to examine a condition of irregularity cracks spreading over concrete.

Three types of crack widths were set, 0.1, 0.2, and 0.4mm, considered the limit value of crack width(0.2mm) and set the near values. For crack depths, they were set at 40mm when cracks were assumed to pass through reinforcing steel (pass through crack); depths were set 1/4(10mm), 1/2(20mm), or 3/4(30mm) of the concrete cover when cracks were assumed not to pass through reinforcing steel (not pass through crack). Another specimen without cracks was prepared at the same time.

There were two types of specimen concrete mix, with a water-cement ratio (W/C) of 45% and 55%, and the volume ratio of fine aggregate and cement (S/C) was 400vol%. As for material characteristics, compressive strength was 39.5N/mm² at W/C 45% and 36.3N/mm² at W/C 55%. Ordinary Portland cement was used and pit sand (passed through a 2.5 mm sieve) was used as a fine aggregate.

Experimental Results and Proposed Equation

Figure 3 shows the relationship between effective diffusion coefficient considering a cracking effect (D_{cr}) and crack area ratio (A/A_{cr}). Regression coefficient of linear approximation was put down together. Regression coefficients were 200-270cm²/year for pass through cracks, and 100-150cm²/year for not pass through cracks, with

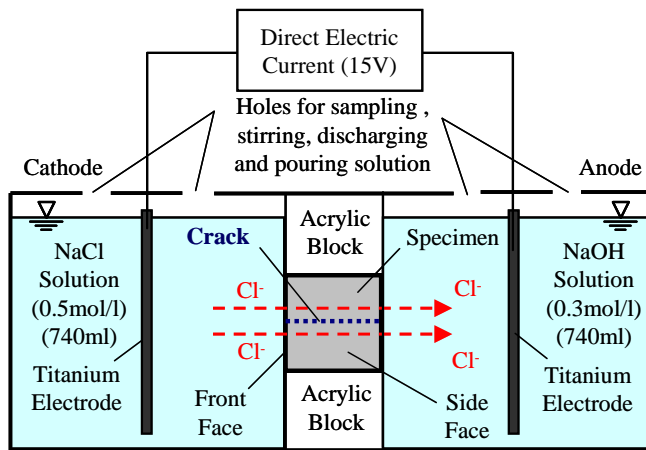


Fig.1. Schematic view of migration cell and experimental set-up

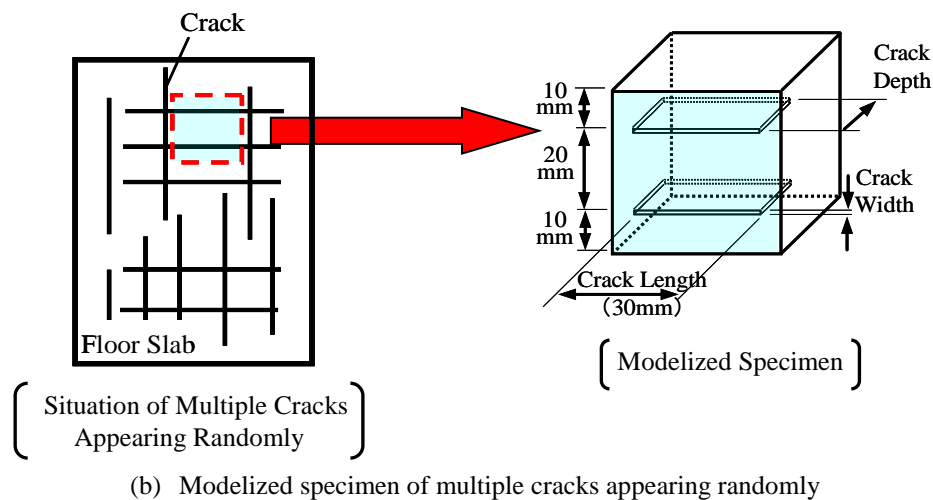
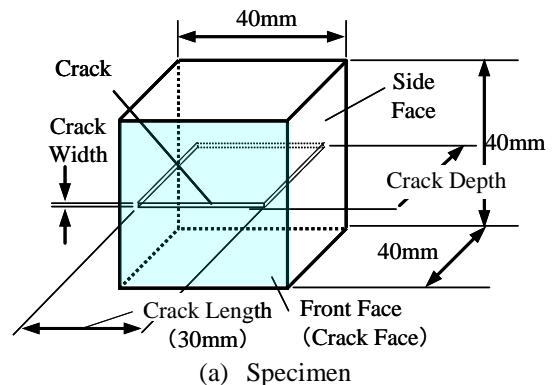


Fig.2 Shape of specimens

approximately a half of it for pass through cracks.

Figure 4 shows the relationship between the mean of the regression coefficient (same meaning as a constant D_0 which represents a cracking effect on transport of chloride ions in concrete) and crack depth in crack area ratio where there was a large number of data items. It shows a line shape; regression coefficients for not pass through cracks became a value that regression coefficient for pass through cracks was proportionally reduced depending on crack depth.

From the above, in the calculation of effective diffusion coefficient considering the cracking effect, pass through cracks can be considered as a product of crack area ratio and regression coefficient. For effective diffusion coefficient for not pass through cracks, the regression coefficient for pass through cracks should be reduced depending on crack depth. In addition, D_0 in JSCE Equation ($=200\text{cm}^2/\text{year}$) seems to be able to be used for the regression coefficient for pass through cracks. Equation (1) is a proposed equation where limits of crack conditions and members of the JSCE Equation were expanded.

$$D_{cr} = \frac{A_{cr}}{A} D_0 \quad (1)$$

In this equation, D_{cr} is the diffusion coefficient considering cracking effect, A_{cr} is the Crack Area, A is the Concrete Area (A_{cr}/A is the Crack Area Ratio) and D_0 is the constant to represent the effect of cracks on transport of chloride ion ($=200\text{cm}^2/\text{year}$).

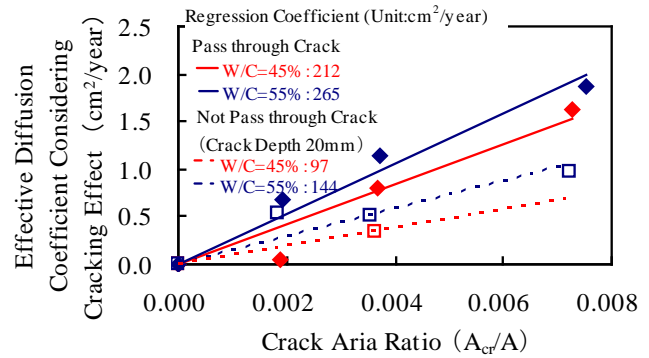
Problem of Proposed Equation

For applying the proposed equation to existing concrete structures, the issue was accompanied with the difference in concrete areas of specimens and existing concrete structures. As shown in Fig.5, concrete areas of existing concrete structures are larger than that of the specimens, and there may be a difference in chloride ions in areas near and apart from cracks into the core in a vertical direction. However, ion distribution in crack spacing is averaged in the proposed equation; chloride ion penetration characteristics are evaluated as in danger on high chloride ion areas near cracks, and as safe on low chloride ion areas apart from cracks. It may mislead the evaluation of chloride ions as it is.

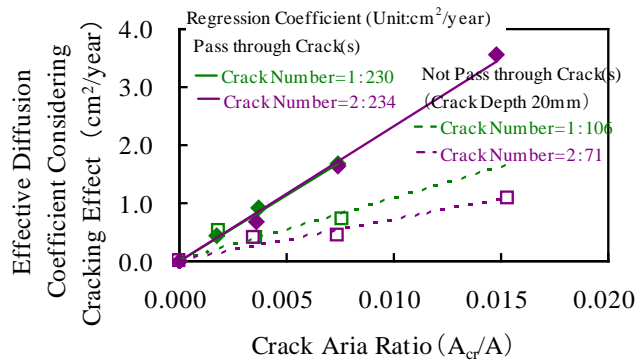
INVESTIGATION TO APPLY THE PROPOSED EQUATION TO EXISTING STRUCTURES

Table 1 Specimens condition

Specimens Condition	Value
W/C (%)	45, 55
Crack Width (mm)	0.1, 0.2, 0.4
Crack Depth (mm)	10, 20, 30, 40
Crack Length (mm)	30
Crack Number	1, 2



(a) W/C=45%,55%



(b) Crack Number=1,2

Fig.3 Relationship between D_{cr} and crack area ratio

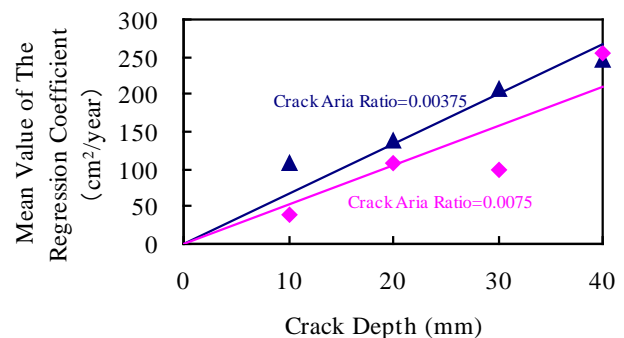


Fig.4 Relationship between D_0 and crack depth

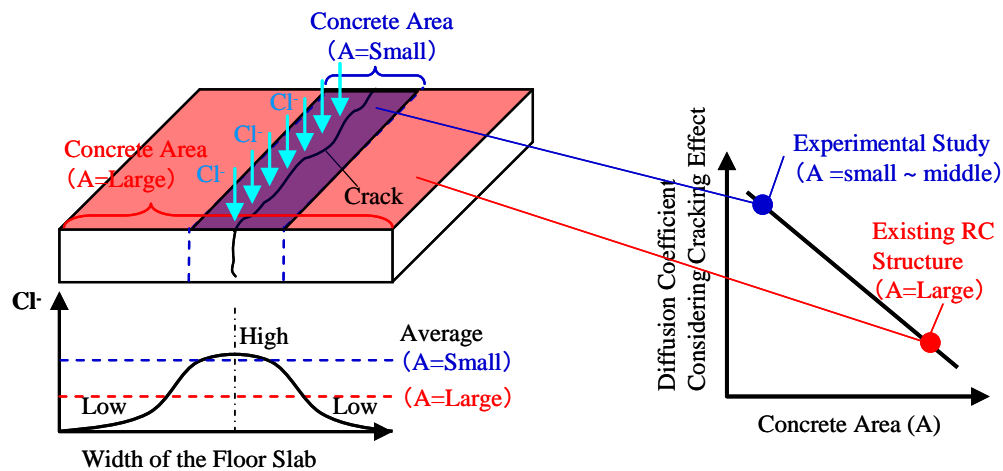


Fig.5 The mean value of the chloride ion in cracked concrete

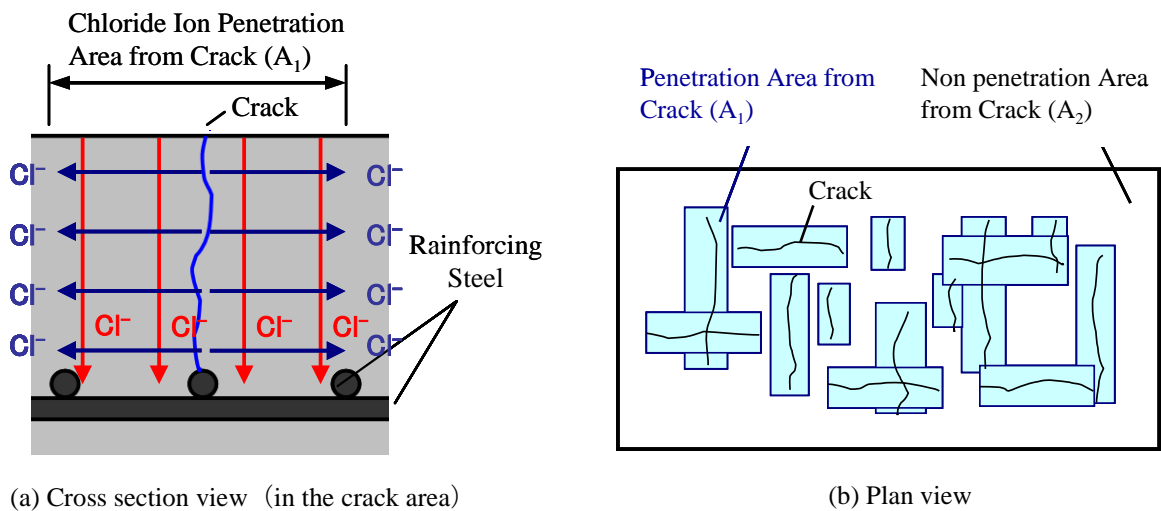


Fig.6 Penetration area from crack

Contents for Investigation

For applying the proposed equation to existing concrete structures, this study suggests a method determining minimum and maximum areas affected by chloride ion penetration from the cracks (penetration area) and using the value of the concrete area to the equation depending on the penetration area to solve the issue coming from the difference in concrete areas. Penetration areas from the cracks were classified as shown in Fig.6; the area where chloride ions penetrate from cracks into the core in a vertical direction in the period chloride ions penetrating from concrete surface to a reinforcing steel in concrete (A_1), and the area out of A_1 areas (A_2). Appropriate setting of the area is important; the area was examined with a back analysis based on experimental results.

Back Analysis Outline

Values for the back analysis were the values obtained in this experiment. Experimental result D_{cr} , various crack conditions (converted to crack area ratio) and D_0 were used to calculate penetration area A via the back analysis. Two kinds of constant D_0 which represents the crack effect on transport of chloride ions in concrete were used for calculation; $200\text{cm}^2/\text{year}$ used in the JSCE Equation and $400\text{cm}^2/\text{year}$ (the diffusion coefficient for chloride ions in water) used in the Kagaku Binran by the Japan Chemical Society (JCS) [6]. For not pass through cracks, D_0 is adjusted by crack depth (Table 2).

The amount of chloride ion supplied to cracks can be considered correlating to crack area A_{cr} . When the constant D_0 which represents the crack effect on transport of chloride ions in concrete is assumed to be fixed, supplied chloride ions are

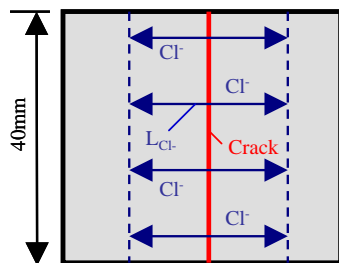
correlated to a product of A_{cr} and D_0 . In contrast, chloride ions supplied to cracks penetrate from cracks into concrete, as shown in Eq.(1), it becomes equivalent to a product of penetration speed (effective diffusion coefficient considering the cracking effect D_{cr}) and penetration area A . That can be said, when the relationship holds, the diffusion coefficient considering the cracking effect D_{cr} becomes larger correlating to the amount of supplied chloride ions because D_{cr} in this experiment was calculated with the constant penetration area (specimen area A). Using Eq.(2) with diffusion coefficient considering the cracking effect D_{cr} , the calculated penetration area A is considered that it theoretically becomes almost the same on specimens with different cracking conditions. The calculated value represents the penetration area.

$$A = \frac{D_o \cdot A_{cr}}{D_{cr}} \quad (2)$$

In this equation, A is the Penetration Area, A_{cr} is the Crack Area, D_0 is the constant to represent the effect of cracks on transport of chloride ion and D_{cr} is the diffusion coefficient considering cracking effect.

Back Analysis Results

Figure 7 shows the relationship between penetration lengths of chloride ion from cracks in a vertical direction L_{Cl^-} and the ratio of penetration area when chloride ions penetrate from the concrete surface to the reinforcing steel. Results from existing studies in Fig.7, the relationship between the chloride ions in cracked concrete and that in non-cracked concrete, and appropriate crack width, were converted values to make them comparable to the values from this experiment using the size of the specimens in this experiment.



Schematic View of L_{Cl^-}

Length of Chloride Ion Penetration from Cracks into the Concrete in a Vertical Direction L_{Cl^-} (mm)

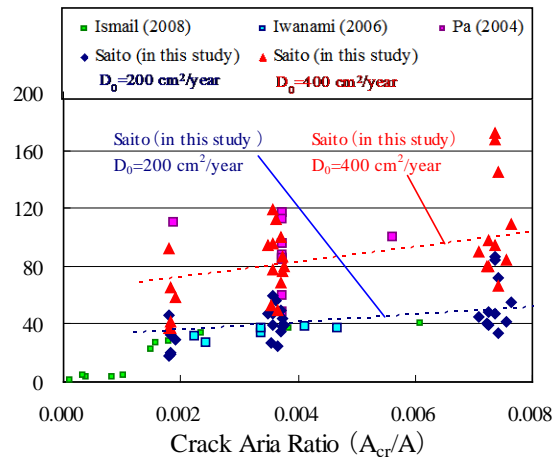


Fig.7 Relationship between L_{Cl^-} and crack area ratio

Table 2 D_0 for back analysis

Crack Depth		Constant to Represent the Effect of Cracks on Transport of Chloride Ion in Concrete	
		$D_0=200 \text{ cm}^2/\text{year}$	$D_0=400 \text{ cm}^2/\text{year}$
		Standard Specifications for Concrete Structures- 2007, Design by JSCE [5]	Kagaku Binran by JCS [6]
Pass Through Crack	Cover	200 ($=D_0$)	400 ($=D_0$)
Not Pass Through Crack	Cover \times 3/4	150 ($=D_0 \times 3/4$)	300 ($=D_0 \times 3/4$)
	Cover \times 1/2	100 ($=D_0 \times 1/2$)	200 ($=D_0 \times 1/2$)
	Cover \times 1/4	50 ($=D_0 \times 1/4$)	100 ($=D_0 \times 1/4$)
No Crack		0	0

In the case of D_0 set at $200 \text{ cm}^2/\text{year}$, L_{Cl^-} was 40mm. This is the same length as the penetration area from the concrete surface (concrete cover). Moreover, when the crack area ratios in this experiment and the existing experiment were the same, the mean of the results in this experiment were a comparable level to the existing experiment such as Ismail et al. [7] and Iwanami et al. [8]. By contrast, in the case of D_0 set at $400 \text{ cm}^2/\text{year}$, L_{Cl^-} was approximately twice the length between the surface and the reinforcing steel, and showed a close value to that in Pa et al. [9].

From the examination above, the concrete area should be used at a smaller set value to take a computationally safe value; it is considered appropriate that a product of concrete cover and crack length obtained in back analysis (in the case of

D_0 set at $200\text{cm}^2/\text{year}$ is equal to the penetration area. The proposed equation becomes more suitable for the application to existing concrete structures by setting an appropriate concrete area to Eq.(1) according to the classification of the area.

CONCLUSIONS

Obtained results in this study are summarized as follows.

- 1) Using a crack area ratio and considering proportionally reduced D_0 for pass through cracks depending on crack depth expand the application conditions for the JSCE Equation.
- 2) It is reasonable to set penetration area as a product of concrete cover and crack length. The proposed equation becomes more suitable by applying appropriate concrete area to the JSCE Equation according to the classification of the area.

ACKNOWLEDGEMENT

This work was supported by JSPS KAKENHI Grant Number 23760430.

REFERENCES

- [1] JSCE Concrete Committee., "STANDARD SPECIFICATIONS for CONCRETE STRUCTURES -2007 "design", JAPAN SOCIETY of CIVIL ENGINEERS(JSCE), 2007, pp.119-122 (in Japanese)
- [2] Saito J., "Experimental Study on the Chloride Permeability of Plate Concrete with Cracks", Journal of Research Institute of Science and Technology College of Science and Technology Nihon University, No.127, 2012, pp.1-10 (in Japanese).
- [3] Saito J., "Experimental Study on Evaluation of Chloride Permeability of Plate Concrete with Multiple Cracks", Proceedings of the Japan Concrete Institute, Vol.34, No.1, 2012, pp.790-795 (in Japanese).
- [4] Saito J. and Simobe S., "Experimental Study on Chloride Ion Penetration in Damaged Concrete under External Force Using Electrical Migration Test Method", Proceedings of the Japan Concrete Institute, Vol.35, No.1, 2013, pp.823-828 (in Japanese).
- [5] JSCE Concrete Committee., "STANDARD SPECIFICATIONS for CONCRETE STRUCTURES -2007 Test Methods and Specifications -JSCE STANDARD-, JAPAN SOCIETY of CIVIL ENGINEERS(JSCE), 2007, pp.277-284 (in Japanese).
- [6] The Japan Chemical Society (JCS)., "kagakubinran kisohen Part2, 2004 (in Japanese).
- [7] Ismail M., Toumi A., Francois R and Gagne R., "Effect of Crack Opening on the Local Diffusion of Chloride in Cracked Mortar Samples", Cement and Concrete Research, Vol.38, 2008, pp.1106-1111.
- [8] Iwanami M., Yokota H. and Nick R B., "Experimental Study on Chloride Transport in Cracked Concrete", Proceedings of the Japan Concrete Institute, Vol.28, No.1, 2006, pp.917-922 (in Japanese).
- [9] Pa P W., Watanabe M. and Machida A., "Penetration Profile of Chloride Ion in Cracked Reinforced Concrete", Cement and Concrete Research, Vol.34, 2004, pp.1073-1079.

OPTIMIZATION OF EFFECTIVE DEPTH OF COMPACTION FOR FINE-GRAINED SOILS

Girum Y. Yesuf¹, Inge Hoff² and Jan Vaslestad³

^{1,2}Faculty of Engineering Science and Technology, Norwegian University of Science and Technology, Norway; ³ Norwegian Public Roads Administration, Norway

ABSTRACT

Soil compaction is an important phase during construction of roads. Its primary aim is to reduce the void ratio, in order to improve the strength of the soil. In this way, a good bearing capacity of pavement foundation is obtained. Consequently, long term deformation in the pavement layers can be substantially reduced. In this paper, a finite element method is used to study the rolling compaction of fine-grained soils. Since compaction is associated with volumetric plastic deformations, the modified Drucker-Prager Cap model, available in Abaqus FEA is used for numerical simulation. The soil-structure interaction of a rolling rigid body over a compressible soil mass is defined using Abaqus/Explicit. The weight of the roller, or the contact pressure, is directly related to the effective compaction depth and density of the soil. The evaluation of these factors has been optimized using the strength characteristics of soils, namely the cohesion and friction angle.

Keywords: Cap model, Compaction, Density, Optimization

INTRODUCTION

Pavement layers are compacted during road construction to maintain the long-term performance of roads. Insufficient compaction leads to distress in pavements such as premature pavement rutting, longitudinal unevenness and cracking. Hence, compaction of bound and unbound materials in roads is highly desired. The increase of vehicles with heavier axle loads demands a good subgrade support. A good bearing capacity of subgrade soils is often obtained by increasing the strength by means of compaction. Compaction increases also the stiffness of the pavement layers so that future settlements due to the traffic loads can be greatly reduced. To a lesser extent, the reduced permeability of soils may prevent undesirable frost heave problems. The common factors that control the extent of compaction are the compaction effort, the type of soil and its gradation, and the water content [1].

In the study presented in this paper, we mainly discuss on the effect of the compaction energy and the strength characteristics of soils for possible optimization techniques by using a Finite Element Method (FEM). The scope of modeling is limited to static roller compaction which is often applied to the fine-grained soils. Since the compaction process is highly dependent on the moisture content, the numerical modeling is more suitable for studying the soil-roller interaction. Moreover, the influence of moisture content in subgrade soils can be related to geotechnical soil parameters such as cohesion and

friction angle. These parameters are not the inherent properties of soil; rather they describe the “condition” of the soil. For soils, the highest strength is frequently obtained by using greater compactive efforts with water contents somewhat below the optimum moisture content. Large scale tests [2] have shown that the confined compressive strength of clayey sand could be doubled by compaction, within the range of practical field compaction procedures.

Rollers with static load drums use the effective dead weight of the machine to apply pressure on the surface. Adequate compaction with static rollers is normally achieved only in the upper layers of the material because the effective depth of static compaction is limited [3]. In some cases, considerable compaction can also be obtained by proper routing of hauling equipment during construction [2]. Although the specifications of these compacting machines are different, the degree of compaction is highly dependent on the static weight of the roller. Road agencies provide regulations on the static load that must be used during compaction and the number of roller passes [4]. In this way, the quality of compaction is ensured or field tests are conducted to evaluate the degree of compaction.

With the advent of high computer speed and availability of advanced finite element modeling tools, the science of terra-mechanics is gaining popularity in the recent years for optimization of soil-structure problems [5]-[7]. Besides, appropriate soil models should be chosen for the specific practical problems. In this paper, the theoretical

formulations of the model used in our analysis is presented from literature [8],[9]. In the conventional elastoplastic soil models, such as the standard Drucker-Prager and Mohr-Coulomb models, the application of compressive hydrostatic pressure alone does not cause plastic flow. Plastic flow under compressive hydrostatic pressure may only be triggered with the superposition of shear stresses. When plastic compaction is relevant the standard Drucker-Prager or Mohr-Coulomb plasticity models are not able to capture the actual material behavior [10]. Instead, the Drucker-Prager Cap model is used for soil compaction.

The analysis presented in this paper is based on the assumption of monotonic loading conditions of static rollers during soil compaction. If the dynamic effect of the roller (i.e. rolling speed, vibration frequency) is to be evaluated, advanced rate-dependent models such as the hypoplastic model formulation must be considered for realistic simulation of the compaction process [11],[12]. Another important aspect of numerical simulation of soil compaction is the geometric and boundary modeling techniques. Such issues are addressed in this paper mainly based on the user manual of the FEM tool used for the numerical simulation [8].

FEM MODELLING

Finite element analysis has been widely used for modeling non-linear soil-structure interaction problems in recent years. The numerical simulation of soil-structure interaction needs the contact boundary conditions to be properly defined. In this study, the finite element program Abaqus FEA has been used for modeling of the roller compaction. The numerical simulations presented in this paper are carried out using Abaqus/Explicit. The explicit scheme provides stable solutions for contact problems, in contrast to the implicit scheme. In the longitudinal direction (direction of rolling), small elements are used to ensure a smooth interaction between the roller surface and the soil.

The objective of the FEM, in this study, is to obtain a relationship between the weight of the roller and the volumetric plastic strains (change in density). It is assumed that the change in density is due to the plastic deformations which do not reach a large deformation limit. The principle is more suitable for surface compaction of wet fine-grained soils in thin layer applications. When large deformation is encountered during compaction, objective stress rates must be considered in the numerical scheme [8]. This is not the scope of this paper.

The three-dimensional model that is used in this study is shown in Fig. 1. It consists of two distinct bodies: a soil bed and a rigid rotating roller.

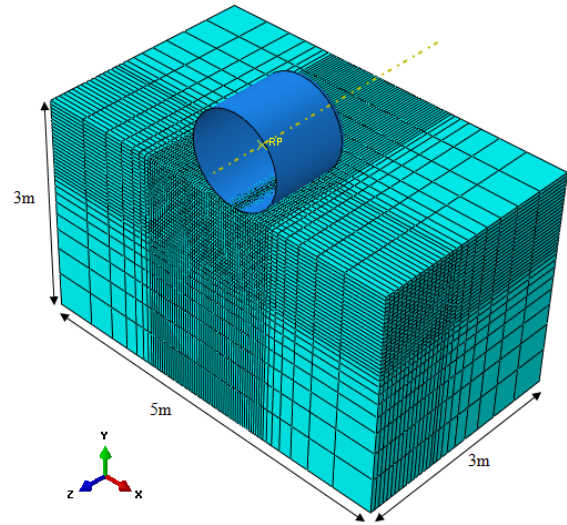


Fig. 1 Geometric model of the soil and roller.

Because of symmetry, only one-half of the geometry is modeled. To ensure the dynamic analysis with a very small inertial effect, a small mass (i.e. 100kg) is assigned for the roller. A point load, equivalent to the weight of the roller) is applied at the center of mass at the reference point. In the numerical model, the motion of the rigid body is controlled by the boundary and loading conditions applied at the reference point.

The Soil Model

The soil is modeled using the modified Drucker-Prager Cap model incorporated in Abaqus FEA. The Drucker-Prager constitutive model for pressure sensitive geo-materials was formulated in the 1950ies [9]. Though the original model is able to simulate a varying yield surface depending on the level of the mean stress, it cannot predict plastic volumetric strain or compaction of soil materials during hydrostatic loading. To alleviate this problem, the model was later modified with a convex end cap [13]. The Cap model provides a plastic hardening mechanism to account for plastic compaction and helps to control volume dilatancy when the material yields in shear. The generalized Drucker-Prager yield criterion is shown in Eq. (1) [8].

$$F_s = t - p \tan \beta - d \quad (1)$$

Where β and d represent the angle of friction and the cohesion of the soil respectively. The deviatoric stress measure t is defined in Eq. (2).

$$t = \frac{1}{2} q \left[1 + \frac{1}{K} - \left(1 - \frac{1}{K} \right) \left(\frac{r}{q} \right)^3 \right] \quad (2)$$

Where $p = -\frac{1}{3} \text{trace } \sigma$

$$q = \left(\frac{3}{2} \sigma^{dev} : \sigma^{dev} \right)^{1/2}$$

$$r = \left(\frac{9}{2} \sigma^{dev} : \sigma^{dev} : \sigma^{dev} \right)^{1/3}$$

σ and σ^{dev} are the stress and its deviatoric component. K is the ratio of the yield stress in triaxial tension to the yield stress in triaxial compression. It can be understood from Eq. (2) that the value of K controls the shape of the yield surface.

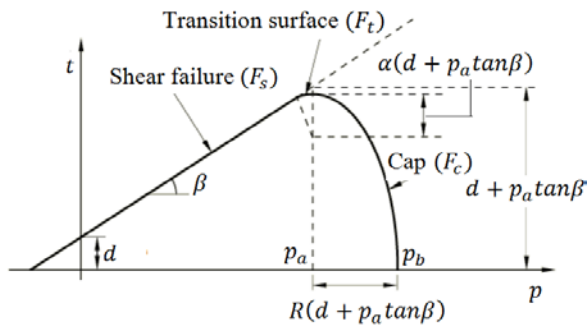


Fig. 2 Density dependent Drucker-Prager Cap model(2D representation) [5].

The cap yield surface includes dependence on the third stress invariant. The cap surface hardens or softens as a function of the volumetric plastic strain. The detail description of the shear failure surface (F_s) and transition surface (F_t) and the Cap surface (F_c) shown in Fig. 2 is available in [8]. The hardening or softening law is a user defined piecewise linear function relating the hydrostatic compression yield stress (p_b) and the corresponding volumetric plastic strain (ε_{vol}^p). The current density (ρ) in reference to initial density (ρ_0) can be obtained from the relation with ε_{vol}^p , as shown in Eqn. (3) and the cap surface as a function of density is presented in Fig. 3.

$$\varepsilon_{vol}^p = \ln \left(\frac{\rho}{\rho_0} \right) \quad (3)$$

The value of $d, \beta, R, \varepsilon_{vol,0}^p, \alpha$ and K are used to define the shape of the yield surface. The elastic behavior of the soil is defined by its Young's modulus and the Poisson's ratio, and is combined with the Modified Drucker-Prager Cap model to model the overall soil behavior during compaction. For triaxial loading condition, the material cohesion (d) and friction angle (β) are obtained from the Mohr-Coulomb parameters, cohesion (c) and

friction angle (ϕ) as shown in Eqs. (4) and (5) for the points where the Drucker-Prager yield surface coincides with the Mohr-Coulomb in triaxial compression.

$$\tan \beta = \frac{6 * \sin \phi}{3 - \sin \phi} \quad (4)$$

$$d = \frac{6 * c * \cos \phi}{3 - \sin \phi} \quad (5)$$

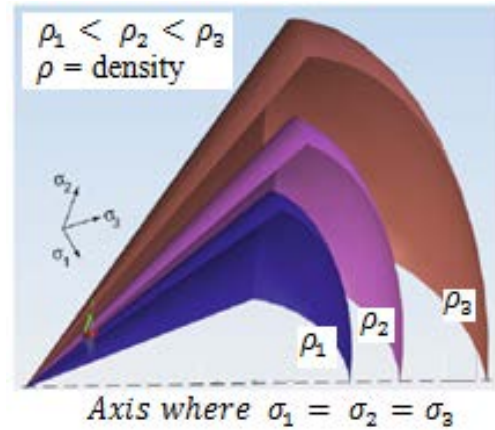


Fig. 3 Density dependent Drucker-Prager Cap model (3D view) [14].

Table 1 Input parameters for the Cap model.

Parameters	Unit	Value
Cap eccentricity parameter, R	[-]	0.2
Initial Cap yield surface position, $\varepsilon_{vol,0}^p$	[-]	0
Transition surface radius parameter, α	[-]	0.01
Flow stress ratio, K	[-]	1.0
Density(initial), ρ_0	[kg / m ³]	1600

The Cap hardening parameters are determined, based on the ratio of compression index (λ) to swelling index (κ) ($\lambda/\kappa = 10$), where $\lambda = 0.2$ is considered. For the initial yield stress level, 60kPa is assumed. The elements selected for the soil were "C3D8R", a 3-dimensional, 8-node with reduced integration, solid elements. This element supports the three translation degrees of freedom in the x , y and z directions.

Roller

A roller with a diameter of 1.2m is used. For low rolling speed, the rotary inertia of the roller is not

considered in the model. The roller is simulated using analytical rigid shell. Analytical rigid surface is chosen for both accuracy and computational performance since analytical surfaces are not discretized into finite elements [8]. A cylindrical shell with edge fillet of radius 0.07m is used to avoid numerical problems arising in the algorithm used to model contact surface between the roller and the soil.

Roller-Soil Interaction

The analytical surface of the roller is constrained to the reference point. An angular velocity of 1.85 rad/sec is applied on the reference point. Since the soil model used in this study is rate-independent, the rolling speed has no influence on the compaction process. The roller is modeled as an analytical rigid body and it is non-deformable in the analysis. A surface-to-surface contact is chosen and a penalty contact method is used in Abaqus/Explicit.

Two surfaces are defined to connect the roller surface. The friction coefficient between the roller and the soil surface is roughly approximated from the friction angle of the soil, i.e. $f = \tan(\phi)$. To be more realistic, a slightly lower value of friction coefficient than the one computed from the friction angle is used. This is to account for the fact that rolling friction is lower than sliding or static friction. For $\phi < 15^\circ$, a friction coefficient of 0.3 is considered to ensure rolling of the roller on the soil surface.

FEM RESULTS AND DISCUSSIONS

Figure 4 shows the result from a single roller pass. The density at the instance of roller loading is computed from the total volume change i.e. both the elastic and plastic volume change in the soil. After the roller is passed, the density is computed only from the plastic volume change. The elastic volumetric change recovers during unloading. The density profile for different weight of rollers is presented in Fig. 5. The relative density (RD) in this context is the density normalized by the maximum density. The stiffness of the soil in the analysis is 50MPa and the Mohr-Coulomb parameters are $c = 40\text{kPa}$ and $\phi = 20^\circ$. It is evident that the effective compaction depth increases as the weight of the roller increases.

Lift Height

During compaction of fine grained soils, the number of passes needed to achieve the desired compaction depends on the lift thickness, the contact pressure and soil moisture content. So, the depth of the soil layer (lift height) is an important factor that

affects compaction cost and machine performance. In addition, the interaction between the soil and the roller affects the compaction efficiency.

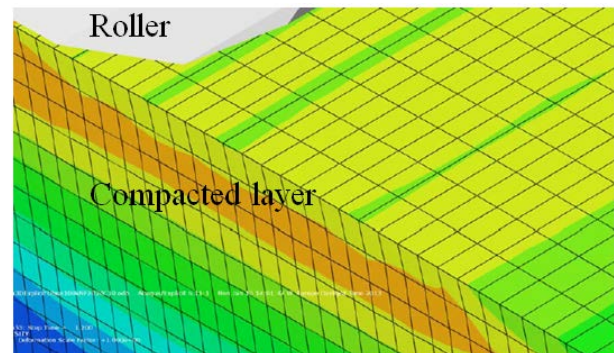


Fig. 4 View of the compaction profile.

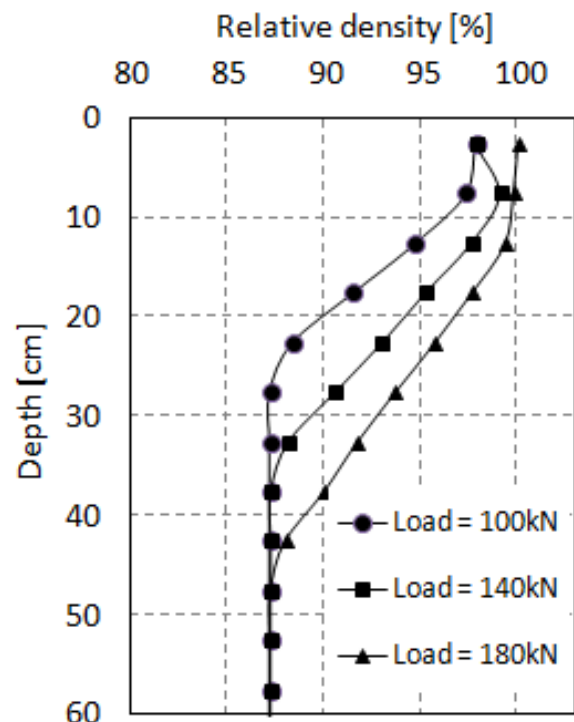


Fig. 5 Compaction density profile for different weight of roller.

Different road agencies have their own specification for the lift height. When different compacting equipment is available in the field, economical compacting effort can be carried out by proper planning. Figure 6 shows the principle of optimization techniques of the lift height for the minimum allowable relative density. The effect of friction angle on effective compaction depth for a roller weight of 10tonn is shown in Figs. 7 and 8. In the model, the cohesion value of the soil is 15kPa and the value of friction angle is varied.

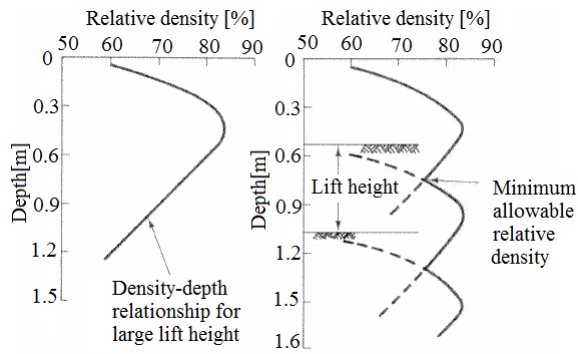


Fig. 6 Principle of an approximate method for determining lift height to achieve a minimum compacted relative density [2].

A critical height is noted at a depth of 0.3m above which soils with low friction angle are compacted to a lesser extent. The highest density is obtained for moderate friction angle and the density closer to the surface of compaction reduces for higher friction angle, possibly due to the effect of dilation. Dilation in soils is associated with increase in volume which consequently reduces the density.

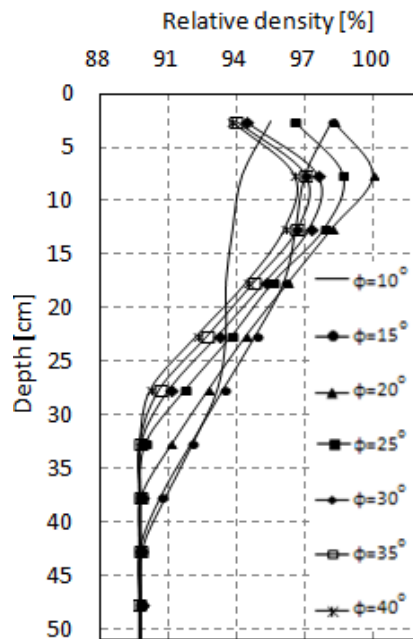


Fig. 7 The effect of friction angle on soil compaction

When the depth of compaction increases, there is no significant change for low friction angle since the compaction depth is controlled by cohesion. At higher values of friction angle, the change in effective compaction depth is small as the soil becomes strong enough and additional compaction effort is required.

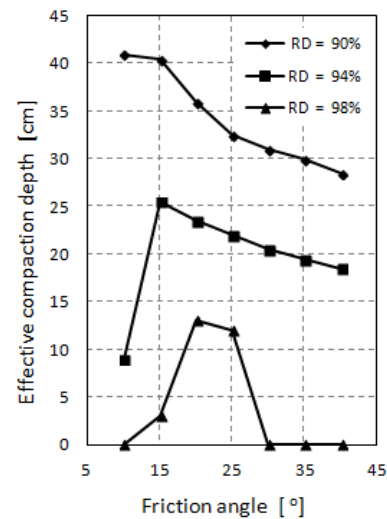


Fig. 8 Effective compaction depth at different relative densities based on friction angle.

The relationship between the relative density and cohesion for specific depths in the soil is presented in Figs. 9 and 10. In this case, the value of friction angle is kept constant ($\phi = 20^\circ$) and the cohesion is varied. The compacted density appears to be independent of the cohesion of the soil in the top 0.1m for high cohesion values. As the depth increases, the effect of cohesion is clearly shown. For the same load, the effective depth of compaction for highly cohesive soils is very limited and it increases as the cohesion decreases.

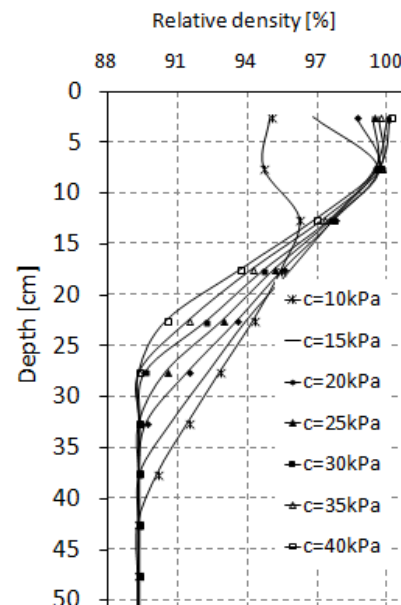


Fig. 9 The effect of cohesion on compaction.

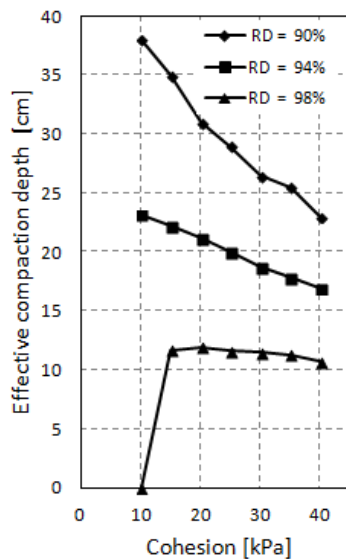


Fig. 10 Effective compaction depth at different relative densities based on cohesion.

CONCLUSION

The study presented in this paper is mainly for smooth wheel rollers. These types of rollers are commonly used when adequate compaction is obtained under relatively low pressure. The effect of soil strength parameters during the compaction process can be used as an input to optimize the compaction depth. The rule of thumb in practice is to use a specified lift height (the same thickness for a range of fine grained soils). Though the general understanding of soil parameters on the response of soil is well known, the quantitative understanding is yet to be investigated.

The numerical investigation shows that soil cohesion highly affects the effective compaction depth. Depending on the amount of stress induced from the roller and the relative density required, the lift height can be chosen as a function of the strength parameters. Based on the knowledge of the friction angle and cohesion of fine grained soils, the rolling strategy can be adjusted and the compaction practice can be improved.

ACKNOWLEDGEMENTS

This research is conducted at the Norwegian University of Science and Technology with the research fund support from the Norwegian Public Roads Administration.

REFERENCES

- [1] Proctor, RR, Fundamental principles of soil compaction. Engineering News-Record, Vol.111, No.9, 1933, pp. 286-289.
- [2] Holtz RD, and Kovacs WD, "Compaction", An introduction to geotechnical engineering, Prentice-Hall, Inc.,1981, pp.109-165.
- [3] Briaud JL, Seo J, Intelligent Compaction: Overview and Research needs, Texas A&M University, 2003, pp. 1-84.
- [4] NPRA, Handbook 018: Road Design and Construction Guidelines (in Norwegian), Norwegian Public Roads Administration, 2011.
- [5] Xia K., Masud A, You Z, A large deformation finite element formulation for subgrade soil compaction, Pavements and Materials, 2008, pp. 122-130.
- [6] Chiroux RC, et al., Three-dimensional finite element analysis of soil interaction with a rigid wheel. Applied Mathematics and Computation, Vol. 162 ,No.2, 2005. pp. 707-722.
- [7] Hambleton JP, Drescher A, Development of improved test rolling methods for roadway embankment construction. 2008, Minnesota Department of Transportation.
- [8] Abaqus FEA, Simulia, Dassault Systèmes, 2011
- [9] Drucker DC, Prager W, Soil mechanics and plastic analysis for limit design. Quarterly of Applied Mathematics, Vol.10,No.2,1952. pp. 157-165.
- [10] Neto EDS, Peric D, Own DRJ, "Advanced Plasticity Models", Computational Methods for Plasticity: Theory and Applications, John Wiley & Sons Ltd,2008, pp. 403-433.
- [11] Hügél, H.M., S. Henke, and S. Kinzler, High-performance Abaqus simulations in soil mechanics, in Abaqus Users' Conference. 2008.
- [12] Kelm M. and Grabe J, Numerical simulation of the compaction of granular soils with vibratory rollers, in Cyclic Behavior of Soils and Liquefaction Phenomena, Taylor & Francis Group, 2004, pp. 661-664.
- [13] Chen WF and Mizuno E, Nonlinear Analysis in Soil Mechanics - Theory and Implementation. Elsevier. 1990.
- [14] Han LH, et al., A modified Drucker-Prager Cap model for die compaction simulation of pharmaceutical powders. International Journal of Solids and Structures, Vol.45, No.10, 2008, pp. 3088-3106.

COMPRESSIVE STRENGTH OF CEMENT PASTES EXPOSED TO ELEVATED TEMPERATURE AND DETERIORATION MITIGATION

Abdoullah Namdar¹, Ideris Bin Zakaria¹ and Gurumurthy Hegde²

1. Faculty of Civil Engineering & Earth Resources, Universiti Malaysia Pahang, Malaysia

2. Faculty of Industrial Science & Technology, Universiti Malaysia Pahang, Malaysia

ab_namdar@yahoo.com

ABSTRACT

Kaolin-bentonite mixture [1] is mixed with cement paste for introducing a green and fire sustainable concrete. The effects of Kaolin-bentonite (additive is grounded particles sized of $<75\mu\text{m}$) as mineral admixtures on the hydration behaviour and mechanical properties of ordinary Portland cement (OPC) have been investigated. The crystalline modification, changes in microstructure and minerals mixtures in hydration of cement by using X-ray diffraction (XRD) and also the compressive strength of specimens have been investigated. The specimen exposed to elevated temperature of 500 and 1000 °C for 3 h in ceramic furnace and cooled down to the room temperature. The compressive strength test made after specimens are cooled down to room temperature. It observed if OPC-Kaolin-bentonite imposed by 500 °C heat for 3 hours resulted in improve 25% of compressive strength compare to OPC. Increasing heat to 1000 °C almost resulted in failure of all type of specimens and one day after cooling down specimen exposed to 1000 °C heat the compressive strength reach to absolute zero. The certain level of heat in limited time will improve OPC-Kaolin-bentonite, it is revealed possibility of using this method for improving cement paste in construction industry.

Keywords: Kaolin-bentonite mixture, compressive strength, hydration, XRD.

INTRODUCTION

The effect of elevated temperature on cement paste and concrete are two enormous topics in civil engineering research work. There are several reasons available these two parts of investigation integrated each other. This reconnaissance takes concentration on effect of elevated temperature on cement paste and comparing with previous work was on concrete.

The effect of CaO rehydration in reducing strength of OPC after 800 °C has been reported. It was find that the rate of water absorption is a factor governs the extent of deterioration caused by CaO rehydration, and also water absorption quantity it is a reason in accelerating rehydration of CaO into CaOH₂. This phenomenon is impossible to observe in concrete [2]. The maximum of water reduction occurs between 300 and 500 °C is due to the dehydration-dissociation of CaOH₂. And OPC produce is calcium hydroxide (CaOH₂) during hydration [3]. In an investigation on micro-level and macro-level properties of cement pastes mixed with different fiber contents to study role of PP fiber at elevated temperature in self-compacting cement paste samples, is observed in higher temperatures micro cracks is influences the gas permeability [4]. Reducing amount of concrete spalling and enhance the fire-resistance has mitigate by using fire-resistant spray materials for ensure an effective level of fire-resistance [5-6]. The polypropylene fiber in concrete

is exposed to temperatures of 400 °C extend crack compare to not used polypropylene fibers in concrete. When the fibers dissolve with water, the concrete expands, creating a tensile strength within its matrix, and hence generating cracks [7-8]. The quartz powder (QP) as mineral admixture used in Portland cement (PC) from 0 to 20 wt % in increment of 5% and subsequently exposed to elevated temperatures up to 1000 °C for 2 h, which started from 200 °C and in each stage 200 °C is increased. The result indicated that the QP improves both elevated temperature and thermal shock resistance of the cement pastes [9]. It has been indicated that compressive strengths of mortars containing pozzolan were less affected high temperature than that of control mortars [10]. Not any studies have been performed on OPC-Kaolin-bentonite mixture properties after elevated temperatures. It is very promising method, in understanding mechanical properties of this composite material after elevated temperatures. In this paper a comparative study on OPC and OPC-Kaolin-bentonite exposed to elevated temperature has been investigated. The mechanical properties, compressive strength and hydration of pastes have been analysed, to find appropriate effect of heat level and room temperature during curing as well as exposed high level temperature deterioration mitigation of cement paste.

2. Experimental program

Materials

The produced additive is made from Kaolin-bentonite mixture exposed to 800 °C has ability to enhance compressive strength of concrete [1]. These are natural commercial minerals. The produced additive from Kaolin-bentonite mixture exposed to 800 °C (12%) for one hour has been used as mineral admixtures along with OPC (43 G) as a binding material. The produced additive created from Kaolin-bentonite mixture under 800 °C have been blended with OPC. Subsequently the compressive strength is measured after exposed to temperature of 500 °C and 1000 °C for 3 hours in ceramic furnace (figure 1) and cooling down. The mix designs of the additive and water to cement ratio are indicated in Table 1.

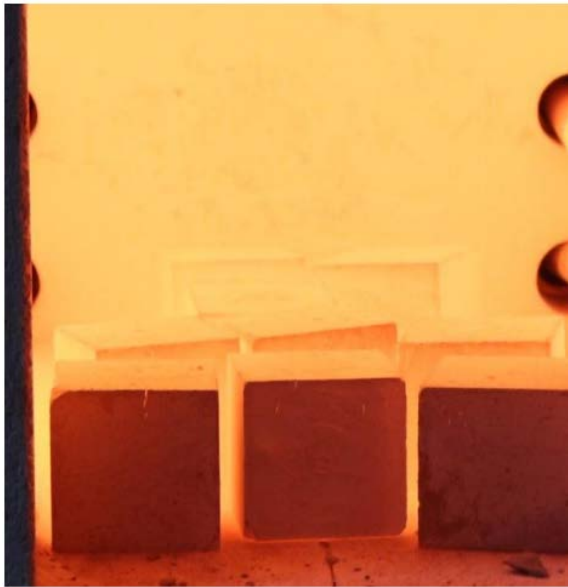


Figure.1. Paste cube exposed to temperature of 1000 °C after 3 hours in ceramic furnace.

Cement paste mix design

The Kaolin-bentonite mixture [1] admixture has been used for studying mineralogical reform and chemical reaction of cement paste. It is not discovering any specific methods for cement past mix design used Kaolin-bentonite, this research work is established by trial mixes. The ACI methods could not be applied to the cement past mix design with this new material for micro properties investigation and analyzing their effect on macro characteristics of concrete. In this research work for the identification of appropriate natural additive and establish optimization of materials mix ratio the additives are mixed based on weight of cement paste.

Compressive strength

To obtain the effect of Kaolin-bentonite mixture (12%) on the compressive strength of OPC, cubical molds (5 cm × 5 cm × 5 cm) were prepared according water to cement ratio indicated in Table 1. After initial curing of 1 day, the specimens were kept at water 30 ± 5 °C for 28 days. The compressive strength has been done as per ACI and the average value of three specimens has been selected for interpretation.

XRD

X-ray diffractometry (XRD) has been used to investigate in hydration process of OPC and OPC-produced additive [1] (figure. 2.1-2), mixture after 28 days of curing. The samples were grounded to a particle size of <75 µm for application of XRD, to reconnaissance on hydration and morphological characteristic of cement pastes.

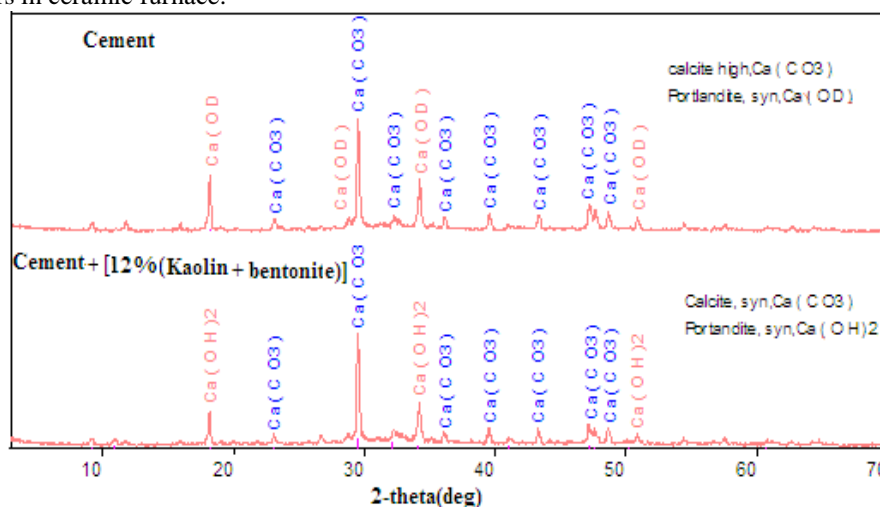


Fig. 2.1 XRD pattern of cement, and cement- kaolin-bentonite mixture, the kaolin-bentonite was submitted to 800 °C heat for 1 hour [1].



Figure. 2.2 Paste cube exposed to temperature of 1000 °C after 3 hours in ceramic furnace.

Table. 1. Mix designs of the solidified wastes.

Identity	W/C ratio	Produced Additive
OPC only - C 0	0.34	-
OPC + Kaolin -bentonite (12%)	0.34	12

RESULT AND DISCUSSION

A large amount of heat was released from the hydration process evaporating water inside the specimens during curing due to minerals-cement reaction. The method is suitable in cold region based on mentioned phenomenon. The specimen subjected to high level of heat is faced accelerating rehydration due to high level of water absorption and resulted in extending crack in specimen (figure 3-7) and drastically reducing compressive strength. According to Petzold and Rohrs [11], the reason for this cracking is the expansive, and hence disruptive, rehydration (due to reaction with airborne water vapour) of previously dissociated CaOH_2 . It has been reported [12-13] using pozzolanic materials due to consume calcium hydroxide in cement paste by pozzolanic reaction between calcium hydroxide in hydrated cement and reactive SiO_2 in mineral admixtures help to reduce cracking due to post cooling. It has good agreement with figures 6-7 in Ordinary Portland cement subjected to 1000 °C for 3 hours bigger crack is appear, based on table 2 strength of Ordinary Portland cement paste-Kaolin-bentonite mixture subjected to 1000 °C for 3 hours has lower compressive strength compare to Ordinary Portland cement subjected to 1000 °C for 3 hours. And one day after fully cooling down both specimens exhibited with zero compressive strength. The pozzolanic materials in high temperature have more negative effect on material due to fast reaching to end of hydration process. According to reported mentioned in [1], the quantity of 12% Kaolin-bentonite additive produced by 800 °C heats has shown best result in improving concrete

compressive strength. But in recent investigation has not agreement with previous work, it is enough reason for investigate effect of elevated temperature on both cement paste and concrete. From other hand the room temperature has specific effect on cement paste hydration. The room temperature was $30 \pm 5^\circ\text{C}$ for curing concrete and the room temperature was $20 \pm 3^\circ\text{C}$ and more humidity for curing cement paste. Test results showed [14] that the compressive strength of concrete cooled in water cooling is higher than that cooled in natural and furnace. It can be understand humidity and room temperature are important factors in mitigating elevated temperature of paste fire resistance. The finding in [1] and recent research work has good agreement with which reported in [14]. Pozzolanas are defining as siliceous and aluminous materials they react with lime to form calcium silicate and calcium aluminate silicate hydrates in moist environments [15]. The room temperature also play important role in hydration process and time. The compressive strength of cement paste is exposed to high temperature can be partially recovered by providing appropriate environment contents sufficient humidity and temperature. Figure 3 indicated OPC after elevated temperatures of 500 °C for 3 hours and cooling in open area for 2 hours in this case 70% of specimens separated due to self-weight of specimen in furnace but in same condition if Kaolin-bentonite mixed to OPC this deterioration reduced (Figures 3-4). In condition eliminating surcharge it is possible to increase temperature up to 1000 °C without this deterioration (figures 5-6). Figure 7 is shown OPC after elevated temperatures of 500 °C for 3 hours and cooling in open area for 2 days, it is faced sever deterioration. Figure 8 indicated that OPC-Kaolin-bentonite after elevated temperatures of 500 °C for 3 hours and cooling in water immediately in this case the paste change color to black but not faced any deterioration even after long term and its compressive strength is improved. From other hand if temperature increased to 1000 °C cooling down of specimen immediately in water resulted in fully collapse (figure 8) and even after cooling down in open area after 1 hour when the specimen can transport by naked hand keeping in water it shown collapse (figure 9). From above indications find that cooling down of specimens can be done only in specific environments which depend on specimen temperature.

Table. 2. Cement paste-additive mixture ratio

Sl No	Heat level	Time of Heat in hours	Type of additive	(%)	Compressive strength after 28 days (MPa)
1	Room temperature	-	-	0	30.1
2	500 °C	3		0	33.8
3	1000 °C	3		0	4.57
4	Room temperature	-	Additive produced by 800 °C (%) [1]	12	27.71
5	500 °C	3		12	42.29
6	1000 °C	3		12	3.55



Fig. 3. OPC after exposed to elevated temperatures of 500 °C for 3 hours and cooling in open area for 2 hours.



Fig 4. OPC-Kaolin-bentonite after exposed to elevated temperatures of 500 °C for 3 hours and cooling in open area for 2 hours.



Fig. 5. OPC after elevated temperatures of 1000 °C for 3 hours and cooling in open area for 2 hours.



Fig. 6. OPC-Kaolin-bentonite mixture after exposed to elevated temperatures of 1000 °C for 3 hours and cooling in open area for 2 hours.



Fig. 7. OPC after exposed to elevated temperatures of 500 °C for 3 hours and cooling in open area for 2 days.



Fig. 8. OPC-Kaolin-bentonite after exposed to elevated temperatures of 500 °C for 3 hours and cooling in water immediately.



Fig. 9. OPC-Kaolin-bentonite after exposed to elevated temperatures of 1000 °C for 3 hours and cooling in water immediately.



Fig. 9. OPC-Kaolin-bentonite after exposed to elevated temperatures of 1000 °C for 3 hours and cooling in water after 2 hours.

CONCLUSION

This is well known that the elevated temperature changes engineering properties of construction materials. In this investigation has been observed that the certain level of heat in limited time will improve OPC properties if appropriate additive has been used. Both cement paste and concrete has to be investigated for accurate design construction materials. The humidity, room temperature and elevated temperature are important factors in fire resistance mitigation of concrete and concrete curing time. The compressive strength of cement paste exposed to 1000 °C for 3 hours is reduced continuously and is reached to absolute zero even after cooling down, and stopping exposing high temperature not stopping reducing compressive strength of specimen and deterioration process of micro properties of cement paste destroy whole compressive strength gradually. The compressive strength of cement paste is exposed to high temperature can be partially recovered or reduce deterioration of concrete structure by providing appropriate environment contents sufficient humidity and temperature. There is possibility for improve paste characteristics using appropriate temperature, method and additive.

REFERENCES

- [1] Namdar A, "Natural minerals mixture for enhancing concrete compressive strength", *Frattura ed Integrità Strutturale*, 22, 2012, pp.26-30; DOI: 10.3221/IGF-ESIS.22.04.
- [2] Mendes A, Sanjayan J. G, Gates W.P, Collins F, "The influence of water absorption and porosity on the deterioration of cement paste and concrete exposed to elevated temperatures, as in a fire event", *Cement & Concrete Composites*, 34, 2012, pp. 1067-1074.
- [3] Y. Lea FC, Stradling RE, "The resistance to fire of concrete and reinforced concrete", *Engineering*, 144, 1922, pp.341-4.
- [4] Liu X, Ye G, Schutter G. De, Yuan Y, Taerwe L, "On the mechanism of polypropylene fibres in preventing fire spalling in self-compacting and high-performance cement past", *Cement and Concrete Research*, 38, 2008, pp.487- 499.
- [5] International research institute of cooperation between industry and academia. Exfoliation of the concrete tunnel of shinkansen and spalling of concrete structures, University of Tokyo, Tokyo, Japan; 2002.
- [6] ITA Working group No. 6. maintenance and repair, Guidelines for structural fire resistance for road tunnels; 2004.
- [7] Kalifa P, Menneteau FD, Quenard D, "Spalling and pore pressure in HPC at high temperatures", *Cem Concr Res* 30, 2000, pp.1-13.
- [8] Pierre K, Grégoire C, Christophe G, "High-temperature behaviour of HPC with polypropylene fiber from spalling to microstructure", *Cem Concr Res* 31, 2001, pp.1487-99.
- [9] Rashad A. M, Zeedan S.R, "A preliminary study of blended pastes of cement and quartz powder under the effect of elevated temperature", *Construction and Building Materials*, 29, 2012, pp. 672-681.
- [10] Yazıcı S, Sezer G.I, Sengül H, "The effect of high temperature on the compressive strength of mortars", *Construction and Building Materials*, 35, 2012, pp.97-100.
- [11] Petzold A, Rohrs M, "Concrete for high temperatures", Second ed, London, 1970, Maclaren and Sons Ltd.
- [12] Aydın S, Baradan B, "Effect of pumice and fly ash incorporation on high temperature resistance of cement based mortars", *Cem Conr Res*, 37(6), 2007, pp.988-95.
- [13] Xu Y, Wong YL, Poon CS, Anson M, "Influence of PFA on cracking of concrete and cement paste after exposure to high temperatures", *Cem Conr Res*, 33(12), 2003, pp. 2009-16.
- [14] Karakoç M.B, "Effect of cooling regimes on compressive strength of concrete with

lightweight aggregate exposed to high temperature”, *Construction and Building Materials*, 41, 2013, pp.21-25.

- [15] Heikal M, El-Didamony H, Sakkary T.M, Ahmed I.A, “Behavior of composite cement pastes containing microsilica and fly ash at elevated temperature”, *Construction and Building Materials*, 38, 2013, pp.1180-1190.

PARTICLE SIZE AND OTHER FACTORS AFFECTING THE PULLOUT BEHAVIOR OF GEOCELLS EMBEDDED IN GRAVELLY SOIL BACKFILL

Xinye Han¹, Takashi Kiyota², Michiyuki Harata³ and Fumio Tatsuoka⁴

^{1,2} Institute of Industrial Science, University of Tokyo, Japan; ³ Plastic Products, Technical & Engineering Plastic Products Sales Division, Tokyo Printing Ink MFG.CO.LTD, Japan; ⁴ Department of Civil Engineering, Tokyo University of Science, Japan

ABSTRACT

In order to study whether geocell can be worked as tensile reinforcement in retaining walls, pullout tests were performed on two types of geocell which have diamond-shaped cells and square-shaped cells embedded in two different compacted gravelly soils under the surcharge of 1 kPa at constant pullout rate. Different pullout behaviors were found due to the effect of in-plane geometry which can be explained by different interaction mechanisms. In particular, the dilatancy effects on the pullout strength of geocell were also discussed. Moreover, a preloading method was applied to reduce the slackness of transverse members of square-shaped geocell, and therefore enhance the initial stiffness.

Keywords: Pullout test, Diamond-shaped geocell, Square-shaped geocell, Preloading method

INTRODUCTION

Geocells, as a three-dimensional soil confinement system, have been widely applied in construction roads over soft soils, stabilization soils on embankments, protection steep slopes.

The common type of geocell has a diamond pattern, on which many studies were carried out mainly to check the function as base reinforcements subjected to vertical loads, such as roads, embankments and light houses. The influencing factors for the performance of geocell-reinforced bases, such as geometric structures and dimensions, properties of geocell material and properties of infilled soil, loading methods, etc., were investigated by previous works [1]-[4], etc. However, the application of geocell as tensile reinforcement to soil structures, such as retaining walls, is relatively new due to the lack of related research. Ling et al. (2009) [5] investigated the seismic performance of several soil retaining walls having a geocell facing by shaking table tests. The results showed that walls having a geocells facing are flexible exhibiting much better seismic performance than conventional type retaining walls. In addition, the performance of a retaining wall with the backfill reinforced with geocell layers is better than with geogrid layers.

In order to check whether geocell can be worked as tensile reinforcement, two types of geocell which have diamond-shaped cells (traditional type geocell) and square-shaped cells (new developed geocell) were evaluated by pull-out tests embedded in two different compacted gravelly soils.

TEST APPARATUS, PROCEDURES AND MATERIALS

Pullout Test Apparatus

Figure 1 shows the schematic diagram of pullout test apparatus that was developed at IIS, the University of Tokyo. The tests are carried out on plane-strain condition. The soil box is rectangular in shape and made of steel. The dimensions of inner soil box are 700mm (length) × 400mm (width) × 500mm (height). The opening size of the front wall could be changed for pulling out the model geocells of different heights. Leads shots are applied on the crest of the backfill to provide a surcharge of 1 kPa as a flexible top boundary, which is preferred for the purpose of measuring vertical deformation of backfill, which caused by the dilatancy of soil around the geocell reinforcements in the pullout process.

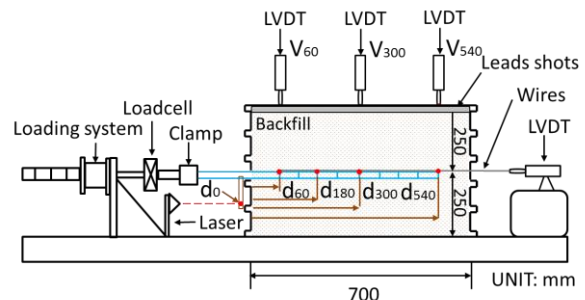


Fig. 1 Schematic diagram of pullout test apparatus

Pullout Test Procedures

Gravels were poured into the soil box and compacted in 25 cm-thick sub-layers arranging geocell model at the prescribed level in the backfill. The target density of the backfill was 1.76g/cm^3 . As indicated in Fig. 1, the front displacement (d_0) was monitored by laser deformation transducer. The displacements along the geocell, for example, the locations at distances of 60 mm (d_{60}), 180 mm (d_{180}), 300 mm (d_{300}), and 540 mm (d_{540}) from the face of front wall were measured with linear variable differential transformers (LVDTs). Monitoring the displacements along the geocell reinforcement allows proper interpretation of the interface force transfer mechanism and provides appropriate evaluation of the pullout resistance as well. Inextensible stainless wires were connected to the designated locations of geocell reinforcement to measure the displacements along the geocell reinforcement. The wires were protected by stiff tubes and connected to the LVDTs, which were mounted on the rear wall of soil box. In addition, the vertical deformation of the backfill surface at distances of 60 mm (V_{60}), 300 mm (V_{300}), and 540 mm (V_{540}) from the face of the front wall were also measured with three LVDTs. The tests were conducted by pulling out the geocell at a constant displacement rate of 2.5 mm/min using a precision jack driven by a motor. The pullout force was measured with a load cell. All instrumentations were linked to an electronic data logger which can scan the measurements at desired time intervals.

Soil Materials and Tested Geocell Models

The backfill soils used in this study were poorly graded sub-round gravelly soils, Gravel No.1 and Gravel No.3 (Fig. 2). Their particle sizes are 3~5 mm and 7~10 mm, respectively. As shown in Fig. 3, two types of geocell reinforcements were prepared: diamond-shaped geocell (conventional type geocell) and square-shaped geocell (new developed type geocell), both of which were made of polyethylene terephthalate (PET) covered with PVC for protection, having a thickness of 1 mm. The ultimate tensile strength of the material is 56 kN/m at a strain of 20%.

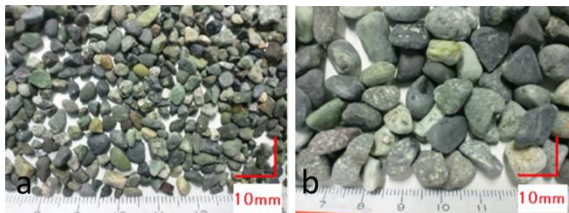


Fig. 2 Soil materials: (a) Gravel No.1; (b) Gravel No.3

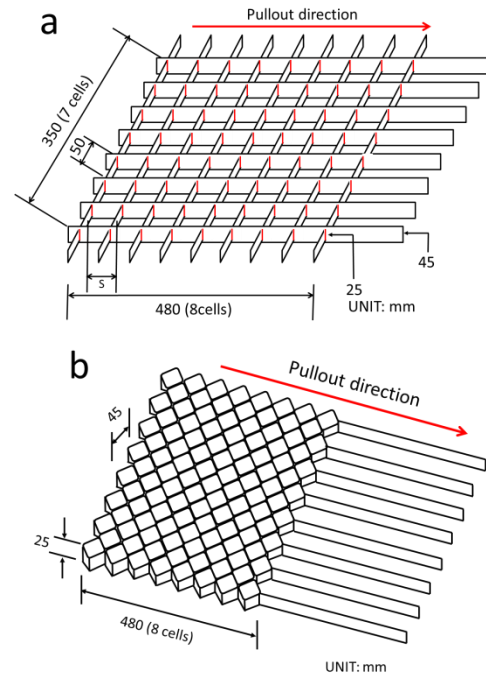


Fig. 3 Schematic diagram of: (a) square-shaped geocell and (b) diamond-shaped geocell

RESULTS AND DISCUSSION

Effects of Geometry of Geocell

Typical pullout behavior

Typical pullout test results on square-shaped geocell and diamond-shaped geocell embedded in Gravel No.1 and Gravel No.3 are presented in Fig. 4. The pullout resistance (P) versus horizontal displacement (d_{60}) of geocells is plotted in Figs. 4a and 4c, while the vertical displacement (V_{60}) of the backfill surface and horizontal displacement (d_{60}) of geocells is plotted in Figs. 4b and 4d. It is found that square-shaped geocell shows both higher peak pullout resistance and higher initial stiffness than diamond-shaped geocell in both soil materials. It is interesting to note that, for square-shaped geocell embedded in Gravel No.1, with increasing pullout horizontal displacement (d_{60}) there is a high peak pullout resistance indicating a contribution from dilatancy of soil (Fig. 4b), and then as pullout continues the resistance decreases to a residual state. The peak pullout resistance at 16mm horizontal displacement coincides with the steepest slope of the vertical displacement line (Fig. 4b). This behavior is quite similar to the typical behavior of granular dense soils which indicates that the dilatant contribution equals the work done against the normal stress as pullout progresses, thereby increasing the pullout resistance, as pullout continues, the shear zone around the geocell reinforcement eventually achieves to a stable state-

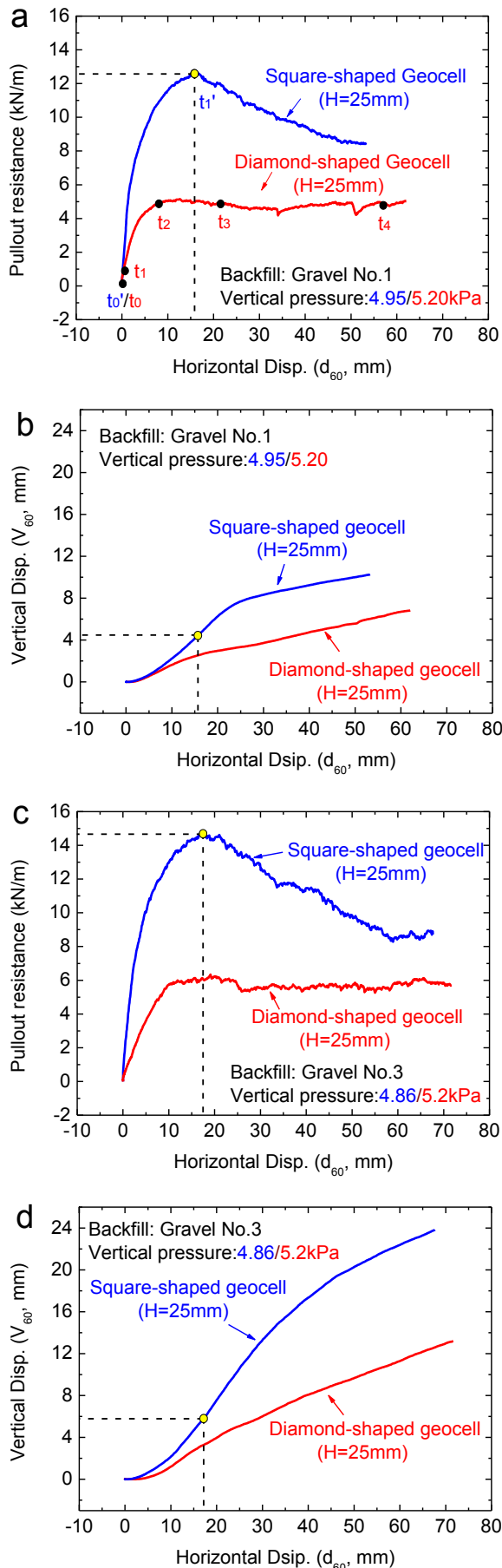


Fig. 4 Typical pullout behaviors of square-shaped geocell and diamond-shaped geocell: (a) and (c), pullout resistance against horizontal displacements (d_{60}); (b) and (d), relationships between vertical displacement (V_{60}) and horizontal displacement (d_{60})

sliding state, in which the pullout resistance reaches residual state. While for diamond-shaped geocell, the dilatant contribution is lower than square-shaped geocell (Fig. 4b), which is associated with the value of the pullout resistance is lower than square-shaped geocell in both peak state and residual state (Fig. 4a). From Figs. 4c and 4d, similar pullout behavior of square-shaped geocell and diamond-shaped geocell embedded in Gravel No.3 are also investigated. In both cases, as shown in Fig. 5, square-shaped geocell exhibits not only higher peak pullout resistance but also higher residual pullout resistance than diamond-shaped geocell. These differences are due likely to the different geometries of the geocell, in particular the shape of aperture (Fig. 3). Moreover, as particle size increases from Gravel No.1 to Gravel No.3, the peak pullout resistance increases associated with an increase of dilatancy for both diamond-shaped geocell and square-shaped geocell.

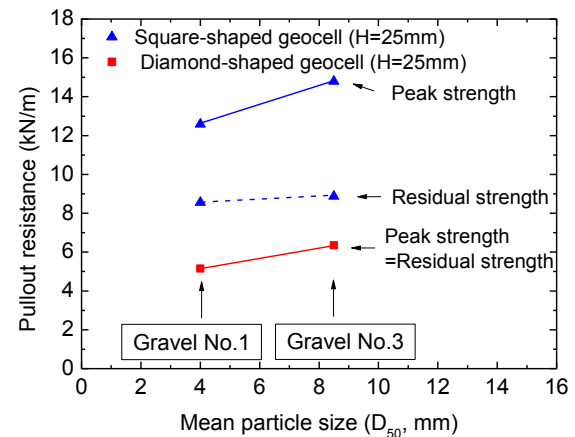


Fig. 5 Peak and residual pullout resistances for geocell reinforcement in different backfill soils

Stress-deformation mechanism

Figure 6 represents the distribution of local horizontal displacements of the geocell reinforcements for different values of the applied pullout forces, and the slope of the curve represents local strain. It is found that, for square-shaped geocell (Fig. 6a), two different phases are observed to characterize the pullout behavior of the reinforcement: (1) In Phase 1 (force-transfer phase), the local strain increases as the pullout force increases, which indicates that the tensile force is progressively transferred to the geocells and the each cell provides its passive anchorage resistance or shear resistance consecutively from the front cells

near the point of pullout load application to the end cells until the peak pullout state ($P=12.59\text{kN/m}$) of geocell reinforcement after which no increment of strain along the geocell reinforcement occurs. Note again, at peak state, the steepest slope of vertical-horizontal displacements curve ($V_{60}-d_{60}$) is reached (Fig. 4b); (2) In Phase 2 (sliding phase), two adjacent curves are parallel each other, indicating that the geocell reinforcement move as a whole and the shear bands form where the residual shear force determines the residual pullout resistance.

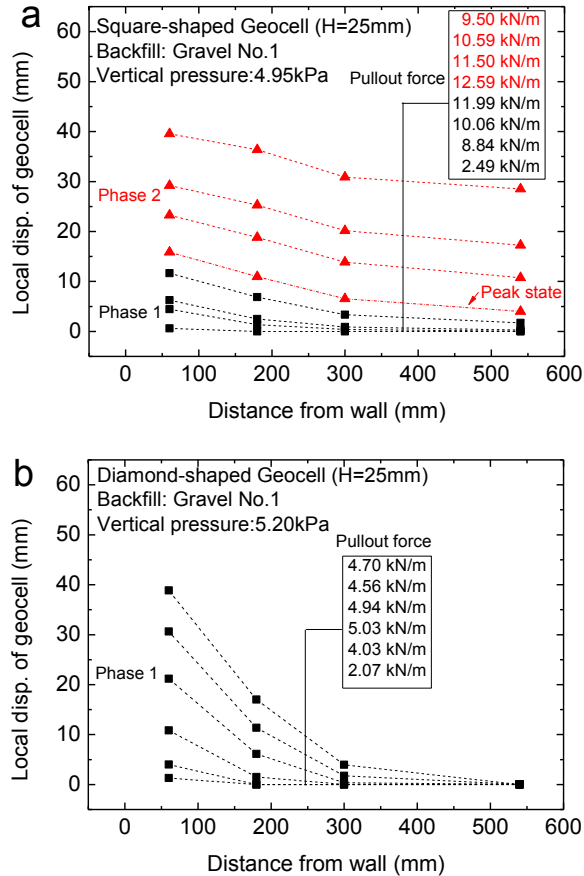


Fig. 6 Local horizontal displacements at different pullout force levels: (a) square-shaped geocell and (b) diamond-shaped geocell

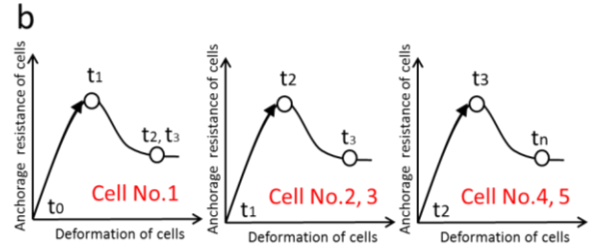
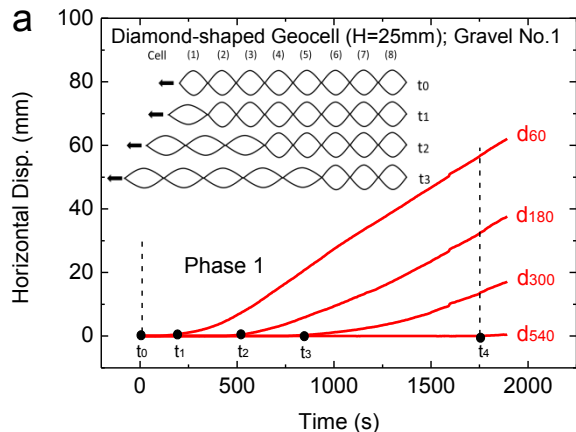


Fig. 7 Schematic stress-deformation characteristics of diamond-shaped geocell: (a) horizontal displacement versus time history; (b) schematic diagram of stress-deformation mechanism

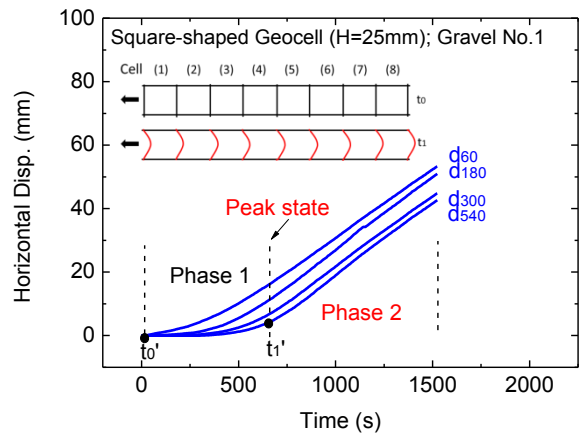


Fig. 8 Stress-deformation characteristics of square-shaped geocell

In the case of diamond-shaped geocell (Fig. 6b), only Phase 1 (force-transfer phase) occurs. It is noteworthy to highlight that, due to large deformation of diamond-shaped cell itself, the last node of geocell does not move at large displacement of the first node, which restricts the development of shear band along the geocell resulting in a lower peak resistance.

Figures 7 and 8 show the stress-deformation characteristics of diamond-shaped geocell and square-shaped geocell varying with time when subjected to a pullout force. The schematic diagrams of deformation status varying with time are given in the inset of the figures. In particular, the stress-deformation mechanism of diamond-shaped geocell is shown in Fig. 7b. For diamond-shaped geocell (Figs. 4a and 7), from t_0 (initial state) to t_1 (the first state), the first diamond cell starts to deform and provide corresponding pullout resistance (Fig. 4a and 7b) until other cells reach the residual resistance state of the first cell. Afterwards from t_1 to t_2 , the second and the third cells deform and provide their pullout resistances until the rest cells reach the residual state of them. This procedure repeats from t_2 to t_3 until all cells work in the pullout Phase 1 (force-transfer phase). This deformation characteristics of diamond-shaped geocell can be characterized as

progressive deformation in Phase 1 (force-transfer phase), which would induce the soil surrounding the diamond-shaped geocell not fully mobilized, and therefore cause a lower peak pullout resistance and initial stiffness compared with the square-shaped geocell. However, as shown from Figs. 4a and 8, the square-shaped geocell only shows a slightly progressive deformation in Phase 1 (force-transfer phase) from t_0 (initial state) to t_1 (peak state). After that, all square cells work immediately which could provide larger peak pullout resistance and higher initial stiffness than diamond-shaped geocell. It is possible to observe the final deformation states of diamond-shaped geocell (Fig. 9a) and square-shaped geocell (Fig. 9b), showing shrink deformation characteristics and non-shrink deformation characteristics close to the position of clamp, respectively.

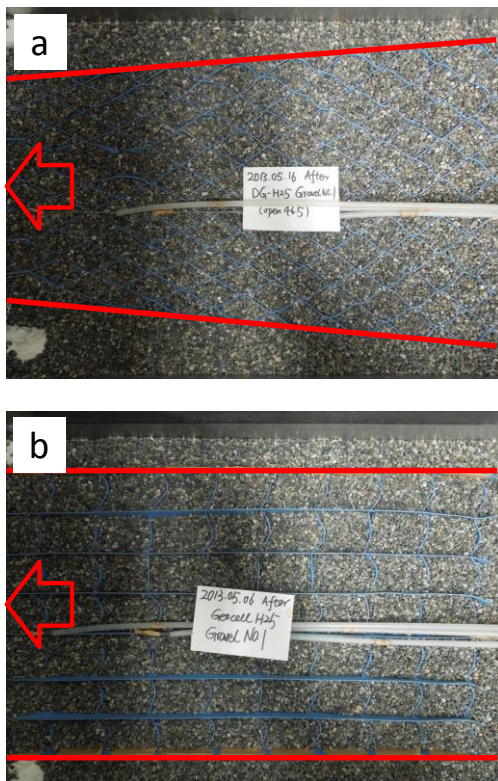


Fig. 9 Final deformation states of: (a) diamond-shaped geocell and (b) square-shaped geocell

Enhancement of Initial Stiffness

With square-shaped geocell, the peak pullout resistance and initial stiffness are mainly determined by the anchorage resistance provided by transverse members or shear resistance around geocell reinforcements in Phase 1 (force-transfer phase). In particular, initial stiffness would increase as an increase in the stiffness of transverse members and better initial arrangements of transverse members would also be of prime importance. As shown in

Fig. 10, a preloading was applied at the value of residual strength in order to decrease the slackness of transverse members as presented in Fig. 11. From Fig. 12a, with Gravel No.1, the initial pullout stiffness of square-shaped geocell increases significantly by preloading method, while from Fig. 12b, with Gravel No.3, the initial pullout stiffness increases slightly. However, the preloading method has little influence on the peak resistance and residual resistance in both cases.

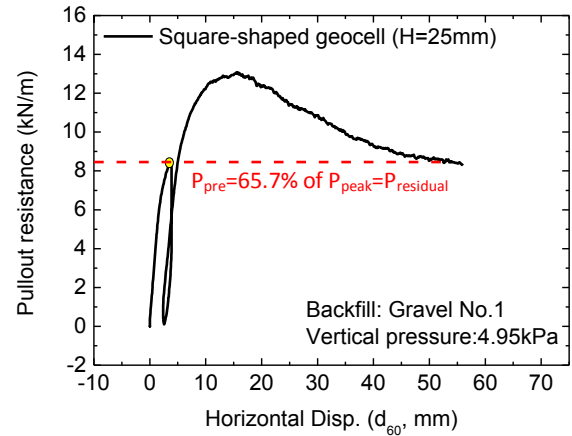


Fig. 10 Preloading method for square-shaped geocell

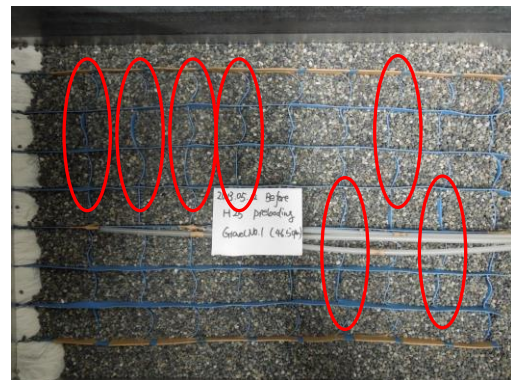
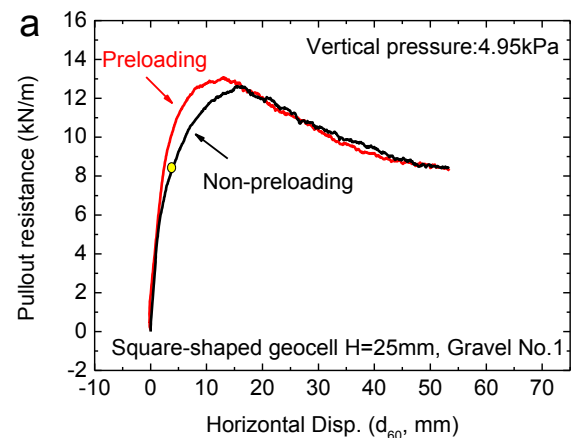


Fig. 11 Arrangements of transverse cell members before test



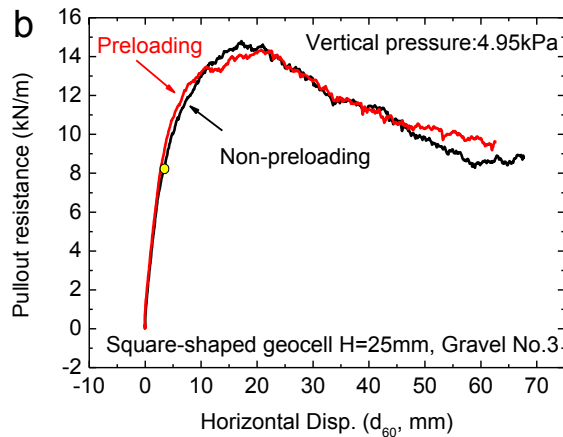


Fig. 12 Enhancement of square-shaped geocell by preloading method with: (a) Gravel No.1 and (b) Gravel No.3

CONCLUSION

The pullout tests were conducted using diamond-shaped geocell and square-shaped geocell embedded in compacted granular soils under the surcharge of 1 kPa at constant pullout rate. The main conclusions could be summarized as follows;

- a) The square-shaped geocell exhibits much higher peak pullout resistance and higher initial stiffness than the diamond-shaped geocell, and with an increase in particle size from Gravel No.1 to Gravel No.3, the peak pullout resistance increases for both types geocell, associated with an increase of soil dilatancy.
- b) These differences are related to the effect of geometry of geocell on the mobilization of interface mechanisms. With diamond-shaped geocell, a large progressive mobilization of the interface interaction mechanism develops indicated as Phase 1(force-transfer phase), which determine the total pullout resistance; on the other hand, square-shaped geocell firstly experiences slightly progressive deformation indicated as Phase 1 (force-transfer phase) in which passive anchorage

resistance provided by transverse members or shear resistance of the shear band determines the total pullout resistance until the peak state, after that, in Phase 2 (sliding phase), the geocell reinforcement moves as a whole and the shear bands form where the residual shear force determines the residual pullout resistance.

- c) A preloading method was applied to reduce the slackness of transverse members of square-shaped geocell, and therefore enhance the initial stiffness.
- d) In Phase 1 (force-transfer phase), the dimension of geocell, such as height of geocell and spacing between transverse members determines the mobilization of interaction mechanism and therefore the peak pullout resistance, which should be investigated in the future.

REFERENCES

- [1] Mhaikar, S.Y. and Mandal, J.N. (1994). "Three dimensional geocell structure: performance under repetitive loads", 5th International Conference on Geotextile, Geomembranes and Related products, Singapore, 155-158.
- [2] Dash, S.K., Krishnaswamy, N.R., and Rajagopal, K. (2001). "Bearing capacity of strip footings supported on geocell-reinforced sand." *Geotextiles and Geomembranes*, 19(4), 235-256.
- [3] Dash, S.K., Sireesh, S., and Sitharam, T.G. (2003). "Model studies on circular footing supported on geocell reinforced sand underlain by soft clay." *Geotextiles and Geomembranes*, 21(4), 197-219.
- [4] Dash, S.K., Rajagopal, K. and Krishnaswamy, N.R. (2004). "Performance of different geosynthetic reinforcement materials in sand foundations." *Geosynthetics International*, 11(1), 35-42.
- [5] Ling, H.I., Leshchinsky, D., Wang, J.P., Mohri, and Y., Rosen, A. (2009). Seismic response of geocell retaining walls: experimental studies. *ASCE Journal of Geotechnical and Geoenvironmental Engineering* 135, 515-524.

EFFECT OF LOADING RATE ON STRENGTH CHARACTERISTICS OF GRANULAR BASE COURSE MATERIAL

Yuan Zhang¹, Tatsuya Ishikawa² and Tetsuya Tokoro³

¹Graduate School of Engineering, Hokkaido University, Japan; ²Faculty of Engineering, Hokkaido University, Japan; ³Tomakomai National College of Technology, Japan

ABSTRACT

This paper examines the effect of loading rate on the shear behavior of granular base course material under a series of degrees of saturation through monotonic triaxial compression tests. In this study, monotonic triaxial compression tests under consolidated drained condition (CD test) were carried out. The experimental results show that peak strength of base course material increases with the increase of loading rate, especially in air-dried condition. Besides, it is appeared as the loading rate plays a remarkable part in the shear strength parameters obtained for granular base course material. Under air-dried and saturated condition the internal friction angle increases with the increase of loading rate, while the cohesion decreased with the increase of loading rate. Loading rate effects under unsaturated condition do not appear to be the same regularity as under air-dried and saturated conditions.

Keywords: Unsaturated soil, Monotonic triaxial compression test, Suction, Shear strength

INTRODUCTION

The pavements have to transfer traffic loadings with different loading speeds from the asphalt-mixture layer to subgrade course layer, which causes deterioration on the pavement structures. However, throughout a year, the water content of pavement will be affected by the infiltration of water through various means. Especially, in snowy cold regions, such as Hokkaido, Japan, the water content of the pavement rises due to the inflow of thaw water or thawing of ice lenses. As a result, the bearing capacity of the subgrade and base course temporarily degrades. Therefore, it is of great significance to understand the influence of loading rate on the mechanical characteristics of unsaturated base course material under different degree of saturation.

Many different types of unsaturated soil have been studied by various researchers, however, there is limited available information in existing literature on mechanical behavior of unsaturated base course material which has maximum particle size of almost 40mm. This is because laboratory element tests for unsaturated soils with large-size specimens are quite time-consuming due to the ceramic disk with very low permeability usually used in the test apparatus for unsaturated soils. Recently, Nishimura et al. [1] performed some kinds of laboratory element tests for unsaturated soils using a cellulose filter, and were able to confirm the validity of using this filter as a substitute for a ceramic disk and thus shorten the testing time. On the other hand, based on the usefulness of membrane filters, we proposed testing methods adopting the pressure membrane method

with a medium-size specimen, which were highly useful in water retention tests and triaxial compression tests in terms of the reduction of total testing time as in [2].

In this paper, in order to examine the effects of loading rate on the shear behavior of a granular base course material (C-40), a series of monotonic triaxial compression tests for C-40 with different degree of saturation were conducted under different loading rates with the medium-size triaxial compression apparatus. Here, the monotonic triaxial compression tests were carried out under fully drained condition (CD test) during shearing process.

TEST MATERIAL

The base course material (C-40) was employed as a test material in this study, which is a natural crusher-run made from angular, crush, hard andesite with maximum particle size of 40mm. C-40 is encountered in subbase course layer of Japanese pavement structures. Physical properties and grain-size distribution curves for test specimen are shown in Table 1 and Fig. 1, respectively. Note that according to the results of sieve analysis before and after the test as shown in Fig. 1, the particle breakage of C-40 under air-dried condition at effective confining pressure of 34.5kPa was not largely caused during the monotonic triaxial compression test with loading rate of 0.05%/min.

When we performed the monotonic triaxial compression test under unsaturated condition, the prescribed degree of saturation can be obtained by applying corresponding suction based on the soil

water characteristic curve (SWCC). Figure 2 shows the relationship between matric suction ($s=u_a-u_w$) and degree of saturation (S_r) obtained from the water retention test on C-40 with the degree of compaction of 95% in the previous study [2]. The residual degree of saturation of C-40, which was 23.94%, can be determined through the fitting curve by LG model [3]. On the basis of Fig. 2, in order to get the approximate degree of saturation as the same value as regular degree of saturation (about 35%) in the real long-time field measurement [4], the suction of 10kPa was selected.

Table 1 Physical properties of base course material.

ρ_{dmax}^{*1} (g/cm ³)	w_{opt} (%)	F_c (%)	PI	ρ_{dmax}^{*2} (g/cm ³)	ρ_{dmin}^{*2} (g/cm ³)
2.070	8.2	5.20	NP	2.270	1.680

Note: *1 is compaction E-b method (JIS A 1210, 2009). *2 is test method for minimum and maximum densities of gravels (JGS 0162, 2009).

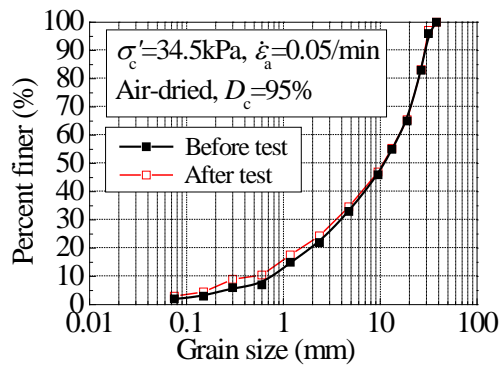


Fig. 1 Grain size distributions of C-40 before and after test.

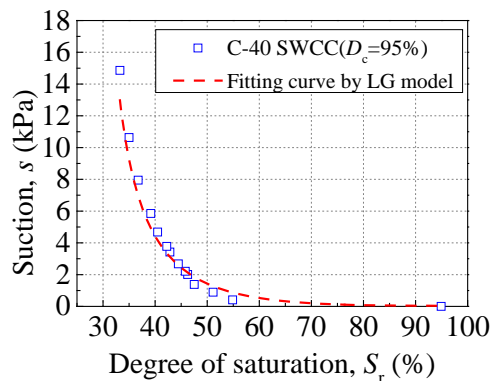


Fig. 2 Soil-water characteristic curve of C-40.

TEST APPARATUS

A schematic diagram of the medium-size triaxial apparatus for unsaturated coarse granular materials and the structure of cap and pedestal are shown in

Fig. 3. In the cap and pedestal, the pore water pressure is applied to a specimen through a versapor membrane filter attached to the water plumbing path, while the pore air pressure is applied through a hydrophobic polyflon filter attached to the air supply path in the cap and pedestal. Physical properties of the filters are shown in Table 2.

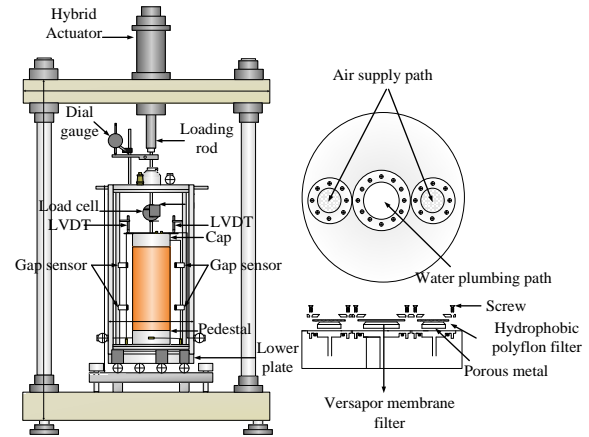


Fig. 3 Medium-size triaxial apparatus and structure of cap and pedestal.

Table 2 Physical properties of filters.

Name	Thickness (μm)	Pore size (μm)	AEV/WEV ^{*1}
Versapor	94.0	0.8	60
Polyflon	540.0	-	14.3

Note: *1 AEV is the air entry value of versapor membrane filter, while WEV is the water entry value of hydrophobic polyflon filter.

The measurements of stress and strain of a specimen were performed as follows. Axial stress (σ_a) was measured by a load cell installed inside the triaxial cell. Axial strain (ϵ_a) was obtained by measuring the displacement of loading piston with an external displacement transducer (dial gauge) and two linear variable differential transducers (LVDTs). Volumetric strain (ϵ_v) was measured by two sets of two proximity transducers (Gap sensors). As shown in Fig. 3, the gap sensors were fastened on two pillars diagonally opposite to each other around the specimen diameter. To ensure the accuracy for ϵ_v including unsaturated condition, the ϵ_v was calculated by taking the average value between two methods. One approach was that specimen was deemed to maintain a cylinder in the ideal case during shearing. And then diameter change of specimen during shearing could be measured by gap sensors, while vertical displacement change can be measured by dial gauge. Hence, the volume change can be calculated in accordance with the diameter

change and axial displacement change. The another method was as below: The initial positions of gap sensors were at the point of $\frac{1}{4}$ and $\frac{3}{4}$ of the specimen, therefore, with the increase of shearing, the measuring positions on specimens by gap sensors were also changed. During shearing the specimen was postulated to have a vertical cross section of a “beer barrel shape”, and the curve parts of which were represented approximately by parabolas. The parabolas can be drawn by the measurement data of gap sensors and the axial displacement change. Then the volume change of specimen can be calculated by the parabola, which was assumed to be equal to the rotator of the parabola [5]. Finally, ε_v of the specimen was obtained by the mean value of volumetric strain calculated from the two above mentioned methods. In case of saturated specimens, the volume of drainage during testing was also measured with a double tube burette.

TESTING METHOD

Monotonic triaxial compression tests were performed with different loading rates of 0.05%/min and 0.5%/min under three different degrees of saturation, namely “air-dried”, “unsaturated”, and “saturated” in conformance with the standards of Japanese Geotechnical Society (JGS 0524 & JGS 0527, 2000).

A cylindrical specimen for C-40 with initially 300mm in height and 150mm in diameter was prepared with air-dried sample by tamping with a woody rammer and compacting with a vibrator in five layers. And more detail about the specimen preparation method was described in previous study [2]. Note that after finishing all the tests under unsaturated condition, the air entry value (AEV) of versapor membrane filters would be checked by applied suction increasingly until air passed through the filters. Measurements of versapor membrane filters attached to the cap and the pedestal showed that the AEV after the test were nearly equal as before. This indicates that the versapor membrane filter suffers little degradation from the wear and tear during monotonic triaxial compression tests on coarse granular material.

Next, a consolidation process was conducted. Note that there are two effective confining pressure (σ_c'): 68.9kPa and 34.5kPa. The loading condition of σ_c' loaded on roadbed middle were estimated based on stress analysis of Japanese paved road model by GAMES (General Analysis Multi-layered Elastic Systems) [6]. Fig. 4 is the result of stress state inside typical Japanese pavement structure with different coefficients of slip interface calculated by GAMES, and AASHTO is the testing sequence for base/subbase of MR test [7]. Here, the maximum confining pressures of roadbed middle calculated by

GAMES with coefficients of slip interface of 0.0 and 0.5 are 33.4kPa and 67.6kPa, respectively, which are close to the confining pressure of 34.5kPa and 68.9kPa in AASHTO standard. Therefore, the σ_c' in this paper were selected as 34.5kPa and 68.9kPa.

For the air-dried specimen, the S_r was 8.2%. All saturated specimens ($S_r=100\%$) were saturated by CO_2 method and the B-value of each saturated specimen was insured as 0.96 or more. For the unsaturated specimen, the S_r of specimen was about 35% by applying an intended suction of 10kPa. Reference [2] presents detailed operation approaches of consolidation for specimens with different S_r .

Upon attaining an equilibrium condition in the consolidation process, the specimen was continuously sheared by applying an axial deviator stress ($q=\sigma_a-\sigma_c$) at a designated loading rate of 0.05%/min or 0.5%/min under fully drained condition (CD test) regardless of the water content, while all other testing parameters were held constant. Here, σ_a is the axial stress. Note that the loading rate of 0.05%/min in drained test was selected based on the standard of Japanese Geotechnical Society (JGS 0527, 2000), while the loading rate of 0.5%/min was designed by referring to the axial strain rate of 1.0%/min in quick shear test of MR test [7].

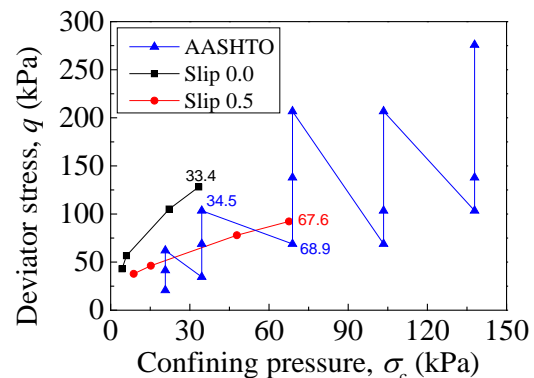


Fig. 4 Stress state inside typical Japanese pavement structures.

TEST RESULTS AND DISCUSSION

Stress-strain Behavior

Fig. 5 and Fig. 6 show typical relationships for air-dried, unsaturated and saturated specimens among the q , ε_v and ε_a obtained from CD tests under different loading rates at σ_c' of 68.9kPa and 34.5kPa, respectively. It should be noted that in Fig. 5(c) and Fig. 6(c), the results of volumetric strain were measured by gap sensors and burette under saturated condition. The dash dot lines denote the volumetric strains obtained by burette. As what to be confirmed previously, the two methods of gap sensors and burette were in reasonable agreement with each

other in the change of ε_v during shear up to the ε_a of 6 % approximately until the q reached peak. Accordingly, we do not adopt the ε_v calculated with the lateral displacements of the specimens measured by gap sensors as an experimental data in the range of ε_a of 6% or more from the viewpoint of the measurement precision.

According to set of curves in Fig. 5 and Fig. 6, the dense compacted C-40 exhibits strain softening behavior irrespective of loading rates during shearing process. With increasing ε_a , q sharply increases to the peak strength at ε_a of about 4% to 6%, and then it gradually decreases to the residual strength at $\varepsilon_a=12\%$ or over. Further, the volumes of all the specimens initially decrease, and then the specimens dilate with the increment of ε_a during shearing, irrespective of loading rates and S_r .

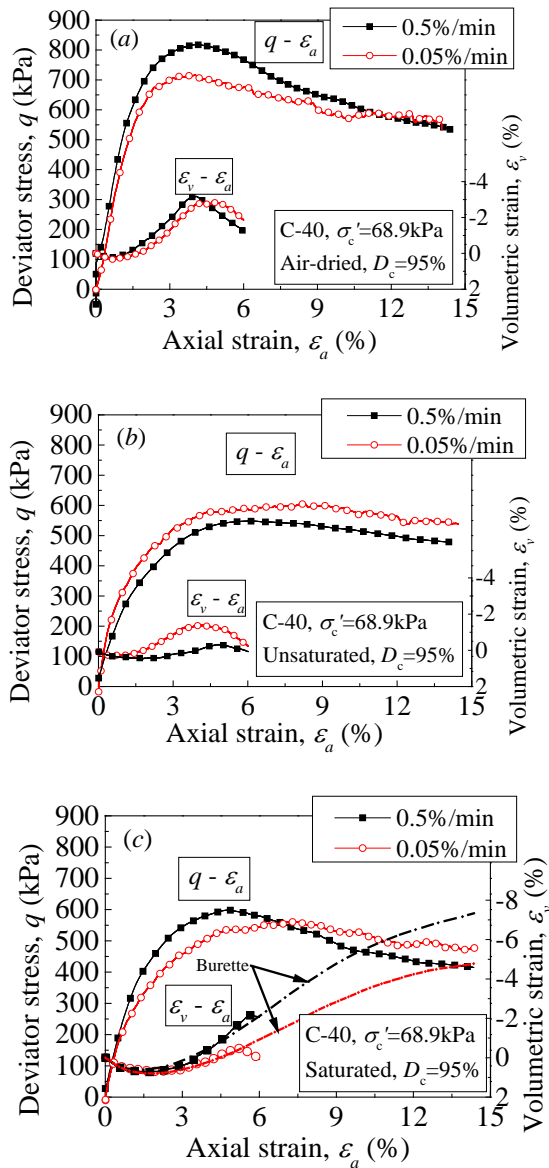


Fig. 5 Relationships among q , ε_v and ε_a under $\sigma'_c=68.9\text{kPa}$.

When comparing two curves obtained from tests under air-dried condition with different loading rates at the σ'_c of 68.9kPa and 34.5kPa as shown in Fig. 5(a) and Fig. 6(a), the results clearly show that behavior of C-40 was affected by loading rate. The q - ε_a relationship with higher loading rate locates above of that with lower loading rate and peak strength is increasing with increase of loading rate as shown in Fig. 7. The reason for the increase in peak strength would be related with corresponding volume changes during shearing as discussed in reference [8], which analyses from the view of particle crushing and rearranging during shearing. Since there is not obvious particle breakage on the basis of sieve analysis, the particle rearranging could be considered to play an important role in peak strength during shearing. As shown on ε_v - ε_a curves,

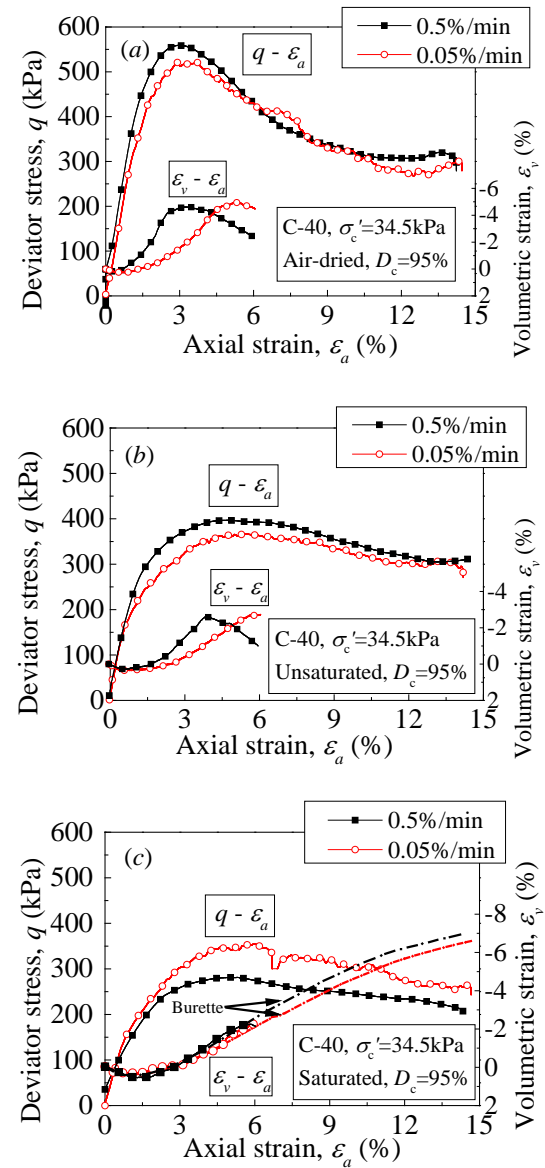


Fig. 6 Relationships among q , ε_v and ε_a under $\sigma'_c=34.5\text{kPa}$.

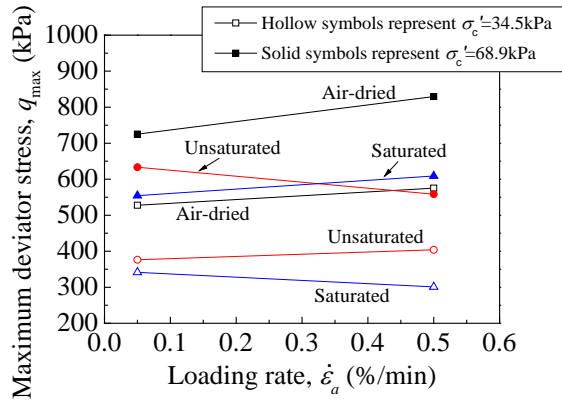


Fig. 7 Maximum deviator stresses related to different loading rate of all the tests.

specimens with higher loading rate are prone to dilation instead of compression. That is because the time for rearranging soil particle reduces, and then amount of particle compression decreases due to short of time. Therefore, the specimens are inclinable to expand. The same result is shown in reference [8] that higher strain rates induce volume change that are slightly less compressive than that in lower tests. These small amounts of volumetric compression changes make the specimens appear more dilation.

In case of unsaturated condition of σ'_c of 34.5 kPa as shown in the Fig. 6(b), the trend is consistent with those of the air-dried specimens, and specimen with higher loading rate exhibits more dilation than specimen with lower loading. However, opposite regulation obtained under σ'_c of 68.9 kPa that the larger loading rate is, the smaller the peak strength is as shown in Fig. 7. Since the two different trends discussed above are not satisfactory for each other, it would be desirable to redo unsaturated tests with loading rate of 0.5%/min under σ'_c of 68.9 kPa in the near future.

Saturated condition of σ'_c of 68.9 kPa are shown in Fig. 5(c), which shows specimen with higher loading rate has related higher peak strength. The reason for such phenomenon is associated with the volume change. The volume change with higher loading rate appears to be slightly less compressive while more dilated than that of slower loading rate. As for Fig. 6(c), it expresses that peak strength of higher loading rate is smaller than that of lower one. That is because the specimen with higher loading rate shows more compression during shearing.

Except loading rate, S_r related with suction also has a deep effect on strength characteristic of C-40. As shown in Fig. 7, with increase in S_r , the peak strength is decreasing, except the unsaturated test with loading rate of 0.5%/min under σ'_c of 68.9 kPa. The same result was obtained for rockfills by Kohgo [9]. Based on the reference [10], the resistance of soil to plastic deformation is strongly influenced by

shear resistance between grain contact points. It is supposed that the suction here is capillary force which acts perpendicularly on grain contact points and attracts soil particles together. Then this force restrains relative sliding between soil particles [11]. For this reason the peak strength is correspondingly increasing with decrease of S_r .

Influence on Strength Parameters

In order to show how to calculate strength parameters under different loading rates, the typical relationships between maximum deviator stress (q_{max}) and mean effective principal stress (p') are shown in Fig. 8. Here, Eq. (1) was employed to calculate mean effective principal stress (p') in saturated and air-dried soils, where the effective stress plays a main role for saturated condition and the pore water pressure (u_w) is equal to zero in air-dried condition [12].

$$p' = \frac{1}{3}(\sigma_a + 2\sigma_c) - u_w \quad (1)$$

Based on Fig. 8, the failure envelope can be plotted by linear fitting curve. Then friction coefficient, internal friction angle, and cohesion are expressed as Eq. (2), and Eq. (3) as in [12].

$$M = \frac{q_{max}}{P} = \frac{6 \sin \phi}{3 - \sin \phi} \quad (2)$$

$$c = b \frac{3 - \sin \phi}{6 \cos \phi} \quad (3)$$

Where, M represents friction coefficient, ϕ is internal friction angle, c signifies cohesion, and b is intersection of fitting curve on the vertical axis.

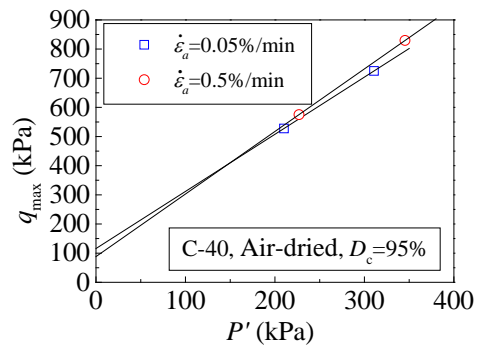


Fig. 8 Failure envelopes under air-dried condition of loading rate of 0.05%/min and 0.5%/min.

The calculated internal friction angles ϕ and cohesion c under different loading rates are shown in Table 3. Note, the ϕ and c in Table 3 were calculated by adding results under σ'_c of 49 kPa. The values of ϕ

under different loading rates are not the same. In air-dried and saturated condition, the corresponding ϕ increases slightly with the increase of loading rates, which agrees the result obtained by Yamauro and Lade [8]. While under unsaturated condition the ϕ reduces with decrease in loading rate, which is different regulation from above mentioned conditions, and it should be affected by the test result of unsaturated condition as mentioned previously. On the other hand, the loading rate is influential in the c . In air-dried and saturated conditions, with the increase of loading rate, the c decreases. While under unsaturated condition, when increasing the loading rate, the viscosity resistance increases. In conclusion, considering the different trends of c obtained from various degrees of saturation, more tests will be performed in near future.

Table 3 The strength parameters.

	ε_a (%/min)	M	ϕ (°)	c (kPa)
Air-dried	0.05	2.07	50.21	23.50
	0.5	2.15	52.23	19.88
Unsaturated	0.05	2.15	52.42	6.95
	0.5	1.80	43.71	27.90
Saturated	0.05	2.21	53.73	2.36
	0.5	2.30	56.10	1.25

CONCLUSION

The following findings were obtained from the present study:

- (1) Loading rate has strongly impact on shear behavior of granular base course material. Especially in air-dried condition, the shear strength of base course material increases with the increase in loading rate, and also specimens with higher loading rate are prone to dilation instead of compression.
- (2) Under air-dried and saturated conditions, internal friction angle slightly increases with increase in loading rate, while the cohesion decreases with the increase of loading rate.

REFERENCES

[1] Nishimura T, Koseki J, Fredlund DG and Rahardjo H, Microporous membrane technology for measurement of soil-water characteristic curve, *Geotechnical Testing Journal*, Vol. 35, No. 1, 2012, pp. 61-77.

[2] Ishikawa T, Zhang Y, Segawa H, Miura S and Tokoro T, Development of medium-size triaxial

apparatus for unsaturated granular base course materials, in *Proc. 2nd In. Conf. on ICTG*, 2012, pp. 534-540.

[3] Mori T, Kamiya K, Chiba T, Uzuoka R and Kazama M, The functional model of the soil-water characteristic curve used the logistic function during cyclic shearing, in *Proc. 44th Japan national Conf. geotechnical engineering*, 2009, pp. 1519-1520(in Japanese).

[4] Ishikawa T, Kawabata S, Kameyama S, Abe R and Ono T, Effects of freeze-thawing on mechanical behavior of granular base in cold regions, in *Proc. 2nd In. Conf. on ICTG*, 2012, pp. 118-124.

[5] Kato S and Kawai K, Deformation characteristics of a compacted clay in collapse under isotropic and triaxial stress state, *Soils and foundations*, Vol. 40, No. 5, 2000, pp. 75-90.

[6] Maina JW, and Matsui K, Developing software for elastic analysis of pavement structure responses to vertical and horizontal surface loading, *Transportation Research Record*, No. 1896, 2004, pp. 107-118.

[7] American Association of State Highway and Transportation Officials, Standard method of test for determining the resilient modulus of soils and aggregate materials (T 307-99), 2007, pp. T 307-1-T 307-42.

[8] Yamamuro JA and Lade PV, Effects of strain rate on instability of granular soils, *Geotechnical testing journal*, 1993, Vol. 16, No. 3, pp. 304-313.

[9] Kohgo Y, Asano I and Hayashida Y, Mechanical properties of unsaturated low quality rockfills, *Soils and Foundations*, 2007, Vol. 47, No. 5, pp. 947-959.

[10] Kohgo Y, Nakano M and Miyazaki T, Theoretical aspects of constitutive modelling for unsaturated soils, *Soils and Foundations*, 1993, Vol. 33, No. 4, pp. 49-63.

[11] Kohgo Y, Asano I and Hayashida Y, An elastoplastic model for unsaturated rockfills and its simulations of laboratory tests, *Soils and Foundations*, 2007, Vol. 47, No. 5, pp. 919-929.

[12] Nishimura T, Toyota H and Waguri M, Influence of high soil on angle of internal friction and cohesion for a statically compacted non plastic silty soil, *Japanese Geotechnical Journal*, 2008, Vol. 3, No. 4, pp. 321-329(in Japanese).

EXPERIMENTAL STUDY OF PLYWOOD COMPARING TO FOAM FILLED HONEYCOMB STRUCTURE

Phacharaporn Bunyawachakul, Chattarin Sunsin, and Thammakorn Sasanawin
Department of Aerospace Engineering, Faculty of Engineering, Kasetsart University, Thailand

ABSTRACT

In the current study, results of an experimental analysis of plywood panel used in Thailand for construction purposes are presented comparing to sandwich panel composed of two plywood sheets separated by a kraft paper core whose cells were filled with two different types of foam. The honeycomb core was initially formed in hexagonal shape. Flexural properties were determined according to the guidelines specified by the Thai Industrial Standard No.876-2547 for flat pressed particleboards (TIS No. 876-2547). The plywood samples were 25.4 mm x 350 mm, two-ply and five-ply, 6 mm and 15 mm thick. They were fabricated both face grain parallel and perpendicular to span direction to test in order to identify flexural stiffness, flexural strength, shear stiffness, and shear strength. The sandwich beam samples were fabricated by filling PU and PVC foam into each cells of the core. The failure mechanism of each sample was observed and it was found that the sample failures were identical for the same type of specimen. The experimental result in this study will be implemented in a model that can be used to observe the correlation between the flexural strength and stiffness of plywood and foam filled honeycomb structure.

Keywords: Plywood, Honeycomb, Flexural properties, Shear properties, Failure

INTRODUCTION

In Thailand, plywood panels are widely used in construction, furniture, interior decoration, and flooring purpose. Market survey shows several plywood products in common trade name, such as black coated plywood, natural teak plywood, engineered teak plywood, commercial plywood, Medium-Density Fiberboard (MDF), Particleboard or chipboard, Oriented Strand Board (OSB), and others. All plywood panels as mentioned use different type of wood species to fabricate. It is hard to classify following any standard as shown in [1] because we use tropical wood to be basic sheet to manufacture. From the list of common trade name of plywood in Thailand, the plywood type covered by this paper is classified by type of cover sheet and by price without specific structural meaning as follows:

Table 1 List of plywood in Thailand

Plywood type	Cover sheet	Price
Black coated	synthetic	high*
Natural teak	teak	medium
Engineered teak	synthetic	medium
Commercial	tropical wood	low
MDF/ Particleboard or Chipboard	synthetic	vary
OSB/others	Imported wood	medium

*reusable 5-8 times.

This paper focuses on commercial plywood type which uses tropical wood for fabrication and has low price as shown in Table 1. In the market, plywood panel has standard size about 1.22 m x 2.44 m with available thickness range from 3 mm to 20 mm. Not all thicknesses are readily available. Plywood panel having thickness of 3 mm is selected in this study. The panel is constructed of small pieces of wood united under pressure and temperature by a bonding agent. The face and back plies are also covered by tropical wood sheet and have the grain direction oriented parallel to the long dimension of the panel. It is usually found in indoor application and can make more benefits in case of knowing structural limitation.

Additionally, in recognition of required mechanical properties for each plywood panel, it is very interesting to compare their strength when the panel is separated by other lightweight materials, called sandwich structure. This type of structure consists of two thin but stiff face sheets attached to a lightweight thick core as shown in Fig.1. The core supports shear load and increases flexural stiffness and strength to the overall structure.

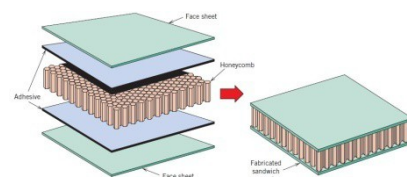


Fig. 1 Schematic of honeycomb structure. [2]

The flexural stiffness and strength efficiency of sandwich panel are illustratively compared to solid plate in Fig.2. Solid plate is split at the middle of its thickness then inserted by a typical core material having the same thickness as solid plate and double. The result is two more sandwich panel with 2 and 4 times of the total thickness. Two new panels present very good flexural stiffness and strength. By doubling the thickness of the core material, the flexural strength is increased by 3.5 with only 3 percent of additional weight while 9.2 is the flexural strength number for tripling the thickness of the core material. The maximum core thickness panel gives sandwich structure having 37 times of flexural stiffness while only 6 percent of weight increasing is observed.




	Solid Material	Core Thickness t	Core Thickness $3t$
			
Stiffness	1.0	7.0	37.0
Flexural Strength	1.0	3.5	9.2
Weight	1.0	1.03	1.06

Fig. 2 Comparison of solid and sandwich beam in terms of weight, flexural stiffness, and strength. [3]

In this study, commercial plywood is used as face sheets. Porous materials, e.g., foam, paper or metallic formed in different shape, are commonly used for core material. More details on the various core materials are demonstrated in [4-7]. Basically, foam is the most famous to be selected as core material in general application because of its variety and continuity in macroscopic scale. However, in high performance application, Nomex core or Rohacell or honeycomb as shown in Fig.1 are widely used due to high strength to weight ratio. This paper will investigate the combination of foam and honeycomb as core material. Sandwich panels which the cell were filled by foam are studied in order to expanded requirements for construction and industrial uses.

Survey on the selection of the core material is in this paragraph. Many core materials were listed from market place in Thailand. Kraft paper in hexagonal shape, polyurethane (PU), and Polyvinyl chloride foam (PVC) have light weight and suit to be selected for sandwich panel construction due to ease of fabrication and cost. The benefits of PU foam are used to prevent heat, cold, acid, and alkali. PU foam has usually lightweight and strong. The benefits of the PVC foam are lightweight, weather-resistant, heat and sound insulation, and excellent protection against chemicals substances.

RELATED THEORY

The typical sandwich beam theory is used in this paper to calculate the deflection of sandwich beam. Consider a simply supported sandwich beam of span l and width b loaded in three-point bending with a central load P as illustrated in Fig.3.

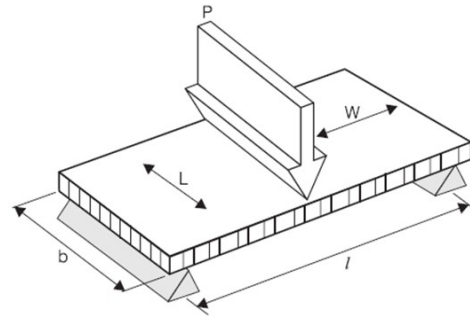


Fig. 3 Beam with central load and simple support condition. [3]

The beam deflection or vertical displacement of the beam is induced by bending and shear with assumption of perfect bonding of the whole panel, and it can be obtained from the equation:

$$\delta = \frac{2Pl^3}{48E_s t_s^2 h^2 b} + \frac{Pl}{4bhG_c} \quad (1)$$

where δ = Mean deflection of the beam
 E_s = In-plane Young's moduli of the skin
 t_s = Skin thickness
 h = Beam thickness
 G_c = Out-of-plane shear modulus of the core

The beam deflection depends on some parameters of sandwich beam material properties in Eq. (1), for example, E_s and G_c . The first unknown properties can be obtained by a variety of reports conducted by three-point bending test of plywood panel with a simply supported beam of span l loaded with a central load P . The beam will be deformed under the effect of bending moment and shear force controlled by support distance. The longer support distance gives lower effect of shear force. Therefore, the deflection of beam in classical beam theory can be calculated as;

$$\Delta = \frac{Pl^3}{48EI} + \frac{Pl}{AG} \quad (2)$$

where Δ = Mean deflection of the beam
 E = Young's moduli of beam material
 I = Moment of Inertia
 A = Cross-sectional area of the beam
 G = Shear modulus of beam material

From Eq. (2), the longer number of support span makes more effects on the beam deflection by the first term. In contrast, if the beam is short, the second term in Eq. (2) will play more important role.

PLYWOOD PROPERTIES INVESTIGATION

Many of the questions that arise with plywood application have to do with mechanical properties of plywood, especially properties of plywood in Thailand compare with those of plywood in other country. The mechanical property data was presented in many reports show a wide range of the properties [8] occurred in the manufacturing of plywood and correspondingly changes in design information. There are several standard test methods for evaluation of the basic properties of plywood, for example, Young's modulus, modulus of rigidity, and strength properties. The procedure to determine Young's modulus is described in TIS No. 876-2547 which the flexural stiffness of the board can be calculated from test (Fig.4).

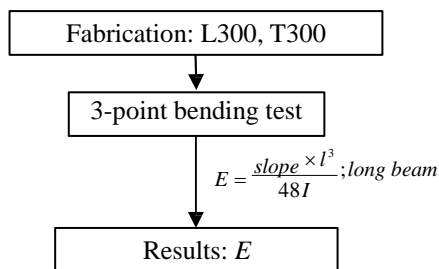


Fig. 4 Diagram for plywood testing procedure.

Specimen manufacturing

One test piece was cut from 3-mm thick plywood panel in two different directions of the grain of outer layer: parallel and perpendicular to the longitudinal axis of the specimen. Both layers were bonded together under pressure forming specimen with total thickness of 6 mm indicated by L300 and T300 (Fig. 5). 'L' and 'T' denote the outer face ply of specimen in longitudinal and transverse direction respectively. The test specimens measured 350-mm in length, 25.4-mm in width, and the distance between the supports was 300-mm as indicated by following number '300'. Three specimens of each type are manufactured to investigate flexural stiffness by experiment.

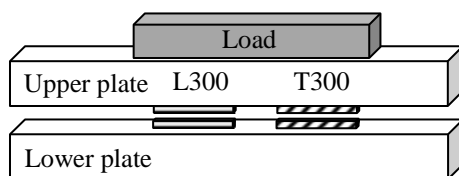


Fig. 5 Fabrication of L300 and T300 specimen.

The following study is focused on comparing the flexural stiffness of sandwich beam. The dimension of all specimens is 25.4 mm x 350 mm. Four types of sample were fabricated based on the same effective thickness of 15 mm. The 15 mm thick specimens are:

- 1) LO: 5-ply of plywood with [L/T/L/T/L] orientation (see in Fig. 6)
- 2) 4SLOT: Sandwich beam consists of a Nomex honeycomb core with a cell size of 12.5 mm and a density of 270 kg/m³. The skin is 3-mm thick plywood panel with outer face orientation parallel to beam axis (see in Fig. 7)
- 3) PU: 4SLOT sandwich beam filled the honeycomb cells with PU foam (see in Fig. 7)
- 4) PVC: 4SLOT sandwich beam filled the honeycomb cells with PVC foam (see in Fig. 7)

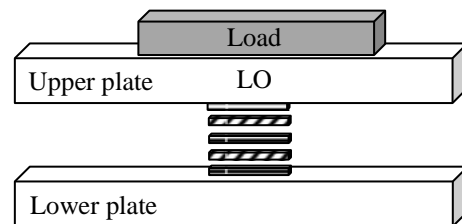


Fig. 6 Fabrication of the LO specimen.

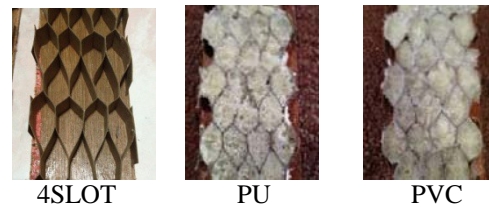


Fig. 7 Typical photograph of 4SLOT, PU, and PVC specimen before attaching upper skin.

Testing procedures of the 15-mm thick specimen

The modulus of rigidity, load at yield, and load at peak of these specimen configurations are to be investigated. The bending tests were conducted on a Testometric MICRO 500 50 kN universal testing machine. Samples were installed in the compression zone of test unit between the support base of 300 mm and the thrust punch at its central point. Regardless of dynamic response of the beam, only one cross-head speed was done. The test is performed under quasi-static condition with cross-head speed of 0.5 mm/min. The data acquisition system which was linked with the Testometric machine was used to record all the necessary results

including the maximum load or load at peak, average load, vertical displacement or deflection, and useful related mechanical properties. Photograph of PU and PVC specimen are illustrated in Fig. 8. During the test, sample failure behaviors were observed and recorded to identify the loss of linear proportion of the load-deflection curve.



Fig. 8 PU and PVC specimen.

RESULTS AND DISCUSSIONS

Two-ply Specimen

Load-deflection curves of representative 2-ply specimens in the bending test are illustrated in Fig. 9, showing the flexural stiffness of the L300 and T300 specimens in different value with a high level of reproducibility for each sample type. The flexural stiffness is higher for the samples having face grain parallel to span direction with 5.77-6.29 GPa, compared to 1.3-1.88 GPa of T300 (see in Table 2). Compared to few studies in [9] and information about a variation of these properties, the Modulus of elasticity of plywood is 6.96-8.55 GPa. The results obtained by tropical wood-based plywood in Thailand as shown by L300 bending test are slightly less than international product which is probably caused by temperature and moisture content.

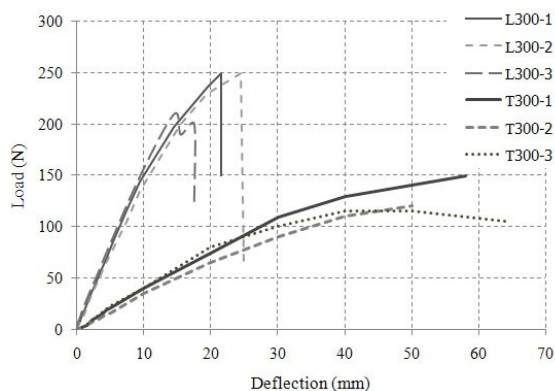


Fig. 9 Load-deflection curve of 2-ply specimen.

The failure scenario is also investigated during the test. It is obvious that the T300 specimen is very flexible and can be deflected as much as the cross-

head moves down as shown in Fig. 10 while the deflection of the L300 specimen is limited at 15-25 mm by a total rupture at static peak load.

As observed in Fig. 9, a slight drop of the load level applied to the L300 specimen is appeared about 150-160 N, then the upper and lower skin start to crack until reaching the maximum load-carrying capacity of the sample in bending at about 35-45 percent of peak load as shown in Table 2. To investigate failure behavior from the first to final damage for both specimens, the glue-bonding between plies was in good condition. Fig. 10 shows the L300 specimen at break and T300 one at stop that no slipping between the layers is found. Only some noises were observed after the first damage indicated by a slight loss of slope was reached as shown Fig. 9. The total failure of L300 specimen can be seen by a sudden drop caused by the outer face grain's fiber breaking of its upper and lower face skin which the highest flexural stress is basically occurred.



(a) L300 test

(b) T300 test

Fig. 10 Photographs of (a) L300 specimen at break and (b) T300 specimen at stop.

Comparison of the first damage of both specimens, it is found that L300 can carry higher load at yield at approximately 2 times. So the strength shall be about 2 times as well by using the same rectangular size in cross section. The same effect is occurred in case of the ultimate load as shown by load at peak in Table 2.

Table 2 Elastic modulus, load at yield, and peak load of the L300 and T300 specimens.

Sample type	E (GPa)	Load (N)	
		@yield	@peak
L300-1	6.21	150	250
L300-2	5.77	160	250
L300-3	6.29	160	210
T300-1	1.72	60	150
T300-2	1.30	55	125
T300-3	1.88	80	115

There is more information about failure scenario for 2-ply sample of two different orientation angles. The load-deflection curves of L300 sample is obviously illustrated into two main parts: the elastic

and plastic zone. The first zone represents the linearity of the curve, whereby the sample deformed as a part of circle regardless of shearing effects. The second zone show plastic behavior of the sample, whereby the sample is still intact until the lowest point touched the machine base about 70 mm so the test was stopped. No catastrophic failure appears to T300 sample after removing the load. This would be advantage of T300 to be good performance in energy absorption.

Fifteen-mm thick Specimen

As previous mentioned, four types of specimens under flexural test are performed as follows:

LO samples

The load-deflection response of three LO samples is shown in Fig. 11. At the start, all the LO specimens were pressed at the mid-point of the supports. The load increased with displacement linearly up to the first damage at a variation of load from 400 to 520 N (see in Table 3). The flexural stiffness of all the specimens was found by this linearity to be the same, which is not surprising since it is determined by the intrinsic material properties. After the first damage, a slight increasing of load was applied till the first drop was occurred. Three tested specimens had different response after the drop. Two-third could be recovered as seen in additional exerted load. However, an increasing load after the first drop was less than the first peak and samples were broken. The maximum load is 620-760 N. With respect to the sheared surface A, this results in a shear strength of 1.63-1.99 MPa:

$$\tau = \frac{P_{\max}}{A} = \frac{620 \text{ N}}{25.4 \text{ mm} \cdot 15 \text{ mm}} = 1.63 \text{ MPa} \quad (3)$$

The shear strength properties vary because of different failure modes corresponding to crack between layers and outer skin fiber breaking.

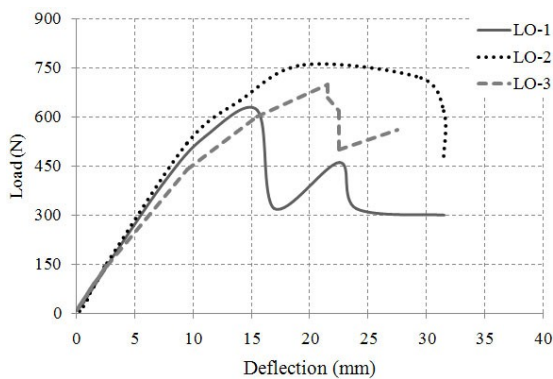


Fig. 11 Load-deflection curve of the LO specimen.

Table 3 Weight, shear modulus, load at yield, and peak load of the 15-mm thick specimens.

Sample type	Weight* (g)	G (MPa)	Load (N)	
			@yield	@peak
LO-1	158.5	24.24	400	620
LO-2		27.44	520	760
LO-3		17.18	440	700
4SLOT-1	87	11.59	97	161
4SLOT-2		28.28	153	187
4SLOT-3		21.97	157	174
PU-1	95	8.72	99	154
PU-2		8.68	93	190
PU-3		5.45	55	150
PVC-1	100	7.78	55	125
PVC-2		5.56	60	150
PVC-3		5.17	80	115

*average value

4SLOT samples

Three load-deflection curves of 15-mm thick 4SLOT samples are almost congruent for the elastic regime until the first failure occurs as illustrated in Fig. 12. From experimental results, two specimens show the load has two peaks. The second peak is higher than the first peak. Load level is gradually increased after the first drop except one specimen. However, the second slope seems to coincide for all specimens testing results. It corresponds to failure of the bonding between skin and core as observed during the test. The separation started from the end and grew to the centre of the sample. At this point, skins and core individually work to resist the bending. Sudden and dramatic drop occurs indicating an outer face rupture which visually appears during the test. Shear strength which is calculated by Eq. (3) yields 0.44-0.46 MPa. The deflection reaches a large amount at breaking point.

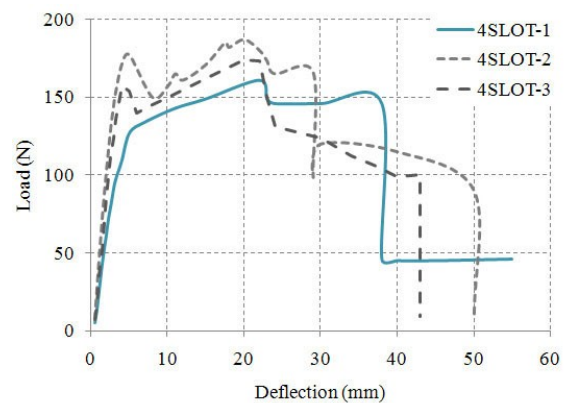


Fig. 12 Load-deflection curve of the 4SLOT samples.

4SLOT, PU, and PVC samples

Fig. 13 shows three curves obtained from one of each type of sandwich beam specimen. The trend of PU and PVC specimen was found to be similar to the 4SLOT sample. There were crack growth from the edge to the center of sample during a constant force level from the deflection of 3-35 mm. Photograph of PU specimen when the maximum load was reached are illustrated in Fig. 14. The flexural stiffness of all three types are close each other. Shear strength which is calculated by Eq. (3) yields 0.3-0.4 MPa. The filled foam specimen has shear strength less than the sample without foam filling. This drop is observed by many defects from manufacturing processes. The slipping is occurred by imperfect bonding between skin and core.

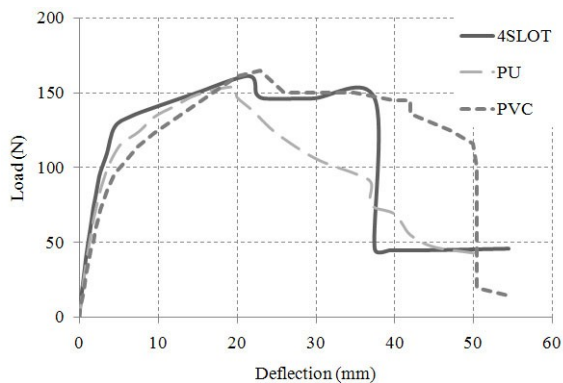


Fig. 13 Comparison of load-deflection curve in experiment for 4SLOT, PU, and PVC samples.



Fig. 14 Load at peak of PU specimen testing.

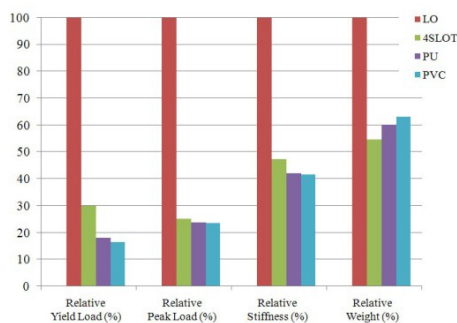


Fig. 15 Bar chart of the 15-mm thick samples test.

From a summary bar chart in Fig. 15, the height of the bar shows comparison of load at yield, load at peak, shear modulus, and weight based on LO specimen. For sandwich sample, the two first terms is relatively low with the imperfect bonding during manufacturing processes.

CONCLUSION

The modulus of elasticity of tropical wood-based plywood in Thailand is identified with slightly less value than international standard plywood. These properties can be useful for Thailand construction industry. The development of a finite element modeling will be validated by implementation of the flexural properties obtained from testing results. Manufacturing processes and environmental control is needed for specimen fabrication. The bonding plays very important role to increase strength of the sample.

REFERENCES

- [1] ASM Handbook: Composites Vol. 21. Ohio: ASM International, 2001.
- [2] Voluntary Product Standard: PS1-95 Construction and Industrial Plywood. Washington: APA-The Engineered Wood Association, 2002, sec. 4.
- [3] Hexcel composites, "HexWeb™ Honeycomb sandwich design technology", 2000.
- [4] Bitzer T, "Honeycomb Technology: Materials, Design, Manufacturing, Applications and Testing", Chapman & Hall, 1997.
- [5] Zenkert D, "The Handbook of Sandwich Construction", EMAS/Engineering Materials Advisory Services Ltd., 1997.
- [6] Strong AB, "Fundamentals of Composites Manufacturing: Materials, Methods and Applications", 2nd ed., SME/Society of Manufacturing Engineers, 2008.
- [7] Marshall AC, "Lightweight Structural Cores, ASM Handbook: Composites", ASM International, 2001. Composite Basics, Marshall Consulting Publishing, 7th ed., Vol. 21, 2005, pp. 180-183.
- [8] Biblis EJ, "Effect of weathering on surface quality and structural properties of six species of untreated commercial plywood siding after 6 years of exposure in Alabama", Forest Products Journal, Vol. 50, 2000, pp. 47-50.
- [9] Cai Z and RJ Ross, "Wood Handbook, Chapter 12: Mechanical Properties of Wood-Based Composite Materials", General Technical Report FPL-GTR-190, Madison, WI: U.S. Department of Agriculture, Forest Service, Forest Products Laboratory, 2010, pp. 12-1-12-12.

X-RAY IMAGE ANALYSIS OF POROSITY OF POROUS CONCRETES

Jaehun Ahn¹, Jinwoo Jung² and Seungbae Kim³

¹Faculty, Pusan National University, Korea; ^{2,3}Student, Pusan National University, Korea

ABSTRACT

The use of permeable pavement is one of most promising tools to control runoff and water quality, therefore enabling low impact development, along with several other benefits. The porosity of the permeable pavement is the most important property of the pavement in current state of the practice. In this article, the porosity of a porous concrete sample made in laboratory was evaluated by two approaches: measuring weights and X-ray image analysis. Two different X-ray equipment, 2D and 3D, were used to construct cross-sectional planar images of a cylindrical porous concrete sample. It was found that the porosity estimate from 2D X-ray was close to the results with measuring weights, but that of 3D X-ray was rather larger. The difference in porosity (not ratio) from 2D X-ray and weight measurement was about 2%, but the differences from 3D X-ray and weight about 9%. The observed trend corresponds to the authors past experience with field core sample.

Keywords: Porosity, Porous Concrete, Permeable Pavement, Green Infrastructure, Low Impact Development

INTRODUCTION

In urban area, many traffic infrastructures such as highways, parking lots, sidewalks, and small roads (say, for bike) are paved, and therefore impervious, which adversely affect the stormwater management as these infrastructures generally replace natural permeable greens or at least soils with impervious paved surface. In addition to the effective control of runoff, the pervious pavement are told to have more benefits such as skid resistance, water quality control, noise control, and surface temperature decrease.

The concept of pervious pavement is, though, not very new but some of early pervious pavements have been a couple of decades, and there are some but no unified design guides available (NRMCA, 2004; Paul et al., 2004; John et al., 2009; ACI, 2008; ACI, 2010). In current state of the practice, the most important property of pavement material is the porosity, the ratio of the volume of internal pore and the gross (total) volume of the pavement.

Montes et al. (2005) used the submerged weight of the pervious concrete for porosity estimation, and Neithalath et al. (2006) the difference of saturated and drained weights of the concrete. There are also studies that utilize the X-ray image to identify the pore in porous materials: concrete, asphalt, and geotechnical materials (Jung et al., 2011; Kim et al., 2012; Kang et al., 2012).

This paper presents the preliminary results on the estimation of the porosity of a laboratory porous concrete sample using X-ray images.

POROUS CONCRETE

A porous concrete sample with 4.8-cm diameter and 8.5-cm length was made in laboratory as shown in Fig. 1. The crushed stone was used for aggregates of the concrete sample. Before mixing, the crashed stone was screened to be in 1.18 ~ 2 mm range, and washed 3 times with water. Portland cement was used as a binding material; the mixture proportion is shown in Table 1.



Fig. 1 Porous concrete sample

Table 1 Mixture proportion

Material	Weight per volume (kg/m ³)	Content (%)
Aggregate	1,590	70.7
Cement	477	21.2
Water	183	8.13
Total	2,250	100.0

Montes et al. (2005) used the submerged weight of the pervious concrete for the porosity estimation. In this paper, the porosity estimation was made

following the work of Montes et al. (2005). The porosity P of porous concrete can be estimated based on the following equation.

$$P = 1 - \frac{(W_D - W_S)}{\gamma_w V_T} \quad (1)$$

where W_D and W_S are the dry and submerged weights of the sample, V_T is the total volume and γ_w is the unit weight water.

The submerged weight of the pervious concrete sample was measured by using the electronic scale and a wired mesh basket attached shown in Fig. 2.



Fig. 2 Equipment to measure the submerged weight

The sample was saturated more than 3 hours under water to measure W_S . For the measurement of W_D , the saturated sample was drained in the air for 24 hours and assumed that the sample is in saturated-surface-dry condition. The 3-hr saturated and 24-hr air-drained weights were 147.47g and 247.69g, respectively. Given the volume of the sample 153.81 cm^3 , the porosity was calculated to be 34.8%.

X-RAY IMAGE ANALYSIS

X-ray CT is a powerful tool to look inside the sample of a porous material and analyze the pore characteristics. Pusan National University has three X-ray machines with different specifications. In this study, two X-ray equipment (one 2D and one 3D) with the specifications in Tables 2 and 3 were used to get the images of the pervious concrete sample.

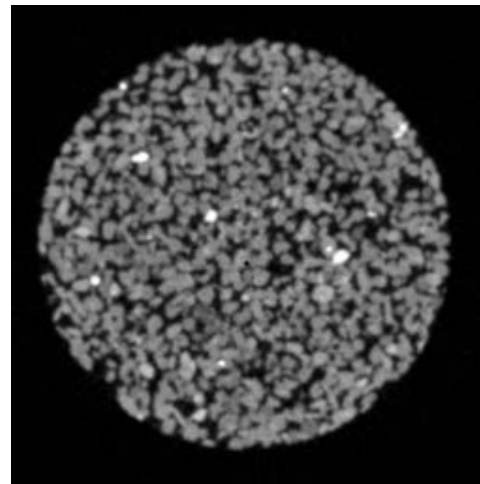
Table 2 Specifications of 2D X-ray equipment

Item	Description
Manufacturer	X-Tek
Model number	VENLO450-ACTIS
X-ray tube voltage	450 kV
X-ray tube current	4.8mA

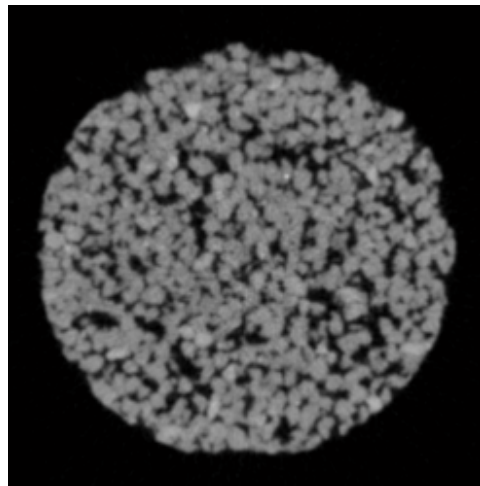
Table 3 Specifications of 3D X-ray equipment

Item	Description
Manufacturer	X-Tek
Model number	HMK CT – 225
X-ray tube voltage	225Kv
X-ray tube current	1.0mA

Fig. 3 presents the planar images from 2D and 3D X-ray equipment. It was found that the image from 3D X-ray was not clear with more noise than that of 2D X-ray. (Noise may be observed better in Fig. 4.)



(a) 2D X-ray



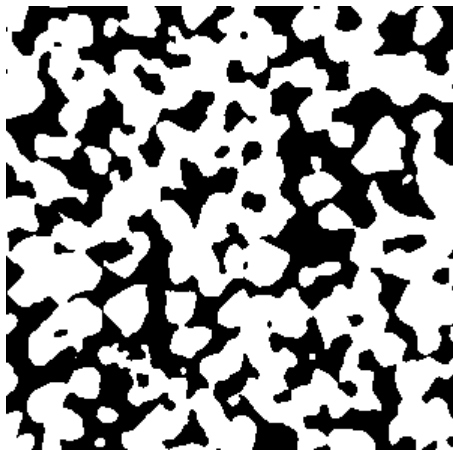
(b) 3D X-ray

Fig. 3 Planar images from X-ray equipment

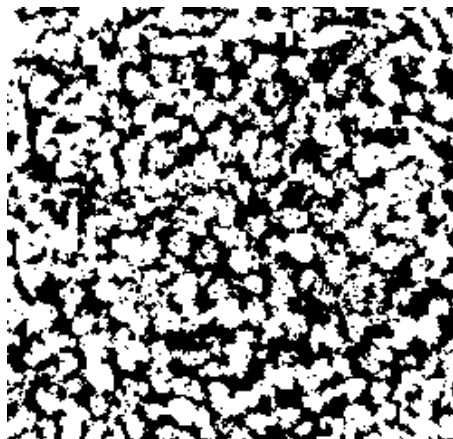
For image processing and estimation of the porosity, the image inside the sample was first cropped. Given cross-sectional images were 16-bit grayscale, which means that $2^{16} = 65536$ gray levels can be used to represent different shades of gray from black (gray level = 0) to white (gray level = 65535). To distinguish the pore (dark) from the solid (bright), the cropped images were converted to

purely black and white image by taking the limit of black and white based on the Otsu's method (Otsu, 1979) implemented in MATLAB Image Processing Toolbox (MathWorks, 2011). Based on black and white images in Fig. 4, the numbers of black and white pixels were counted; the number of black pixels over the total pixels makes the porosity.

The results of porosity estimates are presented in Fig. 5 with respect to the depth of the sample. The averages of the porosities from 2D and 3D X-ray equipment are 37.9% and 44.2%, respectively. It is noted that the result of 2D equipment is closer to the porosity measured using submerged weight 34.8%. This trend corresponds to authors' experience with another sample (field core). In case of field core, the porosity from weights was 29.9%; the results from 2D and 3D X-rays were 30.9 and 35.2, respectively.

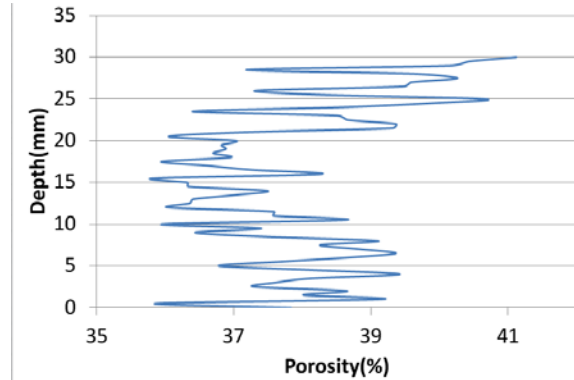


(a) 2D X-ray

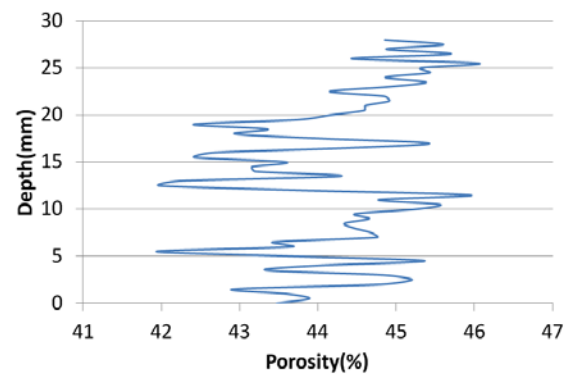


(b) 3D X-ray

Fig. 4 Black and white images



(a) 2D X-ray



(b) 3D X-ray

Fig. 5 Porosity with depth

DISCUSSION

There are several sources to make scatters in the porosity values based on both weight measurement and X-ray image analysis. In evaluating the porosity from Eq. (1), the sample should be completely saturated when the submerged weight is measured. The weight of drained or dried solid sample can also differ corresponding to how it was drained or dried. As of X-ray image analysis, first concern is to take X-ray image of the sample under proper setup, that is tube voltage and current, which may determine the quality of the image. Then, proper image processing should be done to filter out noise and scatters, which was conducted by commercial software VGStudio (2004) in this paper. The limit of black and white, which is void and solid, should be properly made, and in fact there is no real proof that the limit value based on Otsu's method (Otsu, 1979) is correct. The fact that the results of Eq. (1) and 2D X-ray image are close may sooth this argument, but does not clear out. But still the X-ray image analysis will be a useful tool inspecting pore spaces of the pervious pavement; for example, Kayhanian et al. (2012) was able to successfully inspect the degradation of the porosity of the permeable concrete pavement due to clogging.

CONCLUSION

The porosity of the porous concrete material was evaluated by measuring weights and analyzing images from two different X-ray machines in this paper. The result from 2D X-ray was close to that of weight measurement; not the case for 3D X-ray. The averages of the porosities from 2D and 3D X-ray equipment are 37.9% and 44.2%, respectively. This trend corresponds to authors' experience with a field core sample.

In near future, authors plan to investigate the effect of gradation of aggregate in porous concrete on the pore shape and hydrologic performance of porous concrete. The saturated and unsaturated permeability of porous concrete will also be investigated.

ACKNOWLEDGEMENTS

This work was supported by the National Research Foundation of Korea (NRF) grant funded by the Korea government (MEST) through the Mid-Career Researcher Program (2012-047702) and the Human Resource Training Project for Regional Innovation (2011-07-Univ-04-034).

REFERENCES

- [1] ACI Committee 522.1-08 (2008) Specification for pervious concrete pavement an ACI standard, American concrete institute.
- [2] ACI Committee 522R-10 (2010) Report on pervious concrete, American concrete institute.
- [3] John, T.K., Wang, K. and Vernon, R.S. (2009) Test methods for characterizing air void systems in Portland cement pervious concrete, Journal of ASTM International, 6(9)
- [4] Jung, Y.J. and Yun, T.S. (2011) Quantification of 3D pore structure in glass bend using micro X-Ray CT, KGS collection of dissertations, 27(11), 83-92.
- [5] Kang, D.H., Yun, T.S., and Kim, K.Y. (2012) Image processing techniques relevant to geomaterials, Advances in civil, environmental, and Materials research, ACEM'12(August 26-30)
- [6] Kayhanian, M., Anderson, D., Harvey, J.T., Jones, D. and Muhunthan, Balasingam. (2012) Permeability measurement and scan imaging to assess clogging of pervious concrete pavements in parking lots. Journal of Environmental management, 95(2012), 114-123
- [7] MathWorks. (2011) MATLAB R2011b, <http://www.mathworks.co.kr>.
- [8] Montes, F., Valavala, S. and Haselbach, M.L. (2005) A New test method for porosity measurements of portland cement pervious concrete, Journal of ASTM International, January 2005, 2(1).
- [9] Neithalath, N., Weiss, J. and Olek, J. (2006) Characterizing enhanced porosity concrete using electrical impedance to predict acoustic and hydraulic performance, Elsevier cement and concrete research, 36 (2006), 2074-2085.
- [10] Otsu, N., "A Threshold Selection Method from Gray-Level Histograms," IEEE Transactions on Systems, Man, and Cybernetics, 9(1), 1979, 62-66.
- [11] Paul, D.T., Michael, L.L. and David, J.A. (2004) Pervious concrete pavements, Portland Cement Association, Illinois.
- [12] VGStudio MAX (2004) User's Manual Version 1.2

STRESS - STRAIN BEHAVIOUR OF SLAG CEMENT CONCRETE

Mustapha BOUKENDAKDJI
College of Engineering, University of Hail, Saudi Arabia

ABSTRACT

The paper describes the results of test carried out on OPC concrete and slag cement concretes. Ten blended slag-cement concretes, made with typical slags from four countries (United Kingdom, Belgium, South Africa and Japan), are compared with a control OPC concrete. The slags replaced 30 to 70% of cement by mass. The bobbin shaped specimens were used in the direct tension test and 300x150 mm dia. cylindrical specimens were used in the axial and lateral strain tests. Poisson's ratio in compression was determined as the ratio of the lateral to axial strain at the ages of 14 and 84 days. Concretes at the age 84 days exhibits more linearity than at the age of 14 days and slag concrete becomes more brittle when stored in the dry environment. There was no difference between the Poisson's ratio of slag and OPC concretes.

Keywords: Slags, Stress-strain, Compression, Tension, Poisson's ratio

INTRODUCTION

The main objective of this investigation was to study the stress-strain of concrete containing different slags as a cement replacement in compression and tension.

From typical stress-strain curves for aggregates, hydrated cement paste, and concrete loaded in uniaxial compression, relative to aggregate and cement paste, concrete is really not a linear elastic material. The deformation of concrete under a short-term loading has been shown to be directly related to progressive internal microcracking at both the cement paste-aggregate interface and through the mortar itself [1], [2]. The non-linearity of the stress-strain relation is related to the cumulative effects of this cracking. Such microcracking occurs as a result of differential volume changes between the cement paste and the aggregate, i.e. due to differences in stress-strain behaviour, and in thermal and moisture movements.

The rate of strength development at early ages is generally inversely proportional to the amount of slag used in the blend because the initial rate of reaction of slag and water is slower than that of OPC and water [3]. Brooks and Neville [4] found that the secant modulus in tension is greater than that in compression and Stutterheim [5] found that for water-stored specimens Poisson's ratio was substantially the same irrespective of the cement type and ranged between 0.23 and 0.3.

EXPERIMENTAL DETAILS

The materials used to make eleven concretes were ordinary Portland cement (OPC), ground granulated blastfurnace slag and quartzitic

aggregate. Slags were obtained from the U.K., Belgium, Japan and South Africa. Chemical analysis and physical properties are given in Table 1.

Table 1 Chemical analysis of OPC and slags (%)

	OPC	U.K. slag	B. slag	S.A. slag	J. slag
SiO ₂	20.5	36.11	33.08	38.59	32.99
Al ₂ O ₃	5.79	10.84	12.93	12.94	15.20
Fe ₂ O ₃	2.50	0.38	1.17	0.56	0.37
CaO	65.8	40.45	39.80	35.02	42.49
MgO	1.25	9.46	9.79	9.40	6.22
MnO	0.08	0.57	0.50	1.07	0.49
TiO ₂	0.25	0.70	0.57	0.64	0.98
Sulphur	0.97	1.22	1.13	0.89	0.83
Sulphide	0.04	1.13	1.07	0.82	0.78
SO ₃	2.33	0.28	0.15	0.18	0.13
Na ₂ O	0.28	0.32	0.40	0.22	0.24
K ₂ O	0.62	0.51	0.60	0.78	0.36
L.O.I	1.27	1.78	0.98	0.05	0.53
Fineness (m ² /kg)	391	412	402	407	465

Potential compound composition

C ₃ S	62.73				
C ₂ S	11.59				
C ₃ A	11.12				
C ₄ AF	7.6				
chemical modulus		1.68	1.89	1.48	1.96

$$\text{chemical modulus} = \frac{\text{CaO} + \text{MgO} + \text{Al}_2\text{O}_3}{\text{SiO}_2}$$

The first concrete was an OPC control mix having mass proportions of 1:1.62:2.49 with a water/cement ratio of 0.43 and the cement content was 437 kg/m³. The ten slag concretes had 30 to 70% of the mass of OPC replaced by equal masses of slags, with the same aggregated proportions and water/cementitious ratio as the control concrete.

All moulded specimens were cured for 24 hours under wet hessian, then demoulded and cured in water for 13 days. Thereafter, the specimens were stored in two storage environments: in water at 20±2° C, and in air at 65±5% RH and 20±2° C.

The bobbin shaped specimens were used in the direct tension test and 300 x 150 mm dia. cylindrical specimens were used in the axial and lateral strain tests. The strain gauges used were 60 mm and 30 mm foil electrical resistance and were embedded in both the bobbin and the cylindrical specimens; the 30 mm gauges were used for lateral strain, and the 60 mm gauges for axial strain. The ages of testing were 14 and 84 days and the average curve of two specimens was obtained.

Secant modulus of elasticity in compression and tension were obtained at a stress equal to 0.3 of the strength. Poisson's ratio in compression was determined as the ratio of the lateral to axial strain at the ages of 14 and 84 days. In addition, for each mixture, 100 mm cubes were made to determine the compressive strength

TEST RESULTS AND DISCUSSION

Compressive Strength

Figure 1 shows the average influence of replacement of cement by slag on strength of water-stored concrete.

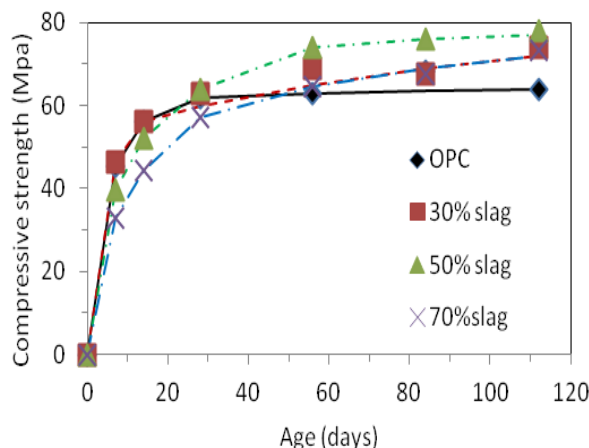


Fig. 1 Average influence of cement replacement by slag on compressive strength.

The behaviour follows the expected trend in that an increase of slag content reduces the early-age

strength, but later-age strengths are similar to, or slightly greater than, the strength of OPC concrete. For concrete stored dry from the age of 14 days, the strength was greater than for wet storage. The 300 x 150 mm dia. cylinder strength followed the same pattern, and the relationship between the two strengths was similar for both the wet and dry storage conditions. The mean and standard deviations of the cylinder to cube strength ratio was 0.82 ± 0.042 , which is close to the generally accepted ratio of 0.80.

Stress-Strain in Compression

Figures 2 to 4 show the stress-strength ratio plotted against axial and lateral strain as measured on 150 x 300 mm. cylindrical specimens for OPC, 50% U.K.slag and 50% S.A.slag cement concrete, respectively. It can be seen that the shape of the curves are similar for OPC and slag concretes. The maximum variability was ± 6 and ± 25% for the stress-strain test in axial and lateral, respectively.

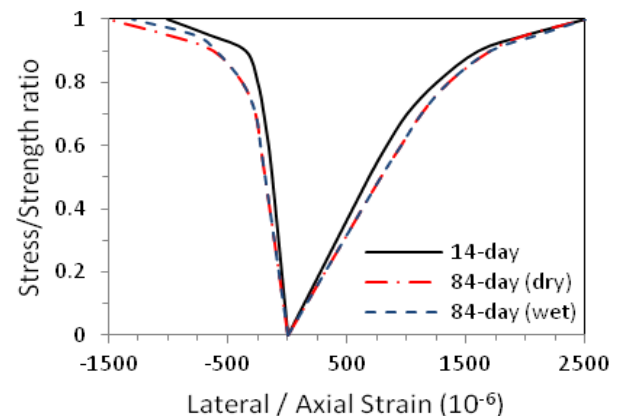


Fig. 2 Stress-strain curves for OPC concrete in compression.

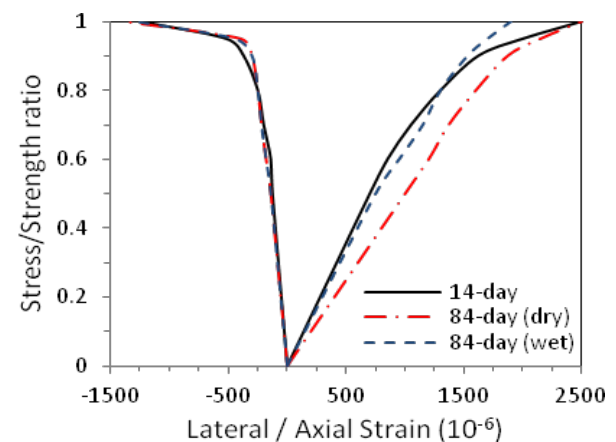


Fig. 3 Stress-strain curves for 50% U.K.slag concrete in compression.

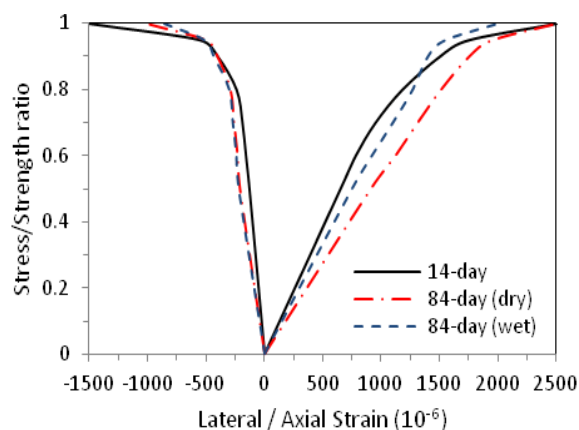


Fig. 4 Stress-strain curves for 50% S.A.slag concrete in compression.

The secant modulus of elasticity, as measured at a stress-strength ratio of 0.3 is shown in Table 2. Compared with OPC concrete, the 14-day values of slag-cement concrete are similar, but the 84-day strengths are greater. The 84-day modulus of dry-stored slag-cement concrete was less than for wet-storage by approximately 12%. However, for OPC dry-stored concrete, the 84-day modulus was 14% greater than for wet storage.

Table 2 Secant modulus of elasticity of water-cured OPC and slag concretes obtained from 150 x 300 mm cylinders (GPa)

Age (days)	14	84	84 *
Control Mix	31.5	33.9	38.6
U.K.slag 30%	27.8	37.1	33.8
50%	29.9	37.3	31.9
70%	27.4	38.6	33.2
B.slag 30%	30.4	35.1	30.9
50%	28.4	39.5	34.5
70%	27.6	35.5	32.3
S.A.slag 50%	30.6	41.6	36.8
70%	32.1	38.4	34.5
J.slag 50%	28.1	41.6	32.6
70%	26.1	35.9	33.7

* specimens were stored in dry environment after 14-days of water curing and tested dry.

A comparison of the strain at which the initial secant modulus decreased by 5% is made. A similar approach has been adopted previously by Kaplan [6]. The strain measured at this particular point is defined as the strain at the limit of proportionality (L.O.P.) and the values obtained are tabulated in Table 3. It appears that generally, the strain increases with age which implies concrete at the age 84 days exhibits more linearity than at the age of 14 days. This difference is probably due to the fact that the concrete tested at 84 days is stronger; Mindess and Young [7] have stated that stronger concrete exhibits a more linear stress-strain behaviour

because it leads to a higher bond-strength between aggregate and cement paste, and the curve also becomes more linear when the stiffness of the matrix approaches the aggregate stiffness and it is known that stiffness of the matrix increases with age.

Table 3 Axial strain in compression at limit of proportionality (L.O.P.) of OPC and slag concretes (Microstrain).

Age (days)	14	84	84 *
Control Mix	440	550	555
U.K.slag 30%	785	625	952
50%	672	555	1375
70%	745	932	1350
B.slag 30%	490	602	905
50%	640	930	860
70%	420	560	750
S.A.slag 50%	600	945	917
70%	350	864	1400
J.slag 50%	410	575	950
70%	420	920	1010

* specimens were stored in dry environment after 14-days of water curing and tested dry.

It seems that while the effect of storing slag concrete specimens in the dry environment is to increase the strain at L.O.P., compared with those stored wet, there was no effect on OPC concrete. Therefore, it can be concluded that the slag concrete becomes more brittle when stored in the dry environment. It is difficult to notice any differences between the effect of slag types or slag content in view of the scatter.

As the stress-strength ratio versus axial strain curve becomes asymptotic at failure, it is difficult to assess any value for limiting axial strain. However, comparison can be made on the basis of 95% of failure stress, i.e. the stress at a stress-strength ratio of 0.95. These values are tabulated in Table 4.

Table 4 Axial strain at a stress:strength ratio of 0.95 of OPC and slag concretes (Microstrain).

Age (days)	14	84	84 *
Control Mix	1750	1930	1850
U.K.slag 30%	1950	1510	1780
50%	1900	1680	2065
70%	1745	1642	1915
B.slag 30%	1875	1650	2110
50%	1725	1600	1860
70%	1585	1595	1865
S.A.slag 50%	1735	1535	1920
70%	1585	1735	1852
J.slag 50%	1820	1784	2426
70%	1640	1860	2313

* specimens were stored in dry environment after 14-days of water curing and tested dry.

It can be seen that for concrete stored wet and tested at 84 days, the slag concrete has a lower limiting axial strain than OPC concrete. On the other hand, for concrete stored dry, the limiting axial strain was similar or higher in the case of slag concrete. Also, for any slag concrete mix, the effect of storing concrete dry after 14 days of water-curing was to increase the limiting axial strain which implies that dry specimens can withstand higher axial strain at failure compared with those wet stored in the case of slag concrete.

A comparison of the limiting lateral strain at a stress-strength ratio of 0.95 is given in Table 5 and there are no apparent differences between OPC and slag concretes at the age of 14 days, the average value being about 560 microstrain. On the other hand, generally at 84 days, the OPC concrete exhibited higher limiting lateral strain for both wet and dry storage conditions which implies more ductile behaviour and the capacity to sustain a higher stress. This may explain the higher indirect tensile strength of slag concrete compared to OPC concrete [8].

Table 5 Lateral strain at a stress:strength ratio of 0.95 of OPC and slag concretes (Microstrain).

Age (days)		14	84	84 *
Control Mix		550	775	887
U.K.slag	30%	540	372	702
	50%	500	445	405
	70%	595	300	510
B.slag	30%	462	500	610
	50%	445	560	475
	70%	610	460	475
S.A.slag	50%	505	497	465
	70%	525	640	415
J.slag	50%	775	700	750
	70%	650	670	700

* specimens were stored in dry environment after 14-days of water curing and tested dry.

Stress-Strain in Tension:

Figures 5 to 7 show the average stress-strain curves for OPC, 50%UK slag and SA slag concretes in tension and the maximum variability between two specimens obtained was $\pm 14\%$. It can be seen that in tension most failures were sudden. This behaviour could have been due to the fact that failure did not occur at the centre of the specimens (within the gauge length) and, therefore, strength and strain at failure may not considered to be representative. For the case of elastic-pseudo plastic behaviour (Fig. 7), the tensile strain at failure, for concrete tested at 84 days, was up to about 125 microstrain.

The development of direct tensile strength of OPC and slag-cement concretes is similar to that of compressive strength. The results of direct tensile strength of concrete are listed in Table 6. Unlike the compressive strength which was about 8% stronger for dry storage than for wet storage, tensile strength was stronger for wet storage.

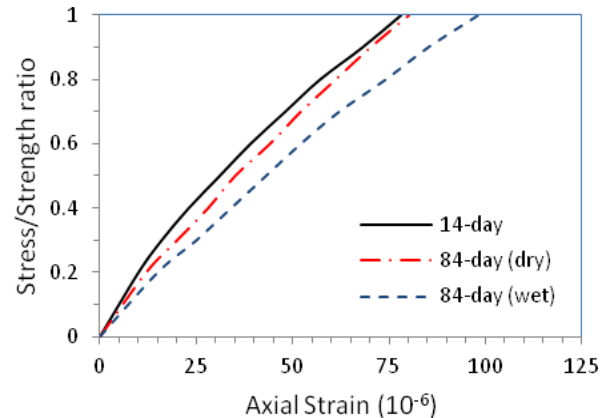


Fig. 5 Stress-strain curves for OPC concrete in tension.

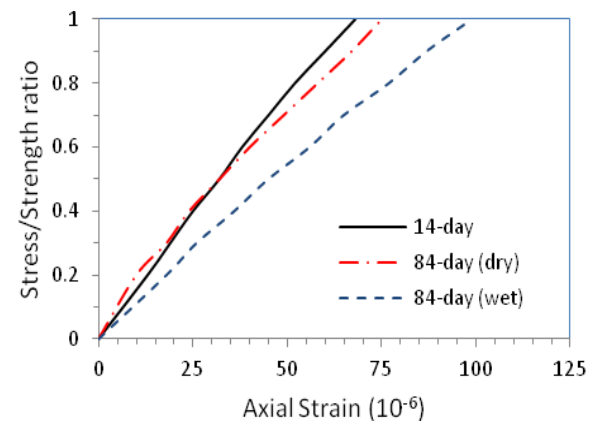


Fig. 6 Stress-strain curves for 50% U.K.slag concrete in tension.

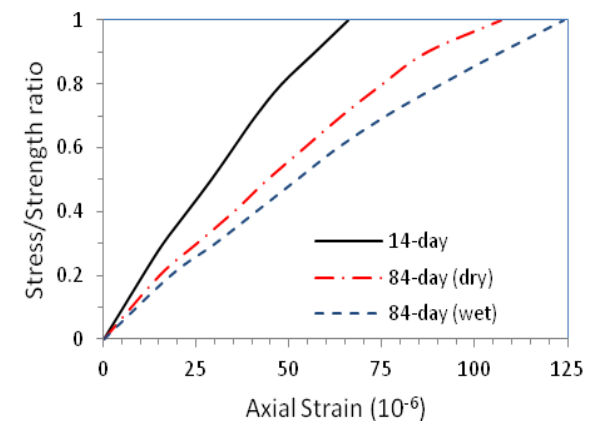


Fig. 7 Stress-strain curves for 50% S.A.slag concrete in tension.

Table 6 Direct tensile strength of OPC and slag-cement concrete (MPa).

Age (days)	storage environment	OPC mix	50% U.K.slag concrete	50% S.A.slag concrete
14	water	2.30	2.35	1.54
84	air	3.13	3.13	3.52
84	water	3.74	3.72	3.74

The secant modulus calculated from these curves are tabulated in Table 7. It can be seen that the modulus increases with age following a similar trend to that of modulus in compression. The secant modulus in tension is greater than that in compression because the modulus decreases with an increase in stress [9] and the modulus in tension is measured at a lower stress than that in compression. This confirms the finding of Brooks and Neville [4] whose explanation for this trend was that, at low stresses, the stress-strain curve is concave to the stress axis owing to the closing of microcracks and, at high stresses, the stress curve is convex owing to the opening of microcracks and to creep.

Table 7: Secant modulus of water-cured OPC and slag-cement concretes in tension (GPa)

Age (days)	storage environment	OPC mix	50% U.K.slag concrete	50% S.A.slag concrete
14	water	41.3	37.8	34.8
84	air	44.8	44.1	35.0
84	water	46.9	52.2	42.1

Poisson's Ratio:

Poisson's ratio at a stress-strength ratio of 0.3 represents the elastic portion of the stress-strain curve, and is generally used for practical design; the values are shown in Fig. 8. For OPC and slag concretes tested at 14 days, Poisson's ratio ranged between 0.139 and 0.22 and for slag concretes stored dry, and at 84 days the range was between 0.122 and 0.209. These values for slag concrete are lower than those of the same concrete stored in water; the latter varied between 0.161 and 0.24. This difference is mainly due to the fact that the wet-stored slag concrete exhibited a higher axial strain than that stored dry, whilst the lateral strains remained fairly constant. This confirms the conclusion of Mindess and Young [7] that Poisson's ratio of saturated concretes lies in the range 0.2 to 0.3, but decreases to about 0.18 on drying. However, the Poisson's ratio of OPC concrete stored either in water or dry are similar (Fig. 8) because the axial strains of specimens stored dry or in water are similar. From the results shown in Fig. 8 it is not easy to see any effect of slag content or slag type on the Poisson's

ratio due to the scatter of the results. Also, there does not seem to be difference between Poisson's ratio of slag concrete and OPC concrete, apart from the effect of storage environment. Stutterheim [5] found that for water-stored specimens Poisson's ratio was substantially the same irrespective of the cement type and ranged between 0.23 to 0.30 at the age of 28 days.

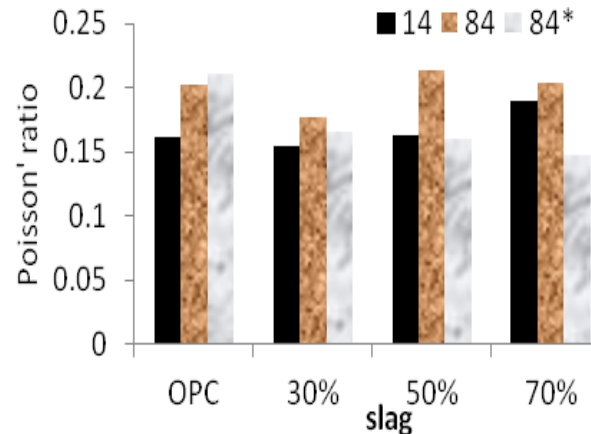


Fig. 8 Poisson's ratio at a stress:strength ratio of 0.3 of water-cured OPC and slag concretes.

CONCLUSION

For the range of typical international slags and replacement levels used in this investigation, a comparison with OPC concrete had led to the following conclusions:

- 1) An increase of slag content reduces the early-age strength, but later-age strengths are similar to, or slightly greater than, the strength of OPC concrete which confirms the conclusion of Boukendakdji [10].
- 2) The secant modulus of elasticity in compression of water-stored slag-cement concretes was similar at early ages, and greater at later ages. However, the opposite trend occurred for mature dry-stored concrete.
- 3) Concretes at the age 84 days exhibits more linearity than at the age of 14 days and slag concrete becomes more brittle when stored in the dry environment.
- 4) The secant modulus in tension is greater than that in compression
- 5) There was no difference between the Poisson's ratio of slag and OPC concretes which confirms the conclusion of Stutterheim [5]. However, the values for specimens stored dry was slightly higher than those stored wet for slag concretes.

ACKNOWLEDGEMENTS

The author wishes to acknowledge the facilities and assistance provided by the University of Hail. The

support of this research program by The Saudi Binladin Group is gratefully acknowledged as well.

REFERENCES

- [1] Hsu, T.C. et al. "Microcracking of plain concrete and the shape of the stress-strain curve", American Concrete Institute Journal, Vol.60 No.2, 1963, pp.209-223.
- [2] Shah, S.P. and Winter, G. "Inelastic behaviour and fracture of concrete", American Concrete Institute Journal, Vol.63, No.9, 1966, pp.925-930.
- [3] Boukendakdji, M. "Mechanical properties and long-term deformation of slag cement concrete", PhD thesis, Dept. of Civil Engineering, University of Leeds, 1989, 290 pp.
- [4] Brooks, J.J. and Neville, A.M. "A comparison of creep, elasticity and strength of concrete in tension and in compression" Magazine of Concrete Research, Vol.29, No.100, 1977, pp.131-41.
- [5]. Stutterheim, N. "Properties and uses of high - magnesia Portland slag cement concretes" American Concrete Institute Journal, Vol.56, April, 1960, pp.1027-45.
- [6] Kaplan, M.F. "Strains at stresses of concrete at initiation of cracking and near failure" ACI journal, July 1963, pp.853-78.
- [7] Mindess, S. and Young, J.F. Concrete, New Jersey, Prentice-hall, Inc, Englewood Cliffs, 1981.
- [8] Boukendakdji, M , Brooks, J.J. and Waiwright, P.J. "Strength Development of Concrete with and without slag" ConChem International Exhibition and Conference, Brussels, Belgium, 28-30 Nov. 1995.
- [9] Neville, A.M. Properties of concrete, London, Pitman third edition, 1981.
- [10] Boukendakdji O., Kadri E., and Kenai S. "Effects of granulated blast furnace slag and superplasticizer type on the fresh properties and compressive strength of self-compacting concrete" Cement and concrete composites, Vol 34, 2012, pp 583-590.

ESTIMATION AND EXPERIMENTAL STUDY ON DIVERSION LENGTH OF CAPILLARY BARRIER USING CRUSHED SHELL PARTICLES

Kazunobu Matsumoto¹, Kaoru Kobayashi², Satoru Nakafusa³ and Toshihiro Morii⁴

^{1,2}Tobishima Corporation, Japan; ³ Japan Atomic Power Company, Japan; ⁴ Niigata University, Japan

ABSTRACT

A simple soil layer system which is composed of a finer soil layer underlain by a coarser soil layer provides an excellent property of capillary barrier. In order to realize the best performance of the capillary barrier function, it is necessary to make a sharp contrast of soil particle diameter between sand and gravel. The authors found that an employment of crushed shells instead of gravel in the lower layer greatly reduces transport of the finer particles in the upper layer into the lower layer, and provides an effective function of capillary barriers. In this study, the diversion lengths are measured in the laboratory soil box tests using crushed shells instead of gravel, and compared those with the estimations calculated by the theoretical equation proposed by Steenhuis *et al.* In addition, we compared it with the diversion lengths which were measured in the laboratory soil box tests using a sand layer underlain by a gravel layer. As the result, the authors make clearly the applicability of the theoretical equation proposed by Steenhuis *et al.* in estimating the diversion length of the capillary barrier.

Keywords: Capillary barrier, Soil water characteristic curve, Diversion length, Crushed shell particles

INTRODUCTION

Capillary barrier (CB) is simply composed of a finer soil (usually sand) layer underlain by a coarser soil (usually gravel) layer [1]. The CB has been employed in a top cover of waste landfills to reduce water infiltration into the protected waste materials [2]. The length along which water infiltration is diverted is limited to some value, because water flow downward along the interface of CB accumulates gradually its mass of flow due to continuous infiltration from the soil surface, and, at some length along the interface, water percolates into the coarser soil layer.

As the CB effect is brought by a sharp contrast in water retention capacity between the finer and coarser soils, it is necessary to select a large difference in the grain size of two soils. But a significant performance deterioration is concerned because sand particles may move down into voids of gravel layer by earthquake or water infiltration for an extremely long duration [3]. To solve this problem, Nakafusa *et al.* [4], [5] and Matsumoto *et al.* [6] focused on the water retention characteristics of crushed shell particles, and selected as an alternative material for the lower layer soil (gravel) of the CB. They have shown that the movement of the upper sand into the lower crushed shell particles can be well prevented because the crushed shell particles have flat and finer grain size distribution while maintaining the CB function.

In this study, the performance of CB using the crushed shells instead of gravel is investigated. At

first, some fundamental properties (grain size and its distribution) and soil water characteristic curve (SWCC) of crushed shell particles are measured to show a practical effectiveness of crushed shell particles in the CB system. Then the diversion lengths [7] are measured by the laboratory soil box test, and compared with ones estimated by Steenhuis *et al.* [8]. The applicability of the theoretical equation proposed by Steenhuis *et al.* [8] in estimating the diversion length of the CB employing the crushed shell particles instead of gravel.

DIVERSION LENGTH OF THE CB AND ESTIMATED EQUATION

In the CB system, water which infiltrates into soil is suspended just above the interface between soil layers due to a physical difference in the water retention characteristics of the finer and coarser soils (Fig. 1). When the interface between soil layers has an slope as shown schematically in Fig. 1, the suspended water flows downward along the interface. This water flow downward along the interface between soil layers gradually accumulates its mass of flow due to continuous infiltration from the soil surface, and, at some length along the interface, water percolates vertically into the coarser soil layer. A horizontal length from the beginning of water flow to this percolation (breakthrough) into the coarser soil layer is called a diversion length [7].

Some theoretical equations have been proposed to estimate the diversion length of the CB by several researchers [8]-[10]. Among these, the equation

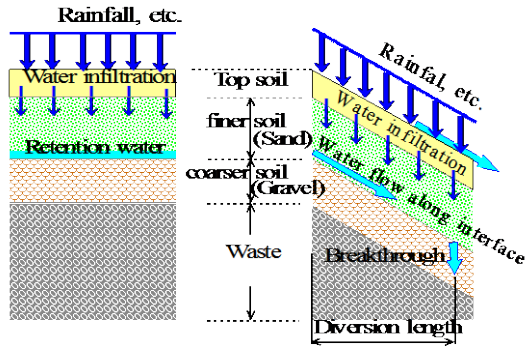


Fig. 1 Schematic layout of water flow downward along an interface between soil layers in the CB system.

proposed by Steenhus *et al.* [8] is effectively adaptable [11], [12]. In the case where an infiltration rate, q , is much smaller than a saturated hydraulic conductivity of sand, K_s , the equation of the diversion length, L , is given by

$$L \leq \frac{K_s}{q} \tan \phi [\alpha^{-1} + (h_a - h_w)] \quad (1)$$

where ϕ is the slope angle of the interface, h_a and h_w are the air entry value of sand and the water entry value of gravel, respectively. α is an exponential constant describing the relationship between negative pressure head, h , and unsaturated hydraulic conductivity, K , of sand near saturation:

$$\begin{aligned} K &= K_s & h < h_a & ; \\ K &= K_s \times \exp[-\alpha(h - h_a)] & h \geq h_a & \end{aligned} \quad (2)$$

In Eq. (1), q may depend on a thickness of the top soil layer above the sand as well as rainfall intensity and duration.

PHYSICAL PROPERTIES AND SWCC OF THE CRUSHED SHELL PARTICLES AND SAND

Materials

Scallop shell and silica sand no.6, which are available widely and easily, were used in the study. The shell was crushed by a small crusher machine after washing and being dried for 24 hours in the drying oven (80 degree Celsius). Table 1 shows the result of soil test of crushed shell and silica sand. Grain size distribution curves are given in Fig. 2. The crushed shell particles have the effective distribution curves which can prevent the movement of the upper sand into lower crushed shell particles [6].

Test Method

The crushed shell particles and the sand were compacted into a cylindrical specimen, 10 cm in diameter, by using a compact plate. Dry densities of

Table 1 Result of laboratory soil tests

Terms		unit	samples	
		—	crushed shell	silica sand no.6
density	ρ_s	g/cm ³	2.671	2.701
natural water content	W_n	%	0.3	0.8
grain size	gravel (2~75mm)	%	55	53
	sand (0.075~2mm)	%	39	41
	silt (0.005~0.075mm)	%	6	6
	clay (under 0.005mm)	%	0	0
	maximum grain size	D_{max} mm	19.00	0.45
	uniformity coefficient	U_c	14.00	1.74
	coefficient of curvature	U_c'	1.48	0.938
	50% grain size	D_{50} mm	2.340	0.194
	20% grain size	D_{20} mm	0.564	0.499
minimum void ratio	e_{min}		0.763	0.672
maximum void ratio	e_{max}		1.463	1.055
dry density	ρ_d	g/cm ³	1.321	1.334
saturated hydraulic conductivity	K_s	cm/s	1.82×10^{-1}	1.31×10^{-2}

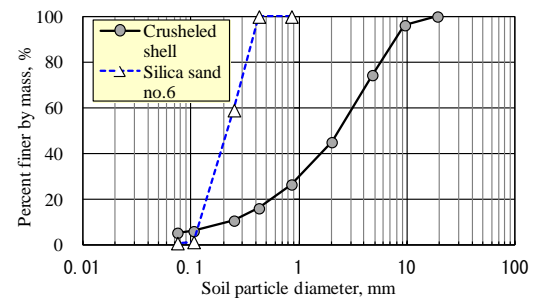


Fig. 2 Grain size distribution of crushed shell particles and silica sand employed in the CB.

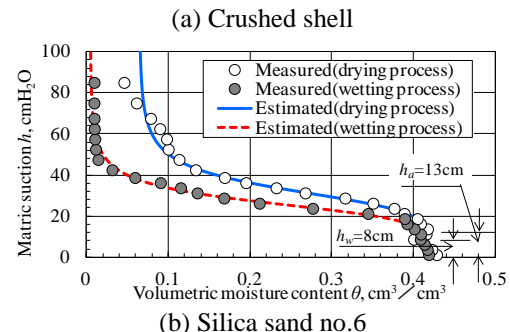
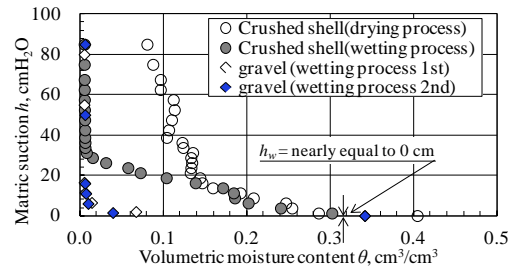


Fig. 3 SWCC measured by soil column tests and estimated by using van Genuchten equation.

crushed shell particles and sand were 1.321 Mg/m^3 (relative density $D_r=60 \%$) and 1.334 Mg/m^3 (compacted $D_c=90\%$), respectively.

Results of Soil Box Test

Change of volumetric moisture content (θ)

The volumetric moisture contents measured along the line C given in Fig.4 during the soil box test are given in Fig.5.

Comparing θ measured at S3, S8 and S13, it is found that the moisture content becomes larger along the depth in the sand layer. As the sand layer was compacted uniformly, the larger value of moisture content means higher degree of saturation above the interface. In addition, the volumetric moisture contents become higher with the increase of rainfall intensity. Conversely, the volumetric moisture contents become lower with the decrease of rainfall intensity.

In case G with 2.5 degrees in slope and 5 mm/h of infiltration rate (rainfall intensity), rainfall was supplied steadily during about 7 days. As the result, the volumetric moisture contents are constant both in sand and crushed shell layers as shown in the Z section devoted in Fig.5. The condition of moisture in CB remains stable for a long duration of rainfall. A series of laboratory soil box tests was carried out continuously by changing the rainfall intensity and by jacking up the one side of soil box to obtain the tilting interface of the CB. The volumetric moisture contents show the same values under the condition of the same slope and rainfall intensity during the period from the start of rainfall to the end of a series of tests (about 21 days). Tests were carried out 2 times, 3 times, and 2 times under the same condition to recognize the reproductiveness, 10 degrees in slope and 5 mm/h of rainfall intensity, 10 degrees and 10 mm/h, 10 degrees and 20 mm/h, respectively. As shown for sensor number S13 in Fig.5, the volumetric moisture contents in steady state, is about 0.20 (in 2 times), about 0.23 (in 3 times), and about 0.26 (in 2 times), respectively. Thus, reproductiveness is verified.

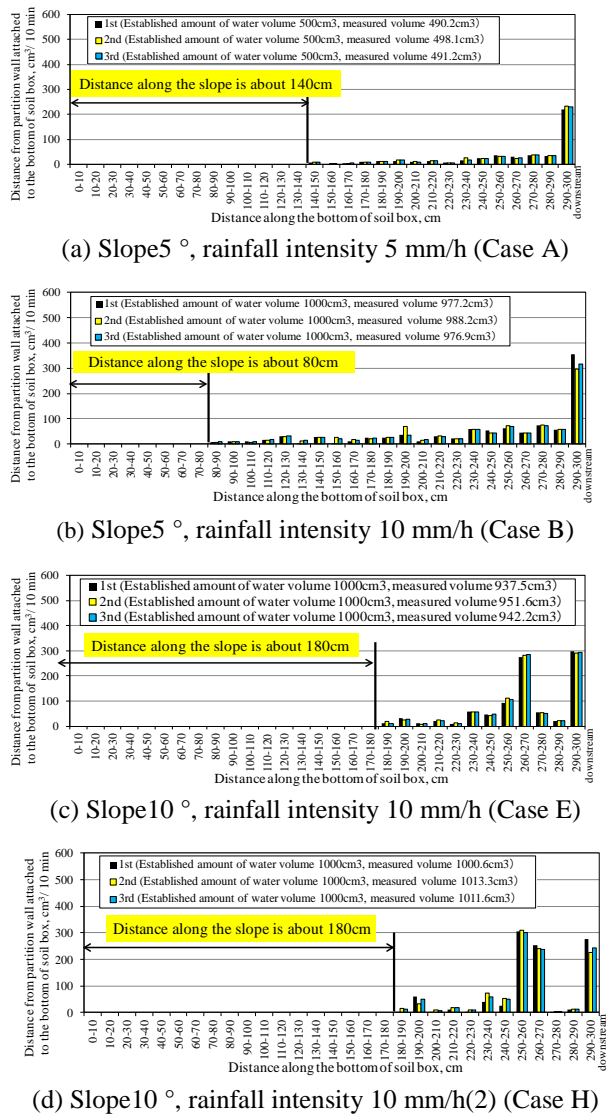


Fig. 6 Typical measurement of water volume collected along the bottom of the soil box to determine the diversion length .

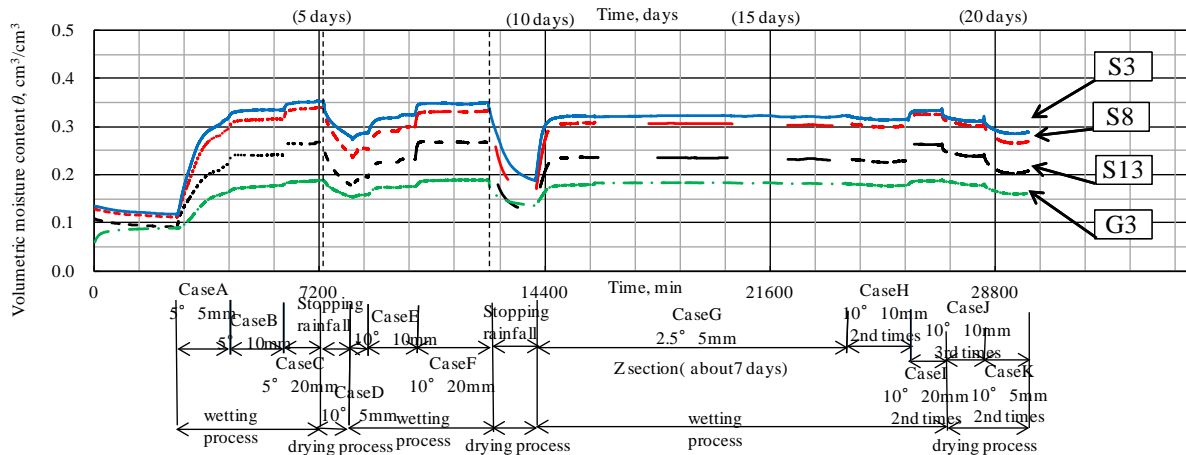


Fig. 5 Volumetric moisture content measured in CB constructed in the soil box. S3, S8, S13 and G3 are sensor numbers and given in Fig. 4.

Table 3 Diversion lengths measured in the soil box test. Note that the upper asterisk “*” shows the diversion length measured during drying processes.

		(Unit: cm)		
Slope angle, degree		Established rainfall intensity, mm/h		
		5	10	20
2.5		90	-	-
5.0		139	80	30
10.0	1st time	246	177	89
	2nd time	246*	177	89
	3rd time	-	187*	-

As a result, in the case where a certain rainfall intensity is given for a long duration, soil moisture contents remain constant and the condition of moisture is in a steady state. The volumetric moisture contents of CB fluctuate according to the repetition of wet and dry conditions for about 21 days. The volumetric moisture contents have the same values and reproductiveness is found under the same condition for about 21 days. The performance of CB using crushed shells is stable for a long duration of rainfall and in the case of repetition of wet and dry conditions.

Diversion length of the CB

Figs. 6(a)-(d) show the volume of water collected along the bottom of the soil box. Horizontal axis shows the distance along the interface from the most upstream of the soil box. In Fig. 6, the distance from the upstream of the soil box to a point where the water volume collected firstly gives the diversion length of the CB. Table 3 summarizes the diversion lengths measured in all cases, in which the diversion lengths are converted into the horizontal lengths by taking the angles of slope of the soil box into account. The diversion length measured by the soil box test is affected by the rainfall intensity and slope. The lower the rainfall intensity is and the larger the slope angle is, the longer the diversion length becomes.

To examine whether the CB can reproduce the same diversion length, the test of 10 degrees in slope angle and 5 mm/h of rainfall intensity were repeated twice (Cases D and K), the test of 10 degrees and 10 mm/h 3 times (Cases E, H and J), and the test of 10 degrees and 20 mm/h twice (Cases F and I). As shown in the lowest line of Table 3, almost the same diversion lengths were measured. This means the CB can provide a stable diversion of infiltration water.

According to the results as mentioned above, it was clarified that the CB using crushed shell particles instead of gravel provides an excellent and stable performance of water diversion.

APPLICABILITY OF ESTIMATION EQUATION INTO THE CB COMPOSED OF SAND AND CRUSHED SHELL PARTICLES

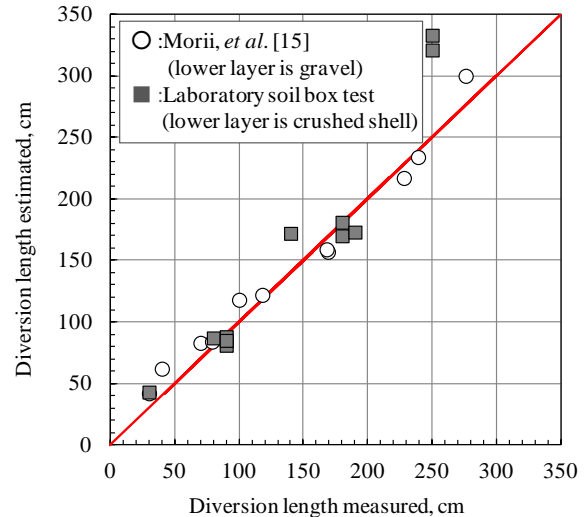


Fig. 7 Comparison of the diversion lengths measured in the soil box test with ones estimated by Steenhuis et al. [8]. The diversion length of the CB composed of sand and gravel are also given for comparison.

The diversion lengths of CB were estimated by Eq. (1) considering the test conditions. As shown in Fig. 3(b), the air entry value (h_a) of silica sand was 13 cm, and the water entry value (h_w) was set to 1 cm because there was no definite value as shown in Fig. 3(a). Saturated hydraulic conductivity of sand, $K_s = 1.31 \times 10^{-2}$ cm/s, was measured as given in Table 1. α near saturation of silica sand can be estimated to be 0.118 cm^{-1} .

The diversion lengths which were measured in cases A to K are compared with ones estimated by Eq. (1) in Fig. 7 by using gray squares. Laboratory results using gravel instead of crushed shells published by Morii *et al.* [15] are also plotted by white circles. As the diversion lengths in the case of crushed shells are almost same as values in the case of gravel, it may be found that Eq. (1) can be well employed to estimate the diversion length of the CB.

According to the results as mentioned above, it is concluded that the crushed shell particles are applicable to the CB system. This alternative of the crushed shell particles will keep good performance for a long duration because of small deterioration of shell material.

CONCLUSION

In order to determine the diversion length of the CB composed of sand and crushed shell particles, the laboratory soil column test and the soil box test were carried out. The diversion lengths measured by the soil box test were compared with ones estimated by Steenhuis *et al.* [8]. In addition, the applicability of the equation proposed by Steenhuis *et al.* [8] in

estimating the diversion length of the CB was discussed.

The following are obtained:

(1) The SWCC of crushed shell particles during the drying and wetting processes show only very small air entry value (h_a) and water entry value (h_w). They are similar to the air entry value and the water entry value of gravel. From the point of view of soil-water characteristic, crushed shell particles can be well employed in CB instead of gravel.

(2) The volumetric moisture contents have the same values under the condition with the same slope and rainfall intensity in the soil box test during a period from the start of rainfall to the end of a series of tests (about 21 days) and reproductiveness is found. So, the CB using the crushed shells displayed the stable function during a long-term rainfall and under repetitive dry and wet condition.

(3) It was confirmed experimentally that the lower the rainfall intensity is and the larger the slope angle is, the longer the diversion length becomes. The diversion length measured several times under the same condition had almost the same value and reproductiveness of diversion length was verified.

(4) As the diversion lengths in the case of crushed shells are almost same as values in the case of gravel, Eq. (1) can be well employed to estimate the diversion length of CB.

According to the results as mentioned above, it is concluded that the crushed shell particles instead of gravel are applicable to the CB system. The reuse of fishery by-product (shell) may contribute to construct a recycling society in Japan with scarce natural resources.

ACKNOWLEDGEMENTS

The present study was supported by JSPC KAKENHI Grant Number 22560507. Messrs. K. Taguchi and N. Someya, TNS Co., Ltd., Japan, are sincerely grateful for their help in conducting the laboratory soil box test.

REFERENCES

- [1] Morii T., "Capillary barrier of soil", *Geotechnical Engineering Magazine*, Vol.59, No.2, 2011, pp. 50-51.
- [2] Rahardjo H., Krisdani H. and Leong E-C., "Application of unsaturated soil mechanics in capillary barrier system", *Proceedings of the 3rd Asian Conference on Unsaturated Soils* edited by Yuan, J. and Chiu, A. C. F., 2007, pp. 127-137.
- [3] Nakafusa S., Nishimura T., Kobayashi K. and Morii T., "Soil water characteristic curve of soil mixed by sand and gravel", the 2011 JAGH Autumn lecture and symposium, 2011, pp. 138-141.
- [4] Nakafusa S., Kobayashi K., Morii T. and Matsumoto K., "Study on capillary barrier of using fishery byproducts to reduce the infiltration of sand particles into the low layer", *Journal of JSCE (B3)*, Vol. 68, No. 2, 2012, pp. I_462-I_467.
- [5] Nakafusa S., Kobayashi K., Morii T. and Nishimura T., "Alternative employment of crushed shell particles in capillary barrier of soil", *Int. J. of GEOMATE*, Vol.1, No.1, 2011, pp.50-55.
- [6] Matsumoto K., Kobayashi K. and Morii T., "An examination of crushed shells by constructive heavy machinery for the alternative to gravel constituting the capillary barrier", *Proceedings of the 57th Japan Geotechnical symposium*, 2012, pp. 235-238.
- [7] Miyazaki T., "The diversion capacity of an inclined capillary barrier", *Journal of JSIDRE*, No. 179, 1995, pp. 49-56.
- [8] Steenhuis T. S., Parlange J. -Y. and Kung K -J., "Comment on 'The diversion capacity of capillary barriers' by Benjamin Ross", *Water Resources Research*, Vol. 27, No. 8, 1991, pp. 2155-2156.
- [9] Ross B., "The diversion capacity of capillary barriers", *Water Resources Research*, 26(10), 1990, pp. 2625-2629.
- [10] Kung K. -J. S., "Preferential flow in a sandy vadose soil 2, Mechanism and implications", *Geoderma*, 46, 1990, pp. 59-71.
- [11] Walter M. T., Kim J. -S., Steenhuis T. S., Parlange J. -Y., Heilig A., Braddock R. D., Selker J. S. and Boll J., "Funneled flow mechanisms in a sloping layered soil: Laboratory investigation", *Water Resources Research*, 36(4), 2000, pp. 841-849.
- [12] Smeets J. K. and Selker J. S., "Effect of soil-particle size contrast on capillary barrier performance", *Journal of Geotechnical and Geoenvironmental Engineering*, 127(10), 2001, pp. 885-888.
- [13] van Genuchten M. Th., "A closed-form equation for pre-dicting the hydraulic conductivity of unsaturated soils", *Soil Science Society of American Journal*, Vol. 44, pp. 892-898, 1980.
- [14] Stephens D. B., "Vadose Zone Hydrology", CRC Press, pp. 183-187, 1996.
- [15] Morii T., Kobayashi K., Matsumoto K., Suzuki T., Kawai T. and Nakafusa S., "Practical application of capillary barrier of soil into a shallow land waste repository", *Proceedings of the Fifth China-Japan Geotechnical symposium*, 2012.

EXPERIMENTAL STUDY OF CONCRETE AND MORTAR MIXING WASTE TIRE RUBBER

Man-Kwon Choi ¹, Yuki Hasegawa ², Shushi Sato ³, Shinsuke Matsumoto ³ and Hyeon-Tae Kim ⁴

¹Institute of Agriculture & Life Science, Gyeongsang University, Korea

²The United Graduate School of Agricultural Science, Ehime University, Japan

³Faculty of Agriculture, Kochi University, Japan

⁴Department of Bio-Industrial Machinery Engineering, Gyeongsang National University (Institute of Agriculture & Life Science), Korea

ABSTRACT

Waste tire disposal is one of the most important issues in all over the world. The use of waste tire as a material to concrete is a possible disposal solution. In this study, the fundamental properties in harden state of concrete and mortar mixed waste tire rubber were examined. The volume percentage of aggregate and sand was replaced by waste tire rubber. Focusing on the mechanical properties, the use of waste tire rubber of replaced volume was shown compressive and flexural strength concerning both rubberized concrete and mortar. As a result, the reduction rate of flexural strength was smaller than that of the compressive strength. In addition, ultrasonic pulse velocity showed the same tendency that rubberized mortar decrease more than rubberized concrete.

Keywords: Waste Tire Rubber, Mechanical Properties, Mixture Proportions, Concrete, Mortar

INTRODUCTION

Japan is generating millions of waste tires every year. All over the world, waste tire disposal have been occurred many environmental problems. As a result, several studies have been carried out to find substitution and application for this rubber waste. Waste rubbers disposal have two main uses; the first one is the reuse of rubber tires left over retreading process, and the second one is incorporating it into cement-based material [1]. As for the latter use, many authors have studied the use of waste tire rubber in applications to such as aggregate of concrete, asphalt pavement and shock absorber structures. In the last utilization method, they called it as the rubber concrete [2-4]. Experimental investigations of rubber concrete indicated that chipped or crumbed tire rubber particles results the significant change in mechanical properties. Almost all investigators reported a substantial decrease (10-80%) in compressive and tensile strengths of rubberized concrete with increasing waste tire rubber content [5-12]. The level of strength reduction was related to the waste tire rubber content and low bond strength between the cement based matrix and the waste tire rubber particles. Eldin and Senouci reported that the concrete mixtures exhibited lower compressive and splitting tensile strength than those of normal concrete [5]. Also, a mathematical model is used to describe the effects of rubber aggregate on the compressive and tensile strength reduction of concrete. Papakonstantinou and Tobolski reported that compressive strength

reduced when crumb rubber and tire chips in Portland cement concrete [6]. But, the main variable in the mixtures was the toughness of the material greatly increases. Moreover, workability was not significantly affected. Li et al. investigated the performance of the waste tire chip and waste tire fiber modified concrete [7]. They observed that fibers performed better than chips did. Atahan and Sevim produced concrete mixed shredded waste tire chips and measured compressive strength, modulus of elasticity and dynamic impact using the identical mix design [8]. They found that specimens with 20 to 40% aggregate replacement gave the best impact performance without significant reduction in concrete strength. Yuksel et al. investigated how the usage of bottom ash, granulated blast furnace slags [9]. They observed that compressive strength loss due to freezing-thawing effect for low replacement ratio (10-30%) and abrasion resistance of concrete incorporation non-ground blast furnace slag did not decrease when replacement of non-ground blast furnace slag with fine aggregate up to 50%.

Although numerous investigations have been performed for rubberized concrete with waste tire particles, there are a limited number of studies related to the mechanical properties rubberized mortar. In this study compressive strength, flexural strength and ultrasonic pulse velocity were investigated for both rubberized concrete and mortar at each mixed design.

The objective of this study was to evaluate the feasibility and performance of waste tire rubberized concrete using larger sized chips, rubberized mortar

Table 1 Mix proportion of rubberized concrete and mortar

Specimen	Cement (kg/m ³)	Water (kg/m ³)	Fine aggregate (kg/m ³)	Coarse aggregate (kg/m ³)	Rubber added (kg/m ³)	Admixture (g/m ³)
RC0 (control)	373	212	732	849	0	75
RC10	373	212	732	810	39	75
RC20	373	212	732	771	78	75
RC30	373	212	732	733	116	75

Specimen	Cement (g)	Water (g)	Fine aggregate (g)	Coarse aggregate (g)	Rubber added (g)	Admixture (g)
RM0 (control)	450	225	1350	-	0	-
RM10	450	225	1215	-	53.7	-
RM20	450	225	1080	-	107.4	-
RM30	450	225	945	-	161.1	-
RM50	450	225	675	-	268.5	-

using waste tire powder.

EXPERIMENTAL DESIGN

Materials and Mix Design

In this study, the concrete specimen was designed with a constant water cement ratio of 56 %. Ordinary Portland cement, crushed stone (as coarse aggregate), crushed sand (as fine aggregate) and tap water were basic components for the fundamental materials of all concrete specimens. The densities of coarse and fine aggregate were 2.58 g/cm³ and 2.54g/cm³, respectively.

The mortar specimen was designed with same water cement ratio of 50 %. Ordinary Portland cement, standard sand and tap water were used as the fundamental materials of mortar specimen. The mix proportions of rubberized concrete and mortar were given in Table 1.

The waste tire rubber chips were collected from a tire recycling company in Kochi prefecture. These chips were shredded and thieved into maximum size of 25 mm for concrete specimens, and gathered less than 5 mm of diameter for mortar specimens. The density of waste tire rubber was 1.18 g/cm³. The waste tire rubber was mixed into concrete against the volume of coarse aggregate at ratio of 0%, 20% and 30%. In addition, the waste tire rubbers were mixed into mortar against the volume of fine aggregate at ratio of 0%, 20%, 30% and 50%.

Specimen Preparation and Testing

All specimens were placed and unmolded after 24 hours of casting, and cured with standard water curing under a constant temperature 20 ± 1 °C. A total of 72 concrete specimens were made and cured according to JIS A 1132 [14]; of these, 36 cylindrical specimens (10cm×20cm) were tested for compressive strength and 36 rectangular specimens (10cm×10cm×40cm) were tested for flexural strength. On the other hand, total of 40 mortar specimens were made and cured for this experiment. The size of all mortar specimens were controlled in height, width, and length of 4cm×4cm×10cm, respectively. All mortar specimens were tested at age 7, 28 and 91 days for compressive, flexural and ultrasonic pulse velocity tests. The flexural and compressive strength tests were conducted at age 7, 28, 91 days using Hi-ACTIS 200 (MARUI CO. LTD).

For the flexural strength test of concrete, three specimens in each mixture were prepared and tested by three point loading configuration. Compressive strength test of concrete were performed three cylindrical specimens in each mixture. Compressive strength test of mortar specimens were used six broken pieces of test prisms left after testing the flexural strength. Ultrasonic pulse velocity was measured against each test age.

RESULTS AND DISCUSSIONS

The test results of the compressive strength, flexural strength and ultrasonic velocity of each

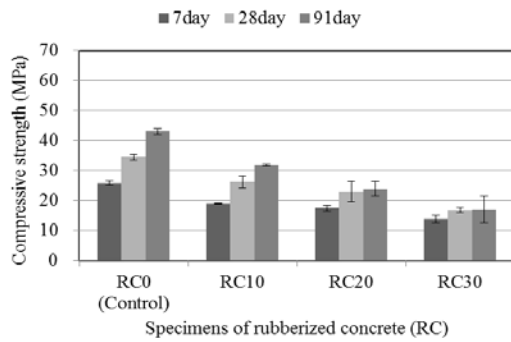


Fig. 1 Compressive strenght variations of the concretes

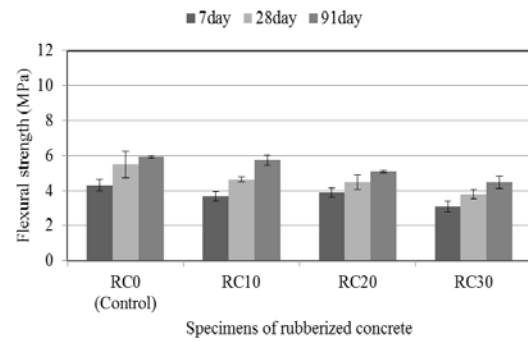


Fig. 3 Flexural strength variations of concretes

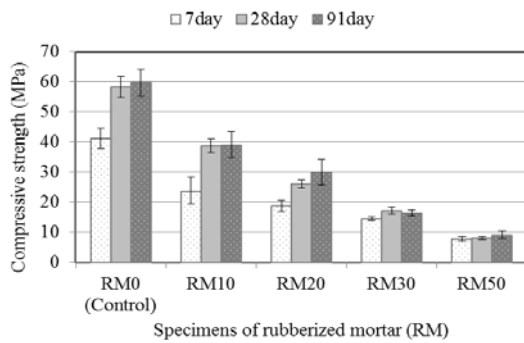


Fig. 2 Compressive strength variations of the mortars

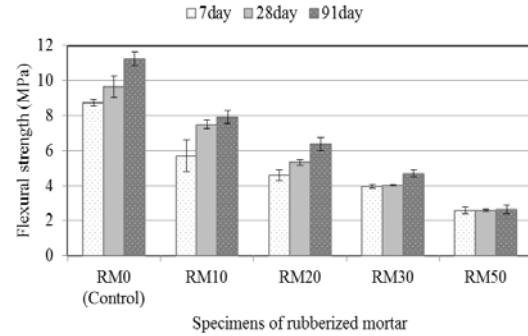


Fig. 4 Flexural strength variations of mortars

specimen were shown in Fig.1 to Fig.6. These results were analyzed and described as follows.

Effect on Waste Tire Rubbers to the Compressive Strength of the Rubberized Concrete and Mortar

The compressive strength of rubberized concrete and mortar was determined at 7, 28 and 91 days respectively. It was calculated based on the average in each specimen. The test results were given in Fig. 1 and Fig.2.

From these test results, the compressive strength of all rubberized concrete and mortar were lower than that of the control regardless the replacement ratio. It was natural results because waste tire rubbers were softer than the concrete and mortar matrix such as aggregate or cement hydrates. In general, soft part acts as the concentration of stress in the composite [7]. The compressive strength of the control mix for concrete specimens was evaluated as 25.87MPa, 34.47Mpa and 43.03MPa at age 7, 28, 91 days, respectively. Comparing these values above, the reduction of compressive strength at age 28 day were 24.0% (RC10), 33.5% (RC20) and 51.6% (RC30). On the other hand, the compressive strength of the control mix for mortar specimens was evaluated as 41.15MPa, 58.22MPa

and 59.69MPa at 7, 28, 91 days respectively. Comparing these values above, the reduction of compressive strength at age 28day was 33.6% (RM10), 55.2% (RM20), 70.6% (RM30) and 86.2% (RM50).

It was concluded that the large amount of rubber mixing led to huge losses of compressive strength and the reduction ratio of compressive strength of mortar was higher than that of concrete due to increment of replacement ratio.

Effect on Waste Tire Rubbers to the Flexural Strength of the Rubberized Concrete and Mortar

The flexural strength of rubberized concrete and mortar was determined at age 7, 28 and 91 days. The test results were presented in Fig. 3 and Fig.4. Flexural strength of control mixed for concrete was evaluated as 4.31MPa, 5.49MPa and 5.92MPa at age 7, 28 and 91 days, respectively. The result of flexural strength test also indicated the similar tendency of the result of compressive strength. Comparing with the control mixture of concrete (RC0), the reduction of flexural strength at age 28 days were 15.7% (RC10), 18.4% (RC20) and 31.1% (RC30). The flexural strength of the control mixture for mortar specimens was evaluated as 8.72MPa,

9.65MPa and 11.23MPa at age 7, 28 and 91 days, respectively. Comparing with these values above, the reduction of flexural strength at age 28day was 22.4% (RM10), 44.7% (RM20), 58.3% (RM30) and 73.3% (RM50).

These results indicated that the reduction rate of flexural strength was lower than that of the compressive strength. Thus, there was possibility that the rubber particles in concrete affect to a good bonding than rubberized mortar.

Effect on Waste Tire Rubbers to the Ultrasonic Pulse Velocity (UPV) of the Rubberized Concrete and Mortar

Ultrasonic pulse velocity (called UPV, here after) method is one of the non-destructive tests and utilized for the evaluation of strength development. The effect on mixed waste tire rubber to the mechanical property of various specimens was investigated. Fig. 5 and Fig.6 showed the change of UPV with the age of rubberized concretes and mortars. The UPV reduced significantly with increment of the replacement ratio concerning to the both concrete and mortar specimen. From the Fig. 5, the UPV values of age 28 days were 4.21km/s (RC10), 4.19 km/s (RC20) and 4.02km/s (RC30), respectively. All of these values were lower than the value of control mixture (4.4km/s). Additionally, it

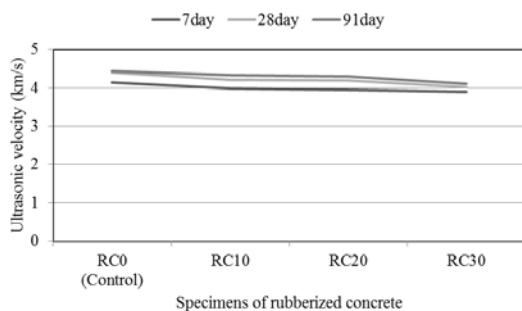


Fig. 5 Ultrasonic Pulse Velocity variations of concretes

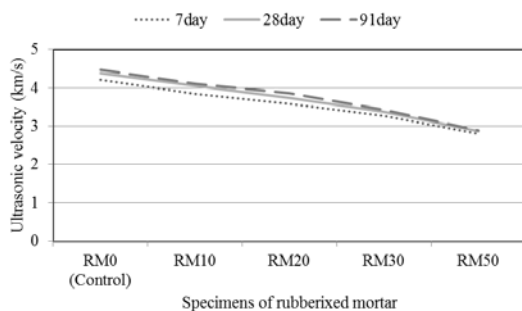


Fig. 6 Ultrasonic Pulse Velocity variations of mortars

was observed that the change of UPV had tendency of increment with the advance of age at three rubberized concrete mixture.

According to the previous study by Malhotra (1976), the specimens are classified in “good” condition as their UPV values ranged in 3.66km/s-4.58km/s [13]. Rubberized concrete in this research were evidently in “good” conditions.

From the Fig. 6, the UPV values of mortar specimen showed the same tendency with rubberized concrete. However, UPV value at age 28 days of mortar mixture tended to decrease more than that of concrete mixture.

CONCLUSION

Rubberized concrete and mortar was prepared and tested. The compressive and flexural strength and ultrasonic pulse velocity tests of rubberized concrete and mortar were conducted. The effect of various design variables on the compressive and flexural strength decrease while the amount of rubber replacement increases, respectively. At age 28 days, compressive and flexural strength of mortar tended to decrease more than that of concrete with same replacement ratio due to the advance of curing time. Also, ultrasonic pulse velocity showed the same tendency that rubberized mortar decrease more than rubberized concrete.

ACKNOWLEDGEMENT

A part of this study was supported by JSPS KAKENHI Grant Number 24580356. Authors are thanks to Ms. Uchida Mika, Mr. Matsuura Satoru, Ms. Aoki Anna, Mr. Kagawa Haruhiko, Mr. Kanaoka Hiroki, Ms. Hara Shizuka and other members of water use and environmental engineering laboratory in Kochi University, for their kindly cooperation on experiment.

REFERENCES

- [1] Ozbay E, Lachemi M, Sevim UK, “Compressive strength, abrasion resistance and energy absorption capacity of rubberized concretes with and without slag”, *Materials and Structures*, Vol. 44, Dec. 2011, pp. 1297-1307.
- [2] Yilmaz A, Degirmenci N, “Possibility of using waste tire rubber and fly ash with Portland cement as construction materials”, *Waste Management*, Vol. 29, Dec. 2009, pp.1541-1546.

- [3] Son KS, Hajirasouliha I, Pilakoutas F, "Strength and deformability of waste of waste tyre rubber-filled reinforced concrete columns", *Construction and Building Materials*, Vol. 25, Jan. 2011, pp. 218-226.
- [4] Cao W, "Study on properties of recycled tire rubber modified and asphalt mixtures using dry process", *Construction and Building Materials*, Vol. 21(5), May 2007, pp. 1011-1015.
- [5] Eldin NN, Senouci AB, "Rubber-tire particles as concrete aggregate", *J. of Materials in Civil Engineering*, Vol. 5(4), Nov.1993, pp. 478-496.
- [6] Papaloustantinou CG, Tabolski MJ, "Use of waste tire steel beads in Portland cement concrete", *Cement and Concrete Research*, Vol. 36, Sept. 2006, pp. 1686-1691.
- [7] Li G, Stubblefield MA, Garrick G, Eggers J, Abadie C, Huang B, "Development of waste tire modified concrete", *Cement and Concrete Research*, Vol. 34(12), Dec. 2004, pp. 2283-2289.
- [8] Li G, Garrick G, Eggers J, Abadie C, Stubblefield MA, Pang SS, "Waste tire fiber modified concrete", *Composites Part B: Engineering*, Vol. 35, Jan. 2004, pp. 305-312.
- [9] Yuksel I, Bilir T, Ozkan O, "Durability of concrete incorporating non-ground blast furnace slag and bottom ash as fin aggregate", *Building and Environment*, Vol. 42 (7), Jul. 2007, pp. 2651-2659.
- [10] Atahan AO, Sevim UK, "Testing and comparison of concrete barriers shredded waste tire chips", *Materials Letters*, Vol. 62, Aug. 2008, pp. 3754-3757.
- [11] Khatib ZK, Bayomy FM, "Rubberized Portland cement concrete, *J. of Materials in Civil Engineering*, Vol. 11(3), Aug. 1999, pp. 206-213.
- [12] Toutanji, HA, "The use of rubber tire particles in concrete to replace mineral aggregates", *Cement and Concrete Composite*, Vol. 18(2), Jan. 1996, pp. 135-139.
- [13] Malhotra VM, "Testing hardened concrete: nondestructive methods", *American Concrete Institute, Monograph*, NO. 9, 1976
- [14] Japanese society of civil engineers, *Guideline for Experiment on Materials of Civil works*, JSCE, 2009 Edition.

PILE DRIVING EFFECTS ON NEARBY BUILDING

Adhilla Ainun Musir¹ and Abdul Naser Abdul Ghani²

¹Faculty of Civil Engineering, UiTM Penang, Malaysia; ²School of Housing Building and Planning, Universiti Sains Malaysia, Malaysia

ABSTRACT

Piles are used to support many major structures such as buildings and bridges. It is known that pile driving activity creates vibrations in the ground and may affect nearby building and structure. However, the different pile size and shape as well as installation distances factors remain as interesting subjects for studies. The effect of hammer driven piles installation were studied using laboratory scale model. Three main effects were studied in which they are the response on top and bottom of a building, the vibration creates by three different distances of driven pile and the vibration produced by two different pile sizes. It can be concluded that the effect of vibrations are higher at the bottom of the building. The result also indicates that the nearest distance of piling activity produced higher vibration. However, it is interesting to note that the smaller pile creates larger vibrations.

Keywords: Pile, Piling Vibration, Building, Laboratory Model.

INTRODUCTION

It is known that pile driving activity creates vibrations in the ground and may affect nearby building or structure. Propagation of vibrations to the surroundings depends on the weight of the ramming equipment, impact velocity, impact duration, shape of the pile, surrounding and underlying soil, cross-sectional area of the pile, straightness of the pile and eccentric or oblique strokes. Piling and sheet piling work on construction sites affects the environment in different ways depending on geological conditions. Usually, piling cause noise, vibration, settlement or heaving close to the site. The effects are dominated by the energy introduced into the subsoil, the distance from the source and because of subsoil condition. Settlement quickly occurs in non-cohesive soil.

It is expected that vibration level associated with pile driving may vary with distance from the pile driving site. This is because the resulting wave is of periodic nature which is highly attenuated after short distance and harmonic frequencies are low vibration level.

Ground vibration generated by construction sources consists of transient vibration and steady state vibration. Transient vibration is the single event or sequence vibrations. Each transient pulse of varying duration decaying before the next impact occurs. For example air, diesel or steam impact pile drivers by dynamic compaction of loose sand and granular fills by highway and quarry blast. Abdel-Rahman [1] surveyed and concludes that the force vibration caused by pile driver, double acting impact hammers operating at high speed and heavy machineries affect surrounding buildings. It causes or propagates crack and failure.

Energy that is produced by pile driving and

spread into the ground travels from the pile to structures within. The amplitude of this vibration depends on many factors. The energy propagating away from driven pile depends on pile driver and the pile type itself [2]. Massarsch and Fellenius [3] described three types of ground waves created by pile driving namely surface wave, spherical wave from the pile toe and cylindrical wave from the pile shaft.

The main thrust of this study is to identify the various physical parameters involve in the propagation of vibration energy that affect surrounding building or structure by means of laboratory model. Over the years, several researchers ([2], [4], [5], [6] and [7]) have used scale model to carry out experiments related to piling. In this study, it is expected that relationship of the various parameters such as pile size, pile type, distance, trench depth and driving methods can be established. The empirical relationships can then be used in the actual operational condition as preliminary strategy to reduce or eliminate pile driving effects on nearby building or structure.

MATERIAL AND METHODS

Laboratory scale model was used to carry out experiments. A suitable sand container was fabricated to be used as a testing ground. The laboratory testing container was scaled from real construction site with 1:20 scale. This box was filled with river sand as soil. The size of container is 1.35 meter for the length, 1.0 meter for the width and 0.6 meter from the depth. Figure 1 shows the testing container used in this study. The size of the container is designed to accommodate dimensional similitude of a model building structure. Similar container size has been used before by other researchers as described in previous paragraph.



Figure 1: Sand container

Building/Structural Model

Model of building was built by using stainless steel bar. This model was scaled as 1:20 from 3 storey building and the height of the model building is 0.9 meter. The width and the length of the building is 0.3 meter. Stainless steel were cut into pieces and welded to the shape of skeleton building structure. The foundation of this building is raft foundation. The model of the building is shown in Figure 2.



Figure 2: Building Model

Pile

Piles used for this study are squared piles with 150mm x 150 mm and 200mm x 200 mm dimension. The size of pile was scaled down to 7.5mm x 7.5mm for the size of 150mm x 150mm and 200mm x 200mm was scaled to 10mm x 10mm. The pile shoe scaled to 20 mm for both types of pile.

The assumed length of piles is 6m on site and it was scaled to 300 mm for the model. There are three piles for each size and will be allocated at different distance. The two sizes of piles chosen was the common pile sizes used for low rise building construction. The difference of pile size is expected to produce different level of vibration to the nearby

building.

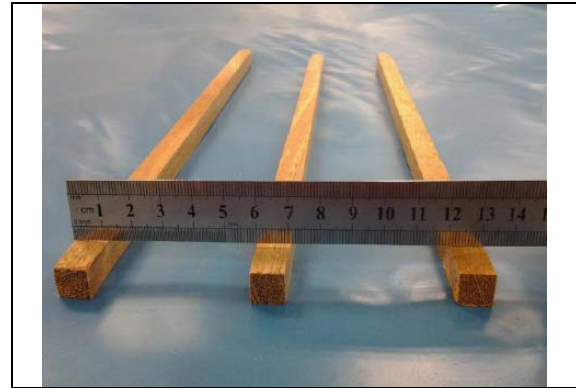


Figure 3: Equivalent 200mm square Pile of 10mm x 10mm

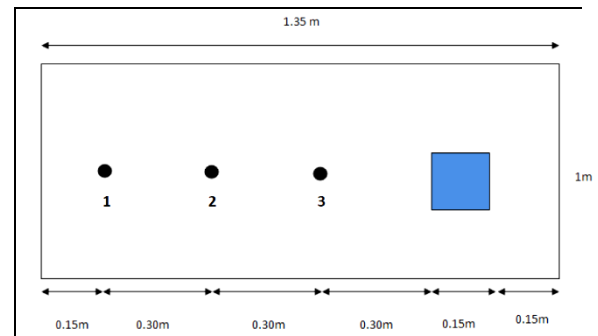


Figure 4: Pile arrangement at various distance from building

Pile driving hammer

On site hammer weight considered for this study is 1 ton and it was scale down to the ratio 1:20. The model hammer weight now becomes 120 gram. The dimension of container is 50 mm x 50 mm x 50 mm and filled with sand to the required weight. Hammer weight will be released at 150 mm height to the top of pile. Vibration at nearby model building were recorded when the hammer reach the pile. Hammer weight and hammer drop distance are constant throughout this experiment.



Figure 5: Hammer system

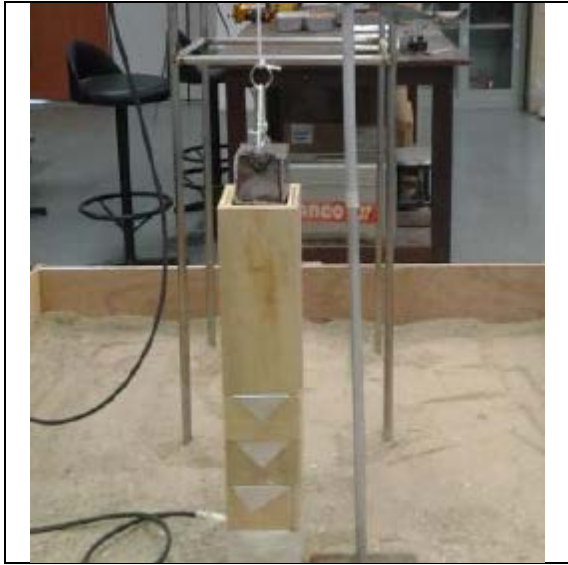


Figure 6: Use of special casing to make sure hammer drop on top of pile.

Testing Procedure

The steps conducting this experiment were explained further as below:

1) Two vibration transducers (accelerometer) were connected to the top and bottom of building and also connected to a dynamic data-logger as it will record the vibration data in computer.

2) Pile with the size 7.5 mm x 7.5 mm was positioned at point three. Pile was aligned at the centre of building as measured before. Pile was braced by formwork to make sure pile still standing correctly during driven activity.

3) When pile is ready, the hammer will be aligned with the pile. A casing with 150 mm height was installed to make sure hammer drop distance is constant and the hammer will be drop just over the pile. It also to make sure there is no disturbance from others such as wind or any movement.

4) The vibration data will be recorded for every 10 mm penetration of pile to the sand.

5) Formwork was divided into parts. After 50 mm penetration, part of formwork will be dismantling to hammer pile again.

6) The process will be continued until pile penetrated up to 250 mm. The steps will be repeated to the other pile for point 2 and point 1.

7) The process continuously repeated for other pile installation.

RESULTS AND DISCUSSION

Laboratory testing model result is based on vibrations occurs during pile driving. These results were divided into three parts. The first is the result of comparison between vibration impact on top and bottom of the nearby building. It involved both sizes of piles which is 7.5 mm x 7.5 mm (150 mm x 150 mm) on site and 10 mm x 10 mm (200mm x 200 mm) on site. The scale ratio of sizes of pile is (1:20).

The next part involves the analysis and discussion of comparison of vibration impact on nearby building based on three different distances which are 900 mm, 600 mm and 300 mm from the building. The scale used is 1:20 and it means the real distance from buildings is 18 m, 12 m and 6 m on site.

The last part of analysis for this study is comparison of vibration impact on existing building with different sizes of piles. The comparison values of vibration impact based on two sizes of piles that were driven on same distance from the building.

Effect based on pile size

Table 1(a): The comparison between sizes of pile on top of building (vibration level in mV/g)

TOP	7.5 X 7.5	10.0 X 10.0
Point 1	1810	1392
Point 2	1560	1884
Point 3	4394	5061

Table 1(b): The comparison between sizes of pile on bottom of building (vibration level in mV/g)

BOTTOM	7.5 X 7.5	10.0 X 10.0
Point 1	2037	1602
Point 2	3119	2690
Point 3	5656	6241

At the top of building, it shows that the resulting vibration was higher from point 1 (farthest) for the smaller 7.5 mm pile. As piling work moved closer to the building the bigger pile produce higher vibration at the top as indicated by point 2 and point 3 (nearest).

This is possibly because heavier pile reduces the vibration amplitude. It was similarly reported before that when the pile is small, the vibration amplitude can be inadequate at the pile base. This can also result in too much transverse vibration and sometime lead to a broken pile [9].

Similarly, the bottom transducers produce higher

vibration record as a result of 7.5mm pile from position 1 and 2. Only when it is very close to the model building at position 3 that the bigger 10mm pile cause higher impact.

Effect based on driving distance

Table 2 (a): The comparison on the effect based on of 7.5 x 7.5 mm piles (vibration level in mV/g)

7.5 x 7.5	POINT 1	POINT 2	POINT 3
Top	1810	1560	4394
Bottom	2037	3119	5656

Table 2 (b): The comparison on the effect based on of 7.5 x 7.5 mm piles (vibration level in mV/g)

10.0 x 10.0	POINT 1	POINT 2	POINT 3
Top	1392	1884	5061
Bottom	1602	2690	6241

Table 2 clearly indicates that the vibration level from various pile sizes increases as it moves closer to the model building.

The risk of driving piles next to a building may vary according to the types of structure and method of piling but in general vibration will be higher nearer to the building.

Effect to the top and bottom of building

Table 3(a): The comparison between top and bottom vibrations on 7.5 x 7.5 mm piles (vibration level in mV/g)

7.5 x 7.5	TOP	BOTTOM
Point 1	1810	2037
Point 2	1560	3119
Point 3	4394	5656

Table 3(b): The comparison between top and bottom vibrations on 7.5 x 7.5 mm piles (vibration level in mV/g)

10.0 x 10.0	TOP	BOTTOM
Point 1	1392	1602
Point 2	1884	2690

Point 3 5061 6241

The tables above show that the effect of driven pile activity was higher at the bottom for both sizes of pile. This is mainly because the ground vibrations is nearer to the bottom part of the building and the effect is diminishing towards the top.

CONCLUSION

It is known that pile driving activities creates vibrations in the ground. Those vibrations may affect the nearby structures or disturbed people in the neighborhood of pile driving activity.

In this study, the result naturally shows that vibrations effect were higher at the bottom of building compared to the effect on the top of building. Also, the nearer distance cause higher vibrations compared to the one further from the building. However, the smaller pile creates more vibrations towards the nearby building. This could be due to pile density reaction towards resisting forces from soil. Further study is required to identify a matrix of pile type, sizes and suitable distance for use in practical selection of pile size in works associated with pile installation near existing building or structure.

REFERENCES

- [1] Abdel-Rahman, S.M (2002), "Vibration associated with pile driving and its effects on nearby historical structure". In: *Proceedings-Spie the International Society for Optical Engineering*, 2002, USA. 1251-1258
- [2] Woods, R. C. and Sharma V. M. (2004), "Dynamic Effect of Pile Installation on Adjacent Structures", A. A. Balkema, India.
- [3] Massarsch, K.R. and Fellenius, B.H. (2008). "Ground Vibrations Induced by Impact Pile Driving.", In *Proceedings of 6th International Conference on Case Histories in Geotechnical Engineering*, 2008. VA USA.
- [4] Dowding, C.H. (1996) *Construction Vibrations*, New Jersey: Prentice-Hall
- [5] Pak, R. Y. S. and Guzina, B. B. (1995), Dynamic Characterization of Vertically Loaded Foundation on Granular Soils, *J. Geotech. Engrg.*, 121(3),274-286.
- [6] Ali, H., J. Castellanos, Hart, D. and B. Nukunya (2003), Real Time Measurement of the Impact of Pile Driving Vibrations on Adjacent Property during Construction, TRB Annual Meeting.
- [7] Teh, M. (2010), Flac 2D Analysis of a Single Pile under Lateral Loading, Unpublished Master Thesis, UiTM.
- [8] Selamat, M. R., Ramli, N. A. and Abdul Aziz, H. M. (2004), "Pile Driving Tests for Mitigating

Structural Damage due to Ground Vibrations”,
*Proceeding 3rd National Conference in Civil
Engineering*, Copthorne Orchid, Tanjung
Bungah, Malaysia.

- [9] Huybrechts, N., Legrand, C. and Holeyman, A.
(2002), “Drivability Prediction of Vibrated Steel
Pile”, *International Conference on Vibratory
Pile Driving and Deep Soil Compaction*, Swets
& Zeitlinger, Lisse

LABORATORY STUDY ON THE PERFORMANCE OF RECYCLED CONCRETE AGGREGATES BLENDED WITH RECLAIMED ASPHALT PAVEMENT AS A PAVEMENT GRANULAR MATERIAL

S. Jayakody, C. Gallage, J. Ramanujam, A. Kumar

School of Earth, Environment and Biological Sciences, Science and Engineering Faculty, Queensland University of Technology, Brisbane, Australia

ABSTRACT

Production of recycled concrete aggregates (RCA) from construction and demolition (C&D) waste has become popular all over the world since the availability of land spaces are limited to dispose. Therefore it is important to seek alternative applications for RCA. The use of RCA in base and sub-base layers in granular pavement is a viable solution. In mechanistic pavement design, rutting (permanent deformation) is considered as the major failure mechanisms of the pavement. The rutting is the accumulation of permanent deformation of pavement layers caused by the repetitive vehicle load. In Queensland, Australia, it is accepted to have the maximum of 20% of reclaimed asphalt pavement (RAP) in RCA and therefore, it is important to investigate the effect of RAP on the permanent deformation properties of RCA. In this study, a series of repeated load triaxial (RLT) tests were conducted on RCA blended with different percentage of RAP to investigate the permanent deformation and resilient modulus properties of RCA. The vertical deformation and resilient modulus values were used to determine the response of RCA for the cyclic loading under standard pressure and loading conditions.

Keywords: Recycled concrete aggregates, Granular pavements, RLT testing, Permanent deformation, Resilient modulus

INTRODUCTION

Road constructions are typically demanded a huge volume of crushed aggregates which causes for the depletion of natural resources. Therefore, investigations on the alternatives are becoming more popular to replace the crushed aggregates. Utilization of recycled materials in pavement construction leads the sustainability in the development of infrastructures. Reuse the crushed concrete as an unbound pavement material is a promising concept from both environmental and economic standpoints.

The subsurface layers (e.g: base and sub base) of flexible pavement usually made up from compacted aggregates. The absolute strength of these layer materials is very important to have a good stiffness in spreading traffic loading efficiently to the underlying subgrade soil. Thus these aggregates should be high quality and stringent materials. These granular layers exhibit two types of deformation when subjected to repeated loading; resilient deformation and permanent deformation. The resilient deformation provides an indication of elastic response and causes for fatigue cracking on bound layers (e.g asphalt, concrete layers) [1]. The permanent deformation is due to the accumulation of small increments of plastic strain over large number

of load repetitions [2]. Rutting failure of the pavements is due to the increment of these gradual accumulation plastic deformations of the granular layers.

The conventional classification test procedure for the pavement materials typically describe properties of the aggregates and then compared to those of an adequately performing material. But this is not appropriate for an alternative aggregate like crushed concrete because the material constituents are differ substantially from those of traditional materials. Therefore the most appropriate method of material assessment is to simulate the insitu loading and determine the performance. The materials can be performed in Repeated Load Triaxial test (RLT) in laboratories to observe the permanent deformation and resilient responses. The RLT test is significance to predict the performance and to determine the responses of the materials under different confining pressures and loading stresses.

This paper presents the results of RLT tests on RCA mixed with different percentages of RAP. The effects of RAP on RCA are determined through the permanent deformation and resilient modulus values. RAP is the major constituent that could be mixed with RCA at the crushing process. The asphalt is being mixed with crushed concrete aggregates when the rigid pavement concrete

structures are crushing. The possible mixing percentage of RAP with RCA is usually around 20% at the crusher plant [3]. Therefore it is important to investigate the influence of RAP in RCA on its performance under repetitive loading in order to assess RCA as unbound pavement materials. Further RLT tests on RCA will be conducted to investigate the effects of number of load repetitions, stress levels, and moisture content on plastic deformation and resilient modulus and the results will be published in subsequent journal/conference papers.

MATERIAL USED

The crushed concrete which is commercially named 'RM 001' is the main material and obtained from a leading concrete recycling plant in Queensland, Australia. RM001 is produced as a pure crushed concrete aggregates by avoiding the possible constituents such as asphalt, bricks, glass and wood. In order to evaluate the performance of RCA with and without the RAP, another three samples were prepared by mixing 10%, 15% and 20% of RAP with RCA. The maximum percentage of RAP was kept as 20% because it is the maximum possible amount of RAP content that could be mixed at the production process of RCA [3]. Table 1 shows the names of the tested samples and percentage of material mixed by mass.

Table 1 New RCA samples with blending percentages

Material name	Mixing percentage by mass	
	RM001	RAP
RM1-100/RAP0	100	0
RM1-90/RAP10	90	10
RM1-85/RAP15	85	15
RM1-80/RAP20	80	20

EXPERIMENTAL METHOD

Standard proctor compaction test in accordance with the Australian standard [4] was performed on each sample to determine the optimum moisture content (OMC) and maximum dry densities (MDD). Results are shown in Table 2. The RLT tests were performed at OMC to determine the permanent deformations at their maximum compactions.

Table 2. Optimum Moisture Content and Maximum Dry Density for four Samples

Material name	Optimum Moisture Content %	Maximum Dry density (g/cm ³)

RM1-100/RAP0	13.2	1.748
RM1-90/RAP10	12.7	1.785
RM1-85/RAP15	12.3	1.789
RM1-80/RAP20	12.9	1.789

Sample Preparation

Each sample was compacted at corresponding MDD with OMC. Prior to the compaction the water mixed samples were cured in sealed containers for 3 hours as it is the sufficient time period for moisture homogenization for crushed concrete aggregates [5]. Sample compaction was done using standard compaction method within 25 blows in 3 layers in standard triaxial mould, 100 mm in diameter and 200 mm in height. Since cement fines are presented in crushed concrete samples, it is required a specific time period for strength gaining in the specimens. Thus, the compacted samples were again cured in sealed containers for 4 days to steady their strength. Curing the RCA samples in hermetic boxes for 3 hours prior to the compaction and 4 days after the compaction were found to be adequate to guarantee the completion of strength gaining due to the cement fines as well as other organic constituents [5]. In the case of determining the performance characteristics, the curing period is significance to expose the precise responses of RCA specimens under cyclic loading.

Repeated Load Triaxial test

Repeated Load Triaxial test was performed on the compacted specimens to simulate the repeated passage of loaded vehicle wheels over the materials. The standard test method of Department of Transport and Main Roads Q137 for permanent deformation and resilient modulus of granular unbound materials was followed for the permanent deformation and resilient modulus test [6]. The UTM-4 digital servo control testing machine was used with the UTM-14 Resilient modulus test application software to determine the performance characteristics. The RLT equipment is shown in the Fig. 1.

Stresses were decided according to the Q137; 125kPa confining pressure was applied and held over the test. The total vertical pressure 750kPa was applied to represent the tire pressure of a standard axle. Therefore constant stress ratio of 750/125 was kept for 50000 loading cycles.



Fig. 1 Repeated load triaxial apparatus

RESULTS AND DISCUSSION

RLT test results aimed to characterize the resistance of the specimens to the incremental plastic strain responses and the resilient modulus (M_R) of the RCA samples. Figure 2 shows a typical vertical stress vs. axial strain behavior of a granular material after a certain number of load cycles at fixed loading and pressure condition [7].

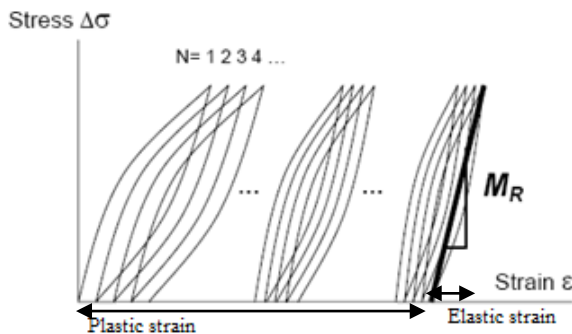


Fig. 2 strains and resilient behavior of granular materials

Usually it can be observed a rapid accumulation of plastic strain at the beginning of load cycles and the plastic response of the material becomes gradually decreased and then stabilized. The elastic response also gradually decreased as seen in the Fig. 2 and it shows non linear behavior for the load repetitions. However a stable resilient behavior can be observed after a large number of load cycles [2]. The results of the RLT tests of this study have been discussed in accordance with the above behavior of RCA specimens.

Effect of RAP in RCA on Its Permanent Deformation

Figure 3 shows the values of permanent deformation of the four samples. Rapid deformations of the four

samples are seen at the beginning of the cyclic loads. It is noted that the capability to lower the deformation by increasing the compaction effort at the sample preparation on the four specimens. It is significant that RM1-100/RAP0 and RM1-90/RAP10 exhibit almost similar values but on the other hand RM1-90/RAP10 has slightly lower value of deformation than 100% pure crushed concrete. The deformation curves of these two specimens in Fig. 3 shows that the rapid deformation of RM1-90/RAP0 is slightly lower than RM1-100/RAP0 at the initial loading cycles. This indicates that RM1-90/RAP10 sample is well compacted than RM1-100/RAP0 specimen. The 10% RAP particles are caused for appropriate gradation of the particles for better compaction and higher stiffness by sound interlocking of the particles. Therefore the combination of RM001, 90% and RAP 10% has shown higher resistance for the repetitive load.

Other two specimens had comparatively higher deformation and the values have been increased with the portion of RAP percentage. Further the increasing rate of deformation also higher than the RM1-100/RAP0 and RM1-90/RAP0. Increase of RAP portion as 15% and 20% caused for the lack of coarser particles and led for lower stiffness of the compacted specimens. In addition, the bitumen coat around the asphalt particles could be facilitated for further compression of the specimens with increasing cyclic loading. The rapid deformations of these two samples also indicate higher values for the initial load cycles. This specifies that the mixing RAP more than 15% do not sustain for better compaction with particles size distribution of the specimens. However, having a higher deformation at the beginning of load cycles is a common feature for the four samples. Therefore this rapid deformation could be minimized by applying a higher compactive effort at the sample preparation.

Limitation of the rut depth in pavement construction is the key aspect in pavement designing. The prediction of rutting in flexible pavement is extremely complex since it is basically depend on the quality of the base and sub base aggregates as well as the environmental conditions. Therefore, appreciate the nature of permanent deformation of a pavement material is the foremost thing to understand and assess the behavior of materials in pavement rutting [8]. The overall results of permanent deformation of the four samples are less than 7mm for the 750 kPa loading pressure with 125 kPa confining pressure after 50000 loading cycles. This is a satisfactory result and more tests are continuing to investigate the behavior of axial deformation of RCA under different stress conditions.

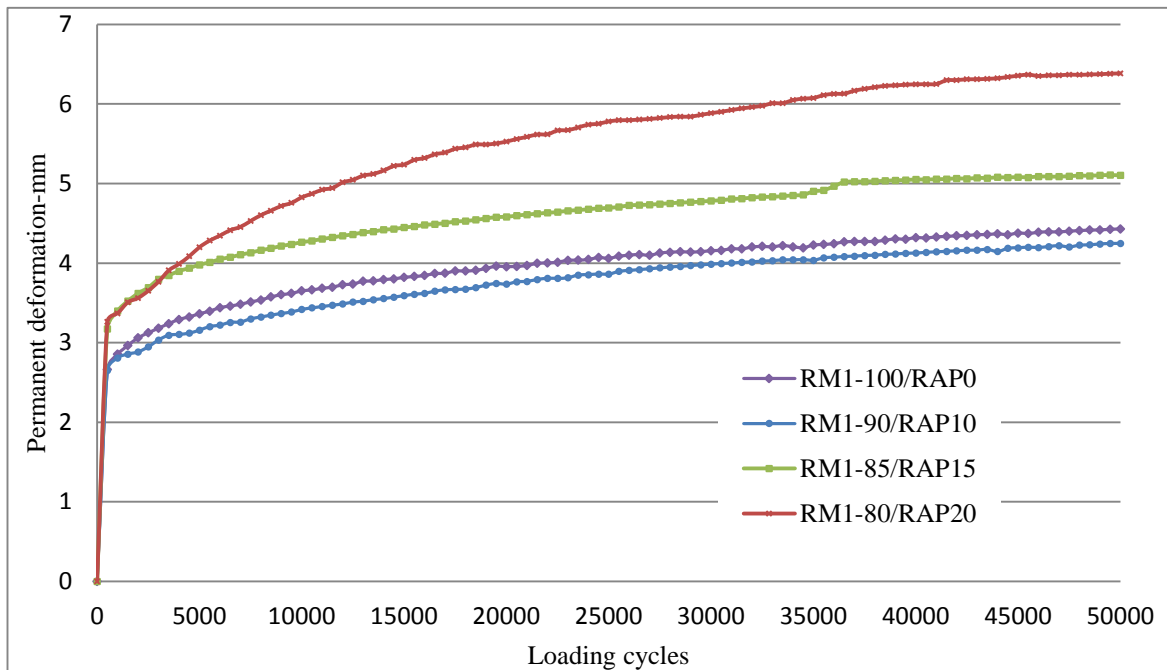


Fig. 3 Permanent deformation values for 50000 cycles

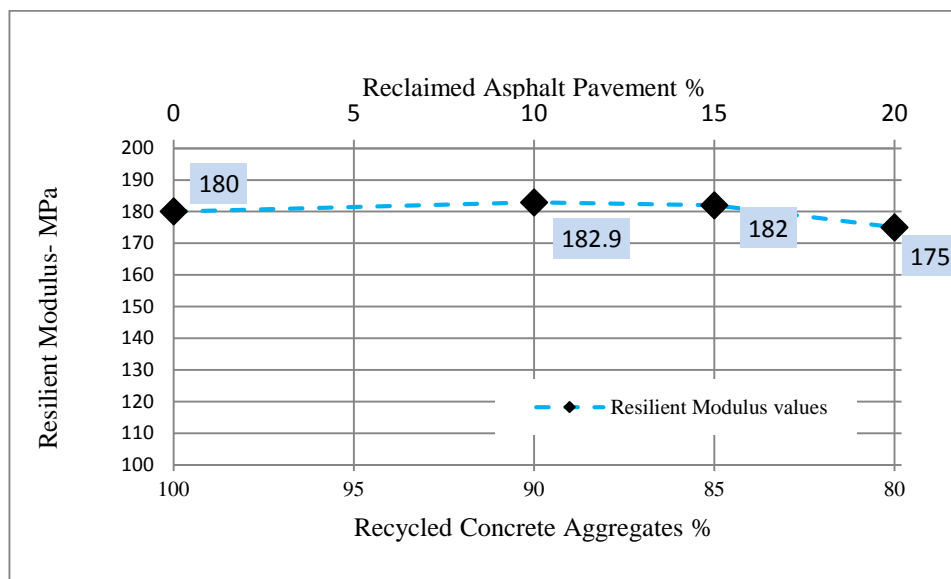


Fig. 4 Resilient Modulus values after 50000 cycles

Effect of RAP in RCA on Its Resilient Modulus

The resilient modulus is a key property of granular material characterization which indicates the stiffness and elastic response of aggregates. Mr is

highly stress dependent and for the pavement designing a representative Mr value should be selected according to the stress state for the selected pavement structure and loading [9]. Figure 4 shows the Mr values of four samples with the variation of

RCA and RAP content after 50000 load cycles. They have almost similar Mr values at the end of 50000 load cycles. But RM1-80/RAP20 shows slightly low value of Mr and this makes a sign that the elastic response of the RCA samples could be higher with the increasing of RAP over 15%. Four samples also show considerably high Mr values for 750kPa cyclic pressure. It can be noted that the compacted materials perform higher stiffness and the elastic strain becomes lower after 50000 cycles on the specimens. This is a good sign for a pavement material since higher resilient modulus values indicate lower elastic responses of the materials for cyclic loads.

CONCLUSION

RLT tests were aimed to evaluate the RCA as it is used as unbound pavement material. On the basis of the test results of this study following conclusions are made.

- Modified RCA sample by mixing 10% RAP shows the best performance with lowest permanent deformation
- High percentage of RAP as 15%, 20% lead for lower stiffness of the RCA and show higher permanent deformations
- After 50000 loading cycles the deformation is not resilient in four samples and permanent deformation is acceptable for more load repetitions. These materials could reach the failure for a great number of load repetitions
- It is seen that resilient modulus is not significantly affected by the RAP content if the amount of RAP in RCA is equal or less than 15%. However, further increase in RAP content (e.g: 20%) cause to decrease in resilient modulus of RCA samples. Therefore the elastic response could be higher when increasing the RAP content over 15%

Further studies are continuing to investigate the resilient behavior and permanent deformation of RCA with respect to the number of load repetitions, stress levels, and moisture content and the results will be published in future.

REFERENCES

[1] Lekarp F, Dawson A, "Modelling permanent deformation behavior of unbound granular materials", Construction and Building Materials, Vol. 12, 1998, pp. 9-18.

[2] Chazallon C, Hornych P, Mouhoubi S, "Elastoplastic model for the long-term behavior modeling of unbound granular materials in flexible pavements",

International Journal of Geomechanics, 2006, pp. 279-289.

[3] Department of transport and main roads Q, Australia, "Recycled materials for pavements", State of Queensland, Department of Transport and Main Roads, 2011.

[4] Australia CoS, "Method 5.1.1: soil compaction and density tests—determination of the dry density/moisture content relation of a soil using standard compactive effort", Standards Australia International Ltd, Sydney, NSW 2001, Australia, 2003.

[5] Jayakody S, Gallage C, A.Kumar, "Assessment of recycled concrete aggregates for road base and sub-base", Second international conference on Geotechnique, Construction Materials and Environment - GEOMATE 2012, pp. 575-579.

[6] Department of transport and main roads Q, Australia, "Permanent deformation and resilient modulus of granular unbound materials", The state of Queensland, Department of transport and main roads, 2012.

[7] United State Department of Transportation FHA, "Geotechnical Engineering ", 2011.

[8] Lekarp F, Dawson A, "State of the art. II: Permanent strain response of unbound aggregates", Journal of transportation engineering, Vol. 126, 2000, pp. 76-83.

[9] Jameson G, Vuong B, Moffatt M *et al.*, "Assessment of rut-resistance of granular bases using the repeated load triaxial test", Austroads Limited, Sydney, New South Walse, Australia, 2010.

BEHAVIOR OF PENETRATION AND LEACHING OF CESIUM IN MORTAR HAVING VARIOUS FINE AGGREGATES AND MOISTURE CONTENT

Masashi ITO¹, Kenichiro NAKARAI¹, Akihiko HAYASHI¹ and Kenji KAWAI¹
¹Graduate School of Engineering, Hiroshima University, Japan

ABSTRACT

The accident at the Fukushima Daiichi Nuclear Power Plant resulted in spreading a huge amount of the radioactive cesium (cesium-137) widely. It is important to decontaminate the radioactive cesium and dispose the radioactive waste safely as soon as possible. This study aims to investigate the basic behaviors of the cesium-133 in mortar such as adsorption, penetration and leaching. From the experimental results, it was observed that the cesium was hardly adsorbed on the cement hydrates as well as lime sand and silica sand prepared as aggregate in this study. In the penetration test, in the water-saturated mortar specimens, around 80% of the penetrated cesium in the whole area of specimens was soluble. On the other hand, in the dried specimens, 80% of the penetrated cesium was soluble only in the inner area of the specimen. In the surface, 60% of the cesium was soluble. It was thought that the surface of the dried specimens were carbonated during the drying process before the penetration tests, and then fixed more cesium.

Keywords: Cesium, Adsorption, Penetration, Leaching, Zeolite

INTRODUCTION

The accident at the Fukushima Daiichi Nuclear Power Plant caused by the Great East Japan Earthquake resulted in spreading a huge amount of radioactive cesium widely [1]. The cesium-137 has a half-life of thirty years and remains longer than other main radioactive substances released by the accident. We need to decontaminate the radioactive cesium appropriately.

Disposing a huge amount of radioactive waste that resulted from decontamination has been also problems. It is necessary to prevent radioactive waste from scattering and diffusion to the environment again during transportation and storage.

From the above, it is demanded to investigate the behavior of the cesium in concrete. To discuss the behavior of the cesium in concrete, the sorption properties for cement materials have already been investigated by several researchers [2]. However, the studies on the mass transfer considering the time histories of moisture contents in the concrete under cyclic drying and wetting conditions are very few.

Therefore, this study aims to investigate the cesium behaviors such as adsorption, penetration in the cyclic drying and wetting conditions, and leaching from mortar. Because of the limitation of

the experimental installation, the non-radioactive cesium (cesium-133) was used in this study.

EXPERIMENT METHODS

Materials

The materials used in this experiment were ordinary Portland cement (the density was 3.16 g/cm³ and the chemical composition is shown in Table. 1), unwashed lime sand (the density in saturated surface-dry condition was 2.68 g/cm³ and the water absorption was 1.46 %), washed lime sand and zeolite. The zeolite prepared in this study was the synthetic mordenite, which was reported to adsorb a large quantity of the radioactive cesium [3], [4]. In the adsorption test, silica sand (the density in saturated surface-dry condition was 2.64 g/cm³ and the water absorption was 0.18 %) was also used. The commercially available cesium-133 chloride was used.

Specimens

The mortar specimens with different fine aggregates were used in the penetration and leaching tests. The fine aggregates were the unwashed lime

Table. 1 Chemical composition of cement

Chemical composition (%)									
LOI	SiO ₂	Al ₂ O ₃	Fe ₂ O ₃	CaO	MgO	SO ₃	Na ₂ O	K ₂ O	Cl
1.75	20.82	5.15	2.92	64.69	1.12	2.22	0.23	0.38	0.005

Table. 2 Mixture proportion of mortar specimens

(a) Penetration test

W/C	Unit content kg/m ³			
	Water	Cement	Sand	Zeolite
0.60	430	717	872	0
			918	6.8

(b) Leaching test

W/C	Unit content kg/m ³				
	Water	Cement	Sand	Zeolite	CsCl
0.45	386	858	918	0	6.5
			872	6.8	
0.60	430	717	918	0	7.2
			872	6.8	

Table. 3 Ponding and drying condition

Specimen name	Moisture content	Condition
S	Saturation	Ponding in Cesium chloride solution for 28 days
D (P)	Dry	Ponding in Cesium chloride solution for 6 hours
D (P-D)	Dry	Ponding in Cesium chloride solution for 6 hours ↓ Drying for 1 week
		Ponding in Cesium chloride solution for 6 hours ↓ Drying for 1 week ↓ Ponding in Pure water for 6 hours

sand, the washed lime sand, and the unwashed lime sand partially replaced by zeolite (5 % in volume).

For the penetration test, the above materials and water were mixed mechanically at the water-cement ratio of 0.60, and then the mortar was casted in molds of 40×40×160 mm. After 24 hours, specimens were demolded and cured in the high humid condition for 28 days. The mix proportions of mortar specimens were shown in Table. 2 (a).

The specimens for the leaching test, were prepared in the similar manner to that for the penetration test, but we used 0.1 mol/L of cesium chloride solutions as the mixing water of the mortar specimens. The water-cement ratios were 0.45 and 0.60 and the mortar was casted in molds of 40×40×40 mm. The mix proportions of mortar specimens were shown in Table. 2 (b).

Adsorption test

The samples used in the adsorption test were cement paste powder with a water-cement ratio (W/C) of 0.40 (hand mixed, and cured for 28 days) and fine aggregates such as unwashed lime sand, washed lime sand, silica sand and zeolite. Those samples were pulverized to smaller than 75 μm . In addition, the mixed samples that consist of equivalent amount of cement paste powder and fine aggregates were prepared.

One gram of samples including cement paste powder was added in 20 mL of deionized water, and then they were stirred for 10 hours to stabilize pH. After that, 1mL of the cesium chloride solution was added, and then stirred for 6 more hours again. In this test, 5, 10 and 15 g/L of cesium chloride solutions were added (the initial cesium concentration were 0.0018, 0.0036, and 0.0054 mol/L, respectively). After stirring, the solution was filtrated with a membrane-filter and the equilibrium concentration of cesium in the solution was measured by an atomic adsorption spectrophotometer.

Measurement of pore size distribution

In the measurements, the total porosity and the pore size distribution were measured by mercury intrusion porosimetry (MIP). Before the measurements, the mortar specimens with W/C=0.45 and 0.60 at the age of about 64 days (cured in high humid condition) were cut by an oil cutter and crushed with a hammer to become less than 1 cm in grain size. The crushed specimens were ponded in acetone and dried by the vacuum deaeration. The measurement range of pressure was 0.01~413 MPa and the diameter was 0.003~121 μm .

Penetration test

In the penetration tests, two types of specimens with different moisture contents, saturated and dried specimens, were prepared. The saturated specimens were prepared with vacuum saturation technique [5], while the dried specimens were dried to be constant weight in the conditions of 20 °C and 60 % RH. Five surfaces of each specimen were coated with epoxy resin before the test in order to discuss one-dimensional penetration behavior.

The ponding and drying condition during the penetration test is shown in Table. 3. The specimens were ponded in 0.1 mol/L of the cesium chloride solutions or the deionized water. After that, the specimens were cut into slices of 2.5 mm in thickness from the exposure surface by an oil cutter, and pulverized in order to measure the distribution of total and soluble cesium. The measurement of the quantity of cesium in every sample was conducted based on “Methods of test for chloride ion content in hardened concrete” (JIS A 1154). The total cesium was derived by nitric acid and the soluble cesium was derived by hot water of 50 °C. The concentration of cesium in the solution was determined with an atomic adsorption spectrophotometer.

Leaching test

The mortar specimens were placed in a tank filled with the deionized water. The deionized water volume was 480 mL, which was equated to 5 mL per 100 mm² of the surface area of the specimen. The tank was capped to avoid the evaporation of the water and the carbonation of the specimen. The deionized water was renewed at the periods of 0.25, 1, 2.25, 4, 9, 16, 25, 36, 49 and 64 days. After that, the solution was filtrated with a membrane-filter and the concentration of cesium was measured by an atomic adsorption spectrophotometer.

RESULTS AND DISCUSSION

Adsorption test

The results of the adsorption test are shown in Fig. 1. The distribution ratio K_d calculated by Eq (1) was used to discuss the cesium adsorptivity of the samples [6].

$$K_d = \frac{V}{M} \times \frac{C_0 - C}{C} \quad (1)$$

where V : volume of liquid (mL)

M : mass of samples (g)

C_0 : initial concentration (mol/L)

C : equilibrium concentration (mol/L)

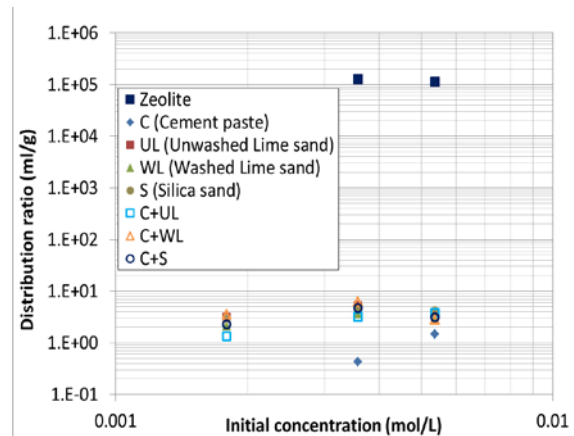


Fig. 1 The results of adsorption test

The distribution ratio is the ratio of the concentration in the solid-phase to the concentration in the liquid-phase. For example, the high distribution ratio at the same initial concentration of the solution means that cesium was adsorbed by the materials easily. From Fig. 1, it was found that the distribution ratios were around 1 mL/g for cement paste powder and 2~4 mL/g for fine aggregates, respectively. On the other hand, the distribution ratio of zeolite was approximately 1×10^5 mL/g, and it was significantly higher than those of cement paste powder and fine aggregates.

The distribution ratios for unwashed and washed lime sand were almost same although the decrease in the distribution ration by the washing was expected. It was thought that pulverizing might relatively decrease the influence of the fine grains in the unwashed lime sand on the adsorption.

The equilibrium concentrations in the liquid-phase of the samples including zeolite were too low to be measured accurately. Although the values of the distribution ratios should be used as a guide, it can be said that a large amount of cesium could be adsorbed on zeolite.

Measurement of pore size distribution

The results of measurement of the total pore volume, and pore size distribution of the mortar specimens with $W/C=0.45$ and 0.60 are shown in Figs. 2, 3, and 4. From Fig. 2, it was observed that the specimens with $W/C=0.60$ had larger total pore volume than the specimen with $W/C=0.45$ regardless of the kinds of the fine aggregates. Figs. 3 and 4 indicate that the specimens containing zeolite had the largest total pore volume with the increase in the cumulative pore volume in the range of pore size of $0.01 \sim 0.1 \mu\text{m}$. Especially, the increase in the pore volume was significant in the specimen with $W/C=0.60$.

Regarding to the effect of the washing of the sand, the clear differences in the pore size

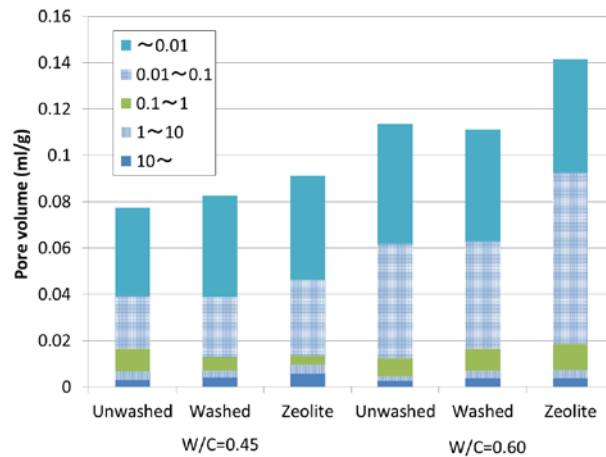


Fig 2 The cumulative pore volumes

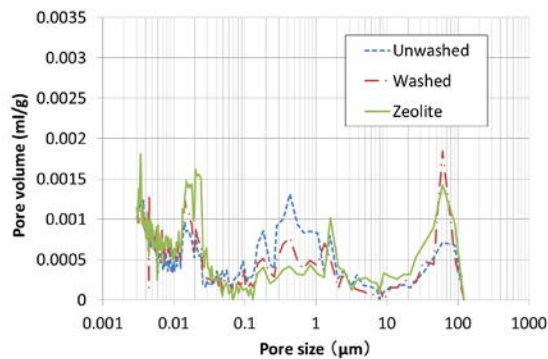


Fig. 3 The distribution of pore volume (W/C=0.45)

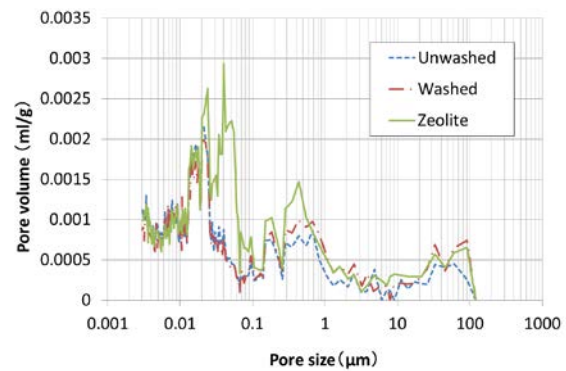


Fig. 4 The distribution of pore volume (W/C=0.60)

distributions and the cumulative pore volumes were not observed between the specimens containing unwashed and washed lime sands.

Penetration test

First, as the results of the penetration test of the specimen containing the unwashed lime sand, the distributions of the measured total and soluble cesium from the exposure surface of the specimens are shown in Fig. 5. The distribution of the total cesium showed that the cesium penetrated to the deeper area in the saturated specimen than in the dried specimen. It was because the ponding periods were 28 days, which was longer than that of the dried specimens. The apparent diffusion coefficients of the saturated specimens were about $1 \times 10^{-7} \text{ cm}^2/\text{s}$ and those of the dried specimens [D (P)] were about $1 \times 10^{-6} \text{ cm}^2/\text{s}$. Since they were calculated based on Fick's laws of diffusion, the apparent diffusion coefficients of the dried specimens [D (P)] significantly increased by the effect of advection. It means that the cesium penetrates to the dried specimens deeper than the saturated specimens when the ponding periods were same.

Regarding the solubility of the penetrated cesium, 80 % of the penetrated cesium was soluble not only in the inner area of the specimen but also at the

surface.

As for the dried specimens [D (P)], in the inner area of the specimen, 80 % of the penetrated cesium was soluble. On the other hand, large amounts of the cesium were fixed as insoluble at the surface, where 60 % of the total cesium was soluble. It was reported that the distribution ratio of cesium in carbonated part was 1.5 times as much as non-carbonated part [7]. From the above, it was thought that the surface of the dried specimens were carbonated during the drying process before the penetration tests, and then fixed more cesium.

For the transportation of cesium during ponding and drying processes, the total quantity of cesium increased at the surface of specimen, and decreased at 6~12 mm from the surface for the specimen [D (P-D)] compared with the specimen [D (P)] during the drying process. It was thought that soluble cesium in the inner area were transported to the surface with dissipating of water, and adsorbed during the drying process. The quantity of cesium increased at near 8 mm from surface of the specimen for the specimen [D (P-D-P)] again. It was also thought that a part of insoluble cesium which was fixed at the surface became soluble, and was transported to the inner area with water penetration when the specimen was ponded in the deionized water.

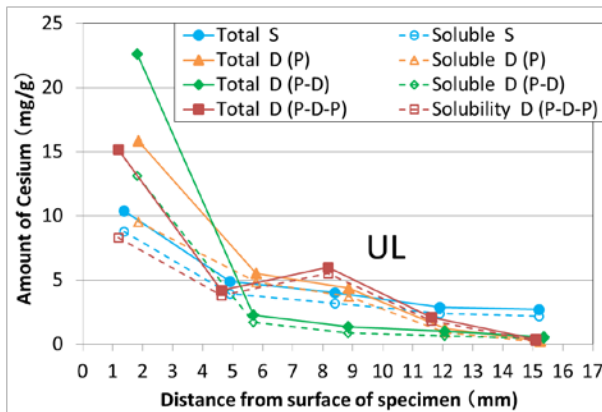


Fig. 5 The distribution of total and soluble Cesium (UL)

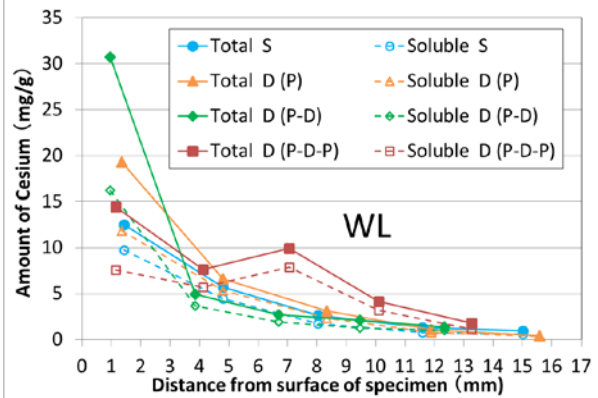


Fig. 6 The distribution of total and soluble Cesium (WL)

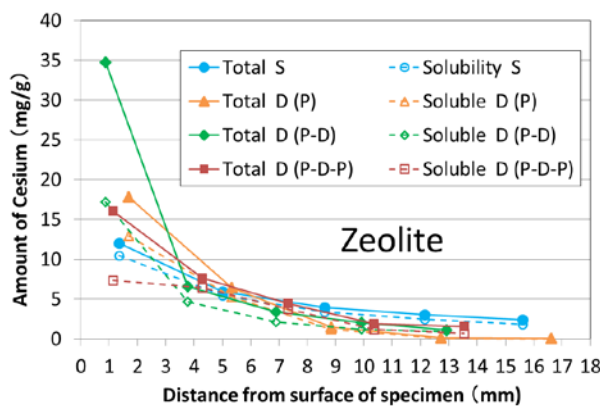


Fig. 7 The distribution of total and soluble Cesium (Zeolite)

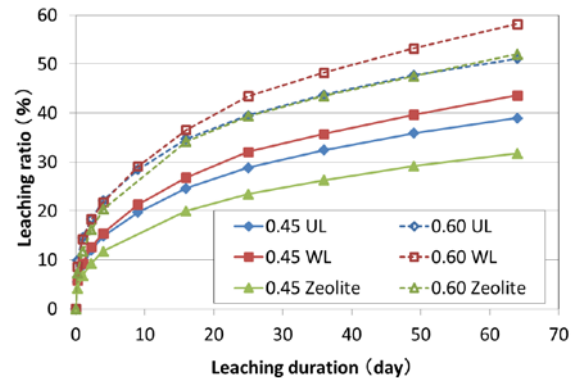


Fig. 8 The result of leaching test

Next, the results of the specimen containing the washed lime sand were shown in Fig. 6. The trend of penetration for the specimen containing washed lime sand were similar to the specimen containing unwashed lime sand, while the total quantity of cesium increased.

Finally, the results of the specimen containing zeolite were shown in Fig. 7. The profiles of the penetrated cesium were almost similar with the other specimens. However, the quantity of cesium did not increase at near 8 mm from surface of the specimen for the specimen [D (P-D-P)]. It was caused by the zeolite's high adsorption reducing the transportation of cesium to the inner area associated with the advection.

Leaching test

As results of the leaching test, the leaching ratio are shown in Fig. 8. The leaching ratio was the percentage of the cumulative amount of cesium leached from a specimen to the amount of total cesium. The amount of total cesium was the amount of cesium contained in a specimen at the time of test start, calculated by mixture proportion. The leaching ratios of specimens with $W/C=0.60$ were higher than

specimens with $W/C=0.45$ regardless of fine aggregates because the specimen with $W/C=0.60$ had larger total pore volume as seen in Fig. 2, and the internal structure was porous.

About the differences in the fine aggregates, the leaching ratio of the specimen containing washed lime sand was higher than that of the unwashed lime sand because of the high specific surface area of the small particle lime sand. In addition, the leaching ratio of the specimen containing zeolite was equal or lower than that of unwashed lime sand in spite of the result that the specimen has the largest total pore volume. It is considered that adsorption performance of the zeolite reduced the leaching ratio for the specimen containing zeolite.

CONCLUSIONS

In this study, we investigated the cesium behaviors in the mortar such as adsorption, penetration in the cyclic drying and wetting conditions, and leaching by using cesium-133. As a result, it was found that the cesium was hardly adsorbed on the cement paste powder and fine aggregates, while significantly adsorbed on zeolite.

In the penetration test, around 80% of penetrated cesium was soluble in the surface and inner area of saturated specimens. On the other hand, in the dried specimens, 60% of the penetrated cesium was soluble in the surface. We thought that large amounts of the cesium were fixed as insoluble at the surface, and it was caused by carbonation of the specimen. In the inner area of the dried specimens, 60% of the penetrated cesium was soluble.

The leaching ratios of the specimens with $W/C=0.45$ and 0.60 were 30~40 % and 50~60%, respectively, and the leaching ratio of cesium was high.

From the study, it was found that the cesium was transported with the water penetration or dissipating in the cyclic drying and wetting conditions.

REFERENCES

- [1] Digital Japan, "Extension site of distribution map of radiation dose, etc."
<http://ramap.jmc.or.jp/map/eng/>
- [2] Mine T., et al, "Adsorption tests of Iodine and Cesium in various cementitious material" Power Reactor and Nuclear Fuel Development Corporation, PNC TN8410 97-258, 1997, p.40
- [3] National Environmental Research Institute, "Proper waste disposal behavior of radioactive material from technical documentation version3", December, 2012, pp.43-44
http://www.nies.go.jp/shinsai/techrepo_r3_121220.pdf
- [4] Ogawa M., "Zeolite", Journal of the Japan Research Association for Textile End-Uses, Vol.24, No.7, 1983, pp.293-302
- [5] Watanabe H., et al, "Effect of vacuum saturation method for concrete specimen on results of rapid chloride permeability test", Proceedings of annual meeting of Japan Society of Civil Engineers, Vol.57, No.5, 2002, pp.1057-1058
- [6] Sugiyama D., "Experimental measurements and integrated modeling studies of actinide sorption onto cement", CRIEPI report T02025, April, 2003, p.3
- [7] Mochizuki M., et al, "Effect of Carbonation of Concrete on the Distribution Coefficient of Cs and Co", Atomic Energy Society of Japan, Autumn convention proceedings 1991, p.569

EFFECTS OF COARSE AGGREGATE CONTENT ON THE EROSION RATE OF CONCRETE DUE TO SULFURIC ACID ATTACK

Yuji Hatano¹, Yutaka Okame¹ and Kenji Kawai¹

¹ Hiroshima University, Japan

ABSTRACT

The deterioration of concrete structures caused by sulfuric acid attacks has been serious. However, a prediction method for concrete deterioration due to sulfuric acid attack has not been established yet. In this study, the effects of the coarse aggregate content on sulfuric acid deterioration of concrete were investigated. In the experiment, the coarse aggregate content and water cement ratio of concrete were varied and concrete specimens were immersed in two different concentrations of sulfuric acid solution (1 mol/L, and 2 mol/L). The erosion depth, mass loss and neutralization depth were measured at fixed periods. The results showed that the increase in the coarse aggregate content led to the decrease in the rate of sulfuric acid deterioration of concrete. Coarse aggregate was found to contribute to preventing the removal of gypsum produced by the reaction of sulfuric acid with calcium compounds.

Keywords: Sulfuric acid attack, Coarse aggregate, Erosion depth, Mass loss, Neutralization depth

INTRODUCTION

There are various acid solutions that cause chemical deterioration of concrete, and a particular attention has been paid to sulfuric acid. Recently, the deterioration of concrete caused by sulfuric acid attacks in sewage and waste water treatment plants has been reported. In sewage and waste water treatment plants, sulfuric acid is generated by microorganisms, and this causes sulfuric acid deterioration of concrete. However, a prediction formula of sulfuric acid deterioration of concrete is not yet established. In the previous studies^{1,2,3)}, it was reported that the deterioration of concrete due to sulfuric acid is affected by the concentration of sulfuric acid and the water cement ratio of concrete. However, most of the experiments were carried out using cement paste and mortar specimens. Even in the case where

concrete specimens were used, the effect of coarse aggregate on the deterioration was barely considered. For this reason, it is hard to apply the results of previous studies to the prediction of the deterioration of existing concrete structures. It is necessary to consider the effect of coarse aggregate on the deterioration in order to apply the results of previous studies using mortar to existing concrete. In this study, using two different concentrations of sulfuric acid solutions, the effect of coarse aggregate on the erosion of concrete and the sulfuric acid penetration into the concrete was investigated.

EXPERIMENTAL OVERVIEW

Materials

Normal Portland cement (density: 3.16 g/cm³;

Table 1 Mix proportion of concrete specimens.

Names	W/C	Unit Content(kg/m ³)						G/V
		W	C	S	G	AE	Thickener	
G0	0.40	266	664	1146	0	3.3	-	0
G17		220	549	949	452	2.8	0.3	17
G35		174	435	751	905	2.1	-	35
G50		132	332	573	1310	1.7	-	50
G0	0.55	274	498	1253	0	2.5	-	0
G18		224	407	795	479	2.0	0.2	18
G37		174	316	795	958	1.6	-	37
G50		137	249	626	1310	1.3	-	50

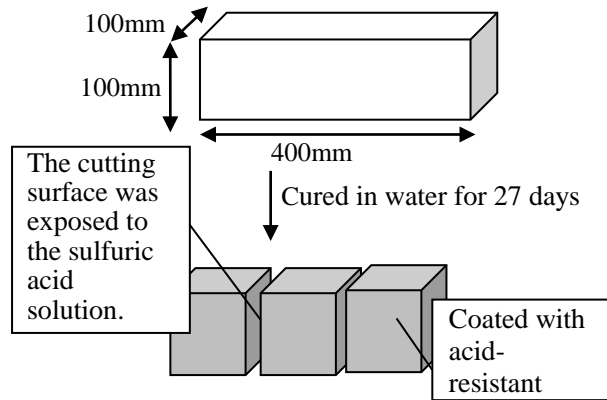


Fig. 1 Schematic diagram of the specimen

specific surface area: 3360 cm²/g), crushed sand (saturated and surface-dry density: 2.60 g/cm³; absorption 1.06 %), crushed stone (saturated and surface-dry density: 2.62 g/cm³; absorption 0.69 %) were used as cement, fine aggregate, and coarse aggregate, respectively. In addition, a thickener (methyl cellulose type) was used to disperse coarse aggregate homogeneously in concrete when the volume ratios of coarse aggregate in concrete were 17 % and 18 %.

Mix proportion of specimens

The mix proportion of concrete used in this study is shown in Table 1. The water cement ratios of concrete are 0.55 and 0.40, and the volume ratios of the coarse aggregate in concrete are 0 %, 18 % (17 %, in the case of W/C=0.40), 37 % (35 %, in the case of W/C=0.40), 50%. Based on the mix proportions for G35 (W/C=0.40) and G37 (W/C=0.55) concretes, the volume ratios of water, cement, and fine aggregate in concrete were kept constant so as not to change the properties of mortar.

Outline of specimens

Figure 1 shows the outline of specimens. Prismatic concrete specimens measuring 100×100×400 mm in size (W/C=0.55, 0.40) were prepared and demolded after 24 hours, and cured in water for 27 days. At the age of 28 days, the specimens were cut into three pieces. These pieces were then coated with acid resistant acrylic epoxy, except for one cutting surface exposed to the sulfuric acid solution. Before the following immersion test, the specimens were immersed in

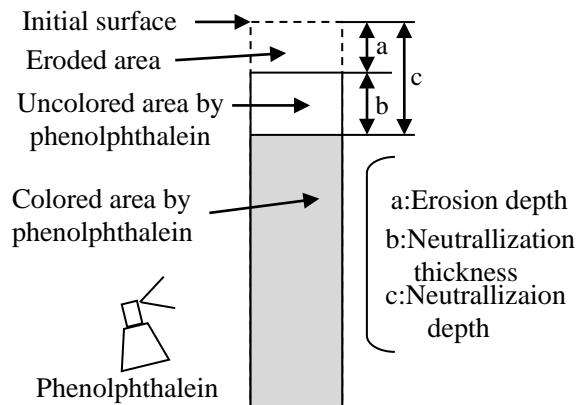


Fig. 2 Schematic diagram of deterioration depth

water for 1 day in advance to prevent rapid penetration of sulfuric acid due to water absorption.

Immersion test

Specimens were immersed in sulfuric acid solution at concentrations of 1 mol/L and 2 mol/L. The concentration of the solution was measured periodically, and the concentration was adjusted by adding sulfuric acid every week.

Measurement

Mass loss

The mass loss of a specimen was measured at fixed periods. The mass loss was defined positive when the mass of the specimen became smaller than the initial mass.

Erosion depth

The erosion depth is the difference between the initial length and measured length of the specimen. The length of each specimen was measured at given 4 points at fixed periods. The erosion depth was defined negative when the specimen was expanded because of reaction products.

Neutralization depth

After being immersed for a fixed period, specimens were split into two pieces and phenolphthalein solution was sprayed on the cross-section. The length of the uncoloured area was measured and the sum of that length and the

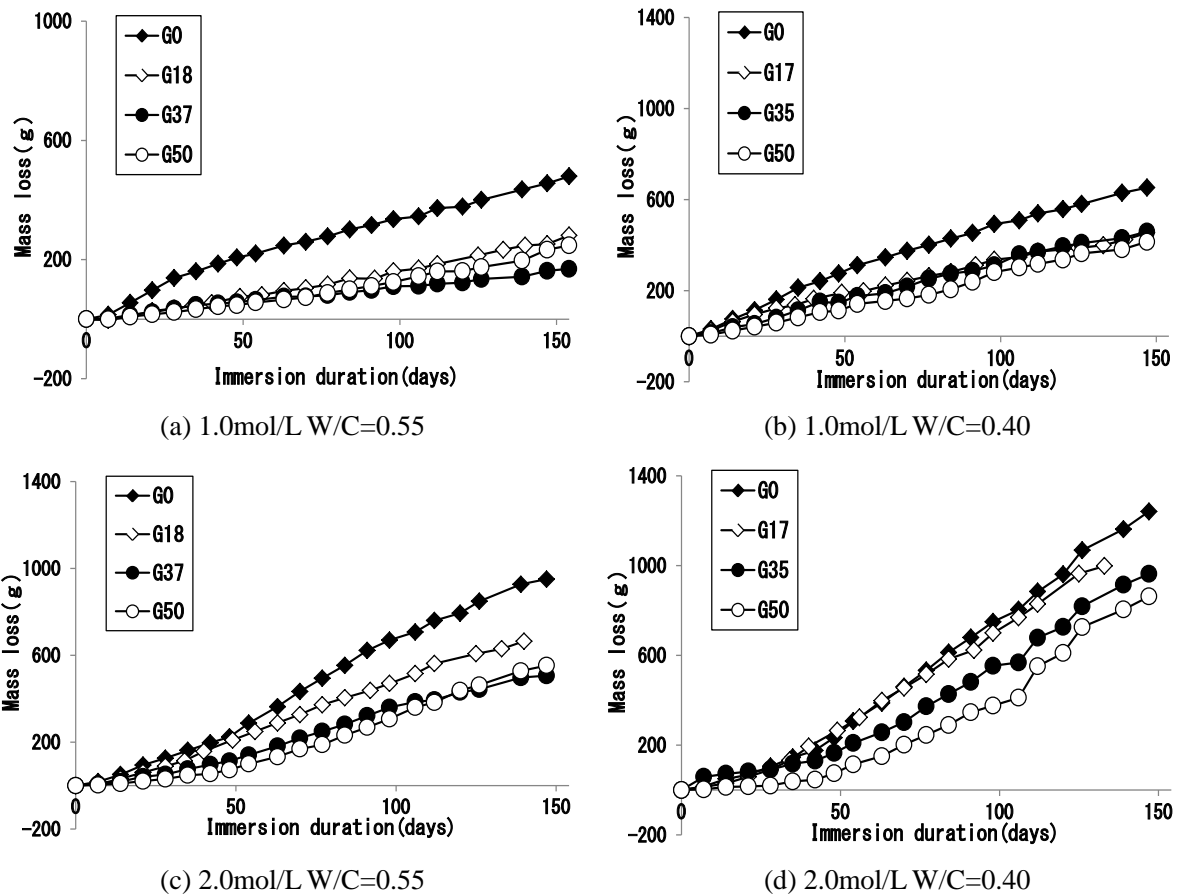


Fig. 3 Relationship between immersion duration and mass loss

erosion depth of the same specimen was defined as neutralization depth.

EXPERIMENTAL RESULTS

Mass Loss

Figure 3 indicates the relationship between the immersion duration and mass loss. From this figure, the mass loss for G0 is the largest in all cases. The mass loss for G50 having the highest coarse aggregate content is becoming gradually larger than that for G37 in the case of W/C=0.55. It is suggested that coarse aggregate could control the mass loss of concrete due to the sulfuric acid attack. However, little difference can be seen in the mass losses for G35 and G50 (W/C=0.40) immersed in 1.0mol/L of sulfuric acid solution and for G37 and G50 (W/C=0.55) in 2.0mol/L. The effect of the coarse aggregate content on the sulfuric acid deterioration could be

different in the water cement ratio of concrete and the concentration of sulfuric acid solution.

Erosion depth

Figure 4 indicates the relationship between immersion duration and erosion depth. In all cases, the specimen for G0 began to be eroded earlier compared with the other specimens. For specimens other than G0, the time when the specimen began to be eroded was different. The larger the coarse aggregate content, the later the erosion starts. The Erosion depth for G0 increased almost linearly with time, while the erosion depth for others seems to increase in a stepwise manner. Although the value shown in Figure 4 is the average of three different specimens, the raw data measured at given four points of the specimen for G0 with W/C=0.40 immersed in 1.0 mol/L and for G35 with W/C=0.55 immersed in 1.0 mol/L are shown in Figure 5. From each data in this figure, a linear increase for G0 and a stepwise increase for G35 can be also confirmed. When a space between coarse aggregates is small, it is thought that the aggregates keep gypsum produced

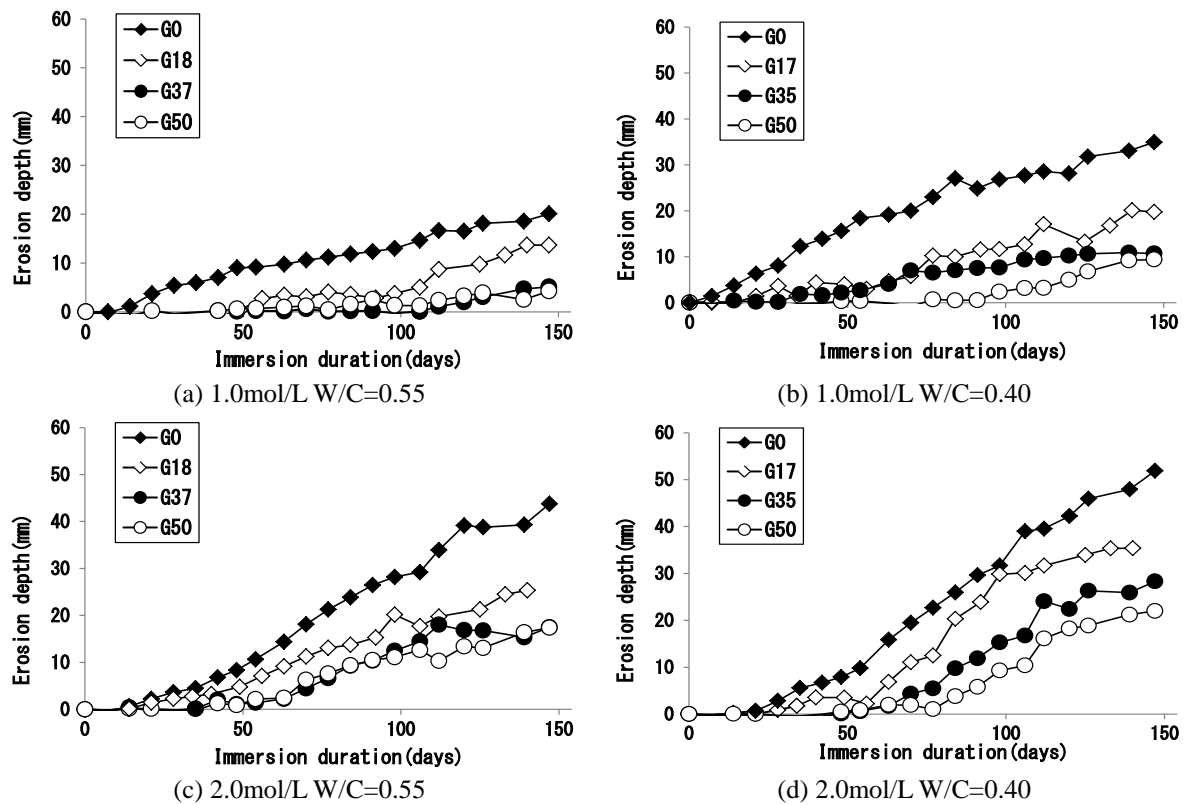


Fig. 4 Relationship between immersion duration and erosion depth

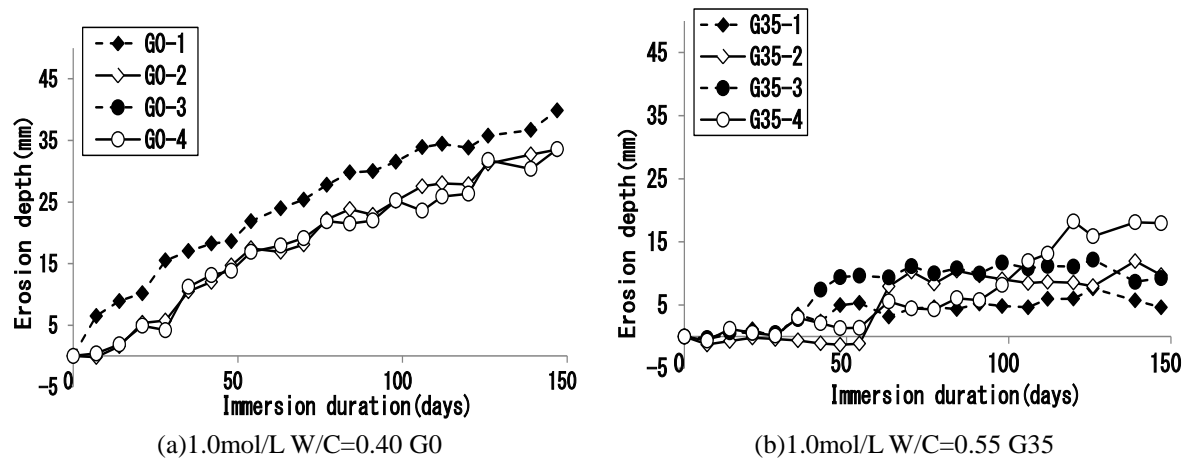


Fig. 5 Erosion depth at every measuring point of specimen

by sulfuric acid and retard the erosion of concrete. This could be the reason why the time when the specimen began to be eroded is different and delayed for the specimen having larger coarse aggregate content, and the erosion depth increases in a stepwise manner instead of linear.

Erosion rate

Based on the results of the erosion depth, the erosion rate was calculated. The erosion rate is

defined as an increment of the erosion depth after the specimen began to be eroded. The regression line for each specimen is shown in Figure 6 and the value in this figure represents the erosion rate (mm/day). Figure 7 shows the relationship between the coarse aggregate content and erosion rate. The larger the coarse aggregate content, the smaller the erosion rate, although the erosion rates for G50 with W/C=0.40 immersed in 1.0 mol/L and with W/C=0.55 immersed in 2.0 mol/L are larger than those for G35 with W/C=0.40

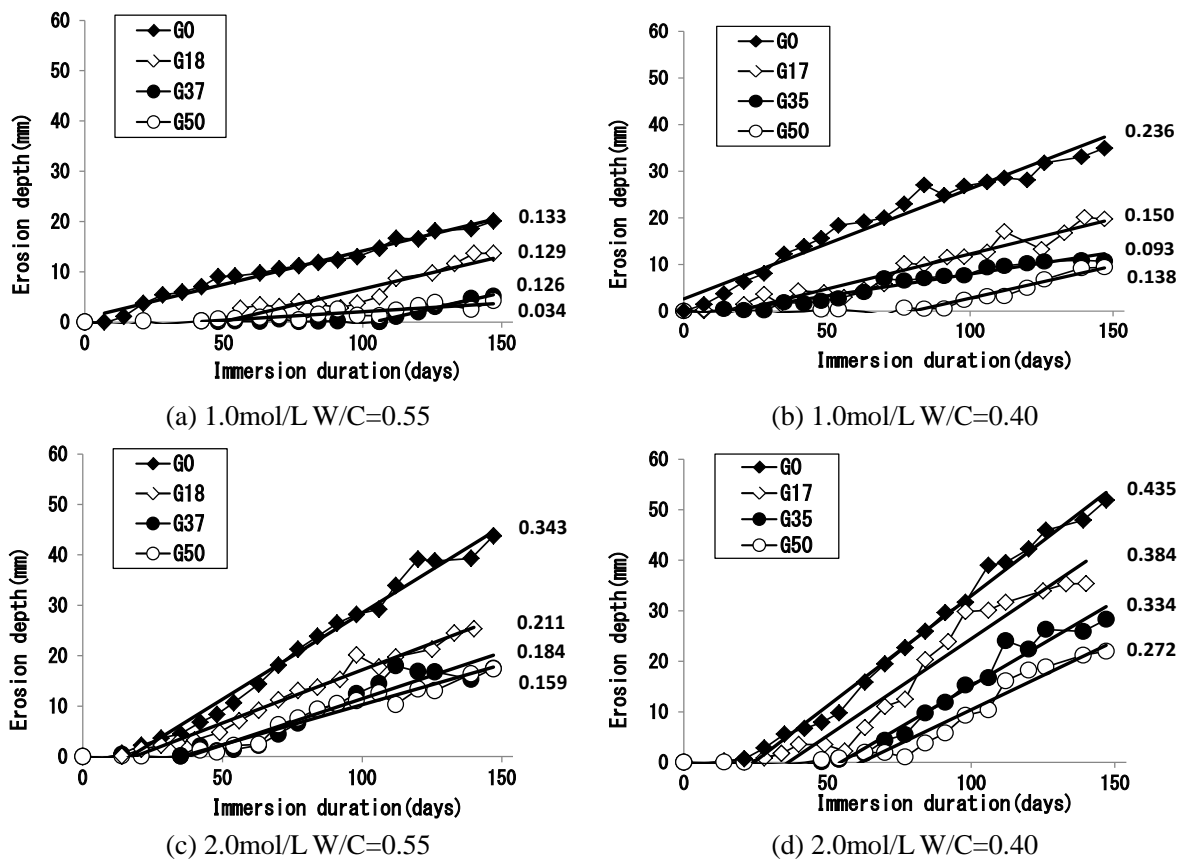


Fig. 6 Regression line for Erosion depth

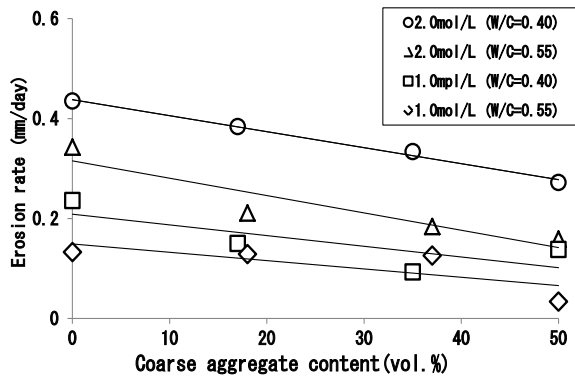


Fig. 7 Relation between coarse aggregate content and erosion rate

immersed in 1.0 mol/L and G37 with W/C=0.55 immersed in 2.0 mol/L, respectively. There is a possibility that the optimum coarse aggregate content can exist to control the erosion of concrete. effect and the control effect was became constant or degraded over define coarse aggregate content.

Neutralization depth

Figure 8 indicates the results of neutralization depth. The larger the coarse aggregate content, the smaller the neutralization depth. This result also suggests that the existence of coarse aggregate contributes to controlling neutralization.

CONCLUSIONS

- (1) The coarse aggregate content affects the deterioration of concrete due to sulfuric acid attack.
- (2) The increase in the coarse aggregate content leads to the decrease in the sulfuric acid deterioration of concrete.
- (3) The increase in the coarse aggregate content also reduces the erosion rate in the sulfuric acid deterioration of concrete.
- (4) The effect of the coarse aggregate content on the deterioration differs in the water cement ration of concrete and the concentration of sulfuric acid solution

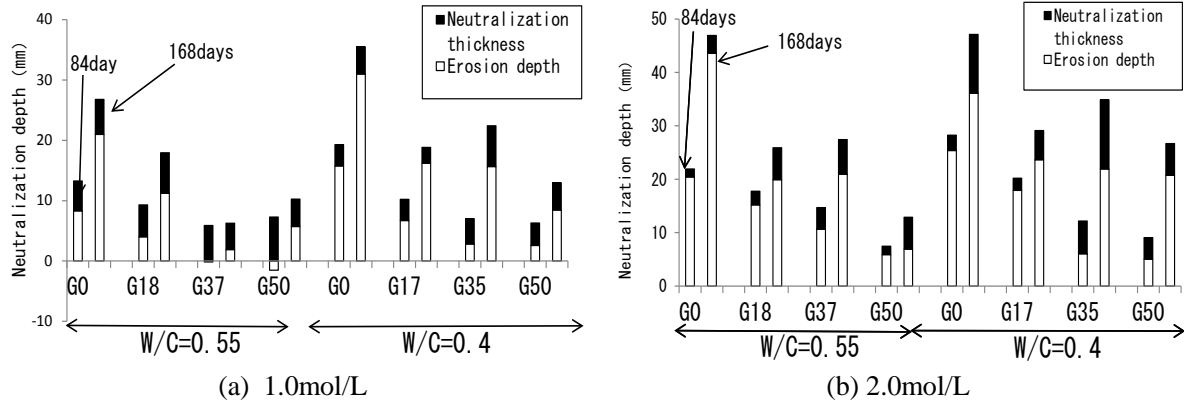


Fig. 8 Neutralization depth

REFERENCES

- [1] Terabayashi A, "A study about the influence which sulfuric acid density gives to the deterioration of concrete", Progression of The Japan Concrete Institute, Vol. 29, 2007, pp. 921-926.
- [2] Kurashige I, "Effect of Cement Hydration Products and Microstructure of Concrete on the Resistance to Sulfuric Acid attack", Progression of The Japan Concrete Institute. Vol. 23, No. 2, 2001, pp. 469-474.
- [3] Kurashige I, "Mechanisms of Scaling-off of Hardened cement paste due to sulfuric acid attack", Cement Science and Concrete Technology, No. 55, 2001, pp. 458-464
- [4] Hisada M, "Progression of Deterioration of Hardened Cement under Sulfuric Acid Environment", Journal of Materials, Concrete Structures and Pavements, Vol. 64, No. 3, Aug. 2008, pp. 449-459

STUDY ON PHYSICAL PROPERTIES AND USABILITY OF SOME SELECTED RECYCLED FINE AGGREGATES

Mohammad Raihanul ISLAM¹, Satoru ISHIGURO²

¹Doctoral Student, ²Faculty, Graduate School of Bioresources, Mie University, Japan.

ABSTRACT

The study was accomplished to know the usability of the experimental recycled aggregates through physical properties, lightness, skid resistance and light irradiation behavior. The saturated and dry density of the slag aggregates (2.64 g/cm³ & 2.6 g/cm³) was highest and the roof tiles (2.27 g/cm³ & 2.13 g/cm³) was the lowest among the experimental recycled aggregates. Roof tiles aggregates absorbed highest percentage of water (6.61%) and the lowest absorption showed the glass aggregates (0.02%). The highest increased inside and surface temperature showed the slag aggregate made sample block and the lowest showed the ceramic aggregate block during the light irradiation test. The skid resistance test value was in between 75 to 83 for the all test aggregate block. According to the color test result ceramic block will reflect most of the light and hold minimum; slag block will hold the maximum. The test results of the recycled aggregates were satisfactory and sometimes better in compare with the standard aggregate sand test results.

Key Words: Recycled Aggregates, Physical Properties, Lightness, Skid Resistance and Light irradiation.

INTRODUCTION

In the recent years, industrial and construction wastes become a big problem because of their risky and expensive management system. On the other hand the demands of the construction materials are increasing day by day. This increasing demand is creating pressure on environmental sustainability. To save the environment and to continue the present construction activities in the world, use of recycle construction aggregates can play a vital role.

In Japan, the treatment and disposal of municipal solid waste (MSW) come under the jurisdiction of the municipality where it is generated, and it is the common practice to incinerate the waste and landfill the subsequent residue (bottom and fly ash, etc.) [1].

Japan produced glass and ceramic wastes of 10947 thousand ton in 2005, 11004 thousand ton in 2006, 11461 thousand ton in 2007 and 8776 thousand ton in 2008. There also produced slag wastes of 4555 thousand ton in 2005, 4922 thousand ton in 2006, 5183 thousand ton in 2007 and 6174 thousand ton in 2008 [2].

Fukushima, Miyagi and Iwate prefecture generated 320 and 11 times larger amount of wastes in compare with their usual waste generating amount due to the great east Japan earthquake in 2011 [3].

Recycling of ceramic and glass wastes is a challenge for the electric power generation companies worldwide. In the year 2009, The Kansai Electric Power Co. Inc. generated 3,100 ton of glass and Ceramic wastes those they use as insulator and other purposes [4].

A number of research studies have completed and continuing in the field of recycled construction

aggregate. The main objective of this study was to investigate the physical properties of the selected recycled aggregates, making mortar to test their lightness, light irradiation motive and skid resistance for understanding the usability of the selected recycled aggregates.

MATERIALS AND METHODS

The investigation was accomplished with four recycled fine aggregates; ceramic, roof tiles, glass and slag aggregate and a traditional standard fine aggregate sand.

Sand: River bed sand with size 0-5 mm was used in this study.

Ceramic Aggregates: The ceramic tiles aggregates were collected from Yamamura Co. Matsusaka City, Japan. Size of the recycled ceramic aggregates in this study was 0-3mm.

Roof Tiles Aggregates: The roof tiles aggregates were collected from Manen Co. Tsu City, Japan. This recycle center producing roof tiles aggregates by crushing used roof tiles. Size of the recycled roof tiles aggregates in this study was 0-3mm.

Glass Aggregates: The used glass aggregates were collected from Yamamura Co. Matsusaka City, Japan. Size of the recycled glass aggregates in this study was 0-2.5mm.

Slag Aggregates: The used Slag aggregates were collected from Yokkaichi City, Mie, Japan. Size of the recycled slag aggregates in this study was 0-5mm.

To achieve the objectives of the investigation the basic physical parameters of the above mentioned recycled aggregates were determined with standard methods.

Sieve Analysis

Sieve analysis was accomplished according to the “JIS A 1102: Method of test for sieve analysis of aggregates” [5].

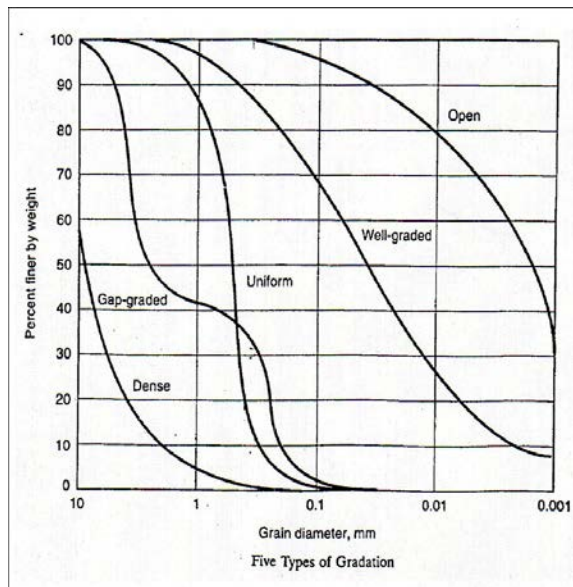


Fig.1 Shape of the standard gradation curve [6]

Dense and well-graded aggregates are desirable for making concrete, gap-graded aggregates can make good concrete, for the uniform grading, only a few sizes dominate the bulk material, The open graded contains too much small particles and easy to be disturbed by a hole [6].

Test of Density and Absorption

The aim of the experiment was to determine the saturated density (d_s), oven dry density (d_d) and absorption of the fine aggregates. The experiment followed the instructions of “JIS A 1109: Method of test for density and water absorption of fine aggregates” [7].

Color Test

This test was performed with Digital Color Reader (CR -13, Konica Minolta Optics Inc.) by the instructions of the instrument manufacturer which was followed by JIS Z8721 [8].

Light Irradiation Test

The concrete-mortar samples were prepared and stored for the test in a controlled room at 25°C and with R.H. 50%. Every sample placed in cork sheet frame (30cm x 30cm x 5cm) and was kept in the light irradiation test room for 24 hours before the test for

the temperature adjustment with the room temperature. The beam lamp Irradiation was continued on the sample block for four hours. The data logger was received data for 24 hours and stored.

Skid Resistance Test

The test was performed by using British Pendulum Tester. The experiment was accomplished by following the “ASTM E 303: Standard Test Method for Measuring Surface Frictional Properties Using the British Pendulum Tester” [9].

RESULTS AND DISCUSSIONS

Sieve analysis

The results of sieve analysis were expressed as fineness modulus (FM) and as graphical presentation by gradation curve. The fineness modulus of sand, roof tiles, ceramic, slag and glass were 3.1, 2.9, 3.0, 4.0 and 3.4 respectively. The limit of the fineness modulus of fine aggregates is 2 to 3.5[10].

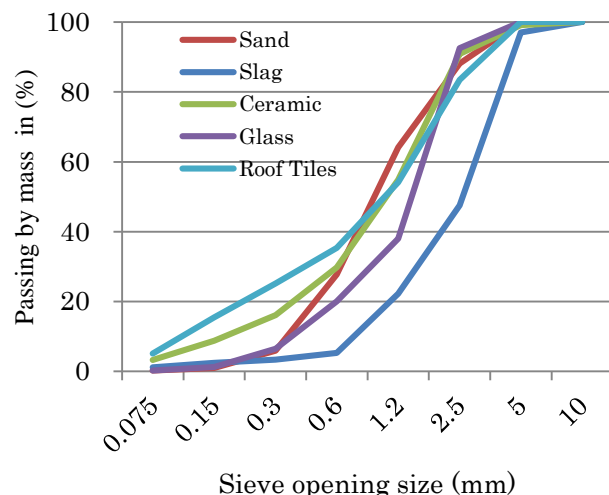


Fig.2: Gradation curve of the experimental aggregates

According to the above gradation curve sand can be defined as uniformly graded when ceramic tiles and glass aggregates can be defined as well graded, slag was dense graded and the roof tiles aggregate was gap-graded[6]. The recycle slag, ceramic tiles and glass aggregates were desirable for making concrete. As gap-grading aggregates have lacks of one or more intermediate size, roof tiles could be use to prepare concrete with relatively low workability and with high workability, segregation might be occurred and that could make problem.

Density of the fine aggregates

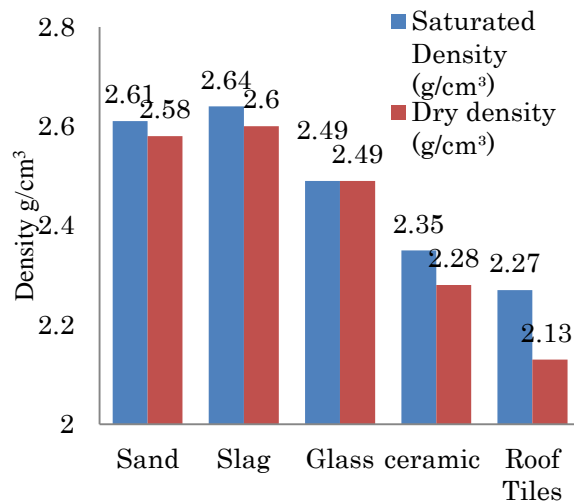


Fig.3 Saturated and dry density of the experimental aggregates

The saturated and dry density of the slag aggregates (2.64 g/cm^3 & 2.6 g/cm^3) was the highest and the roof tiles (2.27 g/cm^3 & 2.13 g/cm^3) was the lowest among the experimental recycled aggregates when the value was 2.61 g/cm^3 & 2.58 g/cm^3 for the standard reference aggregate sand.

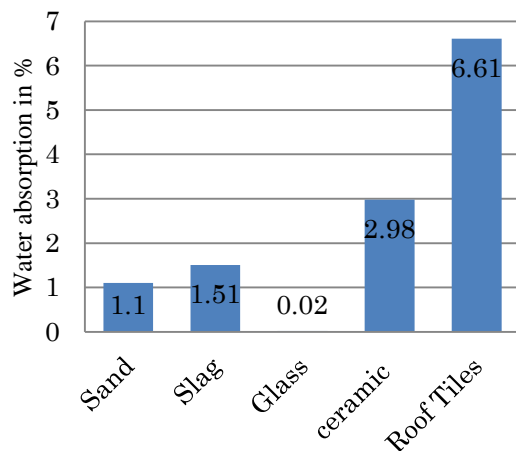


Fig.4 Water absorption of the study aggregates

Roof tiles aggregates absorbed highest (6.61%) and slag absorbed the lowest (1.51) percentage of water within the recycled aggregates. The absorption of the glass aggregates (0.02%) was very negligible and could be count as zero absorbent.

Color Test

The value of the lightness parameter indicates the lightness as well as the reflection and heat control property of the sample block. According to the color test result ceramic block will reflect most of the light and hold minimum; slag block hold the maximum.

More light holding property indicates the hotter surface and less indicates the cooler block surface.

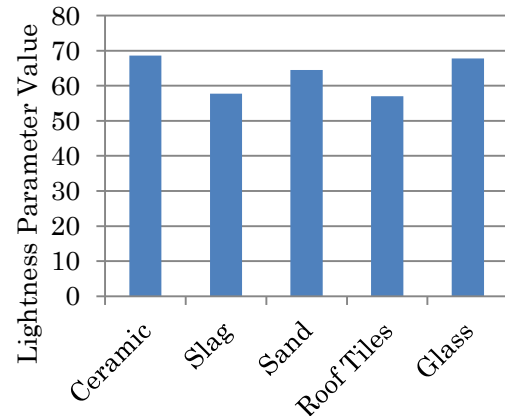


Fig.5 Lightness Status of the Sample Blocks surface.

Lamp Irradiation

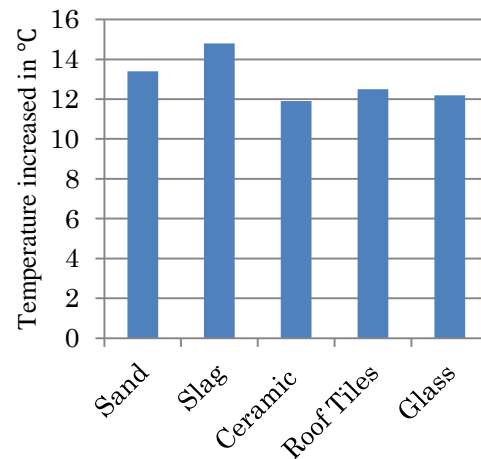


Fig.6 Sample block increased inside temperature

The highest increased inside and surface temperature showed the slag aggregate made sample block and the lowest showed the ceramic aggregate block during the light irradiation test.

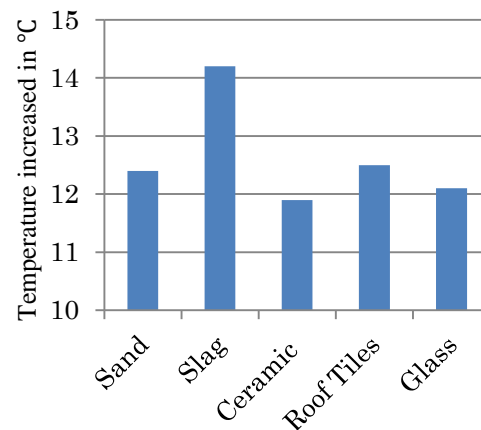


Fig.7 Sample block increased surface temperature

Skid Resistance

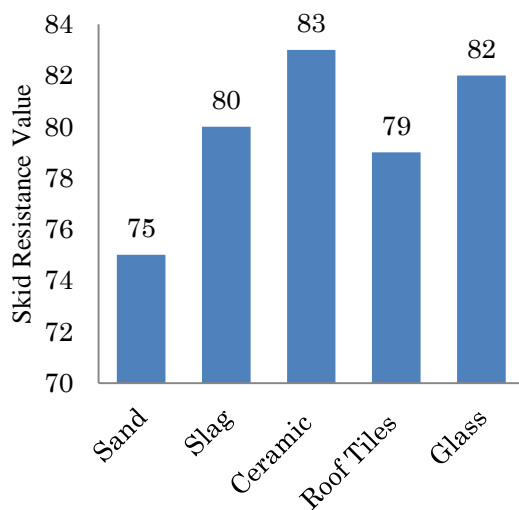


Fig.8 Skid Resistance Test Result

The highest skid resistance test value showed the ceramic tiles aggregate block surface and the lowest value showed the sand made mortar block surface.

Skid resistance value should be ≥ 65 for round, bend, gradient and unrestricted roads. It should be ≥ 55 for motorways and ≥ 45 for all other sites [11]. So, all of the recycled aggregates could be used safely to make walkways and pavements including bend and slop condition.

CONCLUSION AND RECOMMENDATIONS

The outcomes of the experiment can be concluded as follows:

The experimental aggregates can be used in construction industry as the replacement of sand and other traditional fine aggregates to reduce the cost and save the environment for green and sustainable construction. Ceramic aggregates would be the good choice where normal surface temperature is needed and slag could be used where hot surface temperature is needed. Other aggregates also could be used with satisfactory light irradiation motive. Ceramic aggregates would be the best choice where high skid resistance is needed and other aggregates also could be used in all conditions (walk-ways, motor-ways, with bend or slop condition) to make road and pavement surface.

The following Recommendations were prepared from the experiment:

- These types of experiment could be set for new recycled aggregates to increase the re-use of aggregates for sustainable environment.
- More and more new experiment should be set for the safe use and finding new ways of use of the

aggregates.

- The same type of experiments could be set for the aggregates collecting from new sources.

REFERENCES

- [1] Masahide Nishigaki. Producing permeable blocks and pavement bricks from molten slag. Waste Management, Volume 20, Issues 2-3, April 2000, Pages 185-192.
- [2] Waste Report, Environmental Statics 2012 (Chapter: 3.6, 2.37, 3.19), Ministry of Environment, Government of Japan. http://www.env.go.jp/en/statistics/contents/index_e.html#haikibutu
- [3] Report on the: Tohoku Area Pacific Offshore Earthquake, Department of Urban Engineering, The University of Tokyo, Japan. <http://www.recwet.t.u-tokyo.ac.jp/kurisu/gsls/report2.html>
- [4] The Kansai Electric Power Co. Inc., Japan <http://www1.kepc.co.jp/corporate/csr/data/data02.html>
- [5] Japanese Industrial Standards Committee. JIS A 1102: Method of test for sieve analysis of aggregates. <http://teaching.ust.hk/~civl111/CHAPTE R3.pdf>
- [6] Japanese Industrial Standards Committee. JIS A 1109: Methods of test for density and water absorption of fine aggregates.
- [7] <http://www.konicaminolta.jp/instruments/knowledge/color/part1/09.html>
- [8] American Society for Testing and Materials (ASTM). ASTM E 303: Standard Test Method for Measuring Surface Frictional Properties Using the British Pendulum Tester
- [9] The Constructor. <http://theconstructor.org/practical-guide/grain-size-analysis/2261/>
- [10] MUNRO, Skid Tester. http://munroinstruments.co.uk/pdf/PSR_T_Manual.pdf

Environment

COMPUTER MODELING AND ANALYSIS OF THREE PHASE INDUCTION MOTOR UNDER TEMPORARY SHORT CIRCUIT FAULT IN STATOR USING WAVELET TRANSFORM

Dicky Nova Wardana^{1,2}, Dimas Anton Asfani¹, Ardyono Priyadi¹, and Mauridhi Hery Purnomo¹

¹Electrical Engineering Department, Institut Teknologi Sepuluh Nopember (ITS), Indonesia

²PT PLN Persero, Indonesia

ABSTRACT

The stator winding deterioration at the early stage does not affect to the motor performance i.e. torque, vibration, etc. Therefore, in most cases the deterioration is not detected until short circuit fault is occurred. This circumstance can produce a worse short circuit fault, overheating and end up with catastrophic failure as long as motor operation. The early warning system is necessary for detecting this condition to avoid the operation motor failure. This paper proposes mathematical model and simulations of temporary short circuit in induction motor winding. Moreover, the detection method is proposed to detect the symptoms of fault while motor operate normally. This method uses wavelet transform that able providing both of frequency and time information. Low current short circuit with short duration represents the symptoms of winding and insulation deterioration. Simulation analysis shows that the proposed method can detect very low short circuit current and short time duration as a spike fault. Moreover, the information of fault occurring can be provided

Keywords: Induction Motor, Temporary Fault, Short Circuit, Wavelet Transform

INTRODUCTION

Stator and bearing faults are the most common fault that occurred on the induction motors. 30% - 40% from all faults on the induction motors related to stator fault. Stator fault initiated with inter-turn short circuit caused by degradation of stator winding insulation. Early stage of inter-turn short circuit virtually no effect on the motor performance, but it will develop phase-to-phase or phase-to-ground short circuit if it is not detected immediately. Phase-to-phase or phase-to-ground short circuit cause catastrophic damage on the stator core and motor winding due to high current flows [1].

Several detection methods with varied parameters and variables have been proposed. Non-invasive method is more attractive due to its ability to detect fault without disassembly the machine. Motor current signature analysis (MCSA) is a common method that used to detect motor fault because different type of fault yields different harmonics current [2]. MCSA has very low accuracy in detecting temporary and nonperiodic faults. Harmonic frequency is unable to represent nonperiodic faults since the current of this type of fault doesn't periodic. Therefore, wavelet transform was used as alternative method to handle this problem. Several experiments on the laboratory have been conducted to acquire temporary short circuit current characteristic from real motor and classified them using wavelet transform. The results show that this method very effective and can be used as faults identifier [3-6].

Beside laboratory experiment, induction motor

modeling is also widely developed in order to investigate the characteristic of the induction motor under faulty condition. Asymmetrical stator winding of induction motor is developed and simulated under Matlab-Simulink environment [7-8]. However, most models simulate permanent fault and only few models simulate temporary fault in stator winding that use negative sequence current as fault identifier of this type of fault [9].

This paper presents theoretical analysis and simulation of temporary and non-periodic stator faults in phase-A of induction motors. A three-phase induction motor is simulated under normal operation and faulty condition: non-periodic and temporary inter-turn short circuit windings to represent early stage of faults on the stator induction motor. The fault severity can be changed by varying number of shorted turn. By simulating this model, current characteristic when fault occur can be investigated and wavelet transform is proposed as identifier of temporary short circuit.

ASYMETRICAL INDUCTION MOTOR MODEL

Symmetrical three-phase induction motor's model is well described in [10-11]. In this paper, the mathematical model of the mathematical model of an induction machine consisting of inter-turn stator winding short circuit [7] is used to simulate asymmetrical induction motor due to non permanent and nonperiodic short circuit as shown in Fig. 1. In order to derive equations for this type of induction

motor, the following assumptions have been made:

- (1) Stator phase-A of the motor has a different number of turns (N_a) caused by inter-turn short circuit and $N_b=N_c=N_s$.
- (2) Magnetic saturation, friction and windage losses are neglected.
- (3) Mutual and self-inductance on the rotor are constant.
- (4) Rotor resistances are same each phase $r_{ar} = r_{br} = r_{cr} = r_r$.

The voltage equation of induction motor consists of current and magnetic flux can be expressed as follows:

$$V_{abc}^s = r_{abc}^s i_{abc}^s + \frac{d}{dt} \lambda_{abc}^s \quad (1)$$

$$0 = r_{abc}^r i_{abc}^r + \frac{d}{dt} \lambda_{abc}^r \quad (2)$$

$$\text{where } r_{abc}^s = \begin{bmatrix} r_{assc} & 0 & 0 \\ 0 & r_{bs} & 0 \\ 0 & 0 & r_{cs} \end{bmatrix}; \quad r_{abc}^r = \begin{bmatrix} r_{ar} & 0 & 0 \\ 0 & r_{br} & 0 \\ 0 & 0 & r_{cr} \end{bmatrix}$$

and r_{assc} is stator resistance due to short circuit.

Applying stationary reference frame transformation to this equation yields the corresponding qd0 equations and (1,2) becomes:

$$V_{qd0}^s = r_{qd0}^s i_{qd0}^s + \frac{d}{dt} \lambda_{qd0}^s \quad (3)$$

$$0 = r_{qd0}^r i_{qd0}^r - \omega_r \begin{bmatrix} 0 & 1 & 0 \\ -1 & 0 & 0 \\ 0 & 0 & 0 \end{bmatrix} \lambda_{qd0}^r + \frac{d}{dt} \lambda_{qd0}^r \quad (4)$$

where,

$$r_{qd0}^s = \begin{bmatrix} k_{r1} r_s & 0 & k_{r2} r_s \\ 0 & r_s & 0 \\ k_{r3} r_s & 0 & k_{r3} r_s \end{bmatrix}, \quad r_{qd0}^r = r_r \begin{bmatrix} 1 & 0 & 0 \\ 0 & 1 & 0 \\ 0 & 0 & 1 \end{bmatrix}$$

and k_r is constant of resistance due to short circuit.

The flux linkages of the stator and rotor windings are written as follows:

$$\begin{bmatrix} \lambda_{abc}^s \\ \lambda_{abc}^r \end{bmatrix} = \begin{bmatrix} L_{abc}^{ss} & L_{abc}^{sr} \\ L_{abc}^{rs} & L_{abc}^{rr} \end{bmatrix} \begin{bmatrix} i_{abc}^s \\ i_{abc}^r \end{bmatrix} \quad (5)$$

where stator and rotor mutual inductances are:

$$L_{abc}^{ss} = \begin{bmatrix} L_{asas}^{ss} & L_{asbs}^{ss} & L_{ascs}^{ss} \\ L_{bsas}^{ss} & L_{bsbs}^{ss} & L_{bscs}^{ss} \\ L_{csas}^{ss} & L_{csbs}^{ss} & L_{cscs}^{ss} \end{bmatrix}$$

$$L_{abc}^{rr} = \begin{bmatrix} L_{arar}^{rr} & L_{arbr}^{rr} & L_{arcr}^{rr} \\ L_{brar}^{rr} & L_{brbr}^{rr} & L_{brcr}^{rr} \\ L_{crar}^{rr} & L_{crbr}^{rr} & L_{crcr}^{rr} \end{bmatrix}$$

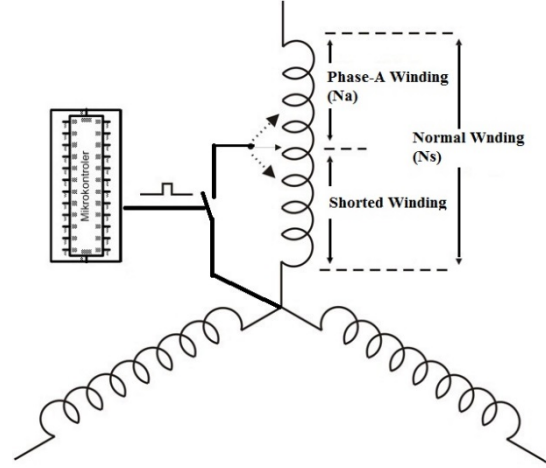


Figure 1. Wiring Diagram

In the symmetrical stator condition, stator mutual inductance will be $L_{asbs}=L_{bsas}$, $L_{ascs}=L_{csas}$, $L_{bscs}=L_{csbs}$. Similar to stator, rotor mutual inductance and self-inductance have $L_{arbr} = L_{arcr} = L_{brcr} = L_{brar} = L_{crar} = L_{crbr}$ and $L_{arar} = L_{brbr} = L_{crcr}$, respectively.

Based on machine's parameters, the stator self-inductances for phase as, bs and cs can be calculated as follows:

$$L_{asas} = \frac{N_a^2}{N_s^2} (L_{ls} + \frac{2}{3} L_m) \quad (6)$$

$$L_{bsbs} = L_{csbs} = L_{ls} + \frac{2}{3} L_m \quad (7)$$

The stator mutual inductances can be calculated as follows:

$$L_{asbs} = L_{bsas} = L_{ascs} = L_{csas} = -\frac{1}{3} N_a L_m \quad (8)$$

$$L_{bscs} = L_{csbs} = -\frac{1}{3} L_m \quad (9)$$

Assuming rotor has symmetrical parameters, the rotor self and mutual inductances can be calculated as follows:

$$L_{asar} = L_{asbr} = L_{ascr} = \frac{2}{3} N_a L_m \quad (10)$$

$$L_{bsar} = L_{bsbr} = L_{bscr} = L_{csar} = L_{csbr} = L_{cscr} = \frac{2}{3} L_m \quad (11)$$

Mutual inductance of stator to rotor and rotor to stator are dependent on the rotor position (angle), therefore:

$$L_{abc}^{sr} = \begin{bmatrix} L_{asar}^{sr} \cos \theta_r & L_{asbr}^{sr} \cos \theta_{r1} & L_{ascr}^{sr} \cos \theta_{r2} \\ L_{bsar}^{sr} \cos \theta_{r2} & L_{bsbr}^{sr} \cos \theta_r & L_{bscr}^{sr} \cos \theta_{r1} \\ L_{csar}^{sr} \cos \theta_{r1} & L_{csbr}^{sr} \cos \theta_{r2} & L_{cscr}^{sr} \cos \theta_r \end{bmatrix} \quad (12)$$

where $\theta_{r1} = \theta + \frac{2\pi}{3}$ and $\theta_{r2} = \theta - \frac{2\pi}{3}$.

The inductance matrix $L_{abc}^{rs} = L_{abc}^{sr'}$ where (') means transpose of the matrix. The coefficients of matrix L_{abc}^{sr} are peak values of stator-to-rotor mutual inductance. Because of rotor symmetry $L_{asar} = L_{asbr} = L_{ascr}$, $L_{bsar} = L_{bsbr} = L_{bscr}$ and $L_{csar} = L_{csbr} = L_{cscr}$.

The stator and rotor $qd0$ flux linkages are obtained by applying transformation to the stator and rotor abc flux linkages in (5), can be written as follows:

$$\lambda_{qd0}^s = L_{qd0}^{ss} i_{qd0}^s + L_{qd0}^{sr} i_{qd0}^r \quad (13)$$

$$\lambda_{qd0}^r = L_{qd0}^{rs} i_{qd0}^s + L_{qd0}^{rr} i_{qd0}^r \quad (14)$$

where,

$$L_{qd0}^{ss} = \begin{bmatrix} L_{11}^{ss} & L_{12}^{ss} & L_{13}^{ss} \\ L_{21}^{ss} & L_{22}^{ss} & L_{23}^{ss} \\ L_{31}^{ss} & L_{32}^{ss} & L_{33}^{ss} \end{bmatrix} \quad L_{qd0}^{sr} = \begin{bmatrix} L_{11}^{sr} & L_{12}^{sr} & L_{13}^{sr} \\ L_{21}^{sr} & L_{22}^{sr} & L_{23}^{sr} \\ L_{31}^{sr} & L_{32}^{sr} & L_{33}^{sr} \end{bmatrix},$$

$$L_{qd0}^{rs} = \begin{bmatrix} L_{11}^{rs} & L_{12}^{rs} & L_{13}^{rs} \\ L_{21}^{rs} & L_{22}^{rs} & L_{23}^{rs} \\ 0 & 0 & 0 \end{bmatrix} \quad L_{rr} = \begin{bmatrix} L_{11}^{rr} & 0 & 0 \\ 0 & L_{22}^{rr} & 0 \\ 0 & 0 & L_{33}^{rr} \end{bmatrix}$$

Normally, induction machine is supplied with three wire connection without neutral wire. Hence, stator, rotor and inductance of the asymmetrical can be written compactly as:

$$r_{qd}^s = \begin{bmatrix} k_{r1} r_s & 0 \\ 0 & r_s \end{bmatrix} \quad \text{and} \quad r_{qd}^r = \begin{bmatrix} r_r & 0 \\ 0 & r_r \end{bmatrix} \quad (15)$$

$$L_{qd} = \begin{bmatrix} L_{11}^{ss} & L_{12}^{ss} & L_{11}^{sr} & L_{12}^{sr} \\ L_{21}^{ss} & L_{22}^{ss} & L_{21}^{sr} & L_{22}^{sr} \\ L_{11}^{rs} & L_{12}^{rs} & L_{11}^{rr} & 0 \\ L_{21}^{rs} & L_{22}^{rs} & 0 & L_{22}^{rr} \end{bmatrix} \quad (16)$$

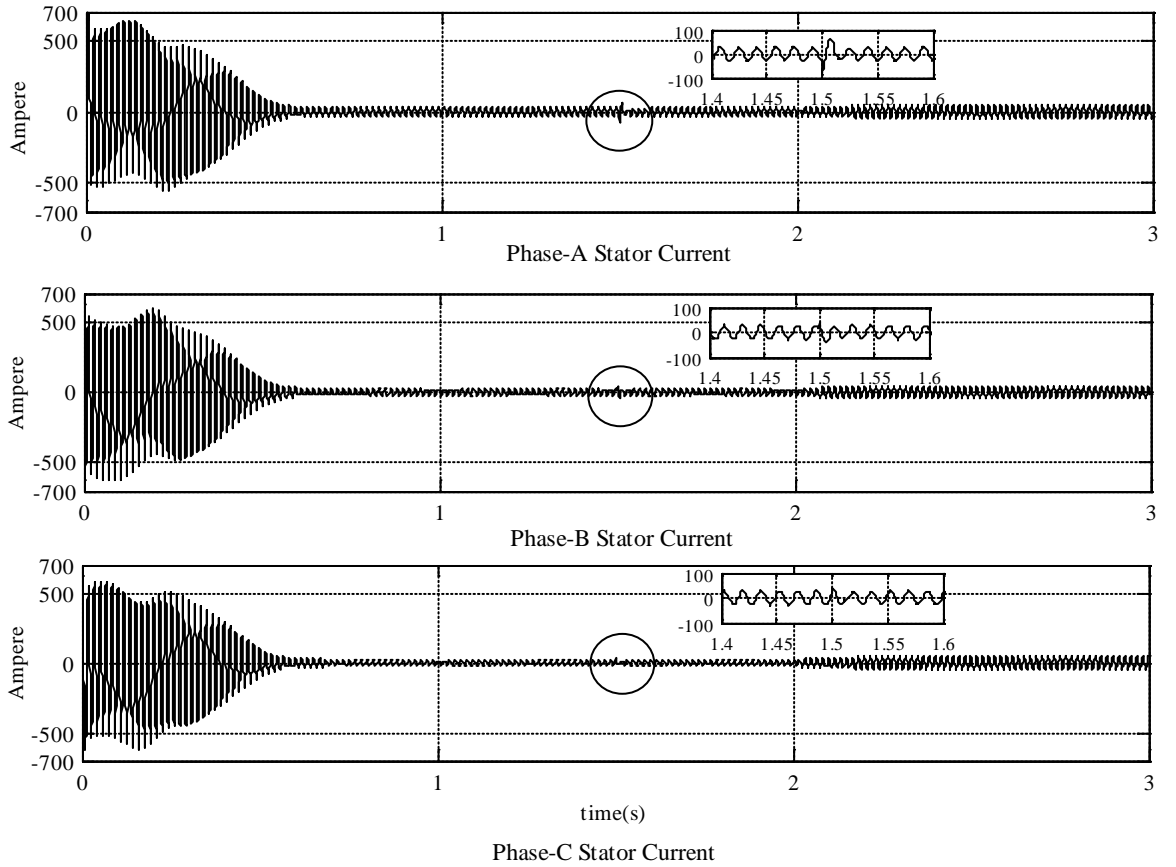


Figure 2. Phase current of the motor

Table 1. Machine's parameters

Parameter	Value
Horse power	50 hp
Line voltage	460 V
Rated speed at 60 Hz	1705 rpm
Stator winding resistance	0.087 Ω
Stator leakage inductance	0.302 Ω
Magnetizing inductance	13.08 Ω
Stator leakage inductance (stator refereed)	0.302 Ω
Rotor winding resistance (stator refereed)	0.228 Ω
Inertia	1.662 kg.m ²
Number of poles	4

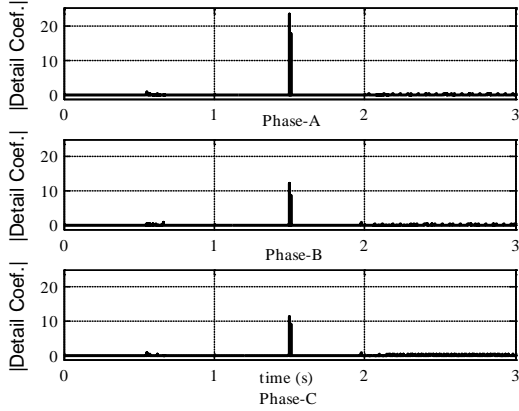


Figure 3. Detail coefficient each phase

Table 2. Detail coefficient with different number of shorted turn

SC Severity	Absolute Detail Coefficients		
	Phase A	Phase B	Phase C
10% Total Winding	23.68	12.25	11.43
25% Total Winding	73.31	37.07	36.25
50% Total Winding	215.8	108.3	107.5
75% Total Winding	484	242.4	241.6

SIMULATION AND ANALYSIS OF TEMPORARY SHORT CIRCUIT IN STATOR WINDING

Machine parameters used in this paper are shown in Table 1. Temporary and non periodic short circuit is simulated using model based on the mathematical equation derived above. Short circuit causes resistances and inductances parameter of the motor changed. At that period of time, the parameters are calculated using Eq. 15 and 16.

The qd voltages can be obtained by applying qd transformation from stator phase voltage as follows:

$$v_q^s = \frac{2}{3} [v_{as} - \frac{1}{2}(v_{cs} + v_{bs})] \quad (17)$$

$$v_d^s = \frac{1}{\sqrt{3}} [-v_{bs} + v_{cs}] \quad (18)$$

Flux linkages in qd axis can be obtained by rearranging voltage equation in Eq. 3 and 4, the results are expressed as follow:

$$\lambda_{qs} = \int \left\{ V_{qs} + \frac{r_s}{aL_{ls}} (\lambda_{mq1} - \lambda_{qs}) \right\} dt \quad (19)$$

$$\lambda_{qr} = \int \left\{ \omega_r \lambda_{dr} + \frac{r_r}{L_{lr}} (\lambda_{mq2} - \lambda_{qr}) \right\} dt \quad (20)$$

$$\lambda_{ds} = \int \left\{ V_{ds} + \frac{r_s}{L_{ls}} (\lambda_{md} - \lambda_{ds}) \right\} dt \quad (21)$$

$$\lambda_{dr} = \int \left\{ -\omega_r \lambda_{qr} + \frac{r_r}{L_{lr}} (\lambda_{md} - \lambda_{dr}) \right\} dt \quad (22)$$

where

$$\lambda_{mq1} = L_m \left[\frac{b(\lambda_{qs} - \lambda_{mq1})}{aL_{ls}} + \frac{c(\lambda_{qr} - \lambda_{mq2})}{L_{lr}} \right]$$

and

$$\lambda_{mq2} = L_m \left[\frac{c(\lambda_{qs} - \lambda_{mq1})}{aL_{ls}} + \frac{(\lambda_{qr} - \lambda_{mq2})}{L_{lr}} \right]$$

Torque and speed of motor is expressed as follows:

$$\omega_r(t) = \frac{P}{2J} \int (T_{em} + T_{mech}) dt \quad (23)$$

$$T_{em} = \frac{3}{2} \frac{P}{2} (\lambda_d^s i_q^s - \lambda_q^s i_d^s) \quad (24)$$

SIMULATION RESULT

Initially, motor is operated in normal condition. After starting transient has finished and motor running in nominal speed, microcontroller send a signal to activate temporary short circuit at 1.5 second with 0.01 second duration (half cycle) and load change begins at 2 second. The current characteristics during free acceleration from stand still to full speed consist of 10% short circuit of total winding are shown in Fig. 2. As it can be seen from this figure, only slight different between normal and faulted current during motor operation, this problem makes identification system less accurate. Fig. 3 shows absolute detail coefficients obtained using wavelet transform. The significant difference between normal and faulty condition is shown in this figure. This result is makes detection of fault is easier. Moreover, it is founded that magnitude of detail coefficient is linear with the number of shorted turn as shown in Table 2.

CONCLUSION

Mathematical model of asymmetrical induction motor has been presented in this paper. This model is used to simulate temporary and non-periodic inter-turn short circuit on the phase-a of induction motor winding. Simulation results show that wavelet transform is an effective tool to identify temporary short circuit in induction motor winding. Wavelet transform is used to provide detail coefficient of the stator current which is used as variable detection. Analysis of some fault cases varied by different number of shorted turn is resulting that the magnitude of detail coefficient is linear with the number of shorted turn.

ACKNOWLEDGEMENTS

The authors gratefully acknowledge to the Directorate General for Higher Education (DGHE), Ministry of national Education, the Republic of Indonesia and JICA PREDICT-2 for supporting this research under program of "Joint – Research Predict Batch-2".

REFERENCES

- [1] Rasool Sharifi and M. Ebrahimi, "Detection of Stator Winding Faults in Induction Motor Using Three-Phase Current Monitoring", *ISA Transactions* 50(2011) 14-20.
- [2] Neelam Mehla and Ratna Dahiya, "An Approach of Condition Monitoring of Induction Motors Using MCSA", *International Journal of System Application, Engineering & Development*, Vol. 1, Issue 1, 2007.
- [3] D. A. Asfani, Syafaruddin, D. N. Wardana, M. H. Purnomo, and T. Hiyama, "Temporary Short Circuit Identification in Induction Motor Winding Using Wavelet Transform", Presented at the 3rd International Student Conf. on Advanced Science and Technology (ICAST), Seoul, Korea, 2009.
- [4] D. A. Asfani, Syafaruddin, M. H. Purnomo, and T. Hiyama, "Wavelet Level Evaluation for Temporary Short Circuit Detection in Induction Motor Winding", Presented at the 5th International Student Conf. on Advanced Science and Technology (ICAST), Kumamoto, Japan, 2010.
- [5] Dimas A. Asfani, Syafaruddin, Dicky N. Wardana, M. H. Purnomo, and T. Hiyama, "Characterization of Temporary Short Circuit in Induction Motor Winding using Wavelet Analysis", *Proceedings of the 2010 International Conference on Modelling, Identification and Control (ICMIC)*, Okayama, Japan, July 17-19, 2010.
- [6] D. A. Asfani, Syafaruddin, M. H. Purnomo, T. Hiyama, "Temporary Short Circuit Detection in Induction Motors Winding using Second Level Haar-Wavelet Transform", *IEEJ Transactions on Industry applications*, Vol. 131 No. 9, pp. 1-10, 2011.
- [7] M. Arkan, D. Kostic-Perovic, and P. J. Unsworth, "Modelling and Simulation of Induction Motors with Inter-Turn Faults for Diagnostics", *Electric Power System Research*, vol. 75, pp. 57-66, 2005.
- [8] S. Sivakotaiah, Mini V.P., Shajialal A. S., "Fault Detection of Induction Motor by Fuzzy Logic Algorithm", *10th National Conference On Technological Trends (NCTT09)*, pp. 85-90. Nov 2009.
- [9] D. A. Asfani, Syafaruddin, M. H. Purnomo, T. Hiyama, "Simulation and Detection of Temporary Short Circuit in Induction Motor Windings Using Negative Sequence Current", *The International Conference on Advanced Power System Automation and Protection (APAP)*, pp. 2304-2308. 2011.
- [10] P. Krause, O. Wasynczuk, S.D. Sudhoff, "Analysis of Electric Machinery", *IEEE Inc*, 1995.
- [11] C. M. Ong, "Dynamic Simulation of Electric Machinery", *Prentice Hall PTR*, 1998.

ANALYTICAL SOLUTION TO CONTAMINANT EXTRACTION CONSIDERING SMEAR EFFECT

H.Y Wang¹, X.W Tang¹ and B. Bai¹

¹Research Center of Coastal and Urban Geotechnical Engineering, Zhejiang University, China

ABSTRACT

The smear zones are usually caused by the installation of vertical drains in fine-grained soil. An analytical solution to contaminant extraction utilizing well injection depth extraction (WIDE) system is developed. The effect of the smear zone around the vertical drains is considered. The injection rate is assumed to be equal to the retrieval rate to maintain full saturation and a steady-state seepage flow. The results obtained by the proposed analytical solution agree well with those obtained from the finite element method. An illustrative example is presented to show the influence of the smear zones and results revealed that the smear zone can have a great influence on the contaminant extraction from contaminated soils. The 500-hour base concentration of acetone in the middle of the contaminated soil increases by a factor of approximately 1.9 when the effect of the smear zone is considered in the model. The proposed analytical model is relatively simple to verify complicated numerical methods, and evaluate experimental data.

Keywords: Contaminant Extraction; Smear Effect; Analytical Solution; Well Injection Depth Extraction (WIDE);

INTRODUCTION

Remediation of contaminated low-permeability soils utilizing conventional technologies, such as pump-and-treat and vapor extraction systems is typically ineffective. Well injection depth extraction (WIDE) is an improved pump-and-treat system which is demonstrated to be effective for depth-specific removal of contaminants in fine-grained soils, because the use of prefabricated vertical wells (PVW) installed in a relatively close spacing shorts the flow path (Gabr et al., 1996; Quaranta et al., 1997; Welker and Gilbert, 2003; Kunberger et al., 2003; Warren et al., 2006; Sharmin et al., 2008).

The models for contaminant extraction using WIDE technology in the literature are usually completed by numerical models. For instance, Welker and Gilbert (2003) developed MODFLOW with MT3D method to numerically model the bench-scale PVD remediation system. Sharmin et al. (2008) analyzed the impact of the extraction process of WIDE technology on the groundwater head distribution and contaminant transport using the finite element model. Although many sophisticated must be solved numerically, simplified analytical solutions are still an economical and efficient alternative to the numerical models. Gabr et al. (1996) have given the analytical solution for contaminant extraction through an axisymmetric model with semi-infinite boundary.

The installation of vertical drains by means of a mandrel causes significant remolding of the subsoil, especially in the immediate vicinity of the mandrel (Hansbo, 1981; Indraratna and Redana, 1998, 2000; Sathanathan and Indraratna, 2006). The

characteristics of the smear zone investigated using a large-scale consolidometer are found with reduced permeability, decreased water content and increased compressibility (Indraratna and Redana, 1998; Sathanathan and Indraratna, 2006). Porter et al. (1960), Barraclough and Tinker (1981), So and Nye (1989) observed that the solute diffusion coefficient in soil decreased with increasing bulk density and decreasing water content. Therefore, it is of great importance to research the smear effect on contaminant transfer in soils.

In this paper, an analytical solution of 1D contaminant extraction using WIDE system considering the smearing effect is obtained under conditions of steady-state flow. In order to simplify the sophisticated problem and emphasize the smear effect on contaminant transfer, the PVWs are substituted by sand-wall (Fig. 1). Similarly to the classical model of consolidation (Hansbo, 1981), the presented model is described as an idealized three-zone model, where the smear zone is the disturbed region in the immediate vicinity of the sand-wall, and the middle zone is the intact region. In the remainder of the paper, the results obtained by the proposed method are compared with those obtained by the finite element method (FEM) provided by GeoStudio 2007. An illustrative example is performed to investigate the smear effect based on the proposed analytical solutions.

MATHEMATICAL MODEL

As shown in Fig. 1, the flushing solutions are injected through a row of sand-wall, and retrieved through another row of sand-wall that runs parallel

to the injection sand-wall, and the rate of the injection which remains constant is equal to the rate of the extraction. The model mainly includes the sand-walls, the smear zones, and the undisturbed contaminated soil which are considered to be homogeneous and fully saturated. The co-ordinate x has its origin at the border of the injection sand-wall, and its direction is parallel to the ground surface. It is assumed that the piezometric heads in the injection sand-wall and extraction sand-wall are steady, and the piezometric head varies linearly between the injection sand-wall and extraction sand-wall. Based on Darcy's law, the flow of the flushing solution can be occurred only in the x direction and if the piezometric heads in the injection sand-wall and extraction sand-wall are fixed, the seepage velocity must be invariable.

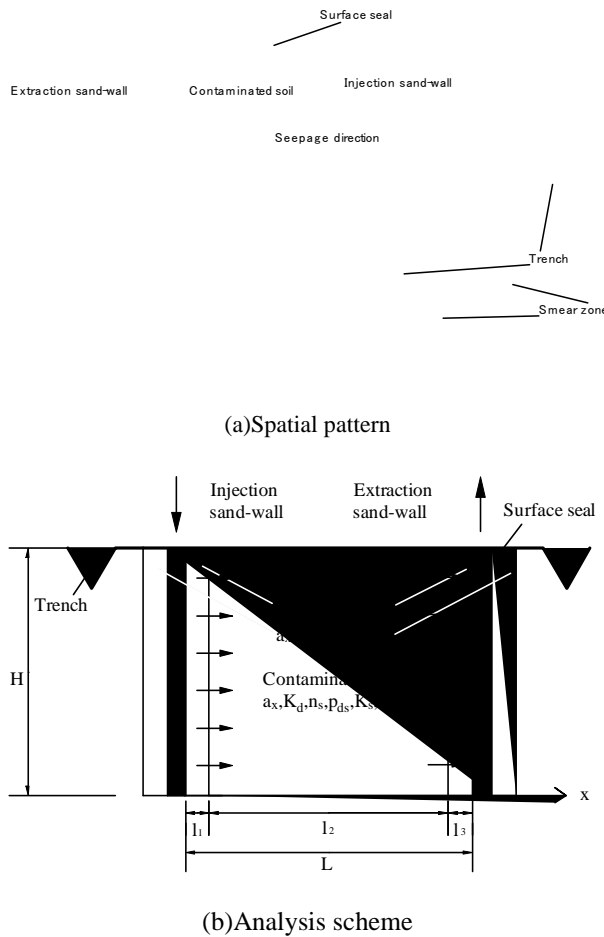


Fig. 1 Schematic diagram of contaminant extraction with smear zones.

The governing equations for solute transport through the smear zones and the undisturbed contaminated soil at a particular distance x and time t are expressed respectively:

$$R_{ds} \frac{\partial C_{si}(x,t)}{\partial t} = D_s \frac{\partial^2 C_{si}(x,t)}{\partial x^2} - \frac{1}{n_s} \frac{q_x \partial C_{si}(x,t)}{\partial x} \quad (i=1, 2) \quad (1)$$

$$R_d \frac{\partial C(x,t)}{\partial t} = D \frac{\partial^2 C(x,t)}{\partial x^2} - \frac{1}{n} \frac{q_x \partial C(x,t)}{\partial x} \quad (2)$$

where R_{ds} , R_d are the retardation factor of the smear zone and the undisturbed soil, respectively; C_{s1} is the contaminant concentration in the smear zone near the injection sand-wall; C_{s2} is the contaminant concentration in the smear zone near the extraction sand-wall; C is the contaminant concentration in the undisturbed soil; D_s , D are the coefficient of the hydrodynamic dispersion of the smear zone and the undisturbed soil; and n_s , n are the porosity of the smear zone and the undisturbed soil, respectively. q_x is the seepage velocity and based on the Darcy's law it is determined by

$$q_x = K_H \frac{\Delta h}{L} = \frac{l_1 + l_2 + l_3}{l_1 / K_s + l_2 / K + l_3 / K_s} \frac{\Delta h}{L} \quad (3)$$

where K_H is the horizontal equivalent permeability coefficient; K_s , K are the permeability coefficient of the smear zone and the undisturbed soil; Δh is the water head difference between the injection sand-wall and the extraction sand-wall; l_1 , l_3 are the width of the smear zone; l_2 is the width of the undisturbed soil; and L is the span between the injection sand-wall and the extraction sand-wall.

Using the Henry's law, R_{ds} , R_d can be represented as follows:

$$R_{ds} = 1 + \rho_{ds} K_d / n_s \quad (4)$$

$$R_d = 1 + \rho_d K_d / n \quad (5)$$

where ρ_{ds} , ρ_d are the dry bulk density of the smear zone and the undisturbed soil, respectively; and K_d is the equilibrium distribution coefficient, which is usually obtained by the Batch test, as the soil type of the smear zone and the undisturbed zone are same, K_d in the both regions are assumed to be equal.

On the basis of the Eq. (3), D_s , D can be obtained:

$$D_s = D_s^* + \alpha_x K_H \frac{\Delta h}{n_s L} \quad (6)$$

$$D = D^* + \alpha_x K_H \frac{\Delta h}{nL} \quad (7)$$

where D_s^* , D^* are the effective diffusion coefficient of the smear zone and the undisturbed soil; and α_x is the dispersivity of the x direction, likewise, α_x in the both regions are assumed to be equal.

The initial condition is

$$C_{si}(x, 0) = C(x, 0) = C_0 \quad (i = 1, 2) \quad (8)$$

where C_0 is the initial contaminant concentration which is a constant.

For the left boundary, the contaminant concentration of the flushing solution is zero:

$$C_{s1}(0, t) = 0 \quad (9)$$

The Neumann boundary condition is considered at the right boundary:

$$\left. \frac{\partial C_{s2}(x, t)}{\partial x} \right|_{x=L} = 0 \quad (10)$$

The contaminant concentration at the interface of the smear zone and the undisturbed zone are the same, and the continuity of the contaminant flux must be obeyed as well:

$$-n_s D_s \frac{\partial C_{si}(x, t)}{\partial x} + q_x C_{si}(x, t) \quad (11)$$

$$= -nD \frac{\partial C(x, t)}{\partial x} + q_x C(x, t) \quad (i = 1, 2)$$

$$C_{si}(x, t) = C(x, t) \quad (12)$$

where the coordinate $x = l_1$ as $i=1$, and $x = l_1 + l_2$ as $i=2$.

ANALYTICAL SOLUTION

The process of the contaminant extraction is analogous to the process of the small-strain consolidation because their governing equations are both the same form of a second-order partial differential equation. Similarly to the problem of one-dimensional consolidation of layered systems, the method of separation of variables mentioned by Lee et al. (1992) is applied. The solution to the governing Eqs. (1) and (2) satisfying the boundary conditions given by Eqs. (9) and (10) and the continuity conditions given by Eqs. (11) and (12)

can be expressed as follows:

$$C_{si}(x, t) = \exp\left(-\frac{q_x x}{2n_s D_s} - \frac{q_x^2 t}{4n_s^2 R_{ds} D_s}\right) \times \sum_{m=1}^{\infty} \xi_m h_{smi}(x) e^{-\frac{D_s}{R_{ds}} \beta_{sm} t} \quad (i = 1, 2) \quad (13)$$

$$C(x, t) = \exp\left(-\frac{q_x x}{2nD} - \frac{q_x^2 t}{4n^2 R_d D}\right) \times \sum_{m=1}^{\infty} \xi_m h_{mi}(x) e^{-\frac{D}{R_d} \beta_m t} \quad (14)$$

where

$$\beta_{sm} = \lambda_{sm}^2 \quad (15)$$

$$\beta_m = \lambda_m^2 \quad (16)$$

$$\beta_{sm} = \frac{DR_{ds}}{D_s R_d} \beta_m + \left(\frac{q_x^2}{4n^2 R_d D} - \frac{q_x^2}{4n_s^2 R_{ds} D_s}\right) \frac{R_{ds}}{D_s} \quad (17)$$

$$h_{smi}(x) = A_{smi} \sin \lambda_{sm} x + B_{smi} \cos \lambda_{sm} x \quad (i=1, 2) \quad (18)$$

$$h_m(x) = A_m \sin \lambda_m x + B_m \cos \lambda_m x \quad (19)$$

$$\xi_m = \frac{C_0 [n_s D_s e^{\frac{q_x x_1 + q_x x_2}{n_s D_s} - \frac{q_x^2 x}{2n_s D_s}} \int_0^{x_1} h_{sm1}(x) e^{-\frac{q_x x}{2n_s D_s}} dx + \frac{D_s R_d}{DR_{ds}} n D e^{\frac{q_x x_1 + q_x x_2}{n D} - \frac{q_x^2 x}{2n D}} \int_{x_1}^{x_2} h_m(x) e^{-\frac{q_x x}{2n D}} dx + \frac{D_s R_d}{DR_{ds}} n D e^{\frac{q_x x_1 + q_x x_2}{n D} - \frac{q_x^2 x}{2n D}} \int_{x_1}^{x_2} h_m^2(x) dx + n_s D_s e^{\frac{q_x x_2 + q_x x_1}{n_s D_s} - \frac{q_x^2 x}{2n_s D_s}} \int_{x_2}^L h_{sm2}(x) e^{-\frac{q_x x}{2n_s D_s}} dx] + n_s D_s e^{\frac{q_x x_2 + q_x x_1}{n_s D_s} - \frac{q_x^2 x}{2n_s D_s}} \int_{x_2}^L h_{sm2}^2(x) dx}{n_s D_s e^{\frac{q_x x_1 + q_x x_2}{n_s D_s} - \frac{q_x^2 x}{2n_s D_s}} \int_0^{x_1} h_{sm1}^2(x) dx + \frac{D_s R_d}{DR_{ds}} n D e^{\frac{q_x x_1 + q_x x_2}{n D} - \frac{q_x^2 x}{2n D}} \int_{x_1}^{x_2} h_m^2(x) dx + n_s D_s e^{\frac{q_x x_2 + q_x x_1}{n_s D_s} - \frac{q_x^2 x}{2n_s D_s}} \int_{x_2}^L h_{sm2}^2(x) dx} \dots \quad (20)$$

The coefficients A_{smi} , B_{smi} , A_m and B_m in Eqs. (18) and (19) can be obtained as follows:

$$[A_{sm1} \ B_{sm1}]^T = [1 \ 0]^T \quad (21)$$

$$[A_m \ B_m]^T = T_1^{-1} S_1 [A_{sm1} \ B_{sm1}]^T \quad (22)$$

$$[A_{sm2} \ B_{sm2}]^T = S_2^{-1} T_2 [A_m \ B_m]^T \quad (23)$$

where

$$S_i = \begin{bmatrix} E_{si} & F_{si} \\ G_{si} & H_{si} \end{bmatrix} \quad (i=1, 2), \quad (24)$$

in which:

$$\begin{aligned} E_{si} &= \sin \lambda_{sm} x_i e^{\frac{q_x x_i}{2n_s D_s}}, & F_{si} &= \cos \lambda_{sm} x_i e^{\frac{q_x x_i}{2n_s D_s}}, \\ G_{si} &= (-n_s D_s \lambda_{sm} \cos \lambda_{sm} x_i - \frac{q_x}{2} \sin \lambda_{sm} x_i) e^{\frac{q_x x_i}{2n_s D_s}}, \\ H_{si} &= (n_s D_s \lambda_{sm} \sin \lambda_{sm} x_i - \frac{q_x}{2} \cos \lambda_{sm} x_i) e^{\frac{q_x x_i}{2n_s D_s}}. \end{aligned}$$

$$T_i = \begin{bmatrix} E_i & F_i \\ G_i & H_i \end{bmatrix} \quad (i=1, 2), \quad (25)$$

in which:

$$\begin{aligned} E_i &= \sin \lambda_m x_i e^{\frac{q_x x_i}{2nD}}, & F_i &= \cos \lambda_m x_i e^{\frac{q_x x_i}{2nD}}, \\ G_i &= (-nD \lambda_m \cos \lambda_m x_i - \frac{q_x}{2} \sin \lambda_m x_i) e^{\frac{q_x x_i}{2nD}}, \\ H_i &= (nD \lambda_m \sin \lambda_m x_i - \frac{q_x}{2} \cos \lambda_m x_i) e^{\frac{q_x x_i}{2nD}}. \end{aligned}$$

The determinant of the following which is equal to zero yields the values of λ_m :

$$\left| U \cdot S_2^{-1} \cdot T_2 \cdot T_1^{-1} \cdot S_1 \cdot \begin{bmatrix} 1 & 0 \end{bmatrix}^T \right| = 0 \quad (26)$$

where

$$U = \begin{bmatrix} \lambda_{sm} \cos \lambda_{sm} L + \frac{q_x}{2n_s D_s} \sin \lambda_{sm} L \\ -\lambda_{sm} \sin \lambda_{sm} L + \frac{q_x}{2n_s D_s} \cos \lambda_{sm} L \end{bmatrix}^T \quad (27)$$

COMPARISONS WITH THE FINITE ELEMENT METHOD

To demonstrate the method is reasonable and verify the analytical solution gives the correct results, the proposed analytical solutions are compared with the finite element method (FEM) provided by GeoStudio 2007. The width of the sand-wall is assumed to be 4cm and smear zone is taken to be 0.1m, which is 2.5 times the width of the mandrel

based on large-scale consolidation studies, as described by Sathananthan and Indraratna (2006). The porosity and permeability in the undisturbed contaminated soil and the smear zone are extracted from Indraratna and Redana (1998, 2000). Toluene is chosen to represent the contaminant in the soil, and the initial constant concentration of toluene is assumed to be 1mg/L. The material and chemical properties of the soil are taken directly from Foose et al. (2002) for the similar property of the compacted clay liner from Foose et al. (2002) and the clay used in Indraratna and Redana (1998). The effective diffusion coefficient D^* in the smear zone is assumed to be decreased by 10% than D^* in the undisturbed zone. The properties of the undisturbed zone and smear zone are shown in Table 1.

In this case, the Neumann boundary condition, i.e., $\partial C_{s2}(L, t) / \partial x = 0$, is adopted at the extraction sand-wall. The comparisons of contaminant concentration profiles in the contaminated soil consisting of two smear zones and an undisturbed zone obtained by the presented analytical solution and GeoStudio 2007 are shown in Fig.2. The presented analytical solutions are agreed with the results obtained by the finite element method excellently. This result further validates the proposed analytical solutions.

Table 1 Parameters of the model for comparison with GeoStudio 2007

Property	Toluene
n_s	0.52
n	0.55
$\rho_d(\text{g/cm}^3)$	1.25
$\rho_{ds}(\text{g/cm}^3)$	1.30
Δh	12m
$K(\text{cm/s})$	3.36×10^{-7}
$K_s(\text{cm/s})$	2.7×10^{-8}
$K_d(\text{ml/g})$	1.0
$\alpha_x(\text{m})$	2.0
$D^*(\text{cm}^2/\text{h})$	7.34×10^{-3}
$D_s^*(\text{cm}^2/\text{h})$	6.6×10^{-3}
$l_1(\text{cm})$	10
$l_2(\text{cm})$	80
$l_3(\text{cm})$	10

RESULTS AND DISCUSSION

An illustrative example is presented to show the influence of the smear zones. Acetone is selected to represent the contaminant in the soil, and the initial constant concentration of acetone is assumed to be 1mg/L. The diffusion and distribution coefficients of the clay are from Kalbe et al. (2002). The effective

diffusion coefficient D^* in the smear zone is assumed to be 90% of D^* in the undisturbed zone. The properties of the smear zone and the undisturbed zone are extracted from Indraratna and Redana (1998, 2000). The material and the chemical properties of the undisturbed zone and smear zone are summarized in Table 2.

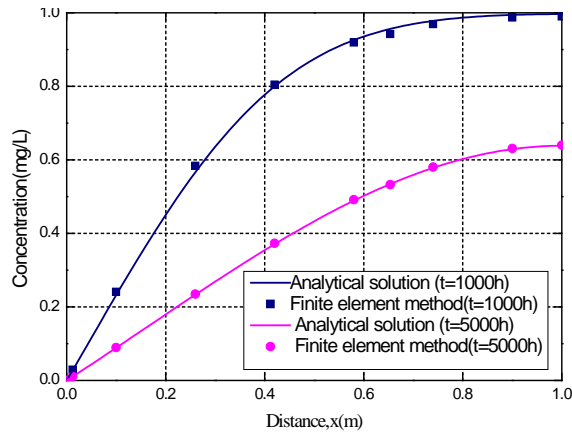


Fig. 2 Comparisons of the analytical solution with the finite element method.

Table 2 Parameters of the model for analysis

Property	Acetone
n_s	0.52
n	0.55
$\rho_d(\text{g/cm}^3)$	1.25
$\rho_{ds}(\text{g/cm}^3)$	1.30
Δh	12m
$K(\text{cm/s})$	3.9×10^{-8}
$K_s(\text{cm/s})$	3.4×10^{-9}
$K_d(\text{ml/g})$	0
$\alpha_x(\text{m})$	2.0
$D^*(\text{cm}^2/\text{h})$	1.22×10^{-2}
$D_s^*(\text{cm}^2/\text{h})$	1.09×10^{-2}
$l_1(\text{cm})$	10
$l_2(\text{cm})$	30
$l_3(\text{cm})$	10

Three different conditions are considered for this discussion. The comparison of the concentration profile for the case considering the effect of the smear zone and that assuming no smear zone is shown in Fig. 3. Both concentration profiles of the two cases are obtained on the basis that the water head difference is maintained at 12m, and correspondingly the seepage velocities of the two cases are $6.49 \times 10^{-6} \text{m/h}$ and $3.37 \times 10^{-5} \text{m/h}$ respectively. The 500-hour base contaminant concentration at the distance of 0.25m decreases

from 0.88 for the case considering the smear zone to 0.46 for that assuming no smear zone. Meanwhile, the contaminant concentration at the distance of 0.5m decreases from 0.996 to 0.66 when the smear zone is not considered in the model. The results suggest that the smear zone has a great effect on the contaminant extraction from contaminated soils.

Another case considering the smear zone is performed that the seepage velocity of the case is promoted to be equal to that assuming no smear zone. The 500-hour base contaminant concentration of this case is slightly less than that assuming no smear zone for the actual flow velocity in the pore of the smear zone is a little more than that of the pore of the undisturbed zone, correspondingly, the action of advection and dispersion can be greater. It is indicated that the smear zone has a slight influence even though the effect of smear zone on the flow velocity is not considered.

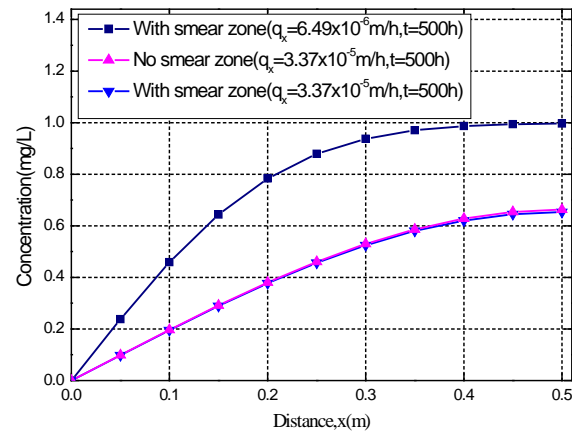


Fig. 3 Effect of smear zone on contaminant concentration profiles.

CONCLUSION

An analytical solution for one-dimensional contaminant extraction considering the effect of the smear zone is presented in this paper. The results obtained by the proposed analytical solution agree well with those obtained by the finite element method. The results suggested that the smear zone can have a great influence on the contaminant extraction from contaminated soils. The 500-hour base concentration of acetone at the distance of 0.25m increases by a factor of approximately 1.9 when the effect of the smear zone is considered in the model. Even though the flow velocities of the smear zone and undisturbed zone are identical, the smear zone still has a slight effect.

ACKNOWLEDGEMENTS

The authors would like to express their sincere gratitude to National Natural Science Foundation of

China (Grant 51179168) and the National Basic Research Program of China (Grant 2012CB719800) for the financial support to this study.

REFERENCES

- [1] Barraclough PB and Tinker PB, "The determination of ionic diffusion coefficients in field soils. i. diffusion coefficients in sieved soils in relation to water content and bulk density", *Journal of Soil Science*, Vol. 32, June. 1981, pp. 225-236.
- [2] Foose G, Benson C and Edil T, "Comparison of Solute Transport in Three Composite Liners", *Journal of Geotechnical and Geoenvironmental Engineering*, Vol. 128, May. 2002, pp. 391-403.
- [3] Gabr MA, Wang J and Bowders JJ, "Model for efficiency of soil flushing using PVD-enhanced system", *Journal of Geotechnical Engineering*, Vol. 122, November. 1996, pp. 914-919.
- [4] Gabr MA, Bowders JJ, Wang J and Quaranta JD, "In situ soil flushing using prefabricated vertical drains", *Canadian Geotechnical Journal*, Vol. 33, 1996, pp. 97-105.
- [5] Hansbo S, "Consolidation of fine-grained soils by prefabricated drains", in *Proc. 10th Int. Conf. SMFE*, 1981, pp. 677-682.
- [6] Indraratna B and Redana IW, "Laboratory determination of smear zone due to vertical drain installation", *Journal of Geotechnical and Geoenvironmental Engineering*, Vol. 124, February. 1998, pp. 180-184.
- [7] Indraratna B and Redana IW, "Numerical modeling of vertical drains with smear and well resistance installed in soft clay", *Canadian Geotechnical Journal*, Vol. 37, February. 2000, pp. 132-145.
- [8] Kalbe U, Müller WW, Berger W and Eckardt J, "Transport of organic contaminants within composite liner systems", *Applied Clay Science*, Vol. 21, April. 2002, pp. 67-76.
- [9] Kunberger T, Quaranta J and Gabr MA, "Remediation of Former Lockbourne Air Force Base using well injection depth extraction (WIDE)", in *Proc. 12th Pan-American Conf. on Soil Mechanics and Geotechnical Engineering*, 2003, pp. 1575-1581.
- [10] Lee PKK, Xie KH and Cheung YK, "A study on one-dimensional consolidation of layered systems", *International Journal for Numerical and Analytical Methods in Geomechanics*, Vol. 16, November. 1992, pp. 815-831.
- [11] Porter LK, Kemper WD, Jackson RD and Stewart BA, "Chloride diffusion in soils as influenced by moisture content", *Soil Science Society of America Journal*, Vol. 24, November. 1960, pp. 460-463.
- [12] Quaranta JD, Gabr MA, Cook EE and Szabo D, "Developments in prefabricated vertical drain enhanced soil flushing", in *Proc. 7th Int. Conf. on Offshore and Polar Engineering*, 1997, pp. 703-706.
- [13] Sathananthan I and Indraratna B, "Laboratory evaluation of smear zone and correlation between permeability and moisture content", *Journal of Geotechnical and Geoenvironmental Engineering*, Vol. 132, July. 2006, pp. 942-945.
- [14] Sharmin N, Kunberger T, Gabr MA, Quaranta JD and Bowders JJ, "Performance modeling and optimization of contaminant extraction using prefabricated vertical wells (PVWs)", *Geosynthetics International*, Vol. 15, March. 2008, pp. 205-215.
- [15] So HB and Nye PH, "The effect of bulk density, water content and soil type on the diffusion of chloride in soil", *Journal of Soil Science*, Vol. 40, December. 1989, pp. 743-749.
- [16] Warren KA, Gabr MA and Quaranta JD, "Field study to investigate WIDE technology for TCE extraction", *Journal of Geotechnical and Geoenvironmental Engineering*, Vol. 132, September. 2006, pp. 1111-1120.
- [17] Welker AL and Gilbert RB, "Calibration of flow and transport model with a bench-scale prefabricated vertical drain remediation system", *Journal of Geotechnical and Geoenvironmental Engineering*, Vol. 129, January. 2003, pp. 81-90.

MECHANISM OF C₆H₆ OXIDATION IN THE THREE-WAY CATALYTIC CONVERTER EQUIPPED A GASOLINE ENGINE

Akio Takigawa¹, Akihiro Mieda¹ and Yongzhen Peng²

¹Department of Civil and Environmental Engineering, Meibashi Institute of Technology, 460-1, Kamisatory-cho, Maebashi, Gunma 371-0816, Japan,

²Key Laboratory of Beijing for Water Quality Science and Water Environment Recovery Engineering, Beijing University of Technology, 100Pingleyuan, Chaoyang District, China

ABSTRACT

The mechanism C₆H₆ oxidation was investigated in a tubular-flow reactor containing a three-way catalyst a three-way catalyst. Experiments were performed to investigate the effects of coexistence gas components, temperature, gas flow rate and operating age of catalytic converter. The components of C₆H₆, H₂, CO, H₂O, HC, O₂ and N₂ were selected from the gasoline engine exhaust gas. The experimental results show that the oxidation of C₆H₆ was effect by the presence of coexistence gas component, and C₆H₆ oxidation was enhanced by the presence of O₂ and CO, while the presences of H₂, HC and H₂O have suppressive effect on the oxidation of C₆H₆ than O₂ and CO. The results reveal that catalyst has lower catalytic oxidation activity for C₆H₆ oxidation at lower temperature, and has higher catalytic oxidation activity for C₆H₆ than CH₄, C₂H₆ and C₃H₈, and decomposition of C₆H₆ via catalytic was similar to the decompositions of C₂H₄ and C₃H₆. The operating age of catalytic converter has lower effect on the oxidation of C₆H₆ with an increase in the operating time of catalytic converter from 0 to 80,000km at lower temperature range.

Keywords: C₆H₆, Catalytic Converter, Coexistence Gas, Temperature, Operating Age

INTRODUCTION

Volatile chlorinated hydrocarbons such as chloroform, trichloroethylene, aromatic compounds, such as benzene, xylene etc. 18 substance are in the substance on the hazardous air pollutants list defined as atmospheric pollutants with long term toxicity. 18 substances is also a substance in hazardous air pollutants list, high detection rates in our living environments, especially in the indoor air. Carcinogenic substance has been demonstrated to 18 types of being measured in benzene only. Benzene was also given priority initiatives substance of atmospheric organic harmful substances in Environment Agency, a revision of the Clean Air Act air quality guideline value less than 3μg/m³^[1]. Automobile exhaust gas, petroleum industry and various combustion systems etc. are the major C₆H₆ emission sources. C₆H₆ is estimated to about 83% in automotive-related source of C₆H₆ ^[2]. For building measures to prevent air pollution caused by C₆H₆, there is a need to clarify the discharge mechanism from the Automobile. Most modern gasoline engines equipped with three-way catalytic converters that simultaneously convert NO_x, CO and HC into non-polluting forms by means of precious metal-based heterogeneous catalyst. However, gasoline engine exhaust contains up 150 different hydrocarbons, except for NO_x and CO^[3]. Among these, the reactivity of C₆H₆ on the three-way catalytic converter is different with the other components. The three-way catalytic converter varies extremely with the change of driving mode of the automobile, and the operating

age of catalytic converter has been pointed out to potentially result in higher pollutant emissions.

The experiments reported here were designed to investigate the emission of C₆H₆ from a gasoline engine equipped with a three-way catalytic converter under different operating conditions. The effect of degradation of the catalytic converter on the C₆H₆ emission is also discussed.

EXPERIMENTS

The experimental apparatus is shown in Fig.1, and the reaction tube is shown in Fig.2. The reaction tube consisted of a preheating zone and a reaction zone. To achieve as near isothermal conditions as possible, the temperature of reaction tube was controlled by an electric furnace. The reaction tube was 18mm of inside diameter and 1300mm long. The preheating zone occupied 850 mm of the length and main reaction zone was 150mm in length. The reaction tube housed a commercial catalyst of 17mm outside diameter and 150mm in length used in an automobile. A rapid cooling zone, 10mm inside diameter and 300mm long, below the main reaction zone, was used to halt the reaction at the outlet of the reactor as rapidly as possible. The gas mixture was made up from seven streams (C₆H₆, CO, H₂, HC, H₂O, O₂ and N₂) supplied by calibrated mass controllers. The experiments were carried out for various flow rates of individual stream, using individual control valves so as to keep the concentration at the inlet of the reactor at the stated level. Measurement of C₆H₆, CO, H₂, HC and O₂ concentration was then performed after

the temperature of the reaction zone stabilized. The experiments were carried out for the various gas compositions, flow rate and reaction temperature. C_6H_6 and HC were measured using aflame ionization detector (FID) gas chromatograph

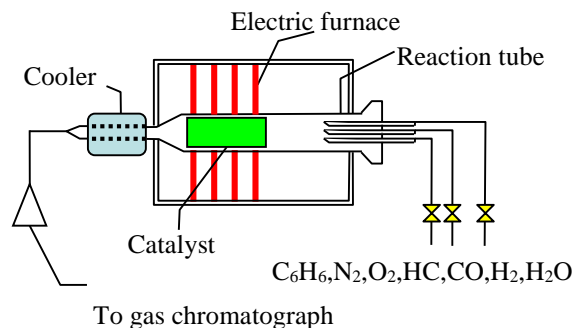


Fig.1 Experimental apparatus

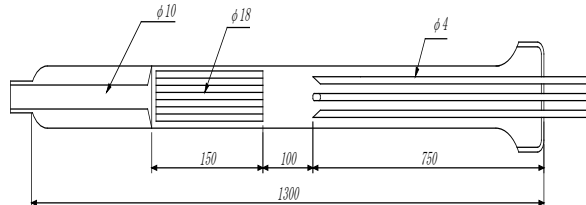


Fig.2 Details of reaction tube

Table 1 Experimental conditions

Gas component and concentration							
C_6H_6 : 30ppm, O_2 : 0.5%, HC: 1800ppm, CO: 0.2%, H_2 : 2.0%							
No.	N_2	C_6H_6	O_2	CO	H_2	H_2O	HC
1	○	○	○				
2	○	○	○	○			
3	○	○	○		○		
4	○	○	○			○	
5	○	○	○				○
6	○	○	○	○	○	○	○

gas flow rate: 10-24(ℓ /min), reaction temperature: 300-700°C, catalyst: 0km, 40000km, 80000km

(G2500, Hitachi). The concentrations of CO, H_2 were measured using a thermal conductivity detector (TCD) gas chromatograph (G5000, Hitachi). The activity of the catalytic converter is expected to be greatly dependent on the operating age. In order to elucidate the operating age with respect to C_6H_6 emission, three three-way catalytic converters were employed in these experiments. The catalytic converters tested are the same type in the composition and model water was injected in a manner to pass gas into the distilled water in the reaction tube inlet.

RESULTS AND DISCUSSION

Effects of O_2 , H_2 , CO, H_2O and HC on the Oxidation of C_6H_6

Initial experiments were carried out with the $C_6H_6/O_2/N_2$ gas system in the absence and presences of H_2 , CO and H_2O . The reactions were investigated as the function of gas flow rate (Fig.3). The decomposition of C_6H_6 is 100% in the range

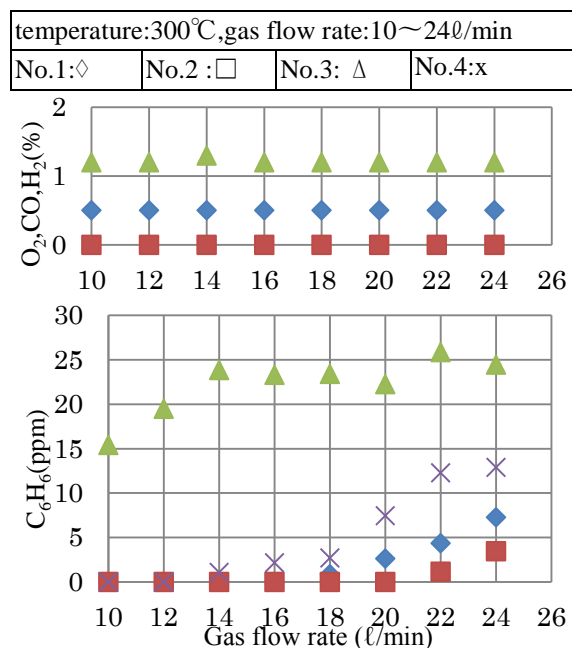
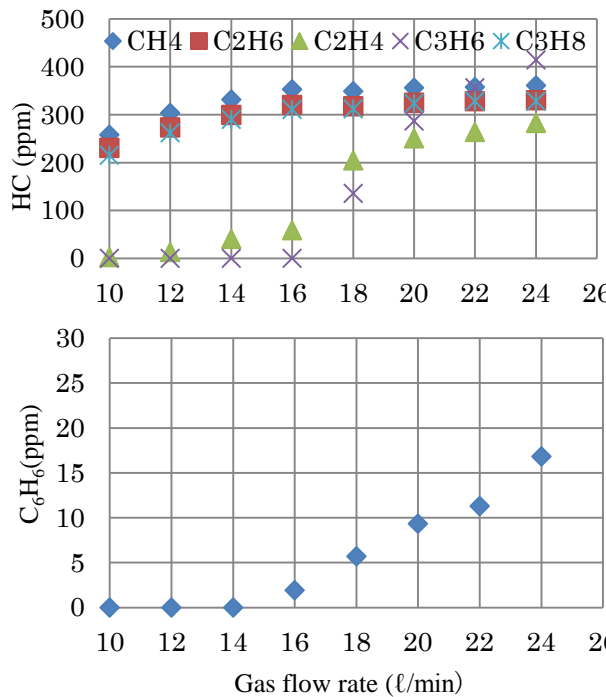


Fig.3 Effects of O_2 , CO, H_2 and H_2O on the oxidation of C_6H_6

from 10 ℓ /min to 16 ℓ /min and the concentration of C_6H_6 increases from 0ppm to 7ppm as the gas flow rate is increased from 16 ℓ /min to 24 ℓ /min in the $C_6H_6/O_2/N_2$ gas system. The variation of C_6H_6 concentration in the presence of CO is similar to that shown in $C_6H_6/O_2/N_2$ gas system, however, the emission of C_6H_6 is observed at 22 ℓ /min and maximum concentration of C_6H_6 of 4ppm is much lower than that for the $C_6H_6/O_2/N_2$ gas system. In the gas system of H_2O presence, the concentration of C_6H_6 increases from 0ppm to 3ppm with the increase in the gas flow rate from 10 ℓ /min to 18 ℓ /min, while the concentration of C_6H_6 increase sharply from 3ppm to 13ppm in the range of gas flow rate of 18 ℓ /min ~ 24 ℓ /min. For the $C_6H_6/H_2/O_2/N_2$ gas system, as the gas flow rate is increased from 10 ℓ /min to 14 ℓ /min, the concentration of C_6H_6 increases from 15ppm to 24ppm. Above 14 ℓ /min, the concentration of C_6H_6 maintains nearly a same value. In these experimentations CO was decomposed completely and the concentration of H_2O was not measured.

Fig.4 shows the variation in Paraffin (CH_4 , C_2H_6 , C_3H_8), olefin (C_2H_4 , C_3H_6) hydrocarbon concentrations and benzene (C_6H_6) concentration

No.5, gas flow rate: 10~24 ℓ /min
temperature: 300°C

Fig.4 Effect of HC on the oxidation of C₆H₆

at the outlet of converter with respect to gas flow rate. The variation in concentrations of CH₄, C₂H₆ and C₃H₈ show the similar tendency for the change of the gas flow rate, and show the lower decomposition rate at any gas flow rate. The variation in concentrations of C₂H₄, C₃H₆ and C₆H₆ also show the similar tendency for the change of the gas flow rate, however, the concentrations of C₂H₄, C₃H₆ and C₆H₆ show higher decrease in the range of lower gas flow rate.

Comparison of the effects of O₂, CO, H₂O, H₂ and HC on the decomposition of C₆H₆ shows that at 300°C, addition O₂, CO, H₂O, H₂ or HC to C₆H₆/N₂ gas system can strongly influence the C₆H₆ decomposition. These also evident that by contrast H₂O, H₂ and HC, O₂ and CO have significant accelerating effect respectively on the decomposition of C₆H₆.

Fig.5 shows effect of coexistence of CO, H₂O, H₂ and HC with C₆H₆/O₂/N₂ gas system on the decomposition of C₆H₆. When increasing the gas flow rate from 10 l/min to 18 l/min, the concentration of C₆H₆ increases from 15 ppm to 25 ppm. Above 18 l/min, the concentration of C₆H₆ maintains nearly a same value. These results resemble with the variation of C₆H₆ concentration in the C₆H₆/H₂/O₂/N₂ gas system, show that the inhibition of H₂ for C₆H₆ degradation is greater than the coexistence of other gas.

Effect of Temperature on the Oxidation of C₆H₆

No.6, gas flow rate: 10~24 l/min

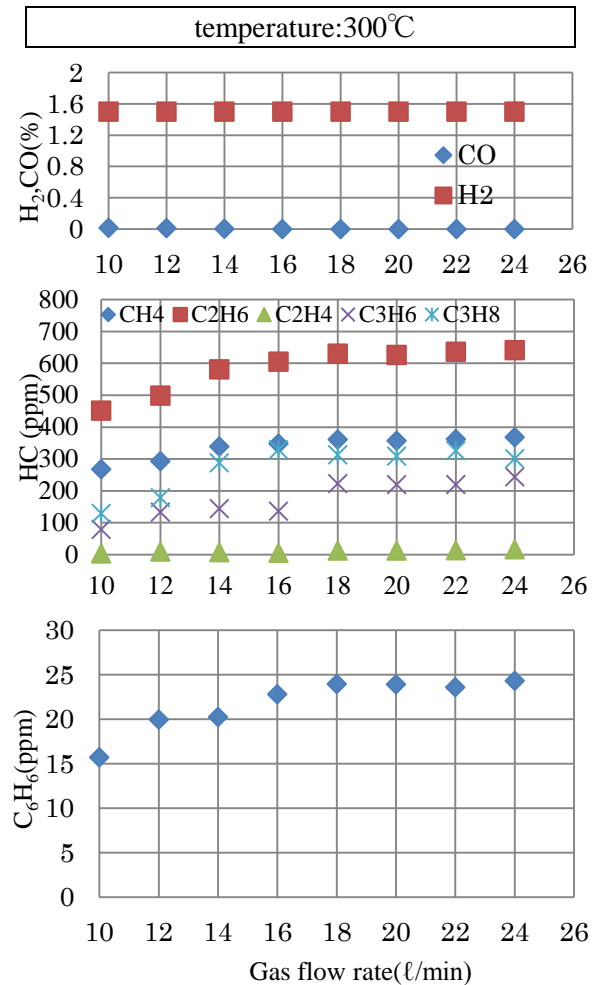
Fig.5 Effect of coexistent gas on the C₆H₆ oxidation

Fig.6 shows effect of temperature on the C₆H₆ oxidation in the C₆H₆/CO/H₂/H₂O/HC/N₂ gas system. Car exhaust gas temperature will vary with changes in the running speed of the car. Usually, under normal pressure, gasoline catalyst performs oxidation and reduction reactions in a range of 300°C~600°C^[4]. As shown in Fig.6, C₆H₆ is about 20 ppm at the temperature less than 500 °C, and maintained a constant concentration substantially, as the catalyst temperature rises from 500 °C to 700 °C, C₆H₆ concentration is reduced to about 11 ppm.

Comparing the results in Figure 5, these results indicate that the decomposition of C₆H₆ in the catalyst is influenced by temperature, and there is a temperature range, in which the C₆H₆ decomposition is enhanced. When increasing the temperature from 500°C to 700°C, the concentrations of CH₄, C₂H₆ and C₃H₈ were impaired, while the concentrations of C₃H₆, C₂H₄ were increased conversely. These experimental results differ from the experimental results shown in Fig.5. These results indicate that the temperature direct influence the decomposition process of each component in the catalyst, and also

influence to that by the shortening of the reaction time due to temperature rise.

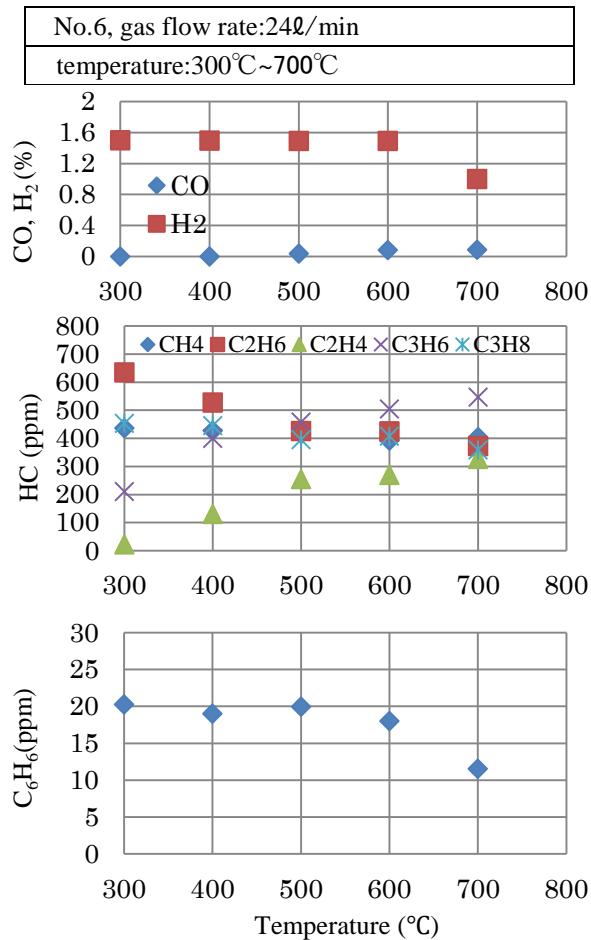


Fig.6 Effect of temperature on the C₆H₆ oxidation

Effect of Catalyst Degradation on the Oxidation of C₆H₆

It is believed that the performance of the gasoline catalyst to decline with an increase in the mileage of the car. Besides mechanical destruction, wear, alteration, catalyst degradation is also advanced by the alteration and dissipation of the active substance, and adsorption of toxic substance.

Fig.7 is the results of the experiment with three catalyst taken from used gasoline car. The mileage of the car is 0km, 40000km and 80000km respectively. As shown in Fig.7, C₆H₆ concentrations are hardly affected by the increase in the mileage from 0km to 80000km. There is no significant difference on the concentrations of H₂, and CO concentration was not detected. However, the effect of mileage on the CH₄, C₂H₆, C₃H₈ concentration is small in the range of the mileage, and concentrations of C₂H₄, C₃H₆ significantly

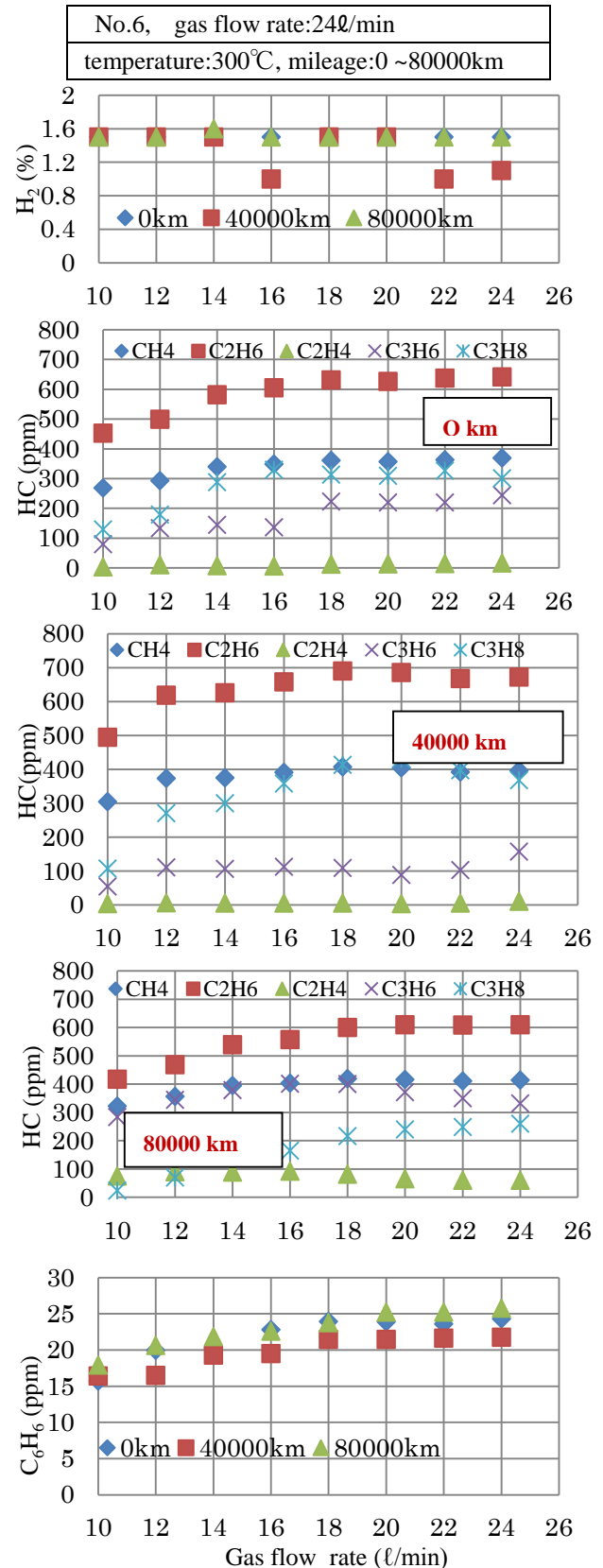


Fig.7 Effect of catalytic degradation on the C₆H₆ oxidation

increase with the increasing in the mileage from 0km to 80000km. These results indicate that the effect of degradation of the catalyst with increasing mileage of

the car on the decomposition of the gas components depend on the components.

CONCLUSION

The effects of the engine operating conditions on the C_6H_6 emission have been investigated with respect to gas flow rate, coexistence gas components and temperature in a tubular-flow reactor containing a three-way catalyst. The comparisons of the effects of coexistence gas components and gas flow rate on the C_6H_6 decomposition have clarified that the oxidation of C_6H_6 is effected by the presence of coexistence gas component, and C_6H_6 oxidation is enhanced by the presences of O_2 and CO , while the presences of H_2 , HC and H_2O have suppressive effect on the oxidation of C_6H_6 than O_2 and CO . The results also reveal that there is a certain range of the temperature, at which the catalysts have higher catalytic activity for C_6H_6 oxidation. The effect of catalyst degradation on the oxidation of C_6H_6 has also investigated. It was found that in the range of the mileage from 0km to 80000km, the degradation of catalyst has lower effect on the decomposition of C_6H_6 .

REFERENCES

- [1] Environmental preservation measures technical committee, Basic knowledge of air pollution, Japan, Japan environmental management association for industry, 2003, ch1.
- [2] NITE, Initial risk assessment of chemicals, japan, 2007, No.104
- [3] John E. S, Silvestre T, William R, et al, "Volatile organic compound emissions from 46 in use passenger cars", J. of Environ. Sci. Technol., Vol.21, No.5, 1987, pp.466-475.
- [4] Abe E, Present and future of automobile exhaust gas catalyst, Science and technology developments, Vol.117, 2010, pp. 8-6

ROLE OF CURBSIDE CRACK OF ROAD IN URBAN BIODIVERSITY

Taizo Uchida¹, Xue J. Huan¹, Daisuke Hayasaka², Teruo Arase³, William T. Haller⁴ and Lyn A. Gettys⁴

¹Faculty of Engineering, Kyushu Sangyo University, Japan; ²Faculty of Agriculture, Kinki University, Japan; ³Faculty of Agriculture, Shinshu University, Japan; ⁴Center for Aquatic and Invasive Plants, University of Florida, USA

ABSTRACT

The objective of this study is to collect basic information on flora along roadside, especially in curbside cracks of road, for evaluating biodiversity in urban landscape. A curbside crack in this study was defined as a linear space (under 20 mm in width) between the asphalt pavement and curbstone. The species composition of plants invading curbside cracks was surveyed in 38 plots along the serial National Route, over a total length of 36.5 km, in Fukuoka City in southern Japan. In total, 113 species including native plants (83 species, 73.5%), perennial herbs (57 species, 50.4%) and woody plants (13 species, 11.5%) were recorded in curbside cracks. Buried seeds were also obtained from soil in curbside cracks, which means the cracks would possess a potential as seed bank. Incidentally, no significant differences were found in the vegetation characteristics of curbside cracks among land-use types (Kolmogorov-Smirnov Test, $P > 0.05$). From these results, curbside cracks would be likely to play an important part in offering habitat for plants in urban area.

Keywords: Biodiversity, Curbside Crack, Roadside Vegetation, Seed Bank, Urban Area

INTRODUCTION

Roads are important infrastructure components that provide critical corridors for transporting goods and humans. Expansion and integration of asphalted road networks would symbolize urban landscape. Some plants, however, become established in curbside cracks of road and cause deterioration of asphalt and curbs, reducing road surface longevity and safety. Therefore, road managers spend a considerable amount of time and money on roadside vegetation management [4]. In this context, several ecological traits of plants in curbside cracks of road have been also shown for effective road management [4], [5], [18].

On the other hand, there has been growing interest in the effect of urbanization on the biodiversity and ecosystems [12], [19], [20]. And, to evaluate the urban biodiversity and ecosystems, the sites where could be habitats for plant, such as wetland, riverside, garden, park or shrine in the cities, have been surveying [12].

In this study, we hypothesize that roadsides, especially curbside cracks of road, can be site where some plants establish including ecologically valuable species, and be evaluated as useful habitat for plant. To investigate above hypothesis, we surveyed plant that invades curbside cracks of road; we compared species composition and characteristics in the curbside cracks among land-use types in urban area. The objective of this study is to collect basic information on flora along roadside, especially in curbside cracks of road, for evaluating biodiversity in urban area.

MATERIALS AND METHODS

Study Area

Surveying of vegetation in curbside cracks was conducted in Fukuoka City, southern Japan, in September 2012 along National Route 3, 202 and 263, over a total distance of 36.5 km (Fig. 1).

Fukuoka City is one of the biggest cities in Japan besides Tokyo, Osaka and Nagoya, and the population is around one and a half million, the density is 4,392 km⁻², as of May 1, 2013 (Fukuoka City Environmental Data System). According to AMEDAS (Automated Meteorological Data Ac-

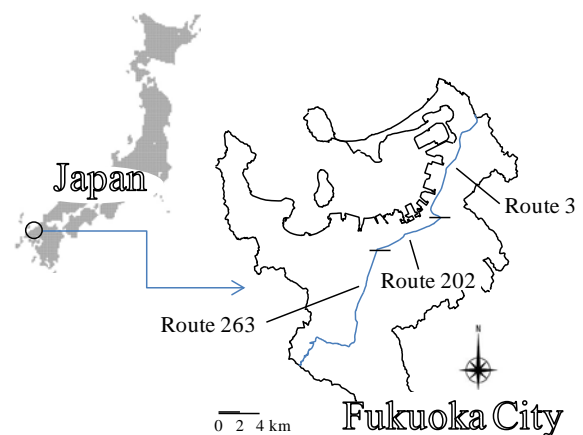


Fig. 1 Location of study sites.

Table 1 Vegetation characteristics of curbside cracks among land-use types.

Land-use types	Vegetation characteristics				
	Number of survey plots	Total number of species	Average number of species	Sannon-Wiener's diversity index (H')	Percentage of non-native species
Forest	8	63	13.3	1.670	19.0
Business area	12	45	10.6	1.952	35.6
Residential districts	14	41	8.7	1.785	39.0
Developed land	1	20	20.0	2.987	40.0
Dry fields	3	23	10.0	1.675	30.4
Paddy fields	0	-	-	-	-
<i>P</i> -value	-	0.200 ^{ns}	0.194 ^{ns}	0.053 ^{ns}	0.200 ^{ns}

$P > 0.05$: ns indicates not significant using Kolmogorov-Smirnov test.

quisition System) from 2003 to 2012, Fukuoka City lies in the warm-temperature zone, with values of Kira's Warmth Index [9] ranging from 143.4 to 155.5 °C and with annual precipitation of 1,020 to 2,018 mm.

Species Composition and Characteristics

The species composition of vegetation in curbside cracks was recorded according to the methodology of Braun-Blanquet cover-abundance scale [2]. A curbside crack was defined as a linear space (under 20 mm in width) between the asphalt pavement and curbstone [4]. We located 38 survey plots along the route at intervals of approximately 1 km. The size of the plots was 50 m (length) × 20 mm (maximum width of the crack).

Plant nomenclature used in this paper followed Miyawaki et al. (1994), Baba (1999) and Shimizu (2003). All the recorded species were categorized by life form (dormancy form, disseminule form, radicle form and growth form) and invasive status (native or non-native), in order to characterize the vegetation surveyed. Life form was based on the description by Raunkiaer (1934) and Numata (1990), and we distinguished non-native from native species based on published literature [1], [11], [17]. Using aerial photographs and field observation, dominant land-use types within a radius of 100 m from each survey plot were classified as residential districts, dry fields, developed land, paddy fields, forest, and business area.

Soil Property

The soil was collected from curbside crack in each survey plot, using stainless spatula, for measurement of pH and EC.

And then, in order to estimate the potential flora in curbside crack, the soil obtained from the crack was spread over 20 cm² with thickness of 1.5 cm on the vinyl pot filled with expanded vermiculite. Pre-

pared pots were put under the constant temperature of 25 °C with 12 hours light of 3,300-3,600 lux a day for 3 months, and plant emerged from the soil was regularly identified.

Data Analysis

Braun-Blanquet cover-abundance scale (r, +, I, II, III, IV and V) was transformed as follows: r and +, 0.1%; I, 5.0%; II, 17.5%; III, 37.5%; IV, 62.5%; and V, 87.5%.

To test whether characteristics of vegetation in curbside cracks were different among land-use types, we conducted a Kolmogorov-Smirnov test, under the null hypothesis that vegetation characteristics of curbside cracks were equivalent across land-use types [3], [21]. The vegetation characteristics employed were the following: the total number of species, average number of species, Sannon-Wiener's diversity index (H') and the percentage of non-native species.

Horn's measurement of overlap [6] was done with mean cover data of species in each land-use type in order to examine the similarity of species composition among land-use types. According to the Eq. (1), Summed Dominance Ratio (SDR) of species [14] in each land-use type was also calculated;

$$\text{SDR} = (F' + C') / 2 \quad (1)$$

Where F' and C' is the ratio of frequency and cover of each species to the numbers of the most abundant species, respectively.

To find out whether the proportion of each life form was different among land-use types, we conducted a two-way ANOVA. The differences in pH and EC of curbside crack soil among land-use types were also analyzed using an ANOVA. All of the data for the ANOVAs were used after transforming to $\ln(x + 0.5)$ value.

Table 2 Number of species emerged from soil of curbside crack obtained in each vegetation type.

Vegetation types	Study parameter				
	Number of survey plots	Total number of species	Average number of species	Maximum number of species	Minimum number of species
V1	26	17	3.4	7	1
V2	9	14	3.1	6	1
V3	3	10	4.3	8	1
Total	38	20	3.4	8	1

See Fig. 2 and Appendix 1. Eight unknown species were excluded. Of the 20 species identified, 2 plants, *Juncus tenuis* Willden. and *Aira caryophylla* L., were not recorded at the field survey.

RESULTS

Species Composition and Characteristics

In total, 113 species including 83 (73.5%) natives were observed in curbside cracks along the surveyed routes (Appendix 1), of which 100 (88.5%) species were herbaceous and 13 (11.5%) species were woody plants. In the former, 57 perennials (50.4%) were recorded. Of the 36 families obtained in this survey (Appendix 1), Poaceae and Asteraceae accounted for the majority of herbaceous plants (47/100 species), and Ulmaceae was dominant in woody plants recorded (4/13 species).

No significant differences were found in the vegetation characteristics of curbside cracks across land-use types ($P > 0.05$) (Table 1).

Using Horn's measurement of overlap three vegetation types could be distinguished (Fig. 2). Type V1 contained business area and residential districts ($n = 26$), and Type V2 included forest and developed land ($n = 9$). Type V3 consisted of dry fields ($n = 3$). Common species to all vegetation types (12/113 species) were *Artemisia princeps* Pamp., *Digitaria ciliaris* (Retz.) Koel., *Eleusine indica* (L.) Gaertn., *Euphorbia supina* Rafin., *Lactuca indica* L., *Oxalis corniculata* L., *Paspalum dilatatum* Poir., *Sagina japonica* (Sw.) Ohwi, *Setaria viridis* (L.) Beauv., *Solidago altissima* L., *Taraxacum officinale* Weber and *Youngia japonica* (L.) DC. (Appendix 1). On the other hand, species that emerged just in some specific type or other were also observed. The species occurred only in Type V1 were 35 plants, e.g. *Cynodon dactylon* (L.) Pers., *Gnaphalium japonicum* Thunb. and *Trifolium dubium* Sibth., and those in Type V2 were 39 plants including *Bidens frondosa* L., *Carex lenta* D. Don, *Clinopodium micranthum* (Regel) Hara, *Festuca arundinacea* Schreb., etc. Four species of *Euphorbia muculata* L., *Lespedeza cuneata* (Dum. Cours.) G. Don, *Ulmus davidiana* Planch. var. *japonica* (Rehder) Nakai and *Viola mandshurica* W. Becker

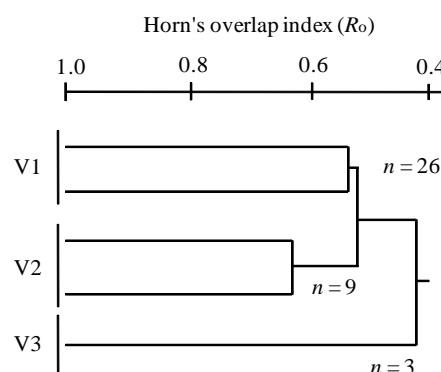


Fig. 2 Classification among 5 land-use types based on mean cover of component species, using Horn's measurement of overlap. See Appendix 1.

were found only in Type V3.

In the top 10 species of SDR in each type (Fig. 3), lots of perennials (H and Ch) were found as well as ephemeral plants (Th(w) and Th), and barachory (D4) or anemochory (D1) was the dominant dispersal modes. Definite tendency was not shown in radicoid and growth forms. Incidentally, the proportion of life forms of vegetation in curbside cracks was not statistically different among the types ($P > 0.05$).

Soil Property

There was no significant difference in pH and EC of curbside crack soil across the types ($P > 0.05$) (Appendix 1).

Seedlings from curbside crack soil which spread over the pot were shown in every pot (max., 8 species; and min., 1 species) (Table 2 and Appendix 1). In total, 20 species emerged from the pot, of which 2 species had not been observed at the field survey.

DISCUSSION

Investigating the vegetation in curbside cracks of road, 36 families with 113 species were observed (Appendix 1). Our results are not surprising because

road has also become an important corridor for dispersal and expansion of plants as well as transporting humans and all the goods we need [8], [10].

Ephemeral (annual and biennial) and non-native plants are species having the highest advantages in curbside cracks [5]. Of 113 species recorded in this survey (Fig. 3 and Appendix 1), however, plenty of perennial (61.9%), native (73.5%) and woody (11.5%) species were confirmed. The characteristics including diversity index (H') were not also affected by land-use types (Table 1). Furthermore, 20 species including 2 species not recorded at the field survey were obtained from the soil in curbside cracks of road (Table 2 and Appendix 1). Therefore, we suggest that curbside cracks would be likely to play an important part in offering habitat and seed bank for plants regardless of surrounding land-use types in urban area although there is the problem of deteriorations of road [4], [5].

Hayasaka et al. (2011, 2012) mentioned that the main ecological types of curbside crack vegetation were species with gravity dispersal (barochory) or wind dispersal (anemochory) mechanisms. Suto et al. (2006) reported the similar opinion of view too. Additionally, both of them were also referred that Poaceae and Asteraceae were dominant families in curbside crack environments [4], [5], [18]. These previous studies support our results that species with barochory or anemochory mechanisms and those in

Poaceae and Asteraceae dominated the plants observed in this survey (Fig. 3 and Appendix 1). Incidentally, correlation between these dispersal modes and families is definite.

A common species among vegetation types would be defined as a typical species in curbside crack vegetation (Fig. 2 and Appendix 1); to name a few, *Artemisia princeps* Pamp., *Digitaria ciliaris* (Retz.) Koel., *Taraxacum officinale* Weber, etc. Conversely, a unique species in each vegetation type could be a peculiar species which affected by the surrounding land-use, e.g. *Phyllanthus urinaria* L., *Talinum crassifolium* Willd., *Impatiens textori* Miq. and *Viola mandshurica* W. Becker. To obtain biodiversity more from curbside cracks of road in urban landscape, therefore, securing various land-use types in the city would be also needed.

Recognizing road is one of the serious problems today in natural ecosystems would be required- for instance, expansion and integration of road networks, which accompany urbanization, can cause fragmentation and extinction of plant populations and communities [7], [16]. And furthermore, roads become dispersal corridors for plants, including non-native species [8], [10]. However, to appreciate the role of curbside cracks of road in offering habitat and seed bank place for plants, including much native species, might be also very important in urban biodiversity.

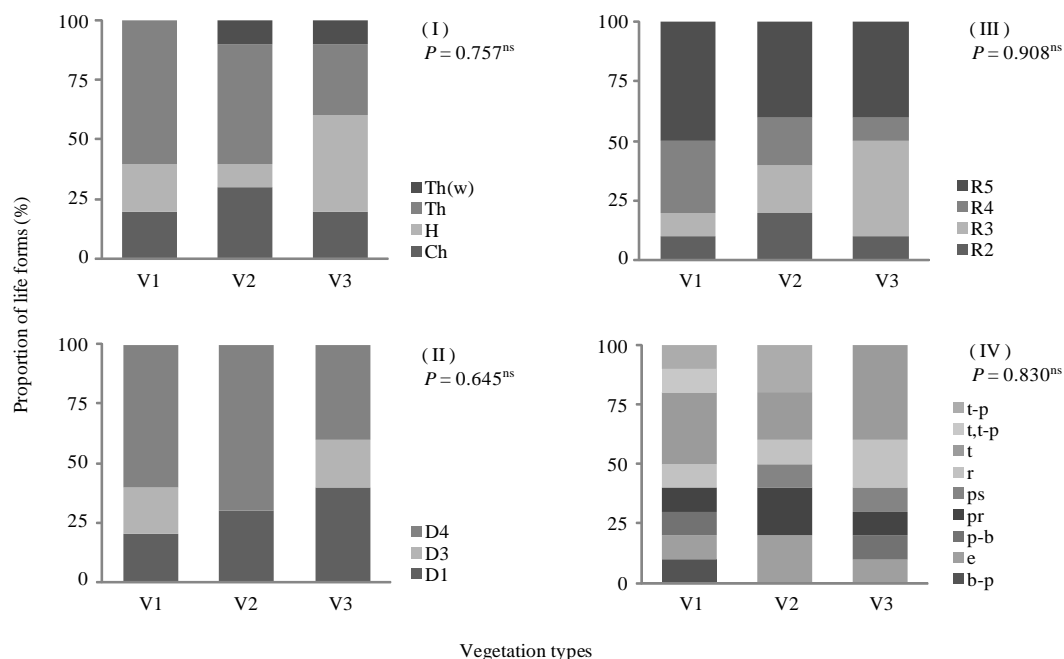


Fig. 3 Proportion of life forms of the top 10 species in SDR in each vegetation type. Life forms are as follows: (I), dormancy form; (II), disseminule form; (III), radicoid form; and (IV), growth form. $P > 0.05$: ns indicates not significant using a two-way ANOVA. See Fig. 2.

Appendix 1 Species recorded in this survey and they were listed, according as component species in each vegetation type.

Species	Family	Common name	Vegetation types			Occurrence frequency (%)
			V1 (n = 26)	V2 (n = 9)	V3 (n = 3)	
<i>Artemisia princeps</i> Pamp. #	Asteraceae	Japanese mugwort	II	V	V	81.6
<i>Digitaria ciliaris</i> (Retz.) Koel. † #	Poaceae	Southern crabgrass	III	II	I	84.2
<i>Eleusine indica</i> (L.) Gaertn. †	Poaceae	Indian goosegrass	III	II	II	47.4
<i>Euphorbia supina</i> Rafin. * †	Euphorbiaceae	Milk purslane	III	I	I	55.3
<i>Lactuca indica</i> L. † #	Asteraceae	Indian lettuce	II	II	II	36.8
<i>Oxalis corniculata</i> L. #	Oxalidaceae	Sorrel	III	II	III	63.2
<i>Paspalum dilatatum</i> Poir. *	Poaceae	Dallis grass	+	+	I	7.9
<i>Savina japonica</i> (Sw.) Ohwi † #	Caryophyllaceae	Pearlwort	+	+	I	10.5
<i>Setaria viridis</i> (L.) Beauv. † #	Poaceae	Green bristlegrass	V	II	II	76.3
<i>Solidago altissima</i> L. *	Asteraceae	Canada goldenrod	I	IV	I	23.7
<i>Taraxacum officinale</i> Weber *	Asteraceae	Dandelion	III	III	III	78.9
<i>Youngia japonica</i> (L.) DC. †	Asteraceae	Oriental false hawkbeard	r	+	II	13.2
<i>Amaranthus spinosus</i> L. * †	Amaranthaceae	Spiny amaranth	r			2.6
<i>Ambrosia ambrosioides</i> (L.) Spach * †	Chenopodiaceae	Mexican tea	r			2.6
<i>Ambrosia artemisiifolia</i> L. var. <i>elatiore</i> (L.) Descurt. † #	Asteraceae	Ragweed	r			2.6
<i>A. virginicus</i> L. *	Poaceae	Broomsedge bluestem	r			2.6
<i>Anhananthe aspera</i> (Thunb.) Planch.	Ulmaceae	Aphananthe	II			5.3
<i>Calystegia hederacea</i> Wall.	Convolvulaceae	Japanese false bindweed	r			2.6
<i>Capsella bursa-pastoris</i> Medicus † #	Brassicaceae	Shepherd's purse	r			2.6
<i>Cayratia japonica</i> (Thunb.) Gagn.	Vitaceae	Bushkiller	r			2.6
<i>Celtis sinensis</i> Pers. var. <i>japonica</i> (Planch.) Nakai	Ulmaceae	Chinese hackberry	+			2.6
<i>Cynodon dactylon</i> (L.) Pers.	Poaceae	Bermuda grass	III			23.7
<i>Cyperus iria</i> L. †	Cyperaceae	Rice galangale	r			5.3
<i>Cyperus rotundus</i> L.	Cyperaceae	Nut grass	r			2.6
<i>Digitaria violascens</i> Link. †	Poaceae	Violet crabgrass	I			5.3
<i>Eraerostis multicaulis</i> Steud. †	Poaceae	-----				2.6
<i>Stenactis annuus</i> (L.) Cass. * †	Asteraceae	Annual fleabane	I			18.4
<i>Glechoma hederacea</i> L. subsp. <i>grandis</i> (A. Gray) Hara #	Lamiaceae	Alehoof	r			2.6
<i>Gnaphalium japonicum</i> Thunb. #	Asteraceae	Japanese cudweed	I			2.6
<i>Isachne elobosa</i> (Thunb.) O. Kuntze	Poaceae	Dwarf white-striped bamboo	r			2.6
<i>Kalmia latifolia</i> L.	Asteraceae	-----	+			2.6
<i>Melastoma azeedarach</i> L. var. <i>subtrinervata</i> Miao	Meliaceae	Chinaberry	+			2.6
<i>Muhlenbergia japonica</i> Steud.	Poaceae	-----	+			2.6
<i>Ophiopogon japonicus</i> (L. fil.) Ker Gawl.	Liliaceae	Mondo grass	+			10.5
<i>Panicum dichotomiflorum</i> Michx. * †	Poaceae	Fall panicum	r			2.6
<i>Phyllanthus urinaria</i> L. † #	Phyllanthaceae	Chamberbitter	r			5.3
<i>Phytolacca americana</i> L. *	Phytolaccaceae	Pokeweed	r			2.6
<i>Polygonum lapathifolium</i> (L.) S. F. Gary †	Polygonaceae	Curlytop knotweed	r			2.6
<i>Portulaca oleracea</i> Cvs. * †	Portulacaceae	Purslane pusley	r			2.6
<i>Portulaca oleracea</i> L. †	Portulacaceae	Common purslane	+			7.9
<i>Rorippa indica</i> (L.) Hiern †	Cruciferae	Variableleaf yellowcress	+			2.6
<i>Sedum bulbiferum</i> Makino †	Crassulaceae	-----	+			2.6
<i>Talinum crassifolium</i> Willd. * #	Portulacaceae	Coral flower	r			5.3
<i>Trifolium dubium</i> Sibth. * † #	Fabaceae	Suckling clover	r			2.6
<i>Zanthoxylum schinifolium</i> Sieb. et Zucc.	Rutaceae	-----	r			2.6
<i>Zephyranthes candida</i> (Lindl.) Herbert *	Amaryllidaceae	Fairy lily	r			2.6
<i>Zostera japonica</i> Steud.	Poaceae	Lawnglass	II			18.4
<i>Acalypha australis</i> L. † #	Euphorbiaceae	Australian acalypha		+		2.6
<i>Achyranthes bidentata</i> Blume var. <i>Tomentosa</i> (Honda) Hara	Amaranthaceae	-----		+		2.6
<i>Amorpha fruticosa</i> L. *	Fabaceae	Desert false indigo		+		2.6
<i>forma citrullifolia</i> (Lebas) Rehd.	Vitaceae	-----		+		2.6
<i>Aster ageratoides</i> Turcz. subsp.	Asteraceae	Wild chrysanthemum		+		2.6
<i>Kalmia latifolia</i> (L.) DC.	Asteraceae	-----		I		5.3
<i>Bidens frondosa</i> L. * †	Asteraceae	Devil's beggartick		+		2.6
<i>Urtica thunbergiana</i> Sieb. et Zucc.	Urticaceae	Ramie		II		10.5
<i>Boehmeria tricuspidata</i> (Hance) Makino	Urticaceae	-----		+		2.6
<i>Boehmeria spicata</i> (Thunb.) Thunb.	Urticaceae	-----		+		2.6
<i>Boenninghausenia japonica</i> Nakai	Rutaceae	-----		+		2.6
<i>Carex lenta</i> D. Don	Cyperaceae	Flat sedge		+		2.6
<i>Chenopodium centrorubrum</i> (Makino) Nakai † #	Chenopodiaceae	Fat hen		+		2.6
<i>Cirsium discolor</i> (Maxim.) Matsum.	Asteraceae	-----		+		2.6
<i>Clerodendron trichotomum</i> Thunb.	Verbenaceae	Harlequin glory bower		+		2.6
<i>Clinodendron micranthum</i> (Reisch Hara)	Lamiaceae	-----		+		2.6
<i>Dactyloctenium aegyptium</i> (L.) Beauv. *	Poaceae	Crowfoot grass		+		2.6
<i>Dioscorea japonica</i> Thunb.	Dioscoreaceae	Japanese yam		+		2.6
<i>Duchesnea indica</i> (Andr.) Focke	Rosaceae	Mock strawberry		+		2.6
<i>Echinochloa crus-galli</i> (L.) Beauv. var. <i>caudata</i> (Roshev.) Kitag. † #	Poaceae	Barnyardgrass		+		2.6
<i>Festuca arundinacea</i> Schreb. *	Poaceae	Tall fescue		+		2.6
<i>Ficus erecta</i> Thunb.	Moraceae	-----		+		2.6
<i>Geranium nealense</i> Sweet subsp. <i>Thunbergii</i> (Sieb. et Zucc.) Hara	Geraniaceae	Oriental geranium		I		5.3
<i>Impatiens textori</i> Miq. †	Balsaminaceae	Touch-me-not		+		2.6
<i>Justicia procumbens</i> L. †	Acanthaceae	Common asystasia		II		10.5
<i>Opismenus undulatifolius</i> (Arduino) Roemer et Schultes	Poaceae	Wavyleaf basketgrass		+		2.6
<i>Opismenus compositus</i> (L.) Beauv.	Poaceae	-----		+		2.6
<i>Paspalum thunbergii</i> Kunth	Poaceae	Japanese paspalum		+		2.6
<i>Petasites japonicus</i> (Sieb. et Zucc.) Maxim.	Asteraceae	Fuki		+		2.6
<i>Picris hieracioides</i> L. subsp. <i>japonica</i> (Thunb.) Krylov †	Asteraceae	Hawkweed ox-tongue		+		2.6
<i>Plantago lanceolata</i> L. *	Plantaginaceae	Ribwort plantain		+		2.6
<i>Polygonum caespitosum</i> Bl. var. <i>laxiflorum</i> Meisn. †	Polygonaceae	Asiatic smartweed		I		5.3
<i>Reynoutria japonica</i> Houtt.	Polygonaceae	Japanese knotweed		+		2.6
<i>Persicaria longisetata</i> (De Bruyn) Kitag. †	Polygonaceae	Tufted knotweed		I		5.3
<i>Persicaria thunbergii</i> (Sieb. et Zucc.) H. Gross † #	Polygonaceae	Water pepper		+		2.6
<i>Rubus buergeri</i> Miao	Rosaceae	-----		+		2.6
<i>Rumex japonicus</i> Houtt.	Polygonaceae	-----		I		5.3
<i>Trifolium repens</i> L.	Leguminosae	White clover		+		2.6
<i>Viola verecunda</i> A. Gray	Violaceae	Japanese violet		I		5.3
<i>Euphorbia maculata</i> L. * †	Euphorbiaceae	Eyebane			I	2.6
<i>Lespedeza cuneata</i> (Dum. Cours.) G. Don	Fabaceae	Sericea lespedeza			I	2.6
<i>Ulmus davidiana</i> Planch. var. <i>japonica</i> (Rehder) Nakai	Ulmaceae	Japanese elm			I	2.6
<i>Viola mandshurica</i> W. Becker	Violaceae	Violet			II	2.6
<i>Artemisia capillaris</i> Thunb.	Asteraceae	Capillary artemisia	+	+		5.3
<i>Conyza bonariensis</i> (L.) Cronq. * †	Asteraceae	Flax-leaf fleabane	II	+		23.7
<i>Cyperus microiria</i> Steud. † #	Cyperaceae	Asian flatsedge	+	I		10.5
<i>Dactylis glomerata</i> L. *	Poaceae	Orchard grass	r	+		5.3
<i>Digitaria timorensis</i> (Kunth) Balansa †	Poaceae	-----	II	II		26.3
<i>Eraerostis poaeoides</i> Beauv. * †	Poaceae	-----	III	II		21.1
<i>Gnaphalium spicatum</i> Lam. *	Asteraceae	Spiked cudweed	r	I		7.9
<i>Leptochloa chinensis</i> (L.) Nees †	Poaceae	Asian sprangletop	r	+		5.3
<i>Paspalum urvillei</i> Steud. *	Poaceae	Knot grass	+	+		10.5
<i>Persicaria capitata</i> (Buch.-Ham. ex D. Don) H. Gross * #	Polygonaceae	Pink-head knotweed	+	+		5.3
<i>Plantago asiatica</i> L.	Plantaginaceae	Chinese plantain	r	II		15.8
<i>Oenothera laciniosa</i> Hill * †	Onagraceae	Cutleaf eveningprimrose	I	III		10.5
<i>Sambucus chinensis</i> Lindley	Caprifoliaceae	Chinese elderberry	r			7.9
<i>Setaria glauca</i> (L.) Beauv. †	Poaceae	Yellow foxtail	I	II		13.2

Appendix 1 Continued.

Species	Family	Common name	Vegetation types			Occurrence frequency (%)
			V1 (n = 26)	V2 (n = 9)	V3 (n = 3)	
<i>Solanum nigrum</i> L. †	Solanaceae	Black nightshade	r	I		7.9
<i>Zelkova serrata</i> (Thunb.) Makino	Ulmaceae	Japanese zelkova	r	+		5.3
<i>Cleistocleis hackelii</i> (Honda) Honda	Poaceae	-----	I		I	13.2
<i>Erigeron canadensis</i> L. * †	Asteraceae	Canadian horseweed	I		I	13.2
<i>Oxalis corymbosa</i> DC. *	Oxalidaceae	Violet wood-sorrel	+		I	10.5
<i>Zanthoxylum ailanthoides</i> Sieb. et Zucc.	Rutaceae	Japanese prickly-ash	+		I	5.3
<i>Eraerostis ferruinea</i> (Thund.) Beauv.	Poaceae	Korean lovegrass		+	I	5.3
<i>Miscanthus sinensis</i> Anders.	Poaceae	Eulalia		I	II	7.9
<i>Sporobolus fertilis</i> (Steud.) W. Clayton	Poaceae	Giant paramutta grass		+	IV	5.3
pH of soil in curbside cracks; mean ± S.D.			7.5 ± 0.4	7.2 ± 0.6	7.2 ± 0.4	
EC (μS cm ⁻¹) of soil in curbside cracks; mean ± S.D.			162.1 ± 53.6	157.3 ± 65.0	173.0 ± 22.3	

Roman numerals and other symbols for each species indicate SDR classes, defined as follows: r, under 5%; +, under 10%; I, under 20%; II, under 40%; III, under 60%; IV, under 80%; and V, above 80%. $P > 0.05$: ns indicates not significant using an ANOVA. *, non-native species; †, ephemeral species (annual and biennial plants); and #, species emerged from soil [See Table 2]. Highlight; woody species. -----; unknown.

ACKNOWLEDGEMENTS

We sincerely thank Atsuhiro Tanaka, Masaaki Furuno and Hisae Yonao, Ecol. Lab., Kyushu Sangyo Univ., for assistance with the field work.

REFERENCES

- [1] Baba, T., 1999. Identifying woody species by their leaf appearances. Shinano Mainichi Shinbunsha, Nagano. 396 pp. *In Japanese*.
- [2] Braun-Blanquet, J., 1964. Pflanzensozologie. Grundzüge der Vegetationskunde, 3rd ed. Springer-Verlag, Vienna. 865 pp.
- [3] Davis, J.C., 1986. Statistics and data analysis in geology, 2nd ed. John Wiley & Sons, New York. 656 pp.
- [4] Hayasaka, D., Asasaka, M., Miyauchi, D. and Uchida, T., 2011. Classification of roadside weeds along two highways in different climatic zones according to ecomorphological traits. Weed Technol. 25, 411-421.
- [5] Hayasaka, D., Asasaka, M., Miyauchi, D., Elgene, O.B. and Uchida, T., 2012. Qualitative variation in roadside weed vegetation along an urban-rural road gradient. Flora 207, 126-132.
- [6] Horn, H.S., 1966. Measurement of "Overlap" in comparative ecological studies. Am. Nat. 100, 419-424.
- [7] Jantunen, J., Saarinen, K., Valtonen, A., Saarnio, S., 2006. Grassland vegetation along roads differing in size and traffic density. Ann. Bot. Fenn. 43, 107-117.
- [8] Kalwij, J.M., Milton, S.J., McGeoch, M.A., 2008. Road verge as invasion corridors? A spatial hierarchical test in an arid ecosystem. Landscape Ecol. 23, 439-451.
- [9] Kira, T., 1977. A climatological interpretation of Japanese vegetation zones. In: Miyawaki, A. and Tüxen, R. (Eds.), Vegetation science and environmental protection. Maruzen Co., Ltd., Tokyo. pp. 21-30.
- [10] Kowarik, I., 2003. Human agency in biological invasions: secondary releases foster naturalisation and population expansion of alien plant species. Biol. Invasions 5, 293-312.
- [11] Miyawaki, A., Okuda, S. and Fujiwara, R., 1994. Handbook of Japanese vegetation. Shibundo Co., Ltd., Tokyo. 646 pp. *In Japanese*.
- [12] Niemelä, J., 2011. Urban ecology. Oxford University Press Inc., New York. 374 pp.
- [13] Numata, M., 1990. The ecological encyclopedia of wild plants in Japan. Zenkoku Noson Kyoiku Kyokai, Tokyo. 664 pp. *In Japanese*.
- [14] Numata, M. and Yoda, K., 1957. The community structure and succession of artificial grasslands (1). J. Jap. Soc. Herb. Crops Grassl. Farm. 3, 4-11. *In Japanese*.
- [15] Raunkiaer, C., 1934. Life forms of plants and plant geography. Oxford University Press, London. 632 pp.
- [16] Rentch, J.S., Fortney, R.H., Stephenson, S.L., Adams, H.S., Grafton, W.N. and Anderson, J.T., 2005. Vegetation-site relationships of roadside plant communities in West Virginia, USA. J. Appl. Ecol. 42, 129-138.
- [17] Shimizu, T., 2003. Naturalized plants of Japan. Heibonsha Ltd., Publishers, Tokyo. 337 pp. *In Japanese*.
- [18] Suto, Y., Takahashi, Y. and Ogasawara, M., 2006. Summer weed vegetation of road pavement seams in Route 4. J. Weed Sci. Tech. 51, 1-9. *In Japanese*.
- [19] Tiébré, M.-S., Saad, L. and Mahy, G., 2008. Landscape dynamics and habitat selection by the alien invasive *Fallopia* (Polygonaceae) in Belgium. Biodivers. Conserv. 17, 2357-2370.
- [20] Tyser, R.W. and Worley, C.A., 1992. Alien flora in grasslands adjacent to road and trail corridors in Glacier National Park, Montana (USA). Conserv. Biol. 6, 253-262.
- [21] Zar, J.H., 1984. Biostatistical analysis, 2nd ed. Prentice Hall, Englewood Cliffs. 718 pp.

DYE TRACER EXPERIMENTS FOR IDENTIFYING SOLUTE DISPERSIVITY IN UNSATURATED POROUS MEDIA

Kazuya Inoue¹, Takayuki Fujiwara¹ and Tsutomu Tanaka¹

¹Graduate School of Agricultural Science, Kobe University, Japan

ABSTRACT

A methodology using spatial moment analysis linked with image processing of a dye tracer behavior in porous media was applied to identify time-series variation of dispersivities not only in longitudinal but in transverse directions under saturated and unsaturated conditions. Dye tracer experiments were carried out in a two-dimensional and vertically placed water tank with the dimensions of 100 cm width, 100 cm height and 3 cm thickness under saturated and unsaturated flow conditions. An image processing technique based on digitalized spatial distributions of dye tracer allowed to link with a spatial moment approach to identify the temporal change of the longitudinal and transverse dispersivities. Dispersivities exhibited an increasing and decreasing tendency associated with infiltration rates and showed a marked difference between estimates under saturated and unsaturated conditions. Transverse dispersivities under unsaturated conditions were approximately one order larger than those under saturated conditions. This attributed to the effect of air distributions in porous media on the temporal and spatial change of solute dispersion phenomena.

Keywords: Dispersivity, Dye tracer, Unsaturated porous media, Spatial moment, Image analysis

INTRODUCTION

Fertilizers and pesticides have ensured high productivity of agriculture and a quality supply of food in past decades. However, use of fertilizers and pesticides can raise concerns about health risks from residues in food and drinking water such as methemoglobinemia and neurodegenerative disorders like Parkinson [1], [2]. Fast transport of fertilizers and other agrochemicals into subsurface or groundwater systems has been recognized as a serious threat due to high concentration of solutes. Thus, an understanding of solute transport mechanism through not only saturated but unsaturated zones under various hydraulic conditions is important in environmental protection and agricultural activity.

In order to understand and express the transport behavior of contaminants in a subsurface, the transport parameters such as longitudinal and transverse dispersivities are some of the key factors that play an important role in spreading the contaminants. Several studies have been conducted through column experiments with well defined boundary conditions [3]-[5]. In such studies, solute breakthrough curves typically are measured in the column's effluent. They provide integrated and flux-averaged information on the processes governing solute transport in the column. Time domain reflectometry has been also used to determine resident solute concentrations in a nondestructive manner both in the laboratory and in the field [6],[7]. However, this method is restricted to local

measurements while the spatial resolution is therefore limited.

In a nondestructive manner, laboratory scale experiments at different spatial scales have shown that techniques based on image analysis of dye tracer movements could be successfully used to study solute mass transport processes in porous media [8]-[11]. The objectives of this study are to determine the both longitudinal and transverse dispersivities in unsaturated porous media using image analysis linked with spatial moment analysis and to elucidate the nature of dispersion phenomena in unsaturated porous media compared to saturated porous media. A new laboratory flow-tank experiment designed to study this issue is also described in this paper.

DYE TRACER EXPERIMENTS

Materials and Methods

In the experiments, Brilliant Blue FCF is used as a dye tracer which differentiates the tracer evolution visually from the ambient pore water. The initial concentration of the Brilliant Blue FCF dye tracer was set to 1.0 mg/cm³. Although the specific gravity of dye tracer is 1.0001 measured using the specific gravity meter and the initial concentration of tracer is determined to be low enough to avoid density-induced flow effects, there is no denying that the effect of gravity on solute transport. This dye is chosen based on good contrast with soil for

visualizing transport patterns of tracer plume and low toxicity implied by its food dye designation [12].

In this study, as a soil material, silica sand with a low uniformity coefficient of 1.80 was selected in order to reflect a relatively high hydraulic conductivity fields. Silica sand of concern had 0.085cm, 2.68 g/cm³ and 0.751 cm/s of physical properties such as the mean particle size, the particle density and the hydraulic conductivity, respectively. Silica sand was washed and dried at 110 °C before the use to remove organic chemicals attached to the particle surface.

Experimental Procedure under Saturated Conditions

Dye tracer experiments were carried out in a two-dimensional and vertically placed water flow tank with the dimensions of 100 cm width, 100 cm height and 3 cm thickness. The water flow tank allowed to contain soils in order to form transparent quasi two-dimensional solute transport phenomena and consisted of two glass plates with 2 cm thickness. Schematic diagram of experimental apparatus is shown in Fig.1.

Soils were completely washed and saturated before packing to avoid entering air and to conduct experiments under the saturated condition. In the process of creation of flow field, water flow tank was filled with water and silica sand from bottom to top in 5 cm layers to achieve uniform packing. In this process, soil was funneled using an extended funnel. Each layer of interest was compacted prior to filling the next layer, resulting in 0.42 of the porosity. The porosity of each flow field was able to be estimated indirectly from measurements of the particle density and the dry soil bulk density.

After packing, water was applied to the flow tank under a specific hydraulic gradient controlled by constant head water reservoirs at the upstream and downstream sides, while maintaining saturated condition of porous media. A steady saturated flow field was established when fluctuations in the observed drainage rate, which was effluent from the constant head water reservoir, and piezometer readings could become negligible. After reaching steady state flow conditions, dye tracer with the volume of 25 cm³, which made flow paths visible, was uniformly injected along the whole thickness of the flow tank. During the experiment, the profiles of tracer migration were periodically recorded using a digital camera, which located about 100 cm away

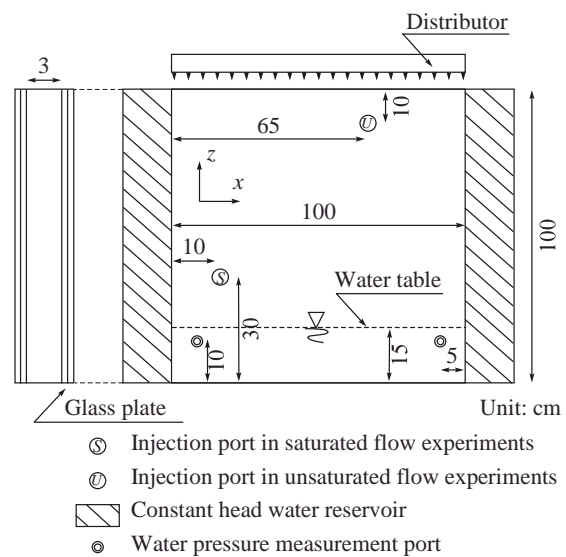


Fig. 1 Schematic drawing of the experimental apparatus used in this study.

from the front face of the water flow tank.

Experimental Procedure under Unsaturated Conditions

Dye tracer experiments under unsaturated conditions were conducted in a similar manner. Internal drainage using constant head reservoirs allowed for approximately one day to create an unsaturated flow field after the flow tank was filled with water and silica sand. Water table was maintained at the 10 cm from the bottom of the water tank. After steady state condition was established, dye tracer with the volume of 25 cm³ was injected in the same manner as saturated experiments. Following that, water was applied using a distributor placed 10 cm above the top of the experimental apparatus, or the ground surface, as shown in Fig.1. Three rainfall rates of 125, 190 and 290 mm/day, were set with no rainfall case. In these experiments, geomembrane was placed on the ground surface to avoid the erosion due to waterdrops.

Spatial Moment Analysis Linked with Image Processing

Each of the pixels representing an image has a pixel intensity which describes how bright that pixel is. In order to establish the relationship between the pixel intensity of a pixel and dye tracer concentration, a calibration was conducted in the same manner reported by Inoue et al. [11]. Under identical experimental conditions, a known

concentration of dye tracer was injected into a corresponding porous formation without a hydraulic gradient. The spread of dye was captured by the digital camera. The same procedure was repeated using different concentrations of dye tracer. Consequently, the concentration of the dye tracer as a function of the pixel intensity varied over the range of 0 mg/cm³ to 1.0 mg/cm³.

A commonly used measure of dilution is the spatial moments of aqueous concentrations, which are calculated from snapshots of tracer plume at given times as follows [13].

$$M_{ij}(t) = \int_{-\infty}^{\infty} \int_{-\infty}^{\infty} c(x, z, t) x^i z^j dx dz, \quad i, j = 1, 2 \quad (1)$$

where x and z are the Cartesian coordinates, c is the solute concentration, t is the time, M_{ij} is the spatial moments associated with the distribution of tracer plume at a certain time, and i and j are the spatial order in the x and z coordinates, respectively.

The pixel intensity distribution can be converted to a concentration distribution by the calibration, providing an analogy between Eq.(1) and Eq.(2).

$$M_{ij}(t) = \int_{-\infty}^{\infty} \int_{-\infty}^{\infty} H(x, z) B(x, z, t) x^i z^j dx dz, \quad i, j = 1, 2 \quad (2)$$

where $H(x, z)$ is the area per unit pixel and $B(x, z, t)$ is the intensity at a corresponding pixel. The centroid of plume concentration distribution is calculated as the normalized first order spatial moment by the following equation.

$$x_c = \frac{M_{10}}{M_{00}}, \quad z_c = \frac{M_{01}}{M_{00}} \quad (3)$$

where x_c and z_c are the centroid locations of plume concentration distribution in the x and z coordinates, respectively. The second order spatial moments are also computed as follows.

$$\sigma_{ij} = \begin{pmatrix} \sigma_{xx} & \sigma_{xz} \\ \sigma_{zx} & \sigma_{zz} \end{pmatrix} = \begin{pmatrix} \frac{M_{20}}{M_{00}} - x_c^2 & \frac{M_{11}}{M_{00}} - x_c z_c \\ \frac{M_{11}}{M_{00}} - z_c x_c & \frac{M_{02}}{M_{00}} - z_c^2 \end{pmatrix} \quad (4)$$

where σ_{ij} is the second order spatial moments.

Longitudinal and transverse dispersivities from spatial moments of the distributed tracer plume are calculated as the following Eqs. (5) and (6) under saturated and unsaturated conditions, respectively [11].

$$\alpha_L = \frac{1}{2} \frac{\sigma_{xx}}{\xi_c}, \quad \alpha_T = \frac{1}{2} \frac{\sigma_{zz}}{\xi_c} \quad (5)$$

$$\alpha_L = \frac{1}{2} \frac{\sigma_{zz}}{\xi_c}, \quad \alpha_T = \frac{1}{2} \frac{\sigma_{xx}}{\xi_c} \quad (6)$$

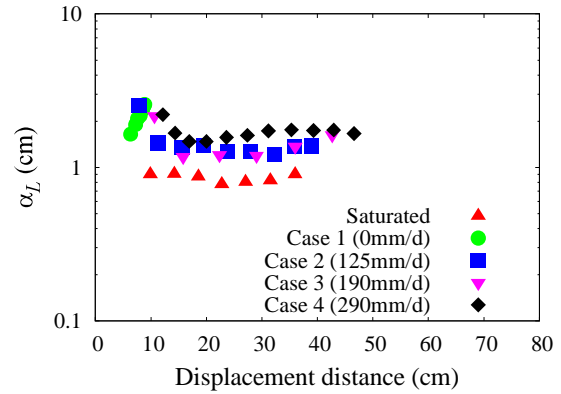


Fig. 2 Results of the longitudinal dispersivity estimates.

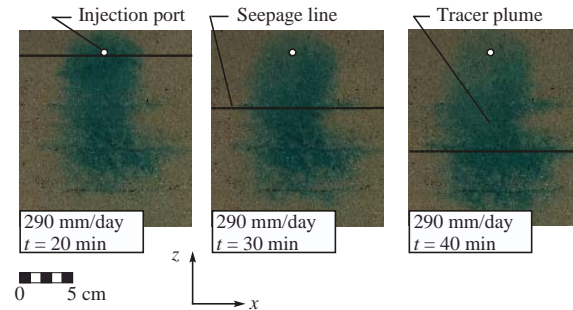


Fig. 3 Representative images of the change of dye tracer distribution.

where α_L is the longitudinal dispersivity, α_T is the transverse dispersivity and ξ_c is the travel distance of the center of tracer plume in the mean flow direction at a given time t .

RESULTS AND DISCUSSION

Longitudinal Dispersivity

The results of longitudinal dispersivity α_L as a function of the displacement distance under saturated and unsaturated conditions are shown in Fig.2. Longitudinal dispersivity estimates under unsaturated conditions are two to four times larger than those under saturated conditions. The increase of the longitudinal dispersivity may be induced from diversity of solute movement due to the effect of air distribution. Several studies have pointed out the same tendency in unsaturated soils [14].

Except for the case without the rainfall intensity and under the saturated flow condition, longitudinal dispersivity estimates also exhibit a rapid decreasing and gradual increasing tendency and show a less dependency on infiltration rates. Water applied to the ground surface infiltrates and reaches an upper

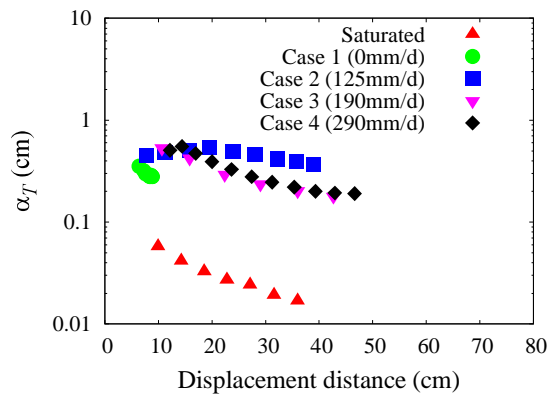


Fig. 4 Results of the transverse dispersivity estimates.

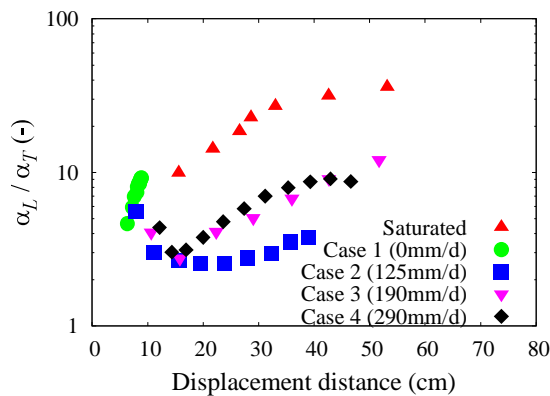


Fig. 5 Results of the ratio of longitudinal to transverse dispersivities.

part of dye tracer. Because flow velocity is larger than solute velocity in unsaturated zone and affects the change of tracer migration patterns, shape of dye tracer distribution is shrunk longitudinally. In Fig.3, representative images of the change of dye tracer distribution are shown with seepage lines, which were visually observed through the experiments. This duration may correspond to the decreasing process of the longitudinal dispersivity due to temporarily shrunk shape of dye distribution. After infiltrating water reaches a front of dye tracer, dye tracer migrates mainly with interstitial water. However, part of dye tracer has relatively low velocities due to the effect of air entrapped within pores. Therefore, shape of dye tracer extends longitudinally, leading to the increase of longitudinal dispersivity estimates. Basically, as solutes move with interstitial water, the intensity of infiltration rates has little effect on the magnitude of the longitudinal dispersivity under the experimental conditions adopted in this study.

Transverse Dispersivity

The results of transverse dispersivity α_T as a function of the displacement distance under saturated and unsaturated conditions are shown in Fig.4. Transverse dispersivity estimates under unsaturated conditions are also larger than those under saturated conditions. Unlike the results of the longitudinal dispersivity, the values of the transverse dispersivity under unsaturated conditions more than ten times larger than those under saturated conditions. Except for the case without the rainfall intensity, transverse dispersivity estimates show a slight increase and a gradual decreasing tendency. It is inferred that transverse solute displacement depends largely on mixing of water and air whose distribution varies with the depth. As aforementioned above, the mobility of part of dye tracer may be extremely low due to the effect of air entrapped within pores. This point leads to larger values of the transverse dispersivity under unsaturated conditions.

On the contrary to the case in longitudinal dispersion phenomena under the unsaturated condition, when water applied to the ground surface reaches an upper part of dye tracer and affects the change of dye tracer distribution, a shape of dye tracer distribution extends horizontally, or laterally. This implies the increase of the transverse dispersivity as well as the decrease of the longitudinal dispersivity.

As a whole, both the longitudinal and transverse dispersivities exhibit a less dependency on infiltration rates. Although the degree of increase of water content induced from rainfall application decreases as rainfall intensity is lower, silica sand employed in this study has a relatively high hydraulic conductivity. Thus, it is inferred that the initial water distribution in the entire domain rather than the rainfall intensity influences the subsequent solute transport pathways.

Ratio of Dispersivity

The results of the ratio of the longitudinal dispersivity α_L to the transverse dispersivity α_T as a function of the displacement distance under saturated and unsaturated conditions are shown in Fig.5. For all cases, the ratio increases with the increase of the displacement distance. This indicates the shape of dye tracer distribution extends longitudinally. Under saturated condition, initial shape of dye tracer and its geometric shape strongly affect the initial value of the transverse dispersivity [11], which is relatively larger value than an inherent transverse dispersivity, or microdispersivity. According to the dye migration, the transverse dispersivity approaches to an asymptotic value. Therefore, the transverse dispersivity in Fig.4 shows

Table 1 Comparison of dispersivities with other experimental results.

Longitudinal dispersivity (cm)	Transverse dispersivity (cm)	Displacement distance (cm)	Condition of water content	Reference
0.78 – 0.82	0.020 – 0.060	5 – 50	Saturated	This study
0.025 – 0.10	0.005 – 0.018	35 – 60	Saturated	Inoue et al. [15]
0.522 – 0.756	–	30.2	Saturated	Maraqa et al. [16]
–	0.000039 – 0.013	30	Saturated	Robbins [17]
1.0 – 2.6	0.25 – 0.60	5 – 50	Unsaturated	This study
–	0.0029	30	Unsaturated	Massabò et al. [18]
1.02 – 1.67	0.320 – 0.577	5 – 25	Unsaturated	Inoue et al. [19]
2.6 – 18.3	0.03 – 2.20	6 - 14	Unsaturated	Abbasi et al. [20]
0.966 – 1.631	–	30.2	Unsaturated	Maraqa et al. [16]

an increasing tendency. On the other hand, the results under unsaturated conditions reflect the change of the degree of solute dispersion both in longitudinal and lateral directions.

Comparison with Other Studies

In order to confirm the accuracy of identified parameters, Table 1 compares the longitudinal and transverse dispersivities identified in this study with flow tank results reported in the literature that were conducted in a similar displacement distance. The results obtained in this study are in good agreement with other experimental results, although it seems that the maximum value of the longitudinal dispersivity is a slight larger value. This is probably because pulse input of dye tracer effects on the temporal change of the magnitude of the flow velocity during the short time period at the beginning of the experiments, leading to an overestimate of the longitudinal dispersivity.

CONCLUSION

In the present study, dye tracer experiments under saturated and unsaturated flow conditions have been conducted for homogeneous flow field filled with silica sand in order to investigate transport characteristics. Spatial moment approach linked with image analysis has applied to the estimation of not only the longitudinal dispersivity but also the transverse dispersivity in porous media. Experimental results revealed that transport parameters depend strongly on the water content where solute passes through, leading to the larger estimates under unsaturated conditions than those

under saturated conditions. These estimation values agree with experimental results in the literature, indicating that employed methodology is useful to identify these transport parameters.

ACKNOWLEDGEMENTS

The work reported here was supported by JSPS Grant-in-Aid for Young Scientists (B).

REFERENCES

- [1] Knobeloch L, Salna B, Hogan A, Postle J, Anderson H, "Blue babies and nitrate-contaminated well water", *Environmental Health Perspectives*, Vol.108(7), 2000, pp. 675–678.
- [2] Mostafalou S, Abdollahi M, "Pesticides and human chronic diseases: Evidences, mechanisms, and perspectives", *Toxicology and Applied Pharmacology*, Vol.268(2), 2013, pp.157–177.
- [3] Matsubayashi U, Devkota LP, Takagi F, "Characteristics of the dispersion coefficient in miscible displacement through a glass bead medium", *Journal of Hydrology*, Vol.192, 1997, pp. 51–64.
- [4] Vanderborght J, Vanclooster M, Timmerman A, Seuntjens P, Mallants D, Kim D-J, Jacques D, Hubrechts L, Gonzalez C, Feyen J, Diels J, Deckers J, "Overview of inert tracer experiments in key belgian soil types: Relation between transport and soil morphological and hydraulic properties", *Water Resources Research*, Vol.37(12), 2001, pp.2783–2888.

- [5] Javaux M, Vanderborght J, Kasteel R, Vanclooster M, "Three-dimensional modeling of the scale- and flow rate-dependency of dispersion in a heterogeneous unsaturated sandy monolith", *Vadose Zone Journal*, Vol.5, 2006, pp.515–528.
- [6] Vanclooster M, Mallants D, Vanderborght J, Diels J, Van Orshoven J, Feyen, J, "Monitoring solute transport in a multi-layered sandy lysimeter using time domain reflectometry", *Soil Science Society of America Journal*, Vol.59, 1995, pp. 337–344.
- [7] Weihermuller L, Kasteel R, Vanderborght J, Putz T, Vereecken H, "Soil water extraction with a suction cap: Results of numerical simulations", *Vadose Zone Journal*, Vol.4, 2005, pp.899–907.
- [8] Jia C, Shing K, Yortsos YC, "Visualization and simulation of non-aqueous phase liquids solubilization in pore networks", *Journal of Contaminant Hydrology*, Vol.35(4), 1999, pp.363–387.
- [9] Huang W, Smith CC, Lerner DN, Thornton SF, Oram A, "Physical modeling of solute transport in porous media: evaluation of an imaging technique using UV excited fluorescent dye", *Water Research*, Vol.36(7), 2002, pp.1843–1853.
- [10] Jones EH, Smith CC, "Non-equilibrium partitioning tracer transport in porous media: 2-D physical modeling and imaging using a partitioning fluorescent dye", *Water Research*, Vol.39(20), 2005, pp.5099–5111.
- [11] Inoue K, Takenouti R, Kobayashi A, Suzuki K, Tanaka T, "Assessment of a UV excited fluorescent dye technique for estimating solute dispersion in porous media", *Journal of Rainwater Catchment Systems*, Vol.17(1), 2011, pp.1–9.
- [12] Flury M. and Flühler H., "Tracer characteristics of Brilliant Blue FCF", *Soil Science Society of America Journal*, Vol.59(1), 1995, pp.22-27.
- [13] Freyberg DL, "A natural gradient experiment on solute transport in a sand aquifer 2. Spatial moments and the advection and dispersion of nonreactive tracers", *Water Resources Research*, Vol.22(13), 1986, pp.2031–2046.
- [14] Vanderborght J, Vereecken H, "Review of dispersivities for transport modeling in soils", *Vadose Zone Journal*, Vol.6, 2007, pp.29-52.
- [15] Inoue K, Kobayashi A, Matsunaga N, Tanaka T, "Application of particle tracking method to dispersivity identification and its experimental verification", *Journal of Rainwater Catchment Systems*, Vol.13(2), 2008, pp.7-16.
- [16] Maraqa MA, Wallace RB, Voice TC, "Effects of degree of water saturation on dispersivity and immobile water in sandy soil columns", *Journal of Contaminant Hydrology*, Vol.25, 1997, pp.199-218.
- [17] Robbins GA, "Methods for determining transverse dispersion coefficient of porous media in laboratory column experiments", *Water Resources Research*, Vol.25(6), 1989, pp.1249-1258.
- [18] Massabò M, Catania F, Paladino O, "A new method for laboratory estimation of the transverse dispersion coefficient", *Ground Water*, Vol.45(3), 2007, pp.339-347.
- [19] Inoue K, Setsune N, Suzuki, F, Tanaka T, "Determining transport parameters for unsaturated porous media in flow-tank experiments using image analysis", *Water Pollution VIII Modelling, Monitoring and Management*, WIT Press, 2006, pp.309–319.
- [20] Abbasi F, Simunek J, Feyen J, van Genuchten MTh, Shouse PJ, "Simultaneous inverse estimation of soil hydraulic and solute transport parameters from transient field experiments: homogeneous soil", *Transactions of the ASAE*, Vol.46(4), 2003, pp.1085–1095.

REUSE OF AGRICULTURAL AND FOOD RESIDUES FOR RETARDING AND ATTENUATING NITRATE IN POROUS MEDIA

Kazuya Inoue¹, Saki Matsuyama¹ and Tsutomu Tanaka¹

¹Graduate School of Agricultural Science, Kobe University, Japan

ABSTRACT

Nitrate pollution in groundwater is related to surplus nitrate fertilizers and animal waste disposal. As high nitrate concentration leads to health concern, mass reduction of nitrate in a contaminated site is important. From the perspective of recent reuse streams, this paper assessed the potential of agricultural and food residues such as rice husk, rice straw and used coffee as a nitrate attenuation material in porous media. Under saturated flow conditions, column experiments were carried out in silica sand with a mixture of residues. KNO₃ or NaCl solutions were injected into columns and were analyzed using temporal moment approaches to characterize the mobility of nitrate and chloride ions. The results showed that the mixture of rice straw leads to the increase of the retardation factor. The results also revealed that the use of rice husk and used coffee decreases the mass of both anions, whereas the rice straw has little effect on attenuation of these anions.

Keywords: Nitrate, Agricultural and food residues, Reuse, Column experiments, Attenuation

INTRODUCTION

Man-made nitrogen fertilizers became widely used not only in Japan and the United States but also around the world, providing an inexpensive source of nitrogen and other plant nutrients that resulted in huge increases in agricultural productivity. In the past century, the global nitrogen cycle has been increasingly affected by nitrogen fixation for agricultural activities, which now exceeds the amount that occurs naturally. Both groundwater and surface water can be contaminated by excess nitrate as a result of agricultural activities. Human exposure to nitrate and nitrite is mainly from the ingestion of food and drinking water [1]. Therefore, public water utilities are required to maintain nitrate levels below a Maximum Contaminant Level of 10 mg/L nitrate-nitrogen that was instituted to protect against methemoglobinemia, to which infants are especially susceptible. In addition to methemoglobinemia, a range of other health effects have been associated with ingesting nitrate-contaminated drinking water, including various cancers, neural tube defects and thyroid conditions [2],[3].

In associated with agricultural activities, large amounts of agricultural wastes are discharged, for example, from the harvesting of rice, instant coffee manufacture and field preparation [4]. Rice husk and rice straw are the main agro-industrial residues from the rice milling industry. Coffee is also one of the largest agricultural products that are mainly used for beverages. According to the U.S. department of Agriculture, the world's coffee production in 2012/13 is forecast at a record 151 million bags, up

almost 7 million from the previous year [5] and large amount of spent coffee grounds are discharged. Although part of them as well as rice husk and rice straw is reused as compost or biodiesel [6], most of these are burned as a waste, which results in production of carbon dioxide, the green house gas. Thus, it is necessary to develop new technologies enabling to reuse agricultural residues for useful purposes.

This paper assessed the potential application of agricultural residues including rice husk, rice straw and spent coffee grounds for retarding and attenuating nitrate in porous media. Some quantity factors such as the dispersivity, the retardation factor, the mass recovery fraction and the degradation rate constant were identified using temporal moment approaches based on a time series of leachate concentration of nitrate or chloride ions. Additionally, quantity parameters for assessing the potential use of agricultural residues were also discussed.

MATERIALS AND METHODS

Materials

In this study, as a soil material, silica sand with a low uniformity coefficient of 1.25 was selected in order to reflect a relatively high hydraulic conductivity fields. Silica sand of interest had 0.050mm, 2.68 g/cm³ and 0.11 cm/s of physical properties such as the mean particle size, the particle density and the hydraulic conductivity, respectively. Since silica sand was washed and dried at 110 °C

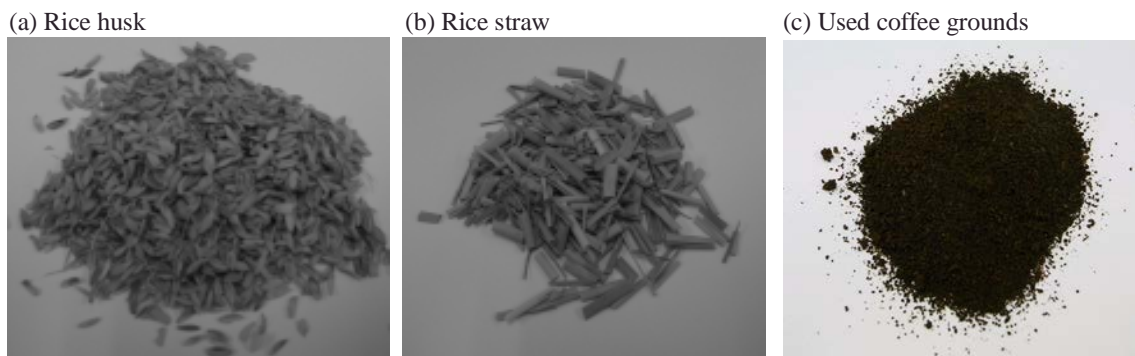


Fig. 1 Images of agricultural residues and food residue used in column experiments: (a) rice husk, (b) rice straw and (c) used coffee grounds.

Table 1 Physical properties of agricultural and food residues mixed with silica sand.

Residues	Weight ratio (%)	Porosity (-)	Hydraulic conductivity (cm/s)
Rice husk	0.95 – 2.6	0.44 – 0.47	0.10 – 0.11
Rice straw	1.0 – 2.2	0.45 – 0.46	0.053 – 0.11
Used coffee	2.3 – 8.9	0.46 – 0.56	0.070 – 0.10

repeatedly, there were no microbes onto the soil surface.

In this study, two types of agricultural residues such as rice husk and rice straw were employed, which were taken from the paddy field after the harvest. In addition, Lion Coffee's "Hawaii coffee" used coffee grounds were used throughout as one food residue in order to compare the degree of nitrate attenuation among agricultural residues. Images of these residues are shown in Fig.1. As shown Fig.1, the length of artificially chopped rice straw was adjusted in approximately 5 mm length. All residues were dried at 110 °C before column experiments.

Column Experiments

Column experiments under the saturated condition were carried out at room temperature (18 ± 2 °C) under an air atmosphere. The soil columns were constructed of acrylic cylinders having 5 cm of inner diameter and 30 cm length and also had filter meshes attached to the top and bottom.

In column experiments, the weight ratios of rice husk, rice straw and used coffee to the total weight of silica sand were varied in order to examine the effect of the amount of residues on the degree of nitrate transfer. From the practical viewpoint, the weight of silica sand equivalent to the column height

of 1.5 cm, 2.1 cm and 3.4 cm was replaced with residues of concern. These soils with one of the residues were completely saturated with deionized water before packing to avoid the entrance of air and were filled into the column in increments of 2.5 cm, homogeneously. Each layer was compacted with a rammer to adjust the porosity prior to packing the next layer. In Table 1, physical properties of each residue mixed with silica sand are listed. The porosity was estimated in each experiment indirectly from the measurements of the total weight of residue and silica sand filled in the column. The hydraulic conductivity was measured using the discharge rate of water from the column under a hydraulic gradient and the sectional area of the column.

After packing, deionized water was applied to the column up to a specific level controlled by constant head reservoirs at the top and bottom of the saturated media, while maintaining the saturated condition of porous media. Steady saturated flow field was established in the column when fluctuations in the observed drainage rate from the bottom reservoir became negligible. A volume of 40cm³ of KNO₃ solution or NaCl solution was applied to produce a pulse input with an initial concentration of 1.5×10^{-4} g/cm³ of NO₃-N or NaCl.

Despite of the condition of the weight ratio of residues, pore water velocities were set to approximately 0.012 cm/s under the control of the

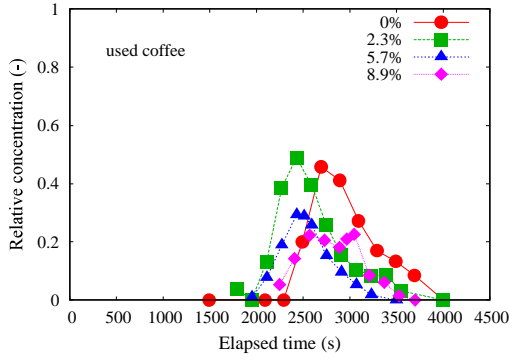


Fig.2 Representative BTCs for nitrate ion in used coffee columns

hydraulic gradient. Pore water samples at the end of the column were taken at specific intervals using a fraction collector to measure experimental breakthrough curves (BTCs). Nitrate ion in the pore water samples was analyzed by capillary electrophoresis (G1600A, Agilent technologies, USA). The basic anion buffer and a fused silica capillary with 104 cm in length and 5 cm internal diameter were obtained from Agilent technologies. The temperature-controlled cartridge for fused silica was set at 15 °C. On the other hand, electrical sensors were used to measure the voltage readings of electrical sensors using a calibrated relationship between the specific concentration of NaCl solution and the corresponding voltage via a data logger.

PARAMETER ESTIMATION

Consider a sorbing and degradable chemical moving through a homogeneous medium at a steady, uniform, flow rate. Assuming linear, equilibrium sorption and first-order kinetic degradation for the solute, the governing transport equation can be written as :

$$R \frac{\partial c}{\partial t} = \alpha v \frac{\partial^2 c}{\partial x^2} - v \frac{\partial c}{\partial x} - \lambda c \quad (1)$$

where c is the concentration of solute, x is the coordinate, t is the time, R is the retardation factor estimate, v is the average pore water velocity, α is the dispersivity, and λ is the degradation rate constant [7].

Temporal moment analysis is a useful approach to characterize experimental BTCs without solving solute transport model [8]. The normalized temporal moment μ_n at a location x , is defined as :

$$\mu_n = \frac{\int_0^\infty t^n c(x,t) dt}{\int_0^\infty c(x,t) dt} \quad (2)$$

In this study, the dispersivity, the degradation rate, the mass recovery fraction and the retardation factor were identified using temporal moment approaches based on a BTCs of nitrate or chloride ions as quantity factors reflecting the effect of agricultural and food residues. Representative BTCs as a function of the elapsed time for nitrate ion under different weight ratios of mixed used coffee are shown in Fig.2.

The dispersivity from temporal moments was calculated as [8] :

$$\alpha_L = \frac{\xi_p}{2} \frac{\mu_2}{\mu_1^2} \quad (3)$$

where ξ_p is the distance between the source and the observation location. The retardation factor was expressed as [9] :

$$R = \frac{(\mu_1 - 0.5t_0) \sqrt{v_p^2 + 4\alpha_L v_p \lambda}}{x} \quad (4)$$

where t_0 is the pulse duration. In all experiments, t_0 was set to 30 seconds to reflect the injection situation of solute.

The mass fraction of solute was used to estimate the mass recovery fraction (MRF) [7] :

$$MRF = \frac{\int_0^\infty Q(L,t)c(L,t)dt}{\int_0^\infty Q(0,t)c(0,t)dt} \quad (5)$$

where Q is the volumetric flow rate and H is the length of the soil column. The degradation rate constant was also calculated by [6] :

$$\lambda = \frac{1}{\mu_1} \ln \left(\frac{1}{MRF} \right) \quad (6)$$

Prescribed solute source conditions in column experiments was designed to clarify the transient concentrations of nitrate and chloride ions and to effectively provide the parameter identification relevant to solute transport using temporal moment approaches.

RESULTS AND DISCUSSION

Solute Dispersivity

From the practical viewpoint, larger dispersion of solute is the consequence of significant mixing or dilution in field. The dispersivity is one of the solute

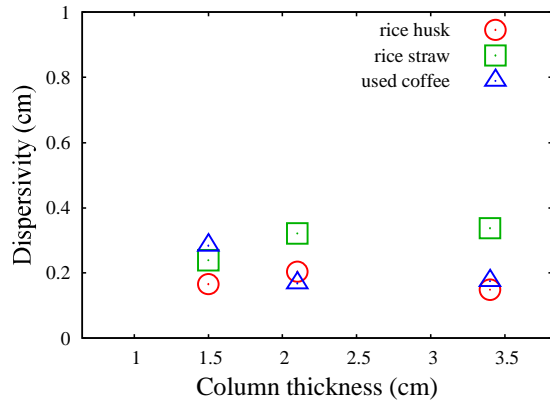


Fig. 3 Relation between the column thickness of residues and the dispersivity for nitrate ion

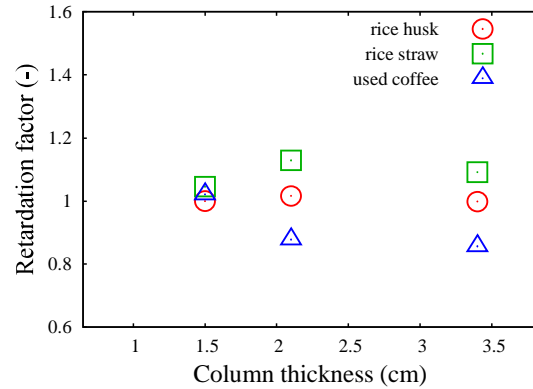


Fig.5 Relation between the column thickness of residues and the retardation factor for nitrate ion.

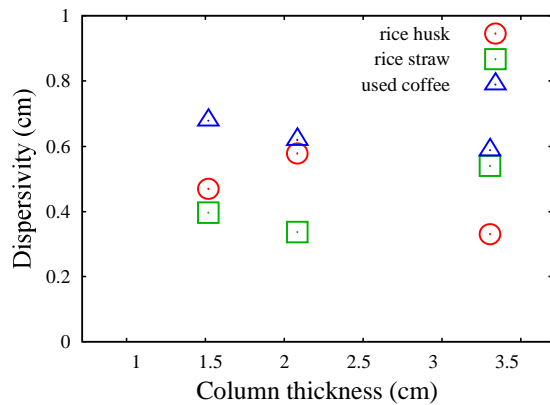


Fig. 4 Relation between the column thickness of residues and the dispersivity for chloride ion

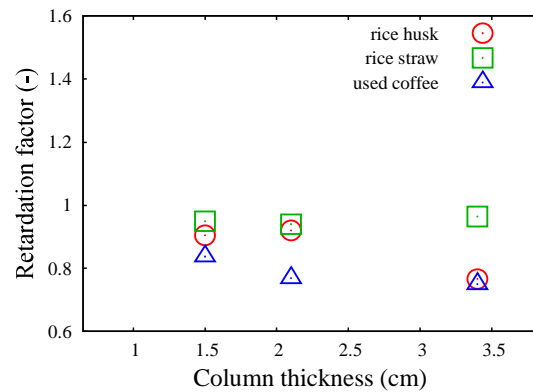


Fig. 6 Relation between the column thickness of residues and the retardation factor for chloride ion.

transport parameters that characterizes solute dispersion in porous media [10]. The results of the dispersivities in rice husk, rice straw and used coffee, which were identified based on Eq.(3), in nitrate and chloride ions are shown in Figs. 3 and 4, respectively, as a function of column thickness of each residue. In the column having only silica sand, the values of the dispersivity for nitrate and chloride are 0.16 cm and 0.32 cm, respectively. The mixture of rice husk and rice straw provides an increase tendency of the dispersivity for nitrate ion, while the opposite tendency is shown in used coffee as well as chloride ion. The dispersivity in nitrate ion exhibits lower values than that in chloride ion. This feature reflects that each anion has its own degree of solute spread with respect to mixed agricultural and food residues. The difference of the dispersivity between the anions or the agricultural residues may appear in the outcome of the retardation factor.

Retardation of Solutes

In order to quantify the degree of the variation of

anion mobility, the retardation factor was employed as a measure and estimated using Eq.(4). The relation between the column thickness of residues and the retardation factor for all residues are shown in Figs.5 and 6, in terms of nitrate and chloride ions, respectively. As seen in Fig.5, the retardation factor in rice husk remains constant value of about 1.0 despite of the mixture of rice husk. This means that no retardation or no sorption occur in porous formations. The retardation factor in rice straw becomes slightly larger than the value of 1.0, indicating that the mobility of nitrate ion decreases during the transport in porous formations. Therefore, from a viewpoint related to the application of rice straw in a field, it is expected that nitrate decomposition by microbes may occur and contribute to the reduction of nitrogen mass in porous media during a transport with retarded velocity.

On the other hand, the results of the nitrate mobility exhibit below the unity in used coffee grounds. This implies the solute transport velocity becomes larger than the seepage velocity in columns

filled with used coffee grounds. On average, the used coffee grounds contain up to 15% oil, although the amount of oil in the coffee source depends on its types [11]. It is inferred that surface hydrophobicity of used coffee provides the increase of the velocity of nitrate and results in the lower values of the retardation factor. Rice husk also has the surface hydrophobicity and may affect the variation of the retardation factor in chloride ion. As a whole, the degree of retardation in nitrate ion is larger than that in chloride ion, indicating that the mobility of chloride ion is higher than that in nitrate ion. At a microscopic level, it is likely that the degree of reaction between the anion and the surface of residues is substantially different.

Mass Recovery Fraction and Degradation of Solutes

The change of mass balance is of interest and of significance during a course of transport associated with the mixture of agricultural and food residues. As another quantity of anion transfer, Table 2 summarizes the results of the mass recovery fraction (*MRF*) and the degradation rate (λ), which were estimated from Eqs. (5) and (6), respectively. Results in rice straw are not listed, since *MRF* and the degradation rate became 1 and 0 in all experimental cases.

As shown in Table 2, in all experimental cases, values of *MRF* are less than 1 and the corresponding degradation rate appears as non-zero values. In Table 2, up to 44% and 56% attenuation of the total mass in nitrate can be seen in nitrate and chloride ions, respectively. This implies that part of nitrate or chloride ions may be strongly adsorbed onto the surface of rice husk or used coffee and may be trapped within pores. This is because rice husk and used coffee have a relatively high surface area [12].

From a practical viewpoint, the degradation of solute mass in a cropland is expected to attenuate the impact on water quality in soils as well as in groundwater. Therefore, the use of agricultural and food residues in soils has a potential to the attenuation of nitrate and chloride ions.

CONCLUSIONS

In this study, the reuse of agricultural and food residues in order to retard and attenuate the impact of nitrate or chloride ions in porous media was assessed through column experiments under saturated flow conditions. Temporal moments associated with observed breakthrough curves were used to quantify the dispersivity, the retardation factor, the mass recovery fraction and the degradation rate. The increase of the mixture of rice husk and rice straw resulted in the slight increase of the dispersivity, while the opposite tendency was shown in used coffee columns. Remarkably, the mobility of anions showed the increase tendency in used coffee columns. Moreover, rice husk and used coffee were found to have a property to decrease the mass balance in both anions. These findings may be attributed to the nature of nitrate and chloride ions having its own degree of solute spread associated with mixed residues.

ACKNOWLEDGEMENTS

The work reported here was supported by JSPS Grant-in-Aid for Young Scientists (B).

REFERENCES

- [1] Bryan N, Alexander DD, Coughlin JR, Milkowski AL, Boffetta P, "Ingested nitrate and nitrite and stomach cancer risk: An updated

Table 2 Results of the mass recovery fraction and the degradation rate.

Column thickness (cm)	<u>Nitrate ion</u>		<u>Chloride ion</u>	
	<i>MRF</i> (-)	λ (hr ⁻¹)	<i>MRF</i> (-)	λ (hr ⁻¹)
<i>Rice husk</i>				
1.5	0.77	0.43	0.44	1.6
2.1	0.95	0.072	0.71	0.50
3.4	0.73	0.50	0.44	1.7
<i>Used coffee</i>				
1.5	1.0	0.	0.53	1.0
2.1	0.59	0.76	0.59	0.86
3.4	0.56	0.76	0.61	0.65

- review", Food and Chemical Toxicology, Vol.50, 2012, pp.3646-3665.
- [2] Grosse Y, Baan R, Straif K, Secretan B, El Ghissassi F, Coglian V, "Carcinogenicity of nitrate, nitrite, and cyanobacterial peptide toxins", The Lancet Oncology, Vol.7(8), 2006, pp.628-629.
- [3] Tsugane S, "Salt, salted food intake, and risk of gastric cancer: epidemiologic evidence", Cancer Science, Vol.96(1-6), 2005, pp.1-6.
- [4] Safarik I, Horska K, Svobodova B, Safarikova M, "Magnetically modified spent coffee grounds for dyes removal", European Food Research Technology, Vol.234, 2012, pp.345-350.
- [5] U.S. Department of Agriculture, Coffee: World markets and trade, 2012.
- [6] Kondamudi N, Mohapatra SK, Misra M, "Spent coffee grounds as a versatile source of green energy", Journal of Agricultural Food Chemistry, Vol.56, 2008, pp.11757-11760.
- [7] Das BS and Kluitenberg GJ, "Moment analysis to estimate degradation rate constants from leaching experiments", Soil Science Society of America Journal, Vol.60, 1996, pp.1724-1731.
- [8] Valocchi AJ, "Validity of the local equilibrium assumption for modeling sorbing solute transport through homogeneous soils", Water Resources Research, Vol.21(6), 1985, pp.808-820.
- [9] Pang L, Goltz M and Close M, "Application of the method of temporal moments to interpret solute transport with sorption and the degradation", Journal of Contaminant Hydrology, Vol.60(1-2), 2003, pp.123-134.
- [10] Fetter CW, Contaminant Hydrology 2nd edition : Prentice Hall, 1998.
- [11] Daglia M, Racchi M, Papetti A, Lanni C, Govoni S, Gazzani G, "In vitro and ex vivo antihydroxyl radical activity of green and roasted coffee", Journal of Agricultural Food Chemistry, Vol.52(6), 2004, pp.1700-1704.
- [12] Kaupp A, "Gasification of Rice Hulls: Theory and Practices", Deutsches Zentrum Fuer Entwicklungs Technologien (German Appropriate Technology Exchange, GATE), Eschborn, Germany, 1984.

MICROSCOPIC RANGE OF IMMOBILIZATION BETWEEN HEAVY METALS AND AMENDMENT IN SOIL THROUGH WATER MIGRATION

Shouhei Ogawa¹, Masahiko Katoh² and Takeshi Sato³

¹ Graduate School of Engineering, Gifu University, Japan; ^{2,3} Faculty of Engineering, Gifu University, Japan

ABSTRACT

In order to identify the microscopic range of immobilization in soil, the pot test was conducted to evaluate the distance that lead (Pb) and antimony (Sb) transport through water migration and the transport phases during immobilization. The amount of amendment required to immobilize Pb and Sb was investigated on the basis of the microscopic range of immobilization. The results clearly showed that Pb and Sb were transported a maximum of 5 mm and 6 mm, respectively, through water migration which corresponded to precipitation for one month. Both metals were accumulated 1 mm from contaminated soil. The primary Pb transport phase was sorbed on Fe/Mn oxide, while that of Sb was water-soluble. The amount of amendment required for Pb and Sb immobilization was estimated to be 4.62% (w/w) from the microscopic range of immobilization (1 mm).

Keywords: Amendment ratio, Antimony, Immobilization, Lead, Water migration

INTRODUCTION

Removing heavy metals, which are highly persistent in soil, is difficult compared to other contaminants, such as oil and volatile organic compounds that readily decompose in soil [1]. Therefore, soil remediation techniques, including excavation and transportation to landfill sites, that can easily reduce risk are often applied to heavy-metal-contaminated soil. However, in addition to construction costs, excavation and transportation to landfills incur conveyance and management costs, which in all probability would lead to an increase in total cost [2].

Chemical immobilization is one of the most economical in situ techniques because the soil can be reused at the site after treatment [3]. The addition of an immobilization amendment to the soil can transform a heavy metal into chemically stable phases and thus reduce solubility, which prevents leaching of heavy metal into groundwater. In this context, immobilization has been investigated for lead (Pb-) and antimony (Sb-) contaminated soil from a shooting range, where contamination is more extensive and asset value is very low [4], [5]. Pb can be immobilized by an apatite, precipitating Pb phosphate minerals, such as pyromorphite [6], and Sb can be immobilized by an iron compound, particularly iron hydroxide, forming surface complexation [7]. However, if the amount of the amendment is not sufficient to immobilize Pb and Sb completely, the treatment can potentially lead to Pb and Sb redissolving in the soil [7].

The required amount of immobilization amendment in the soil is calculated on the basis of

the amendment's maximum sorption capacity estimated by a sorption experiment in solution [8]. However, Pb and Sb would be unstable in the soil unless stable phases are formed, even though the amount of amendment is sufficient to immobilize them. This is because heavy metal transport through water migration, and subsequent contact and reaction with the immobilization amendment, would be essential before the stable phases are formed. Thus, to calculate the required amount of immobilization amendment, it is necessary to identify the microscopic range of Pb and Sb immobilization, i.e., the transport distance of Pb and Sb through water migration during the period of immobilization.

Heavy metals in soil particles would be transported through water migration, repeating various processes, such as ion exchange, precipitation and dissolution, sorption and desorption to soil minerals and organic matters, and colloidal transportation [9], [10]. In addition, heavy metal phases would be altered during transportation. Therefore, to identify the microscopic range of Pb and Sb immobilization, Pb and Sb phases during transport should be taken into consideration.

As stated above, elucidation of the microscopic range of Pb and Sb immobilization during the immobilization period is also necessary to calculate the amount of amendment required for reliable immobilization. However, the required amount of immobilization amendment has not been evaluated in relation to the microscopic range of Pb and Sb immobilization, although heavy metal transport in the soil has been well investigated [10] – [13].

The present study represented Pb and Sb

microscopic transport through water migration in soil from a shooting range by using a compartmentalized pot to represent water flow in unsaturated soil. The objective of this study was to evaluate the distance of Pb and Sb transport and transport phases during the immobilization period, and to identify the microscopic range of their immobilization in the soil. In addition, the required amount of immobilization amendment was investigated on the basis of the microscopic range of immobilization.

MATERIALS AND METHODS

Study Area

This study was conducted using soil from a shooting range located at 35° 28' 6" N and 137° 29' 2" E in Tajimi, Gifu Prefecture, Japan. The mean annual precipitation and temperature at the shooting range are 2200 mm and 14 °C, respectively.

Soil Preparation and Characterization

The Pb- and Sb-contaminated soil was collected from depths of 5–15 cm. The contaminated soil sample was air-dried, passed through a 2 mm sieve, and used for chemical analysis and the water migration experiment. Table 1 shows the physicochemical properties of the soil samples. Total Pb and Sb content of the contaminated soil was 19700 and 261 mg/kg, respectively. The water-

soluble Pb of the contaminated soil was 95.7 mg/kg, which is 1000 times greater than the standard (0.1 mg/kg) for soil in Japan. The physicochemical properties of non-contaminated soil collected outside the contaminated site were similar to those of the contaminated soil, except for Pb and Sb. The non-contaminated soil was passed through a 1 mm sieve prior to the water migration experiment. Commercial Andosol was used as cultivation soil.

Materials Preparation and Characterization

Apatite and iron hydroxide were used as Pb and Sb immobilization amendments, respectively. The apatite was synthesized from gypsum and diammonium hydrogen phosphate [14]. Apatite can immobilize Pb in soil through the precipitation of Pb phosphate minerals such as pyromorphite. The iron hydroxide was synthesized from iron nitrate hydrate [15]. Iron hydroxide can immobilize Sb in soil through the formation of an inner-sphere complex. Both amendments were passed through a 0.425 mm sieve, and equal amounts were well mixed prior to use. Table 1 shows the physicochemical properties of the amendments.

Water Migration Experiment

Figure 1 is a schematic of the experiment. The experimental pot was comprised of four layered compartments: contamination, non-contamination, amendment, and plant compartments (CC, NCC, AC, PC).

Table 1 Physicochemical properties of the soil and immobilization amendment

Soils and Immobilization amendment	pH _(H₂O)	Particles density [g/cm ³]	Total						Water-soluble	
			C	Fe	Ca	P	Pb	Sb	Pb	Sb
			[mg/kg]							
Contaminated soil	7.18	2.62	51000	33700	7570	386	19700	261	95.7	7.6
Non-contaminated soil	6.06	N.A.*	14300	25500	1390	39.3	11.3	1.7	0.1 >	0.1 >
Cultivation soil	5.56	N.A.	71200	40100	5650	1710	58.3	5.8	0.1 >	0.1 >
Immobilization amendment	7.70	3.29	N.A.	254000	181000	45500	14.8	3.5	0.1 >	0.1 >

* : Not Analyzed

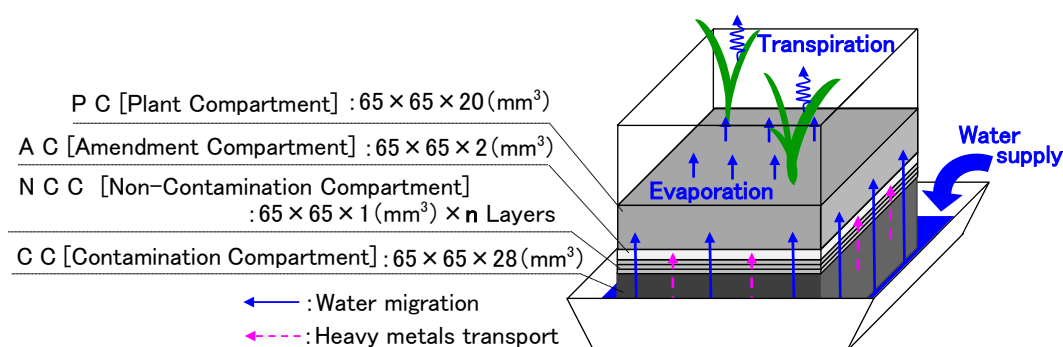


Fig. 1 Water migration schematic

and PC, respectively). NCC was composed of five or ten 1-mm-thick layers (5 mm NC-Pot and 10 mm NC-Pot, respectively). Then, 107.50, 4.68, 8.60, and 100.00 g of contaminated soil, non-contaminated soil, amendment, and cultivation soil, respectively, were added to each layer. The layers were separated using a 25- μ m nylon mesh. Ultra-pure water was added to maintain 50% of the water-holding capacity of each soil or amendment. After adding 5 mL of solution containing nitrogen, phosphorus, and potassium as fertilizer at 10 mg/kg to the PC, two Guinea grass (*Panicum maximum* J.) plants were grown in the compartment. Guinea grass can tolerate Pb toxicity. The plants were grown at room temperature (25 °C). This experimental design represented water flow in unsaturated soil. The bottom of the pot had 25 holes with a diameter of 5 mm. The plants were watered the amount corresponding to the lost weight of pot from the last water supply from the bottom at 2 or 3 times a week (Fig. 1). The total water supply was 170 mm, which corresponded to precipitation for one month at the shooting range site. The period of immobilization was defined as one month. After the experiment, the NCC soil samples were collected, air-dried, and passed through a 2 or 0.425 mm sieve.

Methodology

The pH value of the soil sample was measured in ultrapure water using a pH meter (MM-60R, DKK-TOA Co., Japan). The total carbon (C) content of the soil sample was determined using an NC analyzer (MT-6, Yanaco New Science Inc., Japan). The water-soluble Pb and Sb in the soil was extracted using ultra-pure water (1:10 soil:solution ratio). The total Pb, Sb, calcium (Ca), iron (Fe), and phosphorus (P) content of the soil was determined by acid digestion with 14.5 M HNO₃ and 12 M HCl using a microwave. Sequential extraction was performed on the soil sample following the procedure described in [16]. Then, 1.0 g of soil that had been passed through a 0.425 mm sieve was extracted with 25 mL of a 1 M MgCl₂ solution (exchangeable). The soil remaining after the first extraction procedure was extracted with 25 mL of a 1 M sodium acetate solution with pH 5 (carbonate). The soil remaining after the second extraction was further extracted with 20 mL of 0.04 M NH₂OH-HCl in 25% (v/v) HOAc in a 95 °C water bath with occasional agitation (bound to Fe/Mn oxide). The soil remaining after the third extraction was extracted with 3 mL 0.02 M HNO₃ and 5 mL 30% H₂O₂ solution in an 85 °C water bath with occasional agitation. After extraction for 3 h, 5 mL 3.2 M NH₄OAc in 20% (v/v) HNO₃ was added and the soil was shaken for 20 min (bound to organic matter). The remaining soil was digested with 5 mL HNO₃ and 2 mL HCl using a microwave oven (residual)

and diluted in a 50 mL measuring flask. All the extracted or digested solutions were passed through a 0.45 μ m filter, and analyzed to determine the elemental concentrations by inductively coupled plasma optical emission spectrometry (ICP-OES; ULTIMA2, HORIBA Ltd., Japan) or inductively coupled plasma mass spectrometry (ICP-MS; 7500cx, Agilent Technologies Inc., USA).

RESULTS AND DISCUSSION

Distance of Pb and Sb Transport through Water Migration

Figure 2 shows the levels of total Pb and Sb in each NCC layer in the 5 mm NC-Pot. The levels of total Pb in all the layers were more than twice as high as those in the original non-contaminated soil, indicating that Pb was transported 5 mm from CC in the NCC through water migration during the immobilization period. The highest levels of total Pb were found in the 1 and 4 mm layers of NCC, and the lowest was in the 5 mm layer. The levels of total Sb in all the layers were also more than twice as high as those in the original non-contaminated soil. The highest level of total Sb was found in the 1 mm layer, and the lowest was in the 5 mm layer. This result indicated that Sb was also transported 5 mm. Moreover, it is reasonable to conclude that the levels of transported Pb and Sb would decrease with the increase in transport distance because the lowest level of total Pb and Sb was found in the 5 mm layer of NCC. The Pb and Sb transport distance through water migration in unsaturated soil may depend on the distance between CC and PC. Therefore, another water migration experiment was conducted using the 10 mm NC-Pot to compare with the results using the 5 mm NC-Pot.

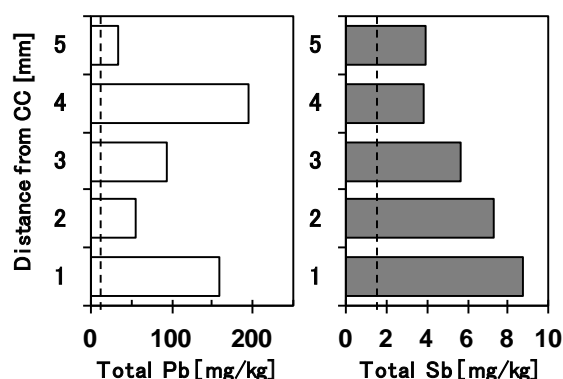


Fig. 2 Total heavy metal levels in NCC (5mm NC-Pot). Broken lines indicate the background levels in the original non-contaminated soil.

Figure 3 shows the level of total Pb and Sb in each NCC layer in the 10 mm NC-Pot. The level of total Pb in the 1 mm layer of NCC, which was nearest to CC, was the highest; it was 14 times higher than that in the original non-contaminated soil. In addition, the level of total Pb in the 3 mm layer was approximately two times higher than that in the original non-contaminated soil. However, the level of total Pb in the layers 6 mm or more, which was not provided in the 5 mm NC-Pot, was the same as that in the original non-contaminated soil. These results suggested that Pb was transported 3 mm from CC in the NCC through water migration during the immobilization period in the 10 mm NC-Pot. The level of total Sb was the highest in the 1 mm layer, reduced with the distance, and was the same as the original non-contaminated soil in layers 7 mm or more. Thus, in contrast to Pb, these results demonstrated that Sb was transported 6 mm through water migration during the immobilization period in the 10 mm NC-Pot.

The Pb and Sb transport distances did not differ significantly in the water migration experiments using a 5 mm NC-Pot and a 10 mm NC-Pot. Accordingly, these results demonstrated that Pb and Sb can be transported 3-5 mm and 6 mm, respectively, through water migration, which corresponds to precipitation for one month. Tlustoš *et al.* [17] and Fitz *et al.* [18] conducted a plant growth experiment using a rhizobox and reported that the plant absorbed Pb and arsenic through water uptake from rhizosphere soil, which is a few millimeters away from the root. These results are consistent with those obtained in this study. Thus, the Pb and Sb transport distances in this study would be valid.

Steely *et al.* [12] and Cao *et al.* [19] have observed that the levels of Pb and Sb in the shooting

range soil decreased relative to soil depth. However, in this study, Sb was transported farther than Pb in NCC (Fig. 3). This observation suggested that, compared to Pb, Sb was transported easily through water migration. Sb would exist as an anion ($\text{Sb}(\text{OH})_6^-$) of Sb (V) in the shooting range soil under oxic conditions, and Sb would be transported as $\text{Sb}(\text{OH})_6^-$ through water migration. In contrast, Pb would exist primarily as a Pb compound, such as PbCO_3 and PbO . The Pb compounds were dissolved; dissolved Pb would be transported and sorbed onto the colloid containing iron oxide and organic matter [10], [19]. Therefore, Sb was probably transported easily because transport of a colloid is more difficult than that of an anion. These results suggest that Sb is effectively immobilized in soil because easy transport in soil results in frequent contact and reaction with immobilization amendment.

Transporting Phases of Pb and Sb

The ratios of water-soluble Pb and Sb to total Pb and Sb in NCC in the 5 mm NC-Pot are shown in Fig. 4. The ratios of water-soluble Pb to total Pb in all layers were very low. The ratio in the 1 mm layer, in which the highest level of total Pb was found, was less than 2%. In contrast to Pb, the ratios of water-soluble Sb in all layers were high, and 30% of the total Sb in the 1 mm layer was water-soluble.

Figure 5 shows the ratios of water-soluble Pb and Sb to total Pb and Sb in the 10 mm NC-Pot. As was observed with the 5 mm NC-Pot, the ratios of water-soluble Sb were higher than those of water-soluble Pb in all layers. The ratio of water-soluble Pb in the 1 mm layer was 2%, while that of water-soluble Sb was 42%. Furthermore, 30% to 40% of the total Sb in the 1 to 6 mm layers, in which the level of total Sb exceeded that of the original non-

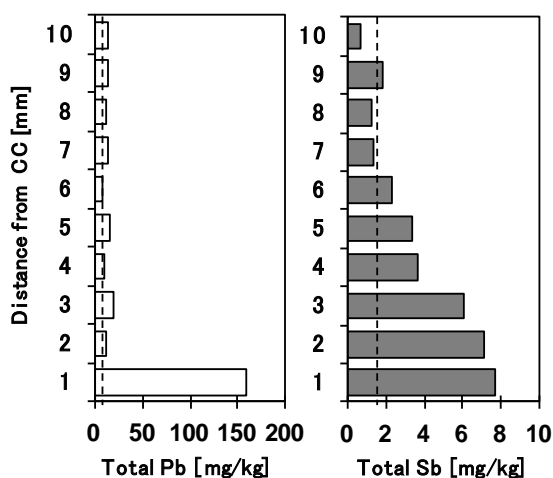


Fig. 3 Total heavy metal levels in NCC of 10 mm NC-Pot. Broken lines indicate the background levels in the original non-contaminated soil.

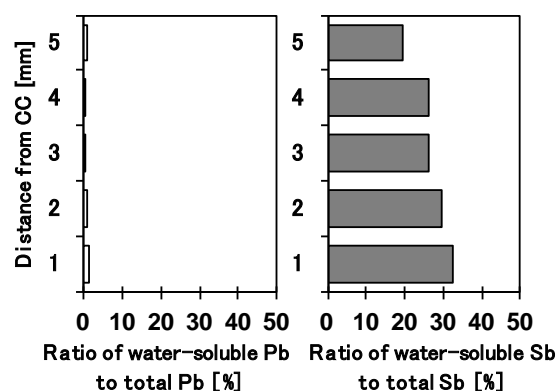


Fig. 4 Ratios of water soluble to total in NCC of 5 mm NC-Pot

contaminated soil, was water-soluble. These ratios are consistent with the results (Pb: 2%–10%, Sb: 4%–72%) obtained by Sanderson *et al.* [20]. These results demonstrated that Sb in the shooting range soil would be more water-soluble, and thus, Sb would have higher mobility through water migration than Pb.

The Pb and Sb that were passed through the 0.45 μm filters were defined as water-soluble in this study. However, Pb underwent colloid transport in the soil, and Pb transport would strongly relate with 0.45–0.8 μm colloid particles [10]. Thus, approximately Pb transported into the layers of NCC likely existed in the sorbing phase on the colloid; Pb would be transported as non-water-soluble phases. Sb was also sorbed on iron oxides. However, the level of Sb sorption was reduced under neutral to alkali soil pH [20]. Therefore, in the soil used, Sb was less likely to be sorbed, which probably induced Sb to be more water-soluble.

Sequential extraction was performed to evaluate Pb transporting phases because Pb was probably transported in non-water-soluble phases. The levels of each Pb fraction in the 1 and 5 mm layers of NCC in the 5 mm NC-Pot are shown in Fig. 6. The level of Pb fraction in the 1 mm layer was highest in the fraction bound to Fe/Mn oxide at 27 mg/kg. The level of Pb fraction in the 5 mm layer, where the level of total Pb was the lowest, was also highest in the fraction bound to Fe/Mn oxide at 6 mg/kg. The levels of the carbonate and Pb fractions bound to Fe/Mn oxide in the 1 mm layer were significantly higher than those in the 5 mm layer. The level of the residual fraction, which was the most stable, was the same for the 1 and 5 mm layers. Therefore, Pb phases transported through the layers appeared to be Pb compounds, such as carbonate. In addition, the Pb phase bound to Fe/Mn oxide; the Pb phase transported with the colloid would be phase sorbed on the iron oxide. In acid soil, Pb carbonate and Pb sorbed on iron oxide are likely to be dissolved and desorbed, respectively [20]. However, in the soil used, the dissolution and desorption was suppressed because of neutral soil pH.

These results indicate that the distance and phases during transport in the soil differed between

Pb and Sb. Therefore, to enhance the effectiveness of immobilization, the type of heavy metal should be taken into account. In this study, only one type soil was used. Further investigation should consider more soil types because soil particle size and chemical composition strongly affect Pb and Sb sorption on the soil surface.

Required Amount of Immobilization Amendment by Microscopic Range

It was anticipated that, in the case of immobilization in contaminated soil, Pb and Sb would be transported through water migration a maximum of 5 to 6 mm, which corresponds to precipitation for one month. However, the transported Pb and Sb were particularly accumulated in the 1 mm layer. Therefore, assuming that the transporting distance to immobilize Pb and Sb is 1 mm, the required amount of amendment was calculated from the following equations on the basis of the microscopic range of immobilization. The overview of the microscopic range is shown in Fig. 7. The microscopic range of Pb and Sb immobilization was calculated according to the following equation:

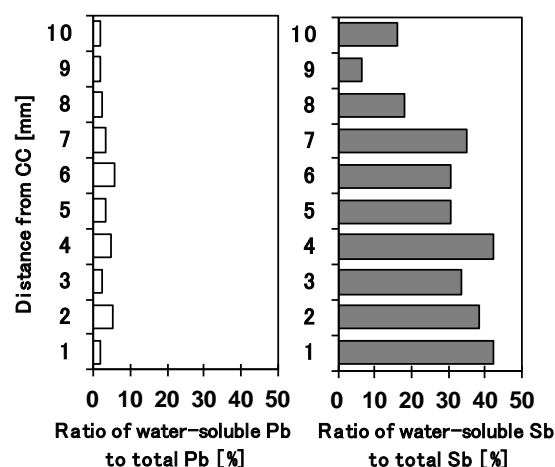


Fig. 5 Ratios of water soluble to total in NCC of 10 mm NC-Pot

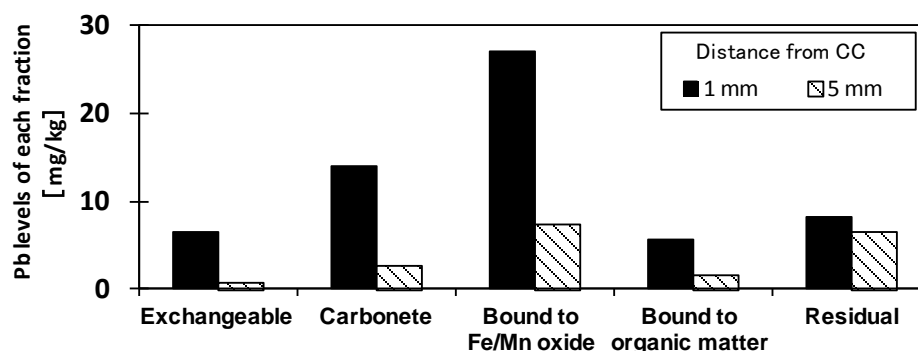


Fig. 6 Pb fractions of sequential extraction in NCC of 5 mm NC-Pot

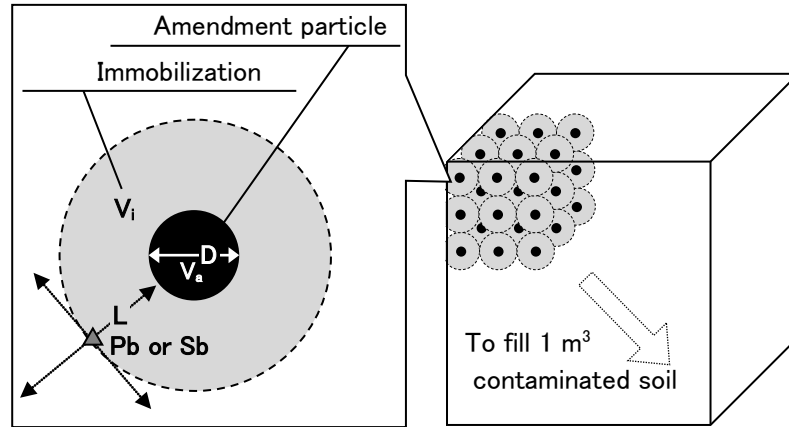


Fig. 7 Overview of microscopic range for immobilization

$$V_i = \frac{4\pi \cdot (L + D/2)^3}{3} \quad (1)$$

where V_i is the microscopic range of Pb and Sb immobilization (mm^3), L is the transporting distance during the immobilization period (1 mm), and D is the diameter of the amendment particle. In case that $D = 1$ mm, the value of V_i was obtained as 14.1 mm^3 using Eq. (1). The required number of immobilization amendment particles to fill 1 m^3 of contaminated soil for the established range of Pb and Sb immobilization (N) can be expressed as

$$N = \frac{1 \times 10^9}{V_i} \quad (2)$$

The value of N was calculated to be 7.09×10^7 .

The volume of one immobilization amendment particle (V_a) can be calculated as

$$V_a = \frac{4\pi \cdot (D/2)^3}{3} \quad (3)$$

Moreover, using V_a and N , the required volume of immobilization amendment (A_v) in 1 m^3 of contaminated soil can be expressed as

$$A_v = \frac{V_a \cdot N}{1 \times 10^9} \times 100 \quad (4)$$

The value of A_v was calculated to be 3.72% using Eq. (4). By converting the volume ratio to weight ratio using the density of the amendment and the contaminated soil (Table 1), the weight ratio of amendment was calculated to be 4.62%.

It would be effective for chemical immobilization to add the phosphorus amendment with 0.6 molar ratio of Pb in the soil and P in the amendment because Pb is immobilized in soil with the precipitation of Pb phosphate minerals such as pyromorphite ($\text{Pb}_5(\text{PO}_4)_3\text{OH}$); its P/Pb molar ratio is 0.6 [6]. In the case that the amendment has been added to the soil at 5% (w/w), the molar ratio of Pb in the soil and P in the amendment would be 0.771. Thus, addition of amendment with 5% (w/w) is probably sufficient to immobilize Pb. Moreover, Álvarez-Ayuso *et al.* [7] added 5% (w/w) iron oxide to the Sb-contaminated soil in which the level of total Sb was 25 times higher than that in the soil used in this study. The results of that study indicated that Sb was completely immobilized. Therefore, in the soil used in the current study, the addition of amendment with 5% (w/w) would be sufficient for Pb and Sb immobilization. Further investigation is necessary because this study simplified estimation conditions to calculate the required amount of immobilization amendment.

CONCLUSION

The present study evaluated the distance of Pb and Sb transport through water migration and their transporting phases during the immobilization period to identify the microscopic range of immobilization in the soil. In addition, the required amount of immobilization amendment was investigated on the basis of the microscopic range of immobilization. The results obtained in this study are as follows:

- 1) Pb and Sb were transported 5 mm and 6 mm at most, respectively, and were particularly accumulated 1 mm from contamination.
- 2) Thirty to forty percent of transported Sb was water-soluble, which suggests that Sb was easily transported in soil to contact and react with immobilization amendment. Pb phases transported through water migration sorbed on Fe/Mn oxide and carbonate. Thus, Pb probably has lower mobility than Sb.

- 3) The distance and phases during transport in the soil differed between Pb and Sb. To enhance the effectiveness of immobilization, the type of heavy metal should be considered.
- 4) The required amount of immobilization amendment was estimated from the range of immobilization (1 mm) to be 4.62% (w/w).

ACKNOWLEDGMENTS

The ICP-OES and CHO analyzer used for chemical analysis in this study was made available by the Division of Instrumental Analysis at Gifu University. The authors are grateful to Prof. F. Li and Prof. T. Yamada (Gifu University) for allowing the use of the ICP-MS. This study was partly supported by Japan Society for the Promotion of Science (JSPS) KAKENHI Grant Number 23710089 and the Maeda Engineering Foundation.

REFERENCES

- [1] Dickinson NM, "Strategies for sustainable woodland on contaminated soils", *Chemosphere*, Vol. 41, 2000, pp. 259–263
- [2] Allen A, "Containment landfills: the myth of sustainability", *Eng. Geol.*, Vol. 60, 2001, pp. 3–19
- [3] Mulligana CN, Yong RN, Gibbs BF, "An evaluation of technologies for the heavy metal remediation of dredged sediments", *J. Hazard. Mater.*, Vol. 85, 2001, pp. 145–163
- [4] Sorvari J, Antikainen R, Pyy O, "Environmental contamination at Finnish shooting ranges—the scope of the problem and management options", *Sci. Total Environ.*, Vol. 366, 2006, pp. 21–31
- [5] Siebielec G, Chaney RL, "Testing amendments for remediation of military range contaminated soil", *J. Environ. Manage.*, Vol. 108, 2012, pp. 8–13
- [6] Chrysoschoou M, Dermatas D, Grubb DG, "Phosphate application to firing range soils for Pb immobilization: The unclear role of phosphate", *J. Hazard. Mater.*, Vol. 144, 2007, pp. 1–14
- [7] Álvarez-Ayuso E, Otones V, Murciego A, García-Sánchez A, "Evaluation of different amendments to stabilize antimony in mining polluted soils", *Chemosphere*, Vol. 90, 2013, pp. 2233–2239
- [8] Chiang YW, Santos RM, Ghyselbrecht K, Cappuyns V, Martens JA, Swennen R, Gerven TV, Meesschaert B, "Strategic selection of an optimal sorbent mixture for in-situ remediation of heavy metal contaminated sediments: Framework and case study", *J. Environ. Manage.*, Vol. 105, 2012, pp. 1–11
- [9] Zhang W, Tsang DCW, "Conceptual framework and mathematical model for the transport of metal-chelant complexes during in situ soil remediation", *Chemosphere*, Vol. 91, 2013, pp. 1281–1288
- [10] Yin X, Gao B, Ma LQ, Saha UK, Sun H, Wang G, "Colloid-facilitated Pb transport in two shooting-range soils in Florida", *J. Hazard. Mater.*, Vol. 177, 2010, pp. 620–625
- [11] Garrido F, Helmhart M, "Lead and soil properties distributions in a roadside soil: Effect of preferential flow paths", *Geoderma*, Vol. 170, 2012, pp. 305–313
- [12] Steelya S, Amarasiriwardena D, Xing B, "An investigation of inorganic antimony species and antimony associated with soil humic acid molar mass fractions in contaminated soils", *Environ. Pollut.*, Vol. 148, 2007, pp. 590–598
- [13] Wanga S, Choi JH, "Simulating fate and transport of chromium in saturated sediments", *Appl. Math. Model.*, Vol. 37, 2013, pp. 102–111
- [14] Furuta S, Katsuki H, Komarneni S, "Removal of lead ion using porous hydroxyapatite monoliths synthesized from gypsum waste", *J. Ceram. Soc. Jap.*, Vol. 108, 2000, pp. 315–317
- [15] Mitsunobu S, Sakai Y, Takahashi Y, "Characterization of Fe(III) (hydr)oxides in arsenic contaminated soil under various redox conditions by XAFS and Mössbauer spectroscopies", *Appl. Geochem.*, Vol. 3, 2008, pp. 3236–3243
- [16] Tessier A, Campbell PGC, Bisson M, "Sequential extraction procedure for the speciation of particulate trace metals", *Anal. Chem.*, Vol. 51, 1979, pp. 844–851
- [17] Tlustoš P, Száková J, Kořínek K, Pavlíková D, Hanč A, Balík J, "The effect of liming on cadmium, lead, and zinc uptake reduction by spring wheat grown in contaminated soil", *Plant. Soil Environ.*, Vol. 52, 2006, pp. 16–24
- [18] Fitz WJ, Wenzel WW, Zhang H, Nurmi J, Štípek K, Fischerová Z, Schweiger P, Köllensperger G, Ma LQ, Stinger G, "Rhizosphere characteristics of the arsenic hyperaccumulator *Pteris vittata* L. and monitoring of phytoremoval efficiency", *Environ. Sci. Technol.*, Vol. 37, 2003, pp. 5008–5014
- [19] Cao X, Ma LQ, Chen M, Hardison Jr DW, Harris WG, "Lead transformation and distribution in the soils of shooting ranges in Florida, USA", *Sci. Total Environ.*, Vol. 307, 2003, pp. 179–189
- [20] Sanderson P, Naidu R, Bolan N, Bowmanc M, McLure S, "Effect of soil type on distribution and bioaccessibility of metal contaminants in shooting range soils", *Sci. Total Environ.*, Vol. 438, 2012, pp. 452–462

SUB-DARCY-SCALE MODELING OF NON-UNIFORM FLOW THROUGH POROUS MEDIA WITH MIXED WETTABILITES

Junichiro Takeuchi¹, Takuya Takahashi², and Masayuki Fujihara³

^{1,3}Graduate School of Agriculture, Kyoto University, Japan; ² Kawasaki Kisen Kaisha, Ltd., Japan

ABSTRACT

A physically-based conceptual model is developed using spatially distributed sub-Darcy-scale clusters in a regular grid to reproduce both the hydraulic properties and the non-uniform wetting and drainage fronts through porous media mixed with hydrophilic and hydrophobic grains. In the model, cellular automaton-like algorithm is employed to route water- and air-intrusion paths through the mixed porous media. Water retention characteristics, which are ones of the macroscopic properties of porous media, are estimated by accumulating a certain numbers of clusters after reaching equilibrium states in a wetting or drainage process. In the experimental part of this study, normal (hydrophilic) and artificially hydrophobized glass spheres, whose diameter is about 0.2 mm, are used as materials, and hydraulic properties of homogeneously mixed glass spheres with various rates are measured. The measured data are compared to model estimation, and the availability of the model is shown.

Keywords: Glass Spheres, Water Retention Properties, Hydrophilicity, Hydrophobicity, Cellular Automaton Modeling

INTRODUCTION

From the early 1900's, it has been reported that there exist soils that have resistance to water infiltration in various countries such as New Zealand, Australia, Netherlands, and so on, and major concerns have been raised because such soils, which are referred to as water-repellent soils, cause soil erosion and productivity reduction in farmlands [1]. In some cases of a natural environment, soil gains water repellency by being coated with organic matters decomposed by fungi, and it is observed that interfusion of hydrophobic grains into hydrophilic grains makes dramatic differences in flow behavior and hydraulic properties [2].

Various works assessing and quantifying water repellency and hydraulic properties of artificial water-repellent soils as well as natural ones have been conducted, and it is shown that the hydraulic properties of soils change gradually with the increasing mix rate of hydrophobic grains [3][4]. While measured properties could be represented with relative ease in some functional form such as van Genuchten-Mualem model, predicting those properties effected by grains' wettabilities needs microscopic approaches. For instance, a functional model is proposed by Ustohal *et al.* (1998) [3], in which the Brooks-Corey model is extended using probability distribution of apparent contact angles on grain clusters with mixed wettabilities. And pore-scale network modeling also proficiently predicts multiphase flow properties through mixed porous media [5]. But this approach requires large computational load even for several cubic centimeters of porous media.

In this study, a physically-based conceptual model, which needs relatively low computational load, is developed by adopting the concept on the cluster of grains. The model realizes a spatial distribution of clusters and makes it possible to reproduce non-uniform wetting and drainage fronts through porous media mixed with hydrophilic and hydrophobic grains. And water retention properties of the mixed porous media are estimated from the computed results in a bottom-up manner.

MODEL

Model Structure

The physically-based conceptual model proposed here employs a cellular-automaton-like algorithm to track water- and air-intrusion paths through porous media. Generally, a cellular automaton is referred to as a collection of cells that have several variable states in a regular grid, and the cells evolve according to a set of rules based on the states of neighboring cells during iteration of discrete time steps. The rules are applied to initial cell states, and new cell states are obtained according to the rules. This process is repeated for as many time steps as desired [6].

In this study, cells correspond to clusters of multiple grains as illustrated in Fig. 1. This figure depicts a schematic of the model two-dimensionally, but grains, cells and capillary tubes are defined as three-dimensional objects in the model. The concept about the cluster is originally used by Ustohal *et al.* (1998) [3] for modeling hydraulic properties of mixed porous media by using a functional form,

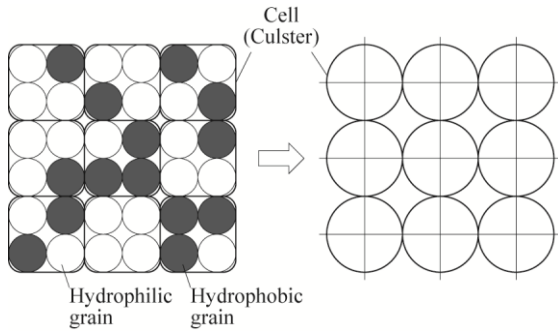


Fig. 1 Relation between grains and cells in a case of a square grid.

and they presumed that the contact angle in each cluster is homogeneous, based on the Cassie's law. The contact angle, which is apparent one synthesized from mosaic of various contact-angle surfaces, is determined, depending on the ratio of hydrophilic and hydrophobic surface areas included in each cluster. While Ustohal *et al.* (1998) [3] treated a cluster itself as a meso-scale wall surface, we assume in this model that each cluster conceptually possesses a bundle of circular tubes with various diameters. And it is also assumed that each tube has constant diameter through a single cell, and that the apparent contact angle of the tubes in a cell has identical value. The apparent contact angle is estimated from the Cassie-Baxter equation, depending on the ratio of surface areas of the grains with different contact angles. When grains with different n^a types of contact angle are included, the apparent contact angle of the i th cell ($i = 1, \dots, n^c$; n^c is the number of cells) is represented as follows.

$$\cos \varphi_i^c = \sum_{j=1}^{n^a} f_{ij} \cos \varphi_j \quad (1)$$

with

$$f_{ij} = A_{ij} / \sum_{k=1}^{n^a} A_{ik} \quad (2)$$

where φ_i^c is the apparent contact angle of the i th cell, φ_j is the j th contact angle among n^a types, f_{ij} is the ratio of the surface area with j th contact angle to the total area, and A_{ij} is the surface area. If the size of all grains is equal and two types of wettability, *i.e.*, hydrophilic and hydrophobic grains, are included, Eqs. (1) and (2) could be represented as follows.

$$\cos \varphi_i^c = f_i^D \cos \varphi^D + (1 - f_i^D) \cos \varphi^P \quad (3)$$

$$f_i^D = n_i^D / n^g \quad (4)$$

where n^g is the number of grains included in a cell, and n_i^D is the number of the hydrophilic grains in the i th cell. Equations (3) and (4) imply that apparent contact angle of a cell that has n^g grains can have $(n^g + 1)$ types of realization, depending on the number of n_i^D ($= 0, 1, \dots, n^g$). When the fraction of the hydrophobic grains included in a whole

apparent contact angle (deg)	30.0	58.4	79.5	99.1	120.0
probability (binominal distribution)	0.004	0.05	0.21	0.42	0.32

Fig. 2 Realizations of a cell, apparent contact angles, and probabilities in a case where the mix rate of hydrophobic grains is 0.75.

porous medium is p^p , the probability of the realization that has n_i^D ($= 0, 1, \dots, n^g$) hydrophilic grains is described by the binominal distribution.

$$P(n_i^D, n^g) = \frac{n^g!}{n_i^D!(n^g - n_i^D)!} (1 - p^p)^{n_i^D} (p^p)^{n^g - n_i^D} \quad (5)$$

In a case where a cell has four grains, the contact angles of hydrophilic and hydrophobic grains are 30.0 degrees and 120.0 degrees, respectively, and the mix rate of hydrophobic grains is 0.75, a cell has five realizations. The apparent contact angles and probabilities of the realizations are shown in Fig. 2.

Capillary tubes in each cell have an ability of capillary rise or fall, depending on the apparent contact angle and the radius of tube, if the lower end of tube is connected to a water pool. The height of the capillary rise or fall from the surface of the water pool is termed 'potential' capillary height here, and the height is represented based on the Young-Laplace equation for circular tubes.

$$h_{ij}^c = \frac{2\sigma \cos \varphi_i^c}{\rho g r_{ij}} \quad (6)$$

where h_{ij}^c and r_{ij} are the potential capillary height and the radius of the j th tube in the i th cell, respectively, σ and ρ are the surface tension and the density of water, respectively, and g is the gravitational acceleration. Equation (6) means that capillary rise could occur when h_{ij}^c is positive ($\varphi_i^c < 90$ degrees), and that capillary fall when h_{ij}^c negative ($\varphi_i^c > 90$ degrees).

There are various options for arrangement of cells and grains. For cell arrangement, the following grids are considered, such as a simple cubic grid and body-centered cubic grid as shown in Fig. 3. Two classes of grain packings are introduced in Ustohal *et al.* (1998) [3]: tetrahedral packings and cubic packings. One of the essential indices for selection of grid is connectivity of cells, which is the number of neighboring cells. It is reported that the connectivity of pores is an essential factor that effects hydraulic properties of porous media by Gharbi and Blunt (2012) [5]. In this case, the cell connectivity has an effect on likelihood of state change of cells.

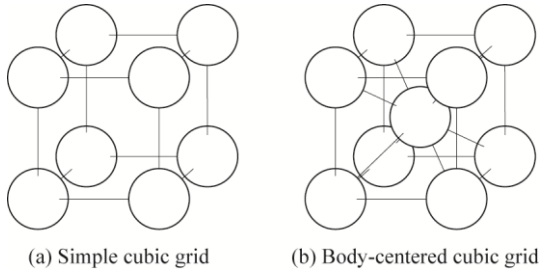


Fig. 3 Three-dimensional cell arrangement.

Rules for Wetting and Drainage Processes

In this model, each cell has two states: dry state and wet state. And one state of a cell could change into the other, depending only on the current states of its own and neighboring cells. After all cells are evaluated based on the current states, all the cells are updated simultaneously and a new set of states is obtained. This process is iterated until any change does not occur or desired time steps are satisfied. To simulate water intrusion into a dry porous medium (wetting process) or air intrusion into a fully wet medium (drainage process), the conditions for state change are given as described below.

In the wetting process, initially each cell in an objective domain is set to be dry state, and cells at the upper end and at the bottom end are supposed to connect to exterior air and water pools, respectively. An objective dry cell changes into wet, if the cell holds the following four conditions:

- 1) the objective dry cell connects to the air pool through other dry cells or directly,
- 2) any of its neighboring cells is wet,
- 3) any of the neighboring wet cells connects to the water pool through other wet cells or directly, and
- 4) the potential capillary height of any of the capillary tubes in the objective dry cell satisfies the following inequality.

$$h_{ij}^c > h_i^p \quad \forall j \in \{1, \dots, n^i\} \quad (7)$$

where $h_i^p (= -p_i / \rho g)$, p_i is the water pressure placed on the i th cell) is equal to the height from the surface of the water pool.

The first condition assumes that the air pressure in dry cells that connect to the exterior air pool is equal to atmospheric pressure, which is supposed to be constant here, and that the air pressure of enclosed air in dry cells that do not connect to the air pool could change and constrict water entry by air pressure increase. The third condition assumes that the water pressure in wet cells that connect to the water pool is hydrostatic one.

In the drainage process, initially all cells are set to be wet. Cells at the top end and at the bottom end connect to exterior air and water pools, respectively, in the same way with the wetting process. An objective wet cell changes into dry, if the wet cell

holds the following four conditions.

- 1) the objective wet cell connects to the water pool through other wet cells or directly,
- 2) any of its neighboring cells is dry,
- 3) any of the neighboring dry cells connects to the air pool through other dry cells or directly, and
- 4) the potential capillary height of all the capillary tubes in the objective wet cell satisfies the following inequality.

$$h_{ij}^c < h_i^p \quad \forall j \in \{1, \dots, n^i\} \quad (8)$$

Estimation of Water Retention Properties

The proposed model treats water and air intrusions in a sub-Darcy scale as mentioned above. The hydraulic properties of porous media such as the water retention property and permeability are macro-scale ones. So, to estimate such macroscopic properties, some operation such as integration and averaging over some part of a computational domain is needed using a computed result.

To evaluate water retention properties, saturation at a certain water pressure head is calculated from cells within a certain range of water pressure heads as follows.

$$S_w(p) = \frac{\sum_{i \in \Omega(p)} \sum_{j=1}^{n^i} \alpha_{ij} r_{ij}^2}{\sum_{i \in \Omega(p)} \sum_{j=1}^{n^i} r_{ij}^2} \quad (9)$$

with

$$\alpha_{ij} = \begin{cases} 1 & \text{if the } j\text{th tube in the } i\text{th cell is wet} \\ 0 & \text{if the } j\text{th tube in the } i\text{th cell is dry} \end{cases} \quad (10)$$

$$\Omega(p) = \{i \in 1, \dots, n^c \mid p - \Delta p < p_i \leq p + \Delta p\} \quad (11)$$

where α_{ij} is a coefficient that distinguishes whether the tube is wet or dry, $\Omega(p)$ is a set of cells under water pressure head from $p - \Delta p$ to $p + \Delta p$, n^c is the number of cells, and p_i is the pressure head placed on the i th cell.

EXPERIMENT

The soil column method is employed to measure the water retention properties of porous media mixed hydrophilic and hydrophobic grains. The soil column is made by piling up acrylic circular cylinders whose inner diameter is 4.8 cm and height is 4.0 cm, and each cylinder is taped together strictly to avoid air and water leaking (Fig. 4). Dry materials are packed in the column at a prescribed density, and the top and bottom of the column are covered by porous filters to prevent air entrapment. In a case of a wetting process, preliminarily materials are dried adequately in a desiccator. In a case of a drainage process, a packed column is saturated by the vacuum method, because materials containing a high percentage of hydrophobic grains will not inundate spontaneously. Then, a certain water pressure is constantly placed on the bottom of the column until

the column reaches an equilibrium state (72 hours in this study), and weights of materials in each cylinder is measured before and after oven-dry. All these procedures are conducted in a room whose temperature is kept at 20 degrees Celsius.

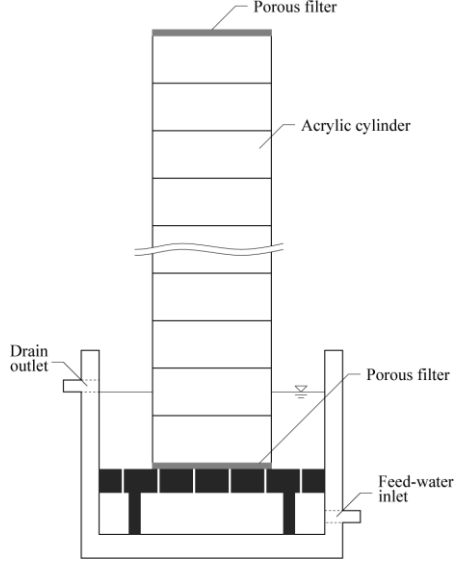


Fig. 4 Soil column method.

MATERIAL

In this model, we assume a uniform grain size for each wettability. So, for the experiments glass spheres whose diameter is 0.2 mm are used as hydrophilic materials. It is checked that the distribution of the diameter is narrow enough from images taken by a microscope. After washing and drying, the original glass spheres are hydrophobized by vapor-depositing octadecyltrichlorosilane ($\text{CH}_3 - (\text{CH}_2)_{17}\text{SiCl}_3$, OTS), which is a popular chemical material used in other works [3][4]. Specimens are made by homogeneously mixing hydrophilic and hydrophobic spheres at the following mass-based rates of hydrophobic grains: the mix rates of hydrophobic grains are 0.00, 0.25, 0.50, 0.75, and 1.00. And the bulk density of specimens is controlled to be 1.58 g/cm^3 , when materials are packed in the acrylic cylinders.

RESULTS AND DISCUSSION

Experimental Results

The measured water retention properties of both wetting and drainage processes are shown in Figs. 5 and 6, respectively. These results show that the mix rate of hydrophobic grains has a great effect on water retention properties, and that the water retentivity decreases as the rate increases in both wetting and drainage processes.

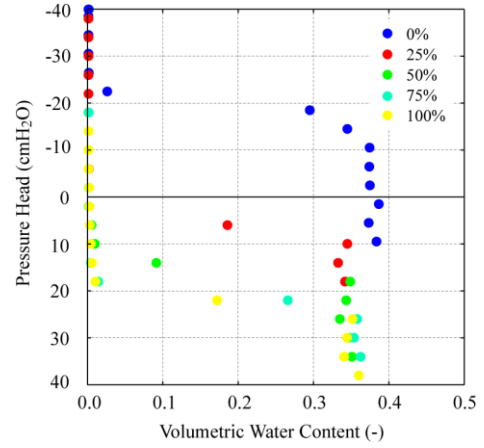


Fig. 5 Measured water retention properties at various mix rates of hydrophobic grains (wetting process).

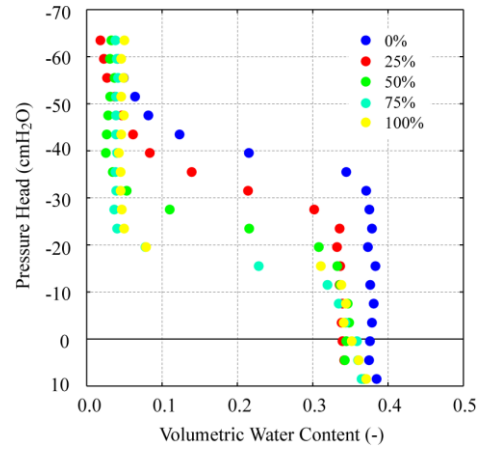


Fig. 6 Measured water retention properties at various mix rates of hydrophobic grains (drainage process).

Parameters and Computational Conditions

In this study, a simple cubic grid, in which inner cells have six neighboring cells, is employed. The grid interval is estimated from the following equation, based on the diameter of grains and the number of grains in one cell.

$$l = \left(\frac{4\rho_g \pi r_g^3 n^p}{3\rho_b} \right)^{\frac{1}{3}} \quad (12)$$

where l is the grid interval, ρ_g is the density of glass, ρ_b is the bulk density of the specimen, and r_g is the radius of the glass sphere. The number of capillary tubes in a cell is also estimated, assuming grains are arranged in a simple cubic grid.

$$n^t = \text{round} \left(l^2 \left\{ \left(\frac{3\rho_b}{4\rho_g \pi r_g^3} \right)^{\frac{1}{3}} + 1 \right\}^2 \right) \quad (13)$$

where $\text{round}(\cdot)$ is the function that rounds input value off to the closest whole number.

The computational domain is set as a cuboid and the size is $\sqrt{10} \text{ cm} \times \sqrt{10} \text{ cm} \times 80 \text{ cm}$, which is based on the experimental column used here. Simulations are conducted with three types of grain number included in one cell: the number is 4 in Type I, 8 in Type II, and 27 in Type III. The parameters included in the model are given or estimated based on the materials used for experiments and those are summarized in Table 1. The radius of the capillary tubes is determined here by the normal distribution whose average μ^t and standard deviation σ^t are 0.04 mm and 0.006 mm, respectively. These values are based on the previous work that estimated hydraulic conductivity of porous media using a pore-scale network model [7].

Table 1 Parameters Used for Each Type.

	Type I	Type II	Type III
ϕ^D (deg)		45	
ϕ^P (deg)		120	
μ^t (mm)		0.04	
σ^t (mm)		0.006	
n^s	4	8	27
n^t	3	4	9
l (mm)	0.298	0.376	0.564

Computed Results

Some of the computed results of non-uniform water-intrusions in wetting processes are shown in Fig. 7. The mix rate of hydrophobic grains is 0.50 and the height of the depicted samples is 5 cm. The pressure head placed on the bottom of the samples is 5 cmH₂O. Though the samples are cut out from the original computed domains in the same position, those are markedly different in appearance except

for the cell size. This implies that the number of grains in a cell has an influence on computed results.

Next, the computed water retention properties of wetting and drainage processes are shown in Figs. 8 and 9, respectively. These figures show that water retentivity decreases clearly as the mix rate of hydrophobic grains increases. While all the saturations varies smoothly in Type III, there exist several step-like changes in Type I and Type II. Such a step-like change is also observed in Fig. 7 (b), which shows that the ratio of dry cells increases obviously above about three-quarters of the sample height. The cause of the sudden change in saturation is considered that each realization of the apparent contact angle in Type I and Type II has relatively large probability compared with Type III because the number of grains in a cell is small. This also means that cells become more homogeneous as the number of grains in a cell increases.

Compared with the experimental results (Figs. 5 and 6), the computed results shows some differences. In wetting processes, water enters capillary tubes under negative water pressure even in the case of 0.50 of the mix rate, while spontaneous water-entry is prevented from only 0.25 of the mix rate. This indicates that in actual cases a single hydrophobic grain has an influence on all the hydrophilic neighboring grains, and which is left out of consideration by dividing the grain gathering into many clusters in the model.

In drainage processes, water is drained promptly depending of the mix rate in the computed results, while much water is kept up to $-20 \text{ cmH}_2\text{O}$ even in the high rate cases of the measured results. The reason is considered that speed of air-water interface movement is not considered in the model. In actual cases, water in large pores is drained in advance of that in small pores, and such non-uniform drainage could make water isolation in a pore-network. But in

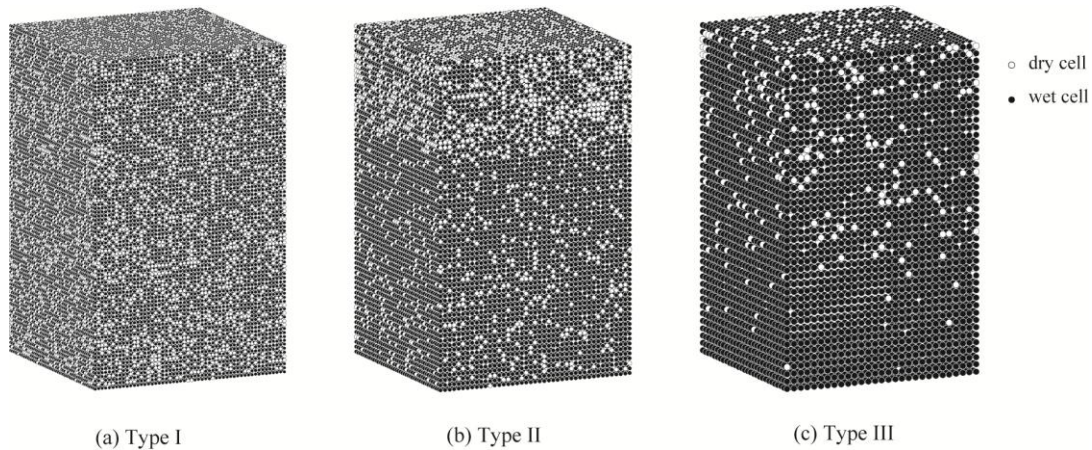


Fig 7 Water intrusions in a case where the mix rate of hydrophobic grains is 0.50.

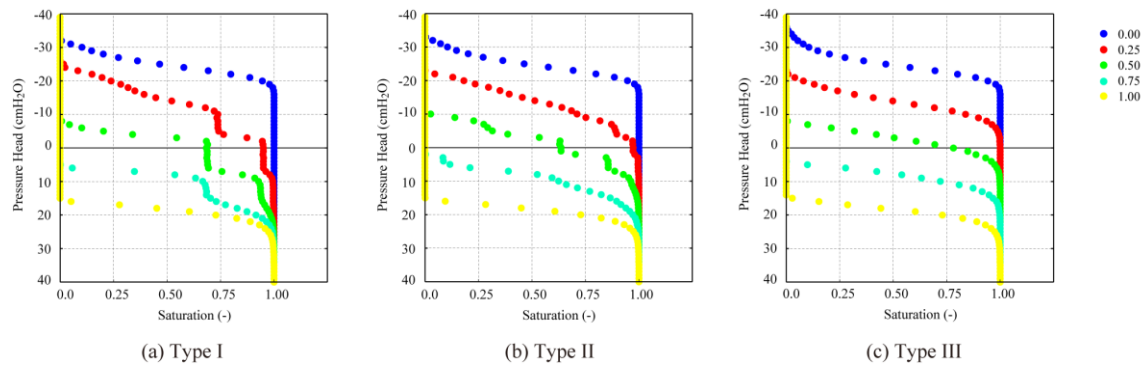


Fig. 8 Water retention properties of wetting processes.

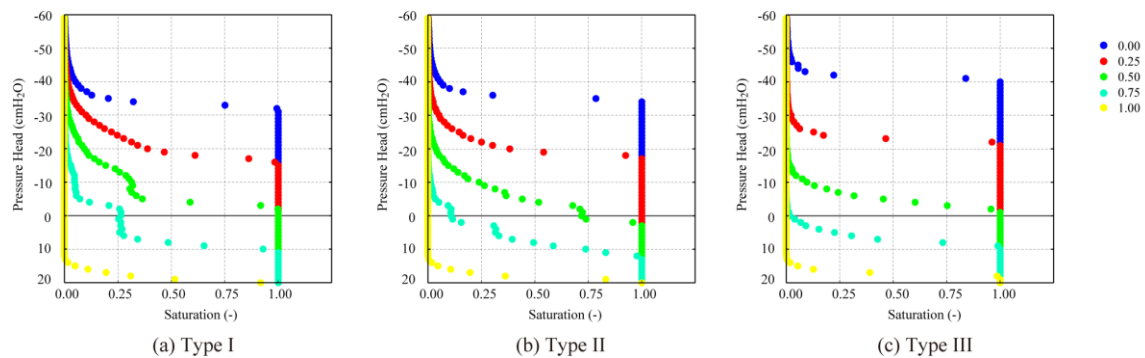


Fig. 9 Water retention properties of drainage processes.

the model all waters included in cells that satisfies the drain conditions are drained at once in one discrete time step.

CONCLUSION

A physically-based conceptual model was proposed to reproduce non-uniform water- and air-intrusions through porous media mixed with hydrophilic and hydrophobic grains. In the model, the cellular automaton-like algorithm was employed to figure out the intruding paths, and the hydraulic properties were estimated from the computed intrusion paths in a bottom-up manner.

The computed results that had reproduced wetting and drainage processes were compared with the experimental results using glass spheres hydrophobized by OTS. Although there were discrepancies in the water-entry pressure for the wetting processes and in the air-entry pressure for the drainage processes, the dependence of water retentivity on the mix rate of hydrophobic grains and non-uniform water and air intrusions were illustrated. And it was also shown that the number of grains in a cell was one of the essential factors in this model, because it effects the value and probability of the apparent contact angle in cells. From these results, it is concluded that the proposed model has the possibility of being provided as a useful tool to estimate the hydraulic properties of porous media with different wettabilities.

REFERENCES

- [1] DeBano LF, "Water repellency in soils: a historical overview", J. of Hydrol., Vol. 231-232, 2000, pp. 4-32.
- [2] Bauters TWJ, Steenhuis TS, DiCarlo DA, Nieber JL, Dekker LW, Ritsema CJ, Parlange JY, and Haverkamp R, "Physics of water repellent soils", J. of Hydrol., Vol. 231-232, 2000, pp. 233-243.
- [3] Ustohal P, Dtauffer F, and Dracos T, "Measurement and modeling of hydraulic characteristics of unsaturated porous media with mixed wettability", J. of Contam. Hydrol., Vol. 33, 1998, pp. 5-37.
- [4] Annaka T, "Wettability indices and water characteristics for sands of mixed wettability", J. Jpn. Soc. Soil Phys., Vol. 102, 2006, pp. 79-86.
- [5] Gharbi O and Blunt MJ, "The impact of wettability and connectivity on relative permeability in carbonates: A pore network modeling analysis", Water Resour. Res., Vol. 48, W12513, 2012.
- [6] Chopard B and Droz M, Cellular Automata Modeling of Physical Systems, Cambridge University Press, 2005.
- [7] Ijiri Y, Takeuchi J, and Fujihara M, "Estimation of hydraulic conductivity by pore-scale network", in Proc. Applied Hydraulics Workshop, JSIDRE, 2012, pp. 92-92 (in Japanese).

CAPTURING PEDESTRIAN MOVEMENT SAFETY AND SECURITY ISSUES AT MAJOR TRANSPORTATION INTERCHANGES

Zulfadly Azizi Bohari¹, Syahriah Bachok¹ and Mariana Mohamed Osman¹

¹*Kulliyah of Architecture and Environmental Design, International Islamic University Malaysia*

ABSTRACT

More often than not, transportation nodes such as stations, interchanges and terminals were designed without much consideration to the needs, ergonomics and behavior of prospective passengers and public transport users. This research reports the first phase of the validation of data for the capturing of pedestrian behaviours at major interchanges. Applying the methods of video recording and manual passenger counting, the study used a case study of *Masjid Jamek* public transport interchange in Kuala Lumpur, to record and validate the pedestrian access and egress movements. This research aims at analyzing these empirical data to estimate these movements to estimate and calibrate the more appropriate models for improving pedestrian flows at these interchanges. Public transport operators and authorities may use the models to plan and design these nodes more effectively and ensure safety and security of passengers and users, especially during peak hours and irregular influx of trip making during seasonal holidays or major events.

Keywords: *Pedestrians, Public Transport Interchanges, Multimodal, Movements, Modelling*

INTRODUCTION

This study attempts at evaluating the movement characteristic of passenger in the interior space of a station building. The case study of a typical multimodal interchange facility, found in Kuala Lumpur, Malaysia, has been selected to represent commuting trip makings involving more than one modes of public transport.

Using the case study of *Masjid Jamek* Interchange, where passengers transferred from one light rail system to another, this research applied two types of data collection namely passenger counting and video recording. *Masjid Jamek* Interchange or station is located at the heart of the city, a busy and rapidly growing district in Kuala Lumpur. Major landuses are commercial, retails, businesses and financial.

In an urban centre, public transport plays an important role in transporting the passenger from one place to another. The services efficiency provided by the transit agencies has resulted in a high number of public transport ridership. Numbers of projects such as increasing train frequencies and capacities, upgrading the ticketing and information system, improving the station integration are conducted in order to meet the demand of users. In such improvements, transit agencies also take into account the circulation of passengers in station buildings. Heavy flows of people moving through station buildings especially during peak hours require careful planning during the design phase.

PROJECT BACKGROUND

The research aims at determining the pedestrian volumes and movement patterns in a crowded public transport interchange station. Kuala Lumpur, with a population of 2.1 million and a size of 243 km², is the capital of Malaysia. It is currently served by five main rail-based public transportation services, namely RAPIDKL systems (Ampang and Kelana Jaya Lines), Monorail system, KLIA Ekspres and KLIA Transit systems and the heavy rail KTM Komuter system (Figure 1).

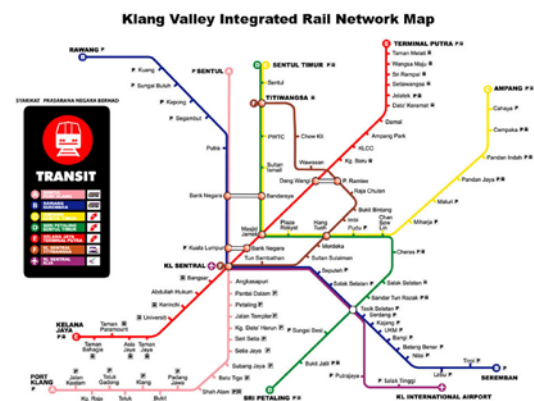


Figure 1: Kuala Lumpur rail network map (source: www.kuala-lumpur-rail-transit.com)

Previously, *Masjid Jamek* Station served as regular station between two separate lines, namely *Kelana Jaya Line* (KLJ Line) and *Ampang Line*

(AMG Line). However, passengers could not accomplish their transfer movement directly because of different ticketing system from both lines. Due to that, passengers who wanted to transfer between KLJ Line to AMG Line and vice versa needed to exit the paid area before completing their transfer activities (required to buy new ticket) to the next line.

Recently, in November 2011, the integration of ticketing system was implemented between KLJ Line and AMG Line to meet the demands of passengers and to encourage direct transfer activity. Integration of *Masjid Jamek* Station and ticketing system has resulted in direct paid to paid movement between KLJ Line and AMG Line. This requires some improvement towards the interior space of Masjid Jamek Interchange Station such as raising the floor level of existing Concourse 1 of AMG Line station; relocating of the ticketing counter of AMG Line Station and the new ticket gates. The changes of interior space of *Masjid Jamek* Station influenced the passengers' movement especially at the concourse area and have led to confusion among passengers. Hence, pedestrian movement in a crowded public transport interchange is an area less studied by scholars, particularly in Malaysia. There is a limited research on crowd movement issues, warranting a research such as this to be conducted.

Crowd Movement Study

Microscopic

Researchers [1], [2] & [3] highlighted that microscopic level refer to individual pedestrian behavior that exists in the crowd. Several behaviors such as collision avoidance and selecting the shortest path to the target are taken into account at this level.

Macroscopic

Meanwhile, macroscopic level is different from microscopic. It deals only with the general properties of the whole crowd such as flow and density, disregarding the interactions of an individual pedestrian with the environment and others [3]. Macroscopic models use the relation of density to walk speed and flow to calculate overall movements of the crowd.

Some attempts have been identified to have been lacked in modeling of the agent-based or disaggregated models of pedestrian movements in crowded places. In particular, limited studies have been focused on the comparison of peak and off-peak hours of commuting trips. It was also inconclusive as to how pedestrians' typological and physiological variations affected the speed and volume of movements in these places. Moreover, travelling speed from the point of origin towards the end destination could not be modeled appropriately

for case studies in developing cities due to the variations in buildings' or facilities' architectural designs, evacuation strategies and pedestrians' characteristics.

Safety issues in public transport interchange facility

A public transport interchange or transfer facilities are the first points of contact between the passengers and multimodal public transport services. The spacing, location, design, and operation of interchanges significantly influence the transit system performance and pedestrian movements. As a basic necessity for interchanges or transfer facilities, the design of these buildings or sections of buildings should fulfill certain parameters such as distance from origin/destination to the platforms and the walking time, whilst its physical conditions should be ergonomic and weather proof in design.

Entry and exit points location are crucial elements to improve the quality of interchanges. The determination of these points is an important aspect for operational consideration as the strategic and easily identified and accessible points will ensure a timely and systematic and smooth evacuation procedures, minimising the number of casualties and damages to properties. It should also be visible for pedestrians to identify exits or entry gates or turntiles for safety and must have the easy exit to the congregation areas and the criteria of comfort and convenient. In addition, these facilities should instill the feeling of safety and security among passengers, away from the fear of crime.

The use of cameras in determining and capturing the pedestrian movements, particularly in crowded areas is very common nowadays. There are so many issues related to the CCTV and real time cameras provided in the present practice of precautionary safety and security measures, these included that:

- i. In certain blind spots, two cameras maybe required to cover the varied movements of pedestrian entering and exiting the transfer facilities.
- ii. Capturing, digitising and separating the required frames for purposes of modelling, estimating and calibrating required great effort and longer time period.
- iii. The dataset such as speed, volume, direction and way finding behaviours may need to be confirmed and validated using another set of methods such as CCTV and pedestrian counting or observations.

PROBLEM STATEMENTS

The review of literature has established the following problem statements:

- i. There are inconsistent pedestrian behaviors in way finding especially during off-peak and peak hour of commuting in developing cities' interchanges facilities.
- ii. It is still unclear which primary factors influence the speed and movement of pedestrians in crowded situations such as during multimodal transfers activities.

RESEARCH QUESTIONS AND OBJECTIVES

Research questions raised from the above problem statements are:

- i. What are the pedestrian behaviours in way finding in especially during off-peak and peak hour of commuting in developing cities' interchanges facilities?
- ii. How best can the speed and movement of pedestrians in crowded situations such as during multimodal transfer activities be modelled?

The objectives are:

- i. To identify the pedestrian behaviours in way finding in interchanges facilities.
- ii. To evaluate the factors influencing speed and movement of pedestrians in crowded situations.

METHODOLOGY AND APPROACHES

This section will highlight the methods and approaches that were adopted in the study. The two methods applied in the study were video recording and manual passenger counting. Studies [4] and [5] illustrated that the significance video recording in pedestrian study provide many advantages such as the ability to represent the movement of pedestrians and the variables interactions in real time.

Three types of primary data were collected for the modelling exercise. First, three cameras were set up at different points in the stations to capture real time movement of the pedestrians. Second, passengers or pedestrian counts were conducted on the selected days and time period. Finally, stations' and interchange facilities' layout designs were hand-drawn to identify possible routes, entry and exit areas as well as potential conflicts and collision points. Secondary data collected through the recordings of CCTV and computer-aided designed/drawn stations and facilities layout were to reinforce and reconfirm the following variables:

- i. passenger' travelling speed (meter/second),
- ii. Passengers' typological and physiological attributes,

- ii. Variation in peak and off-peak passenger volumes, and
- iv. Travel distance between entrance and exit points (in meter).

Three cameras were set at strategic locations to capture passengers' or pedestrians' movements. During the site appraisal, several blind spots were identified.

Due to mobility and logistics reasons, several limitations during the surveys have been overridden by increasing the number of equipments and personnel in charge as enumerators. Enumerators were assigned to record the pedestrian counts using traffic counters.

The camera setting activities were undertaken during the weeks of 27th December 2012 (Thursday) until 14th January 2013 (Monday). Pilot survey of pedestrian count and pedestrian movement observation were also conducted during this period. Pedestrian counts were carried out during the week beginning 18th February until 22nd February 2013.

Video Recording of Pedestrian Activities

During the pilot study, video recording has been performed to identify the strategic points for locating recording equipments. This was important to ensure the installed video cameras covered all the section of the study area and high data accuracy can be ensured. Figures 2 through to 5 show the location of cameras and the recorded angles.

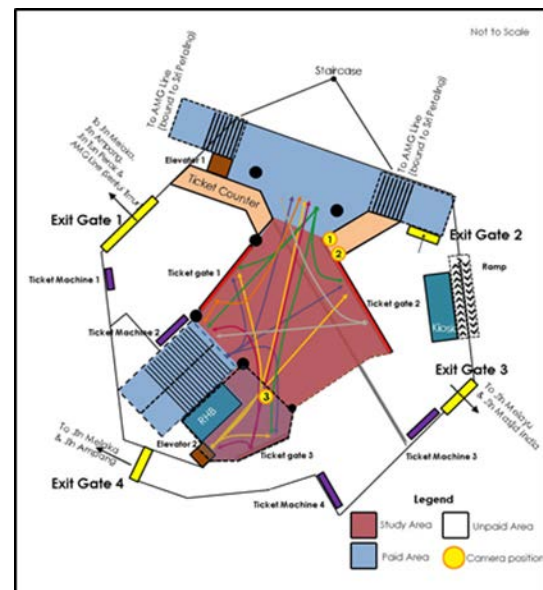


Figure 2: Three points are identified for video camera installation.

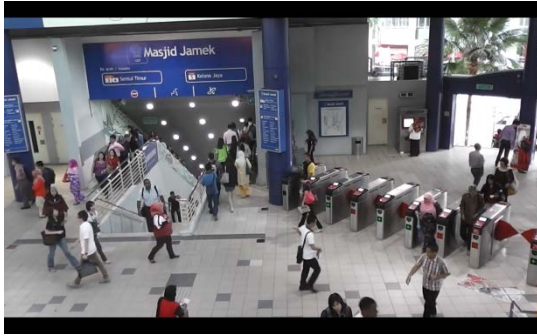


Figure 3: Recorded angle from Camera 1.



Figure 4: Recorded view from Camera 2



Figure 5: The view from Camera 3 location with enumerators, positioned at strategic points in the interchange facility, were capturing the pedestrian movement by the utilization of traffic counters.

Passenger Counting

Passenger counting was also performed in this study. It was one of the manual count methods in pedestrian study [4]. The manual counts bring huge benefits towards the study, for example providing large set of necessary data (i.e. age, gender, physical attributes and behavior). Further, manual counts also could capture and gather significant data such as classifying volumes and recording observations [4].

The passenger counting survey required a large number of enumerators. They were located mainly at the ingress and egress points of the concourse area (Figure 6). Their task was to count the number of passengers passing the ingress and egress point based on gender, physical attributes and age. Enumerators are equipped with mechanical counter

and survey forms. Passenger number were recorded and transcribed into the forms. The lapse intervals were set to 5 minutes so as to evaluate variations in the data. The collection of field data was made for sample length of 7 hours per during both peak and off peak periods for comparison purpose.

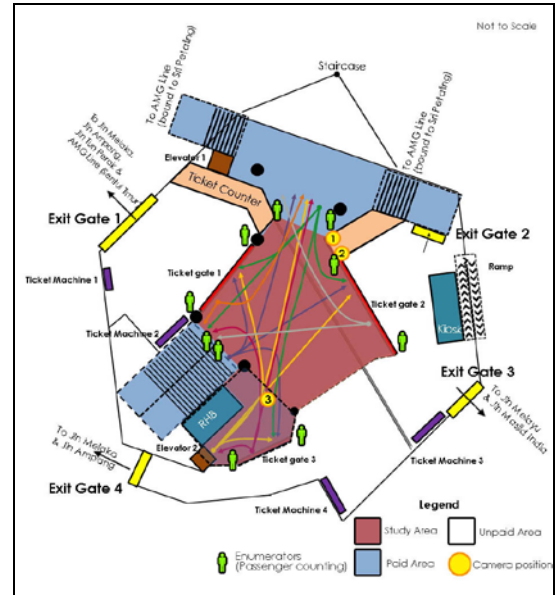


Figure 6: Position of enumerators in Masjid Jamek Interchange Station.

Sampling

The sample size was selected from movement of one direction i.e. from point O-D at 7.15 am to 7.45 am. Figure 7 shows the direction of movements from O (escalator and staircase) to D (ticket gates).

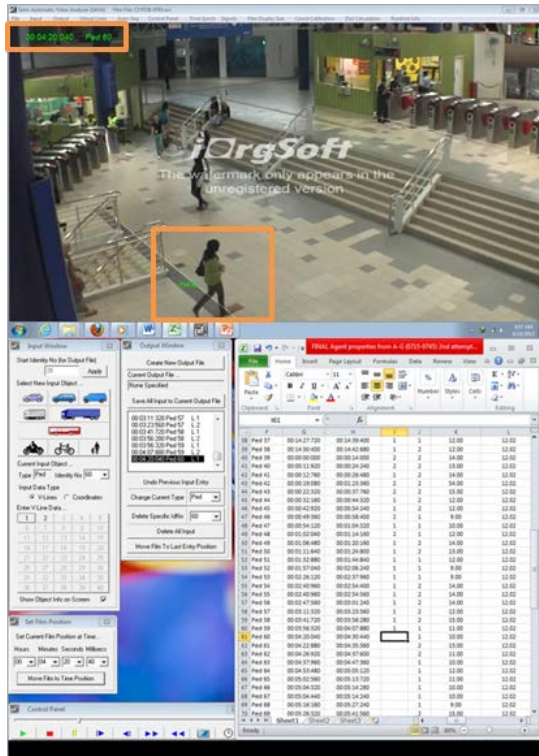


Figure 7: Movement direction of passenger from escalator/elevator (point O) to ticket gates (point D).

Performing Video Analysis and Speed Capture

A video analysis phase was carried out in Semi-Automated Video Analysis (SAVA) program. Then video analysis was performed on the segmented frames to determine the agent's gender, physical attribute, age, familiarity, travel time and walk

speed. Figures 8 and 9 show the process of video analysis.



In Figure 8, the orange boxes indicate the labeled pedestrian number and the starting time. For example, the pedestrian labelled 60 was a female and she reached the first line at 00:04:20:040.

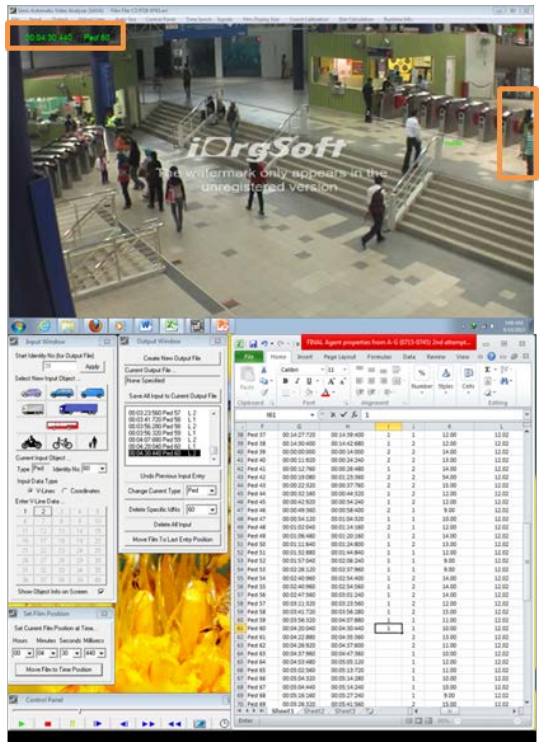


Figure 9: Pedestrian numbered 60 has reached the second line at 00:04:30:440.

DATA ANALYSIS

Based on the manual counting data, it was found that there were 35 males, 68 females and one physically impaired pedestrian traveling from point O-D between 7.15am and 7.45am. The highest number of passenger moving from point O-D was between 7.30am -7.35am. Within this time interval, the total number of passenger moving from O-D was 33. In the tabulated data, females walked at slower speed to reach the destination points, ranging from 0.22 meter/second to 1.34 meter/second. Meanwhile, male pedestrians walked slightly faster, ranging from 0.75 meter/second to 1.5 meter/second.

Several attempts at modeling the agent-based movement have been carried out. Two of the alternative models were estimated in Tables 1 and 2.

Table 1: Regression Analysis Output 1

Variables	Regression Statistics		
	Coefficient	T-statistics	p-value
Constant	1.07841	14.0719	0.0001
Gender	-0.0292	-0.6558	0.5134
Physical Attributes	-0.1732	-0.7986	0.4263
Familiarity	-0.2951	-9.4991	0.0001
Directional Movement	-0.1254	-2.5282	0.0129

Table 2: Multiple Regression Analysis Output 2

Variables	Regression Statistics		
	Coefficient	T-statistics	p-value
Constant	1.8214	10.1464	0.0001
Gender	-0.1067	-3.3503	0.0011
Physical Attributes	-0.0877	-0.5761	0.5658
Familiarity	-0.3079	-9.9916	0.0001
Directional Movement	-0.0647	-1.8052	0.0740

From the tables, the estimated models have r^2 values ranging from 0.47 to 0.54 indicating a

moderate relationship between the combinations of parameters in determining the speed of pedestrian.

The estimations have also indicated that at 95% confidence level, factors such as familiarity with the station layout and facilities, walking pattern or directional movements and gender may influence the speed of travel from the escalators to the ticketing exit gates and from the ticketing entry gates to the escalators.

DISCUSSION AND CONCLUSION

The safety levels in an interchange can be influenced by the transfer facilities' layout design, the locational distribution of the facilities, entry and exit points as well as pedestrians' movement speed from an entry point to an exit point.

This research has employed a combination of camera, CCTV and manual pedestrian counts to identify pedestrian movement and speed in a crowded rail station where users transferred from one rail mode to another. The use of cameras, CCTV, and manual counts were not without their drawbacks. Analyzing the videos recording also proved to have posed some challenges to the research team.

Accuracy and validity of the research data depended very much on the methodology adopted for this research. The moderate correlations between the speed and factors influencing the movement of pedestrian have been explained in the previous sections. In essence, gender, familiarity with the stations or interchanges facilities and directional movements of pedestrian indeed determined the levels of speed with which passengers can ensure their safe and smooth transfer from one mode to another.

This research is limited, however, by the interpretation of physiological attributes of the pedestrians including the height, shoulder width and personal characteristics.

Based on the estimation carried out, the following conclusions can be drawn:

- i. To reach the exit and assembly points within 2 minutes of an emergency situations, the distance from the escalator should not be more than 150 meters, while ensuring 95% of passengers to be evacuated safely and smoothly.
- ii. During crowding and evacuation activities, pedestrians such as females, those who are unfamiliar with the station layout design and those who has lesser

tendency of walking systematically in a group should be properly guided and assisted by evacuation or emergency personnel to congregation areas.

This research has attempted to model pedestrian movements in a crowded interchange facility, with the aim of minimizing the impacts of safety and increasing the smooth and systematic evacuation strategy during an emergency. The models estimated can be of great use to operators and other stakeholders so as to increase the safety levels and ensure security is kept at the highest level possible. In the era where safety and security threats have also impacted and effected public transportation operations, safeguarding the pedestrians and preventing an emergency should always be first considered in designing and planning of public transport transfer infrastructure and facilities.

ACKNOWLEDGEMENTS

The authors would like to express their gratitude to Research & Development Division of *Syarikat Prasarana Negara Berhad* for their assistance, advice and resources rendered during the undertakings of this research project.

REFERENCES

- [1] Steenbakkens J. and Van der Weij S. (2010), *Pedestrian Logistics Simulation– Crowd Management in Stadiums*, Gert Zülch & Patricia Stock (Hrsg.) Karlsruhe, KIT Scientific Publishing
- [2] Sarmady S. (2008), *Modelling and Simulation of Movements and Behaviours in Large Crowd Using Cellular Automata*
- [3] Burger M., Markowich P., Pietschmann J. F. (n.d), *Continuous Limit of a Crowd Motion and Herding Model: Analysis and Numerical Simulations*
- [4] Miranda and Carrasco, 2011, "Pedestrian Volume Studies: A case study in the city of Gothenburg", Department of Civil and Environmental Engineering, Chalmers University of Technology.
- [5] Teknomo K, Takeyama Y, and Inamura H., 2000, data collection method for pedestrian movement variables. Jurusan Teknik Sipil, Fakultas Teknik Sipil dan Perencanaan – Universitas Kristen Petrra
- [6] <http://www.spad.gov.my>
- [7] [http:// www.kuala-lumpur-rail-transit.com](http://www.kuala-lumpur-rail-transit.com)

ASSESSMENT OF CHROMIUM CONTAMINATION IN SEDIMENTS OF SOUTHERN KAOHSIUNG HARBOR, TAIWAN

Cheng-Di Dong¹, Chih-Feng Chen¹ and Chiu-Wen Chen¹

¹ Department of Marine Environmental Engineering, National Kaohsiung Marine University, Kaohsiung 81157, Taiwan, ROC

ABSTRACT

Major objectives of this study are to evaluate the enrichment, accumulation, and potential ecological risk of chromium (Cr) in the surface sediments of southern Kaohsiung Harbor, Taiwan. Twelve sampling locations were installed of southern Kaohsiung Harbor to collect sediment samples for analyzing Cr. Results showed that the Cr concentrations varied from 13.4–265.7 mg/kg with an average of 53.2 ± 71.2 mg/kg. The spatial distribution of Cr reveals that the Cr concentration is relatively high in the river mouth region, especially in Jen-Gen River, and gradually diminishes toward the harbor entrance region. This indicates that upstream industrial and municipal wastewater discharges along the river bank are major sources of Cr pollution. Results from the enrichment factor and geo-accumulation index analyses imply that the sediments collected from the river mouth can be characterized between severe and very severe degree enrichment and between moderately strong and strong to very strong accumulation of Cr, respectively. However, results of potential ecological risk index indicate that the sediment has low ecological potential risk.

Keywords: Accumulation, Chromium, Ecological Risk, Enrichment, Sediment.

INTRODUCTION

Chromium (Cr) is moderately toxic to aquatic organisms; its presence threatens the water ecological environment. [1]. Therefore, much research effort has been directed toward the distribution of Cr in water environment. Anthropogenic activities including tanning, mining, smelting, domestic and industrial wastewaters, steam electrical production, and sewage sludge are the major source of Cr pollution [1,2]. In receiving water body, Cr is presented essentially as hydroxy-complexes of low solubility associated with the water-borne suspended particles [3,4]. After a series of natural processes, the water-borne Cr finally accumulates in the sediment, and the quantity of Cr contained in the sediment reflects the degree of pollution for the water body [5].

Kaohsiung Harbor is located on the southwestern shore, and it is the largest international harbor in Taiwan. the harbor receiving effluents from four contaminated rivers, including Love River, Canon River, Jen-Gen River, and Salt River. Results of previous research indicate that the Kaohsiung Harbor is heavily polluted with Cr, and the Jen-Gen River and Salt River are both major pollution sources [6]. The two rivers flow through the downtown area of Kaohsiung City and finally discharged into Kaohsiung Harbor (Fig. 1). The major pollution source includes domestic wastewater discharges, industrial wastewater discharges (e.g. tanning, metal processing, chemical production,

electronic and foundry), municipal surface runoff, and transportation pollution [6]. All the pollutants will eventually be transported to the river mouth and/or harbor to deposit and accumulate in the bottom sediment.

The objective of this study is to investigate the Cr distribution in the surface sediment of the water body between river mouths (i.e., Jen-Gen River and Salt River) and harbor entrance of Kaohsiung Harbor so that the degree of Cr enrichment, accumulation, and potential ecological risk can be evaluated.

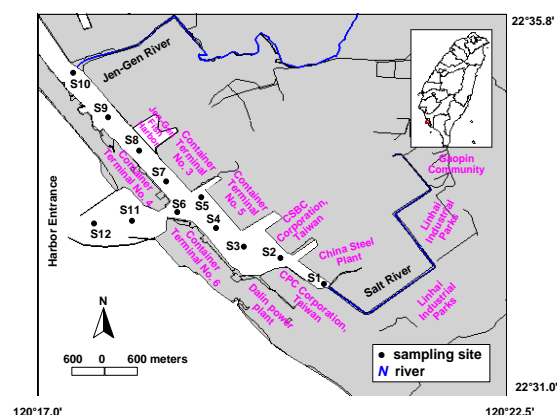


Fig. 1 Map of the study area and sampling locations.

MATERIALS AND METHODS

Twelve sampling stations were distributed in southern Kaohsiung Harbor, Taiwan (Fig. 1). Surface sediment samples were collected at 12 stations selected in this study in February, 2011 with Ekman Dredge Grab aboard a fishing boat. The collection, pre-processing and analysis program of sediment sample have been detailed previously [7,8]. The collected samples were characterized for aluminum (Al), chromium (Cr), grain size, water content, and organic matter (OM). The Al and Pb contents were determined using a flame atomic absorption spectrophotometry (Hitachi Z-6100, Japan) after digestion procedures [7,8]. The sediment grain size was measured using a Coulter LS Particle Size Analyzer; water contents were determined by oven-drying at 105°C; OM was determined using the LOI (loss-on-ignition) method at 550°C. The characteristics of sediment (e.g. grain size, water content, and OM) have been reported in detail previously [8].

RESULTS AND DISCUSSION

Distribution of Chromium in Sediments

All surface sediment samples collected at 12 monitoring stations studied contain 13.4–265.7 mg/kg with an average of 53.2 ± 71.2 mg/kg. Spatial distributions of Cr concentration in the surface sediment shown in Fig. 2 reveal that the sediment Cr content is relatively higher near the mouths of Jen-Gen River (site 10), and Salt River (site 1), and gradually decreases in the direction toward the mouth of harbor (sites 11 and 12). These observations clearly indicate that the upstream pollutants brought over by rivers are the major source of harbor Cr pollution. The both rivers receive a great amount of industrial and domestic Cr from Kaohsiung city because about 40% domestic wastewater is discharged directly without adequate treatment [6]. Moreover, several industrial plants (e.g. metal processing, paint and dye, chemical manufacturing, electronic, motor vehicle plating and finishing, and foundries) discharge industrial wastewater effluents into the tributaries in or adjacent to Kaohsiung city, and the pollutants are transported by river flow and finally accumulate near the river mouth. Some pollutants may drift with sea current to be dispersed into open sea [6].

The Pearson correlation between the sediment characteristics and Cr content was carried out. The surface sediment Cr content is not obviously correlated to OM content ($p > 0.05$) and particle size ($p > 0.05$). However, based on the 11 sites, except site 10, the significant correlation ($r = 0.920$, $p < 0.01$) between Cr and organic matter content was found (Fig. 3). The results suggest that the sediment organic matter played an important role in controlling the Cr distribution in sediments, whereas

pollution source can influence the partition of Cr in sediment organic matter.

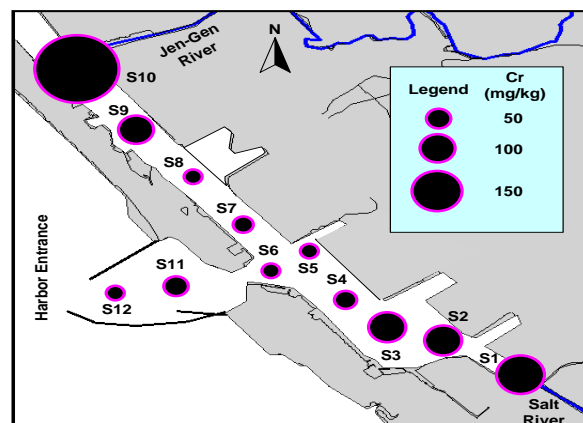


Fig. 2 Spatial distribution of chromium (Cr) contents in the surface sediment of southern Kaohsiung Harbor.

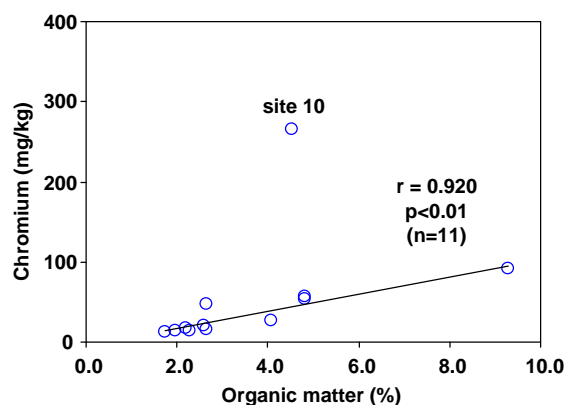


Fig. 3 Correlation between the organic matter and Cr content in the surface sediment of southern Kaohsiung Harbor (except site 10).

Comparison with Sediment Quality Guidelines

Several numerical sediment quality guidelines have been developed for assessing the contamination levels and the biological significance of chemical pollutants recently [9,10]. One of the widely used sediment toxicity screening guideline of the US National Oceanic and Atmospheric Administration provides two target values to estimate potential biological effects: effects range low (ERL) and effect range median (ERM) [10]. The guideline was developed by comparing various sediment toxicity responses of marine organisms or communities with observed metals concentrations in sediments. These two values delineate three concentration ranges for each particular chemical. When the concentration is below the ERL, it indicates that the biological effect is rare. If concentration equals to or greater than the

ERL but below the ERM, it indicates that a biological effect would occur occasionally. Concentrations at or above the ERM indicate that a negative biological effect would frequently occur. Fig. 4 shows the measured concentrations of Cr in comparison with the ERM and ERL values. Among the 12 sediment samples collected, the Cr is between ERL (81 mg/kg) and ERM (370 mg/kg) in 2 samples. This indicates that the sediment concentrations of Cr found in sites 1 and 10 may cause adverse impact on aquatic lives. All other samples are below ERL for Cr indicates that biological effects would rarely occur.

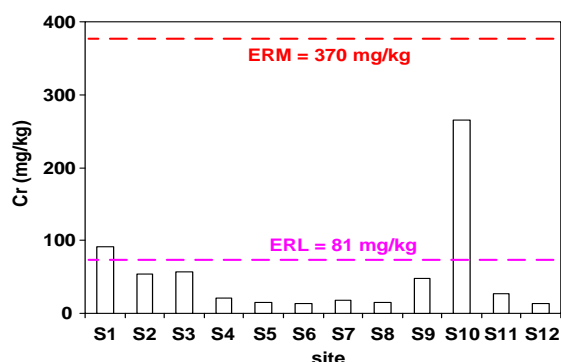


Fig. 4 Distribution of chromium (Cr) contents in the surface sediment of southern Kaohsiung Harbor.

Enrichment Factor

The enrichment factor (EF) is a good tool for differentiating the man-made and natural sources of metal contamination [6,11]. This evaluating technique is carried out by normalizing the metal concentration based on geological characteristics of sediment. Aluminum is a major metallic element found in the earth crust; its concentration is somewhat high in sediments and is not affected by man-made factors. Thus, Al has been widely used for normalizing the metal concentration in sediments [6,11]. EF is defined as: $EF = (X/Al)_{\text{sediment}} / (X/Al)_{\text{crust}}$, where (X/Al) is the ratio of Cr to Al. The average Cr and Al content in the earth crust were 100 mg/kg and 8.23%, respectively, which excerpted from the data published by Taylor (1964) [12]. When the EF of a metal is greater than 1, the metal in the sediment originates from man-made activities, and vice versa. The EF value can be classified into 7 categories [13]: 1, no enrichment for $EF < 1$; 2, minor for $1 < EF < 3$; 3, moderate for $3 \leq EF < 5$; 4, moderately severe for $5 \leq EF < 10$; 5, severe for $10 \leq EF < 25$; 6, very severe for $25 \leq EF < 50$; and 7, extremely severe for $EF \geq 50$.

Table 1 show EF values of the sediment Cr for 12 monitoring stations studied; the Cr concentration is consistent with the Cr EF value for

all sampling stations, and EF values in the river mouths of Jen-Gen River (site 10) and Salt River (sites 1-3) are greater than 1. This indicates that the sediment Cr has enrichment phenomenon with respect to the earth crust and that the Cr originates from man-made sources. Sites 1-3 are classified as minor enrichment, site 10 is classified as moderate enrichment, and the other sites are classified as no enrichment, respectively. These results point out that the sediment near the mouth of rivers experiences minor to moderate enrichment of Cr that originates from the upstream sources of pollution. Additionally, the average EF value of 4.5 obtained in site 10 (Jen-Gen River mouth) is lower than the average EF value of 8.4 reported earlier [11] indicating that the upstream pollution has been reduced so that the accumulation of pollutants in sediments is not as serious as during earlier years. This observation may show the effectiveness of intercepting the river flow and dredging the river mouth.

Table 1 Enrichment factor of Cr for each station studied at southern Kaohsiung Harbor

Site	EF value	EF class	EF level
S1	1.4	2	minor
S2	1.1	2	minor
S3	1.1	2	minor
S4	0.4	1	no enrichment
S5	0.3	1	no enrichment
S6	0.3	1	no enrichment
S7	0.3	1	no enrichment
S8	0.3	1	no enrichment
S9	0.9	1	no enrichment
S10	4.5	3	moderate
S11	0.5	1	no enrichment
S12	0.3	1	no enrichment

^a 1: $EF < 1$ (no enrichment), 2: $1 < EF \leq 3$ (minor), 3: $3 < EF \leq 5$ (moderate), 4: $5 < EF \leq 10$ (moderately severe), 5: $10 < EF \leq 25$ (severe), 6: $25 < EF \leq 50$ (very severe), and 7: $EF \geq 50$ (extremely severe) [13].

Geo-accumulation Index

Similar to metal enrichment factor, geo-accumulation (I_{geo}) index can be used as a reference to estimate the extent of metal accumulation. The I_{geo} values for the metals studied were calculated using the Muller's (1979) [14] expression: $I_{\text{geo}} = \log_2 (C_n / 1.5B_n)$, where C_n is the measured content of element Cr, and B_n is the background content of Cr 100 mg/kg, in the average shale [6]. Factor 1.5 is the background matrix correction factor due to lithogenic effects. The I_{geo} value can be classified into 7 classes: 0, none for $I_{\text{geo}} < 0$; 1, none to medium for $I_{\text{geo}} = 0-1$; 2, moderate for $I_{\text{geo}} = 1-2$; 3, moderately strong for $I_{\text{geo}} = 2-3$; 4, strong for $I_{\text{geo}} = 3-4$; 5, strong to very strong for $I_{\text{geo}} = 4-5$; and 6,

very strong for $I_{geo} > 5$. Based on the I_{geo} data and Muller's (1979) [14] geo-accumulation indexes, the accumulation levels with respect to Cr at each site are ranked in Table 2. Site 10 is classified as none to medium accumulation, and all other sites are classified as none accumulation.

Table 2 Geo-accumulation (I_{geo}) index of Cr for each station studied at southern Kaohsiung Harbor

Site	I_{geo} value	I_{geo} class	I_{geo} level
S1	-0.7	0	none
S2	-1.5	0	none
S3	-1.4	0	none
S4	-2.9	0	none
S5	-3.4	0	none
S6	-3.5	0	none
S7	-3.1	0	none
S8	-3.3	0	none
S9	-1.7	0	none
S10	0.8	1	none to medium
S11	-2.5	0	none
S12	-3.4	0	none

^b 0: $I_{geo} < 0$ (none), 1: $I_{geo} = 0-1$ (none to medium), 2: $I_{geo} = 1-2$ (moderate), 3: $I_{geo} = 2-3$ (moderate to strong), 4: $I_{geo} = 3-4$ (strong), 5: $I_{geo} = 4-5$ (strong to very strong), and 6: $I_{geo} > 5$ (very strong) [14].

Potential Ecological Risk

The potential ecological risk index (PERI) is applied to evaluate the potential risk associated with the accumulation of Cr in surface sediments. PERI that was proposed by Hakanson (1980) [15] can be used to evaluate the potential risk of one metal or combination of multiple metals. The PERI is defined as [15]: $PERI = PI \times T_i$, where PI (pollution index) = (C_i/C_f) ; C_i is the measure concentration of Cr in sediment; C_f is the background concentration of Cr; T_i is its corresponding coefficient, i.e. 2 for Cr [15]. In this study, the average Cr concentration in earth crust of 100 mg/kg Taylor (1964) [11] was taken as the Cr background concentration. The calculated PERI values can be categorized into 5 classes of potential ecological risks [15]: low risk ($PERI < 40$), moderate risk ($40 \leq PERI < 80$), higher risk ($80 \leq PERI < 160$), high risk ($160 \leq PERI < 320$), and serious risk ($PERI \geq 320$). Table 3 lists the PI value, PERI value, and risk classification for the Cr contained in the surface sediment samples collected in this study. All stations are classified as low risk with respect to Cr pollution. The above evaluation results indicate that the Cr contained in surface sediments at the study area has low potential ecological risks. However, the PERI value near the river mouth of sites (sites 1–3 and 10) are higher than other sites (Table 3).

Table 3 Potential ecological risk index of Cr for each station studied at southern Kaohsiung Harbor

Site	PI	PERI	Risk level
S1	0.9	1.8	low
S2	0.5	1.1	low
S3	0.6	1.1	low
S4	0.2	0.4	low
S5	0.1	0.3	low
S6	0.1	0.3	low
S7	0.2	0.4	low
S8	0.2	0.3	low
S9	0.5	0.9	low
S10	2.7	5.3	low
S11	0.3	0.5	low
S12	0.1	0.3	low

^c $PERI < 40$ indicates low risk, $40 \leq PERI < 80$ is moderate risk, $80 \leq PERI < 160$ is higher risk, $160 \leq PERI < 320$ is high risk, and $PERI \geq 320$ is serious risk [15].

CONCLUSIONS

The surface sediment samples collected from the southern Kaohsiung Harbor contain 3.4–265.7 mg/kg with an average of 53.2 ± 71.2 mg/kg. The distribution of Cr in surface sediments reveals that the Cr originates from the river upstream discharges of industrial and domestic wastewaters; it is transported along the river and finally deposited and accumulated near the river mouth. Results from the EF and I_{geo} analyses imply that the sediments collected from the river mouth can be characterized between minor and moderate degree enrichment and between none to medium accumulation of Cr, respectively. Compared to the EF values reported earlier [4], the degree of Cr enrichment at the Jen-Gen river mouth has been obviously reduced. Based on the comparison with SQGs, the concentrations of Cr in the mouths of Jen-Gen River and Salt River sediments may cause acute biological damage. Results of PERI evaluation show that the Cr contained in surface sediment at southern Kaohsiung Harbor has low potential ecological risks. The results can provide regulatory valuable information to be referenced for developing future strategies to renovate and manage river mouth and harbor.

REFERENCES

- [1] Callender E, "Heavy metals in the environment: historical trends", Treatise on Geochemistry, Holland HD, Turekian KK, Eds. New York: Elsevier, 2003, pp. 67–105.
- [2] Pertsemli E, Voutsas D, "Distribution of heavy metals in Lakes Doirani and Kerkini, Northern

- Greece”, *J. Hazard. Mater.*, Vol. 148, 2007, pp. 529–537.
- [3] Kotaś J, Stasicka Z, ” Chromium occurrence in the environment and methods of its speciation”, *Environ. Pollut.*, Vol. 107, 2000, pp. 263–283.
- [4] Pawlikowski M, Szalińska E, Wardas M, Dominik J, “Chromium Originating from Tanneries in River Sediments: a Preliminary Investigation from the Upper Dunajec River (Poland)”, *Pol. J. Environ. Stud.*, Vol. 15, 2006, pp. 885–894.
- [5] Selvaraj K, Ram-Mohan V, Szefer P, “Evaluation of metal contamination in coastal sediments of the Bay of Bengal, India: geochemical and statistical approaches”, *Mar. Pollut. Bull.*, Vol. 49, 2004, pp. 174–185.
- [6] Chen CF, Dong CD, Chen CW, “Evaluation of sediment toxicity in Kaohsiung Harbor, Taiwan”, *Soil. Sediment. Contam.*, Vol. 22, 2013, pp. 301–314.
- [7] Chen CW, Chen CF, Dong CD, “Distribution and accumulation of mercury in sediments of Kaohsiung River Mouth, Taiwan”, *APCBEE Procedia*, Vol. 1, 2012, pp. 153–158.
- [8] Dong CD, Chen CF, Chen CW, “Evaluation of mercury contamination in surface sediments of southern Kaohsiung Harbor, Taiwan”, *Adv. Mater. Res.*, Vol. 716, 2013, pp. 459–464.
- [9] Riba I, Casado-Martínez MC, Forja JM, delValls TA, “Sediment quality in the Atlantic coast of Spain”, *Environ. Toxicol. Chem.*, Vol. 23, 2004, pp. 271–282.
- [10] Long ER, Macdonald DD, Smith SL, Calder FD, “Incidence of adverse biological effects within ranges of chemical concentrations in marine and estuarine sediments”, *Environ. Manage.*, Vol. 19, 1995, pp. 81–97.
- [11] Chen CW, Kao CM, Chen CF, Dong CD, “Distribution and accumulation of heavy metals in the sediments of Kaohsiung Harbor, Taiwan”, *Chemosphere*, Vol. 66, 2007, pp. 1431–1440.
- [12] Taylor SR, “Abundance of chemical elements in the continental crust: a new table”, *Geochem. Cosmochim. Acta*, Vol. 28, 1964, pp. 1273–1285.
- [13] Birth G, “A scheme for assessing human impacts on coastal aquatic environments using sediments” In: Woodcoffe CD, Furness RA, Eds. *Coastal GIS 2003*, Wollongong University Papers in Center for Maritime Policy, 14, Australia. 2003.
- [14] Müller G, “Die Schwermetallbelastung der sedimente des Neckars und seiner Nebenflüsse: Eine Bestandsaufnahme“, *Chemiker Zeitung*, Vol. 105, 1981, pp. 157–164.
- [15] L. Hakanson, “An ecological risk index for aquatic pollution control. a sedimentological approach”, *Water Res.*, Vol. 14, 1980, pp. 975–1001.

GPS/GIS IDENTIFICATION OF POTENTIAL BUS STOP LOCATIONS AND PASSENGER'S ACCESS AND EGRESS POINTS

Syahriah Bachok¹, Zakiah Ponrohono¹, Mariana Mohamed Osman¹, Zulfadly Azizi Bohari¹

¹ Kulliyah of Architecture and Environmental Design, International Islamic University Malaysia

ABSTRACT

This research reports the study of identification and determination of bus stop locations and passengers boarding and alighting positions through the application of Global Positioning System (GPS) and Geographical Information System (GIS) methods. Previously, the locations of bus stop were designed without much consideration to the access and egress points of prospective passengers and other users. Using the case study of public bus operation in Kerian, Perak, a district in Malaysia, GPS method captured the locational points during on-board surveys while the GIS method produced the points mapping. As a result, the possible bus stop locations can be recorded and validated based on the passengers access and egress points and volume patterns. This research aims to analyse these empirical data to estimate the possible location of new bus stops within certain distance ratios. From this findings, public bus operators and authorities can determine/allocate/distribute the bus stop locations that may reduce the waiting time.

Keywords: GIS mapping, GPS points, Bus stop, passengers access, passengers egress

INTRODUCTION

This paper deals with the application and implementation of Geographic Information and Global Positioning System in the identification and determination of bus stop locations and passengers boarding and alighting positions. This research is funded partially by the Government of Malaysia, State of Perak. The case study has been selected to be a district in Perak, a state still rapidly experiencing economic and social growths, to achieve its development mission by 2015. District of Kerian, Perak has a population of approximately 180,340 people, with a density of 7 people per km².

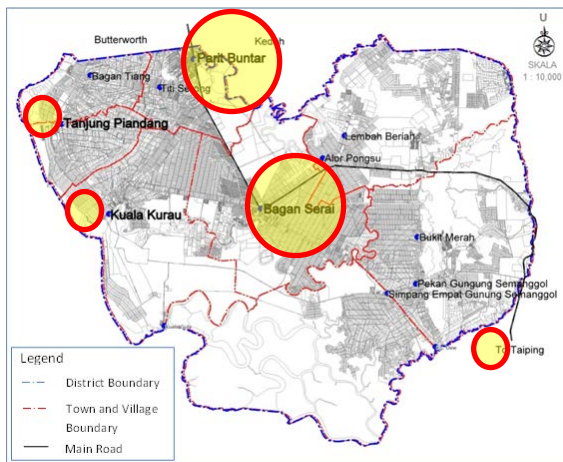


Figure 1: Kerian District

District of Kerian (Figure 1) is located in the State of Perak Darul Ridzuan. In the north are Penang and Kedah states. In the east and south, Kerian borders

with Larut, Matang and Selama districts; and in the west is the Strait of Malacca. The uniqueness of this case study is that the public transport routes plies through the Kerian River which is the borderline of three states namely Penang, Kedah and Perak. There are eight (8) sub-districts under the administration of Kerian District Council: Parit Buntar, Bagan Tiang, Tanjung Piandang, Kuala Kurau, Bagan Serai, Beriah, Gunung Semanggol and Selinsing [13 and 14].

Kerian has a good road and highway network. The network stretches approximately 225.0 km and connects the eight sub-districts. The main north-south road that cuts through this district is Ipoh-Butterworth road. Kerian District road is accessible from Kampung Dew, Simpang Ampat, Changkat Lobak and Kuala Kurau. The major town is Parit Buntar that is located at the border of Penang and Kedah. As the district has a large commercialized agricultural area with ample buildings and facilities, Kerian contributes to Perak's economics growth and capital generation, with a 5.7% GDP growth rate in 2012 [13 and 14].

LITERATURE REVIEW

Transportation planning is an art and science of arranging the transportation infrastructure and facilities according to suitability and appropriateness of the distribution basing on the population and socio-demographic needs of the locality. It deals largely with issues and problems encountered by transportation services, operation, infrastructure and

facilities, as highlighted by the contemporary literature.

Public transportation system includes all multiple occupancy vehicles services designed to transport people/customers on local and regional routes and their sub-systems. The systems include vans, buses, taxis, or rails or other conveyance, privately or publicly owned, providing their services to the public general or segmented group of users. Generally, the public transportation system in Malaysia comprises bus, railway and taxi services and plays a significant role in finding solutions to the numerous challenges. Whether it is more jobs, a cleaner environment, higher energy independence or a better quality of life, public transportation gets the right to be included [9, 10 and 11].

A more sustainable future can be promoted when more trips are made by public transport modes as it will reduce the number of trips made by private vehicles, leading to less congestion on the roads and a more efficient road system. Apart from that, efficient public transportation services enhance personal opportunities, save fuel, provide economic opportunities, save money and reduces carbon footprint [5]. It will contribute towards rapid economic growth and healthy social development of a city. However, there are a number of issues relating to public transportation services such as the limitation of facilities, the use of low quality of public transport facilities and interchanges, inconvenience of fleet, low passenger trips and long waiting time [8].

All public transport demand will relate to what the operators can offer to the passengers such as route frequency, availability and affordability. Additionally, the demand also depended on the facilities and accessibility to the bus stop [1]. A bus stop is the first point of contact between the passengers and the bus services. The spacing, location, design, and operation of bus stops significantly influence the transit system performance and customer satisfaction. As a basic necessity for public bus service, the design of bus stop location should fulfill certain parameters such as distance from origin/destination point to the bus stop and the walking time, its physical conditions should be ergonomic and weather proof [1].

The consideration of bus stops location is an important aspect for operational purposes as the strategic location of bus stop will ensure a comprehensive coverage and easy accessibility to all categories of users [7]. Bus stops should also be visible for users. Safety and easy access to the servicing buses are essential. Bus stops must fulfill the criteria of comfort and convenience. Moreover,

bus stop keep passengers away from the fear of crime [1]. There are various issues relating to the bus stop location provided in the current public transportation services, [3] including that:

- I. In certain areas, two bus stops maybe are closely located resulting depletion of resources.
- II. In other areas the bus stops are sparsely sited forcing the people to walk far distances or to take other modes of transport to reach their destinations.
- III. Some bus stop locations are found to be hazardous, posing danger to other vehicles and may also cause traffic congestion.

One method to locate the best location of bus stop is by applying Geographic Information Systems (GIS). GIS also offers a better solution in overcoming the above issues. The use of GIS in determining and planning the public transport facilities particularly bus stop location is very common nowadays [2]. This approach to locate the bus stop will help in modelling preferred solutions to different forms of spatial issues [3]. In short, the review of literature has established the following problem statements:

- i. There are inconsistent hierarchy, operation systems and supply-demand gaps of bus services in Kerian District.
- ii. Bus stops locations and passengers' pick-up and drop-off points in Kerian District have not been clearly identified for policy making and implementation purposes.

RESEARCH QUESTIONS AND OBJECTIVES

Research questions arising from the above problem statements are:

- i. What are the hierarchy, operation systems and supply-demand gaps of bus services in Kerian District?
- ii. How best can bus stops locations and passengers' pick-up and drop-off points in Kerian District be identified for policy making and implementation purposes?

The objectives are:

- i. To identify the existing of hierarchy, operation systems and supply-demand gaps of bus provided in Kerian District.
- ii. To evaluate possibility of determining bus stops locations and passengers' pick-up and drop-off points in Kerian District using geographical information and geo-positioning systems.

In order to provide convenient bus services, some performance indicators such as bus operation characteristics were analysed to determine the

effectiveness of the bus service [8]. These performance measurements are known as levels of services or LOS and the variables of measurement are shown in the Table 1 and 2:

Table 1: Fixed-route Service Frequency LOS

LOS	Average Headway (min)	Vehicle per hour	Comments
A	<10	>6	Passengers do not need schedules
B	10-14	5-6	Frequent service, passengers consult schedules
C	15-20	3-4	Maximum desirable time to wait if bus/train missed
D	21-30	2	Service unattractive to choice riders
E	31-60	1	Service available during the hour
F	>60	<1	Service unattractive to all riders

Table 2: Fixed-route Hour of Service LOS

LOS	Hours of service	Comments
A	19-24	Night 'owl' service provided
B	17-18	Late evening service provided
C	14-16	Early evening service provided
D	12-13	Daytime service provided
E	4-11	Peak hour service only or limited midday service
F	0-3	Very limited or no service

On the other hand, other parameters that can be used to measure the efficiency of the bus services [5] are such as:

Terminal, Bus Stop and the Route

Terminal or station is where the end/start of bus route at which transit vehicle may arrive and depart. It is the station for the vehicle to have layover/recovery time, used for resting, administrative purposes and for maintaining proper headways. The preliminary observation showed that there was no layover/recovery time provided at bus stations in Parit Buntar and Bagan Serai,. The bus lay by areas were used for the passengers to embark and alight only. A bus stop is the first point of contact between the passenger and the bus service. The spacing, location, design, and operation of bus stops significantly influence transit system performance and customer satisfaction.

Travel Time and Schedule and Operating Speed in Mixed Traffic

It is important to study the travel time and schedule of bus service in order to assess the level of efficiency and satisfaction of the riders. Operating speed is another variable that can measure the bus service performance as the condition of mixed traffic

could affect the operating speed of the bus service. Variation of speed may contribute towards the delay of travel time and schedule.

Stage Bus Service Characteristics and Regularity of Bus Service

A study of bus stop location for loading and unloading passengers is to measure the level of bus service efficiency. It also important to determine the regularity of bus service and the actual acceptable range of departure times so as to provide a better bus service scheduling.

METHODOLOGY AND APPROACHES

The data for analysis was collected through a series of on-board surveys. For service frequency survey, observation was done by locating enumerators on road sides to record the number of buses and the frequency of buses passing the observation points. . Based on the service frequency survey, bus performance indicators were computed including:

- time headway (minute),
- cycle time (minute),
- number of trips (trip/bus/day), and
- travel distance (km/bus/day).

On-board Survey

The survey was conducted from 6 November 2012 to 10 November 2012 with target of 100 convenience sampling unit of on-board passengers due to mobility and logistics reasons. During the on-board surveys for purposes to observe the bus route enumerators have identified the name and the distance between bus stops or others point of stops. The enumerator assigned inside one particular bus would record the number of passengers' boarding or alighting at or between stops, excluding him/herself as a passenger. This task was conducted repeatedly between the two terminals (start and end points) for the operating duration of the bus services, but the enumerator did not necessarily ride the same bus repeatedly. Since intercity buses have one door for passengers to embark and disembark, therefore only one enumerator was required to be located at the front door of the bus. Another enumerator was assigned to read and record the GPS of passengers' access and egress points. The bus speed was also recorded using the GPS apparatus that was synchronized with the mobile satellite.

Plotting of GPS point Using GIS

The use of GPS for the co-ordinates collection and GIS for the spatial analysis will offer the following advantages:

- Graphical and attribute data input and editing

ii. Use of spatially referenced data

For this study the co-ordinates/GPS points of passenger's access and egress were recorded through the on-board survey, where the points were plotted on the projected map using GIS.

DATA FINDINGS

The generalization of findings from this study is subject to the data collected according to the specific time and routes. Survey was conducted during the both peak and off-peak of public transport services.

Travel Time, Schedule, Fare and Regularity of Bus Service for Inter-city and Intra-city

Bus services in Kerian district offered both intra-city and inter-city services that can be accessed by the case study population. The inter-city bus services to Kuala Lumpur, Johor, Singapore, and Pulau Pinang were offered by the express bus operators. The intra-city bus routes were within the Kerian district and the concentration of service was within residential in Kuala Kurau, Tanjung Piandang and Kuala Kurau (Table 3) [4]. However, there was only one bus under one operator to cover each intra-city route. As such, the frequency of bus was low, i.e. one service per up to 45 - 70 minutes. Previously there was additional route to Selama but the route has been discontinued recently. The minimum bus fare was RM1.00 and the maximum bus fare was RM5.20.

Table 3: Intra-city Bus route and frequency

Route Number and Route	No. of buses	Frequency (min)	Distance (km)	Travel time (min)
Bus services at Parit Buntar station				
A Parit Buntar-Taiping	1	70	98	60
B Parit Buntar-Kuala Kurau	1	45	16	30
C Parit Buntar-Tanjung Piandang	1	45	13	30
Bus services at Bagan Serai station				
A Bagan Serai-Tanjung Piandang	1	70	36	60
B Bagan Serai-Kuala Kurau	1	70	44	60

Existing Bus Condition and Ticketing System

Observation on the existing bus condition showed that buses were not equipped with air conditioning system and some of the buses needed to be

upgraded. The buses also used the ring button system that was located at the bottom of passengers' seats. The system was not universally designed to cater for physical disability users. Bus conductors and paper tickets were the operational systems applied by Red Omnibus Sdn. Bhd, which was the sole intra-city bus service operator. The fare rate was calculated based on the distance and interval time.

Terminal and Bus Stop

Kerian District has two bus stations: Hentian Raya Parit Buntar and Hentian Raya Bagan Serai. The station design was a sheltered ground floor building with the waiting seats at each route's bus bay. Both of the bus station buildings were of two levels with the upper level providing the public toilets and prayer room facilities. The ground level has the ticket counters placed facing the bus bays. The location of bus station was in the middle of town center and it was easy to access with ample size of road width for buses to reverse or manoeuvre. Bus stations' main entrance were diverted from the main road of the town centre and managed to avoid the traffic flow conflicts at the main access point. However, there was no specific bus layover provided in Kerian bus stations.

The bus stops were provided along the Kerian main road with no specific standard design. Each of the bus stop were of different types of shelter and size. Some of the bus stops were not equipped with seating facilities and there was no loading and unloading kerb for passengers. Most of the bus stops were not provided with proper lighting or public phones. Additionally, from the secondary sources and observation conducted, the buses services were only till 7.00pm and most passengers embarked and disembarked at door-to-door points along the main road of the routes.

Bus Route, Bus Stop Locations and Passengers' Access and Egress Points

Three major bus service routes (Figures 2, 3 and 4) provided by the Red Omnibus Sdn. Bhd were selected as the case study. The data recorded was presented in the GIS route map with attached the attributes of GPS data table. There were five possible points along route 3 to be proposed as bus stop locations. Along route 5, there were 7 points identified as potential locations for future bus stops. For route 8, there were 15 points of possible bus stop locations, determined using the number of passengers accessing and egressing.

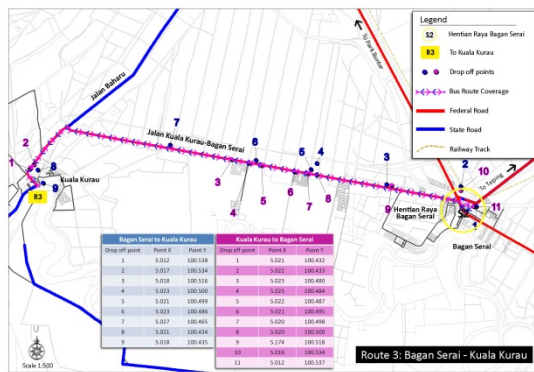


Figure 2: Route 3 Bagan Serai – Kuala Kurau Passengers' Drop Off Points Map.

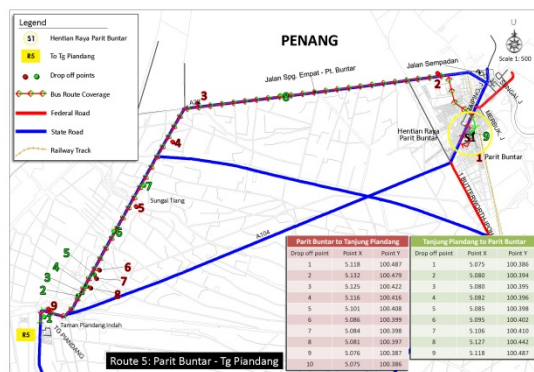


Figure 3: Route 5 Parit Buntar-Tanjung Piandang Passengers' Drop Off Points Map.

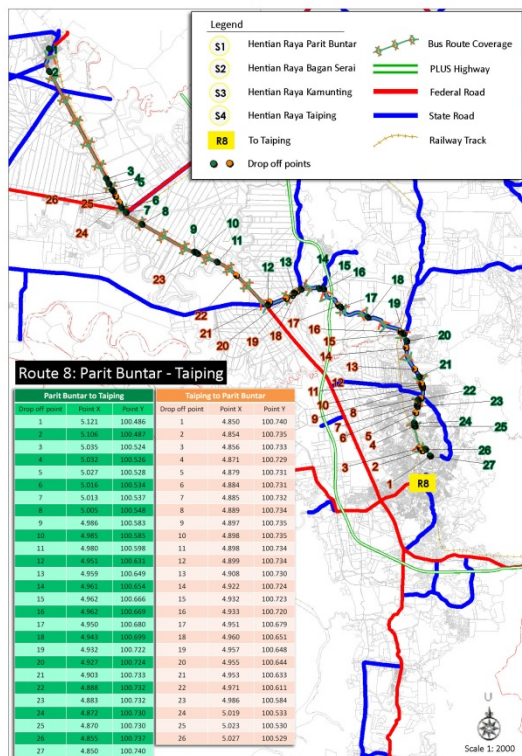


Figure 4: Route 8 Parit Buntar-Taiping Passengers' Drop Off Points Map.

SUMMARY OF FINDINGS

Overall findings showed that the Kerian District needed better bus services operations. The dependency on the future demand of public transportation service in the district was still high with 68% of respondents expressing their willingness to use public bus at least 3 days per week. It is recommended that the local authority and state government to provide an allocation to upgrade and enhance the public transport service and its facilities to sustain the mobility of Kerian District's people in economic and other daily activities. Level of Service (LOS) of public transport service analysis was very important in determining the efficiency and the quality of current service provided. The LOS is a factor that influences the future demand on public transport services. Table 4 shows the LOS matrix.

Table 4: Matrix of LOS for Public Transport Services in Kerian

Criteria	Bus Service			Taxi Service		Train Service	
	R3	R5	R8	Station 1	Station 2	Station Bagan Serai	Station Parit Buntar
Fixed-route Service Frequency LOS	A	A	C	-	-	D	D
Fixed-route Hour of Service LOS	D	D	C	-	-	A	A
LOS Scheme for transit speed	D	E	E	-	-	-	-
Passengers Loading LOS Thresholds (Off-peak)	A	A	C	A	A	-	-
Service Frequency LOS Thresholds (Off-peak)	E	E	E	A	A	-	-

Source: Kerian Bus Services Surveys, November 2012.

DISCUSSION AND CONCLUSION

The points where high number of passengers were dropped off can represent the possible suitable locations to designate a bus stop. However, there were some issues arising during the stage of plotting the GPS points into GIS maps. Some maps showed errors in alignment of their north points. This may be due to the GPS readings being recorded on moving buses and determination of points was influenced by the satellite connectivity in cloudy areas. The level of accuracy of the GPS points were accepted, with 90% from the points recorded being able to be plotted into the maps. Those errors in GPS points were eliminated to avoid inconsistency and can be represented using the nearby points where the east points were referred. Even though the GPS points were accepted, there was a 5% to 10% inaccuracy of actual points on the ground. As a

result, a mapped GPS points in GIS application can model the overview of bus routes and passengers' access and egress points for the purpose of determining possible areas to locate bus stop facilities.

In general, the overall bus service in Kerian has many areas to be improved based on the passengers' perception of overall bus service, trip frequency, bus condition, bus punctuality, bus efficiency and effectiveness. Based on the responses obtained from the survey, it can be concluded that:

- i. Route 3 from the station to Kuala Kurau respondents needed more frequent bus trips with at least 30 minutes interval for waiting time. 13 respondents had chosen the 30 minutes interval, 4 respondents preferred the 20 minutes interval and 19 respondents selected the 15 minutes interval.
- ii. All respondents of the three routes agreed to pay higher fares if services were upgraded with comfortable bus interiors with air conditioning system.

ACKNOWLEDGEMENTS

This research was funded by Institute Darul Ridzuan (IDR) <http://www.idrperak.com>. The authors wish to thank IDR for funding this research.

REFERENCES

- [1] Giuseppe SALVO and Simona SABATINI, ND, A Gis Approach To Evaluate Bus Stop Accessibility. Retrieved at <http://www.iasi.cnr.it/ewgt/16conference/ID108.pdf> on 10/5/2013 at 11.45am.
- [2] John C. Sutton, 2005, GIS Applications in Transit Planning and Operations: A Review of Current Practice, Effective Applications and Challenges in the USA, Transportation Planning and Technology, August 2005, Vol. 28, No. 4, pp. 237_250, ISSN 0308-1060 print: ISSN 1029-0354 Taylor & Francis DOI: 10.1080/03081060500247655
- [3] Khaled Hazaymeh, 2009, GIS-Based Safety Bus Stops— Serdang and Seri Kembangan Case Study, Journal of Public Transportation, Vol. 12, No. 2.
- [4] Laporan Penemuan Rancangan Tempatan Kawasan Pentadbiran Majlis Bandaraya Kerian, 2020
- [5] Madzlan Napiah, Amirah Suriati Ahmad Farid and Suwardo, 2010, Trip Productivity Evaluation Of Bus Service: Medan Kidd Bus Station, MUTRFC 2010.
- [6] Noorfakhriah Yaakub and Madzlan Napiah, 2001, Quality of Service and Passenger's Perception – A review on Bus Service in Kota Bharu, International Journal of Civil & Environmental Engineering IJCE-IJENS Vol: 11 No: 05, p. 1-9.
- [7] Olowosegun Adebola and Okoko Enosko, 2012, Analysis of Bus-stops locations using Geographic Information System in Ibadan North L.G.A Nigeria, Industrial Engineering Letters, ISSN 2224-6096 (print) ISSN 2225-0581 (online), Vol 2, No.3, 2012, www.iiste.org
- [8] Suwardo, M. Napiah and I. Kamaruddin, 2007(a), "Bus Operation Characteristics and Performance Indicators as a Preliminary Study in Promoting Public Transport: A Case Study based on the Kerian-Lumut Corridor in Perak", *Prosiding Kebangsaan Awam '07*, Pusat Pengajian Kejuruteraan Awam, USM.
- [9] Suwardo, M. Napiah and I. Kamaruddin 2008 (b), Review on Motorization and Use of Public Transport in Perak Malaysia: Realities and Challenges, 2nd International Conference on Built Environment in Developing Countries (ICBEDC 2008).
- [10] Suwardo, Madzlan B. Napiah, and Ibrahim B. Kamaruddin, 2008(c), Punctuality and Expected Waiting Time of Stage Buses in Mixed Traffic, Jurnal Transportasi Vol.8 Edisi Khusus no.3 Oktober 2008: 213-226.
- [11] Suwardo, Madzlan B. Napiah, and Ibrahim B. Kamaruddin, 2009 (d), On-Time Performance and Service Regularity of Stage Buses in Mixed Traffic, International Journal of Business, Economics, Finance and Management Sciences 1:3 2009
- [12] (<http://mdkerian.gov.my/web/guest/latar>).
- [13] (<http://mdkerian.gov.my/web/guest/latar>).
- [14] <http://www.spad.gov.my>

GEOCHEMISTRY OF PALEOGENE RED BEDS IN THE NORTHERN IRAQ FORELAND BASIN: EVIDENCE FOR PROVENANCE

Muatasam Hassan,^{1,2*} Brian G. Jones,¹ Ali Ismail Al Jubory,² Sabah Ahmed Ismail,³
Abdual Salalm Mehdi Saleh⁴

¹School of Earth and Environmental Science, University of Wollongong, Australia; ²College of Science, Mosul University, Iraq; ³School of Earth Science, University of Kirkuk, Iraq; ⁴School of Earth science, University of Tikrit, Iraq

ABSTRACT

The Paleogene Red Bed deposits in northern Iraq crop out as a narrow northwest-southeast trending belt within the thrust zone in an active foreland basin developed adjacent to the Zagros orogenic belt. The Red Beds are divided vertically into four units. The lower part (unit 1) is mainly composed of red mudstone and siltstone. The middle part (unit 2) is mainly composed of sandstone with thin interbeds of red siltstone. The upper part is composed of conglomerate (unit 3) covered by 100-120 m of red mudstone, siltstone and sandstone (unit 4).

The geochemical stratigraphy shows an increase in transition elements and REEs while LILE and HFSE elements decrease in the lower part of the sequence. These features indicate that a mafic source supplied detritus during the deposition of the lower Red Beds and decreased in importance during the deposition of the middle and upper parts as a result of erosion or tectonic activity.

Keywords: Red Beds, Mafic Source, Iraq, Zagros Orogenic Belt

INTRODUCTION

The geochemical composition of rocks is generally a useful tool to determine the chemical characteristics of the source area [1] and draw tectonic conclusions [2]. The diagenesis, nature of the source rock and the weathering of the source area can also be deduced from the geochemical composition of clastic rocks [3], [4], [5], [6].

One section was selected from the Mawat area (Sorakalat section) in the south-eastern part of the basin and one section was selected from Qandel area (Suwais section) on the northwest side of the basin (Fig. 1). Rare earth element studies are very useful because their distribution is stable in various rocks and minerals under different conditions, such as weathering, transportation and metamorphism.

Rare earth elements were normalized to chondrite, average shale and upper continental crust and plotted on spider diagrams and showed that the lower parts of the sequence in the Mawat area is enriched in HREEs in comparison to the middle and upper parts of the Red Beds which have less HREEs. Trace elements were normalized to Upper Continental Crust [7] and plotted on spider diagrams and also plotted versus stratigraphic height to assess their vertical distribution.

The REE patterns indicate the lower part derived from a mafic source with minor contributions from a felsic source. This is distinctly different from the middle and upper parts of the sequence. Trace element diagrams show a concentration of transition elements and high field

strength elements (HFSE) in the lower parts of the Red Beds and depletion of HFSE upward towards the middle and upper parts. This pattern probably reflects regressive erosion of the mafic components upwards through the section with the effect of a minor felsic source in the middle and upper parts of the Red Bed sequence.

Laterally, the Mawat-Chwarta area section has been more affected by mafic and ultramafic sources than Qandel area section (Suwais).

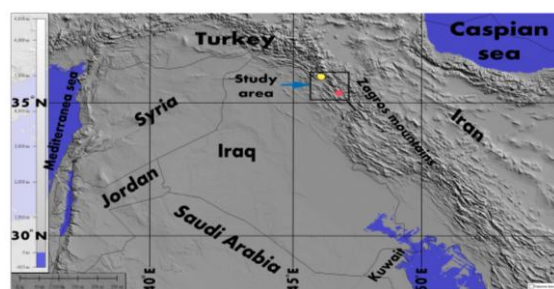


Fig. 1. Location map of the study area (Qandel and Mawat-Chwarta areas).

GEOLOGICAL SETTING

The Zagros Mountains of northern Iraq are geologically part of the extensive Alpine mountain belt. They form a narrow strip along the border between Iraq and Iran and include two main zones: the Zagros Simply Folded Belt in the southwest and the Zagros Suture Zone in the northeast. These zones are included in the Zagros Orogen. A

foreland basin occurs southwest of the Zagros Mountains. The tectonic development of the Zagros Mountains indicates that the foreland basin was initiated in the Late Cretaceous during ophiolite obduction along the Zagros Suture Zone followed by continental collision of the Arabian plate with Eurasia in the Cenozoic [8], [9]. Late Cretaceous and Paleogene foreland basin deposits have been folded and are therefore now part of the Zagros Simply Folded Zone. In northeast Iraq, the former Zagros foreland basin included Cretaceous shallow-marine deposits of the Shiranish and Tanjero Formations overlain by continental deposits of the Paleogene Red Beds (Fig. 2). The Paleogene sedimentary rocks in the foreland basin record sedimentation developed during the Alpine orogeny. The Red Beds are structurally overlain by thrust sheets that are part of the Zagros Suture Zone. In the Mawat-Chwarta area the Red Beds are structurally overlain by the volcanic rocks of the Naopurdan Group [10] whereas the contact with the underlying Tanjero Formation is gradational as confirmed by the current study.

Tanjero Formation (Maastrichtian)

The Tanjero Formation is another rock unit of the Late Cretaceous succession in the study area. It is widespread in the Kurdistan region of northern Iraq [11] (Fig. 3). The formation is over 2010 m thick. The upper part of the Tanjero Formation contains foraminifera consistent with a Maastrichtian age for the unit. The lower part of the succession is composed of 480 m of globigerinal marl and rare siltstone. Its upper part consists of 1530 m of mixed siliciclastic and carbonate sedimentary rocks including silty marl, siltstone, sandstone, conglomerate, and organic detrital limestone. An interfingering interval ~45 m thick with gradational contacts between the Tanjero and Aqra Formations occurs in the Mawat-Chwarta area (Sorakalat section). It is composed of sandy detrital limestone, which progressively changes upwards to a calcareous sandstone, rich in shell debris. The boundary between the Tanjero Formation and the overlying Red Beds in the Mawat-Chwarta area is locally marked by Quaternary sediments. Furthermore, such a boundary is also recognized in nearby Sorakalat village, where fossiliferous limestone beds are recognized within the lowermost part of the Red Beds.

Red Beds (Paleocene-Eocene)

The Red Beds are composed of mudstone, sand stone and conglomerate. Clastic sedimentary rocks are distributed throughout the succession while

carbonate beds are confined to the lower part of the unit. In most places the lower contact of the Red Beds with the Tanjero Formation is conformable, as occurs in the Mawat-Chwarta area (Fig. 3). This contact is sharp in some areas and a transition in others [12]. An angular unconformity was also recorded in the study area close to the Suwais sections (Fig. 3). The variety of detrital components in the stratigraphic column through the Red Beds reflects the unroofing history of the thrust sheets that provided the components to the Red Bed basin.

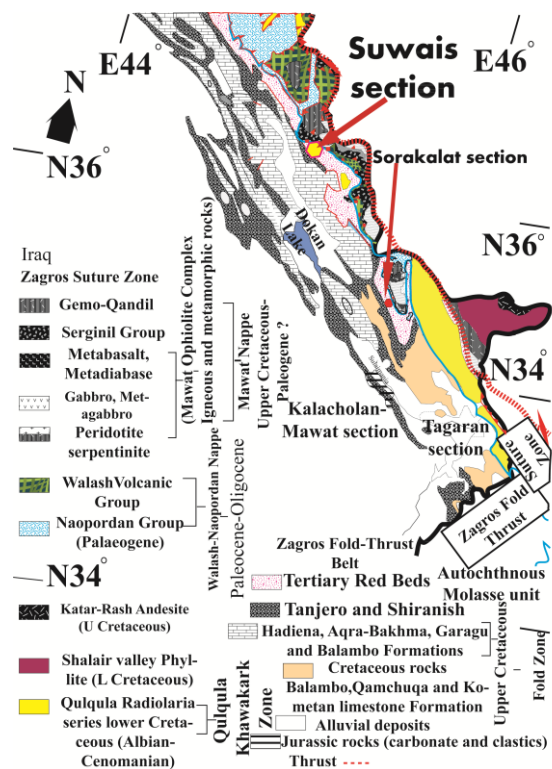


Fig. 2. Regional geological map of northern Iraq (Kurdistan area) and northwestern Iran showing locations of the study areas and Late Cretaceous formations and thrust sheets [13].

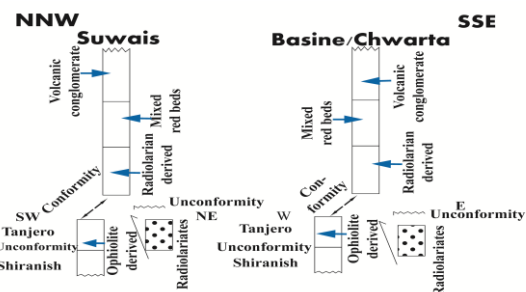


Fig. 3. The stratigraphic relationships of the Late Cretaceous-Paleogene rocks from the Suwais section (Qandel area) and Basina-Chwarta area within the former foreland basin [13].

Geochemical studies show that a diversity of source rocks supplied detritus to the Red Beds, reflecting uplift of older rocks coupled with intensive orogenic movements during Red Bed deposition. The Red Beds are divided on the basis of provenance into two parts. A lower unit is dominated by radiolarian chert detritus with a minor component of ophiolitic detritus. An upper unit lacks radiolarian chert and ophiolitic detritus and has a mixed provenance of volcanic, metamorphic and sedimentary rocks.

SAMPLING AND METHODS

The current study used conventional geological methods including geological surveys in the field; X-ray fluorescence (XRF) and inductively coupled plasma-mass spectrometer (ICP-MS) analysis.

Fifty five samples from the Suwais and Sorakalat sections were analysed by XRF for trace elements in the School of Earth and Environmental Sciences at the University of Wollongong. Twenty four samples were analysed using ICP-MS in Brisbane for REEs from two sections (Suwais and Sorakalat, Tables 1-2).

RESULTS AND DISCUSSION

Rare Earth Elements (REEs)

Rare earth elements (Tables 1-2) provide very important evidence for determining sedimentary source rocks because they are stable in different rocks and minerals and are not modified during metamorphism [14].

Fig. 4 shows the different patterns for the average shale [16] and upper continental crust [12] normalized to chondrite [17]. The figure shows enrichment in the LREE in the upper continental crust as a result of the LREEs fractionating into the liquids generated during magma formation and intrusion into the upper crust. For this reason the composition of REEs in the MORB and upper continental crust is different. The enrichments of La to Sm are similar in the Qandel and Mawat areas but with some increase in La in the Mawat area.

All the samples were plotted on spider diagrams after being normalized to chondrite [4] (Figs 4-5). Generally there is a similarity pattern of the geochemical signatures between all the samples in the current study. These patterns are stratigraphically characterized by non-uniformity of REE distributions showing relative enrichment of LREEs with little flat pattern or depletion of HREEs. The LREEs increase in abundance towards the middle and upper parts of the Red Beds in

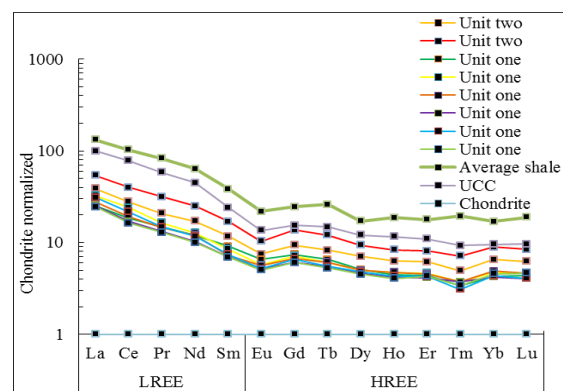


Fig. 4. Plots of REEs from average shale [16], upper continental crust [12] and the selected samples from the Suwais section normalized to chondrite values [17].

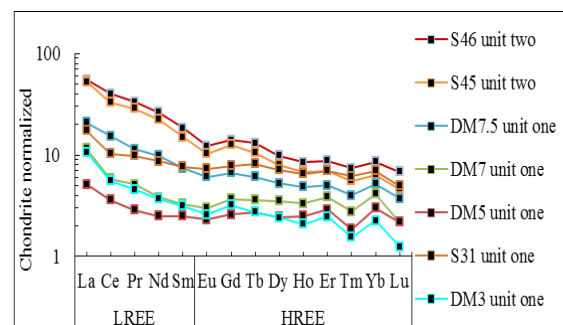


Fig. 5. Plots of REEs from selected samples in the Sorakalat section normalized to chondrite values [17].

Table 1. Average REE results for Suwais section.

LREEs								
Units	La	Ce	Pr	Nd	Sm	GdYb	LaSm	
Unit1	4.9	8.2	1	4.4	1.1	3.5	4.5	
Unit2	7.7	16	2	8.2	2.1	2.4	3.1	
HREEs								
Eu	Gd	Tb	Dy	Ho	Er	Tm	Yb	Lu
0.4	1.5	0.3	1.5	0.3	1.0	0.1	1.0	0.1
0.6	2.4	0.4	2.6	0.6	1.8	0.2	2.1	0.3

Table 2. Average REE results for Sorakalat section.

LREEs								
Units	La	Ce	Pr	Nd	Sm	GdYb	LaSm	
Unit1	8.6	16	1.8	6.9	1.5	1.8	5.8	
Unit2	14	27	3.2	13	2.8	1.8	5.3	
HREEs								
Eu	Gd	Tb	Dy	Ho	Er	Tm	Yb	Lu
0.4	1.7	0.3	1.6	0.3	0.9	0.1	0.9	0.1
0.7	2.0	0.5	2.6	0.5	1.5	0.2	1.6	0.2

comparison to the lower parts. The increase of LREEs in the lower mudstone-dominated facies probably results from their adsorption onto clays, which coincides with findings in the eastern desert of Egypt [15].

The Gd/Yb ratio ranges from 1.06-3.2 in the lower and middle parts decreasing to 0.6-0.8 in the upper part. The pattern of the samples is ordered from bottom to top of the sections. In Figs 4-5 the pattern of the elements in all sections was similar but there are differences between samples from the lower, middle and upper parts. Samples from units one and two reflect high ratios of HREEs while samples from units three and four have lower HREE ratios. The chondrite normalized samples also show positive anomalies represented by Eb, Er and Gd with negative anomalies represented by Tm, Eu and Ce. In sandstone samples the Ce content from the lower, middle and upper parts is very high ranging from 32-118 ppm.

The patterns in the middle and upper parts are similar to each other with similar HREE patterns and a little enrichment by LREEs in the upper part relative to the middle part. Although the middle and upper parts were at least partly derived from felsic or different thrust source rocks, the patterns for these parts are slightly less than 1; therefore, a mafic source has still affected these parts as well. In contrast, patterns from the lower part of the Red Beds are well below 1 which indicates that a main mafic and ultramafic source has affected this part. Also the depletion of LREEs within this lower part indicates that the source area for this part was different from the middle and upper parts and it was not derived from the upper crust. The REE patterns in the current research are similar to the clayey-siliceous rocks (normalised to shale) from the Bazhenov Formation in Russia [18]. They also stated that the Ce distribution was not affected by early diagenesis and variable redox conditions which is similar to the Red Beds. The enrichment of LREEs in some samples from the lower and middle parts does not necessarily mean that these samples were affected by the felsic source because of two reasons.

Transition trace elements (TTE)

This group, also called ferromagnesian trace elements, is composed of V, Co, Ni, Cr and Cu which show convergent behaviour during the evolutionary processes of volcanic rocks and they decrease with increasing silica content. These elements are very important for determining provenance and tectonic setting [19]. It is well known that these elements concentrate in mafic and

Table 3. Average concentrations of transition elements in the Suwais section of the Red Beds.

Units	V	Co	Ni	Cr	Cu	Ce
Unit1	56	26	26	237	484	26
Unit2	63	24	23	172	459	32

Table 4. Average concentrations of transition elements in the Sorakalat section of the Red Beds.

Units	V	Co	Ni	Cr	Cu	Ce
Unit1	98	40	39	399	711	29
Unit2	64	64	71	22	38	40

ultramafic rocks and they are more common in pelitic rocks than in shale and the NASC [6]; [20]; [21].

V in the Red Beds includes high values reaching up to 208 ppm in some parts of the Red Beds, especially within the Kalacholan-Mawat section (Table 3). This element occurs in the structure of pyroxene, amphibole, biotite and the oxides that contain titanium [22]. Therefore, V has high values in some samples that are probably rich in pyroxene. Cr occurs in igneous rocks in spinel minerals, such as chromites, and it also occurs in ferromagnesian minerals, such as pyroxene and olivine [23]. In ultramafic igneous rocks Cr content is more than 2000 ppm, in basalt it ranges between 150-200 ppm; it reduces to 25-80 ppm in intermediate rocks while it decreases to less than 20 ppm in granitic rocks. During weathering of the source rocks the behaviour of Cr^{+3} , which occurs in the silicate minerals, is geochemically similar to Fe^{+3} and Al^{+3} , therefore, it occurs in the clay minerals. During more intense oxidation conditions Cr^{+3} is probably oxidised to Cr^{+6} to form CrO_4^{2-} that may be deposited in chromate minerals such as $CaCrO_4$ and $PbCrO_4$. The Cr that occurs in chromite and spinel is generally resistant to geochemical weathering; therefore, it is transported from the source area to the sedimentary environments in the resistant minerals which strongly reflect the Red Beds.

The increase of Co and decrease of other transition elements may not reflect a mafic rock origin but could reflect sedimentary sorting processes [21]. This has happened in the Red Beds in the Mawat-Chwarta area in the upper part (unit 2) of the Sorakalat section (Table 4). There is a negative relationship between Co/Ni versus Cr in several samples from the upper part of unit two in the Sorakalat and Suwais sections (Tables 3 and 4) while generally there is similarity in the Co/Ni in the other samples although strong variability occurs in Cr contents in unit one. This probably indicates that the Cr in the Red Beds occurs mainly in detrital chromite mineral grains. Chromite was not

uniformly distributed in the source rocks but was concentrated in pockets and, therefore, the amount of chromite derived from this source depends on the surface area of chromite bodies that were exposed to weathering.

The ratio of Co/Ni in the Red Beds is not affected by the previous factors because these elements occur in the silicate minerals and their abundance is related to weathering products such as illite-smectite and montmorillonite that are common in the Red Beds. The small variation in the Co/Ni ratio in the lower part of the Red Beds indicates little variation in the nature of the source rocks during their sedimentation. The stronger variation of this ratio in the upper parts of the Red Beds reflects contribution from another source whereas there is little variability in the Cr content in this part of the sequence relative to the lower parts. When the Co/Ni ratios and Zr contents were compared to data from other rocks from northern Iraq and elsewhere it was shown that most of the lower Red Bed samples were close to values from dunite, harzburgite, lherzolite and basalt while most of the middle Red Bed samples plus sample S20 from the lower part are similar to the upper continental crust analyses (Table 3). Recently analysed Cr-spinels from serpentines in northern Iraq showed that much of the matrix of the serpentines was derived from harzburgite and lherzolite of forearc affinity [24].

The amount of Ni in the Red Beds increases in the upper parts within the conglomerate facies, which probably reflects a contribution of felsic components. It should be mentioned that the Cr and Ni in the Red Beds have low concentrations in the Merga and Kanarroy sections which probably reflects less exposure to an ultramafic source during the deposition of these sections or because a different river channel supplied these deposits to the basin. The Cr contents in the Taconian orogen from North America reached 3950 ppm [1]. If Cr and Ni > 100 ppm and they show a high correlation they probably indicate derivation from ultramafic components in the source area [3]. A Cr/Ni ratio of 2 or more indicates a mafic source and, therefore, since most Cr and Ni values from the lower part of the Red Beds plotted within this range they would have come from a mafic source while the middle (sandstone) and upper part (conglomerate) of the sequence were under this range and would have had a less mafic source. These results exactly coincide with findings from the Bastar craton [21].

Pelite samples tend to be enriched with Cr and Ni [21] but contents are slightly lower than the actual mafic volcanic rock samples from the Bastar craton [22]. In contrast, their coarser grained samples of sandstone and quartzite plotted in the

field of post-Archean crust reflecting derivation from granite and gneiss in the Bastar craton [25].

CONCLUSIONS

Generally, the trace and REEs indicated that the sediments in the Red Beds were affected by a major ultramafic to mafic source, especially in the mudstone facies from the lower part, and the geochemical data were compatible with a mixed to mafic impact especially within the coarse-grained sediments in the middle and upper parts. The data also indicated that the Red Beds were affected by a moderate degree of weathering and a lack of recycled sediments. Rare earth elements were normalized to chondrite, average shale, upper continental crust and mid oceanic ridge values. The diagrams of chondrite normalised values generally show enrichment in LREEs with negative Eu anomalies and the lower part of the Red Beds is mainly enriched with HREEs ascribed to mafic and ultramafic source rocks contrary to the middle and upper parts which have less HREEs and were probably affected by a felsic source.

The concentration of transition elements the lower parts and depletion in the upper parts reflect regressive erosion of the mafic components upwards through the section with little effect from a felsic source. Spider diagrams reflect the main derivation of mafic sediment in lower parts of the Red Beds with a minor felsic contribution fed into the middle and upper parts.

According to their geochemical signatures the Red Bed sediments were deposited in a range of sedimentary environments and derived from a source area with varied source rocks. The provenance of the Red Beds can be inferred from the geochemical evidence to be predominantly mafic as shown by the REEs and transition elements.

REFERENCES

- [1] Etemad-Saeed N, Hosseini-Barzi M, John S & Armstrong-Altrin, "Petrography and geochemistry of clastic sedimentary rocks as evidences for provenance of the Lower Cambrian Lalun Formation, Posht-ebadam block, Central Iran", *J. Afr. Earth Sci.*, Vol. 61, 2011, pp. 142-159.
- [2] Bhatia MR, "Plate tectonics and geochemical composition of sandstones", *J. Geol.*, Vol. 6, 1983, pp. 611-627.
- [3] Garver JI, Royce PR & Smick TA, "Chromium and nickel in shale of the Taconic foreland; a case study for the provenance of fine-grained sediments with an ultramafic

- source", *J. Sedim. Res.*, Vol. 66, 1996, pp. 100-106.
- [4] Hossain HMZ, Roser BP & Kimura JI, "Petrography and whole-rock geochemistry of the Tertiary Sylhet succession, northeastern Bengal Basin, Bangladesh: provenance and source area weathering", *Sed. Geol.*, Vol. 228, 2010, pp. 171-183.
- [5] Meinhold G, Kostopoulos D, Reischmann T, Frei D & BouDagher-Fadel MKF, "Geochemistry, provenance and stratigraphic age of metasedimentary rocks from the eastern Vardar suture zone, northern Greece", *Palaeo. Palaeo.*, Vol. 277, 2009, pp. 199-225.
- [6] Osae S, Asiedu DK, Banoeng-Yakubo B, Koeberl C & Dampare SB, "Provenance and tectonic setting of Late Proterozoic Buem sandstones of southeastern Ghana: evidence from geochemistry and detrital modes", *J. Afri. Earth Sci.*, Vol. 44, 2006, pp. 85-96.
- [7] Rudnick RL & Gao S, Eds, *Composition of the Continental Crust*. Oxford: Pergamon, 2003.
- [8] Agard P, Omrani J, Jolivet L, Whitechurch H, Vrielynck B, Spakman W, Monie P, Meyer B & Wortel R, "Zagros orogeny: a subduction-dominated process", *Geol. Mag.*, Vol. 148, 2011, pp. 692-725.
- [9] Alavi M, "Regional stratigraphy of the Zagros fold-thrust belt of Iran and its proforeland evolution", *Am. J. Sci.*, Vol. 304, 2004, pp. 1-20.
- [10] Al-Mehaidi HM, "Tertiary Nappe in Mawat Range, N.E Iraq", *J. Geol. Soc. Iraq*, Vol. 8, 1975, pp. 31-44.
- [11] Buday T, "The regional geology of Iraq", *Stratigraphy and Palaeogeography*, Geological Survey Mining. Baghdad, 1, 1980, 445pp.
- [12] Karim KH, Koyi H, Baziany MM & Hessami K, "Significance of angular unconformities between Cretaceous and Tertiary strata in the northwestern segment of the Zagros fold-thrust belt, Kurdistan Region, NE Iraq", *Geol. Mag.*, Vol. 148, 2011, pp. 925-939.
- [13] Hassan MM, 2012. "Sedimentology of the Red Beds in NE Iraq", PhD thesis, University of Wollongong, 400pp (unpublished).
- [14] Gao S & Wedepohl KH, "The negative Eu anomaly in Archean sedimentary rocks: Implications for decomposition, age and importance of their granitic sources", *Earth Plan. Sci. Lett.*, Vol. 133, 1995, pp. 81-94.
- [15] Dawood YH, Abd El-Naby HH & Sharafeldin AA, "Influence of the alteration processes on the origin of uranium and europium anomalies in trachyte, central Eastern Desert, Egypt", *J. Geochem. Explor.*, Vol. 88, 2004, pp. 15-27.
- [16] Piper DZ, "Rare earth elements in the sedimentary cycle". *Chem. Geol.*, Vol. 14, 1974, pp. 285-304.
- [17] Boynton WV, Ed. *Cosmochemistry of the Rare Earth Elements: Meteorite Studies*. Amsterdam: Elsevier, 1985.
- [18] Zanin YN, Eder V, Zamirailova A & Krasavchikov VO, "Models of the REE distribution in the black shale Bazhenov Formation of the West Siberian marine basin, Russia", *Chemie der Erde*, Vol. 70, 2010, pp. 363-376.
- [19] Armstrong-Altrin JS, Lee YI, Verma SP & Ramasamy S, "Geochemistry of sandstones from the Upper Miocene Kudankulam Formation, southern India: implications for provenance, weathering, and tectonic setting", *J. Sedim. Res.*, Vol. 74, 2004, pp. 285-297.
- [20] Feng R & Kerrich R, "Geochemistry of fine-grained clastic sediments in the Archean Abitibi greenstone-belt, Canada - implications for provenance and tectonic setting", *Geochim. Cosmochim. Acta*, Vol. 54, 1990, pp. 1061-1081.
- [21] Wani H & Mondal MEA, "Petrological and geochemical evidence of the Paleoproterozoic and the Meso-Neoproterozoic sedimentary rocks of the Bastar craton, Indian Peninsula: implications on paleoweathering and Proterozoic crustal evolution", *J. Asian Earth Sci.*, Vol. 38, 2010, pp. 220-232.
- [22] Mason B & Moore CB, *Principles of Geochemistry*. New York: Wiley, 1982.
- [23] Wedepohl KH, *Handbook of Geochemistry*. Heidelberg: Springer-Verlag, 1978.
- [24] Aswad KJA, Aziz NRH, & Koyi HA, "Cr-spinel compositions in serpentinites and their implications for the petro-tectonic history of the Zagros Suture Zone, Kurdistan region, Iraq". *Geol. Mag.*, Vol. 148, 2011, pp. 802-818.
- [25] Mondal MEA, Hussain MF & Ahmad T, "Continental growth of Bastar craton, central Indian shield during Precambrian via multiphase subduction and lithospheric extension/rifting: evidence from geochemistry of gneisses, granitoids and mafic dykes. *J. Geosci. Osaka City Univ.*, Vol. 49, 2006, pp. 137-151.

DEVELOPMENT OF BASE MATERIALS FOR SEAWEED BEDS USING VOLCANIC ASHES AND RECYCLING MATERIALS OF INDUSTRIAL WASTES

K. Yamamoto¹, T. Negami², T. Nakajima¹, H. Yano³, Y. Futsuhara³ and K. Shima³
¹Kagoshima University, ²Saga University and ³Infratec Company, Japan

ABSTRACT

The frequency of eruptions at Mt. Sakurajima in Kagoshima peaked in 2011, the highest since observations began in 1955. Large amounts of volcanic ashes from Mt. Sakurajima were falling in the surrounding areas. The total volcanic ashes have been observed to be over 6.1 million tons in 2012. Most of the volcanic products have been disposed as industrial wastes, but the supply of these volcanic products is anticipated to be unending for the foreseeable future. On the other hand, the area of Japanese seaweed beds has decreased by around 40% in the last 40 years. Seaweed beds play a very important role in the ecosystem of the coastal area. The purpose of this study is to develop maintenance-free base materials for seaweed beds artificially using volcanic ashes and recycled materials of industrial wastes.

Keywords: Volcanic ashes, Recycled materials, Seaweed beds, Solidification, Low-environmental load

INTRODUCTION

An active volcano, Mt. Sakurajima is located in Kagoshima, Japan. Due to the cyclic nature of magma, a number of eruptions have recently been activated. A large amount of volcanic ashes are already supplied in the Kagoshima area and a constant supply of these ashes is anticipated from now on.

Seaweed beds are communities consisting of large benthic plants (seaweed/seagrass) and they form rich underwater forests. These forests play an important role in the ecosystem of the coastal area, serving as nursery grounds for fish and shellfish, including egg-laying sites and feeding grounds [1]–[3]. But they have been remarkably reduced in Japan. Not only coastal engineering works such as reclamation and dredging but also the phenomenon known as barren ground (called “isoyake” in Japanese) has led to the deterioration of coastal environments. It is also important to consider that a stable supply of iron indispensable for seaweed growth is lacking under the sea due to the change in the nutritional composition of the sea caused by deforestation and the development of dams in the land.

This study develops the base materials for seaweed beds using volcanic ashes and recycled materials of industrial wastes for the maintenance of natural environments. The mixture of industrial wastes is recycled gypsum, scrapped ceramics, iron powder, cement and so on. The main solidification material is recycled gypsum and the use of cement is additional. Figure 1 shows the image of carbon

fixation and environmental restoration produced by the base materials for seaweed beds in this study. As shown in this figure, seaweed beds are an important part of the marine food system through the photosynthetic activities, absorbing carbon dioxide and discharging oxygen. Furthermore, seaweed beds play a virtual role in the ecology of the aquatic ecosystems, serving as buffers of seawater quality.

PHYSICO-CHEMICAL PROPERTIES OF VOLCANIC ASHES

The volcanic ashes of Mt. Sakurajima were sampled in Kagoshima city. The following fundamental properties were obtained from the soil test [4]–[5]: soil particle density $\rho_s=2.708 \text{ g/m}^3$; coefficient of permeability $k=2.0 \times 10^{-4} \text{ cm/s}$; and $\text{pH}=7.91$ (weak alkaline). Figure 2 shows the grain size distribution curve. This figure shows that the percent finer by weight is over 40% when the grain size is less than 0.1 mm.

Next, the compaction curve is shown in Fig. 3. The compaction test was conducted using the A-b method [6], where the compaction energy is low and the sample is not repeatedly used. The optimum water content and the maximum dry density are 15.1% and 1.62 g/cm^3 , respectively. Thus, it is found that the volcanic ashes are good materials suitable for compaction.

RESULTS OF TEST PIECES

The unconfined compression test was carried out

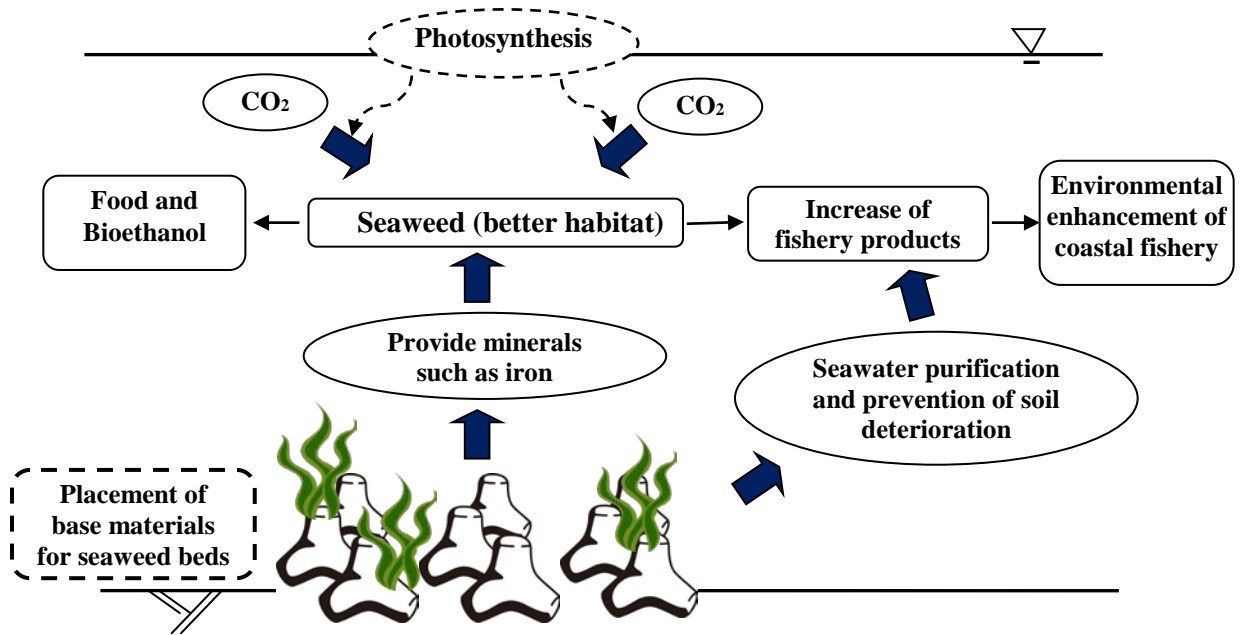


Fig. 1 Image of carbon fixation and environmental restoration produced by base materials for seaweed beds.

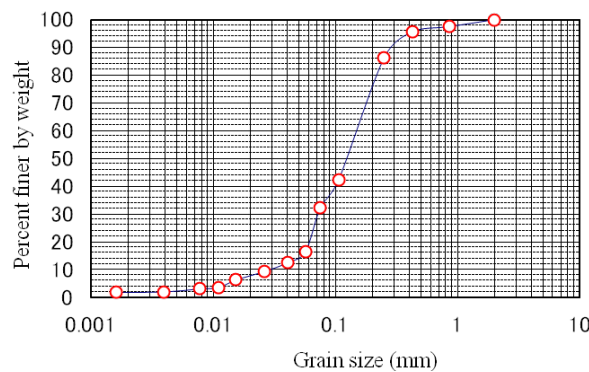


Fig. 2 Grain size distribution curve.

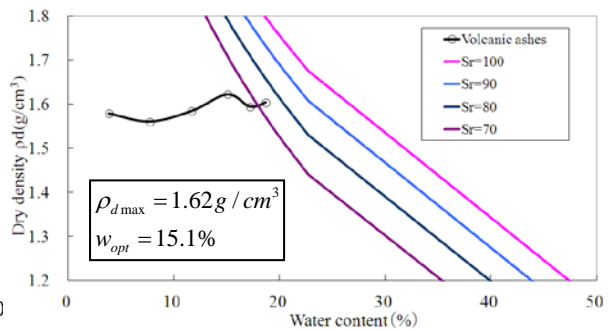


Fig. 3 Compaction curve.

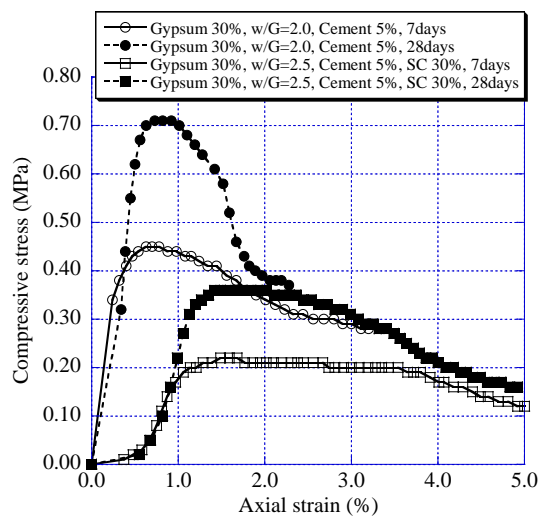


Fig. 4 Stress-strain curve (7 and 28 days curing).

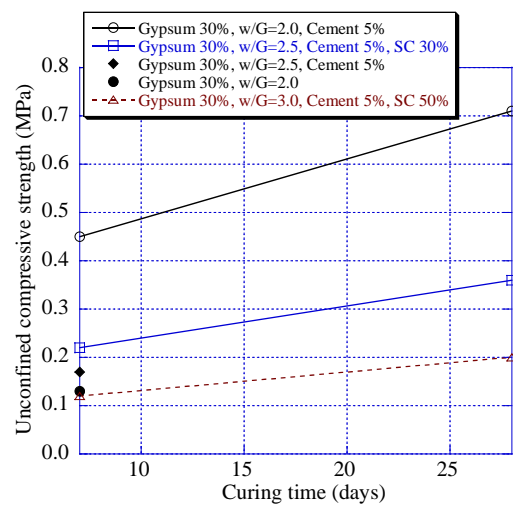


Fig. 5 Relationship between unconfined compressive strength and curing time.

in our laboratory to obtain the unconfined compressive strength of test pieces. Figure 4 shows an example of compressive stress – axial strain curves after 7 and 28 days curing. In the graph legend, the mixture ratio is the weight ratio for the absolute dry condition of volcanic ashes. Note that w/G and SC mean water-gypsum ratio and scrapped ceramics, respectively. The volumes of gypsum and cement are 30% and 5%, respectively in this paper. For the mixing of the cement, water is added at a ratio of w/C (water-cement ratio)=0.8. Three specimens were prepared for each test case to consider the imperfection of specimens and the variation of test results. The cases with w/G=2.0 show higher peak compressive stress than those with w/G=2.5. Naturally the compressive stress after 28 days curing is higher than that after 7 days curing for each case. Also, the stress-strain curves for the cases of mixing with scrapped ceramics showed toughness on materials after the peak compressive strength. It is found that a higher compressive stress can be obtained when the water content is moderate (w/G=2.0) and cement is additionally added.

The Relationship between unconfined compressive strength and curing time is shown in Fig. 5. The increase of unconfined compressive strength for the case of Gypsum 30%, w/G=2.0 and Cement 5% is remarkable with the increase of curing time. In particular, the use of small amounts of cement and scrapped ceramics is more effective for the preservation of the shape of the base materials and the improvement of interlocking.

PRODUCTION OF BASE MATERIALS FOR SEAWEED BEDS

The unconfined compression and dissolution tests and the analysis of components were carried out on the specimens of the developed base materials. Figure 6 shows the compressive stress -

axial strain curves for the base materials after 28 days curing. In the graph legend, the mixture ratio is the weight ratio for the whole weight. Particularly in the cases with cement 14.7% and 12.3%, the compressive stress reduces noticeably after the peak strength. Fig. 7 shows photographs of the specimen before and after completion of the unconfined compression test after 28 days curing. The specimen is composed of volcanic ashes 29.4%, recycled gypsum 23.5%, water 14.7%, scrapped ceramics 17.6% and cement 14.7%. It is found from Figs. 7(a) and (b) that the whole surface of specimen is quite smooth before the test and the noticeable longitudinal crack can be seen after the failure. Also, the fragments in the crack are scrapped ceramics as shown in Fig. 7(b).

Table 1 contains a summary of results obtained

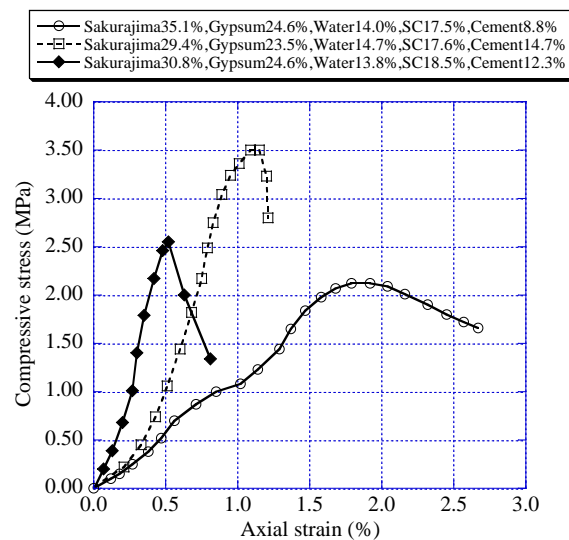


Fig. 6 Stress-strain curve (base materials for seaweed beds, 28 days curing).



(a) Before test



(b) After failure

Fig. 7 Specimen before and after unconfined compression test (Volcanic ashes 29.4%, Recycled gypsum 23.5%, Water 14.7%, Scrapped ceramics 17.6%, Cement 14.7%, 28days curing).

Table 1 Results obtained from unconfined compression test (base materials for seaweed beds, 28 days curing)

Mixing ratio (%)	Volcanic ashes	35.1	29.4	30.8
	Recycled gypsum	24.6	23.5	24.6
	Water	14.0	14.7	13.8
	Scrapped ceramics	17.5	17.6	18.5
	Cement	8.8	14.7	12.3
Unconfined compressive strength (MPa)		2.12	3.50	2.55
Water content (%)		19.0	19.7	19.5
Wet density (g/cm ³)		1.91	1.93	1.76

from the unconfined compression test. The water content for each case is over 19.0% and the specimen shows the same black color as the volcanic ashes including some extent of water. The unconfined compressive strength becomes higher when the mixture ratio of cement increases. In addition, it is noted from visual observations that the surface of specimen in the case of volcanic ashes 30.8%, recycled gypsum 24.6%, water 13.8%, scrapped ceramics 18.5% and cement 12.3%, was very rough and the wet density was the smallest among all cases due to the small amount of water for the cement.

As a result of the dissolution test, a change on pH of specimen after 28 days curing, dipping in artificial seawater is shown in Fig. 8. The graph legend is the same as that in Fig. 6. The initial pH value for the artificial seawater was 9.37. The pH values of all cases were increased by more than 1.0 immediately after dipping the specimen and the values were almost constant after 5 days dipping. The reason why the pH value increased rapidly was that the curing of the specimen was not long enough from visual observations, the specimen was not completely hardened and the volume of artificial seawater for the specimen was small. In the element analysis of constituent parts of artificial seawater, the dissolution of hazardous elements like mercury and hexavalent chromium was not detected within 30 days dipping.

Finally, examples of developed base materials for seaweed beds (6 cases) are shown in Fig. 9. As shown in Fig. 9, the surface of first specimen has many small circular holes and is different with other cases due to the mold. The weight for each base material is approximately 23.0 Kg. In the second to sixth specimens, the half part of the surface is washed by water after the curing to make the rough surface. The pieces of scrapped ceramics on the surface can be seen in the rough part. These would be effective for the rooting of seaweed pores in

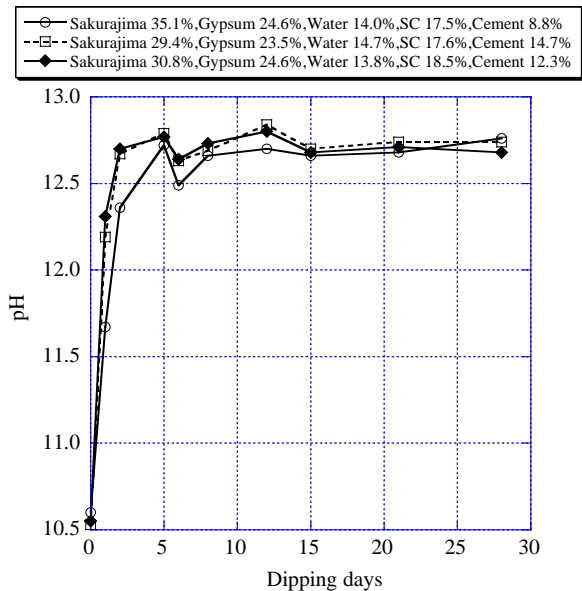


Fig. 8 Change on pH of specimen dipping in artificial seawater.

comparison with the smooth surface of non-washed part. The third, fourth and sixth specimens are the cases with the inclusion of iron powders. In the third specimen, the iron powders of 300g were covered on the surface of the half part of mold, and the same amount of iron powders were mixed into the half part of mold in the fourth specimen. The sixth specimen was the case of mixing the iron powders (3.0% of the whole weight) into the whole part of mold. Additionally, 10.1% shells of the whole weight were mixed into the whole part of mold for increasing the rooting of seaweed in the fifth specimen.

Thus, the effects of the roughness of surface, the mixture of iron powders and shells are regularly monitored for the rooting and growth of seaweed after setting the base materials into Kagoshima Bay. It was observed that the color of surface of the base

■ first specimen

mixing ratio				Cement
Volcanic ashes	Recycled gypsum	Water	Scrapped ceramics	8.8%
35.1%	24.6%	14.0%	17.5%	



■ second specimen

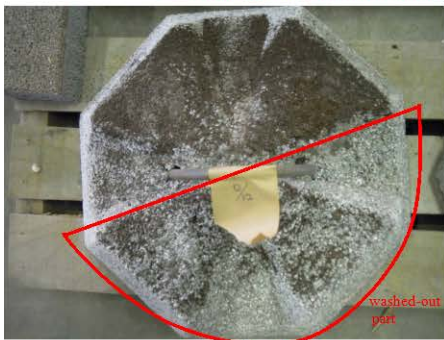
mixing ratio				
Volcanic ashes	Recycled gypsum	Water	Scrapped ceramics	Cement
29.4%	23.5%	14.7%	17.6%	14.7%



■ third specimen

mixing ratio				
Volcanic ashes	Recycled gypsum	Water	Scrapped ceramics	Cement
30.8%	24.6%	13.8%	18.5%	12.3%

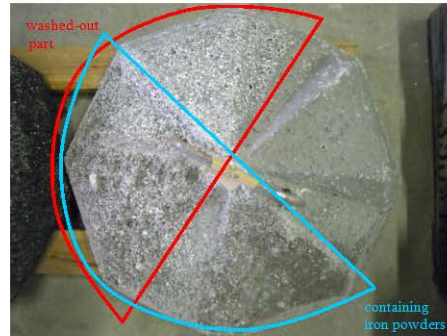
※ cover with iron powders (300g) on the surface



■ fourth specimen

mixing ratio				
Volcanic ashes	Recycled gypsum	Water	Scrapped ceramics	Cement
30.8%	24.6%	13.8%	18.5%	12.3%

※ mix iron powders (300g) into the half part



■ fifth specimen

mixing ratio					
Volcanic ashes	Recycled gypsum	Water	Scrapped ceramics	Cement	Shells
26.8%	21.5%	12.1%	16.1%	13.4%	10.1%



■ sixth specimen

mixing ratio					Iron powder
Volcanic ashes	Recycled gypsum	Water	Scrapped ceramics	Cement	3.0%
29.9%	23.9%	13.4%	17.9%	11.9%	

※ mix iron powders into the whole part



Fig. 9 Example of developed base materials for seaweed beds (6 cases).

materials changes gradually from black to white and small amount of calcium hydroxide comes from the surface, when the base materials are becoming dry. The tendency which the base materials require some time to harden has been confirmed from visual observations in the process of curing.

CONCLUSION

In this study, the base materials for seaweed beds which reduce the environmental impact could be developed using volcanic ashes and recycled materials of industrial wastes. Now the developed base materials have been set into Kagoshima Bay and long-term survey has begun to monitor the rooting and growth of seaweed for these materials at fixed intervals.

ACKNOWLEDGEMENTS

Scrapped ceramics and recycled gypsum are provided by Fukushima Youzai limited company. The authors appreciate the kind cooperation.

REFERENCES

- [1] Terawaki T, Nakayama N, Arai S and Shikida A, "For the restoration of seagrass and seaweed bed", *Aquabiology* 145, Vol. 25 No. 2, Seibutsu Kenkyusha Co. Ltd., 2003, pp. 100–106 (in Japanese).
- [2] Terada R, "A review of a long-term survey for seaweed/seagrass communities in Japan", *Aquabiology* 195, Vol. 33 No. 4, Seibutsu Kenkyusha Co. Ltd., 2011, pp. 291–297 (in Japanese).
- [3] Okuda K, "Coastal environment and seaweed-bed ecology in Japan", *Kuroshio Science* 2-1, 2008, pp. 15–20.
- [4] Yamamoto K, Negami T, Hira M, Aramaki N and Hayashi Y, "Mechanical properties of volcanic products applied physical improvement", *Proc. of the Tenth National Symp. on Ground Improvement*, 2012, pp. 439–442 (in Japanese).
- [5] Negami T, Yamamoto K, Hira M, Hayashi Y and Aramaki N, "Unconfined compressive strength of volcanic ash treated with hardening materials", *Proc. of the Tenth National Symp. on Ground Improvement*, 2012, pp. 443–446 (in Japanese).
- [6] Japanese Geotechnical Society, *Soil test –basis and guideline- (first revised edition)*: Maruzen Print Co. Ltd., 2011, pp. 71-78 (in Japanese).

CARBON FOOTPRINT AWARENESS – AN INVESTIGATION FROM TRAVEL DIARY SURVEY

Nur Sabahiah Abdul Sukor¹ and Nur Khairiyah Basri²

^{1,2} School of Civil Engineering, Engineering Campus, Universiti Sains Malaysia, 14300, Nibong Tebal, Penang, Malaysia.

ABSTRACT

In this study, hundred university students were recruited to fill in the seven days travel diary that described their use of privately owned motor vehicles. The diaries were collected and the respondents were given a motivation session on the carbon emission caused by motor vehicles. Then, they were asked to record their travel pattern for another seven days and were encouraged to change their travel pattern to be more pro-environment. A statistical analysis was done to examine the differences of the individual's carbon footprint before and after the motivation session. The result revealed the significant differences in the carbon footprints between first and second travel diaries. The structural equation modeling demonstrated that among the psychological variables, pro-environment attitude was the most significant factor affecting the respondent's intention to reduce the usage of motor vehicle, thus influencing the respondents' behavior to be more pro-environmentalist.

Keywords: Carbon Footprint, Travel Diary, Theory of Planned Behavior, Pro-Environment

INTRODUCTION

The continuous rise in the number of vehicles together with increasing mileages of travelling on the road have triggered a serious issue of air pollution from these motor vehicles [1]. In fact, the number of motor vehicles, as oppose to human population, in the world is growing more rapidly as since 1960's, 3.5 billion people having 50 million cars in 1950 to over 600 million cars for 6.7 billion people. It was estimated that there will be about a billion cars produce by 2020.

Moreover, Stern [2] reported in his book that the transportation sector accounts for 14 % of total global world GHG emissions, in which the road transport contributes three-quarters of the emissions. In addition, the World Energy Outlook project claimed that the global transport demand appears to be growing up to 45 % by 2030 [3]. Therefore, GHG emissions, resulting from the transportation sector, are undoubtedly posing a serious concern and require attention because of its grievous consequences of the global warming.

The impact of human activities on global warming was usually measured via the carbon footprint calculation [4]. Nowadays, there are numerous carbon calculators available online as well as from consultants regarding the voluntary carbon foot-printing [5]. Wright, Kemp and Williams [6] stated that individual carbon footprint calculator is used to calculate the individual GHG emissions in order to link them to the more pro-environment lifestyle and activities.

However, according to Wiedman and Mix [7], there is still no common consensus has been developed on how to measure the carbon footprint whilst the definition is also still intangible. There are few studies which introduce the carbon footprint concept by measuring the CO₂ together with other greenhouse emissions in units of carbon dioxide equivalent (CO₂-e) [8-12]. However United States Environmental Protection Agency [13] stated that greenhouse emissions such as CH₄ and N₂O are complex to calculate due to their dependency control equipment, vehicle miles travelled, maintenance and operational practice.

In GHG protocol mobile v1.3 [14] it is stated that either fuel-based or distance-based method can be applied to straightforward calculate CO₂ emission for all transportation sources. Fuel-based Method is calculations that based on aggregate fuel consumption data meanwhile distance-based method is calculations based on distance travelled and distance based emission factors.

Lifestyle-travel pattern and psychological impact towards carbon emissions.

Individual lifestyle is also claimed as one of the factors that contributed to the individual carbon footprint, including the individual travel patterns. Vanderbergh, Barkenbus and Gilligan [15] in their study reported that the use of private cars usually related with the idling of the motor vehicle engine. This can be a source of increase in CO₂ emissions. Meanwhile, Susilo and Stead [16] found that the individuals that were young with high income, members of smaller household, and with privately

owned vehicle were more likely to travel farther. These indicators unfortunately lead to the high carbon emissions which are instigated by their travel pattern and lifestyle. They also revealed that some proportion of their respondents were in the favor of this suggestion that in order to reduce the CO₂ emissions, the public transport system should be strategized and promoted.

In order to promote the pro-environment lifestyle Stern [17] suggested that psychology can contribute to the reduction of carbon emissions through developing the understanding of climate relevant to the household, individual and organizational behaviors. For example, the voluntary actions in order to reduce the carbon emissions (by reducing the use of cars) were always directed to the awareness and knowledge towards the environmental issues [18]. In the psychology and behavioral study, the Theory of Planned Behavior (TPB) is renowned in explaining the diversity of human behavior through the prediction of intention, attitude, subjective norms and perceived behavioral control (Fig.1).

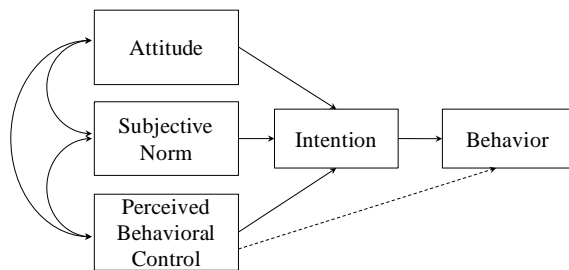


Fig. 1 Theory of Planned Behavior [19]

The extended of TPB were also used to measure the psychological effects towards the pro-environment travel behaviour. For example, Anable [20] in her study to promote the alternative modes for car users found that the voluntary behaviour of switching to more pro-environment mode of transports were affecting by psychological factors such as attitude and beliefs. She stated that the person who die-hard drivers were likely to create reluctant attitude to switch their mode.

On account of believing that psychology could give positive impact in reducing the emission caused by the private vehicles, Fuji and Taniguchi [21] implemented the motivational approach towards groups of people at different county in Japan in order to promote the pro-environment travel behavior. Their study resulted in reduction of CO₂ emissions and car use thus increased in public transport use.

Study Objective

Therefore, the objective of this study is to discover the underlying psychological factors of the

individual carbon footprint based on the altered Theory of Planned Behavior after a motivation session on carbon emissions. This research applies the distance-based method obtained from the travel diary to calculate the CO₂ emissions. For this purpose, this study performed several analyses based on the respondents' travel diary survey. In reporting this study, this paper is organized as follows: Section 2 describes the travel diary, questionnaire and how the survey was implemented; Section 3 presents the results of the analysis of data; finally, section 4 is devoted to discussion and conclusion from the results found.

METHOD

The sample and travel diary

This study is focused on the factors affecting the university students' carbon footprint throughout their use of private motor vehicles. A hundred students from School of Civil Engineering, Universiti Sains Malaysia were recruited and asked to fill in a 7 day travel diary that reported their daily activities and travel patterns. The information from the diaries was used to indicate each of the individual carbon footprints. After they finished with the 7 day diary, they were required to attend a motivational session that was aimed at increasing their awareness towards carbon emission and environmental issues. At the end of the session, they were requested to answer the questionnaire survey pertaining to the psychology. After that, they were asked to fill in another 7 day travel diary in order to check any behavioral change towards their way of travel.

Carbon footprint calculation

Data on distance traveled were collected through the travel diary survey that included the vehicle type and fuel type. The distance estimated from the each individual travel diary was converted to CO₂ emissions by multiplying with distanced-based emissions factor. In this study the distanced-based emission factor was using the source from GHG protocol mobile guide v1.3 [14]. The equation to calculate CO₂ emissions based on the distance traveled method is presented below.

$$CO_2 = \sum Distance_j \times d_j \quad (1)$$

$$d = b \times f \quad (2)$$

where

d = distance based emission factors (kg/100km)

j = different modes of transportation

b = liters per 100km (liter/100km)

f = fuel based emission factors (kg/liter)

In this study, all the respondents were consumed RON95 for their motorized vehicle.

Questionnaire survey

Table 1 Questionnaire statements for psychological variables

Statement	Psychological variables	Answer scale
It is an obligation for each individual to reduce the usage of private motor vehicles to reduce the carbon emissions.	Moral obligation	1= Strongly Agree 2= Agree 3=Disagree 4=Strongly Disagree
In my opinion, an attempt to travel without using private motor vehicles is one of the best acts to reduce the carbon emissions.	Opinion	1= Strongly Agree 2= Agree 3=Disagree 4=Strongly Disagree
I do not attempt to travel by private motor vehicles to reduce the consequences of carbon emissions.	Attitude	1= Strongly Agree 2= Agree 3=Disagree 4=Strongly Disagree
It is hard for me to travel by not using private motor vehicles.	Perceived Behavior Control	1= Strongly Agree 2= Agree 3=Disagree 4=Strongly Disagree
The people that close to me do not support me to reduce the usage of private motor vehicles.	Subjective Norms	1= Strongly Agree 2= Agree 3=Disagree 4=Strongly Disagree

The questionnaire form to measure the psychological effects were given after the motivation session. Since Ajzen [19] suggested that the TPB is open to expansion, so the questionnaire was constructed according to the TPB variables with the addition of moral obligation and opinion. The statements measuring the psychological variables in the questionnaire form are shown in Table 4. The data for all the psychological variables listed below was examined through the structural equation modeling (SEM).

RESULTS

Descriptive analysis

The results of frequency analysis in Table 2 revealed that the age range for the sample recruited is within 19 to 33. The male and female categories are almost balanced with 52% of male and 48% of female. 36.7% of the respondents possessed a car, 17.3% owned a bicycle, 8.2% owned a motorcycle and 31.6% with no vehicle ownership. However in this study, students with bicycle and no vehicle ownership were included in the same group namely students without motor-vehicle ownership.

Table 2 Descriptive statistic of the respondents

Variable	% (N)	Mean (S.D)
Age	-	23.08 (2.82)
Gender		
Male	52 (52)	0.56 (0.502)
Female	48 (48)	0.37 (0.489)
Vehicle ownership		
At least one motorized vehicle ownership	49 (49)	0.49 (0.502)
No motorized vehicle ownership	31.6 (52)	0.52(0.502)

Individual Carbon Footprint

T-test statistical analyses were undertaken in order to examine the differences of carbon footprint values in travel diary 1 and 2. The results showed that there were significant differences on individual carbon footprint emission before and after the motivational lecture session according to gender and motor vehicle ownership. This demonstrates that the motivation session was a success in terms of increasing the students' awareness towards carbon emission issues. The findings also disclosed that after the lecture session, 62% of the respondents had intention to reduce the usage of motor vehicles. However, the respondents who did not own motor vehicles demonstrated no significant difference of carbon footprint between travel diary 1 and 2. It indicates that they kept their carbon footprint low.

Table 3 Statistical t-value for carbon footprint before and after motivation session according to gender and vehicle ownership

Variable	CF before	CF after	t-stat
Gender			
Male	17.024	9.717	1.825*
Female	16.823	12.105	2.169 [#]
Vehicle ownership			
Motorized vehicle ownership	26.348	16.775	2.176*
Non-Motorized vehicle ownership	7.876	5.184	1.665

Note: p-value for male (0.035), female (0.074), motorized owner (0.035), non-motorized owner (0.102); [#]p<0.10, *p<0.05, **p<0.01, ***p<0.001

Psychological Effect

Table 5 presents the estimation results of psychological factors based on the structural equation modeling. Results are presented in terms of estimated parameters and their corresponding t statistics. The overall maximum likelihood estimation of the model yields a chi-square value of 2.799 with 4 degrees of freedom. A review of the goodness-of-fit statistics showed that the model provides a reasonably good fit to the data. In particular, the RMSEA value is lower than 1. The chi-square/d.f. of 0.67 is well below the recommended value of 3.00. The GFI, NFI and CFI values seem probably acceptable and exceed the cutoff value of 0.90

Table 4 Estimated causal effects (standardized) among variables

Path To	Path From	E.P	S.E	C.R
Intention	Atd	-0.205 ***	0.071	-2.123
Intention	PCB	0.143	0.061	1.497
Intention	SN	-0.138	0.059	-1.467
Intention	MO	-0.146	0.082	-1.531
BC	SN	-0.052	2.827	-0.534
BC	Intention	0.197 ***	4.542	2.002
BC	Opinion	-0.160	3.419	-1.646

Note: Atd = Attitude, PCB = Perceived Behavior Control, SN = Subjective Norm, MO = Moral Obligation, BC = Behavior Change, E.P = estimated parameters, S.E = standard error, C.R = critical ratio, *p<0.05, **p<0.01, ***p<0.001

Furthermore, according to the estimation results, several path coefficients were statistically significant. Fig. 5 illustrates the path diagram with the resulting estimates of entire structural parameters have shown on the path. For statistical analysis purpose, the variations in the students' individual carbon footprint were used as the dependent variable. The results indicated that attitude was the only important psychological factor, related to the intention of reducing the individual carbon footprint, whereas, other psychological variables were not that significant. In addition, the attitude also delivered the strongest coefficient value among the psychological variables associated with the behavioral intention of the respondents. The negative coefficient of attitude indicates that the respondents who were not willing to travel by private motor vehicles in order to reduce the carbon footprint are most probably on the verge of making a plan to change their travelling behavior to be more pro-environment, after the lecture session.

The results also indicated that intention was also an extremely important variable associated with the respondents' behavioral change. The positive coefficient showed that the respondents who have an intention to be pro-environment are likely to demonstrate some changes in their individual carbon footprint, after the lecture session. In the case of correlation between the psychological variables, moral obligation was found to be significantly related with the respondents' opinion and attitude. It also disclosed that the respondents who felt it is an obligation to avoid using the privately owned vehicles in order to reduce the carbon emissions are expected to decrease their usage. On the other hand, the respondents with moral obligation were also likely to agree that travelling without using motorized vehicle would be one of the best options to be a pro-environment.

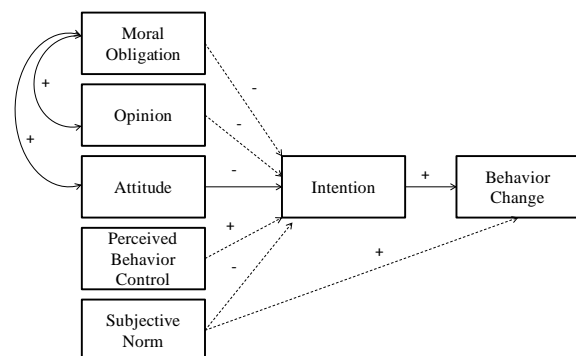


Fig. 2 Estimated model of relationships among psychological variables towards individual carbon footprint behavioral change

Note: N = 100; Cmin = 2.799; d.f.=4; Cmin./d.f.= 0.670; CFI = 1.0; GFI = 0.992; AGFI=0.945; 90% confidence interval

Discussion and Conclusion

This study emphasized on the effectiveness of a motivation session in order to increase the awareness of the carbon footprint that caused by the individual's pattern of travel. The individual carbon footprints were collected through two time frames (each time frame constitutes 7 days) and interspersed by a motivation session that was related to environmental awareness. At the end of the motivation session, the respondents were required to answer the psychological questionnaire.

Our findings reinforced existing evidence for the importance of attitude and intention in predicting changes towards pro-environmental travel behavior. Among the psychological factors, the attitude displayed significantly stronger effect than the intention. However intention was statistically noteworthy towards the behavioral changes. Other psychological antecedents were found to be not that significant.

The differences of carbon footprint value between diary one and diary two revealed that the motivation sessions have delivered a positive impact on the respondents' attitude towards carbon emission issues that instigated by human travel patterns. Male students were found to be more committed with the reduction of their carbon footprint value as compared to female students. This is because most of the male students owned motor vehicles and the motivation session seemed managed to convince them to reduce the use of their private motor vehicle. It is consistent with the t-test findings where the students who owned motor vehicle reduce their carbon print more than those who do not own a vehicle.

However, this study did not confirm whether the motivation session will affect the students' behavior in the long term. It is suggested to assess the respondents' behavior at 6 months interval after the motivation session. Furthermore, other psychological variables except for attitude and intention were not found to be significant that might be due to the small sample size for this study. This might have an impact on the SEM results. Nonetheless, the aim of this study is also to examine the capability of travel diary to gain the carbon footprint data. This is because the travel diary survey is less concerned to be implemented in Malaysia. Therefore, for future research it is aimed to increase the number of samples to gain more accurate results. As a conclusion, this study suggested that a travel diary survey can be used to collect the data for carbon footprint. In addition, this study also confirmed that motivational sessions are effective for increasing awareness on individual's carbon emission, thus affecting the individual's way of travelling.

REFERENCES

- [1] Tiwary, A. and Colls, J. Air Pollution. Measurement, Modelling and Mitigation, 3rd ed., London: Routledge, 2010.
- [2] Stern, N., Stern Review: The Economics of Climate Change. London: HM Treasury, 2006
- [3] Oh, TH and Chua, SC., "Energy Efficiency and Carbon Trading Potential in Malaysia", Renewable and Sustainable Energy Reviews, Vol. 14, No. 7, 2010, pp. 2095 – 2103
- [4] Stiglitz, J., Sen, A. and Fitoussi, J.P., "Mis-Measuring Our Lives", The Report by the Commission on the Measurement of Economic Performance and Social Progress, New York: The New Press, 2010, pp. 113-116.
- [5] Pandey, D., Madhoolika A. and Jai S. P. "Carbon Footprint: Current Methods Of Estimation." Environmental monitoring and assessment Vol 178, no. 1-4, 2011, pp. 135-160.
- [6] Wright, LA., Kemp, S., Williams, I., "Carbon Footprinting: Towards A Universally Accepted Definition", Carbon Management, Vol.2, No. 1, 2011, pp. 61-72.
- [7] Wiedmann, T. and Minx, J. "A definition of 'Carbon Footprint' ", Ecological Economics Research Trends, Nova Science Publishers, 2008, pp. 1–11.
- [8] Lynas M., Carbon Counter. Glasgow: Harper Collins Publishers, 2007.
- [9] UK POST (Parliamentary Office of Science and Technology), Carbon Footprint of Electricity Generation, 2006, pp. 268.
- [10] BSI (British Standard Institute), 'Guide to PAS 2050, How to Assess the Carbon Footprint of Goods and Services', British Standards, London, 2008.
- [11] Browne, D., O'Regan, B., and Moles, R., "Use Of Carbon Footprinting To Explore Alternative Household Waste Policy Scenarios In An Irish City-Region", Resources, Conservation and Recycling, Vol. 54, 2009, pp. 113–122
- [12] Mathez, A., Manaugh, K., Chakour, V., El-Geneidy, A. and Hatzopoulou, M., "How can we alter our carbon footprint? Estimating GHG emissions based on travel survey information", Transportation, Vol.40, 2013, pp 131-149
- [13] "Direct Emissions from Mobile Combustion Sources", United States Environmental Protection Agency, 2008 .
- [14] "Calculating CO2 Emissions from Mobile Sources" GHG Protocol-Mobile Guide (03/21/05)v.13 Available at http://cf.valleywater.org/Water/Where_Your_Water_Comes_From/Water%20Supply%20and%20Infrastructure%20Planning/Climate%20Change/Guidance_for_mobile_emissions_GHG_protocol.pdf. Accessed on 13 February 2013

- [15] Vanderbergh ,MP., Barkenbus, J. and Gilligan, J., "Individual Carbon Emissions: The Low-Hanging Fruit", Vanderbilt University Law School Public Law and Legal Theory, 2008
- [16] Susilo, YO and Stead,D., "Individual CO2 emissions and the potential for reduction in the Netherlands and the United Kingdom ", 88th Annual Meeting of the Transportation Research Board, 2010.
- [17] Stern, P., "Contributions of Psychology to Limiting Climate Change", American Psychologist, Vol. 66, No. 4, 2011, pp. 303 – 314.
- [18] Nilsson, M. and Kuller, R., " Travel behaviour and environmental concern", Transportation Research Part D, Vol.5, 2000, pp. 211-234..
- [19] Ajzen, I., "The Theory Of Planned Behavior." Organizational Behavior And Human Decision Processes, Vol. 50, no. 2 1991,; 179-211.
- [20] Anable, J., "'Complacent car addicts' or 'aspiring environmentalists'? Identifying travel behaviour segments using attitude theory." Transport Policy Vol. 12, no. 1, 2005, 65-78.
- [21] Fujii, S. and Taniguchi, A. "Reducing Family CarUse by Providing Travel Adviceor Requesting Behavioral Plans: An Experimental Analysis of Travel Feedback Programs", Transportation Research D, Vol. 10. No. 5, 2005, pp. 385 – 393.

OPTIMAL MONITORING NETWORK DESIGN FOR EFFICIENT IDENTIFICATION OF UNKNOWN GROUNDWATER POLLUTION SOURCES

Om Prakash^{1,2} and Bithin Datta^{1,2}

¹ Discipline of Civil and Environmental Engineering, School of Engineering and Physical Sciences, James Cook University, Townsville QLD 4811, AUSTRALIA.

² CRC for Contamination Assessment and Remediation of the Environment, Mawson Lakes SA 5095, AUSTRALIA.

ABSTRACT

Application of linked simulation-optimization approach for solving groundwater identification problems is well established. Pollutant concentration measurements from different sets of monitoring locations, when used in a linked simulation-optimization approach, results in different degrees of accuracy of source identification. Moreover, the accuracy of source identification results depends on the number and spatiotemporal locations of pollutant concentrations measurements. This study aims at improving the accuracy of source identification results, by using concentration measurements from an optimally designed monitoring network. A linked simulation optimization based methodology is used for optimal source identification. Genetic programming based impact factor is used for designing the optimal monitoring network. Concentration measurement data from the designed network is then used, in the Simulated Annealing based linked simulation-optimization model for efficient source identification. The potential application of the developed methodology is demonstrated by evaluating its performance for an illustrative study area. These performance evaluation results show improvement in the efficiency in source identification when such designed monitoring networks are utilized.

Keywords: Optimal Monitoring Network; Groundwater Pollution; Genetic Programming; Multi-Objective Optimization; Pollution Source Identification; Simulated Annealing

INTRODUCTION

The most common problem encountered in remediation of a polluted aquifer, is the accurate identification of pollution source locations and their release histories from sparse set of spatiotemporal concentration measurements. In scenarios where potential source locations and activity duration are known with fair degree of certainty, linked simulation-optimization based approach is often applied for solving groundwater pollution source identification problem for recreating the flux release history of the sources.

A large number of concentration measurements spread over time and space is necessary for accurate identification of pollution sources. However, long term monitoring over a large number of monitoring locations has budgetary constraints. Hence monitoring locations should be chosen such that concentration measurements from such designed monitoring network when used in a linked simulation-optimization approach, improves the accuracy of source identification results. Contrary to this, monitoring locations often consists of arbitrarily located single water supply well, or a group of arbitrarily placed wells which may not be optimally located for accurate source identification.

Design of monitoring networks may have different underlying objectives, such as optimal sampling plan for groundwater quality monitoring

[1], cost-effective sampling design [2], sampling strategy in space and time using Kalman filter [3], optimal monitoring network for early detection of pollutant [4], [5], minimizing the number of monitoring wells [6]. Optimization based solution for reducing the redundancy in a groundwater quality monitoring network [7], sequential monitoring network design [8], and variation of dynamic monitoring network design methodology is discussed in [9].

Most of the existing methodologies of source identification using linked simulation-optimization use concentration measurements from arbitrarily located monitoring wells. Limited amount of work has been reported for improving the accuracy of source identification using concentration measurements from an optimally designed monitoring network. A methodology is proposed for design of optimal monitoring network for improving the accuracy of source identification results using concentration measurements from a designed monitoring network. The simulated response of the aquifer is compared to the observed response of the aquifer at these optimal monitoring locations in a classical linked simulation-optimization technique.

The monitoring network designed to improve the accuracy of source identification is based on two conflicting objectives, (1) reduce the possibility of missing an actual source, and (2) decreases the degree of non uniqueness in the set of possible

aquifer responses to subjected geo-chemical stresses. The proposed methodology uses genetic programming (GP) models to calculate the impact factor of a source on a candidate monitoring location. This impact factor is utilized as the design criteria for choosing the optimal monitoring locations out of the candidate well locations. The conflicting objectives considered are, (1) maximization of the normalized impact of all potential pollution sources at selected monitoring locations and (2) to maximize the relative impact of a potential source at the chosen monitoring location. The Pareto-optimal solutions obtained from the two objective model is utilized to relate the variation in the accuracy of source identification results and the trade-off between the above stated conflicting objectives for designing an optimal monitoring network. Performance of the proposed source identification methodology is evaluated by solving an illustrative problem. The results of source identification are compared for different random monitoring networks with that of the optimal network. This method can be applied to practical scenarios where the observed concentration data is to be restricted to a few monitoring locations.

METHODOLOGY

In this proposed methodology, first GP models are trained against a large set of data pattern comprising of source flux history for all the potential sources as input and corresponding aquifer response at all potential monitoring locations as the output. Based on R^2 value specified, a number of fittest GP models are chosen for calculating the impact factor of potential source on a monitoring location. The impact factor is calculated for all candidate monitoring locations at each monitoring time step. A multi-objective optimization formulation is applied to select the optimal set of monitoring location for source identification using linked simulation-optimization technique. In the second step, a SA based linked simulation-optimization model for source identification is solved to minimize the deviation between the simulated and measured pollutant concentrations at these optimally chosen monitoring locations.

Genetic Programming and Impact Factor

GP is an evolutionary optimization algorithm based on the concepts of genetics and natural selection. It starts with an initial population of randomly generated computer programs and optimizes the parameter values of a given model structure within predefined parameter space to find a highly fit computer program that produces desired output for particular set of input. Each GP model is essentially a computer program that represents the mathematical relationship between the dependent

variable (pollutant concentration at chosen monitoring locations and times) and the independent variables (flux values of pollutant at potential pollutant source locations).

Specified number of best individual GP models is used for computing the impact factor. The impact factor is described as a measure of how much an input variable accounts for the output result i.e., a factor by which the result would differ if the variable was removed. This essentially implies that, if by removing a variable from the mathematical function (GP model) there is a large change in the output, then the removed variable has a high impact on the output and hence the impact factor of that variable will be high. The impact factor value is then used as design criteria in a multi-objective optimization formulation for designing an optimal monitoring network.

Multi-Objective Optimization for Monitoring Network Design Model

An SA based multi-objective optimization model is utilized for choosing monitoring locations such that the possibility of missing an actual source is reduced, and at the same time reduces the degree of non-uniqueness due to overlapping of multiple pollutant plumes. This is accomplished by an SA based multi-objective optimization model that finds monitoring well locations with the following objectives (1) finding well locations with maximum normalized impact from all the potential sources and (2) finding well locations with maximum normalized relative impact from an individual potential source over a chosen observation period. Finding well locations with maximum normalized average impact (objective 1) reduces the possibility of missing an actual source as it chooses locations where overlapping of plumes due to potential sources is maximum. This also reduces the likelihood of choosing monitoring locations where the impact of potential sources are small. However objective 1 is in conflict with objective 2 of finding well locations with maximum normalized relative impact from an individual potential source. The second objective essentially reduces the non-uniqueness due to overlapping of different pollutant plumes resulting from different sources.

A multi-objective optimization model is formulated to design an optimal monitoring network with multiple conflicting objectives. One of the objectives is traded off to improve the other objective and vice versa. The constrained method is utilized, which iteratively maximizes one of the objectives subject to the other objective achieved at a specified level. The number of monitoring wells to be selected is essentially governed by budgetary constraints. The formulation for the multi-objective optimization for monitoring network design is given in Eq. (1) through Eq. (11).

$$IF_{iob}^S = \sum_{t=1}^{nt} (F_{iob}^{St}) \quad (1)$$

IF_{iob}^S is the impact factor of source S on monitoring well location iob

F_{iob}^{St} is the impact factor of source S on monitoring well location iob at stress period t

$$SumIF_{iob}^S = \sum_{k=1}^{nk} (IF_{iob}^S)^k \quad (2)$$

$SumIF_{iob}^S$ is the sum of the impact factors of a potential source S at any given monitoring location iob for nk sampling steps

$$SumIF_{iob}^{norm} = \sum_{S=1}^{nS} \frac{SumIF_{iob}^S}{\frac{1}{nob} \sum_{iob=1}^{nob} SumIF_{iob}^S} \quad (3)$$

$SumIF_{iob}^{norm}$ is the normalised sum of impact factor at any monitoring location iob due to all the potential sources nS for all nk monitoring time steps

nt is the total number of stress periods

nk is the total number of monitoring time steps

$\frac{1}{nob} \sum_{iob=1}^{nob} SumIF_{iob}^S$ is the average impact factor due to a source S at all monitoring well locations nob

$$Rel SumIF_{iob} = Max\{SumIF_{iob}^S\} - ((\sum_{S=1}^{nS} (SumIF_{iob}^S)) - Max\{SumIF_{iob}^S\}) \quad (4)$$

$Rel SumIF_{iob}$ is the relative impact factor due to all the sources nS at a given monitoring well location iob

$$Rel SumIF_{iob}^{norm} = \frac{Rel SumIF_{iob}}{\frac{1}{nS} \sum_{S=1}^{nS} SumIF_{iob}^S} \quad (5)$$

$Rel SumIF_{iob}^{norm}$ is the normalized relative impact factor at monitoring well location iob for all potential sources

$\frac{1}{nS} \sum_{S=1}^{nS} SumIF_{iob}^S$ is the average impact factor at monitoring well location iob for all potential sources

The two objectives $F1$ and $F2$ of the multi-objective optimization model for optimal monitoring network design for accurate identification of unknown pollution sources is defined by Eq. (6) and Eq. (8) respectively.

$$Maximize F1 = \sum_{iob=1}^{nob} SumIF_{iob}^{norm} f_{iob} \quad (6)$$

$$Maximize F2 = \sum_{iob=1}^{nob} Rel SumIF_{iob}^{norm} f_{iob} \quad (7)$$

$$\sum_{iob=1}^{nob} f_{iob} \leq \alpha \quad (8)$$

α is integer constant representing the maximum number of wells that can be chosen

f_{iob} represent the binary decision variable to select a monitoring well location $f_{iob} \equiv \{0,1\}$ such that when f_{iob} value equal to 1 representing monitoring well to be selected at location iob , and zero otherwise

$$\sum_{iob=1}^{nob} Rel SumIF_{iob}^{norm} f_{iob} - \lambda \geq 0 \quad (9)$$

$$Max F2 \geq \lambda \quad (10)$$

$$F2_{Max F1} \leq \lambda \quad (11)$$

The two objective multi-objective optimization model is solved using the constrained method where one of the objective function (F1) is maximized keeping minimum level of satisfaction (λ also termed as the trade-off constant) of the second objective function (F2) as shown in Eq. (9). All solutions lying on the Pareto-optimal front corresponds to a different monitoring network.

Linked Simulation-Optimization Model for Source Identification

Groundwater flow (MODFLOW) and solute transport (MT3DMS) simulation model are used to simulate the physical process within the optimization model. Simulated Annealing (SA) is used as an optimization algorithm to solve the optimization problem. Candidate values of unknown variables (source fluxes) are generated in optimizations algorithm for simulations of flow and transport models. The difference between simulated and observed pollutant concentrations are computed, and finally obtain an optimal solution that minimizes the difference between observed and simulated values.

$$Minimize F = \sum_{k=1}^{nk} \sum_{iob=1}^{nob} ABS(cest_{iob}^k - cobs_{iob}^k) \quad (12)$$

$$cest_{iob}^k = f(q_s, C_s) f(q_s, C_s, cest_{iob}^k) \quad \forall iob, k \quad (13)$$

$q_s C_s$ is the pollutant source fluxes

q_s is the volumetric flux

C_s is the concentration of the sources or sinks

ABS is the absolute difference

$cest_{iob}^k$ is the simulated concentration

nk is the total number of monitoring time steps

nob is the total number of observation wells

$cobs_{iob}^k$ is the observed concentration

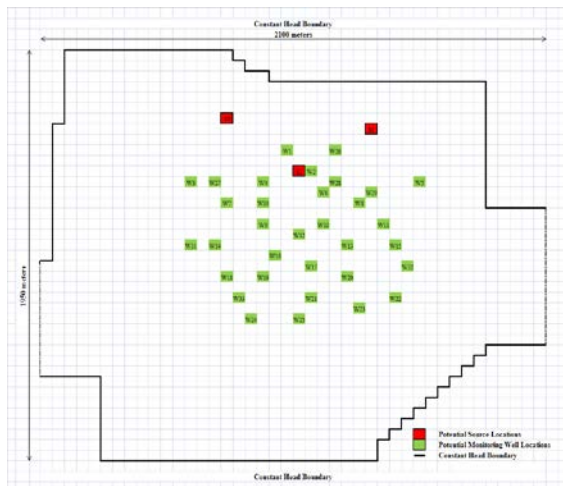
PERFORMANCE EVALUATION

The performance of the developed methodology was evaluated for the study area shown in Fig. 1, with hydro-geological parameters as given in Table

1. Three sources with three stress periods of 500days each were considered. The pollutant flux from each of the sources is assumed to be constant over a stress period. Four temporal concentration measurements at each potential location (starting $t = 1600$ days) are taken after every 200 days.

Fig. 1 Plan view of the Illustrative Study Area

Table 1 Hydro-geological Parameters



Parameter	Unit	Value
Maximum length of study area	m	2100
Maximum width of study area	m	1950
Saturated thickness, b	m	30
Grid spacing in x-direction, Δx	m	50
Grid spacing in y-direction, Δy	m	50
Grid spacing in z-direction, Δz	m	30
Hydraulic conductivity, K	m/d	20
Effective porosity, θ		0.3
Longitudinal Dispersivity, αL	m/d	20
Transverse Dispersivity, αT	m/d	10
Horizontal Anisotropy		1
Initial contaminant concentration	g/l	0
Diffusion Coefficient	g/s	0-100
Contaminant Flux		

Genetic Programming Impact Factor

The impact factor is calculated for 3 sources and 25 (W1 to W25 as shown in Fig. 1) potential monitoring well locations. The input data consists of flux values for each source at every stress period. The corresponding output data consists of the resulting pollutant concentration measurement due to these source fluxes at all the 25 potential monitoring well at $t = 1600$, $t = 1800$, $t = 2000$ and $t = 2200$ days. 3000 data patterns are used of which 50% is used for training, 40% for validation, and

10% for testing the GP models. DiscipulusTM 5.1 (RML Technologies, Inc.) is used for training, validation and testing. Based on R^2 fitness value, top 30 GP models are used for computing the impact factor. The impact factor for all the potential monitoring locations at every sampling time step is calculated likewise which is then used to calculate the normalized relative impact factor $^{Rel} SumIF_{iob}^{norm}$ and normalised sum of impact factor due to all the potential sources $SumIF_{iob}^{norm}$.

Optimal Monitoring Network and Arbitrary Monitoring Network

The optimal monitoring design model is solved using normalised impact factor values as calculated above. The value of the minimum satisfaction level of objective function F2 is varied from a minimum - 1.7 to a maximum of 8.06 to obtain 12 different Pareto-optimal solutions representing different Pareto-optimal monitoring networks: MN1 to MN12. To show the comparison, 10 arbitrary monitoring networks ARMN1 to ARMN10 are chosen. A total of 6 monitoring wells are selected in each monitoring network.

Source Identification using Data from Pareto-Optimal Monitoring Networks and Arbitrary Monitoring Network

To evaluate the performance, observed concentration measurements are generated synthetically. These simulated measurements are then perturbed with random error term (maximum deviation of 10 percent of the measured concentration data) to incorporate realistic measurement errors (Eq. 17 to Eq. 18). A linked simulation-optimization model is solved using measurements from 12 Pareto-optimal monitoring networks (MN1 to MN12) and 10 arbitrary monitoring networks (ARMN1 to ARMN10). The source identification model is solved with error free data and perturbed erroneous data.

$$^{Pert} cobs_{iob}^k = cobs_{iob}^k + err \quad (14)$$

$$err = \mu_{per} \times rand \quad (15)$$

$^{Pert} cobs_{iob}^k$ is the perturbed concentration value

$cobs_{iob}^k$ is the numerically simulated concentration value

err is the error term

μ_{per} is the specified maximum deviation expressed as a fraction < 1

$rand$ is a random fraction between -1 and +1

RESULTS AND DISCUSSION

The Pareto-optimal solution for the two-objective optimal monitoring network design model is shown in Fig. 2. The first objective function values $F1$ is plotted against the minimum satisfaction level of the second objective function value $F2$. The non-inferior solutions show the conflicting nature of the two objective functions and

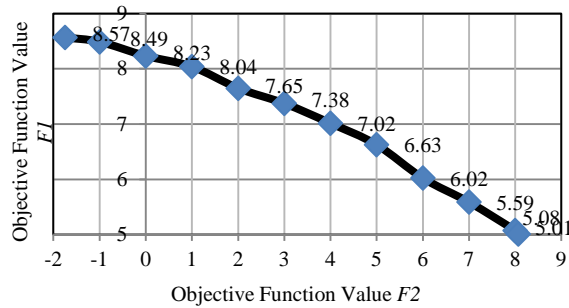


Fig. 2 Pareto Optimal Solution Front

their trade-off.

The results of source flux identification solution results obtained by using linked simulation-optimization model is compared for all the 12 Pareto-optimal monitoring locations (MN1 to MN12), obtained as solutions, using error free and perturbed error data (Fig 3 and Fig 4).

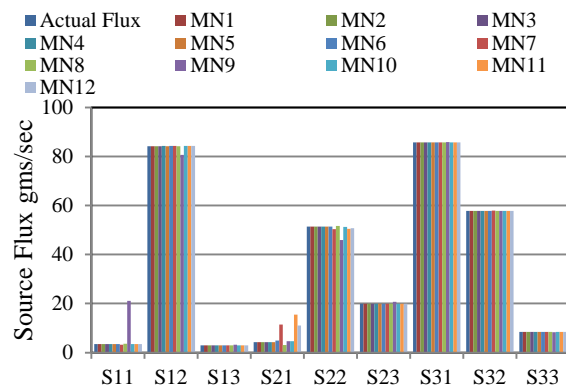
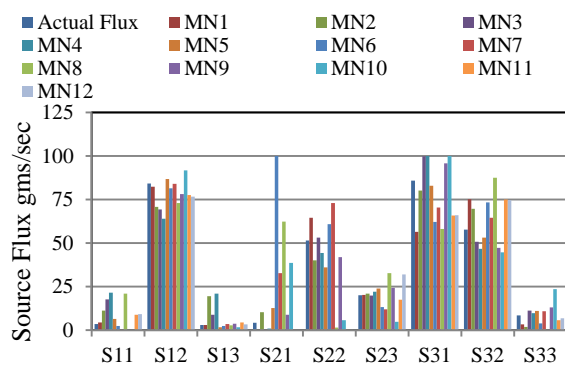


Fig. 3 Identification Results using Error free data



To choose the best monitoring network out of the 12 Pareto-optimal monitoring networks (MN1 to MN12), absolute difference of actual source flux and

the estimated source flux for all the 12 Pareto-optimal monitoring networks is calculated using error free data and erroneous data (Fig. 5 and Fig. 6). Absolute difference of actual source flux and the estimated source flux for all the 12 Pareto-optimal monitoring networks (MN1 to MN12) with error free data and erroneous data show similar trend. The average of the absolute difference, between the actual source flux and the estimated source flux is minimum for monitoring network 5 (MN5), hence can be designated as the optimal monitoring network.

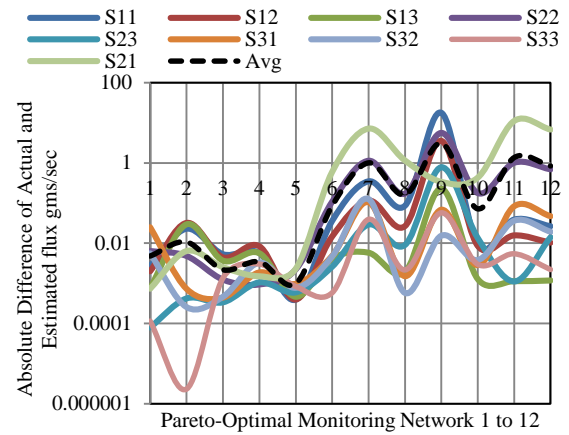
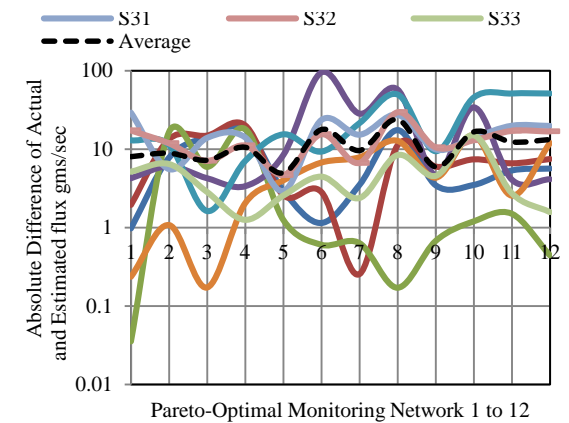


Fig. 5 Difference of Actual Flux and Estimated Flux- Error free Data

Fig. 6 Difference of Actual Flux and Estimated Flux- Erroneous Data



The source identification model is solved for 10 arbitrary networks (ARMN1 to ARMN10) with both error free data and erroneous data. The estimated flux values using the arbitrary networks is averaged and compared with the actual flux values and estimated flux value from monitoring network 5 (MN5), both for error free data and erroneous data (Fig. 7 and Fig. 8). It is seen that the estimated flux using monitoring network 5 (MN5), are closer to the actual flux values as compared to the flux estimated using the arbitrary networks (AVG-AR).

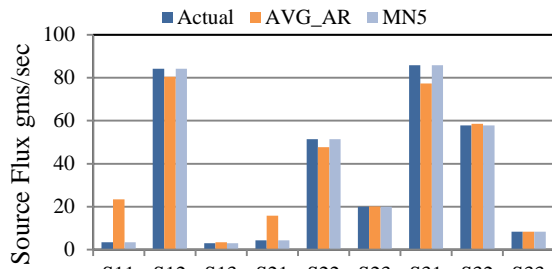
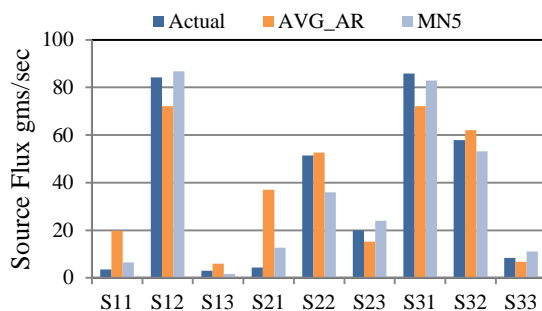


Fig. 7 Comparison of Identification Results using Optimal Network and Arbitrary Networks: Error free Data

CONCLUSIONS



Not all monitoring locations are ideally located for accurate identification of source flux using linked simulation-optimization. The solution results in the illustrative example problem show that the accuracy of source flux identification varies when using pollutant concentration measurement data from different monitoring locations. A methodology has been developed for designing an optimal monitoring network for accurate source flux identification. Concentrations measurements from such a designed monitoring network when used in source flux identification, can improve the accuracy of the source identification results.

An optimal monitoring network design for source flux identification is a multi-objective problem. It requires the right balance between well locations where the impact of all the potential sources are significantly large, reducing the possibility of missing an actual source and, well locations where non-uniqueness due to overlapping of source plumes is less. In all real world problems of source identification, the degree of uncertainty in terms of source locations and aquifer response to subjected geo-chemical stress are large. Moreover, the number of monitoring wells to be implemented for concentration measurement data is governed by budgetary constraints. The proposed methodology can be applied to polluted aquifer sites. This method can decrease such uncertainties using limited number of monitoring wells which otherwise will have to be reduced by implementing large number

of monitoring wells, resulting in increased capital cost. This method can increase the accuracy of source identification with concentration measurement data from limited number of monitoring wells in a designed monitoring network.

REFERENCE

- [1] Loaiciga, H. A. (1989), An optimization approach for groundwater quality monitoring network design, *Water Resource Research*, 25(8):1771–1782.
- [2] Mugunthan, P., and C. A. Shoemaker (2004), Time varying optimization for monitoring multiple pollutants under uncertain hydrogeology, *Bioremediation Journal*, 8(3–4):129–146.
- [3] Kollat, J. B., P. M. Reed and R. Maxwell (2011), Many-objective Groundwater Monitoring Network Design using Bias-Aware Ensemble Kalman Filtering, Evolutionary Optimization, and Visual Analytics, *Water Resource Research*, v47, W02529.
- [4] Loaiciga, H. A., and P. F. Hudak (1992), A location modelling approach for groundwater monitoring network augmentation, *Water Resource Research*, 28(3):643–649.
- [5] Loaiciga, H. A., and P. F. Hudak (1993), An optimization method for network design in multilayered groundwater flow systems, *Water Resource Research*, 29, 2835.
- [6] Meyer, P. D., A. J. Valocchi and J. W. Eheart (1994), Monitoring network design to provide initial detection of groundwater pollution, *Water Resource Research*, 30, 2647.
- [7] Dhar, A., and B. Datta (2010), Logic-Based Design of Groundwater Monitoring Network for redundancy Reduction, *Journal of Water Resource Planning and Management*, 136,88(2010).
- [8] Dhar, A., and B. Datta (2007), Multi-objective design of dynamic monitoring networks for detection of groundwater pollution, *Journal of Water Resource Planning and Management*, 133(4):329–338.
- [9] Sreenivasulu, C., and B. Datta (2008), Dynamic optimal monitoring network design for transient transport of pollutants in groundwater aquifer, *Water Resources Management*, 22(6):651–670.

SPATIAL DISTRIBUTION CHARACTERISTICS OF SUBTERRANEAN HOT WATER EVALUATED USING WATER QUALITY CONCENTRATION DATA

Takamitsu Kajisa¹, Si Senfi¹, Yasunori Mori^{1,2}, Homayoon Ganji¹,
Abdul Saboor Rahmany¹, Masaaki Kondo¹, and Hajime Narioka¹

¹Graduate School of Bioresources, Mie University, Japan

²Mie Prefecture Health and Environment Research Institute, Japan

ABSTRACT

Spatial distribution characteristics of subterranean hot water were indexed using correlation coefficient's (R) p -values for hot spring water quality indicators. For example, in a case where the p -value of R was smaller than 5%, the correlations of a set of water qualities for two hot springs were significant. In this study, in a dense hot spring area, the minimum distance with a p -value greater than P_c (critical p -value) was proposed as a stochastic and critical distance (X_c) for both new and existing hot spring owners. By using data from 10 hot springs in each area, 45 sets of distances and p -values were examined. Of the five areas examined, three and four X_c s more than 1,000m were found for P_c 1% and P_c 5%, respectively. The experimental relation between the given X_c and the hot spring depth could not be confirmed. Results indicate that the influence of water quality from new hot springs located outside of the X_c range is not always insignificant, even though the water quality of the new hot springs should primarily influence existing springs located within the X_c range.

Keywords: hot spring, subterranean hot water, hot springs law, correlation coefficient, p-value

INTRODUCTION

In Japan, in areas where wells for hot spring spas are numerous, decaying water quality has been observed. To combat this problem, the "Guideline for the protection of hot spring resources" was developed under the Hot Springs Law by the Japanese Ministry of the Environment [1].

A water source is determined to be a hot spring by the "Hot Spring Law" (Onsen-ho), if the hot water discharged from underground is equal to or above 25°C. When it is below 25°C, it must satisfy at least one of the 19 elements listed in Table 1.

According to the guidelines [1], the limiting distance for new wells, X_g , is 300–500m, as set forth by the questionnaires administered in 23 prefectures. X_g being the critical limiting distance proposed in practice for public judgment (m). Some X_g s were given numerically by questionnaires, water balance and heat balance. From the viewpoint of water balance, X_g is 406 m. For deep hot springs, X_g s are 1,000–2,000 m. By calculating heat balance, X_g s are 1,030–1,780 m. On account of numerous hypotheses applied, the logic of employing these distances is not particularly strong. Hence, using critical limiting distance, X_g , is very simple.

The depth of hot spring wells can substantially differ. Wells with depths of more than 1,000 m are called deep hot springs, whereas those with depths lower than 1,000 m are called shallow hot springs. In

order to receive authorization for a hot spring, it is necessary to obtain water quality data. Therefore, much hot water quality data is available. In this study, we focused on five areas with available hot spring water quality data. Ten hot water springs were used for each area, totaling to 50 hot springs. Particular types of water qualities were selected to determine correlations among the hot springs.

Hot springs with similar water quality may have the same source. Digging a new hot spring with a similar water quality is a potential water resource hazard for the existing hot spring owner. If the water quality difference of two hot springs can be estimated by the distance between them, a parameter that is easily determined, this could help in avoiding such hazards. Therefore, the water quality differences between two hot springs were discussed relative to the distance between the hot springs. For analysis, the following three hypotheses were made.

- 1) Steady state hypothesis is used. The correlation coefficient (R) of water quality between two hot springs can be numerically given as a constant number by a stochastic method.
- 2) In cases where the correlation is significant, as the p -value of R is smaller than the critical value P_c , the water source or root of the flow is expected to be near.
- 3) In cases where the water source or root of the flow is near, digging a new hot spring may affect the

existing hot spring.

Estimation of the critical distance X_c would assist both a new owner digging a new hot spring and the existing hot spring spa owner. In this study, X_c is the critical distance determined by using stochastic method, which is numerically given by evaluating the similarity of certain chemical data measured in each of the hot springs.

OBJECTIVES

Under all three hypotheses given in the Introduction, three objectives were created, which are mentioned as follows:

1) Confirm how the combination samples of X and p -value will be classified by X_c and P_c .

X being the distance between the new and existing hot spring (m).

2) Determine whether X_c varies with hot spring depth.

3) Clarify the essential meaning of X_g s and X_c s by discussing the difference between them.

These three objectives were examined by collecting and analyzing water quality data of existing hot springs.

CALCULATIONS

The mutual relations among the logarithm values

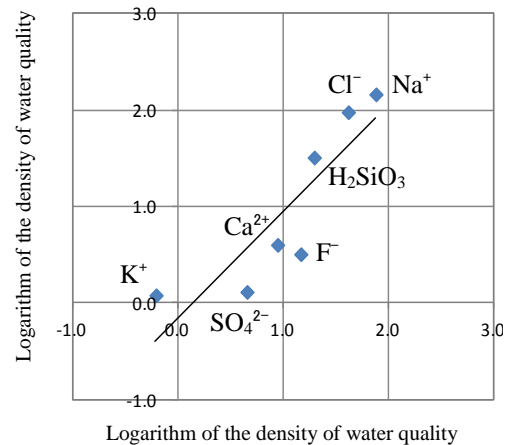
Table 1 Standard of hot spring spa

temperature	$\geq 25^\circ\text{C}$
total soluble component	$\geq 1,000 \text{ mg/kg}$
CO_2	$\geq 250 \text{ mg/kg}$
Li^+	$\geq 1 \text{ mg/kg}$
Si^{2+}	$\geq 10 \text{ mg/kg}$
Ba^{2+}	$\geq 5 \text{ mg/kg}$
$\text{Fe}^{2+}, \text{Fe}^{3+}$	$\geq 10 \text{ mg/kg}$
Mn^{2+}	$\geq 10 \text{ mg/kg}$
H^+	$\geq 1 \text{ mg/kg}$
Br^-	$\geq 5 \text{ mg/kg}$
I^-	$\geq 1 \text{ mg/kg}$
F^-	$\geq 2 \text{ mg/kg}$
HAsO_4^{2-}	$\geq 1.3 \text{ mg/kg}$
HAsO_2	$\geq 1 \text{ mg/kg}$
S	$\geq 1 \text{ mg/kg}$
HBO_2	$\geq 5 \text{ mg/kg}$
H_2SiO_3	$\geq 50 \text{ mg/kg}$
NaHCO_3	$\geq 340 \text{ mg/kg}$
Rn	$\geq 2 \times 10^{-9} \text{ Ci/kg}$
Ra	$\geq 1 \times 10^{-8} \text{ mg/kg}$

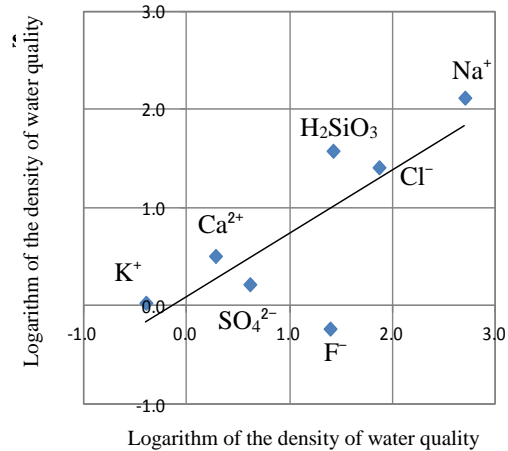
for seven types of water quality indicators (ppm) are illustrated in **Fig. 1**. A logarithmic function was used because of the varying order of magnitude for water quality parameters.

The correlation value for both hot springs can be obtained using a stochastic method. Seven types of water quality indicators, shown in **Table 2**, were selected on the basis of the following three points: (1) The hot spring water qualities as defined by the ministry in the hot-spring standard (**Table 1**). (2) The water qualities derived from previous hot springs, shown in [2][3]. (3) The geology-based water qualities shown in Piper's trilinear diagram. In this study, we selected Na, K, Ca, F, Cl, SO_4 , and H_2SiO_3 . Because these seven water quality indicators were used, the data number n for determining R is seven.

The p -value was used as the index that demonstrates



(a) A case where p -value is 1%



(b) Case where p -value is 5%

Fig. 1 Examples of a set of data.

the significance of the correlation R . Although the procedure for calculating p -value using R and n is essential, it is widely explained in other books and hence not elaborated in this study.

When the p -value of R is larger than P_c , the correlation is not significant. From the second hypothesis given in the Introduction, a high p -value suggests that digging a new hot spring will not affect the water of the existing hot spring.

In sections I and II of Fig. 2, where the p -value is more than the threshold value P_c , the correlation is not significant. In section I, there is no theoretical plot. Therefore, in this study, X_c is defined as the minimum distance X of the plots in section II. The possibility that the new hot springs affect the existing ones is presumed small for this section.

On the other hand, in sections III and IV, the correlation is significant. For the range IV plot group, even if the distance is longer than X_c , the correlation of water quality may be significant. Therefore, the new hot spring may affect the existing spring.

HOT SPRINGS USED FOR ANALYSIS

In this study, the prefecture shown in Fig. 3 was used. Ten spa facilities for each of the five areas were selected; that is, the water quality of 50 hot springs was used. By combining all hot springs in each area, a total of 45 sets of two hot spring combinations were possible (i.e., 45 distances X and R coefficients for each area).

As shown in Table 3, in area 1, most hot springs were deep. On the other hand, in area 5, which was well known for its hot springs, most hot springs were shallow. In areas 2, 3, and 4, deep hot springs were more in number than shallow hot springs.

RESULTS

Table2 Dataset used for analysis

water quality	chemical symbols
Sodium ion ^{2, 3}	Na ⁺
Potassium ion ^{2, 3}	K ⁺
Calcium ion ^{2, 3}	Ca ²⁺
Fluoride ion ^{1, 2}	F ⁻
Chloride ion ^{2, 3}	Cl ⁻
Sulfuric acid ion ^{2, 3}	SO ₄ ²⁻
Metasilicic acid ^{1, 2}	H ₂ SiO ₃

1: water quality shown in the hot-spring standard

2: water quality shown in [2] and [3]

3: water quality used in the trilinear diagram

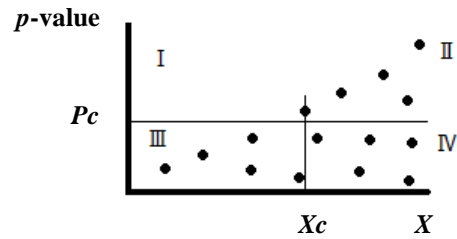


Fig. 2 The condition P_c and selected X_c on X -(p -value) plane, where each point indicates the result for the hot-spring combinations.

Table 3 Major depth types for each area

area	deeper than 1,000 m	shallower than 1,000 m	the major type
1	9	1	deep
2	6	4	deep
3	7	3	deep
4	6	4	deep
5	1	9	shallow

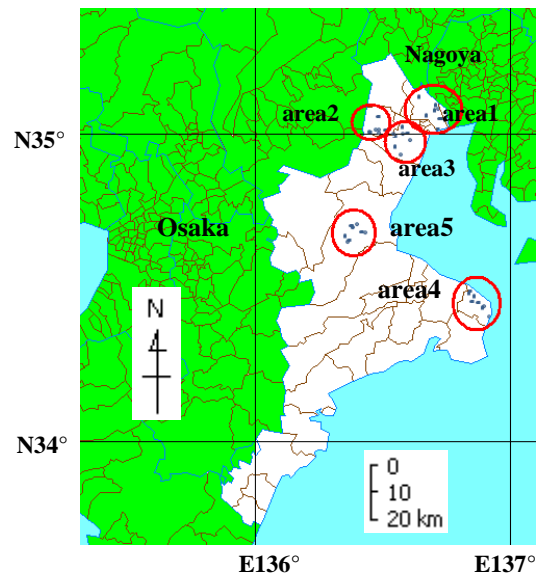


Fig. 3 Map of hot spring locations in each area.

As some of the water qualities are numerically zero, the logarithm of all data points could not be calculated. As the data number (n) was expected to be constant, the R values for such cases were not used in this study. Therefore, the given numbers of R were not always 45, as shown in **Table 4**. For areas 1–5, the numbers of plots were 36, 45, 45, 36, and 45, respectively.

By using the concept of X_c and P_c as shown in **Fig. 2**, the combinations of the X s and p -values were separated by P_c 5% as shown in **Figs. 4 (1)–(5)**. There is no theoretical plot in section I because the vertical line is drawn for making such a situation. Alternatively, there was no area without plots in the section IV. This result was the similar for the combination of X s and p -values separated by P_c 1%.

DISCUSSION

X_c s can also be explained using **Figs. 5 (1)–(5)**, where each hot spring is shown as a plot. The five figures in the left-hand column represent the raw data.

The middle five figures present the distances whose p -values are less than 5%. The right-hand-side figures show the distances whose p -values are less than 1%.

In **Figs. 5 (1)–(5)**, if the group of solid lines show almost the same direction in one area, and yet if such a group is not shown in the figures on the left, it suggests that underground the water is flowing in the same ground layer. However, this type of grouping of solid lines was difficult to see.

1) The samples classified by X_c and P_c

As the combination samples of X s and p -values were classified as shown in **Figs. 4 (1)–(4)**, each could be counted without the samples having water quality that is numerically zero (**Table 4**).

The four samples having the smallest distance had p -values of 0.00001, 0.00040, 0.00202, and 0.00000 for distances of 0, 187, 331, and 392 m, respectively. The order of these numbers means that the p -value becomes very small as distance X becomes very small. Because such a small X is rare, it was lucky for us that the p -value could be obtained.

For large distance X , the numbers of the samples for which there was a combination of X and p -value were not small, as shown in the section IV in **Table 4**. Therefore, digging a new hot spring in such cases may affect the existing hot spring located at a large distance.

2) Order of X_c along the depth

In **Table 5**, for the four deep hot spring areas (areas

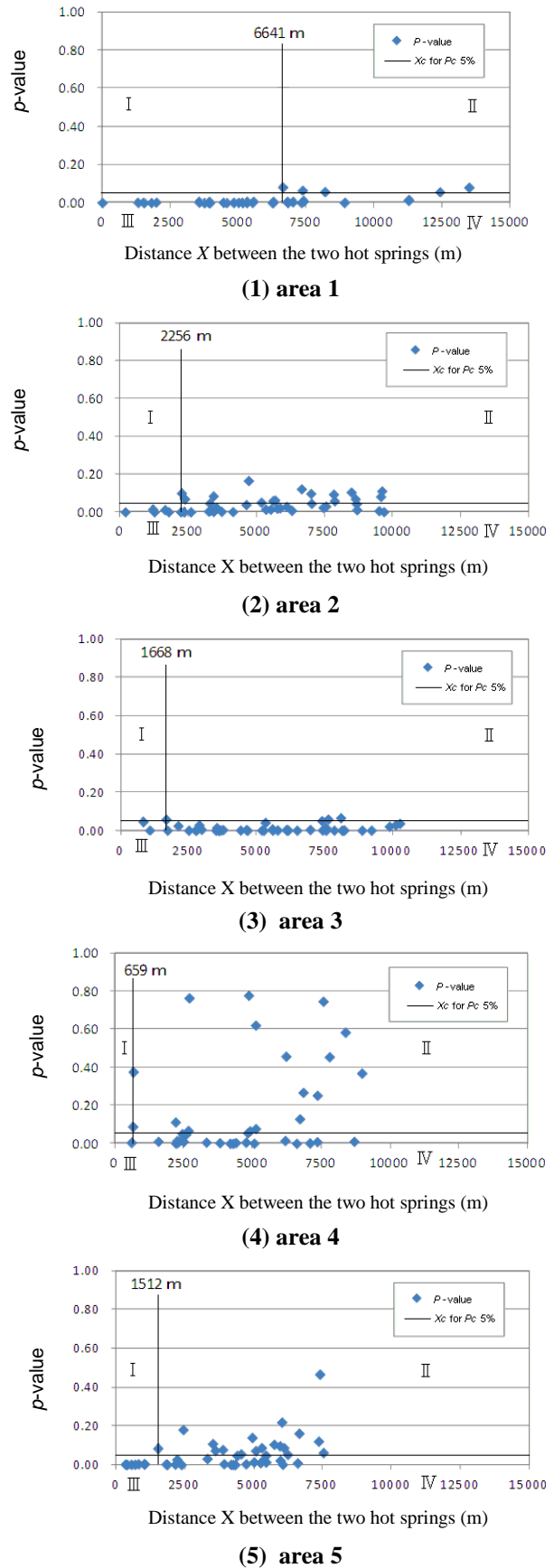


Fig. 4 Given p -values versus distance between two hot springs, in which P_c 5% is applied.

1–4), X_c s are distributed between 659 and 6641 m. For the shallow hot spring area (area 5), X_c s are distributed to 1512 m. Therefore, the relationship between depth and X_c s was not a simple one.

3) Difference of the meaning about X_g and X_c

Prior to the analysis, the given X_c s were numerically nearer to X_g s more than what was expected, as depicted in the second row of **Table 6**.

As shown in **Table 4**, although section I is empty, there are many plots in section IV. This indicates that the p -value which is larger than P_c cannot be distinguished by distance X alone. Thus, correlation of the new hot spring's water quality with an existing spring located outside of the X_c range is not always insignificant as shown in column (4) of **Table 6**. This is despite the fact that correlation of the new hot spring's water quality with an existing spring located within the X_c range should always be significant, as shown in column (2) of **Table 6**.

CONCLUSIONS

With regard to the unclear phenomena occurring very deep in the ground layer, the simple stochastic view was applied because we were expecting some simple rules. Most of the results seem to give some power to existing hot spring owners. The results, however, were not good for new hot spring owners as the critical limiting distance was confirmed to be insufficient for explaining the sustainable digging of hot spring.

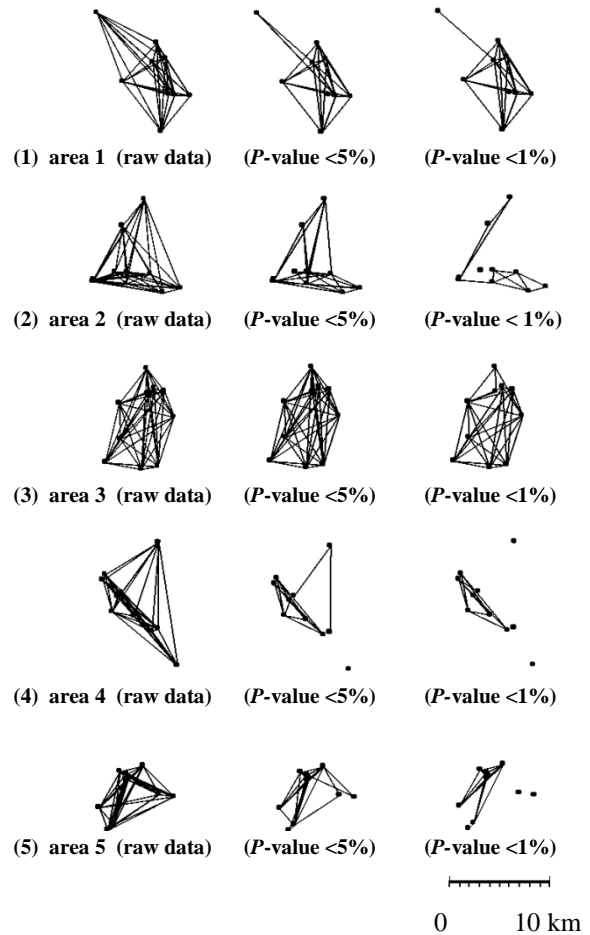


Fig. 5 Distances given for P_c 5% or P_c 1%.

Table 4 Number of the samples of the set of X and p -value

Area	P_c 5%					P_c 1%				
	I	II	III	IV	total	I	II	III	IV	total
1	0	5	24	7	36	0	7	24	5	36
2	0	15	6	24	45	0	31	1	13	45
3	0	3	2	40	45	0	13	0	32	45
4	0	19	1	16	36	0	25	1	10	36
5	0	12	7	26	45	0	26	7	12	45

Table 5 Given critical distance, where P_c indicates critical p -value

Area	Major type of depth	X_c	
		P_c 5%	P_c 1%
1	deep	6641	6641
2	deep	2256	1200
3	deep	1668	824
4	deep	659	659
5	shallow	1512	1512

Table 6 Difference between X_g and X_c

Critical distance	X_g shown in [1]	X_c
Reason of the distance	Questionnaires, water balance, and heat balance.	Stochastic approach
Order of the distance	300–500m or 1,000–2,000m as explained in Introduction	659–6,641m from Table 5
Hot springs at a distance smaller than the critical distance	(1) mutually influenced.	(2) influenced in the section III
Hot springs at a distance larger than the critical distance	(3) not influenced.	(4) not influenced in the section II

References

[1] Ministry of the Environment, Government of Japan: Guideline for the Protection of Hot Spring Resources, 2009 (in Japanese)

[2] Mori Y, Yoshimura H, Maeda A, Shimura K, Ohkuma K, Ogawa M, Hashizume K, Nohara S, Kondo M, Kajisa T: Geochemical Influence of Drilling a New Hole Adjacent to an Existing Hot Spring, *Hot Springs Science* 60(1), The Japanese

Society of Hot Springs Science, 22-36, 2010 (in Japanese with English abstract)

[3] Mori Y, Yoshimura H, Maeda A, Shimura K, Ohkuma K, Kondo M, Kajisa T: Investigation of the Influence of Lift Pump Installation Based on the "Guideline for the Protection of Hot Spring Resources", *Hot Springs Science* 60(2), The Japanese Society of Hot Springs Science, 161-176, 2010 (in Japanese with English abstract)

IDENTIFICATION OF POLLUTANT SOURCE CHARACTERISTICS UNDER UNCERTAINTY IN CONTAMINATED WATER RESOURCES SYSTEMS USING ADAPTIVE SIMULATED ANEALING AND FUZZY LOGIC

Mahsa Amirabdollahian^{1,2} and Bithin Datta^{1,2}

¹School of Engineering and Physical Sciences, James Cook University, Australia; ²CRC for Contamination Assessment and Remediation of Environment, Australia

ABSTRACT

Effective environmental management and remediation strategies are required to remediate contaminated water resources. Accurate characterizing of unknown contaminant sources is vital for selection of appropriate environmental management plan and reduction of long term remedial costs. In order to characterize the sources of contamination, the aquifer boundary conditions and hydrogeologic parameter values need to be estimated or specified. In real life contaminated aquifers, often there are sparse and inaccurate information available. On the other hand, extensive collection of data is very costly. The uncertain and highly variable natures of water resources systems affect the accuracy of contaminant source identification models.

In this study, an optimal source identification model incorporating Adaptive Simulated Annealing optimization algorithm linked with the numerical flow and transport simulation models, is designed to identify contaminant source characteristics. The fuzzy logic concept is used to identify the effect of hydrogeological parameter uncertainty on groundwater flow and transport simulation. The fuzzy membership values incorporate the reliability of specified parameter values in to the optimization model. An illustrative study area is used to show the potential applicability of the proposed methodology. The incorporation of fuzzy logic in source identification model increases the applicability of contaminant source detection models in real-life contaminated water resources systems.

Keywords: Pollution Detection, Aquifer Contamination, Groundwater, Source Identification, Uncertainty.

INTRODUCTION

Groundwater as the major source of potable, agricultural and industrial water is subject to various sources of contamination. The first signs of the presence of contaminate underground water may be detected from the water extracted from current extraction wells. Often surface water quality like rivers or lakes, is affected by contamination of underground water. The spread of pollution in underground water increases the necessity to develop efficient techniques for remediation of contaminated aquifer. The effectiveness of a remediation strategy depends on how efficiently the contamination source characteristics are identified. Accurate identification of the contaminant sources and reconstructing their release history plays an important role in modeling of subsurface flow and transport processes, and help to reduce the long-term remedial costs.

The source identification problem deals with the spatial and temporal variations of the location, activity duration, and the injection rate of the pollutant source and is mostly inferred from the

available sparse and sometimes erroneous concentration measurements at the site. Mainly source identification includes a simulation problem, like groundwater flow and pollutant transport models, which is used to estimate past phenomena or predict future scenario. The estimated values are then compared with observed values. Availability of adequate data is vital regarding the structure of source identification procedure. However, acquiring data is a cost and time intensive task.

The source identification model requires an accurate flow and transport model to estimate the contaminant concentration distribution in aquifer. The lack of adequate geographic and parameter information, results in uncertain groundwater and solute transport model. The solution of source identification model is highly sensitive to measurement errors either in the observation data or model parameters [1].

Various techniques has been proposed in literature to characterize the contamination sources including stochastic methods [2]; response matrix [3], [4]; embedded optimization [5] and linked simulation-optimization [6], [7]. Amirabdollahian

and Datta [8] presented a comprehensive overview on different source identification methods.

Most of the techniques represented in literature are designed for the case where the aquifer hydrogeological parameter values are known. Jha and Datta [7] tested their proposed method under uncertain hydrogeological parameter values. Their method is able to manage moderate degree of uncertainty. By increasing the degree of uncertainty the accuracy and reliability of source identification decreases.

In this study the linked simulation-optimization model is used to characterize the sources of contamination. The Adaptive Simulated Annealing (ASA) is utilized as the optimization method. In contrast to deterministic viewpoint where all the model parameters were considered known, in the proposed methodology the uncertainty in hydrogeologic zonation and parameter values are considered using Fuzzy Logic concept. In this way the available sparse model parameter data, in addition to available uncertain information about hydrogeologic zones are utilized to increase the reliability of pollutant source characteristics identification.

METHODOLOGY

The source identification model consists of an optimization algorithm linked to flow and transport process simulation models. The optimal solution is obtained by minimizing the differences between observed and simulated values. The objective function for the optimization problem is defined as follow.

$$\text{Min } F_1 = \sum_{k=1}^{nk} \sum_{iob=1}^k \mu_{iob}^k (\text{cest}_{iob}^k - \text{cobs}_{iob}^k)^2 w_{iob}^k / (\text{cobs}_{iob}^k)^2 \quad (1)$$

Subject to:

$$\text{cest} = f(x, y, z, D, q, R) \quad (2)$$

The above constraint essentially represents the flow and transport process simulation models.

Where:

cest_{iob}^k = Concentration estimated by the simulation model at observation well location iob and at the end of time period k.

nk = Total number of concentration observation time periods;

nob = Total number of observation wells;

cobs_{iob}^k = Observed concentration at well iob and at the end of time period k;

μ_{iob}^k = The fuzzy reliability factor for well iob and at the end of time period k;

w_{iob}^k = Weight corresponding to observation location

iob, and the time period k.

The weight w_{iob}^k can be defined as follows:

$$w_{iob}^k = 1 / (\text{cobs}_{iob}^k + n)^2 \quad (3)$$

Where n is a constant and it should be sufficiently large so that errors at low concentrations do not dominate the solution [5]. The objective function is constrained by the flow and transport simulation models.

Optimization Method

In this paper the ASA optimization method is utilized to characterize the sources of contamination. Simulated Annealing (SA) optimization starts from a feasible solution and a specific objective function. A new solution is randomly selected from its neighbors and the objective function is evaluated for the new selected solution. If the new solution has a better objective function value, the most recent solution is definitely better than the old one. Therefore, it is then accepted and the search moves to a new point and continues from there. On the other hand, if the new solution is not better than the current one, the new solution may be or may not be accepted depending on the acceptance probability. The acceptance probability is strongly influenced by the choice of a parameter temperature (T). ASA is a variant of SA in which the algorithm parameters that control temperature schedule and random selection are automatically adjusted as the algorithm progresses. This makes the algorithm more efficient and less sensitive to the user defined parameters than SA [9].

Simulation Model

The ASA based source identification model estimates the source fluxes using a linked simulation-optimization model. The simulation model evaluates the contaminant concentration values at monitoring locations corresponding to candidate contaminant source characteristics. Groundwater Flow and contaminant transport simulation models used in this study are, MODFLOW-2000 [10] and MT3DMS [11], respectively.

MODFLOW is a computer program that numerically solves the three-dimensional ground water flow equation for a porous medium by using a finite-difference method. The MT3DMS transport model uses a mixed Eulerian-Lagrangian approach for the solution of the three-dimensional advective-dispersive-reactive equation. The Lagrangian part of the method, used for solving the advection term, employs the forward tracking Method of Characteristics (MOC), the backward-tracking

Modified Method Of Characteristics (MMOC), or a hybrid of these two methods. The Eulerian part of the method, used for solving the dispersion and chemical reaction terms, utilizes a conventional block centered finite-difference method [11].

Fuzzy Reliability Factor

When there is inadequate available information about the hydrogeologic zonation and parameter values, the contaminant source identification model is subjected to uncertainty. The simulation model needs exact aquifer parameter information to accurately estimate contaminant concentration at monitoring locations. In practice usually an interpolation method is utilized to calculate hydrogeologic parameter values for entire aquifer using sparse data. Substantial variation of hydrogeologic parameter values in heterogeneous and non-uniform aquifers impose high level of uncertainty to the contaminant source identification model.

The hydraulic conductivity values are used by the flow simulation model to generate the head distribution in the study area. This head information is used by the simulation model to calculate contaminant concentration at different monitoring locations.

In this study the inverse Distance Weighting (IDW) interpolation technique is used to evaluate hydraulic conductivity value for entire aquifer using available sparse information. The IDW is a type of deterministic method for multivariate interpolation with a known scattered set of points. The assigned values at unknown points are computed using a weighted average of the known values at the known points. A general form of finding an interpolated value u at a given point x based on samples $u_i = u(x_i)$ for $i=1,2,...,N$ using IDW is as below.

$$u(x) = \frac{\sum_{i=0}^N \frac{v_i(x) u_i}{\sum_{j=0}^N v_j(x)}}{\sum_{j=0}^N v_j(x)} \quad (4)$$

Where:

$$v_i(x) = \frac{1}{d(x, x_i)^p} \quad (5)$$

$u(x)$ = Interpolated value at given location x ;
 N = Number of nearest points which are utilized to estimate interpolated value;

u_i = known value corresponding to point i ;

v_j = Weight corresponding to point i ;

$d(x, x_i)$ = distance between point x and x_i ;

p = power;

Power p determines the contribution of values at known points in estimation of value at unknown points with respect to distance between points with known and unknown values. This means that higher value of p results in using more near points with known values by the IDW interpolation method.

The uncertainty in aquifer zonation with respect to hydraulic conductivity value is studied using different p values in IDW interpolation method. To calculate the fuzzy reliability factors, the fuzzy membership function is utilized. The reliability membership function is calculated using Equation 6.

$$\mu_{iob}^k = 1 - (cest_{iob,1}^k - cest_{iob}^k)^2 / (cest_{iob}^k)^2 \quad (6)$$

Where $cest_{iob,1}^k$ is estimated concentration values obtained using simulation model at observation well location iob and at the end of time period k , with $p=M_1$ for the IDW interpolation method (equation 5).

$cest_{iob}^k$ is estimated concentration values obtained using simulation model at observation well location iob and at the end of time period k , with $p=M_2$ for the IDW interpolation method (equation 5). In the optimal source identification model (equation 1) the concentration estimations are based on $p=M_2$. When the available information about field hydraulic conductivity zonation is not adequate, the concentration values estimated using simulation model will not be precise. On the other hand, there would be large discrepancy between simulated concentrations using two different p values by the IDW interpolation technique. Therefore, the fuzzy reliability factor will be less than one.

The fuzzy reliability factor for each observation location and at the end of each time period is estimated progressively using optimization generated candidate source characteristics.

PERFORMANCE EVALUATION

Performance of the developed methodology is evaluated using synthetic hydrogeologic data. The advantage of using synthetic data is that the true source characteristics are known for evaluation. This allows for the testing of the source identification methodology. Figure 1 shows the hypothetical aquifer study area. There are three candidate locations for contamination sources. Two of them are active sources and the third one is dummy source. There are two active extraction wells and 9 monitoring locations. The study area is 1500 meter by 1000 meter and is 40 meter deep. The three-dimensional model of aquifer includes two layers, each of 30 rows and 20 columns. The hydraulic conductivity is generated using truncated Latin hypercube and lognormal distribution.

Three different zones with respect to hydraulic conductivity value are considered. The mean hydraulic conductivity values for low, moderate and high permeable zones are 3, 10 and 20 m/day, respectively. The standard deviation is 0.1 times mean value for all zones. These hydraulic conductivities represent actual field condition and are generated at 50 meter intervals of the study area. The simulation model requires hydraulic conductivity values at each node. These values were obtained by interpolation using Kriging. The resulting field is utilized by the simulation model to estimate the spatial and temporal concentration values. Figure 2 shows the generated actual hydraulic conductivity field.

To evaluate the performance of the proposed methodology the hydraulic conductivity is assumed to be uncertain. Therefore the actual hydraulic conductivity values are assumed to be known at every 300 meters distance. By this assumption the known actual hydraulic conductivity values are reduced from 1303 values to 61 values. Using these 61 values, the uncertain hydraulic conductivity field is generated by interpolating the available 61 values to entire aquifer using IDW technique. The selected p value is 2.

To conduct the fuzzy ASA source identification the fuzzy reliability factor needs to be calculated using candidate source characteristics. The fuzzy membership function is estimated using equation 6. The selected M_1 and M_2 values are 4 and 2, respectively. Figures 3a and 3b show the hydraulic conductivity generated fields using IDW method. In Figs 3a and 3b, the p value (equation 5) is set to 2

and 4, respectively. Since the hydraulic conductivity data used to generate both fields is the same, the illustrated difference is due to uncertainty and lack of adequate amount of data.

RESULTS AND DISCUSSION

Table 1, 2 and 3 show the results of source identification model for sources 1, 2 and 3, respectively. In these tables, the first row shows the actual source fluxes during each stress period. The fluxes corresponding to source 2 is zero which means that it is a dummy source.

Second rows show the result of crisp source identification model solution where there is unaccounted uncertainty in the estimation of hydraulic conductivity field. For the crisp source identification the ASA optimization model uses the same objective function (Equation 1). However, in this case the fuzzy reliability factor is considered to be always equal to one.

The huge discrepancy between the resulting source fluxes and actual ones show the deficiency of the crisp source identification model in estimating of source characteristics while there is inadequate available data for the hydraulic conductivity field

The third rows show the result of fuzzy ASA source identification model. Comparing the results show that the fuzzy model is able to increase the accuracy of the source identification.

Results show that the use of fuzzy logic can improve the source identification results by 47.3 and 25.6 percent for sources one and three, respectively.

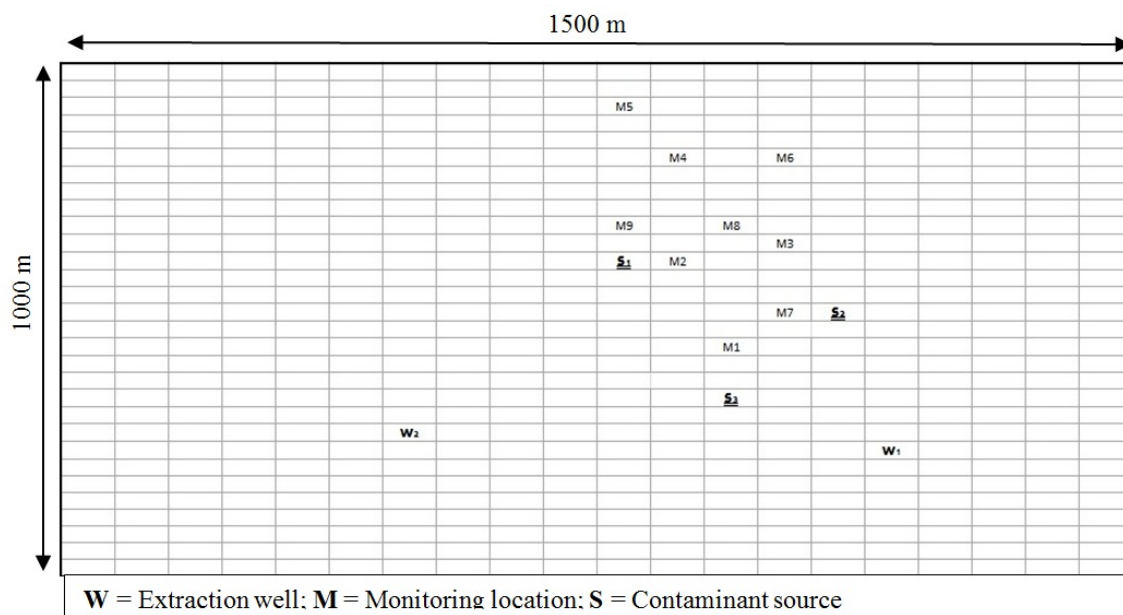


Fig. 1 Study area

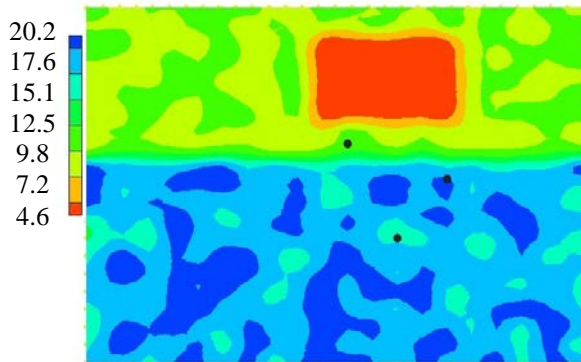


Fig. 2 Actual hydraulic conductivity values (m/day) (Dot points show the candidate source locations)

Although both models are not able to specify zero fluxes for source two (dummy source), the estimated source fluxes by both models are small comparing to the magnitude of flux for other sources. However, the performance of both models will improve if more precise information about hydraulic conductivity field or more monitoring data are actually available. Since the inputs for the flow simulation model have associated high level of uncertainty, limited accuracy in source identification results is expected. However, by using the fuzzy model, the error in estimation of source fluxes has been reduced. Table 4 shows the estimation error using crisp and fuzzy ASA source identification models, and demonstrates improvement in estimation of source fluxes using fuzzy logic concept.

Table 1 Estimated contamination fluxes for source one (g/s)

Method	Stress Period 1	Stress Period 2	Stress Period 3
a	70	90	35
b	5.7	40.4	55.1
c	46.9	59.7	52.3

Note: a: Actual source fluxes
b) Result of crisp source identification.
c) Result of fuzzy ASA source identification.

Table 2 Estimated contamination fluxes for source two (g/s)

Method	Stress Period 1	Stress Period 2	Stress Period 3
a	0	0	0
b	0.3	9.55	15.6
c	1.2	11.5	19.2

Note: a: Actual source fluxes
b) Result of crisp source identification.
c) Result of fuzzy ASA source identification.

Table 3 Estimated contamination fluxes for source three (g/s)

Method	Stress Period 1	Stress Period 2	Stress Period 3
a	95	85	75
b	39.3	65.1	52.1
c	40.68	78.8	62.3

Note: a: Actual source fluxes
b) Result of crisp source identification.
c) Result of fuzzy ASA source identification.

Table 4 Error in estimation of contamination fluxes (g/s) and the improvement percentage

Source	Source 1	Source 2	Source 3
b	134	25.45	98.5
c	70.7	31.9	73.22
Improvement (%)	47.3	-*	25.7

Note: b) Result of crisp source identification.
c) Result of fuzzy ASA source identification
* Source two is dummy.

CONCLUSION

A new methodology for unknown groundwater pollution source identification, using Adaptive Simulated Annealing (ASA), linked simulation-optimization, and fuzzy logic is proposed. Uncertainties in hydrogeologic parameters are incorporated by using fuzzy membership function. Limited performance evaluations show the improvement in source identification using the proposed methodology.

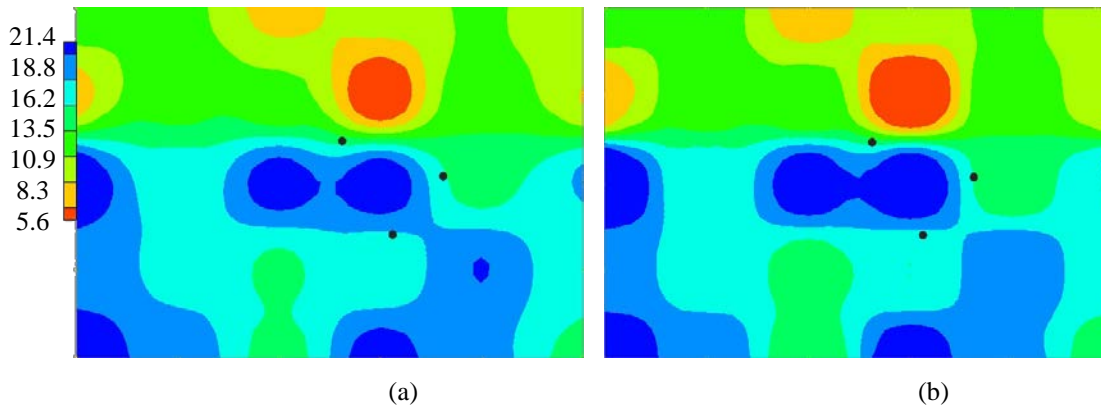


Fig. 3 Uncertain hydraulic conductivity fields (m/day). Generated using IDW interpolation method where a) $p=2$; and b) $p=4$

REFERENCES

- [1] Sun NZ, Inverse problems in groundwater modeling. Boston: Kluwer academic, 1994.
- [2] Gelhar LW, "Stochastic subsurface hydrology from theory to applications", Water Resource Research, Vol. 22, No. 9. 1986, pp. 135-145.
- [3] Gorelick, SM, Evans B, and Remson, I, "Identifying Sources of Groundwater Pollution: An Optimization Approach", Water Resource Research, Vol. 19, No. 3. 1983, pp. 779-790.
- [4] Datta B. et al., Development of an Expert System Embedding Pattern Recognition Techniques for Pollution Source Identification. Virginia: National Technical Information Service, 1989.
- [5] Mahar, PS, and Datta, B, "Optimal identification of ground-Water pollution sources and parameter estimation", Water Resource Planning and Management- ASCE, Vol. 127, No. 1. 2001, pp. 20-29.
- [6] Chadalavada, S, Datta, B, and Naidu, R, "Optimal identification of groundwater pollution sources using feedback monitoring information: a case study", Environmental Forensics, Vol. 13, No. 2. 2012, pp. 140-153
- [7] Jha, M, and Datta, B, "Three dimensional groundwater contamination source identification using adaptive simulated annealing", J. of Hydrologic Engineering, Vol. 18, No. 3. 2012, pp. 307-313.
- [8] Amirabdollahian, M, and Datta, B, "Identification of contaminant source characteristics and monitoring network design in groundwater aquifers: an overview", J. of Environmental Protection, accepted, 2013.
- [9] Zheng C, and Bennett, GD, Applied contaminant transport modeling. New York: Wiley-Interscience, 2002.
- [10] Zheng C, Hill, MC, and Hsieh PA, MODFLOW-2000, the U.S. Geological Survey Modular Ground-Water Model- User guid to the LMT6 Package, the linkage with MT3DMS for Multi-Species Mass Transport Modeling. Denver, Colorado: U.S.G. Survey, 2001.
- [11] Zheng C, and Wang, PP, A Modular Three-Dimensional Multispecies Transport Model for simulation of advection, dispersion, and chemical reactions of contaminants in groundwater systems. Documentation and user's guide. Denver, Colorado: U.S.G. Survey, 1999.

POINT-BASED RENDERING FOR MASSIVE POINT CLOUD VISUALIZATION

Masafumi Nakagawa

Department of Civil Engineering, Shibaura Institute of Technology, Japan

ABSTRACT

A laser scanner can acquire a 3-D point cloud by measuring the distance to a surface and the scanning angles. Accurate 3-D point data are used for various applications in urban areas. An advantage of 3-D point-cloud data is that it allows accurate display from an arbitrary viewpoint. In contrast, panoramic imagery has the advantage of providing more attractive images with fewer data. We test whether these advantages can be combined by a point-cloud projection into panoramic space. Our objective is to develop a point-based rendering application with a simple filtering algorithm, which we call a layered image-based depth arrangement refiner for versatile rendering (LIDAR VR). We have focused on the following features. First, panoramic imagery can be generated from arbitrary viewpoints from several observation data sets. Second, a spatial interpolation with rendering results can reduce the processing task. These features have been verified using case studies.

Keywords: Laser scanning data, Point-cloud, Point-based rendering, Spatial interpolation

INTRODUCTION

Accurate 3-D scanning techniques such as terrestrial laser scanning are used for various applications such as geographical information systems (GIS) data acquisition in urban areas [1]-[3]. A laser scanner can acquire a 3-D point cloud by measuring the distance to a surface and the scanning angles. Moreover, a calibrated digital camera with a laser scanner can be used to acquire color information with the point-cloud data.

An advantage of 3-D point-cloud data is that they allow accurate display from an arbitrary viewpoint and 3-D modeling [4]-[7]. In contrast, panoramic imagery has the advantage of providing more attractive images with fewer data [8], [9]. In addition, panoramic image georeferencing and distance-value-added panoramic image processing show that both advantages can be combined for 3D-GIS visualization [10], [11]. Thus, we tested whether these advantages can be combined by a point-cloud projection into panoramic space.

Point-cloud visualization has two issues. The first is a near-far problem caused by distance differences from the viewpoint to scanned points. The second is a transparency effect caused by rendering hidden points among near-side points. These effects degrade the quality of a point-cloud visualization.

Splat-based ray tracing [12] is a methodology that generates a photorealistic curved surface on a panoramic view using normal vectors from point-cloud data. A problem is the large amount of time required for surface generation in the 3-D work space. Furthermore, the curved-surface description is

inefficient at representing urban and natural objects as GIS data. In particular, we consider that a simpler filtering algorithm is important to achieve high volumes of point-cloud processing with high speeds.

Thus, our objective is to develop a point-based rendering application with a simpler filtering algorithm, which we call a layered image [13] based depth arrangement refiner for versatile rendering (LIDAR VR). We have focused on the following features. The first feature is panoramic imagery generation with a translated viewpoint from several observation data sets. In general, an image from a viewpoint should be created from an observation. Moreover, when panoramic images are taken from several viewpoints, position data from RTK-GPS and rotation data from a gyrosensor are required to calculate relative positions and rotations between cameras. LIDAR VR images from many viewpoints can be simulated from observation data through our proposed approach. Moreover, the proposed methodology can simulate camera translation and generate new simulated imagery without the position and rotation sensors. The second feature is real-time spatial interpolation. In general point-cloud interpolation processing, missing points can be interpolated by a traditional 3-D filter from other points in the space. This type of 3-D interpolation requires huge amounts of processing capability. Therefore, we tested whether spatial interpolation with rendered results can reduce the processing task. We have also developed a pixel-selectable averaging filter. This function can replace spatial filtering in 3-D space by spatial filtering in 2-D space with real-time processing. Thus, any quality reduction caused by viewpoint translation can be solved in real time.

METHODOLOGY

The processing flow of the proposed methodology is described below. First, sensors acquire a point cloud with additional color data such as RGB data or intensity data. The sensor position is defined as the origin point in a 3-D workspace. If color data cannot be acquired, distance values are attached to a color index. Thus, for example, we can use a laser scanner or a stereo camera. Second, a LIDAR VR image from the simulated viewpoint is generated using the point cloud. Finally, the generated LIDAR VR image is filtered to generate missing points in the rendered result using distance values between the viewpoint and objects.

LIDAR VR image generation using point-cloud

The colored point cloud is projected from 3-D space to panorama space. This transformation simplifies viewpoint translation, filtering, and point-cloud browsing. The LIDAR VR data consist of a panorama model and range data. The panorama space can be a spherical model, a hemispherical model, a cylindrical model, or a cubic model. Here, the spherical model is described. The measured point data are projected onto a spherical surface, and can be represented as range data as shown in Figure 1. The range data can preserve measured point data such as X , Y , Z , R , G , B , and intensity data in the panorama space in a multilayer style. Azimuth and elevation angles from the viewpoint to the measured points can be calculated using 3-D vectors generated from the view position and the measured points. When azimuth angles and elevation angles are converted to column counts and row counts in the range data with adequate spatial angle resolution, a spherical panorama image can be generated from the point cloud.

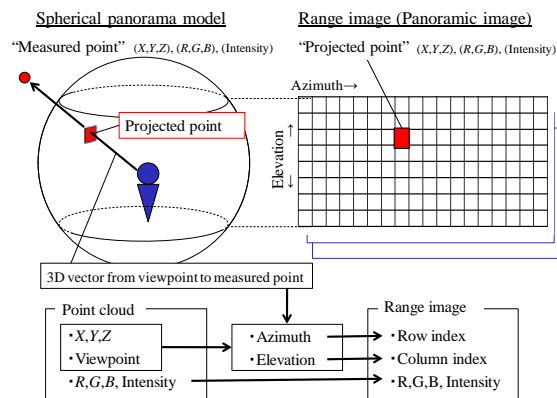


Fig. 1 LIDAR VR consisting of a spherical panorama (left side of the figure) and range data (right side of the figure)

Based on this spherical panorama, the range data are generated using the point cloud with a translated viewpoint, as shown in Figure 2. When points from P_1 to P_{10} are projected into a panorama space generated from a viewpoint X_o , these points are arranged continuously from P_1 to P_{10} in the range data. An azimuth or elevation angle from a viewpoint X_o to a measured point P_1 is denoted as R_o . When the same scene is captured from a different viewpoint X_t , the angle from the viewpoint X_t to the measured point P_1 is denoted as R_t . The position of the projected point in the range data moves according to the change in angle from R_o to R_t .

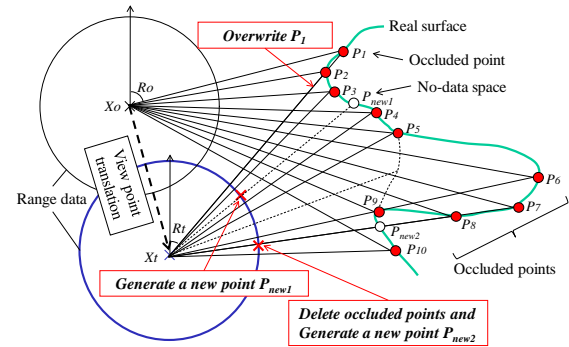


Fig. 2 Point distribution calculated by viewpoint translation in range data, occlusion detection using the point cloud, and point-cloud interpolation with distance information

Filtering using distance values between a viewpoint and measured points

Three types of filtering are performed after the viewpoint translation, as shown in Figure 2. The first filtering is the overwriting of occluded points. When the viewpoint is translated to X_t , the projected point P_1 becomes an occluded point behind P_2 . Therefore, P_1 is overwritten by P_2 .

The second filtering is the generation of new points in the no-data space. This occurs when the viewpoint is translated to X_t and a no-data space exists between the projected points P_3 and P_4 . Thus, Figure 2 shows that P_{new1} is generated.

The third filtering is the detection of occluded points and generation of new points to replace detected occluded points. When the viewpoint is translated to X_t , point P_8 exists between points P_9 and P_{10} after the first filtering. However, the actual point P_8 should be occluded because the point P_8 exists behind the real surface. Therefore, the occluded point P_8 should be given a new distance value as P_{new2} , calculated using interpolation processing and the distance values of points P_9 and P_{10} . In addition, new points are generated with the pixel-selectable averaging filter developed in this research, which we now describe.

Pixel-selectable averaging filter

In general, when an image is transformed, each pixel in the image has its color data resampled by using pixel values around it. Points projected into the panorama space are also processed using a similar technique to improve the quality of the range data. However, general resampling techniques such as nearest interpolation reduce the quality of the range data because valid, erroneous, and missing data are blended in the resampling. Therefore, we apply a focused pixel-selectable averaging filter to this problem. The filtering processing uses only valid pixels around a pixel for the resampling, as shown in Figure 3. This processing is equivalent to missing-point regeneration without reducing geometrical accuracy by a uniform smoothing effect. For example, a three by three block of pixels in the range data set is prepared. The center point in the block is the focus point in the range data set. When the focus point is a missing point and the other points are valid points in the point cloud, a new pixel value is given to the focus point using the other points. This processing is applied to each channel in the RGB image and to an intensity image.

Thus, this processing uses only valid points in the range data. The detailed flow of the pixel-selectable averaging filter is described as follows. First, the data are checked to see whether valid points exist. When more than one pixel in a three by three block exists, including the focus point and the points around it, processing proceeds to the next step. If no point exists in the block, the next processing step is omitted.

Second, the number of valid pixels in the block is counted. When there are more than two valid pixels, the processing proceeds to the next step. If there is only one valid pixel and the extracted point is the focus point, it is deleted as spike noise. If there is only one valid pixel and the extracted point is not the focus point, the focus point remains without the filtering processing.

Third, after these point-extraction steps, a range of search distances is given to extract valid points. The start value of the search range is the distance from the viewpoint to the nearest point found among the extracted points, while the end value is the start value plus a defined distance parameter. Then, all valid points in the block within the search range are extracted. The defined distance parameter depends on the continuity of the points in the point cloud. For example, when trees and building walls are measured, the defined parameter would be 10 cm to

1 m from experience.

Finally, an average distance value from the viewpoint to the valid points is calculated. Then, the focus point value is overwritten by the average value. However, when the focus point has a distance value within the search range, the point is defined as the nearest surface approximately, and the overwriting processing is not performed in that case. This processing sequence is applied to all points.

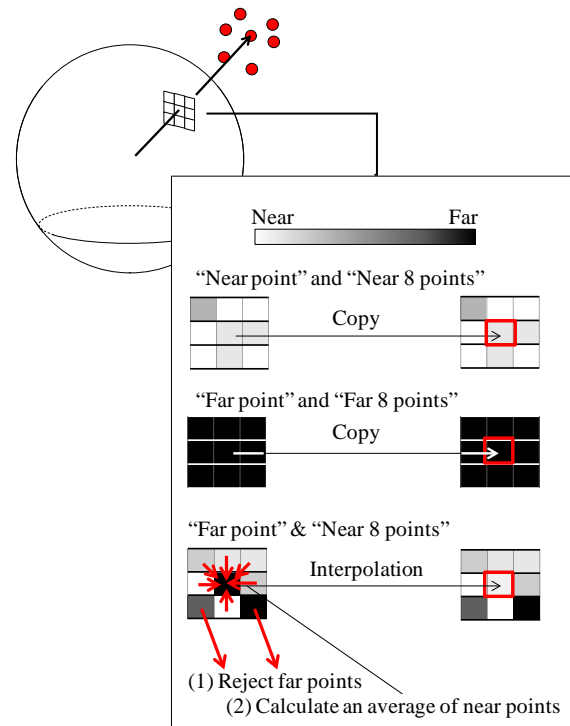


Fig. 3 Pixel-selectable averaging filter

EXPERIMENTS

We conducted experiments using a point cloud taken from a terrestrial laser scanner VZ-400 produced by RIEGL Laser Measurement Systems GmbH. This scanner can acquire panoramic distance data and corresponding color data over 360° in the horizontal direction.

We prepared three test sites. The first site was a gymnasium consisting of flat planes. The second site was a park (Tsukuba city) that has good visibility, including flat ground planes and individual trees. The third site was a historical building ("Goryokaku" in Hokkaido), including tiles, facades, and signboards.

RESULTS

Gymnasium data set

We acquired 200 million points in the indoor and

outdoor environments from 10 viewpoints. A panoramic image (1800×450 pixels) was rendered with 0.20° angle resolution after 3 cm^3 spatial filtering. The average processing time for the panoramic image conversion and iterative filterings (three times) by parallel programming in C was 0.13 s (Intel Core i7, 2.80 GHz, eight threads) for one-shot generation in multiple viewpoints without file I/O. Figure 4 shows a part of the panoramic image-generation result after a viewpoint translation. Figure 5 shows the same part of the panoramic image-generation result after viewpoint translation and filtering.



Fig. 4 Part of the panoramic image-generation result after viewpoint translation



Fig. 5 Part of the panoramic image-generation result after viewpoint translation and filtering

Park (Tsukuba city) data set

We acquired 400 million points in outdoor environment from 28 viewpoints. A part of an ortho image map generated from the point cloud is shown in Figure 6. A panoramic image (3600×900 pixels) was rendered with 0.10° angle resolution after 1 cm^3 spatial filtering. Figure 7 shows a part of the panoramic image-generation result after a viewpoint translation. Figure 8 shows the same part of the panoramic image generation result after viewpoint translation and filtering.

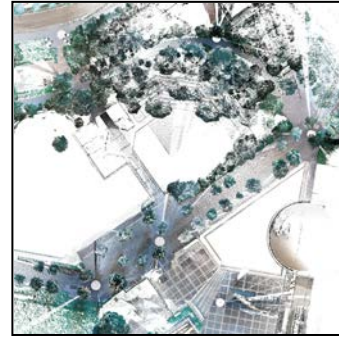


Fig. 6 Part of an ortho image map



Fig. 7 Part of the panoramic image-generation result after viewpoint translation

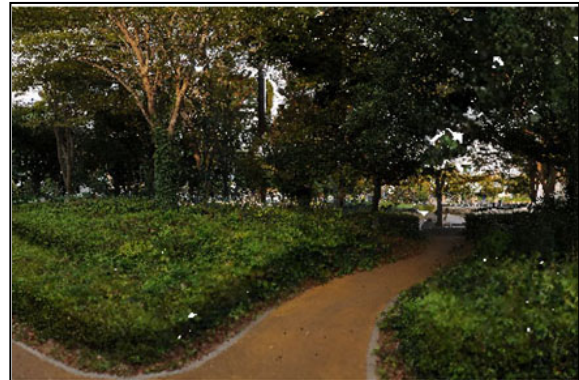


Fig. 8 Part of the panoramic image-generation result after viewpoint translation and filtering

Historical building ("Goryokaku" in Hokkaido) data set

We acquired 800 million points in outdoor environment from 30 viewpoints. A panoramic image (3600×900 pixels) was rendered with 0.10° angle resolution after 1 cm^3 spatial filtering. Figure 9 shows a part of the panoramic image-generation result after a viewpoint translation. Figure 10 shows the same part of the panoramic image-generation result after viewpoint translation and filtering.



Fig. 9 Part of the panoramic image-generation result after viewpoint translation



Fig. 10 Part of the panoramic image-generation result after viewpoint translation and filtering

DISCUSSION

We can verify the features of our LIDAR VR generation as follows. The first feature is panoramic image generation with an arbitrary viewpoint. We have verified that the proposed methodology can successfully generate panoramic images with several observation data sets from one viewpoint automatically. Moreover, we have verified that camera movement and rotation from a viewpoint can be simulated successfully to generate a new image without a position sensor such as RTK-GPS or a direction sensor such as a digital compass. In addition, we have confirmed that continuous camera trajectory simulation can achieve panoramic imagery generation from accurate viewpoints.

The second feature is real-time spatial interpolation using the point cloud. We have confirmed that spatial interpolation with rendering can be processed in real time (approximately 8 fps with parallel processing) including panoramic image generation. First, a panorama projection is performed successfully as shown in Figure 4. Next, a viewpoint translation simulates a new panoramic image with some missing point data as an interleaved pixel array. Then, the interpolation

processing for missing points in the panorama space generates new point data from the new viewpoint. Thus, almost all of the missing data are recovered after filtering. As a result, a higher-quality image is generated, as shown in Figure 5. Finally, although the panorama projection requires a long processing time in proportion to the number of points, we have confirmed that the proposed overall processing can be achieved in real time. Moreover, even if missing points remain, they can be removed via two or more iterative filterings in most cases.

In addition, Figure 11 shows an example of missing points caused by puddles. Generally, median filtering is applied to improve a noise affect in image processing. However, missing points are interpolated from surrounding pixels with noise. Thus, a blending effect occurs, as shown in Figure 12. We have confirmed that our approach can avoid this blending effect, as shown in Figure 13.

However, larger translations of the viewpoint expose more occlusions in the point cloud. Therefore, even if iterative processing is applied to a generated image from a more distant viewpoint, the interleaved pixels may not be correct. This is not a critical problem because a common interpolation is undesirable in a case with data.

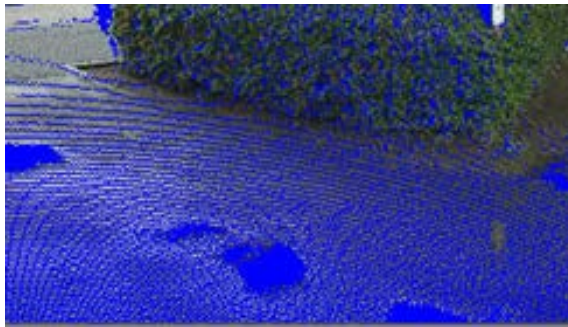


Fig. 11 Input point cloud



Fig. 12 Result after median filtering



Fig. 13 Result after proposed filtering

SUMMARY

We have developed a point-based rendering application called LIDAR VR with high-speed spatial interpolation using a point cloud. This application has achieved not only a transformation from point cloud to panoramic image but also automatic regeneration of missing points in the rendered result from a chosen viewpoint. Moreover, we have focused on two features, panoramic imagery generation from arbitrary viewpoints and the processing task reduction in spatial interpolation with rendering results. Finally, we have presented results that confirm these features in case studies.

ACKNOWLEDGEMENTS

This work is supported by the Strategic Information and Communications R&D Promotion Programme (SCOPE) of the Ministry of Internal

Affairs and Communications, Japan. This work is also supported by RIEGL Japan Co. Ltd. in our data acquisition.

REFERENCES

- [1] Jan B, "Terrestrial LiDAR in Urban Data Acquisition", Photogrammetric Week '09, pp.169 – 178, 2009.
- [2] Shi P, George V, "Knowledge based reconstruction of building models from terrestrial laser scanning data" ISPRS Journal of Photogrammetry and Remote Sensing, Volume 64, Issue 6, pp. 575–584, 2009.
- [3] Eloïse D, Renaud B, Caroline B, "Towards road modelling from terrestrial laser points", IAPRS, Vol. XXXVIII, Part 3A, pp.293-298, 2010.
- [4] George V, "Advanced point cloud processing", In: Photogrammetric Week '09, pp. 137-146, 2009.
- [5] Remondino F, "From point cloud to surface : the modeling and visualization problem", International Archives of the Photogrammetry, Remote Sensing and Spatial Information Sciences, Vol. XXXIV-5/W10, 2003.
- [6] Augustine T, Chun.F H, I-Chou H, Wen-Kai Liu, "Plane and Boundary Extraction from LiDAR data using Clustering and Convex Hull Projection", International Archives of the Photogrammetry, Remote Sensing and Spatial Information Sciences, Vol. XXXVIII - Part 3A, pp.175-179, 2010.
- [7] Jan B, Maria P, "From Point Samples to Surfaces", On Meshing and Alternatives ISPRS Image Engineering and Vision Metrology, XXXVI, pp.50 – 55, 2006.
- [8] Shenchang, E.C, "QuickTime VR - An image-based approach to virtual environment navigation". Proceedings of ACM SIGGRAPH'95: 29–38, 1995.
- [9] Katsushi I, Masao S, Hiroshi K and Imari S, "Constructing Virtual cities by Using Panoramic Images", International Journal of Computer Vision, Vol. 58, No.3: 237-247, 2004.
- [10] Jason D, "An approach to virtual environments for visualization using linked geo-referenced panoramic imagery", Computers, Environment and Urban Systems 24, 127-152, 2000.
- [11] Edward V, Sisi Z and Sander D, "Distance-value-added panoramic images as the base data model for 3D-GIS", Panoramic Photogrammetry Workshop, 2005.
- [12] Lars L, Karsten M and Paul R, "Splat-based Ray Tracing of Point Clouds", Journal of WSCG, Vol.15, Issue: 1-3: 51-58, 2007.
- [13] Jonathan S, Steven Gortler, L. He, and Richard S, "Layered Depth Images", SIGGRAPH '98, pp.231-242, 1998.

REDRAWING AN UNKNOWN MASONRY CAISSON BY GEOPHYSICAL METHODS

Ming-Hung Chen¹, Shun-Min Lee², Yung-Chuan Chou², Yao-Jen Hsu² and Chih-Hsin Hu³
¹ China Engineering Consultants, Inc., Taiwan; ² CECI Engineering Consultants, Inc., Taiwan; ³ HCK Geophysical Company, Taiwan

ABSTRACT

An old railway bridge built in 1911 was damaged in a series of typhoon events from 2005 to 2009. The rail bridge was out of service since a new bridge was built beside, and this old bridge became as a reserved heritage. Knowing the true depth and size of the caisson is significant before the rehabilitation designing. Unfortunately, the original design plot was not well stored for such an aged structure, which leads to extremely difficult situation when the local government considered rehabilitating this vulnerable historical structure. Hence, seven different non-destructive investigation ways were implemented to confirm the real geometry of pier beneath the ground surface. These methods include 2D & 3D ERI (electrical resistivity image), cross-hole resistivity tomography, ultra-seismic, parallel seismic, borehole GPR (ground penetration radar), and multiple offsets of vertical seismic profiling. All the tests were used to finalize the estimation of actual foundation depth with confidence. Not alike most reinforcement concrete structures constructed with steel bar inside, a masonry structure is more challengeable when employing resistivity method.

When doing the NDT tests, three boreholes were drilled to survey the subsurface soil property at site. These investigations gave not only the opportunity to plot stratum profiles of the investigating area, but also provided essential information for judging the resistivity variation between primary deposits and artificial configurations. A proving excavation was also executed within the overall survey work. All the test results conclude that geophysical survey could explore the masonry structures nondestructively, when it is well designed and finely conducted.

Keywords: NDT, bridge, caisson, masonry, geophysics

INTRODUCTION

The design drawings of bridges built decades ago were mostly lost and can not assure the actual penetration depth and size of pier foundations. These unknown bridge foundations pose a significant problem to the bridge managing agencies because of scour vulnerability concerns. The foundation depth information in particular is needed to achieve an accurate scour evaluation at each bridge site, along with as much other information on foundation type, geometry, materials, and subsurface conditions as can be obtained. Assessing and characterizing pier foundations at existing bridges for scouring problem has become an essentially necessary task.

Surface geophysics can provide information concerning substructure geometry and relevant material properties. The methodologies currently available to determine unknown foundations can be grouped as (1) direct methods such as probing, augering, drilling or digging, (2) deductive methods with borings alongside the foundation such as parallel seismic method, borehole ground penetration radar method, vertical seismic profiling method, cross-hole electrical resistivity tomography method and, (3) surface interpolation methods such as seismic refraction method, ultra-seismic method,

electrical resistivity imaging method and other wide variety of geophysical or Non Destructive Tests (NDT). The tops of footings and pile caps may be buried below riprap, backfill, and/or channel soils. The bridge conditions may range from dry riverbed to marsh to flowing water with water conditions ranging from fresh to brackish to saltwater. The actual type of NDT method chosen is site specific depending on access, foundation configuration, nature of subsurface soils, etc.

Olson et al. [1] studied some NDT determinations of unknown bridge foundations in terms of their capabilities and limitations. Six surface methods and four borehole methods were discussed. Wightman et al. [2] summarized some Surface NDT Methods and Borehole NDT Methods to determine the unknown depth of foundations.

BACKGROUNDS AND ENVIRONMENTAL CONDITIONS

The historical rail bridge selected in this study was built in 1911~1913 by Japanese technicians. The old bridge was assigned as national heritage and retired from service in 1987 as a new bridge constructed alongside. It crosses a wide and flat river section in alluvial plain field. Total length of the rail

bridge is 1,526 m with 23 brick-masonry-made piers along with simple supported steel truss superstructure. After a series of typhoon events from 2005 to 2009, several piers were destroyed in scouring. Some existed piers were temporally reinforced by micro-piles as shown in Fig. 1.



Fig. 1 An existed pier in the water way with temporally reinforced by micro-piles

From Fig. 1, the upper part of pier is formed by 3 different layers. The investigated pier is illustrated as Fig. 2 (pointed by the yellow arrow). For designing an effectively strengthen method, it is necessary to realize the actual depth of the existed pier foundations. For that reason, the bridge owner originated an investigation project to confirm the actual depth of these foundations. For these masonry piers, however, without steel reinforced rebar inside cuts the advantage of judging the distinct resistivity variation between metal and soil, which leads to evaluate through resistivity methods become more difficult.



Fig. 2 The environmental condition of studied pier

INSPECTION METHODS

To evaluate the real depth of foundation, all the potential and available methods were applied on this study case. The tests comprise Surface NDT Methods and Borehole NDT Methods, as well as a proof excavation was also conducted at the same site.

There were seven test methods adopted in this study as: 2D & 3D ERI, ultra-seismic, parallel seismic, cross-hole resistivity tomography, borehole ground penetration radar, and multiple offsets of vertical seismic profiling. Although an excavation can't be classified as a nondestructive test, it is agreed to be the most convincing manner. Generally speaking, it is unusual to put so many various ways to be applied at the same time. The only explanation is the investigating team did really want to discover the true solution of foundation geometry,

RESULTS

The entire investigation process took months to finish. The process should be divided into two phases, separated by the proof excavation. A preliminary survey was executed in Phase I, followed by the proof excavation thereafter. The proof excavation, however, gave the answer that the preliminary conclusion needs to be corrected. Therefore, some supplementary tests were added to gain better solution in Phase II. In Phase II the Borehole NDT Methods were mainly taken into account. Results from each test are illustrated as follows.

Phase I

2D ERI

For conducting 2D Electrical Resistivity Image, survey line was deployed along the longitudinal axis of bridge to test the resistivity of underground materials. In Fig. 3, there is a clear boundary at 5 m below ground surface, which refers to the interface between granite and brick (layer 3 and layer 4). The bottom of foundation is unrevealed in 2D ERI since the lower part on the image exhibits uniform resistivity distribution.

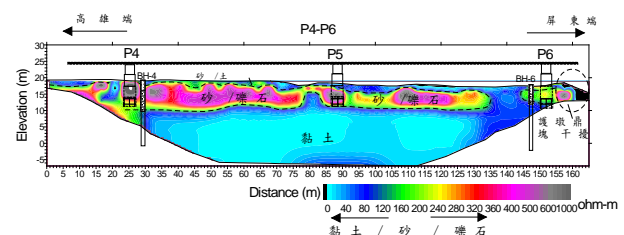


Fig. 3 2D ERI image profile

3D ERI

3D ERI was achieved by two perpendicular survey lines to construct a set of cross images at the crossing location. Again, an obvious interface was indicated at -5 m as shown in Fig. 4, same as 2D ERI. According to 2D and 3D ERI results, as has been mentioned, the resistivity methods can not get

well outcomes since no steel rebar consisted inside the foundation. The shallower part of foundation shows lower electrical resistance is constructed by granite. Below the granite is made by brick, where resistance becomes closer to the surrounding geological materials. For such condition, not much findings can be expected through just resistivity method.

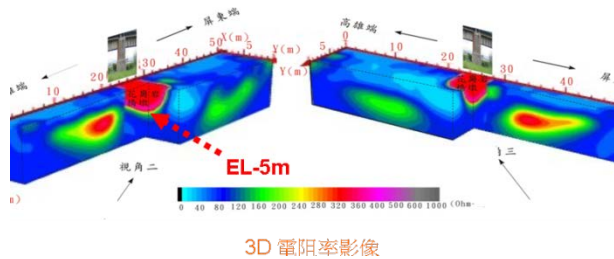


Fig. 4 3D ERI cross images profile

Ultra-Seismic

For Ultra-Seismic Test, the source is given on the pier and the receivers are attached along the side wall of pier. When every strike hits on the source point, it produces a downgoing flexural wave down to the lower part of pier, and then reflects from bottom of foundation. The interface of different layers of foundation, or the bottom of foundation can be calculated from the intersection of downgoing and upgoing events. The downgoing flexural waves have a linear positive moveout with travel time increasing with distance and upgoing events having a negative linear moveout. For this field geometry, the interface of the foundation is easily found at -4.9 m as shown in Fig. 5.

Parallel Seismic

Parallel Seismic Test is performing by using a hammer to produce some artificial impact wave onto the pier, then measuring the transmitting wave at different depth in an adjacent borehole. The measurement was recorded every 0.5 m from the bottom of hole (-20 m) upward to surface.

The crucial character of wave sequence in Fig. 6 is to find some depth at which the frequency or amplitude of wave behaves discontinuously. This character denotes some material interface encountered when stress wave traveling downward, and induces another source effect. In Fig. 6, at depth of -5 m and -10 m exist two diffraction responses which can be concluded as interfaces identified by parallel seismic test.

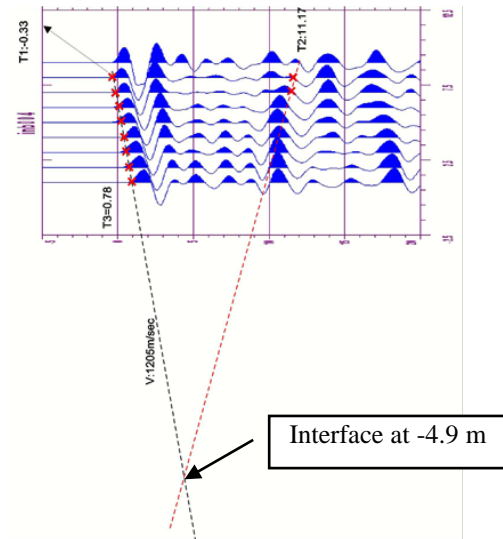


Fig. 5 Ultra-seismic vertical profiling dataset

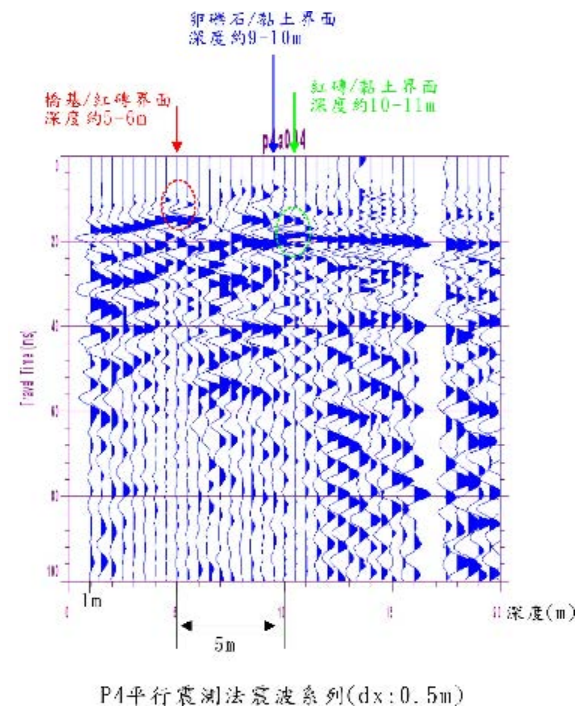


Fig. 6 Wave sequence of parallel seismic for Phase I

Proof Excavation

The project includes a proof excavation to verify NDT results. After finishing four NDT tests mentioned above, a proof excavation was used to confirm the actual solution. Based on the preliminary founding from Phase I, the depth of foundation was assumed to be about -9 m mainly fitting to the judgment from parallel seismic. Fig. 7 presents a design for the temporal retaining wall with steel sheets of 13 m at length. The excavation level was lowered down to -4 m with an open

excavation of 1:1 slope. Another two struts were used to provide horizontal support to against lateral earth pressure.

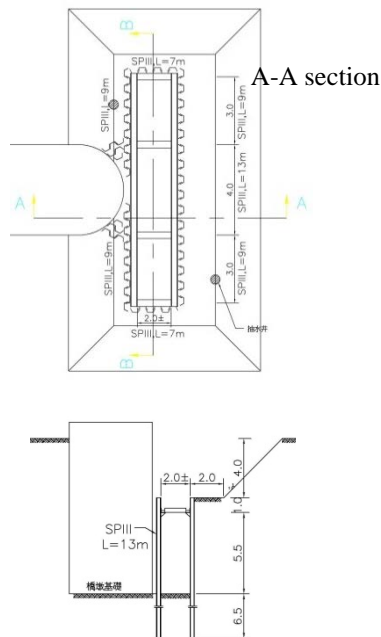


Fig. 7 Design drawing of temporal retaining wall for proof excavation

Fig. 8 displays side wall of brick caisson of investigated foundation, which implies to the layer 4. It is amazing to realize the marvelous craft at the early age as seeing the smooth and ordered brick wall. Considering the geological condition and construction technique at the early 19th century, it is thought the estimated foundation depth of -9 m should be reasonable. The caisson bottom, however, was not met at that depth. The excavation even continued to proceed 4 m further to -13 m, but could not reach the bottom yet. For the sake of safety, the excavation finally stopped at -13 m and remained the foundation bottom unrevealed.



Fig. 8 The brick portion (layer 4) of the studied foundation exposed by excavation

Phase II

After knowing the foundation depth might be deeper than -13 m, more NDT tests were applied to reconfirm the true depth.

Ultra-Seismic

The ultra-seismic vertical profiling data was reanalyzed. In addition to an interface of the foundation is clearly found at -4.9 m, another interface is at -12.36 m (end of brick caisson). Moreover, it is found an indistinct pair of upgoing and downgoing events intersect at the lowest position is about 17.36 m underneath the ground surface (Fig. 9).

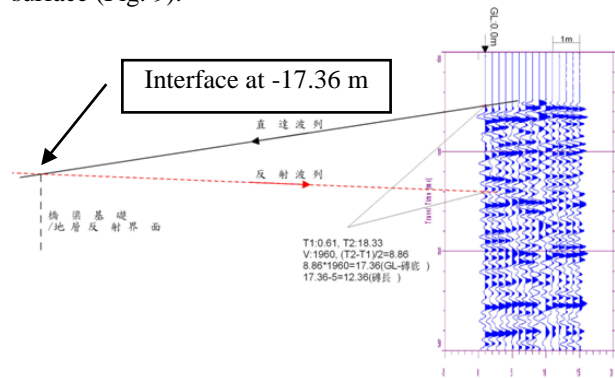


Fig. 9 Another deeper interface estimated from ultra-seismic vertical profiling

Cross-hole Resistivity Tomography

For conducting some Borehole Nondestructive Tests, two boreholes with depth of 20 m were drilled next to the study pier. Fig. 10 shows an image plotted from the cross-hole resistivity tomography. This image gives also strong electrical resistance transformation at -5 m as well as some further information because the electrical rods are closer to the foundation. An unclear layer was found at -9.5 m. Furthermore, another possible interface is guessed at -16.5 m ~ -17 m only with slight variation in resistivity.

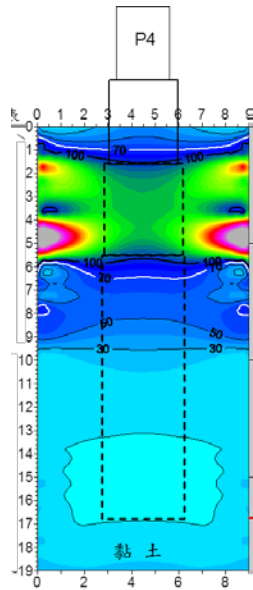


Fig. 10 Cross-hole resistivity image

Parallel Seismic

By the second parallel seismic test, wave sequences were collected deeper than the first time. The crucial clues are commonly hidden in wave sequence, and should accompany with extra hints to discover. Through a carefully picking, three interfaces at -5 m, -17 m and -22 m were identified by parallel seismic test.

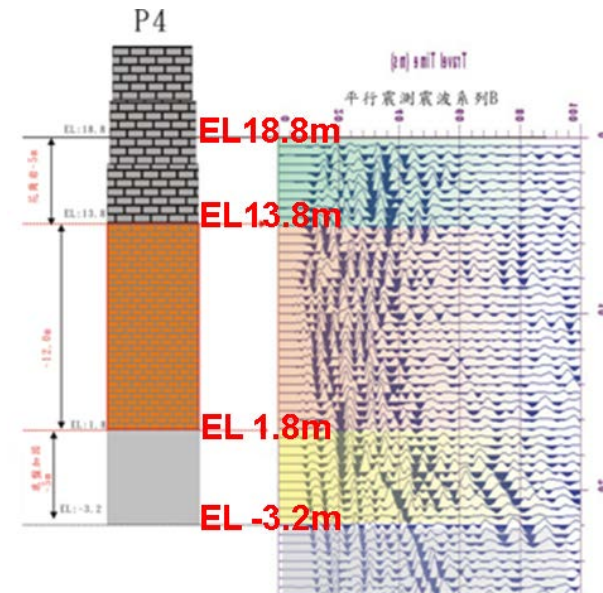


Fig. 11 Wave sequence of parallel seismic for Phase II

Borehole GPR

Ground Penetration Radar (GPR) is a very

popular test on underground investigation. Borehole GPR holds same function but puts the sensors in a borehole to get closer to the investigating target. As shown in Fig. 12, from ground surface to -5 m presents fast radar signals refer to granite portion. From -5 m to -9.5 m demonstrates diffraction due to gravel material. The signals become uniform from -9.5 m to -20 m in which an interface is discovered at -16.5 m to -17 m. Beneath -20 m is another gravel layer and followed with clay layer. It is more likely the foundation bottom at -16.5 m to -17 m by borehole GPR result.

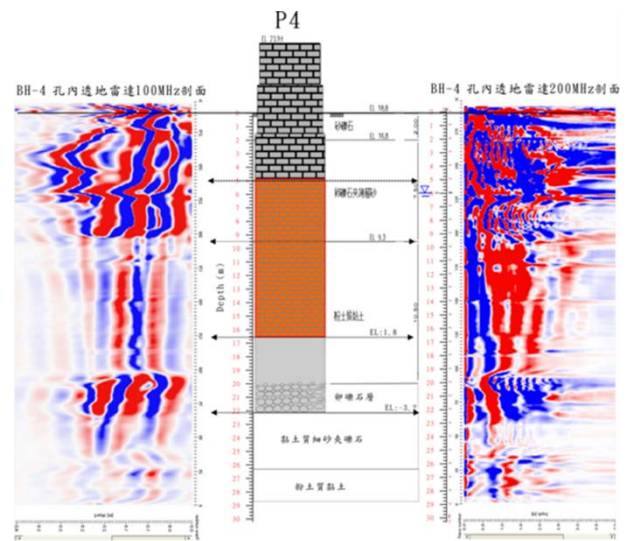


Fig. 12 Profile image of borehole GPR test

Multiple Offsets of Vertical Seismic Profiling

Multiple Offsets of Vertical Seismic Profiling uses a series of receivers in a borehole, and the seismic source hits on ground surface at different offsets away from the borehole. As the investigated foundation sits between the source and borehole, every stress wave will pass through the foundation before arriving at the receivers in borehole. Each stress wave trace can reflect its path-dependent effect. Fig. 13 shows a record of multiple offsets of vertical seismic profiling where the offset was set at 26 m. It is found there are three dispersion points at -16 m, -21 m and -18 m, respectively.

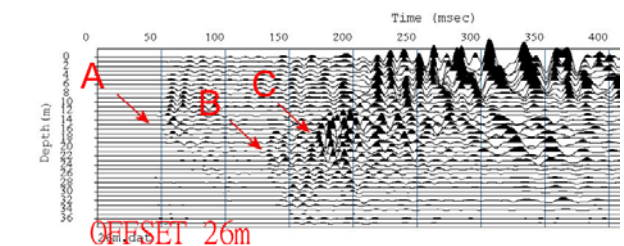


Fig. 13 A record of Multiple Offsets of Vertical Seismic Profiling at offset of 26 m.

According to all the investigating methods employed in this study, different test results are listed as Table 1. The major interfaces of interesting are the interface of layer 3 and layer 4, and foundation bottom. ERI can effectively find only the interface of layer 3/4. Cross-hole resistivity tomography, ultra-seismic, parallel seismic, and borehole GPR can relatively detect lighter dissimilarity and give similar answers at deeper ground. In addition, multiple offsets of vertical seismic profiling is another promising method to determine the foundation bottom within an acceptable range.

Table 1 Summary of NDT results in this study

	Method	Investigated Pier	
		Interface of layer 3/4	Foundation bottom
1	2D ERI	-5.0	NA
2	3D ERI	-5.0	NA
3	Cross-hole Resistivity Tomography	-5.0	-17.0
4	Ultra seismic	-4.9	-17.4
5	Parallel Seismic	-5.0	-17.0
6	Borehole GPR	-5.0	-17.0
7	Multiple Offsets of Vertical Seismic Profiling	-	-16 ~ -18

CONCLUSION

An old rail bridge was surveyed in this study to investigate the original foundation depth. This investigated masonry bridge caisson represents a real construction technical art as well as a heritage which should be well preserved. Thus as many as seven NDT methods were used in the meantime to discuss the foundation depth. From the seven NDT methods, to put it briefly, the Surface NDT Methods provide fundamentally understanding about the stratum profile and likely foundation depth. Some ambiguous messages mixed with unanalyzable data need to be verified cautiously. It is suggested to combine several methods to give a more confident solution. Conversely, Borehole NDT Methods give more accurate information of foundation boundary. It should be concluded, from what has been said

above, that wisely picking the suitable geophysical methods is essential in surveying unknown underground structures. In addition, a solid conclusion only could be made if two or more methods obtain the same answer.

ACKNOWLEDGEMENTS

The authors would like to express the special gratitude and thanks to Bureau of Cultural Affairs of Kaohsiung City Government for funding this project.

REFERENCES

- [1] Olson LD, F Jalinoos, and MF Aouad, "Determination of Unknown Subsurface Bridge Foundation," Federal Highway Administration, Geotechnical Notebook Issuance No. 16, 1998.
- [2] WE Wightman, F Jalinoos, P Sirles, and K Hanna, Application of Geophysical Methods to Highway Related Problems, FHWA, 2003.

CONTRIBUTION OF GEOLOGICAL MAPPING AND NEW TECHNOLOGIES TO THE IDENTIFICATION OF A MAJOR, PRE-EXISTING AND ACTIVE FAULT OVER THE CAPITAL OF TUNISIA

Adnène KASSEBI^{1,2} and Fouad ZARGOUNI¹

¹ Faculty of Sciences of Tunis, University of Tunis El Manar, Tunisia; ² National Center for Mapping and Remote Sensing, Tunis, Tunisia

ABSTRACT

Greater Tunis, which covers a quarter of the population, is an area of vulnerability to natural hazards, because it is built on a series of hills sloping down to the lake of Tunis, and has a steep slope in away from the top of a bowl direction: sebkha Sejoumi. Among the active north-east of Tunisia, the El Nahli-Ben Arous and Kechabta major faults are the most dynamic. The application of a directional filtering on HRVIR images SPOT-4 and Landsat-7 ETM+, combined with digital elevation models produced from topographic data and aerial photographs combined with geomorphological and geological observations on the field. We identified the existence of a pre-existing fault, deep and active. The potential and low activity of the major fault can cause catastrophic damage for the state of buildings in the city and taking into account the results of past earthquakes.

Keywords: Structural, Microtectonic, lineaments, satellite imagery, Seismicity

1. INTRODUCTION

Orientation NS to NNW-SSE of limestone outcrops south of the city of Tunis, in contrast to the major direction of the rest of Atlasic folds trending NE-SW. has led us to establish a tectonic and structural study of these outcrops at the end to understand their geodynamic significance and structural feature.

The discussion major tectonic events that led to the deformation of the study area: the thickness variation, the pre-existing fracture, folds or twists that affect the superficial layers geological levels related to fault movements and states constraints that are closely related to this structure.

The analysis of satellite imagery and aerial photographs, in addition to the analysis of historical earthquakes in the city of Tunis, we identified the existence of a major and active fault above the capital Tunisia.

2. GEOGRAPHICAL AND GEOLOGICAL SETTING OF THE STUDY AREA

The study area belongs to the north-east of Tunisia, which is an area of interference major structural zones of Tunisia, namely the eastern area, the north-south alignment and fault Zaghouan and Atlas North, including the dome zone [1]. It consists of limestone outcrops south of the city of Tunis, from El Jellez cemetery in the north to the outcrop of Souk el Jomla South. This area is often called "horst Tunis" [2], [3], [4] and [5] because of its morpho-structural position between Sebkhet Essijoumi raised in the West and Lake Tunis East

(Fig. 1).

The Greater Tunis area is characterized by outcrops often disjointed and plains lined with quaternary geological structures, which makes it difficult to understand the whole approach to geometric and kinematic relationships between the various structural elements.

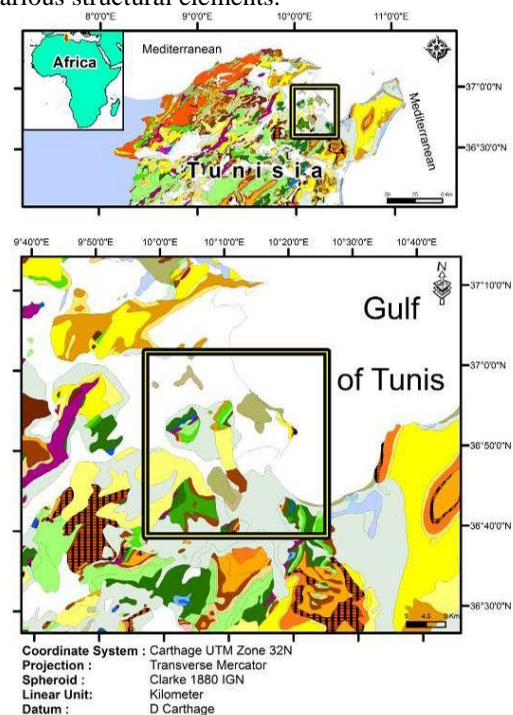


Fig. 1 Geographical and geological map of the study area.

3. GEOMETRIC AND STRUCTURAL ANALYSIS

3.1. Geometry structures

In our study area, attempts to detail geometric analysis and determination of the kinematics of deformation of fold structures and / or faulted are few [2], [3] and [6]. They are intended to demonstrate the complex appearance [4] and [5] and often disharmonic structures [5] without defining a model of folding. Lithological heterogeneities present within the sedimentary pile involve different attitudes to deformation. Thus, levels of incompetent lithologies locate separations and are causing disharmony. Relevant levels proportionally fewer and thinner form markers within the structures.

Because of the abundance of fracturing and abundance of directions within the limestone outcrops, we tried to represent the outcrops by the various major structures indicating the landscape of the outcrop and small details like small horst and graben. The folding and minor flaws will be described in part microtectonic analysis.

Mass in the study area are distinguished by their different sizes and geometries. The major structures are all asymmetrical and show only one periclinical termination. The layout of all structures in space has a more or less rectangular.

3.2. Structural framework

The structural study of the study area, has allowed us to reconstruct the geometry of the main structures that shape the landscape of the area, as well as major faults that affect it.

The major direction of fold axes in our study area is NW-SE to north-south (Fig. 2). This direction may be related to a rotation in the space of the direction of the major constraint known across Tunisia NW-SE to NE-SW to NS.

Structural cuts were made at the end to simplify the structure of these outcrops (Fig. 2). The reversal of the dip is the most widespread in these outcrops landscape with same rotation sets in space. This is due to the presence of a preexisting deep and caused this accident chaotic deformation, indicating the blockage which is pronounced by the geological feature of the area: a sign of tectonic interference region of the main structural zones of Tunisia, North-South alignment and fault Zaghouan in southern sector of the basin-Kechabta Messefine north, the area of the water and the dome zone to the west.

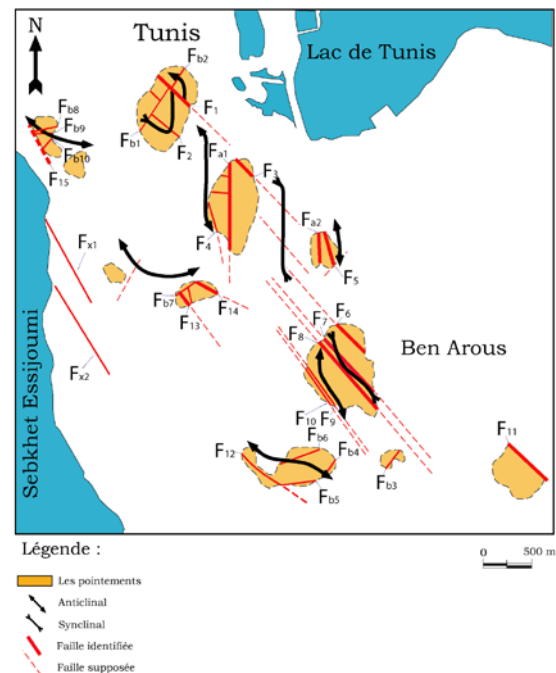


Fig. 2 Interpretive structural diagram of limestone outcrops, south of the city of Tunis [7].

This block is identified in contact with major faults in the sector, while in the center, where the shortening is less strong, there are series in Horizontal (Jbel Boulaâdham).

3.3. Discussion

The tectonic study of beam folds the study area showing major faults that are often parallel to the large structures (Fig. 2). Other faults assumed effective, are derived from the geometry and spatial arrangement relay certain structures. So off faults, low emissions, related folds themselves. According to the different outcrops.

- Flaws numbered from F1 to F15 (Fig. 2) have a major NW-SE direction. The majority of these faults indicate normal oblique very important games, putting yprésienne series abnormal contact with the Campanian-Maastrichtian series, or clays Santonian. The normal game these existing accident before the game setback sinister dexter or even a game as reverse faults.

- Flaws in Fa1 Fa2 (Fig. 2) have a NS direction and has normal games that precede the inverse operation of these major accidents.

- Flaws numbered Fb1 to Fb10 (Fig. 2) have a major NE-SW direction. The majority of faults that this direction have a game in normal fault followed by the reverse Thurs Some vulnerabilities have a winning dexter sinister in some localities of the study area Thurs

- Flaws and Fx2 Fx1 direction N160 to N165 (Fig. 2) affect the quaternary land border East Sebkhet Essijoumi.

4. MICROTECTONIC ANALYSIS

4.1. Related criteria chronology

In the field study, since the age of the youngest rocks with the means of microtectonic data is the Campanian-Maastrichtian. Criteria for timing are essential to approach the Cenozoic tectonic history. The kinematics deduced devices mirror flow have been detailed by several authors [2], [3], [4] and [5], but the criteria of chronology were rarely discussed in detail. Several traps can be produced, which can lead to erroneous conclusions. These criteria can be distinguished cross cutting relationships between all devices and chronologies vectors of tectonic faults on mirrors.

4.1.1. Slot against Slot

The division between two slots can be of three types: X, λ and χ -type, with different interpretations (Fig. 3). For the X-type crossing, if mineral fillers are clearly different for each direction, it clearly defines two distinct generations with σ_3 (Fig. 3 B and C).

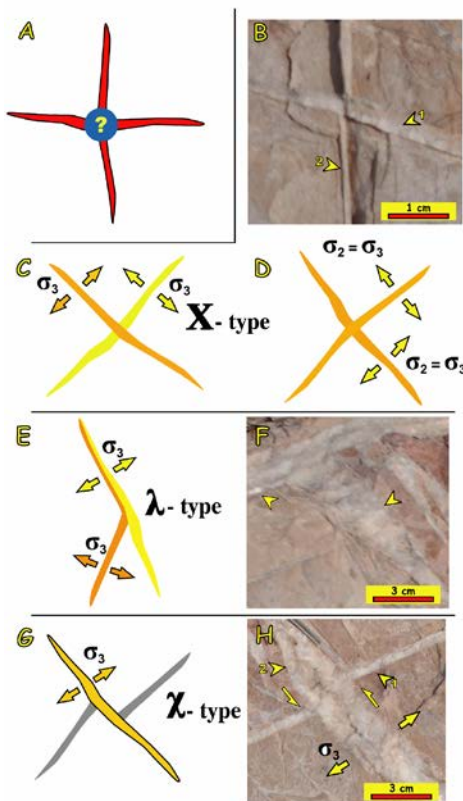


Fig. 3 Criteria relative chronologies between tension gashes; A: problem of determining chronology B: photography with a slot oldest NW voltage (1), cut by a younger slot voltage NE-SW (2); C: theory for the X-type with the first generation and the second yellow orange, D: theory for the X-type with a generation for the radial extension, E: Theory of λ -type for the first generation gray the second in

orange, F: photography with a slot voltage NW-SE older (1) blocking a younger slot voltage NE-SW (2) G: χ deviation theory with the first generation in gray the second in orange, H photography with a slot voltage older NE-SW (1) cut by a younger slot voltage NE-SW (2).

If filling is homogeneous it involves synchronous opening due to a simple radial extension ($\sigma_2 = \sigma_3$) (Fig. 3 D). For λ -Type, cross the broken slot is actually the second generation as the spread was blocked by the previous straight slot (Fig. 3 E and F). In such a case the filling slot is clearly different [8].

4.1.2. Timelines involving flaws

The film features recorded on mirrors faults are frequently associated with pressure-solution process and conduct a detailed analysis of the relationship between the striations, the stylolites and fills ore.

There are two kinds of relative chronologies, first intersection between devices and other tectonic reactivation of the same discontinuity Paléochamps under different constraints.

The first is more obvious since the intersections are very clear, for example, a slot voltage can be striped or striated plane can cross without being moved, a stylolitique plan can be displaced by a fault where the mirror flaw can be affected by stylolitiques ridges or fault plane can be moved by reactivation of the fault itself.

As in a single scheme palaeostress conjugate faults, cracks and stylolitiques plans have very different directions [9], such a division is very common and is not significant in determining the timing of Paléochamps constraints [10]. On opposite changes and film for the same asserted discontinuity, changing Paléochamps constraints is clear.

Fills minerals observed mirrors faults are of primary interest to establish the chronology of Paléochamps constraints, according to their types. The first example is affected by a fault movement (Fig. 8) slot.

4.2. Age and significance of structures

The first extensional tectonic phases have arisen from the Campanian-Maastrichtian, then from the upper Paleocene-Eocene. As in all of Tunisia, the phases of the deformation are more visible in the Neogene. After these phases Neogene most of currently observable structures in place, but on a smaller scale deformations, continue to be felt. Recent movements of age post-Villafranchian have affected the older Quaternary formations.

The three tectonic features: faults, tension gashes and stylolites were associated with a step or normal movement, when their directions σ_3 were consistent with stylolites and / or flaws in the same location. In

some cases it was not possible to remove the ambiguity between the two tectonic regimes.

5. EXTRACTION OF LINEAMENTS AND VALIDATION

5. 1. Image processing of Landsat-7 ETM +

The Principal Component Analysis (PCA) was performed on seven soundtracks ETM + Landsat-7 image of Grand Tunis has generated neo-channels (principal components). The first three components contain a high percentage of the total variance (Table 1). This table shows a strong correlation of the visible bands (1, 2 and 3) with coefficients of 0.9. There is also a correlation in the order of 0.7 those of the infrared. The combined use of these channels gives redundant information because they contain common data. The CPA has helped identify the information contained in these multispectral images by eliminating data redundancy: the linear geostructures are best seen in the first principal component (principal component 1 or PC1) on the multispectral image.

Table 1 Correlation matrix of the Landsat ETM+ bands of the area of Great Tunis

Band ETM+	1	2	3	4	5	6	7
1	1,00						
2	0,96	1,00					
3	0,95	0,95	1,00				
4	0,88	0,87	0,79	1,00			
5	0,87	0,91	0,93	0,86	1,00		
6	0,66	0,66	0,64	0,58	0,66	1,00	
7	0,78	0,79	0,91	0,74	0,88	0,75	1,00

Some details in the images obtained could then be enhanced through the application of the technique of combining images using simple mathematical operations that generate reports bands (PC1 / ETM +7) and indices standardized (ETM+6 – ETM+4) / (ETM+6 + ETM+4).

Table 2 The application of high-pass filter (Laplacian modified) 5X5

0	0	-1	0	0
0	-1	-2	-1	0
-1	-2	16	-2	-1
0	-1	-2	-1	0
0	0	-1	0	0

The application of high-pass filter : Laplacian modified (Table 2), directional Sobel filter type 7x7 and finally gradient filter Yésou [11] bands ETM+7,

ETM+4 and PC1 can raise even more discontinuities images corresponding to structural lineaments.

5. 2. Natural lineaments from the analysis of the DTM

The realization of a mapping project, using the Leica Photogrammetry following LPS extraction field, we succeeded in the automatic generation of a digital terrain model (DTM for each display quality indicators) by correlation of ten IKONOS 2004 satellite imagery (Fig. 4) oriented.

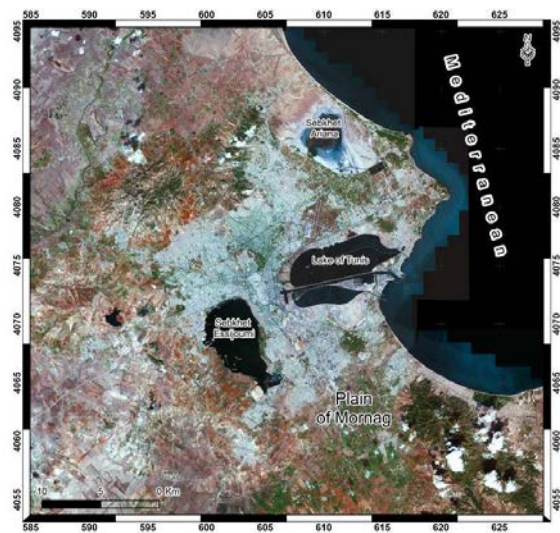


Fig. 4 Correlation of ten IKONOS 2004 satellite imagery.

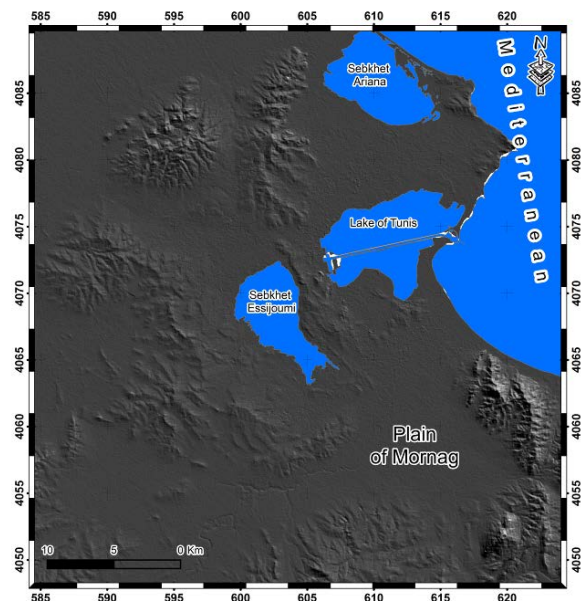


Fig. 5 Hillshading from the DTM of the Greate Tunis region.

Existing data (support points, field points control connection (aerial triangulation) and text files), digital terrain model and external vectors from the triangulation of an image block, and extraction of

elevation and creation from orthorectified aerial photography (2012) images, are used to improve the correlation process.

Using the "3D Surfacing Tool" tool LPS Core was merged NCD and added line breaks.

The extraction of lineaments from MNT (Fig. 5), corrected and validated, with the manual method, takes into account the removal of the water system and human lineaments and other lineaments that can not correspond to a fault or fracture.

5.3. Discussion

The extraction of lineaments was performed in part on the initial and transformed bands (or filtered from the ACP) and secondly the DTM extracted. Treatment and filtering have been to accentuate and facilitate the detection of discontinuities-images, allowing them lifted by visual observation. Only the origin of structural lineaments, have an interest in this study. Also, by synthesis of information through a GIS anthropogenic previously vectorized linearities (paved roads, trails, power line, transects bounding forest and cultivated land ...) have been identified in all the lineaments and eliminated.

Geological and structural lineaments identified in previous mapping [2], [3], [4], [5] and [7], but few based on aerial photographs and field observations therefore considered as true, were found in our network of lineaments. The ability of the method, based on the interpretation of satellite images, find real fractures already known, not only among the largest, validates our extraction method. This validation leads us then extrapolated to give a structural value to all our lineaments and move from the use of the term lineament than divide.

This work on satellite images finally provides a new structural map and much richer in Greater Tunis, where it has been introduced by mistake or overlook some fractures, especially among smaller (length of a few kilometers) to the observation scale images.

6. ACTIVE SEISMICITY

6.1. Historical seismicity

The historical seismicity of Tunisia is very poorly known, the documents produced by several authors [12], [13] and [14] show that the Greater Tunis known in the history of destructive earthquakes as shown in Table 3.

It is noted that the historical earthquakes in the study area often affect areas of Tunis city northern suburbs, and Mornaguia-Borj Amri.

Table 3 The history of destructive earthquakes in Great Tunis area.

Area	Date
Utica	5th century (between 410 and 412 BC)
Kairouan	9th century (855) 13 villages destroyed around Kairouan
Tunis	In 856; 45000 victims
Tunis (Zerkachi)	In 1425
Tunis	In 1735, 1750 and 1758 AD C.
Tunis Bab El Mejaz	March 14, 1872
Tunis, Ariana and La Goulette	15 to 21 December 1863
Tunis	March 17, 1904
Tunis Mejaz El Bab	25 February 1920
Tunis Mornaguia	October 7 and September 26, 1922
Tunis	27 and June 28, 1927
Tunis	July 22, 1929
Tunis - Khereddine	February 21, 1932
Tunis	19 and May 21, 1948
Tunis	1st December 1970; magnitude 6
Tunis	December 16, 1976; magnitude 4.5

These locations are located just within the alignment seismotectonic NE-SW Tunis-Mornaguia in with data from the instrumental seismicity. The most violent earthquakes that are at the northern edge of Lake Tunis, seem to be related to the NW-SE fault. This fault extends about ten miles and shifts the anticline Jbel Nahli sinistral strike-slip. Recent activity of this accident is shown by the fact that it affects the last limestone crust and upper Pleistocene [16] red silts.

Further south in the region of Tunis, the moderate seismic activity seems, but in reality it is important for the large number of low shaking whose magnitudes do not exceed 3 degrees Richter and have not been shown in card. It seems that some events are to be attached to the accident Zaghuan and others are to be attached to the N-S fault M'hamdia and NE-SW fault Jbel Tella [16].

The instrumental seismicity data from the National Institute of Meteorology (INM) and correspond to recorded from 1976. It is generally low to moderate seismicity (magnitude between 2 and 5 degrees).

6. 2. Macroseismic companion

A macroseismic companion made following the earthquake April 29, 2003, in the Greater Tunis, reveals an epicentral area, elongated along a NNW-SSE, which follows the same direction of our major flaw identified in the field [7]. This is an earthquake of magnitude 3.5 and intensity VI on the MSK scale. This earthquake caused a lot of damage to the old Medina founded in 698 and the outskirts of the city

that are currently at risk of collapse, and moisture in buildings spread in very bad condition. This shows the current risk associated with stronger and possible earthquake damage.

7. INTERPRETATION

Major tectonic lineaments regional extension, often coincide with pre-existing map vulnerabilities directions N060, N090, N180 and N140. The faults trending N065 el Mannoubia of N140 direction Nahli Ben Arous and Mhamdia define structural panels NE-SW direction, they form a system strap tectonic shear associated with anticlinal megastructures NS to N140.

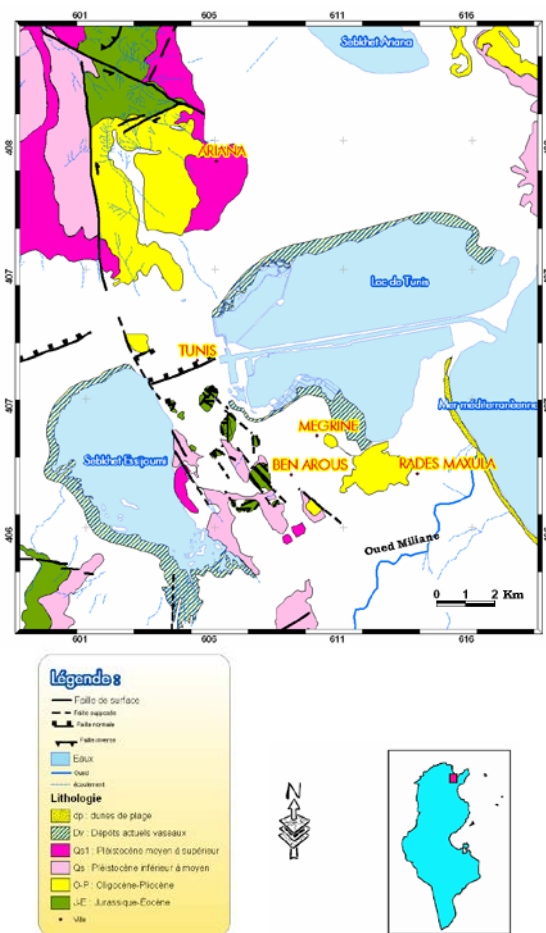


Fig. 6 Seismotectonic map of the study area and its surroundings ([7], modified).

The major faults trending N120-140 N060-070 are involved in the genesis and deformation of the upper Pliocene basin Cretaceous.

The Late Cretaceous is the most demonstrative when major faults are subject to a transtensional regime resulting from the opening of the Tethyan areas mesogean and Atlantic [18]. Faults NW-SE to EW were activated primarily from the Upper Cretaceous, while the NS faults in the N060 is the

oldest directions. Therefore, we can provide a base cut by accidents NS who suffered during the time of raised portions repetitive image of the domain alignment NS.

8. CONCLUSIONS

Our study area has a great diversity of viewpoint geodynamics, structural and tectonic. Though this is a natural extension of the Tunisian Atlas, its tectonic features also recall NS alignment (Fig. 6); it is also up on its northern extension. It can thus be seen as an interference area structures. Indeed, the tectonic division is configured holes directions N60-70 and N120-140 known the Atlas area.

Therefore, these limestone outcrops correspond to folds associated with a major setback to NW-SE to NS. This accident is presented in the study area by several segments, probably corresponds to the extension of the accident affecting NS el-Manar Nahli area. This even affects the Quaternary deposits of the sector [13].

9. REFERENCES

- [1] Zargouni F. et Abbès C., 1987. Zonation structurale de la Tunisie. Rev. Sci. Terre, édition I.N.R.S.T., Tunisie, V-3. pp. 63-69.
- [2] Solignac M., 1927. Etude géologique de la Tunisie septentrionale. Dir. Gen. Trav. Pub., 756 p; Thèse es Sciences, Lyon.
- [3] Jauzein A., 1967. Contribution à l'étude géologique des confins de la dorsale tunisienne (Tunisie Septentrionale). Ann. Mines Géol., Tunis, N°22, 475 p, 92 fig., 5 pl. Ht.
- [4] Ben Ayed N., 1986. Evolution tectonique de l'avant-pays de la chaîne alpine de Tunisie du début du Mésozoïque à l'actuel. Thèse d'Etat, Univ. de Paris, Sud- centre d'Orsay.
- [5] Boutib L., 1998. Tectonique de la région du Grand Tunis : évolution géométrique et cinématique des blocs structuraux du Mésozoïque à l'actuel (Atlas nord oriental de la Tunisie). Thèse de Doctorat, Univ; Tunis, 151p.
- [6] Boutib L. et Zargouni F., 1997. Évolution géométrique des mégastructures anticlinales et découpage en lanières tectoniques de l'Atlas centro-méridional de Tunisie. 14ème Coll. Bassins Sédimentaires. Marocains, p. 142.
- [7] Kassebi, A. 2007. Signification géodynamique des pointements calcaires au Sud de la ville de Tunis. Thèse de 3ème Cycle, Faculté des Sciences de Tunis, 95 P.
- [8] André G., 2002. Evolution des paleocontraintes tectoniques le long d'un accident régional, exemple de la faille de Vittel, Journée de l'Ecole Doctorale RP2E, Nancy. CD-R.
- [9] Arthaud F. et Mattauer M., 1969. Exemple de stylolites d'origine tectonique dans le

- Languedoc, leurs relations avec la tectonique cassante. Bull. Soc. Géol. de France (7), XI, n°5, pp. 738-744.
- [10] André G., 2003. Caractérisation des déformations méso-cénozoïques et des circulations de fluides dans l'Est du Bassin de Paris. Thèse de 3ème cycle, Université Henri Poincaré, Nancy, 311 p.
- [11] Yésou, H., Besnus, Y., Rolet, J. et Pion, J.-C. (1993) Comparaison et évaluation des données SPOT, ERS-1, Seasat, Landsat et des données combinées lors d'études de géologie structurale. In 8e congrès de l'Association Québécoise de Télédétection, 16ème Symp. Télédétection, Sherbrooke, pp. 521-526.
- [12] Ambrassey N. N. (1962) - The seismicity of Tunis. Anali di geofisica, vol. XI, n°2-3, Roma.
- [13] Rothe J. P. (1969) - Mission d'information seismologique, Moyen-Orient et Afrique du nord. UNESCO, n° de serie: 1759/BMS. 336p. 24 fig., 50 tabl., Paris.
- [14] Zenati H. (1990) - Etablissement dun catalogue des seismes historiques de la Tunisie: evolution des donnees recueillies pour la periode 365-1950. Tome I, Soc. Tun. Elec. Gaz (rapport inedit).
- [15] Kassebi, A., Khémiri S., Ajmi M., Hamza M. H. et Zargouni F. 2010. Les risques d'inondation associés à l'évolution de l'environnement urbain dans le Grand Tunis. Congrès International Géotunis : 5ème édition, intitulé : « L'utilisation des SIG et la Télédétection pour le développement durable ». pp. 21-22.
- [16] Kacem J., 2004. Etude sismotectonique et évaluation de l'Aléa sismique régional du Nord-Est de la Tunisie : apport de la géophysique dans l'identification des sources sismogéniques. Thèse Es Sciences Géologique, Univ. Tunis II, Fac. Sc. Tunis, 389 p.
- [17] Dlala M. et Kacem J., 2006. Carte sismotectonique du grand Tunis, programme de collaboration INM-FST, et OTC-Tunis.
- [18] Dlala M., 2002. Les manifestations tectono-sédimentaires d'âge Campanien-Maastrichtien en Tunisie : implication sur l'évolution géodynamique de la marge Nord-Africaine. C.R Geoscience, 334, pp. 135-140.

EFFECT OF GRAIN SIZE ON MINERAL CARBONATION OF COAL COMBUSTION FLY ASH FOR CO₂ SEQUESTRATION

N. L Ukwattage and P.G Ranjith

Deep Earth Energy Lab, Bld 60, Monash University, VIC 3800, Australia

ABSTRACT

Mineral sequestration with alkaline waste materials is being studied extensively for its application as a way of reducing the increased level of CO₂ in the atmosphere. Coal combustion fly ash has the potential to react with CO₂ to form minerals which are stable over geological times. For industrial level application of this concept, the mineralization reaction is required to enhance. One possible way of achieving it is through selection of best reactive material. Therefore, the objective of the present study was to investigate the effect of the grain size of fly ash on rate and efficiency of mineralization reaction. In the study, three Australian fly ashes from Hazelwood, Loy Yang and Yallourn power plants were carbonated inside a closed reactor at 3 MPa CO₂ pressure and 40 °C temperatures. For each fly ash type, 50 g of oven dried samples from four different particle size classes as < 100 µm, 100-250 µm, > 250 µm and bulk particles were tested and compared for the weight gain after carbonation. From the results 100-250 µm samples were found as the best particle size range for the mineral carbonation reaction of all three tested fly ashes whereas particles larger than 250 µm diameters gave the least sequestration. Also, Yallourn fly ash showed the highest sequestration potential at each particle size of all three tested fly ashes which could be attributed to its available oxide content and purity.

Keywords: Mineral sequestration, CO₂, Fly ash, Grain size

INTRODUCTION

Mineral sequestration of CO₂ using alkaline materials is another novel CO₂ sequestration concept which provides a beneficial use for certain rapidly accumulating waste materials [1]. Solid wastes produced during coal combustion (fly ash and bottom ash), municipal solid waste incineration (fly ash, bottom ash and air pollution control residues) and by-products such as steel slag are some of the residues which are being evaluated for their potential for CO₂ sequestration [1]-[3]. In mineral sequestration, atmospheric CO₂ is taken up by alkaline oxides and hydroxides present in the candidate materials to form thermodynamically stable forms of carbonates [1], [4]. Basically, mineral carbonation is an acid base reaction where an acid formed by dissolution of CO₂ in water (H₂CO₃) is neutralised by a solid base (alkaline mineral). It is one of the steps in natural rock weathering which comprises of a complex series of chemical and mineralogical transformations [3].

Under ambient conditions Ca and Mg-bearing silicate minerals are naturally carbonated to form Ca and Mg carbonates. But this natural weathering takes geological times to complete [5]. Therefore in order to achieve quick transformation of CO₂ into stable minerals, for the applications in CO₂ sequestration, the natural reaction should be enhanced through aqueous mineral carbonation. In this, the carbonation reaction is accelerated through

the ex-situ carbonation with manipulated reaction parameters such as temperature, CO₂ pressure, moisture content and mixing [6, 7]. In addition, selection of a suitable candidate material helps to increase the sequestration efficiency and also the rate of reactions.

Coal combustion fly ash is a solid waste material contains oxides such as CaO and MgO that can be converted to carbonates in the presence of CO₂. Also it is an abundant solid waste of which, production is expected to increase as a result of the world's increasing reliance on coal-fired power generation over the next few decades. Although there are many potential uses of fly ash including cement production, road sub-base construction, mine reclamation and as aggregate substitute material, it is presently identified as a resource that is significantly under-utilized [8]. Each year a large mass of fly ash is collected in storage ponds, which emphasizes the need for the investigation of large- scale applications for this waste product.

Over the last few decades fly ash has attracted attention as a potential source in the mineral sequestration process, which involves the capture and storage of atmospheric C in alkaline materials [6], [9]. The utilization of fly ash to capture and fix CO₂ has an added advantage, since it assists in the management of this potentially hazardous waste. As the carbonation process helps to alter the chemical stability of the fly ash, the leachability of heavy metals such as Pb, Zn tends to reduce after

carbonation [10]. This allows the safe disposal of carbonated fly ash into landfills or dumpsites.

However the mineral carbonation of coal fly ash for CO₂ sequestration is still not implemented in industrial level due to several drawbacks in the process which needs to be solved through further research on the discipline. One of the identified research needs is to optimize the carbonation reaction by investigating the effect of parameters on the mineralization process. As a material characteristic, the grain size of the fly ash being carbonated can influence the overall reaction rate and efficiency. Therefore, the objective of the present study is to evaluate the effect of fly ash grain size on the mineral carbonation for CO₂ sequestration.

MATERIALS AND METHODS

The fly ash samples for the test were collected from three power plants (Hazelwood, Loy Yang and Yallourn) located in Latrobe valley, Victoria, Australia. Victorian brown coal is the parental material for all three of these ashes. The morphology of the Latrobe valley ash particles is generally irregular and ranges from sub-angular through to rounded, sometimes spherical. The powder used in the study came from the collection ponds and initially contained large clods of ash which needed to be broken into individual particles for testing.

Fly ash samples were then sieved with 250 µm followed by 100 µm sieves to get material under 100 µm, between 100 to 250 µm and above 250 µm diameters. Bulk sample was randomly drawn from the bulk material. Then the samples were oven dried at 105 °C for 24 hours to remove all moisture. From the dried material 50g of samples belong to each grain size category were taken for testing. For each test two replicates were taken. Then these samples were added with 20% weight of distilled water and placed in stainless steel dish containers for reaction.

The carbonation reactions were carried out inside the pressure chamber shown in Fig. 1. Sample containers were placed inside the reactor cell and the cell was heated up to 40°C temperature. Then CO₂ gas was charged into the cell until the cell inside pressure becomes 3 MPa. After achieving the pressure the reactor cell was isolated and the ash was allowed to react with gas for 10 hours. After 10 hours' time the remaining gas in the cell was discharged and the samples were taken out. Reacted samples were then oven dried until a constant weight and then the final dry weights were recorded. Weight gain after the carbonation in different particle size category was analyzed for all the three fly ashes tested. In order to confirm the carbonation, the reacted samples were looked under the scanning electron microscopy (SEM).

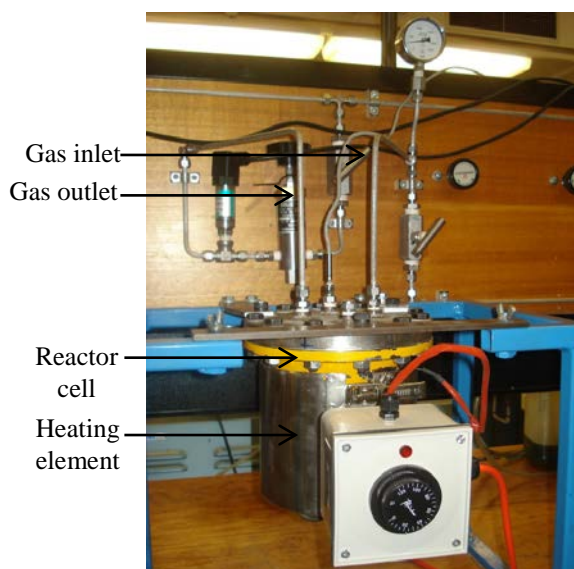
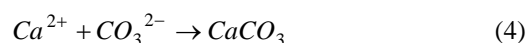
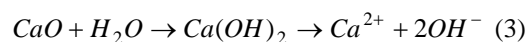
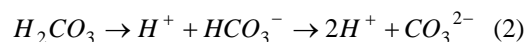
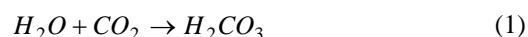


Fig. 1 the reactor setup used for the carbonation reaction

RESULTS AND DISCUSSION

The optimum grain size of coal fly ash for the mineral carbonation reaction for CO₂ sequestration was determined using the percentage dry weight gain after the carbonation. During the carbonation process the formation of carbonates from oxides increases the dry weight of the solid material. Out of all available oxides, CaO forms the most stable form of carbonate, Calcite (CaCO₃) at the presence of moisture and CO₂. The series of mineralogical transformations occur during the carbonation process is shown under Eq. (1) to (4).



According to the chemical reactions ultimately the gaseous C occurred in CO₂ is stored within calcite as carbonate carbon. Therefore after the reaction fly ash material gain some weight due to stored carbon. Fig. 2 shows the average weight gain after carbonation of different grain size categories of each fly ash type.

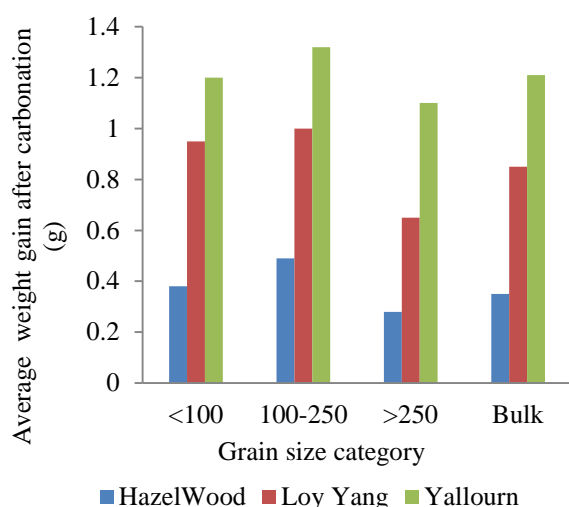


Fig. 2 Weight gain after carbonation

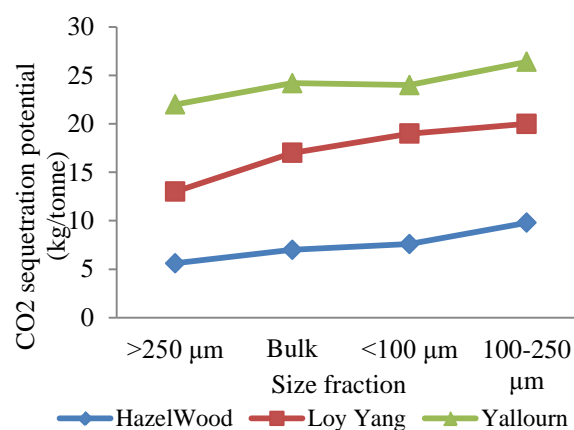
According to the results shown in Fig. 2 all three fly ash types had their maximum weight gain after carbonation for the grain size category of 100 to 250 μm . Also all three ashes showed the least weight gain for the ash particles > 250 μm diameter. In order to verify the significance of the differences in weight gain obtained for different grain size classes, two factor ANOVA statistical test was performed for all the samples. Fly ash type and the grain size category were considered as the sources of variance. According to the test results, at α level of 0.05 there was a significant difference in the weight gain after carbonation among different grain size categories (F test 14.51 > F critical 4.75). Also, the average weight gain for the same experimental conditions was significantly different on the fly ash type.

These results can be interpreted with the different factors affecting on the rate and efficiency of the mineralization reaction. Particle size can influence the overall carbonation efficiency of solid waste materials due to several reasons. Smaller the size of the particles the reactivity of those tends to be increased. Smaller particles become more reactive for two reasons: 1) they have a larger specific surface area for reactions, 2) as they cool faster upon exiting the combustor they undergo more changes. Therefore they possess a more reactive structure [11]. In addition to the increased reactivity, the comparatively high CaO content found in smaller particles is another factor which helps them to show a higher degree of carbonation efficiency than larger ones. Usually the CaO content increases with decreasing particle size. Therefore the largest particle size category records the lowest weight gain after carbonation.

However, the maximum weight gain was observed for the grain size of 100 to 250 μm . Therefore the optimum grain size of coal fly ash for

mineral carbonation lies within this grain size range. The results of the present study are in agreement with similar studies done on municipal solid waste incineration (MSWI) ash and coal fly ash by some other workers. In their experiment on carbonation of air pollution control residues (APC ash) of MSWI, [9] observed that the fraction below 212 μm as the optimum for carbonation. Also [6] studied the effect of particle size on the carbon sequestration potential of coal fly ash and concluded that 20–150 μm particle size range as the optimum. The least potent was observed for the >150 μm fraction.

Considering the average weight gain after carbonation for each sample tested, the sequestration potential could be estimated. Fig. 3 compares the CO₂ sequestration potential of three different coal fly ashes for each particle size range.

Fig. 3 CO₂ sequestration potential of different size fractions

The highest sequestration potential for all three types of ashes was observed for the size range of 100 to 250 μm . Among three tested fly ashes Yallourn ash showed the highest sequestration potential of 26.4kg per tonne of fly ash. The lowest potential was shown by Hazelwood fly ash. This is mainly due to the change in the chemical composition of three different fly ashes. Hazelwood fly ash has the highest CaO content among all three ashes followed by Yallourn and Loy Yang fly ashes. However the Hazelwood ash used for the study were already weathered heavily due to long term storage in waiting ponds. Therefore it showed the lowest capacity to capture CO₂. Yallorn and Loy Yang ashes were subjected to almost similar degree of natural weathering and therefore the available CaO content for the reaction was much higher.

The results of the present study were compared with some other studies (results are under review of journal publication) done by the authors on the same fly ashes. During those tests authors observed grater

sequestration potentials for all the three fly ashes compared to the present study. Table 1 summarizes the results of present study and the past study.

Table 1 This is the example for table formatting

Study	Highest sequestration potential (kg/tonne)		
	HazelWood	LoyYang	Yallourn
Present	9.8	20	26.4
Past	10.7	22.1	28.4

This change in the maximum potential of sequestration could be mainly attributed to the reaction conditions used in the present study. The past study was conducted with the continuous stirring provided to the ash material with CO₂ in which the reaction was observed to be completed within 8 hours. But in the present study only a set time duration of 10 hours was used for the reaction without provision of any stirring. This resulted incomplete carbonation at the end of reaction time and therefore the sequestration potential was slightly lower than the maximum.

Finally, in order to confirm the carbonation occurred in the samples SEM pictures were obtained for the tested samples with NOVA Nano SEM 450 available at Monash University. Fig.4 shows the SEM picture.

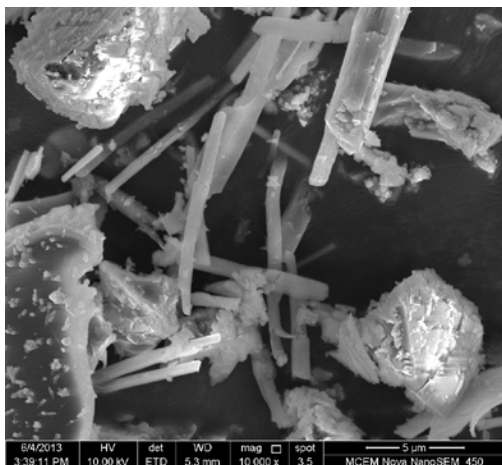


Fig. 4 SEM picture of a carbonated fly ash sample

Formation of carbonate crystals was clearly visible in the SEM images as seen in Fig.4. Rod shape carbonate crystals were abundantly observed all the reacted samples scanned through the microscope. Therefore the weight gain due to carbonation is evident.

CONCLUSIONS

Mineralization of alkaline coal fly ash has the potential to store CO₂ permanently. The sequestration of carbon in fly ash can be enhanced through optimization of parameters affecting the mineral carbonation reaction. Fly ash particle size is an important material characteristic that can be optimized. According to the results of the present study Latrobe valley fly ashes showed the maximum sequestration within the grain size range of 100 to 250 µm. Larger particles (>250 µm) had the lowest sequestration. Also, among the tested fly ashes Yallourn ash had the highest sequestration which is 26.4 kg per tonne of fly ash. The insufficient reaction time under provided reaction conditions did not allow obtaining the maximum sequestration potential recorded in a past study done by the authors.

ACKNOWLEDGEMENTS

Authors are thankful to everyone who contributed in different ways for the success of the present study. Special thank goes to the supervisor of the PhD research of the first author and the lab staff of the Department of Civil Engineering.

REFERENCES

- [1] Huijgen WJJ, Witkamp GJ, Comans RNJ. "Mineral CO₂ sequestration by steel slag carbonation", *Environmental Science and Technology* Vol. 39(24), 2005, pp 9676-82.
- [2] Reddy KJ, Weber H, Bhattacharyya p, Argyle M, Taylor D, Christensen M, Foulke T, Fahlsing P. "Instantaneous capture and Mineralization of Flue Gas Carbon Dioxide: Pilot Scale Study", *Nature Precedings* available at <http://dxdoiorg/101038/npre201054041>. 2010. Accessed on 28 May 2012.
- [3] Fernandez Bertos M, Li X, Simons JR, Hills CD, Carey PJ. "Investigation of accelerated carbonation for the stabilisation of MSW incinerator ashes and the sequestration of CO₂", *Green Chemistry*, Vol. 6(8), 2004, pp 428-36.
- [4] Baciocchi R, Poletti A, Pomi R, Prigiobbe V, Nikulshina V, Zedwitz V, Steinfeld A. "CO₂ sequestration by direct gas solid carbonation of air pollution control (APC) residues", *Energy and Fuels*, Vol. 20, 2006, pp 1933-40.
- [5] Costa G, Baciocchi R, Poletti A, Pomi R, Hills C, Carey P. "Current status and perspectives of accelerated carbonation processes on municipal waste combustion residues" *Environmental*

Monitoring and Assessment, Vol 135(1), 2007, pp 55-75.

[6] Nyambura MG., Mugeru GW., Felicia PL., Gathura NP “Carbonation of brine impacted fractionated coal fly ash: Implications for CO₂ sequestration” Journal of Environmental Management. Vol 92, 2011, pp 655-64.

[7] Fernandez Bertos M, Simons SJR, Hills CD, Carey PJ, “A review of accelerated carbonation technology in the treatment of cement based materials and sequestration of CO₂” Journal of Hazardous Materials. Vol 112, 2004, pp 193-205.

[8] Da Costa JCD, Prasad P, Pagan RJ. “Modern environmental improvement pathways for the coal power generation industry in Australia” Process Safety and Environmental Protection, Vol 82(3 B), 2004, pp 191-9.

[9] Montes-Hernandez G, Pérez-López R, Renard F, Nieto JM, Charlet L. “Mineral sequestration of CO₂ by aqueous carbonation of coal combustion fly-ash” Journal of Hazardous Materials, Vol 161(2-3), 2009, pp 1347-54.

[10] Van Gerven T, Van der Eerden E, Arickx S, Jaspers M, Wauters G, Vandecasteele C. “Carbonation of MSWI bottom ash to decrease heavy metal leaching, in view of recycling” Waste Management, Vol 25, 2005, pp 291-300

[11] Iyer RS. and Scott JA. “Power station fly ash - review of value-added utilization outside of the construction industry” Resources, Conservation and Recycling, Vol 31(3), 2001, pp. 217-228.

STUDY SEISMICITY PARAMETERS OF RUDBAR REGION AND SEISMOLOGICAL ASSESSMENT OF RUDBAR-MANJIL (IRAN) EARTHQUAKE OF JUNE1990

Noushin Naraghi Araghi , Mohd. Nawawi and Syed Mustafizur Rahman
School of Physics, University Science Malaysia (USM), 11800, Penang, Malaysia

ABSTRACT

This paper presents the seismicity characteristics of Rudbar and adjacent regions, the study area is a radius of 100 km from the center of Rudbar (36.80°N –49.41°E) where it was destroyed seriously on June 20, 1990 by one of the largest earthquake in Iran with magnitude of 7.7 (M_s) and the peak ground acceleration greater than 0.6g. More than 40,000 people were killed, and 60,000 were injured. Geological maps were used to provide the faults map of this region. Using global database of earthquakes provided as well as a catalog of historical (pre-1900) and early- instrumental (1900-1963) earthquakes, a uniform catalog of earthquakes for the interest region has been provided. To unify the scale of earthquake magnitude, we established empirical relations to convert m_b to M_s . Based on this uniform catalog and after eliminating foreshocks and aftershocks, seismicity of the interest region was studied, and seismicity parameters were calculated. In order to achieve more reliable results, the completeness of the catalog and uncertainty of magnitudes have been estimated and considered in our calculations for the interest region, the results show that b-value is equal to 0.82 ± 0.3 , λ is equal to 0.40 ± 0.08 for $m_c=4$ and $M_{max}=8.20 \pm 0.54$.

Keywords: Seismicity, Seismotectonic, Seismic Parameters, Completeness of Catalog, Rudbar

INTRODUCTION

In 20 of June 1990 a large magnitude ($M_s = 7.7$, $M_w = 7.3$, $M_b = 6.4$, focal depth of 19 km) earthquake with the peak ground acceleration greater than 0.6g was recorded, located about 10 km from the earthquake fault in north of Iran near Rudbar [1]. Rudbar is a city situated in Gilan Province and 268 kilometers from Tehran. This huge event was referred as the Manjil earthquake [2] and Rudbar – Tarom earthquake [3].

In the literature, the epicenter of the Rudbar earthquake (36.95°N–49.40°E) is determined by the USGS in 1990. It affected both urban and rural regions, where it completely destroyed 700 villages in the Sefidrud river valley and also the cities of Rudbar, Manjil and Loshan, killing more than 40,000 people, injuring 60,000 and making more than 500,000 homeless [3], so seismicity studies is essential in this area.

One of the power-law relations commonly employed in seismicity studies is the frequency-magnitude earthquake distribution .

$$\log N = a - bM \quad (1)$$

which predicts the distribution of earthquakes with respect to magnitude. In Eq. (1), M is magnitude, a and b are constants and N is number of earthquakes equal to or larger than M . The b-value is in most cases close to unity for long time periods and large areas [4].

The a-value is related to the seismic activity and so

for the time and the volume of the considered window. The b-value (size distribution) is a measure for the relative abundance of the strong to the weak earthquakes and is considered to be related to the tectonic regime of the area [5].

A variation of the b-value in region is commonly correlated with characteristics of regional seismic activities [6] .

Previous studies pointed out that the region with low b-value implies large stress.[7]

The objectives of this research are to carry out a preliminary analysis of seismicity studying in this hazardous area and assessment of seismic hazard parameters .

SEISMOTECTONIC AND SEISMICITY OF THE AREA

The study region is an area in the radius of 100 km from the center of the Rudbar city (36.80°N – 49.41°E). According to some geological, geophysical and seismological similarity with the assumption of uniform earthquake potential, Iran could be divided into seismotectonic provinces. The seismotectonic province of Iran is defined as an area bounded by geological features which make a difference in seismic characteristics of one province from its neighboring provinces. Each province has equal seismic potential and uniform geological structure and trends. This study area is situated in Azerbaijan-Alborz seismotectonic province as shown in Fig1 [8].

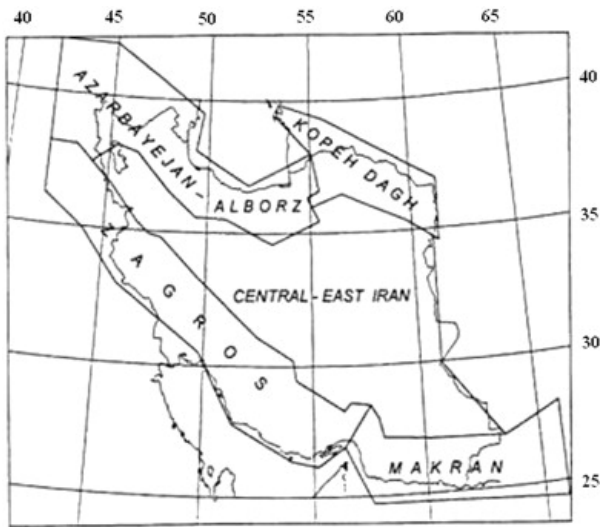


Fig .1 Sesimotectonic provinces in Iran [8]

Alborz mountains (north of Iran) are considered as mountains without root that its uplift is due to thrusting of allochthonous masses over each other in a compressional tectonic regime [9]. The depth of Moho in Alborz mountains is less than 35km [10]. Geological - tectonic investigations in the Alborz mountains obviously show that these mountains have been formed by thrusting of folded rocks over each other [11], [12]. The focal mechanism of Alborz's earthquake indicates the strike - slip mechanism with some reverse component [13]. The focal mechanism of the Rudbar- Tarom earthquake shows a left- lateral strike slip. Although reverse faults and folding contributed an important role in the formation of Alborz folded and thrust active mountains but the occurrence of the Rudbar- Tarom earthquake indicates that the Alborz belt in the Rudbar-Tarom area is affected by left- lateral shear. Main active faults of the study area can be seen in Fig2.

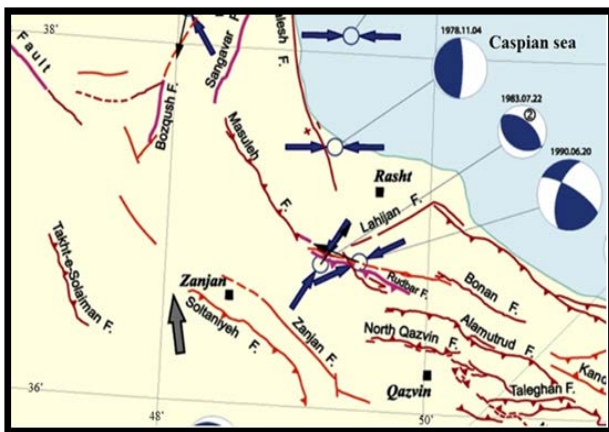


Fig .2 Major active faults of the study area with the focal mechanism solution for earthquakes

DATA

The first step in the seismic hazard study is preparation of complete data in the study area. The available earthquake catalogs usually contain two types of information: Macro seismic observations of major seismic events that occurred over a period of a few hundred years and complete instrumental data for relatively short periods of time (last 50 years the most).

Earthquake catalog of Iran includes two kinds of data.

- The historical or pre-instrumental earlier 1900
- The instrumental period . (1900-present)

The instrumental era includes early instrumental (1900-1963) and modern instrumental era post 1963 to present [14] .

For historical data in this area we used Ambraseys and Melville [15]. Six historical events were recorded which can be seen in table 1. (Quality in table 1 indicates the quality and quantity of Macro seismic information marked by A to F).

Instrumental data for this research provided by global and local databases as followed.

- USGS (U.S. Geological Survey)
- ISC (International Seismological Centre)
- BHRC (Building and Housing Research Center)

Table .1 historical events in study Area

Date	Latitude (°)	Longitude (°)	M_s	Quality
1052	36.60	50.30	6.8	B
1119	36.38	50.00	6.5	C
1367	37.30	49.90	5.5	D
1678	37.20	50.00	6.5	B
1803	36.33	48.95	5.3	C
1844	37.50	48.00	6.9	B

Relation between m_b and M_s

Normally earthquake catalog includes different magnitude scales , M_s is the surface wave magnitude, m_b is the body wave magnitude, M_w is the moment magnitude and M_l is the local magnitude .

The historical earthquake in Iran has been defined in M_s also M_s and m_b are the most reported magnitudes for instrumental events in this area.

The saturation level of m_b is around magnitude 6.2 whereas the saturation level of M_s is 8 so surface wave magnitude is the most appropriate magnitude scale for this region [16].

To evaluate seismic hazard parameters a homogenized catalog is needed .

To unify the scale of earthquake magnitude for each sesimotectonic province, we established empirical relations to convert m_b to M_s . Since

historical earthquake in Iran have been defined in M_s and lack of events with magnitudes above the saturation level of M_s in the interest region, surface wave magnitude is the most appropriate magnitude scale for the region,. There is a linear relation between M_s and m_b as in Eq. 2.

$$M_s = dm_b + c \quad (2)$$

d and c are constants. In order to establish empirical relations between m_b and M_s we applied the regression method as shown in Fig.3. This relation was used for converting all magnitudes to M_s .

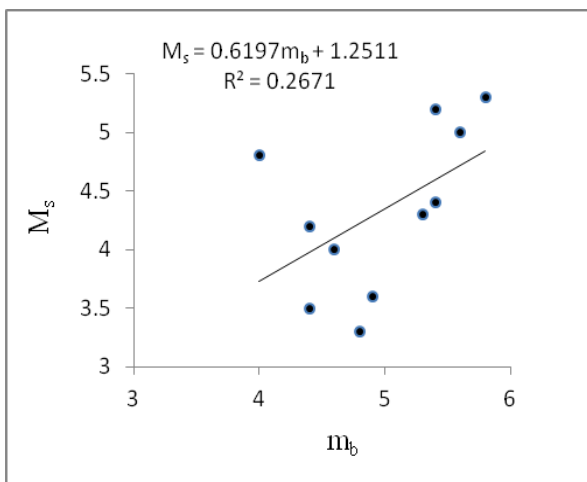


Fig.3 Regression between M_s and m_b

DATA ANALYSIS

The event list was homogenized and surface magnitude, M_s was applied in the analysis. When mapping b-value completeness of the employed earthquake catalogue is crucial.

Obviously, an incomplete catalogue can substantially modify the b-values. The fractions of missing (small) events will result in a reduction of b .

Magnitude of completeness (M_c) is the minimum magnitude which above it is thought that all earthquakes are reliably recorded, so assessing magnitude of completeness is prerequisite to seismicity analysis. M_c magnitude was estimated from the observed frequency magnitude distribution. As follows from the diagram in Fig. 3 M_c is magnitude of completeness where the frequency-magnitude curve starts to deviate from a linear trend [17]. $M_c = 4$, meaning that the event list, covering the catalogue period, is complete for magnitude 4 and bigger [18].

Based on the uniform catalog, seismicity of the region studied, seismicity parameters were calculated utilizing the method proposed by Kijko and Sellevoll [14]. In order to achieve more reliable results, the completeness of the catalog and uncertainty of magnitudes was estimated and considered in our calculations. In this method, dataset of the catalog was divided into extreme and complete part. Using a global and local database of earthquakes provided by USGS, BHRC and ISC for complete part, as well as catalog of historical (pre-1900) and early-instrumental (1900-1963) earthquakes provided by Ambraseys and Melville for extreme part, a uniform catalog of earthquakes for the interest region has been provided. To estimate the magnitude threshold (M_c) maximum curvature method was used. Fig. 4 shows the cumulative number of earthquakes with magnitude and calculation of M_c . Before and after the main shock, foreshocks and aftershocks happen and since the complete list of earthquake usually do not follow the Poisson distribution, all foreshocks and aftershocks must be excluded from the catalog by windowing method in time and space domains by Gardner and Knopoff [19]. According to this algorithm all events under the time-magnitude and distance-magnitude curve were considered as dependent events and should be eliminated from catalog for further analysis (Fig.5).

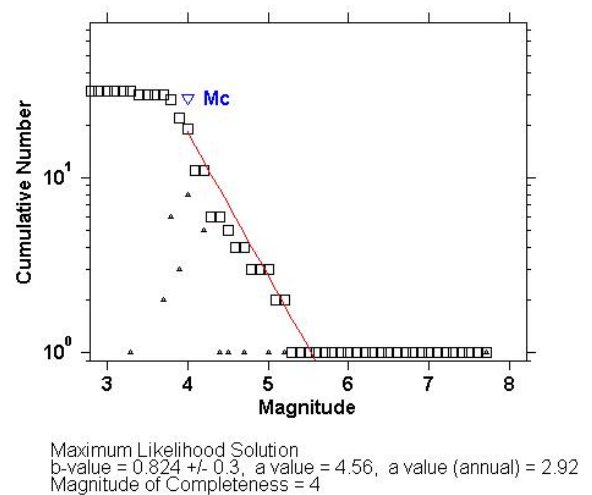


Fig. 4 Distributions of frequency Magnitude

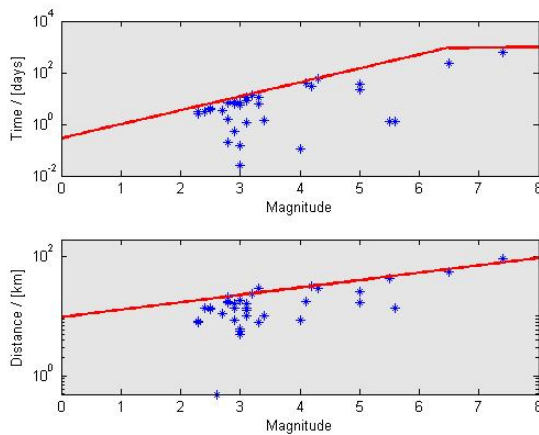


Fig.5 the time- magnitude and distance-magnitude curve

The maximum regional magnitude M_{\max} of an earthquake is the maximum limit of the magnitude of a seismic tectonic source [20]. By constraining the observed largest magnitude to be the expected value of the largest observed magnitude, Kijko has obtained an estimator for M_{\max} , which requires knowledge of the mean seismic activity rate λ ($\lambda=N/T$) and the parameter b [21].

The constant coefficients a -value and b -value of Gutenberg–Richter was obtained by the seismicity data for this area. The constant ‘ a ’ is defined as the number of seismic events with a magnitude greater than M in a definite time interval and dependent on the number of earthquakes, area of seismic zone and the length of the time interval. The b -value is the slope of the b line is the seismicity factor and shows the relation of number of weak and strong seismic [22].

CONCLUSION

The significant results of this research is the generation seismic parameters. In this study, the parameter of Magnitude completeness (M_c) plays an important role in determining the b -value and a -value, the M_c value in research location is around 4. The results show that b -value is equal to 0.82 ± 0.3 , the recurrence rate of the seismic events λ is equal to 0.40 ± 0.08 for $M_c=4$ and $M_{\max}=8.20 \pm 0.54$ (table 2). The seismicity analysis is just one part of an integrated research about the vulnerability characteristic of a region of the earthquake, therefore other studies related to geotectonic, geology, fault row, as well as earthquake history can help in supporting the calculation and analysis of seismic hazard in the region to mitigate earthquake disaster.

Table 2. Seismic parameters for study area

Seismic Parameters	M_c	M_{\max}	λ	a -value	b -value
Value	4.0	8.20 ± 0.54	0.40 ± 0.08	4.56	0.82 ± 0.3

ACKNOWLEDGEMENTS

The support for the research presented in this paper had been provided by the Universiti Sains Malaysia (USM) Short Term Grant No 304/PFIZIK/6312025. The support is gratefully acknowledged.

REFERENCES

- [1] Moinfar A A and Naderzadeh A .1990. "An immediate and preliminary report on the Manjil, Iran earthquake of 20 June 1990", Building and Housing Research Center, Ministry of Housing and Urban Development, pp. 68-119
- [2] Niazi M and Bozorgnia Y. 1992. "The 1990 Manjil, Iran, earthquake: Geology and seismology overview, PGA attenuation, and observed damage", Bulletin of the Seismological Society of America, Vol 82, pp. 774-799.
- [3] Berberian M, Qorashi M, Jackson J, Priestley K and Wallace T. 1992. "The Rudbar-Tarom earthquake of 20 June 1990 in NW Persia: preliminary field and seismological observations, and its tectonic significance", Bulletin of the Seismological Society of America, Vol. 82, pp. 1726-1755.
- [4] Gutenberg B and Richter CF. 1942. "Earthquake magnitude, intensity, energy, and acceleration " Bulletin of the Seismological Society of America ,Vol 32, no. 3 ,pp. 163-191.
- [5] Jafari MA. 2008. "The distribution of b-value in different seismic provinces of Iran". International Association for Earthquake Engineering.
- [6] Sanchez JJ, Nutt S R, Power J A, Wyss M.2004. "Spatial variations in the frequency– magnitude distribution of earthquakes at Mount Pinatubo volcano" Bulletin of the Seismological Society of America ,Vol 94,pp. 430 –438.
- [7] Schorlemmer D, Wiemer S and Wyss M. 2005. "Variations in earthquake-size distribution across different stress regimes" Nature 437 Vol 22,pp. 539– 542.
- [8] Mirzaei N. Mengtan G and Yuntai C. 1998. "Seismic source regionalization for seismic zoning of Iran: major seismotectonic provinces", Journal of Earthquake Prediction Research, Vol.7, pp. 465-495.
- [9] Abdi F, Mirzaei N and Shabani E. 2013 . "Ground-motion scenarios consistent with PSH deaggregation for Tehran, capital city of Iran", Nat. Hazards Earth Syst. Sci, Vol. 13, pp. 679-688.
- [10] Dehghani G A and Makris J. 1983. "The Gravity Field and Crustal Structure of Iran", Geol. Survey Iran, Rep, No. 51, pp. 51-68.
- [11] Stocklin J. 1968. "Structural History and Tectonics of Iran; A Review", Bull. Am. Assoc. Petrol. Geol,Vol. 52, pp. 1229-1258.
- [12] Berberian M. 1982. "Continental Deformation in the Iranian Plateau (Contribution to the Siesmotectonics of Iran (Part IV))", Geol. Surv. Iran, Rep. No. 52, 625p.
- [13] McKenzie D P. 1972. "Active Tectonics of the Mediterranean Region", Geophys. J. R. Astr. Soc, Vol.30, pp.109-185.
- [14] Kijko A and Sellevoll M. 1992. "Estimation of earthquake hazard parameters from incomplete data files. PartII. Incorporation of magnitude heterogeneity", Bulletin of the Seismological Society of America, Vol. 82 (1), pp 120-134.
- [15] Ambraseys N N and Melville CP. 2005. "A history of Persian earthquakes. ", Cambridge University Press.
- [16] Singh S K, Rodriguez M and Esteva L. 1983. "Statistics of small earthquake and frequency of occurrence of large earthquakes along the Mexican subduction zone", Bull. Seism. Soc. Am, Vol 73, pp. 1779-1796.
- [17] Nuannin P, Kulhánek O and Persson L.2012. "Spatial and temporal characteristics of aftershocks of the December 26, 2004 and March 28, 2005 earthquakes off NW Sumatra", Journal of Asian Earth Sciences, Vol 46, pp.150-160.
- [18] Nuannin P, Kulhanek O, Persson L. 2012. "Variations of b-values preceding large earthquakes in the Andaman-Sumatra subduction zone".Journal of Asian Earth Sciences, Vol 61,pp.237-242
- [19] Knopoff L. and Gardner J. 1969. "Homogeneous catalogs of earthquakes", Proceedings of the National Academy of Sciences,Vol. 63, pp.1051-1054.
- [20] Reiter L. 1990. "Earthquake hazard analysis", Columbia University Press, New York, pp. 245.
- [21] Kijko A and Sellevoll M A. 1989. "Estimation of earthquake hazard parameters from incomplete data files. Part I. Utilization of extreme and complete catalogs with different threshold magnitudes ",Bulletin of the Seismological Society of America Vol 79, no. 3, pp. 645-654.
- [22] Amiri GG, Motamed R, Hashemi R and Nouri H. 2006. "Evaluating the seismicity parameters of Tehran, Iran", Proceedings of the Institution of Civil Engineers-Geotechnical engineering, Vol. 159, pp.275-283.

UNDERSTANDING TO PREDICT SOIL BEHAVIOR

J. Rajaraman¹ K.Thiruvengatasamy² and S. Narasimha Rao³

ABSTRACT

Geotechnics is a branch of civil engineering which is firmly founded on experience. Theoretical concepts are developed and continuously improved through a continuous analysis and interpretation of experimental data; in turn, experiments are used to validate the new theoretical concepts. A clear example is the development of the Critical State Theory which is based on evidence coming from laboratory testing on reconstituted saturated clay. Its extension to unsaturated soils, has been developed based on laboratory experiments on unsaturated soil samples. The important Geotechnical property shear strength links of coastal soils, stability of slopes, landslides and turbidity currents. Sometimes inter and multi-disciplinary approach is needed to analyze and predict soil behavior. It is surprising to note that when additional, new environmental information, or parameters are included, the present estimated shear strengths take paradigm shift. Thus the modified approach becomes more reliable. In other words the new environmental information increases Reliability. Based on the analysis and interpretation of documented cases as stated above, this paper makes a new conceptual model in interpretation of the influence of Carbonate Compensation depth on turbidity currents in Abyssal plain and the geotechnical behavior of the sediments in Abyssal plains. Documented Cases are: 1) Liquid Limit of a soil calculated by using distilled water is not representative sample in marine condition. The distilled water overestimates Geotechnical property. 2) The failure envelope of reconstituted clay mixed with distilled water is different from the one mixed with NaCl solution. 3) The Oedometer test on undisturbed specimens exposed to distilled water display higher strains than tested in solution. Turbidity current consists of hydraulic loading (Saline water) inorganic /organic loading (includes mineral skeletons /organic remains) and velocity. When the turbidity current approaches Lysocline layer. It begins to lose calcium carbonate particles. The velocity of the turbidity current slows down and on the way sheds inorganic load and further slows down. At this point the concept of Soil is Rock on its way to Ocean stops. The abyssal plain maintains moderate Shear strength. The abyssal plain is a controlled environment which controls any events of the restless earth around it. Thus the Carbonate Compensation Depth influences both Turbidity Currents and Abyssal plain.

Keywords: Abyssal plains Carbonate Compensation depth Lysocline layer Reliability Shear Strength.

1.0 INTRODUCTION

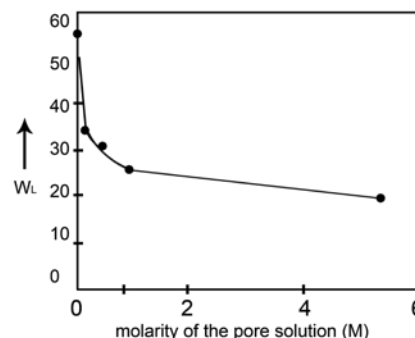
Turbidity currents are a subclass of the broader category of density currents. Density Currents also are termed gravity currents. A density Current “is the flow of one fluid within another caused by the density difference between the fluids. Turbidity currents exist when the density difference is due to suspended sediment and of course the fluids involved are both water. Soil is Rock on its way to Ocean (Abyssal Plain). Through Subduction Zone soil is returned to continental crust as Rock. The next cycle begins.

The weathering and stress history of the continental Rock transported as sediment as varying stages to abyssal plain meets varying or different environmental conditions on the way. Any Experimental data collected on Continental areas should be viewed with environmental information as an additional parameter to interpret Marine conditions. A few documented cases are discussed below.

2.0 DOCUMENTED CASES

2.1 Case (i):

The liquidity limit obtained with distilled water is about two times the one obtained with NaCl solution, regardless its molarity.



Take y axis twice the given scale. (wl in %) [1]

A soil with a higher liquid limit will settle more. Distilled water is not a suitable pore liquid because it helps to obtain more settlement. In this context saline water is a better pore fluid compared to

distilled water. The salinity of fresh water is in between distilled and Saline Sea water.

2.2 Case (ii):

An example of possible effects of infiltration of fresh water in a natural deposit subjected to swelling is shown in fig (2). The results of a Oedometer tests carried out on two couples of undisturbed specimens of a type of clay shale taken respectively at a depth of 2.5 and 21m. A specimen of each couple was tested in a 1 m NaCl solution. The influence of the nature of the bath does not appear significant in the stage of compression, when the pore water is expelled from the specimen, but becomes prominent in the following stages of swelling, when some liquid is absorbed from the bath. The specimens tested in the distilled water (and specially the one taken at the greatest depth) display higher strains than those tested in the solution.

At the end of the tests performed in the NaCl solutions, when the axial stress was 10 kPa, the solution was substituted with distilled water giving immediately rise to further strong soil deformation.

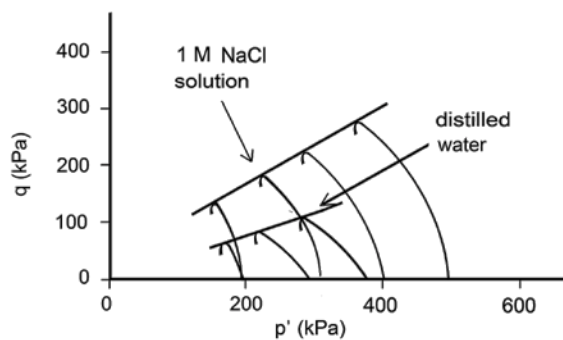
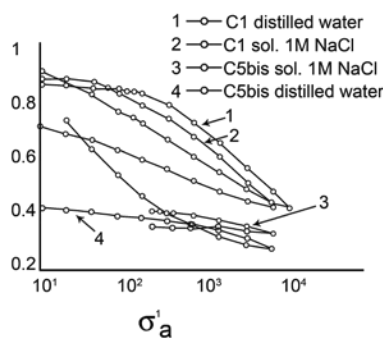


Fig.2

[1] [2]

2.3 Case (iii):

Fig (3) shows the results if a triaxial tests on reconstructed normally consolidated specimen obtained by mixing powdered clay with distilled water and a 1M NaCl solutions. It suggests that that a friction angle at constant volume (i.e. the critical friction angle) can strongly depend on the nature of the liquid. Similar data feature the residual friction angle.



[1] [2]
ratio

X axis MPa Fig. 3a

Y axis Void

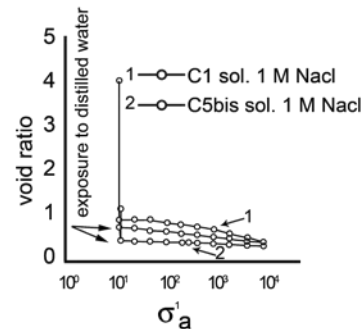


Fig.3b

[1] [2]

2.4 Case (iv):

Figure 4 shows the results of conventional tests conducted under a normal stress lower than swelling pressure (around 0.6 MPa) while part of specimens were allowed to swell, as usual, for 48h, others were sheared only after 10-100 days during which they experienced a high volumetric strain. The difference in shear strength is very clear.

All data show that swelling in distilled water as usual in laboratory, is responsible for a radical change in soil behavior. In addition fig 4 shows that the effect of swelling is higher if secondary swelling is allowed.

The conceptual qualitative model of Turbidity currents: Repeated short term environmental changes influence in the long run the initiation of Turbidity currents.

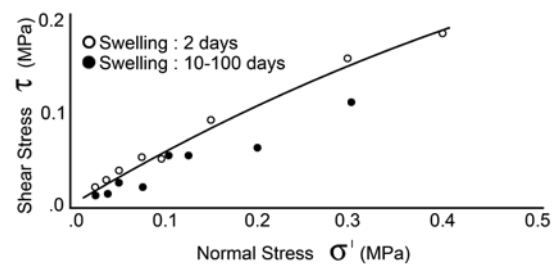


Fig. 4 .

[1] [2]

3.0. RELIABILITY AND SOIL BEHAVIOR

3.1. Understanding To Predict Land Fill (Soil) Shear Strength to Increase Reliability [4] [5] Decrease In Shear Strength Due To Man Induced Reasons In A Bioreactor Land Fill.

Injection of Liquids in a Bio-Reactor Land Fill endangers the stability of waste mass slopes, for the following reasons.

1) Increased driving force due to the increase in unit weight of the waste mass due to liquid injection.

2) Decrease in strength due to decrease in the effective (inter-granular) stress corresponding to the increase in pore pressure that result from liquid injection(leach-ate head build-up).

3) Decrease in strength due to transformation of

Waste mass by the biological and chemical processes that enhance degradation, turning the waste into an inherently weaker material.

Lack of reliable data on shear strength of degraded waste is the main reason for all the problems/.

Isenberg et al (2001) conducted sensitivity modeling using a typical land fill.

Configuration to better understand how potential reduction in shear strength coupled with increases in unit weight will influence waste mass (soil) slope stability.

3.2 Understanding to Predict Shear Strength of Coastal and Shallow Water Marine Sediment with Increase in Reliability.

Hyperpycnal flow: At a river mouth, a flow of river water that is denser than the water in the basin receiving it. This occurs during floods. The dense water flows beneath the basin water, as a density current, carrying sediment beyond the shore and inhibiting the pro-gradation of a delta

When Hyperpycnal flow erodes a shallow bed changes the soil behavior. Shallow layers of highly plastic marine OC clay subjected to swelling Udepending shear strength decrease due to infiltration of fresh rain water which presents a very different composition than the natural pore liquid. The accumulated influence of the above changes in the environment will induce long term slope failure even in a gentle slope

3.3 Understanding to Predict Shear Strength of Marine Slope Sediments of Intermediate Water Depth with Increase in Reliability.

Like Mineral Particles (Solids of the Soil Predominant) CaCO_3 Skeleton (particles) could be classified as Angular, Sub-angular, Sub-rounded, Rounded and well rounded. The angle of the internal resistance (ϕ) decreases due to weathering of particles from angular to well rounded stages. In the down slope depths the shear strength is less because angle of friction is less.

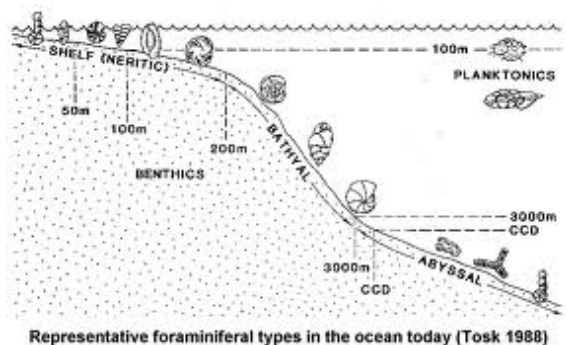


Fig.5.a

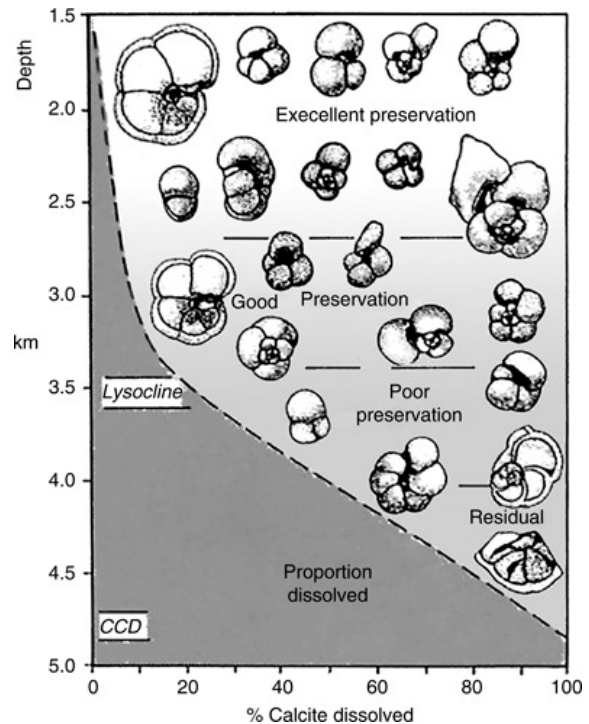


Fig. 5 b.

3.4 Understanding to Predict Shear Strength of Marine Turbidity Sediments of Deep Water before Passing through CCD, with Increase in Reliability.

Carbonate Compensation Depth (CCD). CaCO_3 shells (tests) sink from surface water Tests may reach a depth where water is significantly under-saturated with respect to CaCO_3 . At this depth, called Lysocline, shells begin to dissolve. In the modern Oceans, there is also a depth at which there is no longer any free CaCO_3 . This depth, called the Carbonate Compensation depth $\text{CCD} = - 4 \text{ Km}$. CaCO_3 tests accumulate only if they settle on Sea Floor above the CCD.

3.5 Understanding to Predict Shear Strength of Marine Turbidity Sediments of Deep Water after passing through CCD with Increase in Reliability.

The final stage of Turbidity Current consists of hydraulic loading (saline water) Inorganic/Organic loading (includes mineral skeletons/Organic remains) and Velocity. The turbidity Current Passing through CCD it begins to lose all the Calcium Carbonate particles. The Velocity of Turbidity Current slows down and the Shear Resistance decreases and spreads as Submarine fans. At this point the concept of Soil is Rock on its way to Ocean stops.

Turbidity deposits on a horizontal slope with contours. Before passing ccd.

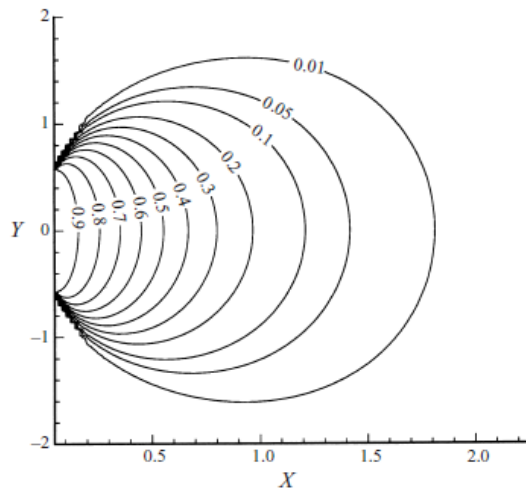


Fig. 6a

x- position of down slope y-position of cross slope. After passing ccd.

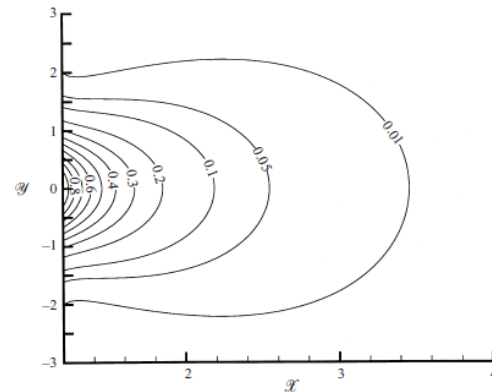


Fig.6b.

3.5.1 A Conceptual hypo- Cycloidal Model and Explanation for the Behavior of Turbidity Current.

In Fig (7) the pore with Saline Water as Pore Fluid is shown as a circle with radius 'a' and the Solid Calcium Carbonate representing angle of internal friction, is shown as solid circle with radius 'b'. In other words a solid circle with radius 'b' is rotating inside a fluid circle of radius 'a'. At selected points on the circumference of this fluid circle the particle (CaCO_3) makes contact to mobilize shear resistance. Taking $a = R$ and $b = r$. The Selected number of contacts depends upon R/r ratio. The figure (7) is a self explanatory for the particle behavior. Here the mathematics part is omitted.

Before reaching lysocline or CCD layer, the pore fluid and solid CaCO_3 fertile balance each other in strength to maintain dynamic equilibrium. The friction resistance is due to solid particle resistance balance each other the pattern of the fan is more or less circular in nature. When these solid particles are dissolved, the pore fluid circle alone exists with radius R . The small 'r' is already dissolved. The disappearance of solid particles and filling by fluid can be imagined, as a reverse consolidations the fluid is expelled and solid particles come closer to each other. Where as in the marine environment (CCD) the solids is expelled and fluid is closer the space occupied by solid (CaCO_3). Under these conditions the fluid dominates and the pattern of the fans are elongated elliptical one because the fluid after the collapse of the Turbidity Current will run further distance creating elliptical fans.

Figure 8 is an illustration of the position of the ccd and lysocline and their relationship to ocean bathymetry, carbonate accumulation rate and CaCO_3 content.

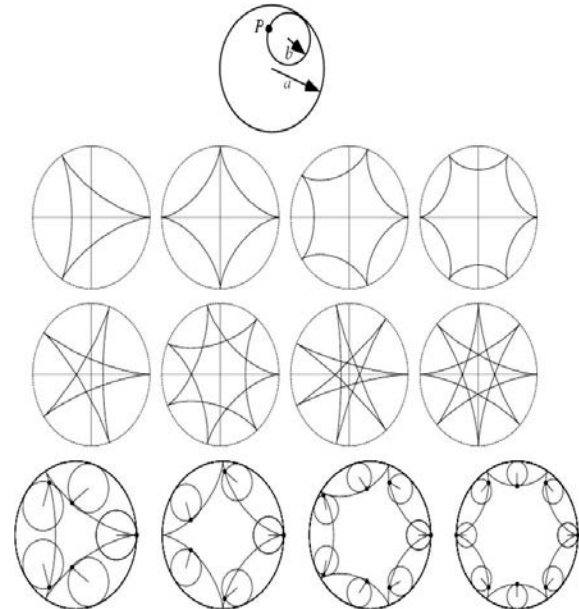


Fig.7 Hypo –cycloidal model with different b.

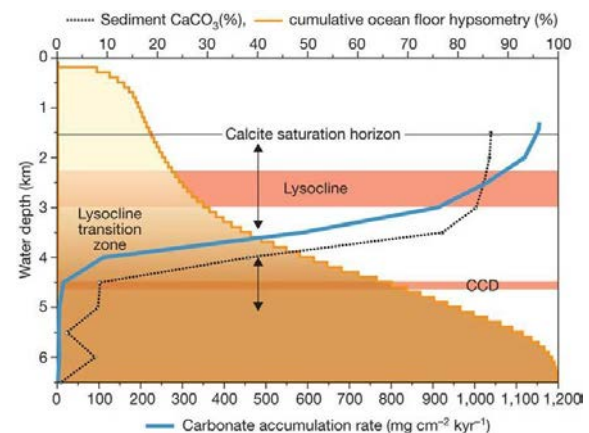


Fig.8.

3.6 Understanding to Predict Shear Strength of Abyssal Sediments in Abyssal Depths with increase in Reliability.

The abyssal plain is a naturally Controlled environment which controls any event of the restless earth around it. In abyssal plain carbonates can not impart shear strength as particles but in dissolved state Calcium Carbonate with saline water can influence shear strength. In abyssal plain sediments derive shear strength from two sources (1) Cohesion of abyssal clay (pure shear or Coaxial component of shear strength). (2) Angle of internal friction (phi) from sand (Simple shear or Non-Coaxial component of the shear strength) along with mud and oozes. The third factor is saline water which modifies shear strength according to the environmental needs since CCD is not a fixed depth. It changes with environment and sensitive to Carbon stress from Continental areas.

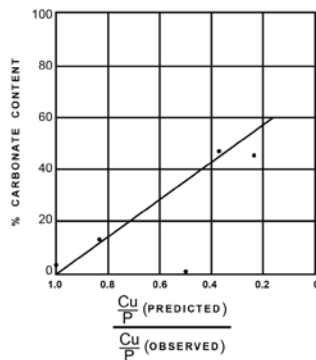


Fig. 9. Influence of carbonate content on undrained strength of sediments from experimental Mohole.

In Fig. 9 . When the Carbonate percentage is very low the C_u/p predicted is equal to C_u/p observed, where C_u = un-drained shear strength and P = Vertical effective stress. This information increases the reliability and prediction becomes meaningful. Any additional information will always help in propagation of the predicted value of shear strength to the true value of shear strength of sediments.

4.0 CONCLUSIONS

1. Soils/ Sediments are Rocks on its way to Ocean.
2. The Moving Sediment is subjected to changing, environmental factors. The Shear Strength changes according to the existing conditions.
3. Starting from (urban) continental areas to deep ocean floor the reduced shear strength is a function of different environmental parameters.
4. The important environmental factors are:
 - i) Saline Water
 - ii) Hyperpycnal flow
 - iii) Oversteepening of slope.
 - iv) Calcium Carbonate shells.
 - v) Lysocline layer.
 - vi) Carbonate Compensation depth .
 - vii) Flat or very slight slope of Abyssal plain.
 - viii) Turbidity Currents.
 - ix) Shape and size of Soil Particles.
 - x) The resistance of sand

and silt even in abyssal depth. Any combination of the environmental factors which will change the Shear strength of sediments will become the additional information and the reliability will increase the correct prediction of shear strength within that particular environment.

5.0 REFERENCES

- [1] Di Maio C, Onorati R (2000) . Influence of pore liquid composition on the shear strength of an active clay In: Bromhead E. N Dixon and M.L Ibsen (eds) , Proceedings. 8th International .Symposium on Landslides, Cardiff 1: 463-468.
- [2] Picarelli L Di Maio C.Olivares L . Urciuoli G (1998). Properties and behavior of tectonised Clay Shades in Italy In:Evangelista A and L Picarelli (eds). Balkema Proceedings Second International Symposium on The Geotechnics of Hard Soils, Soil Rocks, Napoli 3,pp. 1211-1241.
- [3] (1964) . Shear Strength and related properties of sediments from experimental Mohole (Guadalupesite) Journal of Geophysical Research Volume 69. Pp 4271-4291
- [4] Kavazanjian.E ., Hendren D., and Corcoran, G.T ., strength and stability of bio-reactor landfills., PP 63-70 in proceedings of the SWANA land fill symposium, 2001.
- [5] Isenberg, R.H.,Law, J.H. Neill., and Denver, R. J., Geotechnical aspects of land fill bioreactor design is stability a fatal blow? Pp, 51-62 in proceedings of the SWANA land fill symposium, 2001.

CASE STUDY ON SHALLOW FAILURE OF CONGLOMERATE AND SILTSTONE SLOPES DUE TO A HEAVY RAINFALL

Satoshi Kagamiahra¹, Satoru Shibuya¹, Byeong - su Kim², Shunzo Kawajiri³, Tara Nidhi Lohani¹ and Takashi Okimura⁴

¹Kobe University, ²Okayama University, ³Railway Technical Research Institute, Construction Engineering Research Institute

ABSTRACT

This paper describes a case study in which the mechanism of shallow slope failure occurred in Aichi Prefecture on October 8, 2009 has been addressed. The slope that collapsed due to a heavy rainfall of Typhoon No. 18 was comprised of a sedimentary soft rock. The total rainfall by this typhoon accounted as much as 250mm/day, and the rainfall at the instant when the slope failed was 75mm per hour. A field test of the slope section adjacent to the failed site was carried out. The undisturbed soil samples were also collected from the collapsed slope plane so as to determine the strength and saturation characteristics of the soil layer where the failure took place. A series of direct box-shear test (DST) on the undisturbed specimens under low confining pressures were then performed. In addition, a simulation of the rainfall infiltration for Typhoon No. 18 was carried out by using a saturated/unsaturated ground seepage program. A slope stability analysis was also performed based on the results of DST. By comparing the result, it is found that the slope was saturated due to the rainfall infiltration, and the shallow slope failure occurred because of a decrease in the shear strength of the slope.

Keywords: shallow failure, Conglomerate and Siltstone Slopes, direct shear test, the saturated-unsaturated seepage program

INTRODUCTION

The Typhoon No. 18 had knocked the Chita Peninsula of Aichi Prefecture on October 18, 2009 and caused a heavy damage of building structures and flooding. A hill slope facing towards the Nagoya Railway, Tokoname Line, was collapsed and the large amount of accumulated debris has stopped the train operation for quite a long period. The total rainfall by this typhoon accounted for 250mm/day and the rainfall at an instant when the slope actually failed was 75mm per hour.

In this post-failure study, the mechanism behind the slope failure mentioned above was investigated by performing a series field tests, laboratory tests and FEM simulation. The field tests were carried out at a slope section adjacent to the failed portion. The

the collapsed slope surface to determine the strength properties of the soil layer involved. In the laboratory, series of direct shear tests were

considerably low confining pressures, so as to simulate the shallow in-situ condition. The simulation of the rainfall infiltration was done by using a saturated/unsaturated ground seepage Program. A slope stability analysis was then performed based on the results of direct shear test and saturated-unsaturated seepage analysis.

SUMMARY OF SLOPE FAILURE SITE AND THE WEATHER

Figure 1 shows a rainfall observation data of the typhoon No. 18 prepared by the Chita City Fire department at the failure site. As can be observed from this figure, the precipitation, until 5:00 a.m. on October 8 from 0:00 a.m. on October 7, was about 93mm. The record high rainfall for an hour thereafter, reached as high as 75mm per hour and had initiated a shallow slope failure of approximate dimension, 20m wide, 20m high and 1.5m thickness (Photo 1).

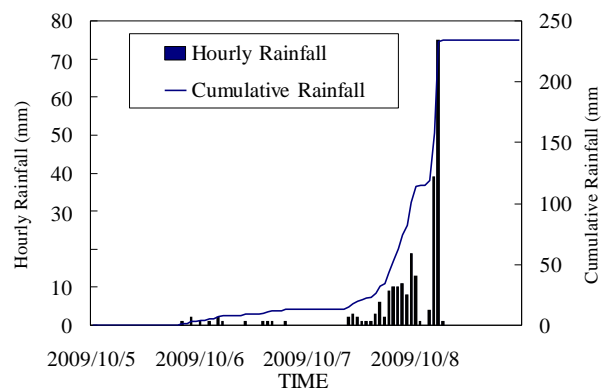


Figure 1 Rainfall observation data at the slope failure site

The Typhoon was also accompanied by strong wind (7~30m/sec) in north-northwest and northwest direction [1]. As the slope failure under investigation was also facing north-west, it is believed that the strong wind blow has also played a partial role in the failure.

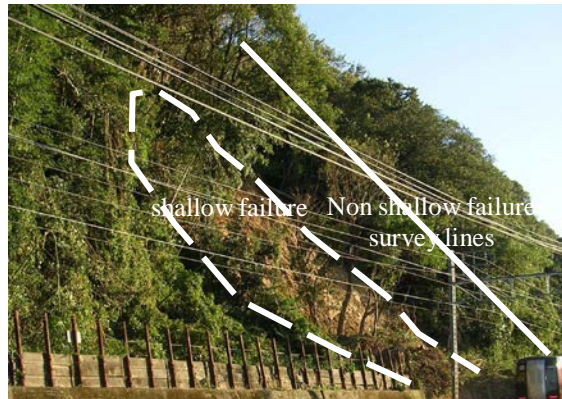


Photo 1 Shallow landslide site at Aichi Prefecture, Japan

The convex type hill slope, where the failure occurred, had relative height of 30m, NW orientation, and the slope gradient of 40-45 degrees. The geology is understandable by the presence of a Tertiary (Tokoname formation) conglomerate and siltstone layers. The dip slope is about 5-15 degrees as compared to the slope inclination. Although most part of slope collapse involves the heavily weathered siltstone rock, some part of heavily weathered conglomerate layer has also slipped together.

FIELD SURVEYS AND LABORATORY TESTS

In-situ investigation

In order to identify the collapsed mechanism, a simple dynamic cone penetration test was performed at the adjacent undisturbed slope section of the failed site, shown by a straight line in Photo 1, by assuming similar topography and cross-section to that of the failed mass. Figure 2 shows the result which indicates that the rate of increase in N_d values with depth is different at around $N_d = 5$. Including the landslide depth from site observation, it can be estimated that failure took place across the section where $N_d < 5$. The information on sectional soil profile was further added by undertaking a PS logging test, a surface wave exploration and by drilling boreholes.

Figure 3 is a two-dimensional shear wave velocity (V_s) sectional profile obtained from this study. The PS logging result was applied in drawing the profile by surface wave exploration analysis in order to increase the accuracy. Besides, the layer boundary identification was done by observing the

borehole data. The red dots in the figure show the section with $N_d = 5$. For the region having $N_d < 5$, V_s of siltstone layer is ≤ 120 m/s and that of conglomerate is ≤ 160 m/s. Therefore, not only N_d values but also the type of geological formation has affected the V_s magnitude. The figure also points that there is strong weathering at shallow depths and the velocity is quite low as compared to the base rock mass.

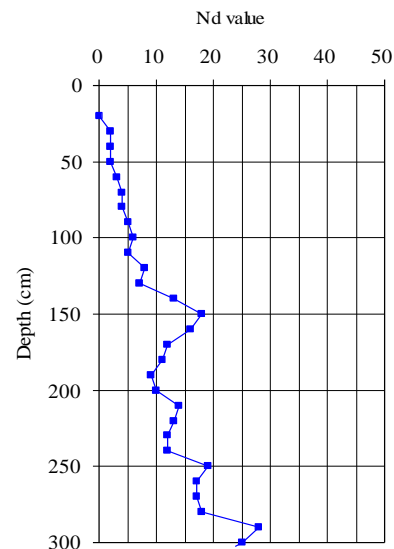


Figure 2 N_d -value against the penetration depth from dynamic cone penetration test

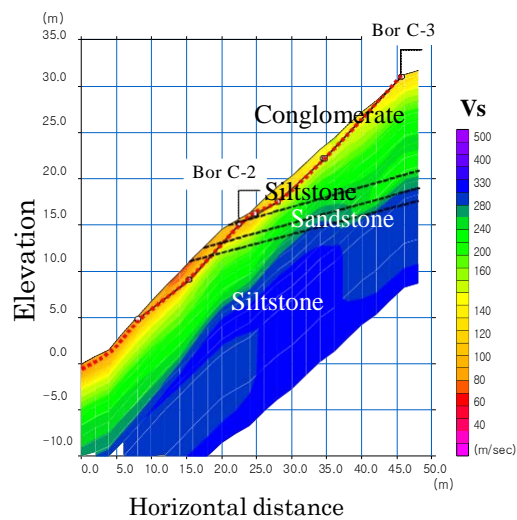


Figure 3 A two-dimensional sectional profile of shear wave velocity (V_s)

Laboratory test

In order to understand physical and mechanical properties of the collapsed soil, undisturbed samples were collected from the strongly weathered siltstone and conglomerate layers by a nail sampling technique [2].

Shear wave velocity of the collected undisturbed samples was evaluated in the laboratory by using a consolidation apparatus fitted with bender elements (hereinafter referred to as BE) [3]. The undisturbed samples were also tested in a direct shear apparatus to determine the shear strength parameters (cohesion, c and friction angle, ϕ). Table 1 shows the physical properties of the undisturbed samples. The physical property tests show that the strongly weathered conglomerate can be classified into a clayey-sandy-gravel, whereas, the strongly weathered siltstone is classified as a sandy clay.

Table 1 Physical properties of soil

	DLc:strongly weathered	DLs:strongly weathered siltstone
Soil classification	clayey-sandy-gravel	sandy clay
Soil particle density ρ (g/cm ³)	2.647	2.602
Natural water content w_n (%)	13.7	18.3
Wet density ρ (g/cm ³)	1.527	1.391
Dry density ρ (g/cm ³)	1.346	1.176

BE tests were performed by using undisturbed samples and those prepared by molding the sampled soil from the site, for which, in-situ moisture content overburden stress and wet density states were reproduced. The consolidation pressures applied to the specimens were relatively low by considering the in-situ stress levels involved in the shallow failure.

Figure 4 shows a shear wave velocity profile for two different types of geologic layers, siltstone and conglomerate. In the plot, shear wave data obtained from the laboratory BE tests for undisturbed, $(V_s)_{lab,u}$, and disturbed siltstone samples, $(V_s)_{lab,d}$, and those evaluated by field PS-logging, $(V_s)_f$ are compared. The following points for siltstone stratum are understandable. Firstly, the $(V_s)_f$ and $(V_s)_{lab,u}$ at about 1m depth, the depth where sampling was done, substantially match each other by confirming the fact that the effect of sample disturbance incorporated during sampling, while transporting to the laboratory and specimen preparation process is quite insignificant. Secondly, at deeper depths below 1.8m, $(V_s)_f$ is larger than $(V_s)_{lab,u}$, suggesting that the in-situ soil is significantly aged and structured at increasing depths, which is absent in the sample that was stressed beyond the in-situ overburden stress. The shear wave velocity for remolded (disturbed) samples, $(V_s)_{lab,d}$, remain slightly on the lower side of $(V_s)_{lab,u}$, inferring a partial deconstruction of undisturbed samples [4]. On the other hand, in case

of conglomerate stratum, $(V_s)_{lab,u}$ is far above the $(V_s)_f$. It is likely that the result was affected because of the presence of large-sized gravel particles in the sample as compared to the propagated shear wave wavelength [3]. The $(V_s)_f$ for disturbed specimen is indeed similar to that shown by field test $(V_s)_f$.

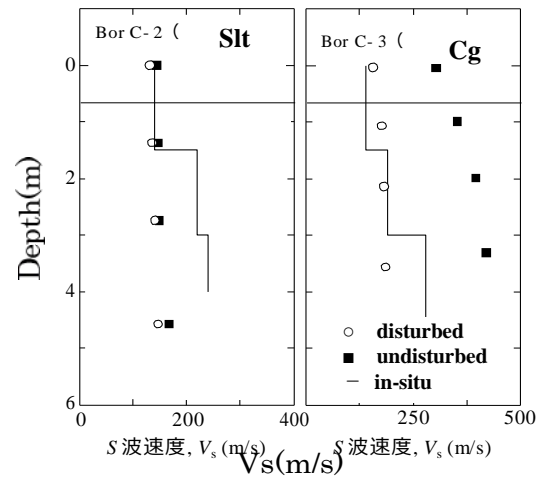


Figure 4 Shear wave velocity profile from in-situ and laboratory tests

In order to determine the shear strength parameters, drained constant pressure direct shear test were performed on undisturbed samples, both at unsaturated (natural water content) and saturated conditions [5]. The test was conducted with cylindrical specimens of 6cm diameter and 2cm height. Shearing was conducted at the speed of 0.1mm/min after consolidating at three different vertical stresses, 15kPa, 30kPa, 50kPa respectively, for each series.

Figure 5 is a graph showing a relationship between the applied vertical stress, σ_v , for consolidation and shear stress, τ , for both formations. It clearly confirms a comparatively higher strength of specimens at unsaturated condition than that when they are saturated. On the other hand, on comparing the slope of failure lines, angle of internal friction can be said to be roughly equivalent for both saturated and unsaturated states. Furthermore, cohesion intercept interestingly vanishes on saturation by inferring a non-cohesive nature of soil and also a complete loss of suction during saturation. The above trend is valid for both siltstone and conglomerate formations.

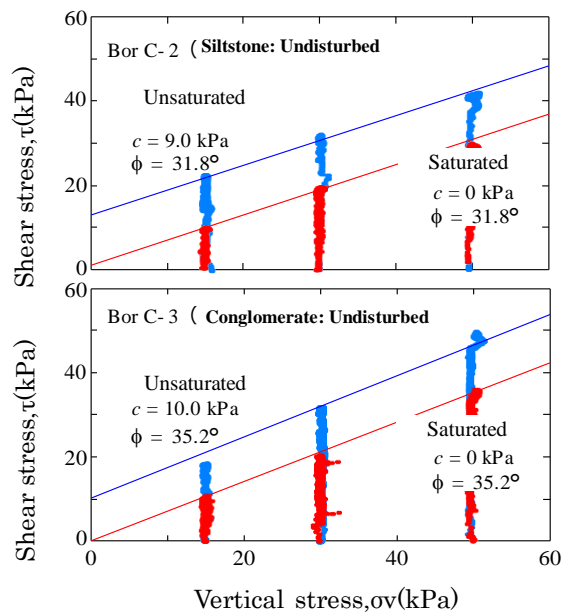


Figure 5 Mohr-coulomb failure line

ESTIMATION OF THE COLLAPSE MECHANISM BY STABILITY ANALYSIS AND SATURATED-UNSATURATED SEEPAGE FLOW ANALYSIS

Saturated-unsaturated seepage flow analysis model

A saturated-unsaturated seepage flow analysis with a two-dimensional cross-section was conducted in order to simulate the rainfall infiltration condition of the landslide area. The model uses a seepage flow advection-dispersion code, "Dtransu-2D". The model X-section before failure was taken as that of the survey line adjacent to the failed slope by Typhoon 18. Boundary conditions were set in the following way. The sloping surface is taken as a permeable boundary for rainfall infiltration, the water level on sideways is kept at a constant level and decided as per the well and river water levels in the close proximity. Figure 6 shows the set boundary conditions and Figure 7, the analysis model.

The permeability parameters used in the analysis, which were obtained from laboratory tests as well as literatures, were as shown in Table 2 [6]. About the unsaturated characteristics of strongly weathered layer, water-retention curve was obtained by laboratory tests. The hydraulic conductivity ratio curve was estimated by Van Genuchten formula [7]. For steady state analysis, a mean annual rainfall of the site from the nearby weather stations, 1340 mm, was used. On the other hand, for non-steady-

state analysis, the rainfall by typhoon No. 18 for two weeks period before the actual slope failure was considered.

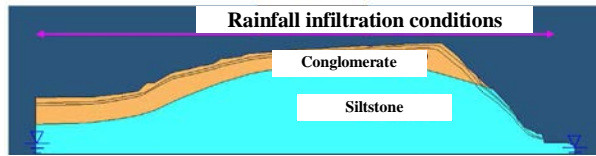


Figure 6 A 2D model section used for seepage analysis

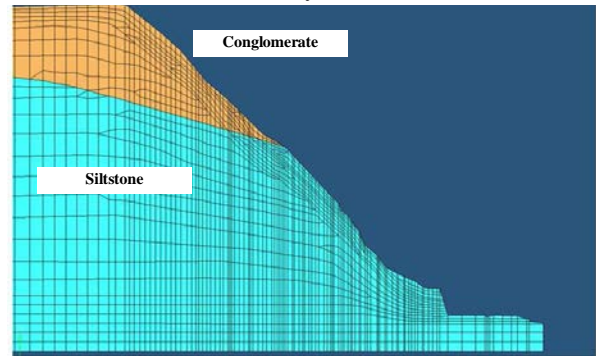


Figure 7 A 2D mesh model used for seepage analysis

Table 2 Seepage flow analysis parameters

	hydraulic conductivity	effective Porosity	specific storage
DLc:strongly weathered conglomerate	2.62×10^{-2}	0.51	2.0×10^{-4}
DHc:weathered conglomerate	1.30×10^{-3}	0.51	1.0×10^{-4}
CLc:gconglomerate	2.76×10^{-6}	0.51	3.3×10^{-6}
DLs:strongly weathered siltstone	2.62×10^{-4}	0.56	2.6×10^{-3}
DHs:weathered siltstone	2.76×10^{-9}	0.56	1.3×10^{-3}
CLs:siltstone	2.76×10^{-9}	0.56	3.3×10^{-6}

Results of saturated-unsaturated seepage flow analysis

The temporal change of degree of saturation is shown in Figure 8. It can be seen that degree of saturation of the strongly weathered rock increases with time. Particularly, a higher degree of saturation due to the pooled water at the boundary of highly permeable weathered conglomerate and less permeable weathered siltstone layer is clearly noted.

Stability analysis model

Stability analysis was performed on the model shown in Figure 9 based on the result of saturated-unsaturated seepage flow analysis. The topography

after the failure has been taken as the shape of slip surface. Table 3 shows the soil parameters used in the analysis. Unit weight of strongly weathered rock was altered depending on the degree of saturation [8]. Shear strength parameters were adopted from the laboratory shear tests conducted at low confining pressure. Suction pressure was estimated by using Van Gennuchten model [9], [10]. Figure 10 shows the relationship for unit weight and the suction stress.

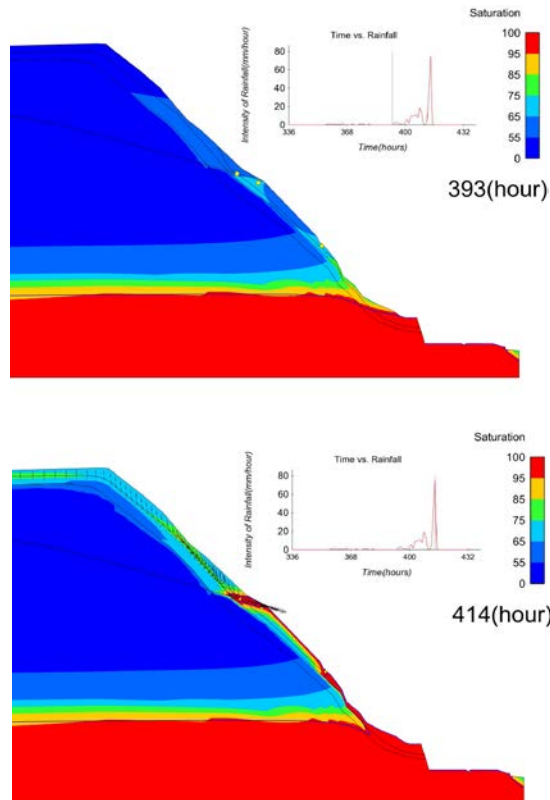


Figure 8 Analysis results (saturation distribution)

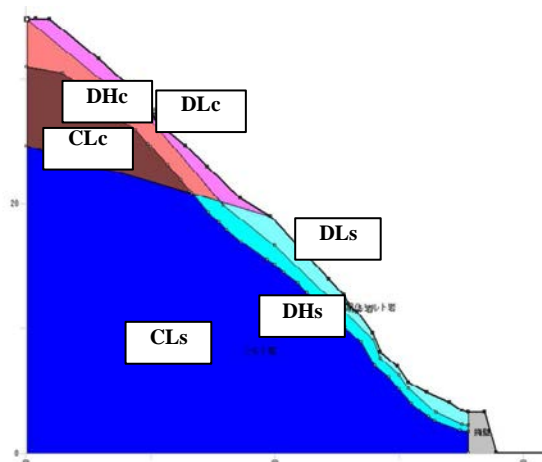


Figure 9 A sectional model used for stability analysis

Table 3 Slope stability analysis parameters

	wet unit weight $\gamma_t(\text{kN/m}^3)$	cohesion $c(\text{kN/m}^2)$	friction angle $\phi(\text{degrees})$
DLc:strongly weathered conglomerate	15.2	10.0	35
DHc:weathered conglomerate	15.2	15.2	35
CLc:conglomerate	17.1	44.3	37
DLs:strongly weathered siltstone	13.9	9.0	31
DHs:weathered siltstone	15.4	19.6	31
CLs:siltstone	16.4	23.5	32

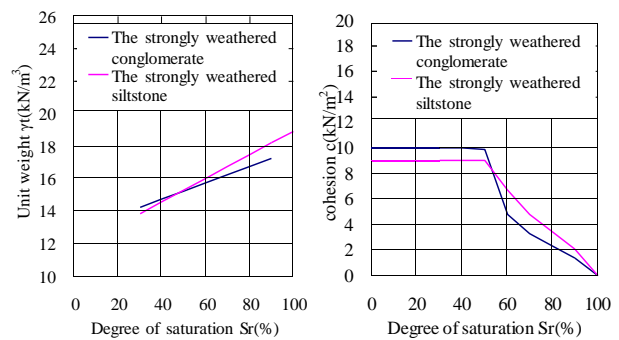


Figure 10 Variation of unit weight and cohesion values against the degree of saturation used in the model

Results of stability analysis

Figure 11 shows a time-wise variation in the factor of safety from the stability analysis. The continuous rainfall infiltration has lowered the safety factor from 1.0, thereby losing the mechanical balance of the sloping mass. The instant is consistent with the time of the largest amount of rainfall per hour that initiated the landslide.

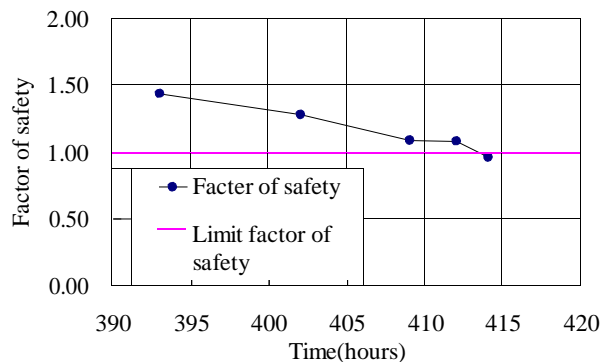


Figure 11 Variation in the factor of safety against the time from stability analysis

CONCLUSION

The findings of this study are summarized below.

- ☒ In this post-failures study of slope failure, a surface wave exploration technique was applied for in-situ testing and the sampled soil was further tested in the laboratory to evaluate strength parameters. When applied at the steep failure site, it was found that shear wave velocity difference observed for various soil strata from surface wave exploration method appeared accordingly in the shear strength parameters in laboratory tests. Therefore, surface wave exploration is quite useful and quick method in order to obtain two-dimensional sectional information of mechanical properties of soil layers.
- ☒ Internal friction angle, ϕ_d , shown by the slope of failure line, is roughly equivalent for both saturated and unsaturated conditions. However, cohesion intercept, c_d , disappears completely confirming a complete loss of suction on saturation. Although conglomerate stratum show slightly higher strength, siltstone formation also has similar trend.
- ☒ Result of the unsaturated-saturated seepage flow analysis shows a tendency of higher degree of saturation at the boundary of highly permeable strongly weathered conglomerate stratum and that of less permeable strongly weathered siltstone.
- ☒ Result of the stability analysis, by using a distribution of degree of saturation obtained from the unsaturated-saturated seepage analysis, shows that factor of safety turned below 1.0 and the slope collapsed at the same instant when the site observed the maximum rainfall per hour.

With the results and discussion above, the collapse mechanism of the weathered conglomerate and siltstone slope could be related to be the combination of, i) heavy rainfall at the site penetrated to the weathered soil layers at shallow depth and unit weight of soil increased, ii) pooling

of water took place at the boundary of two soil formations due to a smaller permeability of soil on the downward side, which then further added saturation of down-slope layers, and, iii) the suction reduced so much so that the disturbing force exceeded the shear strength of soil formations causing a slope collapse.

REFERENCES

- [1] Japan Meteorological Agency web site, <http://www.jma.go.jp/jma/indexe.html>
- [2] Chiaki A, et al. "Physics and mechanics test and sampling of decomposed granite soil is not disturbed", Soil Engineering Society, 1985, pp.89-92.
- [3] Tomohito H, "Shear wave velocity and liquefaction strength of freezing sampling and reconstituted specimens", Proceedings of Japan Society of Civil Engineers Hokkaido branch. Vol. 58, 1994, pp. 526-529.
- [4] Kansai Branch of The Japanese Geotechnical Society, "The disaster investigation by the typhoon No. 9 in 2009", 2009.
- [5] Shibuya S, et al "Interpretation of direct shear box testing of sands as quasi-simple shear", Geotechnique, 47, No. 4, 1997, pp.769-790.
- [6] The Japan Geotechnical Society "Measures and environmental impact assessment for the groundwater flow conservation", 2004.
- [7] Van Genuchten "A closed-form Equation for Predicting the Hydraulic Conductivity of Unsaturated Soil", Journal of Soil Science America, Vol.44, 1980, pp.892-898.
- [8] Japan highway public corporation, "Design guidelines", Vol.2, 2000, pp. 2-9.
- [9] Daizo K, "The relationship between the mechanical behavior and the state of pore water in unsaturated soil", Proceedings of Japan Society of Civil Engineers, Vol. 535, 1996, 83-92.
- [10] Research Committee on Evaluation of permeability characteristics unsaturated "Analysis of the current state on permeability evaluation in unsaturated soil", The Japanese Geotechnical Society, 1996, pp.11-13.

Authors Index

A		B	
A. Kadir Marsono	47	B. A. M. Shahriar	113
A. Nishida	89	B. A. Mir	304
A. Oya	274	B. Bai	416
A.Kumar	389	Bithin Datta	493, 505
A.M.K.N. Nadeesha	164, 169	Brian G. Jones	475
Abdoullah Namdar	339	Bujang B.K.Huat	32
Abdual Salalm Mehdi Saleh	475	Byeong - su Kim	545
Abdul Naser Abdul Ghani	384	C	
Abdul Saboor Rahmany	499	C F Leung	59
Abdul Sukorand	487	C. Gallage	389
Adhilla Ainun Musir	384	C.T. Nguyen	298
Adnène KASSEBI	523	Chattarin Sunsin	357
Afshin Asadi	32	Chen, B.K.	229
AGLIPAY Mary Roxanne	262	Cheng-Di Dong	464
Akihiko HAYASHI	394	Chih-Feng Chen	464
Akihiro Mieda	422	Chih-Hsin Hu	280, 517
Akio Takigawa	422	Chiu-Wen Chen	464
Akira Asaoka	2	Chung-Yue Wang	280
Alejandra María Gómez Jiménez	12	D	
Ali Ismail Al Jubory	475	D.H Lee	154
Aniroot Suksan	235	Dai Nakamura	71
Apichit Kumpala	235	Daisuke Hayasaka	427
Ardyono Priyadi	411	Dicky Nova Wardana	411
Asano Kanako	205	Dimas Anton Asfani	411
Ashish Juneja	304	Donovan Mujah	148
Atsushi Mikami	241	Du N L	286
Ay Lee Saw	59		

Authors Index

E			
Ehsan Momeni	47	Hiroshi Yamato	142
Erwin Oh	53, 310	Hiroyuki Kyokawa	95, 205
		Homayoon Ganji	499
F			
Fauziah Ahmad	148	Hoshina T	286
Ferney Quiñones Sinisterra	12	Houman Sohaie	47
Fouad Zargouni	523	Hyeon-Tae Kim	379
Fumio Tatsuoka	345	I	
		Ideris Bin Zakaria	164, 339
G			
G. Ren	258	Inge Hoff	333
Gary chai	53, 310	Isobe K	286
Girum Y. Yesuf	333	J	
Goh Chin Ong	217	J Wu and M Ryu	154
Guangli Xu	268	J. Rajaraman	540
Gurumurthy Hegde	339	J. Ramanujam	389
		J.F. Camacho-Tauta	187
		J.F. Gaitán-Serrano	187
H			
H. M. Shahin	113, 181, 199, 205	Jaehun Ahn	363
H. Tokhi	258	Jan Vaslestad	333
H. Yano	481	Je-Min Baek	323
H. Yukimoto	89	Jennifer E. Nicks	252
H.Y Wang	416	Jidong Teng	268
Ha H. Bui	274, 298	Jim Shiau	175
Haider Al-Ani	53	Jin-Suk Hur	323
Hajime Narioka	499	Jinwoo Jung	363
Helsin Wang	280	Jirayut Suebsuk	235
Hemanta Hazarika	148	Jun Sugawara	83
Hideto Nonoyama	136	Junichiro Takeuchi	452
		Junpei Saito	327

Authors Index

K		Márcio Muniz de Farias	12
K. Hayano	169	Mariana Mohamed Osman	458, 469
K. Shima	481	Masaaki Kondo	499
K. Yamamoto	481	Masafumi Nakagawa	511
K.Thiruvengkatasamy	540	Masahiko Katoh	445
Kaneda K	286	Masaki Makano	142
Kaoru Kobayashi	193, 373	Masaki Nakano	130, 136
Kato Morihiro	181	Masashi Ito	394
Kazunari Suzuki	142	Masaya Hinokio	142
Kazunobu Matsumoto	193, 373	Masayuki Fujihara	452
Kazuya Inoue	433, 439	Masuda Saki	199
Kenichiro Nakarai	247, 394	Mauridhi Hery Purnomo	411
Kenji KAWAI	394, 400	Md. Shahidul Islam	113
Kimitoshi Hayano	223	Mehdi Pouragha	24
Kiyota Takashi	107	Melia K. Iwamoto	252
KONAGAI Kazuo	262	Michael T. Adams	252
Kyokawa Hiroyuki	107	Michiyuki Harata	345
		Ming-Hung Chen	517
L		Minoru Kawaida	142
Leila Eslami-Andargoli	53	Mio Susumu	199
Lyn A. Gettys	427	Miura Minami	160
		Mohammad Raihanul Islam	406
M		Mohammad Shariful Islam	113
M. Iwata	89	Mohd Ashraf Mohamad Ismail	217
M.P. Ortiz-Pulido	187	Mohd. Nawawi	535
M.R. Islam	169	Morikawa Yukihiro	199, 211
Mabrouk Touahmia	119	Moshe Livneh	65
Maeda Kenichi	211	Muatasam Hassan	475
Mahsa Amirabdollahian	505	Muhammad Ekhlaur Rahman	148
Man-Kwon Choi	379	Muhammad Irfan	292

Authors Index

Musahaq Ali	42	Phacharaporn Bunyawanchakul	357
Mustapha Boukendakdji	367	Phillip S.K. Ooi	252
Mutsumi Tashiro	124		
		R	
N		R. Fukagawa	274, 298
N Minakata	154	Ramli Nazir	47, 77
N. Hiraoka	274	Ranjith, P.G.	229
N. L Ukwattage	530	Richard Wan	24
Na Li	317	Romziah Azit	217
Nakai Teruo	199	Ryan Kemp	175
Nasim Mosavat	310	Ryoki Ohashi	95
Nguyen Hong Son	124	Ryuta Ogawa	223
Noam A. Livneh	65		
Norzani Mahmood	217	S	
Noushin Naraghi Araghi	535	S A Tan	59
Nur Khairiyah Basri	487	S Nishiyama	154
Nur Sabahiah	487	S. Jayakody	389
Nurmunira Muhammad	164	S. Narasimha Rao	540
		Sabah Ahmed Ismail	475
O		Saki Matsuyama	439
Ohashi Ryoki	205	Sarah Khosravani	24
Ohtsuka S	286	Satoru Ishiguro	406
Okuda Kazuaki	181	Satoru Kawasaki	101
Om Prakash	487	Satoru Nakafusa	373
Osman El Hussien	77	Satoru Nakafusa	193
		Satoru Shibuya	323
P		Satoru Shibuya	545
P. Rajeev	274	Satoru Shimobe	327
P.G Ranjith	530	Satoshi Kagamiahra	545
Peng Yin	317	Satoshi Yamashita	71

Authors Index

Seungbae Kim	363	Takayuki Sakai	130, 142
Shao, S.S.	229	Takeshi Sato	445
Sharma Keshab	107	Takuya Takahashi	452
Shibuya Satoru	160	Tara Nidhi Lohani	323, 545
Shigeko Haruyama	42	Taro Uchimura	292
Shinsuke Matsumoto	379	Tatsuya Ishikawa	71, 351
Shotaro Yamada	130	Teruo Arase	427
Shouhei Ogawa	445	Teruo Nakai	95, 181, 205
Shun-Min Lee	517	Tetsuya Tokoro	71, 351
Shunzo Kawajiri	545	Thammakorn Sasanawin	357
Shushi Sato	379	Toshihiro Morii	193, 373
Si Senfi	499	Toshihiro Noda	124, 136
Suksun Horpibulsuk	235	Tsutomu Tanaka	433, 439
Syahriah Bachok	458		
Syahriah Bachok	469	W	
Syed Mustafizur Rahman	535	William T. Haller	427
T		X	
T Yano	154	X.W Tang	416
T. Hara	89	Xinye Han	345
T. Kato	89	Xue J. Huan	427
T. Nakajima	481		
T. Negami	481	Y	
Taizo Uchida	427	Y. Futsuhara	481
Takafumi Inoue	241	Y. Honjo	89
Takamitsu Kajisa	499	Y. Otake	89
Takashi Danjo	101	Yafei Zhang	268
Takashi Kiyota	345	Yao-Jen Hsu	517
Takashi Okimura	545	Yasunori Mori	499
Takayuki Fujiwara	433	Yi Yang	317

Authors Index

YM Cheng	317
Yongzhen Peng	422
Yuan Zhang	351
Yuji Hatano	400
Yuki Hasegawa	379
Yuki Yokoyama	247
Yung-Chuan Chou	517
Yutaka Okame	400

Z

Zakaria Hossain	42
Zakiah Ponrohono	469
Zhang Feng	211
Zulfadly Azizi Bohari	458
Zulfadly Azizi Bohari	469
Zulkifli Nordin	217

Contents of GEOMATE2011-Volume 1(1) and Volume 1(2)

Geotechnique

Developments of geosynthetic-reinforced soil technology in Japan: retaining walls and bridge abutments <i>Fumio Tatsuoka</i>	3
Seepage-deformation coupled numerical analysis of unsaturated river embankment using an elasto-plastic model <i>F. Oka, S. Kimoto and R. Kato</i>	15
Progressive failure of shallow anchor in dense sand evaluated by 2D and 3D finite element analysis and model tests <i>T. Sakai and M. Rokouzzaman</i>	23
Design of single pile foundations using the mechanics of unsaturated soils <i>Vanapalli S. and Taylan Z.N.</i>	31
Problematic soil: in search for solution <i>Bujang B.K. Huat</i>	39
Characterization and modeling of various aspects of pre-failure deformation of clayey geomaterials – fundamental theories and analyses <i>J.N. Mukabi</i>	47
The maintenance of ground anchors in Nippon Expressway <i>Yuu Fujiwara and Toshinori Sakai</i>	57
Stress distribution in khon kaen loess under spread footing <i>Pairoj Yodsa-nga and Watcharin Gasaluck</i>	61
The effect of sheet pile length on the capacity of improved pile foundation on sand under vertical and moment loading <i>Tuan Van Nguyen and Pongsakorn Punrattanasin</i>	65
Investigation of a reliable reinforcing method for embankment ground <i>H. M. Shahin, T. Nakai, M. Kikumoto, R. Sakai, Y. Yoshida, I. Saito, N. Nagao and K. Toda</i>	71
Evaluation of stamps and latex shell influence on stabilometer testing results, modeled with simulia abaqus <i>Dmitriy Volik</i>	77
Characterizing the interaction of geomat with fine grained black cotton soils <i>Wekesa S., Mukabi J., Okado J., Kogi S., Ndeda M. and Ogallo J.</i>	81
Soil liquefaction susceptibility zoning due to earthquake using GIS and geotechnical data <i>Bhuyan Md. Habibullah, Rama Mohan Pokhrel, Jiro Kuwano and Shinya Tachibana</i>	87
Evaluation on the results of multistage shear test <i>Hormdee D. and Kaikeerati N.</i>	93
Verification of effects of countermeasures for seepage of river levees by on-site monitoring of the water level of levees <i>Hiroyuki Masuyama, Yukiko Saito, Masanori Ishihara, Tetsuya Sasaki and Hirotoshi Mori</i>	97
Influence of decreasing of soil suction on unconfined compressive strength for bentonite <i>Tomoyoshi Nishimura</i>	103

Contents of GEOMATE2011-Volume 1(1) and Volume 1(2)

The relationship between soil suction and the maximum unsaturated undrained shear strengths of compacted khon kaen soil <i>R. Nuntasarn and W. Wannakul</i>	107
Interpretation of coaxial and non-coaxial strain on directional variation of undrained strength of clay <i>J.Rajaraman and K. Thiruvengkatasamy</i>	113
FEM analysis of innovative shallow foundation system for reactive soils <i>Mostafa A. Ismail and Mohamed A. Shahin</i>	117
Delay times of elastic waves at discontinuities in laminated specimens <i>Yota Togashi, Kazuo Tani, Tetsuji Okada and Hiroaki Sato</i>	123
Geotechnical investigation of valleys using lightweight dynamic cone penetration test for landslide risk assessment <i>Takashi Hanaoka, Takashi Tsuchida, Shoichi Kawabata and Shota Nakagawa</i>	129
Study on individual landslide risk assessment of natural valleys and slopes during heavy rain based on geotechnical investigation and analysis <i>Shouichi Kawabata, Takashi Tsuchida, Takashi Hanaoka and Shouta Nakagawa</i>	135
Analyses of piping under foundation of weirs in different ground density by FEM <i>Okajima Kenji</i>	141
Shear deformation and failure of sandy slope according to pore pressure generation due to rainfall infiltration <i>Katsuo Sasahara and Naoki Sakai</i>	147
Load settlement relationships of circular footing considering dilatancy characteristics of sand <i>Yusuke Tomita, Tatsuaki Nishigata, Takeshi Masui and Shintaro Yao</i>	153
Thermally modifying bentonite for construction industry <i>Abdoullah Namdar</i>	159
Mesh-free analysis of beam on elastic foundation <i>S. M. Binesh</i>	163
Frictional Performance Of Infilled I-Blocks With Geosynthetic Inclusions <i>Faisal Hj Ali, Md. Zahidul Islam Bhuiyan, Firas A. Salman and Siau Lian San</i>	167
Varying ground water level to minimise liquefaction hazards in urban areas <i>Heitor A., Oka F., Kimoto S. and Higo Y.</i>	173
Development of a new type reinforced soil wall <i>Hara T., Tsuji S., Yoshida M., Ito S. and Sawada K.</i>	177
Development of design charts for reinforced embankment using excel spreadsheet slope stability analysis <i>Ito Kazuki, Md. Zakaria Hossain and Toshinori Sakai</i>	183
Numerical simulation of 2D crack growth with frictional contact in brittle materials <i>Kai Zhang, Jing-cai Jiang and Qing Yang</i>	187
Interface behaviour of basalt geosynthetic with sand in direct shear mode <i>M.B. Hossain, M.Z. Hossain and T. Sakai</i>	191
Effect of soil parameter uncertainty on seismic response of buried segmented pipeline <i>Chaminda Gallage, Pathmanathan Rajeev and Jayantha Kodikara</i>	197

Contents of GEOMATE2011-Volume 1(1) and Volume 1(2)

The sorption capacity of cu by sc-soil from batch and column tests <i>Arwut Yimtae, Pongsakorn Punrattanasin and Noppadol Sangiumsak</i>	203
<i>Construction materials</i>	
Green construction: the role of palm oil fuel ash in concrete <i>A.S.M. Abdul Awal</i>	211
Behavior of collapsible loessic soil after interparticle cementation <i>Arrua Pedro, Aiassa Gonzalo, Eberhardt Marcelo and Claverie Eliana</i>	221
A study on hardened soil brick using liquid type and powder type hardening agent <i>Jin Sung Ki., Jung Seung Yong. and Kim Tae Ho.</i>	227
The effect of salt content in soil on the sorption capacity of heavy metals <i>Lerd Kerdchaiyaphum and Pongsakorn Punrattanasin</i>	233
Manufacture of Housing Construction Materials with Jute Polymer Composite (Jutin) <i>Mubarak A. Khan, Fahmida Parvin, Jahid M M Islam and Md. Zakaria Hossain</i>	239
Evaluation of strength of granulated construction waste sludge with quick lime and its application to soil structure <i>Makoto Kobayashi, Hiroaki Nakamura and Hideaki Mizuno</i>	245
Analysis of enhanced strength and deformation resistance of some tropical geomaterials through application of in-situ based stabilization techniques <i>Kogi S., Ndeda M., Mukabi J.N. and Wekesa S.</i>	251
Further developments in the swelling model of expansive clays under ASTM 4546 and CBR testing <i>Moshe Livneh</i>	257
The effect of clay, lime and rice husk ash contents on the sorption capacity of Cu, Ni and Zn by Soils <i>Pongsakorn Punrattanasin and Noppadol Sanggiumsak</i>	263
The effect of temperature on the sorption capacity of copper by soils <i>Noppadol Sangiumsak and Pongsakorn Punrattanasin</i>	269
Experimental Investigation for Nitrate Reduction Using Iron Powder in Porous Media <i>Haruka Shimada, Kazuya Inoue, Ikko Ihara, Katsutoshi Suzuki and Tsutomu Tanaka</i>	275
Using spatial moments in conjunction with image processing to estimate macrodispersion in stratified porous formations <i>Katsutoshi Suzuki, Kazuya Inoue, Tsutomu Tanaka and Akira Kobayashi</i>	281
The novel technology of desertification control and ecological restoration with an Hydrolysis Polyurethane(W-OH) <i>Weimin Gao, Zhiren Wu, Zhishen Wu, Kentaro Iwashita, Hirondo Inagaki and Caiqian Yang</i>	287
Migration of radioactive materials through porous media: theory and a solution for an unsteady state problem <i>Khaled I. Hamza</i>	293
Fundamental study on ecosystem support canal using porous concrete <i>Masuma Yoshihiro, Hasegawa Yuki, Md.Rokunuzzaman, Yamada Toshio, Kassai Hirofumi and Sato Shushi</i>	299

Contents of GEOMATE2011-Volume 1(1) and Volume 1(2)

Alternative employment of crushed shell particles in capillary barrier of soil <i>Satoru Nakafusa, Kaoru Kobayashi, Toshihiro Morii, Tomoyoshi Nishimura</i>	305
A novel statistical approach for investigating the significant factors that influence the performance score of the Turkish method <i>Kshama Sundar Roy, Kamrul Islam and Md. Shams Arafat</i>	311
Ultimate strength and fatigue life of concrete structural elements reinforced with carbon fiber sheet <i>Hidehori Tanaka and Yutaka Toi</i>	317
Development of functional carbon nanotubes -asphalt composites <i>Tatsuo Shirakawa, Akio Tada and Noriyasu Okazaki</i>	323
Hydraulic character of estimation method on roughness coefficient of concrete canal <i>Koichiro Otagaki, Koji Sai, Kenichi Fujisawa, Shinsuke Matsumoto and Shushi Sato</i>	329
Na-bentonite as rock containment barrier against heavy metals and acid leachates <i>Angelica Naka, Takeshi Katsumi, Toru Inui, Giancarlo Flores and Takehiro Ohta</i>	333
The comparison of monotonic behaviors of two different calcareous sands <i>R. Rezvani, H. Shahnazari, H. Salehzadeh and Y. Dehnavi</i>	337
Soaking effect on strength and performance of fine grained soil stabilized with recycled gypsum <i>Aly Ahmed, Keizo Ugai and Taira Jinno</i>	343
Removal of Zinc in soils using natural zeolite <i>Wiparat Nisapai, Arthit Neramittagapong and Sutasinee Neramittagapong</i>	349
Heat control of pavement surface temperature using oyster shell lime <i>Satoru Ishiguro and Masayoshi Yamanaka</i>	353
Buckling behavior of composite triangular plates <i>T.Farsadi, P.Amani and E.Heydarnia</i>	357
Durability of cement treated highway materials <i>Jiraroeth Sukolrat, Apisit Klummeng and Sekchai Anuvechsirikiat</i>	365
Porous geopolymer concrete <i>Tawatchai Tho-in, Vanchai Sata and Prinya Chindaprasirt</i>	371
Design and Fabrication of Composite Technology for Earth Slope Protection <i>Md. Toriqul Islam, Md. Zakaria Hossain and Masaaki Ishida</i>	375
Study of slump testing for hydraulic plastic grout <i>Hiroyasu Ishii, Kenichi Horikoshi and Masaki Kitazume</i>	381
Behavioral comparison of coarse aggregate from various quarry sites of pakistan, effect on hardened concrete, economics and environment <i>Faisal Malik and S. Muhammad Jamil</i>	387
Methods for execution of concrete piles in corrosive and destructive marine environments, based on study of the Persian Gulf marine installations <i>Nasser Arafati, Abdol Hossein Fazli and Seyed Mehdi Mousavi</i>	393
Fundamental study on particle size distribution of coarse materials by image analysis <i>G.H.A.J.J. Kumara, K. Hayano and K. Ogiwara</i>	399

Contents of GEOMATE2011-Volume 1(1) and Volume 1(2)

Environment

Calibration and simulation of runoff models for developing watershed respond knowledge at tropical area <i>Arien Heryansyah and Zulkifli Yusop</i>	407
Effect of geological succession on macrophyte and microbiota in aquifer ecosystem in urban coastal zone <i>Kazuhito Murakami and Akiko Inoue-Koham</i>	411
Bioclean and liquid biofertilizers a new way to the green area <i>Sittisak Uparivong</i>	417
Massive point cloud acquisition on a soil surface using a stereo camera <i>Masafumi Nakagawa, Anna Nakanishi, Hirotaka Endo and Kenta Ochiai</i>	421
Estimation of earthquake ground motion in Padang, Indonesia <i>Rusnardi Rahmat Putra, J. Kiyono and Y. Ono</i>	425
Groundwater contamination due to irrigation of treated sewage effluent in the werribee delta <i>Hiroyuki Ii, Masanobu Taniguchi, Ataru Satoh, Graeme Allinson, Matt Kitching, George Croatto and Bruce Shelley</i>	431
Process of invading the alien plant species into the river ecosystem <i>Michiko Masuda, Yumie Ito and Fumitake Nishimura</i>	437
Recent meandering pattern of the Irrawaddy, Myanmar <i>Mayumi Matsumoto and Shigeko Haruyama</i>	443
Physical and chemical properties of tsunami deposit in northeast area in Fukushima prefecture after Tohoku-Kanto earthquake <i>Tomonori Fujikawa, Hiromu Okazawa, Takahiko Nakamura, Yasushi Takeuchi and Masaharu Komamura</i>	447
Changes of bottom sediment caused by Construction of the Airport Island in the Ise Bay, Japan. <i>Maki Oyagi, Motohiro Kawase and Akihiko Yagi</i>	453
Proposal of simple measurement method for evaporation rate by using oxygen isotopic ratio in the inawashiro lake <i>Satoshi Miyahara and Hiroyuki Ii</i>	457
Landslide susceptibility mapping using logistic regression model with neighborhood analysis: a case study in mizunami city <i>Wang Liangjie, Sawada Kazuhide and Moriguchi Shuji</i>	463
The evaluation of the river environment and water quality by image analysis in the Yamato River Basin in Japan <i>Masanobu Taniguchi, Hiroyuki Ii and Tatemasa Hirata</i>	469
Distribution of oxygen and hydrogen stable isotopic ratios and estimation of the spring water origin in the Kushiro Moor <i>Natsuki Kawabe and Hiroyuki Ii</i>	473
A debris flow and its risk analysis related to the 2008 Wenchuan earthquake <i>Yange Li, Guangqi Chen, Chuan Tang and Lu Zheng</i>	479
Impact analysis of water price reform of Zhangye, China <i>Atsushi Koike, Zhongmin Xu, Kang Wang and Bunei Itoga</i>	485

Contents of GEOMATE2011-Volume 1(1) and Volume 1(2)

Post earthquake rapid inspection planning for bridges in western Kentucky <i>Norimitsu Koike and Issam E. Harik</i>	491
Organophosphoric acid triesters from landfill sites and sewage plants in Japan <i>Haruki Shimazu</i>	497
Ground water pollution around the Oyachi-Heizu district of Yokkaichi city <i>Yukimasa Takemoto, Masaaki Takahashi, Kayoko Awaya, Mikihiro Ioka and Peng Guo</i>	501
Characteristics of damage to structures induced by the tsunami of the 2011 east Japan mega earthquake <i>Ömer Aydan, Hisataka Tano and Takahiro Iwatate</i>	505
Characteristics of strong motions induced by the 2011 east Japan mega earthquake with an emphasis on Tokyo bay area <i>Takahiro Iwatate, and Ömer Aydan</i>	511
Inquiry of the value of parks in the characteristics and use of park planning through urban revival planning projects in Maebashi city <i>Shinya Tsukada, Tetsuo Morita and Akira Yuzawa</i>	517
A study on evaluation of quality of life in consideration of water/green environment <i>Tetsuo Morita, Yoshihito Kogure, Hiroshi Sugita, Tsuyoshi Baba, Shinya Tsukada and Naoki Miyazato</i>	521
Changes and issues in green space planning in the tokyo metropolitan area: focusing on the "capital region plan" <i>Tetsuo Morita, Yoshihide Nakagawa, Akinori Morimoto, Masateru Maruyama and Yoshimi Hosokawa</i>	527
Application of traffic simulation in road policy assessment accompanied by railway elevation <i>Maekawa Takuya and Hiroshi Inouye</i>	533
Impact estimation of land cover changes of recharge area on spring discharge in marshy environment <i>Masaaki Kondo and Takamitsu Kajisa</i>	541
Numerical Study on Characteristics of Levee Breach Flood Disasters in Alluvial Floodplain <i>Md. Serazul Islam and Tetsuro Tsujimoto</i>	547
Purification system of ocean sludge by activating microorganisms <i>Kyoichi Okamoto, Kenji Hotta, Takeshi Toyama and Hideki Kohno</i>	553
Author index	559

Volume 2

Characterization and modeling of various aspects of pre-failure deformation of clayey geomaterials – applications in modeling <i>J.N. Mukabi and M.Z. Hossain</i>	563
An emergency medical care information system for fetal monitoring <i>Muhammad Ibn Ibrahimy</i>	573
Effects of gypsum on the swelling and dispersion behaviour of fine grained soils from Sudan <i>Abdul Karim, M. Zein and Ahmed M. Elsharief</i>	577

Contents of GEOMATE2011-Volume 1(1) and Volume 1(2)

Comparison of bearing capacity equations for vertical central loading <i>Muhammad Awais Shafique and Tanvir Iqbal Qayyum</i>	583
Pull-out resistance of selected native plants in Hong Kong <i>Leung F.T.Y., Yan W.M., Tham L.G. and Hau B.C.H.</i>	589
Inland navigation in carrying injured and sick disaster victims in case of a massive earthquake in the Tokyo metropolitan area <i>Kazuya Egami, Keiichi Noto, Wataru Miyazaki, Kazukiyo Yamamoto and Takeo Kondo</i>	593
Model calculation and geotechnical interpretation of the correlation co-efficient between finite and incremental strain path of a formation <i>J.Rajaraman and K. Thiruvengatasamy</i>	597
Geocell reinforced bed subjected to simulated traffic loads <i>P. Sharifi, and S.N. Moghaddas Tafreshi</i>	601
Effects of gradation of various sand deposits of Pakistan on strength of hardened concrete <i>Gauhar Sabih and S. Muhammad Jamil</i>	607
Strengthening of landslide retaining pile wall after geodetic monitoring <i>Frangov G., Zayakova H., and Hamova M.</i>	613
Response of tapered piles under lateral harmonic vibrations <i>Ahmad Dehghanpoor and Mahmoud Ghazavi</i>	627
Investigation of ground movement in soil-nailed walls using 1g models and PIV method <i>H. Mahdavi, and M. Hajjalilue-Bonab</i>	623
Author Index	629

Contents of GEOMATE2012 - Volume 2(1)

ID Keynote Papers

1	Use of microbial technology in geotechnical engineering <i>Jian Chu, Volodymyr Ivanov, Jia He and Viktor Stabnikov</i>	1-4
2	A study on slow moving slopes <i>L G Tham and Xu Kai</i>	5-11
3	Bearing capacity and settlement behaviour of shallow foundations in unsaturated sands <i>Sai K. Vanapalli and Fathi M. O. Mohamed</i>	12-21
4	Development of Piled Geo-wall <i>Hara, T., Tsuji, S., Yoshida, M. and Sawada, K.</i>	22-29
5	Measurement of strain distribution along precast driven pile during full scale pile load test <i>Faisal Ali and Lee Sieng Kai</i>	30-39
6	Unique grouting material composed of calcium phosphate compounds <i>S. Kawasaki and M. Akiyama</i>	40-46
7	Stiffness Anisotropy and Resilient Modulus of an Unsaturated Soil under Static and Cyclic loads <i>Charles W.W. Ng, C. Zhou and J. Xu</i>	47-62
8	Nanoparticles for Geotechnical Engineering <i>Mohd Raihan Taha</i>	63-68

Technical Papers

	<i>Geotechnique</i>	69
24	Damage Assessment and Strengthening of R/C Building Constructed on Expansive Soils <i>Osama M. A. Daoud</i>	70-75
29	Gravitational Sphere Packing Method To Find The Porosity Of The Soil Particles With The Identical Size in cylindrical container <i>Mohammad Mahdi Roozbahani , Bujang B. K. Huat, Afshin Asadi</i>	76-78
34	Parametric Study of Piled Raft Foundations to improve the Design Method <i>Tohidi A., MH .Sadagiani</i>	79-84
39	Experimental Study of Suction-Monitored CBR test on Sand-Kaolin Clay Mixture <i>Purwana, Y.M., Nikraz H., and Jitsangiam P.</i>	85-90
41	Foundation Strengthening of Historic Buildings by Micropiles <i>Azza M. Elleboudy</i>	91-96

Contents of GEOMATE2012 - Volume 2(1)

44	Group effects of piles due to lateral soil movement <i>Hongyu Qin1 and Wei Dong Guo</i>	97-102
45	Collapse-Settlement Calculations for Embankments Based on a Collapsible Soil Subgrade <i>Moshe Livneh</i>	103-108
46	The influence of trench soil properties on the accuracy of pressure cell measurements in an earthfill dam <i>D. Elmi, A. A. Mirghasemi</i>	109-112
50	Studying the effects of considering dilation angle over the performance of geotechnical elements using numerical methods <i>Salman Hanifi, Amin Naeimabadi , Mohammad Reza Atrchian</i>	113-117
50a	Comparing the excavating effect of single and twin tunnels on the earth surface settlement by numerical methods <i>Amin Naeimabadi, Salman Hanifi , Mohammad Reza Atrchian</i>	118-124
107	Excess Pore Pressure Characteristics of Sand Mat using Dredged Soil <i>M.S LEE, K. ODA</i>	125-130
110	Effect of clays fraction to california bearing ratio laboratory test value with and without soaked <i>Soewignjo Agus NUGROHO, Syawal Satibi and Ferry Fatnanta</i>	131-136
111	Compressibility Characteristics of Residual Soil Subjected to Microbial Treatment <i>Lee Min Lee, Ng Wei Soon, and Yasuo Tanaka</i>	137-140
115	Strength and aging of cement treated low plastic soils <i>Fabien Szymkiewicz, Antoine Guimond-Barrett, Alain Le Kouby</i>	141-145
119	Performance Of Cantilever Sheet Pile Supporting Excavation Adjacent To Strip Footing <i>Yousry M. Mowafe, Ahmed M. Eltohamy and Ahmed A. Mohamed</i>	146-153
119a	Enhancing Stability of Slopes with Cement Kilin Dust Sand Mixture Layer <i>Al Serif M. Abd Alazez1, Ahmed M. Eltohamy and Ahmed Rusdy Towfek</i>	154-161
122	The effect of confining stress on the analysis of excavations with adjacent existing buildings <i>Sabzi Zahra, Fakher Ali</i>	162-166
125	Bored Pile Socket in Erratic Phyllite of Tuang Formation <i>D.E.L. Ong</i>	167-171
133	Swelling deformation of the bentonite mixed with silica fume or sodium carbonate in calcium hydroxide solution <i>Yuki YOKOYAMA and Kenichiro Nakarai</i>	172-175
136	A Combined Probabilistic Method for Engineering Failure analyses and Applications in Typical Geotechnical Structures <i>Duruo Huang</i>	176-181
137	Parametric Study of Crossing Tunnels at Different Level <i>A. Tohidi, MH.Sadagiani</i>	182-189
143	Use of post-floatation copper tailings in the construction of dump dams <i>Tschuschke W., Wierzbicki J.</i>	190-195

Contents of GEOMATE2012 - Volume 2(1)

150	Effects of Slope Inclination on the Rain-induced Instability of Embankment Slopes <i>Chaminda Gallage, Shiran Jayakody and Taro Uchimura</i>	196-201
225	Extension of an integrated AHP and TOPSIS approach in the earth dam site selection <i>Minatour Yasser, Khazaie Jahangir</i>	202-208
227	Using Geogrid Boxes as a New Approach for Reinforcement of Rock Slopes <i>Ahmad Fahimifar, Arvin Abdolmaleki</i>	209-214
228	Volume Change Characteristics of Clay Mixes with Different Bentonite Percentages <i>J. M. Kate, Sunil Kumar, M. P. Bhorkar</i>	215-218
236	FE Analysis for Settlement of Peat Ground under Embankment Loading <i>Satoshi Nishimoto and Hirochika Hayashi</i>	219-224
237	Seismic behavior of pile group in soil slopes: 1g shake table tests <i>H. Elahi, M. Moradi, A. Ghalandarzadeh and A. Elahi</i>	225-229
239	Electrophoresis of Bacteria and Electro-Biogrouting <i>Hamed A. Keykha, Bujang B. K. Huat, Afshin Asadi, Satoru Kawasaki</i>	230-232
240	Consideration concerning reasonable modified form of Floating-type Improved Ground <i>Hijiri Hashimoto, Satoshi Nishimoto and Hirochika Hayashi</i>	233-236
241	Numerical Study Effect of Nail Angle Change on Stability and Displacement of Excavation Wall in Cohesive and Cemented Non-Cohesive Soils <i>Navid Shahnazi, Jahangir Khazaie, Mohamad Sharifipour and Kiarash Ashtari</i>	237-241
242	An investigation on behavior of geogrid reinforced soil retaining walls applying finite difference method (F.D.M) <i>Jahangir Khazaie and Alireza Sadeghabadi</i>	242-252
243	Effects of humic acid and salt additives on the behaviour of lime-stabilised organic clay. <i>N.Z. Mohd Yunus, D. Wanatowski, and L.R. Stace</i>	253-256
244	Sodium Tripolyphosphate For Stabilizing Of Contaminated Soil <i>Amin Falamaki, Hossein Tavallali and Shahrbanoo Rezanejad Farahmand</i>	257-260
246	Evaluation of Soil Water Characteristic Curves for Sand-Expansive Clay Mixture <i>T. Y. Elkady, M. A. Dafalla, A. M. Al-Mahbashi and Mosleh Al Shamrani</i>	261-265
247	Coastal soils improvement <i>Mohammad reza Atrchian, Morteza Ala, Amin Naeimabadi</i>	266-269
248	A Hybrid Intelligent System of Fuzzy C-Mean Clustering and Neural Networks to Predict the Compaction Characteristics of Fine Grained Soils <i>Iman Ashayeri, Mahnoosh Biglari</i>	270-273
249	Equivalent linear seismic ground response analysis of unsaturated soil deposits <i>Mahnoosh Biglari, Iman Ashayeri</i>	274-278
251	The Correction of Shallow Foundation Settlement Equations by Finite Element Method <i>Mohammad Arab Ameri, Hakime Rabbanifar and Mehdi Arab Ameri</i>	279-284

Contents of GEOMATE2012 - Volume 2(1)

255	Numerical study of earthquake hazards of liquefaction occurring on the site and sustainable transport pipes <i>Hamed Bavanpouri, Jahangir Khazaie, Dr.Hasan Sharafi</i>	285-288
266	Analysis of geogrid reinforced soil retaining walls with limit equilibrium and finite difference method <i>Alireza Sadeghabadi, Jahangir Khazaie and Mostafa Yousefi Rad</i>	289-293
270	Recent Development in Electrokinetic Stabilization of Soft Soil, A review <i>Hossein Moayed, Sina Kazemian, and Bujang B. K. Huat</i>	294-298
275	Application of ion-exchange solution soil stabilizer in increasing CBR values of clayey soils <i>Reza Ziaie Moayed, Seyed Ali Hashemi and Farzad Allahyari</i>	299-302
276	Assessment of Low Strain Wave Attenuation for Piles Cast in Very Dense Granular Soil <i>Ramli Nazir and Osman El Hussien</i>	303-307
279	Dynamic Soil-Structure Interaction Considering Pore-Water Pressure Coupling <i>Qutayba Nazar Al-Saffar, P Akram Y. Al-Sa'aty, Mohamad T. Al-Layla</i>	308-325
281	Analysis and design of tunnel lining in alluvial soil deposits <i>Nuri al-Mohamadi</i>	326-330
285	Effect of silt content on the anisotropic behaviour of silt-sand mixtures <i>Navid Khayat, Abbas Ghalandarzadeh</i>	331-337
288	Optimizing the twin tunnels position for reduction the surface ground movements <i>Mehdi Mokheri, Seyed Ali Farjam</i>	338-344
290	Evaluation of pile lateral capacity in clay applying evolutionary approach <i>Alkroosh I., Nikraz H</i>	345-348
293	Effect of Reservoir Drawdown Rate on Phreatic Line Recession in Homogeneous Earth Dams <i>R. Ziaie Moayed, V. Rashidian</i>	349-352
294	The effect of lime-microsilica stabilization on California Bearing Ratio of silty soils <i>R. Ziaie Moayed, Y. Daghighi, B. Pourhadi and N. Sahebzamani</i>	353-356
295	Effect of elastic modulus varieties in depth on modulus of subgrade reaction on granular soils <i>Reza Ziaie Moayed, Mahdi Ali Bolandi</i>	357-360
296	Flexural Buckling Behavior of Steel Pile with Vertical Load in Liquefied Soil <i>Yoshihiro Kimura and Koichi Onohara</i>	361-365
305	Two-dimensional finite difference pseudo-static deep-seated slope stability analysis of embankments over stone column-improved soft clay <i>Farshad Fayyaz Jahani, Mohammad Sharifipour</i>	366-371
308	Parametric study of Geo-grid soil reinforced retaining walls under dynamic loading by ABAQUS software <i>Artrchian mohammad reza, Daghighi younes, Ghanbari namin hamed</i>	372-380
2010	Sensitivity analysis in soil nail wall for Tehran-Tabriz railway by considering the coefficient of variation for effective parameters in stability analysis <i>Mohammad Moghadaripour, Ardalan Akbari Hamed, Ali Ghozat</i>	381-384

Contents of GEOMATE2012 - Volume 2(1)

2012	Evaluation of Strength Parameters of Improved Collapsible Soils with Current Additives (Case study: Atrak zone, Iran) <i>Mohammad Arab Ameri, Samaneh Kargar and Mehdi Arab Ameri</i>	385-390
2100	Influences of soil material parameters in compaction simulation with soil/water/air coupled F.E. code <i>S. Sakamoto, K. Kawai, V. Phommachanh and A. Iizuka</i>	391-396
2105	Lower bound limit analysis of strip footings resting on cohesive soils <i>S.M. Binesh, A. Gholampour</i>	397-402
2106	Upper bound limit analysis of strip footings resting on cohesive soils <i>S.M. Binesh, S. Raei</i>	403-408
2108	Evaluating and optimizing different methods of treating and cleaning contaminated soil <i>Mohammad Reza Atrechian, Seyed Salman Musavi Khosro Ebrahimkhani</i>	409-412
2112	Experimental study concerning impact characteristics by collision of weight on sand cushion over steel beam <i>Tam Sy Ho, Hiroshi Masuya and Naoto Takashita</i>	413-419
2114	Landslides in Tea Plantation Fields in Shizuoka, Japan <i>Jun Sugawara</i>	420-425
2115	Natural base isolation system for earthquake protection <i>Srijit Bandyopadhyay, Aniruddha Sengupta and G.R. Reddy</i>	426-431
2116	Comparison of Effect of Percent of Compaction, Sand and Cement on The Amount and Time of Swelling of Bentonite <i>Mohammad S. Pakbaz and B. Rafiee</i>	432-435
2118	Prediction of the Axial Bearing Capacity of Piles by SPT-based and Numerical Design Methods <i>Issa Shooshpasha, Ali Hasanzadeh and Abbasali Taghavi</i>	436-439
2120	Application of recently developed mechanistic-empirical methods for the design of heavily loaded pavement structures <i>John N. Mukabi</i>	440-447
2121	Design of support system for excavation in black cotton soils in Guntur, India <i>D. Neelima Satyam, Akhila Manne</i>	448-451
2127	Numerical modeling of pullout capacity of a pile in sand under oblique load <i>Md. Iftakharuzzaman and Dr. Bipul Hawlader</i>	452-457
2130	Slope Failure in Residual Soils of Peru <i>A. Carrillo-Gil</i>	458-461
2131	Back-analysis of Frictional Jacking Forces Based on Shear Box Testing of Excavated Spoils <i>Choo Chung Siung and Dominic Ong E. L.</i>	462-467
2132	Lime Stabilization of Tropical Soft Soils <i>Dygku Salma Awg Ismail, Tan Jui Siang and Siti Noor Linda Taib</i>	468-471
2138	Increase Of Piles Bundle Capacity By Making A Base Joining Them <i>Jan Jaremski</i>	472-478

Contents of GEOMATE2012 - Volume 2(1)

2139	The Effects of soil-Pile Interaction on Seismic Parameters of Superstructure <i>Mahdy KhariI, Khairul Anuar Bin Kassim, Azlan Bin Adnan</i>	479-484
2140	Investigation on Finite Element Modeling of Group of Stone Columns <i>M. Mirshekari, C. Behnia and S. Fakhretaha</i>	485-488
2147	Suction Controlled Triaxial Apparatus for Saturated-Unsaturated Soil Test <i>Luky Handoko, Noriyuki Yasufuku, Kiyoshi Oomine, Hemanta Hazarika</i>	489-493
2154	Monitoring Program and Dilapidation Survey for Grouting of Karst Cavities <i>Hasan A. Kamal and Hassan J. Karam</i>	494-497
2156	Numerical Analysis of Soil Nail Walls under Seismic Condition in 3D Form Excavations <i>Siavash Zamiran, Hamidreza Saba</i>	498-501
2159	Shear strength improvement of fibrous peat due to consolidation pressure <i>Vivi Anggraini, Nurly Gofar and Bujang bin Kim Huat</i>	502-506
2164	Factors affecting the stability analysis of earth dam slopes subjected to reservoir drawdown <i>T. Souliyavong, C. Gallage, P. Egodawatta and B. Maher</i>	507-512
2165	Lateral stress induced due root-water-uptake in unsaturated soils <i>Mu'azu Mohammed Abdullahi and Nazri Bin Ali</i>	513-517
2166	The effect of pre-tensioned rock bolts on seismic behavior of urban tunnels <i>Farshad Fayyaz Jahani, Mohammad Sharifipour</i>	518-523
2170	Effect of silt content on the anisotropic behaviour of silt-sand mixtures <i>Navid Khayat, Abbas Ghalandarzadeh</i>	524-530

Construction Materials

24b	Production and Properties of High Strength Concrete for Concrete Dam Heightening Project in Sudan <i>Osama M. A. Daoud and, H. S. Sagady</i>	531-537
27	Effect of openings locations of quadratic folded plate roofing systems on their static and dynamic behavior <i>Ahmed Hassan</i>	538-544
48	Improving concrete compression strength using natural additive <i>Abdoullah Namdar, Ideris Bin Zakaria and Nurmunira Binti Muhammad Atan</i>	545-548
53	DEM simulations and laboratory experiments on physical and mechanical properties of sand-gravel mixtures <i>Janaka J. Kumara, Kimitoshi Hayano, Yuuki Shigekuni and Kota Sasaki</i>	549-554
120	Rock slope stability problems in Gold Coast area in Australia <i>Shokouhi Ali, Gratchev Ivan, Charrismanagara Arry</i>	555-558
121	Techno-commercial development of pre-fabricated structures using geopolymer concrete <i>J. Santhosh, R.Sanjeev, P.Sethu Raja, A. Rajendra Prasad, A. Abdul Rahman</i>	559-563

Contents of GEOMATE2012 - Volume 2(1)

124	Mechanical Properties of Recycled Steel Fibre Reinforced Concrete <i>A.S.M. Abdul Awal, Lim Lion Yee, M. Dianah1 and M. Zakaria Hossain</i>	564-569
134	Effects of Gradation of Various Sand Deposits of Pakistan on Strength of Hardened Concrete <i>Gauhar Sabih , S. Muhammad Jamil and Kamran Akhtar</i>	570-574
203	Assessment of recycled concrete aggregates for road base and sub-base <i>S. Jayakody, C. Gallage, A.Kumar</i>	575-579
232	Estimation of consolidation properties of Holocene clays with artificial neural network <i>Kazuhiro ODA , Minsun Lee and Shotaro Kitamura</i>	580-585
250	Measurement of The Crack Displacement Using Digital Photogrammetry for Evaluation of The Soundness of Tunnels <i>A. Kanazawa, S.Nishiyama, T.Yano, T.Kikuchi</i>	586-592
259	Numerical modelling of a small scale shallow foundation reinforced by Soil-Mixing <i>Anna Grzyb, Mahmoud Dhaybi and Frederic Pellet</i>	593-598
262	Physical modelling of a small scale shallow foundation reinforced by Soil-Mixing <i>Mahmoud Dhaybi and Frederic Pellet</i>	599-604
282	Prediction compressive strength of concretes containing silica fume and styrene-butadiene rubber (SBR) with a mathematical model <i>A.Hagholahi, M.Shafieyzadeh</i>	605-610
283	Sliding stability of dry masonry block retaining structure with a resistance plate <i>Akihiro Hashimoto, Noriyuki Yasufuku, Yoshio Suematsu, Kazuo Fujita1 and Toshimitsu Komatsu</i>	611-616
287	Evaluation and Prediction Method on Neutralization of Supplied Long-term Hydraulic Concrete Structure <i>Man-Kwon Choi , Yuki Hasegawa, Shinsuke Matsumoto, Shushi Sato and Tsuguhiro Nonaka</i>	617-621
297	Measurement of tensile properties of geogrids <i>Raid R. Al-Omari and Mohammed K. Fekheraldin</i>	622-631
306	Modeling the Swelling strain and pressure of Weak Rock using Adaptive Network-Based Fuzzy Inference System <i>Ramin Doostmohammadi</i>	632-636
309	Centrifuge Modeling Of Reinforced Embankments On Soft Foundation <i>Ali Sobhanmanesh, Nurly Gofar</i>	637-642
2102	Centrifuge model tests and finite element analyses on the seismic behavior of the quay walls backfilled with cement treated granulate soils <i>Hayano, K., Morikawa, Y., Fukawa, H., Takehana, K. and Tanaka, S.</i>	643-650
2109	Response of Piered Retaining Walls to Lateral Soil Movement Based on Numerical Modeling using Matlab <i>Siamak Pahlevanzadeh</i>	651-654
2122	Evaluation of Thermal Response Tests in Energy Piles <i>Seung-Rae Lee, Seok Yoon, Hyun-Ku Park , Gi-Dae Oh</i>	655-659
2134	Experimental Study on Mechanical Characteristics of Soil-Geosynthetic Interface <i>Md. Bellal Hossain, Md. Zakaria Hossain and Toshinori Sakai</i>	660-665

Contents of GEOMATE2012 - Volume 2(1)

2136	An Interpretation of Mechanical Properties of Bentonite as a Non-linear Elastic Material <i>Y. Takayama, S. Tsurumi, A. Iizuka, K. Kawai</i>	666-671
2149	Effect of carbonation on strength of cement treated sand <i>Kenichiro Nakarai and Tomomi Yoshida</i>	672-675
2167	Application of PML to Analysis of Nonlinear Soil-Structure-Fluid Problem using mixed element <i>Pahaiti Rehemani, Hiroo Shiojiri</i>	676-681

Environment

28	Recycled Bassanite as a Stabilizing Agent for Cohesion-less Soil <i>Aly Ahmed and Keizo Ugai</i>	682-687
31	The effects of environmental on today construction industry <i>Mahdy KhariI, Khairul Anuar Bin Kassim, Azlan Bin Adnan</i>	688-692
33	A Case History of Quay Wall Failure and Remedial Design <i>C. S. Chen</i>	693-696
37	Environmental economical efficiency in treatment/reutilization of construction sludges considering delay in process flow <i>Shinya Inazumi, Hiroyasu Ohtsu and Takayuki Isoda</i>	697-702
42	Evaluation and validation of elastic-fragile damage modeling for unsaturated porous media in θ -stock <i>B. Gatmiri , M. Fathalikhani</i>	703-708
43	Estimation of the Landslide Dam Sustainability in the Gigantic Seimareh Landslide Using the Rate of Sedimentation <i>Zieaoddin Shoaie</i>	709-7012
47	Influence of soil and rock mineralogy and geomorphology on Landslides Occurrence and soil erosion in the Merek Catchment, Iran <i>Mosayeb Heshmati , Nik Muhamad Majid, J. Shamshuddin, Arifin Abdu and Muhamad Ghaituri</i>	713-719
112	The effect of historical land use on landslide initiation <i>Gholamreza Shoaie</i>	720-723
114	Integrated Environmental Management for Sustained Development <i>J.Rajaraman and K.Thiruvenkatasamy</i>	724-729
114a	Lowland Environmental Geotechnology of Seismosediments of Kandla Port In India <i>J.Rajaraman and K.Thiruvenkatasamy</i>	730-735
123	Single step extraction to find out soluble lead in soil <i>Masahiko Katoh, Satoshi Masaki, Takeshi Sato</i>	736-741
127	Biogas Production from Tannery Sludge <i>A.Rajendra Prasad, A.Dhanalakshmi, S.Usha and A.Abdul Rahman</i>	742-746
131	Water Harvesting and Salinization Prevention by Capillary Barrier of Soil <i>Toshihiro Morii, Mitsuhiro Inoue, Kaoru Kobayashi, Tetsuya Suzuki and Takayuki Kawai</i>	747-752

Contents of GEOMATE2012 - Volume 2(1)

204	Study of the Performance of anaerobic digestion of greasy skim as a renewable energy source <i>Salam J. Bash Al-Maliky</i>	753-756
209	Seismic evaluation of NARGES soil nailed wall under Cyclic loading and Pseudo Static forces <i>Ardalan Akbari Hamed , Mohammad Moghadaripour , Ali Ghozat</i>	757-761
229	Purification System of Ocean Sludge by and Using Coagulants and then Activating Microorganisms <i>Kyoichi Okamoto and Kenji Hotta</i>	762-767
233	Mechanical properties of volcanic products mixed with industrial wastes <i>K. Yamamoto, T. Negami2, M. Hira, N. Aramaki and Y. Hayashi</i>	768-771
235	Measurement of Hydraulic Conductivity for Peat Ground Using CPTU <i>Hirochika Hayashi and Satoshi Nishimoto</i>	772-775
252	Extraction of temporal and spatial properties on habitat of snail by means of statistical approach <i>Masaaki Kondo and Takamitsu Kajisa</i>	776-781
265	The use of Nano Zero Valent Iron to remediation of contaminated soil and groundwater <i>Taghizadeh Maryam , Yousefi Kebria Daryoush and Gholamreza Darvishi</i>	782-785
267	A Multi-parameter Water Quality Analysis by onsite filtered 2mL Sample to Monitor Urban River Eutrophication <i>Akira Kikuchi, Nor Eman Ismail, Narges Janalizadeh, Musa Mutah and Muhamad Faiz</i>	786-790
268	The intelligent performance installations in energy efficiency in green buildings <i>Hooman Abadi, Rouzbeh Abadi, Poona Abadi</i>	791-796
271	Study the Effect of Polyvinyl Chloride (PVC) Addition on the Permeability of Anbar Soils <i>Ahmed H. Abdul Kareem & Omar Mustafa</i>	797-802
274	Monitoring deforestation and rangeland destruction through land use alteration during 1955- 2002, using GIS and RS in Merek sub-basin, west Iran <i>Mohammad Gheitury, Mosayeb Heshmati, Mohammad Ahmadi and Nik Muhamad Majid</i>	803-807
280	The comparison of phytoremediation and electrokinetic methods in remediation of petroleum hydrocarbons contaminated soil <i>Gholami Meade, Yousefi Kebria Daryoush</i>	808-811
286	Using Metacognitive Strategies On Listening Comprehension <i>Mahshid Mirzaaghaee</i>	812-822
298	Evaluation of Run-Off Supply Projects in Hamedan Province(Iran) <i>N. Rostam Afshar, M. Abdoli</i>	823-827
299	Protective measures of the monumental pine in Rikuzentakada with soil-water-air-solved material coupled model <i>Y. Sugiyama, S. Nomura, K. Kawai and A. Iizuka</i>	828-833
304	Effects of Biosurfactants in Electrokinetic Remediation of contaminated soils <i>Bour Moslem and Yousefi kebria Daryoush</i>	834-838
2117	Change in structure of ground-beetle assemblage on river areas after construction of biotopes using the technique, "Nature oriented river works" <i>Michko Masuda, Takaaki Tsukada and Fumitake Nishimura</i>	839-844

Contents of GEOMATE2012 - Volume 2(1)

2123	Dense granular-fluid mixture: the effects of the natural grains characteristics and the interstitial fluid viscosity <i>Anna Maria Pellegrino and Leonardo Schippa</i>	845-850
2131	Back-analysis of Frictional Jacking Forces Based on Shear Box Testing of Excavated Spoils <i>Choo Chung Siung and Dominic Ong E. L.</i>	851-856
2137	An idea of multi-functional reservoirs in mountain regions <i>Jan Jaremski</i>	857-862
2141	Estimation Method of Amount of Tsunami Disaster Wastes during the 2011 off the Pacific Coast of Tohoku Earthquake <i>Minoru Yamanaka, Naoya Toyota, and Shuichi Hasegawa, Atsuko Nonomura</i>	863-866
2143	Assessment of Runoff in the High Humid Foot-hill Areas of Arunachal Himalayas Using Thornthwaite Equation <i>Md. Eahya Al Huda and Surendra Singh</i>	867-871
2161	Natural Radiation level in Groundwater from Katsina, a Semi Arid Region of Northern Nigeria <i>B.G. Muhammad and M.S. Jaafar</i>	872-876
2163	Cost-Performance Studies of Abandoned Shell Husks (ASH) for Soil Reinforcement Applications <i>Md. Toriqul Islam, Md. Zakaria Hossain, Masaaki Ishida, Md. Bellal Hossain and Md. Jamal Uddin</i>	877-880
2171	Cyclones Path and Severities: Effect on Flood Height and Damages of Land and Embankments in Bangladesh <i>Musahaq Ali, Zakaria Hossain and Shigeko Haruyama</i>	881-884
	Author index	885

ISBN978-4-9905-9580-1
C3051 ¥5000E



定価 (本体5000+税)



- The “International Journal of GEOMATE” is a Scientific Journal the GEOMATE International Society that encompasses a broad area in Geotechnique, Construction Materials and Environment.
- The key objective of this journal is to promote interdisciplinary research from various regions of the globe.
- The editorial board of the journal is comprised of extensively qualified researchers, academicians, scientists from Japan and other countries of the world.
- It is peer-reviewed journal that is published quarterly. All articles published in this journal are available on line.
- For more details, please visit:
<http://www.gi-j.com/>

VOLUME 4
Number 1 & 2
March-June 2013

ISSN: 2186-2982 (Print)
ISSN: 2186-2990 (Online)
Serial 7 & 8

International Journal of GEOMATE

**Geotechnique, Construction
Materials and Environment**



Tsu, Japan

<http://www.gi-j.com/>
geomate@gi-j.com

THE GEOMATE INTERNATIONAL SOCIETY

GEOMATE 2014

**Fourth International Conference on
Geotechnique, Construction Materials & Environment**

19-21 November 2014

University of Southern Queensland, Springfield Campus, Brisbane, Australia

Invitation to participate

Geotechnique, Construction Materials & Environment

VOLUME 3(2)



**Edited by
Md. Zakaria Hossain
Hossain Md. Shahin**



GEOMATE 2013 NAGOYA, JAPAN
GEOTECHNIQUE, CONSTRUCTION MATERIALS AND ENVIRONMENT

PROCEEDINGS OF THIRD INTERNATIONAL CONFERENCE – GEOMATE 2013
GEOTECHNIQUE, CONSTRUCTION MATERIALS AND ENVIRONMENT NAGOYA, JAPAN
13-15 NOVEMBER, 2013

Geotechnique, Construction Materials and Environment

Edited by

Md. Zakaria Hossain
*Graduate School of Bioresources
Mie University*

Hossain Md. Shahin
*Graduate School of Engineering
Nagoya Institute of Technology*



THE GEOMATE INTERNATIONAL SOCIETY

Copyright @ 2013 by The GEOMATE International Society

All rights reserved. In principle, no part of this publication or the information contained herein may be reproduced in any form or by any means, translated in any language, stored in any data base or retrieval system, or transmitted in any form or by any means without prior permission in writing from the publisher.

Disclaimer: The editors and the publisher have tried their best effort to ensure the integrity and the quality of this publication and information herein. However, they give no warranty of any kind, expressed or implied with regard to the material contained in this book, and will not be liable in any event for the consequences of its use.

Published by:
The GEOMATE International Society
Tsu city, Mie, Japan
E-mail: geomate@gi-j.com
www.gi-j.com

ISBN Number: 978-4-9905958-2-1 C3051

Table of Contents

	Preface	x
	Organization	xi
ID	Keynote Papers	1
	GROUND DEFORMATION DURING AND AFTER EARTHQUAKES	2
1k	–SIMULATION AND PREDICTION BASED ON ELASTO-PLASTIC SOIL MECHANICS- Akira ASAOKA	
	USE OF RECYCLED AGGREGATES FROM CONSTRUCTION AND DEMOLITION WASTES FOR THE	12
2k	CONSTRUCTION OF FLEXIBLE PAVEMENTS Márcio Muniz de Farias, Alejandra María Gómez Jiménez and Ferney Quiñones Sinisterra	
	EFFECTIVE STRESS IN UNSATURATED GRANULAR MEDIA IN THE PENDULAR REGIME	24
3k	Richard Wan, Sarah Khosravani and Mehdi Pouragha	
	RECENT GEOTECHNICAL RESEARCH ADVANCES IN UNIVERSITY PUTRA MALAYSIA	32
4k	Bujang B.K.Huat and Afshin Asadi	
	Technical Papers Volume 3(1)	40-573
ID	Technical Papers Volume 3(2)	574
	DEVELOPMENT OF RAINFALL INFILTRATION INTO UNSATURATED SOIL COLUMN USING	
3120	ELECTRICAL CAPACITANCE VOLUME-TOMOGRAPHY (ECVT) Aniza Ibrahim, Muhammad Mukhlisin and Othman Jaafar	575
	SITE RESPONSE ANALYSIS TO DERIVE GROUND MOTION SIGNALS FOR ENGINEERING	
3126	APPLICATIONS Thayalan Nall, Greg Hackney and Harry Poulos	580
	A STUDY OF THE PARAMETERS AFFECTING THE PERFORMANCE OF ROADS UNDER AN EXTREME	
3131	RAINFALL EVENT Helen Fairweather and John Yeaman	586
	EFFECT OF STIFFNESS OF LOAD-BEARING LAYER ON RESISTANCE CHARACTERISTICS AT PILE TOE	
3167	OF STEEL PIPE PILE ON THIN LAYER Kazuhiro Oda and Shuhei Takegawa	592
	INFLUENCE OF SHEAR SPEED ON DIRECT SHEAR STRENGTH FOR COMPACTED BENTONITE WITH	
3186	DIFFERENT SOIL SUCTIONS Tomoyoshi NISHMURA and Junichi KOSEKI	598
	EFFECTS OF HYDROLOGICAL PARAMETERS ON DESERTIFICATION IN CHINA BASED ON THE	
3194	SATELLITE DATA Nozomu Hirose, Fengzhi DAI and Keiko Okada	604

3213	STRENGTH PARAMETER SELECTION IN STABILITY ANALYSIS OF RESIDUAL SOIL NAILED WALLS Atefeh Asoudeh and Erwin Oh	608
3231	TENSILE STRENGTH AND SUCTION OF SATURATED NSF CLAY AND THEIR RELATIONSHIPS WITH UC STRENGTH Surendra Bahadur Tamrakar and Toshiyuki Mitachi	613
3255	COUPLED ANALYSIS OF BIFURCATION AND SHEAR BAND IN SATURATED SOILS: EFFECT OF CHARACTERISTIC LENGTH SCALE Peijun Guo	619
3260	BEARING CAPACITY OF SOIL REINFORCED WITH SOIL-CEMENT COLUMNS FORMED BY THE DEEP MIXING METHOD Ahmad Safuan A Rashid and Jonathan A Black	625
3261	INTEGRATED QUALITY ASSURANCE AND CONTROL FOR DEEP SOIL MIXING IN WATERWAY PROJECT S.H. Chew, C.Y. Tan, T.Y. Yap, K.E. Chua, H.M. Yim, S.Y. Kee, T.K. Khoo and Ja Naw	631
3263	EMPIRICAL CORRELATION OF SHEAR WAVE VELOCITY AND N-SPT VALUE FOR JAKARTA Achmad Fauzi, Masyhur Irsyam, Usama Juniansyah Fauzi, and Muhammad Addifa Yulman	637
3265	ELECTRICALLY CONDUCTIVE GEOMEMBRANE ENHANCES LINER LEAK DETECTION SURVEYS AT POST INSTALLATION H.B. Ng, D. Gallagher and A. Beck	642
3266	INVESTIGATION OF CESIUM DIFFUSION IN CRACKED CONCRETE BY USING MICROFOCUS X-RAY CT Ivan Sandi Darma, Shohei Ikeda, Takafumi Sugiyama	646
3278	MODELLING THERMO-ELASTO-PLASTIC BEHAVIOUR OF NORMALLY CONSOLIDATED AND OVERCONSOLIDATED SOILS Yang-Ping Yao and Annan Zhou	652
3279	STABILITY OF A ROCK SLOPE SUSCEPTIBLE TO SEASONAL MOVEMENTS A. K. Alzo'ubi	658
3289	REAL-TIME BRIDGE SCOUR MONITORING SYSTEM BY USING CAPACITOR SENSOR S. M. A. Motakabber, M. I. Ibrahimy and A. H. M. Zahirul Alam	664
3291	SKIN FRICTION TESTS ON MODEL PILE IN WET SOIL Mohamed M. Shahin	667
3299	A NEW UPPER BOUND SOLUTION TO QUANTIFY THE ULTIMATE BEARING CAPACITY OF SHALLOW FOUNDATIONS ON RESTRICTED SOIL Reza Afshar-mazandaran, Hadi Khabbaz	673
3304	SOME THOUGHTS ON THE ULTIMATE RESISTANCE OF PILES Stephen Buttlng	679
3307	WIRELESS SENSOR NETWORK FOR LANDSLIDE MONITORING S. M. A. Motakabber, M. I. Ibrahimy and F. Anwar	685
3311	INFLUENCE OF THE SOIL-STRUCTURE INTERACTION ON THE SEISMIC BEHAVIOR OF BUILDINGS ON SHALLOW FOUNDATIONS Z. Benadla, K. Hamdaoui, S. Aissaoui and A. Baouch	688
3328	NUMERICAL STUDY OF PLASTICITY-BASED CONSTITUTIVE MODELS FOR SOIL IN SIMULATION OF BRACED EXCAVATION Samuel J. Verghese, Ha H. Bui	694

3339	A NUMERICAL MODEL TO PREDICT SETTLEMENT OF CHEMICALLY STABILISED LANDFILL Behnam Fatahi, Hadi Khabbaz	700
3340	SHEAR PROPERTIES OF HIGH-DENSITY BENTONITE-SAND MIXTURE UNDER UNSATURATED AND SATURATED CONDITIONS Takeshi Kodaka, Ying Cui and Hidenori Takada	706
3352	ENVIRONMENTAL CONDITION INDEX FOR ESTIMATION ON EUTROPHIC STATE OF ENCLOSED AQUIFER ECOSYSTEM Kazuhito Murakami, Michio Gomyo, Saki Agatsuma and Yoshimasa Amano	711
3170	SHALE FAILURE AND CRACKING IN A SEMI-ARID AREA Muawia Dafalla, Mutaz E. , Mansour Al humimidi, Loni Allafouza Oumar and Mosleh Al Shamrani	717
3300	EARTH MASONRY UNIT: SUSTAINABLE CMU ALTERNATIVE Joseph Dahmen, Jose F. Muñoz	721
3285	CONSTRUCTION AND MAINTENANCE OF EMBANKMENTS USING HIGHLY ERODIBLE SOILS IN THE PILBARA, NORTH-WESTERN AUSTRALIA J.V. Smith and L.A. Sullivan	728

Preface

On behalf of the GEOMATE 2013 Organizing Committee, it is our great pleasure to welcome you to the International Conference on Geotechnique, Construction Materials and Environment held at the Meitetsu New Grand Hotel, Nagoya, Japan organized in conjunction with Nagoya Institute of Technology, GEOMATE International Society, Japanese Geotechnical Society, AOI-Engineering, Useful Plant Spread Society, HOJUN and Glorious International. On Friday 11 March 2011, at 14:46 Japan Standard Time, the north east of Japan was struck and severely damaged by a series of powerful earthquakes which also caused a major tsunami. This conference was dedicated to the tragic victims of the Tohoku-Kanto earthquake and tsunami disasters. Since this is the third conference in this series, we have received a lot of positive feedback from the participants.

The conference covers three major themes with 17 specific themes including:

- Advances in Composite Materials
- Computational Mechanics
- Foundation and Retaining Walls
- Slope Stability
- Soil Dynamics
- Soil-Structure Interaction
- Pavement Technology
- Tunnels and Anchors
- Site Investigation and Rehabilitation
- Ecology and Land Development
- Water Resources Planning
- Environmental Management
- Public Health and Rehabilitation
- Earthquake and Tsunami Issues
- Safety and Reliability
- Geo-Hazard Mitigation
- Case History and Practical Experience

This year we have received many paper submissions from different countries all over the world, including Albania, Algeria, Australia, Bahrain, Bangladesh, Belarus, Benin, Canada, China, Colombia, Czech Republic, Egypt, Ethiopia, Germany, Hong Kong, India, Indonesia, Iran, Iraq, Japan, Kenya, Libya, Malawi, Malaysia, Norway, Poland, Romania, Russia, Saudi Arabia, Singapore, South Korea, Sri Lanka, Sudan, Taiwan, Thailand, Tunisia, Ukraine, United Arab Emirates, United States and Vietnam. The technical papers were selected from the vast number of contributions submitted after a review of the abstracts. The final papers in the proceedings have been peer reviewed rigorously and revised as necessary by the authors. It relies on the solid cooperation of numerous people to organize a conference of this size. Hence, we appreciate everyone who support as well as participate in the joint conferences. Last but not least, we would like to express our gratitude to all the authors, session chairs, reviewers, participants, institutions and companies for their contribution to GEOMATE 2013. We hope you enjoy the conference and find this experience inspiring and helpful in your professional field. We look forward to seeing you at our upcoming conference next year.

Best regards,

Prof. Teruo Nakai, Conference Chairman



Dr. Md. Zakaria Hossain, Conference General Secretary



Dr. Hossain Md. Shahin, Conference Secretary



Organization

Scientific Committees:

Conference Chairman: Prof. Dr. Teruo Nakai, Nagoya Institute of Technology, Japan

Conference Honorary Chairman: Emeritus Prof. Dr. Sohji Inoue, Mie University, Japan

Conference Organizing Committee:

Prof. Dr. Teruo Nakai, Nagoya Institute of Technology, Japan

Prof. Dr. Feng Zhang, Nagoya Institute of Technology, Japan

Prof. Dr. Kenichi Maeda, Nagoya Institute of Tech., Japan

E/Prof. Dr. Sohji Inoue, Mie University, Japan

A/Prof. Dr. H.M. Shahin, Nagoya Institute of Tech

A/Prof. Dr. Zakaria Hossain, Mie University

National Advisory Committee:

Prof. Dr. Fumio Tatsuoka, Tokyo University of Science, Japan

Prof. Dr. Toshinori Sakai, Mie University, Japan

Prof. Dr. Masaki Nakano, Nagoya University, Japan

Prof. Dr. Toshihiro Noda, Nagoya University, Japan

Prof. Dr. Jing-Cai Jiang, University of Tokushima, Japan

Prof. Dr. Noriyuki Yasufuku, Kyushu University, Japan

Prof. Dr. Masuya Hiroshi, Kanazawa University, Japan

Prof. Dr. Toshihiro Morii, Niigata University, Japan

Prof. Dr. Nishimura Tomoyoshi, Ashikaga Inst. of Tech., Japan

Prof. Dr. Yoshihiro Kimura, Tohoku University, Japan

Prof. Dr. Kimitoshi Hayano, Yokohama National Univ., Japan

A/Prof. Dr. Kenichiro Nakarai, Hiroshima University, Japan

International Advisory Committee:

Prof. Dr. Sai Vanapalli, University of Ottawa, Canada

Prof. Dr. M. Bouassida, National Sch. of Engg. of Tunis

Prof. Dr. L.R. Austriaco, Angles Univ. Found., Philippines

Prof. Dr. A.S.M. Abdul Awal, Univ. Technology Malaysia

Prof. Dr. M. Ibn Ibrahimy, Int. Islamic Univ., Malaysia

Prof. Dr. Md. Zahurul Islam, BUET, Bangladesh.

Prof. Dr. Bujang B.K. Huat, Univ. Putra Malaysia

Prof. Dr. Nemy Banthia, UBC, Canada

Prof. Dr. Ian Jefferson, Univ. of Birmingham, UK

Prof. Dr. John Bolander, Univ. of California, USA

Prof. Dr. Shamsul Chowdhury, Roosevelt Univ., USA

Prof. Dr. Isabel Pinto, University of Coimbra, Portugal

Prof. Dr. Mark Jaksa, University of Adelaide, Australia

A/Prof. Dr. Mohamed Shahin, Curtin University, Australia

A/Prof. Dr. Jim Shiau, Univ. of Southern Queensland Toowoomba

A/Prof.. Dr. Hj. Ramli Bin Hj. Nazir, UTM, Malaysia

A/Prof. Dr. Aly Ahmed, Beni-Suef University, Egypt

Dr. J.N. Mukabi, President of Kenya Geotech Soc., Kenya

Conference Secretariat:

Dr. H.M. Shahin, Secretary, A/Prof. NIT, Japan
Dr. Zakaria Hossain, General Secretary, A/Prof. MU, Japan
Mr. Musahaq Ali, Assistant Secretary
Division of Environmental Science and Technology
Graduate School of Bioresources
Mie University, 1577 Kurima Machiya-cho
Tsu-city, Mie 514-8507, Japan
E-mail: geomate@gi-j.com
Tel+Fax: +81-59-231-9578

Editorial Committee:

Dr. Md. Zakaria Hossain
Dr. Hossain Md. Shahin

Executive Committee:

A/Prof. Dr. Md. Zakaria Hossain
A/Prof. Dr. Hossain Md. Shahin
Prof. Dr. Teruo Nakai
E/Prof. Dr. Sohji Inoue
Mr. Musahaq Ali

Note- A: Associate, E-Emeritus

Technical Papers Volume 3(2)

DEVELOPMENT OF RAINFALL INFILTRATION INTO UNSATURATED SOIL COLUMN USING ELECTRICAL CAPACITANCE VOLUME-TOMOGRAPHY (ECVT)

Aniza Ibrahim^{1,2}, Muhammad Mukhlisin^{1,3} and Othman Jaafar¹

¹Department of Civil and Structural Engineering, Universiti Kebangsaan Malaysia,

²Faculty of Engineering, Universiti Pertahanan Nasional Malaysia,

³Department of Civil Engineering, Polytechnic Negeri Semarang, Indonesia.

ABSTRACT

Infiltration caused by rainfall will effect to the changes of moisture content and pore water pressure of the soil. These changes indicate the behavior of the soil especially during wetting and drying process, which leads to the soil instability especially slopes. The objective of this paper is to study the effect of rainfall intensity and duration to the image developed by ECVT during infiltration process. Normally, most of the studies of infiltration for unsaturated soil used time-domain reflectometer (TDR) and tensiometer that attached to the soil column to measure the parameters. This paper present the experimental result that not only obtaining the data of volumetric water content and pore water pressure, but also images of water infiltration throughout the column. This real time 3 dimension images were developed by Electrical Capacitance Volume Tomography (ECVT) that attached to the soil column. Type of soil used in this study is gravelly sand which is commercially obtained. Two types of simulated rainfall with designated duration were applied to the soil column. The result showed that the real time images were successfully performed throughout the wetting and drying process by ECVT. The 3 dimensional images show that the water infiltration pattern is responded with the gravelly sand. Other than real images, the normalized permittivity obtained can be used to obtained volumetric water content, which normally obtained by TDR in the infiltration study. This new technology is expected to enhance the understanding soil behavior especially in the area of water infiltration relates to soil instability.

Keywords: Infiltration, Pore water pressure, Soil column, ECVT, , Volumetric water content.

INTRODUCTION

There are several factors that caused soil instability; human activities especially on slope, rainfall, hillside development, and climatic condition such as geological features, topography, vegetation, or combination. For tropical country, high seasonal rainfall is the main reason for many slope instability event [1],[2]. In Malaysia, the residual soil is composed with the negative pore water pressure above the groundwater table, which vigorously subjected by climatic and hydrological changes such as precipitation, infiltration, evaporation and transpiration [8]. Therefore, these rainfall-induced slope failures are caused by the loss of pore water pressure of soils by rainwater [1],[6].

The mechanism of rain water infiltration into the soil event is complex due to its high nonlinearity of soil water characteristic and soil permeability [12]. Supported by [3] and [5], the complexity is concerning the parameters such as soil initial moisture condition, soil water retention ability, soil porosity, evaporation rate and others. For that reason, the desires to study the infiltration mechanisms are essential with the intention of understanding the behavior of soil under various

rainfall intensity and duration, with the rationale that the parameters mentioned can be achieved.

Soil column apparatus is widely known as an apparatus to perform simulate water infiltration into soil. This apparatus has been used extensively to facilitate understanding of rainfall infiltration mechanism. Normally, few equipments are attached to soil column to measure the parameters such as TDR and tensiometer. Even soil column apparatus can attained parameters related to rainfall induced soil instability, the parameters that obtained are at the point where the equipments are installed. The high quantity of equipment attached, more parameters obtained, and higher understanding of the soil behavior. As a result, there are limited space of locating TDR into the soil column. On the other hand, the result will measure only at the points where the equipments are installed.

ECVT is the innovative technology in civil engineering especially in geotechnical engineering research. Previously the principle of tomography was widely used for other area such as Magnetic resonance imaging (MRI), X-ray micro tomography, Optical tomography, resistive tomography, Acoustic tomography, Positron-emission tomography (PET), Capacitance tomography, and others [11]. ECVT is

the 3 dimensional real-time imaging system considered as " the most promising technique for dynamic flow imaging, which has a relatively high temporal resolution, up to few milliseconds , with reliable spatial resolution "[4].

The basic principle of ECVT is based on the measurement of electrical properties with forward and inverse problem [10]. Forward problem engage with the collection of capacitance data from electrodes to the data acquisition system. These electrodes act as sensors are located at the perimeter of ECVT wall vessel. Then, inverse problem will be conducted which including retrieving the capacitance data by personal computer. Subsequently, the measured data capacitance is used for the reconstructing images.

Previously, the principle of ECVT has been used to explore the transient occurrence in the entrance region of column using a single nozzle gas distributor with paraffin liquid, air, and glass beads as flow media [9]. In this research, these technique was proved to facilitate a real time 3D imaging of experiment perform for the moving object. On the other hand, [7] used ECVT to capture real time imaging of water infiltration that can be seen in each layer of the vessel.

The objective of this paper is to study the effect of rainfall intensity and duration to the image developed by ECVT during infiltration process. The imaging of 3 dimension real-time imaging is captured along the experiment, and the capacitance data is then converted to evaluate volumetric water content for the gravelly sand.

MATERIALS AND METHOD

Properties of soil

Soil used for the experiment was gravelly sand, and basic properties of the soil such as moisture content, porosity, and bulk density were determined in the laboratory. Other than that, saturated hydraulic conductivity, k_s was measured through constant head permeability test. Plate pressure extractor apparatus was used to measure Soil Water Characteristic Curve (SWCC) of the soil, which the result was fitted using Van Genuchten Method (1980). The results of soil properties are as in the Table 1.

Experimental set up

The infiltration test was conducted in a soil column apparatus which consists of water supply system, soil column, and percolation collection system.

Water supply system

Water flow regulator for rainfall simulation was used as a water supply in infiltration test. The pump which is manufactured by Cole-Parmer, model 07554-80 Masterflex L/S economy with variable-speed console and the speed are varies from 1 to 10, was attached with Masterflex L/S Easy –Load II pump heads.

Table 1: Soil Properties of Gravelly sand.

Soil Properties	Symbols	Gravelly Sand
Moisture content	θ_w	0.0013
Bulk density	g cm^{-3}	1.572
Saturated volumetric water content	θ_s	0.0883
Residual volumetric water content	θ_r	0.0313
Fitting parameters	α	1.2931
	n	1.4396
	m	0.3054
Saturated hydraulic conductivity (m/s)	K_s	6.333e-4

Soil Column Apparatus

The main component of soil column in this experiment was the ECVT apparatus system which include the vessel with sensors, data acquisition system, and the parameters can be retrieved by personal computer. Size of the vessel is 11.5 cm x 27 cm, and there are 32 pixel for all x, y, and z axes. Therefore, the length of vessel is divided by the total pixel resulted of 0.844 and 0.11 cm³ per voxel. The parameters were set to be logged for every 1 minute throughout the experiment.

Using the equation proposed by [7], the value of normalization permittivity, and volumetric water content can be determined.

Normalized permittivity,

$$\epsilon_N = \frac{\epsilon - \epsilon_{res}}{\epsilon_{sat} - \epsilon_{res}} \quad (1)$$

Volumetric water content,

$$\theta = \eta \left(\frac{\epsilon - \epsilon_{res}}{\epsilon_{sat} - \epsilon_{res}} \right)^{0.5} \quad (2)$$

where ϵ_N , ϵ , ϵ_{res} , and ϵ_{sat} are normalized, relative, residual, saturated permittivity respectively, and η is the porosity.

It is noted that the relative permittivity for air, water, residual soil , and saturated soil are 1, 80, 2-4, and 23-28 respectively.

However, the ECVT vessel which attached to the sensors cannot be intruded for assembling of TDR and tensiometer. Therefore, top of the vessel was extended with acrylic tube for this purposes. TDR used in this experiment was TRIME-IT Time domain Reflectometry with Intelligent MicroElements by IMKO Micro modultechnik GmbH. Other than that, mini tensiometer used was type T5, from UMS GmbH product. All data from ECVT, TDR and tensiometer were obtained through separately data acquisition system attached to the soil column for every ten minutes except from ECVT which was every 1 minute. The schematic diagram of the soil system component is illustrated in Figure 1.

Percolation Collector System

Water percolation collection system in this experiment was used to measure the discharge of rainwater through infiltration. Rainlog Datalogger by Rainwise was used to collect discharge from soil column. The 8 inches diameter collector tipping bucket will collect 0.01 inch/tip and 0.5 min/tip minimum and maximum respectively. This battery operated logger fits inside the polypropylene rain gauge and will measure the total rainfall at every ten minute. For this experiment, rain gauge was set for 0.01 inch/tip.

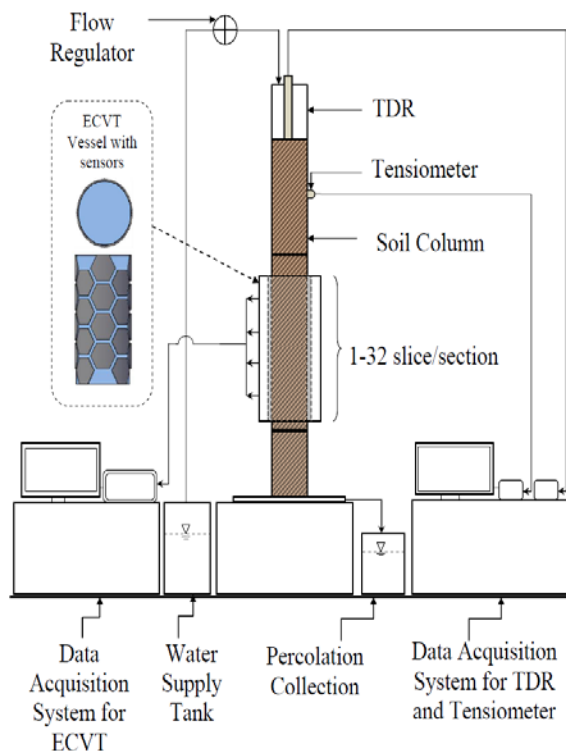


Figure 1 : Schematic diagram of soil column apparatus using ECVT

The experimental schedule

The infiltration tests were carried out with two simulated rainfall flow rate and durations. The first experiment was carried out with 1.93 mL/s flow rate, for 3 days. In addition, second experiment was done with 10 mL/s flow rate, for 1 day. 1 hour is allocated for drying process for each test respectively.

RESULTS AND DISCUSSION

ECVT images

3-Dimensional images

For the imaging of ECVT, there are 32 slices/sections produced for every frame. Total frame is indicated by the duration times for the experiment is conducted. In other word, there are 32 slices or sections per frame for 6347 minutes, which the total of 203,104 sections altogether from top to bottom of the vessel.

The example of the images captured by sensors as shown in Figure 2. The images that obtained were converted to the video, before slicing the sections to show the details of rainfall infiltration. In Figure 2, the normalized permittivity which indicates the value of zero approaching 1, was represented by the color code of red, orange, yellow, light blue, and blue.

In this example, infiltration of water was clearly verified by the Figure 2(a) to Figure 2 (h). As a start, the vessel was filled with soil, showed by the red color code. (Figure 2a). Figure 2(b) demonstrated blue color on the top of the vessel which indicated that water started to infiltrated into the vessel after simulated rainfall was applied. Then the water infiltration continued approaching bottom of the vessel, as proved in Figure 2 (c), and (d). In Figure 2(e), while the whole vessel was occupied by the water, but there was light blue color on the top of vessel, which indicated that the drying process was started on that particular sections. Subsequently, Figure 2 (f) and (g) suggested that the soil in the vessel continued to dried up after simulated rainfall has stopped. Finally, the color of the whole vessel was changed to red color indicated that soil in most of the sections was in drying process.

Volumetric Water Content(ECVT)

The parameter obtained from ECVT was normalized permittivity, which can be converted to relative permittivity for analysis. Equation (1) was used for conversion in the analysis. After obtaining relative permittivity, equation (2) was use to convert the value of relative permittivity to volumetric water content. Figure 3(c) shows the effect of rainfall infiltration to the volumetric water content for the

selected points along the height of ECVT vessel, which represent the differences among each level of vessel.

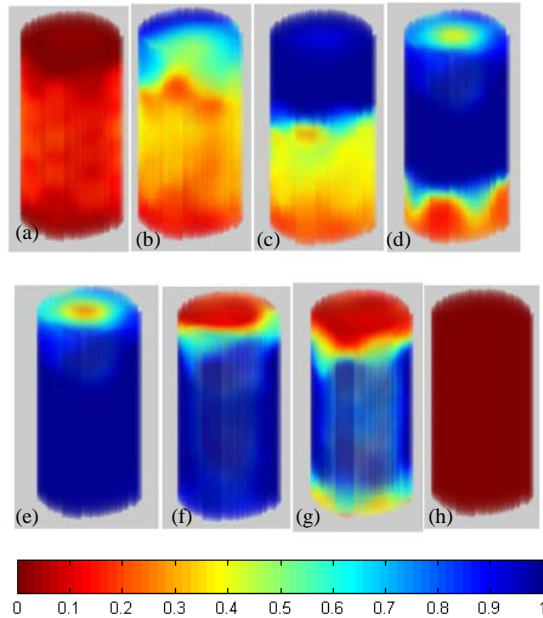


Figure 2: 3-Dimensional images of ECVT

The graph shows that the pattern of volumetric water content moves from the left to right side of the graph, proved that the water infiltration affect the value of volumetric water content. The volumetric water content increased when applying the first rainfall event, then decreased as drying process took place. In addition, the second rainfall event was also having the same pattern as the first event.

It was being observed that the middle section of the vessel achieve higher value of volumetric water content compared to others. This phenomena was perceived due to the fact that the water infiltrates into the soil, and trapped into the middle section, before leaving the section, and continue infiltrates into the bottom section. Other than that, the conditions was the effect of the soil porosity, rainfall intensity, and the soil capacity of holding water.

Pore water pressure (tensiometer) and percolation system

Other than results acquire by ECVT, the experiment also acquire results from the equipments attached to the soil column system. The TDR, and tensiometer were used to compare the pattern of parameters of volumetric water content and pore water content from ECVT. As shown in Figure 3(b), the result for pore water pressure has the same pattern of volumetric water content along the experiment. As rainfall was applied to the column,

water infiltrates into the soil resulted in decreasing the value of pore water pressure, but increasing while drying process. On the other hand, volumetric water content was increased while wetting, but decreased during drying process. For the percolation, Figure 3 (d) indicated the first drop of water at the 50.5 hours after the experiment started.

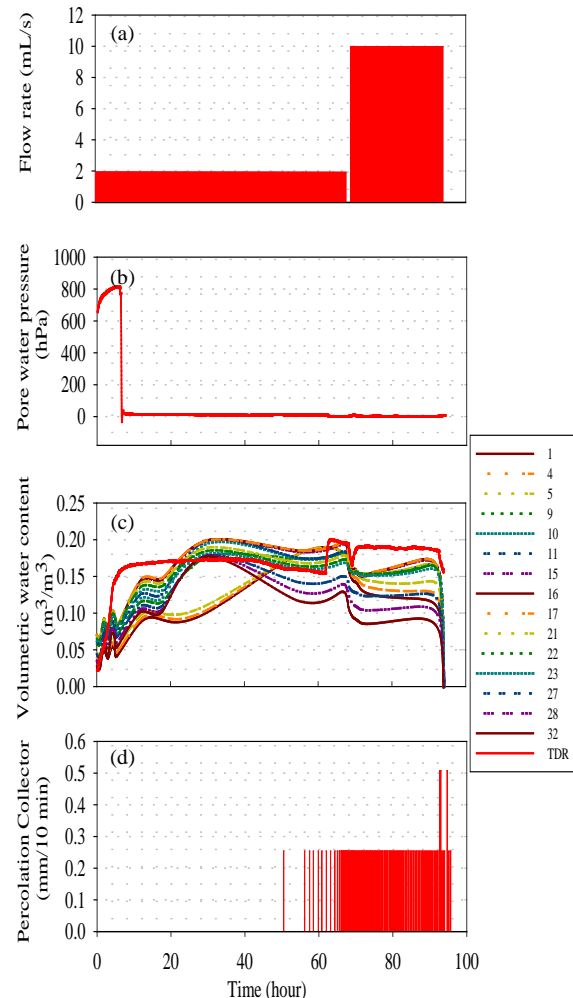


Figure 3: Relationship of (a)Flow rate, (b)Pore water pressure, (c)Volumetric water content, and (d)Percolation

CONCLUSION

In this study, one dimensional infiltration test using soil column was conducted in the two components; attaching TDR and tensiometers to the soil column, and using real time imaging of ECVT sensors. The analysis and results show that real time imaging of water infiltration can be captured by ECVT method. The 3 dimensional images produced the water infiltration pattern response with the gravelly sand.

Other than real images, the normalized permittivity obtained can be used to obtain volumetric water content, which normally obtained by TDR in the infiltration study. It is suggested that 2 dimensional images also can be produced in order to check the performance of the infiltration parameters at the points selected. Finally, this new technology is expected to enhance the understanding the complexity of soil behavior especially in the study of water infiltration.

ACKNOWLEDGEMENTS

The authors would like to express their appreciation to the financial supports provided by Universiti Kebangsaan Malaysia through ERGS/1/2012/TK03/UKM/02/2, and the Faculty of Civil Engineering and Built Environment.

REFERENCES

- [1] B. B.K, Ali F. H and Low T.H, "Water Infiltration Characteristics of Unsaturated Soil Slope and its Effect on Suction and Stability," *Geotechnical and Geological Engineering*, vol. 24, 2006, pp. 1293-1306.
- [2] Gofar N, Lee L. M, and Kassim A, "Instrumented Soil Column Model for Rainfall Infiltration Study," presented at the GEOTROPIKA 2008.
- [3] Lee L. M, Kassim A, and Gofar N, "Performance of Two Instrumented Laboratory Models for the Study of Rainfall Infiltration into Unsaturated Soils", *Engineering Geology*, vol. 117, 2011, pp. 78-89.
- [4] Marashdeh Q, Fan L.S, Du B, and Warsito W, "Electrical Capacitance Tomography - A Perspective," *Ind. Eng.Chem. Res.*, vol. 47, 2008, pp. 3708-3719.
- [5] Mukhlisin M, Kosugi K, Satofuka Y, and Mizuyama T, "Effects of Soil Porosity on Slope Stability and Debris Flow Runout at a Weathered Granitic Hillslope", *Vadose Zone J*, Vol 5, 2006, pp. 283-295.
- [6] Mukhlisin, M., and Taha, M.R., "Numerical Model of Antecedent Rainfall Effect on Slope Stability at a Hillslope of Weathered Granitic Soil Formation", *Journal Geological Society of India*, Vol 79, 2009 ,pp.525-531 .
- [7] Mukhlisin M, Saputra A, El-Shafie A, and Taha M. R, "Measurement of Dynamic Soil Water Content Based on Electrochemical Capacitance Tomography," *Int. J. Electrochem. Sci.*, vol. 7, 2012, pp.5457-5466.
- [8] Rahardjo H, Ong T.H, Rezaur R. B, Leong E.C, and Fredlund D.G, "Response Parameters for Characterization of Infiltration," *Environment Earth Science*, vol. 60, 2010, pp. 1369-1380.
- [9] Van Genuchten M.TH, "A Closed-form Equation for Predicting the Hydraulic Conductivity of Unsaturated Soils", *Soil Sci. Soc. Am. Journal*, vol.44(5),1980,pp. 892-898.
- [10] Warsito W and Fan L.S, "Dynamics of spiral bubble plume motion in the entrance region of bubble columns and three-phase fluidized beds using 3D ECT", *Chemical Engineering Science*, vol. 60, 2005, pp.6073-6084.
- [11] Warsito W, Marashdeh Q, and Fan L-S, "Electrical Capacitance Volume Tomography", *IEEE Sensors Journal*, vol. 7, 2007, pp.525-535.
- [12] Williams R. A and Beck M. S., 'Introduction to process tomography', *Process Tomography: Principles, Techniques and Applications.*, 1 ed.: Butterworth-Heinemann, 1995, pp.3-10.
- [13] Yang H, Rahardjo H, and Leong E. C, "Behavior of Unsaturated Layered Soil Columns during Infiltration," *Journal of Hydrologic Engineering*, July / August 2006, pp. 329-337.

SITE RESPONSE ANALYSIS TO DERIVE GROUND MOTION SIGNALS FOR ENGINEERING APPLICATIONS

Thayalan Nall¹, Greg Hackney² and Harry Poulos³
Coffey International, Australia

ABSTRACT

Design ground motions for earthquake related analyses are typically specified as 'rock outcrop' motions. Often they have to be modified for use as input signals at depth for engineering assessments of stress, strain and displacement. Modifications are often undertaken using a site response analysis with commercially available programs such as SHAKE, Proshake and Quake/W, which have been developed based on wave propagation techniques. This is seemingly a simple process; however is often the subject of considerable confusion. In a recent study, site response analyses have been undertaken to de-convolute and convolute free-field outcrop ground motion signals using Proshake. Convolved signals from various other commercially available and in-house programs were examined and compared. This paper outlines the concepts, discusses compatibility issues and presents examples illustrating the process and verification of the resulting input ground motion signals. This study highlights it is imperative that a suitable site response analysis is undertaken to arrive at an appropriate input signal for engineering applications. Further when two different programs are used care should be taken to ensure that material models and functions adopted are compatible.

Keywords: Site Response, Earthquake, De-convolution, Convolution, Acceleration-Time Signal

INTRODUCTION

For earthquake engineering assessments design earthquake ground motion signals are generally developed based on site specific Seismic Hazard Studies (SHS) and are usually presented as free field rock outcrop motions (i.e. the signal that would be measured by a seismograph positioned on a rock outcrop). However for seismic analyses, (finite element or semi-empirical methods), the seismic input must be relevant to the ground model and the location in the model that the signal is applied. For Finite Element Models (FEM), Acceleration-Time (A-T) functions are usually applied at the base of the model and for liquefaction assessments; the Peak Ground Acceleration (PGA) must be relevant to the liquefiable layer. This gives rise to the question: what input motion should be considered in order to adequately simulate the design ground motion?

In a recent study, site response analyses have been undertaken to de-convolute and convolute free-field outcrop ground motion signals to obtain a design input motion. De-convolution was performed using Proshake to obtain input signals for Dynamic PLAXIS modeling to assess earthquake-induced displacements. While convolution has been performed to validate the de-convolution process and assess compatibility between Proshake and PLAXIS, additional site response analyses were undertaken to examine and compare convoluted A-T signals from programs such as ERLS (Earthquake Response of Layered Soils, a Coffey in-house program), Proshake, PLAXIS and Quake/W, as each

method has fundamentally different mathematical formulations to solve for ground response.

FORMULATIONS

The formulations adopted for the various programs are described below:

ProShake is based on a frequency domain formulation. This method uses a Fast Fourier Transform (FFT) to convert the input motion from a time domain into a Fourier series in the frequency domain. The response at any location in the frequency domain can be obtained by using the input motion together with a transfer function. After computing the response in the frequency domain, the method uses an inverse FFT to transform the solution back to the time domain [1].

QUAKE/W is based on a finite element formulation which uses Wilson Theta integration scheme in the time domain. This does not involve transformation of the motion equations into the frequency domain and the motion equations are solved directly using a finite-difference time-stepping procedure [2].

PLAXIS is also based on a finite element formulation which uses a damped implicit Newmark integration scheme. The advantage of an implicit scheme is that it is more stable and less dependent on the chosen time step [3].

ERLS is a one-dimensional program that employs a forward marching explicit finite difference scheme in the time domain [4]. This is based on the lumped mass model as developed by

Seed and Idriss [5]. The basis of this model is the replacement of each soil layer with a series of lumped masses connected by strain-dependent springs and dash-pots.

NONLINEARITY OF MATERIALS

The characterization of dynamic material properties is a fundamental consideration in dynamic site response analyses. It is well known from laboratory testing that soils exhibit pronounced nonlinear behavior under shear loading conditions. Shear modulus decreases with increasing strain and is accompanied by an increase in material damping. As this behavior is applicable to *in situ* geotechnical materials subjected to earthquake loading, site response calculations need to accommodate strain dependent nonlinearity of stiffness and damping.

Although it has been long recognized that there are problems such as sample disturbance and laboratory tests that do not exactly simulate the dynamic stress path caused by shear waves in the frequency range up to 20Hz, various parametric relationships have been proposed based on laboratory test results for use in dynamic analysis. Each nonlinear model has its advantages and limitations in describing the response of soil to the type of loading produced by seismic disturbances. The goal of the de-convolution and convolution exercise through site response analysis is to estimate the appropriate base input motion to the model such that the design outcrop motion is recovered at the top of rock (outcrop) level. Within the PLAXIS model, the nonlinear Hardening Small Strain (HSS) model was adopted [6]. Both Proshake and Quake/W have the flexibility of user defined strain dependent shear modulus and material damping functions [2], [7]. However in ERLS, the coefficients of reference parameters were adjusted to arrive at similar strain dependent relationships [4].

PLAXIS and Quake/W also have the capability to incorporate pore pressure build up and dissipation [2], [3]. In the site response analysis described herein this capability was used only in PLAXISTM by adopting the 'Undrained A' drainage model. All other programs used a total stress approach.

DYNAMIC ANALYSIS IN PLAXIS

Dynamic PLAXIS (2-D) has been used as the primary tool in a study to assess earthquake induced stress, strain and displacement for an earth and rock structure in an active earthquake zone. A key focus of the site response analysis was to establish appropriate A-T signals as inputs into the modeling. Earthquakes are usually modeled by means of prescribed horizontal displacements at the base of the model, while maintaining zero vertical

displacements. To assess earthquake induced parameters in relation to those mobilized at the base of the model, input ground motion signals are generally modified to yield zero displacement. PLAXIS adopts an 'absorbent' boundary to absorb incremental stresses caused by dynamic loading and to avoid reflection into the soil body [3].

SITE DESCRIPTION AND INPUT DATA

The subject site comprised a complex profile of marine, alluvial and variable strength rock to considerable depth, which would be used to support an earth-and rock structure, as described in Figure 1.

A-T signals as rock outcrop motions (for material having a shear wave velocity (V_s) of 1000m/s) were obtained for the site from the SHS. For the dynamic analysis, ground conditions down to 450m depth were modeled. Broadly, this profile comprised 115m of sediments and weak rocks, underlain by two distinct high strength rock layers. The upper rock layer is approximately 135m thick and was characterized by V_s value of 1000m/s. The lower rock layer is approximately 200m thick and is characterized by a V_s value of 1200m/s. A site response analysis was undertaken to de-convolute the outcrop A-T signals through the two high strength rock layers to obtain suitable input signals at the base of the model.

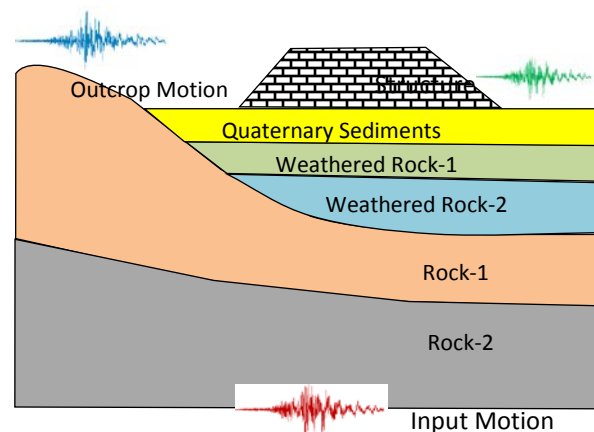


Fig. 1 Earthquake Ground Motions

NONLINEAR MODEL IN PLAXIS

Functions for shear modulus and material damping used in the PLAXIS model are described briefly.

Strain Dependent Shear Modulus

To characterize the degradation of the shear modulus of soil and rock with strain, PLAXIS uses a hyperbolic law proposed by Santos & Correia [8]

which is a modified version of the Hardin & Drnevich [9] relationship. The function is defined using the small-strain shear modulus (G_0) and the shear strain ($\gamma_{0.7}$) at which the secant shear modulus (G_s) reduces to about 70% of G_0 .

$$G_s = G_0 / (1 + 0.385 \gamma / \gamma_{0.7}) \quad (1)$$

PLAXIS, incorporates a lower cutoff shear modulus at G_{ur} , so that the stiffness reduction curve does not extend far into the plastic region. G_{ur} and cutoff strains are computed as per the expressions below.

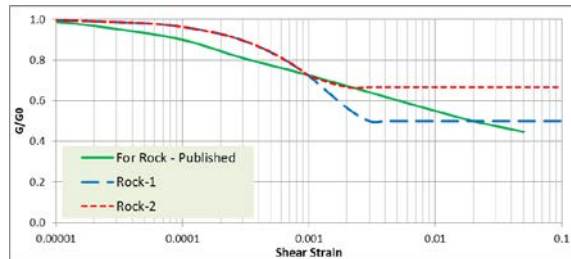
$$G_{ur} = E_{ur} / 2(1 + \nu_{ur}) \quad (2)$$

$$\gamma_{(cut-off)} = a(G_0 / G_{ur} - 1)^{0.5} \quad (3)$$

$$a = \gamma_{0.7} / 0.385 \quad (4)$$

Therefore in PLAXIS in addition to G_0 and $\gamma_{0.7}$, the ratio G_0 / G_{ur} is user defined to establish the shear modulus verses shear strain relationship. The strain dependent modulus reduction function adopted in the analysis, along with a published reduction function [10], is shown in Figure 2.

Fig. 2 Shear Modulus Reduction Function



Stress Dependent Shear Modulus

At each analysis step, PLAXIS updates the material shear modulus based on stress state. This stress dependent shear modulus is implemented by a power law, as given below.

$$G_0 = G_{0ref} \{ (\sigma'_3 \sin\phi + c \cot\phi) / (\sigma_{ref} \sin\phi + c \cot\phi) \}^m$$

The stress dependency of the G_0 is incorporated in the other programs by dividing the layers into number of sub-layers of thickness 4m and 5m for Rock-1 and Rock-2 respectively and assigning each layer a G_0 computed as per the above power law.

Strain Dependent Material Damping

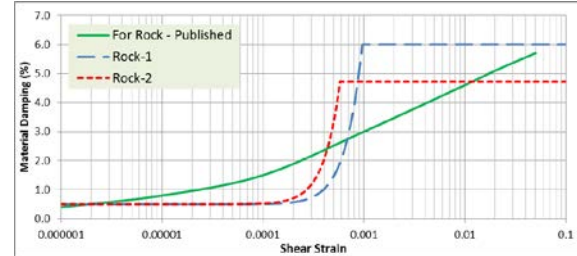
PLAXIS incorporates hysteretic material damping in addition to viscous damping [11]. The hysteretic damping is estimated as the ratio of energy dissipated between each cycle of loading (E_D) and maximum strain cycle (E_s). Hysteretic damping increases with increasing shear strain as shear modulus decreases, but remains constant as soon as the cutoff modulus G_{ur} is reached.

$$D_h = E_D / (4\pi E_s) \quad (6)$$

$$E_D = 4aG_0 \{ 2\gamma_c - \gamma_c / (1 + a/\gamma_c) - 2a \ln[1 + (\gamma_c/a)] \} \quad (7)$$

$$E_s = G_0 \gamma_{(cut-off)}^2 / (2 + 2a\gamma_{cut-off}) \quad (8)$$

At small strains, hysteretic damping is insignificant. PLAXIS incorporates viscous damping through Rayleigh damping parameters. For this study, a viscous damping ratio of 0.5% has been adopted and the Rayleigh parameters α and β were estimated based on the natural site period (T_s). The strain dependent material damping adopted in the



analysis is shown in Figure 3, together with a published damping function [10].

Fig. 3 Material Damping Function

DE-CONVOLUTION USING PROSHAKE

As the SHS did not consider upper soil or weak rock layers in the derivation of the design outcrop motions, it was considered reasonable not to consider these in the de-convolution analysis. The 'rock outcrop' level was considered as the top of the high strength Rock-1, which was evident around RL 880m (site datum), whilst mean sea level is RL 1000m (site datum). The base of the analytical model was at RL 550m (site datum). The ground model considered in de-convolution process is shown schematically in Figure 4.

De-convolution was performed using the program Proshake considering the two provided horizontal components (H1 and H2) of the design earthquake.

The outcrop earthquake signals used are shown in Figures 5 and 6, while the de-convoluted motions obtained through site response analyses at the base level of the model are shown in Figs 7 and 8.

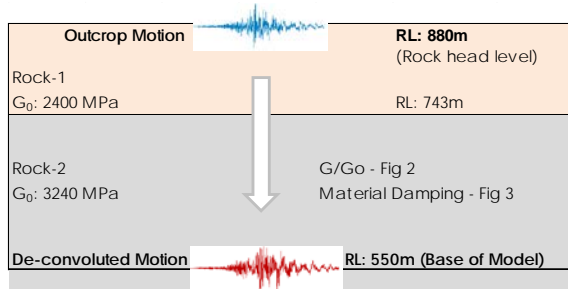


Fig. 4 Ground Model

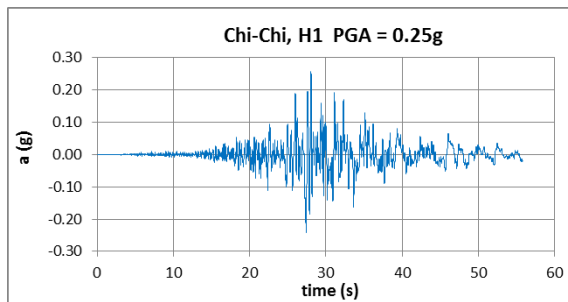


Fig. 5 Outcrop Earthquake Ground Motion H1

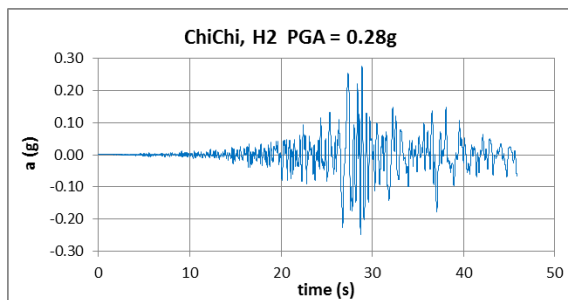


Fig. 6 Outcrop Earthquake Ground Motion H2

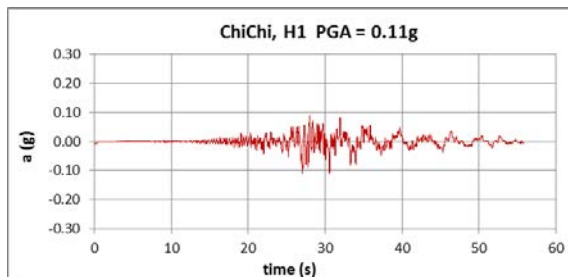


Fig. 7 De-Convolved Ground Motion H1 (RL 550m)

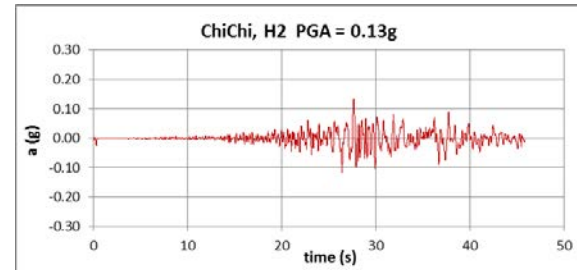


Fig. 8 De-Convolved Ground Motion H2 (RL 550m)

These analyses indicated that there was a significant reduction in the amplitude of the de-convoluted ground motion signal. Given the potential influence on the measured earthquake induced stresses, strains and displacements, a validation process to convolute the base motion signals was undertaken using PLAXIS to compare and assess the ground motion signal recovered at the rock outcrop level.

CONVOLUTION USING PLAXIS

In these analyses, the de-convoluted A-T signals were applied on a prescribed displacement boundary at the base of PLAXIS model. The ground model was constructed with the two rock layers and the analyses were performed using the HSS constitutive model with modulus reduction and material damping as discussed above. The convoluted A-T signals measured at the top of the model were then compared with the design outcrop earthquake motions shown in Figures 5 and 6. These details are given in Figures 9 and 10.

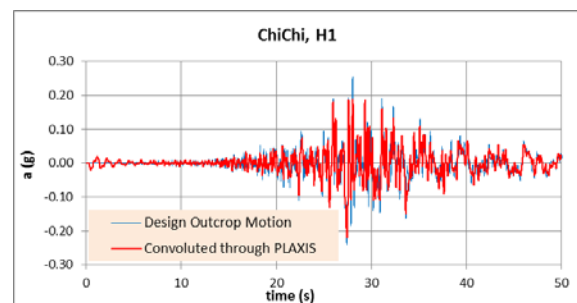


Fig. 9 Comparison of Earthquake Motion H1 (Outcrop Motion)

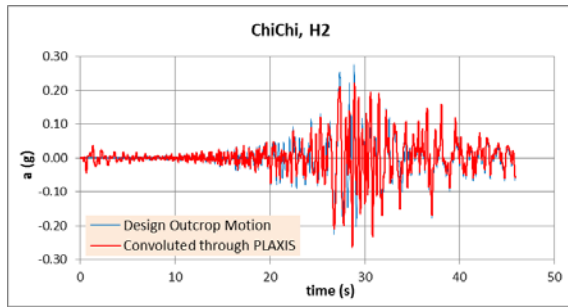


Fig. 10 Comparison of Earthquake Motion H2 (Outcrop Motion)

Convolved A-T signals obtained through above analyses show reasonably close agreement with the design outcrop signals. To further verify the process, acceleration response spectra of the convolved and outcrop earthquake ground motions were compared and are shown in Figures 11 and 12. These functions show close agreement, providing a high level of confidence in the site response process and the use the de-convoluted A-T signals for assessment of other earthquake induced parameters using PLAXIS.

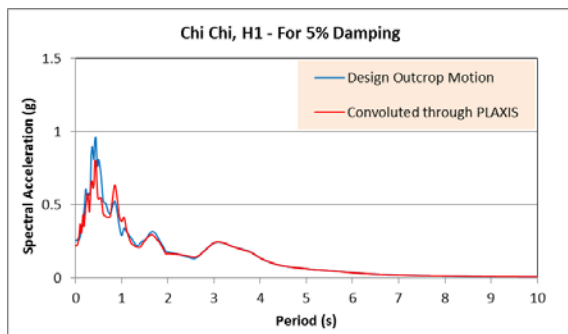


Fig. 11 Response Spectra Earthquake Motion H1

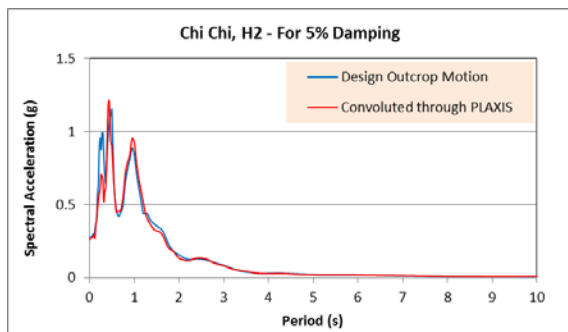


Fig. 12 Response Spectra Earthquake Motion H2

COMPARISON WITH OTHER PROGRAMS

The study was extended to compare de-convoluted A-T signals from other programs such as Quake/W and ERLS. For these assessments, the de-convoluted A-T signals from Proshake were used as input ground motions. Shear modulus degradation

and material damping functions as per the PLAXIS and Proshake models were adopted, except in ERLS, where the cutoff modulus G_{ur} and damping could not be incorporated. The functions employed in ERLS are shown in Figures 13 and 14.

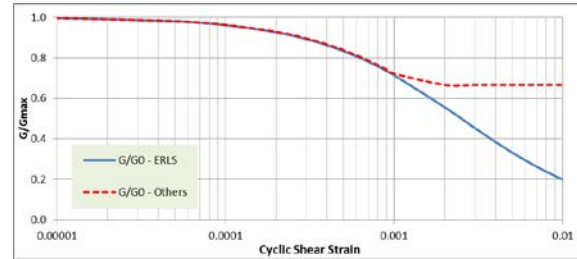


Fig. 13 Implemented G/G_0 Functions

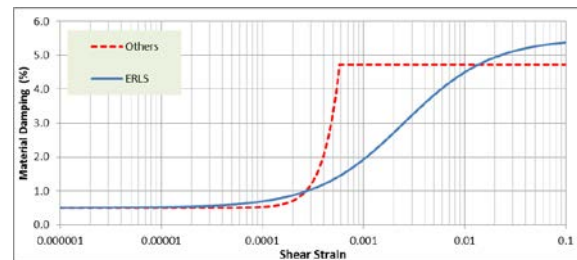


Fig. 14 Implemented Material Damping

Computed A-T signals are shown in Figures 15 and 16 along with the design outcrop earthquake motion for comparison. The results indicate good agreement in spite of the varying mathematical formulations used.

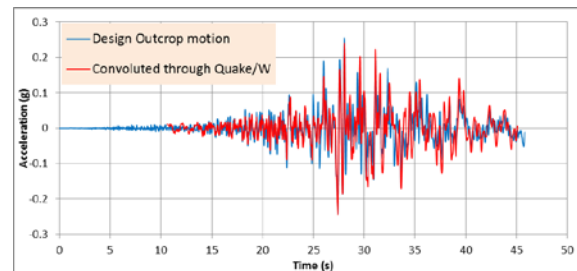


Fig.15 Quake/W Convolved Earthquake Motion H2

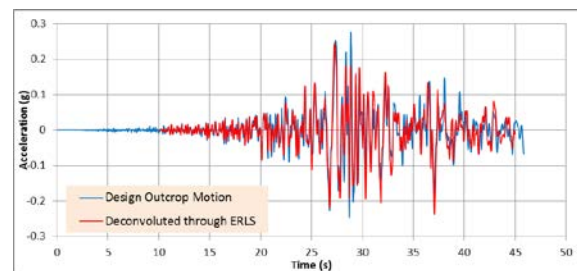


Fig. 16 ERLS Convolved Earthquake Motion H2

CONCLUSION

This study highlights the relevance of site response analysis in earthquake engineering assessments. As input of an earthquake motion into PLAXIS is generally achieved through a prescribed displacement boundary at the base of the model, it is imperative that a suitable site response analysis is undertaken to arrive at an appropriate input signal. Depending on the available design or target earthquake signals, they may have to be either de-convoluted or convoluted to arrive at input earthquake ground motions.

Few commercially available site response programs can perform de-convolution of signals; but all have the capability to convolute the signals to the surface and within layers at higher elevations. Except for PLAXIS and Quake/W, the others programs considered herein are 1-D programs and are suited for horizontally layered strata. PLAXIS and Quake/W are multi-faceted and their site response capability is only a secondary module. As a result they involve more computation time and require more storage capacity. For this study, Proshake was used successfully to perform de-convolution of earthquake ground motion signals to obtain input signals for PLAXIS and arrive at Peak Ground Acceleration parameters in the upper soil layers for pseudo static and liquefaction susceptibility analyses.

It is important that, when two different programs are used (i.e. one to obtain input earthquake signal and the other to obtain earthquake induced displacement) care should be taken to ensure that material models and functions adopted are compatible and that the target earthquake signal is recovered at designated levels in the subsequent analysis.

From the comparative A-T plots presented, it is evident that PLAXIS, Proshake, Quake/W and ERLS are remarkably close, considering that these packages are based on different theoretical formulations. Whilst there are some differences, it is hard to identify any one formulation being more accurate than the others.

REFERENCES

- [1] Kramer SL "Geotechnical Earthquake Engineering" Prentice Hall, Upper Saddle River, New Jersey, 1996.
- [2] Geo-Slope international Ltd, "Dynamic modeling with Quake/W – an engineering methodology" 2012.
- [3] PLAXIS, "Material Model Manual" 2012.
- [4] Coffey Partners International Pty Ltd, "Earthquake response of layered soils – User guide" 1991.
- [5] Seed HB, and Idriss IM. "Soil moduli and damping factors for dynamic response analyses" 1970, Report No. EERC 70-10, Earthquake Engineering Research Center, University of California, Berkeley.
- [6] Schanz T, Vermeer PA, Bonnier PG, "The hardening soil model: Formulation and verification" in proc. Beyond 2000 in computational geotechnics, 1999, Balkema, Rotterdam, pp. 281-290.
- [7] EduPro Civil Systems, "Proshake user's manual version 1.1", 2005.
- [8] Santos JA, Correia AG, "reference threshold shear strain of soil" in 15th International Conference on Soil Mechanics and Geotechnical Engineering, 2001, Istanbul Turkey, vol. 1, pp. 267-270.
- [9] Hardin BO, Drnevich VP, "Shear modulus and damping in soil" Proc. ASCE: Journal of the Soil Mechanics and foundation Division, 1972, 98(SM7), pp. 667-692.
- [10] Schnabel PB, Lysmer J, and Seed HB "SHAKE: A computer program for earthquake response analysis of horizontally layered sites" Report No. EERC 72-12, Earthquake Engineering Research Center, University of California, Berkeley, California 1972.
- [11] Brinkgreve RBJ, Kappert MH, Bonnier PG, "hysteretic damping in a small-strain stiffness model" in Proc. NUMCOG X, pp. 737-742.
- [12] Seed HB, Wong RT, Idriss IM, and Tokimatsu K "Moduli and damping factors for dynamic analyses of cohesionless soils" Journal of Geotechnical Engineering, ASCE, 1986, Vol. 112, No. 11, pp. 1016-1032.
- [13] Kokoshu T, "Cyclic triaxial test of dynamic soil properties for wide strain range", Soils and Foundations, 1980, Vol. 20, No. 2, pp. 45-60
- [14] Dobry R, and Vucetic M, "Dynamic properties and seismic response of soft clay deposits", Proceedings, International Symposium on Geotechnical Engineering of Soft Soils, 1987, Mexico City, Vol. 2, pp. 51-87.

A STUDY OF THE PARAMETERS AFFECTING THE PERFORMANCE OF ROADS UNDER AN EXTREME RAINFALL EVENT

Helen Fairweather and John Yeaman

Faculty of Science, Health, Education & Engineering, the University of the Sunshine Coast, Australia

ABSTRACT

Sunshine Coast Regional Council has recently upgraded a section of Sippy Downs Drive adjacent to the University of the Sunshine Coast campus. Prior to opening, the pavement was instrumented to monitor strain and moisture in the surface and the subgrade layers and the temperature under the surface layer. At the time of installation, traffic was light, as University classes had not yet commenced. Traffic increased when classes commenced in February 2013 and is projected to grow substantially as a new suburb and two major shopping centres are built over the next three years. Data are recorded every minute and downloaded by mobile phone connection every 24 hours. These data are analysed automatically every day. Six weeks after opening, a major rainfall event occurred with nearly 500mm of rain recorded over three days. The paper discusses the impact on pavement strain as a function of changing moisture content and temperatures. These data have potential for identifying future maintenance requirements.

Keywords: Pavement Monitoring, Subgrade, Asphalt Pavements

INTRODUCTION

The Sunshine Coast Council undertook an upgrading of Sippy Downs Drive adjacent to the University of the Sunshine Coast (USC) during 2012. The road works included a duplication of the carriageway, the installation of traffic lights at the main entrance to the University, an upgrade of the secondary entrance and street scaping including drainage incorporating Water Sensitive Urban Design (WSUD) installations.

The purpose of the road works was not only to provide improved access to the university for the ever burgeoning student population but also to cater for future traffic demands of the growing Sippy Downs Township. This township includes a planned new suburb of 50,000 residents and two major shopping malls.

During late 2011, Engineering at USC was seeking projects for students completing their final year in Civil Engineering. These major projects are equivalent to a 0.5 study load conducted over a full year. The projects are designed to test the student's knowledge gained over the previous three years of study. In addition the project thesis should be as demanding as a Science Honours Thesis, which is conducted over a full year.

Engineers with the Sunshine Coast Council agreed that the Sippy Downs road works provided a suitable site to install instrumentation to assess pavement performance parameters under operational conditions. An additional advantage of the Sippy Downs site is that it will be under the influence of increasing traffic (volumes and loads) over the next five to ten years.

This report is limited to an analysis of data received from the instruments at the site between the 24th and 28th January 2013 during a cyclonic rainfall depression.

The configuration of the instruments also fits in with the research being undertaken by a Higher Degree (by research) student whose study is "Intelligent Highway Engineering and Maintenance Optimisation". Therefore the data being collected will be utilised by this student over the next three years. It is anticipated that further final year undergraduate engineering projects will also be possible using this site over the coming years.

EXPERIMENTAL DESIGN

The first undergraduate engineering student working on this project in 2013 was tasked with sourcing preferred equipment and arranging its

installation into the pavement. The aim of the monitoring is to determine the pavement performance as a function of strain and moisture measured at two locations (bottom of the bound layer and top of the subgrade layer) and pavement temperature underneath the bound layer.

The instrumentation and road works were completed in December 2012 and monitoring commenced on the 19th December. Over the Australia day long weekend (25th to 28th January 2013) a cyclonic rainfall depression passed through Sippy Downs with total rainfall over the period of three days of nearly 500mm. During this period the monitoring station remained operational and continued to provide details of the strain, moisture and temperature every minute.

STUDY BACKGROUND

The objective of this study is to understand the behaviour of a newly constructed section of road under extreme weather conditions. Achieving this objective will provide the basis to use this study site to further investigate pavement behaviour under real traffic conditions.

Traditionally pavement performance has been tested using Accelerated Pavement Testing (APT) facilities. These facilities generally include a heavy vehicle simulator [1]-[2].

Instrumentation of pavements in-situ is a relatively new advancement, but has mostly been limited to a localised and short-term installation [3]. These authors are developing a smart monitoring system using a 'pebble' sized strain sensor. The size of this sensor and the development of a reliable long-term energy supply will eventually allow a multitude of these sensors to be installed during construction [3]. However, to date, it appears that this system has only been installed in a test facility.

MONITORING THE TEST SITE

The pavement under test is part of a major upgrading of Sippy Downs Drive (Fig. 1). During the construction it was decided to instrument the pavement so that the parameters affecting pavement performance could be monitored continuously.



Fig. 1 Test site location, Sippy Downs Drive, Queensland.

The test site is on the upstream direction from the traffic lights at the intersection and in the outer wheel path of the median lane. It is now recognised that this may not be the optimum position as the traffic is relatively fast moving. In addition the surface layer of this lane may not be fully compacted due to the closeness of the kerb and concern of the roller operator that damage may occur to the gauges.

From observations, this lane receives the least traffic except in peak periods such as start and finish times at the adjacent school and university. In hind-site the optimal position would be where the traffic is slower moving and is generally concentrated.

Notwithstanding the above limitations, measurements being taken every minute of every day provide considerable data for analyses. Data are being streamed to the writers' desks on a daily basis, with updated data being streamed every three minutes for strain and moisture content and temperature.

Monitoring Equipment and Placement

The configuration of the instrumentation and data logger are described below with the indicated depths all measured from the top of the asphalt. The centres of the strain gauges are at depths of 115mm and 395mm in the surface and subgrade layers, respectively. The moisture content gauges are placed at the bottom of the surface and subgrade layers at depths of 395mm and 670mm, respectively. The temperature sensor is installed in the surface layer at a depth of 70mm.

Data logger

The key to the data collection facility is the data logger. For this installation a dataTaker DT82EM Series 3 Data Logger was chosen as it has several desirable features; ultra-low power design, integrated cellular modem, automatic data transfer to email or FTP, support for up to 10 SDI-12 sensors, and can house up to 6 (30V) sensor units.

The software associated with this equipment provides a continuous and visual data feed. The logger is configured so that each morning the previous day's data is emailed direct to the researcher's computer. This process has enabled real time processing of the 1400 lines of data from 5 transducers, with the ability to upgrade to more transducers as deemed necessary.

Strain transducer KM 5000

The KM series strain transducers are designed to measure strain in materials such as concrete and pavement layers. Their extremely low modulus ($40 \frac{\text{N}}{\text{mm}^2}$) and waterproof construction make them ideal for this type of test. The built in thermocouple sensor in the surface layer measures temperature in addition to strain. Both strain gauges were embedded in the pavement vertically.

The installation of the strain gauges was according to the manufacturers' convention. For vertical installation, the manufacturer advised positive strain (+ve) indicates values in compression and negative values (-ve) indicates value in tension.

Soil moisture content sensor

For this study the Theta probe ML2X was chosen as the preferred instrument for measuring moisture. The measurement accuracy of this probe is quoted at $\pm 1\%$ with a measurement range of up to 50% volumetric moisture content. This capability was considered ideal for this study.

Power source

The whole system is powered by a 13.5 long-life battery charged by a solar panel; Steca Solsum Range - 6.6F, Solar Charge Regulators, 12/ 24 V, load current 6A, with LVD 1 Solarwatt Solar panels rated at 40W.

LOGGING AND CALIBRATING THE DATA**Equilibrium Moisture Content**

From the 19th December 2012 through to the 23rd January 2013 (43 days) a period of stable hot and dry weather conditions dominated. The readings (at one minute intervals) for this period were analysed to determine if this stability translated to a stable moisture content measured in each of the layers.

The optimum moisture content for each of the unbound component materials is 8.6% [4]. The moisture content measured over the 43 day hot and dry period is considered to provide the equilibrium state. The average moisture content over this period was 15% and 18% from the surface layer and subgrade layers, respectively. An analysis of the 6300 moisture contents measured during the hot and dry period indicated reasonable consistency as the baseline for detecting changes in moisture content with time (Table I).

Table I Equilibrium moisture contents

Layer	Mean	Std Dev	C of V
Surface	15.5%	0.69%	4.4%
Subgrade	18.5%	0.51%	2.8%

Calibration of Strain Data

In an attempt to relate the strain measurements to axle loads, a calibration exercise was undertaken on the 6th March 2013. The Sunshine Coast Council provided a single axle, dual tyre truck loaded with 8.2 tonnes on the rear axle. Tyres were inflated to 760 KPa. This unit made 10 passes over the test site between the hours of 9:30AM and 10:30AM and again between the hours of 1:30PM and 2:04PM. These times were chosen as this is when the pavement appears to be generally at the median of the temperature regime. The strains, moisture contents and temperature were recorded for each pass (Table II).

Considering only the 'TEST TRUCK' results shown in Table II, the temperature in the morning test run increased from 27 to 28°C. During this time the strain in the surface layer varied from -23 to -30µε for a moisture content stabilised at ~18.1%. For these runs, the strain in the subgrade layer varied from -4 to -9µε for a relatively steady moisture content of ~18.74%.

For the afternoon runs, and again considering only the 'TEST TRUCK' results in Table II, the surface temperature increased from 33.7 to 34.4°C. The corresponding surface layer strain increased from -81 to -84µε (tension), while the moisture content remained steady at ~18.03%. In the subgrade layer the strain ranged from -51 to -54µε, for a moisture content steady at 18.79%.

During the calibration test two other heavy different vehicles drove over the instrumentation

and these results are recorded in Table II for interest. The very large strains recorded when the TEST TRUCK was parked on the test site for 3 minutes (-971 and -305µε in the surface and subgrade layers, respectively) indicates the impact of this static load is greater in the surface, though the change in the subgrade layer is substantial.

Table II Calibration data collected on the 6th March 2013 using a vehicle with a known load (TEST TRUCK)

Time	Surface layer			Subgrade layer		Remarks
	Strain (µε)	Moisture (%)	Temperature (°C)	Strain (µε)	Moisture (%)	
9:48:00	-24	18.1	27.0			TEST TRUCK
10:06:23	-27	18.2	27.6	-4	18.76	TEST TRUCK
10:14:25	-55	18.1	27.8	-23	18.74	Truck with Excavator
10:17:32	-35	18.1	27.8	-9	18.74	TEST TRUCK
10:23:25	-23	18.1	28	-7	18.74	TEST TRUCK
10:30:30	-57	18.1	28.1	-20	18.74	Bus followed by TEST TRUCK
13:30 to 13:33	-971	18.03	33.5	-305	18.79	TEST TRUCK parked on site for 3 minutes
13:36:33	-84	18.03	33.7	-53	18.79	TEST TRUCK
13:43:24	-82	18.03	33.9	-51	18.79	TEST TRUCK
14:03:38	-81	18.04	34.4	-54	18.79	TEST TRUCK

EXTREME WEATHER EVENT RESULTS AND DISCUSSION

Australia Day Weekend, 2013

Between commissioning of the equipment on the 19th December 2012 and 24th January 2013, a period of high temperatures and zero rainfall was experienced at the site. During this period the streetscape planting of grasses, trees and shrubs was watered manually.

Rainfall

From the 25th to 28th January a cyclonic depression passed over the site with high winds and large rainfall amounts recorded (Table III). Over the five days the total rainfall recorded was 479mm.

Table III Rainfall at Sippy Downs during the cyclonic depression in January 2013

Day	Date	Rainfall (mm)
Thursday	24 th	42
Friday	25 th	52
Saturday	26 th	92
Sunday	27 th	198
Monday	28 th	95

Moisture content

In the surface layer the moisture content was stable, fluctuating between 16.5 to 17% on the 24th and 25th January. The moisture content rose rapidly from 5:00PM on the 26th January to a

maximum of 20% at 4:30PM on the 28th and falling to 18.3% by 9:00AM on the 29th January (Fig. 3).

Similarly, the subgrade layer had a stable moisture content fluctuating between 17.8 to 17.9% between the 23rd and 25th January. The moisture content in the subgrade layer rose steadily from about 2:00PM on the 27th January to a maximum of 19.6% at 3:00PM on the same day (Fig. 4).

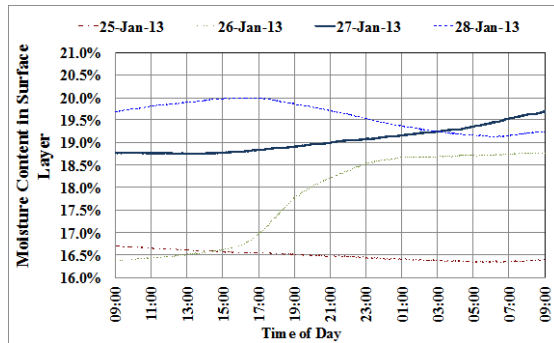


Fig. 2 Surface layer moisture contents recorded over the period 24th to 29th January 2013.

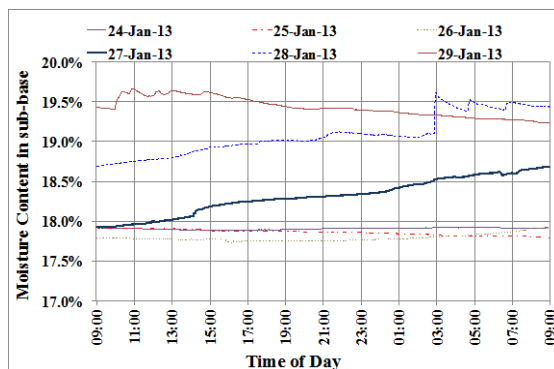


Fig. 3 Subgrade layer moisture contents recorded over the period 24th to 29th January 2013.

Temperature

The temperature of the surface layer varied from a minimum of 35°C at 9:00AM and maximum of 51°C at 4:30PM on the 24th January. From the 26th to the 29th January the temperature remained relatively constant fluctuating between 27°C and 29°C (data not shown).

Surface layer temperatures averaged ~42°C prior to the event. However, during the event the average dropped to ~25°C. The temperature returned to the pre-event average on the 29th January. This behaviour prompted a further evaluation of the respective influence of temperature and moisture on the critical strains.

Critical Strains

During this cyclonic event the surface layer strain moved from compression to tension on the 25th January. The surface layer strain returned to compression on the 31st January (after the extratropical cyclone event).

At the time of the above surface layer strain changes, the subgrade strain moved from compression to tension with a maximum tensile strain of around 60µε on the 29th January. Subgrade strain showed signs of recovery by the 30th January after which no further rainfall was recorded (Fig. 4).

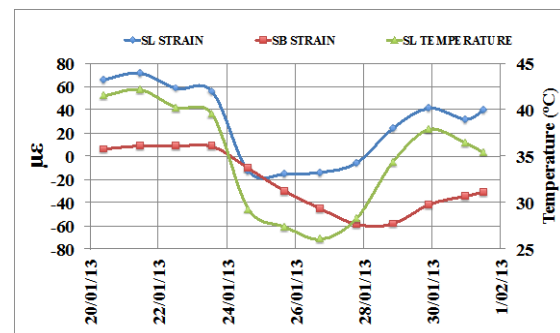


Fig. 4 Surface layer strain (SL STRAIN, blue diamond and line) and temperature (SL TEMPERATURE, green triangle and line) and subgrade strain (SB STRAIN, red square and line) measurements.

Strain and moisture content relationships

There is reasonable correlation between surface layer strains and change in moisture ($R^2=0.31$), at a constant temperature. The surface layer strains increase in tension with increasing moisture content, when both variables are averaged over a constant temperature (Fig. 5).

The correlation between the strain and moisture in the subgrade layer is slightly higher ($R^2=0.58$), with the strain increasing in tension as moisture content rises (Fig. 5). Again a constant temperature is used to average strain and moisture content.

There is good correlation ($R^2=0.73$) between the strain in the subgrade layer and the surface layer moisture (both averaged over constant temperature). The strain in the subgrade layer increases in tension as surface layer moisture content increases (figure not shown).

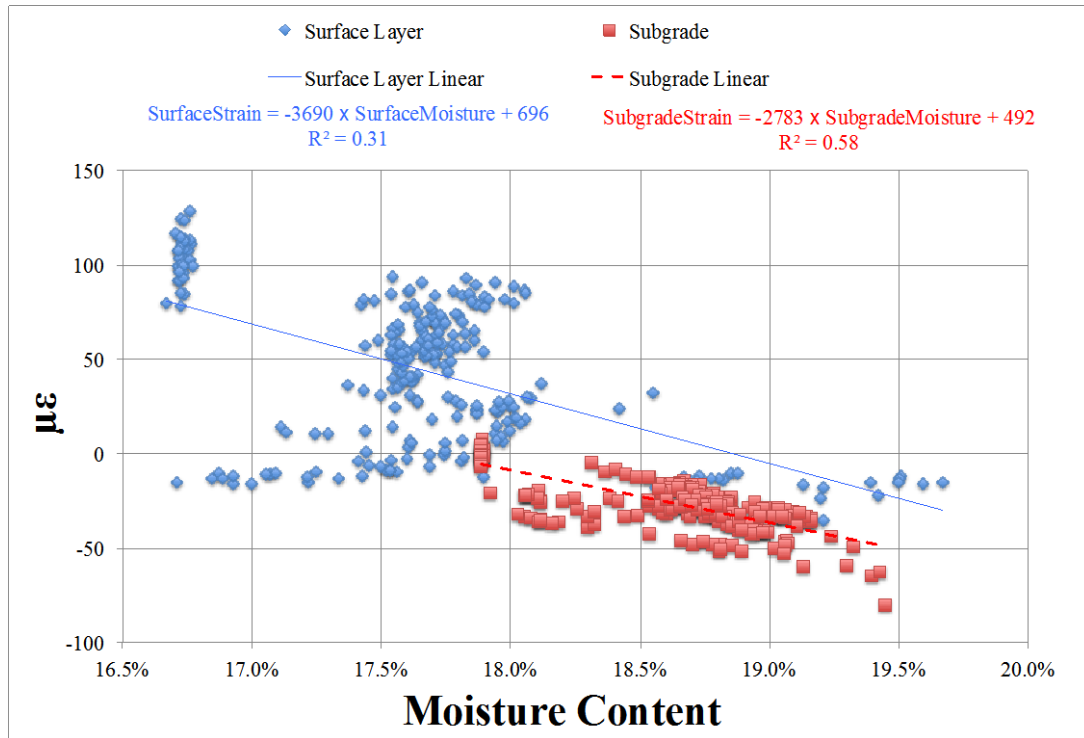


Fig. 5 Strain as a function of moisture content (averaged over constant temperatures) for surface and subgrade layers.

Strain and temperature relationships

There is a strong relationship between surface layer strain and temperature ($R^2=0.85$), with strain becoming increasingly positive with increasing temperature. At temperatures above $\sim 32^\circ\text{C}$ the strain switches from tension (-ve) to compression (+ve) (Fig. 4).

The relationship between the strain in the subgrade layer and surface layer temperature is not strong ($R^2 = 0.20$).

CONCLUSIONS

An extreme weather event over a four-day period provided an opportunity to assess the potential damaging effect to a roadway from known critical damage determinants. These determinants are tensile strains at the underside of the bound pavement and compressive strains on the subgrade.

The collected data showed that in the surface layer the temperature is a key determinant of pavement performance. The strains in the subgrade layer were seen to be predominately in tension irrespective of surface layer temperature.

There is only a small correlation between surface layer strain and moisture. A stronger

correlation was observed between the strain and moisture in the subgrade layer.

Further research will develop methods to utilise these data to more precisely predict pavement failure and therefore better target road maintenance.

REFERENCES

- [1] Chen D, Zhou F, Cortez E "Determination of load damage relationships through Accelerated Pavement Testing", J of Testing and Evaluation, ASTM, Vol. 34, Jul. 2006, pp. 312-318.
- [2] Chen T, Chang J, Chen D, "Applying data mining technique to compute LDE for rutting through full scale Accelerated Pavement Testing", Road Materials and Pavement Design, Vol. 9. 2, 2008, pp. 227-246.
- [3] Lajnef N, Rhimi M, Chatti K, Mhamdi L and Faridazar F, "Toward an integrated smart sensing system and data interpretation techniques for pavement fatigue monitoring", Computer-Aided Civil and Infrastructure Engineering, Vol. 26, 2011, pp. 513–523.
- [4] Cardno Bowler, Density and moisture ratio test results, "Unpublished", Report Number 3747/R/2157-1, 2012.

EFFECT OF STIFFNESS OF LOAD-BEARING LAYER ON RESISTANCE CHARACTERISTICS AT PILE TOE OF STEEL PIPE PILE ON THIN LAYER

Kazuhiro Oda¹, Shuhei Takegawa²

^{1,2} Graduate School of Engineering, Osaka University, Japan

ABSTRACT

It has been known that the sufficiently stiff layer can be considered as a load-bearing layer of piles, even if its thickness is thin. The authors have studied the toe bearing resistance of pile on a thin load-bearing layer, in order to establish the design method about pile on a thin load-bearing layer. In this paper, the effect of stiffness of load-bearing layer on characteristics of toe resistance of steel pipe pile on a thin load-bearing layer is discussed through a series of numerical simulations. First, a field loading test of steel pipe piles with a concrete bulb on a thin load-bearing layer is reproduced through the numerical simulations, in which a soil-water coupled with an elast-plastic finite element method is applied, to confirm the availability of the numerical analysis proposed. Second, a series of numerical simulations are carried out in which the deformation modulus of the load-bearing layer is chosen as a variable parameter. The results of the numerical simulations show that the stiffness of load-bearing layer does not remarkably affect the resistance when the yielding of load-bearing layer occurs.

Keywords: Steel pipe pile, stiffness of load-bearing layer, Load-bearing resistance at the pile toe, Thin load-bearing layer, Numerical simulation

INTRODUCTION

Most big cities in Japan have been constructed on Holocene plains. In general, such plains are composed of sand or sandy gravel layers and thick clay layers what accumulated alternatively. A stiff and thick layer which can be considered as load-bearing layer for piles could not be found in many cases. In particular, it has become more difficult to find a sufficiently stiff and thick load-bearing layer because a large number of pile foundations with large diameters have been constructed recently.

The appropriate estimation of toe bearing resistance of pile on a thin load-bearing layer can give the economical advantage for construction of pile foundations. The authors have studied the characteristics of toe bearing resistance of pile on a thin load-bearing layer in order to establish the design method about pile on a thin load-bearing layer. It is elucidated that the toe bearing resistance of pile on a thin load-bearing layer is affected significantly by the thickness of load-bearing layer in the case where it is less than 3 times pile diameter. Also, the yielding of thin load-bearing layer must be dominated by the punching shear failure [1], [2], [3].

In this paper, the effect of stiffness of load-bearing layer on the characteristics of toe resistance of pile on a thin load-bearing layer is elucidated through a series of numerical analyses. First, a field loading test of steel pipe piles with a concrete bulb on a thin load-bearing layer is reproduced through numerical simulations, in which a soil-water coupled with an elasto-plastic finite element method is applied. Second, a series of numerical simulations are carried out in which the deformation modulus of

the load-bearing layer is chosen as a variable parameter. The effect of stiffness of load-bearing layer on characteristics of toe bearing resistance of pile on a thin load-bearing layer is discussed by focusing on both the relationship resistance and displacement at pile toe and the development of local failure in the bearing ground.

TEST PILE AND FIELD LOADING TEST

Figure 1 shows the configuration of the instruments that were used to measure the displacement of pile with a concrete bulb, the displacements of bearing ground below the concrete bulb, and the axial force [4]. As shown in Fig.1 (a), a standard penetration test (SPT) was carried out to investigate the ground conditions at the southeast part of the Osaka Bay area. Based on the results of the SPT, it was found that the ground is composed of alternate layers of clay and sand or sandy gravel. The sand layers that show an N-value of more than 50 in the SPT were found to have a thickness of less than 2 m, which indicates that no clear load-bearing layer is available.

The tested pile was a steel pipe that is 34 m in length and 1 m in diameter, with a concrete bulb that is 1 m in length and 1 m in diameter. The length of the embedded part of the pile is about 27.9 m. The pile was born on a sand layer that is 0.9 m thick, which is underlain by a stiff clay layer. First, the pile was installed by a combination of inner excavation and penetration into the ground, until the pile toe reached the bearing ground. Second, the ground below the pile toe was excavated and a cavity was created in the bearing ground. Third, a cement mix

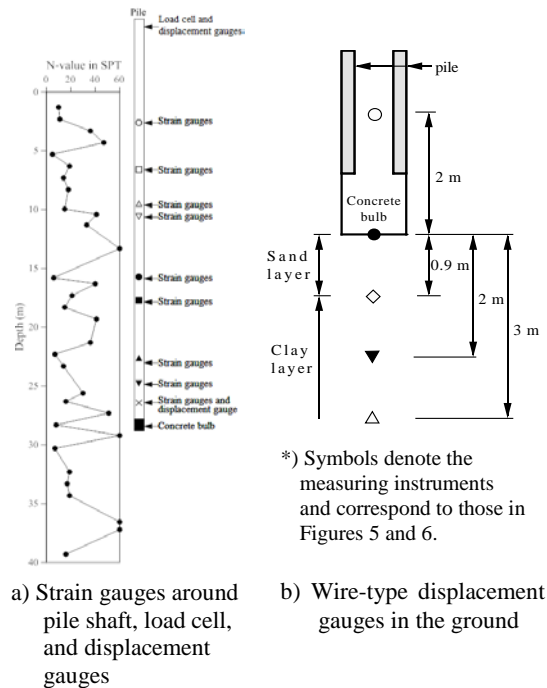


Fig.1 Configuration of instruments used to measure the displacement of pile with concrete bulb, the displacements of the bearing ground below the concrete bulb, and the axial force

with high pressure of about 20 MPa was injected into the cavity, creating a concrete bulb below the pile toe.

The load and displacement at the pile head were measured by a load cell and a displacement gauge. A displacement gauge was also set up at the pile toe. The displacements of the concrete bulb and the bearing ground below the concrete bulb were measured by wire-type displacement gauges. Strain gauges were also set up around the pile shaft. The axial force, which is denoted by symbols, was calculated from the measured strain. The axial force, which was calculated from the measurements of the strain gauges closest to the pile toe, was defined as the pile toe load.

ANALYTICAL MODEL

A soil-water coupled elasto-plastic finite element method with an axisymmetric condition was used in the numerical simulation. Figure 2 and Table 1 show the analytical model and the values of the soil parameters used in the simulation, respectively. The soils were fundamentally modeled as elasto-plastic materials to realistically reproduce the complicated behavior of the ground. The steel pipe pile and the concrete bulb were modeled as being composed of elastic materials. For almost all sandy soils, the *tij*-sand model, which was proposed by Nakai [5], was used, provided that soil stresses did not reach the

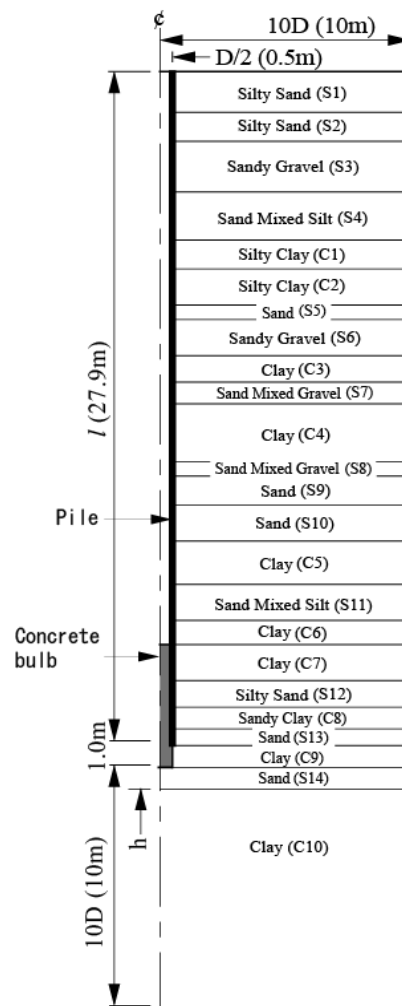


Fig.2 Analytical model

failure threshold of the model. When the stresses did reach the failure threshold, the constitutive model of sandy soils was replaced with the Drucker-Prager model. For clayey soils, an elasto-plastic model proposed by Matsui and Abe [6] was used. When the stresses reached the failure threshold of the elasto-plastic model, the constitutive model of clayey soils was replaced with the von Mises model. A joint element proposed by Goodman et al. [7] was used to represent the discontinuity between pile and soil.

The soil parameters used in the numerical simulation were determined from data from soil investigations that included the SPT and unconfined compression test. Few parameters were reasonably rearranged to fit the results of the numerical simulation to the field measurements.

RELIABILITY OF NUMERICAL ANALYSIS

Figure 3 shows the relationship between the applied load and the displacement at the pile head. In the analytical relationship between the applied load and displacement, the slope of the analytical

Table 1 Values of soil parameters used in the analysis

Division	Model	Parameters
S1	Elasticity	$E = 18.9 \text{ MPa}$, $\nu = 0.2$
S2	Elasticity 2	$E = 37.8 \text{ MPa}$, $\nu = 0.2$
S3	Elasticity 3	$E = 72.5 \text{ MPa}$, $\nu = 0.2$
S4	Elasticity 4	$E = 15.8 \text{ MPa}$, $\nu = 0.2$
C1	Elasticity 5	$E = 18.9 \text{ MPa}$, $\nu = 0.2$
C2	Elasticity 6	$E = 25.2 \text{ MPa}$, $\nu = 0.2$
S5	Elasticity 7	$E = 31.5 \text{ MPa}$, $\nu = 0.2$
S6	Elasticity 8	$E = 72.5 \text{ MPa}$, $\nu = 0.2$
C3	Matsui-Abe model	$\lambda = 0.0360$, $\kappa = 0.00899$, $M = 1.635$, $\nu = 1/3$, $\eta_{k0} = 0.75$
S7	tij-sand model	$C_t = 8.77 \times 10^{-3}$, $C_e = 6.20 \times 10^{-3}$, $m = 0.3$, $\alpha = 0.90$, $R_e = 5.83$, $D_f = -0.36$, $\nu = 0.325$
C4	Matsui-Abe model	$\lambda = 0.0450$, $\kappa = 0.00563$, $M = 1.551$, $\nu = 1/3$, $\eta_{k0} = 0.75$
S8	tij-sand model	$C_t = 1.90 \times 10^{-2}$, $C_e = 1.35 \times 10^{-2}$, $m = 0.3$, $\alpha = 0.85$, $R_e = 4.49$, $D_f = -0.3$, $\nu = 0.325$
S9	tij-sand model	$C_t = 5.93 \times 10^{-2}$, $C_e = 4.19 \times 10^{-2}$, $m = 0.3$, $\alpha = 0.65$, $R_e = 3.36$, $D_f = -0.15$, $\nu = 0.325$
S10	tij-sand model	$C_t = 2.56 \times 10^{-2}$, $C_e = 1.48 \times 10^{-2}$, $m = 0.3$, $\alpha = 0.85$, $R_e = 4.56$, $D_f = -0.20$, $\nu = 0.325$
C5	Matsui-Abe model	$\lambda = 0.0257$, $\kappa = 0.00642$, $M = 1.551$, $\nu = 1/3$, $\eta_{k0} = 0.75$
S11	tij-sand model	$C_t = 6.43 \times 10^{-2}$, $C_e = 3.71 \times 10^{-2}$, $m = 0.3$, $\alpha = 0.55$, $R_e = 2.49$, $D_f = -0.15$, $\nu = 0.325$
C6	Matsui-Abe model	$\lambda = 0.0692$, $\kappa = 0.0173$, $M = 1.179$, $\nu = 1/3$, $\eta_{k0} = 0.75$
C7	Matsui-Abe model	$\lambda = 0.0309$, $\kappa = 0.00773$, $M = 1.551$, $\nu = 1/3$, $\eta_{k0} = 0.75$
S12	tij-sand model 6	$C_t = 4.80 \times 10^{-2}$, $C_e = 2.77 \times 10^{-2}$, $m = 0.3$, $\alpha = 0.75$, $R_e = 3.89$, $D_f = -0.18$, $\nu = 0.325$
C8	Matsui-Abe model	$\lambda = 0.0592$, $\kappa = 0.0148$, $M = 1.221$, $\nu = 1/3$, $\eta_{k0} = 0.75$
S13	tij-sand model	$C_t = 5.99 \times 10^{-2}$, $C_e = 4.14 \times 10^{-2}$, $m = 0.3$, $\alpha = 0.80$, $R_e = 4.02$, $D_f = -0.20$, $\nu = 0.325$
C9	Matsui-Abe model	$\lambda = 0.1021$, $\kappa = 0.00681$, $M = 1.551$, $\nu = 1/3$, $\eta_{k0} = 0.75$
S14	tij-sand model	$C_e = 4.94 \times 10^{-2}$, $m = 0.3$, $\alpha = 0.90$, $R_e = 4.60$, $D_f = -0.45$, $\nu = 0.325$
C10	Matsui-Abe model	$\lambda = 0.247$, $\kappa = 0.0124$, $M = 1.418$, $\nu = 1/3$, $\eta_{k0} = 0.75$

curve changes at about 3 MN of the applied load at the pile head. Then, the slope of analytical curve becomes gradually steeper with an increase in the applied load at the pile head. Finally, the analytical displacement of the pile head significantly increases at an applied load of about 4.8 MN. It is considered that the resistance of the pile head at this load level is closer to the ultimate bearing resistance of the test pile.

Figure 4 shows the relationship between the resistance and displacement at the pile toe. The slope of the analytical curve hardly changes up to a

resistance of about 1.8 MN. The analytical displacement then significantly increases at a load level of about 1.8 MN. It is found that the yield of the resistance and displacement behavior at the pile toe occurs at this load level.

Figure 5 shows the axial force distribution of the test pile. The numerical simulation reasonably reproduces the friction behavior around the pile shaft.

Figure 6 shows the relationship between the resistance at the pile toe and the displacements in the underlying bearing ground, in addition to that of the

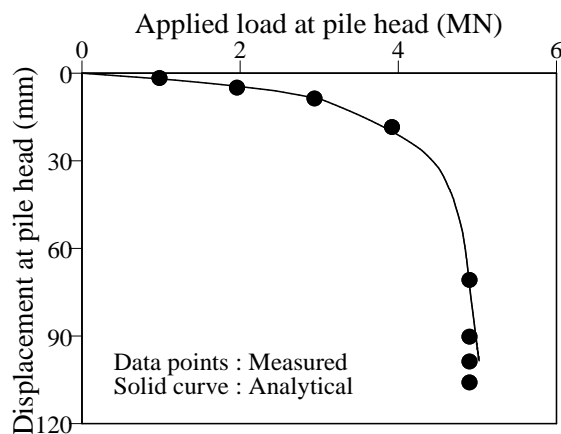


Fig.3 Relationship between applied load and displacement at pile head

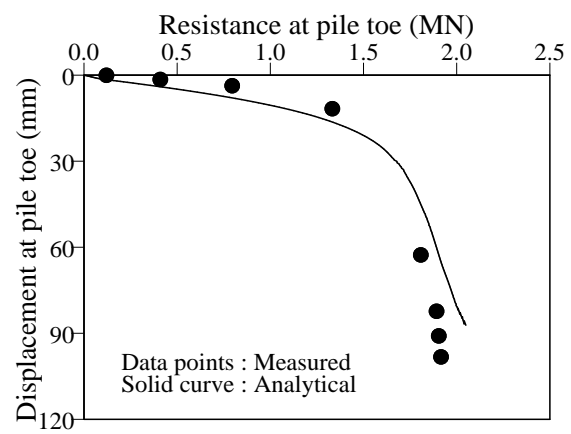


Fig.4 Relationship between resistance and displacement at pile toe

concrete bulb. The analytical relationship between the resistance and displacement, which is indicated by a solid circle at the toe of the concrete bulb, agrees closely with that which is indicated by an empty circle at the inner concrete bulb, indicating that the concrete bulb acts in coordination with the steel pipe piles. In addition, it is considered that failure of the concrete bulb did not occur. It should be noted that the displacement at a point 1 m below the toe of the concrete bulb, i.e., at the bottom of the sand layer, which is denoted by an open rhombus, increases more significantly than that at the point 2 m below the toe, which is denoted by a solid triangle, as the resistance and displacement behaviors at the pile toe begin to yield.

As shown in Figures 3, 4, 5 and 6, the agreement between the measured and analytical results is good, thus confirming that the numerical simulation realistically reproduces the bearing behavior of the pile and the foundation behavior of the ground around the pile toe in the field loading test [2].

Figure 7 shows the analytical results of the deformation of the bearing ground below the concrete bulb in the final stage of loading. The bearing ground behaves as if the pile might punch through the thin load-bearing layer. In particular, the finite elements of the thin load-bearing layer directly below the perimeter of the concrete bulb deform as if they were subject to simple shearing. This suggests that the punching shear failure occurs in the bearing ground below the concrete bulb.

ANALYTICAL CASES IN PARAMETRIC STUDY

Table 2 shows the analytical cases in the parametric study. In this paper, the stiffness of load-bearing layer could be considered as the compressibility of sands or sandy gravels which forms the load-bearing layer. C_t , which is one of the most important parameters in tij-sand model, was chosen as variable parameter, in order to change the deformation modulus of the load-bearing layer. C_t is mechanical parameter for controlling the volumetric compression behavior. The volumetric strain rate, $\dot{\epsilon}_{vol}$, can be defined by the following equation.

$$\dot{\epsilon}_{vol} = m C_t p'^{m-1} \dot{p}' \quad (1)$$

where p' is mean principal stress at the initial condition and m is a material parameter. Also, the dot denotes the rate. On the other hand, the volumetric strain rate in the elastic media is defined by the Eq.(2).

$$\dot{\epsilon}_{vol} = K \dot{p}' \quad (2)$$

where K is bulk modulus. Also, K can be given by the following equation.

$$K = \frac{E}{3(1-2\nu)} \quad (3)$$

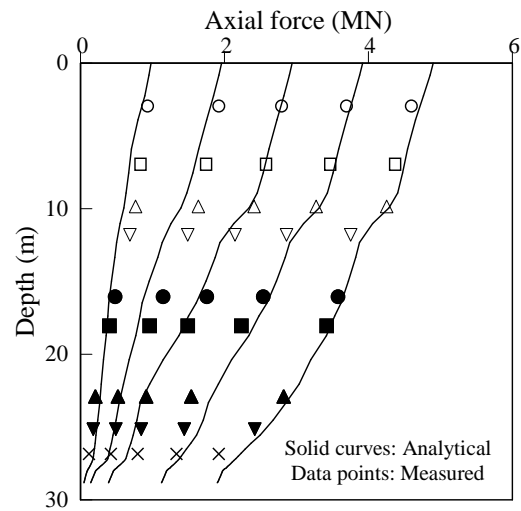


Fig.5 Axial force distribution of pile

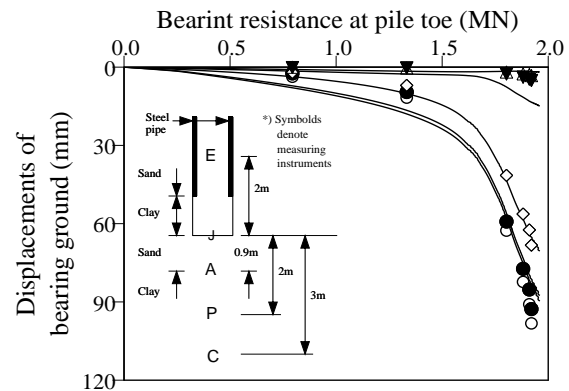


Fig.6 Relationship between resistance at pile toe and displacement of the concrete bulb and underlying bearing ground

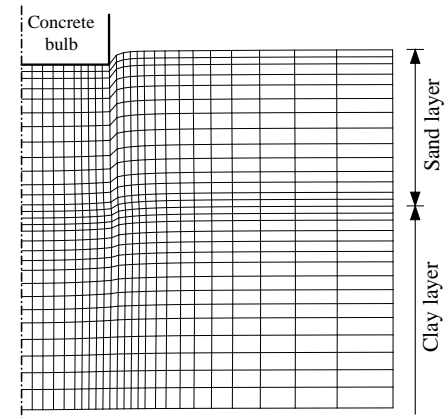


Fig.7 Analytical results of the deformation of bearing ground around concrete bulb at the final stage of loading

Table 2. Analytical cases

Case	Deformation Modulus	C_t
E1014	1014 kgf/cm ²	5.69×10^{-3}
E830	830 kgf/cm ²	6.95×10^{-3}
E670	670 kgf/cm ²	8.60×10^{-3}

where E is deformation modulus and ν is poisson's ratio. From Eq.(1), Eq.(2) and Eq.(3), E is given by

$$E = 3(1 - 2\nu)m C_i p^{m-1} \quad (4)$$

Strictly speaking, E does not imply the elastic modulus in this paper.

EFFECT OF STIFFNESS OF LOAD-BEARING LAYER ON BEARING CHARACTERISTICS AT PILE TOE

Figure 8 shows the relationship between resistance and displacement at pile toe in the case where the thickness of the load-bearing layer is equal to 1.5m. The resistance at pile toe increases as the deformation modulus of load-bearing layer is greater at the same displacement before the yielding of the relationship between resistance and displacement at pile toe occurs. In the case of E1014, the yielding in relationship between resistance and displacement at pile toe occurs at toe displacement of about 4.0cm and at toe resistance of about 2.8MN. Also, in the case of E830, the yielding in relationship between resistance and displacement at

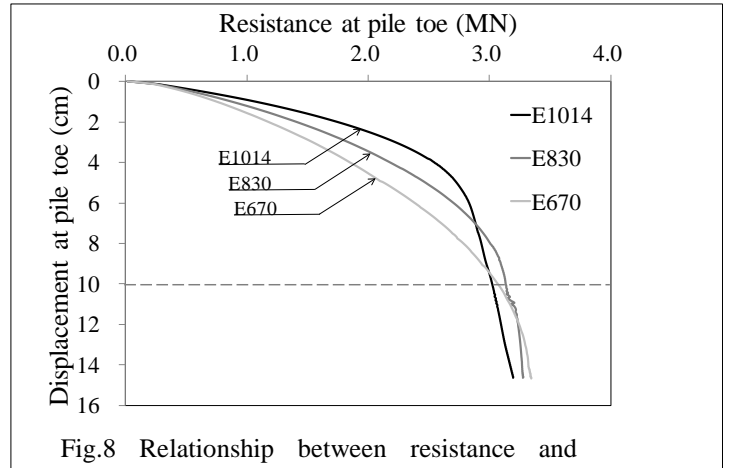


Fig.8 Relationship between resistance and displacement at pile toe

pile toe occurs at toe displacement of about 8.0cm and at toe resistance of about 3.1MN. However, in the case of E670, the yielding does not occur until the displacement at pile toe reaches 10cm which is equal to 10% of the pile diameter. In general, the toe resistance at the displacement of 10% of pile diameter can be estimated as the ultimate bearing

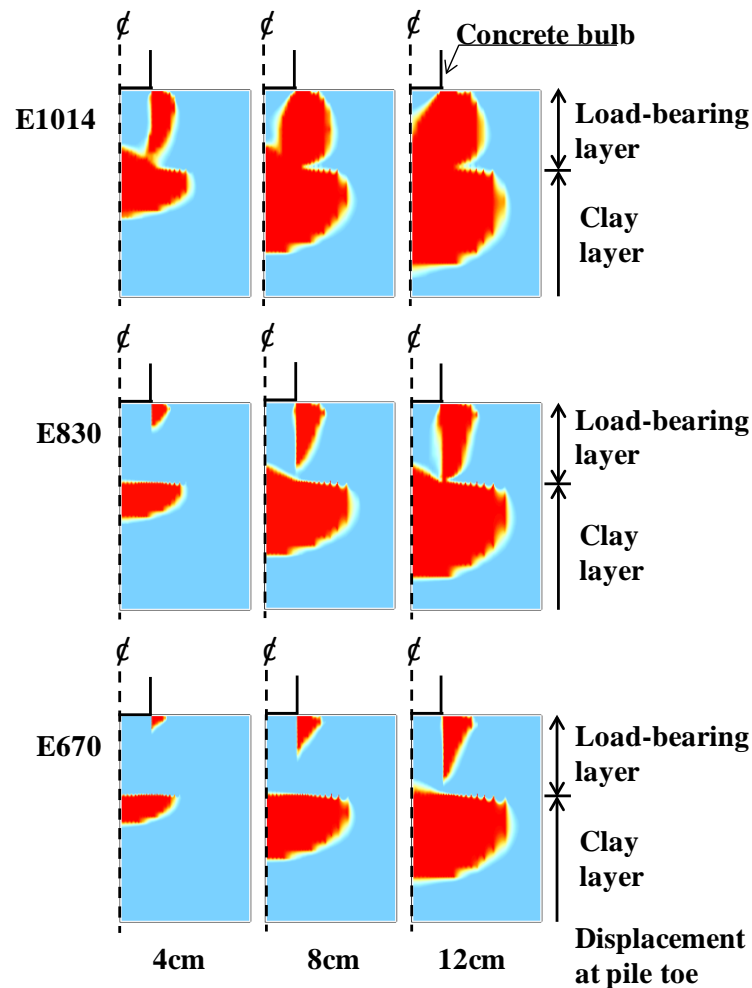


Fig.9 Development of local failure in the bearing ground underneath a concrete bulb

resistance in design method, in Japan. The yielding occurs at the toe displacement of about 12cm and at toe resistance of 3.3MN in the case of E670. After the yielding occurs, the resistance at pile toe hardly increase with the displacement in each analytical case. Also, the resistance at pile toe in each case is closely agreed with those in the other cases at the displacement of 15cm.

Figure 9 shows the development of the local failure in the bearing ground underneath a concrete bulb. In figure 9, the zone in which the local failure occurs is painted red. In E1014, the local failure zone surrounds the compressed zone underneath the toe of concrete bulb in the load-bearing layer and reaches nearly the clay layer underlying the load-bearing layer at toe displacement of about 4cm. The yielding of relationship between resistance and displacement at pile toe occurs at toe displacement of 4cm in E1014, as shown in Fig.8. It is, therefore, suggested that the punching shear failure, in which a highly compacted core of soils is formed underneath a concrete bulb due to the installing the pile into the load-bearing layer, is the prevailing bearing mechanism.

In E830, the local failure develops slowly than in E1014. The local failure zone does not reach the clay layer underlying load-bearing layer at toe displacement of about 4cm surrounding the compressed zone underneath the toe of concrete bulb. The failure zone in the bearing layer reaches nearly the clay layer underlying at toe displacement of about 8cm. At toe displacement of about 8cm, the occurrence of yielding is confirmed as shown in Fig.8. It is suggested that punching shear failure is the prevailing bearing mechanism in E830, too.

In E670, the local failure zone surrounding the compressed zone underneath the toe of concrete bulb reach nearly the clay layer underlying at displacement of 12cm.

CONCLUSIONS

In this study, the effect of stiffness of load-bearing layer on bearing characteristics of a steel pipe pile with concrete bulb on a thin load-bearing layer was investigated through a series of numerical simulations. The main conclusions are summarized as follows.

1. The numerical analysis which was developed by authors, realistically reproduces the bearing behavior of the steel pipe pile with concrete bulb on a thin load-bearing layer in a field loading test.

2. The resistance at pile toe increases as the stiffness of load-bearing layer is higher at the same level of displacement before the yielding of relationship between resistance and displacement at pile toe occur.
3. The resistance at pile toe at the displacement of 10% of pile diameter might be not significantly affected by the stiffness of load-bearing layer.
4. The punching shear failure is the prevailing bearing mechanism, regardless of the stiffness of load-bearing layer.

ACKNOWLEDGEMENT

The authors would particularly like to thank the Japan Iron and Steel Federation for scholarship.

REFERENCES

- [1] Matsui, T., K. Oda, and M. Nakabayashi, "End bearing mechanism of bored pile on thin bearing layer", Proceedings of 9th Asian Regional Conference on Soil Mechanics and Foundation Engineering, Vol. 1, 1991, pp.251-254.
- [2] Matsui, T., K. Oda, and M. Nakabayashi, "Deformation behavior of bored steel pipe piles with concrete bulb on a thin bearing layer", Proceedings of the 4th International Offshore and Polar Engineering Conference, 1994, pp.548-553.
- [3] Takegawa, S., Oda, K., Ikefuji, Y., "Effect of strength of bored steel pile pipes with concrete bulb on end bearing characteristics on a thin layer", Proc. 47th annual meeting of J.G.S, 2012, pp. 1075-1076.
- [4] Koike, M., F. Yasuda, T. Takasuga, and T. Katayama, "Loading test of large-scale bored steel pipe pile on a thin bearing layer", Proc. 46th annual meeting of J.S.C.E., 1991, pp. 828-829.
- [5] Nakai, T. "An isotropic hardening elastoplastic model for sand considering the stress path dependency in three-dimensional stresses", Soils & Foundations, (29), 1, 1989, 119-137.
- [6] Matsui, T. and N. Abe. "Multi-dimensional elasto-plastic consolidation analysis by finite element method", Soils & Foundations (21), 1, 1981, 79-95
- [7] Goodman, R.E., R.L. Taylor and T.L. Brekke, "A model for the mechanics of jointed rock", ASCEM3, 1968, 637-659

INFLUENCE OF SHEAR SPEED ON DIRECT SHEAR STRENGTH FOR COMPACTED BENTONITE WITH DIFFERENT SOIL SUCTIONS

Tomoyoshi NISHMURA¹ and Junichi KOSEKI²

¹Ashikaga Institute of Technology, Japan, ²Institute of Industrial Science, University of Tokyo

ABSTRACT

Geotechnical engineered barriers for isolating nuclear waste disposal at great depths are constructed of compacted bentonite. Hydraulic mechanism of bentonite is widely known to be affected by changes in water content or suction. Soil suction can be used for predicting shear strength of compacted bentonites. Direct shear tests with different shear speed are presented to describe effect of hydraulic process of compacted bentonite. Direct shear tests conducted with different shear speed to reach failure or stable residual conditions. Measured direct shear strength related to soil suction and soil moisture. Shear strength of suction of 2.8 MPa decreased with increasing shear speed. Also, compression curve of compacted bentonite was influenced due to change of soil suction (i.e. total suction). Soil suction is extended to incorporate the effect of external loading, creating a shear resistance.

Keywords: Bentonite, Suction, Direct shear strength, Shear speed, Compression properties

INTRODUCTION

Geotechnical engineered barriers used for isolating nuclear waste disposal at great depth are constructed of compacted bentonite. Hydraulic mechanism of bentonite is a widely known behavior resulting from change in water content. Some governing parameters of compacted bentonite properties are related via the soil-water characteristic curve and therefore, soil suction can be used for prediction of shear strength of compacted bentonites. It is well known that the use of suction as a governing parameter introduces the presence of hydraulic mechanism for compacted bentonite. For compacted bentonite, a non-negligible quantity of water is strongly adsorbed on montmorillonite minerals, and physical-chemical effects related to montmorillonite-water molecular interactions are important. Standard mechanical models are completed to account for the additional complexity related to physical-chemical effects for heavily compacted swelling soils (Cui et al., (1993), Cui et al., 2002).

Hydration-mechanism tests showed some limitation of existing elasto-plastic models for compacted bentonite with collapsible macro-pores resulting from changes in soil suction, and established the concept of critical swelling curves. The concept accounts for the couplings between hydraulic and mechanism effects.

A new direct shear tests are presented that included the effect of hydraulic process for compacted bentonite. Direct shear strengths of compacted bentonite with different suction are conducted with different shear speed to reach

Table 1 Summary of chemical component for bentonite.

Symbol	Percentage %
SiO ₂	69.7
TiO ₂	0.14
Al ₂ O ₃	15.8
Fe ₂ O ₃	1.69
MgO	2.19
CaO	2.00
Na ₂ O	2.04
K ₂ O	0.24

failure or stable residual conditions. The shear speed ranged from 0.004 mm per a minute to 0.5 mm per a minute for a total horizontal displacement of 8 mm. Measured direct shear strengths have relation with soil suction and soil moisture. In addition, volumetric behavior of bentonite in response to change in water content has effect on shear properties.

TEST PROCEDURE

Soil materials

Sodium bentonite was used for this test program. Silica sand was mixed into the bentonite at a ratio of 30 % by dry weight. The bentonite had chemical components shown in Table 1.

The soil specimen was statically compacted in the shear box under a compression stress of 3.5 MPa and had an initial water content of 5.9 %. The soil specimen had a dry density of 1.6 g/cm³, a diameter of 6 cm and a height of 2.5 cm. Initial suction was determined as 105 MPa using soil-water

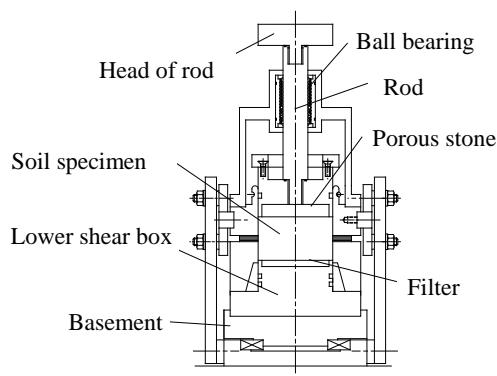


Fig. 1 Direct shear box used in this test program.

characteristic curve obtained from vapor pressure technique with suction range from 2.8 MPa to 296 MPa (Nishimura et al. 2010).

The shear box was shown in Fig. 1. The shear box consisted of upper box and lower box. Five rings were placed between upper box and lower box which were subjected to fluorination treatment for minimizing friction resistance. The shear box was placed in the chamber of modified direct shear apparatus.

The specimens were subjected to two different suction values of 2.8 MPa and zero (i.e. saturation condition). Vapor pressure technique using K_2SO_4 induced to suction of 2.8 MPa for compacted bentonite. Reduction of suction from 105 MPa to 2.8 MPa caused expansion of upper surface of compacted bentonite. This closely related to decreasing dry density and changing of macro-micro structures (Wang, et al., 2012, Nowanmooz and Masrouri (2012)). Nishimura et al. (2012) had measured expansion of compacted bentonite, which had a diameter of 2 cm and height of 1 cm. Applied suction was lower than initial suction. Expansion of volume change of the sample approached to 31.1 %. Many cracks occurred on the surface of sample, and it can be predicted to change micro-macro structure in compacted bentonite. More and more cracks were observed on the surface of sample with time and all cracks advanced to significant depths.

This study performed compression test on compacted bentonite with three different suctions in order to understand compression properties. The compacted bentonite had a diameter of 6 cm and a height of 2.5 cm. Required suctions were 105 MPa, 2.8 MPa and zero value. The suction of 105 MPa was correspond a suction of initial direct shear compacted bentonite specimen. In case of suction of

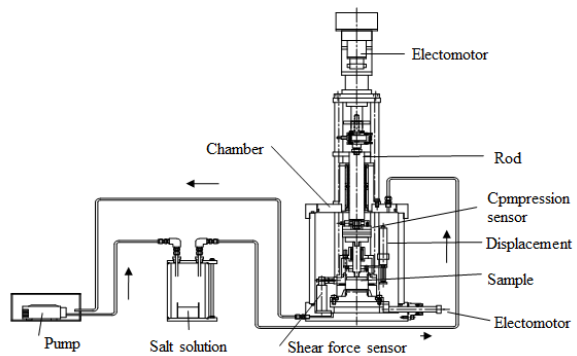


Fig. 2 Relative humidity air circulation system.

2.8 MPa, compacted bentonite applied decreasing of suction under relative humidity of 98 %. Suction of zero value in the compacted bentonite was produced due to swell in de-aired water. The swelled specimen in de-air water was prepared decreasing suction as zero suction value, and it was remained a constant initial height during soaking. The swelling period was at least over than one month. After swelling all specimen approached to saturation condition, and suction of compacted bentonite reduced from 105 MPa to zero value. Each sample was loaded and unloaded the ranged from 20 kPa to 1000 kPa.

Other hands, all specimens controlled of suction were installed in the modified direct shear apparatus as shown in Fig. 2 and a normal stress of 200 kPa was loaded and consolidated to all specimens. It was remained at least twenty four hours before a direct shearing.

This testing program modified a conventional direct shear apparatus to maintain constant suction around specimen and that was performed two different processes before shearing correspond to each specimen. In case of compacted bentonite with suction of 2.8 MPa, air circulation was flowed through direct shear chamber using relative humidity control system which was maintained at relative humidity of 98 % as shown in Fig. 2. Potassium sulfate was put in a container placed outside chamber and a conventional pump circulated the air at relative humidity of 98 % through the system. The air in chamber of direct shear apparatus maintained a constant suction that was predicted for the surface of specimen at constant suction of 2.8 MPa. This air circulation system was similar to the system suggested by Blatz and Graham (2000) or Nishimura and Fredlund (2003).

In case of saturated specimen, the de-aired water was supplied in the chamber of direct shear apparatus till water level approached upper surface

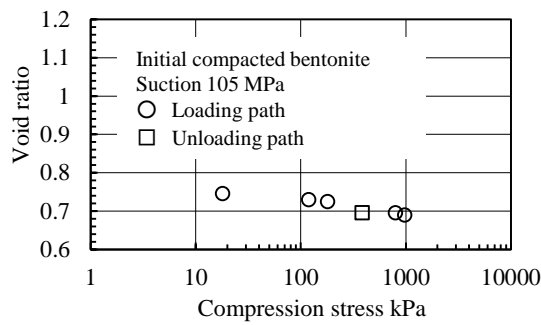


Fig. 3 Compression curve for suction of 105 MPa.

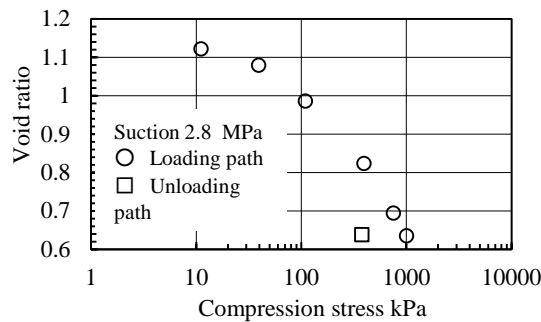


Fig. 4 Compression curve for suction of 2.8 MPa.

of specimen and swelled bentonite remained at saturation condition during direct shear process. It was unknown whether either drained condition or undrained condition existed in bentonite during shearing as excess pore-water pressure was not measured in this testing. Four different shear speeds ranging from 0.004 mm/min to 0.5 mm/min were applied to specimens under constant normal stress of 200 kPa.

TEST RESULTS

Compression properties of compacted bentonite

Compacted bentonite sample subjected to decreasing suction indicated expansion or peeling on upper surface, which controlled suction was 2.8 MPa corresponding to RH of 98 %. Change of macro-micro structure cause its volume deformation. This study conducted compression test for three different suctions such as initial compacted bentonite, suction of 2.8 MPa and bentonite. Each bentonite specimen was maintained to constant suction values in chamber through compression tests. Applied compression stress from 10 kPa to 1000 kPa, both loading path and unloading path were performed that was to determine compression index and swelling index.

The compression curves of bentonite for three different suctions are shown in Figs. 3 to 5. Initial compacted bentonite having a suction of 105 MPa showed not so much reduction of void ratio through

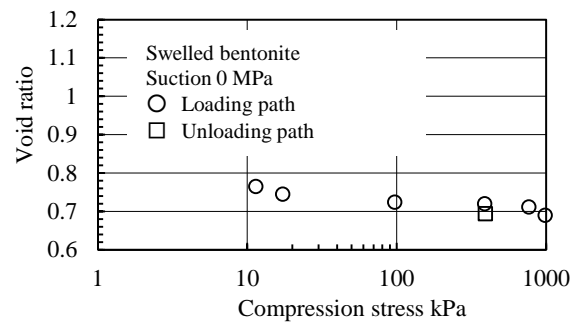


Fig. 5 Compression curve for suction of zero.

Table 2 Summary of compression parameters.

Suction MPa	Cc	Cs
105	0.05	0.04
2.8	0.47	0.01
0	0.05	0.01

Cc: Compression index, Cs: Swelling index

compression stresses approach to a maximum stress value, because a bentonite sample was applied significantly high stress in order to remain a target dry density. Figure 4 shows the curve of bentonite subjected to decreasing suction due to vapor pressure technique, which expansion was observed on upper surface. Hydration effort induced changing of void ratio that increased from 0.75 to 1.12. It was predicted that macro-micro pore distribution and soil moisture distribution were considerable different to initial bentonite. Compression deformation gradually progressed with increasing compression stress. After compression stress was over 40 kPa, reduction of void ratio was large and the curve was seemed to be liner on a semi-logarithmic scale. Determined void ratio was 0.635 when maximum compression stress was loaded. Its deformation was large compare to the curve of initial compacted bentonite shown in Fig. 3. Subsequently, expansion deformation was measured at unloading path.

Swelled bentonite showed similar to the curve of initial bentonite, it seemed to small reduction of void ratio through entire vertical stress ranges. The swelled bentonite may maintained undrained condition in macro structure which had much low hydro-conductivity. It meant draining of pore-water in void structure was not induced due to consolidation, and compression deformation was slightly at loading path. Also, swelling deformation was small at unloading path. Compression index and swelling index were summarized in Table 2. Measured compression index of suction of 2.8 MPa was largest among other two bentonite samples. Regard to swelling index, its value was relatively large compare to other two bentonite samples when suction was 2.8 MPa. Thus, compression properties was clearly difference and the influence of suction

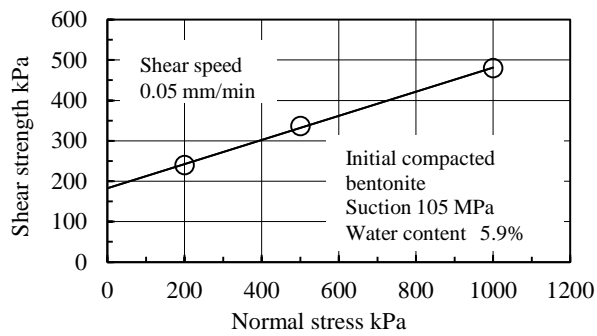


Fig. 6 Relationship between vertical stress and shear strength for initial compacted bentonite.

Table 3 Strength parameters for initial bentonite.

Angle of internal friction	Apparent cohesion
16.6 degrees	182.7 kPa

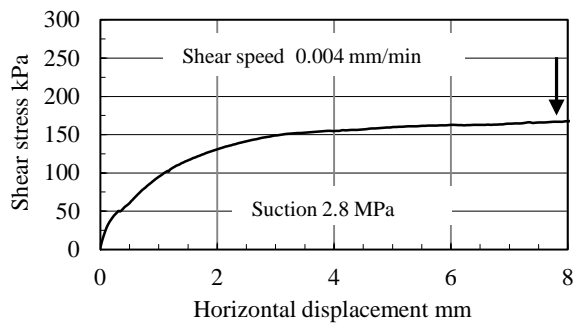


Fig. 7 Stress-strain curve for suction of 2.8 MPa under shear speed of 0.004 mm/min.

was effectively.

Failure envelope for compacted bentonite before changing suction

Initial compacted bentonite samples were conducted out direct shear test under constant normal stress of 200 kPa at a shear speed of 0.05 mm/min and the relationship between vertical stress and shear strength was shown in Fig. 6. Applied normal stresses ranged from 200 kPa to 1000 kPa. Relationship between normal stress and shear strength showed a straight line at this limited normal stress ranges. The measured failure envelope had strength parameters (i.e., angle of internal friction and apparent cohesion). The strength parameters are summarized in Table 3.

Stress-strain behavior in suction of 2.8 MPa

Direct shear tests under constant normal stress of 200 kPa were performed under four different shear speeds for compacted bentonite controlled from initial suction of 105 MPa to 2.8 MPa. These stress-strain behaviors were shown in Figs. 7 to 10. The

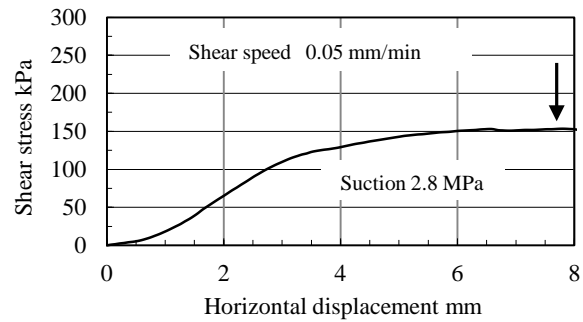


Fig. 8 Stress-strain curve for suction of 2.8 MPa under shear speed of 0.05 mm/min..

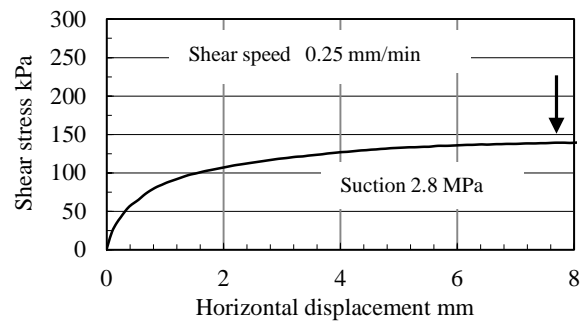


Fig. 9 Stress-strain curve for suction of 2.8 MPa under shear speed of 0.25 mm/min.

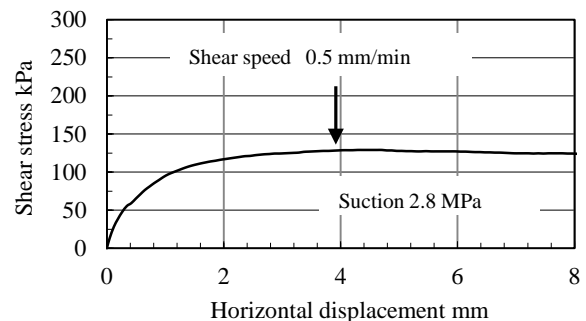


Fig. 10 Stress-strain curve for suction of 2.8 MPa under shear speed of 0.5 mm/min.

maximum shear stresses were indicated on the stress-strain curve using black narrow. The shear stress rapidly increased at beginning of shearing except 0.05mm/min, and gradually increased when horizontal displacement was over 2.0 mm. These specimens described maximum shear stress value till horizontal displacement was 8.0 mm. Each magnitude of horizontal displacement at failure was different. It was difficult to make available tendency with shear speeds. In case of 0.5 mm/min, shear stress showed small reductions such as softening.

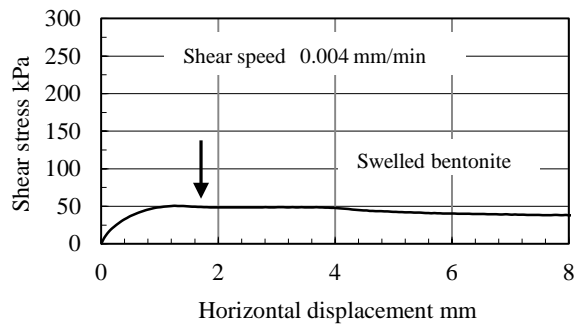


Fig. 11 Stress-strain curve for swelled bentonite under shear speed 0.004 mm/min.

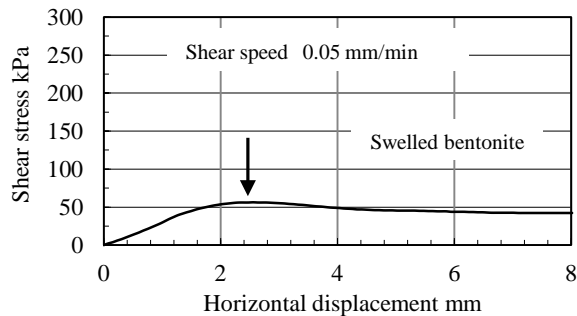


Fig. 12 Stress-strain curve for swelled bentonite under shear speed of 0.05 mm/min.

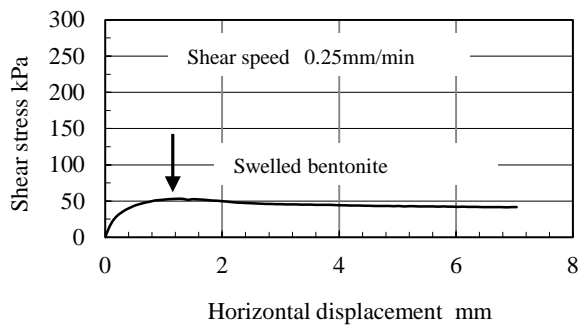


Fig. 13 Stress-strain curve for swelled bentonite under shear speed of 0.25 mm/min.

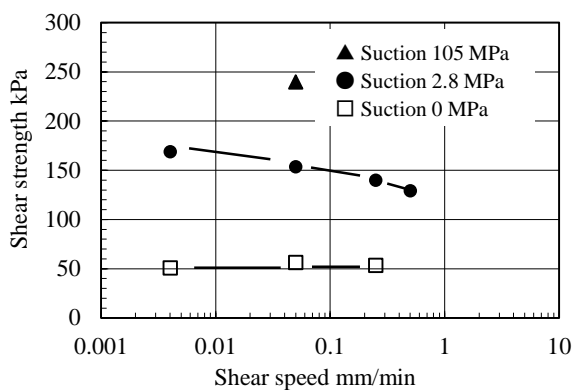


Fig. 14 Relationship between shear speed and shear strength for compacted bentonite.

Table 4 Summary of shear strength of compacted bentonite with four different shear speeds.

Shear speed mm/min	0.004	0.05	0.25	0.5
Suction 2.8MPa	168.8	153.4	140.0	129.0
Suction 0 MPa	50.7	56.4	53.2	—

Stress-strain behavior of swelled saturated bentonite

Stress-strain behaviours of the swelled bentonite at three different shear speed in shown Figs. 11 to 13. Shear stress increase gradually at beginning and maximum shear stress was approached at small horizontal displacement compare to bentonite of suction of 2.8 MPa. Horizontal displacements to reach maximum shear stress were less than 3.0 mm. All specimens showed small reduction of shear stress beyond maximum shear stress and remained at residual shear stress. Maximum shear stresses were close to 50 kPa and these values indicated significant reduction compare to bentonite with both suction of 105 MPa and 2.8 MPa. Also, the difference between maximum shear stress and residual shear stress was small.

Influence of shear speeds on shear strength

Relationship between shear strength obtained constant normal stress in direct shear test under a variety of shear speeds is shown in Fig. 14. Shear speeds were plotted on logarithmic scale, which ranged from 0.001 mm/min to 10 mm/min. Shear strength of bentonite with suction 105 MPa was plotted that it was initial bentonite sample. The shear strength of compacted bentonite with different both suctions and shear speeds was summarized in Table 4. The shear strength of suction of 105 MPa indicated largest among other suction values that mentioned significant effort to shear strength. Shear strengths reduced toward to one fifth at least in comparison between suction of 105 MPa and swelled saturation condition.

The shear strength of 168.8 kPa was described on 0.004 mm/min for suction of 2.8 MPa and the shear strength gradually decreased with increasing shear speed. At shear speed of 0.5 mm/min, shear strength decreased to 129.0 kPa. It described that shear speed influenced to shear strength for compacted bentonite subjected to suction of 2.8 MPa. Other hands, the swelled bentonite indicated similar shear strength regardless of shear speed at limited speed ranges. Magnitude of shear strength indicated around 50 kPa. Eventually, the influence of shear speed on direct shear strength was different to suction value of compacted bentonite.

CONCLUSIONS

This study investigated shear speed influence on shear strength of a compacted bentonite in direct shear test under constant normal stress, while suction was controlled to 2.8 MPa or swelled saturation. As in previous compression test, each compression index and swelling index was described in order to realize the influence of suction changes. The results obtained from this testing program are summarized as following;

- (1) Void ratio of compacted bentonite increased when suction changed from from 105 MPa to 2.8 MPa before compression test. Large compression index was measured. Its index was ten times as high as that of initial compacted bentonite.
- (2) Decreasing of suction influenced on shear strength of compacted bentonite, and induced the decrement of shear strength.
- (3) In case of suction of 2.8 MPa, the shear strength of compacted bentonite decreased gradually with increasing shear speed, while the influence of shear speed was small for swelled bentonite.

ACKNOWLEDGEMENTS

This study was supported by the grant for 2012 from Ashikaga Institute of Technology. Also authors would like to make grateful acknowledgement to Dr. Julian K. GAN, P. Eng. (MDH Engineered Solutions Corp.) for discussions.

REFERENCES

- [1] Blatz, J.A. and Graham, J. A system for controlled suction in triaxial tests. *Geotechnique*, 2000, Vol.50, No.4, 465-469.
- [2] Cui, Y.J. and Delage, P. On the elasto-plastic behaviour of an unsaturated silt. *Unsaturated Soils*, American Society of Civil Engineers, 1993. 125-126.
- [3] Cui, Y.J., Yahia-Aissa, M. and Delage, P. A model for the volume change behavior of heavily compacted swelling clays. *Engineering Geology*, 2002, Vol.64, 233-250.
- [4] Nishimura, T. and Fredlund, D.G. A new triaxial apparatus for high total suction using relative humidity control. *12th Asian Regional Conference on Soil Mechanics and Geotechnical Engineering*, 2003, 65-68.
- [5] Nishimura, T., Rahardjo, H., Koseki, J. Direct Shear Strength of Compacted Bentonite under Different Suctions. *Proceedings of the Fifth International Conference on Unsaturated Soils*, 2010, 323-328.
- [6] Nishimura, T., Koseki, J. and Matsumoto, M. Measurement of swelling pressure for bentonite under relative humidity control. *Unsaturated Soils: Research and Applications, E-UNSAT 2012*, 2012, Vol.1, 235-240.
- [7] Nowanmooz, H. and Masrouri, F. Soil fabric and soil water retention curve of a compacted silt-bentonites. *Geotechnical Testing Journal*, ASTM, 2012, Vol.35, No.1, 18-30.
- [8] Wang, Q., Tang, C., Tang, Anh-M. and Cui, Y-J. Effect of suction changes on the microstructure of compacted crushed argillites under constant-volume conditions. *Unsaturated Soils: Research and Applications, E-UNSAT 2012*, 2012, Vol.1. 185-190.

EFFECTS OF HYDROLOGICAL PARAMETERS ON DESERTIFICATION IN CHINA BASED ON THE SATELLITE DATA

Nozomu Hirose¹, Fengzhi DAI² and Keiko Okada¹

¹Civil and Environmental Engineering, Matsue College of Technology, Japan;

²College of Electronic Information and Automation, Tianjin University of Science and Technology, China;

ABSTRACT

Desertification is defined as land degradation of arid or semiarid ecosystems driven by climate variation and human disturbances. In this study, we explore the expansion of desertification in China and the effects of hydrological change under global warming on it by investigating satellite data. We used Normalized Difference Vegetation Index (NDVI), soil moisture, snow cover, and precipitation from 2002 to 2012. Two study areas are determined by classifying the vegetation type based on IGBP land use.

We found that NDVI in August decreases as soil moisture decreases in June and July in semiarid area. Precipitation in the area is decreased from 1957 to 2011. On the other hand, it is found that the relationship between NDVI and soil moisture in crop land is obscured due to agricultural irrigation.

Keywords: Desertification, NDVI, soil moisture, satellite data

INTRODUCTION

Recently, desertification eastward and sand dust has become one of the most serious ecological and environmental problems in China. The affected areas (where vast dust that is blown by powerful wind in western Inner Mongolia autonomous region falls down after roaming to the east through the air) are not only limited in Beijing and Tianjin, but have expanded to Korea and Japan [1]-[6].

The desertification from western China to Beijing-Tianjin area has raised serious problem in society and damaged the function of the capital of China. In the future, it may be an important factor result moving the capital to another city. In the future, with the temperature rises and the precipitation decreases caused by global warming, the soil will become drier and irrigation will make the water resource drains distinctly. It can be predictable that the process of desertification will be more and more serious.

The United Nations has signed the Convention to Combat Desertification, where pointing out that the climate changes and human activities are the main causes of soil deterioration and environmental destroy. Therefore, it is necessary, with the exception of reducing man-made sabotage, to grasp the annual changes in desertification of earth's surface in a long period, and clarify the influence that climate change could make for desertification by observation and statistical analysis. Furthermore, we can utilize some approaches like numerical analysis to predict the direction and rate of desertification in order to deploy the long-term effective prevention and treatment program of

virescence.

China has done some measures such as eco-migration and large-scale reforestation aiming at the status quo of desertification, but the globally effective strategy appears rarely.

The present governance is aimed at local analysis of a region. However, only global countermeasures resolve the problem in Beijing-Tianjin area. Therefore, widespread monitoring by satellite remote sensing technology is bound to be the important means.

The accurate model for monitoring and analyzing desertification by satellite technology is rare. But it is feasible to obtain data of soil moisture, migration of surface vegetation and from which to calculate the direction and speed of desertification. The research is by the satellites that long-termly monitor the plant growth and water cycles, thereby analysis the current desertification situation as well as its influence on the Beijing-Tianjin region of China.

DATA

Vegetation Index

Vegetation conditions are collected by The Moderate Resolution Imaging Spectroradiometer (MODIS) that are carried on the Terra and the Aqua satellite (spatial resolution is 0.05°). The used vegetation index is the EVI (enhanced vegetation index) since the EVI value changes more remarkably than that of the NDVI (normalized difference vegetation index) [7].

Soil Moisture

Soil moisture [g/cm³] is obtained by using the measured data of AMSR-E carried by the Aqua satellite (spatial resolution is 0.25°) [8].

Air temperature and precipitation

The research adopts the high-resolution dataset of daily precipitation and air temperature from Aphrdpdt's water resources project (spatial resolution is 0.25°) [9]. This dataset is for the sake of ascertaining the impact that global warming makes on water resources in Asia area, collects and provides the long-term daily precipitation and average air temperature in this area.

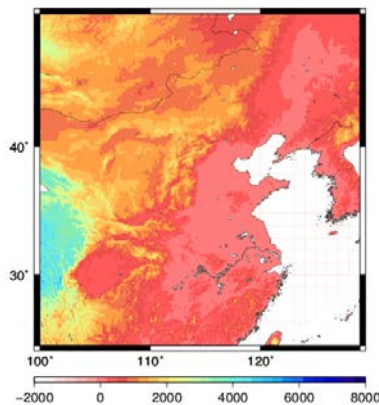


Fig. 1 Altitude figure of the study area.

STUDY AREA

Firstly, an area which contains Beijing-Tianjin area and has significant effect on them is selected. Figure. 1 is the altitude figure of study area. We use the IGBP Land Cover Dataset 2006 to classify the growth status of the land cover vegetation to 17 classes in the study area, which is shown in Fig. 2. It can be seen from Fig.2 that this region is divided to two main parts by a remarkable boundary. More bushes and weeds are located in the arid areas of Northwest (displaying as the yellow parts in color print), yet more crops like rice spread over the humid areas of Southeast (the green parts). By comparing Fig.1 and Fig.2, it is obviously that the boundary is consistent with the varying altitude.

Around the Beijing-Tianjin region within the analytical scope, we differentiate 2 regions (shown as two rectangular frames A and B in Fig.2) near the boundary where vegetation growth and soil humidity change sharply in order for statistics and analysis of data [10], [11].

They are Region A (Longitude: 114°-117°, Latitude: 41°-45°) covered by scrubland plants such

as bushes and weeds in the semi-arid area, and Region B (Longitude: 115°-117°, Latitude: 37°-40°) where more crops like rice grow in humid area.

All the data are collected from September 2002 to December 2011. Fig. 3 and Fig.4 provide the vegetation and soil humidity distribution of this area in August 2011. Notice that the striking distinction of vegetation and soil humidity in different region is also near the boundary basically.

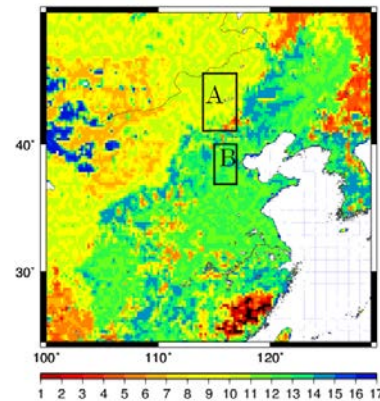


Fig. 2 Land covers classification in the study area.

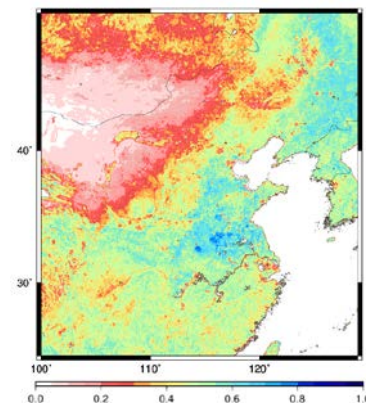


Fig. 3 The distribution of vegetation index (NDVI) in August 2011.

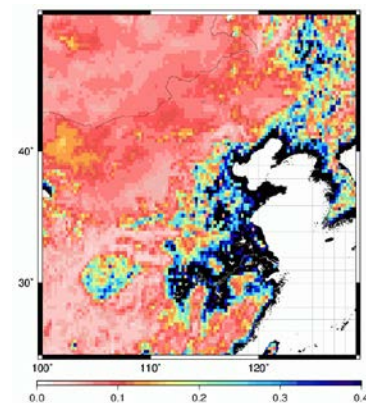


Fig. 4 The distribution of soil moisture in August 2011.

RESULT

Long-term change of vegetation and soil moisture

To analyze long term trend of desertification around target areas, monthly average of vegetation growth and soil humidity of selected areas in Sept. 2002 to Dec. 2011 is used. The vegetation growth and soil humidity change with season: They increased in summer and decreased in winter since there is more rain in summer. And with the increase of precipitation, the growth of plant became actively.

Monthly average change of vegetation and soil moisture

Fig. 5 and Fig.6 illustrate the monthly change of vegetation and moisture. The records are long-term monthly means of vegetation growth and soil moisture, so that we can clearly see the averages that different months influence on vegetation indexes. The curves suggest that it is obviously to find both changes in two areas (just paying attention to summers when vegetation grows): in Region A, the vegetation growth varies greatly from June to September. In contrast, the soil moisture changes largely from May to August. Namely, the rise of soil moisture is ahead of vegetation growth. In Region B, the vegetation growth shifts much from June to September while the soil moisture does this from June to October, especially both the curves of vegetation and soil moisture rises sharply from June [10], [11].

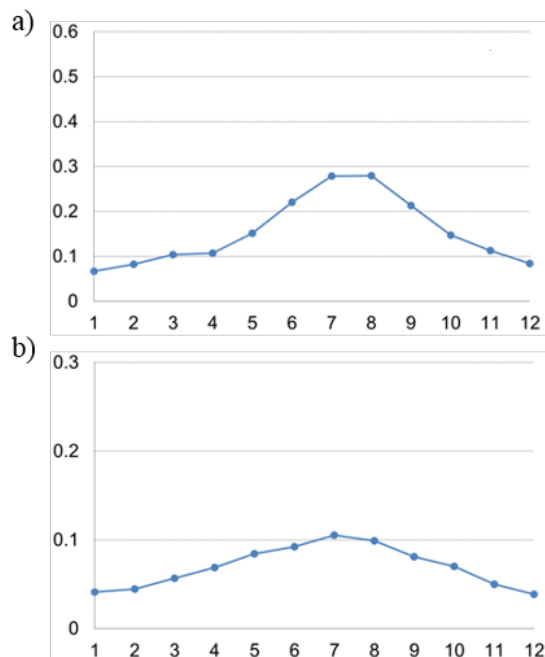


Fig. 5 The Monthly average of a) vegetation index and b) soil moisture with climate in area A.

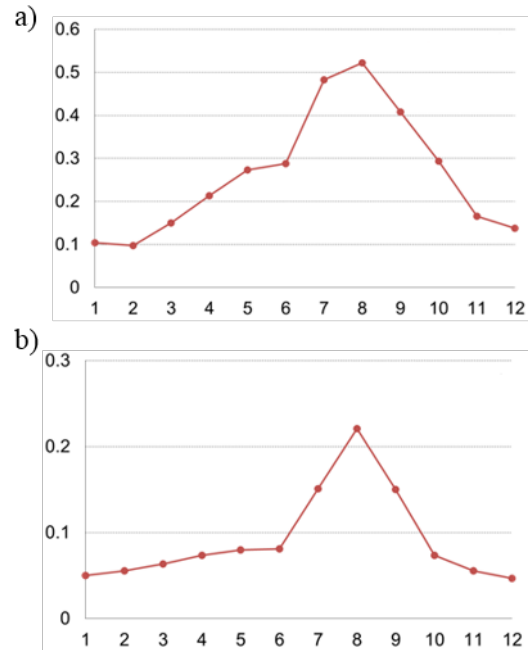


Fig. 6 The Monthly average of a) vegetation index and b) soil moisture with climate in area B.

The curves suggest that it is obviously to find both changes in two areas (just paying attention to summers when vegetation grows): in Region A, the vegetation growth varies greatly from June to September. In contrast, the soil moisture changes largely from May to August. Namely, the rise of soil moisture is ahead of vegetation growth. In Region B, the vegetation growth shifts much from June to September while the soil moisture does this from June to October, especially both the curves of vegetation and soil moisture rises sharply from June [10], [11].

In contrast, the soil moisture changes largely from May to August. Namely, the rise of soil moisture is ahead of vegetation growth. In Region B, the vegetation growth shifts much from June to September, while the soil moisture does this from June to October. Especially both the curves of vegetation and soil moisture rise greatly from June.

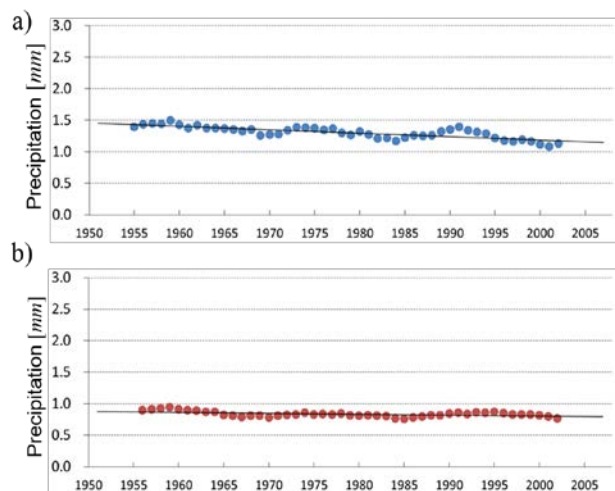


Fig. 7 Long-term changes of precipitation in area a) A and b) B.

The variation of long-term precipitation

Fig. 7 reveals the variation of annual precipitation means from 1951 to 2007. Through the comparison between the precipitations of two regions, we can see that Region A has more precipitation than Region B, but Region A has a downward trend during the last 50 years while there has almost no change in Region B

CONCLUSION

This research monitors the vegetation growth and water circulation in a long period near the Beijing-Tianjin area in China by utilizing the data observed by the satellites. According to the result of analysis, there is an apparent shift, with seasons, for both vegetation growth and soil moisture. And also, the precipitation has a falling tendency year by year. On the contrary, although vegetation growth and soil humidity in Region B keep change with seasons, precipitation in this area has no such inclination. Besides, the soil moisture in Region B increases sharply in June even exceeds Region A, though more precipitation is in Region A. The cause is that at farming area Region B, irrigative leads to a great rise of soil moisture. In terms of the existing data, the areas covered by plants in the semi-arid region in Northwest of China will continuously tend to reduce, following the decreasing of precipitation in future [10], [11].

ACKNOWLEDGEMENTS

The authors thank Hideyuki Fujii for providing newly soil moisture data.

This research is partly supported by the Open Foundation (YF11700102) of Key Laboratory for Water Environment and Resources, Tianjin Normal University; Dr. Fund of Tianjin Normal University (52LX24); Natural Science Foundation of China (41172315).

REFERENCES

- [1] Ishizuka, M., M. Mikami, Y. Yamada, F. Zeng, and W. Gao (2005), An observational study of soil moisture effects on wind erosion at a gobi site in the Taklimakan Desert, *J. Geophys. Res.*, 110, D18S03, doi:10.1029/2004JD004709.
- [2] Myoung, B., Y.-S. Choi, S.-J. Choi, and S. K. Park (2012), Impact of vegetation on land-atmosphere coupling strength and its implication for desertification mitigation over East Asia, *J. Geophys. Res.*, 117, D12113, doi:10.1029/2011JD017143.
- [3] Gu, Y., E. Hunt, B. Wardlow, J. B. Basara, J. F. Brown, and J. P. Verdin (2008), Evaluation of MODIS NDVI and NDWI for vegetation drought monitoring using Oklahoma Mesonet soil moisture data, *Geophys. Res. Lett.*, 35, L22401, doi:10.1029/2008GL035772.
- [4] Kaneko, D., T. Kumakura, P. Yang (2008), Crop yield and CO₂ fixation monitoring in Asia using a photosynthetic-sterility model with satellites and meteorological data, *Proceedings of the Global Conference on Global Warming-2008 (GCGW-08)*, 6-10, July, 2008, Istanbul, Turkey, Paper No.378, 227-238.
- [5] Ishizuka, M., M. Mikami, J. Leys, Y. Yamada, S. Heidenreich, Y. Shao, and G. H. McTainsh (2008), Effects of soil moisture and dried raindroplet crust on saltation and dust emission, *J Geophys Res*, 113, D24212.
- [6] Darменова, Kremena, Irina N. Sokolik, Yaping Shao, Beatrice Marticorena, and Gilles Bergametti (2009), Development of a physically based dust emission module within the Weather Research and Forecasting (WRF) model: Assessment of dust emission parameterizations and input parameters for source regions in Central and East Asia, *J Geophys Res*, 114, D14201.
- [7] Rouse, J. W., Jr., H. R. Haas, D. W. Deering, J. A. Schell, and J. C. Harlan (1974), Monitoring the vernal advancement and retrogradation (green wave effect) of natural vegetation, type III final report, 371 pp., NASA Goddard Space Flight Cent., Greenbelt, Md.
- [8] H. Fujii, T. Koike, and K. Imaoka, (2009), Improvement of the AMSR-E Algorithm for Soil Moisture Estimation by Introducing a Fractional Vegetation Coverage Dataset Derived from MODIS Data, *Journal of The Remote Sensing Society of Japan*, VOL.29, 282-292
- [9] A.Yatagai, K. Kamiguchi, O. Arakawa, A. Hamada, N. Yasutomi, A. Kitoh (2012), Aphrodite: Constructing a long-term daily gridded precipitation dataset for Asia based on a dense network of Rain Gauges. *Bulletin of American Meteorological Society*, Vol. 9: 401-415.
- [10] Okada Keiko, Hirose Nozomu, Dai Fengzhi. Analysis Desertification and its affect in China by satellite data. *Proceedings of 2012 Annual Conference, Japan Society of Hydrology and Water Resources*, September 26-28, Horoshima, Japan, 236-237, 2012.
- [11] Okada Keiko. The condition and influence of desertification in mainland of China based on satellite data. *Matsue College of Technology* 2013.

STRENGTH PARAMETER SELECTION IN STABILITY ANALYSIS OF RESIDUAL SOIL NAILED WALLS

Atefeh Asoudeh¹ and Erwin Oh²

^{1,2}School of Engineering, Griffith University, Australia

ABSTRACT

This paper investigates slope stability of soil nailed walls which are located on sites formed with mostly residual soils. Residual soils, forming from weathered rocks can be found in many parts of the world with different characteristics and appearance based on type of the parent rock they have been formed of. A review on geotechnical properties of residual soils that have been used in previous studies in different parts of the world will be presented and then evaluated to be used as parameters for numerical analysis of soil nailed walls. Slope stability assessment is performed by LEM analysis and a discussion on the results of analysis is presented in this paper.

Keywords: Residual Soil, Slope Assessment, Soil Nailing, Numerical Analysis

INTRODUCTION

Slope stability is one of the most unpredictable problems in geotechnical projects and the cause of this unpredictability can be returned to ambiguity in several factors such as condition and location of failure, geotechnical parameters of soil and history of loading on the slope. This issue gets even more serious when the slope is on residual soil, which means that unlike sedimentary soils, the strength parameters of soil cannot be obtained trustfully based on stress-strain relationships.

Therefore, this paper tries to find a reliable solution in slope stability assessment of residual soil slopes by concentrating on selection of right values for strength parameters in this type of soil. First, a review on previous studies on residual soil slopes will be presented. Afterward, some samples of strength parameters for residual soils that have been used in previous studies will be introduced. Accordingly, critical geotechnical parameters that should be considered in assessment of a residual soil slope will be identified.

A REVIEW ON RESIDUAL SOIL SLOPES

Residual soils form from weathered rocks and can be found in many parts of the world with different characteristics and appearance based on the type of parent rock they have formed of. This large range of difference in residual soils leads to variety of studies that focus on different aspects of this type of soil and therefore in the following paragraphs summary of these studies will be presented based on the area they are focusing on.

General Characteristics of Residual Soils

According to Townsend [1], three main chemical weathering factors that can lead to production of residual soils are: a) climate, b) parent rock's minerals and c) topography. Effect of climate in weathering is obvious as the rainfall provides the required moisture for chemical reactions and then the temperature dictates the chemical reaction's rate and considering these two components, best climate in which weathering can occur and therefore residual soils can be found is tropical weather.

The role of parent rock in weathering process is only predominant on initial stages of weathering and topography can influence the weathering procedure by controlling the surface run off and therefore moisture content of soil and also by rate of erosion.

Chean and Sew [2] highlighted the main traits of residual soils as very heterogeneous with high permeability. They summarized the importance of weathering profile regarding to its role in control of 1) potential failure surface and mode of failure 2) groundwater hydrology and 3) the erosion characteristics of material.

Valuable information regarding to general characteristics of residual soils has been gathered in the book prepared by Wesley [3]. In his book, Wesley presents basic aspects of residual soil and those properties that should be considered by geotechnical engineers while working with this type of soil.

By remarking some important characteristics of residual soils such as a) being heterogonous, b) having specific types of clay minerals and c) having unusual form of structure, Wesley concludes that in design of geotechnical structures on residual soil, engineers should give more attention to observation, experience and judgment instead of just relying on analytical and theoretical part of problem. Moreover, he emphasizes that application of e-log p graph for interpreting the behavior of residual soils is meaningless, as sedimentation process has not formed them.

Engineering Properties of Residual Soils

Townsend [1] also investigated the engineering properties of three different types of residual soil that are Lateritic Soils (highly weathered reddish tropical soils), Allophanic Soils (derived from volcanic ash) and Black Soil (or dark clays). Table 1 presented by Townsend [1] shows the shear strength parameters for the above-mentioned soils that had been obtained in previous studies.

Table 1 Example of Strength Parameters for Residual Soils (Townsend, 1985)

Soil Type & Location	ϕ' (°)	c' (kPa)	Reference
Lateritic gravels, Africa	37.5	0-40	Horn (1982a)
Lateritic clays, Africa	22.5	0-100	Horn (1982a)
Lateritic soil, Panama	38	0	Townsend (1970)
Granitic laterite soil, Venezuela	21.5	20	Pursza (1983)
Granitic laterite, Brazil	31	0	Vargas (1953)
Andosol, Java	36	24	Wesley (1974)
Black clay, Cameroon	16.1-20.1	47-58	Horn (1982b)

Loganathan and others [4] suggested a correlation factor for shear strength of residual soil in order to achieve more accurate results. This correlation factor can be applied into the laboratory shear strength of a specific type of residual soil that has been obtained by specific method of sampling and testing. For instance, the samples should be saturated under an effective stress of 10Kpa and shear strength parameters should be determined

using multistage consolidated undrained triaxial tests using a strain rate of 0.05% per min.

Coutinho and others [5] carried out a project to investigate the instability problems of a road constructed in Brazil after occurrence of a landslide in a natural non-homogenous unsaturated residual soil slope of this road. As a result of an intensive laboratory investigation, geotechnical parameters of residual soil were obtained and have been shown in Table 2.

Table 2 Strength parameters of residual soil by direct shear test (Coutinho & others, 2000)

Soil Type	Depth (m)	Test condition	ϕ' (°)	c' (kPa)
Mature Residual	0.75	Submerged	31.9	10.8
		Nat. M.C.	41.6	71.4
Young Residual	8.70	Submerged	29.3	2.8
		Nat. M.C.	29.5	7.0
Mature Residual	1.9	Submerged	35.5	0.0
		Nat. M.C.	37.8	15.8
Young Residual	4.6	Submerged	30.3	0.0
		Nat. M.C.	31.2	38.3

Azevedo and others [6] performed an extensive laboratory work on undisturbed samples of residual soils and used the results of these tests in modeling the behavior of residual soils with non-associated elasto-plastic model in finite element analysis of a tunnel excavation. They compared the results of numerical analysis with both empirical predictions and field instrumentations and proposed coefficients that can be used in numerical simulation of tunnel construction stages in residual soils.

A series of examinations were conducted by Rahardjo and others [7] in Singapore to specify the relationship between the degree of weathering and soil behavior in residual soils. As a result, they found that the higher the degree of weathering is, the more pore volume is which means a larger range of pore-size distribution.

As a part of their work, they took samples from different depths corresponding to different degrees of weathering and conducted consolidated, drained tri-axial compression tests under both saturated and unsaturated. Table 3 shows the summary of data that they found as a result of the above-mentioned tests.

Rahman and others [8] performed a testing program on reinforced and unreinforced residual soil samples by considering six different stress strain paths. Then, they introduced parameters related to

the Cam Clay model in simulating the finite element analysis of reinforced residual soil and as a result they could find a good agreement between the result of their numerical simulations and measured response.

Table 3 Shear strength of residual soil in different depths (Rahardjo and others, 2004)

Soil Type	Depth (m)	Grade of Weathering	ϕ' (°)	c' (kPa)
Granitic Bukit Timah formation				
Sandy Silt	5-9	VI	27	26
Silty Sand	10-15	V	35	13
Silty Sand	15-21	V	38	12
Sedimentary Jurong formation				
Purple silty sand	3-4	IV	42	125
Purple silty sand	4-5	IV	51	55
Orange silty sand	9-10	IV	45	35
Purple silty sand	22-24	III	50	225

Ogunro and others [9] presented the geotechnical properties of Piedmont residual soil on which some major cities and centers in the east coast of U.S. are founded and it is the result of chemical and mechanical weathering of Piedmont Paleozoic Rocks (schist, gneiss, and granite). Table 4 shows a sample of results from *Borehole Shear Test* (BST) and CU triaxial test in a site located in North Carolina.

Table 4 Sample of result from BST and CU triaxial test for Piedmont residual soil

Borehole#	Depth (m)	Borehole Shear Test (BST)		CU triaxial Test	
		ϕ' (°)	c' (kPa)	ϕ' (°)	c' (kPa)
1	10	45	0	29	5.9
	15	43	0	37	11
	20	40	9.65	41	0
2	5	44	0	30	24.1
	10	23	7.9	30	18.3
	15	40	0	36	14.1
	20	42	6.9	29	20

In another paper, Anderson and Cottingham [10] introduced the average values for Cohesion (c) and friction (ϕ) of Piedmont residual soil equal to 26.9 kPa and 26.3 degree, respectively.

Huat and others [11] collected lots of data and in their book, presented an overview of the index and engineering properties of some tropical residual soils. Based on their findings, values for soil strength in residual soils ranges from 2 to 123KN/m² for cohesion and 10 to 58 for friction angle (ϕ). They related this large range of variety to the great difference of soil formation in residual soils.

Furthermore, Wesley [3] related the high shear strength in these soils to existence of clay minerals. Also, microstructural effect and its contribution to the cohesive component of shear strength (C) can be chosen as another reason.

Slope Stability on Residual Soils

There are several studies that have been carried out to study the stability of slopes in residual soil areas in different parts of the world and the following paragraphs is a brief on some of these studies.

One important part of work carried out by Coutinho and others [5], was a back analysis in order to find the shear strength parameters of residual soil that can lead to the slope failure. As a result they concluded that shear strength parameters obtained from laboratory tests could explain the failure condition ($FoS=1$) by considering a low or very low amount of suction in wet seasoning.

Moreover, they introduced several factors as the impacting factors on the landslide including excavation for the purpose of road construction, sever rainfalls and prolonged high precipitation.

Tan and others [12] performed a parametric study on stability analysis of residual soil slopes in Malaysia and investigated the effect of several factors such as slope geometry, soil parameters, piezometric surface, surcharge and soil nailing reinforcement on the tropical residual soil slope stability. However, the summary of their work does not show any sign of considering specific characteristics for residual soil and therefore, residual soil has been treated and analyzed in the same way that sedimentary soil is examined.

Another important study on residual soil slopes is a section of book prepared by Huat and others [11] on failure of 6 slopes (including natural, man-made and filled slopes) on tropical residual weathered soil located in different parts of Malaysia. As a result of this study they recommended the use of Consolidated Isotropically Undrained (C.I.U.) tri-axial test in obtaining the peak shear strength and use of ring shear test to find the residual shear

strength and they suggested the use of residual strength in residual soil slope stability design.

Discussion and Concluding Remarks From Previous Studies

One important point that can be concluded from previous section is that almost all types of the residual soils that have been studied possess a relatively high value of friction angle (ϕ) with a minimum record of 20 degrees and average value of 35 degrees. Unlike friction angle, cohesion of residual soils has shown a wide range of values in different studies from zero to very high values near to 200kPa in deeper distances from ground level. This important fact demands a crucial attention to impact of cohesion on stability of residual soil slopes. Therefore, a parametric study has been performed and three different cases (Case-I: $\phi=20^\circ$, Case-II: $\phi=35^\circ$, Case-III: $\phi=45^\circ$) were used to investigate the effect of different values of cohesion on stability of nailed slopes in residual soils. Next sections present a summary on detail of slope assessment and results of Limit Equilibrium Method (LEM) of analysis performed by geotechnical software Geo-Slope for the above-mentioned cases.

NUMERICAL ANALYSIS OF DIFFERENT SLOPES IN RESIDUAL SOILS

Three different cases with three different values of friction angle ($\phi=20^\circ$, 35° & 45°) were simulated in geotechnical software Geo-slope, which uses LEM in slope stability analysis. Geometrical properties of slopes and general properties of soil nails were identical for all three cases and it has been presented in Fig.1

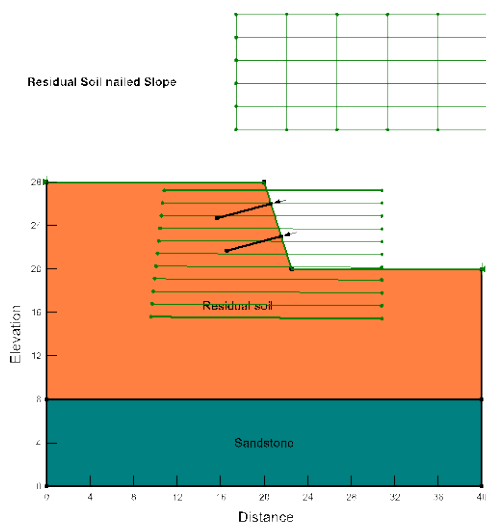


Fig.1 Geometry of modeled soil nailed slope

As shown in Fig.1, two rows of nails with length of 5m, angle of 15° and horizontal space of 2m were considered in stabilization of slope. In order to find the FoS of slopes method of Morgenstern-Price, which is able to satisfy both force and moment equilibriums, was used in LEM analysis.

RESULT OF ANALYSIS AND DISCUSSION

In order to examine the impact of cohesion value (c) on stability of these slopes, a sensitivity check was performed and the obtained Factor of Safety (FoS) for each case has been presented in Figure 2. For the purpose of sensitivity check, a wide range of cohesion changing from zero to 200kPa was assumed for the cohesion parameter of slopes.

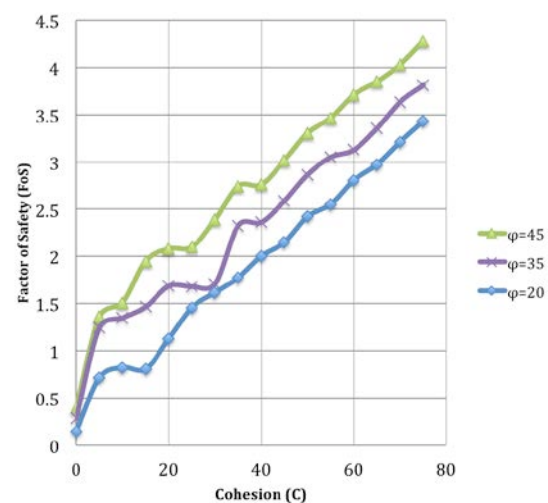


Fig.2 FoS of nailed slope for different values of cohesion

According to result of analysis presented in Fig.2, a nearly linear relationship exists between FoS and cohesion of soil and the slope of this line is almost the same for all three cases. However, this relationship is more variable in low values of cohesion and almost in all three cases the cohesion value of less than 10kPa will lead to unacceptable FoS, which is less than 1.5.

CONCLUSION

A review of previous studies on residual soils and specifically residual soil slopes was presented in this paper and strength parameters of soil which had been considered in each study was presented in separate tables. Based on assumed strength parameters in previous works, three different cases were modeled and analyzed to investigate the impact of cohesion on residual soil slopes. As a result, findings of the present study demonstrated that residual soil slopes with cohesion parameter of less than 10kPa (no matter how much is the friction

angle) and with acceptable amount of reinforcement have the high probability of collapse and these types of slopes are sensitive to value of cohesion. Also, it can be concluded that more attention needs to be taken in finding the cohesion parameter of residual soils.

REFERENCES

- [1] Townsend, F., *Geotechnical Characteristics of Residual Soils*. Journal of Geotechnical Engineering, 1985. 111(1): p. 77-94.
- [2] Chin, I.T.Y. and I.D.G.S. Sew, The Determination Of Shear Strength In Residual Soils For Slope Stability Analysis, in *Seminar Cerun Kebangsaan* 2001: Cameron Highlands, Malaysia.
- [3] Wesley, L.D., *Geotechnical Engineering in Residual Soils*. 2012: Wiley.
- [4] Loganathan, N., S. de Silva, and A. Thurairajah, *Strength Correlation Factor for Residual Soils*. Journal of Geotechnical Engineering, 1992. 118(4): p. 593-610.
- [5] Coutinho, R.Q., J.B.S. Neto, and F.Q. Costa, *Design Strength Parameters of a Slope on Unsaturated Gneissic Residual Soil*, in *Advances in Unsaturated Geotechnics*. 2000. p. 247-261.
- [6] Azevedo, R., A. Parreira, and J. Zornberg, *Numerical Analysis of a Tunnel in Residual Soils*. Journal of Geotechnical and Geoenvironmental Engineering, 2002. 128(3): p. 227-236.
- [7] Rahardjo, H., et al., *Characteristics of residual soils in Singapore as formed by weathering*. Engineering Geology, 2004. 73: p. 12.
- [8] Rahman, M.M., S.A. Mofiz, and M.R. Taha, *Experiments and Finite Element Analysis of Geosynthetics Reinforced Residual Soil*, in *Slopes and Retaining Structures Under Seismic and Static Conditions*. 2005. p. 1-12.
- [9] Ogunro, V.O., et al., *Characterization and Geotechnical Properties of Piedmont Residual Soils*, in *GeoCongress 2008*. 2008. p. 44-51.
- [10] Anderson, J.B. and M.A. Cottingham, *Results of Consolidated Drained Triaxial Tests on Granitic Residual Soil*, in *Contemporary Topics in In Situ Testing, Analysis, and Reliability of Foundations*. 2009. p. 74-78.
- [11] Huat, B.B.K., D. G.Toll, and A. Prasad, *Handbook of Tropical Residual Soils Engineering*. 2012: CRC Press/Balkema.
- [12] Tan, L.P., C.Y. Lee, and T. Sivadas. *Parametric studies of stability of residual soil slopes*. in *ICCBT*. 2008. Malaysia.

TENSILE STRENGTH AND SUCTION OF SATURATED NSF CLAY AND THEIR RELATIONSHIPS WITH UC STRENGTH

Surendra Bahadur Tamrakar and Toshiyuki Mitachi²

¹Associate Professor, Kyoto University, Japan; ² Professor, Nihon University, Japan

ABSTRACT

Tensile strengths of saturated and normally consolidated NSF clays prepared under consolidation pressures (P'_c) 50, 100, 200 and 300 kPa are measured using a modified version of Tensile strength measuring apparatus given by Tamrakar et al. (2005) [2, 3] so that suction could be measured at bottom and mid height of the specimen before as well as throughout the tensile test. Tests were conducted at different tensile pulling rates; 0.01, 0.1, and 1.0 mm/min. Increment in the tensile strength with the increase in tensile pulling rate is seen. Tensile strength and suction measured at 0.1 mm/min tensile rate are compared with the unconfined compression strength and suction measured with the specimens prepared under same condition and compression rate. Strength ratio (q_u/q_t) obtained lies in the range of -2.54 to -2.99. The ratio of q_t/P'_c ranges from -0.13 to -0.21 and similarly, the ratio of q_u/P'_c ranges from 0.34 to 0.56. Also, it is seen that the suction values measured at failure in both tests show the similar value.

Keywords: Tensile strength, Suction, Unconfined compressive strength, Tensile strength measuring apparatus

INTRODUCTION

In order to understand the development of tensile crack which leads to the failure of slopes, earth dams, embankments, pavements and ice lens development process, it is necessary to know the exact value of tensile strength that the particular soil exhibits. At the same time, development of simple and proper method for the determination of tensile strength in the laboratory is necessary.

In the past, tensile strength of soils is generally neglected as its value is very small in comparison with compressive strengths. Also, there is difficulty in measuring the tensile strength directly in the laboratory. In the past, several tests such as uniaxial direct tensile test, simple splitting test, unconfined penetration test, flexure (beam) test, indirect Brazilian test and hollow cylinder test were used. But most of those tests were focused to brittle and elastic materials (stiff, compacted and cement mixed soils) which have higher tensile strength rather than for ductile materials (soft, saturated and clayey soils) which have lower tensile strength. Very few testing methods have been mentioned for the measurement of tensile strength of soils which have lower tensile strength values.

Recently, Nahlawi, et al. [1] and Tamrakar, et al. [2, 3] have introduced new tensile strength measuring apparatus which measures the tensile strength directly. One developed by Tamrakar et al. (2005) [2, 3] could be used for both compacted unsaturated and saturated soils simply and easily. But this apparatus cannot measure the suction. There is importance of measuring suction values along

with tensile strength. But with the apparatus of Tamrakar et al. [2, 3], one cannot measure suction. But it is necessary to measure suction and compare this value with tensile strength. Therefore, here, tensile strength measuring apparatus is modified so that it can measure suction at the mid height and the bottom of the specimen before as well as throughout the test. In order to measure the suction, saturated ceramic discs with air entry value (AEV) equal to 240 kPa is used. To see the effect of tensile pulling rates (0.01, 0.1 and 1.0 mm/min), tensile tests were conducted at different tensile pulling rates.

Unconfined compression tests were also conducted with compression rate of 0.1 mm/min. Here also, suction is measured before and through out the test. Finally, suction behavior and strength values of both tensile and unconfined compression tests were compared.

TESTING APPARATUS

In this paper, tensile testing apparatus and unconfined compression testing apparatus are used. Suction in both tests is measured with pore water pressure measuring transducers. For both tests, test specimens are prepared under at the same time and under same condition.

Tensile Test Apparatus

General layout of the modified tensile test apparatus is shown in Fig. 1. The shape of tensile mold is like that of numeric letter "8" consisting of two equal halves, which are connected to outer mold.

These outer molds are connected to lower plates; one of which is fixed and another is movable. Fixed mold (plate) is directly connected to bottom main horizontal platform whereas the movable mold (plate) is connected to bottom main platform via linear sliding roller. This roller will reduce the friction between movable plate and lower plate. Both halves of tensile mold are kept in contact with each other during specimen preparation (insertion) by two horizontal screws, one on each side. Just before starting the test, those two horizontal screws are unscrewed. Then movable half is pulled away in horizontal direction by the motor at constant tensile pulling rate until the soil specimen fails in tension with tensile crack appearing at the middle of the specimen where two halves of the mold is attached.

Load cell placed between the movable half and motor axis measures the tensile load. This tensile load is then divided by the area of the tensile crack perpendicular to horizontal pulling direction, to get tensile stress. The minimum width at the constricted section of the mold is 3 cm and the depth of the tensile mold is 5 cm, which gives tensile failure plane of 15 cm^2 . Displacement during pulling is measured either by using laser sensor or adjusting

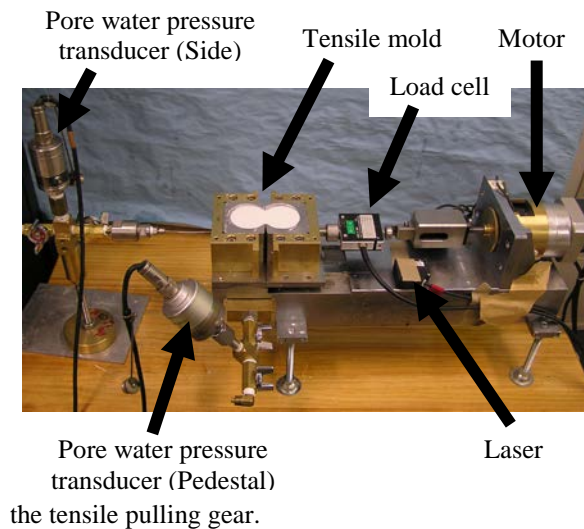


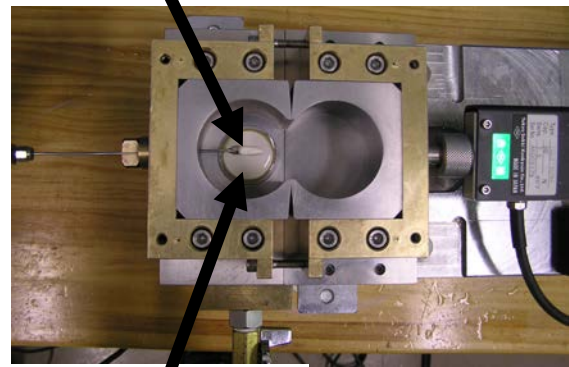
Fig. 1 Newly modified tensile test apparatus.

In contrast to tensile mold used by Tamrakar et al. [2, 3], here two ceramic discs are used to measure the suction (Fig. 2) at two places of test specimen; one at the bottom, i.e., at Pedestal (ped) and another at the mid-height via side; i.e., at side. In the first case, ceramic disc lies at the bottom of the fixed mold whereas in the second case, ceramic disc in from of a small bulb is inserted from the side of the fixed mold upto its center as shown in Fig. 2. Both of these ceramic discs must be fully saturated before the test. Pore-water pressures through these ceramic discs are measured separately using separate pore pressure transducers. Suction measured from the

setup of the specimen into the mold and once the value of suction becomes constant, it is represented as initial suction. Suction measured at tensile failure is generally represented as the maximum (max) values of pore-water pressure.

In this paper, tensile tests are conducted at different tensile pulling rates varying from 0.01 to 1.0 mm/min. Tensile force is measured by load cell is then divided by the tensile failure plane (15 cm^2) to get the tensile stress. By plotting tensile stress and time (or displacement) graph, tensile strength, the maximum value of tensile stress, q_t for the

Ceramic disc (Side)



Ceramic disc (Pedestal)

corresponding test specimen is obtained.

Fig. 2 Tensile test apparatus showing ceramic discs.

Unconfined Compression Test Apparatus

General unconfined compression testing machine is used for the measurement of unconfined compression stress. But in this test also, suction is measured throughout the test. For this, ceramic disc is placed at the bottom pedestal which is then connected to pore-water pressure transducer (Fig. 3). Once the suction becomes constant after the set-up of the specimen, i.e., initial suction values, then unconfined compression test is started. Suction measured at failure (or at 15% of axial strain) is represented as maximum suction at failure.

Unconfined compression test is conducted at displacement rate of 0.1 mm/min. Unconfined compression stress and axial strain relationship is then plotted. Maximum value of unconfined compressive stress within 15% of axial strain is taken as unconfined compressive strength, q_u of that test specimen.

SPECIMEN PREPARATION AND TESTING METHODS

Dried test soil (clay) is mixed with de-aired distilled water for about 30 minutes in a mixture.

The amount of water mixed is equal to two times the liquid limit of the soil specimen. The slurry prepared is then moved into a special cell where mixing as well as simultaneous de-airing is possible. Mixing and de-airing in this cell is done for 3 hours. Slurry is then de-aired by applying suction into that cell.

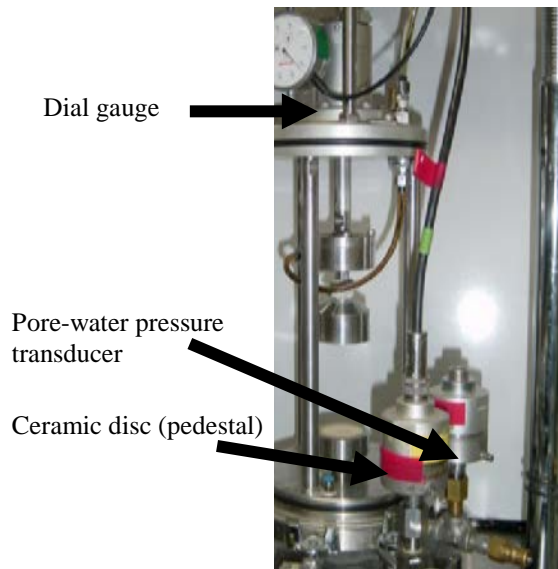


Fig. 3 Unconfined compression test apparatus.

De-aired slurry is then poured into consolidation molds; tensile consolidation mold (TCM) and unconfined compression consolidation mold (UCCM) as shown in Fig. 4. TCM is used for preparing tensile test specimen and UCCM is used for preparing unconfined compression test specimen.

Before pouring the slurry into each consolidation mold, greasing of inner part of consolidation mold is done. Also, upper and lower porous stones used of drainage during consolidation of each mold are de-aired and saturated. Filter paper is placed on the lower porous stone before pouring the slurry into it and then after finishing the pouring, filter paper is placed on the top and with upper porous stone. Both porous stones and filter papers enhance the consolidation. Here, two-way drainage is allowed in both consolidation molds. Consolidation loads are then applied in steps.

Here, five test specimens are prepared by applying consolidation pressure, P'_c equal to 50, 100, 200 and 300 kPa, respectively. All the test specimens are normally consolidated.

The inner cross sections of TCM as well as UCCM are same as that of tensile test specimen and UC test specimen, respectively. Therefore, during the test, only thickness of the test specimen from the consolidation mold is to be adjusted; 5 cm thick for tensile test and 10 cm height for unconfined

compression test. Wire saw is used for cutting as well as trimming the consolidated test specimens. Since side trimming of the test specimen is not required, disturbance to the test specimen is highly reduced.

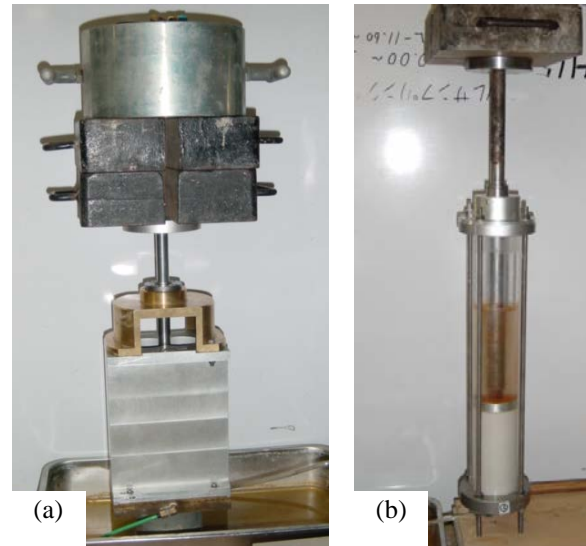


Fig. 4 Special consolidation molds for (a) tensile test and (b) unconfined compression test.

Once the consolidation is finished, then consolidated specimens are shifted to respective testing apparatus. In case of tensile test, direct moving of consolidated specimen from TCM to tensile mold of tensile testing apparatus is done. Adjustment of the positions is made so that the consolidated specimen easily slides into tensile mold when pushed from the top. Proper care is taken to reduce the disturbance. Once the specimen touch the bottom pedestal (ceramic disc), reading of the pore-water pressure starts to change. A small pressure is applied to the specimen so that the test specimen touches the bottom of the mold. After this, ceramic disc from the side of the tensile mold is inserted in order to measure the suction at the mid height of the specimen. Proper care is taken so that side ceramic disc just reaches the center of the fixed mold. Once this is done, then the test specimen is separated from the TCM by cutting it using wire saw which is pre-setup between the TCM and tensile mold. Upper portion of the test specimen is then trimmed and covered with a polythene sheet to avoid moisture loss. Pore-water pressures from both ceramic discs are measured continuously until they reach to certain constant value, called initial suction. Then two horizontal screws which keep the halves of tensile mold combined, are loosened and removed and whole the apparatus is covered by a box. This will

prevent the moisture lost during the test. Tensile pulling is then started at constant rate via motor gear. Tensile load is measured from the load cell and displacement is measured using laser sensor. Continuous measurement of tensile load, displacement and suction ($-u_w$: negative pore water pressure) are done.

In case of unconfined compression test, the consolidated specimen from UCCM (Fig. 3(b)) is pushed out and then cut into a length of little longer than 10 cm. Finally trimming of upper and lower surfaces of this cut specimen is done so that test specimen of exactly 10 cm length is obtained. Test specimen is set up on the unconfined compression testing apparatus shown in Fig. 2. Once the suction measured at the lower pedestal becomes constant then compression is started at a constant rate of 0.1 mm/min. Unconfined compressive stress, displacement (or axial strain) and suction are measured simultaneously.

TEST RESULTS AND DISCUSSIONS

In Figs. 5 and 6, the effect of tensile pulling rate is shown. With the increase in tensile pulling rate, there is increase in tensile stress. Here, the medium value of tensile pulling rate, 0.1 mm/min is chosen for comparing the tensile strengths values with others.

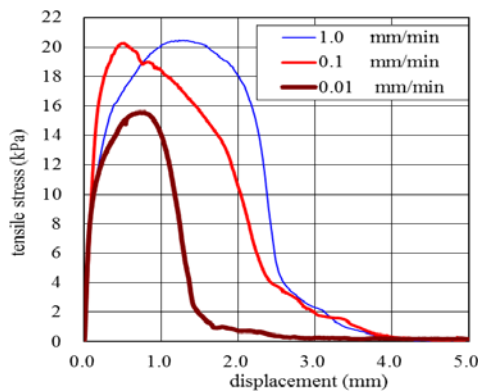


Fig. 5 Tensile pulling rate effect (P'_c 200 kPa).

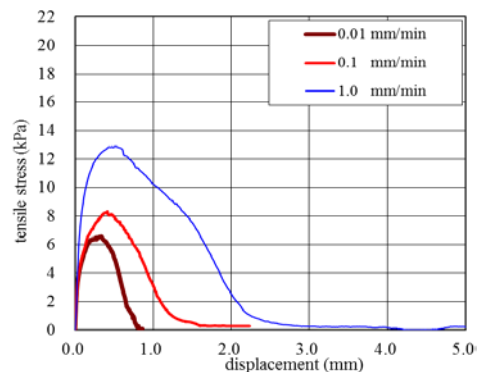


Fig. 6 Tensile pulling rate effect (P'_c 50 kPa).

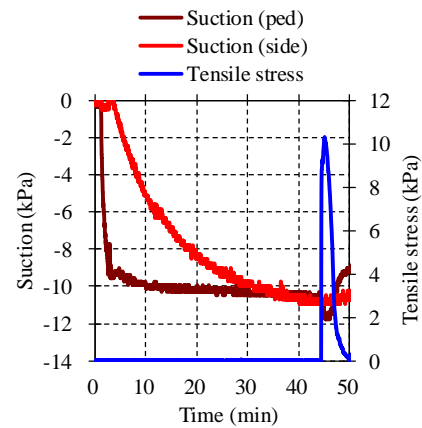
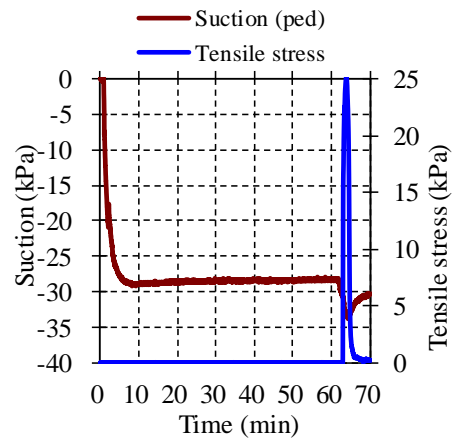


Fig. 7 Tensile stress, suction (ped) and suction (side)



measured during the tensile test (50 kPa).

Fig. 8 Tensile stress, suction (ped) and suction (side) measured during the tensile test (200 kPa).

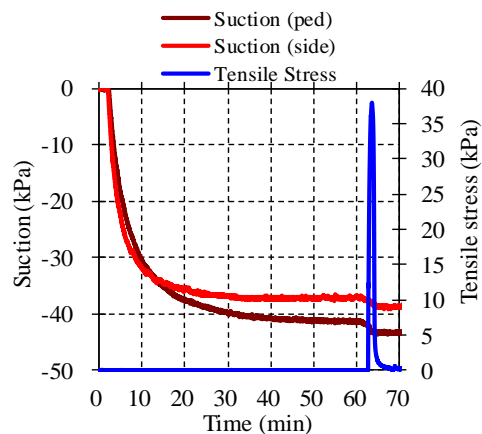


Fig. 9 Tensile stress, suction (ped) and suction (side) measured during the tensile test (300 kPa).

In Figs. 7, 8 and 9, the tensile stress curves along with the measurement of suction at the pedestal

(ped) and side ceramic discs from the start to end of the tensile pulling test are shown. As seen, tensile pulling is started when the values of suction become almost constant. Although there is little variation in the values of suction measured at the pedestal and side ceramic discs, they show almost same trend with almost closer values.

In case of tensile stress curves, a peak value is seen showing the tensile strength (q_t). Around the tensile failure, there is an increase in suction values. (suction at failure).

In Figs. 10, 11 and 12, unconfined compressive stress and suction (measured at pedestal ceramic disc) from the start to end to the test are shown. Here also, the compression is started only after the initial suction value of specimen became constant. The peak value of unconfined compression curve given the unconfined compression strength (q_u). Just near the compressive failure, the change is suction value is seen. Here, in contrary to tensile test, decrease in suction values at failure is seen.

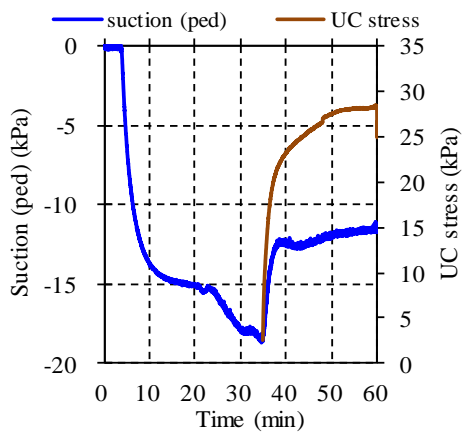


Fig. 10 Unconfined compression test (50 kPa).

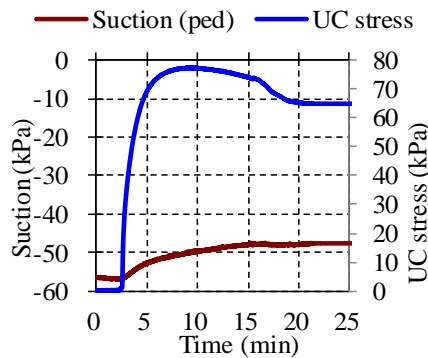


Fig. 11 Unconfined compression test (200 kPa).

Tables 1 and 2 show the values of tensile strength, unconfined compressive strength, and suction values measured just before (initial) the test

and at failure. With the increase in the consolidation pressure, there is increase in tensile as well as unconfined compressive strengths. The ratio of q_t/P'_c lies in the range of 0.13 to 0.21 and the ratio of q_u/P'_c lies in the range of 0.35 to 0.56.

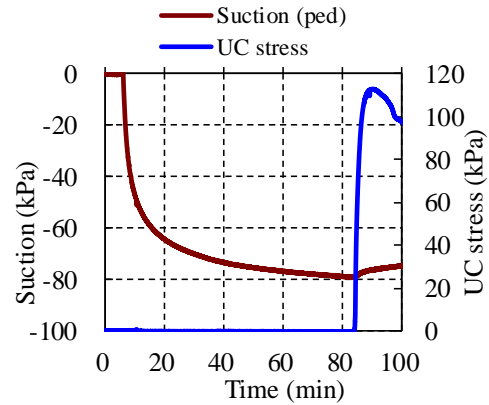


Fig. 12 Unconfined compression test (300 kPa).

Table 1 Tensile test results

P'_c (kPa)	Suction (kPa)		q_t (kPa)	q_t/P'_c
	Initial	Failure		
50	10.5	11.3	-10.3	-0.21
100	17.1	19.7	-17.0	-0.17
150	20.5	27.1	20.9	-0.14
200	28.8	33.2	-25.1	-0.13
300	41.7	43.3	-37.8	-0.13

Table 1 Unconfined compression test results

P'_c (kPa)	Suction (Ped) (kPa)		q_u (kPa)	q_u/P'_c	q_u/q_t
	Initial	Failure			
50	-16.9	-11.5	28.2	0.56	-2.74
100	-30.2	-19.7	43.4	0.43	-2.55
150	-43.3	-25.8	53.1	0.35	-2.54
200	-40.4	-31.2	75.1	0.38	-2.99
300	-77.2	-72.7	111.4	0.37	-2.95

In Tables 1 and 2, the values of q_t , q_u , initial and final (at failure) suction values measured at pedestal (ped) and (side) are shown. Also, the effect of consolidation pressure on q_t and q_u are shown. Accordingly with the increase in consolidation pressure, both strengths show increment. The ratio of q_t/P'_c ranges from -0.13 to -0.21 and similarly, the ratio q_u/P'_c ranges from 0.34 to 0.56.

In the Table 2, the ratio of q_u/q_t for various consolidation pressures is shown. For the saturated NSF clay, this ratio lies between -2.54 to -2.99,

showing almost same ratio.

Comparing the suction values measured at the pedestal (ped) during tensile and compressive failures, their values are almost same (except for 300 kPa). This shows that the suction values at failure in both tests will be same.

CONCLUSION

Here, the effect of tensile pulling rate on tensile strength is checked. At the same time the ratios q_t/P'_c and q_u/P'_c as well as the strength ratio, q_u/q_t and suction measured at failure of both tests are shown. From the tensile test as well as unconfined compression test with suction measurement, following conclusions are made;

1. Tensile strength increases with the increase tensile pulling rate.
2. Both tensile strength and unconfined compression strengths increase with the increase in the consolidation pressure. The ratio of q_t/P'_c and q_u/P'_c are -0.13~-0.21 and 0.34~0.56, respectively.
3. The ratio of q_u/q_t for the saturated NSF clay is found to be in the range of -2.54~-2.99, showing almost the same value.
4. Suction values measured at the pedestal during failure in both tests show almost same values, except for the case of 300 kPa consolidation pressure.

REFERENCES

- [1] Nahlawi, H., Chakrabarti, S. and Kodikara, J., "A direct tensile strength testing method for unsaturated geomaterials", *Geotechnical Testing Journal*, 27, 4, 2004, pp. 356-361.
- [2] Tamrakar, S.B., Toyosawa, Y., Mitachi, T. and Itoh, K., "Tensile strength of compacted and saturated soils using newly developed tensile strength measuring apparatus", *Soils and Foundations*, 45, 6, 2005a, pp. 103-111.
- [3] Tamrakar, S.B., Mitachi, T., Toyosawa, Y. and Itoh, K., "Development of a new soil tensile strength test apparatus, Proc., Geo-Frontiers 2005, Geotechnical Special Publication 138 (CD-ROM) Site Characterization and Modeling, ASCE, Reston, Va., 2005b.

COUPLED ANALYSIS OF BIFURCATION AND SHEAR BAND IN SATURATED SOILS: EFFECT OF CHARACTERISTIC LENGTH SCALE

Peijun Guo

Department of Civil Engineering, McMaster University, Hamilton, Ontario, Canada

ABSTRACT

For saturated soils, owing to its inherent dilation or contraction feature under shearing, the presence of pore fluids alters the deformation process and may either facilitate or delay material instability or bifurcation. A perturbation approach is used to investigate the bifurcation of saturated soils sheared under undrained conditions. Even for rate-independent materials, the diffusion of pore pressure involves a certain characteristic length scale (or time scale) and the rate effect. The coupling between soil skeleton deformation and pore fluid can result in different types of bifurcation, in the form of localization of soil skeleton, the diffuse mode of either soil skeleton or pore pressure. The diffuse mode is activated at the state near the peak deviator stress and it is delayed when the inertia effect is taken into account. When pore pressure bifurcation occurs, the thickness of shear band is affected by the rate of deformation, the amplitude of strain difference across the shear boundary.

Keywords: Bifurcation, Shear band, Instability, Perturbation method

INTRODUCTION

The bifurcation and unstable behaviour of soils have been extensively investigated both analytically and experimentally. It has been shown that soil specimens uniformly stressed may undergo non-uniform strains such as surface buckling, volume instability, or shear banding at certain critical states of stress or strain [1]-[7]. Conventional bifurcation analysis, such as the Thomas-Hill-Mandel shear-band model [7], consists of finding perturbation solutions (i.e., difference between the heterogeneous and homogeneous fields of incremental displacement) that satisfy the constitutive law and that are compatible with boundary condition. Some published researches have different conclusions on the effect of pore fluids on bifurcation and deformation instability of saturated soils under undrained conditions (see, for example, [1], [2], [6] and [7]).

In this paper, a perturbation approach is used to investigate the bifurcation of saturated soils sheared under undrained conditions. The mixture theory is used to formulate the governing equations of the all phases in the soil. Depending on material properties and the rate of shearing, the variation of perturbation in both pore pressure and soil skeleton deformation may result in either diffuse or localized bifurcation modes.

PROBLEM FORMULATION

In this section, the governing equations for fully-saturated soil subjected to simple shear and the

stress-strain relations are formulated using the mixture theory. The sign convention in continuum mechanics is adopted; i.e., compressive stresses and strains are referred to as negative.

Stress-Strain Relations and Governing Equations

Stress-strain relations

Following Rice [6], let us consider a layer of saturated soil sheared in plane strain, as shown in Figure 1. Within this layer, all field quantities vary only with y (across the layer) and time t . The shear strain γ and volumetric strain ϵ are expressed as:

$$g = \frac{\hbar u_x}{\hbar y}, \quad e = \frac{\hbar u_y}{\hbar y} \quad (1)$$

where u_x and u_y are displacement components of a material point. Strain rates are decomposed into

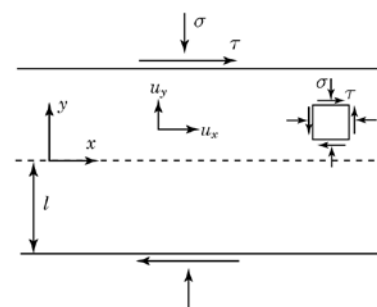


Figure 1: A layer of saturated soil of 2ℓ thickness subjected to simple shear

elastic and plastic components such that $\dot{\epsilon}_{ij} = \dot{\epsilon}_{ij}^e + \dot{\epsilon}_{ij}^p$. The elastic shear and volumetric strain rates are

$$\dot{\epsilon}^e = \dot{\epsilon} / G, \quad \dot{\epsilon}^p = \dot{\epsilon} / M \quad (2)$$

where G and M are the shear and constrained modulus, respectively. The constrained modulus can be related to the shear modulus and Poisson's ratio n by $M = 2G(1 - n) / (1 - 2n)$.

The linear Mohr-Coulomb model is selected as the constitutive model, for which the yield function F and plastic potential Q are expressed

$$F = t + s[m(e, g^p, \dot{g}^p); Q = t + s[b_D(e, g^p, \dot{g}^p) \quad (3)$$

The mobilized friction angle j_m and the angle of dilatancy γ_m (and hence μ and the dilatancy factor $b_D = \sin \gamma_m$) are both assumed to be functions of appropriate hardening variables. It should be noted that b_D is positive for dilation and negative for contraction. The plastic shear strain rate \dot{g}^p is related to plastic volumetric strain rate $\dot{\epsilon}^p$ by

$$\dot{\epsilon}^p = b_D(e, g^p, \dot{g}^p) \dot{g}^p \quad (4)$$

Following the standard procedure in the theory of elasto-plasticity, the incremental stress strain relations are expressed as [6]:

$$\begin{aligned} dg &= \frac{1}{G} \dot{\epsilon}^e + \frac{dt + m \dot{\epsilon}^p}{h} \\ de &= \frac{1}{M} \dot{\epsilon}^p + \frac{ab(dt + m \dot{\epsilon}^p)}{h} \end{aligned} \quad (5)$$

where $h = -s[m] / G$, $h_t = dm / dg^p$, $a = M / G$. Under undrained conditions, setting $de = 0$ results in

$$dt = \frac{h + abm}{1 + h + abm} G dg, \quad ds = -\frac{ab}{H} G dg \quad (6)$$

where $H = 1 + h + abm$, $G^* = G(h + abm) / H$.

Equations of mass balance

When taking into account the compressibility of pore-fluid and soil grains, the equations of mass balance for solid phase and fluid phase read ([7], page 147):

$$\frac{1}{1-n} \frac{dn}{dt} = \frac{de}{t} + \frac{1}{r_s} \frac{dr_s}{dt} \quad (7)$$

$$- \frac{j(nw_y)}{j_y} = \frac{de}{t} + \frac{1}{r_s} \frac{dr_s}{dt} + \frac{n}{r_w} \frac{dr_w}{dt} \quad (8)$$

in which $w_y = v_{wy} - v_{sy}$ is the pore velocity of water, v_w and v_s are the velocity of water and solid particles respectively. By introducing Darcy's law $q = -\frac{k}{r_w g} \frac{dp}{dy}$ in which k is the hydraulic conductivity of the material, $q = n(v_{wy} - v_{sy})$ is the specific discharge and n is the porosity of soil. The mass balance equation, Eq. (8), for the fluid phase can be rewritten as

$$- \frac{j}{j_y} \frac{k}{r_w g} \frac{dp}{dy} = \frac{de}{t} + \frac{1}{r_s} \frac{dr_s}{dt} + \frac{n}{r_w} \frac{dr_w}{dt} \quad (9)$$

Equations of linear momentum balance

The equations of the linear momentum balance are established using the mixture theory. In mixture theory, the linear momentum balance must hold separately for each constituent and for the whole medium. The interaction forces between the solid and fluid phases and the linear momentum resulting from the mass transfer should also be included in the momentum balance. For a constituent α , the balance of linear momentum reads

$$s_{ij,j}^a + n^a r^a g_i + p_i = n^a r^a \frac{D^2 u_i^a}{Dt^2} \quad (10)$$

where s_{ij}^a is the partial Cauchy stress tensor for the α -th phase, p_i is the interaction force (i.e. the drag force) component and g_i the gravity component.

For a two-phase material, the linear momentum balance for the bulk material requires

$$s_{ij,j} + f_i = r \frac{h^2 u_i}{h t^2} + n r_w \frac{h w_i}{h t} \quad (11)$$

with $w_i = v_{wi} - v_{si}$, $f_i = (1 - n)f_i^s + f_i^w$ is the bulk body force per unit volume, $r = r_s(1 - n) + n r_w$ is the bulk density, s_{ij} is the Cauchy stress tensor of the mixture as a whole. The interaction (or the drag force) induced by water flow is expressed as ([8]-[9]):

$$p_i = \frac{n r_w g}{k} q_i = \frac{n^2 r_w g}{k} (v_{wi} - v_{si}) \quad (12)$$

It follows that

$$\begin{aligned}
 & -n \frac{dp}{dx_i} + nr^w g_i - \frac{n^2 r_w g}{k} (v_{wi} - v_{si}) = nr^w \frac{d^2 u_i^w}{dt^2} \\
 & - (1-n) \frac{hp}{hx_i} + \frac{hs_{ij}}{hx_j} + (1-n)r^s g_i \\
 & = (1-n)r^s \frac{d^2 u_i^s}{dt^2} - \frac{n^2 g_w}{k} (v_{wi} - v_{si}) \\
 & - \frac{hp}{hx_i} + \frac{hs_{ij}}{hx_j} + (1-n)r^s + nr^w g_i = r \frac{d^2 u_i^s}{dt^2} + nr^w \frac{dw_i}{dt}
 \end{aligned}$$

for the fluid phase, solid phase and the mixture, respectively.

For a layer of soil subjected to simple shear as illustrated in Figure 1, when applying the stress-strain relations and neglecting the compressibility of water and soil grains, the equation of mass conservation for the fluid phase and the linear momentum balance are simplified as

$$\begin{aligned}
 \frac{k}{r_w g} \frac{h^2 p}{h^2} &= \frac{1+h+ab_D m}{aG(1+h)} \frac{dp}{dt} + \frac{b_D}{1+h} \frac{hg}{t} \quad (13) \\
 \frac{h}{1+h} \frac{G}{G} \frac{h^2 g}{y^2} - \frac{m}{h} \frac{dp}{y^2} &= (1-n)r^s \frac{d^2 g}{dt^2} + \frac{n^2 r_w g}{k} \frac{hg}{t} \quad (14)
 \end{aligned}$$

COUPLED PERTURBATION ANALYSIS FOR SATURATED SOILS

Perturbation Equations

For a shear soil sample under constant normal stress σ as illustrated in Figure 2, let us consider small perturbations, $\tilde{u}(y,t)$ and $\tilde{p}(y,t)$, within the shear band over the homogeneous displacement and in pore pressure fields, $u(y,t)$ and $p(y,t)$, outside the band. For continuous bifurcation, the materials within and outside the shear band can be described by the same stress-strain relation [6]. We study spatial perturbations at zero normal stress perturbation $\tilde{s} = 0$ with the following forms:

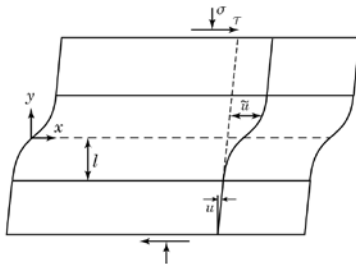


Figure 2: Inhomogeneous displacement field induced by a shear band

$$\begin{aligned}
 \tilde{g}(y,t) &= \frac{h\tilde{u}(y,t)}{ht} = G \exp(St + iby) \\
 \tilde{p}(y,t) &= P \exp(St + iby)
 \end{aligned} \quad (15)$$

where P and G are the amplitude of initial perturbations in the shear strain and pore pressure, respectively; S is a quantity reflects the growth of a perturbation with time; $bl = p/2$ with $l = 2\ell$ being considered as the wavelength of the perturbation. The initial value of maximum perturbation shear strain rate is $\dot{\tilde{g}}_0 = \tilde{g}(y,t)/t|_{t=0} = S$. When $S > 0$, a perturbation grows exponentially with time and eventually becomes infinite. Correspondingly, a negative S shows that the perturbation is stable.

Perturbation induced shear stress and volumetric strain are determined from the stress-strain relation as

$$\tilde{\tau} = -m\tilde{p} + h\tilde{g}^p, \quad \tilde{\epsilon} = \frac{\tilde{p}}{M} + b_D \tilde{g}^p \quad (16)$$

The mobilized frictional coefficient μ , the dilatancy factor b_D and the plastic modulus h should be understood as functions of the unperturbed homogeneous strains. The evolution of the perturbations must satisfy the equations for mass conservation of water and the linear momentum balance:

$$\frac{k}{r_w g} \frac{h^2 \tilde{p}}{h^2} = \frac{1}{1+h} \frac{dp}{dt} + \frac{b_D}{1+h} \frac{hg}{t} \quad (17)$$

$$\frac{h}{1+h} \frac{G}{G} \frac{h^2 \tilde{g}}{y^2} - \frac{m}{h} \frac{dp}{y^2} = (1-n)r^s \frac{d^2 \tilde{g}}{dt^2} + \frac{n^2 r_w g}{k} \frac{hg}{t} \quad (18)$$

Considering the perturbations in Eq. (15), the above equations expressed in terms of the magnitude of initial perturbations are given as

$$-Pb^2 = \frac{r_w g}{k(1+h)} \frac{dp}{dt} + \frac{b_D}{1+h} \frac{hg}{t} S \quad (19)$$

$$\frac{h}{1+h} \frac{G}{G} \frac{h^2 \tilde{g}}{y^2} - \frac{m}{h} \frac{dp}{y^2} = (1-n)r^s S + \frac{n^2 r_w g}{k} \frac{hg}{t} S \quad (20)$$

Elimination of P and G from Eqs. (19) and (20) yields

$$f(S) = A_0 S^3 + AS^2 + BS + C = 0 \quad (21)$$

where

$$A_0 = (1-n)kr^s H / (aG)$$

$$A = (1-n)r^s b^2 k^2 (1+h) + n^2 H / (aG)$$

$$B = kb^2 \frac{aG}{(1+n)}(1+h) + (h+ab_D m)/a$$

$$C = Gb^4 k^2 h; \quad k = k/(r_w g)$$

For perturbations of long wave length (i.e., $b \gg 0$) corresponding diffuse bifurcation, Eq. (21) yields

$$S = - \frac{n^2}{(1-n)kr^s} < 0 \quad (22)$$

The negative value of S shows that the perturbation is stable.

For perturbations of short wave length that corresponds to thin shear band when $b \rightarrow 0$, Eq. (21) takes the following form

$$A_0 S^3 + Gb^2 kh = 0; \quad S = - \frac{aG^2 b^2 kh}{(1-n)kr^s H}^{1/3} \quad (23)$$

which implies that perturbations of very short wave length are generally stable when $h > 0$. Obviously, for the perturbation zone with finite thickness as illustrated in Figure 2, the two extremes at $b \rightarrow \infty$ and $b = 0$, however, undermine the spatial variation of both shear strain and pore pressure. Consequently, it is more relevant to examine evolution of perturbations under general condition with limited values of wave number β or the wave length $l = 2\ell$.

DEFORMATION INSTABILITY ANALYSIS

Instability without Inertia Effects

Let us first examine the stability of deformation when the rate of deformation is small enough and hence the inertia effect can be neglected. Corresponding to this assumption, Eq. (21) is simplified as

$$f_1(S) = A_1 S^2 + BS + C = 0 \quad (24)$$

where $A_1 = n^2 H / (aG)$, B and C are the same as defined previously.

The stability of perturbation evolution can be explored by examining the nature the roots of the quadratic equation in Eq. (24). The determinant of Eq. (24) can be expressed as

$$D = a^{-2} k^2 b^4 (1 - an^2)^2 (h - h_1^{cr})(h - h_2^{cr}) \quad (25)$$

with

$$h_1^{cr} = \frac{a(n + \sqrt{-b_D m})^2}{1 - an^2}, \quad h_2^{cr} = \frac{a(n - \sqrt{-b_D m})^2}{1 - an^2}$$

Eq. (24) has real roots when $h \geq \max(h_1^{cr}, h_2^{cr})$ or $h \leq \min(h_1^{cr}, h_2^{cr})$. During frictional hardening (i.e., $h > 0$), $D = 0$ is possible only when $1 - an^2 > 0$ (or $n < 1/\sqrt{a}$) and $h > h_1^{cr} > h_2^{cr} > 0$. It can be shown that any bifurcation prior to $h = h_1^{cr}$ is stable. At $h = h_2^{cr}$, the root of Eq. (24) is

$$S = - \frac{2an(1 - an\sqrt{-b_D m})(n - \sqrt{-b_D m})}{1 - an^2}$$

which is positive when

$$n < \min\left\{\sqrt{-b_D m}, \frac{1}{a\sqrt{-b_D m}}, \frac{1}{\sqrt{a}}\right\} \quad (26)$$

or

$$\frac{1}{\sqrt{a}} > n > \max\left\{\sqrt{-b_D m}, \frac{1}{a\sqrt{-b_D m}}\right\} \quad (27)$$

In other words, depending on the materials properties, unstable perturbation is possible for saturated soils with the porosity satisfying the above constraints and when $h < h_2^{cr}$.

Instability with Inertia Effects

When the inertia effect of the fluid phase in considered, Eq. (21) can be rewritten as after applying Eq. (24):

$$f(S) = A_0 S^3 + (A - A_1)S^2 + f_1(S) \quad (28)$$

where $(A - A_1) = (1 - n)r^s b^2 k^2 (1 + h)$. As both A_0 and $(A - A_1)$ are positive, for unstable perturbation ($S > 0$), the condition $f(S) = 0$ requires $f_1(S) < 0$. As the value of $f(S)$ decreases with decreasing hardening parameter h , the inertial effect delays the bifurcation of deformation.

DIFFUSE BIFURCATION VS. LOCALIZED BIFURCATION

The bifurcation of saturated soil deformation under undrained conditions may manifest itself in either diffusive mode or localized mode, depending on the wavelength of the perturbation, which is determined as $l = 2\ell = p/b$. We examine the following cases.

Case 1: Zero pore pressure perturbation $P = 0$

For zero pore pressure perturbation (i.e., $P = 0$), according to the mass conservation in Eq. (19), the

non-trivial perturbation solution with non-zero value of G exists only if $b_D = 0$. The balance of linear momentum, Eq. (20), yields

$$\frac{1}{b^2} = -\frac{Gh}{1+h} \frac{1}{(1-n)r^s S^2 + \frac{n^2 r_w g}{k} S} \quad (29)$$

which requires $-\frac{n^2 r_w g}{k(1-n)r^s} < S < 0$ when $h > 0$.

Recalling that the amplitude of shear strain rate associated with the perturbation $\dot{g}_0 = SG$, Eq. (29) becomes

$$\frac{1}{b^2} = -\frac{h}{1+h} \frac{kGG}{n^2 r_w g \dot{g}_0} \frac{1}{1 + \frac{k(1-n)r^s}{n^2 r_w g} \frac{\dot{g}_0}{G}} \quad (30)$$

The minimum perturbation wavelength l_{\min} is determined as

$$l_{\min} = \rho \frac{2k}{n^2 r_w g} \sqrt{\frac{Gh}{1+h}} (1-n)r^s \quad (31)$$

One observes that l_{\min} is affected by the porosity, hydraulic conductivity and the hardening parameter h . However, the bifurcation is stable since $S < 0$.

In general, for saturated soils under undrained conditions, a displacement perturbation may induce local volume change and hence pore pressure variation. As such, zero pore pressure perturbation $P = 0$ is only a special case that is applicable to impermeable soils or soils with very low permeability.

Case 2: non-zero pore pressure perturbation $P \neq 0$

For small perturbations, when neglecting the inertia effect and eliminating Γ from Eqs. (19) and (20), one obtains after applying $\dot{g}_0 = SG$:

$$\frac{1}{b^2} = \frac{k}{r_w g} \frac{(h + ab_D m) - a(1+h)n^2}{ab_D n^2} \frac{P}{\dot{g}_0} \quad (32)$$

Bifurcation is possible when β has real values, which requires

$$b_D < 0, \quad h < h_{cr3}, \quad 1 - an^2 > 0 \quad (33)$$

with

$$h_{cr3} = \frac{a(n^2 - b_D m)}{1 - an^2}$$

The corresponding wavelength of perturbation is

$$l = 2\ell = \rho \sqrt{\frac{k}{r_w g} \frac{(1 - an^2)h + a(b_D m - n^2)P}{ab_D n^2} \frac{P}{\dot{g}_0}} \quad (34)$$

It is found that unstable bifurcation is possible when the hardening parameter $h = h_2^{cr}$, with the wavelength being

$$l = \rho \sqrt{\frac{k}{r_w g} \frac{m}{n} \frac{P}{b_D m \dot{g}_0}} \quad (35)$$

It should be noted that the wavelength tends to increase as h decreases with continuous plastic deformation. In summary, the following conclusions can be drawn:

- Bifurcation with $P \neq 0$ can take place only in contractive soil with $b_D < 0$;
- The perturbation wavelength λ tends to decrease as the shear strain velocity increases;
- Both the hydraulic conductivity and porosity of soil have influence on λ ;
- As the pore pressure difference within and outside the shear band increases, the perturbation wavelength λ will increase.

CHARACTERISTIC LENGTH OF PORE PRESSURE DIFFUSION

It has been known that the time (t_c) required to establish pore pressure equilibrium is related to the characteristic length scale (l_c) and the diffusion (or consolidation) coefficient c_v by $l_c = \sqrt{c_v t_c}$. When l_c is smaller than the perturbation wavelength λ for the time of interest t_c , the inhomogeneous pore pressure distribution described in Eq. (15) could be maintained. For this case, the coupled bifurcation analysis under isochoric conditions as discussed previously is valid. Given $c_v = k / (m_v r_w g)$ that depends on the hydraulic conductivity k and the coefficient of volume compressibility m_v of soil, with a decrease of k and the modulus of soil, the diffusion length may decrease to its minimum value at the material micro-structural length scale that is about the diameter of soil grains [10]. On the other hand, if l_c is larger than λ , the dissipation of pore pressure within the zone of perturbation and pore-water flow will take place, accompanied by the local volume change ([2], [3], [11]). When the diffusion scale length is of the order as the dimension of the specimen, diffuse instability takes place. From a perturbation analysis of pore pressure when both the normal and shear stresses are unchanged (i.e., $s = t = 0$), Garagash [10] related l_c to the shear

strain rate \dot{g} by $l_c = \sqrt{(k/r_w g)M\dot{g}^{-1}}$ with M being the constrained modulus of soil.

For simplicity, let us only examine the bifurcation and deformation stability close to the peak of the effective stress path when $h = h_p = -ab_D$. At this state, the dilatancy factor is generally $b_D < 0$. According to Eq. (34), the wavelength length of perturbation is

$$l_{G^*=0} = \rho \frac{k}{r_w g} \frac{1 - ab_D m P}{b_D \dot{g}_0}^{1/2} \quad (36)$$

which can be related with the characteristic length scale (l_c) as

$$\frac{l_{G^*=0}}{l_c} = \rho \frac{1 - ab_D m P}{b_D M}^{1/2} \quad (37)$$

which implies that perturbation wavelength exists when $b_D < 0$. Depending on the value of b_D , the perturbation wavelength may be smaller than or of the same order as the characteristic length scale (l_c). In addition, since $\dot{g}_0 = SG$, one may conclude that the perturbation growth rate is inversely proportional to the square of the wavelength. Localized deformation mode with small shear band thickness cannot be precluded; however, it will experience maximum amplitude growth and cause instability comparing with diffuse bifurcation at this point.

CONCLUSION

A perturbation approach is used to investigate the bifurcation of saturated soils sheared under undrained conditions. Even for rate-independent materials, the diffusion of pore pressure involves a certain characteristic length scale (or time scale) and the rate effect. The coupling between soil skeleton deformation and pore fluid can result in different types of bifurcation, in the form of localization of soil skeleton, the diffuse mode of either soil skeleton or pore pressure. When uniform pore pressure, bifurcation can only take place when soil has no militancy (i.e., $b_D = 0$). On the other hand, bifurcation with $P \neq 0$ can take place only in contractive soil with $b_D < 0$. The perturbation wavelength λ tends to decrease as the shear strain velocity increases, and it is also affected by the hydraulic conductivity and porosity of soil.

ACKNOWLEDGEMENTS

Funding provided by the Natural Sciences and Engineering Research Council of Canada is gratefully acknowledged.

REFERENCES

- [1] Vardoulakis I, Goldscheider M, Gudehus G, "Formation of shear bands in sand bodies as a bifurcation problem", *Int. J. Numer. Anal. Meth. Geomech.* 2(2), 1987, 99–128.
- [2] Finnno RJ, Viggiani G, "Shear bands in plane strain compression of loose sand", *Geotechnique* 47 (1), 1997, 149–165.
- [3] Desrues J, and Viggiani G, "Strain localization in sand: an overview of the experimental results obtained in Grenoble using stereo-photogrammetry", *Int. J. Numer. Anal. Meth. Geomech.* 28, 2004, 279–321.
- [4] Kodaka T, Higo Y, Kimoto S and Oka F, "Effects of sample shape on the strain localization of water-saturated clay", *Int. J. Numer. Anal. Meth. Geomech.* 31, 2007, 483–521.
- [5] Nicot F, and Darve F, "Diffuse and localized failure modes: Two competing mechanisms", *Int. J. Numer. Anal. Meth. Geomech.* 35, 2011, 586–601.
- [6] Rice JR, "On the stability of dilatant hardening for saturated rock masses", *J. Geophysical Research*, 80, 1975, 1531–1536.
- [7] Vardoulakis I, and Sulem J, *Bifurcation Analysis in Geomechanics*. Chapman & Hall: London, 1995.
- [8] Hueckel TA, "Water-mineral interaction in hydromechanics of clays exposed to environmental loads: a mixture-theory approach", *Can. Geotech. J.* 29, 1992, 1071–1092.
- [9] Loret B and Prevost JH, "Dynamic strain localization in fluid-saturated porous-media", *J. Eng. Mech.* 117(4):, 1991, 907–922.
- [10] Garagash DI and Rudnicki JW, "Stability of undrained deformation of fluid-saturated geomaterials", In: *Proceedings of the 9th International Symposium on Plasticity* (Khan A and Lopez-Pamies O Eds.), 2002, 492–494.
- [11] Guo P, "Undrained shear band in water saturated granular media: a critical revisiting with numerical examples", *Int. J. Numer. Anal. Meth. Geomech.*, 37(4), 2013, 353–373.

BEARING CAPACITY OF SOIL REINFORCED WITH SOIL-CEMENT COLUMNS FORMED BY THE DEEP MIXING METHOD

Ahmad Safuan A Rashid¹ and Jonathan A Black²

¹Faculty of Civil Engineering, University Teknologi Malaysia, Malaysia; ² Department of Civil and Structural Engineering, University of Sheffield, United Kingdom

ABSTRACT

The paper presents on a series of sl-scale pne strain 1g physical model tests designed to examine the bearing capacity of soil-cement columns formed via Deep Mixing (DM). Pre-formed soil-cement columns 24mm in diameter were installed in a soft clay bed with the improvement area ratios, a_p , was 26% beneath a rigid foundation of width 100mm. Two types of column installation which is fully and partially penetrated were investigated in the laboratory scale. Particle Image Velocimetry (PIV) was implemented in conjunction with close range photogrammetry in order to track soil displacement during loading from which the failure mechanisms were derived. Bearing capacity performance was verified using numerical analysis software (LimitState:GEO). The bearing capacity increased between 78% and 140% from the untreated soil model.

Keywords: Bearing Capacity, Soil Cement Column, Deep Mixing Method, Particle Image Velocimetry (PIV)

INTRODUCTION

Deep Mixing (DM) is a soil modification technique commonly employed to improve the bearing resistance of soft soil ground. Soil is mixed in column form with a cement stabilising agent that improves the engineering properties of soft ground, providing increased strength and stiffness, as well as reduced permeability [1], [2], [3]. A number of laboratory physical model and field tests have been conducted in order to evaluate the ultimate bearing capacity of soft soil reinforced via DM [4], [5], [6], [7], [8], [9], [10], [11], [12]. However, fewer attempts have been made to study the performance between fully and partially penetrated cases of deep mixing method.

This paper presents results obtained from a series of small-scale experiments conducted using fully and partially penetrated soil-cement columns in a rectangular group formation, with improvement area ratios of 26% (corresponding to 9 columns) and loaded to failure under a rigid footing. Failure mechanics throughout the full loading history were assessed in terms of soil displacement measurement using Particle Image Velocimetry (PIV), complemented by post examination of the columns via model dissection. Numerical analysis in the form of an Ultimate Limit State software program (Limitstate:GEO) was employed to validate the laboratory results.

TEST PROCEDURES

Model Preparation

A model of a soft ground was prepared in a rigid 400 mm in length x 150 mm in width x 430 mm in depth aluminum box as shown in Fig. 1. The front side of the box was fitted with a transparent Perspex panel to allow a real time observation on soil movements during the loading tests. Speswhite kaolin clay was used to model 200 mm thick of the soft ground. The foundation soil model was prepared in slurry form and then was consolidated inside the testing chamber to achieve a strength of 5 kPa.

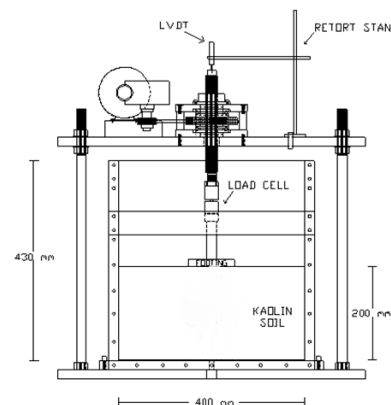


Fig. 1 Equipment and test setup.

Pre-formed 100mm (partially penetrated) and 200mm (fully penetrated) long soil-cement columns were then prepared by mixing the kaolin slurry (twice its liquid limit) with 15% of Ordinary Portland Cement (OPC) derived from a kaolin dry mass. The slurry was subsequently poured in two equal layers into a Perspex tube of 23.5 mm in diameter, 100mm and 200mm in length using a 20

ml syringe, with the ends of the tube sealed using adhesive. Air bubbles were removed by vibration, and the top surface was levelled and sealed using a cap to prevent moisture loss. The soil-cement columns were cured for 7 days at a controlled room temperature of 20°C. The columns were carefully removed from the casing using a specially-designed extruder system before being installed into the clay bed.

Following the removal of the consolidation piston plate and filter sheet, a thin-wall brass tube with a 25 mm outer diameter was pushed inside the model ground at predetermined locations into a rectangular pattern made from a drill template to create a hole for column installation. Three column group configurations of 9 representing area improvement ratios of 26% were considered. An auger of 23 mm in diameter was used to bore a hole inside the tube. The process was conducted in stages to avoid soil disturbance and ground heave. The column was subsequently pushed slowly until it reached a depth of 100 mm from the top of the model's ground. A surcharge of 50 kPa was applied to close the gap between the columns and the surrounding soil. As previously stated, the stress was reduced to 5 kPa. The groups of columns were left inside the soil model for 5 days before the loading test was conducted. Triaxial compression tests were conducted to determine the strength of the soil cement column.

A rigid plate of 100 mm in width and 150 mm in length to replicate the raft foundation of a building then was mounted on the model. All the tests were performed under undrained condition based on normalized velocity, V , approached [13]. During the tests, the stresses and displacements were recorded using a load cell and Linear Vertical Displacement Transducer (LVDT). A digital camera was employed to capture the soil movements in continuous shooting mode during the loading test. The undrained strength and moisture content of the soil were determined after the test was completed.

PIV algorithm was used to determine the soil movements during the tests. The deformation was determined by systematically comparing the intensities of patches in the first image to a predefined search zone in the following images (Fig. 2). Artificial texture (Flock) was used to improve the texture and intensity bandwidth of the kaolin by spreading it on the exposed model surface before the test was conducted. Calibration test was conducted to determine the accuracy and precision of the PIV system. It was found that the difference error between the real coordinate and coordinate produced from the PIV was less than 0.050 mm. The error was considered small and insignificant with less than 0.25% from the total penetration of the footing (20 mm).

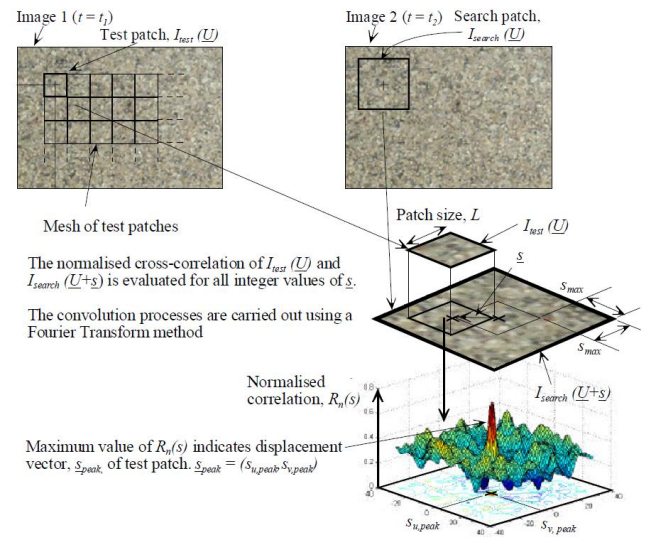


Fig. 2 PIV analysis [14]

RESULTS ANALYSIS AND DISCUSSION

Load – Displacement Relationship

Three series of tests (T1, T2 and T3) consists of untreated, fully and partially penetrated cases were conducted on this study and the mechanical characteristics of the ground model and the failure stress of each test were listed in Table 1. The vertical stress – displacement/width of footing curves recorded in this study are shown in Fig. 3. The vertical load for untreated case (Test T1) increases rapidly with the increase of settlement and reached a plateau at about 0.04 of displacement/footing width. It can be deduced that the soft clay possessed a ductile behaviour. On the other hand, a distinct stress peak was observed in test T3 reinforced with fully penetrated soil cement column followed by strain softening. This brittle response could be attributed to the sudden failure of individual columns in the group, thus triggering a loss in strength of the foundation capacity. Meanwhile, for the partially penetrated columns, a ductile behaviour is observed, even though a group of soil-cement columns is installed inside the model bed. This behaviour is believed to have been due to the group of columns bearing on soft ground.

The load corresponding to the peak and plateau is taken as the ultimate bearing capacity, q_{ult} , of the footing. Equation 1 was used to determine the bearing capacity factor, N_c (dimensionless) and both of the tests were compared base on the N_c value. The average undrained shear strength of the soil, c_{us} , was used for each case to obtain the factor.

$$N_c = q_{ult}/c_{us} \quad (1)$$

Table 1 Mechanical characteristics of the ground model

Test	c_{us} (kPa)	c_{uc} (kPa)	Failure Stress, q_{ult} (kPa)	N_c
T1	5.7	-	33.57	5.89
T2	5.6	83.71	90.11	14.08
T3	6.4	87.21	67.14	10.49

c_{us} = undrained shear strength of surrounding soil

c_{uc} = undrained shear strength of soil cement column

The value of N_c for the all tests are listed in Table 1. A higher result than the theoretical bearing capacity factor of 5.14 for a long rectangular (strip) foundation on clay was found. This might be due to the non-homogeneity of the soil model and wall friction between the testing chamber wall and the soil during the loading. The relative increase in bearing capacity for the reinforced compared to unreinforced soil was 78% and 140% for the partially and fully penetrated respectively.

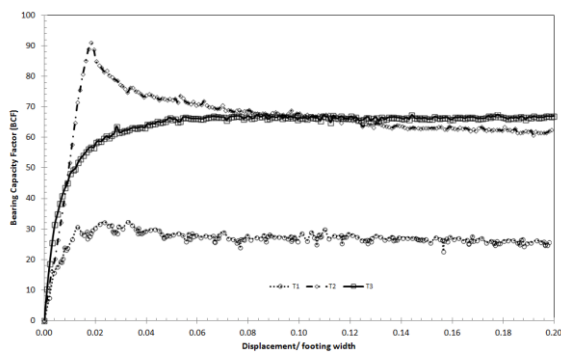
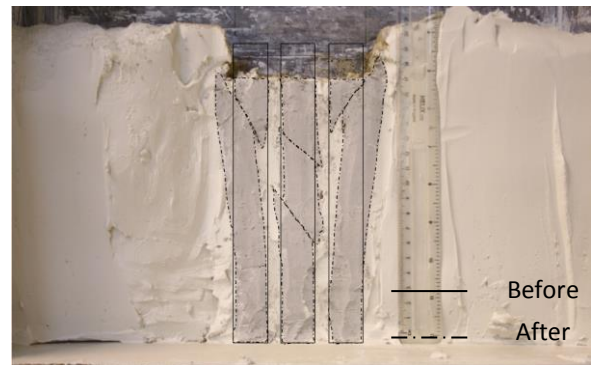


Fig. 3 Vertical Stress vs displacement/footing width curved obtained from experiments.

Column Failure Pattern

The failure patterns from Tests T2 and T3 are presented in Fig 4. In the figures, the initial positions and final positions of the columns are highlighted for better inspection. Due to the approximately similar failure mode of the columns in rows, only the second row from Tests T2 and T3 are presented. The difference in the failure modes of the columns in rows may be due to progressive failure that occurred in the group of columns, in which the columns did not fail at the same time but one by one during loading. For the fully penetrated case, localised shearing of the outer columns was prevalent at the interface with the footing edges and a bending was observed on the middle of the

columns. A shearing failure of the central column produced a double small break-out section at the middle of the column. However, test T3 involved only a bending failure of the columns at both edges of the footing. The column bases move outwards by approximately 20 mm from the top. The column at the centre penetrates almost vertically downwards, approximately, by the same displacement as that of the footing. A combination of shear and bending, and bending failure were observed for fully and partially penetrated columns respectively.



(a) Test T2



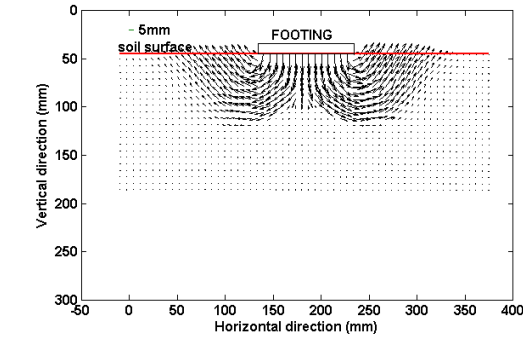
(b) Test T10

Fig. 4 Failure pattern of DM columns under vertical loading

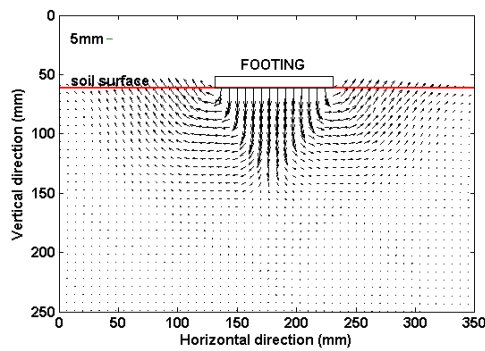
Ground Deformation

The soil displacements over the model soil face were observed through images captured and PIV analyses. Figure 4 shows the accumulated displacement vectors of Tests T1, T2 and T3 derived from the analyses over a series of images prior to the loading right up to the final penetration depth of the footing. It can be observed here that the footing displaced the underlying soil symmetrically. The failure mechanism obtained from the Tests T1 (Fig. 4a) and T2 (Fig. 4b) result compared well to the typical Prandtl failure mechanism. The soil adjacent to and below the footing was deformed over a distance of approximately 100% of the footing

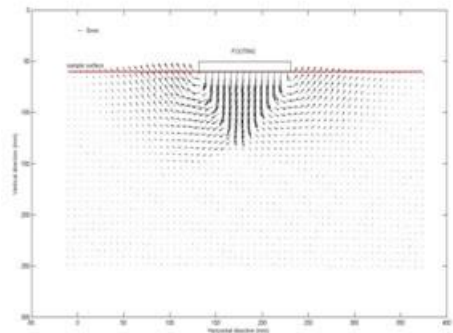
width, which is similar to the Prandtl failure mechanism. Generally, a deeper failure mechanism than the test T1 and T2 sample observed for test T3 as shown in Fig 4c. The soil adjacent to the footing has been mobilised over a lateral distance of about 100% of the footing width, and over a distance of approximately 150% of the footing width below the footing.



(a) Test T1



(b) Test 2



(c) Test 3

Fig. 5 Ground deformation produce by PIV analyses

Validation of the Laboratory Result

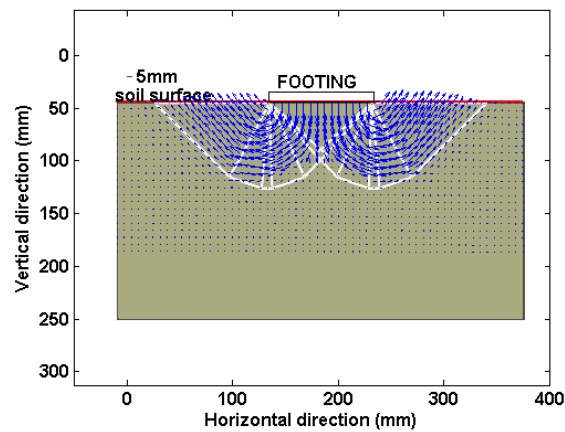
The LimitState:Geo software, developed based on Discontinuity Layout Optimization (DLO) procedure was employed to validate the present laboratory results [15], [16]. The dimensions of the numerical model matched those of the testing chamber. To perform the analysis, a rough interface layer was assumed and applied between the ground model and the rigid footing. In addition, a fixed boundary was applied on the soil model and a nodal density of 1000 nodes was used. An homogenize method was used to analyse the soil model treated by the soil cement column. The values of bearing capacity factor N_c produced from the software are listed in Table 2. Differences ranging from 7.4% to 19.2% are found by comparing the results from the both N_c obtained from the laboratory and the LimitState:GEO software. The difference could be due to the friction between wall and the soil model during the loading test.

Table 2 Comparison of experimental results with LimitState:Geo

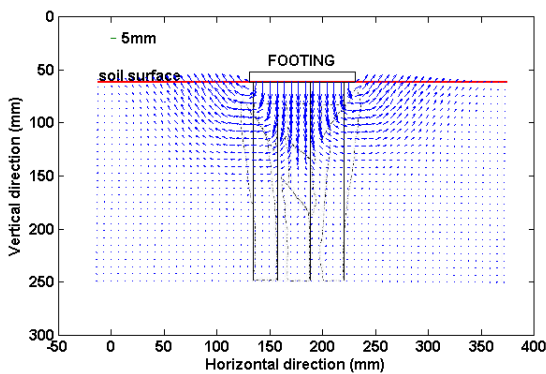
Test	$N_{c,Exp} = (q_{ult}/c_{us})$ (a)	$N_{c,limit} = (q_{ult,limit}/c_{us})$ (b)	Difference (%) (b) to (a)
T1	5.89	5.45	-7.4
T2	14.08	12.16	-13.6
T3	10.49	8.48	-19.2

q_{limit} = Failure stress generate from the LimitState:Geo software.

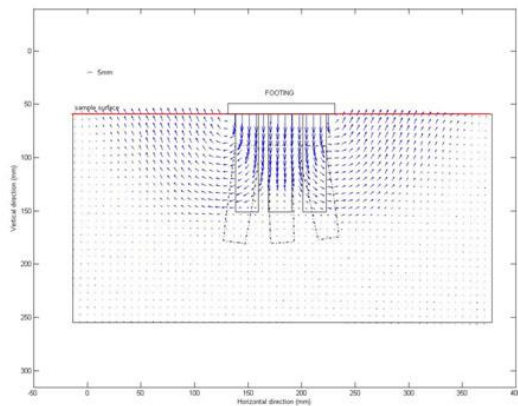
Figure 5 shows the pattern of failure surface produced by the PIV analyses for all tests that was superimposed on the computed failure pattern. Generally, the sense of the soil movements for both cases and the extent of displacement field (PIV analysis) predicted quite well with the software. However, the soil movement tailed off with distance from the footing. For the treated cases, the difference in observations from both analyses could be due to the fact that Limitstate:GEO is based on an ideal rigid plastic material with no pre-failure strain, thus eliminating loading penetration in developing the failure mechanism, in addition to the comparison being limited by 3D column movement away from the viewing window.



(a) Test T1



(b) Test T2



(c) Test T3

Fig. 5 Comparison between failure pattern produce by LimitState:Geo software and PIV analysis .

CONCLUSIONS

The bearing capacity and ground deformation of a soft clay were investigated based on a series of

physical model tests. Numerical modelling based on the Discontinuity Layout Optimization (DLO) approach was used to verify the laboratory results and mechanism patterns produced by the Particle Image Velocimetry analyses (PIV). Several conclusions that could be made from both the physical and numerical modeling are listed below:

- 1) The relative increase in bearing capacity for the reinforced compared to unreinforced soil was 78% and 140% for the partially and fully penetrated respectively
- 2) A combination of shear and bending, and bending failure were observed for fully and partially penetrated columns respectively.
- 3) The soil adjacent to and below the footing for the untreated and fully penetrated was deformed over a distance of approximately 100% of the footing width, which is similar to the Prandtl failure mechanism. While, a deeper failure mechanism than the untreated and fully penetrated sample observed for partially penetrated case.
- 4) LimitState:Geo software shows a good agreement of N_c values with value obtained from the laboratory work.
- 5) The failure patterns for all cases produced by the LimitState:Geo show slight difference compared to the PIV analyses. The difference was due to the different material model and the effect of the columns.

NOTATION

B	Width of the footing
c_{us}	Undrained shear strength of surrounding soil
c_{uc}	Undrained shear strength of soil-cement column
N_c	Bearing capacity factor
q_{ult}	Ultimate bearing capacity

ACKNOWLEDGEMENTS

The work was financially supported by Universiti Teknologi Malaysia and Ministry of Science and Technology of Malaysia, MOSTI under Research University Grant (R.J130000.7922.4S051).

REFERENCES

- [1] Karastanev, D., Kitazume, M., Miyajima, S., and Ikeda, T. (1997). Bearing capacity of shallow foundations on column type DMM improved ground. *Proc. of the 14th Int. Conf. on SMFE*, Vol. 3, 721-724.
- [2] Porbaha, A. (1998). State of the art in deep mixing technology: part I. basic concepts and

overview. *Ground Improvement*, Vol. 2, No. 2, 81-92.

[3] Topolnicki, M. (2004). In situ soil mixing. *Ground Improvement*, New York, NY: Spon Press, 331-428.

[4] Terashi, M. and Tanaka, H. (1981). Ground improved by deep mixing method. *Proceedings of the 10th ICSMFE*, Vol. 3, 777-780.

[5] Kitazume, M., Ikeda, T., Miyajima, S., and Karastanev, D. (1996). Bearing capacity of improved ground with column type DMM. *Proc. of the 2nd International Conference on Ground Improvement Geosystems*, Vol. 1, 503-508.

[6] Kitazume, M., Yamamoto, M., and Udaka, Y. (1999). Vertical bearing capacity of column type DMM ground with low improvement ratio. *Proc. of the Int. Conf. on Dry Dry Mix Methods for Deep Soil Stabilization*, 245-250.

[7] Kitazume, M., Okano, K., and Miyajima, S. (2000). Centrifuge model tests on failure envelope of column type deep mixing method improved ground. *Soils and Foundations*, Vol. 40, 43-55.

[8] Omine, K., Ochiai, H., and Bolton, M.D. (1999). Homogenization method for numerical analysis of improved ground with cement-treated soil columns. *Proc. of the Int. Conf. on Dry Dry Mix Methods for Deep Soil Stabilization*, 161-168.

[9] Boussida, M. and Porbaha, A. (2004). "Ultimate bearing capacity of soft clays reinforced by a group of columns-application to a deep mixing technique". *Soils and Foundations*, Vol. 44, No. 3, 91-101.

[10] Boussida, M. and Porbaha, A. (2004). Bearing capacity of foundations resting on soft ground improved by soil cement columns. *International Conference on Geotechnical Engineering (ICGE 2004)*, 173-180.

[11] Fang, Z. (2006). *Physical and numerical modelling of the soft soil ground improved by deep cement mixing method*. PhD Thesis, The Hong Kong Polytechnic University.

[12] Yin, J.H. and Fang, Z. (2010). Physical modeling of a footing on soft soil ground with deep cement mixed soil columns under vertical loading. *Marine Georesources and Geotechnology*, Vol. 28, 173-188.

[13] Lehané B.M., Gaudin C., Richards D.J., and Rattley M.J. (2008). Rate effects on the vertical uplift capacity of footings founded in clay. *Géotechnique*, Vol. 58, No. 1, 13-22.

[14] White, D.J. and Take, W.A. (2002). *GeoPIV: Particle Image Velocimetry (PIV) software for use in geotechnical testing*. Technical Report CUED/D-SOILS/TR322, Cambridge University, Engineering Department.

[15] Smith, C. and Gilbert, M. (2007). Application of discontinuity layout optimization to plane plasticity problems. *Proceedings of the Royal Society A*, Vol. 463, 2461 -2484.

[16] Gilbert, M., Smith, C., Haslam, I., and Pritchard, T. (2010). Application of discontinuity layout optimization to geotechnical limit. *Proceedings of the 7th European Conference on Numerical Methods in Geotechnical Engineering*.

INTEGRATED QUALITY ASSURANCE AND CONTROL FOR DEEP SOIL MIXING IN WATERWAY PROJECT

S.H. Chew¹, C.Y. Tan², T.Y. Yap³, K.E. Chua⁴, H.M. Yim⁵, S.Y. Kee⁶, T.K. Khoo⁷ and Ja Naw⁸

^{1,2}Department of Civil & Environmental Engineering, National University of Singapore, Singapore; ^{3,4,5,6}Housing & Development Board, Singapore; ^{7,8}Surbana International Consultants Pte Ltd, Singapore

ABSTRACT

Deep soil cement mixing (DSM) method has gained popularity over the years in Singapore due to the increase in underground construction over difficult ground conditions. One of the concerns is the quality assurance and quality control of this technique. Two aspects were evaluated: operational control and evaluation of the treated soil strength. Firstly, for the quality control of the treatment operation, an online record of the mixing efficiency, in terms of mixing time, cement content and mixing energy etc; were recorded and evaluated. After the completion of treatment works, a consistent and rationale methodology was developed for the evaluation of the strength variation of the treated soils over the area and over the depth. These will help in the final development of the acceptance criteria for such ground treatment works. Illustration of the applicability of such methodology was done in conjunction with a mega-project in Singapore – construction of the Punggol Waterway. This paper discusses the proposed quality assurance and quality control methodology. It successfully covers the long stretch of Punggol Waterway in good detail, yielding “accurate” representation of the quality of the DSM columns installed, thereby, ensuring the quality of the soil improvement works by DSM before excavation.

Keywords: Deep Soil Mixing, Soil Improvement, Clay, Quality Assurance, Control

INTRODUCTION

Implemented by the Housing & Development Board, Singapore (HDB), the Punggol Waterway is Singapore's first man-made waterway. Its birth injects a new lease of life to the former agriculture and farmland, transforming Punggol Town into a bustling and vibrant waterfront eco-town. Construction of the Punggol Waterway had to be carried out over difficult soil conditions. As such, Deep Soil Mixing (DSM), which has gained popularity in the past 10 years in Singapore [1], was selected as the ground improvement method for the construction of Punggol Waterway (Part I). The overall features of the Punggol Waterway and the soil profiles at this site can be found in [2]. The properties of the Singapore Marine Clay treated with cement mixing have been well studied [3], [4].

As DSM is carried out underground, it is difficult to ascertain its quality after construction. Furthermore, as deep excavation of about 13m was required for the construction of the waterway, good and consistent results for DSM soil improvement works were required to ensure adequate slope stability. In addition, DSM was carried out massively over the site. As such, a rationale, elaborate and representative quality assurance and quality control methodology with clear acceptance criteria were required for this project.



Fig. 1 Overall site layout

SOIL CONDITIONS & DEEP SOIL MIXING GROUND TREATMENT DESIGN

Soil investigations comprising of a total of 42 boreholes & 66 numbers of Cone Penetration Tests (CPTs) were carried out for the project. Generally, the ground consists of filled material overlaying a layer of either soft marine CLAY or Peaty CLAY, underlined by the original formation of Old Alluvium, which is a compacted, dense sand layer. A typical soil profile is shown in Fig. 2.

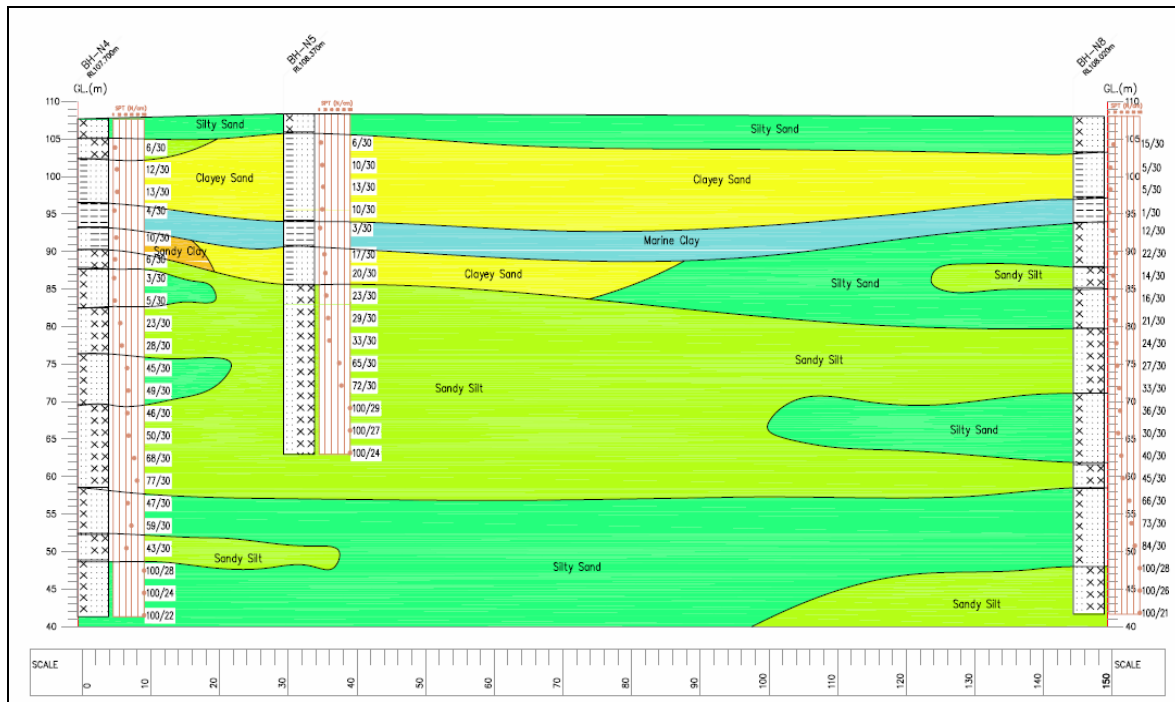


Fig. 2 Soil profile

Deep Soil Mixing (DSM) ground treatment method is proposed and its design consists of column diameters of 850mm, with centre-to-centre spacings of 750mm. Grid patterns of DSM are installed instead of full blocks of DSM (shown in Fig. 3). The composite properties of the treated soil mass were carefully evaluated based on a purposefully defined ratio of area improvement.

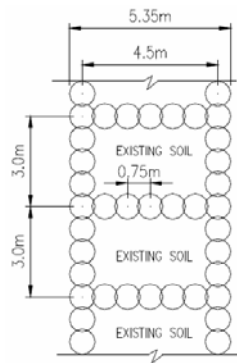


Fig. 3 Typical grid pattern of Deep Soil Mixing (DSM) Columns

The minimum design strength and stiffness of the individual DSM columns were calculated and listed as:

Unconfined Compression Strength, $q_u = 1000 \text{ kPa}$

Undrained Shear Strength, $C_u = 500 \text{ kPa}$

Undrained Young's Modulus, $E_u = 200,000 \text{ kPa}$

A typical geometry of the waterway with the DSM columns in place for slope enhancement is shown in Fig. 4. This was done over the whole 2.4km length of the waterway (Part I).

OPERATIONAL QA/QC CONTROL FOR DSM

To ensure the quality of the DSM columns installed, stringent operational control was set up. For every column installation, an online record of the mixing efficiency, in terms of mixing time, cement content and mixing energy etc; were recorded. Contractors were required to submit records of DSM piles installation and compare that with the designed curve as shown in Fig. 5. In this figure, vertical axis is the depth of penetration, while the horizontal axis is the time. Superimposed on the same diagram is the flow rate in each and every depth. Based on this information, the rate of rotation can be calculated, which gives an indication of the time for mixing. The amount of cement mixed with the soil at that particular depth can be evaluated based on the flow rate at that depth. The calculated rate of mixing and cement used must be consistent with the design value. Any variation will imply that the column was not properly installed and remedial action must be done.

END RESULT EVALUATION

The qualities of the end result of Deep Soil Mixing (DSM) columns were inspected by coring the completed columns after 21 days. To provide consistent and representative quality sampling, the DSM treated area was divided into blocks of 25m along each bank of the waterway. Sampling was carried out with two core locations per block. Each location of coring consists of three sampling points (i.e. top, middle, and bottom) from the selected DSM columns, and the unconfined compressive strength test is carried out.

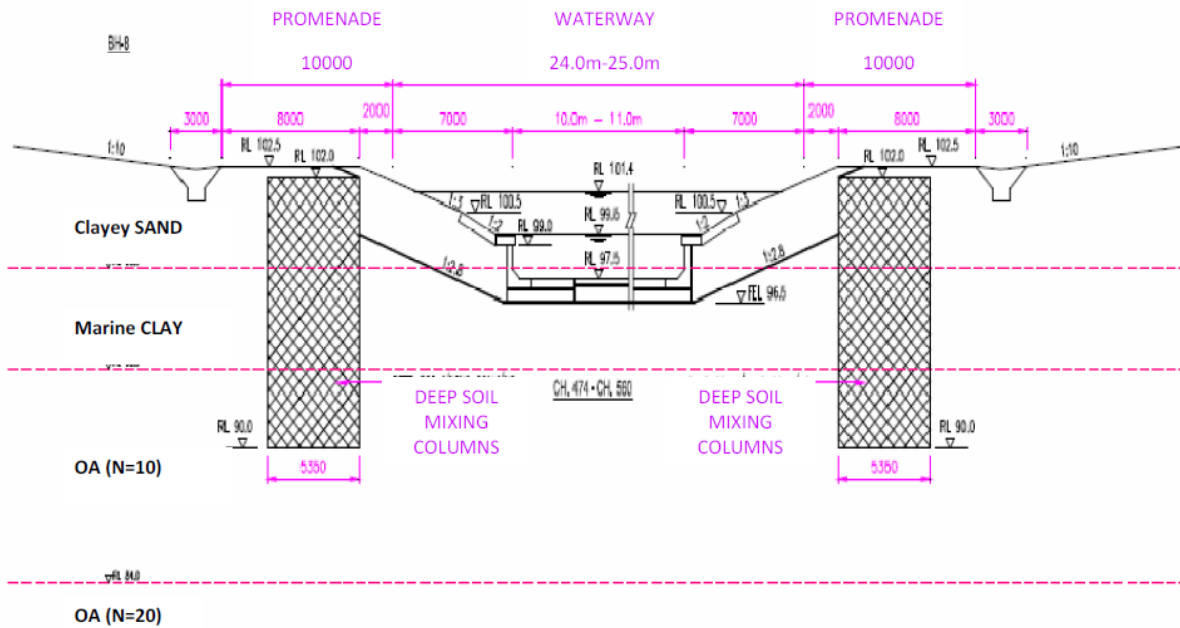


Fig. 4 Typical scheme of DSM and Waterway

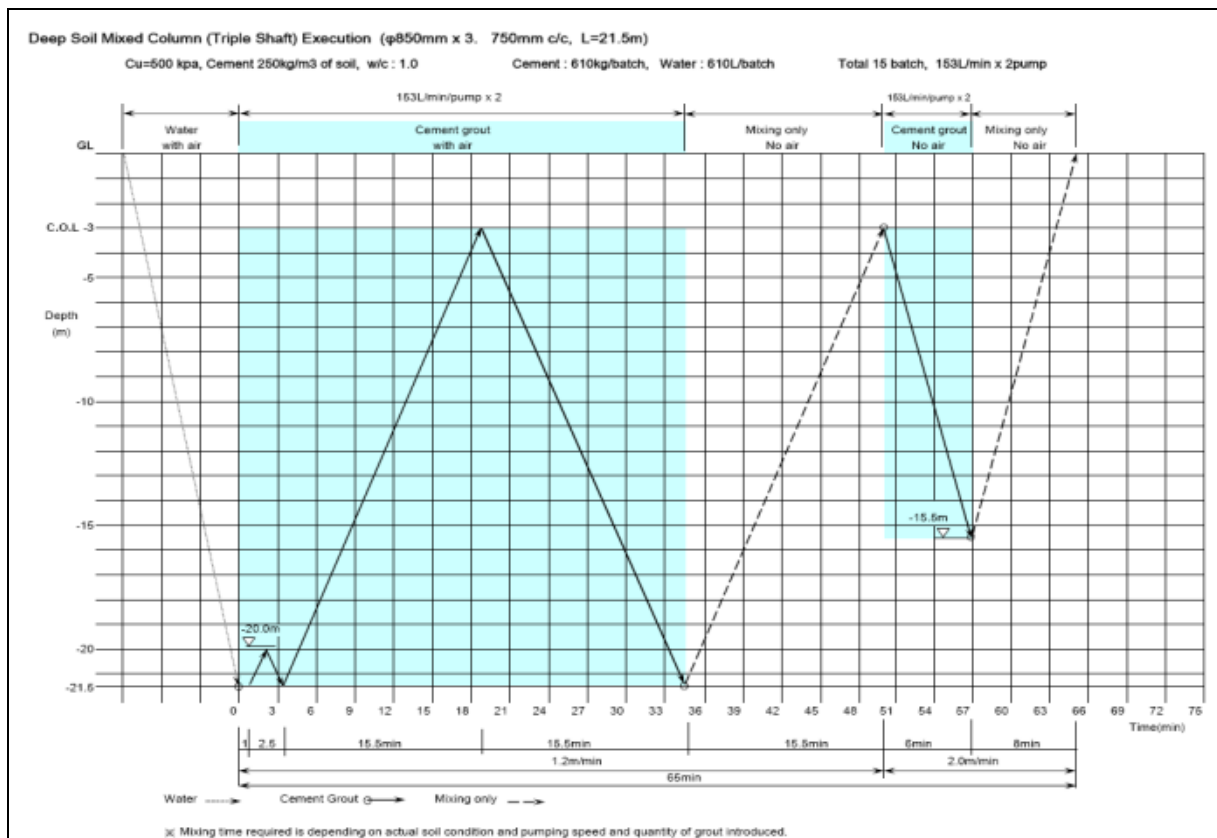


Fig. 5 DSM pile installation record – design curve

The Conventional QA/QC Criteria

The conventional acceptance criteria for this kind of DSM works specified that for each sampling point, the following criteria must be satisfied:

- Total core recovery (TCR) shall be at least 85%
- Unconfined compressive strength (UCS) shall be at least 1000kPa
- Modulus of Elasticity (E) shall be at least 200MPa for each DSM column.

This conventional method indicates highly varied and inconsistent results. It will be difficult to access the overall performance of the DSM blocks based on the conventional criteria. Hence, an improvement of the QA/QC criteria is needed.

Improved QA/QC For Completed DSM Columns

The quality assurance and quality control plan was revised to ensure the quality of DSM columns installed comply with specifications and performance requirements. The outlines of this improved acceptance criteria are as follow:

Coring tests

The quality of Deep Soil Mixing columns should be inspected by coring the completed columns throughout the depth. The coring shall be consisted of at least two cored locations per block of 25m along each bank of the waterway.

Representative zones along DSM columns

Each cored location is divided into three zones, e.g. Upper Zone, Middle Zone and Bottom Zone. At each zone, three cored samples is collected. The samples are taken between each of these cored samples with clear distance of at least 1m and not more than 2m. The collected samples were then sent for laboratory testing for Unconfined Compression Test to obtain the UCS and modulus parameter.

Acceptance criteria for Deep Soil Mixing column

The acceptance criteria for unconfined compressive strength (UCS) are as follows:

- Average UCS for each zone (average of 3 samples) $> 0.9\text{MPa}$
- UCS for each sample $> 0.1\text{MPa}$
- Average UCS for three zones (average of 9 samples) $> 1.0\text{MPa}$

The acceptance criteria for total core recovery (TCR) area as follows:

- Average TCR for each zone $> 75\%$
- TCR for each 1m $> 10\%$
- Average TCR of whole cored location $> 85\%$

The cored location can be accepted if it satisfies all the above mentioned criteria. Vice versa, the cored location cannot be accepted if any one of the criteria has not been met. The acceptance criteria are as illustrated in Fig. 6.

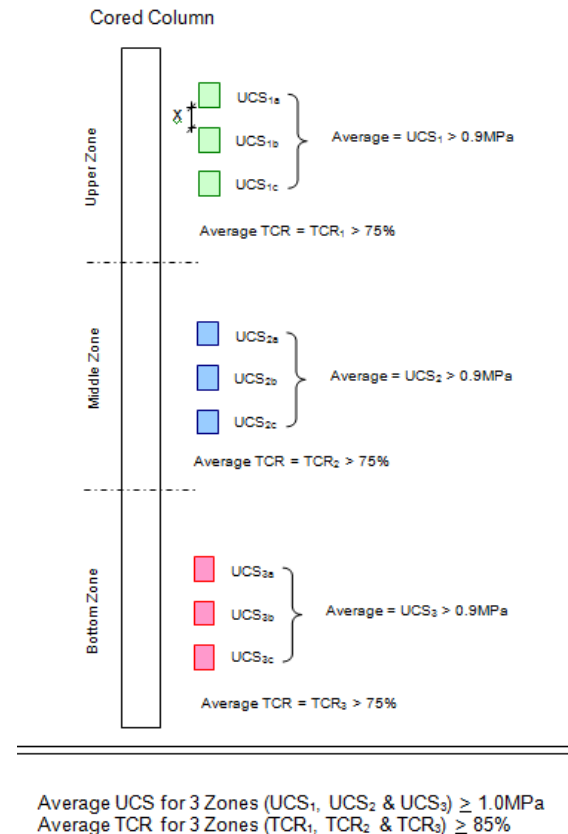


Fig. 6 Acceptance criteria for DSM Column

ACTUAL CONSTRUCTION WORK

Actual construction works of DSM treatment were carried out with the above revised operational QA/QC control.

As an illustration, an operational record very close to the design curve, yielded a very uniform and good DSM column as revealed from the cored sample shown in Fig. 7. In comparison, as an illustration for the opposite, an operational record that deviates significantly from the design curve was found to produce DSM columns that were poor in quality and highly non-uniform as revealed from the cored sample as shown in Fig. 8. The operational mixing curves for the DSM treatment to yield good and bad quality DSM columns are summarized in Fig. 9.

The evaluation of the end result for the treated ground is thus evaluated based on the above end result QA/QC acceptance criteria. The result of the later evaluation is presented below.

Coring samples were extracted from completed DSM columns using wet boring method. Coring samples were taken at least 21 days after the date of completion of the columns. A total of 9 test samples were tested for each coring location. The test results for unconfined compressive strength and the TCR for the two coring locations are summarized in Table 1.



Fig. 7 Good sample photo



Fig. 8 Bad sample photo

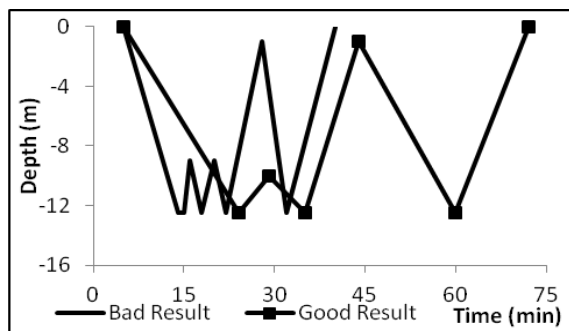


Fig. 9 Sketch of operational mixing curves

The average UCS test results for the top, middle and bottom zone of the sample location N92-06 are 1.23MPa, 1.07MPa and 0.97MPa respectively. These results have met the acceptance criteria with respect to the UCS criteria. In addition, the average TCR for all three zones also passed the acceptance criteria with respect to TCR. Hence, this column has been considered as “passed”.

Table 1 Summary of two coring locations

Ref No.	Zone	UCS (MPa)	Avg UCS (MPa)	TCR (%)	Avg UCS for whole coring location (MPa)	Pass/Fail
N 92-06	TOP	1.06	1.23	90%	1.09	Pass
		1.15				
		1.48				
	MID	1.18	1.07	100%		
		1.14				
		0.88				
	BOT	0.81	0.97	95%		
		1.3				
		0.8				
N 99-01	TOP	1.00	0.99	80%	1.10	Fail
		1.02				
		0.96				
	MID	0.76	0.66	90%		
		0.55				
		0.66				
	BOT	1.84	1.65	85%		
		1.34				
		1.76				

The average UCS test results for the top, middle and bottom zone of the sample location N99-01 are 0.99MPa, 0.66MPa and 1.65MPa respectively. This result has not met the acceptance criteria with respect to the UCS criteria. Even though the average TCR for all three zones passed the acceptance criteria with respect to TCR, this column would be considered as “failed”. Rectification works were then carried out and additional columns were installed for this 25m panel.

RECTIFICATION

The DSM works for a 25m panel is accepted if the results of both coring locations within the panel meet the stated criteria. If at least one coring location is found to be “failed”, DSM works for the entire 25m panel is not accepted and rectification work is required to compensate for it. This will ensure the whole panel achieves the required treatment quality.

Rectification works was carried out by computing the additional number of columns needed to achieve an overall strength equivalent to the design strength by computing the number of columns and the in-situ strength of the “failed” DSM columns with respect to the total TCR.

This concept of compensation takes into account the presence of the actual in-situ quality of the failed DSM columns that has been installed, and does not compromise the overall quality of the DSM panel after rectification.

CONCLUSION

A revised quality assurance and quality control plan for Deep Soil Mixing treatment for Punggol Waterway was developed. It consists of two components: operational mixing control and end result QA/QC check. This revised plan was carried out and the results were found to be successful and effective. It successfully ensured the long stretch of Punggol Waterway was treated with good quality of DSM columns.

The end results QA/QC plan also provided good details, yielding accurate representation of the quality of the DSM columns installed, thereby, ensuring the overall quality of the soil improvement works by DSM before excavation.

ACKNOWLEDGMENTS

Special thanks to contractor Koh Brothers Building & Civil Engineering Contractor (Pte.) Ltd, and geotechnical contractor – Ryobi Kiso (S) Pte Ltd.

REFERENCES

- [1] Tan, T.S., Goh, T.L., and Yong, K.Y., "Properties of Singapore Marine Clays Improved by Cement Mixing", ASTM Geotechnical Testing Journal, Vol. 25 Issue 4, 2002.
- [2] Chew, S.H., Tan, C.Y., Yap, T.Y., Chua, K.E., Ng, K.C., Khong, Y.C., and Goh, P.L., "Improving Soft Peaty Soil by Grouted Stone Columns Punggol Waterway Project, Singapore", 14th Asian Regional Conference on Soil Mechanics and Geotechnical Engineering, 2011.
- [3] Kamruzzaman, A.H.M., Chew, S.H., and Lee, F.H., "Structuration & Destructuration Behavior of Cement-Treated Singapore Marine Clay", ASCE Journal of Geotechnical and Geoenvironmental Engineering, Vol. 135 no. 4, 2009.
- [4] Chew, S.H., Kamruzzaman, A.H.M., and Lee, F.H., "Physiochemical and Engineering Behaviour of Cement-Treated Clay", ASCE Journal of Geotechnical and Geoenvironmental Engineering, Vol. 130 no.7, 2004.

EMPIRICAL CORRELATION OF SHEAR WAVE VELOCITY AND N-SPT VALUE FOR JAKARTA

Achmad Fauzi¹, Masyhur Irsyam², Usama Juniansyah Fauzi³, and Muhammad Addifa Yulman³

¹Faculty of Civil Engineering and Earth Resources, Universiti Malaysia Pahang, Malaysia; ²Faculty of Civil and Environmental Engineering, Institut Teknologi Bandung, Indonesia; ³Former Student at Faculty of Civil and Environmental Engineering, Institut Teknologi Bandung, Indonesia

ABSTRACT

This paper proposes an equation representing shear wave velocity (V_s) as a function of SPT blow count (N-SPT). The equation is generated by statistical regression of site investigation data at many building project in Jakarta. The N-SPT values and V_s values were obtained from the same boreholes between 2005 and 2012. The V_s values were obtained by the downhole seismic survey. A total of 22 building and 35 borings provided 234 pairs of N-SPT and V_s values were used to get a regression equation. The new and previously suggested formulae have been compared and evaluated by using the same dataset. Wave propagation analysis require V_s as an input parameter, and the empirical equation may be useful for estimating V_s at site where only N-SPT data available. The information of empirical correlation can and perhaps should be considered in developing microzonation map of Jakarta as inputs in a continuous process of risk assessment and disaster mitigation risk reduction.

Keywords: Downhole seismic survey, shear wave velocity, standard penetration test, Jakarta soil, in-situ test

INTRODUCTION

The shear-wave velocity of soils plays an important role in the design of geotechnical structures under dynamic loads. It is used mostly for determining the seismic site categories (e.g., Indonesian Building Code SNI 1726-2002) and for input of ground motion prediction equations where Indonesia has large strain problems related to seismic loading. In Indonesia, the shear-wave velocity is typically measured using the seismic downhole test. However, the equipment is not widely available and, consequently, the test is generally too expensive to perform for most construction projects. On the other hand, the standard penetration test method (SPT) is one of the most common in-situ tests because its equipment is widely available and it is easy to perform

Numerous relations between SPT blow count, N-SPT, and shear wave velocity, V_s , exist in the literature. Early efforts utilized laboratory results to develop correlations, and the correlations were subsequently refined as field measurement of V_s became more common and data became available. The most common functional form for the relations proposed in the literature is $V_s = a \times N\text{-SPT}^b$, where the constants a and b are determined by statistical regression of a data set.

A study to develop correlations among penetration test results and shear-wave velocity for soils from Indonesia is currently being conducted. This present paper present the development of a correlation between the resistances obtained from

SPT and shear-wave velocity for soils from Jakarta area.

GEOTECHNICAL AND SEIMOTECTONIC SETTING

Geological condition

Geologically, the study area, Jakarta is dominated by quaternary sediment and, unconformably, the base of the aquifer system is formed by impermeable Miocene sediments which are cropping out at the southern boundary, which were known as Tangerang High in the west, Depok High in the middle and Rengasdengklok High in the east. They acted as the southern basin boundary. The basin fill, which consist of marine Pliocene and quaternary sand and delta sediments, is up to 300 m thick.

Individual sand horizons are typically 1 - 5 m thick and comprise only 20% of the total fill deposits. Silts and clays separate these horizons [1], [2]. In detail, Reference [3] differentiated the lithology in this area into some formations and explained as follows {Figs. 1}.

- a. Rengganis Formation consists of fine sandstones and clay stone outcropped in the area of Parungpanjang, Bogor. Unconformably, this formation is covered by coral limestone, marl, and quartz sandstone.
- b. Bojongmanik Formation consists of interbedded of sandstone and clay stone, with intercalated limestone.

- c. Genteng Formation consists of volcanic eruption material such as andesitic breccias and intercalated tuffaceous limestone.
- d. Serpong Formation, interbedded of conglomerate, sandstone, marl, pumice conglomerate, and tuffaceous pumice.
- e. Coral Limestone, Holocene age and found in Seribu Island Complex in Jakarta Bay, consist of coral colony, coral fragment, and mollusk shell.

Beside those above lithology, there are found Banten Tuff, young volcanic eruptive material, fan deposits, paleo and recent beach ridge deposits which are deposited parallel to recent coastal line.

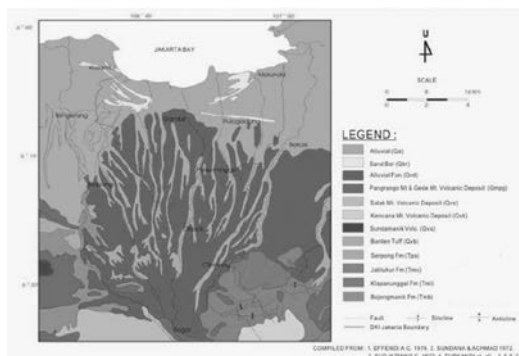


Fig. 1 Geological map of the Greater Jakarta and its surrounding area.

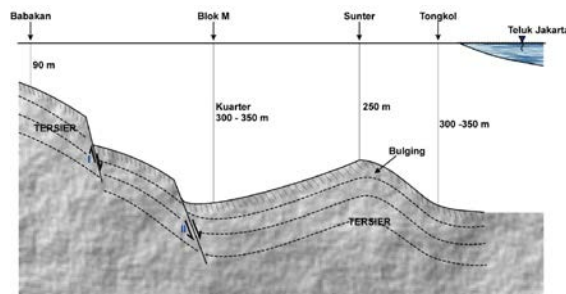


Fig. 2 Bedrock profile of Jakarta

Seismotectonic settings

Jakarta is located in a tectonically very active area. The study site is surrounded by a number of active faults. The Indo-Australia Subduction Zone, Sunda Fault, and Lembang Fault are the most important earthquake sources in the study site. The 2009 West Java earthquake, which resulted in extensive loss of life and damage to structures particularly in the Sukabumi Region, was also felt in Jakarta and its vicinity. General condition of the mayor tectonic features was shown in Fig. 3.

TEST PROGRAM

The test program considered in this study was conducted in 22 locations; in each location a series of standard penetration tests and a series of shear-

wave velocity measurements performed using the seismic downhole test method were conducted in one bore-hole. The coordinate of locations are shown in Table 1 and Fig. 4.



Fig. 3 Major tectonic feature of Jakarta region

Table 1 Test location in this study

ID	Coordinate		Soil Types	ID	Coordinate		Soil Types
	Longitude	Latitude			Longitude	Latitude	
1	106.8336	-6.2282	Soft soil	12	106.8384	-6.30495	Soft to Stiff soil
2	106.8764	-6.17113	Soft soil	13	106.8162	-6.21073	Soft to Stiff soil
3	106.9081	-6.15226	Soft to stiff soil	14	106.6279	-6.24064	Stiff soil
4	106.8277	-6.22972	Stiff soil	15	106.8353	-6.21677	Stiff soil
5	106.788	-6.23653	Stiff soil	16	106.8236	-6.1992	Stiff soil
6	106.7976	-6.21092	Soft to stiff soil	17	-	-	Stiff soil
7	106.7942	-6.24675	Soft to stiff soil	18	106.8143	-6.24707	Stiff soil
8	106.6279	-6.24064	Soft to stiff soil	19	106.7847	-6.23671	Stiff soil
9	106.8267	-6.22923	Soft to stiff soil	20	106.8197	-6.21167	Stiff soil
10	-	-	Stiff soil	21	106.7893	-6.1691	Soft soil
11	106.78	-6.29142	Stiff soil	22	106.8341	-6.22476	sedang

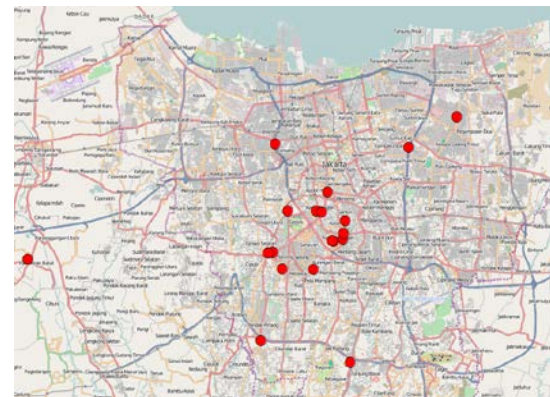


Fig. 4 Locations of geotechnical and downhole investigations

Standard Penetration Tests were performed along borings with intervals of 1.5 m to 2m. Standard Penetration Test procedure and equipment followed the ASTM D 1586 – 84 [4], “Standard Method for Penetration Test and Split Barrel Sampling of Soils”. The resistance of soil is represented by the N-SPT value. The number of blows of hammer striking drilling rod to cause 3x6” penetration of the split spoon at the tip into the soil was counted. The N-SPT value is the total number of blows for the last 2x6” penetration.

The seismic downhole tests were performed in accordance with ASTM D7400 – 08 [5]. The tests

were conducted using 3-component, OYO Borehole Pick Model 3315 geophone and McSeis 24-channel portable engineering seismograph. The shear-wave velocity was measured at 1.0 m interval. The seismic shear-wave was generated using the 28-kgf, T6-6061 aluminum alloy shear-wave source equipped with ground coupling spikes. The method is illustrated in figure below.

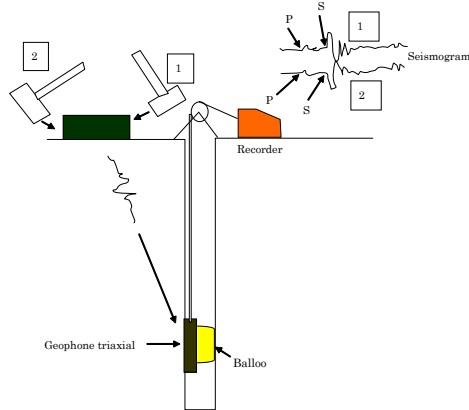


Fig. 5 Downhole seismic survey illustration

PROPOSED EMPIRICAL CORRELATIONS FOR VS-N-SPT

A significant number of correlations have been published on various soil types {Table 2}. Reference [6] pointed out that geological age and type of soil are not predictive of Vs while the uncorrected N-SPT value is most important. Reference [7] examined the influence of the soil type on N-SPT versus Vs correlation using data collected from an earthquake-prone area in the eastern part of Turkey. The results showed that, except for gravels, the correlation equations developed for all soils, sand and clay yield approximately similar Vs values. Reference [8] presented a detailed historical review on the statistical correlation between N-SPT versus Vs. Reference [9] studied similar statistical correlations using 97 data pairs collected from an area in the north-western part of Turkey and developed empirical relationships for sands, clays, and for all soils irrespective of soil type.

Significant differences exist among the various published relations, which are likely partially caused by differences in geology, but also by errors in measurements of N-SPT and Vs. Resolving the differences among published relationships is beyond the scope of this study.

Example data from ID 11 is shown in Fig. 6. The graphs show the Vs profile and N-SPT profile at the site. The Vs profiles were typically recorded at 1 m intervals, whereas the N-SPT values were recorded at much coarser sampling intervals typically 1.5m or larger. A number of possible approaches were considered for selecting an appropriate Vs value to

associate with each N-SPT value for statistical regression.

Table 2 Some existing correlations between N-SPT and Vs

Author(s)	ID	Equation(s)
Ohta and Goto (1978)	A	$85.3N^{0.341}$
Imai and Tonouchi (1982)	B	$96.9N^{0.314}$
Sykora and Stokoe (1983)	C	$100.5N^{0.29}$
Jinan (1987)	D	$116.1(N+0.3185)^{0.202}$
Iyisan (1996)	E	$51.5N^{0.516}$
Jafari et al. (1997)	F	$22N^{0.85}$
Kiku et al. (2001)	G	$68.3N^{0.292}$
Hasancebi and Ulusay (2007)	H	$90N^{0.309}$

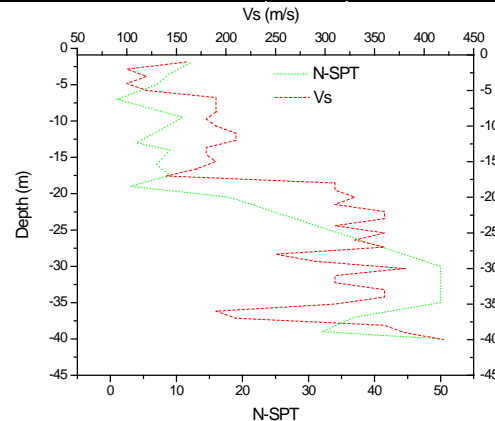


Fig. 6 Example variation of N-SPT and Vs for statistical regression

In this study, 234 data pairs (N-SPT and Vs) were employed in the assessments. The correlations were developed using a simple regression analysis for the existing database. New relationships were proposed between uncorrected Vs (m/s) and corresponding N-SPT. {Fig. 7}. The following relationships with its correlation coefficients (r) are proposed between Vs (m/s) and N-SPT values.

$$Vs = 105.03N^{0.286} \quad (r = 0.675) \quad (1)$$

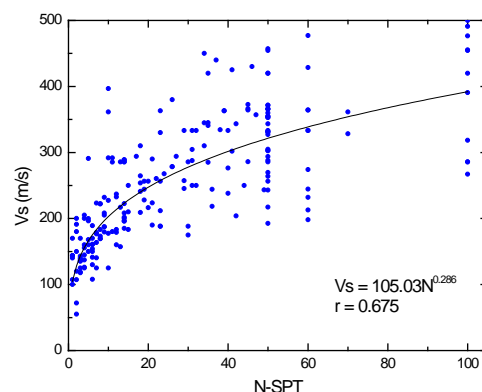


Fig. 7 Present correlation between N-SPT and Vs

Comparisons between the measured Vs and Vs predicted from {Eq. (1)} are presented in Fig. 8. The plotted data are scattered between the lines with 1:0.5 and 1:2 slopes, with smaller Vs values (Vs <

300 m/s) falling close to the line 1:1.

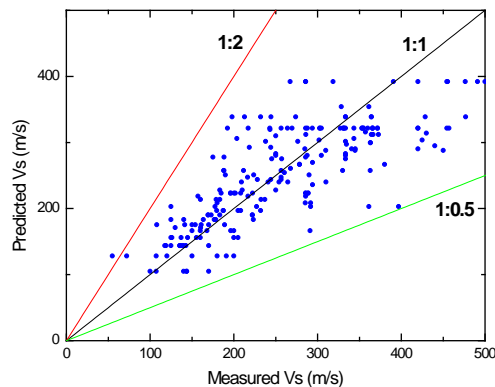


Fig. 8 Measured versus predicted shear wave velocities

Equation (1) are plotted in Fig. 9 together with several of the earlier regression equations given in Table 2. Some of the correlations fit the data points reasonably well, though there is tremendous difference in the range of V_s values predicted for a given N-SPT value. It is unclear how much of these deviations are caused by natural variability in soil deposits, how much is caused by errors in measurements of N and V_s , and how much is caused by exclusion of overburden correction in the existing relations. All the equations including the equation of the present study {Eq. (1)} yield similar V_s values. There is only a slight difference between Eq. 1 and those developed by Reference [10] and Reference [11]; Eq. (1) proposed in this study estimates V_s values considerably closer to those derived from most of the existing equations.

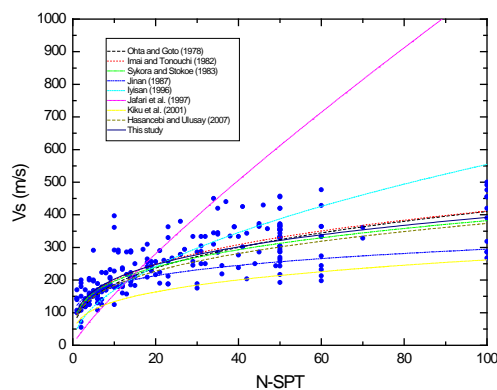


Fig. 9 Comparisons between proposed and previous correlations for N-SPT and V_s

Future efforts should aim to reduce the variability in these relations by utilizing only high-quality measurements of N-SPT and V_s , and properly incorporating the influence of overburden. This effort would involve re-interpretation of the data available in published relations, which is beyond the scope of this paper.

CONCLUSION

In this study, based on the geotechnical and geoseismic data from the Jakarta area, an attempt was made to develop new relationships between N-SPT and V_s to indirectly estimate the V_s to be used for practical purposes. The regression equations developed in this study compare well with most of the previous equations and exhibit a good prediction performance. Therefore, the use of an equation developed for all soils based on uncorrected blow-counts is recommended for practical purposes.

A likely application of the correlations presented in this work is the calculation of the thirty-meter shear wave velocity, V_{s30} , which is defined as 30m divided by the travel time of a vertically propagating shear wave in the upper 30m. V_{s30} is a required input for the Next Generation Attenuation models and is therefore needed to quantify seismic hazard. Geotechnical site investigations at many older sites contain boring logs, but no geophysical measurements. Obtaining a rough estimate of V_{s30} based on the recorded boring logs could therefore be useful for assessing seismic hazard at sites with that lack geophysical measurements, and for identifying whether geophysical measurements are necessary to further refine the estimate of V_{s30} .

The differences between existing and proposed equations are mainly due to the specific geotechnical conditions of the studied sites, the quantity of processed data and the procedures used in undertaking the SPTs and geoseismic surveys. The proposed relations are not an accurate substitute for geophysical measurements, and uncertainty in the predictions should be considered when using the relations.

ACKNOWLEDGEMENTS

The writers wish to his sincerest gratitude to Team for Microzonation Study of Jakarta, for allowing writers to incorporate the valuable data when the Team developed Jakarta Microzonation Map. Financial support for the research was provided by Universiti Malaysia Pahang and Institut Teknologi Bandung, Indonesia.

REFERENCES

- [1] Martodjojo, Evolusi Cekungan Jawa Barat, Doctor Dissertation. Bandung: Bandung Institute of Technology, 1984, ch. 3.
- [2] Assegaf, Hidrodinamika Airtanah Alamiah Cekungan Jakarta, Master Thesis. Bandung: Bandung Institute of Technology, 1998, ch. 2.
- [3] Delinom RM, "Conference proceedings", in International Workshop on Integrated Watershed Management for Sustainable Water

- Use in a Humid Tropical Region, 2007, pp. 40-54.
- [4] ASTM, Standard test method for penetration test and split-barrel sampling of soils. Annual book of ASTM standard, D1586, Vol. 04.08, 1984.
 - [5] ASTM, Standard test methods for downhole seismic testing, Annual book of ASTM standard, D7400, Vol. 04.09, 2008.
 - [6] Sykora and Stokoe, "Correlations of in-situ measurements in sands of shear wave velocity". Soil Dynamic Earthquake Engineering, Vol 20 1983, pp. 125–136.
 - [7] Iyisan, "Correlations between shear wave velocity and insitu penetration test results (in Turkish)", Chamber of Civil Engineers of Turkey, Teknik Dergi, Vol 2, 1996, pp. 1187-1199
 - [8] Jafari, Shafiee A, and Ramzkhah A, "Dynamic properties of the fine grained soils in South of Tehran". Journal of Seismology and Earthquake Engineering, Vol 4, 2002, pp. 25–35.
 - [9] Hasancebi N and Ulusay R, "Empirical correlations between shear wave velocity and penetration resistance for ground shaking assessments", Bulletin of Engineering Geology and The Environment, Vol 65, 2006, pp. 203-213.
 - [10] Ohta Y and Goto N, "Empirical shear wave velocity equations in terms of characteristics soil indexes", Earthquake Engineering Structural Dynamic, Vol 6, 1978m pp.167-187.
 - [11] Imai T and Tonouchi K, "Conference proceedings", in the 2nd European symposium of penetration testing, 1982, pp. 57-72.

ELECTRICALLY CONDUCTIVE GEOMEMBRANE ENHANCES LINER LEAK DETECTION SURVEYS AT POST INSTALLATION

H.B. Ng¹, D. Gallagher² and A. Beck³

¹GSE Lining Technology Co., Ltd., Bangkok, Thailand; ²GSE Environmental Inc., Houston, Texas, USA;

³TRI Environmental Inc., Austin, Texas, USA

ABSTRACT

Construction Quality Assurance (CQA) plays an important role in producing a quality containment system. Electrical leak detection / liner integrity surveys are CQA non-destructive tests that help locate leaks and defects at post-installation of the geomembrane systems before and after covered with soil and water. GSE Leak Location Liner incorporates a thin layer of electrically conductive layer on the bottom surface of an insulating geomembrane which allows it to be sparked tested for defects. The paper discusses the utilization of electrically conductive geomembrane liners in facilitating electrical leak detection surveys at post installation that helps engineers achieve their goal of a leak free geomembrane barrier system. Based on large scale field tests and few commercial scale tests that have been performed by third party surveyors, the surveys indicate that an electrically conductive geomembrane can significantly increase the quality of electrical leak detection surveys used to locate holes in a liner system. An electrically conductive geomembrane also allows the use of leak detection surveys in applications that were previously impossible such as multiple-layer systems, on side slopes and in situation where wrinkling has occurred in the liner.

Keywords: Conductive Geomembrane, Electrical Liner Integrity Survey, Leak Detection, Spark Test.

INTRODUCTION

The electrical leak detection / liner integrity (ELI) survey is currently the most effective and practical means of locating leaks in installed geomembranes after cover soil, as detailed in ASTM D7007. The technology functions along the principle that polyethylene geomembranes are electrically insulative. By applying an electrical potential across a geomembrane, an electrical current will flow only if a hole is present in the geomembrane, allowing the current a less-resistive path through the geomembrane. Various survey methods then track this current flow to pinpoint a leak.

When an ELI survey is performed in an application where a cover material has already been placed over the liner, it requires that a sufficiently conductive material—both above and below—is in intimate contact with the geomembrane. This traditionally meant the cover material above and subgrade below. However, due to various site conditions nonconductive liners can have difficulties meeting these requirements. For instance, with wrinkling or bridging of the liner, air gaps can exist beneath the liner that prevents the intimate contact required. Also, in cases where there is dry subgrade or encapsulated geosynthetic clay liners (GCL), the material beneath the liner may not be sufficiently conductive to conduct the leak survey (Peggs, 2007). It is also because of these two requirements that covered ELI surveys cannot be performed easily on

double-lined ponds and their slopes cannot be surveyed at all when using traditional geomembranes.

Recent studies, outlined below, show that covered ELI surveys are more thorough and accurate over a variety of soil-moisture conditions and liner-contact situations with an electrically conductive geomembrane.

IMPROVING ELI SURVEY QUALITY

The essence of covered ELI survey quality lies in the size and number of leaks that are located in the geomembrane during a survey for subsequent repair. To compare the performance of both traditional and electrically conductive geomembranes, the authors chose to employ the sensitivity test portion ASTM method D7007 to quantify survey quality by measuring the signal-to-noise ratio (signal) of identical holes in identical soil conditions when either type of geomembrane is used. A higher signal means that smaller leaks can be located compared with a lower signal, based on the authors' field experience. To eliminate other variables, all of these comparisons were made in a controlled environment using a bench-scale rig in a climate-controlled lab.

Site conditions vary greatly and a sufficient level of conductivity is a requirement of ELI surveys, so it is important that the relationship between survey performance and subgrade conductivity is well understood. To evaluate this, surveys were

performed using both types of liner on subgrades of various moisture contents. At each moisture content, signals was measured using traditional liner as well as the electrically conductive liner and for ease of understanding these two signals were compared to each other to produce an Improvement Factor at each moisture content. For instance, an Improvement Factor of 2.0 means the signal when the conductive geomembrane was used was twice as strong as when the traditional geomembrane was used. Continuing this data collection at increasing subgrade moisture contents populated the chart in Figure 1, which shows the improvement in signal strength when the conductive geomembrane was used vs. a traditional geomembrane.

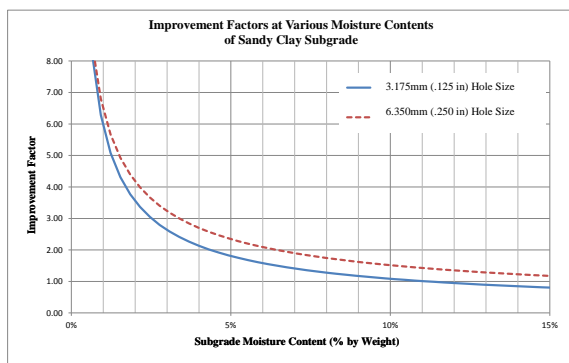


Fig. 1 Improvement factors at various moisture contents of Sandy Clay subgrade

At one moisture content, the signal strength was measured at increasing lateral distances from the hole. The greater signal at the hole was maintained at increasing distances from the hole as shown in Figure 2. This translates to a greater likelihood that a leak will be found by surveyors even if they are not surveying directly over the hole.

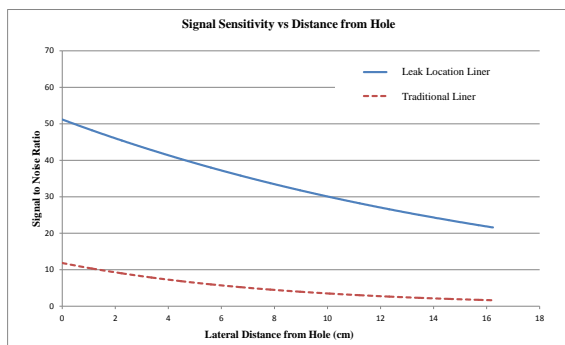


Fig. 2 Signal sensitivity vs. distance from hole

Unlike the prior tests, where improvement was studied in a situation—moist, conductive subgrade in intimate contact with the liner—where traditional liner had historically been successful, the next test was to evaluate performance in finding leaks in

situations where a traditional liner had struggled in the past, particularly when there is not intimate contact between a hole in the geomembrane and the subgrade. In this test, signals were measured multiple times for each contact scenario and the averages were recorded. It was found that when the hole was located over an imperfection in the subgrade that prevented intimate contact as shown in Figure 3, leak signals were eight times stronger when conductive geomembrane was used. Similarly, when the hole is located under a seam flap as shown in Figure 4, leak signals were 10 times greater when conductive geomembrane was used. Lastly, in a situation similar to Figure 5, where the hole is located on a wrinkle, a quantifiable comparison could not be made because no signal was detected when traditional liner was used.



Fig. 3 Hole over imperfection in subgrade

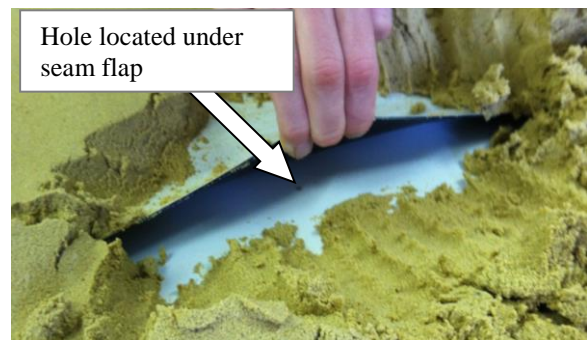


Fig. 4 Hole under seam flap

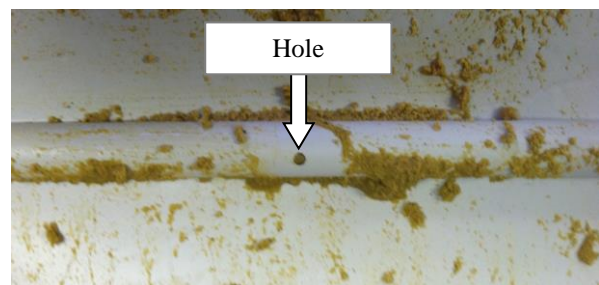


Fig. 5 Hole on simulated wrinkle

RESULTS

The results of these tests have shown that an electrically conductive geomembrane can be used to significantly increase the quality of ELI surveys used to locate holes in a liner system as well as allowing the use of ELI surveys in applications that were previously impossible such as multiple-layer liner systems. The full detailed report of this study was reported by Beck et al., 2013.

FIELD TESTING AND PERFORMANCE

The industry has begun to take notice of these improvements and recently a project was completed at a construction and demolition landfill in southern Minnesota. The site was 1.5 hectares in size with an irregular shape and approximately 3:1 side slopes. The site profile of the lining system was as follows (subgrade to surface): subgrade soils, BentoLiner Geosynthetic Clay Liner (GCL Grade NSL), 1.5 mm thick White Leak Location High Density Polyethylene (HDPE) Geomembrane, Geonet-composite drainage (GSE FabriNet 5mm thick) double sided 130 g/m² nonwoven needle-punched Polypropylene geotextile, 1.2 meters of cover soil and above that, eventual waste placement. Geosynthetic materials were installed by GSI (Geosynthetics Inc.) of Waukesha, Wisconsin.

After installation and cover soil placement a leak location/liner integrity survey was conducted by Leak Location Services Inc. of San Antonio, Texas. Figures 6 and 7 show the ELI survey was conducted through the cover soil and an excavation near defect to locate the leak. The survey took approximately two days to complete and identified two locations of damage to the geomembrane liner, one a crescent shaped cut of small size (Figure 8), the second a series of imperfections adjacent to a pipe penetration that did not appear to visual inspection to penetrate the liner, but were re-paired regardless. The necessary repairs were made and the site is currently in successful service. Detailed information on this project was reported by Ramsey et al., 2012.



Fig. 6 ELI survey was in progress



Fig. 7 Photo of excavation near leak signal and pin-pointing the leak



Fig. 8 Photo of defect found during covered ELI survey

CONCLUSIONS

Completion of this commercial field test has demonstrated the ability of electrically conductive geomembrane to be used to facilitate an ELI survey in applications that would be impossible using traditional liner. By demonstrating that the survey can be completed through cover soils, and in applications where the liner is not in intimate contact with the subgrade opens up the possibilities to a wide range of applications including use over geonets, composites, GCLs, and textiles, as well as on slopes and in situations where wrinkling has occurred in the liner.

Results from testing indicate that the use of electrically conductive geomembrane does not have a negative effect on the ability to perform the ELI survey or in its ability to find small holes when installed properly. Based on the field test that has been performed by third party surveyor, the ELI survey indicates that an electrically conductive geomembrane can significantly increase the quality of electrical leak detection surveys for locating

defects and holes in a liner system. The utilization of electrically conductive geomembrane liners in facilitating electrical leak detection surveys at post installation can assure a leak free geomembrane barrier system before the facility is in operation.

REFERENCES

- [1] ASTM D7007-03 (2003), "Standard Practices for Electrical Methods for Locating Leaks in Geomembranes Covered with Water or Earth Materials."
- [2] Beck A., Gallagher D., Kramer E., "Leak Location Liner Performance Evaluation" Proc. of Geosynthetics 2013 Conference, Long Beach, California, USA, April 1-4, 2013.
- [3] Peggs, Ian D. (2007). "Liner integrity/leak-location survey: The significance of boundary conditions." *Geosynthetics*, February-March 2007, pp. 34-38.
- [4] Ramsey B. J., Peggs I., Gallagher D. et al., "New Electrically Conductive Geomembrane for Post-Installation Liner Integrity Surveys" Proc. of the 5th European Geosynthetics Conference, Valencia, Spain, September 16-19, 2012.

INVESTIGATION OF CESIUM DIFFUSION IN CRACKED CONCRETE BY USING MICROFOCUS X-RAY CT

Ivan Sandi Darma¹, Shohei Ikeda², Takafumi Sugiyama³

^{1,2}Graduate School of Engineering, Hokkaido University, Japan;

³Faculty of Engineering, Hokkaido University, Japan

ABSTRACT

This paper addresses the diffusivity of cesium ions in cracked concrete. Concrete as a construction material is used in radioactive in-ground storage ponds. It is expected that a large amount of highly contaminated solution by radionuclides has been stored. ¹³⁴Cs and ¹³⁷Cs have been considered as the major radionuclides in the waste solutions. The presence of crack due to the application of load might increase the diffusion of cesium in the concrete. In this research small beams made by OPC and fly ash concretes were prepared. The crack was induced using flexural strength test. The unique approach of this research is in the application of microfocus X-ray CT to characterize 3D crack geometry as well as the observation of the presence of cesium in the cracked concrete through the CT number analysis. The result shows the addition of fly ash significantly reduced the diffusion coefficient of cracked concrete.

Keywords: Cracked Concrete, Cesium, Diffusion Coefficient, X-ray CT

INTRODUCTION

Cementitious materials are used in radioactive waste disposal facility construction and also as waste immobilization matrix due to their ability to act as mechanical barriers and to prevent convective water flow. Cementitious materials exhibit diffusion controlled release for many radionuclides although, for some radionuclides, the release mechanism is solubility-limited. ¹³⁴Cs and ¹³⁷Cs have highly solubility limits and therefore their release from cement matrix will be diffusion controlled [1].

A millions of gallons of high level waste solutions which contain radioactive cesium (¹³⁷Cs) in concentrations up to 2×10^{10} Bq/L reported have leaked from concrete storage tank into subsurface at the Hanford site, a former plutonium production complex located in southeastern Washington State, USA [2]. In this way it will be needed to evaluate the transport of cesium in concrete in order to take a preventive measure against leakage in to surrounding environment. The presence of cracks in cementitious materials leads to the more complex problem. Cracks inevitably arise in the most of concrete member. They can be induced by load or volumetric change due to plastic settlement, high curing temperature, various types of shrinkage, and creep. These cracks have negative effect on transport properties of concrete because crack space can act as preferential channels and allow more ions to penetrate.

Recent studies show the application of X-ray CT to evaluate the transport phenomena in cracked

mortars in which the cesium carbonate solution has been employed to trace the diffusivity of solute [3], [4]. Thanks to its relatively larger contrast under the observation with micro-focus X-ray CT the diffusivity has been successfully visualized. In this research by using non-radioactive cesium carbonate solution the transport phenomena of radioactive cesium in cracked mortar have been simulated. It is considered that the transport of the cesium behaves in similar manner in concrete. In addition the crack geometry parameters derived from microtomographic images were also studied.

EXPERIMENTAL PROGRAM

Sample Preparation

Table 1 shows two types of mix proportion for mortar specimens used in this experiment. The Ordinary Portland Cement was used for all mixtures and fly ash was used for FA specimen. Type II fly ash that is specified in the JIS A6201 was used for FA specimen. Due to the limited size of the specimen for the measurement by X-ray CT the maximum aggregate size was 1.7 mm. Fresh mortar was placed in steel molds in a size of 40×40×160 mm and cured in water for 28 days.

Flexural strength tests were used to induce cracks in the specimen. As shown in Figure 1, 10×20×60 mm beam specimens were manufactured from mortars block. The beam was reinforced by FRP sheet so as to avoid its sudden failure due to the bending load.

Table 1 Details of Mortar specimen

Specimen ID	Max. Agg. size (mm)	W/B	S/B	FA/(OPC+FA)	28 days compressive strength (N/mm ²)
OPC	1.7	0.5	2.5	0	45.7
FA				0.3	31.8

Note: W/B is the water to binder ratio by mass, S/B is the sand to binder ratio by mass, and for FA specimen fly ash was replaced for OPC by 30% by mass.

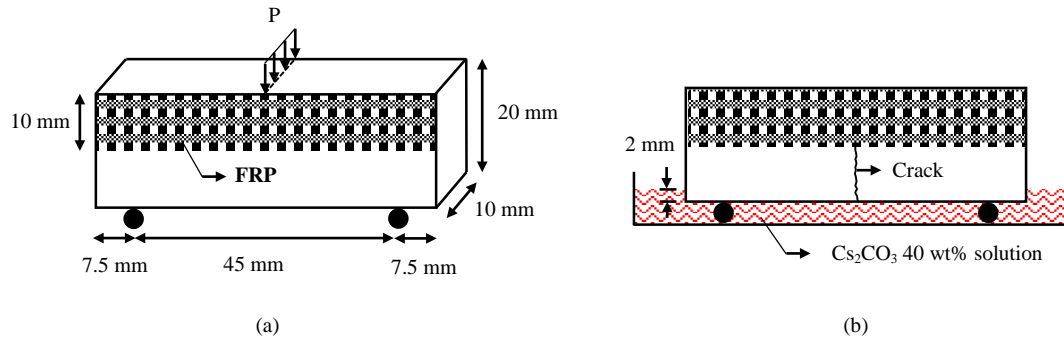


Fig. 1 Experiment set-up (a) Bending test. (b) Cesium penetration test.

The residual crack widths after the removal of bending load in the specimens were planned to be around less than 50 μm . The observation of crack width was conducted using microscope measurement. Since the nature of crack that closes to certain extent after unloading, repetitive tests were performed to obtain the target of crack width. Furthermore, the specimens were oven dried before cesium penetration test.

Cesium Penetration Experiment and Image Acquisition

In radioactive waste depositories, the presence of water, CO_2 gases and carbon containing materials would lead to cesium carbonate. This is why cesium carbonate (Cs_2CO_3) was chosen [5].

Figure 1b shows the illustration of cesium penetration test. Cesium carbonate solution (Cs_2CO_3) 40 wt% with the solution concentration of 1.84 mol/L was prepared [3]. In order to prevent diffusion in lateral direction, side-surfaces of the specimens were sealed. Subsequently, X-ray CT test was conducted after 24 hours exposure time in cesium penetration test.

In this study, tube voltage and tube current of microfocus X-ray CT were set to a value of 130 kV and 28 μA , respectively. The position of FCD and FID were set to 180 and 600 mm, respectively. The stack of these slices provides the reconstructed volumetric data of the scanned object. The reconstructed 3D-image data set was composed of 377 contiguous gray scale images where each slice image contained 1024×1024 pixel. The effective size of pixel in the CT image is $22 \times 22 \mu\text{m}$ with 44 μm in slice thickness.

Crack Width Distribution

To calculate crack width distribution, we implemented one of the plugins in BoneJ [6], [7] called *Thickness*. The operational definition of *Thickness* is based on the following equation [6]:

$$\tau(p) = 2\max(\{r | p \in \text{sph}(x, r) \subseteq \Omega, x \in \Omega\}) \quad (1)$$

Let $p_i \in \Omega$ be the set of an arbitrary point (1 unit voxel) in crack structure (Ω). Subsequently, create the largest spheres with center x and radius r which contains the point ' p_i ' and completely inside the crack structure (Ω). The thickness $\tau(p_i)$ is defined as the diameter ($2r_{\max}$) of the largest sphere. Furthermore, from point ' p_i ' which represent 1 unit voxel we will have one data corresponding to the thickness of crack structure. This algorithm will continue to run until all the points (voxels) covered in the crack structure (Ω). Finally, the information regarding the thickness (diameter) and its volume in crack structure will be obtained.

X-ray CT Number and Cesium Solution Concentrations Relationship

In case of diffusion, the movement of solute is

Table 2 Relationship between Cs_2CO_3 solution and CT Number

	Cs_2CO_3 Concentration [mol/L]				
	0.00	0.01	0.06	0.68	3.68
CT Number	75	119	153	525	2219

caused by different concentration between source of solution and internal crack space. In specific exposure time, the gradient of solute concentration occurred along the crack. This phenomenon can be observed clearly through X-Ray CT by using CT Number as an indicator of solute concentration. Therefore, the relationship between CT number and solute concentration is needed for further analysis.

To clarify the relationship between changes in CT number and solution concentration preliminary test was conducted as follows. $\varnothing 2 \times 50$ mm capillary-glass tubes filled with 0 (water), 0.003, 0.03, 0.34 and 1.84 mol/L of cesium carbonate (Cs_2CO_3) solution were prepared. The average CT number of each solution was obtained. Table 2 shows CT Number values of each solution concentration. It can be seen that the CT number are linearly increased with increasing concentration of ion in solution.

Observation Method of Cesium Diffusion along the Crack

First, a specific slice at the represented elevation from the surface in contact with the solution was chosen from the whole stack of reconstructed slices in solution-exposed condition. Then, several crack locations filled by cesium solution were specified. Line segment which intersect perpendicularly to the crack was applied in selected location. The profile of CT number was obtained from each line segment. Based on the relationship between CT number and cesium solution concentration derived from Table 2, the average of maximum CT number was converted into the cesium solution concentration. By applying the same method for specific position to the exposed surface, cesium solution concentration profile along the crack would be obtained.

Diffusion due to a concentration gradient can in general be described by Fick's second law of diffusion as follows:

$$C_x = C_s \left[1 - \text{erf} \left(\frac{x}{2\sqrt{Dt}} \right) \right] \quad (2)$$

where C_x is the Cs_2CO_3 concentration at distance x , x is the distance from the exposed surface, C_s is the surface Cs_2CO_3 concentration, D is defined as cesium diffusion coefficient in this study, t is the exposure time, and erf is the error function. The best-fit curve was used with the measured Cs_2CO_3 concentration profile along the crack.

Observation Method of Cesium Diffusion in Uncracked Matrix

The similar methods applied to acquire CT number profile in order to determine cesium diffusion coefficient in uncracked body. In the determination of the diffusion coefficient along the

crack used the average of maximum CT number profiles, while in the determination of diffusion in uncracked body, CT number profile is fully used. CT number profile completely shows the Cs_2CO_3 concentration profile both in cracks and uncracked body of mortar at specific height from the surface in contact with the solution. The diffusion coefficient perpendicular to the crack wall then was determined from the best-fit curve represented by Eq.(2) for the measured cesium solution concentration profile.

RESULTS AND DISCUSSION

Distribution of flexural crack width based on 3D crack analysis

Figure 2(c) and (d) shows 3D crack space derived from 3D microtomographic images (Figure 2a and 2b). Despite having slightly different frequency of each value of crack width as shown in Figure 2 (e) and (f), the average crack width for both specimens was coincidentally the same as $88 \mu\text{m}$ based on the 3D crack analysis. This means that the presence of flexural crack for both OPC and FA specimens appears to have the same geometrical effect on the transport of solute in the crack.

Cesium diffusion within the crack space

Figure 3 shows an example to obtain the distribution of Cs_2CO_3 concentration along the given line position in the crack space at a certain elevation surface of 4 mm from the surface in contact with the solution. (FA Specimen). From Figure 3(c) the Cs_2CO_3 concentration in the crack was determined to 0.53 mol/L. This concentration is lower than the concentration of the Cs_2CO_3 in the source solution of 1.84 mol/L meaning that the diffusion process occurs along the crack passage. The same methodology was applied to determine the concentration in the crack at the height of 0, 2, 6 and 8 mm from surface exposed to the solution for both specimens.

Figure 4(a) and (b) shows cesium penetration in both specimens. The presence of cesium in the crack is shown in white because of its large CT numbers. Furthermore, Cs_2CO_3 concentration profiles were obtained as shown in Figure 4(c) and (d). It is obvious that the concentration decreases with the increased heights.

As given in Table 3, the cesium diffusion coefficient along the crack (D_{crack}) in OPC specimen is greater than that of in FA specimen. Considering the crack width distribution for both cracked specimens was similar, we suggest that difference in diffusion coefficient between OPC and FA specimen should be influenced by the movement of cesium toward to the uncracked mortar body.

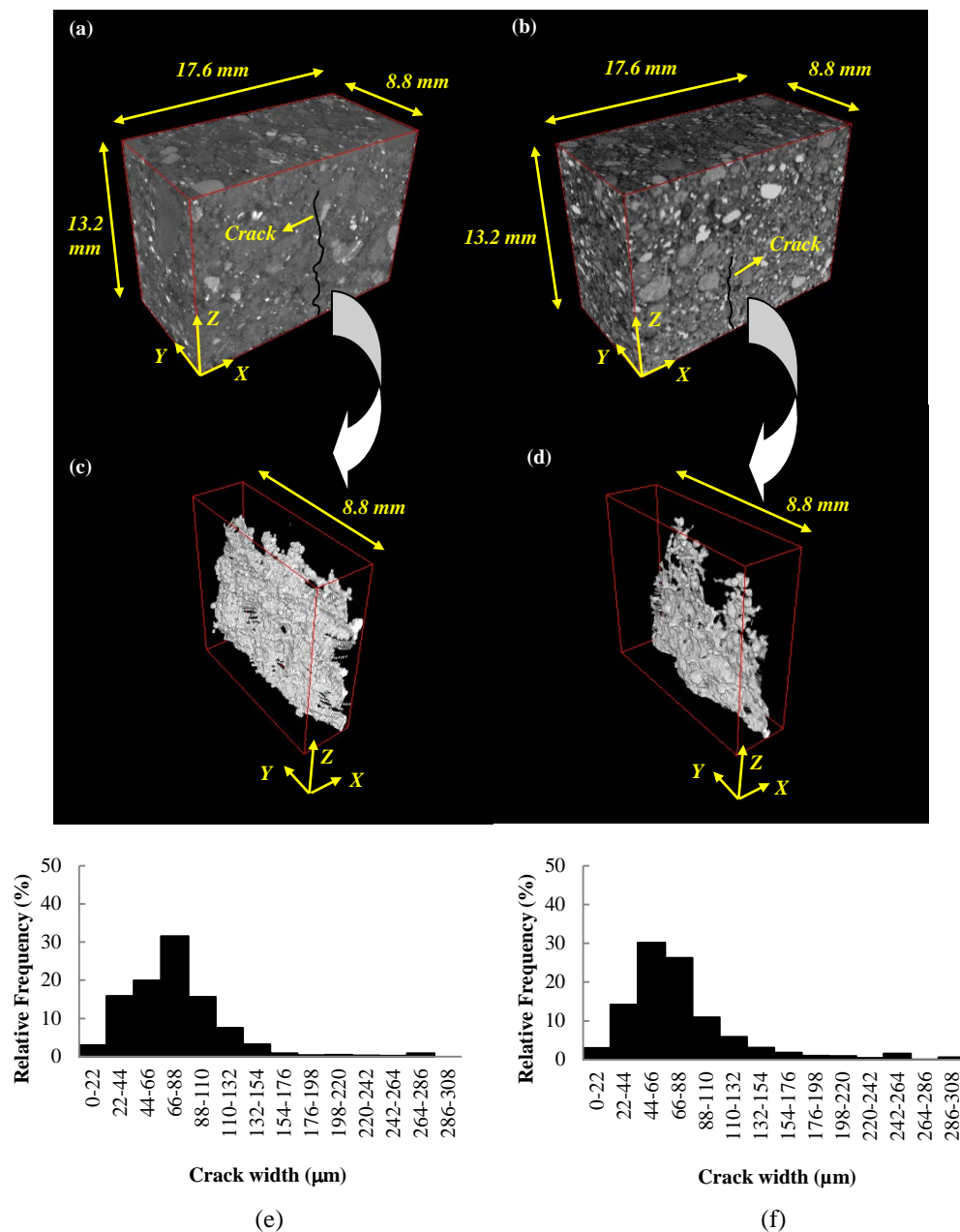


Fig. 2 3-Dimensional cracked specimens, crack structures, and crack width distributions in a volume of interest (VOI) of (a), (c), (e) for OPC specimen and (b), (d), (f) for FA specimen

To discuss the difference in diffusion coefficient along the crack, the diffusion coefficient perpendicular to the crack wall of each specimen were studied.

The diffusion coefficients along the crack for both specimens are lower than the diffusion coefficient of cesium ions in free water ($2.06 \times 10^{-9} \text{ m}^2/\text{s}$, [8]). Although the defined D in this research is based on the Cs_2CO_3 concentration this results implies that the process of cesium moving along the crack is somewhat hindered. Furthermore the capillary absorption would occur because specimens were dried prior to the penetration tests. In this regard more researches will be needed for

clarification.

Cesium diffusion in uncracked matrix

Figure 4(e) and (f) shows the limited diffusion in the uncracked matrix for the FA specimen as compared with OPC. The average apparent diffusion coefficients of uncracked body ($D_{\text{uncracked}}$) for OPC and FA specimens are 9.12×10^{-11} and $3.47 \times 10^{-12} \text{ m}^2/\text{s}$, respectively. In general, at 28 days curing period the diffusivity of ions in fly ash concrete is higher than that of in OPC concrete due to slow in pozzolanic reaction. However, in this research the drying process before penetration test enhanced the

Table 3 Diffusion coefficient of each sample

Sample	Crack width (μm)	CT ^{*2}	Diffusion Coefficient (m^2/s)	
			D_{crack}	$D_{\text{uncracked}}^{*3}$
OPC	20-40	88	1.70×10^{-9}	9.12×10^{-11}
FA	45-55	88	9.30×10^{-10}	3.47×10^{-12}

^{*1} Measured by microscope, ^{*2} Average width by 3D crack analysis, ^{*3} Apparent diffusion coefficient

pozzolanic reaction. This resulted in the increased resistance to diffusivity due to the dense microstructure for FA specimen.

Reduced diffusion coefficient for uncracked matrix in the FA specimen might be the reason why the cesium diffusion coefficient along the crack in the FA specimen was lower than that of OPC specimen. The presence of cesium within the crack space inhibits the movement of cesium toward to the lower gradient. In this condition, a mechanism has been formed where the diffusion in perpendicular direction play important role in diffusivity within the crack space. Cesium diffusion into the uncracked matrix will trigger the diffusion along crack. The easier diffusion into uncracked matrix, the greater diffusion from the source solution along the crack. It is noted that the apparent diffusion coefficients obtained in this study lay within reported ranges by previous research [1], [9].

CONCLUSION

Using flexural strength test, cracked OPC and FA specimens were obtained. From the image analysis of 3D crack analysis, it was found that crack width distribution for both crack spaces were similar although the microscope observation provided their width ranging 20 to 40 and 45 to 55 for OPC and FA specimens, respectively

The addition of fly ash could reduce the diffusivity in uncracked matrix as compared with OPC specimen of equivalent crack width distribution. This condition led to lower diffusion coefficient along the crack for FA specimen than that of in OPC specimen.

ACKNOWLEDGMENT

Part of this research was funded by Japan Society for Promotion of the Science (Research No.23360187). The first author also expresses gratitude for the financial support from JICA.

REFERENCE

- [1] Bucur C., Olteanu M., Cristache C. et al., "Radionuclide transport through cement matrices", *Revista De Chimie*, 61 (5), 2010, pp. 458-461.

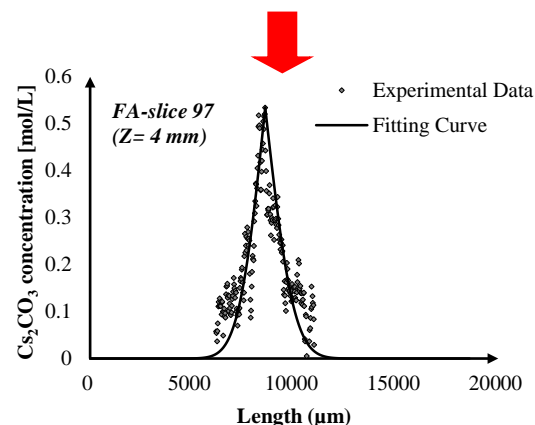
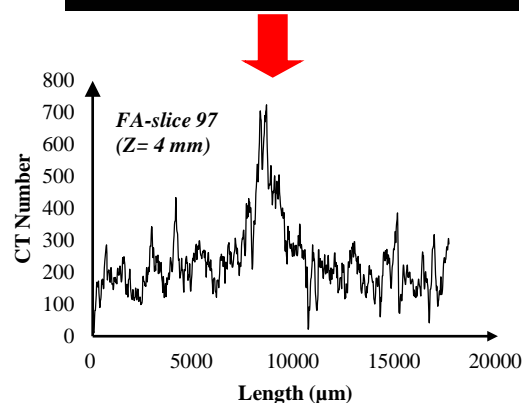
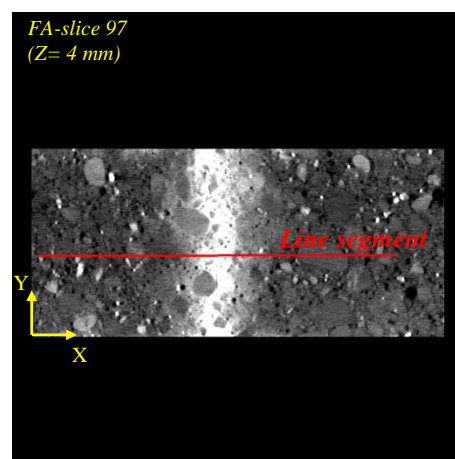


Fig. 3 Method to determine diffusion coefficient from representative microtomographic

- [2] Serne R.J., Zachara J.M., Burke D.S., "Chemical Information on tank Supernatants, Cs Adsorption from Tank Liquids onto Hanford Sediments, and Field Adsorption of Cs Migration from Past Tanks Leaks", Pacific Northwest National Laboratory, 1998, PNNL-11495/UC-510.
- [3] Ikegami H., Kikkawa T., Sugiyama T., "Visualization of solution transport through cracks in concrete by X-ray CT", The 65th Annual Meeting of Japan Cement Association, 2011, pp. 138-139 (in Japanese).

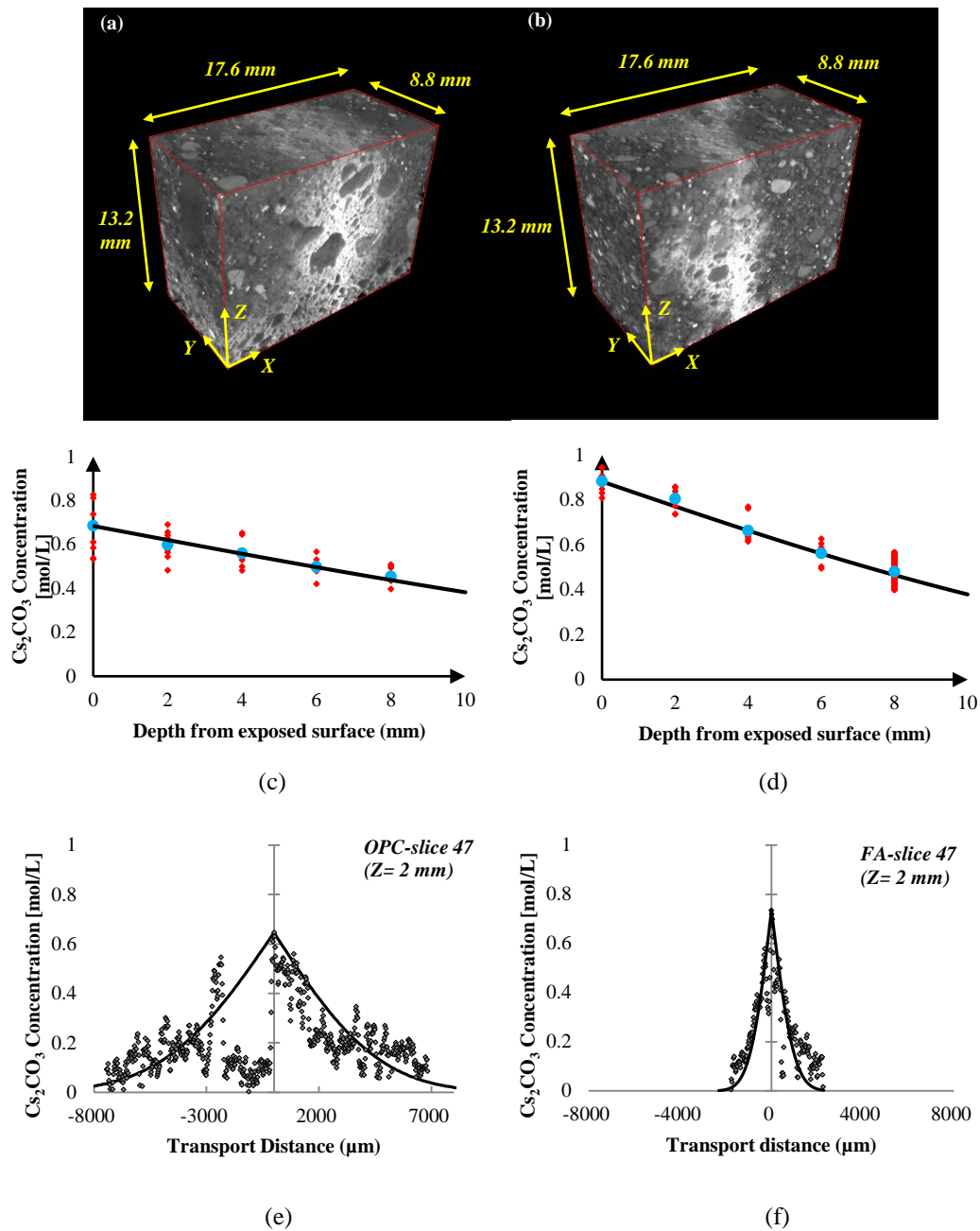


Fig. 4 3-Dimensional cesium penetrated samples of (a) OPC and (b) FA, Cesium concentration profile along the crack of (c) OPC and (d) FA, and representative of Cesium concentration profile of uncracked mortar of (e) OPC sample (f) FA at 2 mm from solution contact surface.

- [4] Kikkawa T., Sugiyama T., Darma I.S., et al., "Observation of flexural cracking and cesium carbonate transport using X-ray CT", *Proceedings of Annual Conference of JCI*, Vol.34 (1), 2012, pp. 1810-1815 (in Japanese).
- [5] Boch Ph., Seiss M., Vetter G., et al., "High-alumina cements for cesium trapping, *Cem. Concr. Res*, Vol 22, 1992, pp. 369-374.
- [6] Doube M., Klosowski M.M., Argenda-Carreras I., et al., "BoneJ: Free and extensible bone image analysis in ImageJ", *Bone*, 47, 2010pp.1076-1079.
- [7] Doube M., "BoneJ [online]", 2009, Available from: <<http://bonej.org>> [December 2012].
- [8] Flury M., Gimmi T., Dane J.H. et al., "Solute diffusion", in *Methods of Soil Analysis, Part 4, Physical Methods*, Soil Science Society of America, Madison, WI, 2002, pp. 1323-1351.
- [9] Kumar A., Roy D.M., "Retardation of Cs^+ and Cl^- diffusion using blended cement admixtures", *J. Am. Ceram. Soc.*, 69(4), 1986, pp. 356-360.

MODELLING THERMO-ELASTO-PLASTIC BEHAVIOUR OF NORMALLY CONSOLIDATED AND OVERCONSOLIDATED SOILS

Yang-Ping Yao¹ and Annan Zhou²

¹Civil Engineering Department, Beihang University, Beijing 100191, China; ²Discipline of Civil Engineering, Royal Melbourne Institute of Technology (RMIT), Melbourne 3001, Victoria, Australia.

ABSTRACT

A constitutive, non-isothermal unified hardening (UH) model is presented to interpret the thermo-elastoplastic behaviours of normally consolidated (NC) and overconsolidated (OC) clays. Two yield surfaces (the current yield surface and the reference yield surface) are adopted in the proposed model. A unified hardening parameter (H) is developed to describe the evolution of the current yield surface, and the plastic volumetric strain is employed to quantify the hardening of the reference yield surface. The similarity ratio (R_T) between the current yield surface and the reference yield surface, which is a function of the temperature and plastic volumetric strain, is developed to govern the volume change behaviour and the shear strength of soils with different stress histories and at varying temperatures. The proposed model is then validated through test results in the literature.

Keywords: Temperature, Non-isothermal conditions, Constitutive modelling, Overconsolidation

INTRODUCTION

Theoretical and experimental studies on the engineering properties of soils are usually restricted to isothermal conditions, although soils in engineering are commonly exposed to non-isothermal conditions. In the natural environment, soils experience seasonal temperature variations, and isothermal conditions exist only in the laboratory environment. In addition to the natural temperature variations, underground structures are also subject to artificial non-isothermal conditions. A typical example is nuclear waste disposal [1], which involves burying high-level radioactive nuclear waste deep into soils with very low permeability. The buried nuclear waste containers keep desorbing energy to the surrounding soils and continually heat the protective soil barriers. Another geotechnical engineering practice related to non-isothermal conditions is buried high-voltage cables [2]. The electric current conveyed through the copper cables produces heat that is continuously transferred to surrounding backfills. Similarly, buried geothermal pipelines that transfer high-temperature fluid also continuously release heat to the surrounding soils, which leads to soil temperature changes.

After realising that soils in geotechnical engineering are not always restricted to isothermal conditions, intensive research on the soils' thermo-mechanical properties has been conducted after the pioneering work by Campanella and Mitchell (see [3]). In the past 30 years, a variety of temperature-controlled laboratory tests were conducted on different soils to investigate their thermo-mechanical properties [4-7]. Based on the experimental observations, a number of constitutive models were

proposed to interpret the thermally-induced yield mechanism and reproduce the temperature-related stress-strain relationships of soils (such as [4, 8-12]).

Because a soil's stress history significantly affects its thermal behaviour, studies (both experimental and theoretical) on the thermal effects are commonly conducted on the soil with different overconsolidated ratios (OCRs). Therefore, a solid and effective constitutive model for both normally consolidated and overconsolidated soils in isothermal conditions should be the starting point for further developing a reliable and robust thermo-elastoplastic model. Very recently, the authors proposed a new elastoplastic model [13] to interpret the mechanical behaviours for both normally consolidated and overconsolidated soils in general stress states based on the sub-loading surface concept. The proposed model, referred to as the original UH model, is simple and practical because it only includes one additional parameter (the Hvorslev slope) compared with the Modified Cam-clay model. The original UH model does not take thermal effects into consideration.

The main purpose of this article is to extend the isothermal UH model (i.e., the original UH model) to non-isothermal states. The thermo-elastoplastic behaviours of both normally consolidated and overconsolidated soils will be interpreted and simulated by the framework of the non-isothermal UH model. For notational convenience, all stress variables in this article are effective stress variables.

ISOTHERMAL UH MODEL: A REVIEW

Current Yield Surface and Reference Yield Surface

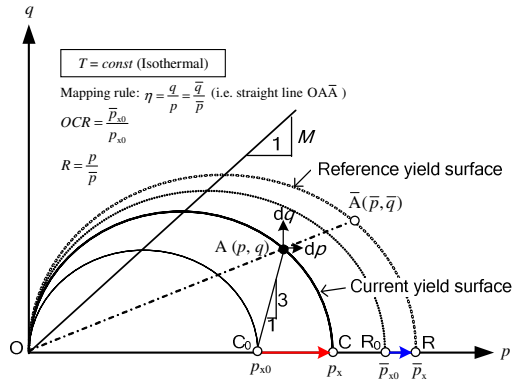


Fig. 1 Current yield surface and reference yield surface for the isothermal UH model.

In the original UH model, an ellipse is adopted as the current yield surface following the Modified Cam-clay model (see Fig. 1, solid ellipse OC). With respect to the current yield surface, the unified hardening parameter (H) is adopted to replace the plastic volumetric strain (ϵ_v^p) that is used as the hardening parameter in the Modified Cam-clay model. The current yield surface and its hardening law are presented as follows:

$$p + \frac{q^2}{pM^2} - p_x = 0; p_x = p_{x0} \exp\left(\int \frac{1+e}{\lambda-\kappa} dH\right) \quad (1)$$

where p and q are the effective mean stress and the deviator stress, respectively. $q = \eta p$, where η is the stress ratio. p_x is the cross point between the current yield surface and the p -axis. p_{x0} is the equivalent initial effective mean stress (i.e., $p_{x0} = p_0 + q_0^2/(M^2 p_0)$), where p_0 and q_0 are initial mean stress and initial deviator stress, respectively). e is the void ratio. κ and λ are the elastic unloading index and elastoplastic compression index for saturated soils, respectively. M is the stress ratio at the critical state. H is the unified hardening parameter proposed by Yao *et al.* (see [13]);, which can be written as:

$$H = \int dH = \int \frac{M_f^4 - \eta^4}{M^4 - \eta^4} d\epsilon_v^p \quad (1)$$

where M_f is the potential failure stress ratio, which will be discussed in detail in the following section, 'Potential Failure Stress Ratio'. The initial size of the current yield surface is determined by the value of p_{x0} (see initial ellipse OC₀ in Fig. 1). During a triaxial loading, e.g., conventional triaxial compression (CTC, see stress path C₀A in Fig. 1), the current state point moves from C₀ to point A, and the current yield surface expands from OC₀ to OC. The increments of the unified hardening parameter (dH) and the plastic volumetric strain ($d\epsilon_v^p$) can be

calculated from Eqs (1) and (2) when the yield surface expands from OC₀ to OC. Conversely, the current yield surface can be determined according to Eqs (1) and (2) with a given increment of the plastic volumetric strain in the strain-controlled loading.

In addition to the current yield surface, the reference yield surface (see Fig. 1, dash ellipse OR), which is completely identical to the yield surface in the Modified Cam-clay model, is adopted to consider the effects of the stress history and further determine the value of M_f (see the following section, 'Potential Failure Stress Ratio'). The reference yield surface and its hardening law can be written as:

$$\begin{cases} \bar{f} = \bar{p} + \frac{\bar{q}^2}{\bar{p}M^2} - \bar{p}_x = 0 \\ \bar{p}_x = \bar{p}_{x0} \exp\left(\int \frac{1+e}{\lambda-\kappa} d\epsilon_v^p\right) \end{cases} \quad (3)$$

where \bar{p} and \bar{q} are the reference mean stress and the reference deviator stress, respectively. \bar{p}_x is the cross point between the reference yield surface and the p -axis. \bar{p}_{x0} is the isotropic preconsolidation pressure. The initial size of the reference yield surface is specified by the value of \bar{p}_{x0} (see initial ellipse OR₀ in Fig. 1). The expansion of the reference yield surface is controlled by the plastic volumetric strain. The plastic volumetric strain produced when the current yield surface expands from OC₀ to OC leads to the expansion of the reference yield surface from OR₀ to OR (see Fig. 1). It is noted that the expansion velocity difference between the current yield surface and the reference yield surface is controlled by the value of the term $(M_f^4 - \eta^4)/(M^4 - \eta^4)$.

Mapping Rule and Similarity Ratio

The reference yield surface can be determined by \bar{p}_{x0} and the term related to the plastic volumetric strain (i.e., $\int [(1+e)/(\lambda-\kappa)] d\epsilon_v^p$). A mapping rule is still required to find the reference point (see point \bar{A} in Fig.1) on the reference yield surface to specify \bar{p} and \bar{q} . A geometric mapping rule between the reference stress point and the current stress point is assumed as below:

$$\eta = \frac{q}{p} = \frac{\bar{q}}{\bar{p}} \quad (4)$$

Following Asoka *et al.* (see [14]), the similarity ratio, i.e., the ratio between the current mean stress (p) and the reference mean stress (\bar{p}), is adopted as a state variable (R):

$$R = \frac{p}{\bar{p}} = \frac{p}{\bar{p}_{x0}} \left(1 + \frac{\eta^2}{M^2} \right) \exp \left(- \int \frac{1+e}{\lambda - \kappa} d\epsilon_v^p \right) \quad (5)$$

Potential Failure Stress Ratio

According to [15], we propose that the relationship between the potential failure stress ratio (M_f) and the similarity ratio (R) is as follows:

$$M_f = \left(\frac{1}{R} - 1 \right) (M - M_H) + M \quad (6)$$

where M_H is the slope of the Hvorslev surface and can be determined by undrained triaxial tests on soils with different OCR s. For clays, M_H is usually $0.5 M \sim 0.9 M$ [15], which can be used to estimate M_H if no test results for the calibration are available. However, Eq (6) in the original UH model neglects the possibility that the value for η exceeds 3. This intrinsic restriction (i.e. $\eta \leq 3$) is taken into account here, and the above equation is revised as:

$$M_f = 3 - \left\langle 3 - \left(\frac{1}{R} - 1 \right) (M - M_H) - M \right\rangle \quad (7)$$

where $\langle \rangle$ are Macaulay's brackets, which indicate the following calculation rules for a variable x :

$$\langle x \rangle = \begin{cases} x & (x \geq 0) \\ 0 & (x < 0) \end{cases} \quad (8)$$

NON-ISOTHERMAL UH MODEL

Volume Change Equation in Non-isothermal Conditions

In addition to the stress change, temperature variation can also induce the volume change of saturated soils, even under constant stress conditions. Thermal volume change can be divided into thermoplastic volume change (irreversible) and thermoelastic volume change (reversible). Compared with the deformation due to a stress change, the deformation caused by a temperature change has its own characteristics. For example, experimental data indicate that the normal compression lines (NCLs, in the plane of e vs. $\ln p$) of a saturated soil at different temperatures can be considered parallel to each other. In other words, the temperature induced void ratio change of normally consolidated soils can be considered independent of stress levels. According to experimental observations ([3, 4, 6, 16, 17]), the following two simple equations are developed to describe the elastic and plastic strains due to both the temperature change and the stress change:

$$\begin{cases} d\epsilon_v^e = \frac{\kappa}{1+e} \frac{dp}{p} + \kappa_T dT \\ d\epsilon_v^p = \frac{\lambda - \kappa}{1+e} \frac{dp}{p} + (\lambda_T - \kappa_T) dT \end{cases} \quad (9)$$

where $d\epsilon_v^e$ is the elastic volumetric strain increment including the elastic and thermoelastic components; $d\epsilon_v^p$ is the plastic volumetric strain increment including the plastic and thermoplastic components; κ_T is the thermoelastic compression index, which could be a function of the current stress, temperature and stress history. However, in this paper, following Cui *et al.* (see [8]), we assume κ_T is a soil constant (i.e. the negative value of the coefficient of thermal expansion) for the simplicity purpose. Thermoelastic swelling during heating is mainly caused by the thermal expansion of the soil skeleton. λ_T is the thermo-elastoplastic compression index and is usually positive for an irreversible contractive volume change due to heating. In this paper, we assume λ_T is a constant for simplicity, but it can be set as a function of temperature, which may involve additional fitting parameters, to simulate the non-linear thermo-elastoplastic compression for normally consolidated soils. It is noted that Eq. (9) is applicable to the normally consolidated soil only. For overconsolidated soils, the volume change equation can be derived from Eq. (9) and the yield surfaces.

If we set the plastic volumetric strain increment in Eq. (9) to zero, the yield surface (p - T yield surface) in the plane of the mean stress (p) and temperature (T) can be solved as:

$$p_{0T} = p_0 \exp[-\beta(T - T_0)] \quad (10)$$

where, v is the specific volume ($= 1 + e$) and $\beta = v(\lambda_T - \kappa_T)/(\lambda - \kappa)$. p_{0T} is the yield stress in isotropic conditions at the observation temperature (T), and p_0 is that at the reference temperature (T_0).

Shear Strength for Non-isothermal Conditions

Experimental results (e.g., [10]) support that the soil's drained shear strength increases during heating. The mechanism of such an increase of the shear strength due to heating can be mainly attributed to the density increase owing to thermal compression. In this paper, we assume the temperature alters the soil's strength by changing its density. The influence of thermal fabric change on soil's strength is not taken into account here, since it is not generally observed.

For a normally consolidated soil with a mean stress ($p = p_0$) (see point A, Fig. 2a and Fig. 2b), increasing temperature (from T_0 to T) leads to a density increase under the same mean stress. The state point moves to point B (p_0, e_1), which is

vertically below point A (p_0, e_0) in the plane of the void ratio and logarithmic mean stress, as shown in Fig. 2a. The soil at point B is still a normally consolidated soil at T because point B is located on the normal compression line at T (see point B, Fig. 2a) and the p - T yield surface (see point B, Fig. 2b). For point B, the critical state stress ratio is $M_T^{(B)}$, which is equal to the potential failure stress ratio ($M_{fT}^{(B)}$) because this soil is normally consolidated at T (the similarity ratio is equal to one; therefore, $M_T^{(B)} = M_{fT}^{(B)}$).

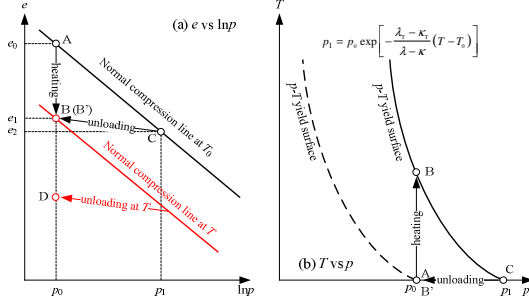


Fig. 2 Density increase due to heating and overconsolidation

However, the soil with the same void ratio (e_1) under the same stress level (p_0) (see point B' in Fig. 2a and Fig. 2b) can be obtained via unloading from point C (p_1, e_2) with a constant temperature (T_0). The mean stress at point C is assumed to be p_1 , which is higher than p_0 . This soil (point B') is an overconsolidated soil at T_0 . The potential failure stress ratio for point B' can be calculated from Eq. (6):

$$M_{fT}^{(B')} = 3 - \left\langle 3 - (R^{-1} - 1)(M - M_H) - M \right\rangle \quad (11)$$

$$= 3 - \left\langle 3 - (p_1/p_0 - 1)(M - M_H) - M \right\rangle$$

where R is the similarity ratio at T_0 , which is equal to p_0/p_1 for point B'. Because the soils at point B and at point B' (see Fig. 2a) have same mean stress and density, it is reasonable to assume they have the same potential failure strength if the temperature remains unchanged during shearing (i.e., shearing at T for point B and shearing at T_0 for point B'):

$$M_{fT}^{(B')} = M_{fT}^{(B)} = M_T^{(B)} \quad (12)$$

Let us substitute Eq. (11) into Eq. (12) and consider the following: (i) p_1 in Eq. (11) can be found from the p - T yield surface, i.e., Eq. (10); (ii) M_H is assumed independent of the temperature (experimentally supported by [9]); and (iii) point B is an arbitrary point. We have:

$$M_T = 3 - \left\langle 3 - (M - M_H) \exp[\beta(T - T_0)] - M_H \right\rangle \quad (13)$$

For overconsolidated soils at T (such as point D in Fig. 2a), the potential failure stress ratio (M_{fT}) can be constructed based on Eq. (6):

$$M_{fT} = 3 - \left\langle 3 - (R_T^{-1} - 1)(M_T - M_H) - M_T \right\rangle \quad (14)$$

where M_T can be found from Eq. (13) and R_T is the similarity ratio at T . If the soil is normally consolidated at T , $R_T=1$ and $M_{fT} = M_T$. For a given temperature (T) and a similarity ratio at this temperature (R_T), the potential failure stress ratio M_{fT} can be calculated via Eq. (14).

Current Yield Surface and Referenced Yield Surface in Non-isothermal Conditions

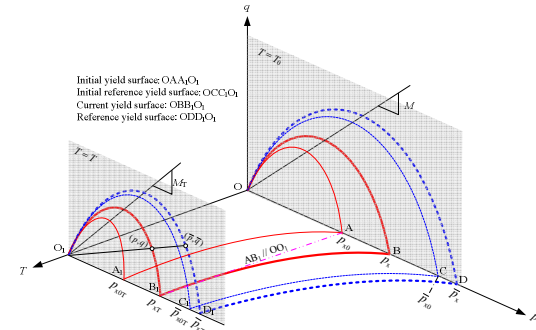


Fig. 3 Conceptual view of the current yield surface and the reference yield surface in non-isothermal conditions

At a given temperature (T), the current yield surface (see C_1O_1 in Fig. 3) is assumed similar to that in the isothermal condition (i.e., Eq. (1)). The p - T yield surface (i.e., Eq. (10), see C_1C in Fig. 3) is adopted to consider the temperature variation. We combine yield surface C_1O_1 and yield surface C_1C together, which generates the current yield surface (3-D) in the space of q - p - T (see OCC_1O_1 in Fig. 3):

$$\begin{cases} f_T = p + \frac{q^2}{pM_T^2} - p_{xT} = 0; p_{xT} = p_{x0T} \exp\left(\int \frac{1+e}{\lambda-\kappa} dH_T\right), \\ dH_T = \frac{M_T^4 - \eta^4}{M_T^4 - \eta^4} d\varepsilon_v^p; p_{x0T} = p_{x0} \exp[-\beta(T - T_0)] \end{cases} \quad (15)$$

where p and q are the current mean stress and deviator stress, respectively, at temperature T . M_T is the critical state stress ratio at temperature T . M_{fT} is the potential failure stress ratio at T , which has been defined in Eq. (14) with a given R_T (see Eq. (18) later). p_{xT} is the cross point between the current yield surface and p -axis at temperature T . p_{x0T} stands for the equivalent initial mean stress when the deviator stress is equal to zero at temperature T . If $\varepsilon_v^p = 0$, p_{xT} is equal to p_{x0T} , and the current yield surface (see OCC_1O_1 in Fig. 3) is the same as the

initial yield surface (see OAA_1O_1 in Fig. 3) because no hardening occurs. H_T is the unified hardening parameter at T . The p - T yield surface (i.e., Eq. (10)) is employed to relate the initial mean stress at temperature T (i.e., p_{x0T}) with that at T_0 (i.e., p_{x0}).

Similarly, based on Eq. (3), the function of the reference yield surface in p - q - T space (see ODD_1O_1 in Fig. 3) can be written on the analogy of the above procedure for the current yield surface:

$$\begin{cases} \bar{f}_T = \bar{p} + \frac{\bar{q}^2}{\bar{p}M_T^2} - \bar{p}_{xT} = 0; \bar{p}_{xT} = \bar{p}_{x0T} \exp\left(\int \frac{1+e}{\lambda-\kappa} d\varepsilon_v^p\right); \\ \bar{p}_{x0T} = \bar{p}_{x0} \exp[-\beta(T-T_0)] \end{cases} \quad (16)$$

where \bar{p} is the reference mean stress and \bar{q} is the reference deviator stress at T . \bar{p}_{x0} is the preconsolidation pressure at T_0 . If $\varepsilon_v^p = 0$, $\bar{p}_{xT} = \bar{p}_{x0T}$, and the reference yield surface (see ODD_1O_1 in Fig. 3) is same as the initial reference yield surface (see OBB_1O_1 in Fig. 3). The reference mean stress at T can be solved from above equation:

$$\bar{p} = \frac{\bar{p}_{x0}M_T^2}{M_T^2 + \eta^2} \exp\left[-\beta(T-T_0) + \int \frac{1+e}{\lambda-\kappa} d\varepsilon_v^p\right] \quad (17)$$

where η is the stress ratio at T ($\eta = q/p = \bar{q}/\bar{p}$). Based on the definition presented in Eq. (5), the similarity ratio at temperature T (i.e., R_T) can be written as

$$R_T = \frac{p}{\bar{p}_{x0}} \left(1 + \frac{\eta^2}{M_T^2}\right) \exp\left[\beta(T-T_0) - \int \frac{1+e}{\lambda-\kappa} d\varepsilon_v^p\right] \quad (18)$$

Once R_T is calculated from Eq. (18), M_{IT} in Eq. (14) can be determined. The flow rule, which is similar to that in the Modified Cam-clay model, is employed here:

$$\frac{d\varepsilon_d^p}{d\varepsilon_v^p} = \frac{2\eta}{M_T^2 - \eta^2} \quad (19)$$

The elastic volumetric strain and elastic deviator strain are defined as follows

$$d\varepsilon_v^e = \frac{\kappa}{1+e} \frac{dp}{p} + \kappa_T dT; \quad d\varepsilon_d^e = \frac{2(1+\nu)}{9(1-2\nu)} \frac{\kappa}{1+e} \frac{dq}{p} \quad (20)$$

where ν is Poisson's ratio, which is assumed as a constant ($= 0.3$) in this paper.

EXPERIMENTAL VALIDATIONS

Drained conventional triaxial compression (CTC) tests on a remoulded kaolin clay with a variety of OCR s are conducted at two different

temperatures, as reported by Cekerevac and Laloui (see [4]). The remoulded kaolin clay is first preconsolidated to 600 kPa ($e_0 = 0.94$) at room temperature ($T_0 = 22^\circ\text{C}$) and then unloaded to 600, 500, 400, 300, 200, and 100 kPa to produce soil samples with different OCR s ($= 1, 1.2, 1.5, 2, 3$ and 6 , respectively). These samples are then triaxially compressed in the drained condition to 20% of the deviator strain at both room temperature (22°C) and 90°C . Isotropic compressions at room temperature (i.e., data set S2-T6 and S2-T8) are employed to calibrate the elastic unloading index and elastoplastic compression index: λ is set to 0.18 and κ is set to 0.05. The isotropic heating test for normally consolidated specimen is adopted to calibrate the thermo-elastoplastic compression index (λ_T). λ_T is set to 1.8×10^{-4} . The thermoelastic compression index is estimated from the ratio between κ and λ because the isotropic cooling test is not available for this kaolin clay, namely, $\kappa_T = -(\kappa/\lambda) \lambda_T = -0.5 \times 10^{-4}$. The triaxial tests results are replotted in Fig. 4 (circles for the 90°C series and triangles for the 22°C series). The critical state stress ratio (M) is calibrated by the triaxial compression test ($OCR=1$) at room temperature (see Fig. 4a). The Hvorslev slope (M_H) can be calibrated by the triaxial compression test ($OCR=1$) at 90°C via Eq. (14) (see Fig. 4a). M and M_H are set to 0.87 and 0.4 for this remoulded kaolin clay, respectively.

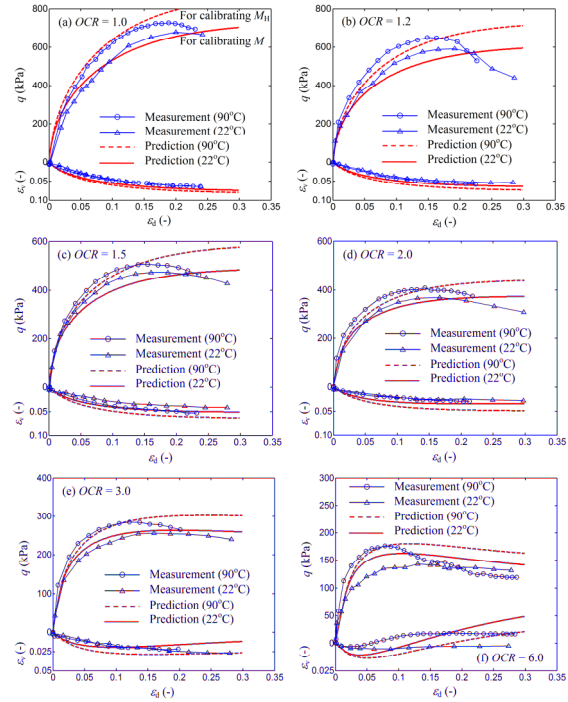


Fig. 4 Drained triaxial compression and predictions by the non-isothermal UH model

The soil responses (the stress strain relationships and the volume change during shearing) are predicted by the non-isothermal UH model and compared with the experimental results in Fig. 4a-f ($OCR = 1, 1.2, 1.5, 2, 3$ and 6 , respectively). In Fig. 4, the solid curves stand for predictions at 22°C and the dashed curves for predictions at 90°C . Three main trends in these tests are visible and predicted reasonably well by the proposed model: (1) the strength at a higher temperature is higher than that with a lower temperature for all OCR s; (2) the softening behaviour during shearing and the peak strength become more visible as the OCR increases for both temperatures; (3) the volume change during shearing gradually turns from compression to dilation with an increase of the OCR for the two temperatures.

CONCLUSIONS

A constitutive model is proposed to interpret the thermo-elastoplastic behaviour of normally consolidated and overconsolidated clayey soils. Compared with the Modified Cam-clay model, the proposed non-isothermal UH model introduces only 3 new parameters, namely, the thermo-elastoplastic compression index, the thermoelastic compression index and the Hvorslev slope. All three parameters have specific physical meanings and can be calibrated by conventional laboratory tests. In addition to the adoption of the double yield surface concept (i.e., the current/reference yield surface) and a novel hardening parameter (H), the other key features of the proposed model include: (1) Strength increase due to heating and overconsolidation is explained in the same framework (i.e., density increase under an unchanged effective mean stress). The critical state stress ratio increases with an increase in the temperature. (2) Both the current yield surface and reference yield surface are extended to p - q - T space. The effects of both the stress history and the thermal history in isotropic and non-isotropic conditions can be considered.

More details about this model can be found in Y. P. Yao & A. N. Zhou (2013) "Non-isothermal UH model: A thermo-elastoplastic model for clays", which has been accepted (Article Number **13-P-035R2**) and will be published on *Geotechnique*.

ACKNOWLEDGEMENT

This study was financially supported by the Discovery Early Career Research Award (DECRA) from the Australian Research Council (Project No.: DE130101342).

REFERENCES

- [1] Gens, A. and S. Olivella, *Clay barrier in radioactive waste disposal*. Revue Française de Génie Civil, 2001. **5**(6): p. 845-856.
- [2] Mitchell, J.K., et al., *Thermal backfill materials*, in *In Underground cable thermal backfill*, S.A. Boggs, Editor. 1982, Pergamon Press: New York. p. 19-33.
- [3] Campanella, R.G. and J.K. Mitchell, *Influence of temperature variation on soil behaviour*. Journal of Soil Mechanics & Foundations Division, ASCE, 1968. **94**: p. 709-734.
- [4] Cekerevac, C. and L. Laloui, *Experimental study of thermal effects on the mechanical behaviour of a clay*. International Journal for Numerical and Analytical Methods in Geomechanics, 2004. **28**(3): p. 209-228.
- [5] Hueckel, T. and G. Baldi, *Thermoplasticity of Saturated Clays: Experimental Constitutive Study*. Journal of Geotechnical and Geoenvironmental Engineering, ASCE, 1990. **116**(12): p. 1778-1796.
- [6] Sultan, N., P. Delage, and Y.J. Cui, *Temperature effects on the volume change behaviour of Boom clay*. Engineering Geology, 2002. **64**(2-3): p. 135-145.
- [7] Kuntiwattanakul, P., et al., *Temperature effects on undrained shear characteristics of clay*. Soils and Foundations, 1995. **35**(1): p. 147-162.
- [8] Cui, Y.J., N. Sultan, and P. Delage, *A thermomechanical model for saturated clays*. Canadian Geotechnical Journal, 2000. **37**(3): p. 607-620.
- [9] Graham, J., et al., *Modified Cam-Clay modelling of temperature effects in clays*. Canadian Geotechnical Journal, 2001. **38**(3): p. 608-621.
- [10] Hueckel, T., B. Francois, and L. Laloui, *Explaining thermal failure in saturated clays*. Geotechnique, 2009. **59**(3): p. 197-212.
- [11] Hueckel, T. and M. Borsetto, *Thermoplasticity of Saturated Soils and Shales: Constitutive Equations*. Journal of Geotechnical and Geoenvironmental Engineering, ASCE, 1990. **116**(12): p. 1765-1777.
- [12] Laloui, L. and B. Francois, *ACMEG-T: Soil Thermoplasticity Model*. Journal of Engineering Mechanics, 2009. **135**(9): p. 932-944.
- [13] Yao, Y.P., W. Hou, and A.N. Zhou, *UH model: three-dimensional unified hardening model for overconsolidated clays*. Geotechnique, 2009. **59**(5): p. 451-469.
- [14] Asaoka, A., M. Nakano, and T. Noda, *Superloading Yield surface concept for highly structured soil behaviour*. Soils and Foundations, 2000. **40**(2): p. 99-110.
- [15] Mita, K.A., G.R. Dasari, and K.W. Lo, *Performance of a Three-Dimensional Hvorslev-Modified Cam Clay Model for Overconsolidated Clay*. International Journal of Geomechanics, ASCE, 2004. **4**(4): p. 296-309.
- [16] Baldi, G., et al., *Developments in modelling of thermo-hydro-mechanical behaviour of Boom clay and clay-based buffer materials (Vols1 and 2, EUR13365/1 and 13365/2)*, 1991, Commission of European Communities: Luxembourg.
- [17] Towhata, I., et al., *Volume change of clays induced by heating as observed in consolidation tests*. Soils and Foundations, 1993. **33**(4): p. 170-183.

STABILITY OF A ROCK SLOPE SUSCEPTIBLE TO SEASONAL MOVEMENTS

A. K. Alzo'ubi¹

¹CECS, Abu Dhabi University, UAE

ABSTRACT

A rock slope, known as the Checkerboard Creek slope located in British Columbia, Canada, is moving under the effect of seasonal temperature changes. Freezing and thawing processes are causing the rock to move at rate of 13 mm/year. A 60 m deep weathered zone has been identified along the slope. This paper discusses the Checkerboard Creek slope, which is moving toward the reservoir, to propose a support system to stabilize the slope.

The numerical simulation conducted in this study shows that the failure is situated near the slope's toe where a road-cut has been made. To stabilize the rock slope, a support system comprising of cables and a shotcrete layer was proposed and installed along the steepest portion of the weathered rock area. Comparison studies showed that the proposed support system could successfully stabilize the moving rock slope at a reduced tensile strength value. By using this support system, the risk of rock slope failure will be reduced to an acceptable limit through increasing the Factor of Safety of the slope to 1.15.

Keywords: Support System, Rock, Slopes, and Stability.

INTRODUCTION

The Checkerboard Creek slope is located at the Revelstoke hydroelectric dam, British Columbia (BC), Canada (Fig. 1). A series of active and old tension cracks were discovered up to 150 m above the highway rock cut immediately after the end of construction of the dam. This finding prompted an intensive geotechnical and geological program carried out by BC Hydro to examine the moving slope, define the moving volume, and monitor the slope to guarantee the safety of the Dam.



Fig. 1 The general location of the Revelstoke Dam

In 1984, BC Hydro began an investigation of the moving slope under question. The thorough investigation was conducted to determine the

possibility of any instability in the slope [1]. The slope was moving toward the reservoir at a rate of 10-13 mm/year. This movement is seasonal movement, beginning as the ground surface cools in October and stopping when the ground begins to warm in May. The investigation established that the moving volume is between 2 to 3 million m³ concentrated in a weathered rock mass.

Monitoring of the rock slope from 1984 onward has determined that the slope movement is triggered by the thermal cycle experienced by the slope. This thermal cycle, along with other environmental effects, weathers the rock mass and results in a weathered region along the slope face. Aydin and Basu [2] found that as the tensile strength of the rock material decreased, the material tends to behave with more ductility and the rupture strain increased as a function of the weathering degree.

Martin *et al* [3] found out that although total collapse of the slope is highly unlikely, the rock mass adjacent to the highway is susceptible to failure under the continuous weathering process. This study presents a supporting system consisted of a shotcrete layer and a cable system to stabilize the slope. The strength reduction factor method was used to evaluate the factor of safety of the supported slope, and was found to be greater than 1.

GEOLOGY AND CLIMATE

The geotechnical and geological settings of the site was discussed by [4], [5], and [6]. The rock mass is composed of igneous rocks, mainly foliated Granodiorite overlying the easterly dipping

Columbia River Fault. Steeply dipping joints and shears were identified. These joints and shears dip in and out of the slope at 60° - 90° from the horizontal. Toppling driven by shearing along these discontinuities at the slope is kinematically possible.

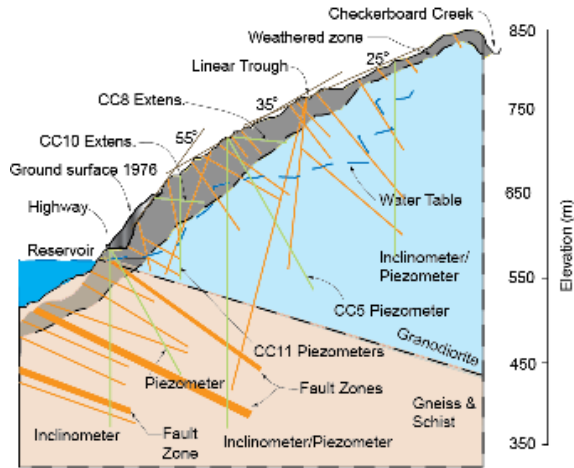


Fig. 2 Cross-section along the Checkerboard Rock Slope (modified from Watson et al, 2006)

A weathered layer exists within the top 60 m of the slope. This layer is composed of poor-quality rocks: highly weathered, weak, altered and disturbed rock with crushed zones and frequent shears. The movement of the slope is concentrated in this weathered region. Underneath this weathered layer, a more competent layer was found of fair-to-good-quality rock. Localized zones of poor-quality rock were found along the shear zones and joints. Figure 2 shows a cross-section through the slope. The weathering of the rock slope was extensive within the first 60 m from the ground surface (Fig. 3).



Fig. 3 Surface weathering of the slope adjacent to the highway cut

Between 1984 and 2000, slope instrumentation was installed in the slope area to monitor the displacement, pore water pressure, and the

temperature change. For the details of the instrumentation and its distribution in the boreholes see [7]. Readings from the instruments were later processed and showed strong relations between the variation in the temperature and the movement of the slope.

Monitoring revealed that the slope is moving in a cyclic mode at a rate between 0.5 to 13 mm/year. The cyclic nature of the displacement was found to be associated with the seasonal temperature. Martin *et al* [3] shows the displacement pattern along with the temperature and water level variation in the slope. The slope movement resumes during the cold weather between early autumn and late winter.

The average air temperature ranges from -25°C to 35°C . Freezing occurs between November and March. Continuous readings were taken from the piezometers installed in the slope; the readings showed that the saturated conditions exist 50 m to 80 m below the ground surface. See Fig. 2 for the interpreted water table location. The water table was incorporated into the numerical model.

THE NUMERICAL MODEL

The discrete element method has been long recognized for its ability to model rock mass behavior in underground and near-surface rock applications. This method can simulate explicitly discontinuities inside the rock mass.

UDEC [8] was originally not designed for isolated joints or for joints terminating in intact rock. However, Lorig and Cundall [9] described the implementation of the voronoi joint option in UDEC for modeling reinforced concrete beams. The introduction of the voronoi joint provided a means for simulating joints that were discontinuous and terminated in heterogeneous intact rock. The voronoi tessellation generator can be used to create randomly sized polygonal blocks between continuous joints [10]. The randomly sized polygons can be considered analogous to flaws in the intact rock.



Fig. 4 Rock mass exposure showing the blocky

nature of the rock mass.

Figure 4 shows the blocky nature of the rock mass that forms the rock slope. As shown in the figure, the rock slope is highly heterogeneous with randomly shaped blocks. This justifies the use of the mosaic block tessellation to generate polygonal blocks in two dimensions that can simulate the rock slope behavior realistically.

A network of flaws was generated numerically inside the rock mass. These flaws have an average length of 1.3 m, formed random polygonal blocks. All the discontinuities and the geological units were included in the simulation along with the weathered region. Figure 5 shows the UDEC-DM used in this paper and fig. 6 shows the details of the UDEC-DM in the area of concern.

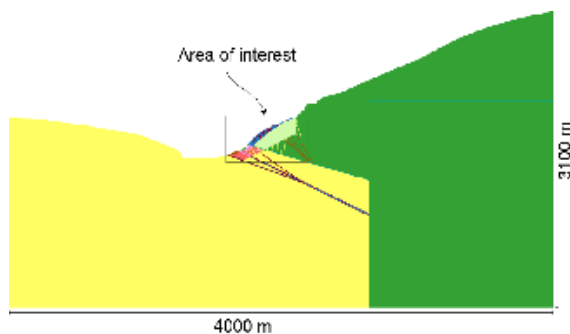


Fig.5 The numerical model of the Checkerboard rock slope.

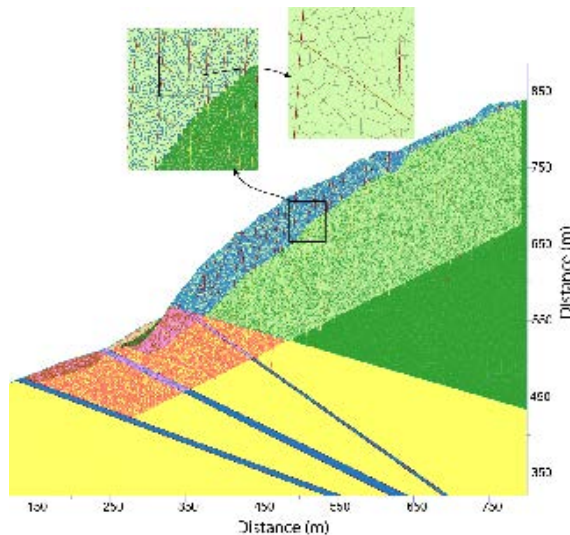


Fig.6 The details of the joints and flaws generated by using UDEC-DM.

The Hoek-Brown failure criterion [11] was used to determine the rock mass cohesion, friction and tensile strength. The discontinuities' properties were taken from [7]. Table 1 shows the material and Voronoi microstructure properties used in this numerical study. The normal stiffness of the flaws and the shear stiffness were assumed to be equal and

then varied to investigate their effect on the slope. The shear stiffness was varied between 1/10 and 4/10 of the normal stiffness. This range was found to have insignificant effects on the displacements from the numerical model measured at the slope surface.

FAILURE PROCESS AND LOCATION

The progressive failure of geo-materials is a gradual and time-dependent failure process at localized areas, followed by the redistribution of the stresses in the slope. These new stresses build up and cause the propagation of the failure. If this fracturing continues, a rupture surface connecting all the failed parts will form. Many factors can cause progressive failure, such as the time-dependent degradation of the strength parameters, increasing pore pressures, and/or thermal stresses. In addition, the presence of non-persistent joints and heterogeneity of the rock mass might cause tensile stresses inside the rock mass and also the initiation and propagation of cracks that might lead to failure.

To study the effect of weathering on the Checkerboard Creek slope, the cohesion and friction of each geological unit was estimated using the Hoek-Brown criterion [11] and the GSI index for each rock formation. The GSI index used in this study was adapted from [7] (see Table 1). Martin *et al* [3] showed that failure will be concentrated near the road cut and tensile strength degradation might cause this failure. Although failure occurred, it was limited to the steepest part of the slope (Fig. 7). As a result of the analysis the region that is prone to movement might be stabilized.

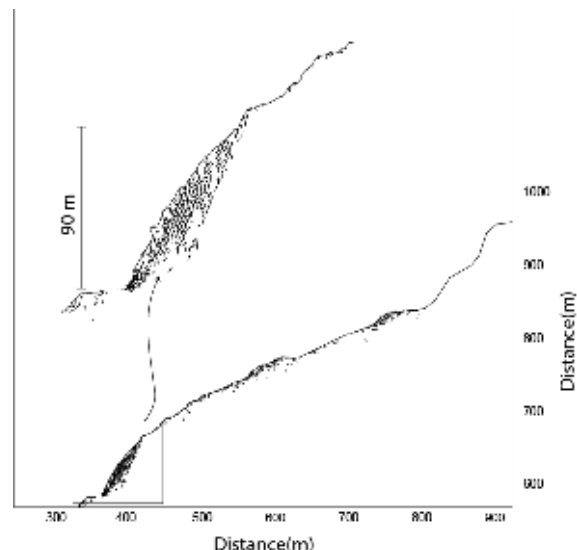
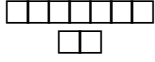
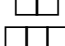
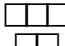
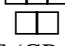
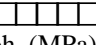


Fig.7 Failure at the rock slope, notice the concentration of the moving rock mass.

Table 1: Properties of the rock mass and the voronoi microstructure used in the UDEC-DM analyses

	Gneiss & Mica Schist		Granodiorite		Columbia River Fault & Shears
	Fresh	Weathered	Fresh	Weathered	
	78	76	133	75	
					
	45	35	60	35	
	26	20	29	26	
E (GPa)	6.5	3.6	17.7	3.6	0.5
ν	0.25	0.27	0.23	0.27	0.3
Voronoi micro-structure					
ϕ 	36	36	48	36	18
Coh. (MPa)	2.4	2.4	5	2.4	0.1
σ_t (MPa)	0.02	0.02	0.22	0.016	0
kn (GPa/m)	18	5	22	6	1.5
ks (GPa/m)	1.8	0.5	2.2	0.6	0.15

It is noteworthy to mention that the tensile strength predicted by [11] ranged between 9 to 20 kPa, while the back-calculated tensile strengths in this analysis range was 25 to 650 kPa depending on the assumed unconfined compressive strength. According to this present study, Hoek-Brown criterion underestimates the tensile strength of rock mass.

Martin *et al* [3] showed the progressive movement of the failed material toward the reservoir as a result of tensile strength degradation. Another attempt was made to simulate the rock slope and to predict the failure mechanism and extent, if any, by assuming the same properties for the entire slope. The flaws in the weathered and un-weathered geological units were assumed to have the same unconfined compressive strength of 60 MPa, and the tensile strength was back calculated.

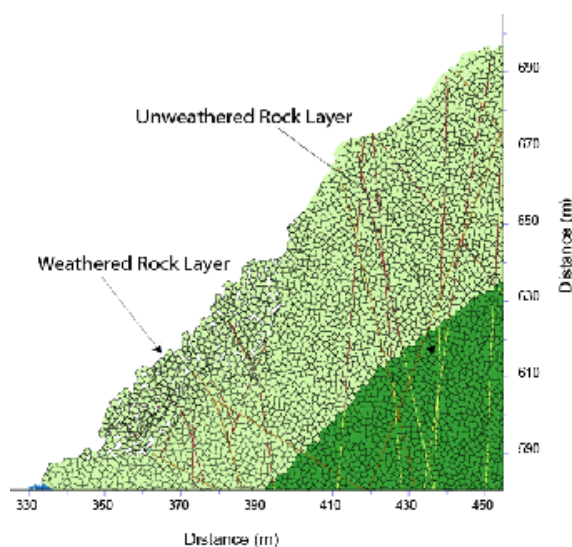


Fig.8 Progressive movement and toppling of the slope toward the reservoir.

Failure was initiated at a tensile strength of 0.2

MPa, which is the same back-calculated tensile strength when the weathered and un-weathered rocks have different properties. The rock mass tends to topple and this toppling was restricted to the steepest slope portion near the highway cut, see Fig. 8.

SUPPORTING SYSTEM

The results of the analysis presented in [3] and in this paper showed that the weathering process might result in failure of the slope near the highway cut. This might lead to retrogressive failure up the slope as a result of steepening of the slope as the failed material moves toward the reservoir. To further investigate this possibility, the moved material at the toe of the slope was excavated. As anticipated, the numerical modeling showed that the previously stable part of the slope started to move toward the reservoir. The newly formed surface resulting from the excavation was a 60° slope, which is very close to the original slope surface prior to movement.

To avoid the consequences of this scenario or any retrogressive failure, a support system composed of a shotcrete layer and a cable system was designed and tested numerically. Passive anchors were used to stabilize the Marble Shear Block slope, which is another slide at the Revelstoke Dam project [12] and the block was successfully stabilized.

In this paper, a cable system was installed inside the weathered rock region and back into the stable rock mass, as shown in Fig. 9. Many configurations of the cables and the shotcrete layer have been modeled numerically to optimize the supporting system. Table 2 shows the properties of the shotcrete layer and the cables.

The best results were achieved when the cables were spaced at an average of 8 m apart, and 10 cm of shotcrete layer was applied at the surface, as shown in Fig. 9. Based on the analysis conducted,

the weathered rock mass was assumed to have weak properties: UCS of 30 MPa and tensile strength of 0.8 MPa to put the slope under marginally stable condition. The tensile strength was then decreased gradually to 0.5 MPa with no significant movement observed. The velocity, displacement and unbalanced forces in the numerical model were watched. According to the numerical analysis of unsupported slope, the model would fail at 0.5 MPa of tensile strength. However, no excessive movement was detected in the numerical model.

Table 2 Support System properties

Property	Shotcrete	Cable
Area (mm ²)		625
Thickness (mm)	100	
E (GPa)	20	98
σ_t at yield	3 MPa	0.55 MN
σ_t (MPa)	30	10 ³
Coh (MPa)	2.0	
Tensile bond (MPa)	1.0	
Grout k_s (GN/m/m)		6
Grout τ (MN/m)		0.32

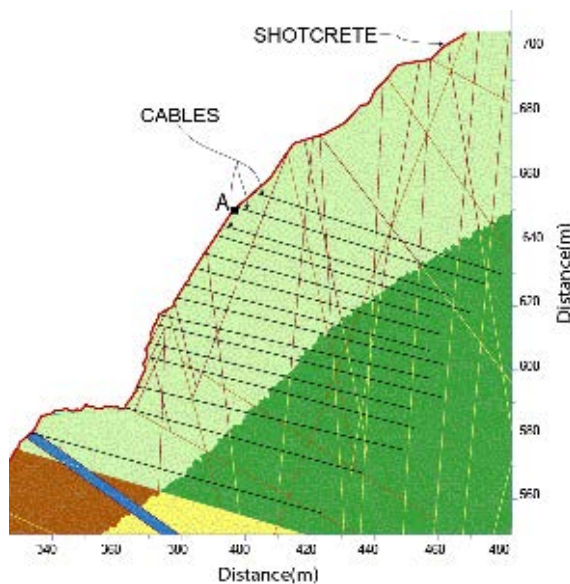


Fig.9 Suggested support system contains of 10 cm shotcrete layer and cables at an average distance of 8 m.

Using the same strength properties for the intact material and the Voronoi micro-structure, two models were examined. The first model was with no support, while the other model was with a support system. The results were compared. As observed, the suggested support system was able to limit the displacement and stabilize the rock slope. Figure 10 shows the effect of a support system on the displacement pattern of the slope.

The Figure shows a comparison between the two

models. As shown in the Figure, the support system was able to limit the displacements in the model, while the unsupported model continued to deform. To further investigate the model, the tensile strength of the supported rock mass prone to movement was reduced to 0.2 and 0.02 MPa, respectively. The results were similar to those obtained from the previous models. Supporting the rock slope stabilized the movement, no excessive fracturing or failure propagation was observed, and such fracturing as was observed was very minimal.

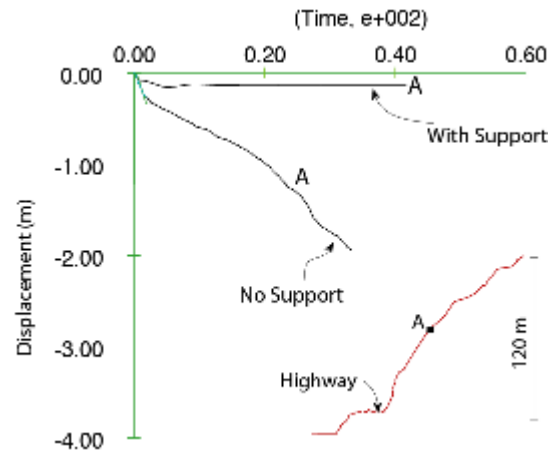


Fig.10 Effect of supporting system on the displacement of surface point A (in the insert).

The cable-shotcrete system proposed and modeled in this paper would hinder the cyclic movement observed at the Checkerboard rock slope. The question remains if this system would perform on site in the same way as in the numerical model. The only way to know is to install the system and monitor the actual performance in the field.

FACTOR OF SAFETY

The strength reduction factor was used to evaluate the traditional factor of safety. The proposed support system showed significant improvement on the displacement pattern as shown on the previous section. The factor of safety of the supported slope was 1.15. As the spacing between the cables was reduced to an average of 6 m, the factor of safety increased to 1.22. The reduction of the distance between successive cables improved the stability of the slope as concluded from the numerical simulation. Although this Factor of Safety is relatively low, it is acceptable as long as the slope is being monitored.

CONCLUSION

The discrete element damage approach was

applied to simulate the Checkerboard Creek rock slope movement and a supporting system. The weathering process at the slope site caused the rock mass properties to degrade. The rock slope undergoes a seasonal movement that might jeopardize the dam's safety. According to the numerical analysis, the failure is concentrated at the slope toe near the road cut at the steepest part of the slope.

To avoid the possibility of retrogressive failure, a support system consisting of 10 cm shotcrete and cables spaced at 8 m, was used successfully to stabilize the rock slope movement toward the reservoir at a reduced tensile strength value.

This hybrid numerical modeling approach (UDE-DM) adapted in this study was used successfully to model this complex rock slope supporting system and showed high potential of success. The strength reduction factor techniques showed that the factor of safety of the supported slope is 1.2. This Factor of Safety is acceptable in such rock slopes, as long as the rock slope remains under close monitoring to avoid sudden failure of the rock slope.

ACKNOWLEDGEMENTS

I would like to acknowledge the financial contribution of the Railway Ground Hazard Research Program sponsored by CP Rail, CN and transport Canada, and the Natural Sciences and Engineering Research Council of Canada. I would like also to extend my thanks to Dr. C. D. Martin for his contribution during the initial stages of this research.

REFERENCES

- [1] Watson A, Moore D, Stewart T "Temperature influence on rock slope movements at Checkerboard Creek", in Proc. International Symposium on Landslides, Evaluation and Stabilization, Lacerda, Ehrlich, Fotoura, Sayao (eds) Rotterdam, Balkema, Rio de Janeiro, Vol 2, 2004, pp. 1293-1304.
- [2] Aydin A, Basu A "The use of Brazilian test as a quantitative measure of rock weathering", Rock Mechanics and Rock Engineering, Vol. 39(1), 2006, pp. 77-85.
- [3] Martin C.D, Alzo'ubi A.K., Cruden D.M. "Progressive failure mechanisms in a slope prone to toppling", in Proc. International Symposium on Rock Slope Stability in Open Pit Mining and Civil Engineering, Vancouver, Canada, 1st ed., Vol. 1, 2011, pp. 12.
- [4] Lane L., "Brittle deformation in the columbia river fault zone near Revelstoke, southeastern British Columbia, Canada", Canadian Journal of Earth Sciences, Vol. 21, 1984, pp.584-598
- [5] Moore D, Imrie A, Enegren E "Evaluation and management of Revelstoke dam reservoir slopes", in Proc. The 19th ICOLD Congress, Florence, Italy, Vol 3, 1997, pp. 1-22.
- [6] Moore DP, Lewis MR "Rock slope reinforcement with passive anchors", in Proc. 23rd United States Symposium on Rock Mechanics, University of California, Berkeley, CA, 1982, pp. 945-952.
- [7] Watson A, Martin C, Moore D, Thomas W, Lorig J., "Integration of geology, monitoring and modelling to assess rockslide risk", Rock and Soil Engineering, Felsbau Vol. 3, 2006, pp. 50-58.
- [8] Itasca "Udec-Universal Distinct Element Code", Version 4.0. Itasca Consulting Group, Inc., Minneapolis. 2004.
- [9] Lorig LJ, Cundall PA " Modeling of reinforced concrete using the Distinct Element Method", in Proc. Fracture of Concrete and Rock, SEM-RILEM international Conference, Shah SB, Swartz SE (eds), Springer-Verlag, New York Inc., Houston, Texas, USA, 1987, pp. 276-287.
- [10] Alzo'ubi, A.K., C.D. Martin, and D. M. Cruden. "Influence of tensile strength on toppling failure in centrifuge tests", International Journal of Rock Mechanics and Mining Sciences Vol. 47(1), 2010, pp. 974-982.
- [11] Hoek E, Carranza-Torres C, Corkum B "Hoek-Brown failure criterion-2002 edition", in Proc. The 5th North American Rock Mechanics Symp, Toronto, Canada, Vol. 1, 2002, pp. 267-273.
- [12] Martin CD, Kaiser PK "Analysis of rock slopes with internal dilatation", Canadian Geotechnical Journal, Vol. 21(4), 1984, pp. 605-624.

REAL-TIME BRIDGE SCOUR MONITORING SYSTEM BY USING CAPACITOR SENSOR

S. M. A. Motakabber, M. I. Ibrahimy and A. H. M. Zahirul Alam
Faculty of Engineering, International Islamic University Malaysia, Kuala Lumpur, Malaysia

ABSTRACT

Scour is the erosion of stream bed or bank material from bridge foundations due to flowing of water. Data logging from sensor and electronic communication systems can monitor scour in real-time to ensure the integrity of bridge structure. A number of parameters are associated with scour, thus different types of sensor are required to measure the individual affecting factor. A simple capacitive type direct scour sensor system is proposed and validated by simulation. The result shows that any change of the river bed dielectric property is a direct indication of scour. Due to simple capacitive structure of the sensor system, it is highly robust and easy to implement. The system can easily be implemented with an existing bridge structure. A wireless telemetry system can be used to send the real-time data from the proposed sensor to a desktop computer at the monitoring lab.

Keywords: Scour, Bridge Monitoring, River Bed Erosion, Capacitor Sensor

INTRODUCTION

Bridge scour is the meaning of removal of soil, sand and rocks from around a bridge supports or piers as shown in Fig. 1. Rapidly moving water can wash out the river bed materials and make scour holes, compromise the existence of a bridge structure [1]. Scour happens under the water and it is hard to see by naked eye. As a result, every year a number of bridges are collapsed all over the world which causes a lot of financial and life losses. The three main reasons of bridge failure are collision, overloading and scour. It has been estimated that 60% of all bridge failures is happened due to scour and other hydraulic-related causes [2]. Scour is a complex natural occurrence and a number of parameters are associated with it. Hence to predict the bridge failures and real time scour monitoring, different types of sensor are required to measure the individual affecting factor [3], [4]. Among them sonar altimeter can be used to measure the distance between sensor and river bottom [5]. A change in distance-to-bottom is an indication of scour. Non-contact radar water level sensor can be used to measure the water level across a wide temperature range and varying water surface conditions [6]. Ultrasonic water velocity sensor and side-looking acoustic Doppler current meter can be used to measure bidirectional velocity of the water. The sensors read all the parameters including scouring, water levels and water flow velocity. These sensors reading is transferred to a computer through wire or wireless communication systems. The reading is programmed to give an early warning to the monitor. These sensors are generally selected and arranged based on local weather conditions, climate change

effect, natural hazards and environmental conditions. Most of these type sensors are complex and very expensive. The dielectric property of different materials such as pure water is 80, dry soil is 5-8 and mud is 30-65. This dielectric property can be used to measure the scour.

A bridge scouring real-time monitoring system [7] can provide a comprehensive, instant and functional monitoring platform to monitor the safety of the bridge. It will reduce the costs of physical monitoring and bridge maintenance. Mobile



Fig.1 Bridge scour [1]

communications can be used to transmit relevant information to bridge maintenance and management units and users when a bridge would be potentially damaged by manmade or natural disasters. The instant conveying of information will allow the bridge management unit to implement instant disaster rescue measures and to notify users to avoid dangerous situation that can protect people's lives and properties.

DEVELOPMENT OF CAPACITOR SENSORS

Design and development of capacitor sensors for measuring the parameters, which are related with the bridge scouring, is a challenging issue. 4 to 6 pairs of separate water-resist metal flat bar electrodes surroundings each of the bridge piers can be used to measure the scour. The electrodes are piled vertically under the river bed and each pair of electrode act as a parallel plate capacitor as shown in Fig. 2. Since the dielectric constant of the water is higher than the dielectric constant of the soil and mud, any amount of soil when washout between the electrodes, increases the capacitance. By measuring the capacitance of individual pair of electrode can give a direct measurement of scouring.

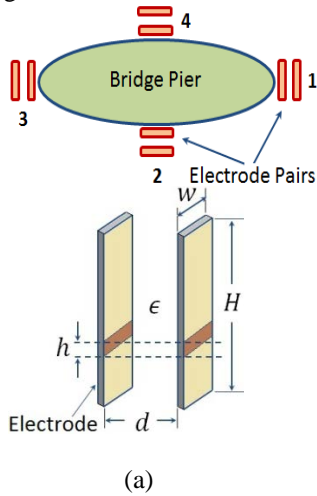


Fig.2 (a) Cross sectional top view of bridge pier and electrodes arrangement, (b) Enlarge view of a single electrode pair

If the dielectric constant ϵ between each electrode pair is considered as constant then the total capacitance of electrode pair can be represented as:

$$C_T = \frac{\epsilon w H}{d} \quad (1)$$

When any scour hole is occurred surrounding the bridge pier, the dielectric constant all over the space between the electrode pair is no longer remained constant. If the electrode pair is divided into n numbers of vertical strips and the dielectric constant between each of the small h strip is considered as a constant then the total capacitance of each electrode pair can be calculated as follows:

$$C_T = \frac{\epsilon_1 w h_1}{d} + \frac{\epsilon_2 w h_2}{d} + \dots + \frac{\epsilon_n w h_n}{d} \quad (2)$$

$$\text{or, } C_T = \frac{w}{d} \sum_{i=1}^n \epsilon_i h_i \quad (3)$$

Here, $H = h_1 + h_2 + \dots + h_n$ and $\epsilon_1, \epsilon_2, \dots, \epsilon_n$ are the dielectric constant of each segments respectively.

The change of dielectric constant at any segment is the result of change of total capacitance of the electrodes. In normal situation the electrode capacitance will be remained constant over a long period of time. An AC Wien bridge oscillator circuit (Fig. 3) can be used to measure the electrodes capacitance change. The frequency of oscillation of the Wien bridge oscillator is determined by Eq. (4).

$$f = \frac{1}{2\pi\sqrt{R_3 R_4 C_{REF} C_{ELECT}}} \quad (4)$$

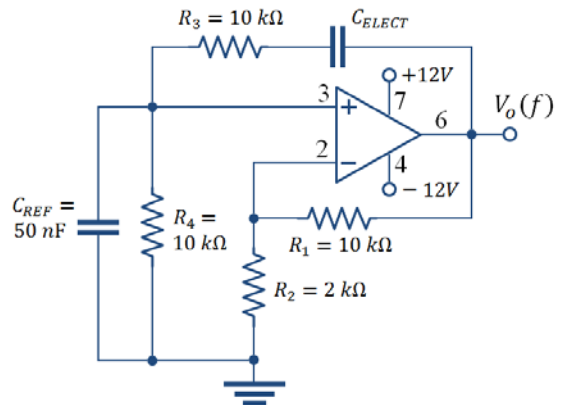


Fig. 3 A basic Wien bridge oscillator circuit

For a particular circuit, the values of resistors R_3 , R_4 and the reference capacitor C_{REF} are generally kept constant. Therefore, the Wien bridge oscillator circuit's frequency is inversely proportional to the square root of the electrode capacitance and the relation can be represented by Eq. (5)

$$f \propto \frac{1}{\sqrt{C_{ELECT}}} \quad (5)$$

Eq. (5) indicates the frequency becomes low when the electrode's capacitance C_{ELECT} increases and it can be happened if there is a scouring. The important thing is that in this case, no need to measure the absolute value of the electrode's capacitance; it can directly show that the change of frequency means there is a scouring.

RESULT AND DISCUSSION

A PSPICE simulation is studied for the proposed bridge scour monitoring system and the result is shown in Fig. 4.

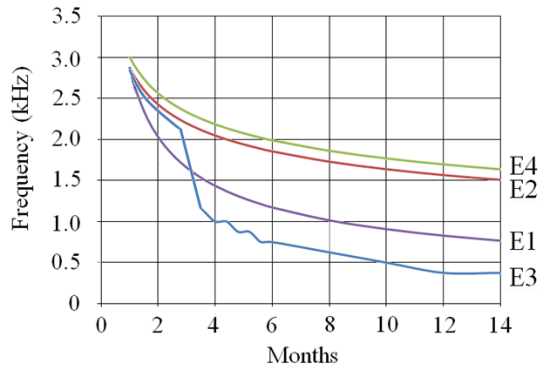


Fig. 4 Variation of frequency with change of electrode capacitance

In this simulation, it is considered that the river water stream direction is from electrode 1 to electrode 3 (Fig. 1). From Fig. 4, it is found that there is a slow scouring effect at the beginning, but near about third month, there is an abrupt change of frequency (low frequency) observed related with the electrode number 3. It means a huge scour is suddenly occurred at this bridge pier.

CONCLUSION

A capacitor type sensor with an oscillator can be used for bridge scour monitoring system. The change of frequency of the oscillator is a direct indication of the scour and it does not need to measure the exact value of sensor capacitor. This

principle may help to develop a simple and low cost real-time bridge scour monitoring system.

REFERENCES

- [1] Warren LP, "Scour at Bridges: Stream Stability and Scour Assessment at Bridges in Massachusetts", US Geological Survey, 2011.
- [2] Parker G, Toro-Escobar CM and Voigt RL, "Countermeasures to protect bridge piers from scour", Vol. 1 (p. 27) and Vol. 2 (p. 360), 1998.
- [3] Glaser SD, Li H, Wang ML, Ou J and Lynch T, "Sensor technology innovation for the advancement of structural health monitoring: a strategic program of US-China research for the next decade", Smart Structure and System, Vol. 3, No.2, 2007, pp. 221-244.
- [4] Lin YB, Lai JS, Chang KC, Chang WY, Lee FZ and Ten YC, "Using MEMS sensors in the bridge monitoring system", Journal of the Chinese Institute of Engineering, Vol. 33, No.1, 2010, pp. 25-35.

SKIN FRICTION TESTS ON MODEL PILE IN WET SOIL

Mohamed M. Shahin
Faculty of Engineering, Misurata University, Libya

ABSTRACT

The shaft resistance of smooth and rough model pile in wet sand, silt and clay under static loading is investigated experimentally in a pile-soil skin friction test apparatus. This apparatus allows independent control of the boundary stresses of a cylindrical soil specimen in the vertical and horizontal directions. The pile installation technique used was designed to minimize soil disturbance so that the failure criterion for pile shaft friction could be investigated. The load transfer along the shafts of smooth and rough surfaces aluminum model piles in wet soil under static load was measured. The study shows that, the magnitude of pile-displacement at failure, which necessary to mobilize the ultimate shaft resistance varies significantly with the soil type and surface roughness of the pile. The study also, shows the importance of the boundary conditions of the soil specimen surrounding the model pile. The results shows the effectiveness of using rough pile in increasing the pile capacity. Also, The results show that the angle of the pile-soil contact depends on the soil type, roughness of the pile surface, void ratio, initial density, and horizontal confining pressure.

Keywords: shaft resistance, model pile, static load, initial density.

INTRODUCTION

The computed values of shaft resistance for all the tests are plotted as a function of the horizontal confining pressure. The relationship is basically a linear one which can be expressed as:

$$f_s = \sigma_h \tan(\delta) = k \sigma_v \tan(\delta)$$

where σ_h is the effective normal stress acting around the pile shaft at failure, δ is the angle of friction between the pile and the soil, k is the coefficient of lateral earth pressure and σ_v is the effective vertical stress around the pile shaft. In this paper the skin friction of smooth and rough model piles under static loading in wet sand, silt and clay is investigated by skin friction tests on model pile.

The influence of the important mechanical parameters is investigated to simulate shear resistance along the pile shaft in different soil densities, For every kind of soil, six tests were carried out on smooth model pile and six tests on rough model pile which were tested in Triaxial apparatus model pile tests as shown in fig, (1).

The test apparatus allows the control of horizontal and vertical pressures on a cylindrical specimen of soil with a circular model pile erected in it. The axial load on the model pile was measured by means of a load cell seated on top of the model pile, while the axial displacement was measured using a dial gage.

EXPERIMENTAL PROGRAM

The specimen can be restrained to generate a condition approximately at rest. The bottom surface of the specimen is supported on a rigid base. The physical properties of the soil testing are shown in

table (1), the specific gravity are 2.65 for sand, 2.70 for silt and 2.80 for clay.

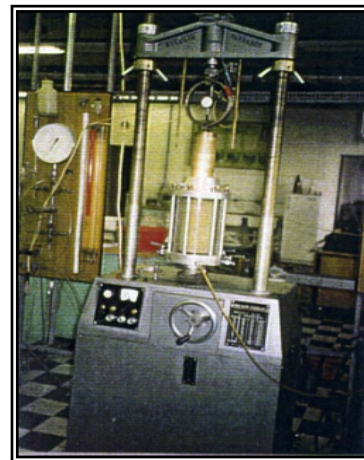


Fig. 1 Test apparatus

A number of static loading tests were performed at a constant rate of displacement to determine the load capacity of an aluminum model pile (200) mm in length and (26.5) mm in diameter for smooth surface and (27.5) mm for rough surface.

Two types of boundary stress and displacement conditions were imposed on the soil element in this study as shown in tables (2) and (3). The successive tests were achieved by increasing the vertical pressure while preventing the lateral deformation of the soil element before and during the load test, where, the specimen was not allowed to expand horizontally.

TEST PROGRAM

The soil specimen, (100) mm in diameter and (200) mm in height, were prepared by pouring the wet soil around the pile into a thin acrylic cylinder which was holding a rubber membrane (100) mm in diameter and (3.0) mm in thickness.

The wet soil was deposited in 5 layers and each layer was tamped by a tamper to achieve a relative density of approximately (28 and 72) % for loose and dense wet sand respectively and (47 and 68) % for loose and dense wet silt respectively in all specimens. After preparing the specimen and before applying any confining pressure, the acrylic cylinder was removed, then lateral confining pressure was applied on the rubber membrane encasing the specimen and the vertical pressure was applied on the top of the soil specimen and the test carried out upon constant volume.

After preparing each specimen the pile was subjected to a static axial load at a constant rate of displacement. The axial load was applied through a downward movement of the pile relative to the fixed soil element at a constant rate of displacement of (0.5) mm per minute. Table (1) shows the physical properties of the sand.

Table 1 Physical properties of soil

Condition of soil	Dry density [gm/cm ³]	Relative density Dr %	Water content %
Loose wet sand	1.45	28	5
Dense wet sand	1.67	72	5
Loose wet silt	1.43	47	10
Dense wet silt	1.80	68	10
Loose wet clay	1.33	---	10
Dense wet clay	1.68	---	10

TEST RESULTS

Tables (2) and (3) list the results and conditions of the load tests on the smooth and rough model piles respectively

Effect of surface roughness

Surface roughness of the pile has an important effect on the skin friction of the pile. The maximum

shear stress developed by rough surface piles is higher than that developed by smooth surface piles.

Hence, the maximum shear stress means the ultimate shaft capacity P_u , where (end bearing resistance = 0). For loose and dense wet sand, the ultimate shaft capacity of the rough piles is in ranges (1.25) times as much as that of smooth piles as shown in tables (2) and (3) for ($k = 0.35$ and 0.26).

Table 2 Summary of loading tests using smooth piles

Soil condition	Test	σ_h KPa	P_u KPa	P_f (mm)
Loose wet sand	S1	100	344	1.0
	S2	200	677	1.25
	S3	300	1022	1.5
Dense wet sand	S4	100	457	1.0
	S5	200	899	1.0
	S6	300	1354	1.5
Loose wet silt	S7	100	352	3.5
	S8	200	706	3.0
	S9	300	1034	6.0
Dense wet silt	S10	100	398	6.5
	S11	200	808	6.5
	S12	300	1219	6.5
Loose wet clay	S13	100	359	6.5
	S14	200	715	6.5
	S15	300	1057	6.5
Dense wet clay	S16	100	382	6.0
	S17	200	791	6.5
	S18	300	1163	6.5

Figures (2) and (3) shows that the shape of the load-displacement curves for the smooth and rough piles is similar until (1.0–2.0) mm of pile displacement. However, after these points we found that the load-displacement curves are different: in the rough piles the axial load is approximately constant, but in the case of smooth piles a slight reduction in axial load is shown, with the amount depending on the density of sand. The ultimate displacement of the model pile p_i to mobilize the maximum shaft resistance is relatively small and is dependent on surface roughness of the piles as shown in tables (2) and (3).

In the case of smooth piles, P_f ranges from (1 - 1.5) mm, whereas, in the case of rough piles, it ranges between (5.0 – 7.0) mm.

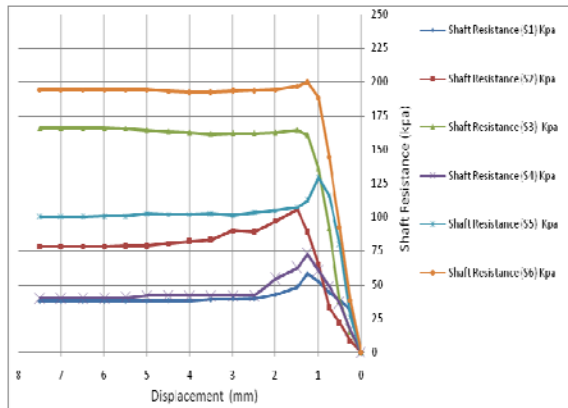


Fig. 2 Typical load-displacement curves for smooth pile surface tests [S1-S6] in wet sand.

Table 3 Summary of loading tests using rough piles

Soil condition	Test	σ_h KPa	P_u KPa	P_f (mm)
Loose wet sand	R1	100	358	6.0
	R2	200	707	6.5
	R3	300	1060	5.5
Dense wet sand	R4	100	462	6.5
	R5	200	914	7.0
	R6	300	1362	7.0
Loose wet silt	R7	100	382	5.0
	R8	200	735	6.0
	R9	300	1087	7.0
Dense wet silt	R10	100	420	6.5
	R11	200	828	7.0
	R12	300	1287	7.0
Loose wet clay	R13	100	400	6.5
	R14	200	814	6.5
	R15	300	1153	6.5
Dense wet clay	R16	100	467	6.0
	R17	200	884	6.5
	R18	300	1280	6.5

The pile displacement at failure values indicate that there is a general trend of increasing pile displacement at failure with increasing lateral confining pressure. The results clearly show that the rough pile requires more displacement to reach failure, which in turn generates more deformation of the soil element.

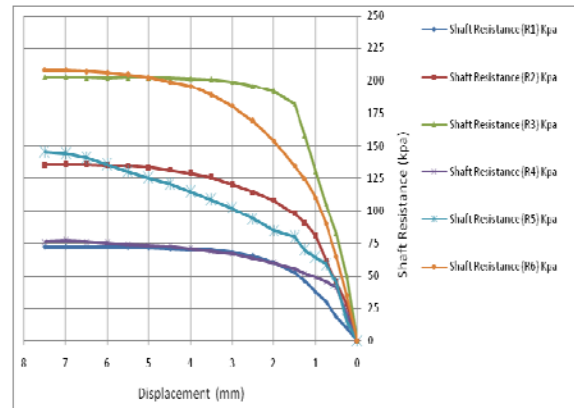


Fig. 3 Typical load-displacement curves for rough pile surface tests [R1-R6] in wet sand.

Tables (2) and (3) shows that, for loose and dense wet silt, the ultimate shaft capacity of the rough piles is equal (1.3) times as much as that of smooth piles for ($k = 0.34$ and 0.28). It should be pointed out that the shape of the load-displacement curves for the smooth and rough piles is similar until (1.5-3.0) mm of pile displacement as shown in figures (4) and (5).

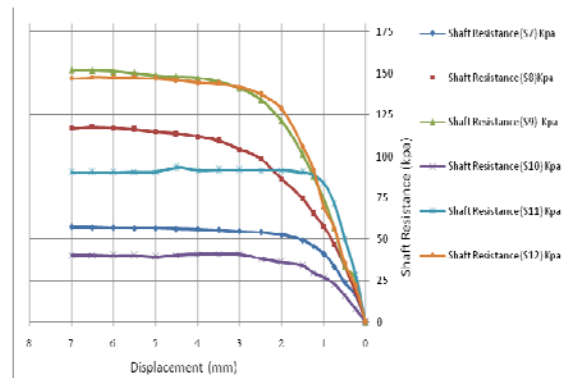


Fig. 4 Typical load-displacement curves for smooth pile surface tests [S7-S12] in wet silt

However, after these points we found that the load-displacement curves are different: in the smooth piles the axial load is approximately constant, but in the case of rough piles a slight increasing in axial load, with the amount depending on the density of silt. The ultimate displacement of the model pile P_f to mobilise the maximum shaft resistance is relatively small and is dependent on surface roughness of the piles as shown in tables (2) and (3).

In two cases of pile surfaces, P_f ranges from (5.0-7.0) mm. The pile displacement at failure values corresponding to the tests on specimens in tables (2) and (3) indicate that there is a general trend of increasing pile displacement at failure with increasing lateral confining pressure.

The results clearly show that the rough pile requires a slight more displacement to reach failure, which in turn generates more deformation of the soil element.

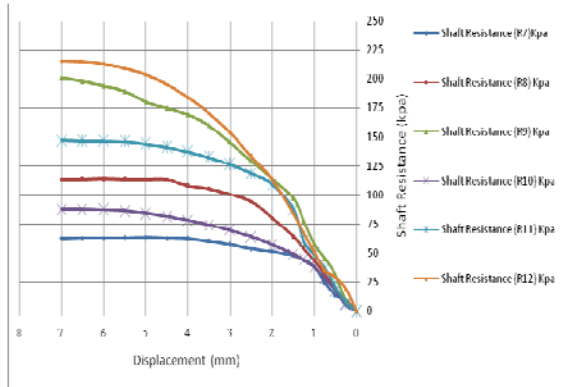


Fig. 5 Typical load-displacement curves for rough pile surface tests [R7-R12] in wet silt

The plastic limit of clay, which used for testing is 20, where we found that the loose and dense wet clay, the ultimate shaft capacity of the rough piles is approximately (1.14) times as much as that of smooth piles as shown in tables (2) and (3) for ($k = 0.32$ and 0.29). From figures (6) and (7) we found that the shape of the load-displacement curves for the smooth and rough piles in wet clay is similar until (1.5–2.5) mm of pile displacement, where, after these points we found that the load-displacement curves are different. In the smooth piles the axial load is approximately constant, but in the case of rough piles a much increasing in axial load, with the amount depending on the density of clay. The ultimate displacement of the model pile p_f to mobilize the maximum shaft resistance is relatively small and is equal (6.0-6.5) mm in two cases of pile surfaces as shown in tables (2) and (3). The pile displacement at failure values corresponding to the tests on specimens in tables (2) and (3) indicate that there is a general trend of equal pile displacement at failure with increasing lateral confining pressure.

The results clearly show that the rough pile requires slight more displacement to reach failure, which in turn generates more deformation of the soil element.

Influence of Lateral Confinement

The shaft capacity P_u of model piles in wet sand, silt and clay increases directly with increasing lateral confining pressure. A similar observation was reported in [1], [3], [4] and [5] for a pile in a sand, kaolinitic clay and silt. From figures (5) and (6) it is observed that the load capacity depends on lateral confining pressure. Furthermore, the rate of increase

of P_u depends on the surface roughness of the piles and it is higher in rough piles than in smooth piles.

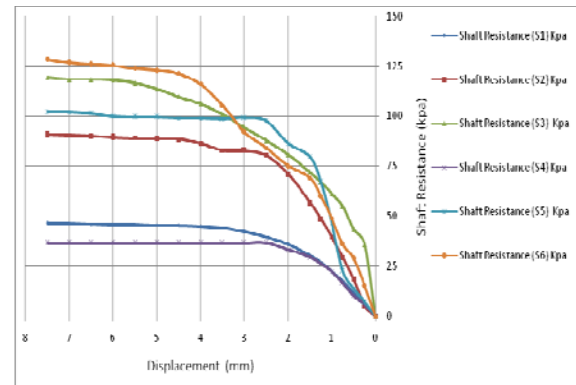


Fig. 6 Typical load-displacement curves for smooth pile surface tests [S13-S18] in wet clay

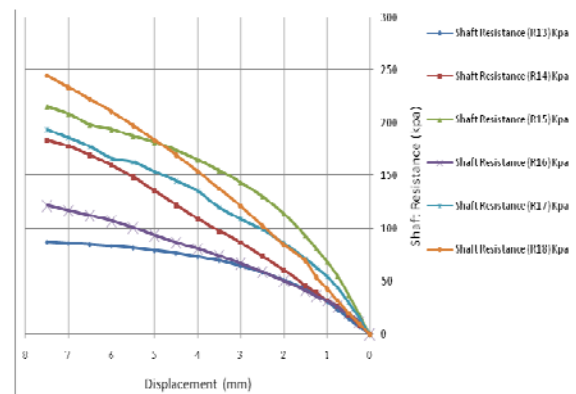


Fig. 7 Typical load-displacement curves for rough pile surface tests [R13-R18] in wet clay

Load-Displacement Response

Typical axial load-pile head displacement curves obtained from the constant rate of displacement tests are shown in figures (2), (3) (4), (5), (6) and (7). The ultimate shaft capacity P_u increases with increasing horizontal pressure applied on the lateral surface of the soil specimen. In case of rough pile model tests in wet sand, the magnitude of the axial load stayed constant after reaching the ultimate displacement P_f , where it showed a very slight reduction of the axial load at displacement larger than P_f in case of smooth pile. This was attributed to the packing of grains of sand. The test results indicated that very little pile displacement is required to reach the maximum axial load and the failure of the friction pile. In two cases of model pile surfaces tests in wet silt and clay, the magnitude of the axial load stayed constant after reaching the ultimate displacement P_f .

The angle of pile-soil friction is seen to be different for each soil specimen tested, depending on the model pile test arrangement (pile diameter,

length of pile-soil contact, and pile surface roughness), the initial density of the soil specimen, the void ratio, relative density and water content.

The value of $(\tan\delta)$ is affected significantly by the surface roughness of the model pile. This is demonstrated by the test results as shown in figures (8), (9) and (10).

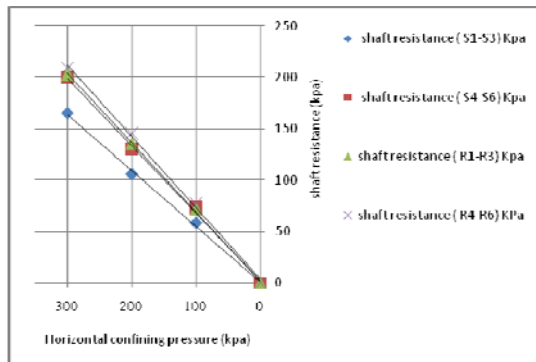


Fig. 8 Shaft resistance versus horizontal confining pressure [S1-S6] and [R1-R6] in wet sand

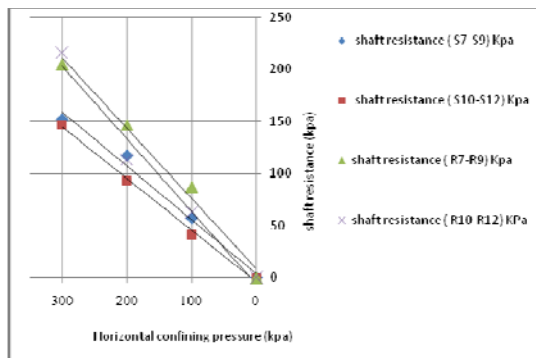


Fig. 9 Shaft resistance versus horizontal confining pressure [S7-S12] and [R7-R12] in wet silt

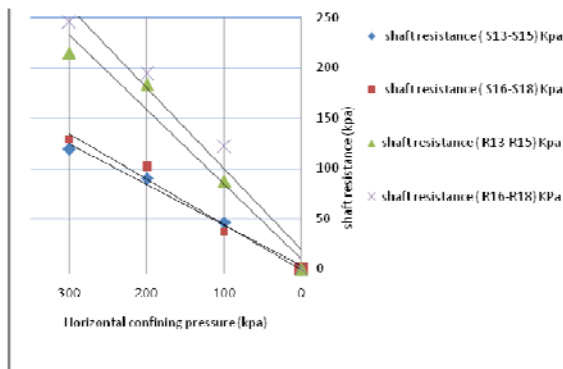


Fig. 10 Shaft resistance versus horizontal confining pressure [S13-S18] and [R13-R18] in wet clay

As seen in figure (11) and table (4) the peak interface friction angle δ_p is affected by the soil type and increasing with increased roughness of the pile and density of the soil. We found that the value of δ_p for sand soil is higher than that for other tested soil, where, for clay soil is the lowest, this attributed to the particle size of the soil.

Table 4 Parameters of the soil

Soil condition	Pile surface	c, kPa	δ_p , deg
Loose wet sand	Smooth	0	28
	Rough	0	33
Dense wet sand	Smooth	0	33
	Rough	0	38
Loose wet silt	Smooth	4	21
	Rough	7	27
Dense wet silt	Smooth	6	26
	Rough	9	32
Loose wet clay	Smooth	9	18
	Rough	13	22
Dense wet clay	Smooth	14	22
	Rough	25	27

SUMMARY

The test apparatus described to measure the load transfer along the smooth and rough shaft surface of an aluminum model pile erected in a specimen of wet soil proved to be a useful tool in studying shaft resistance behaviour. It offers certain features that can be advantageous in analysing the pile-soil interaction.

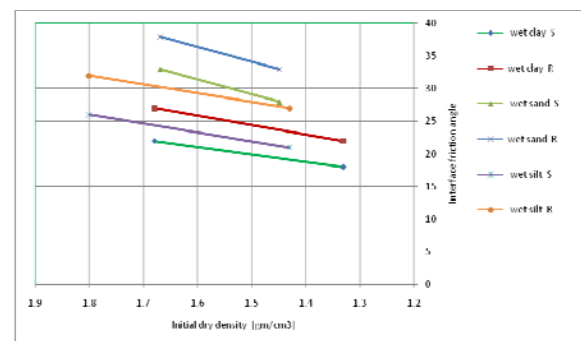


Fig. 11 Relationship between initial compactness and interface friction angle in Triaxial test

The results-based on tests on 18 samples of a wet sand, silt and clay with different initial compactness, show that the angle of pile-soil friction is dependent on the soil type, surface roughness of the piles, the relative density, the void ratio, water content and the stress level.

The magnitude of displacement to mobilise the maximum shaft resistance is relatively small, and is dependent on the soil type, length of the pile-soil contact surface and the surface roughness. The results clearly show that the rough pile requires more displacement to reach failure, which in turn generates more deformation of the soil element.

In summary the test results indicate that the amount of pile displacement to achieve the maximum load and the work done on the soil element increase directly with increasing pile-surface roughness and lateral confining pressure.

CONCLUSION

On the basis of the tests which were done 9-smooth piles and 9-rough piles, the following conclusion can be drawn:

- 1- In this study, the shaft capacity of rough piles is greater-as much as (1.25) than that of similar smooth piles in loose and dense wet sand, where it is equal (1.3) higher than that of similar smooth piles in loose and dense wet silt, but in loose and dense wet clay is higher in rough piles than that of similar smooth piles by 1.15.
- 2- The shaft capacity of pile, P_u increases directly with increasing lateral confining pressure.
- 3- The rate of increase of P_u with confining pressure is much higher in rough piles than in smooth piles
- 4- A small displacement of the pile is sufficient to mobilize the shaft capacity, and varies with surface roughness of the piles and the confining pressure on the soil element surrounding the pile.
- 5- The displacement of failure P_f in wet sand ranges from (1.0-1.5) mm in the case of smooth piles, where, it ranges from (5.5-7) mm in the case of rough piles .

6- The displacement of failure P_f in wet silt ranges from (4-7) mm in the case of loose wet silt for two surfaces of piles, whereas it ranges from (6.5-7) mm in the case of dense wet silt.

7- The displacement of failure P_f in wet clay ranges from (6-6.5) mm for two surfaces of piles.

8- Loading the pile with a vertical load causes downward displacement of the pile, which causes downward deformation of the top surface of the soil element.

9- The value of interface friction angle increases with increasing of initial compactness of the soil, relative density, roughness of pile surface and lateral confining pressure.

REFERENCES

- [1] Edil, T.B. & Abdel Rahman. M A. 1995. Shaft resistance of model pile in granular soil. Deep Foundation on bored and auger piles, BAP 11, Ed. Vane Impe, W.F., A. A. Balkema/ Rotterdam/Brookfield/ pp.279-284.
- [2] Head, K. H. 1986. Manual of soil laboratory testing. volume 3 Effective Stress Tests, ELE Int. Limited. Annnn B, "Unpublished work but accepted", accepted, Year.
- [3] Mochtar, I. B. & Edil, T. B. 1988. shaft resistance of model pile in clay, J.Geotech. Engrg, ASCE, Vol. 114, No..11 November. pp.1227-1242.
- [4] Shahin, M.M .1998. Shaft resistance of model pile in dry sand. proceeding of National Engineering conference 98, Misurata – Libya. pp.43-52
- [5] Shahin M. M. 2006. Shaft resistance of model pile in dry silt. CD of Sixth Asian Pacific Structural Engineering and Construction Conference, Kuala Lumpur - Malaysia, CD E71- E78.

A NEW UPPER BOUND SOLUTION TO QUANTIFY THE ULTIMATE BEARING CAPACITY OF SHALLOW FOUNDATIONS ON RESTRICTED SOIL

Reza Afshar-mazandaran¹, Hadi Khabbaz²

^{1,2} Centre for Built Infrastructure Research, School of Civil and Environmental Engineering, University of Technology Sydney (UTS), Sydney, Australia;

ABSTRACT

One of the controversial issues in geotechnical engineering is the bearing capacity of shallow foundations placed on layered soil when the soil layer is overlying a rigid base; particularly when the soil layer thickness is comparable to or less than the width of the rigid foundation. The effect of the bedrock position and its shear strength properties are often not considered in conventional foundation design. A rigorous bearing capacity solution for a restricted soil layer was introduced by Farzaneh and his co-researchers. In this study the possibility of defining a modified collapse mechanism is investigated and consequently a revised collapse mechanism by extending the original model is presented. The effects of the loading parameters, such as eccentricity and inclination, and the influence of soil-substratum interface roughness on bearing capacity are presented and discussed in detail. In addition, a detailed parametric study is carried out to evaluate the effects of main variables in determining the ultimate bearing capacity of shallow foundations on restricted soil, using the proposed mechanism. Results are finally presented in design charts for practical use in geotechnical engineering.

Keywords: Bearing Capacity, Upper-Bound Limit State Analysis, Rotation-Translation Collapse Mechanism, Rigid Base

INTRODUCTION

The presence of a substratum beneath a restricted soil layer can have significant influence on the bearing capacity of the soil layer. On the other hand the shear strength of soil and substratum interface has a direct proportion on the figuration and size of soil collapse mechanism. This issue has rarely been seen in the evaluation of bearing capacity of confined soil layer. A number of investigations have been conducted in this specific field, Mandel & Salencon [6] focused on the effect of rigid base under a soil layer on bearing capacity. They calculated the capacity of soft ground layer on a rigid base according to the theory of limit equilibrium. They categorized the interface of the soil and the rigid base under two boundary conditions. The friction condition of interface was assumed (i) perfectly rough and (ii) perfectly smooth. They presented the design charts for shallow foundation under eccentric applied load. Farzaneh et al [4] introduced a slip surface equation based on upper bound limit state theorem that can

be applied for calculating the bearing capacity of a confined soil layer overlying a substratum. The presented collapse mechanism included three rigid blocks of which two blocks had rotational-translational movements and the other one just had translational movements. They assumed the interface properties can be indicated on a vast range of between completely smooth and completely rough. They identified no shear strength factors for soil-substratum interface as “perfectly smooth”, on the other hand when these parameters were equal to natural properties of beyond the soil layer; it was assumed “perfectly rough”. The three block failure mechanism is illustrated in Fig. 1. This figure shows a strip footing resting on a thin layer of soil overlying a rigid substratum.

The analysis conducted by [4] was based on an upper bound state theorem; and they used the log-spiral surface algorithm to derive the surface equations. In current research the collapse mechanism is modified by changing the equation of slip surfaces. The modification can optimise the bearing capacity results also introduce the

innovative solution for bearing capacity of shallow foundation on a confined soil layer. In the following, the new collapse mechanism is introduced then verified by comparison with previous solutions and finally the suggested design charts are illustrated.

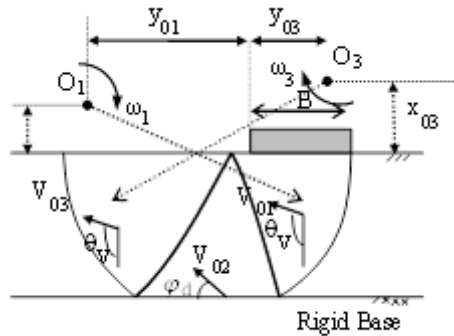


Fig. 1 Translation-rotation failure mechanism [4]

A NEW COLLAPSE MECHANISM

Problem Description

A rigid strip footing of width B is located on a homogeneous cohesive frictional soil. The thickness of the soil layer is H , which is confined by a rigid base. The soil layer is considered to be an isotropic, homogenous and assumed to follow the Mohr-Coulomb plasticity criterion. The parameters e and α signify the amount of eccentricity and inclination of the applied load respectively. The foundation is assumed to be "perfectly rough". A schematic diagram of the problem, analysed in this paper, is shown in Fig. 2.

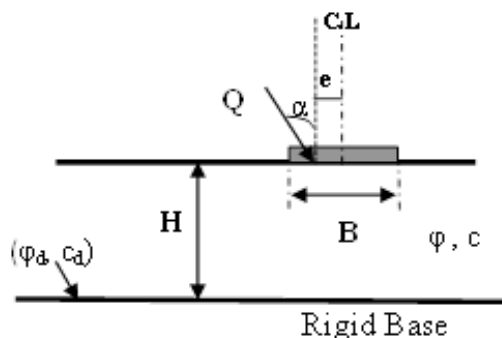


Fig. 2 Strip footing under eccentric and inclined loading based on a thin layer soil.

Derivation of Slip Surfaces

For generating a new failure mechanism which is based on Farzaneh et al [4] solution, a new group of slip surfaces should be introduced in order to form kinematically admissible composite failure mechanism. The new family of slip surfaces is obtained by altering the orientation of convexity of rotational-translational blocks that will be clarified more in the following.

Slip surface for one block failure mechanism

Fig. 3 displays rigid block ABC which is affected by translational and rotational velocities simultaneously. V_0 and $r\omega$ represent the translational and rotational velocities respectively. Rotation takes place clockwise around the origin of polar coordinates (point O) and vector (V_0) is directed to the right side. The assumption velocities are assigned to soil mass. To meet the plastic strain compatibility condition, slip line AB should form an angle ϕ with the vector of the relative velocity ($V_0 + r\omega$) at the whole points. It is assumed that block ABC slips on mass soil. Due to fixed soil mass, the reaction of velocities, such as V_M on an optional point (M), causes to block ABC slips to downward.

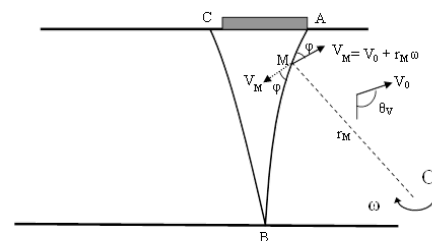


Fig. 3 Determination of the slip surface between a rotational- translational block at the rest of mass soil

Two adjacent points, D and E with coordination factors (r_1, θ_1) and (r_2, θ_2) respectively, should be considered for deriving the slip surface equation on AB slip line. In Fig. 4 the geometric problem and the required angles for obtaining the formulation are illustrated.

In Fig. 4, α is the angle between the velocity vector of block ABC at point D (V_1) with the radius of OD, β is the angle between sector DE and line DF which is drawn perpendicular to OE, and λ is the angle between radius OD and sector DE.

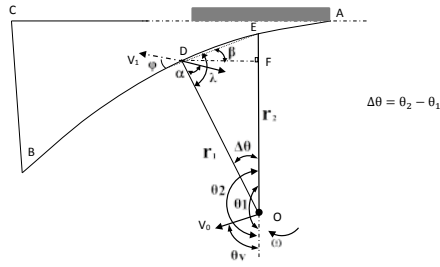


Fig. 4 Determination of the new slip surface equation

According to triangles ODE and DEF yields:

$$EF = (r_1 \sin \Delta\theta) \tan(\lambda + \Delta\theta - \pi/2) \quad (1)$$

At limit, where $\Delta\theta \rightarrow 0$, ED becomes tangent to the slip line at point D and makes following the associated flow rule, angle φ with V_1 , $EF \rightarrow dr$. It follows that:

$$dr = (r_1 d\theta) \tan(\alpha + \varphi - \pi/2) \quad (2)$$

In Eq. (2), angle α needs to be determined.

By considering the velocity diagram at an optional point I on the slip line (Fig. 5) and signifying the angle between $r\omega$ and the resultant velocity, V , by γ , the equation of α can be obtained.

$$\alpha = \arccos \left[\frac{V_0}{\sqrt{V_0^2 + (r\omega)^2 + 2r\omega r_0 \cos(\pi - \theta_V + \theta)}} \cdot \sin(\pi - \theta_V + \theta) \right] \quad (3)$$

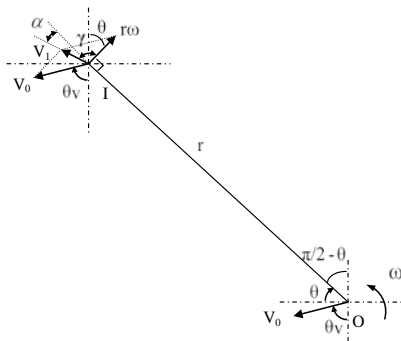


Fig. 5 Velocity Diagram at the point I in slip line AB

Since α is a non-linear function of variables r and θ , obtained differential equation (Eq. 3) cannot

be resolved explicitly. However it can be easily treated by the finite difference method [4].

Slip surface for multiple block failure mechanism

Fig. 6 shows the collapse mechanism of ABCDE including two rigid blocks ABC and BCDE, which are subjected to velocities (V_{01}, ω_1) and (V_{02}, ω_2) , respectively. The first block (block 1) is assumed to rotate about point O_1 and the second one (block 2) about point O_2 .

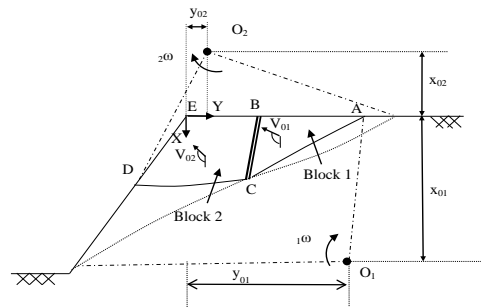


Fig. 6: Slip surface between two rigid blocks with rotational and translational movements

To define the equation of velocity discontinuity between two blocks, BC, it is more convenient to use local Cartesian coordinates (x_1, y_1) and (x_2, y_2) assigned to block 1 and block 2, respectively as shown in Fig. 7.

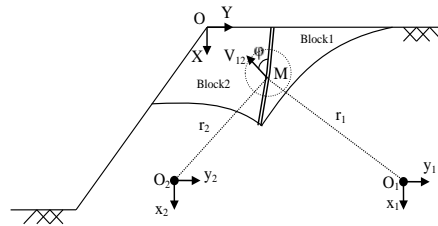


Fig. 7 Relative velocity on optional point

Referring to the associated flow rule (normality condition) the equation of slip surface between two blocks can be derived:

$$\vec{T} \cdot \vec{V}_{12} = |\vec{T}| |\vec{V}_{12}| \cdot \cos(\varphi) \quad (4)$$

where T is the tangential vector of the discontinuity surface at point "M" and V_{12} is relative velocity between two blocks.

As indicated by substituting the local Cartesian coordination in Eq. (4) the final equation can be obtained as follow:

$$\begin{aligned} & (V_{12y}^2 \tan^2 \varphi - V_{12x}^2) dY^2 + 2 V_{12x} V_{12y} \sec^2 \varphi dX dY + \\ & (V_{12x}^2 \tan^2 \varphi - V_{12y}^2) dX^2 = 0 \end{aligned} \quad (5)$$

Complete details of all above equations can be found in [1].

Modified Failure Mechanism

As explained by slip surface introduction, a new collapse mechanism based on upper bound solution can be carried out. Fig. 8 demonstrates the evaluated failure mechanism which can endure the eccentric and inclined applied load. In order to achieve the ultimate upper bound bearing capacity, the internal energy dissipation rate should be equal to the rate of work done by traction and body forces [3].

For minimising obtained ultimate load, requires to use an algorithm by which optimises the variable factors that are affected in bearing capacity. Hence, Generic Algorithms (GAs) [5] is used in the current study.

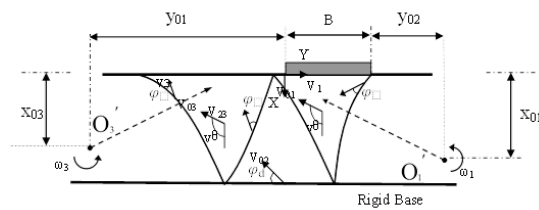


Fig. 8 A schematic diagram indicating the proposed modified collapse mechanism

RESULTS AND DISCUSSIONS

For a comprehensive survey, achieved results are shown as graphical charts. By using this type of chart, the effects of each spectacular parameter can be seen separately. One of the most important parameters is the (H/B) ratio that is the rigid base's depth function. The ultimate applied load indicates as a non-dimensional ratio q_u/C (C is the soil cohesion), although values of N factors can be separately indicated as a result. Eccentricity (e) and inclination (α) of applied load are two significant factors on the bearing capacity of foundation that influence the depth of the failure mechanism. Fig. 9 represents a typical graph that illustrates the bearing capacity results.

The parametric study is more applicable for engineering goals; therefore it needs to identify the specific depth of bed rock which can limit the

collapse mechanism. As it shown on Fig. 9 the bearing capacity stays steady after a particular depth. It means that beyond the special depth the effect of substratum layer is neglected on bearing capacity of overlaying soil layer. In the present study, this depth is called "the effective depth". In the perfectly rough interface, due to inclination of the collapse mechanism to extend the substratum interface, the effective depth is greater than the completely smooth interface when the other parameters are same.

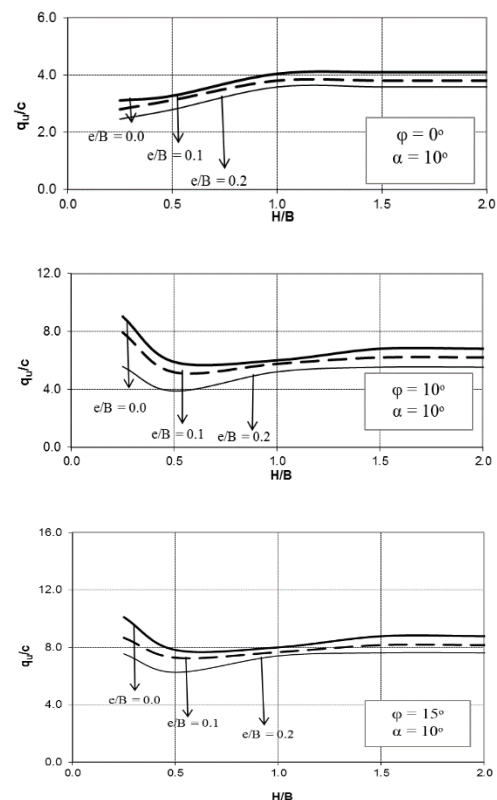


Fig. 9 Practical design graphs for bearing capacity of eccentrically and inclined loaded foundation (perfectly rough interface)

The other significant depth value is the turning point on the bearing capacity of foundation in perfectly smooth interface case. The bearing capacity tends to increase by confining the formation of the failure mechanism, although the lack of shear strength of interface turns to decrease the bearing capacity. The interaction between these two opposing factors causes unsteady raise in the bearing capacity of shallow foundations so that it reaches a minimum value, even less than the amount of bearing capacity in the absence of a rigid base. This specific depth is named "the critical depth".

The inclination of applied load can reduce the bearing capacity. In the current research the inclined load shrinks the depth of the failure mechanism. It causes to vanish the effect of bed rock in a reduced amount of H/B ratio.

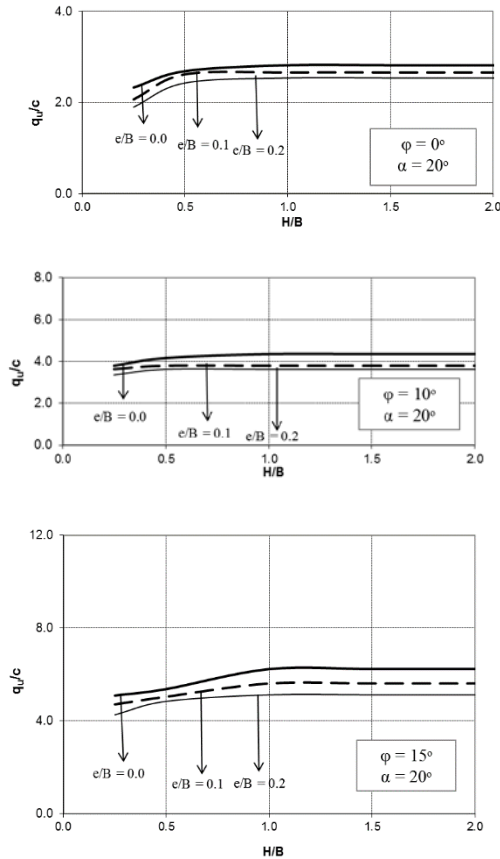


Fig. 10 Practical design graphs for bearing capacity of eccentrically and inclined loaded foundation (perfectly rough interface)

In Fig. 10 the drop of effective depth, in comparison with Fig. 9, is obviously seen with only the angle of inclination increasing. In particular case the increment of α from 10° to 20° decreases the effective depth ratio from 1.5 to 1. The two groups of graphs depict a very similar situation with the single exception being the increase in the angle of inclination.

The factor of presence inclined load on bearing capacity has been considered by previous studies. Hansen introduced inclination factor that was very conservative then it was modified by Vesic [2] Nevertheless the inclination of applied load has rarely been studied on bearing capacity of soil layer overlying a rigid base the current research presents the applied graphs for evaluating the bearing

capacity of foundation and the consequence of bed rock presence on bearing capacity simultaneously.

VERIFICATION

However, a lack of investigation in this specific field of bearing capacity of foundation is completely obvious, the few previously mentioned examples of technical literature that were used for verification. In addition, particular cases [7]-[8]-[9], in the bearing capacity of foundation on two-layer soil in which the failure mechanism because of rigidity of beneath layer is restricted to beyond layer and the layer interface give a good verification in this case.

Comparative results are tabulated in Table 1. According to Table 1 the current study results are compared with the two previous investigations that were mentioned before.

Table 1 Comparison of different methods for calculating the bearing capacity factor (N_c) for vertical loaded foundation on an undrained soil layer ($\phi=0^\circ$), confined by a rigid base.

Perfectly Smooth Interface			
	[4]	[6]	Current Study
H/B	N_c	N_c	N_c
0.10	6.40	6.01	7.12
0.12	6.18	5.50	6.33
0.16	5.27	4.96	5.35
0.20	4.83	4.72	4.80
0.25	4.42	4.42	4.39
0.33	4.11	4.15	4.05
0.50	3.97	3.99	3.75
1.00	4.44	4.43	4.21
2.00	5.17	5.14	5.17
3.00	5.17	5.14	5.17

For further proof, a specific case is investigated in the bearing capacity of a strip footing resting on a two-layer foundation soil sand/clay by a kinematical approach in limit analysis which was introduced by Soubra et al [8]. The collapse mechanism is entirely contained in the sand layer

for high inclination. In that case, a sliding along the clay-sand interface is observed [8].

The verification of current study can be possible with the particular case in Soubra's collapse mechanism [8]. The calculations are performed for a value of load inclination when $\phi = 30^\circ$ $C_d=17$ kPa, $B=1$ m, $\phi_d=0^\circ$ $\gamma=17$ kN/m³ $H/B=0.5$ $\alpha=20^\circ$ and the results are presented in Table 2.

Table 2 The current study result in comparison to [8] and [4] for a specific case

	[8]	[4]	Current Study
$P/\gamma.B$	2.450	2.462	2.701

The main purpose of introducing the modified slip surface is development of Farzaneh et al. collapse mechanism. By combining the original and modified slip surfaces, four collapse mechanisms are presented which only two of them have been explained in this paper. The answer optimization is carried out by choosing the minimum answer of each of them.

CONCLUSIONS

The ultimate bearing capacity of shallow foundations overlaying a soil layer restricted by a rigid base has been investigated using a revised formulation based on the limit state theorem. Rigorous solutions for a wide range of shear strength and geometry parameters of soil and substratum interface have been obtained.

The effects of depth of rigid base on the bearing capacity, inclination and eccentricity of the applied load have been studied. For each kind of situation, there exists a "critical depth" where the appearance of rigid base vanishes on bearing capacity of foundation completely. Finally the results obtained have been demonstrated in terms of bearing capacity factors such as N_c and N_γ in a graphical form to be applicable in solving practical foundation design problems. The modified upper bound can optimise the prior failure mechanism, which was presented by Farzaneh et al [4].

ACKNOWLEDGMENT

The authors would like sincerely to acknowledge the guidance and technical advice provided by Dr Orang Farzaneh, the academic staff member of the University of Tehran, and Dr Farajollah Askari, the academic staff member of the International Institute of Earthquake Engineering and Seismology, Iran.

REFERENCES

- [1] Afshar-Mazandaran R, "Bearing Capacity of Soil Layers on Rigid Base by Upper Bound Method of Limit Analysis", Submitted as a M.sc Thesis, University of Tehran, Iran, 2010
- [2] Bowles JE, "Foundation Analysis and Design", McGraw-Hill, 1996, ch. 4.
- [3] Chen WF & Liu XL, "Limit Analysis in Soil Mechanics", Elsevier Science Publishers B.V. 1990.
- [4] Farzaneh O, Ganjian N, Askari F, "Rotation-Translation Mechanism for Upper-Bound Solution of Bearing Capacity Problems", Computers and Geotechnics, Vol. 37, 2010, pp. 449-455.
- [5] Gen M, Cheng R, "Genetic Algorithms and Engineering Optimization", Wiley, 2000.
- [6] Mandel J & Salencon J, "Force Portante d'un sol Suruneassiserigide (Etude theorique)", Geotechnique, Vol. 22(1), 1972, pp. 79-93.
- [7] Merifield RS, Sloan SW & Yu HS, "Rigorous Plasticity Solutions for the Bearing Capacity of Two-Layered Clays", Geotechnique, Vol. 49, No.4, 1999, pp. 471-490.
- [8] Soubra AH, Abdel Massih DY & El-Hecham E, "Bearing Capacity of Eccentrically and/or Obliquely Loaded Strip Footing over Two-Layer Foundation Soil by a Kinematical Approach", VIII International Conference on Computational Plasticity, Barcelona, 2005.
- [9] Zhu M, "Bearing Capacity of Strip Footing on Two-Layer Clay Soil by Finite Element Method", ABAQUS Users, Conference, 2004.

SOME THOUGHTS ON THE ULTIMATE RESISTANCE OF PILES

Stephen Buttlings¹
¹GHD Geotechnics, Australia

ABSTRACT

Australia was one of the first countries to establish a standard for pile design using Limit State principles. This has since been revised, and the current version is AS 2159-2009. After about 25 years of effort, the Europeans finally produced EN 1997-1 in 2004, and it is apparently slowly gaining acceptance. Japan, Canada, and the USA have also been using limit state, or load and resistance factor, design codes for some time. One of the problems is the confusion surrounding the definition of ultimate pile resistance, or capacity, and this gets highlighted when international competitions are held to predict the outcome of static load tests. In order to try to minimize this confusion, three compatible definitions are proposed, in the hope that this will add clarity.

Keywords: Piling, Ultimate Pile Resistance

INTRODUCTION

When using a limit state design code such as AS 2159 [1] it is important to understand the principles of limit state design in which, when considering the Ultimate Limit State, a design action consisting of loads or deflections which have been factored up to achieve a magnitude which is unlikely to be exceeded, must be less than a capacity which has been factored down such that the actual capacity is unlikely to be less. This ensures that “failure” will not occur. We express this mathematically as:

$$E_d \leq R_{d,g} \quad (1)$$

where E_d = design action effect, and $R_{d,g}$ = design geotechnical resistance.

Characteristic strength

This design geotechnical resistance is factored down by taking account of uncertainty, from what AS 2159 [1] refers to as “the ultimate geotechnical strength of a pile”, R_{ug} , defined in clause 1.3.37 but hardly used in the body of the standard. It is actually only a theoretical value, and is probably the same as what might otherwise be termed the “characteristic ultimate geotechnical strength or capacity” of a pile. This term is used elsewhere around the world, and means the ultimate geotechnical strength which a proportion, typically 95%, of a collection of identical piles would be expected to be stronger than. This is alluded to in the definitions in Table 1.1 of the standard, when it says that R_{ug} “is estimated either by calculation ($R_{d,ug}$) or by testing ($R_{t,ug}$)”. Considering first design by calculation, it may be assumed that a number of boreholes are reviewed, a geotechnical model produced, and design parameters selected which are “a conservative estimate of the value likely to occur at the limit state under

consideration”, in this case the ultimate limit state. These parameters might also be considered as “characteristic strength parameters”, and their use will therefore lead to determination of a characteristic strength, so in this case:

$$R_{ug} = R_{d,ug} \quad (2)$$

This is really the only design method contemplated by AS 2159 [1], although other standards encompass other methods. For example, the European Standard, EC7 [2], allows a number of designs to be produced, one for each borehole on a project. Each one of these is then referred to as a profile or “model pile”, and each will produce an ultimate geotechnical pile capacity, $R_{d,ug}$. A number of possible values of capacity therefore exist, and the characteristic value can be found by dividing the mean value by a factor (ξ_3) or the minimum value by a different factor (ξ_4), and using the lower of the two values calculated. This still satisfies the requirements of AS 2159 [1] in so far as R_{ug} is estimated by calculation from $R_{d,ug}$. Guidance on the factors to be used are given in a table in Annex A to the standard, or in a “National annex” which allows each European country to choose their own, but are in any event dependent on the number of profiles or model piles available, i.e. the number of boreholes. The suggested values from Annex A are shown in Table 1, which illustrates how the “characteristic”

Table 1: Factors to be applied to minimum and mean pile load test results, from EC7 [2]

	ξ for n =						
	1	2	3	4	5	7	10
ξ_3	1.40	1.35	1.33	1.31	1.29	1.27	1.25
ξ_4	1.40	1.27	1.23	1.20	1.15	1.12	1.08

value is produced from a collection of values, the spread of which is taken into account by applying different factors to the mean and the minimum

Geotechnical strength reduction factor

It is not being suggested that these factors should be used in a pile design under AS 2159 [1], since a part of these factors is associated with variability of geotechnical parameters across a site, and this is also assessed within the geotechnical strength reduction factor. Nevertheless the principle still applies, that a characteristic value of the ultimate geotechnical strength can be calculated, either by using characteristic strength parameters, or by applying factors to a collection of individual capacity values. Once this characteristic geotechnical strength has been determined, then the geotechnical design strength can be found by reducing the characteristic strength by the geotechnical strength reduction factor, ϕ_g , and this involves a risk analysis. As explained in detail by Chambers and Lehane [3], the amount of testing proposed has a significant impact on the value of ϕ_g , but this is applied to the ultimate design geotechnical strength, and not to the test value.

It is perhaps easiest to see how this works with a hypothetical case. Taking the example from Figure 1 (a) of Chambers and Lehane [3], a project using 300 driven prestressed precast concrete piles is considered, each with an $E_d = 2,000$ kN. It is further assumed that there are four boreholes, and that these are used to produce a geotechnical model with strength parameters which are a cautious estimate of the strength which will apply at the ultimate limit state. Thus the design geotechnical strength, $R_{d,g}$, is given by:

$$R_{d,g} \geq 2,000 \text{ kN} \quad (3)$$

If it is assumed that 6 tests are carried out (2%), and that the basic geotechnical strength reduction factor, $\phi_{gb} = 0.5$, then this will give $\phi_g = 0.7$ for static load tests and $\phi_g = 0.61$ for dynamic load tests. Therefore the paper design, using the characteristic strength parameters, must produce a design ultimate geotechnical strength, $R_{d,ug}$, of 2,855 kN if static load tests are used, or 3,300 kN for dynamic tests.

For comparison, the model pile method could be used but, as stated above, care must be taken not to make double allowance for soil variability risk. One way to assess this is to check the effect on ϕ_g of changing the site risk ratings from 1 to 5. This is seen to decrease ϕ_g by 0.05, and applying this extra factor to the values for static load tests leads to $R_{d,ug} = 2,665$ kN and for dynamic load tests to $R_{d,ug} = 3,045$ kN. On the basis of 4 boreholes this means that each individual model pile must have a minimum design ultimate geotechnical strength of

3,200 kN for static load tests and 3,655 kN for dynamic load tests, or a mean design ultimate geotechnical strength of 3,490 kN for static load tests and 3,990 kN for dynamic load tests, whichever is the more critical.

Use of pile test results

In this, “conventional” use of pile design and testing, the geotechnical parameters are used to carry out a design on paper, and the testing is used to confirm the design. Thus if the design ultimate geotechnical strength is 2,855 kN, any static load test result above this value confirms the design. On the other hand, if the model pile method has been used, then any static load test result above 2,665 kN confirms the design.

As opposed to a conventional calculation, some designers may choose to actually carry out the design on the basis of pile tests. This appears to be contemplated by AS 2159 [1], since it states in Table 1.1 that the characteristic ultimate geotechnical strength, R_{ug} can be “estimated from $R_{t,ug}$ ”, although it gives no guidance as to how this estimate is to be made. Again this issue has been addressed in EC7 [2], which proposes that:

$$R_{c;k} = \text{Min} \left\{ \frac{(R_{c;m})_{\text{mean}}}{\xi_1}, \frac{(R_{c;m})_{\text{min}}}{\xi_2} \right\} \quad (4)$$

Here the subscript m means *measured*, and hence for comparison with AS 2159 [1]:

$$R_{c;m} \equiv R_{t,ug} \quad (5)$$

The correlation factors ξ to derive characteristic values from static pile load test results (n – the number of tested piles) are given in Table 2.

Table 2. Factors to be applied to static load test results, after EC7 [2]

	ξ for $n =$				
	1	2	3	4	≥ 5
ξ_1	1.40	1.30	1.20	1.10	1.00
ξ_2	1.40	1.20	1.05	1.00	1.00

This method is obviously particularly relevant to driven piling and where a significant amount of testing is utilised. Although conventional design methods may be used to estimate the length of piles and the driveability, it is possible to rely mainly on PDA testing as the means of “designing” the piles.

In the hypothetical case referred to above there were 300 piles on the project, and it was proposed to test 2% of them, so we have 6 test results and 6 values of $R_{t,ug}$. Again R_{ug} is the characteristic ultimate geotechnical strength which it could reasonably be expected that all piles would exceed,

if all of them were tested. Since only 6 piles are to be tested, there is clearly a risk that other piles could have lower $R_{t,ug}$ values if they were tested, so some margin for variability of soil within the site needs to be made. As with the model pile case, care is needed not to make double allowance for this risk, since a ϕ_g factor will still be applied. Again the factors proposed in Annex A to EC7 [2] may be used as a guideline.

The correlation factors ξ to derive characteristic values from dynamic impact test results^{a, b, c, d, e} (n – the number of tested piles) are given in Table 3.

Table 3. Factors to be applied to dynamic pile test results, after EC7 [2]

	ξ for $n =$				
	≥ 2	≥ 5	≥ 10	≥ 15	≥ 20
ξ_5	1.60	1.50	1.45	1.42	1.40
ξ_6	1.50	1.35	1.30	1.25	1.25
^a The ξ -values in the table are valid for dynamic impact tests ^b The ξ -values may be multiplied with a model factor of 0.85 when using dynamic impact tests with signal matching ^c The ξ -values should be multiplied with a model factor of 1.10 when using a pile driving formula with measurement of the quasi-elastic pile head displacement during the impact ^d The ξ -values shall be multiplied with a model factor of 1.20 when using a pile driving formula without measurement of the quasi-elastic pile head displacement during the impact ^e If different types of piles exist in the foundation, groups of similar piles should be considered separately when selecting the number n of test piles					

Therefore, given 6 dynamic pile test results with signal matching on a selection from 300 piles, used as the principal method of design, the minimum total pile capacity must be:

$$R_{t,ug,min} \geq 3045 \times 1.35 \times 0.85 = 3495 \text{ kN} \quad (6)$$

and the mean of the results must be:

$$R_{t,ug,mean} \geq 3045 \times 1.5 \times 0.85 = 3885 \text{ kN} \quad (7)$$

whichever is the more critical.

LIMIT STATES

One of the intentions of introducing limit state design methods into geotechnical engineering was to rationalise the differences which occurred when limit state design methods were being used for structural design, and working stress designs were being used for foundations. It was probably also hoped that this might lead to some simplifications in the processes. However, other complications have

arisen, and not least of these is the definition of the limit states, particularly the ultimate limit state, or ULS. AS 2159 [1] defines the ultimate geotechnical strength as “the resistance developed by an axially or laterally loaded pile or pile group at which static equilibrium is lost or at which the supporting ground fails”. This definition accords with common definitions of ultimate geotechnical capacity, being a load at which deformations continue without increase in load, i.e. the supporting ground fails. However, AS 2159 [1] also defines the ultimate limit state as a “condition for which a system is designed, beyond which it ceases to fulfill its intended function and becomes unfit for use. (Note: There are recognized limit states, e.g. for fire, serviceability, stability and strength.)” Unfortunately a piled foundation can become “unfit for use” to support a structure long before “the supporting ground fails”. AS 1170 [4], wherein the structural design actions are defined, also defines limit states as “states beyond which the structure no longer satisfies the design criteria”, and ultimate limit states as “states associated with collapse, or with other similar forms of structural failure. (Note: this generally corresponds to the maximum load-carrying resistance of a structure or structural element but, in some cases, to the maximum applicable strain or deformation.)” This would also appear to allow that ultimate limit states are associated with collapse, i.e. including foundation failure, but also that they could include states where the design criteria are no longer satisfied, for example as a result of excessive strain or deformation. When we consider piled foundations, particularly single piles which, when tested, tend to increase in capacity, even slowly, as settlement increases, we clearly have difficulty in defining a settlement at which we will say that the ultimate resistance has been achieved. If we cannot define a settlement, then defining the ultimate resistance becomes even more difficult.

Ultimate geotechnical resistance by design

This leads directly to the question of the definition of the ultimate geotechnical strength of a pile. Is it the strength at which the supporting ground fails? This definition would be compatible with a paper design, in which the strength of the soil is estimated, usually layer by layer, and from this the two components of pile resistance, shaft friction and end-bearing are determined. Typically the shaft friction will be calculated by some sort of adhesion factor times the local strength, whether in total stress or effective stress terms, and the end-bearing will be found by applying a traditional bearing capacity theory to the base. By adding these components together we are implicitly assuming that all the soils are elastic/perfectly plastic, and so are not subject to brittle behaviour with post-peak strengths less than the peak, and that the pile is pushed far enough that

all elements have reached their peak strength. This ultimate capacity will be called Q_{u3} . If these strengths are the characteristic strengths of each element, then the calculated pile resistance will also be the characteristic resistance, which is represented by the brown line in the figure below, which we will call $Q_{u3,k}$. In this analysis no consideration is given to settlement.

Ultimate geotechnical resistance by test

A number of complications arise as soon as we try to introduce real physical conditions in a load test. The work of Chin [5, 6] showed that, towards the later part of a static load test, the relationship between load and settlement was hyperbolic, with the load asymptotically approaching the ultimate value. If this is the case then, in theory, the load will only reach the ultimate value at an infinite settlement, which means that this is only a hypothetical value, higher than other more useful estimates of ultimate resistance, and probably compatible with the design value referred to above. It will therefore also be referred to as Q_{u3} . In fact, if a large number of piles are constructed in homogeneous soil conditions, to the same geometry and design, and subsequently tested and the ultimate resistance determined using the Chin method, then the individual values of Q_{u3} might be expected to be distributed normally about the mean, as shown by the blue line in Fig. 6, with the characteristic resistance at 1.96 times the standard deviation below the mean. In this example the mean is 1000 kN, the standard deviation 150 kN, and the characteristic resistance $Q_{u3,k} = 706$ kN.

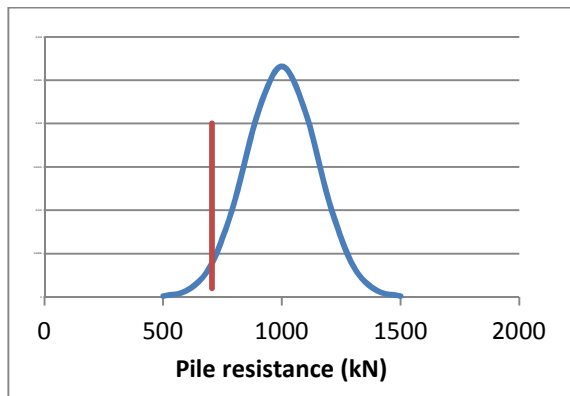


Fig. 6 Distribution of ultimate pile resistance, Q_{u3}

In practice, other than in Constant Rate of Penetration tests, the load in a static load test is applied in small, finite, increments. At some stage, as the ultimate resistance is approached, it may be that the rate at which the pile is settling, multiplied by the area of the hydraulic jack or jacks, is greater than the pump discharge capacity. In this case it will not be possible to reach the next load stage, and it

will be assumed that the ultimate resistance has been reached. However, it may be that a pump with a higher discharge capacity could achieve more increments. This concept is embraced by the Brinch Hansen [7] failure criterion, which defined the failure load of the pile as the load at which the settlement is 4 times the settlement at 80% of that load. In other words, it is defining a point at which the load/settlement curve has become very steep, but not vertical. This will produce an ultimate resistance which is less than that produced by Chin's hyperbolic extrapolation, and will be referred to as Q_{u2} .

A definition commonly used in the UK and Europe, where piles are generally founded on materials which can be described as soil, is that the ultimate resistance is given by the load at which settlement continues without increase in load. It has also been found, in practice, that piles in granular materials may continue to increase in capacity, even if only slowly, with increasing settlement. This has led to definitions which limit the settlement to 10% of the pile diameter, as in EC7 [2], and this has seemed to produce loads and deflections at ultimate capacity, Q_{u2} , for piles in fine grained and in granular soils which are compatible. Fellenius [8] has stated that "the concept of bearing capacity does not apply to a pile toe", and that "toe resistance does not exhibit an ultimate value but continues to increase with increasing toe movement."

Settlement at ultimate geotechnical resistance

To this debate over ultimate strength the question of what settlement should be used to define the ultimate geotechnical strength on a load-settlement chart needs to be added. As mentioned above, for soils in the UK a settlement of 10% of the pile diameter is often taken as defining ultimate end-bearing pressure, and therefore ultimate geotechnical strength, Q_{u2} , since the ultimate shaft friction is usually achieved at much smaller settlements, such as 0.5 to 2% of pile diameter (Fleming et al [9]). However, others have proposed much lower settlement figures, and one of the better known is the Davisson Offset Limit from Davisson [10]. In this criterion the toe settlement is considered to be limited to a fixed amount plus an amount which varies with pile diameter. These were chosen by Davisson [10] as 0.15 inches (4mm) and 1/120 of the pile diameter respectively. These two numbers are added together and applied as an "offset" to the settlement. The remaining component is an elastic component, assuming that all of the load at the pile head is transmitted to the pile toe. This produces a line, drawn from the offset value, for the increasing shortening with increasing load, which has a gradient of L/AE , where L = pile length, A = cross-sectional area, and E = elastic modulus of pile material. The Davisson Offset Limit will generally

produce a lower ultimate resistance, Q_{u1} , than the other criteria, but it is especially popular because of its use in dynamic pile testing. Because it considers the ultimate resistance at a relatively small toe displacement, it is more compatible with dynamic pile testing, with toe shakes in the order of 5 to 10 mm, than other methods where total settlements of 10% of pile diameter are considered.

Nevertheless, there is clearly no agreement on what settlement relates to ultimate pile resistance, and therefore at what point on a load/settlement curve the ultimate resistance can be defined. This has been very well illustrated by Fellenius [11] in his summary of the contributions to a pile prediction event which he organised in 2011, for a CFA pile formed in glacial till near Edmonton, Alberta, Canada. Figure 8 shows the results of predictions by 41 different people from 15 countries and most continents and, while there is clearly a wide scatter in the predicted performance, the main purpose of including this chart is to show the range of values of settlement at which the ultimate capacity of this 406 mm diameter CFA pile was selected. It appears to be from about 5 to 220 mm.

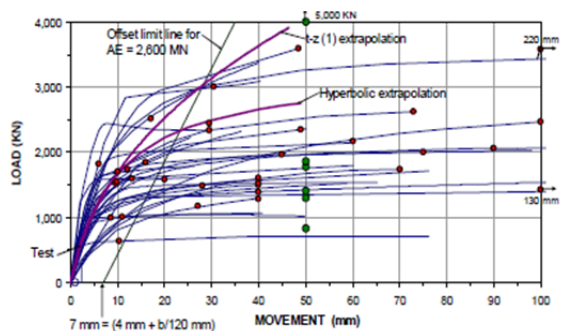


Fig 8. Predicted ultimate resistances and settlements for a 500 mm diameter pile in glacial till, after Fellenius [11]

Fellenius has continued his interest in this aspect of foundation engineering, and carried out another prediction exercise in 2013, based on 4 piles in sandy soil in Bolivia.

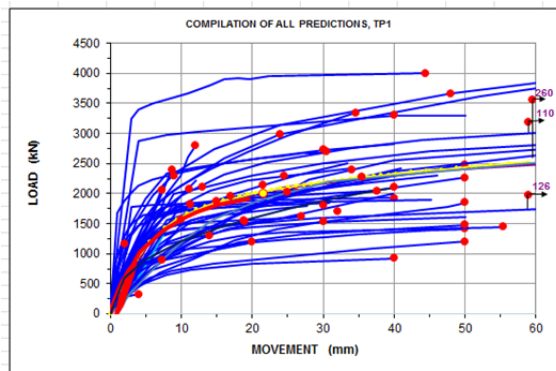


Fig. 9 Predicted ultimate capacities and settlements for TP1, a 450 mm diameter bored pile in sand in Bolivia, after Fellenius [12]

The results are not yet published, but those who made predictions have been sent an initial summary of the results, and Fig. 9, Fig. 10 and Fig. 11 show the same effect for test piles TP1, TP2 and TP3 respectively.

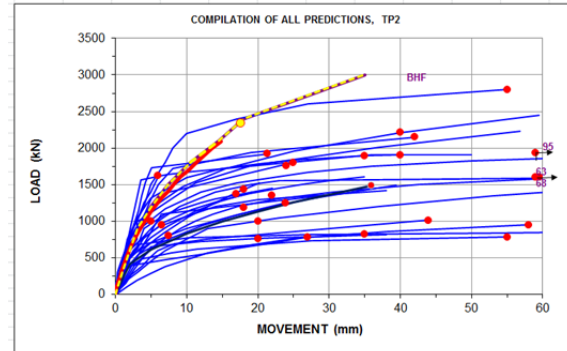


Fig.10 Predicted ultimate resistances and settlements for TP2, a 450 mm diameter auger displacement pile in sand in Bolivia, after Fellenius [12]

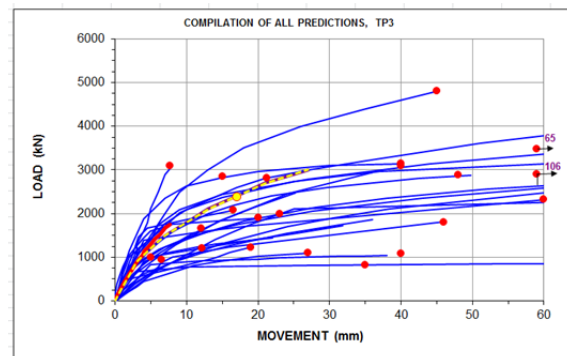


Fig.11 Predicted ultimate resistances and settlements for TP3, a 450 mm diameter auger displacement pile with an expander body in sand in Bolivia, after Fellenius [12]

Again the only aspect of these charts which is being considered here is the range of settlements at which the ultimate pile resistance has been selected, for TP1 this would appear to be about 2 to 260 mm, for TP2 about 5 to 95 mm, and for TP3 about 5 to 106 mm. TP1 was 400 mm in diameter, and piles TP2 and TP3 were both 360 mm diameter. This seems to demonstrate that there are very widely differing views on the settlement at which the ultimate pile resistance should be measured. As stated at the beginning of this section, if there is such a wide disagreement on settlement, then there can be no hope of agreeing on an ultimate pile resistance. It is therefore proposed that three separate definitions of ultimate pile resistance are considered, being Q_{u1} , Q_{u2} and Q_{u3} in order of increasing numerical value. Q_{u1} is based on the Davisson Offset Limit, Q_{u2} on the load at a settlement of 10% of the pile diameter or the Brinch Hansen criterion, and Q_{u3} as the paper

design value or that produced by a Chin extrapolation of a static load test load/settlement curve. It is believed that clear use of these three definitions will enable better comparison between test and analysis methods. When compared to AS 2159, it should be noted that:

$$R_{d,ug} = Q_{u3} \quad (8)$$

and that, if characteristic strengths are used in the design, then:

$$R_{ug} = Q_{u3,k} \quad (9)$$

Similarly:

$$R_{t,ug} = Q_{u2} \quad (10)$$

CONCLUSIONS

1. It is noted that there are numerous definitions of ultimate pile resistance (capacity) in use in different parts of the world, and that these can lead to confusion when working across national borders.
2. It is also noted that, apart from at some theoretical infinite displacement, there is a relationship between load and displacement of a pile, such that the ultimate pile resistance (capacity) corresponds to a prescribed displacement.
3. It is proposed that three ultimate pile resistances (capacities) be defined, corresponding to three different displacements. These are:
 - a. The ultimate pile resistance at a pile head settlement defined by the Davisson Offset Limit Criterion.
 - b. The ultimate pile resistance at a pile head settlement equal to 10% of the pile diameter, or by the Brinch Hansen Criterion.
 - c. The ultimate pile resistance defined by a calculation based on ultimate shaft adhesion and ultimate end-bearing capacity regardless of displacement, or by the Chin Hyperbolic extrapolation of a static load test.
4. Each of these three values will also have a sub-value, being the associated characteristic value from a number of tests.
5. Most existing definitions fit within one of these three, but it is the acknowledgement that the other values are also relevant, and may be used by others, which is important.

REFERENCES

- [1] AS 2159-2009, "Australian Standard: Piling – Design and Installation". Sydney: Standards Australia, 2009.
- [2] EC7, "Eurocode 7: Geotechnical design – Part 1: General rules". BS EN 1997-1:2004. London: BSI, 2004.
- [3] Chambers H and Lehane BM, "An assessment of the geotechnical strength reduction factors specified in the new Australian Piling Standard", Australian Geomechanics, Vol 46 No 4, December 2011, pp. 71-78.
- [4] AS 1170.0:2002, "Structural design actions". Sydney: Standards Australia, 2002.
- [5] Chin FK, "Estimation of the ultimate load of piles not carried to failure", Proc. 2nd South East Asian Conference on Soil Engineering, 1970, pp. 81-90.
- [6] Chin FK, "Discussion on pile test, Arkansas River Project". ASCE, J. for Soil Mechanics and Foundation Engineering, Vol 97, SM6, pp. 930-932.
- [7] Hansen J B, "Discussion on hyperbolic stress-strain response – cohesive soils. ASCE, J. of Soil Mechanics and Foundation Engineering, Vol 89, SM4, 1963, pp. 241-242.
- [8] Fellenius BH, "Recent advances in the design of piles for axial loads, dragloads, downdrag, and settlement". Proc. Seminar by ASCE and Port of New York and New Jersey, 1998, 19p.
- [9] Fleming W G K, Weltman A J, Randolph M F and Elson W K, "Piling Engineering", 3rd Edition, Spon, 2006.
- [10] Davisson MT, "High capacity piles", Proc. Lecture Series on Innovations in Foundation Construction. ASCE, Illinois Section, Chicago, 1972, pp. 81-112.
- [11] Fellenius B H, "Capacity and load-movement of a CFA pile: A prediction event", ASCE GeoInstitute Geocongress, San Diego, Foundation Engineering in the face of uncertainty, ASCE, Reston, VA, 2013, pp. 707-719.
- [12] Fellenius B H and Terceros M, "Pile prediction event in sands in Bolivia", to be published.

WIRELESS SENSOR NETWORK FOR LANDSLIDE MONITORING

S. M. A. Motakabber, M. I. Ibrahimy and F. Anwar

Faculty of Engineering, International Islamic University Malaysia, Kuala Lumpur, Malaysia

ABSTRACT

Every year all over the world many lives and properties are lost due to many geological catastrophes like, landslide or landslip. Manual and electronic monitoring systems are used for predicting the landslide. The manual monitoring system is laborious and not practical. And most of the electronic systems are complex and expensive. A wireless sensor network in conjunction with an underground pretension cable with a strain gage sensor attached at one end is proposed for a simple landslide monitoring system. A mathematical model has been developed for the system and the model is verified by simulation. The result shows that an early prediction of the landslide is possible by using the developed system.

Keywords: *Wireless Sensor Network, Landslide, Automated Monitoring System, Strain Gage Sensor, Geological Catastrophe*

INTRODUCTION

Worldwide, landslides cause about 1,000 deaths per year and property damage of approximately US\$ 4 billion [1]. Existing manual solution is insufficient and sometimes it is costly for landslide prediction and detection. Installing a single sensor for monitoring a wide hilly target area is not sufficient. Most of the cases, the property of the hill is changed in about every 10-15 meters distance. Wiring with multiple sensors to a central data logger is also not reliable and practical as well since it requires frequent maintenance. Therefore, wireless sensor network system is used for real-time landslide monitoring. Thin film strain gage pressure sensor with high accuracy pressure measurement is clamed in the system [2]. A simple pretension underground cable attached with a strain gage at one end can be easily used to measure the pressure of the soil as shown in Fig. 1.

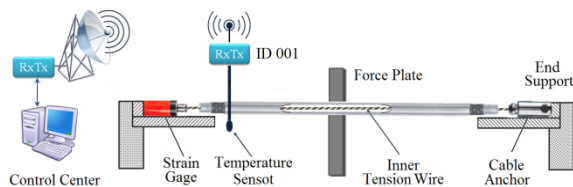


Fig. 1 Basic arrangements of the proposed wireless sensor network system for landslide monitoring.

The measured pressure can be used to calculate the landslide prediction and detection. A number of same kinds of sensor setup can be used for monitoring a wide land area. In this case, each sensor is defined by a unique number within a wireless network. This ID number can be easily used to locate the landslip zone. A majority of the

wireless sensor network arrangements [3], [4] are mainly data collection networks. The wireless sensor network recurrently collects the respective data and collaboratively processes the measurements from the field under study before forwarding them to the central monitoring station. The central monitoring station executes more computationally-intensive algorithms such as finite element modeling and parameter identification [5], [6] and acts as the expert interface to the system. A wireless communication system can be used to transmit the sensors sampled data and relevant information to a distant central database server computer for analysis purpose. The instant conveyed information would allow us to implement instant disaster rescue measures and to notify the land user to protect the people's lives and properties.

SENSOR MODELING

A simplified force diagram of the proposed landslide pressure sensor that is, pretension cable with strain gage is shown in Fig. 2. Assume that a pre tensioned still cable length of L is attached at two end supports under the soil. If the linear expansion coefficient of the cable is α_L and the surrounding temperature of the cable is changed ΔT degree Kelvin then the change of cable length ΔL_T can be calculated as follows:

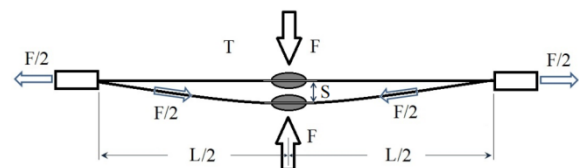


Fig. 2 Simplified force diagram of the proposed landslide pressure sensor.

$$\alpha_L = \frac{1}{L} \frac{\Delta L_T}{\Delta T} \quad (1)$$

$$\text{Or, } \Delta L_T = \alpha_L L \Delta T \quad (2)$$

When the land is slightly moved S distance from its initial position then it creates a force F on force plate as well as on the cable. If the Yang's modulus of the cable is E then at force equilibrium condition,

$$E = \frac{F/A}{\Delta L/L} \quad (3)$$

Where, A is the cross section area of the cable and ΔL is the change in length of the cable due to force.

By considering the temperature effect, Eq. (3) can be rewritten as,

$$\Delta L = \frac{F(L + \Delta L_T)}{EA} \quad (4)$$

The work U_E done by the soil movement can be calculated by Eq. (5).

$$U_E = FS \quad (5)$$

The potential energy U_W stored in the cable can be calculated as follows:

$$U_W = \int_0^{\Delta L} F d\Delta L \quad (6)$$

From Eq. (4) and Eq. (6),

$$U_W = \int_0^{\Delta L} \frac{EA\Delta L}{(L + \Delta L_T)} d\Delta L$$

$$\text{Or, } U_W = \frac{EA\Delta L^2}{2(L + \Delta L_T)} = \frac{\Delta LF}{2} \quad (7)$$

From Eq. (5) and Eq. (7), the potential energy U_S stored in strain gage substrate is calculated as follows:

$$U_S = U_E - U_W = FS - \frac{\Delta LF}{2}$$

$$\text{Or, } U_S = F \left(S - \frac{\Delta L}{2} \right) \quad (8)$$

Again, if the Yang's modulus of the strain gage

substrate is E_S then at force equilibrium condition,

$$F_S = \frac{E_S A_S \Delta L_S}{L_S} \quad (9)$$

Where, A_S and L_S are the cross section area and length of the substrate respectively. F_S is the force on the substrate and ΔL_S is the change in length of the substrate due to force.

From Eq. (9),

$$U_S = \int_0^{\Delta L_S} F_S d\Delta L_S$$

$$\text{Or, } U_S = \frac{E_S A_S \Delta L_S^2}{2L_S} = \frac{E_S A_S \Delta L_S^2}{2} \quad (10)$$

By combining Eq. (8) and Eq. (10)

$$F \left(S - \frac{\Delta L}{2} \right) = \frac{E_S A_S \Delta L_S^2}{2L_S}$$

$$\text{Or, } \frac{\Delta L_S}{L_S} = \sqrt{\frac{2F}{L_{GS} E_{GS} A_{GS}} \left(S - \frac{\Delta L}{2} \right)} \quad (11)$$

If the gage factor and the temperature coefficient of the strain gage are G and α respectively then the change of resistance ΔR of the strain gage with respect to the initial resistance R is calculated as follows:

$$\Delta R = R \left(\frac{G \Delta L_S}{L_S} + \alpha T \right) \quad (12)$$

By combining Eq. (11) and Eq. (12)

$$\Delta R = R \left(G \sqrt{\frac{2F}{L_S E_S A_S}} \left(S - \frac{\Delta L}{2} \right) + \alpha T \right) \quad (13)$$

From Eq. (4), if the Yang's modulus E of the cable is very large then $\Delta T \approx 0$ and Eq. (13) can be rewritten as Eq. (14).

$$\Delta R = R \left(G \sqrt{\frac{2FS}{L_s E_s A_s}} + \alpha T \right) \quad (14)$$

Eq. (14) indicates that the change of strain gage resistance is directly proportional to the square root of the force and displacement of the land.

RESULT AND DISCUSSION

A PSPICE simulation is studied for the proposed landslide sensor for monitoring system. The result is shown in Fig. 3. In this simulation, it is considered that the Yang's modulus E of the cable is infinity and the temperature coefficient of the strain gage is very low. In Fig. 3, it is noticed that a very slow landslide effect is present at the beginning and about four months later, the effect is more visible. The sensor ID number 001 shows that its resistance is changing exponentially; it means a massive landslide would be happened within short time in the region under the sensor.

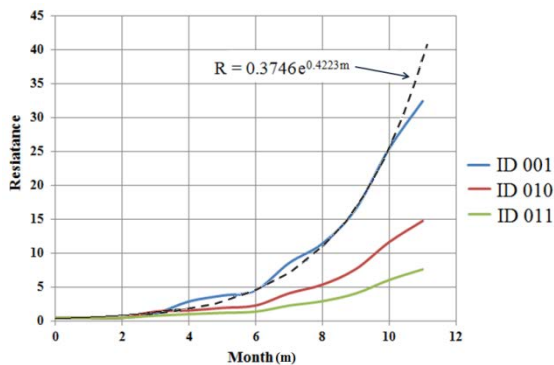


Fig. 3 Change of strain gage resistance with time.

CONCLUSION

A pretension cable and a strain gage sensor can be used for landslide prediction and detection purpose. The change of strain gage resistance is a direct indication of the landslide effect and no need

to measure the exact value of the force or displacement of the soil. This principle can help to develop a simple and low cost real-time landslide or landslip monitoring system. According to the mathematical model, Eq. (13), for an efficient system, the Yang's modulus of the cable must be very large. Since, the still and carbon fiber cable have very large Yang's modulus; they can be used in this development.

REFERENCES

- [1] Lee S and Pradhan B, "Landslide hazard mapping at Selangor, Malaysia using frequency ratio and logistic regression models", *Landslides*, Vol. 4, No. 1, 2007, pp. 33-41.
- [2] Hongye W, Kun L, Zhichou A, Xu W and Xun H, "Ion-beam sputtered thin-film strain-gage pressure transducers", *Sensors and Actuators A: Physical*, Vol. 35, Issue 3, 1993, pp. 265-268.
- [3] Szewczyk R, Polastre J, Mainwaring A and Culler D, "Lessons from a sensor network expedition", in proceedings of the 1st European Workshop on Sensor Networks, January 2004.
- [4] Xu N, Rangwala S, Chintalapudi KK, Ganesan D, Broad A, Govindan R and Estrin D, "A wireless sensor network for structural monitoring", in proceedings of the 2nd international conference on Embedded Networked Sensor Systems, pp. 13-24, USA, 2004.
- [5] Kuppusamy T, Sheng J, Parker JC and Lenhard RJ, "Finite-element analysis of multiphase immiscible flow through soils", *Water Resources Research*, Vol. 23, Issue 4, 1987, pp. 625-631.
- [6] Hoshiya M and Sutoh A, "Kalman Filter-Finite Element Method in Identification", *J. Eng. Mech.*, Vol. 119, Issue 2, 1993, pp. 197-210.

INFLUENCE OF THE SOIL-STRUCTURE INTERACTION ON THE SEISMIC BEHAVIOR OF BUILDINGS ON SHALLOW FOUNDATIONS

Z. Benadla, K. Hamdaoui, S. Aissaoui and A. Baouch

Department of Civil Engineering, Faculty of Technology, University of Tlemcen, Algeria

ABSTRACT

The objective of this work is to study the mobility of shallow foundations relative to the subgrade by considering two cases. In the first, the structure is fixed at its base, as classic cases. For the second, the foundation is replaced by hinges and springs, where their stiffnesses are expressed in terms of the geometry of the foundation and soil shear strength. The comparison is made on a dynamic model when the two tested cases are confronted. Thereafter, a parametric study is considered to see the effect of all the parameters that can play a key role in the structural response. Then, these results will be validated on real structure cases, by considering important Algerian earthquakes: (i) the one of Aïn Témouchent in 1999 and (ii) the earthquake of Boumerdès in 2003. The extracted results will permit to make the point on all the elements that may influence the seismic response of buildings while considering the interface soil-foundation-structure.

Keywords: Dynamic Analysis, Shallow Foundations, Soil Structure Interaction, Shear Velocity.

INTRODUCTION

The design of a structure in a seismic zone is highly dependent on the knowledge of seating elements, namely soil and foundations. These latter are the interface between the soil with which they move, and the superstructure that undergoes inertial forces. In addition to the vertical loads that they ordinarily transmit, the horizontal earthquake action is added. The soil itself is susceptible to deform or even lose its cohesion. Geotechnicians describe the expected behavior of soils, when shaken by deformations, settlements or landslides, or an amplification of waves of certain frequencies. Engineers, in their turn, take this into account for the project in general and the foundations in particular. For the public authority, it takes this into account for planning regulations that prohibit the construction in certain sites or require special foundations.

However, most structural studies do not take into account the foundations mobility relative to the subgrade. Indeed, the building design considers the superstructure fixed on the ground. However, this assumption is not always justified, given that the behavior of a building that is supposed to be fixed in the ground is not the same when the fixed joint is replaced by hinges with springs that schematize the freedom of movement of foundations. In some seismic regulations, such as the Algerian earthquake regulation (RPA 99 V2003, [6]) this matter is not addressed.

In the present work, analyses of the influence of Soil-Structure Interaction (SSI) on the fundamental frequency of building structures are proposed. A model of a simple frame, composed of two columns

and a beam representing the floor, is considered (Fig. 1). The SSI phenomenon is carried by modeling the whole soil-foundation with 6 springs: 3 translations and 3 rotations. This model has been proposed by many authors, as Parmelee in 1967, Veletsos et al. in 1974, 1975, 1977, Jennings et Bielak in 1973, Wolf in 1985 and Aviles et al [4]. in 1996, 1998. The results of this analysis will be compared to those found in another model in which the base is considered as fixed.

SYSTEM MODEL AND FORMULATION

The fundamental frequency of building type structures constitutes an essential parameter in the design and the structural analysis in the seismic zone. This parameter is usually calculated by using empirical formulas provided by the seismic regulations that generally neglect the SSI. However, this interaction can have a significant influence on the fundamental frequency, and thus, can lead to wrong structural design. Indeed, some authors (Gazetas and Mylonakis 1998, 2000, [2], [3]) showed that the post-seismic observations revealed that the SSI can have a detrimental effect on the structures. Additionally, numerical simulations, carried out by Boris et al. (2004) [1], showed that the SSI can have advantageous or harmful effects on the structural behavior, according to the characteristics of soil and those of the seismic loading [4].

The springs' stiffnesses (translation and rotation) are determined using formulas that are available in literature. The formulas of (Newmark and Rosembuth 1971, [5]) express the stiffness in

terms of the soil mechanical characteristics, namely the shear modulus G_s and Poisson's ratio ν . Also, in terms of the geometrical characteristics of the foundation:

$$K_v = \frac{G_s}{(1+\nu)} \beta_z \sqrt{A} \quad (1)$$

$$K_h = 2(1+\nu) G_s \beta_x \sqrt{A} \quad (2)$$

$$K_\theta = \frac{1+\nu}{4} G_s \beta_x (a^2 + b) \sqrt{A} \quad (3)$$

K_v , K_h et K_θ represent respectively the vertical, the horizontal and the rotational translational stiffnesses, and A is the foundation area, $A = a \cdot b$.

The parameters β_x and β_z are two entities depending on the a/b ratio. For the case of a square foundation of $2 \times 2 \text{ m}^2$, $\beta_x = 1$ et $\beta_z = 2.18$ [7].

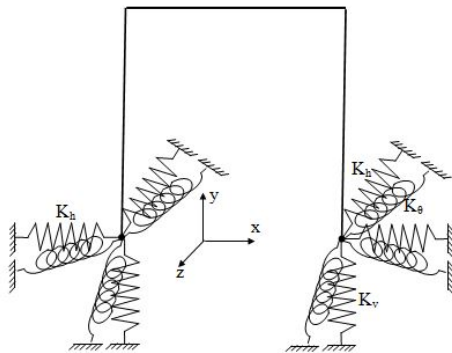


Fig. 1 Reference model

The mechanical characteristics of the used materials are given in the table 1

Table 1 Mechanical characteristics of the studied system

	Density γ (KN/m ³)	Elastic modulus E (MPa)	Poisson's ratio
Soil	20	52	0.3
structure	24.5	32000	0.2

The modal analysis of the selected frame was carried out. The different fundamental modes of the two cases (fixed and by considering the SSI) were extracted. In the first case, the fundamental frequency is found equal to 8.13Hz, where in the second; it is equal to 5.53Hz. Therefore, a reduction of 32% in the fundamental frequency when considering the SSI is seen. The found fundamental mode represents a translation in X direction whatever the treated case is.

PARAMETRIC STUDY

Modal dynamic analyses of the studied frame were carried out for different structural configurations by varying the parameters affecting the fundamental frequency, particularly, the basic parameters relative to the soil and the structure.

The objective is to determine the relationship between the modal fundamental frequency of the fixed model (F_{fix}) and the one of the same model when the SSI is considered (F_{SSI}). The obtained results will permit to bring out the influence of SSI on the fundamental frequency of the buildings.

It should be noted that this can be expressed according to (V_s , E_p , I_p , N_b , N_o , H , L , A). Where V_s is the soil's shear velocities waves, E_p and I_p are respectively, the Young modulus and the moment of inertia of the columns, H is the height of floor, L is the span, and A is the foundation area. N_e is the number of floors, N_b and N_o are the building's openings number in the longitudinal and the transversal directions, respectively.

Initially, the analysis is carried out for a simple frame comprising one floor and one opening. In this case, the fundamental frequency of the frame is expressed only according to V_s , E_p , I_p , H , L , and A . The considered values in this parametric study are summarized in table 2. The soil's shear velocities are taken from the RPA 99 (V2003) [6] regulation for different types of soils: very friable, friable, firm, very firm and rock.

Table 2 Considered parameters values

V_s (m/s)	100 (Very friable)
	150 (Very friable)
	200 (Friable)
	400 (Firm)
	800 (Rock)
E_p (MPa)	20000
	32000
	42000
I_p (m ⁴)	0.000325
	0.00125
	0.00342
	0.00762
	0.0149
H (m)	0.0341
	2.00
	4.00
	6.00
	8.00
A_{column} (cm ²)	10.00
	25x25
	35x35
	45x45
	55x55
	65x65
	80x80

Results

Figs.2 to 5 show the parametric study results for different configurations. The different elements are represented according to the F_{SSI}/F_{fix} frequency ratio. In the case of the V_s influence, this ratio is stabilized for velocities greater than 400m/s. For less resistant soil, the effect of the SSI remains very visible.

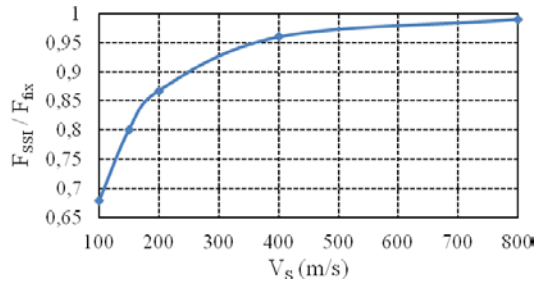


Fig.2 Influence of V_s on the frequencies ratio

The inertia variation of columns influences considerably on the F_{SSI}/F_{fix} ratio (Fig. 3). Indeed, for velocities V_s lower than 400m/s, the reduction of the frequency F_{SSI} can reach the 70%, compared to the case of the fixed structure. It is shown also that more the inertia of columns increases, more it becomes judicious to consider the SSI effect.

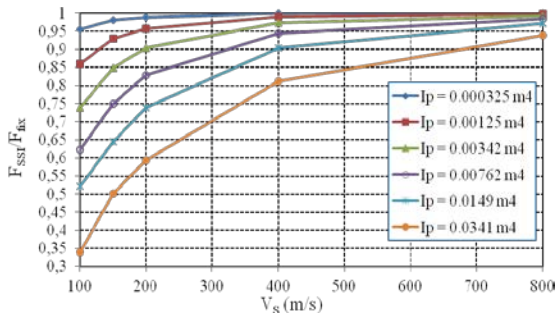


Fig.3 Influence of I_p on the frequencies ratio

The fundamental frequency is affected also by the building's height variation as shown in fig. 4. In the cases where the height H is lower than 8.00m, the variation between the two frequencies F_{SSI} and F_{fix} , and for the same velocities, are not significant. However, the difference becomes clear when $H \geq 8.00$ m. The rigidity of columns does not have a great influence, since the variation of F_{SSI}/F_{fix} has practically the same curve shape for different Young modulus (Fig. 5).

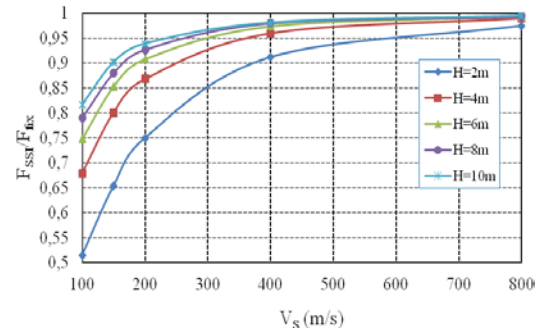


Fig.4 Influence of H on the frequencies ratio

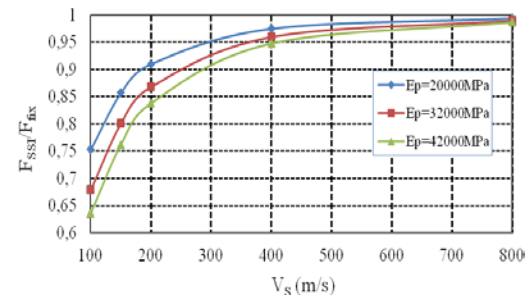


Fig.5 Influence of E_p

Finally, one can note that for some configurations (stiff structures on soft soil), the F_{SSI}/F_{fix} ratio can reach low values, close to 0.3, thing that means that the SSI lead to a reduction of about 70% of the fundamental frequency of the frame. This confirms the need to consider the SSI for the determination of the fundamental frequency for this type of structures.

SSI CONSIDERATION METHOD

A non-dimensional parameter was proposed by Khalil [4], noted K_{SS} , in order to express relative stiffness of soil-structure. This one can be determined according to the parameters used in the previous paragraph: V_s , H , E_p and I_p , determined by Eq. 4.

$$K_{SS} = \frac{N_o \cdot N_b \cdot \rho \cdot V_s^2 \cdot H^3 \cdot \sqrt{\frac{A}{A_0}}}{N_e \cdot E_p \cdot I_p^{0.75}} \quad (4)$$

Where A_0 is a referential area (equal to 1m²), ρ is the soil density and A is the foundation area.

Different configuration cases made possible to trace the abacus of the fig. 6. The found results indicate that for a calculated K_{SS} according to a building data, a corresponding F_{SSI}/F_{fix} ratio will be got.

In order to check the proposed abacus, two cases of constructions implemented in the region of Tlemcen, west of Algeria, are studied. This zone is classified as low seismicity zone (Zone I).

The first is a five story building, with 4 openings in the longitudinal direction and 3 in the transverse one. The second example is a seven story building, with 5 openings in the longitudinal direction and 3 in the transverse one. The case of a five story construction was selected to be based on isolated footings, and the other one (building with seven floors), built on continuous footings. The parameter K_{SS} was calculated according to the data of the two buildings and the result permit to plot the curves of the fig. 6.

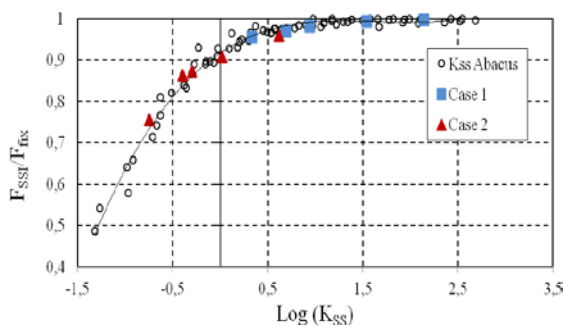


Fig. 6 Relative stiffness influence K_{SS} on the structure frequency in the two buildings

According to the obtained results, we note that the suggested parameter K_{SS} represents well the two buildings cases based on the two types of shallow foundations.

SEISMIC STUDY

In this part, the influence of the SSI on the dynamic response of the structure will be seen. For this effect, the building already studied in the previous paragraph (Case 2) is selected. In that structure, shear walls are added to its frame system. These walls are modelled as SHELL elements type. The numerical model is presented in fig. 7.

Two important Algerian earthquake cases were considered. The first, touched the region of Aïn Témouchent in 1999 (west of Algeria) and the second (Boumerdès) has caused enormous human and material damages in 2003 (north-east region of the country). This earthquake of 6.8 of magnitude was felt for a long distance from the epicentre (Majorque to approximately 300km). The Boumerdès earthquake occurred in a zone where the seismic activity was regarded as moderate.

The zone of Tlemcen, being described as low seismicity compared to the one of Boumerdès, enabled us to consider only one the third (1/3) of the accelerogram recorded at the Keddara station.

Figures 8 and 9 represent the accelerograms of the two studied cases.

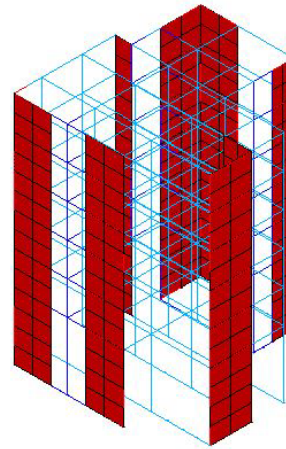


Fig.7 Numerical built model

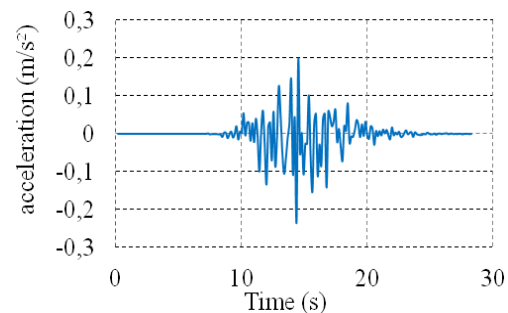


Fig.8 Aïn Témouchent Accelerogram

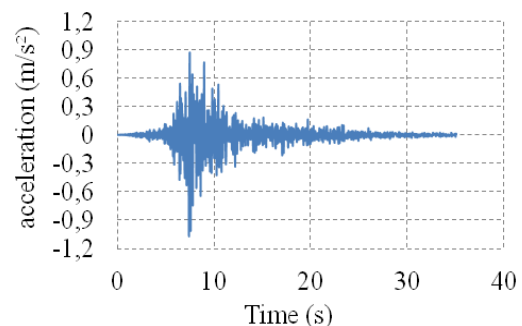


Fig.9 Boumerdès Accelerogram

As results, we presented the obtained accelerations by considering the structure as fixed and considering the spring elements modeling the mobility of the foundations relative to soil, and the displacements of the node at the highest point of construction.

For Aïn Témouchent earthquake, the acceleration graph is composed of two sections (Fig. 10). The first varies from 0 to 10 seconds, where the values are not comparable. They are very significant from

the first moments of the excitation, whereas in the case of the fixed structure, those are minimal. After that, the second interval comes where the values are similar with small differences.

Horizontal displacements are represented in fig. 11. The maximum displacement is seen in the first section (from 0 to 10s), it is equal to 6.74cm in the case of the SSI, whereas in the fixed structure case, this phase illustrates a minimal displacement. Its maximum comes only to after 12.54 seconds from the beginning of the excitation; its value is around 1.66cm. Also, at the end of the excitation, the case of the SSI needs more time to be damped, since the displacement is not vanished, contrary to the fixed structure case.

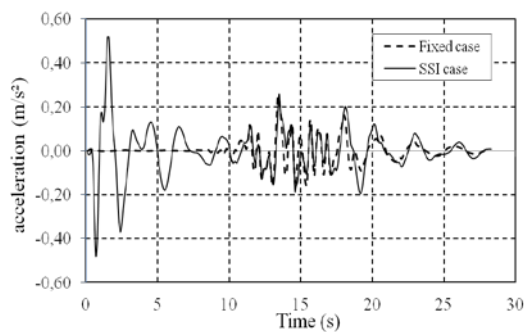


Fig.10 The SSI effect on the acceleration, Aïn Témouchent earthquake

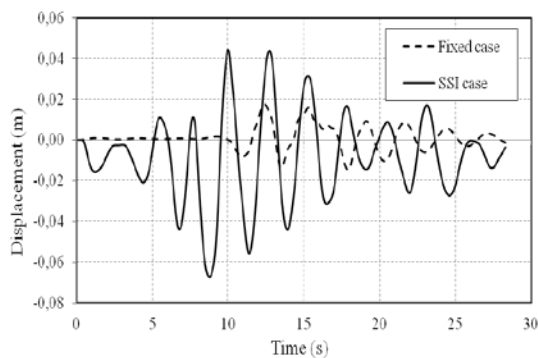


Fig.11 The SSI effect on the horizontal displacement, Aïn Témouchent earthquake.

For the earthquake of Boumerdès, the first noted remark concerns the maximum acceleration that exceeds the 0.33g in the case of the SSI. Indeed, this value exceeds the 0.5g, and it is reached before the one obtained in the fixed case with a gap of around 0.6 seconds (Fig. 12). Furthermore, at the beginning of the excitation, the acceleration is much more significant in the case of the SSI compared to case of fixed structure.

For the displacements (Fig. 13), it is noted that the values are much more significant in the case of the SSI than in the fixed case. The maximum

displacement passes from 2.5cm in the fixed structure case to more than 7.5cm in the SSI case; that is 5cm of difference.

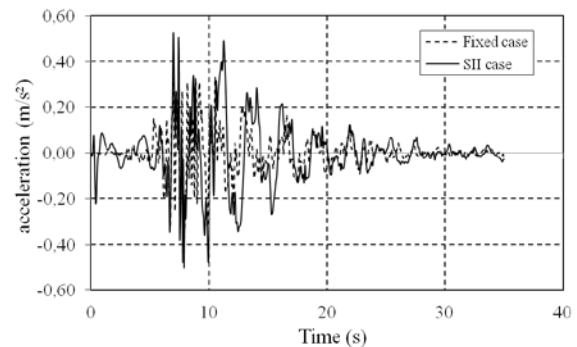


Fig.12 The SSI effect on the acceleration, Boumerdès earthquake.

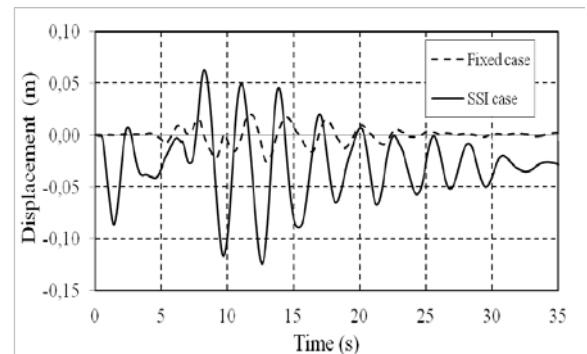


Fig.13 The SSI effect on the horizontal displacement, Boumerdès earthquake.

CONCLUSION

This paper comprised the study of the influence of the soil-structure interaction on building type structures with shallow foundations, using a numerical modeling, and based on the finite element method.

The structure was modeled by beam elements, where the soil-foundation unit was modeled using 6 springs: 3 in translation and 3 in rotation. Their stiffnesses were determined from suggested expressions, available in the literature.

The study on the influence of the soil-structure interaction on the fundamental frequency of the structures showed that this one can reduce very significantly the first frequency of the structures.

The parametric analysis permit the determination of the expression of a non-dimensional parameter, called relative stiffness of soil-structure (K_{SS}), allowing to take into account the influence of the SSI in the calculation of the fundamental frequency of the buildings and this was shown by the treatment of two cases of real buildings.

The study of the seismic response of the buildings was carried out by using two real seismic recordings. It was shown that the fact of considering the effect of the soil-structure interaction increases considerably the acceleration as well as the displacements of last floor of the building. These values seem critical especially at the beginning of the excitation.

REFERENCES

- [1] Boris J., Shashi K. and X. Feng "Influence of Soil-Foundation-Structure interaction on seismic response of the I-880 Viaduct" J. Struc. Engineering, Vol. 26, 2004, pp. 391-402.
- [2] Gazetas G. and Mylonakis G. Seismic Soil-Structure Interaction: New Evidence and Emerging Issues, Emerging Issues paper, Geotechnical Special publication N°75, ASCE Vol. III,.1998, pp. 1119-1174.
- [3] Gazetas G. and Mylonakis G. "Seismic Soil-Structure Interaction: Beneficial or detrimental", Journal Earthquake Engineering, V04, N° 3, 2000, pp. 277-301.
- [4] Khalil L., "Influence de l'interaction sol-structure sur le comportement sismique des bâtiments, analyse dans les domaines linéaire et non linéaire", PhD Thesis, Civil Engineering Department, University Science & Technology of Lille, 2009.
- [5] Newmark N.M. and Rosembueth E., "Fundamentals Earthquake Engineering", Prentice-Hall, 1971.
- [6] Règles Parasismiques Algériennes "RPA 99", document technique réglementaire, DTR B C 2 48,version 2003.
- [7] Tamahoult M and Branci T., "Influence de l'interaction sol-structure sur la réponse dynamique des structures des bâtiments", Civil Engineering Department, Sc. & Sc.Ing. Faculty, University of Chlef, 5^{ème} Symposium International sur la Construction en Zone Sismique. SICZS_2010, 2010.

NUMERICAL STUDY OF PLASTICITY-BASED CONSTITUTIVE MODELS FOR SOIL IN SIMULATION OF BRACED EXCAVATION

Samuel J. Verghese¹, Ha H. Bui¹

¹Department of Civil Engineering, Monash University, Australia

ABSTRACT

Numerical modelling continues to play a unique and intrinsic role in the process of geotechnical design. Of greatest concern are soil constitutive models that are employed within finite element software to predict soil behaviour. The objective of this paper is to provide a numerical study of the Mohr-Coulomb and Hardening Soil constitutive models in simulation of a braced excavation. The Taipei National Enterprise Centre (TNEC) basement construction process was well documented and the commercial finite element code, Plaxis, was selected for this numerical comparative study. It was found that the Mohr-Coulomb soil model, a first order approximation, produced an underestimation of the diaphragm wall deflection, whilst the Hardening Soil model provided a good prediction of the observed in-situ diaphragm wall deflections.

Keywords: Constitutive Soil Models, Plasticity Theory, Finite Element Method, Numerical Modelling

INTRODUCTION

The behaviour of soil varies all over the world and continues to present a unique challenge to geotechnical engineers in professional practice on a daily basis. As a result, numerous soil theorists have emerged attempting to explain the exciting phenomenon observed under various in-situ site conditions. The fundamental knowledge an engineer employs when analysing an engineering system directly correlates to the success, safety, and precision of results.

On April 20th 2004, a 30m deep excavation adjacent to the Nicoll Highway in Singapore collapsed during construction. The transport authorities were constructing an underground railway tunnel when the braced excavation support failed, initiating rapid collapse of the diaphragm walls leaving a collapse zone which was 150m wide, 100m long and 30m deep. This tragedy took the lives of two workers, an engineer and a site foreman. Furthermore, economic losses were substantial with delays contributing to part of the US\$4.14 billion subway project [1]. Upon post failure investigation, it was noted that certain errors in the input data of the original constitutive model used in design ultimately led to incorrect assumptions and underestimated calculations [1]; resulting in catastrophic failure.

In recent times, theoretical developments have significantly grown and with the advance of computer technology and software programming, Finite Element (FE) methods are readily available to assist geotechnical engineers in the interpretation, modelling and design of complex soil systems. Unfortunately, a minority of modern day geotechnical engineers have become accustomed to

user-friendly computer software and consequently fail to comprehend the fundamental theories, principles and assumptions built within.

FE analysis is built upon the concept of continuum mechanics and constitutively models a soil system from its stress-strain characteristics. Various constitutive models have been proposed in literature to capture the properties and features of numerous soil types and model its responses to surface loading, displacements, excavation, slope stability and many other geotechnical actions.

This paper seeks to provide a brief overview into the fundamental principles, which directly influence the level of accuracy and prediction the MC, and Hardening Soil (HS) constitutive models offer.

The Mohr-Coulomb (MC) linear elastic soil model is an example of a commonly used constitutive relationship utilised in industry. This particular model provides a first order approximation helpful in providing a preliminary analysis to the problem. However, for an effective analysis to be carried out, it is imperative for the user to recognise the uncertainties and limitations each model has to offer, and consequently make a judgement between the reliability of the numerical results and the uncertainty therein.

A braced excavation simulation of the Taipei National Enterprise Centre (TNEC) has been modelled using the FE software package Plaxis. Stage by stage construction procedures have been replicated in order to simulate in-situ conditions recorded on site. The diaphragm wall deformations obtained from field data history have been evaluated with respect to numerically computed wall deformations. Both the MC and HS constitutive models have been selected for this numerical comparative study.

NUMERICAL APPROACH

Stress State and Equilibrium

Continuum theory considers solids, in this case soil particles, and fluids to behave as a continuous media. Equations of equilibrium and compatibility are independent of a material's physical properties, and thus form the basis of numerical modelling. There are three normal stress rates ($\dot{\sigma}_{xx}$, $\dot{\sigma}_{yy}$, $\dot{\sigma}_{zz}$) and three shear stress rates ($\dot{\sigma}_{xy}$, $\dot{\sigma}_{yz}$, $\dot{\sigma}_{xz}$). The spatial derivatives of the aforementioned stress rates are then assembled in a vector denoted σ and combined with the body force components, X, Y and Z assembled in a vector b . This presents the static equilibrium of a continuum [18].

$$\underline{L}^T \cdot \sigma + b = 0 \quad (1)$$

where \underline{L}^T is the transpose matrix of a differential operator [18]. Similarly, the kinematic relationship between stress and strain can be formulated accordingly and is referred to as a constitutive relationship seen in Eq. 2 below.

$$\dot{\sigma} = \underline{M} \dot{\epsilon} \quad (2)$$

where $\dot{\sigma}$ and $\dot{\epsilon}$ is the stress and strain tensor respectively and \underline{M} is the material stiffness matrix.

CONSTITUTIVE THEORY

The constitutive relationship for a material depends on the homogeneity, isotropy and continuity of the body material, as well as its response to cyclic loading, and the rate and magnitude of the applied load [5]. General techniques have been developed to characterise soil as elastic, plastic, or viscous in nature to consequently conduct constitutive analyses.

Theory of Plasticity

Classical theory developed by Hill [9] seeks to explain the stress and strain behaviour of plastically deformed solids and is fundamentally analogous to Hooke's law which stipulates the relationship between stress and strain governed by the material's modulus. It is important to note that a material's total strain rate is controlled by an elastic and plastic rate component.

$$\dot{\sigma} = \underline{M}(\dot{\epsilon}^e + \dot{\epsilon}^p) \quad (3)$$

The yield limit of an elastic soil material is defined by a yield function, denoted f , and is a function of the stress components, friction angle, ϕ and cohesion, c . The failure limit under all deviatoric

loading combinations for a perfectly plastic material remains fixed and does not move in principal stress space. Hill [9] states that plastic strain rates are proportional to the derivative of the yield function with respect to the stresses. This notion provides the basis upon which plastic deformation can be determined once the stress point (p-q) reaches the yield surface.

$$\dot{\epsilon}^p = \lambda \frac{\partial f}{\partial \sigma} \quad (4)$$

Experimental data indicates that plastic strain rates are not always orthogonal to the yield surface and hence cannot be accommodated under the coaxial assumption. Therefore, the plastic potential function has been derived to model this type of plastic strain rate behaviour and considers the dilatancy angle, ψ , where $\phi \neq \psi$, to avoid the previous overestimation of dilatancy under the normality rule.

Mohr-Coulomb Soil Model

The MC model in Plaxis captures the linear elastic perfectly plastic stress-strain behaviour of a soil element when considered in its general stress state, and all deformations are fully recoverable upon unloading. Once the stress point (p-q) is loaded past the model's elastic limits, ϕ and cohesion, c , define a fixed shear failure surface upon which the stress point (p-q) is assumed to follow.

$$\tau = \sigma'_m \tan(\phi') + c' \quad (5)$$

The above failure criterion produces a linear failure envelope for a two-dimensional analysis. As the development of plastic strains occur, the yield surface does not admit changes of expansion or contraction and hence is considered a fixed yield surface (perfectly plastic).

Hardening Soil Model

The HS model in Plaxis is a second order constitutive relationship that seeks to describe the non-linear behaviour of soil upon yielding and is derived from the hyperbolic model of Duncan and Chang [8]. The term hardening within this context defines the various changes, in size, location or shape, of the yield surface and is directly related to the loading history measured by a form of plastic deformation [21]. Note, the Plaxis HS model considers isotropic hardening only.

Isotropic hardening is governed by the assumption that expansion or contraction about the centre of the yield surface is uniform, whilst the shape, centre and orientation of the yield surface remain unchanged. Fundamentally this type of hardening behaviour can be characterised into two

components: shear hardening and compression hardening. When a soil body is subjected to primary deviatoric loading, plastic axial strains develop as observed in a triaxial test. These irreversible strains are consequently accounted for by the shear hardening component of the HS model. Furthermore, compression hardening is used to model the irreversible plastic volumetric strains due to primary compression in oedometer loading and isotropic loading. Careful consideration to stress dependent stiffness is a fundamental element of the HS model and is associated with a power law value, m . This power value equates to 1 when a linear analysis is assumed and is typically taken as 0.5 (recommended for hard soils) when attempting to model hyperbolic stress-strain behavior.

This model requires three input stiffness parameters, namely: E_{50} , E_{oed} , and E_{ur} . E_{50} is the confining stress dependent stiffness modulus for primary loading and is described by Eq. (6).

$$E_{50} = E_{50}^{ref} \left(\frac{c \cos \phi - \sigma_3 \sin \phi}{c \cos \phi - p^{ref} \sin \phi} \right)^m \quad (6)$$

For unloading and reloading elastic stiffness, E_{ur} is defined as follows:

$$E_{ur} = E_{ur}^{ref} \left(\frac{c \cos \phi - \sigma_3 \sin \phi}{c \cos \phi - p^{ref} \sin \phi} \right)^m \quad (7)$$

The oedometer stiffness modulus, E_{oed} for primary compression is:

$$E_{oed} = E_{oed}^{ref} \left(\frac{c \cos \phi - \sigma_3 \sin \phi}{c \cos \phi - p^{ref} \sin \phi} \right)^m \quad (8)$$

Note, p^{ref} is defined as the reference pressure and is taken as 100 kN/m² within the Plaxis FEM software [18]. E_{50}^{ref} , E_{ur}^{ref} , and E_{oed}^{ref} are the respective stiffness moduli corresponding to p^{ref} .

The first type of hardening, shear hardening has a linear flow relationship and is characterised by the development of plastic strains when mobilising the soil's material strength, or increasing the soil's preconsolidation stress, commonly referred to as compaction hardening. The fundamental shear hardening yield function is given by [18]:

$$f = \bar{f} - \gamma^p \quad (9)$$

where \bar{f} is a function of stress and γ^p is the strain hardening parameter and is expressed as a function of plastic strains [18]:

$$\bar{f} = \frac{2}{2E_{50}} \frac{q}{1 - \frac{q}{q_a}} - \frac{2q}{E_{ur}} \quad (10)$$

$$\gamma^p = -(2\varepsilon_1^p - \varepsilon_v^p) \quad (11)$$

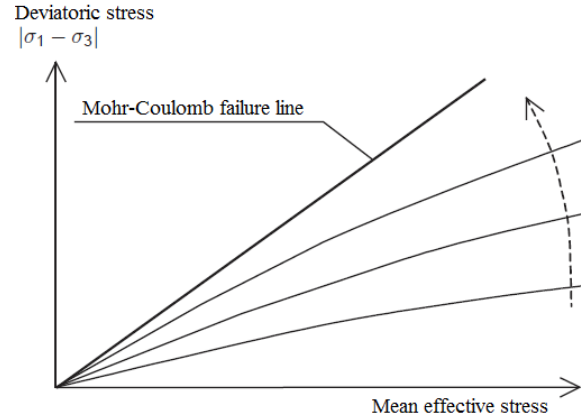


Fig. 1 Yield loci for varying constant values of the γ^p parameter

For hard soils, plastic volume changes tend to be relatively small and hence ε_v^p can be assumed to equal 0 (hard soils only). Hence, the combination of Eq. 10 and Eq. 11 produces multiple yield surfaces with increasing values of γ^p as seen in Fig 1.

The second type of hardening mechanism is plastic volumetric strain. As an element of soil undergoes compressive loading, a stress point asymptotically follows the yield locus respective to its strain hardening parameter, thus the induction of a yield surface limits the elastic region upon which the stress point is asymptotically moving, based on a direct relationship between E_{50}^{ref} and E_{oed}^{ref} . Hence, the shear yield surface is controlled by the triaxial modulus and the cap yield surface by the oedometer modulus respectively [18]. The reader is suggested to make reference to Schanz et al. [19] published paper entitled, "The Hardening Soil Model: Formulation and Verification" for the mathematical derivations of the yield cap surface.

TNEC CASE STUDY

The Taipei National Enterprise Centre (TNEC) is the chosen case study for this paper due to readily available documentation of construction procedures and in-situ conditions released by Ou et al. [15]. The TNEC building was built in 1991 and comprises of 18 storeys and 5 basement levels. The TNEC was excavated to a depth of 19.7m using the top-down construction method and a retaining wall measuring 90cm thick and 35m deep was elected to be supported by a series of temporary steel struts and concrete floor slabs. According to site investigation data, the soil located within the Taipei basin consisted of six layers of alternating silty clay and silty sand deposits overlying a thick gravel formation. The groundwater level was observed at a depth of 2m below the ground surface, with incremental dewatering corresponding to excavation depth. General phreatic level conditions were

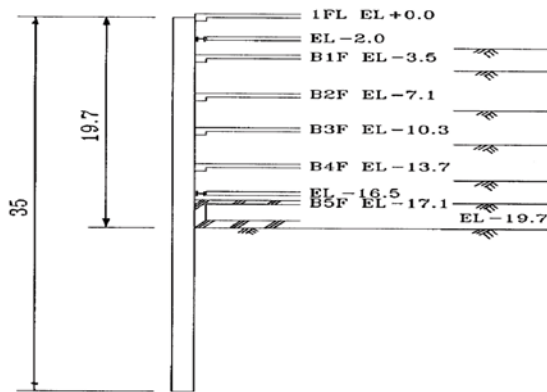


Fig. 2 TNEC excavation cross-section with relevant dimensions in metres [15].

assumed, generating hydrostatic pore pressure distribution. Soil-water coupling was not considered since the CL soil layers were analysed as undrained. Fig. 2 depicts the excavation cross-section. Numerical parameters are as follows.

Table 1 Input parameters of struts and slabs [17]

Strut	Behaviour	EA	L _s
		(kN)	(m)
H300	Elastic	1954810	8
H400	Elastic	3569021	3
B1F	Elastic	3690000	1
B2F	Elastic	3690000	1
B3F	Elastic	3690000	1
B4F	Elastic	3690000	1
B5F	Elastic	3690000	1

Table 2 Input parameters of diaphragm wall [17]

Parameter	Abbr.	Value	Unit
Axial Stiffness	EA	22140000	kN/m
Flexural Rigidity	EI	1494450	kN/m ² /m
Wall Thickness	d	0.9	m
Weight	w	21.6	kN/m/m
Poisson's ratio	ν	0.15	-

Table 3 Input parameters for HS model

Type	GL	m	ν	E_{50}^{ref}	E_{ur}^{ref}	E_{oed}^{ref}
	-m			kN/m ²	kN/m ²	kN/m ²
CL	5.6	0.5	0.2	3531	10594	4414
SM	8	-	0.3	-	-	-
CL	33	0.5	0.2	36022	108067	45028
SM	35	-	0.3	-	-	-
CL	37.5	0.5	0.2	65236	195709	81545
SM	46	-	0.3	-	-	-

Table 4 Input parameters for MC model

Type	GL	γ_t	ϕ'	ν	s_u	E
	-m	kN/m ³	°		kPa	kN/m ²
CL	2	18.25	34	0.5	5	2500
CL	5.6	18.25	34	0.5	30	15000
SM	8	18.93	31	0.3	-	56471
CL	13	18.15	29	0.5	45	22500
CL	18	18.15	29	0.5	35	17500
CL	23	18.15	29	0.5	50	25000
CL	28	18.15	29	0.5	75	37500
CL	33	18.15	29	0.5	100	50000
SM	35	19.62	31	0.3	-	173620
CL	37.5	19.13	0	0.5	125	62500
SM	46	19.62	32	0.3	-	192571

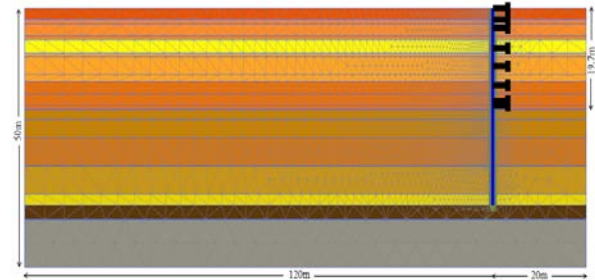


Fig. 3 Finite element mesh of the TNEC

RESULTS AND DISCUSSION

Figure 3 shows the finite element mesh of the TNEC model used for Plaxis modelling. Lateral boundaries have been assumed free-rollers, while the bottom boundary is fixed. In-situ soil parameters were obtained from Ou et al. [15] and Hui & Hie [10]. In the analysis, construction stages were performed by deactivating FE elements in accordance with construction procedures. With consideration to consistency between MC and HS simulations, the drained layers, represented as SM were modelled using MC parameters during the HS simulation. The drained layers consisted of silty sand and hence the MC model provided an accurate representation for those respective layers. It can be seen in Fig. 4 that the MC model underestimated the observed deflections of the diaphragm wall quite significantly. The maximum deflection value predicted by this model was approximately 7.0cm in comparison to the maximum observed deflection of 9.95cm. In contrast, the HS constitutive model provided a much better prediction of the excavation process and slightly overestimated the maximum deflection of the wall by approximately 0.35cm.

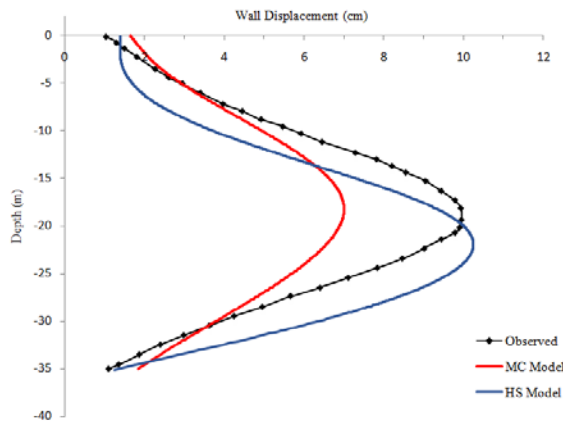


Fig. 4 Comparison of observed diaphragm wall deflections with MC and HS soil models.

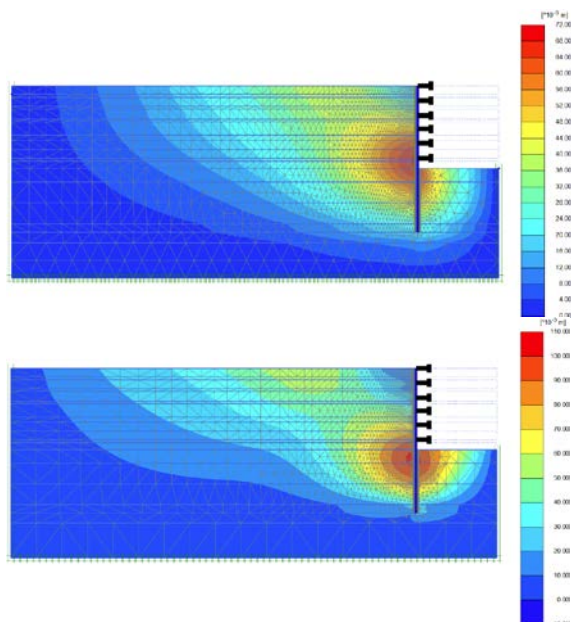


Fig. 5 Comparison of MC and HS simulations.

Firstly, the MC model provides a first order prediction of the excavation procedure and consequently assumes linear elastic behaviour during the excavation process. Within the strain range of 10^{-3} - 10^{-6} , it is common for soils to exhibit non-linear stress-strain behaviour where the variability of stiffness is readily observed. This does not indicate the soil has fully yielded, since the soil is able to almost recover initial stiffness upon unloading, it does however behave differently to the MC assumption of linear elasticity. This directly results in the underestimation of horizontal displacements occurring behind the retaining wall since the soil stress path remains in the linear elastic domain and the development of plastic shear strains are erroneously overlooked. A key feature of the HS model is its capability to capture the elastic non-linear stress-strain relationship that is typically

observed in soils before yielding. This type of hardening mechanism behaviour is referred to as deviatoric hardening, and has been introduced earlier in this paper. When a triaxial test is performed on a soil sample, the shear hardening phenomenon is observed due to the development of shear strains under confining stress conditions. This type of confining stress state is generally experienced by a soil element located behind a retaining wall, where the lateral resistance of the diaphragm wall, coupled with lateral soil pressure induces a deviatoric stress. As the development of plastic deformation increases, the degradation of soil stiffness occurs, thus resulting in considerable diaphragm wall deflection and surface settlement. The MC model is unable to explain this type of behaviour due to its elastic framework which restricts the modelling of plastic shear strain influence.

In addition, the HS model takes into account the stress dependent stiffness of soil. Upon loading, a soil's stiffness is expected to increase due to the densification of soil particles, resulting in a lower volume of voids. This phenomenon is observed when plastic deformation begins to occur, i.e. the permanent rearrangement of the soil's lattice structure. Similarly, when a soil is subject to unloading, exemplary of an excavation scenario, the increasing levels of strain significantly reduce the soil's stiffness attributed by the decrease in confining stress. This highlights the co-dependent relationship between stress and stiffness which the MC model fails to account for. Due to this fundamental behavioural characteristic of soil, constant stiffness cannot be assumed, especially when considering a soil body in undrained conditions. Due to the limitations of the MC model, primary compression stiffness, E_{oed} , is automatically assumed to equal the soil's initial modulus, E_o , and constant elastic stiffness is assumed as a result. This inevitably overestimates the soil body's ability to remain rigid upon unloading as it is unable to account for the softening effect of the soil, thus resulting in the significant underestimation of wall deflection. By alternatively incorporating the three input stiffness parameters into the HS model, E_{50} , E_{ur} , and E_{oed} , this permits the scale of soil deformations to be modelled much more precisely as it takes into account the stiffness variation of soil with loading. Furthermore, this model is able to express a reduction of mean effective stress observed in soft soils when operating in undrained conditions.

The secondary hardening mechanism of the HS model, volumetric hardening, provides an elastic deviatoric hardening limit and when reached plastic volumetric strains are seen to develop. This is another key difference between the MC and HS models, since the MC model is unable to distinguish volumetric strain from shear strain. Thus, when a

soil body is loaded past its preconsolidation pressure, p_o the soil's modulus is typically overestimated. The HS model however derives a cap yield surface based on p_o , which delineates the beginning of plastic volumetric failure, thus avoiding the overestimation of a normally consolidated soil's stiffness. Since the yield surface of the MC model is based upon ϕ and c , the development of plastic strains do not expand or contract the failure surface accordingly. Hence, the yield surface of the MC is fixed. The HS model accommodates the expansion or contraction of the shear yield surface and introduces an additional volumetric cap yield surface which induces the reduction of soil stiffness as a result of high amplitude strain.

CONCLUSION

The TNEC braced excavation case study is one example of the reliability and realistic prediction of soil deformation associated with the application of non-linear elastic constitutive models. The HS model provided a competent result in comparison to observed diaphragm deflections. This was directly due to the model's incorporation of deviatoric and volumetric hardening mechanisms, stress-path dependent stiffness, soil dilatancy and the expansion or contraction of the yield surface with respect to plastic straining. In contrast, the MC model assumed linear elastic perfectly plastic behaviour, i.e. a fixed yield surface, which significantly underestimated the diaphragm wall deflections.

REFERENCES

- [1] Artola J, "A solution to the braced excavation collapse in Singapore" Ph.D. Thesis, 2005, Dep. of Civ. and Env. Eng., Massachusetts Institute of Technology, Cambridge.
- [2] Bishop JFW and Hill R, "A theory of the plastic distortion of a polycrystalline aggregate under combined stresses", Phil. Mag., Vol. 42, 1951, pp. 414-427.
- [3] Calvellido M, "Inverse analysis of a supported excavation through Chicago glacial clays" Ph.D. Thesis, 2002, Dep. of Civ. Eng., North Western University, Illinois.
- [4] Chakrabarty J, Theory of Plasticity, 3rd Ed. Texas: Elsevier Butterworth- Heinemann, 2006.
- [5] Chen WF and Baladi GY, Developments in Geotechnical Engineering- Soil Plasticity. Amsterdam: Elsevier, 1985.
- [6] Clough GW and Reed MW, "Measured behavior of braced wall in very soft clay", J. of Geotech. Eng., Vol. 110, 1984, pp. 1-19.
- [7] Drucker DC, Gibson RE and Henkel D J, "Soil mechanics and work hardening theories of plasticity", Transactions of the American Soc. of Civ. Eng., ASCE, Vol. 122, 1957, pp. 338-346.
- [8] Duncan JM and Chang CY, "Nonlinear analysis of stress and strain in soils", J. of the Soil Mechanics and Foundations Div., ASCE, Vol. 96, 1970, pp. 637-659.
- [9] Hill R, The Mathematical Theory of Plasticity. Oxford: Clarendon Press. 1950.
- [10] Hui X and Hie VAS, "Evaluation of modulus of subgrade reaction for analysis of deep excavation". Ph.D. Thesis, 2007, Dep. of Const. Eng., National Taiwan University of Science and Technology, Taipei.
- [11] Jumikis AR, Theoretical Soil Mechanics. USA: American Book Company, 1969.
- [12] Lim A, Ou C-Y and Hsieh P-G, "Evaluation of clay constitutive models for analysis of deep excavation under undrained conditions", J. of GeoEng., Vol. 5, 2010, pp. 9-20.
- [13] Osouli A, Hashash YMA and Song H, "Interplay between field measurements and soil behavior for capturing supported excavation response". J. of Geotech. and Geoenv. Eng., Vol. 136, 2010, pp. 69-84.
- [14] Ou C-Y, Deep Excavation - Theory and Practice. London: Taylor and Francis Group, 2006.
- [15] Ou C-Y, Liao J-T and Lin H-D, "Performance of diaphragm wall constructed using top-down method", J. of Geotech. and Geoenv. Eng., Vol. 124, 1998, pp. 798-808.
- [16] Ou C-Y, Shiau BY and Wang IW, "Three-dimensional deformation behavior of the Taipei National Enterprise Center (TNEC) excavation case history", Canadian Geotech. J., Vol. 37, 2000, pp. 438-448.
- [17] Phuoc DH, "Excavation behavior and adjacent building response analysis using user defined soil models in PLAXIS" Ph.D. Thesis, 2009, Dep. of Cons. Eng., National Taiwan University of Science and Technology, Taipei.
- [18] Plaxis 2012. Material Models Manual.
- [19] Schanz T, Vermeer PA and Bonnier PG, The hardening soil model: Formulation and verification. Beyond 2000 in Computational Geotechnics – 10 years PLAXIS. Balkema: Rotterdam, 1999.
- [20] Woo SM and Moh ZC, 1990. "Geotechnical characteristics of soils in the Taipei Basin", 10th Southeast Asian Geotech. Conf., Taipei, 1990, Vol. 2, pp. 51-65.
- [21] Yu H-S, Plasticity and Geotechnics. USA: Springer Science and Business Media, 2006.

A NUMERICAL MODEL TO PREDICT SETTLEMENT OF CHEMICALLY STABILISED LANDFILL

Behnam Fatahi¹, Hadi Khabbaz²

^{1,2}School of Civil and Environmental Engineering, University of Technology Sydney (UTS), NSW, Australia,

ABSTRACT

This paper presents the findings of numerical analyses to predict the vertical and horizontal displacements of closed landfills under surcharge load with and without treatment by chemical admixtures. The finite element program, PLAXIS version 9, has been used to evaluate the settlement of a landfill model. The soft soil creep model is used for this analysis. Five layers of solid waste are considered for the landfill to evaluate the effect of depth of stabilisation on settlement of landfill model. Treated and untreated municipal solid waste (MSW) parameters are obtained from the results of the extensive laboratory program performed on MSW samples in this research. The settlement of the landfill model 10 and 20 years after applying the surcharge load for different fly ash-quicklime contents and various depths of improvement is estimated. Results indicate that treatment of MSW reduces the vertical displacement of the landfill model under surcharge load significantly. This reduction is more with higher depths of improvement.

Keywords: Landfill, Settlement, Fly ash, Plaxis

INTRODUCTION

Landfill design and construction technology has progressed rapidly during the past two decades in reaction to more strict controlling requirement and demands. However before any construction on top of landfills, properties of decomposed waste materials should be improved as required. Whether immediately or long time after construction, damage and cracks in structures are a challenging issue for organisation that design and construct foundations on improved landfill sites. Generally, clients require a maximum post construction settlement less than a certain value over the structure's life-time, and limit the differential settlement to a certain change in the grade.

IMPROVEMENT TECHNIQUES

The stabilisation of landfills and waste disposal sites for structural and environmental purposes has been performed through the application of current soil stabilisation and ground improvement techniques. The deep dynamic compaction (DDC) technique is a common ground improvement technique due to its relatively economical and easy application. The deep dynamic compaction technique has been carried out with success in a large range of soils including MSW. Reference [1] reviewed 64 case histories regarding the effectiveness of the DDC on MSW landfill sites.

Their results indicated that the depth of improvement is smaller in MSW compared to cohesionless soils. In addition, the settlement caused by DDC depends on the applied energy and it is in the range of 5% to 25% of the MSW thickness. With deep dynamic compaction large voids reduce and afterward other technique such as fly ash-lime grouting can further reduce the remaining smaller voids. Moreover, the lime/fly ash slurry injection has significant effects on protecting groundwater, neutralising leachate, and for placing curtain walls to prevent leachate migration. Replacement of cement with by-product materials such as fly ash can decrease the stabilisation expenses. Many researchers reported the application of fly ash in geotechnical projects (e.g. [2]-[4]). According to [5], from an economic and environmental viewpoint, rich materials in slaked lime (Ca(OH)_2 , calcium hydroxide), can be treated together with pozzolanic materials, such as fly ash, to develop a cementitious material.

ACTIVATION OF FLY ASH WITH LIME

The reaction of fly ash (FA) with lime results in an immediate improvement of the soil's mechanical properties during stabilisation. It reduces the moisture content of the soil, which has a fast stabilising effect, increases soil pH, preparing a condition for secondary pozzolanic reactions and also it produces heat, which accelerates the chemical

reactions [6]. Many activation methods have been suggested by researchers to treat unstable soils with fly ash. The main purpose of these efforts was to improve the reactivity of the pozzolan, in order to enhance the mechanical and stability characteristics of the mixed product. Extended grinding proposed by [7], curing at high temperatures suggested by [8], alkali activation considered by [9] and [10] and chemical activation procedures presented by [11] are some approaches, which have been practiced to attain that goal.

FINITE ELEMENT MODELING

The finite element program PLAXIS version 9 has been used to evaluate the settlement of stabilised landfill. The cross-section utilised for the numerical analysis is presented in Fig. 1. Five layers of solid waste were considered for the landfill to estimate the effect of depth of stabilisation on landfill settlement. All the dimensions for model are given in Fig. 2. Accordingly, the solid waste properties need to be adjusted to consider various improvement options. The landfill is modeled as a two dimensional plane strain model.

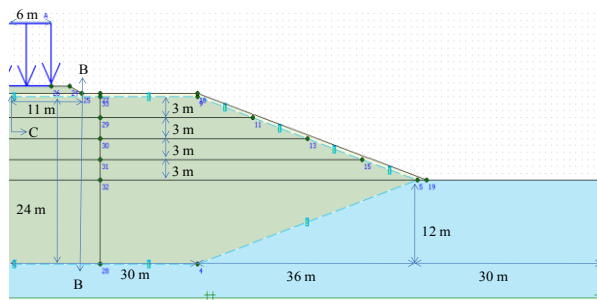


Fig. 1 Dimensions of the model.

MESH GENERATION AND BOUNDARY CONDITIONS

The 15 noded triangle elements were employed in the modeling as shown in Fig. 3 and the mesh generation algorithm of PLAXIS version 9.0 was used in this study. It provides a fourth order

interpolation for displacements and the numerical integration involves twelve stress points. The powerful 15-node element provides an accurate calculation of stresses and failure loads. The two vertical boundaries on both sides are free to move in vertical direction, whereas the horizontal boundary at the base is considered to be fixed in both vertical and horizontal directions as presented in Fig 1. The foundation soil was considered to be stiff soil and its stability and deformation were not considered directly in this analysis. Cross-sections of generated mesh have been shown in Fig. 4.

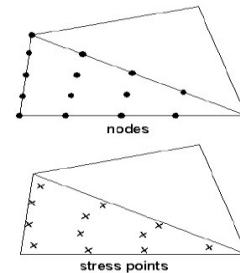


Fig. 3 15-noded triangle element used in modeling.

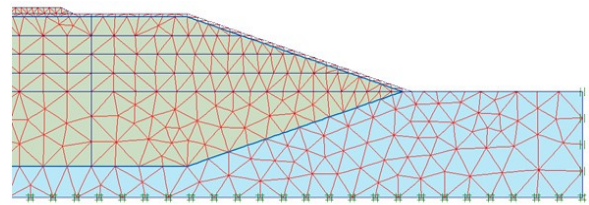


Fig. 4 Cross-section of generated mesh.

ADOPTED MATERIAL MODELS

All soils exhibit some creep, and primary compression is thus always followed by a certain amount of secondary compression. The secondary compression (for instance during a period of 10 or 30 years) can be a certain percentage of the primary compression. This is for instance the case when constructing embankments over closed landfill sites. Indeed, the primary settlement of footings and embankments are usually followed by a substantial

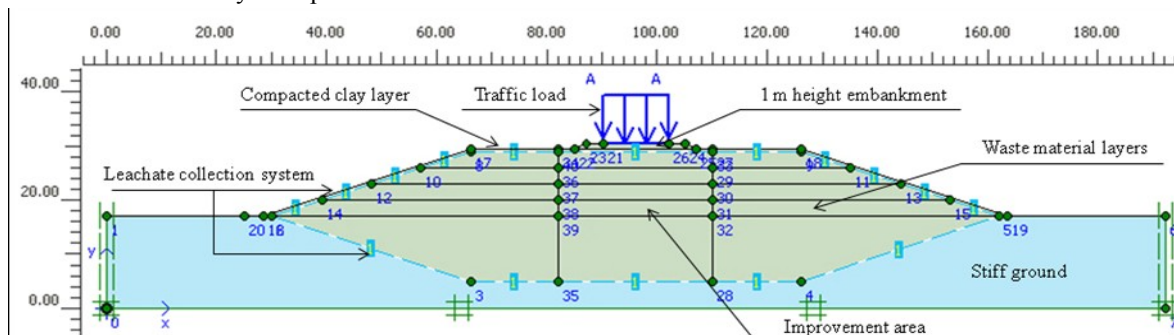


Fig. 2 Cross-section of the numerical model.

creep settlement in later years. In such cases it is desirable to estimate the creep from FEM-computations. The soft soil creep model was used for this analysis due to several characteristics such as:

- Stress-dependent stiffness
- Distinction between primary loading and unloading-reloading
- Secondary compression
- Memory of pre-consolidation stress
- Failure behaviour according to the Mohr-Culomb criterion

Material Parameters

Municipal solid waste parameters used in FEM analysis for different contents of stabiliser are presented in Table 1. In addition, parameters used for compacted clay as a cover layer of closed landfill model and road embankment are summarised in Table 2.

Some of the important waste properties required for the analyses are the unit weight, the shear strength, the permeability, the primary compression index and the secondary compression index. These parameters were obtained from the results of the extensive laboratory program performed on the MSW samples.

The unit weight of solid waste is an important factor in evaluating the settlement of landfills. The unit weight values of MSW specimens changed slightly for specimens mixed with different fly ash-quicklime (QL) contents.

The results obtained from consolidated drained (CD) triaxial tests confirmed that the shear strength parameters are strongly influenced by the fly ash-quicklime content mixed with MSW. The shear strength parameters of solid waste estimated in this study at different fly ash-quicklime content also presented in Table 1. It reveals that c and ϕ values of MSW specimens increased with increasing the fly ash-quicklime content to MSW specimens. In addition, the results from permeability tests indicated that with an increase in fly ash-quicklime content in the MSW specimen, the coefficient of permeability reduced. The corresponding numbers presented in Table 1.

Moreover, from consolidation test performed it has been demonstrated that the value of C_c decreased by 30%, when the fly ash-quicklime content increased from 0 to 26.7%. By increasing the fly ash-quicklime content, the treated specimens indicated more resistance against the compressive loading and less compressibility characteristics. Furthermore, the creep results clearly shows that the value of the secondary compression index, C_{α} , for MSW specimens decreased from 0.052 to 0.033, while fly ash-quicklime content increased from 0 to 26.7%. This means that, for any given time period, the volume change during secondary compression is more for untreated specimens than treated with fly ash-quicklime. Hence, fly ash-quicklime admixture is effective in reducing the volume change during the primary consolidation as well as the secondary consolidation. The corresponding values for the compression index and the secondary compression index are also reported in Table 1.

ANALYSIS TYPE

The settlement of proposed landfill model in PLAXIS was computed using 'consolidation analysis' as a calculation type and 'staged construction' as a loading input. Based on Table 3 the effects of various fly ash-quicklime contents and different depths of improvement were examined. The model presents 30 years old closed landfill and selected MSW materials are decomposed waste. In the first stage of modelling, the filling process of landfill was completed in 4 stages (each stage consisted of 4 metres over 30 days). After filling the site with decomposed waste material, in landfill model, the waste was then covered with a 0.5m layer of compacted clay. After this the model evaluated the settlement of the landfill after 30 years of self weight of MSW. In the next stage a 1m thick road embankment was constructed on the closed landfill model over a 6 month period, and then a traffic loading of 20 kPa with a reduction factor of 0.5 was applied on to the road embankment. In the final step, the vertical and horizontal displacement of the landfill model 10 and 20 years after applying the traffic load for different amounts of fly ash-quicklime and various depths of improvement were calculated.

Table 1 Parameters for soft soil creep model in FEM analysis

FA-QL Content %	Unit weight γ_{sat} kN/m ³	Void ratio e_0	Cohesion C kN/m ²	Friction angle ϕ°	permeability K m/day	Recompression index c_r	Compression index c_c	Secondary compression index c_{α}
0%-0%	14.6	0.63	11	29	0.012	0.075	0.33	0.052
5%-1.7%	14.8	0.61	20	33	0.0092	0.07	0.29	0.045
10%-3.3%	15	0.59	26	36	0.0088	0.068	0.28	0.04
15%-5%	15.2	0.57	29	38	0.0088	0.064	0.24	0.036
20%-6.7%	15.4	0.56	30	39	0.0082	0.061	0.23	0.033

RESULTS AND DISCUSSION

Vertical Settlement 10 Years after Applying Traffic Load

The results of the numerical predictions of the model were estimated in PLAXIS. Table 3 presents the vertical displacements of the landfill model 10 years after applying the traffic load at the midpoint below the embankment. These numbers reported based on different depths of treatment and various fly ash-quicklime contents.

The results predicted that the vertical settlement of untreated landfill model is about 370 mm 10 years after applying traffic load. In addition, the result illustrated that treating MSW with fly ash-quicklime reduced the vertical displacement of the model significantly. This reduction is more with higher depths of improvement. It revealed that for 3m improved landfill with 26.7% fly ash-quicklime the vertical settlement reduced 20% (from 370 mm to 296 mm) and this reduction for 6m, 9m, 12m and 24m improved landfill was 32%, 40%, 46% and 58%, respectively.

Table 2 Model parameters used for cover layer and road embankment.

ID	γ_t kN/m ³	c kPa	ϕ°	ψ°	E kPa	ν
Cover	17.5	10	25	0	2.5E4	0.35
Road	18	5	30	5	6.5E4	0.3

Vertical Settlement 20 Years after Applying the Traffic Load:

The outcomes of the numerical estimation of the model are predicted in PLAXIS. Table 4 shows the vertical displacement of the landfill model 20 years after applying the traffic load at the midpoint below the embankment. These numbers are based on different depths of treatment and various amounts of fly ash-quicklime. The results showed that the settlement of the untreated landfill model is about 536 mm 20 years after applying traffic load. Moreover, these result indicated that treatment of MSW with fly ash-quicklime reduced vertical displacement of the model significantly, and this reduction was more for higher depths of improvement. It showed that 20 years after applying traffic load on 3m improved landfill with 26.7% fly ash-quicklime the vertical settlement reduced by 19% (from 536 mm to 444 mm) and this reduction for 6m, 9m, 12m, and 24m improved landfill is 29%, 37%, 43%, and 55%, respectively.

Furthermore, Fig. 5 and Fig. 6 indicate the effects that the amounts of fly ash-quicklime have

on the vertical displacement versus time for 3m and 9m improvement depths at the midpoint below the embankment. These figures clearly indicated that increasing the amount of fly ash-quicklime reduced vertical settlement to a large extent. It can also be inferred that increasing the depth of improvement significantly decreases vertical settlement in the landfill model.

Table 3 Vertical displacement of the landfill model 10 years after applying traffic load.

Treatment Depth (m)	Vertical displacement for various treatment depth (mm)				
	3	6	9	12	24
FA-QL (%)					
Untreated	370	370	370	370	370
5%FA+1.7% QL	328	309	283	271	248
10%FA+3.3% QL	312	277	255	239	207
15%FA+5% QL	301	258	232	213	172
20%FA+6.7% QL	296	251	221	201	154

Table 4 Vertical displacements of the landfill model, 20 years after applying the traffic load.

Treatment Depth (m)	Vertical displacement for various treatment depth (mm)				
	3	6	9	12	24
FA-QL (%)					
Untreated	536	536	536	536	536
5%FA+1.7%QL	486	451	426	408	372
10%FA+3.3%QL	466	419	387	363	311
15%FA+5% QL	451	394	356	327	262
20%FA+6.7%QL	444	383	339	308	244

Horizontal Displacement 10 Years after Applying the Traffic Load

The result showed that the treatment of MSW with fly ash-quicklime reduced the maximum horizontal displacement of the model, and this

reduction was more for higher depths of improvement. Figure 7 shows the horizontal displacement versus depth for landfill treated with 26.7% fly ash-quicklime with various depths of improvement in a section below the toe of embankment. It can be seen that at any specific depth below the toe of embankment, with increasing depth of improvement, the horizontal displacement was reduced and maximum horizontal displacement occurred at higher depths. Moreover, Fig. 8 shows the horizontal displacement versus depth for 9m improved landfill treated with various amounts of fly ash-quicklime below the toe of embankment. This proves that increasing the amount of fly ash-quicklime reduced the horizontal displacement at any specific depth, and also that maximum horizontal displacement occurred at higher depths.

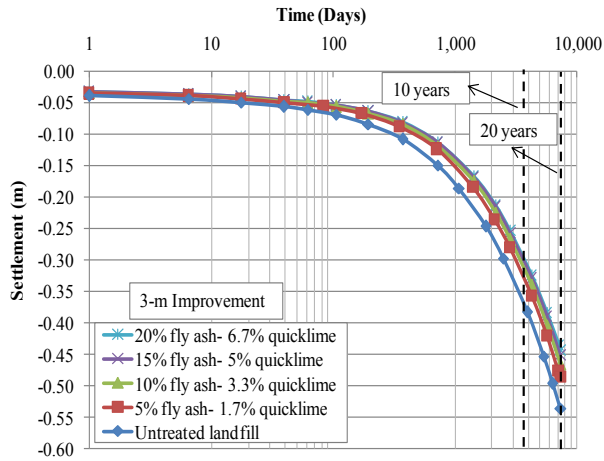


Fig. 5 Vertical settlement versus time for 3-m improved landfill.

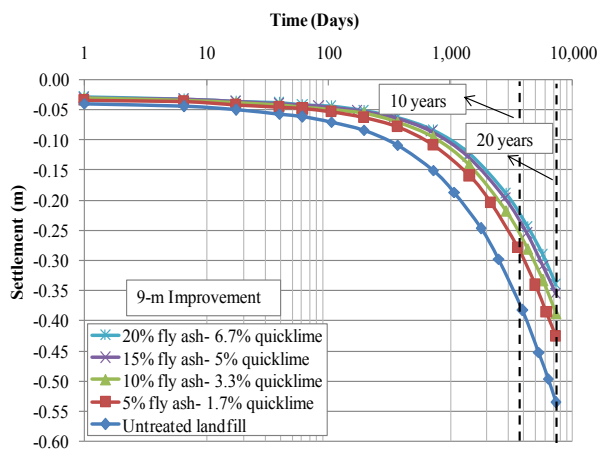


Fig. 6 Vertical settlement versus time for 9-m improved landfill.

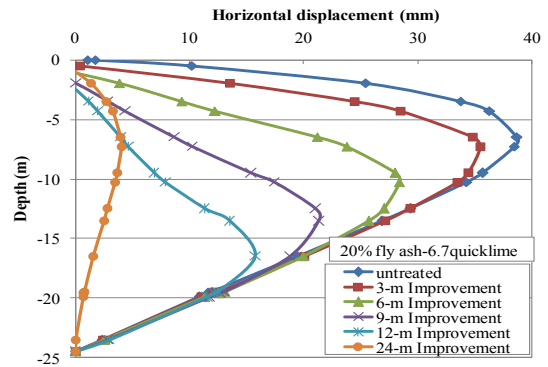


Fig. 7 Horizontal displacement versus depth for the landfill treated with 26.7% fly ash-quicklime content.

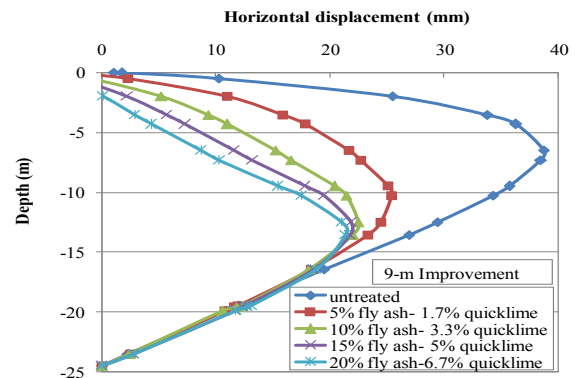


Fig. 8 Horizontal displacement versus depth for 9-m improved landfill.

VALIDATION

Finite element results are validated based on results of triaxial tests conducted in the laboratory on the treated MSW. Finite element analysis of triaxial model (for treated MSW treated with 15% fly ash+5% quicklime and dimensions of 100 mm height and 50 mm diameter) was carried out using PLAXIS 2D. The problem was considered as an axisymmetry model and the nodes on left vertical boundary was restricted to displace horizontally (horizontal fixity) but allowed to undergo vertical displacement whereas all the displacements of the nodes at the bottom surface was arrested (total fixity). A typical axisymmetric model under triaxial loading condition is shown in Fig. 9. The treated MSW material was simulated with soft soil creep model with 15 node triangular elements. The material properties used in the finite element analysis are given in Table 1.

Figure 10 shows the comparison between the laboratory measurement and finite element predictions. As indicated the selected soft soil creep model (which is based on modified cam-clay model)

incorporated in the finite element solution, results in reasonable agreement between the measurements and predictions.

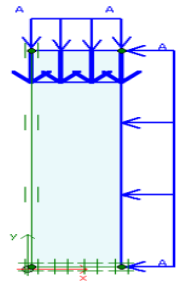


Fig. 9 Typical axisymmetric geometry model

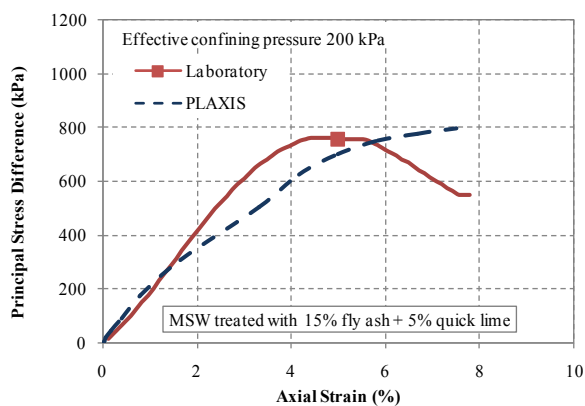


Fig. 10 Comparison between the laboratory measurements and finite element predictions

CONCLUSIONS

A finite element program, PLAXIS version 9, was used to evaluate the settlement of the landfill model under traffic load, with and without treatment by fly ash-quicklime. The soft soil creep model was used for this analysis. Five layers of solid waste were used for the landfill model to evaluate how the depth of stabilisation affected the vertical and horizontal displacement of the model. Treated and untreated MSW parameters used for the model were obtained from the results of the extensive laboratory program performed on treated and untreated MSW samples. The vertical and horizontal displacement of the landfill model 10 and 20 years after applying the traffic load, and with different amounts of fly ash-quicklime and various depths of improvement, were estimated. The results of the model analyses with PLAXIS showed that treating MSW with fly ash-quicklime reduced the vertical displacement under traffic load at the midpoint below the embankment. Horizontal displacement of the landfill model at a specific depth in a section below the toe of the embankment under traffic load was also

significantly reduced. These reductions in vertical and horizontal displacement were greater with higher depths of improvement. For 3m improved landfill with 26.7% fly ash-quicklime, the vertical settlement 10 years after applying traffic load below the embankment was reduced 20% (from 370 mm to 296 mm) and this reduction for 6m, 9m, 12m and 24m improved landfill was 32%, 40%, 46% and 58%, respectively.

REFERENCES

- [1] Zekkos D, Flanagan M (2011) Case Histories-based Evaluation of the Deep Dynamic Compaction Technique on Municipal Solid Waste Sites. *Geo-Frontiers*, pp 529-538
- [2] Kawasaki T, Niina A, Saitoh S, Suzuki Y, Honjo Y (1981) Deep mixing method using cement hardening agent. Proc 10th Int Conf on Soil Mechanics and Foundation Engineering, Southeast Asian Geotechnical Soc Bangkok, pp 721-724
- [3] Kitazume M, Yamazaki H, Tsuchida T (2000) Recent soil admixture stabilization techniques for port and harbor constructions in Japan—deep mixing method, premix method, light-weight method. Proc Int Seminar on Geotechnics in Kochi, ISGK 2000, Kochi, Japan, pp 23-40
- [4] Kehew EA (1995) Geology for engineers and environmental scientists, 2nd edn. Prentice Hall, Englewood Cliffs, pp 295-302
- [5] Horpibulsuk S, Phetchuay C, Chinkulkijniwat A (2012) Soil stabilization by calcium carbide residue and fly Ash. *J Mater Civil Eng* 24(2):184-193
- [6] Janz M, Johansson S (2002) The function of different binding agents in deep Stabilization. *Svensk djupstabilisering Report 9*
- [7] Bouzoubaa N, Zhang MH, Bilodeau A, Malhotra VM (1997) The effect of grinding on the physical properties of fly ashes and a Portland cement clinker. *Cem Concr Res* 27(12):1861-1874
- [8] Shi C, Day RL (1993) Acceleration of strength gain of lime-pozzolan cements by thermal activation. *Cem Concr Res* 23(4):824-832
- [9] Palomo A, Grutzeck MW, Blanco MT (1999) Alkali-activated fly ashes; a cement for the future. *Cem Concr Res* 29 (8):1323-1329
- [10] Xie Z, Xi Y (2001) Hardening mechanisms of an alkaline-activated class F fly ash. *Cem Concr Res* 31(9):1245-1249
- [11] Shi C, Day RL (1995) Acceleration of the reactivity of fly ash by chemical activation. *Cem Concr Res* 25(1):15-21

SHEAR PROPERTIES OF HIGH-DENSITY BENTONITE-SAND MIXTURE UNDER UNSATURATED AND SATURATED CONDITIONS

Takeshi Kodaka¹, Ying Cui¹ and Hidenori Takada¹

¹Department of Civil Engineering, Meijo University, Japan

ABSTRACT

The use of high-density bentonite-sand mixtures as buffer and sealing materials at the disposal sites of radioactive waste is expected. Although the bentonite-sand mixtures at disposal sites will be in an unsaturated condition during the construction period, they will gradually become saturated by reflooding in the ground water after the service commencement. In the present paper, a series of unexhaust-undrained triaxial tests is performed to study the shear properties of a high-density bentonite-sand mixture. A double cell-type triaxial apparatus has been newly developed to observe the dilatancy behavior of the bentonite-sand mixture with various degrees of saturation. As a result, in the case of a low degree of saturation, the shear strength is relatively large and volumetric expansion is observed. However, in the case of a high degree of saturation, the shear strength is small and volumetric compression is observed. These results suggest that the mechanical properties of high-density bentonite rapidly change with an increasing degree of saturation.

Keywords: Bentonite-sand mixture, Triaxial test, Unsaturated soil, Dilatancy, Buffer material

INTRODUCTION

High-density bentonite-sand mixtures are planned for use as buffer materials in the geological disposal of high-level radioactive waste. Their use as buffer and sealing materials at disposal sites of low level radioactive waste is also expected. Since high-density bentonite-sand mixtures are produced from crushed bentonite powder and dry silica sand under an unsaturated condition, the mixtures are thought to remain in an unsaturated condition until reflooding in the ground water after the service commencement. It will take a long time for the mixtures to gradually become saturated due to their extremely low permeability [1]-[2]. It is important, therefore, to study the shear and deformation properties of bentonite-sand mixtures under both saturated and unsaturated conditions in order to design disposal sites.

Triaxial tests on saturated bentonite-sand mixtures have been performed by many other research groups, e.g. [3], [4]. Only a few studies, however, have been done on the mechanical properties of unsaturated bentonite-sand mixtures. Kodaka and Teramoto [2] and Kodaka et al. [5] performed a series of direct shear box tests on unsaturated bentonite-sand mixtures using a high pressure direct shear box apparatus. They showed that the shear properties of unsaturated and saturated bentonite-sand mixtures are quite different from each other. However, the direct shear box test is not an element test, and thus, it is difficult to use the obtained test results for considering the constitutive equation.

In the present study, a series of triaxial tests on

an unsaturated bentonite-sand mixture, with various degrees of saturation, is performed under an unexhaust-undrained condition. A double cell-type triaxial apparatus has been newly developed for this study to observe the dilatancy behavior of the high-density bentonite-sand mixture during shearing.

TESTING PROCEDURE

Testing Sample and Specimen Preparation

Specimens used in this study were prepared by the following method: Powder bentonite (70% wt) and silica sand (30% wt) were mixed well and then distilled water was added to the mixed sample to create a specified moisture content. The mixed wet sample was then put in a rigid cylindrical steel mold and one-dimensionally compressed by a hydraulic jack to become a cylindrical high-density specimen, which has a prescribed dry density and degree of saturation. After the compressed specimen was taken out of the steel mold, about 5 mm were removed from the top and bottom ends of the specimen, since the ends of the specimen are apt to be inhomogeneous due to compression. The specimens prepared in the above manner are 30 mm in diameter and 70 mm in height. The dry density of the compressed specimens is 1.60 Mg/m³.

Three types of specimens, based on degrees of saturation, are adopted. The first type consists of initial moist specimens into which no additional water is added to the mixed sample, except for the water initially contained in the bentonite powder. The second type consists of quasi-saturated specimens, whose degrees of saturation are over

90%. And the third type consists of various moist specimens, which are adjusted by adding water.

Triaxial Test Apparatus and Testing Conditions

The triaxial test apparatus used in this study is a double cell-type, which has an inner pressure cell as well as an ordinary outer pressure cell. An overview of the apparatus and an enlarged photo of the inner cell are shown in Figs. 1(a) and (b), respectively. Figure 2 gives a schematic view of the apparatus. In order to grasp the changes in volume of the unsaturated specimen, the drainage which goes in and out of the inner pressure cell is measured.



(a) Overview of triaxial test apparatus



(b) Specimen set in inner pressure cell

Fig.1 Triaxial test apparatus developed for this study.

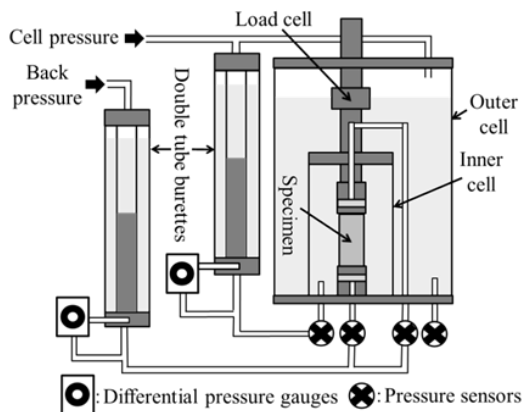


Fig.2 Schematic view of the test apparatus.

A triaxial specimen is set in the inner pressure cell and then isotropically compressed under an undrained–unexhaust condition. Confining pressure levels of 0.1 and 0.5 MPa are adopted here. Triaxial compression is conducted up to the axial strain of 15% under an undrained–unexhaust condition with an axial loading rate of 0.5%/min. The undrained–unexhaust condition is thought to be most suitable for grasping the shear properties of the unsaturated bentonite–sand mixture just at its respective degrees of saturation. Table 1 lists the test cases.

Table 1 Testing cases

Initial moist specimens	$S_r(\%)$	$\sigma_3(\text{MPa})$
IM1-1	32	0.1
IM1-2	34	0.1
IM5-1	34	0.5
IM5-2	34	0.5
Quasi-saturated specimens	$S_r(\%)$	$\sigma_3(\text{MPa})$
QS1-1	92	0.1
QS1-2	90	0.1
QS5-1	91	0.5
QS5-2	91	0.5
Various moist specimens	$S_r(\%)$	$\sigma_3(\text{MPa})$
VM1-1	42	0.1
VM1-2	63	0.1
VM1-3	77	0.1
VM1-4	88	0.1
VM5-1	44	0.5
VM5-2	63	0.5
VM5-3	73	0.5
VM5-4	87	0.5

Note: S_r and σ_3 express the degree of saturation of the specimens and the adopted confining pressures, respectively.

TESTING RESULTS

Test Results of the Initial Moist Specimens

Figure 3 shows the undrained–unexhaust test results for the initial moist specimens. In this case, exactly the same experiments were conducted twice for each confining pressure to check the accuracy and reproducibility. In the deviator stress – axial strain relations, shown in Fig. 3(a), the apparent peak strength, the subsequent strain softening and the residual strength can be seen. The maximum values for the deviator stress in this case are very large compared to those of the cases of a low degree of saturation. This tendency shows the typical shear characteristics of stiff and brittle geomaterials. Clear shear bands and cracks were observed in the specimens at the final stage of shearing.

The volumetric strain – axial strain relations are illustrated in Fig. 3(b). Since positive values for the volumetric strain express the volumetric compression of the specimens, volumetric expansion

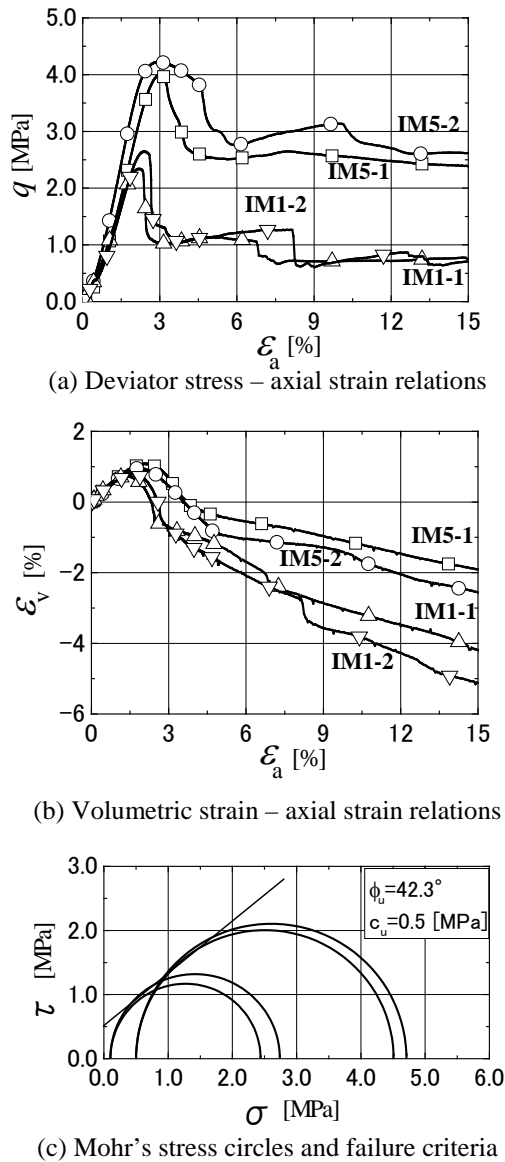


Fig. 3 Test results of the initial moist specimens.

occurs at the state of post-peak and the following residual state. This dilatancy behavior of the unsaturated specimens can be measured using the double cell-type triaxial apparatus.

Figure 3(c) shows the Mohr's stress circles and Mohr-Coulomb failure criteria. A very large internal friction angle is determined from this figure.

Test Results of the Quasi-saturated Specimens

Figure 4 shows the undrained–unexhaust test results for the quasi-saturated specimens. This case was also conducted using the same two specimens for each confining pressure. In all cases, the deviator stress monotonously increases and the maximum values for the deviator stress are very small compared with the peak strengths of the initial moist specimens. Although the specimens for this case are

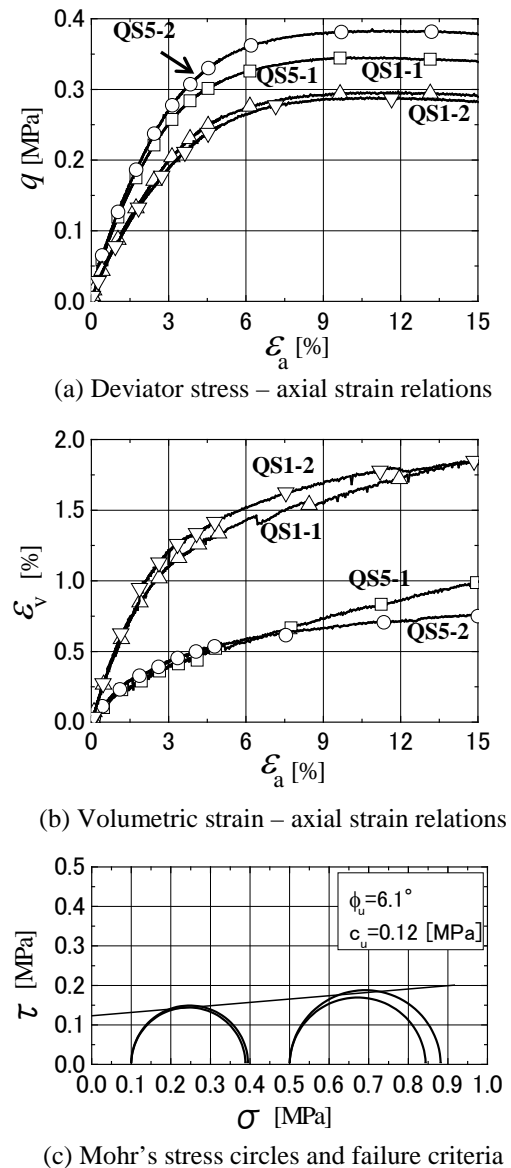


Fig. 4 Test results of the quasi-saturated specimens.

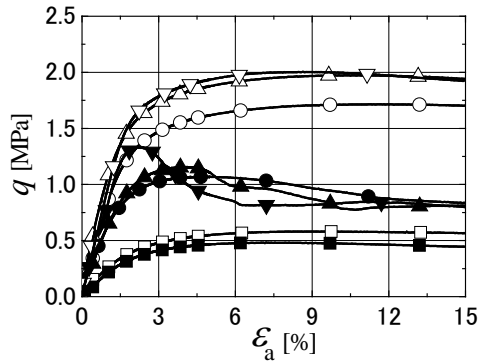
near saturation, relatively small volumetric compression occurs during the undrained–unexhaust shearing. In the case of larger confining pressure, the observed volumetric compression becomes smaller.

As shown in Fig. 4(c), the internal friction angle for the quasi-saturated specimens is very small. However, this angle would be zero if the specimens were fully saturated.

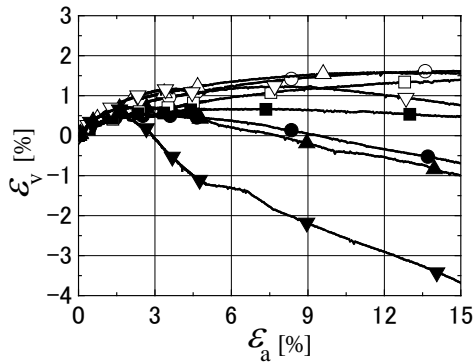
Test Results of Various Moist Specimens

Figure 5 shows the undrained–unexhaust test results for the various moist specimens. Four stages of saturation are adopted, which are covered from low S_r near the initial moist specimens to high S_r near the quasi-saturated specimens. As illustrated in the stress-strain relations for the 0.1 MPa confining

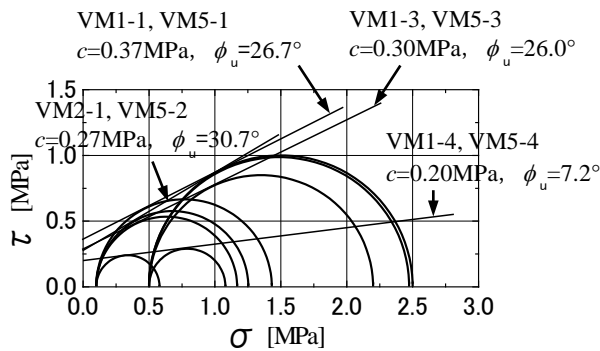
▼ VM1-1 ▲ VM1-2 ● VM1-3 ■ VM1-4
 ▽ VM5-1 △ VM5-2 ○ VM5-3 □ VM5-4



(a) Deviator stress – axial strain relations



(b) Volumetric strain – axial strain relations



(c) Mohr's stress circles and failure criteria

Fig. 5 Test results of the various moist specimens.

pressure case, i.e., VM1-1~4, the tendency of the shear properties dramatically changes with the changing degree of saturation. Typical strain softening behavior is observed in the case of a lower degree of saturation. The degree of strain softening, e.g., the difference between the peak strength and the residual strength, gradually decreases with an increasing degree of saturation. On the other hand, the deviator stress monotonously increases during shearing in all specimens of 0.5 MPa.

The dilatancy characteristics shown in Fig. 5(b) are directly related to the results of the above-mentioned stress-strain relations. Namely, although the apparent changes in dilatancy characteristics with different degrees of saturation can be observed in the lower confining pressure case of VM1-1~4, no clear difference is confirmed in the higher confining pressure case of VM5-1~4.

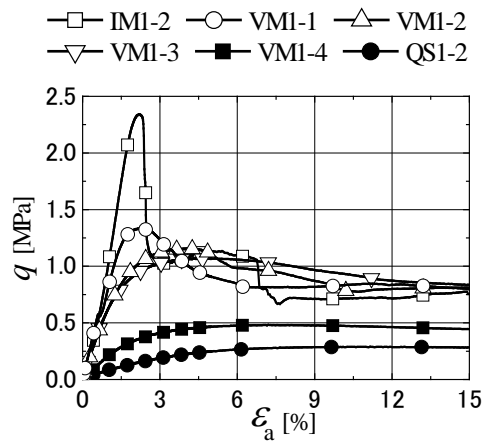
Figure 5(c) shows that the internal friction angles of the unsaturated specimens are more than 26 degrees, except for the high S_r cases, i.e., VM1-4 and VM5-4. In these cases, the internal friction angle slightly decreases with an increasing degree of saturation. However, there is a gap in the internal friction angles between 87% and 75%.

Effects of Degree of Saturation on Mechanical Properties of Bentonite-sand Mixture

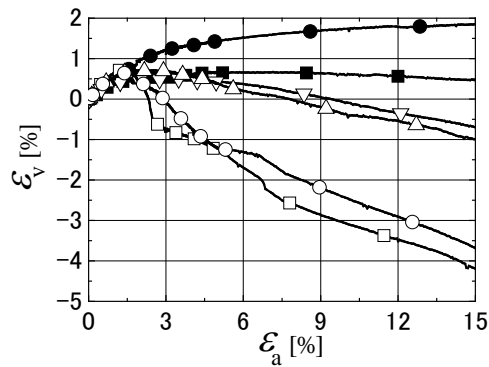
The over-all test results for the cases of confining pressures of 0.1 MPa and 0.5 MPa are shown in Figs. 6 and 7, respectively. There is a large difference in shear strength between the initial moist specimens and the quasi-saturated specimens. The former specimens have quite a high maximum deviator stress and strain softening behavior, while the latter specimens show a very low maximum deviator stress and strain hardening behavior. The dilatancy properties of the two kinds of specimens also show the opposite tendency. Hence, the volumetric strains at the shearing of the former and the latter specimens develop dilatantly and contractively, respectively.

The various moist specimens interpolate between the initial moist specimens and the quasi-saturated specimens. The stress – strain curves of the various moist specimens are placed in between the curves of those two types of specimens, as shown in Figs. 6(a) and 7(a). Therefore, the shear properties of the bentonite-sand mixture depend on the degree of saturation of the specimen. The maximum deviator stress and the internal friction angle decrease with an increasing degree of saturation. There is a gap between VM1-3 (VM5-3) and VM1-4 (VM5-4). This result suggests that the mechanical properties rapidly change at relatively high degrees of saturation.

The supposed saturation process of the bentonite-sand mixture at real disposal sites is that the high-density bentonite-sand mixture is constructed under the condition of a low degree of saturation and then the mixture is gradually saturated. In this study, however, water is added to the granular material mixed with bentonite powder and sand under an unconfined condition and then compacted to be of high-density. Thus, it should be noted that the saturation process of the mixture may be different from the actual condition.

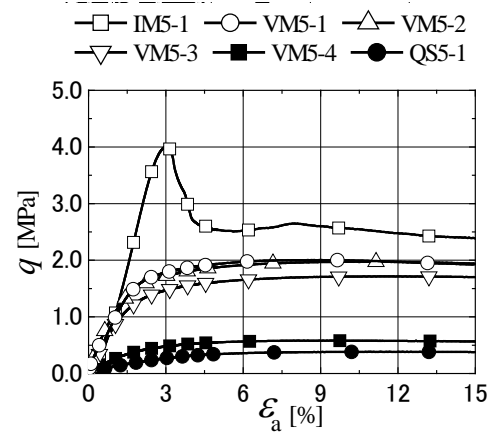


(a) Deviator stress – axial strain relations

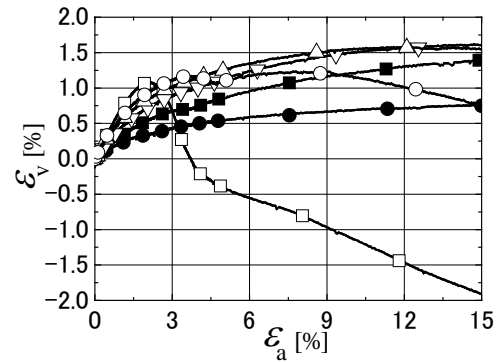


(b) Volumetric strain – axial strain relations

Fig. 6 Test results in the low σ_3 case.



(a) Deviator stress – axial strain relations



(b) Volumetric strain – axial strain relations

Fig. 7 Test results in the high σ_3 case.

CONCLUSION

A series of unexhaust-undrained triaxial tests was performed to study the shear properties of a high-density bentonite–sand mixture. From the test results of this study, in the case of a low degree of saturation, the shear strength is relatively large and volumetric expansion is observed. However, in the case of a high degree of saturation, the shear strength is small and volumetric compression is observed. These results suggest that the mechanical properties of high-density bentonite rapidly change with an increasing degree of saturation.

ACKNOWLEDGEMENTS

The authors wish to express their sincere appreciation to Dr. Kawaguchi of Kitami Institute of Technology for his great support regarding the manufacture of the testing apparatus. Financial support for this study has been provided by the Kajima Foundation, Japan.

REFERENCES

- [1] Komine K and Ogata N, “Experimental study on swelling characteristics of sand-bentonite mixture for nuclear waste disposal” *Soils and Foundations*, Vol.39, No.2, 1999, pp83-97.
- [2] Kodaka T and Teramoto Y, “Shear Failure Behavior of Compacted Bentonite” in *Proc. Int. Symp. on Prediction and Simulation Methods for Geohazard Mitigation, IS-Kyoto 2009*, pp.331-337.
- [3] Namikawa T and Sugano T, “Shear properties of buffer material 1”, *Technical Report of Power Reactor and Nuclear Fuel Development Corporation, PNC TN8410 97-074*, 1997 (in Japanese).
- [4] Takaji K and Suzuki H, “Static mechanical properties of buffer material”, *Technical Report of Japan Nuclear Cycle Development Institute, JNC TN8400 99-041*, 1999 (in Japanese).
- [5] Kodaka T, Teramoto Y, Hirate T and Motoyama Y, “Density changes and sealing performance of damaged compacted bentonite” in *Proc. 14ARC, 2011, Paper ID:197*.

ENVIRONMENTAL CONDITION INDEX FOR ESTIMATION ON EUTROPHIC STATE OF ENCLOSED AQUIFER ECOSYSTEM

Kazuhito Murakami¹, Michio Gomyo¹, Saki Agatsuma¹ and Yoshimasa Amano²

¹Department of Life and Environmental Sciences, Chiba Institute of Technology, Japan; ²Department of Applied Chemistry and Biotechnology, Chiba University, Japan

ABSTRACT

To evaluate the effect of sediment treatment on aquifer ecosystem, a new ecological index that is composed of water quality, sediment quality and biota quantity was proposed in this study. According to ECI (Environmental Condition Index), DAF treatment (Dissolved Air Flotation) + MgO sprinkling was assessed as the most efficiency method for improvement of eutrophicated ecosystem, that is, this method can make the organic matter quantity in aquatic ecosystem minimum level in comparison with other sediment treatment method. Also, for application of this method to real field remediation such as eutrophicated lake, marsh, reservoir and so on, more detailed analysis for treatment function and optimum condition of sediment treatment was considered to be necessary.

Keywords: Environmental condition index, Aquifer ecosystem, COD, IL, Chl.a, Eutrophicated lake

INTRODUCTION

The countermeasure to the nutrient elution from eutrophicated sediment is necessary to be conducted with the cut of the inflow loading of nutrient from a basin area of eutrophicated lake and marsh. Furthermore, it is reported that the eluted nutrient loading from the accumulated sediment reaches 5-10 times of the inflow loading. This constant eutrophication problem is in the point that organic polluted mud is accumulated to the inflow rivers and the lake itself, it is necessary that the organic sediment, which is over quality for water quality and water livings, is taken away from the inside to the outside of the ecosystem [1]. However, the direct removal methods such as digging / boring have a risk, which disturb the lake ecosystem, and some organic matter and nutrient should be left in the sediment to preserve macrobenthos and so on. In this case, water quality purification will be expected by prevention of nutrient elution from the sediment.

In present study, DAF (Dissolved Air Flotation) treatment, MgO sprinkling and CaO sprinkling as CRM (Chemical Remediation Materials) treatment were conducted, and the effect of these treatment methods on the lake ecosystem was evaluated from the viewpoint of ecological influence. Furthermore, a new index that indicating synthetic state of ecosystem was proposed and the effect of sediment treatment on the lake ecosystem was evaluated using this index.

PROPOSAL OF ENVIRONMENTAL CONDITION INDEX

For evaluation and/or assessment of an environment, a variety of index, such as diversity index for biota (for example, Shannon index, Simpson's index, and so on), has been proposed and applied. Most of these indexes are based on biotic diversity, because biota, whether fauna or flora, indicates synthetic results of environmental fluctuations, that is, water and sediment condition are reflected to biota. Although the biotic index can be recognized as one of the most essential indexes to evaluate the environmental condition, it is not enough to indicate the water/sediment condition. It is recognized that water and/or sediment condition is not reflected perfectly to biotic index, and these three elements, *i.e.* water, sediment and biota, are related with one another in multiplication [2].

In this study, a new ecological index for indicating the environmental condition was calculated using the data that is obtained from the results of microcosm experiment.

The environmental condition index (ECI) was calculated by the equation (1) as described below;

$$ECI = \sqrt[3]{C_{(COD)} \times C_{(IL)} \times C_{(Chl.a)}} \quad (1)$$

Where,

$$\begin{aligned} C_{(COD)} &= \sum L_{COD,i} / COD_{mean} \\ C_{(IL)} &= \sum L_{IL,i} / IL_{mean} \\ C_{(Chl.a)} &= \sum L_{Chl.a,i} / Chl.a_{mean} \end{aligned} \quad , \quad \text{and}$$

This index has no mathematical dimension. $L_{COD,i}$, $L_{IL,i}$ and $L_{Chl.a,i}$ mean the existed quantity of COD,

IL and Chl.a in microcosm during the incubation period, respectively. COD_{mean} , IL_{mean} and $Chl.a_{mean}$ mean the average concentration of COD, IL and Chl.a in microcosm. This index means water condition by COD (Chemical Oxygen Demand) concentration, sediment condition by IL (Ignition Loss) concentration, and phytoplankton quantity by Chl.a (Chlorophyll a) concentration. When ECI is low value, the quantity of organic matters in the environment is low level, and when ECI is high value, the quantity of organic matters is high level in the opposite direction. The concept of ECI is indicated in Fig.1. The organic matters are recognized in general as one of main pollutant for aquatic ecosystem. This ECI can indicate the pollution level of organic matters in aquatic ecosystem, such as lake, marsh, reservoir, river, sea, and so on.

EXPERIMENTAL PROCEDURES

Water and sediment were collected from Lake Tega that locates in the northwest area of Chiba prefecture in east Japan and is well known as one of the most polluted enclosed aquifer.

Sediment Treatment

DAF treatment was conducted as follows; 50L of water was poured into 80L volume reactor, then 7kg(w.w.) of sediment was inoculated. Micro bubble was continuously injected under the sediment to water, and the poly ferric sulfate as coagulant (4L of 200mg/L) was added. Sediment with much organic matter can be divided into froth and treated sediment in this process [3], [4].

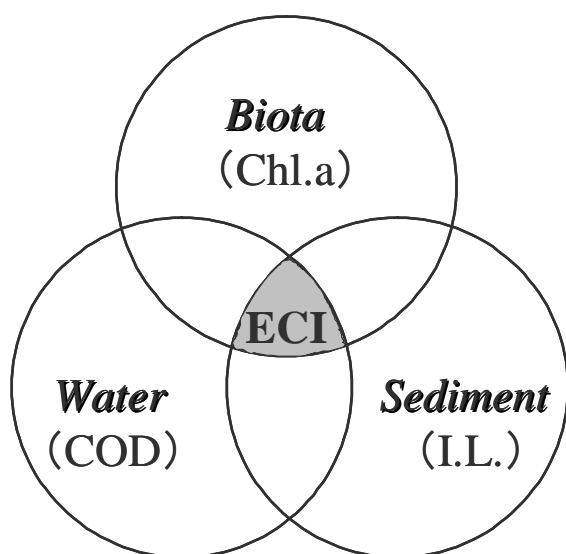


Fig.1 Concept of Environmental Condition Index (ECI)

CRM treatment was conducted as follows; MgO and CaO were prepared to sprinkle on the surface of sediment in experimental microcosm. These chemical agents are expected to control the elution of nutrient salts from sediment layer [4], [5].

Microcosm Culture

The microcosm experiment was conducted using 470ml volume glass vessel, and with 4 series culturing. Those are,

- Run 1 : untreated sediment 100g(w.w.) + Lake Tega water 380mL,
- Run 2 : DAF treated sediment 100g(w.w.) + Lake Tega water 380mL,
- Run 3 : DAF treated sediment 100g(w.w.) + MgO 400g/m² + Lake Tega water 380mL,
- Run 4 : DAF treated sediment 100g(w.w.) + CaO 100g/m² + Lake Tega water 380mL.

As described above, experimental microcosm in this study consisted of water and sediment, like natural lake ecosystem. Thus, system has a characteristic that stability and sustainability of this ecosystem are very high [6], [7]. All glass vessels were sealed up and cultured under unstirring, 20°C, bright (20,000lux) and/or dark condition. Sampling from a boundary between sediment and water was conducted at intervals of 2 days after the cultivation started. The experimental condition of microcosm culture was shown in Fig.2.

Parameters for Evaluation

COD, IL and Chl.a concentrations were measured to calculate ECI. COD is for water quality, IL is for sediment quality and Chl.a is for biota quantity, and ECI was calculated to evaluate the effect of sediment treatment to the lake ecosystem. In addition, phytoplanktonic flora, one of biotic indexes to assess the environmental condition [8], was also analyzed by microscopically observation to compare with ECI.

RESULTS AND DISCUSSIONS

Water Quality Assessment

Total COD quantity in each culture series were; 694.8mg/L/28days in Run 1, 480.5mg/L/28days in Run 2, 361.4mg/L/28days in Run 3, and 886.6mg/L/28days in Run 4, respectively. As shown in Fig.3, COD value increased from 3rd day after the cultivation started, and indicated the maximum value in 10th day, and decreased with gentle slope. This is because removal by DAF treatment and restraint by MgO sprinkling for the elution of nutrient salts from

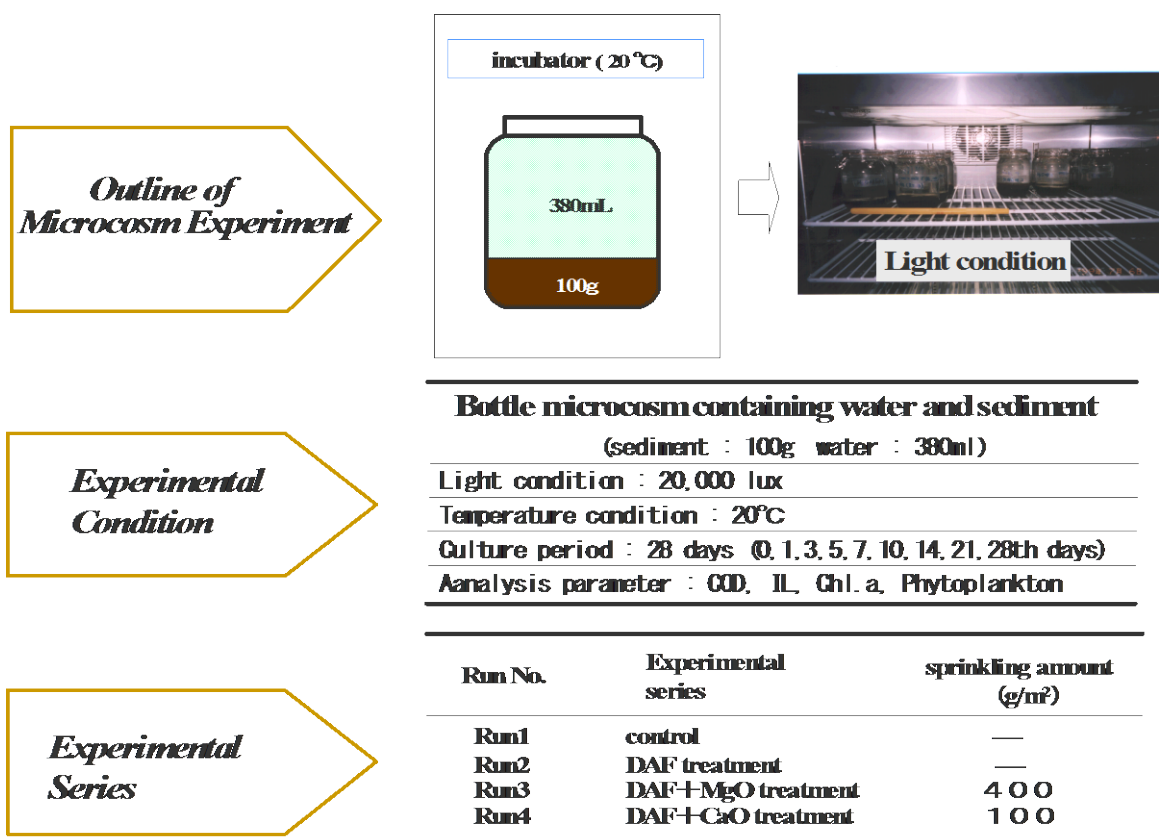


Fig.2 Experimental Condition of Microcosm Culture

the sediment layer lead low growth of phytoplankton and low COD concentration in Run 3. On the other hand, CaO sprinkling made phytoplanktonic growth and COD increasing in Run 4, because of its characteristics, *i.e.* washing out effect of $\text{NH}_4\text{-N}$ from the sediment layer [9]. In comparison with the total COD quantity in Run 1 that is set to value 100%, 69.2% in Run 2, 52.4% in Run 3 and 127.6% in Run 4. Quantity of COD is considered as indicator of water quality, that is quantity of organic matter. From these results, Run 3, that is, DAF treated sediment + MgO sprinkling, was assessed as the most effective improvement method.

Sediment Quality Assessment

Total IL quantity in each culture series were 996mg/g/28days in Run 1, 916mg/g/28days in Run 2, 1,102mg/g/28days in Run 3, and 975mg/g/28days in Run 4. As shown in Fig.4, IL value indicated the maximum value in 1st day, and decreased with gentle slope. This is because DAF treatment removed organic matters from the sediment layer in Run 2, and MgO sprinkling restrained the elution of nutrient salts which introduced bacterial growth in sediment layer, that means IL increasing in Run 3. CaO sprinkling made $\text{NH}_4\text{-N}$ washed out and lead bacterial growth under nitrogen-limiting condition

in Run 4. In comparison with the total IL quantity in Run 1, that was set to value 100%, 91.9% in Run 2, 110.6% in Run 3 and 97.9% in Run 4 were recognized. Quantity of IL is considered as indicator of sediment quality as quantity of organic matter. From these results, Run 2, that is, DAF treated sediment, was assessed as the most effective improvement method.

Biota Quantity Assessment

Total Chl.a quantity in each culture series were 0.512mg/L/28days in Run 1, 0.192mg/L/28days in Run 2, 0.088mg/L/28days in Run 3, and 0.222mg/L/28days in Run 4. Succession of Chl.a concentration in each culture series was shown in Fig.5. The dominant species in each microcosm culture series were cyanophyceae and bacillariophyceae in Run 1, bacillariophyceae in Run 2, bacillariophyceae, chlorophyceae and phytoflagellata in Run 3, and bacillariophyceae in Run 4. This is because these sediment treatments lead the difference of T-N/T-P mass ratio in water. Composition of phytoplanktonic flora is much effected by T-N/T-P mass ratio in water [10]. DAF treatment removes nitrogen peculiarly, and T-N/T-P mass ratio becomes lower, where cyanophyceae cannot grow in Run 2. MgO sprinkling leads higher

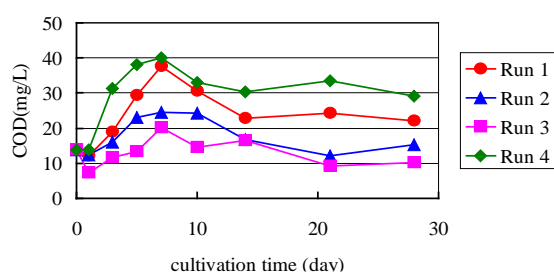


Fig.3 Succession of COD concentration in water

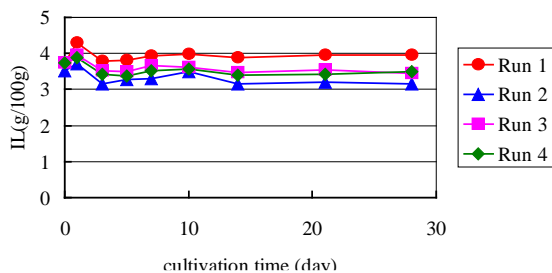


Fig.4 Succession of IL concentration in sediment

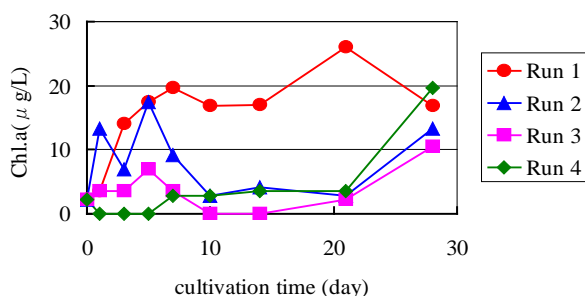


Fig.5 Succession of Chl.a concentration in phytoplankton

T-N/T-P mass ratio, because it has effect to restrain phosphorus. From this, the hybrid treatment of DAF treatment and MgO sprinkling can make nutrient salts concentration lower with keeping T-N/T-P mass ratio properly, like Run 3. CaO sprinkling lead much higher T-N/T-P mass ratio because of its washing out effect on $\text{NH}_4\text{-N}$, even after DAF treatment in Run 4. Concluding these characteristics, DAF treatment lead lower T-N/T-P mass ratio, hybrid treatment, DAF treatment and MgO sprinkling keep proper T-N/T-P mass ratio with low nutrient salts

concentration, and hybrid treatment of DAF treatment and CaO sprinkling introduce high T-N/T-P mass ratio to an extreme. In comparison with the total Chl.a quantity in Run 1, that was set to value 100%, 37.6% in Run 2, 17.2% in Run 3 and 43.3% in Run 4 were recognized. Quantity of Chl.a is considered as indicator of biological quantity, *i.e.* quantity of phytoplankton. From these results, Run 3, that is, DAF treated sediment + MgO sprinkling, was assessed as the most effective improvement method.

Ecological Estimation from Environmental Condition Index (ECI)

ECI value in each culture series were 1.69 in Run 1, 1.22 in Run 2, 0.87 in Run 3, and 1.45 in Run 4. From these results, Run 3, that is, DAF treated sediment + MgO sprinkling, was assessed as the most effective improvement method. Comparison of each index in experimental culture was shown in Table 1.

In comparison with an analysis of phytoplanktonic flora as biotic indicator using microscopic observation, ECI can explain the difference of phytoplanktonic succession in each culture series. Biomass rate of each phytoplankton species, *i.e.* cyanophyceae, bacillariophyceae, chlorophyceae and phytoflagellata in each treatment condition were shown in Fig.6. The dominant species of phytoplankton in each culture series were *Microcystis aeruginosa*, *Anabaena spiroides* (cyanophyceae) and *Melosira granulata* (bacillariophyceae) in Run 1, *M.granulata* and *Nitzschia acicularis* (bacillariophyceae) in Run 2, *M.granulata* (bacillariophyceae), *Scenedesmus quadricauda* (chlorophyceae) and *Chlamydomonas* spp. (phytoflagellata) in Run 3, and *M.granulata* and *N.acicularis* (bacillariophyceae) in Run 4. These species are recognized as biotic indicator for eutrophication and organic pollution of water environment [11]. According to the Saprophylic classification, Run 1, Run 2, Run 3 and Run 4 are under the state of ps, β -ms, os and α -ms respectively. This means Run 1 is the most polluted / eutrophicated state and Run 3 is the most purified / oligotrophic state.

Table 1 Comparison of each index in each experimental series

Run No.	Sediment treatment	total COD	total IL	total Chl.a	ECI	Saprobic index	dominant species of phytoplankton
Run 1	no treat	100	100	100	1.69	ps	cyanophyceae, bacillariophyceae
Run 2	DAF	69.2	91.9	37.6	1.22	ms	bacillariophyceae
Run 3	DAF + MgO	52.1	110.6	17.2	0.87	os	bacillariophyceae, chlorophyceae
Run 4	DAF + CaO	127.6	97.9	43.3	1.45	ms	bacillariophyceae

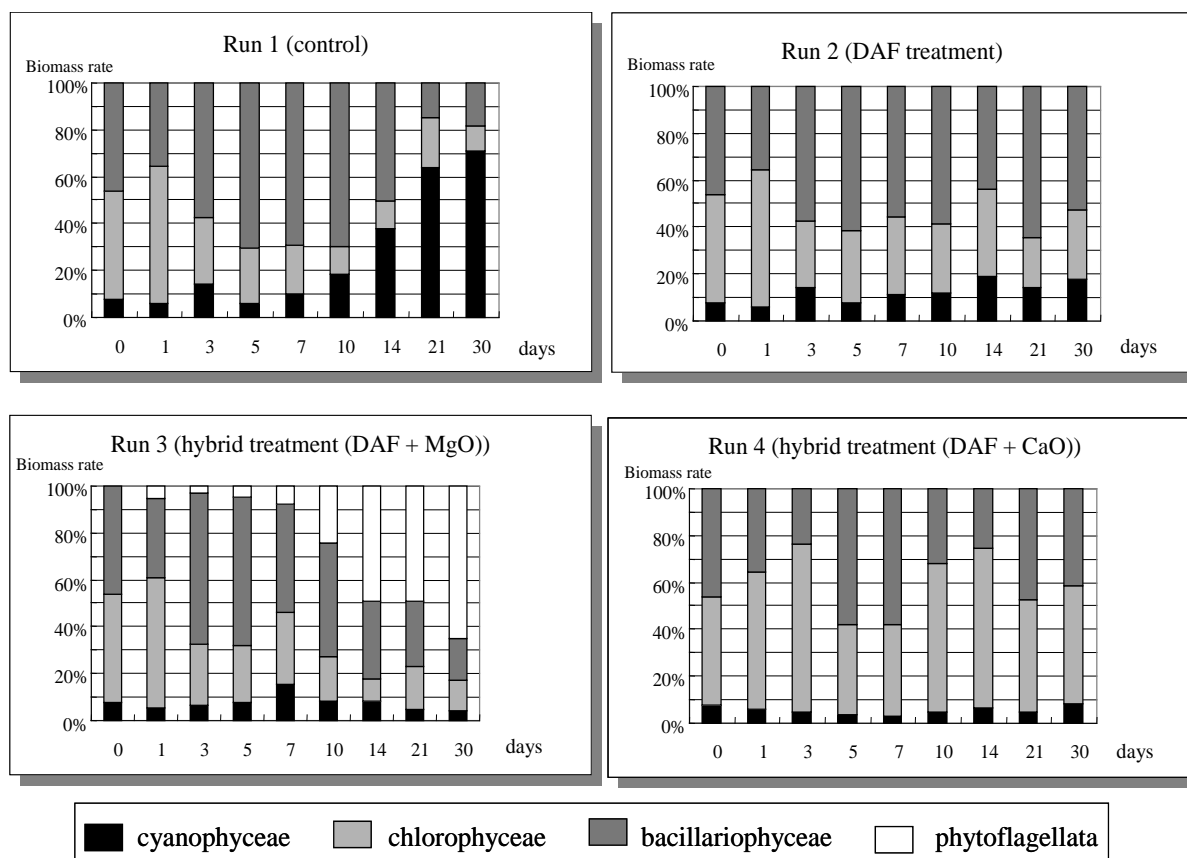


Fig.6 Biomass rate of each phytoplankton species on each experimental series

The experimental results from batch culturing series, were considered to satisfy the theological hypothesis that the hybrid treatment can control nutrient elution from the sediment more effective than DAF and/or no treatment, because water bloom which observed generally in Lake Tega in summer was not observed in grass vessel. Thus, efficiency of this hybrid treatment system of DAF treatment and MgO sprinkling for sediment remediation, possibility of artificial control on phytoplanktonic flora and necessity to establish environmental assessment method on ecosystem level such as ECI proposed in this study were indicated. And to make these treatment methods be applied to real field such as eutrophicated lake and marsh, more detailed analysis for treatment function and optimum condition of sediment treatment was considered to be necessary.

CONCLUSIONS

To evaluate the effect of sediment treatment on aquifer ecosystem, a new ecological index that is composed of water quality, sediment quality and biota quantity was proposed in this study. According to this ECI (Environmental Condition Index), DAF treatment + MgO sprinkling was assessed as the most efficiency method, that is, this method can

make the organic matter quantity in aquatic ecosystem minimum level in comparison with other sediment treatment method. More detailed analysis for treatment function and optimum condition of sediment treatment was considered to be necessary to make these treatment methods be applied to real field remediation such as eutrophicated lake, marsh, reservoir and so on.

ACKNOWLEDGEMENTS

This work is partially supported by the Grant-in-Aid for Scientific Research (24651029) of Japan Society for the Promotion of Science (JSPS).

REFERENCES

- [1] Inamori Y, Jin X, Park J, and Xu K, Guideline on the Management for Establishment of Eco-Sound Watershed Environment of Lakes and Marshes. Tokyo: The Industrial Water Institute, 2007.
- [2] Wetzel RG, Limnology, Third Edition: Lake and River Ecosystems, Academic Press, 2001.
- [3] Agatsuma S, Murakami K, Gomyo M and Amano Y, "Shell Fragment Application as Regional Unused Resources for Nutrients Elution Control from Eutrophicated Sediment", in

- Proc. 5th IWA-ASPIRE Conf. Exhib., 2013, CD-ROM.
- [4] Agatsuma S, Murakami K, Gomyo M and Amano Y, "Water Quality Purification in the Seaside Park Pond using Shell Fragment as Regional Unused Resources", in Proc. Wat. Environ. Technol. Conf. 2013 (WET2013), 2013.
 - [5] Amano Y, Taki K, Murakami K, Ishii T and Matsushima H, "Sediment Remediation for Ecosystem in Eutrophicated Lakes", The Scientific World, Vol.2, 2002, pp.885-891.
 - [6] Odum E P, Ecology, New York: Springer-Verlag, 1963.
 - [7] Beyers R J, and Odum H T, Ecological Microcosms, New York: Springer-Verlag, 1993.
 - [8] Murakami K, Ishii T, Taki K, Matsushima H, "Internal Production Control by Sediment Treatment in Eutrophicated Lakes using Experimental Mesocosm System", Papers on Environmental Information Science, No.22, 2008, pp.487-492.
 - [9] Muto T, Saito T, Matsushima H, Tanaka K, Murakami K, Taki K, "NO₂-N Accumulation through Denitrification Reaction with Lake Sediment", Proc. 2nd IWA Int. Sympo. on Sequencing Batch Reactor Technology (SBRT-2), 2000, CD-ROM.
 - [10] Fujimoto N, Fukushima T, Inamori Y, Sudo R, "Analytical Evaluation of Relationship between Dominance of Cyanobacteria and Aquatic Environmental Factors in Japanese Lakes", J. of Wat. Environ., Vol.18, No.11, 1995, pp.901-908.
 - [11] Watanabe T, Asai K, Houki A, Tanaka S, and Hizuka T, "Saprophilous and Eurysaprobic Diatom Taxa to Organic Water Pollution and Diatom Assemblage Index (DAI_{po})", Diatom, Vol.2, 1986, pp.23-73.

SHALE FAILURE AND CRACKING IN A SEMI-ARID AREA

Muawia Dafalla¹, Mutaz, E², Mansour Al humimidi³, Loni Allafouza Oumar³ and Mosleh Al Shamrani⁴

^{1, 2, 4} Civil Engineering, King Saud University, Saudi Arabia

³ King Abdulaziz City for Science and Technology, Saudi Arabia

ABSTRACT

A semi-arid shale formation in the northern and central part of Saudi Arabia showed frequent near surface cracks and distress at several sites. This phenomenon was found to be of a serious risk to structures founded on or near cracks or failure zones. This study was carried out for an area where several centimeters wide ground cracks extending over more than one kilometer distance across a populated area in Saudi Arabia. The dominant subsurface formation in the area is reddish brown stiff to hard silty to clayey shale underlain by sandstone formation. The subsurface material was explored and clayey shale samples were extracted. The study included borehole drilling and test pit excavations. Soil classification and consistency tests were performed. A series of physical and chemical testing confirmed the expansive nature of the shale. The possible causes of cracks and the mechanisms of failure in semi-arid shale were covered and discussed in sufficient details. Engineering guides for buildings and construction in typical zones were presented.

Keywords: Shale; Expansive; Clay; Cracking; Semi-arid.

INTRODUCTION

The shale is encountered in many parts of Saudi Arabia covering major zones of the central, north and north-western parts of the country. Clayey shales and silty shales were reported in Al Ghatt, Tabuk, Tayma and Aljoaf. Reference [1] highlighted the presence and expansive nature of clay shale in Tabuk. In recent years some ground cracks appeared in several locations causing concerns to municipal authorities. The phenomenon is only associated with shale zones and happened to affect existing structures. Reference [2] presented works covering an area in Madraj near Buraida town in central Saudi Arabia. Earthquake and seismic activities were excluded of being the reason behind this phenomenon as the area does not have any history of tectonic activities and classified within zones of negligible acceleration. This work is part of the studies to investigate the physical and geotechnical nature of the shale where these cracks appeared. Deeda, a small village within the central province was chosen as the study area. Figure 1 presents the geographical location. The area geology belong to Sudair formation consisting of shale, silt, claystone and sandstone. These quaternary deposits are underlain by limestone formation of Triassic age. Cracks in the ground affected several structures and a major mosque had to be removed as a result of excessive distortion. Cracks extended over more than one kilometer causing damage to asphalt roads and other light structures.

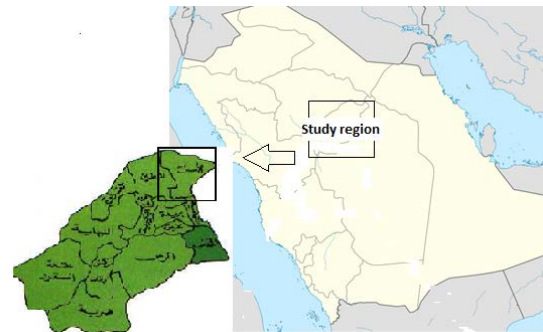


Fig. 1 Study region in Central Saudi Arabia



Fig.2 Typical ground cracks reported in shale formation.

GEOLOGY AND GEOENVIRONMENT

The local geology of area consists of recent deposits of sand, silt and clay with occasional gravels of variable sizes. This is underlain by clayey shale material. Reference [3] presented a geological map for Deeda describing the underlying dolomitic sandstone as belonging to JILH formation

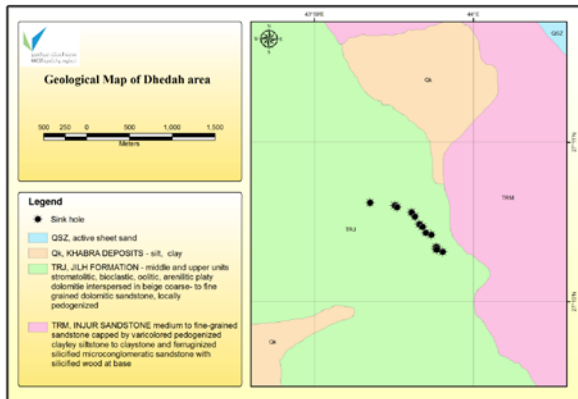


Fig. 3 Geologic map of Deeda Area [3].

The expansive shale like other fat clays is very sensitive to moisture conditions. Drying and wetting are associated with shrinkage and expansion. The temperature range of Al Qassim region vary from -2 degrees in winter to 49 in summer. The annual rainfall varies from year to year with a minimum of 25mm and a maximum of 230mm. Figure 4 presents change of annual precipitation over 60 years.

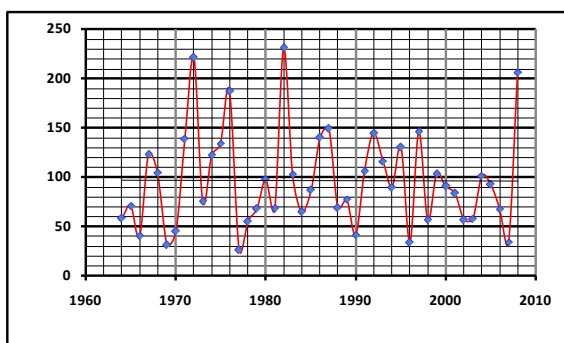


Fig. 4 Annual precipitation changes over 60 years.

EXPLORATION ACTIVITIES

The site was explored by advancing two boreholes within the zones of cracking down to 25 depths. Two test pits were excavated to 3m depth below ground level. Wash boring technique was employed and standard penetration tests were carried out at intervals of 1.5m. On encountering hard formation drilling was continued using double

tube core barrel. Sound and intact rock cores were extracted and transported to the laboratory for further testing. As a part of this investigation seismic explorations were also conducted. Two seismic lines passing through the boreholes were tested. The geotechnical soil profile was constructed based on the outcome of boreholes, seismic data and laboratory tests.



Fig. 5 Drilling Plant on site.



Fig. 6 Typical Shale section from the study area.

RESULTS AND DISCUSSION

The boreholes revealed that the site is overlain by a top soil consisting of brown to reddish brown clayey sand followed by hard sandy clay. The plasticity of clay is increasing with depth. The soil below the level of 3 to 7.5 m is classified within the CH group and this was found extending to a depth of 22.5 m. No open cavities were reported. The drilling fluid used was water. No water loss reported during drilling activities. The sandstone underlying shale formation is weakly cemented on top. The sandstone cementation is improved with depth. Recovery of soils and rock varied from zero to 100% and RQD (rock quality designation factor) varied from zero to 95%. Ground water was encountered at a depth of 24.5 m below ground level. This level is fluctuating

during different season times of the year. Engineering property tests indicated SC (clayey sand soil followed by CL (clay) and CH. The fine material passing sieve number 200 varied from 25% to 94%. The liquid limit varied from 50 to 95 and the plasticity index from 30 to 48. Soil classification, modified proctor and standard penetration tests were carried out in accordance with American standard testing methods [4], [5] and [6].

The seismic profile for borehole (1) indicated two main layers of sediments followed by sandstone. The top layer indicated an average depth of 3m while the second layer extended beyond 18 meters. The seismic profile for borehole 2 yielded the same but indicating 5m thickness for top soil and more than 20 m for shale or claystone.

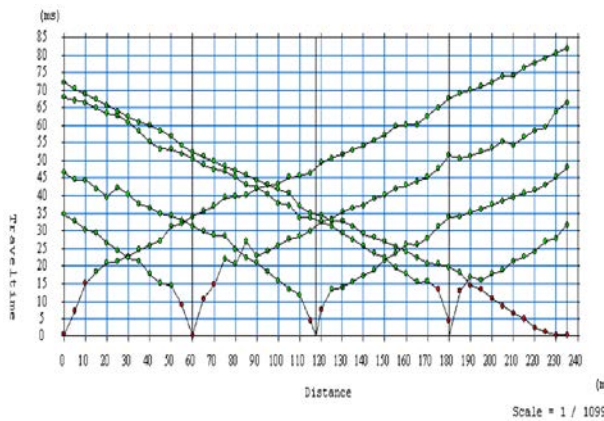


Fig. 7 Travel time and distance profile for line across BH1.

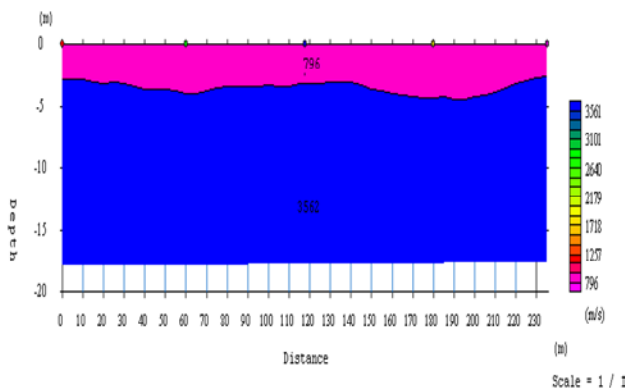


Fig. 8 Geological section derived from seismic line at BH 1.

The engineering properties indicated that the subsurface material belongs to expansive clay group. The cracks can form as a result of drying and shrinkage. The cracks did not show a relative vertical movement that reflects deep failure or any signs of tectonic damage. American Standard

Testing Methods (ASTM) for one-dimensional consolidation properties of soils using incremental loading was used [7]. Swelling pressure tests using odometers indicated swelling pressure of the order of 700 to 800 kPa. This figure is obtained in the laboratory for a confined small sample. The actual swelling pressure in field is far less and can be taken as one third of this value [8]. The swell pressure for non-confined field condition of 250 kPa can be adopted. The overburden pressure for 2.5m is estimated at 50 kPa.

The chemical tests carried out for a sample taken from TP 1 indicated elements as listed in Table 1.

Table 1 Elements concentration in Deeda clay

Elements	Percentage %
Al	5.2
Ca	14.4
Fe	4
Mg	0.6
Si	33.0
Na	14.4
K	6.5

Quartz and calcium are dominant. Aluminium, Calcium and Magnesium are basic components of smectite clay minerals that are associated with expansive clays.

Structures founded on typical soils shall be designed following all instructions listed in Chapter 9 of the Saudi Building Code SBC 303[9]. However, for certain structure it might be feasible to consider pile foundations and transfer the superstructure stresses down to the sandstone formation. Light structures shall have their foundations placed at a minimum depth of 2.5m below ground level and the same time contact pressures from dead loads shall be in the order of 200kN/m². It is also recommended to avoid placing the foundations right on the ground crack lines. A 50m distance away from the cracks will be sufficient to avoid distress and unexpected settlement. Excavations shall extend beyond the bottom level of cracks and careful inspection must be carried out prior to placing footings within the cracks zone.

CONCLUSION

The shale can be subjected to serious shrinkage on drying and can introduce ground cracks. Volume changes in shale can be very serious for light structures. All foundations placed on typical material shall consider all precautions for expansive soils as set in international standards. Special reference is

made to the Saudi Building Code Chapter 9. Foundations placed on expansive soils shall be based on sizing the footing dimensions in such arrangements that contact pressure due to dead loads between concrete and soil is in excess of the swelling pressure. A 200 kN/m² is suggested as a design value for this particular area.

ACKNOWLEDGEMENTS

This research is part of a project funded by King Abdul-Aziz City for Science and Technology, Project Number 542. Authors would like to thank geotechnical and geophysical teams participated in this work.

REFERENCES

- [1] Dhowian, A.W. (1984). Characteristics of Expansive Clay-Shale in the Northern Region of Saudi Arabia. Proc. of 5th Int. Conf. on Expansive Soils, Adelaide, South Australia, pp.316-320.
- [2] Alfozan, F and Dafalla, M (2013). Study of cracks and fissure phenomenon in central Saudi Arabia by applying geotechnical and geophysical techniques. Arab J Geosci. DOI 10, 1007/s12517-013-0884-7.
- [3] Robelin, C., Al-Muallem, M.S., Brosse, J.-M., Fourniguet, J., Garcin, M., Gouyet, J.-F., Halawani, M.A., Janjou, D., Le Nindre, Y.-M., 1994. Geologic map of the Qibah Quadrangle; Sheet 27-G, Scale 1:250,000, Kingdom of Saudi Arabia. Saudi Arabian Ministry of Petroleum and Mineral Resources, Jeddah, Geoscience Map GM-136.
- [4] American Standard Testing Methods (ASTM). American Society for Testing and Material. (ASTM D 2487).
- [5] American Standard Testing Methods (ASTM). American Society for Testing and Material. (ASTM D1557)
- [6] American Standard Testing Methods (ASTM). American Society for Testing and Material. (ASTM D 1586)
- [7] American Standard Testing Methods (ASTM) for One-Dimensional Consolidation Properties of Soils Using Incremental Loading (ASTM D2435 – 04)
- [8] Al-Shamrani, M. A. and Dhowian A. W (2003). Experimental study of lateral restraint effects on the potential heave. Engineering Geology 69 (2003) pp. 63–81
- [9] Saudi Building Code (SBC 303).

EARTH MASONRY UNIT: SUSTAINABLE CMU ALTERNATIVE

Joseph Dahmen¹, Jose F. Muñoz²

¹School of Architecture and Landscape Architecture, University of British Columbia, Canada;

²Watershed Materials LLC, US.

ABSTRACT

This paper provides a justification for a masonry building block fabricated from soil materials that could radically improve the environmental profile of one of the most common construction materials on the planet. Typical concrete masonry units depend on the reaction of ordinary Portland cement to provide strength and durability. While effective at meeting structural requirements, a study has shown that production of ordinary Portland cement causes 6-7% of global greenhouse gas emissions [1]. In contrast, the principal component of stabilized earth mix designs is soil, a ubiquitous, innocuous, and almost unlimited resource that offers the potential of sustainable cradle-to-cradle environmental performance over a full life cycle of products. The paper presents research investigating the characteristics of a range engineered soil blends and natural soil sources. The research is applied toward the production of an environmentally sustainable stabilized earth masonry building block capable of meeting current ASTM concrete block performance specifications while reducing embodied energy by as much as 50% due to the reduction of energy-intensive Portland cement binders, dramatically reducing CO₂ emissions of this common construction material

Keywords: Sustainable Construction Materials, Concrete Masonry Unit, Green Building, Green Materials, Nanotechnology

INTRODUCTION

This paper presents a vision and justification for developing a reduced cement structural masonry building block fabricated primarily from soil materials that could reduce a significant amount of green house gas emissions, radically improve the environmental profile of one of the most common construction materials on the planet. The paper discusses existing concrete masonry unit (CMU) manufacturing practices and their associated impacts, as well as some techniques currently in use to incrementally improve environmental impacts. These conventional practices offer a backdrop against which a radical cement-free block is proposed that would make use of advances in nanotechnology and geopolymerization. The paper briefly describes the current masonry marketplace in the US, identifying the commercial potential of a cement-free masonry building block, and sketches a development pathway to take advantage of the opportunity. These arguments provide justification for the development of a structural masonry building block fabricated from engineered soil materials.

BACKGROUND AND CONTEXT

Concrete is the most voluminous manufactured product in the world, with annual consumption approaching 20,000 million metric tons (MMT). The production of each metric ton of cement results in roughly 900 KG of CO₂ released into the

atmosphere [2] and a study has shown that production of cement causes 6-7% of global greenhouse gas emissions [3]. CMUs, the technical term for common concrete masonry blocks used in construction, are ubiquitous unitized building materials that contain between 10-16% cement by weight. In 2007, 8 billion CMUs were produced in the US, requiring the use of approximately 15.2 million metric tons (MMT) of cement. The manufacture of this cement released approximately 13.7 MMT of CO₂ into the atmosphere. This represents approximately .25% of the 6,000 MMT of CO₂ emissions resulting from energy and industry overall in the US during the same year [4].

The standard CMU is a rectangular 200x200x400 mm (8x8x16-inch) unit comprised of ordinary Portland cement (OPC), gravel, sand, and water. The concrete mixture may also contain ingredients such as supplementary cementitious materials (SCMs), accelerators, retarders, and plasticizers governing setting time and workability, air-entraining agents, coloring pigment, and water repelling admixtures. During the conventional CMU manufacturing process, a machine molds moist, low-slump concrete into the desired shapes, which undergo accelerated curing at elevated temperatures inside a semi-enclosed curing chamber. This is generally followed by a drying and storage phase. The manufacture of CMUs has been characterized by modest, incremental improvement since its introduction over one hundred years ago.

Environmental Impacts of Conventional Concrete Masonry Units

A cradle to gate LCA study conducted by the Portland Cement Association in 2007 indicates that 91% of the GHG released by the manufacture of CMUs are attributable to the OPC constituent used as a binder [5]. This is mainly due to the intense heat required for cement manufacture, together with the CO₂ released during the calcination phase, in which the raw limestone is converted to calcium oxide and CO₂ [6]. It follows that reducing the cement content of a CMU will significantly reduce its overall environmental impact.

Currently, the leading method for reducing the environmental impact of concrete is to replace a portion of OPC binder constituent with SCMs. This class of materials includes fly ash, silica fume, metakaolin and natural pozzolans. In practice, the most commonly used SCMs are industrial by-products such as fly ash and ground granulated blast furnace slag, due to their low cost and general availability. When added to concrete mixes, it has been demonstrated that these materials can reduce the need for OPC binders significantly [7], effectively reducing GHG emissions with only small reductions of strength and durability. However, despite widespread use of fly ash and other SCMs derived from industrial byproducts as a means to reduce embodied energy in the manufacture of concrete, recent research suggests that their use may be limited by geographical availability, and that these materials may also contain significant hazards to human health.

Toxicity is the most pressing issue with respect to SCMs derived from industrial byproducts. The composition of fly ash, one of the most plentiful and widely-used OPC substitutes, varies widely with fuel source, and has been shown to contain such highly toxic elements such as arsenic, beryllium, cadmium, chromium and lead, among others, along with dioxins and polycyclic aromatic hydrocarbons compounds in concentrations that can be up to several percent of the total material [8]. Questions remain as to whether the hydration reaction of fly ash and cement is capable of sufficiently immobilizing the toxic elements in fly ash and leaching of heavy metals, which is of special concern where concrete comes into contact with water [8,9,10]. Past experiences with lead paint, asbestos and arsenic-treated wood should prevent from a widespread use of a product without a full understanding of the impacts on human health [7], and additional research is needed to assure the non-toxicity of concrete incorporating significant amounts of fly ash and other SCMs over the life of the material, particularly where residential construction is concerned.

Issues of toxicity aside, inadequate supply of

conventional SCMs in proximity to areas demonstrating the greatest demand for cement presents another problem. In 2010, the annual global demand of cement was close to 3,300 million tons [11], while the global combined production of fly ash, iron and steel slag, and silica fume accounted for 750 million tons [12,13,14], much of it highly toxic and potentially unusable.

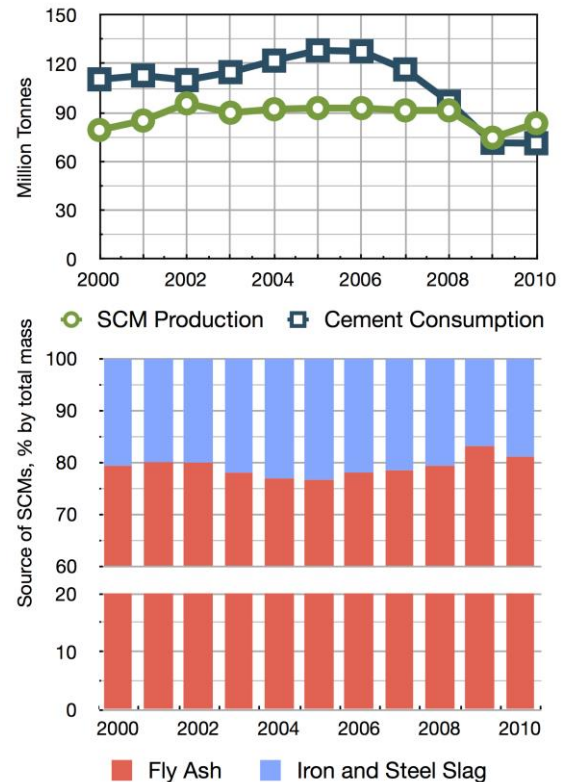


Fig. 1 Evolution of SCM production and cement consumption in U.S. [10-12]

As shown in Figure 1, between 2000 and 2010, fly ash accounted for approximately 80% of the production of these SCMs in the U.S. Life cycle analysis shows that transporting fly ash more than 50 miles from its origin dramatically increases its environmental impacts, reducing its viability as a cement replacement [15]. Fly ash and other combustion co-products must be produced in proximity to cement production sites to ensure their economic and environmental viability as a sustainable cement substitutes.

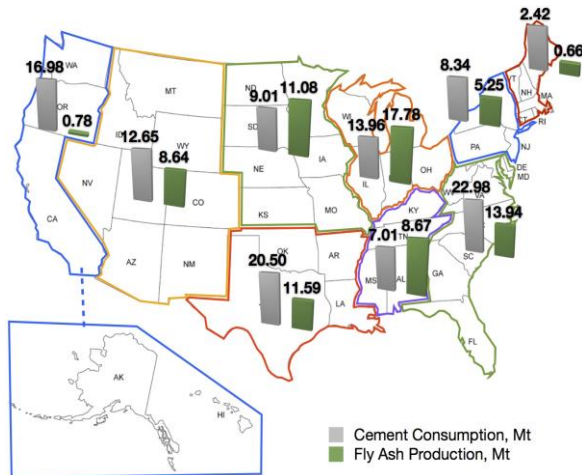


Fig. 2 Cement consumption and fly ash production by US regions in 2007 [11,16]. Fly ash production is estimated from coal consumption data, assuming that 10 tons of coal produce 1 ton of coal combustion products (CCP) [16] and approximately 70% by weight of the total CCP corresponds to fly ash [12]

Cost-effective fly ash availability around the country corresponds to the pattern of coal-fired plant distribution from which it is derived, resulting in uneven geographical availability, as portrayed in Figure 2. For example, in the North, South East Central, and West North Central regions, fly ash production exceeds cement demand. In contrast, other regions such as the Northeast and West Coast US produce insufficient amounts of fly ash to maintain pace with demand, limiting its use as a viable sustainable cement replacement in these areas. Even where fly ash is available in significant quantities, as fly ash is transformed from a liability to a co-product that can be sold at a profit, its widespread utilization as an OPC substitute could subsidize coal-fired electricity generation, which is currently responsible for 20% of the world's total GHG emissions [17].

Despite their growing popularity, the incorporation of conventional SCMs are at best a partial solution to reduce the environmental impacts of cement, and in some cases can even have the opposite effect. The toxicity of the many SCMs discourages their widespread use, particularly in residential applications and where concretes come in contact with moisture. Finally, transporting SCMs long distances required by geographically uneven supply limits their effectiveness as sustainable cement alternatives.

EARTH MASONRY UNITS

In contrast to the incremental environmental gains offered by conventional SCMs derived from

industrial byproducts, properly engineered stabilized soils have the capacity to radically transform traditional concrete-based masonry products at a global scale. Soil, the principal component of stabilized earth materials, is a ubiquitous, innocuous and almost unlimited resource that promises the possibility of sustainable cradle-to-cradle life cycle performance. CMUs typically contain between 10-16% OPC by weight. In contrast, masonry blocks made with minimally processed engineered soil blends are capable of fulfilling the mechanical and durability requirements of contemporary structural applications with as little as 5% OPC content and no additional SCMs, significantly reducing environmental impacts without sacrificing strength and durability. However, challenges must be met before reduced-OPC masonry blocks composed of engineered soil materials will be capable of meeting the structural requirements of CMUs without resorting to the use of conventional SCMs.

Earth masonry materials: opportunities and limitations

Earth-based masonry building materials have been used extensively over the last half-century in civil engineering projects, but poor durability due to the ingress of water [18] has limited their broader acceptance as a replacement for conventional concrete and masonry products. However, research suggests that key aspects of the earth materials such as packing density, soil mineralogy, and type of chemical binder can be manipulated to improve overall durability, suggesting new uses and applications.

Packing Density

The pore structure of the mixes is the major factor controlling the durability of the material. The size and the pore connectivity in the stabilized earth system are linked to the pressure applied, the packing efficiency, and the moisture content. An optimization of the gradation ensures a better packing of the particles and therefore less inter-particle space [19]. The results are mixtures with high density, and lower water and binder demand. Therefore, these mixes will have higher resistance to freeze-thaw damage.

Quantity and Type of Microfines

The amount of microfines (P200 material), together with their mineralogy, is another important factor with direct impact on the durability of the earth masonry materials. Different soils exhibit diverse mineralogies depending on their geographic location, but a common attribute of soils suitable

for stabilization is the presence of clay minerals. The presence of clay minerals plays an important role in the durability of the overall material due to their water absorption demand. The effects of quantity and type of P200 material on dry density and water absorption of soil-cement are illustrated in Figure 3. Increasing content of P200 materials with significant content of clays reduces packing efficiency (low dry density) causing an increase in overall porosity and water absorption.

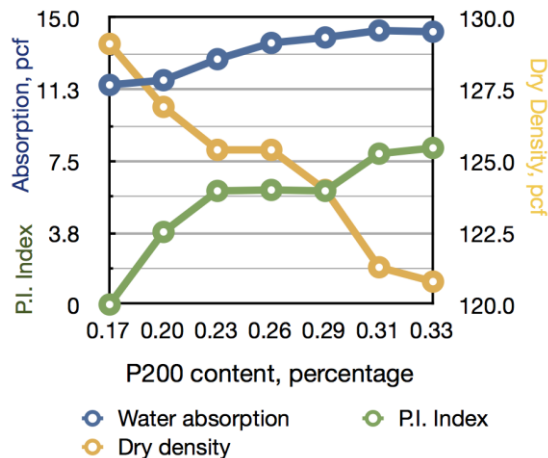


Fig. 3 Effect of varying P200 content and plasticity index (P.I.) on dry density and water absorption of soil-cement materials. Note: 1 pcf is equivalent to 10.018 Kg/m³

Different strategies based on the nature of the clay minerals can be adopted to mitigate the clay mineral water demand. These strategies can be classified as traditional and non-traditional techniques. The use of cement, lime, fly ash, and bituminous products are considered traditional techniques. Other less conventional methods are the use of ionic stabilizer, lignosulfonates, salts, or enzymes. The objective of these two types of products is to impair the water demand of the clay minerals. This is achieved through a variety of mechanisms such as cation exchange, flocculation and agglomeration, pozzolanic reaction, and basal charge destabilization, among others. These treatments have shown to be effective on the stabilization of pavement subgrades [20, 21]. The type of clay mineral to be stabilized dictates the suitability of each particular treatment.

Chemical Binder

Finally, the type and amount of chemical binder is another factor with a high degree of influence on the final performance of the product. Portland cement is the most widely used binder on stabilized earth materials. However, the cement content can be drastically reduced with adequate optimization

of above factors. Research conducted to date has established positive results designing size-engineered mixtures of soil and aggregate by-product stabilized with 6% Portland cement by weight to produce a reduced-cement earth masonry building units that meets the compressive strength, water absorption and wet-dry durability of the ASTM C90 Standard Specification for Loadbearing Concrete Masonry Units and ASTM D559 Standard Specification for Wetting and Drying Compacted Soil-Cement Mixtures. These results already represent a 40% reduction in cement from a conventional CMU.

While significant challenge remain to be solved, packing density, microfine ratios, and careful control over chemical binders have the capacity to transform traditional concrete-based masonry products at a global scale.

NANOTECHNOLOGY IN EARTH MATERIALS

The application of advances in nanotechnology is another approach that offers great promise in addressing the lack of durability in conventional earth masonry products. It is instructive to look at the evolution from regular to high-performance concrete in this regard. Continuous refinement of the particle size of the additives played an important role in making the transition to high strength concretes as illustrated in Figure 4. Similar understanding of characteristics at the nano scale can be applied to earth masonry to increase its strength and durability.

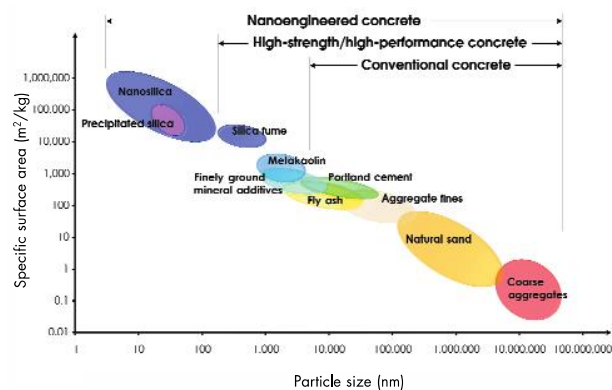


Fig. 4 Particle Size vs. Specific Surface Area of Principal Components and SCMs of Concrete Materials [22]

In earth materials, the specific surface area of the microfine fraction can be modified to influence the void fraction and the capillarity suction of stabilized earth materials [23, 24]. Currently, the aggregate industry offers a wide selection of mineral products and by-products that can be used to engineer the soil's finer fraction from 150

microns down to nanoscale. This enables significant enhancements to the overall performance of the material and, more precisely, the durability of the finished product.

Current scientific advances in nanomaterials may further reduce the energy-intensive cement content in earth masonry building blocks in the future. As an example, the precipitation reaction of the Portland cement binder can be improved by the addition of nano-size materials, which is known as nano-seeding effect. This approach has been proved to be successful to accelerate the hydration reaction of Portland cement and its degree of hydration [25, 26].

The characterization of amorphous hydration gels responsible for the cohesiveness and strength of cementitious materials is another promising area. Thanks to the progress in analytical technique, the structure of these gels can be characterized down to nanoscale, and correlations have been established with mechanical performance at the microscale. The structure of calcium silicate hydrated gel (C-S-H) formed during the hydration of Portland cement has been well studied [27, 28]. Significantly, recent studies have indicated that calcium aluminum silicate gels [29-30] and minerals [31] could achieve even better performance than C-S-H.

It is hypothesized that smaller amount of these gels would need to be nucleated to improve the durability in earth masonry than in cement-based materials. Earth masonry products are dense systems characterized by aggregates with a high degree of connectivity. It is therefore logical to assume that slight chemical reactions at their surface might potentiate the formation of new amorphous phases. The new-formed phases will reinforce the connectivity between particles through direct chemical bond or through cohesiveness attractions (Van der Waals forces). This connectivity among aggregates is capable of creating a rigid skeleton inside the matrix of the earth specimens, contributing to the overall improvement of the integrity and durability of the system.

Applying current advances in nanotechnology offers great promise in generating a new class of earth masonry materials capable of delivering structural performance with significantly reduced environmental impacts.

MASONRY MATERIALS MARKETPLACE

The green building industry currently represents a US\$49B market in the US and is the fastest growing segment of the construction market. It is characterized by the following attributes:

- 280% growth in 5 years, from \$17B in 2005 to \$49B in 2010
- Green Building market is projected to be

\$96–140 billion market by 2014

- \$14.3B (12% of total) of this will be spent on masonry materials

The authors have co-founded a company dedicated to the development of a new class of durable sustainable masonry building blocks called Earth Masonry Units (EMUs) capable of offering reliable structural performance with reduced OPC binder content. To date the company has developed an environmentally sustainable masonry building block with recycled aggregates and 50% less cement than conventional CMUs that meets standard CMU specifications. The company has constructed two demonstration houses utilizing over 13,000 of these blocks, marketed under the name of E-CMUs. The company will continue to capitalize on its existing product line of E-CMU during the development of the transformational zero-cement EMUs. This phased market entry strategy will generate early revenue for the company that will defray development efforts for the future range of radically sustainable masonry materials and products.



Fig. 5 Watershed Materials' demonstration house under construction in the Bay Area of California. Photo by David Easton

CONCLUSION

This paper presents a vision for developing a structural masonry building block fabricated from soil materials. The development of the block could eliminate the need for 15.2 million metric tons (MMT) of cement and the release of 13.7 MMT of CO₂ into the atmosphere. Moreover, soil-based masonry building block could represent a viable business opportunity. Existing CMU manufacturing practices are ripe for transformative change that a radical cement-free masonry block could provide. Such an effort could make use of existing manufacturing capability and distribution networks on the way to developing the commercial potential

of cement-free masonry building block. These arguments provide justification for the development of a structural masonry building block fabricated from engineered soil materials.

ACKNOWLEDGEMENTS

The authors would like to thank David Easton of Rammed Earth Works for his role in the development of the ideas in this paper.

REFERENCES

- [1] Chaturvedi, S. and Ochsendorf, J., "Global Environmental Impacts Due to Concrete and Steel," Structural Engineering International, 14/3, Zurich, Intl. Assoc. of Bridge and Structural Engineers, August 2004, 198-200.
- [2] US Energy Information Administration (EIA), 2009. "Emissions of Greenhouse Gases in the United States 2008" retrieved Nov. 2012 from <http://www.eia.gov/oiaf/1605/ggrpt/carbon.htm>
- [3] Chaturvedi, S. and Ochsendorf, J., "Global Environmental Impacts Due to Concrete and Steel," Structural Engineering International, 14/3, Zurich, Intl. Assoc. of Bridge and Structural Engineers, August 2004, 198-200.
- [4] US Energy Information Administration (EIA), 2009. "Emissions of Greenhouse Gases in the United States 2008" retrieved Nov. 2012 from <http://www.eia.gov/oiaf/1605/ggrpt/carbon.htm>
- [5] Marceau, M., Nisbet, M. and VanGeem, M., 2007. "Life Cycle Inventory of Portland Cement Concrete". Portland Cement Association.
- [6] Worrell, E., Price, L., Martin, N., Hendriks, C. , and Meida, L., 2001. "Carbon Dioxide Emissions from the Global Cement Industry" Annual Review of Energy Environment, 26: 303-29.
- [7] Glazer B., Graber C., Roose C., Syrett P., Youssef C., and Farrah K. 2011. "Fly Ash in Concrete", Perkins and Will.
- [8] Qijun Yu, S. Nagataki, Jinmei Lin, T. Saeki, M. Hisada, 2005. "The leachability of heavymetals in hardened flyash cement and cement-solidified fly ash", Cement and Concrete Research, 35(6): 1056-1063
- [9] R.H. Rankers, I. Hohberg, 1991. "Leaching Tests for Concrete Containing Fly ash - Evaluation and Mechanism". Studies in Environmental Science, 48: 275-282
- [10] Min-Hong Zhang, Marcia C. Blanchette, and V. Mohan Malhotra, 2001. "Leachability of Trace Metal Elements from Fly Ash Concrete: Results from Column-Leaching and Batch-Leaching Tests". ACI Materials Journal, 98 (2): 126-136.
- [11] U.S. Geological Survey, January 2012. "Cement", Mineral Commodity Summaries.
- [12] American Coal Ash Association, 2010. "Coal Combustion Product (CCP) Production & Use Survey Report".
- [13] World Steel Association, 2010. "Steel Industry By-Products Fact Sheet."
- [14] ACI Committee 234, 2006. "Guide for the Use of Silica Fume in Concrete", ACI 234R-06.
- [15] Babbitt C.W., Lindner A.S., 2008. "A life cycle comparison of disposal and beneficial use of coal combustion products in Florida; Part 1: Methodology and inventory of material, energy, and emissions. International Journal of Life Cycle Assessment 13(3): 202-211.
- [16] U.S. Energy Information Administration, 2008. "Annual Coal Report".
- [17] Jos G.J. Olivier, Greet Janssens-Maenhout, Jeroen A.H.W. Peters, 2012. "Trends in global CO2 emissions", PBL Netherlands Environmental Assessment Agency.
- [18] Kerali, A.G. (2001). "Durability of Compressed and Cement-stabilized Building Blocks." PhD Thesis, University of Warwick, School of Engineering.
- [19] Houben, H. and Guillaud, H., 1994 "Earth Construction: A Comprehensive Guide," Intermediate Technology Publications, London.
- [20] Prusinski, J.R. and Bhattacharja, S., 1999, "Effectiveness of Portland Cement and Lime in Stabilizing Clay Soils", Transportation Research Record: Journal of the Transportation Research Board, 1652, 215-227.
- [21] Tingle, J.S., Newman, J.K., Larson, S.L., Weiss, C.A. and Rushing, J.F., 2007, "Stabilization Mechanisms of Nontraditional Additives", Transportation Research Record: Journal of the Transportation Research Board, 1989 (2), 59-67.
- [22] Sobolev, K., and Gutiérrez, M. F., 2005, "How nanotechnology can change the concrete world", *American Ceramic Society Bulletin*, 84(10), 14.
- [23] Suzuki. M., Sato, H., Hasegawa, M. and Hirota, M., 2001, "Effect of size distribution on tapping properties of fine powder", *Powder Technology*, 118 (1-2), 53-57.
- [24] Hall, M. and Djerbib, Y., 2004, "Moisture Ingress in Rammed Earth: Part 1 The Effect of Particle-Size Distribution on the Rate of Capillary Suction", *Construction and Building Materials* 18, 69-280.
- [25] Thomas, J. J., Jennings, H. M., and Chen, J. J., 2009. Influence of nucleation seeding on the hydration mechanisms of tricalcium silicate and cement. *The Journal of Physical Chemistry C*, 113 (11), 4327-4334.

- [26] Sanchez, F., and Sobolev, K., 2010. Nanotechnology in concrete—a review. *Construction and Building Materials*, 24 (11), 2060-2071.
- [27] Constantinides, G., and Ulm, F. J., 2007. The nanogranular nature of C–S–H. *Journal of the Mechanics and Physics of Solids*, 55 (1), 64-90.
- [28] Jennings, H. M., 2008. Refinements to colloid model of CSH in cement: CM-II. *Cement and Concrete Research*, 38 (3), 275-289.
- [29] Qomi MJA, Ulm FJ, and Pellenq RJM., 2012. Evidence on the Dual Nature of Aluminum in the Calcium-Silicate-Hydrates Based on Atomistic Simulations. *Journal of American Ceramic Society*, 95 (3): 1128-1137.
- [30] Hong S and Glasser FP., 2002 Alkali Sorption by C-S-H and C-A-S-H gels. Part II: Role of Alumina. *Cement and Concrete Research*, 32 (7): 1101-1111.
- [31] Jackson, M. D., Moon, J., Gotti, E., Taylor, R., Chae, S. R., Kunz, M., and Monteiro, P. J., 2013. Material and Elastic Properties of Al Tobermorite in Ancient Roman Seawater Concrete. *Journal of the American Ceramic Society*.

CONSTRUCTION AND MAINTENANCE OF EMBANKMENTS USING HIGHLY ERODIBLE SOILS IN THE PILBARA, NORTH-WESTERN AUSTRALIA

J.V. Smith¹ and L.A. Sullivan²

¹School of Civil, Environmental and Chemical Engineering, RMIT University, Australia; ² Southern Cross Geosciences, Australia

ABSTRACT

Many soils and sediments in the Pilbara region of north-western Australia are highly susceptible to erosion. Large quantities of construction materials are required as iron ore mining and the extensive railway lines used to transport ore to port continue to be developed in the region. Simply avoiding the use of highly erodible materials is often considered to be too high a cost where alternatives are scarce. Constructing embankments to survive the cyclonic wet season from material highly susceptible to erosion, is a major challenge. Highly erodible materials encountered in the Pilbara include some bedrock shales, dispersive alluvial silts and sands and slaking clays and mudstones. Dispersive materials can erode internally by the formation of pipes or tunnels. Piping erosion can be difficult to detect and can cause severe internal damage to embankments before being detected. Similarly, slaking material can undergo compaction during wetting and drying cycles resulting in unexpectedly large settlements. The effect of erosion, in general, is controlled by appropriate embankment design and construction, in particular compaction standards. Erosion controls include sacrificial batters, surface protection, encapsulation and stabilisation. For many mining projects achieving short-term construction deadlines is a high priority and adding erosion control measures after construction may be preferred. Predicting the time by which erosion control needs to be installed or rehabilitated should be a part of the embankment design process. Material selection has direct implications for the on-going asset management of embankment structures.

Keywords: Embankment, Erosion, Dispersion, Slaking, Pilbara

INTRODUCTION

Many soils and sediments in the Pilbara region of north-western Australia are highly susceptible to erosion. Large quantities of construction materials are required as iron ore mining and the extensive railway lines used to transport ore to port continue to be developed in the region. Constructing embankments to survive the cyclonic wet season from material highly susceptible to erosion, is a major challenge. Simply avoiding the use of highly erodible materials is often considered to be too high a cost as alternatives are scarce.

Highly erodible materials encountered in the Pilbara include some bedrock shales, dispersive alluvial silts and sands and slaking clays and mudstones. Dispersive materials can erode internally by the formation of pipes or tunnels. Piping erosion can be difficult to detect and can cause severe damage to embankments before being detected. The effect of erosion can be controlled by appropriate embankment design, construction and maintenance. Erosion controls include sacrificial batters, surface protection, encapsulation and stabilisation.

For many mining projects achieving short-term construction deadlines is a high priority and adding

erosion control measures and maintenance after construction is often preferred. Predicting the time by which erosion control needs to be installed or rehabilitated should be a part of the embankment design process. Material selection has direct implications for the on-going asset management of embankment structures. Field observations and laboratory tests show that the coastal and fluvial sediments, dominated by the silty 'Pindan' sand, contain dispersive clays, which are prone to erosion even where clay content and sodicity is low.

Conventional lime stabilisation would be impeded by the alkaline condition of the soil. In contrast, tests show gypsum can achieve 0% Exchangeable Sodium Percentage (ESP) with applications less than 100 grams per ton of soil. The use of gypsum in embankment stabilisation is novel and requires further investigation. In agricultural applications gypsum provides a permanent control on dispersion by the replacement of sodium and magnesium with calcium and also has a temporary 'electrolyte effect' which may last from two to five years depending on water movement. The 'electrolyte effect' is temporary which is not normally acceptable in civil engineering projects. However, the very low initial ESP of these materials indicates permanent stabilisation will be achieved by additions of even

minimal quantities of gypsum. The dynamic nature of mining infrastructure projects means that gaining an additional life prior to rehabilitation works can represent a significant financial incentive.

The Pilbara region is undergoing rapid expansion of railways and other transport infrastructure to link the inland mines with ports to the north. The Economic Regulation Authority [1], the independent economic regulator for Western Australia, has factored in a 100 year life when estimating the asset value of for railway earthworks, including some in the Pilbara. Meanwhile, construction is occurring at record rates with an emphasis on low cost construction. From an asset management viewpoint, there is inevitably a trade-off between up-front construction costs and on-going maintenance costs which should be made explicit during the design process [2].

A detailed understanding of soil behaviour is fundamental to predicting the durability of embankments constructed from soils and sediments of the Pilbara region.

MATERIAL TYPES

The geology of the Pilbara region comprises bedrock of banded iron formation (BIF), consisting of alternating layers of chert, siltstone, mudstone and haematite in varying proportions, shale (referring generally to interbedded fine sandstones, laminated siltstones and mudstones), dolomite, and thick sequences of basic and acidic igneous rocks. According to a regional study, formations in the Pilbara prone to erosion include the Weeli Wolli Dolerite, Mt McRae Shale, Mt Sylvia Formation shales, Bee Gorge Member shales, and various other granites and basalts [3]. The implications of the erodible nature of these materials on borrow pit stability has been investigated [4].

Materials overlying bedrock include alluvial gravels, sands, silts and clays in fans, channels or on flood plains. Colluvial and taluvial sands, gravels and boulders occur on slopes. In the northwest part of Western Australia, scree gravel slopes comprised of materials useful for construction purposes can be expected near outcrops of chert, quartzite and banded ironstone, whereas, deposits of gravel on slopes over dolerite, basalt and other dark igneous rock should be treated with caution because of highly active (montmorillonitic) clays which, they state, almost always occur in the gravel fines or overburden [5]. Weathering profiles developed on bedrock and unconsolidated sediments can be clay-rich or have siliceous or ferruginous duricrusts.

According to the Department of Main Roads of Western Australia [5], well graded sand with small amounts of clay has been extensively used as basecourse in the northwest of the State. The red coloured sands are often referred to as “pindan” and

the yellow coloured sands are sometimes called “wodgil”.

Investigations for the Broome Airport [6] described the pindan sand as a collapsible silty-sand or clayey-sand soil, typically red in colour. Pindan sand is usually considered deleterious, but may display a self-cementation property upon dry-back during construction. The substantial strength gain upon drying, which is lost upon re-wetting, was thought to be due to the bridging effect of clay in the pindan sand. Previous work also attributed the effect to iron oxide, and further evidence from the laboratory testing has suggested that the bridges also form from Fe-kaolinite which contains both iron and aluminium (hydr)oxides. Suction testing suggests that the strength gain of the pindan upon dry-back is not just due to the cementing action of the bridges, but is also due to increased suction from the changed void geometry after the bridges have formed.

A review of approximately 50 laboratory tests of pindan sand material from south of Port Hedland for this study found that gradings were consistent but Atterberg limits were variable with most samples exceeding the recommended value (Table 1).

EMBANKMENT CONSTRUCTION IN THE PILBARA

A review of the construction of railway embankments in the Pilbara [3], described embankments up to 45 m high constructed of rockfill typically compacted in lifts of 750–1000 mm thickness with about 10% by weight of water added during placement. The design slopes of these high rockfill embankments are typically based on precedent with angles of 1.5 horizontal to 1 vertical, that is, 34°. A settlement value of 1% for the embankment height has been considered appropriate and is allowed for by cambering and by increasing the crest width so that an increased thickness of ballast can be applied to compensate for long-term settlement [3].

When durable and non-durable (slaking) rocks in embankments are subjected to compressive contact forces in the presence of water, the non-durable rock fragments are converted to soil that moves into the space between the durable rock fragments causing the settlement of the embankment [7]. Their study calculated the amount of settlement experienced by a mixture of non-durable shale with durable rock fragments subjected to embankment loads. The amount of settlement varied with the percentage by weight of the shale in the mixtures. The greatest settlements were recorded in 100% shale.

It has been observed that shortfalls in suitable borrow material commonly occur in railway construction projects in the Pilbara [3]. This situation is due to variations in overburden depth, incursions of unsuitable materials and environmental

constraints such as a need to keep borrow pits shallow to allow drainage and prevent water ponding.

Table 1: Test results reviewed for this study (approximately 50) relative to published pindan sand recommended interim criteria for use as a sub-base or selected subgrade in a semi-arid or arid climate [6].

Test	Criteria	Proportion of samples meeting criteria
Sub-base DCP-CBR after dry-back	≥ 40	59%
Select subgrade DCP-CBR after dry-back	≥ 20	74%
Sub-base Compaction density (Modified MDD)	95%	Not tested
Select subgrade Compaction density (Modified MDD)	93%	Not tested
Grading %passing 425 μ m sieve	30-100	98%
Grading %passing 75 μ m sieve	15? – 40 ⁽¹⁾	92%
PI x %passing 75 μ m sieve	> 150	87%
Liquid limit %	≤ 25	51%
Plasticity index %	4-12	32%
MDD modified t/m ³	≥ 2.0	Not tested
OMC %	5-10	Not tested
Al ₂ O ₃ + Fe ₂ O ₃ %	>8	Not tested

1. The lower limit is not known. Some of the better performing pindan sand had %passing 75 μ m sieve >25, and this may be a guide for sub-base quality. However it is suggested that the characterisation of suitable pindan should be done by strength testing or the use of PI x %passing 75 μ m sieve rather than grading alone [6].

EROSION OF EMBANKMENTS

Appropriate material selection and compaction is intended to protect embankments from scouring erosion from the wash of surface water during heavy rainfall. Armouring around bridge abutments and culverts is typically installed to protect embankments from sheet flow and flooding.

Erosional processes which can be more difficult to control are those which occur by internal erosion of fine particles by water infiltrating through the embankment. Evidence of this type of erosion is

often concealed until the collapse of pipes or tunnels which have formed below the surface.

Figure 1A shows an embankment constructed from gravelly soil with deep surface scouring. Bridges of soil are present over some of the scours indicating that erosion is, at least in part, a sub-surface process. The scouring is concentrated in a band approximately 1.5 m above the base of the embankment suggesting that either the material type or the construction method at that level was the cause of the erosion.

Figure 1B shows an embankment constructed of silty sands with narrow surface scours. Local erosion of the embankment toe by surface water has revealed that open channels of piping erosion 250 mm across had formed within the embankment.

Embankment slope design should not only take into account stability against slumping but also the role that the slope angle plays in controlling erosion. Slopes of 1.5 horizontal to 1 vertical (34°) may be too steep for embankments constructed of non-cohesive silty sands as this angle can be expected to be close to the friction angle of such sands.

The role of vegetation in embankment stabilisation has been considered elsewhere [8] but will not be considered here due to the climatic limitations on vegetation growth in the Pilbara region.

SACRIFICIAL BATTERS

A commonly applied approach to the use of highly erodible materials is to add additional mass to embankments to delay the impact of erosion on the critical part of the embankment. The additional mass may be in the form of flatter batters or wider crests. Ideally, this approach should incorporate an estimated erosion rate and a predicted lifetime at which rehabilitation is expected to be required. There should also be survey-based monitoring of the actual erosion losses so that predicted performance can be validated. The occurrence of piping erosion, in particular, can occur without equivalent surface scouring being visible.

Figure 2A shows an eroding embankment being managed by the construction of a buttress embankment constructed to approximately half the height of the existing embankment. The width of the buttress is determined by the need to accommodate construction equipment and greatly exceeds the width necessary to provide erosion control. However, the same construction material is being used and the buttress should be considered sacrificial as it is expected to develop similar erosional problems.

SURFACE PROTECTION

Surface protection can be applied at the time of construction or later as rehabilitation. Figure 2B

shows the application of geotextile with a physical and ultraviolet barrier of rock rip-rap. In this case, the surface protection is a rehabilitation measure not anticipated in the original project. Figure 3 shows an example drawing of such surface protection works.

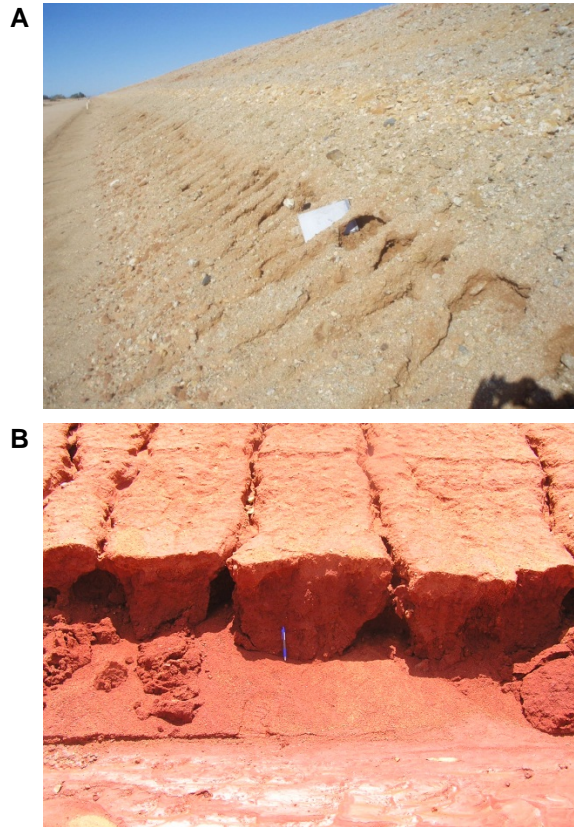


Figure 1. Piping-type erosion on embankments in the Pilbara. A) Concentration of piping erosion at a horizon within the embankment constructed of weathered granite. An A4 size folder shows the scale and highlights the presence of soil bridges in the deeply eroded part of the embankment. B) Fine surface runnels approximately 300 mm apart overlie erosion pipes in an embankment constructed of alluvial sands.

Figure 2C shows surface protection which has been applied in a more *ad hoc* manner by dozing of blasting spoil against eroding batters. Figure 2D shows that in the absence of geotextile or where the applied materials are uniformly coarse, fine soil in the embankment readily washes through this type of protection.

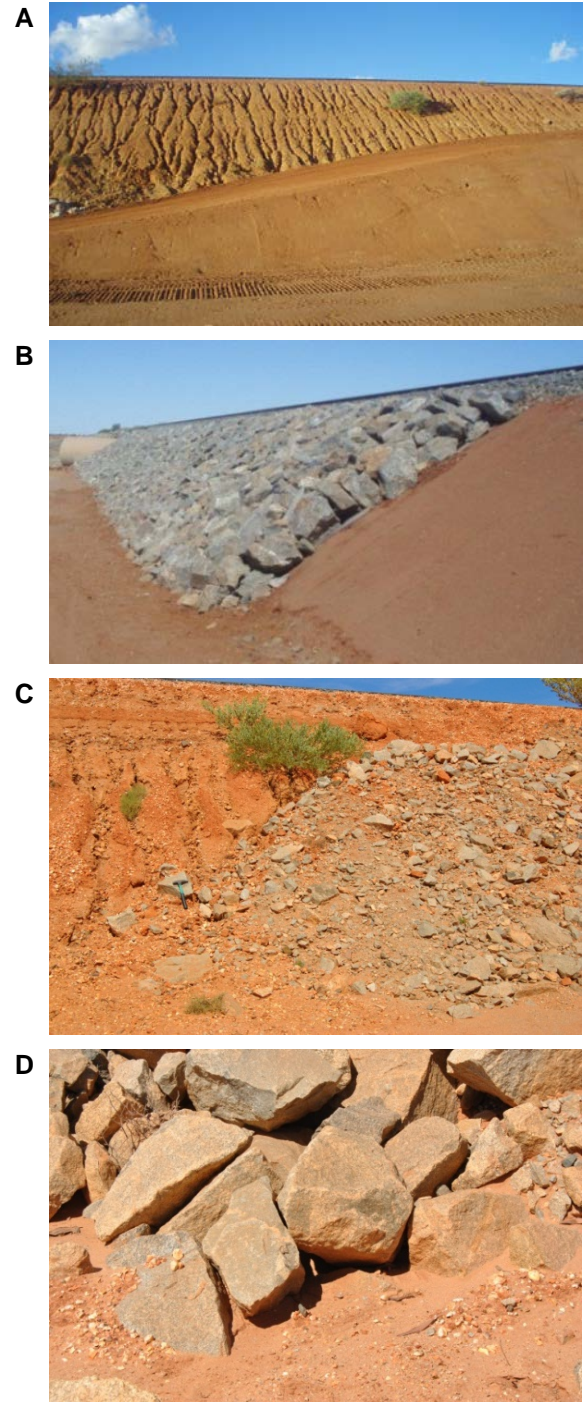


Figure 2. Post-construction rehabilitation of eroded embankments. A) Extending the width of the earth embankment to control embankment erosion. B) Placement of geotextile and rip-rap. C) Excess blast spoil dozed against embankment face to control embankment erosion. D) Fines appear to readily migrate through the improvised rip-rap shown in photograph C.

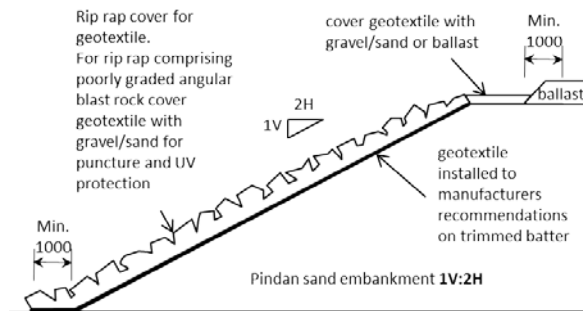


Figure 3. Example detail of recommended geotextile and rip rap protection on erodible embankments.

ENCAPSULATION

In a review of engineering geology for railway construction in the Pilbara [3], it was recommended that weathered shale or dolerite bedrock which can be prone to erosion should be encapsulated by 2 m of non-erodible soil. Encapsulation introduces the potential problem of differential settlement across embankments and requires significant material investigations and trials to be conducted.

STABILISATION

Stabilisation of low plasticity soils with agents such as lime and cement is well documented [9]. Soil stabilisation has been used in the Pilbara on various projects. For example, the stabilisation of highly reactive clay soil known as gilgai soil for the Karratha to Tom Price road [10]. In that study, hydrated lime and a combination of lime and cement were found to have a significant effect in improvement of California Bearing Ratio, unconfined compressive strength and shrink and swell characteristics of the reactive subgrade material.

A case of study ground improvement was undertaken at the stockyard berms of a large iron ore handling facility located in the Pilbara region [11]. The stabilisation involved addition of 3% cement to the berm materials carried out in situ using a Bomag stabiliser machine. Plate load tests were undertaken to assess degree of ground improvement of the clayey gravels. Cement not only provides physical strengthening of a soil but also contributes calcium to the chemical balance in the embankment which can exchange for sodium on clay and thereby influence erodibility of dispersive soils. The role of cement as a chemical stabiliser requires further investigation.

Tests conducted at the Southern Cross GeoScience laboratory have shown that some of the silty pindan sands of the Pilbara contain dispersive clays. The tests indicated that this soil must be managed carefully to avoid structural problems such as

crusting and erosion. These findings indicate that the soils are likely to be prone to dispersive erosion even if their clay content and sodicity are low. Stabilisation of embankment soils with mineral additives may provide significant improvements in erosion susceptibility. Conventional lime stabilisation can be impeded by the alkaline condition of the soil which inhibit the release of calcium from the lime. Alternatively, gypsum releases calcium more readily in alkaline conditions. Gypsum is typically only used to control dispersion of soil in agricultural practice due to the anticipated short-term effect [12]-[15], however, the use of gypsum in embankment construction has been proposed [16].

Tests at Southern Cross Geosciences on dispersive soils from the Pilbara found that an Exchangeable Sodium Percentage of near 0% could be achievable with extremely low applications of less than 100 grams of gypsum per ton of soil. The use of gypsum in embankment stabilisation is novel and requires further investigation. In agricultural applications gypsum provides a permanent control on clay dispersion by the gradual exchange on the clay of the two 'dispersion causing' cations sodium and magnesium, with the more stable calcium cation derived from gypsum dissolution. In addition, gypsum provides a fast acting, but temporary, control on dispersion via the 'electrolyte effect'. The electrolyte effect is due to the flocculating effect of the higher salinity in water caused by gypsum dissolution and may last from two to five years depending on water movement. The electrolyte effect, being temporary, is not normally acceptable in civil engineering projects, but this effect serves to provide effective control during the period of cation exchange that leads to permanent dispersion control. Of course, the dynamic nature of mining infrastructure projects means that gaining even an additional 2-5 years of life prior to rehabilitation works can represent a very significant financial incentive.

CONCLUSIONS

The use of highly erodible material to construct embankments is generally discouraged so that embankments are of high quality and longevity. However, the demand for short construction times means that the most abundant materials at hand will often be used in construction. Consequently, some form of erosion control will be required during or soon after construction. Erosion control may be in the form of surface protection, encapsulation or stabilisation. Surface protection can be conducted as part of the original construction or as later rehabilitation. Encapsulation requires good quality material to be available or stabilisation of material for the outer part of embankments. Stabilisation has

been applied on some previous projects in the region and further investigations are required.

Table 1: Summary of erosion controls for embankment construction

Control	During construction	Rehabilitation
Sacrificial flanks	Yes	Possible
Encapsulation	Yes	Possible
Stabilisation	Yes	Possible
Surface Protection	Yes	Yes

Given the need for many projects to achieve short-term deadlines for construction, it is likely that a significant amount of highly erodible materials will continue to be used in embankment construction. Erosion control and/or embankment rehabilitation will continue to be an integral part of infrastructure management in the Pilbara region.

ACKNOWLEDGEMENTS

Discussions with colleagues at Coffey geotechnical consultants were much appreciated.

REFERENCES

- [1] www.erawa.com.au/ accessed December 2011.
- [2] Sloan, A, Garland, R, & Lloyd, J, "Towards an asset management system for railway embankments and cuttings", Proceedings of the Railway Infrastructure Conference, Railway Engineering, London, Engineering Technics Press. 2000, pp. 9.
- [3] Baynes, FJ, Fookes, PG, & Kennedy, JF, "The total engineering geology approach applied to railways in the Pilbara" Western Australia Bull Eng Geol Environ 64, 2005, 67-94.
- [4] Smith, JV & Sullivan, LA, "Long-Term Environmental Stability of Borrow Pits in Highly Erodible Soils in the Pilbara" International Conference on Ground Improvement and Ground Control, Wollongong, NSW. 2012, pp. 1729-1734.
- [5] Butkus, F, "Gravel Search Manual" Pavements Engineering Report No. 2001-6M, Main Roads Western Australia, 2003, pp. 104.
- [6] Emery, S.J, Masterson, S, & Caplehorn, MW, "Sand-clay Pindan material in pavements as a structural layer" In Proceedings 21st Australian Road Research Board Conference, Cairns, 2003, 15pp.
- [7] Vallejo LE, & Pappas D, Effect of Nondurable Material on Settlement of Embankments. Transportation Research Record, 2170, 2010, 84-89.
- [8] Indraratna, B, Rujikiatkamjorn, C, Vinod, J, Khabbaz, H, "A review of ballast characteristics, geosynthetics, confining pressures and native vegetation in rail track stabilisation (Technical report)". Transport Engineering in Australia. 12.1, 2009, p25.
- [9] Szymkiewicz, F, Guimond-Barrett, A, Le Kouby, A, Reiffsteck, P & Fanelli S "Strength and Aging of Cement Treated Low Plastic Soils" Int. J. of GEOMATE, Vol. 4, No. 1, 2013, pp. 490-494.
- [10] Cocks, G, Clayton, R, Hu, Y Han, G, & Chakrabarti, S "Treatment of Reactive Soil Subgrade for Pavement Construction in Western Australia" 24th ARRB Conference – Building on 50 years of road and transport research, Melbourne, Australia, 2010.
- [11] Chakrabarti, S, Tabucanon, J, "Improvement of iron ore stockyard berms using cementitious stabilization" Australian Geomechanics 45, 2010, 53-64.
- [12] Sullivan, LA, & Fosbery, G, "Gypsum improves soil stability" *Farmnote* 32/85 Western Australian Department of Agriculture, 1984.
- [13] Moore, G, (Editor) "Soil Guide: A Handbook for Understanding and Managing Agricultural Soils" Agriculture Western Australia Bull. 4343, 2001.
- [14] Davies S, & Lacey, A, Identifying Dispersive Soils, *Farmnote* 386. Western Australian Department of Agriculture and Food, 2009.
- [15] Davies S, & Lacey, A, "Managing Dispersive Soils" *Farmnote* 387. Western Australian Department of Agriculture and Food, 2010.
- [16] Biggs AJW, & Mahony KM, "Is Soil Science Relevant To Road Infrastructure?" Conserving Soil and Water for Society: Sharing Solutions 13th International Soil Conservation Organisation Conference – Brisbane, July 2004.

Authors Index Volume 3(2)

A. Baouch	688	K. Hamdaoui	688
A. Beck	642	K.E. Chua	631
A. H. M. Zahirul Alam	664	Kazuhiro Oda	592
A. K. Alzo'ubi	658	Kazuhito Murakami	711
Achmad Fauzi	637	Keiko Okada	604
Ahmad Safuan A Rashid	625	L.A. Sullivan	728
Aniza Ibrahim	575	Loni Allafouza Oumar	717
Annan Zhou	652	M. I. Ibrahimy	664, 685
Atefeh Asoudeh	608	Mansour Al humimidi	717
Behnam Fatahi	700	Masyhur Irsyam	637
C.Y. Tan	631	Michio Gomyo	711
D. Gallagher	642	Mohamed M. Shahin	667
Erwin Oh	608	Mosleh Al Shamrani	717
F. Anwar	685	Muawia Dafalla	717
Fengzhi DAI	604	Muhammad Addifa Yulman	637
Greg Hackney	580	Muhammad Mukhlisin	575
H.B. Ng	642	Mutaz, E.	717
H.M. Yim	631	Nozomu Hirose	604
Ha H. Bui	694	Othman Jaafar	575
Hadi Khabbaz	673	Peijun Guo	619
Hadi Khabbaz	700	Reza Afshar-mazandaran	673
Harry Poulos	580	S. Aissaoui	688
Helen Fairweather	586	S. M. A. Motakabber	664, 685
Hidenori Takada	706	S.H. Chew	631
Ivan Sandi Darma	646	S.Y. Kee	631
J.V. Smith	728	Saki Agatsuma	711
Ja Naw	631	Samuel J. Verghese	694
John Yeaman	586	Shohei Ikeda	646
Jonathan A Black	625	Shuhei Takegawa	592
Jose F. Muñoz	721	Stephen Buttlng	679
Joseph Dahmen	721	Surendra Bahadur Tamrakar	613
Junichi KOSEKI	598	T.K. Khoo	631

T.Y. Yap	631
Takafumi Sugiyama	646
Takeshi Kodaka	706
Thayalan Nall	580
Tomoyoshi Nishmura	598
Toshiyuki Mitachi	613
Usama Juniansyah Fauzi	637
Yang-Ping Yao	652
Ying Cui	706
Yoshimasa Amano	711
Z. Benadla	688

ISBN978-4-9905-9580-1
C3051 ¥5000E



定価 (本体5000+税)



- The “International Journal of GEOMATE” is a Scientific Journal the GEOMATE International Society that encompasses a broad area in Geotechnique, Construction Materials and Environment.
- The key objective of this journal is to promote interdisciplinary research from various regions of the globe.
- The editorial board of the journal is comprised of extensively qualified researchers, academicians, scientists from Japan and other countries of the world.
- It is peer-reviewed journal that is published quarterly. All articles published in this journal are available on line.
- For more details, please visit:
<http://www.gi-j.com/>

VOLUME 4
Number 1 & 2
March-June 2013

ISSN: 2186-2982 (Print)
ISSN: 2186-2990 (Online)
Serial 7 & 8

International Journal of GEOMATE

**Geotechnique, Construction
Materials and Environment**



Tsu, Japan

<http://www.gi-j.com/>
geomate@gi-j.com

THE GEOMATE INTERNATIONAL SOCIETY

GEOMATE 2014

**Fourth International Conference on
Geotechnique, Construction Materials & Environment**

19-21 November 2014

University of Southern Queensland, Springfield Campus, Brisbane, Australia

Invitation to participate